University of Glasgow

Riggs, Christopher J. (2025) *A game of rISC – strategic molecular design for high efficiency OLEDs.* PhD thesis.

https://theses.gla.ac.uk/84923/

Copyright and moral rights for this work are retained by the author

A copy can be downloaded for personal non-commercial research or study, without prior permission or charge

This work cannot be reproduced or quoted extensively from without first obtaining permission from the author

The content must not be changed in any way or sold commercially in any format or medium without the formal permission of the author

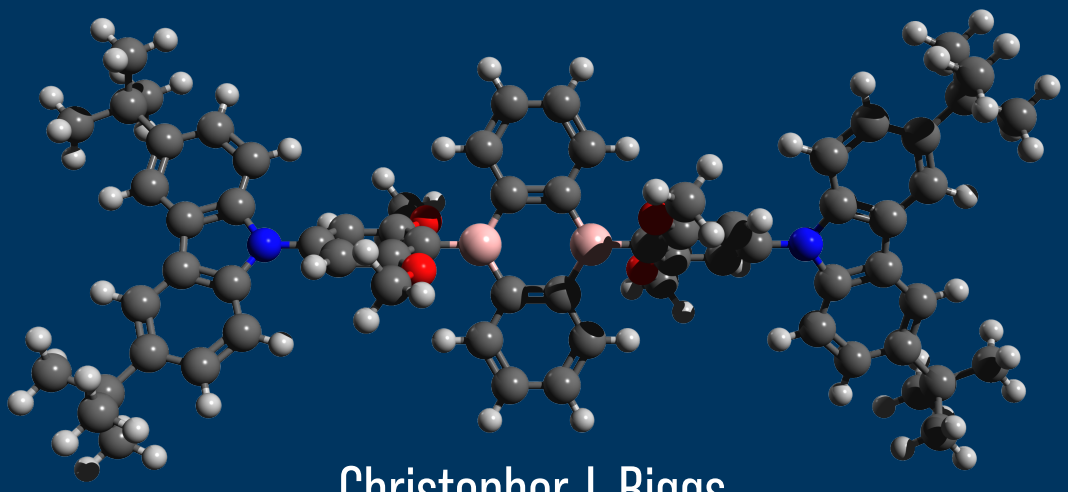
When referring to this work, full bibliographic details including the author, title, awarding institution and date of the thesis must be given

Enlighten: Theses
https://theses.gla.ac.uk/
research-enlighten@glasgow.ac.uk

University of Glasgow

A Game of rISC

Strategic Molecular Design for High Efficiency OLEDs



Christopher J. Riggs

Submitted in fulfilment of the requirements for the degree of
Doctor of Philosophy in Chemistry

School of Chemistry
College of Science and Engineering
University of Glasgow

October 2024

A Game of rISC – *Strategic Molecular Design for High Efficiency OLEDs*

Abstract

As society becomes ever more concerned with energy efficiency, the performance of light emitting devices must improve significantly. Organic light emitting diodes (OLEDs) are now a mainstream display technology. Their high brightness and contrast, excellent colour tunability, ultra-fast refresh rates and the ability to be prepared in seemingly limitless form factors, makes them a highly attractive replacement for traditional display methods. Their flexibility makes them attractive to both medical applications and alternative lighting technology as well, and the fact that they can be fabricated from entirely organic materials allows them to be fully biodegradable and recyclable.

Unfortunately, they still suffer from roll-off effects and degradation through prolonged use, particularly for emitter materials utilising higher energy transitions, such as for blue pixels. As such, development of novel deep blue emitter molecules is vital for the more widespread adoption of this technology.

This thesis explores the synthesis and characterisation of novel, entirely organic, emitter molecules for OLED application. A broad review of the current literature of OLED materials is presented, followed by four synthetic themes.

Chapter 1 provides the reader with a history of light emitting devices and organic electronics, before summarising the basic requirements of, and fabrication of OLEDs.

Chapter 2 delves into the physics of semiconductors and introduces the photophysics of excited states and fluorescent and phosphorescent processes. It goes on to summarise the types of photophysical processes observed in emissive organic molecules.

Chapter 3 explores how chemical structure influences TADF in organic molecules and examines the literature, highlighting key developments that have led to our current understanding about the rules governing the fine tuning of the rISC process in state-of-the-art emitter molecules.

Chapter 4 explores a family of simple boron-based D-A type molecules, their photophysics and chemical stability, which helped to inform the design of further compounds in this thesis.

Chapter 5 reports the successful synthesis and photophysical characterisation of a family of six boron-based emitter molecules with varying acceptors and π-bridge structures. The interesting potential for non-covalent interactions between oxygen and the empty p-orbitals of the boron atoms are explored, giving promising results with attractive properties.

Chapter 6 builds upon the non-covalent interactions of Chapter 5 to produce a highly emissive and efficient D-A-D type molecule with a diboron acceptor core. Whilst its stability is poor, it possesses record-breaking emission lifetimes for its colour and demonstrates the highly effective nature of non-covalent interactions in producing HOMO-LUMO decoupling in the excited state.

Chapter 7 takes the interesting, but understudied, dibenzocarbazole donor moiety explored in Chapter 4, and produces a large family of novel emissive molecules. Not only do they mostly possess TADF, but they also all exhibit striking thermochromism and mechanochromism thanks to the quasi-helical nature of the extended carbazole moiety.

All experimental procedures, UV-vis absorption coefficient calculations, NMR and mass spectroscopy data and crystallography data, are collated in the appendices.

Table of Contents

Abstract ..... *v*

Preface ..... *xvii*

Acknowledgements ..... *xix*

Author's Declaration ..... *xxii*

Definitions/Abbreviations ..... *xxiv*

Chapter 1 Introduction *29*

1.1 A brief history of lighting technology **32**

1.1.1 Pyroluminescent lighting 32

1.1.2 The electric lamp 36

1.2 What are organic electronics? **39**

1.2.1 An introduction 39

1.2.2 The advantages of organic electronics 39

1.3 What makes organic materials conductive? **41**

1.3.1 Polymers 42

1.3.2 Molecules 43

1.4 Types of devices **44**

1.4.1 OLEDs 44

1.4.2 OPVs 44

1.4.3 OFETs 46

1.4.4 Flexible electronics 47

1.5 General principles and structure of OLEDs **48**

1.6 Materials for OLEDs **52**

1.7 Progress of the industry **54**

1.7.1 OLED vs QLED and QD-OLED 55

1.8 Applications of OLEDs **58**

1.8.1 Display technology 58

1.8.2 Solid-state lighting 59

1.8.3 Medical applications of OLEDs 60

1.9 Evaluation of current LEDs and OLEDs **61**

1.10 Characterising OLEDs **62**

1.11 Making OLEDS **65**

1.11.1 Vacuum deposition 65

1.11.2 Solvent methods 66

1.12 Environmental and sustainability benefits of OLEDs **67**

1.13 Summary **68**

Chapter 2 Physics of luminescent materials *69*

2.1 What is light? **70**

2.2 Band theory **72**

2.3 Organic semiconductors **77**

2.4 Band theory in organic semiconductors 78

2.5 The physics of phosphorescence and fluorescence in organic molecules 84

2.5.1 Excited states 84
2.5.2 Electronic transitions and molecular spectra 89
2.5.3 HOMOs, LUMOs and states 92
2.5.4 Mobile excited quasiparticles - excitons 94
2.5.5 Dimers, excimers and exciplexes 94
2.5.6 Types of excitons 99

2.6 Excited state decay kinetics 100

2.6.1 Quantum yield 102

2.7 Quenching of fluorescent molecules 105

2.8 Triplet harvesting 110

2.9 The role of charge transfer states 118

2.10 The physics of charge transfer 118

2.10.1 Investigating the SOC mechanism 125
2.10.2 Charge transfer and additional donors 128
2.10.3 Solvatochromism and CT states 130

2.11 Förster and Dexter energy transfer 134

2.11.1 Trivial energy transfer 134
2.11.2 Forster resonance energy transfer (FRET) 136
2.11.3 Dexter energy transfer 138
2.11.4 Oxidative mechanism 142
2.11.5 Reductive mechanism 142

2.12 Efficiency roll-off 144

2.12.1 What is it? 144
2.12.2 The causes of efficiency roll-off 145
2.12.3 How to prevent roll-off 149

2.13 Summary 157

Chapter 3 Design of TADF molecules 159

3.1 General concepts 160

3.2 *Donor – acceptor* and *donor – acceptor – donor* 161

3.3 Isomerism 162

3.4 Π-bridging 163

3.5 Spiro compounds 167

3.5.1 General background 167
3.5.2 Varying substituent groups on spiro-compounds 170

3.6 TADF design methodology 171

3.7 Boron-based TADF 174

3.7.1 Why is boron suitable? 174
3.7.2 Boron moiety structural types 176

3.8 Carbazole based TADF 182

3.8.1 Structure of carbazole – why it is a donor? 182

3.9 Conformational effects 184

3.10 Non-covalent interactions 186

3.11 Modification to π-bridges 193

3.12 Broad emission profiles in TADF molecules 195

3.13 Aggregation induced emission 198

3.14 Summary 199

Chapter 4 An investigation into novel small molecule donor-acceptor-type TADF molecules 200

4.1 Introduction 201

4.2 Results and Discussion 204

4.2.1 Synthesis 204
4.2.2 Computational chemistry 206
4.2.3 Crystal structures 210
4.2.4 Thermal properties 222
4.2.5 Optical and electrochemical properties 225
4.2.6 Molar absorption coefficient 231
4.2.7 Electrochemical analysis 232
4.2.8 Photoluminescence and UV-vis spectroscopy 238
4.2.9 Thermochromism in MBCz-DMB 243
4.2.10 Phosphorescence 244
4.2.11 Solvatochromism 247
4.2.12 Lifetime measurements 252
4.2.13 CCD time-resolved measurements 257
4.2.14 Hydrolysis of the B-N bond in DBCz-DMB (3) 261
4.2.15 Aggregation induced emission of IMSB-DMB 267

4.3 Conclusions 271

Chapter 5 Novel carbazole - boron molecules and the impact of methoxy groups on non-covalent interactions 273

5.1 Introduction 274

5.2 Experimental 279

5.2.1 General 279
5.2.2 Synthesis 279

5.3 Results and discussion 285

5.3.1 Thermal properties 285
5.3.2 Optical and electrochemical properties 291
5.3.3 Solid-state photoluminescence properties 297
5.3.4 Electrochemical properties 300
5.3.5 Molar absorption coefficient 303
5.3.6 Solvatochromism 304
5.3.7 Lippert-Mataga analysis for solvatochromism 306
5.3.8 TCSPC Lifetime measurements 310
5.3.9 CCD Time-resolved measurements 314
5.3.10 Computational chemistry 326
5.3.11 Crystal structures 331
5.3.12 Crystal packing 338

5.3.13 Intramolecular phenoxy interactions....344
5.3.14 Chemical stability....348

5.4 tBu-DMeOP-Cz-OBA (11)....350

5.5 Conclusions....352

Chapter 6 Rod-like donor-acceptor-donor π-bridged boron-based TADF molecules exploiting non-covalent interactions to improve the rate of rISC....354

6.1 Introduction....355

6.2 Modifications....357

6.3 Recent advancements with CzDBA-type molecules....358

6.4 Results....364
6.4.1 Synthesis....364
6.4.2 Thermal properties....373
6.4.3 Electrochemical properties....374
6.4.4 Molar absorption coefficient....376
6.4.5 Photophysical properties....376
6.4.6 Lifetimes....382
6.4.7 Solvatochromism....388
6.4.8 CCD time-resolved measurements$^{\delta}$....394
6.4.9 Fluorescence and phosphorescence$^{\delta}$....405
6.4.10 Chemical stability....411

6.5 Conclusions....415

Chapter 7 An investigation into novel application of dibenzocarbazole as a quasi-helical donor for D-A type TADF molecules....416

7.1 Introduction....417

7.2 Experimental....420
7.2.1 Synthesis....420

7.3 Results and discussion....422
7.3.1 Thermal properties....422
7.3.2 Optical and electrochemical properties....430
7.3.3 Solid-state photophysics....435
7.3.4 TCSPC Lifetime measurements....439
7.3.5 CCD time-resolved measurements....443
7.3.6 Room temperature phosphorescence of 4MBCzIPN (20)....448
7.3.7 Electrochemical properties....450
7.3.8 Molar absorption coefficients....452
7.3.9 Solvatochromism....454
7.3.10 Investigating CT Peaks....460
7.3.11 Computational chemistry....461
7.3.12 Crystal structures....468
7.3.13 Aggregation-induced emission of 2DBCzPN (18)....477
7.3.14 Aggregation-induced emission of 4DBCzIPN (19) and 4MBCzIPN (20)....478

7.4 Thermochromism....482
7.4.1 Powder X-ray diffraction measurements....500

7.5 Comparison to single crystal XRD....509

7.6 Mechanochromism 511
7.6.1 Comparison of XRD data 526
7.7 Variable temperature NMR 530
7.8 Comparison to literature compounds 532
7.8.1 On thermal properties 532
7.8.2 On photophysical and electrochemical properties 534
7.9 Conclusions 538
Chapter 8 Conclusions and future work 540
Chapter 9 Appendices 545
Appendix 1 – Molar absorption coefficients 546
9.1 Chapter 4 546
9.1.1 IMDB (1) 546
9.1.2 MBCz-DMB (2) 547
9.1.3 DBCz-DMB (3) 548
9.1.4 DPhCz-DMB (4) 549
9.2 Chapter 5 550
9.2.1 tBu-DMP-Cz-OBA (10) 550
9.2.2 tBu-DMP-Cz-DMB (12) 551
9.2.3 tBu-DMeOP-Cz-DMB (13) 552
9.2.4 tBu-MPhOP-Cz-DMB (14) 553
9.2.5 tBu-DPhOP-Cz-DMB (15) 554
9.3 Chapter 6 555
9.3.1 tBu-MeOCzDBA (17) 555
9.4 Chapter 7 556
9.4.1 2DBCzPN (18) 556
9.4.2 4DBCzIPN (19) 557
9.4.3 4MBCzIPN (20) 558
9.4.4 DBCz-PS (21) 559
9.4.5 DBCz-BZPN (22) 560
Appendix 2 – Experimental Procedures 562
9.5 General experimental details 562
9.6 Analytical Characterisation 562
9.7 Thermal analysis 562
9.8 Electrochemical characterisation 563
9.9 X-ray crystallography 563
9.10 Molecular structures 564
9.11 Computational Calculations 564
9.12 Photophysical properties 564
9.13 Synthesis Procedures 566
9.13.1 Chapter 4 566
9.13.2 Chapter 5 574
9.13.3 Chapter 6 587

9.13.4 Chapter 7 596

Appendix 3 NMR and mass spectrometry 605

9.14 Chapter 4 605

9.14.1 IMSB-DMB (1) 605
9.14.2 MBCz-DMB (2) 609
9.14.3 DBCz-DMB (3) 613
9.14.4 DPhCz-DMB (4) 617

9.15 Chapter 5 621

9.15.1 9-(4-bromo-3,5-dimethylphenyl)-9H-3,6-di-tert-butylcarbazole (5.3) 621
9.15.2 4-bromo-3,5-dimethoxyaniline (5.5) 625
9.15.3 2-bromo-5-iodo-1,3-dimethoxybenzene (5.6) 628
9.15.4 9-(4-bromo-3,5-dimethoxyphenyl)-9H-carbazole (5.8) 632
9.15.5 9-(1,3-dimethoxyphenyl)-9H-3,6-di-tert-butyl-carbazole (5.10) 636
9.15.6 Bis-(2-trimethylsilylphenyl)ether (5.12) 640
9.15.7 10-bromo-10H-dibenzo[b,e][1,4]oxaborinine (5.13) 641
9.15.8 tBu-DMP-Cz-OBA (10) 642
9.15.9 tBu-DMP-Cz-DMB (12) 646
9.15.10 tBu-DMeOP-Cz-DMB (13) 650

9.16 Chapter 6 653

9.16.1 9-(4-bromo-3,5-dimethylphenyl)-9H-carbazole (6.5) 653
9.16.2 1,2-bis(trimethylsilyl)benzene (6.2) 655
9.16.3 Dibromodiboraanthracene (DBDBA – 6.4) 657
9.16.4 CzDBA (16) 659
9.16.5 tBu-MeOCzDBA (17) 662

9.17 Chapter 7 666

9.17.1 2DBCzPN (18) 666
9.17.2 4DBCzIPN (19) 669
9.17.3 4MBCzIPN (20) 673
9.17.4 DBCz-PS (21) 677
9.17.5 DBCz-BZPN (22) 680

Appendix 4 – Crystallography data 684

9.18 Chapter 4 684

9.18.1 IMDB (1) 684
9.18.2 DBCz-DMB (3) 689
9.18.3 DPhCz-DMB (4) 694

9.19 Chapter 5 702

9.19.1 tBu-DMP-Cz-OBA (10) 702
9.19.2 tBu-DMP-Cz-DMB (12) 710
9.19.3 tBu-DMeOP-Cz-DMB (13) 715
9.19.4 tBu-MPhOP-Cz-DMB (14) 720
9.19.5 tBu-DPhOP-Cz-DMB (15) 726

9.20 Chapter 6 733

9.20.1 tBu-MeOCzDBA (17) 733

9.21 Chapter 7 734

9.21.1 2DBCzPN (18) 734
9.21.2 4DBCzIPN (19) 739

Appendix 5 List of conferences 747

9.22 Poster 1 748

9.23 Poster 2 749

9.24 Poster 3 750

Appendix 6 List of collaborative visits..... 751

Bibliography 753

"Ein Chemiker, der kein Physiker ist, ist gar nichts"

[*A chemist who is not also a physicist, is nothing at all*]

Robert W. Bunsen (1811 - 1899)

"*No plan survives first contact with implementation*"

Adam Savage

"*Never say 'no' to adventures. Always say 'yes,' otherwise you'll lead a very dull life.*"

Ian Fleming

Preface

Assembling a thesis is very much like a game of Rummy. One must produce a hand, or meld, composed of either a *set* (cards of the same value, but different suit) or a *run* (same suit, but consecutive cards in order). In many ways, Chapter 4 represents a *set* of molecules – all with completely different donors, (with iminostilbene representing a *piques*, monobenzocarbazole the *carreaux*, dibenzocarbazole the *cœurs* and finally diphenylcarbazole the *trèfles*), but with the value determined by the acceptor they all have in common, dimesityl boron, the *Jack* of this deck of molecules. Chapter 5 on the other hand, would perhaps be better represented as a *run* – all the molecules in question have strikingly similar structures, analogous to being of the same *suit*, but are different enough so as to be unique. But perhaps this analogy falls apart, as one could argue that the OBA acceptor should be better represented by a *Queen*, with DBA in Chapter 6 being the *King*. I shall leave it up to the reader to decide the analogy for the remaining chapters, though possibly the suggestion of *52-card pickup* would perhaps be rather apt for Chapter 7, given the mess involved in some of the aqueous workups…

Acknowledgements

This PhD has been almost 5 years in the making! I would like to thank Professor Peter Skabara for giving me the opportunity to explore chemistry further than I ever would have dreamt possible. For giving me a chance to be a part of such a fantastic research group, and for the help and support you have given me over the course of this journey. I cannot begin to describe how grateful and fortunate I am to have had this opportunity.

I would also like to thank Dr. Joseph Cameron, to whom I am indebted. Your advice and assistance have been invaluable to me throughout my PhD. I'd like to thank you for your patience and support, and willingness to chat about even the wildest of synthetic concepts.

Thanks also to Dr. Andrea Pinto. Your help with the rISC project was greatly appreciated. I can only apologise for the awful synthetic route we stuck with for so long! You kept me sane for much of the boron project, and your arrival marked a turning point in our success.

I would also like to thank Dr. Lyuda Kanibolotsky and Dr. Oleks Kanibolotsky, who were always happy to provide assistance and advice during my projects. I would also like to thank the hard work of our technicians, Dr. Holly Yu, Dr. Valentin Fell and Dr. Joe Steel.

Thanks to all the Skabara Group members during my time in Glasgow for making it a truly wonderful working environment. You have all been superb friends and colleagues for the past five years.

Thanks also to Dr. Gordon Hedley and Dr. Nicola Fairburn for your advice and assistance with identifying the limitations of our fluorometer for the NIR emissions in Chapter 7.

Further thanks must go to the members of my fellow cohort, *The Skabara Four*: Michael Johnson, Peter Martin and Wendy Onabule. You three have been fantastic friends ever since I joined the group a few months later than yourselves. The three of you have helped me stay sane throughout my time here, and I wish you all the best with your theses too. Michael in particular, your humour in the lab sustained me throughout, and whilst part of me feels I should apologise for some of the teasing and nonsense, you gave as good as you got – after all, whomsoever sings Christmas carols at the top of his voice in the sweltering heat of July deserves no quarter! Also, thanks to Alasdair Dennis – I think only the pair of us could keep Michael in check!

Thanks must also go to Professor Andrew Monkman, Dr. Suman Kuila, Kamile Bareikaite and Dr. Andrew Danos for your help with the photophysical measurements in this thesis. Also, thanks to Professor Andrew Monkman and Professor Thomas Penfold for your stimulating discussions and advice for interpreting the results for our rISC molecules.

Additional thanks must go to Professor Sebastian Reineke, Dr. Sebastian Schellhammer and Dr. Heidi Thomas of the Lexos group at the Integrated Centre for Applied Physics and Photonic Materials at Technische Universität Dresden for hosting me and supporting my work during my secondment during the MEGA H2020 project.

I would like to give thanks to my family and friends who have had to put up with me spending many nights and weekends working. My Mum, Dad and brother (and dogs), your support and encouragement throughout this time (and indeed throughout my life) has been so valuable and appreciated. Nick, the time we spent unwinding together has helped more than you know.

I must also thank Fred, Sandy and Liana, to whom my decision to return to academia from a comfortable existence teaching must have seemed bamboozling. Your continued friendship and support are greatly appreciated. The walks and coffee post-lockdown were a most welcome distraction, Fred. Thanks must also go to Julie and Mikki. You helped me immensely, even if you didn't realise it.

I feel it important to also thank Dr. Hugh Ferrier and Mr Jimmy Maxwell. It was your lessons that inspired me to take my first steps down this path. Since 2003, chemistry has been by favourite subject, a lifelong passion ignited by the pair of you.

Finally, thank you to Lucy. Your kind support and patience has gotten me through this final year despite the challenges.

Author's Declaration

University of Glasgow

College of Science and Engineering

Statement of Originality to Accompany Thesis Submission

Name: Christopher J. Riggs

Registration Number: _____

I certify that the thesis presented here for examination for a PhD degree of the University of Glasgow is solely my own work other than where I have clearly indicated that it is the work of others (in which case the extent of any work carried out jointly by me and any other person is clearly identified in it) and that the thesis has not been edited by a third party beyond what is permitted by the University's PGR Code of Practice.

The copyright of this thesis rests with the author. No quotation from it is permitted without full acknowledgement.

I declare that the thesis does not include work forming part of a thesis presented successfully for another degree.

I declare that this thesis has been produced in accordance with the University of Glasgow's Code of Good Practice in Research.

I acknowledge that if any issues are raised regarding good research practice based on review of the thesis, the examination may be postponed pending the outcome of any investigation of the issues.

Signature: …….

Date: ……25 October 2024……..

Printed Name : Christopher J. Riggs

Definitions/Abbreviations

°C	Degrees Celsius
1 / 2 / 3D	1, 2 or 3-dimensional
^{1}CT	Singlet charge transfer state
^{3}CT	Triplet charge transfer state
^{3}LE	Locally excited triplet state
A	Ampere
Å	Ångström (10^{-10} m)
AMOLED	Active matrix organic light emitting diode
CBP	4,4′-Bis(N-carbazolyl)-1,1′-biphenyl
CCT	Correlated colour temperature
cd	Candela
CIE	Commission Internationale d'Eclairage
CT	Charge transfer
Cz	Carbazole
D	Debye
D-A	Donor-acceptor
D-A-D	Donor - acceptor - donor
D-π-A	Donor - π-bridge - acceptor
D-π-A-π-D	Donor - π-bridge - acceptor - π-bridge - donor
DBA	Diboraanthacene
DBCz	Dibenzocarbazole
DBDBA	Dibromodiboraanthracene
DCM	Dichloromethane / methylene chloride
DFT	Density Functional Theory
DMB	Dimesitylboron
DMeOP	Dimethoxyphenyl
DMF	N,N-Dimethylmethanamide
DMP	Dimethylphenyl
DMSO	Dimethyl sulfoxide
DPEPO	Bis[2-(diphenylphosphino)phenyl]ether oxide
DPhCz	Diphenylcarbazole
DPhOP	Diphenoxyphenyl
DSC	Differential scanning calorimetry
EBL	Electron blocking layer
EL	Electroluminescence
EML	Emitter layer
EQE	External quantum efficiency
Et_2O	Diethyl ether
ETL	Electron transport layer
EtOAc	Ethyl acetate
EtOH	Ethanol
eV	Electron volts

Fc	Ferrocene
Fc^+	Ferrocenium
FRET	Förster resonance energy transfer
FWHM	Full width at half maximum
HBL	Hole blocking layer
HOMO	Highest occupied molecular orbital
HTL	Hole transport layer
Hz	Hertz
I	Illuminance
IC	Internal conversion
iCCD	Intensified charge coupled device
ICT	Internal charge transfer
IMSB	Iminostilbene
IQE	Internal quantum efficiency
IR	Infrared
irr	Irreversible
ISC	Intersystem crossing
K	Kelvin
LE	Locally excited state
LED	Light emitting diode
lm	Lumen
LUMO	Lowest unoccupied molecular orbital
m	Meters
MBCz	Monobenzocarbazole
MCH	Methylcyclohexane
mCP	1,3-Di(9H-carbazol-9-yl)benzene
MeOH	Methanol
MPhOP	Monophenoxyphenyl
MS	Mass spectrometry
ms	Milliseconds
n	Non-bonding orbital
n-BuLi	n-butyl lithium
NBS	N-bromosuccinimide
NIR	Near infrared
nm	Nanometer
NMR	Nuclear magnetic resonance
NR	Non-radiative
ns	Nanosecond
OBA	10H-phenoxaborin
OFET	Organic field-effect transistor
OLED	Organic light emitting diode
OPV	Organic photovoltaic
OSC	Organic semiconductor
PEDOT:PSS	Poly(3,4-ethylenedioxythiophene) : polystyrene sulfonate
PHOLED	Phosphorescent organic light emitting diode
PL	Photoluminescence

PLQY	Photoluminescent quantum yield
ppm	Parts per millions
PVK	Polyvinylcarbazole
qr	Quasi-reversible
rISC	Reverse intersystem crossing
s	Seconds
S_0	Singlet ground state
S_1	First excited singlet state
S_n	N^{th} excited singlet state, where n = any positive integer, including 0 for the ground state
SOC	Spin-orbit coupling
T_1	First excited triplet state
TADF	Thermally activated delayed fluorescence
tBu	Tert-butyl
TGA	Thermal gravimetric analysis
THF	Tetrahydrofuran
TLC	Thin layer chromatography
TMEDA	N,N,N′,N′-Tetramethylethylenediamine
TMS	Trimethylsilane
TMS-Cl	Trimethylsilyl chloride
T_n	N^{th} excited triplet state, where n = any positive integer
Tol	Toluene
TTA	Triplet-triplet annihilation
UV	Ultraviolet
UV-vis	Ultraviolet - visible
V	Volt
µm	Micrometer
µs	Microsecond

Symbols

E_g	Energy gap. Unless otherwise stated, this refers to the HOMO-LUMO energy gap
E_{opt}	Optical energy gap
E_{ox}	Electrochemical oxidation potential
E_{red}	Electrochemical reduction potential
h	Planck's constant 6.62607015×10^{-34} J Hz^{-1}
k_{DF}	Rate of delayed fluorescence
k_F	Rate of fluorescence
k_{IC}	Rate of internal conversion
k_{ISC}	Rate of intersystem crossing
k_{nr}	Non-radiative rate constant
k_{Ph}	Rate of phosphorescence
k_r	Radiative rate constant
k_{rISC}	Rate of reverse intersystem crossing
γ	Charge balance factor
ΔE_{ST}	The energy gap between the first excited singlet and triplet states
η_{int}	IQE
η_{out}	Light outcoupling efficiency
Φ_{PL}	PLQY
χ_{ST}	Spin formation ratio

Greek Symbols

δ	Chemical shift
ε	Molar absorption coefficient
λ	Wavelength
λ_{max}	Wavelength at maximum absorption
λ_{PL}	Wavelength at peak emission
μ	Dipole moment
π	Pi-bonding orbital
π^*	Pi-antibonding orbital
σ	Sigma-bonding orbital
σ^*	Sigma-antibonding orbital
τ	Lifetime

Chapter 1 Introduction

Artificial lighting has been of fundamental importance throughout human history. The means by which illumination is achieved through the hours of darkness has changed from the experiences of our ancestors, but its advantages remain as relevant today. Despite the relatively recent advancement with universally accessible lighting sources, it is estimated that mankind has utilised artificial lighting for half a million years[1], from early man's use of fire until the late 1800s, where gas lighting was superseded by electrical lighting. In the twenty first century, light emitting devices are of fundamental importance, not just to domestic lighting, but also for illuminating displays in electronic devices.

Modern electronics is firmly based upon the silicon-based semiconductor. The principle of semi-conductivity can trace its roots back to the coinage of the term by Alessandro Volta "semicoibente" (literally 'semi-insulating')[2] and the work of Michael Faraday, who in 1833, established one of the key properties of semiconductors, namely the relationship of their resistance to temperature by measuring the conductivity of silver sulfide at different temperatures[3]. Semiconductor science languished in doldrums of mere curiosity for some time, before a practical application in the form of the invention of the cat's whisker transducer used in crystal radios[4]. Further advancements were largely empirical until the advent of quantum mechanics and the first physical explanation of semiconductivity by A.H. Wilson[5], which revolutionised semiconductor design and enabled the massive acceleration of this field throughout the twentieth century.

Whilst originally thought to be confined to inorganic materials, some organic compounds were found to display semiconducting behaviour too, even photoconductivity, such as in anthracene. Additionally, many organic materials were found to be suited to the emission of light; anthracene also being an example, as well as gonacrin, carbazole and brilliant acridine orange E [6].

Organic-based semiconductors possess many advantages over their inorganic counterparts, namely their flexibility in both design architecture and synthesis methods. If based solely upon organic materials, it is quite within the realms of conceivability that organic devices be much cheaper to produce and more sustainable, whilst also avoiding potentially toxic heavy metal components. OLED devices are beginning to make strong headway into everyday technology, from viewfinders on cameras[7], high end television screens[8], and even on mobile telephone displays[9]. Further development of their component materials through a greater

understanding of their photophysics and chemical synthesis is therefore vital for this field to continue to grow.

1.1 A brief history of lighting technology

Combustion-driven illumination, such as that found when burning wood or oil, is very inefficient, with the largest proportion of energy being released in the form of heat, rather than the desired form of light. They also suffer from the limitation of having a relative lack of colour control, as this is dictated by the energy gaps of electron transitions, which is specific to the material being burnt. Converting the emissions to a different colour requires the use of a pyroluminescent compound added to the flame, which would be costly as well as wasteful. Early electrical methods of lighting suffered a similar problem and would necessitate the use of a phosphor to control the colour, as in the mercury vapour lamp, where ultraviolet light is produced (which is of little use to humans as a direct lighting source). The process to produce the ultraviolet light is only 63% efficient[1], which in turn is used to excite electrons in a phosphor, emitting visible light, resulting in further energy loss. The visible light at the end of the overall process is only 28% efficient[1]!

Natural white light from the sun contains wavelengths between 380 and 780 nm[1], which is the visible spectrum, as well as containing ultraviolet and infrared radiation. A good lighting device should encompass this visible spectrum and as the human eye has evolved to be sensitive to this range, any wavelengths beyond this would be wasted energy.

1.1.1 Pyroluminescent lighting

For millennia, pyroluminescence (the emission of light when a compound is burnt – where ions and atoms are excited and electron transitions emit radiation) was used as the method of lighting, in the form of torches, braziers, *etc*. The burning of wood is thought to have been used for between 0.5 and 1.5 million years when *homo erectus* learnt to harness fire. Later, the fuel would have come from wood with oil, pitch, resin, or animal fat smeared into it[10]. Archaeological evidence suggests that at least 17,300 years ago (with some suggesting even 30,000 to 70,000 years ago), humans were using stone lamps, such as that found in the Lascaux caves in Montignac, France[11] which utilises a wick to draw up fuel for combustion and light emission, as well as those used for burning oil (see Figure 1-1).



Figure 1-1 The Lascaux lamp (left) - carved from stone, this would have contained burning oil for illumination. Image taken from Guarniri[11]. Middle and right show oil burning lamps from *circa* 400 – 200 B.C. held in the Weston Park Museum, Sheffield (images taken by myself).

In 1991, a Neolithic man (later named *Otzi*) was discovered, preserved in ice in a glacier in the Alps. Among his possessions were the materials required to produce a fire – flint and pyrite for ignition, as well as kindling in the form of fungus and burnt wood[10].

During the Roman period, candles made of wax (paraffin or beeswax) which melts in the heat to be drawn into the flame, were used for lighting homes[1]. These had the advantage of being easy to extinguish and relight at a later date and could be small and portable, perhaps allow for better lighting conditions at night thus enabling for increased scholarly output.

A scientific approach to advancing lighting technology was set off following the pioneering work in chemistry by Antoine Lavoisier, who's experiments in oxidation in 1774 established that oxygen was an element required in combustion reactions. This completed the principle of the 'fire triangle' – that fuel, heat and now oxygen are required to initiate combustion. Using this knowledge, Ami Agrand[1] developed an oil lamp design which maximised oxygen contact with the wick and produced a ten times increase in brightness (see Figure 1-2).

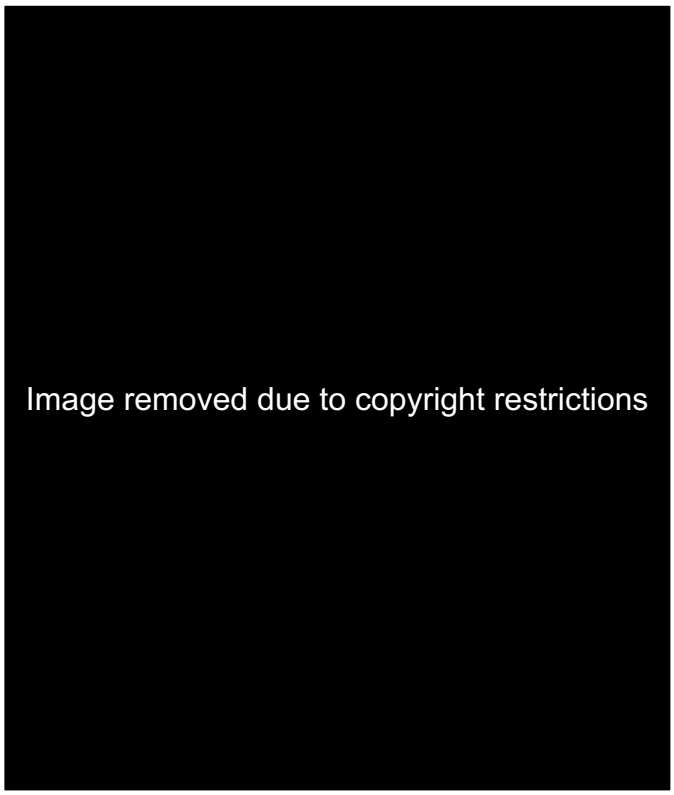


Figure 1-2 Diagram of the Argand lamp. Image from the Library of Congress archive[12].

Throughout the 1800s, gas lighting was used in big cities throughout Europe. This technology, invented initially by William Murdoch in 1798[13], was cheap and easy to incorporate into the buildings of the time, but has of course, numerous drawbacks: high flammability of the gas, carbon dioxide and carbon monoxide production during burning in enclosed spaces, accidental gas leaks, to name but a few, but it also resulted in numerous cases of gas asphyxiation[14] when left on after extinguishing or during leaking, and explosions[15].

The gas light contributed significantly to the acceleration of the industrial revolution, as it allowed businesses and industry to work through evenings and nights[16], dramatically increasing productivity.

Portable lighting had an advancement in this time too in the form of the Humphry Davy Lamp (Figure 1-3), providing safe combustion-based illumination for coal miners[17].

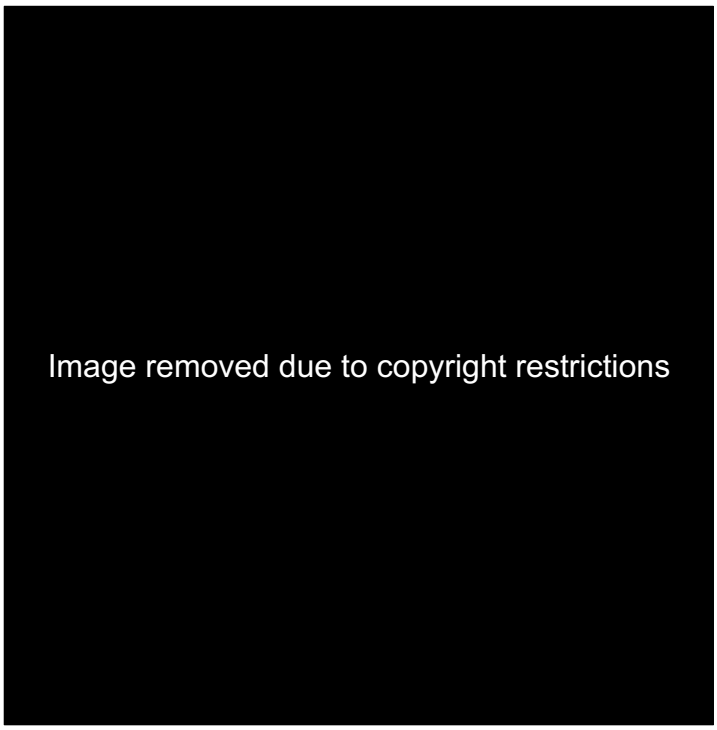


Figure 1-3 Diagram and cross-sectional view of the Humphry Davy Lamp[18].

Analogous to the modern use of phosphors in mercury vapour lamps and LEDs, gas mantles were used to enhance lighting quality, consistency and brightness. One such device was the Clamond basket. This device was made from a gauze containing common and rare earth metal oxides which emitted bright light when the flame heated it[19], further improving the light intensity. This technology survives today in gas camping lamps.

Artefacts from the evolution of lighting technology remains today in the modern lexicon. The phrase "being in the limelight" used to describe the attention given to someone, or indeed something, has its etymology in the Victorian invention of Sir Goldsworth Gurney[20] known as the "limelight". The device was so named because it utilised calcium oxide (quicklime). This device functioned by reacting calcium oxide with hydrogen and oxygen[21] and was initially planned to be used for illuminating survey stations by Thomas Drummond, such that they could be spotted up to a hundred miles away during the 1820s geological survey of the UK[20,22]. Perhaps more famous was its use in theatres for highlighting actors on stage. Drawbacks of the limelight include the inherent flammability of the hydrogen used as well as the reactivity of the oxygen. Fires resulting from accidents during its use were commonplace, and it was soon replaced by the electric arc lamp. The limelight was further improved and patented in 1839 and named the 'Bude light' after the Cornish village where Gurney was born.

1.1.2 The electric lamp

The electric arc lamp involves using two carbon rods separated by a gap. As a current is passed through the circuit, electricity jumps the gap between the rods and light is produced from the arc itself as well as glowing from the heat of the rods. Sir Humphry Davy, once again, is credited with the invention of the arc lamp, using a 4-inch gap between charcoal rods in 1807 (powered by a voltaic pile provided by Alessandro Volta), however it was not until the 1870s, some 60 years later, that they found more widespread usage, owing to the low availability of electricity in the early 19th century.

Perhaps the most common and instantly recognisable form of lighting throughout the 20th century was the incandescent filament bulb. Invented by Joseph Wilson Swan and Thomas Alva Edison separately in 1897 (though Swan was ever so slightly first by a couple of months)[1]. So successful an invention it was, that the businesses they set up to sell their light bulbs still remain at the forefront of the lighting industry today, over 140 years later.

The design of the incandescent filament lamp is of an elegant simplicity. A thin filament of a metal, often tungsten, is connected to a circuit and it begins to glow as the metal's resistivity excites atoms in its structure. As the electrons of the atoms absorb the thermal energy, they are promoted to higher energy levels[23]. Upon relaxation the electrons lose energy in the form of a photon emission. The filament is protected from destructive oxidation by a glass bulb purged and filled with an inert gas, often argon. Incidentally, Edison's original patent describes the design of a lightbulb as having a "carbon wire" as the filament, or a coiled and carbonised "cotton thread"[24], highlighting the intricate craftmanship required to construct lightbulbs in the late 19th century.

Another abundant lighting source still in use today is the fluorescent tube. The precursor to the modern fluorescent tubing was instigated commercially by Peter Cooper Hewitt in 1900 with the development of the mercury vapour lamp and was further enhanced through application of a phosphor in 1938 by Westinghouse Electric Corporation and General Electric[1].

Mercury vapour lamps function by first heating mercury to cause it to evaporate, then ionising the vapour[25]. After being excited, electrons relax and emit ultraviolet radiation, along with visible light containing mostly blue wavelengths. As the blue cast to the light is

not ideal for domestic lighting, phosphors are used. Upon absorption of the ultraviolet light, the phosphors emit light of much longer wavelengths, making the overall colour cast much more pleasing to the human eye. The mercury vapour lamp proved to be much more efficient than the filament bulb, however this was to be superseded by the sodium lamp for widespread usage.

The sodium lamp works by a very similar principle to the mercury vapour lamp, however in this case, sodium is vaporised, ionised and electron transitions result in the emission of radiation. Lacking the propensity for ultraviolet emission however, the sodium vapour lamp has no need of a phosphor owing to the emitted light falling well within the visible range of wavelengths.

Solid-state lighting came into the fray commercially much later, however it was discovered in 1907 that crystals of silicon carbide (SiC) could emit yellow light, which, depending on the quality of the crystal and connections to it, could range in colour from orange to blue[26]. At the time it was not practical as a domestic lighting technology since 10 V was required to initiate luminescence from only a few of the best quality crystals; to ensure all crystals emitted light, some 110 V was required. This, although unknown at the time, was the first example of a light emitting diode.

Holonyak and Bevacqua[27] are credited with the first demonstration of a visible wavelength emitting, light emitting diode (LED) in 1962, with Hall, Fenner, Kingsley, Soltys and Carlson[28] demonstrating emission of infrared shortly before. Holonyak and Bevacqua's red LED involved a p-n junction using gallium arsenide doped with phosphorous. These red LEDs proved to be significantly more efficient than all previous forms of lighting, but with one problem – they were limited to one small band of wavelengths: in this case only red light. For LEDs to have a place in domestic and street lighting, further wavelengths would need to be accessed. 1994 saw the discovery of materials yielding blue emission in LEDs by Nakamura, Mukai and Senoh[29], which exhibited emissions in excess of 1 cd, having record breaking luminous intensity. Nakamura would go on to win the Nobel prize for physics for his work on blue LEDs, along with Isamu Akasaki and Hiroshi Amano[30].

The beginnings of the field of organic light emitting diodes (OLEDs) can be traced back to the work of Bernance, Conte and Vouaux (1955)[6] and Pope, Kallmann and Magnante (1963)[31]. However, the first recognisable OLED was produced by Eastman-Kodak in

1987[32]. The first polymer OLED came in 1990, followed by the active and passive matrix OLEDs (AMOLEDs and PMOLEDS) in 1996 and 1997[32]. Phillips were the first to commercially produce OLED devices in 2002, whereas the first OLED television was produced by Sony in 2007[32].

TADF, originally discovered in Eosin in 1961[32], was exploited by Adachi *et al*. in 2012 and has revolutionised the third generation of OLEDs[33]. As of 2020, OLED technology has found extensive use as display technology, from televisions to tablets and phones, to smart watches and camera viewfinders.

1.2 What are organic electronics?

1.2.1 An introduction

Whilst originally assumed to be confined to the realms of metals and semimetals, throughout the twentieth century it became abundantly clear that organic materials can also be effective electrical conductors, opening the door to applications in devices previously solely manufactured from inorganic materials, but with much more desirable and controllable properties.

Organic electronics consist of small molecules (often less than 1,000 Daltons in size) or indeed polymers, which exhibit electrical properties[34]. The properties could be simple conductivity; or even the ability to generate a current (*via* absorption of light or heat); or to produce an effect upon application of current, such as the emission of light or heat; or even exhibiting electronic device properties such is acting as a transistor, producing dielectric effects or electrochromism[35].

1.2.2 The advantages of organic electronics

The advantages of using organic materials in lieu of metals or inorganic compounds are diverse. One of the more headline-grabbing features of organic electronics is their flexibility, allowing for bendable and foldable or rollable devices[36,37]. The flexible characteristics of organic devices allows for paper thin displays, which handle much like real paper (or closer to overhead projector transparencies in reality). Organic materials can also be stretchable, allowing for application in medicine and healthcare to monitoring health and tracking overall fitness, as well as being engineered to have the ability to self-heal[38], which makes them very attractive for wearable applications, both in terms of comfort for the user, as well as being resistant to damage from everyday wear and tear. Organic electronics also possess high thermal stability, making them not as efficient conductors of heat when compared to metals. They are particularly easy to modify as well, in order to tune their behaviour to a specific requirement by adding on different functional groups to their structures, or by combining different dopants, *etc*., which leads to the fine tuning of their HOMO-LUMO gap. This can lead to two very similar molecules based on the same (cheap

and accessible) precursor structure, with slight alterations to their molecular structures yielding significantly different emission wavelengths for example (blue to red), or wildly different solubilities.

Current inorganic electronic devices are made from unsustainable materials (rare earth metals for example), whereas organic electronics are built from mostly carbon and hydrogen, with some oxygen, nitrogen, sulphur and phosphorous in some cases, as well as halogens and boron. All these elements are in much more abundant supply the world over and when combined with novel methods of hydrocarbon petrochemical synthesis from renewable stocks or even carbon capture, provide a much more sustainable approach to their manufacture. Add to this the feature of disposability – organic devices can be biodegradable (unlike their inorganic counterparts) or even ingestible (making edible electronics for internal analysis of the body) so present little hazard to the environment in landfill, as well as avoiding contamination issues in medical applications[39]. Recycling of disposed organic devices is also possible[40], bringing a revolutionary degree of sustainability to modern electronics.

Physical flexibility of organic devices was previously mentioned, however organic electronics also present a greater flexibility in the device form factor and industrial design of technology. Take for example curtains – simple household 'devices' used for hundreds of years to prevent light creeping through windows. Organic electronics can create a surface on the window itself which, upon application of a current, turns completely opaque. The press of a button immediately returns its transparency[41]. This technology has the power to massively radicalise architectural design, allowing for more homes and offices to be designed to maximise the entry of natural lighting (saving energy in daylight hours). This can be combined as well with so called 'smart glass' which uses an organic film coating which self-cleans the window, cutting down on the need to manually maintain them – they can even be drawn over the walls of a building[42]. Thin-film-based transparent solar cells can also be incorporated into windows where they absorb only the wavelengths necessary to drive a current and transmit visible light[43,44]. New designs are opened up in computing and televisual technology as well. LG have recently announced a rolling 65 inch television, which rolls itself up into a box when not in use[45] – saving significant storage space. In keeping with minimising storage, foldable[46–49], and now rollable[50,51] mobile telephones have also been announced allowing designers to provide innovative new forms to their devices, which some may consider a mere gimmick, however they do offer, when unfolded/rolled

out, larger displays on which the user may be more productive if using the device for work related purposes, as well as offering the screen more protection from scratches when pocketed, or cracks when dropped. Considering protection, self-healing polymers combined with OLEDs also open the door to devices which, when damaged, repair themselves immediately – cutting down on the disposable nature of consumer devices. Organic devices can also be transparent. TOLEDS (transparent organic light emitting diodes) provide the ability to now design displays built into windows or display cabinets[52], such as the Panasonic Design 'Vitrine' concept screen, allowing for space-saving entertainment devices, or even enhancing the quality of augmented reality headsets or camera optical rangefinders or viewfinders.

1.3 What makes organic materials conductive?

Electrical conductivity, put simply, is the movement of charge across a material such that an electrical circuit may be established. In organic materials, electrons are not delocalised across a lattice like in metals. Instead, molecules (or polymers) are able to transport a charge across their structures. This could be either positive or negative charge, where the positive charge arises from a hole (absence of an electron) and the negative charge comes from the presence of an electron. Where an electron is the charge carrier, the mobility is labelled as n-type (negative) and in the case of the hole, p-type (positive). These molecules can accept or donate electrons respectively, a process which can be facilitated by application of heat or light to promote electrons out of the HOMO and into the LUMO. As a semiconductor, this process is temperature dependent. As such, the size of the HOMO-LUMO gap plays a pronounced role in dictating the properties of semiconducting organic materials. Tuning this allows one to control these properties.

In order for organic molecules and polymers to be able to conduct, they must exhibit conjugation across their structures, with aromatic character. They can aid conjugation by the inclusion of heteroatoms such as nitrogen and sulfur, providing lone pairs of electrons. Atoms like boron with empty p-orbitals, can also aid increasing acceptor character in molecules. In order for conjugation to be extended across the molecule, it must remain planar. If the molecule is elastic, or contains a bend in its structure, it will not be aromatic and conjugation cannot extend across it, as the HOMO will encounter breaks in its form.

Continuing along this line of thought, if the molecule, when in the excited state, is able to flex, then it can distort the shapes of the HOMO and LUMO, altering conjugation which can actually act in a deleterious manner to the molecule's semiconductor properties. This is elaborated upon further in Chapter 2 – Section 2.4. The first example of an organic semiconductor was reported in violanthrone by Akamatu and Inokuchi in 1950[53,54], with its photoconductivity established in 1954[55].

1.3.1 Polymers

In Figure 1-4, a selection of conductive polymers is assembled. Note that they all possess some similarities, namely planarity, aromatic rings, heteroatoms or carbon to carbon double bonds. These structural features provide electron-rich groups. They can be used in electron blocking layers, preventing electrons moving in the wrong direction in devices, or as electron transport layers, which feed electrons into an active layer in a device, as well as the active layers themselves. These structures are by no means a complete picture of organic electronic polymers. Many polymers are based upon them, but with subtle differences, such as additional functional groups attached, or different combinations of monomers in their repeating patterns.

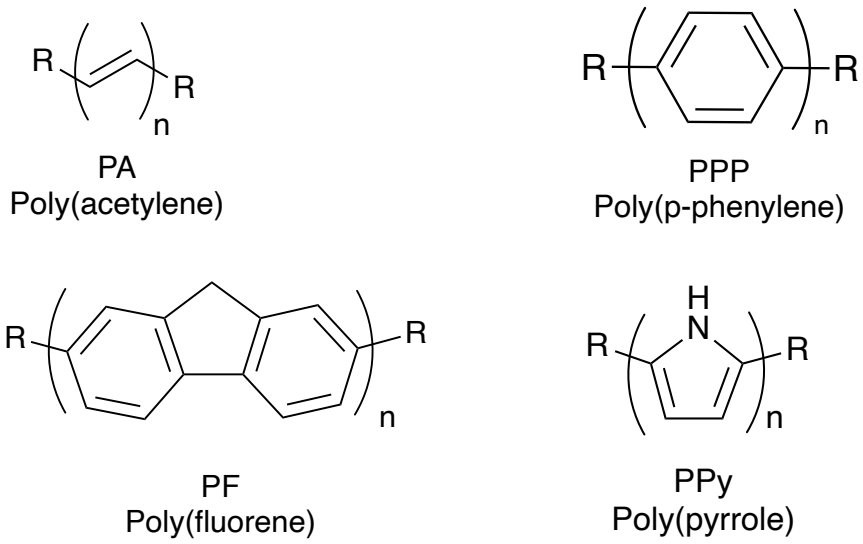


Figure 1-4 A collection of conductive polymers.

1.3.2 Molecules

Organic molecules with semiconductor properties are also planar and aromatic. They can form stacks through π-stacking, van der Waals forces, hydrogen bonding, *etc*., allowing supramolecular structures to form, across which charge can travel. Some examples are included in Figure 1-5.

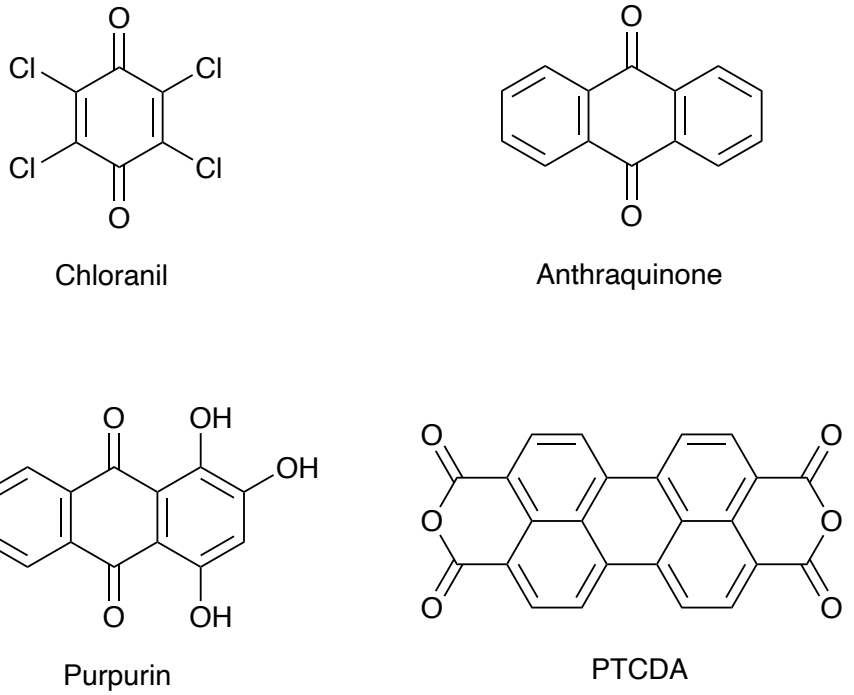


Figure 1-5 A collection of several conductive molecules.

To these structures, electron donating and/or withdrawing substructures, or functional groups, can be added to fine-tune the molecule's properties, such as solubility or even control of the HOMO-LUMO gap.

Whilst not a planar molecule, fullerenes such as buckminsterfullerene (C_{60}) can be used in organic electronics since it is electron deficient, allowing it to be used as an electron acceptor molecule or moiety. One such example of its uses is in OLEDs, where it is a co-active layer with electron-donating molecules, such as rubrene[56].

1.4 Types of devices

As with inorganic materials, there are a number of electronic devices that can be made from purely organic materials. Here follows a summary of a few of the more common examples:

1.4.1 OLEDs

Based upon the concept of the light emitting diode (LED), the organic light emitting diode replaces the inorganic active layer with an organic molecule or polymer. OLEDs provide the potential for highly efficient and pure emission, with devices constructed from highly abundant, and potentially recyclable materials, omitting potentially toxic components as used by inorganic equivalents. This thesis is largely concerned with the synthesis of novel molecules for the use in OLED emissive layers, and will be discussed in greater detail later.

1.4.2 OPVs

In the most basic sense, OPVs are organic-based devices that convert light into electricity. They work by absorbing a photon whose energy is in excess of that of the HOMO-LUMO gap of the active molecule, allowing for promotion of electrons[34]. This is not quite so clear cut in organic photovoltaics because some lower energy photons can be absorbed, giving rise to charge transfer states, as well as absorption where the device is in contact with metals. This gives rise to tailing in their absorption spectra.

The earliest instances of organic photoconductivity were established as far back as 1906 with Pochettino observing it in anthracene[57] (notably being prior to the first known organic semiconductor, violanthrone in 1950[53]), followed by rhodamine B in 1954[58]. The first organic photovoltaic device was reported in 1975[59], incorporating phthalocyanine into the device architecture.

The earliest devices were based on a simplistic design of an organic semiconductor held between metal electrodes of differing work functions. One contact with the organic semiconductor forms a Schottky diode. The active layer is irradiated with light and excitons are formed (see Figure 1-6). When an excited molecule reaches the junction, it dissociates, producing free charges (electrons and holes), which generate a current. Compounds used in

the active layer include merocyanine, phthalocyanine and H_2Pc[60,61]. Later devices began to incorporate C_{60} and other fullerenes into their structures.

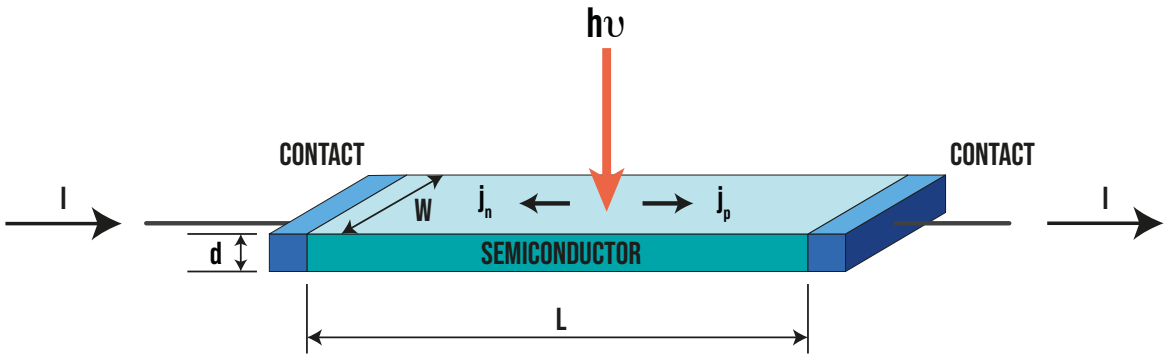


Figure 1-6 Photoconductor illustrating the passing through of a current (I). The current densities of the holes (j_p) and electrons (j_n) are generated by the absorbed photon energy hν. Based on Forrest[34].

There are three main types of photovoltaic cells: the single layer structure; double layer structure; and the bulk heterojunction layer structure. All three consist of a transparent substrate with an indium tin oxide layer connected to a metal electrode and are illustrated in Figure 1-7. This layer is then followed by the active layer(s), then the second electrode in the third layer. The three structural types differ in the following ways. In the single layer structure, the central layer contains the active molecule or polymer only, and is sandwiched between the two electrode layers. The second type, the double layer, also known as a planar heterojunction (PHJ), is similar to that of the first, however in 1986[62], it was discovered that placing an organic semiconductor which acts as an electron donor, above a layer of another organic semiconductor which acts as an electron acceptor, allows for a charge transfer process to occur at the contacts between the two layers. Therefore, these layers need to be very thin in order to work efficiently (~10nm). Whilst these types of OPVs offer a significant improvement on their single layer predecessors, with a ten-fold improvement in efficiencies, the single contact surface limits much in the way of further improvements. The bulk heterojunction structure works by maximising the surface area of donor to acceptor contacts by suspending nanoscale particles of each with the other. This was demonstrated by Yu and Heeger in 1994[62] by blending poly[2-methoxy-5-(2'-ethyl-hexyloxy)-1,4-phenylene with MEH-PPV to be used as an electron donor, and homogenising it with a blend of cyano-PPV and CN-PPV as the electron acceptor. This allowed excitons to survive long enough to dissociate at the donor-acceptor surface, an improvement that Yu and Heeger noted was as good as some inorganic photovoltaics of the time.

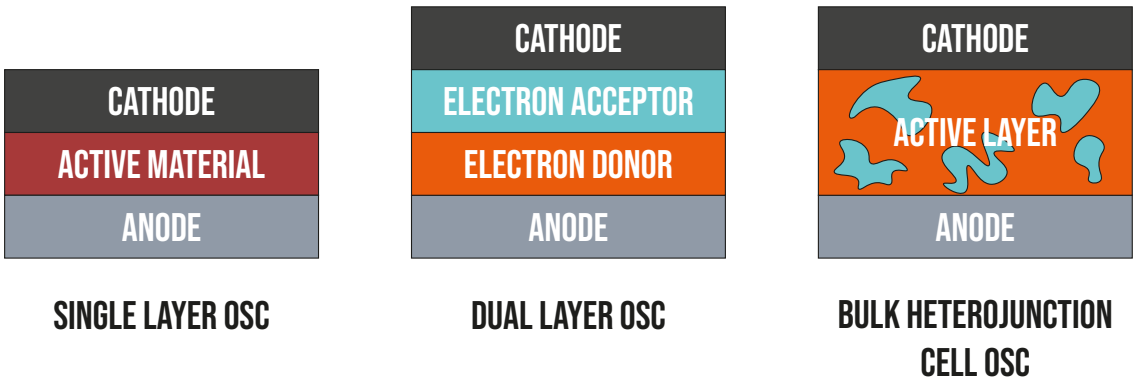


Figure 1-7 The three main types of OSC architecture. Like with OLEDs, additional transport layers can also be added to aid charge carrier transport.

Current OPVs have lifetimes in excess of 20 years and with efficiencies exceeding 16%.

1.4.3 OFETs

Organic Field Effect Transistors (OFETs) are transistors fabricated from organic molecules or polymers. As with all organic electronics, the structure of these molecules and polymers must be comprised of conjugated π-systems (either double bonds or aromatic rings). They also have the advantage of being flexible – allowing for devices to be fabricated with a variety of form factors. As with OLEDs, modification by addition of various electron-withdrawing or donating groups can modify the electronic properties of OFET molecules, as well as altering solubility.

OFET devices consist of several components, chief among them are: the three terminals (gate, source and drain), organic semiconductor channel, gate insulation layer[63] (see Figure 1-8). OFETs find use in the active matrix component of OLED displays, as TFT layers (thin film transistors) in organic devices, RFID tags (radio frequency identification).

Whereas OLEDs and OPVs deal with light emission and absorption, OFETS are concerned with the actual electronics in devices.

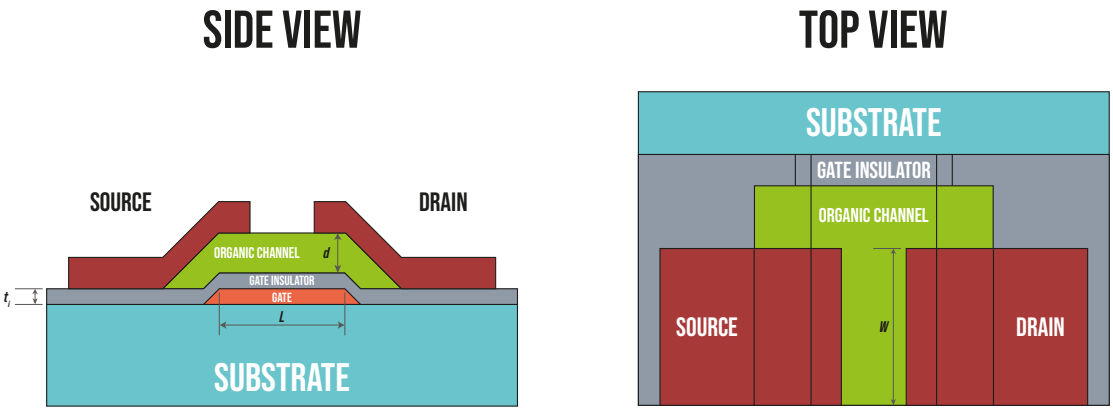


Figure 1-8 Side and top view of an OFET. W is the gate width, L is the gate length, *d* is the channel thickness and t_i represents the insulator thickness. Based on Forrest[34].

1.4.4 Flexible electronics

One of the major selling points of organic electronics is the flexibility of devices. Flexible electronics is not a new field, with flexible circuit boards being widely adopted in numerous devices for a number of years. The premise involves mounting electronic circuits on flexible substrates (often plastic). However, the components themselves (resistors, capacitors, LEDs) are standard available components – not necessarily organic in origin.

One advantage of a flexible circuit board is that they can replace multiple rigid circuit boards and can conform to the internal structure of devices (such as digital camera bodies, *etc*.) thereby saving space, and keeping device size to a minimum.

Use of inorganic circuitry components in flexible circuit boards presents opportunity for damage upon repeated bending and flexing. However, many of the components in standard circuitry can be replaced with organic counterparts, allowing for far more robust devices.

Some examples of the application of flexible electronics include flexible displays (foldable phones, or even flat panel monitors which can bend forming a curved display), whilst OFETs can be used as biological function monitors (such as heart rate and neurological function monitors) which conform to the skin[64,65]. Storage devices using flexible substrates are also possible, along with photonic sensors[65].

1.5 General principles and structure of OLEDs

In the most basic sense, the structure of an OLED can be simplified down to an emissive layer sandwiched between a cathode and an anode. Electrons from the anode and holes from the cathode flow into the emissive layer (EML) and recombine to form an excited state on a molecule, known as an exciton, which decays to emit photons of light.

Arguably, the first reported, albeit very crude, OLED was fabricated by Pope, Kallmann and Magnante in 1963[66]. This 'device' comprised of a single crystal of anthracene (although they also reported devices with 0.01% mol doping with tetracene, whereby anthracene acted as a host matrix). This simple and (by modern standards) poorly optimised device used 10-20 μm thick crystals as the EML, prepared from vapour deposition and solution methods; and either silver paste electrodes or 0.1 M sodium chloride depositions used as electrodes. Electroluminescence was observed at ~ 400 V making them of limited commercial or domestic use. It was not until 1987 that Eastman Kodak would develop a device which operated at a more convenient and reasonable voltage, achieved through careful consideration of charge injection and transportation layers[67].

Holes and electrons have different mobilities. Electrons are normally less mobile than holes in various materials, meaning that the point of recombination will not always be in the same location in different emissive material. This means that excitons can be quenched if they form too close to the cathode for example, or even fail to form entirely if charge carriers leave the emitter layer before combining. To counteract this, additional layers are added to the device to aid charge injection and to coax recombination to occur in a more effective and desirable location to maximise emissions. These materials must also be highly transparent, so as to prevent the loss of photons by absorption before they can even escape the device structure (it's no use fabricating an OLED from opaque materials after all!).

If the right combination of materials is used for each layer, then devices can become very efficient. However, additional layers can result in second order effects such as outcoupling efficiency (extra layers mean more material for emitted light to travel through), charge balance (ensuring that equal quantities of holes and electrons reach the EML to permit recombination) and the exciton dynamics (ensuring the recombination is confined to the EML and does not drift to any of the transport or injection layers) are affected.

Standard OLED devices consist of the following seven layers above a substrate (see Figure 1-9), though the injection layers can be omitted to fabricate five layered devices:

- The substrate (surface on which the device is mounted – can be glass or a polymer, *etc*.)
- The anode, which is usually made from the electrically conductive indium tin oxide, chosen for its transparency.
- Hole Injection layer (HIL), such as TCNQ
- Hole Transport Layer (HTL), such as PEDOT : PSS
- Emission Layer (EML), a pure film of molecules or polymers, or suspended in a host matrix like DPEPO or PVK
- Electron Transport Layer (ETL), such as lithium fluoride
- Cathode, often a metal, such as aluminium, silver or calcium

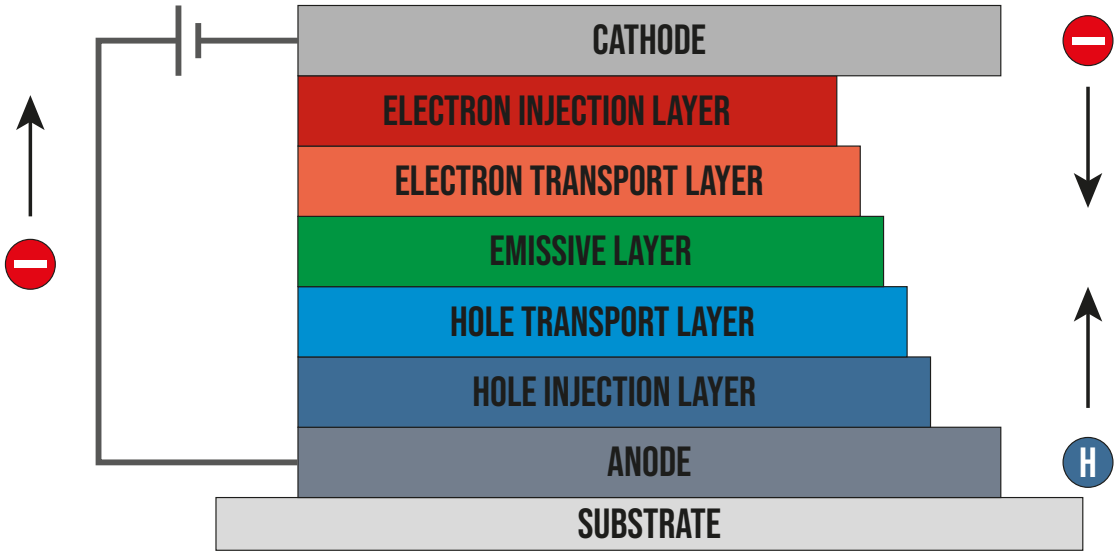


Figure 1-9 Structure of a 7-layer OLED. A similar five layered device works without the injection layers.

The electron and hole injection layers (EIL and HIL) can be thin films or bi-layers on top of the cathode and anode. Additionally, some devices have Electron Blocking (EBL) and Hole Blocking (HBL) layers on either side of the emissive layer to prevent charges from recombining outside the emissive layer (see Figure 1-10). This could be two separate layers, or the HTL and ETL could be designed to serve this purpose instead.

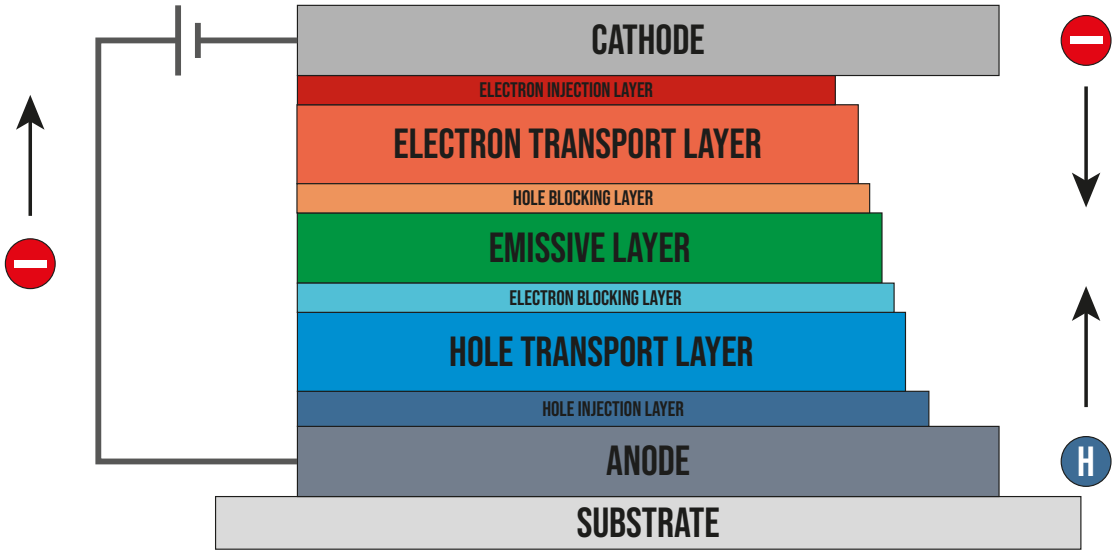


Figure 1-10 OLED structure with blocking layers and injection layers as bi-layers.

Strictly speaking, the cathode is not actually a metal. Often it is lithium fluoride on the surface of aluminium. The lithium fluoride is also the electron injection layer and dictates the Fermi / injection level of the device. In this context, the aluminium is just a support on which the lithium fluoride is placed.

The key component of any OLED is the central emissive layer. This can be is a mixture of materials. For efficient function, both electrons and holes must be readily transported into the emissive layer with equal efficiency. Similarly, the number of electrons and holes entering the emissive layer should be equal, and the rate by which they are transported there should be identical so that none are wasted. It is not desirable for electrons or holes to pass through the emissive layer and out the other side as fewer excitations will happen per charge carrier.

Hole transport and electron transport layers separate the core from the ITO anode and LiF cathode respectively. They can be around 100 nm thick in some cases. A great deal of effort is spent developing hole transport and electron transport materials with dopants. The reason these layers are so large is that they are needed to ensure that the charge recombination zone does not shift too close to the metal. If this were to happen, the excited state encounters its *image charge* in the metal and cancels out its charge - transferring energy to the metal and quenching occurs and less emission occurs in the EML. This problem is also present with the ITO layer and electron transport layer but is not such a concern because ITO is not as effective a ‘metal’ as the cathode is.

The distance between the cathode and anode needs to be ~140 nm so as to maximise light output and minimise destructive interference from reflections of light back into the emissive layer cavity.

In the emission layer, charge trapping occurs on the emitter molecules - either a hole or an electron. This is followed by the opposite charge carrier entering and recombining on the now charged molecule. This forms an excited state, followed by emission. To assist this process, two blocking layers (electron blocking - EBL, and hole blocking - HBL) are placed on either side of the emissive layer, separating it from the hole and electron transporting layers. The reason for this is to stop the *dark current* - the escape of electrons or holes beyond the emissive layer. This is achieved by selecting materials with energy levels sufficient to trap the charge in the emissive layer - making the LUMO too high in energy in the EBL to prevent the escape of electrons into the HTL, and the HOMO too low in energy in the HBL to prevent holes escaping into the ETL.

Additional consideration needs to be taken for fluorescent and phosphorescent emitters because excitons can 'hop' out of the emissive layer into the hole and electron transport layers[34]. Excitons of singlet states have short lifetimes, so they do not 'hop' very far, however triplet states in phosphorescent emitters can travel much further when they 'hop' due to their greater lifetimes. The blocking layers therefore have to be designed to prevent triplet exciton hopping. The TADF process does not have this issue, despite exploiting triplet states. The reason for this is that the charge transfer state cannot hop out of the emissive layer or migrate by energy transfer. In TADF compounds, once the excited state is formed, it is trapped in place and emits from where it is.

In some cases, combinations of different layers can result in unexpected effects, such as electroluminescence coming from hole or electron transport layers when charge carriers travel too far into them instead of being confined to the emissive layer.

1.6 Materials for OLEDs

First of all, the substrate on which an OLED is mounted needs to be transparent (there is no point making a light emitting device and blocking off all light emitted from it). This could be glass, or even a flexible polymer – giving the potential for a wide variety of form factor possibilities.

The anode (as mentioned previously) is most commonly made from indium-doped tin oxide as this is both a suitable electrical conductor and, rather importantly, transparent.

The hole injection layer (HIL) next to the ITO anode needs to be made from a material which has very little difference in energy of its HOMO to that of the anode so that injection of holes into it requires very little effort. This often results in a HOMO which is of lower energy than that of the anode's work function. HILs are normally made from conducting polymers such as a mixture of poly(3,4-ethylenedioxythiophene) and poly-(styrenesulfonate), commonly abbreviated to PEDOT:PSS[68].

After the injection layer, holes are transported to the emitter layer *via* a hole transport layer (HTL). The HTL's HOMO level should be as close to that of the emitter layer's (EML) as possible. An ideal HTL will have a LUMO with energy much higher than that of the emitter layer so that it is incredibly difficult for electrons to traverse the intersection between the EML and HTL – helping to trap them in the emitter layer. This makes the HTL both a hole transporting layer, and an electron blocking layer (EBL). Alternatively, if the LUMO is not high enough, an additional layer can be added to achieve this – a dedicated electron blocking layer (EBL). Electron rich TCTA (see Figure 1-11) is commonly used as both a HTL and HIL. It is also an effective EBL thanks to its high LUMO energy (-2.4 eV)[69].

$Ir(ppz)_3$ (see Figure 1-11) has been used as an electron blocking layer[70] thanks to its high LUMO energy (-1.6 eV[71]) and relatively high HOMO energy (-5.0 eV[71]), making it compatible with HTLs such as PEDOT:PSS.

The emitter layer normally consists of a host matrix (which is used to aid transfer of charge carriers to the emitter molecules *via* Förster or Dexter interactions and holds emitter molecules apart to prevent aggregation caused quenching[72]), in which an emissive molecule (molecules) or polymer is held. The host matrix needs to be selected to have a suitable

polarity to permit efficient emissions in the emitter molecule and allowing for the optimal and desired emission wavelength to occur (*i.e.* any solvatochromic effects are not shifting the emitted colour). As such, many different host matrices are available. Some common examples for TADF-type OLEDs are bis[2-(diphenylphosphino) phenyl] ether oxide (DPEPO) and 4,4′-bis(N-carbazolyl)-1,1′-biphenyl (CBP)[73] (see Figure 1-11).

A selection of materials used for their respective layers are illustrated in Figure 1-11.

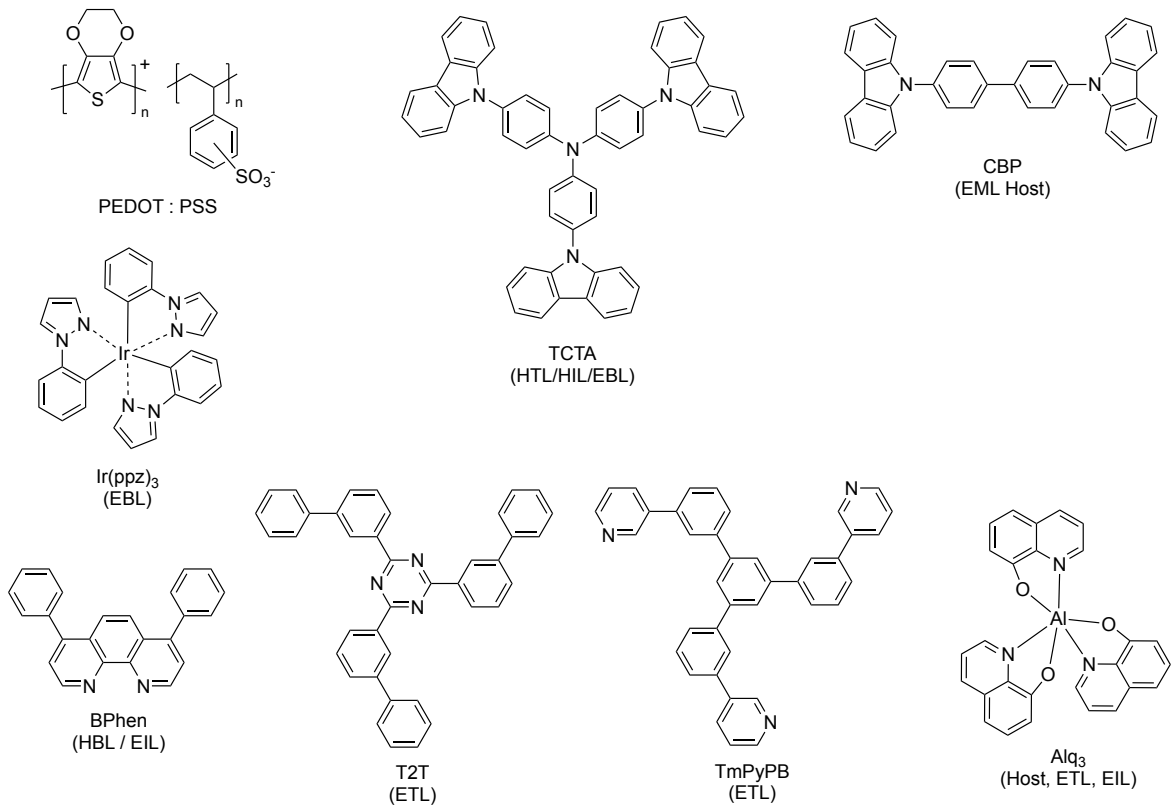


Figure 1-11 Examples of molecules and polymers used in OLED fabrication.

On the other side of the emitter layer is an electron transport layer (ETL). Much like the hole transport layer (HTL), its job is to transport electrons to the emitter layer (EML). To do this effectively, it needs to possess a LUMO close in energy to that of the EIL and cathode, so that injecting electrons requires little energy. The LUMO must also be close in energy to the emitter layer, but its HOMO should be much lower than it in order to prevent holes from leaving the EML. Once again, an alternative is to place a hole blocking layer between the ETL and EML with a much lower HOMO if this is not possible in the selected ETL material. Triazine and pyridine based molecules such as 2,4,6-tris(biphenyl-3-yl)-1,3,5-triazine (T2T) and 1,3,5-tris(3-pyridyl-3-phenyl)benzene (TmPyPB) (see Figure 1-11) are used as ETLs[74,75] and phenanthronline-based compounds such as bathophenanthroline (BPhen) have been used as effective hole blocking layers[76].

The electron injection layer (EIL) must have a similar LUMO energy to both the cathode's work function and the HTL to aid electron injection to the system. The choice of material is closely related to the choice of cathode, because the EIL and cathode are normally incorporated as a bi-layer.

The cathode needs to possess a low work function to support the injection of electrons from the external circuit into the organic materials. Lithium and magnesium make suitable cathodes, however, being very reactive elements as they are, they are susceptible to rapid oxidation upon exposure to moisture and oxygen. Normally they will be incorporated onto less reactive metals such as aluminium, as thin layers (or bi-layers) of alkali metal salts (such as LiF, or Cs_2CO_3) as a thin electron injection layer (EIL). The EIL need only be very thin (~1 nm) to enhance the lowering of the electron injection barrier. If the cathode's workfunction is unfavourable for electron injection, an EIL is inserted between the cathode and the EML. Relatively reactive alkali metals make for good injection layers, however their poor stability requires alternative salts such as LiF or Cs_2CO_3. During deposition of the cathode material, decomposition of these layers can occur, which can be beneficial if paired with the right cathode material (the alkali metal originally in the salt instead behaves as an n-type dopant and makes electron injection easier)[77]. However in other cases it can be detrimental if their work functions differ significantly. EIL bi-layers can enhance the electron injection instead by acting as an injection contact between the EIL and cathode – preventing incompatible mixing of work functions.

1.7 Progress of the industry

OLEDs represent a significant proportion of the organic electronics market. A few years ago, an OLED television cost >£10,000 and was considered a luxury item. Today the cost is closer to £1,000, which is still prohibitively expensive for most people, however it is much more palatable when one is considering investment in a higher quality display. More recently mobile phones, tablets and smart watches have adopted OLEDs in much smaller displays, often below the £1,000 threshold, but still characterising the more expensive end of device lineups.

Nevertheless, the OLED market was estimated to be worth $38.44 billion in 2022, increasing to $46.36 billion in 2023 and currently resides at an estimated $55.95 billion in 2024

according to recent market research by Precedence[78], with an estimation that it will more than double to $119.75 billion by 2028. As such, research in this field is of great strategic and commercial importance over the next decade as devices become much more efficient, sustainable and affordable.

1.7.1 OLED vs QLED and QD-OLED

As of 2024, there are three major display technologies advertised for devices: long-standing liquid crystal displays (LCDs); organic light emitting diodes (OLEDs), and quantum dot LED displays (QLED).

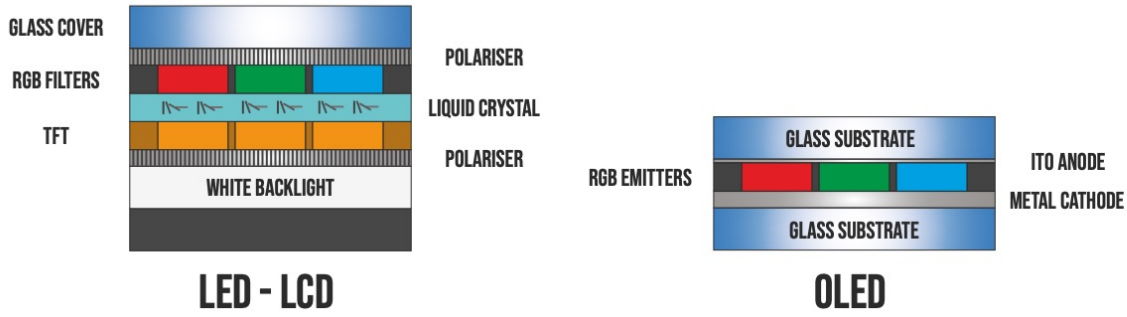


Figure 1-12 General architectures of LED driven LCD display (left) and an OLED display (right).

LCD-LED

LCD displays function by means of a white backlight shining through a polarising filter, TFT array and liquid crystal field, red, green or blue colour filters, a second polarising filter and transparent cover glass (see Figure 1-12). The TFT array and liquid crystals act as digital shutters which block light from reaching the filters, allowing for control of the overall colour of the light which comes out of the device.

Whilst this technology is well established and reasonably cheap to manufacture, it possesses an inherently lossy architecture, since the backlight must be on at all times – the blocking of light means that photons are lost when that particular colour is not viewed, and the colour filter also filters out all other wavelengths. Unfortunately, the contrast of images produced by LCD displays is often poor, since the LED backlight is constantly switched on, some light bleeds through the liquid crystal and TFT matrix, meaning blacks items and dark scenes display as grey, which can be distracting for viewers.

Quantum dots

Quantum dot displays work by a similar principle, however, instead of only releasing transmitted light, the quantum dots absorb excitation wavelengths from the backlight and then reemit it at a very pure and intense wavelength (red, green or blue). Since quantum dots have very broad absorption profiles, they are significantly more efficient than colour filters, and since they achieve high brightnesses, can display excellent contrast, although, depending on the excitation source, some bleeding effects can be observed and blacks are sometimes rendered as grey as a result. Figure 1-13 illustrates the difference between QD displays, and QD-OLEDs.



Figure 1-13 General architectures of a quantum dot (QD) display (left) and QD-OLED display (right).

OLEDs

OLED displays differ from LCDs in that they require no colour filter to make up the pixels – for each red, green or blue pixel, the pixel itself is its own emitter (see Figure 1-12). As such, no liquid crystal shutter is needed either – if a colour is not required, the emitter is simply switched off! This means the devices have the potential for ultra-high efficiency. In terms of image quality, they have superb contrast ratios, since blacks are produced by turning the OLEDs off so that there are no unsightly greys shown in dark images. Unfortunately, OLEDs suffer from roll-off effects – the more energetic blue emitters degrade relatively rapidly, meaning colour accuracy deteriorates. This is particularly noticeable in OLED computer monitors where taskbars and icons are displayed on screens for extended periods. In this case a phenomenon known as “burn-in” can be problematic. Like with CRT displays, where if a static image was rendered on the screen for a long time, the electron beam would have a damaging effect on the phosphor on the screen, burning in place a “ghost image”, OLED displays show a similar artefact when different display pixels degrade at different rates. Owing to the higher energy excited states required for blue emitter materials, blue pixels are likely to break down sooner, giving a redder shift to the overall image. “Burn in”

in OLED displays can also lead to static items on the screen remaining in place after the intended image has moved on to the next.

Software techniques are adopted on some displays to counteract this; however, some methods involve lowering the intensity of all pixels at the same rate as those that are degrading to hide the change – which is not good value for the user's experience.

QD-OLEDs

QD-OLEDs circumvent the issues that standard OLEDs possess by using the OLEDs as the back light. This may be a white source, or blue or purple. This allows for a large array of OLEDs, permitting each red, green or blue quantum dot sub pixel to be excited by its own independent OLED, allowing for ultra deep blacks matching that possible by standard OLED displays (see Figure 1-13).

This technique is perhaps better thought of as a temporary solution. As OLED research and development continues, eventually it is hoped that the issues with device degradation and short lifetimes will be overcome and there will be no need for the quantum dot layer.

Of note is also the mini-LED display. This functions in the same manner as the traditional LCD display. However, in this architecture, instead of large LED backlights, much smaller LEDs are used addressing significantly fewer LCD filters each. This means deeper blacks (and hence higher contrast ratios) are achievable when individual LEDs are switched off. Since the LEDs are driving multiple pixels, this does mean that a halo-effect is sometimes observed around bright objects on dark backgrounds, although this is only noticeable when the display is viewed in a dark environment and is particularly pronounced when white text is shown on a black background.

1.8 Applications of OLEDs

1.8.1 Display technology

Perhaps the most widely reported application of OLED technology is in television and display screens. Currently, the market leader in OLED televisual commercial applications is LG electronics, whose main rival is from Samsung with their support of the QLED and QD-OLED systems. Figure 1-14 illustrates a handful of common display applications for OLEDs.

OLED displays have the great advantage of a wider colour gamut than existing systems, and by virtue of their engineering, produce deep blacks in images. The reason for this is simply because there is no need for a backlight, which can exhibit leakage around pixels and when liquid crystals are blocking light to make a black pixel, some backlight will still make it through, making black scenes appear grey. Without the need for a backlight, a black pixel in an OLED is simply an OLED switched off – so absolutely no light can leak to the viewer. This gives a much richer contrast ratio, and in displays with ultra-high brightness potential; allows for a true high dynamic range (HDR) experience.

Displays also have the potential to be flexible, as the recently released Samsung Galaxy Z[49] and Motorola Razr[79].

Thanks to the thin and light nature of OLEDs, they are also finding applications in the so called 'wearable' technologies, such as fitness trackers (such as the Fitbit Luxe[80]) and smartwatches (such as Apple's Apple Watch[81] and Samsung's Galaxy Watch 4[82]).

Signage also has the potential to be revolutionised by OLEDs – the LG automatic doors for example,[83] function by means of transparent OLED displays affixed to glass doors displaying welcome messages from their owners or advertisements



LG Posé display[84] Motorola Razr 40[79] OLED automatic doors[83]

Figure 1-14 Examples of recent devices incorporating an OLED display.

1.8.2 Solid-state lighting

Whilst the most commonly discussed application of OLEDs is that of display applications, they can also be applied to lighting.

Unlike incandescent bulbs and fluorescent tubes, the luminance of OLEDs is typically lower (lest they exhibit unsatisfactorily short lifetimes), making them a poor choice for point source lighting for entire rooms (however they can be applied to desk lamps, *etc*.[85,86]). To use as a main room lighting source, the form factor of lights using OLEDs would need rethinking. One concept is to apply broad wavelength, white light-emitting OLEDs as a wide surface area emitter – literally light emitting wallpaper or artworks – to illuminate interior environments. Additionally, OLEDs have found application in signalling lights, such as the taillight of the Audi Q5[87] where the manufacturer claims it offers the potential for "greater homogeneity, efficiency, compactness, safety and personalisation". Figure 1-15 illustrates a selection of examples.



Tree Jade desk lamp [86] | OMLED One d2[85] | LivingShapes interactive wall[88]

Corning LumiCurve Wave[89] | OLED tail light on Audi Q5[87] | LG High efficiency OLED light panels[90]

Figure 1-15 A selection of OLED light sources.

1.8.3 Medical applications of OLEDs

OLEDs can also be used for pulse oximetry[91] photodynamic therapy, as muscle contraction sensors, wound healing, optogenetics and fluorescence sensing[92]. In pulse oximetry, OLEDs provide a solution to incorporating the red and infrared emitters into much more compact devices, permitting their incorporation into wearables to allow for self-measurement of blood oxygen levels. The potential flexibility of the geometry of OLED devices lends them to application to the human body both for health monitoring and therapy. Conformation to the contours of the human skin can allow for cutaneous wound healing, permitting consistent uniform exposure of the skin to specific wavelengths for light therapies.

1.9 Evaluation of current LEDs and OLEDs

OLEDs provide numerous advantages to current technologies, although they are not without their drawbacks.

Firstly, OLEDs have very fast response times – in the μs range instead of the ms range afforded by LCD devices. This permits very high image frame rates, making them attractive for gaming, but also for the currently blossoming field of virtual and augmented reality headsets, where low latency displays are necessary to avoid motion sickness for users. As mentioned previously, OLEDs provide deep blacks – since no backlight is required in the display, they yield excellent contrast. They can be fabricated upon flexible substrates, enabling novel use cases and form factors. Displays incorporating OLEDs can have low power consumption compared to LCDs since when dark scenes are displayed, less energy is required to drive the emissions and when black is rendered, the OLEDs at that particular pixel are simply switched off. The photophysical processes involved in the emission process also yield reduced heat emission, so the bulk of the energy conversion is from electricity to light, minimising energy loss. OLEDs have greater luminous efficacy compared to LCDs (more luminous flux per W of power used), making them more efficient.

Unfortunately, OLEDs tend to have low luminance compared to LED displays. They also suffer from shorter lifetimes – particularly the blue emitters[93]. The shorter lifetimes can come from poor encapsulation, resulting in chemical degradation from oxygen or moisture (known as extrinsic effects), as well as roll-off effects. At higher currents, roll-off becomes a much greater issue for OLEDs (hence most OLEDs are driven at a voltage below that which would result in the brightest emissions). This is because of the chemical changes that the emitter materials in OLEDs can undergo owing to intrinsic effects causing bond dissociations or instigating chemical reactions. This is less of an issue in inorganic LEDs since a much greater driving force is required to cause similar issues.

Degradation is not unique to OLEDs and the display industry adopts a system of describing a device's operational longevity – the device lifetime, LT50. This is the time taken for an OLED to degrade such that its luminance drops to half the intensity of its original value. OLED displays have demonstrated an LT50 of up to 100,000 hours, making them satisfactory for consumer use[94]. Adding confusion for the average consumer however are

two additional lifetimes often reported – the LT90 and LT70 – the time it takes for the luminance to drop to 90% and 70% of its original intensities respectively.

1.10 Characterising OLEDs

The human eye does not perceive all wavelengths equally, with it being most sensitive for around 555 nm[95]. In order to describe the quality of the emissions from a light emitting device, the Commission Internationale d'Eclairage (CIE) chromaticity standard was developed. This consists of a diagram with x and y coordinates describing the colour of an emission (see Figure 1-16). The extreme points on this diagram represent the pure colours of red, green and blue, and the device being studied is shown by a point somewhere within the triangle made by the pure RGB emitters. A white light source is represented by coordinates 0.33, 0.33.

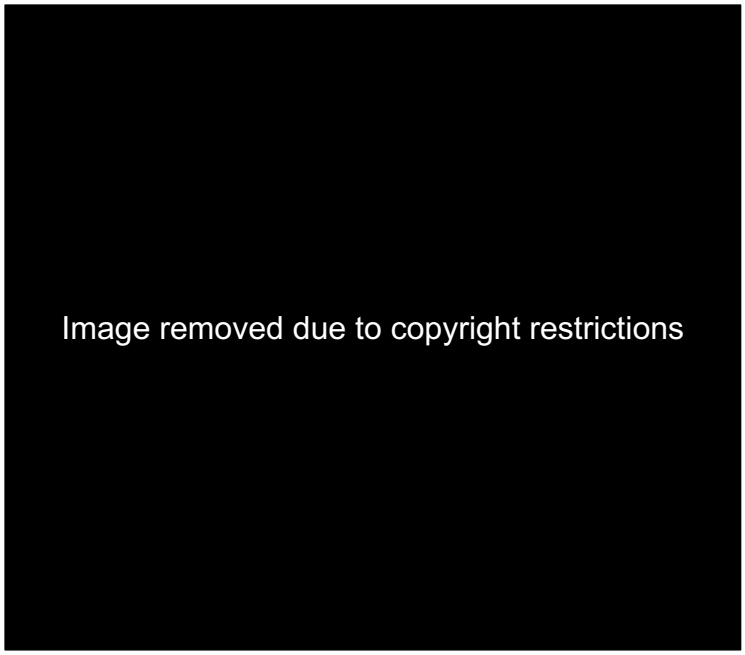


Figure 1-16 CIE colour coordinate diagram. Solid triangle represents the sRGB colour space and the dashed line represents the NTSC colour space. Taken from Forrest[34].

The vertices of the triangles shown in the CIE colour coordinate diagram (an example of which is shown in Figure 1-16) are adjusted to represent the particular device the diagram is representing, meaning that the diagram can show the range of the "colour space" that device is capable of rendering. This colour space is also known as the colour "gamut". A device which covers a larger colour gamut can more accurately render an image and produce images with greater bit depth. There are several widely adopted colour space standards, such as

sRGB, Adobe RGB 1998 and NTSC (National Television System Committee) among others. Commercially available displays are rated against how much of a specific colour space they are capable of accurately covering (usually by a percentage coverage).

Colour correction temperature (CCT) is often quoted as a means of how blue or red white-light appears to be shifted. This is measured in Kelvin (K) and is shown in Figure 1-16 as the grey curve. This curve is referred to as the "Planckian locus"[34]. This refers to the temperature of an ideal black body radiator, or a "Planckian radiator". Since most emitters do not represent such an ideal black body emission, colour correction temperature (CCT) is used as a metric to define it with reference to a black body radiator. Linguistically, the shifting is referred to as *warm* if it is to the red side of white, or *cool*, if it is bluer.

Whilst CIE coordinates and wavelength are perfectly suitable for describing pure (or mostly pure) colour emitters for OLEDs, when it comes to white light for domestic lighting applications, the quoted CCT of that emitter gives a better descriptor for how close the white light is to the daylight spectra (*i.e.* as close to the sun's CCT as possible, being as it is 5780 K[34] with variance throughout the day from 5000 – 6000 K). Cool white light has a blueish tint, and has a CCT of > 5000 K, whereas white light, which is considered to be warm, has a CCT of between 2700 K and 3000 K[34]. Interestingly from a sociological standpoint, what is considered to be an acceptable CCT for use in a domestic setting varies between cultures, with eastern peoples preferring cooler whites, and western cultures typically preferring warmer whites[96].

Colour quality is not the only metric by which an OLED is judged. In addition to this are two types of efficiencies - the internal quantum efficiency (IQE) and the external quantum efficiency (EQE). The IQE is a measure of how efficient the *emitter molecule* is as a percentage of how many incident electrons are converted into the final emission photons (be they *via* fluorescence, phosphorescence, TADF, *etc*.). EQE on the other hand is a measurement of the overall efficiency of a *device* in terms of how many excitons generated are converted into photons *that leave the device.* EQEs will always be lower than their respective IQE owing to the potential loss pathways in devices. EQE can be calculated from the formula in Equation 1-1 :

$$EQE = \eta_{int} \times \eta_{out} = \gamma \times \chi_{ST} \times \eta_{PL} \times \eta_{out}$$

Equation 1-1 The EQE equation as described by Forrest[34].

Where η_{int} is the IQE, η_{out} is light outcoupling efficiency (a ratio of the photons generated to that which make it out of the device - basically driven by the refractive index of the EML, which is typically ~20% for glass substrates thanks to reabsorption by various layers and internal reflections), η_{PL} is the PLQY of the emitter material (a ratio between the absorbed and emitted photons, γ is the charge balance factor (owing to differences in the balance between the numbers of holes and electrons reaching the EML) and χ_{ST} is the spin formation ratio (the ratio of singlets to triplets formed – fluorescent emitters having 25% singlets and 75% triplets, will have a χ_{ST} of 0.25)[34].

Luminous flux (units of lumens, lm) is the power of a light source weighted as seen by the human eye. This is considered a photometric measurement owing to its relevance to human sight (the visible spectrum)[34]. The radiometric analogue (*i.e.* that which is weighted spectrally) is the optical power (using units of Watts, W)[34]. Connecting these metrics is the observation that, for a monochromatic light source at the average human eye's most sensitive wavelength (555 nm), if it is emitting with an optical power of 1.46×10^{-3} W, then the luminous flux will be 1 lm.

Related to the luminous flux is the luminous intensity. This modification records the luminous flux at a specific angle, giving units of lm/sr, or lumens per steradian. This is more commonly referred to as candela, and units of cd are used instead. Another modification of luminous flux is illuminance (I, with units of lux), which is the luminous flux per unit area (lm/m^2). Similarly, the area normalised luminous intensity is the luminance (L, units of cd/m^2). Typically, the "brightness" of a display is reported to consumers as the device's luminance. Display applications can have luminances of 100 – 400 cd/m^2, with displays rated for higher quality high dynamic range (HDR) exceeding 1,000 cd/m^2 in some cases. Consumers are also exposed to an alternative unit for luminance – the nit, where 1 nit is the same as 1 cd/m^2.

When characterising OLEDs, additional consideration must be given to their electrical performance, not just their optical performance. One measurement routinely performed is the current efficiency (CE). This links the luminance to the electrical current that flows through a unit area of an OLED reported as cd/A[34]. Additionally, the luminous power efficiency is a measure of how much luminous flux is produced for a given quantity of power driving the device and possesses units of lm/W[34].

1.11 Making OLEDS

1.11.1 Vacuum deposition

Vacuum deposition typically yields high quality morphology (provided the deposition rate is stable). The process involves heating the material to be deposited to a high temperature under high vacuum. This is usually achieved with an evaporation chamber attached to a turbopump (reducing the pressure to ~10^{-7} – 10^{-6} mbar). The material can be held in a ceramic crucible (which is in turn held by a tungsten wire), or upon a metal boat, through which a current is passed resulting in an increase in temperature. As the temperature is gradually increased, the material sublimes and travels to the top of the chamber where the substrate is held in place, ready to receive the coating.

To control the thickness of deposited layers, a quartz thickness monitor is used to detect the thickness of material that builds up on it (as a function of the vibrational frequency of the crystal under current) as well as the rate of deposition. When the deposition rate is deemed by the user to be acceptable (high enough to build up on the device, but not too high so as to yield poor morphology), a shutter blocking the substrate holder from the evaporation source is pneumatically swung out of the line of sight of the heated crucible or boat, and evaporation onto the substrate can begin. In order to pattern the substrate with separate contacts, a mask is placed between the evaporation source and substrate to cast a "shadow" upon its surface in accordance to the deposited design required. This process can up to take several hours to complete, depending on how long the vacuum pump takes to get the system down to pressure, and how many layers are to be deposited, and how often the chamber needs to be opened up to replace materials or masks, but the actually deposition process itself can take as little as 15 minutes and can be performed in bulk, coating several devices simultaneously. Top of the range systems such as the Lesker Super-SPECTROS 200[97] can be programmed to automatically follow device recipes even be controlled remotely over the internet.

Vacuum deposition is a very lossy process however, as much material is lost prior to the shutter opening, which continues after closing as the evaporation source cools. In addition, sublimation is not aimed solely at the substrates, rather it is jettisoned in a cone upwards from the crucible much like a molecular blunderbuss, coating the entirety of the inside of the evaporation chamber (later necessitating extensive cleaning). Additionally, the evaporation of material is highly dependent on the thermal properties of the material in question. If the

sublimation point of a compound is too high, or the molecular weight too heavy, then evaporation is unlikely to be possible, even at ultra-low pressure. In this case, alternative methods such as spin coating are preferable (which is often the case for high molecular weight EMLs).

1.11.2 Solvent methods

1.11.2.1 Spin coating

Thin films of material can be prepared *via* a process known as spin coating. This involves taking a solution of the emissive material (or indeed any material required for a particular layer in an OLED) and pipetting it onto a substrate (on which there may or may not be prior layers above which this layer will be prepared). The substrate is then spun at a high speed (typically around 2,000 – 3,000 rpm) in order to spread the solvent across its surface. The thin layer will evaporate quickly, leaving a fine film of the deposited material. Films as thin as 100-900 nm can routinely be prepared in as little time as 60 seconds.

This particular technique is suitable for materials with large molecular weights or strong intermolecular interactions that would otherwise decompose when one attempts to sublime them. A wide variety of solvents are usable for this technique – so long as the material being deposited is soluble in it, it can be used. Whilst this technique is attractive for fabricating thin films for analysis, this does however raise the issue of the solubility of layers below that which is being deposited. If the layer onto which the material is being spin coated is also soluble in the solvent being used, then that layer could deteriorate or be completely removed by the solvent – even having regions dissolved and thrown off by centrifugal force, creating an uneven surface. It would also raise the possibility of diffusion of material between two adjoining layers, potentially resulting in a deleterious effect (or even a difficult to reproduce enhancement) on device performance.

1.11.2.2 Printing

An alternative method for preparing OLEDs (if the active materials have good solubility) is printing[98]. Much like ink-jet printing, the active material is deposited upon a substrate when in solution (or as a suspension). This allows for low cost and more efficient and quicker

production methods, allowing for significant upscaling in terms of product size and volume of output, all done at room temperature and atmospheric pressure. Additionally, printing opens up opportunities for a wider variety of substrates – standard glass or other transparent media, but also foils and paper, and depending on the flexibility of the printing mechanism, it is even possible to print on non-planar geometries.

Unfortunately, current printing methods suffer from poorer morphologies when compared to more traditional fabrication techniques, and the deposited material tends to have reduced resolution (*i.e*. being thicker and more on the μm scale of resolution compared to the nm scale achieved with other methods). They also have the added complication in that consideration must be given to the solvent, viscosity caused by the concentration of the active material, binders, surfactants and wetting agents, used – all of which contribute to the quality of the print morphology and final properties of the deposition. As such printing is currently not suitable to high quality display applications but is nevertheless attractive to other areas. OLEDs have potential for where resolution is not important – such as lighting and medical roles.

1.12 Environmental and sustainability benefits of OLEDs

Current production of traditional LEDs and some top of the range phosphorescent OLEDs requires the use of toxic heavy metals. As such, both the manufacturing process and eventual disposal presents an opportunity for environmental contamination.

The use of entirely organic materials in the fabrication of OLEDs (as novel TADF molecules promise) provides a much safer and sustainable alternative[99]. Making use of aromatic compounds and heteroaromatic compounds incorporating lighter elements such as hydrogen, carbon, oxygen, nitrogen, sulfur and boron, and avoiding metals in their entirety, means that the feedstocks for the synthesis of active materials for OLEDs can be far more affordable, fully recyclable and potentially even biodegradable[100].

1.13 Summary

The history of lighting, semiconductors and quantum mechanics are intrinsically linked. Both lighting and semiconductor science developed empirically throughout most of human history, they converged in the mid twentieth century with the advent of quantum mechanics as a means to describe their function and processes physically. This culminated in the development of solar cells, transistors and light emitting diodes which have revolutionised modern life with novel technology. A shift to organic electronic equivalents presents numerous advantages and the opportunity to rethink the design and application of technology, whilst also providing the opportunity to shift to more sustainable components, further aiding recyclability and less environmentally damaging precursor material sources.

In an increasingly environmentally conscious society, moving on from the inorganic to the organic paradigm, will open up an exciting future of previously unimaginable possibilities.

Chapter 2 Physics of luminescent materials

In order to develop novel, highly efficient emitter materials for OLEDs, a thorough understanding of the physics of semiconductors and the photophysics of organic molecules is vital.

2.1 What is light?

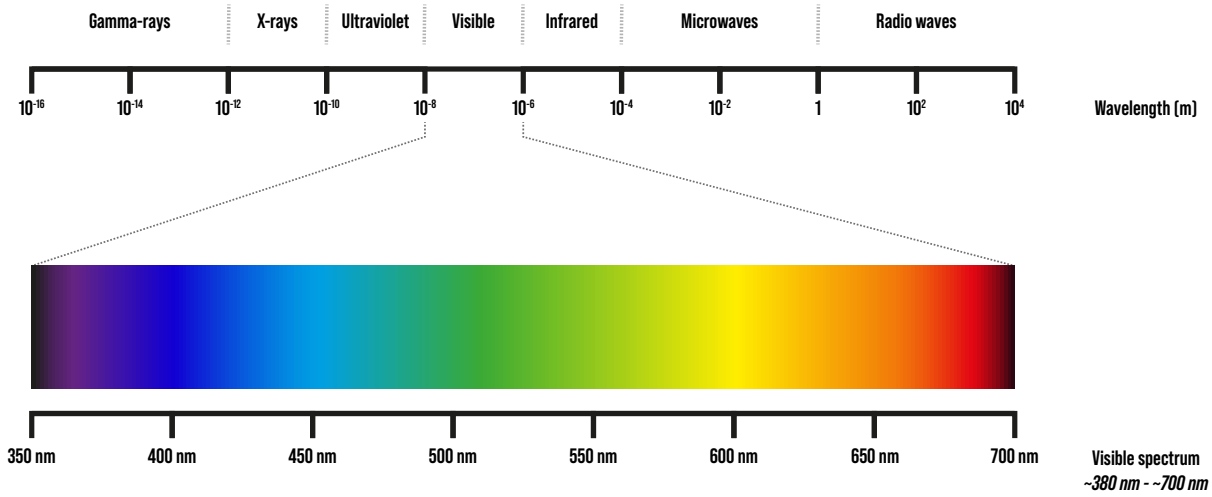


Figure 2-1 The electromagnetic spectrum. The visible region is zoomed in between ~380 nm and 700 nm. Beyond this is the ultraviolet and other high energy wavelengths (below 380 nm) and infrared and longer (above 700 nm).

When a molecule in an excited state decays to the ground state, a photon can be released. The difference in energy between the initial state and the final state corresponds to the energy of the photon emitted. This energy is related to the frequency and wavelength of that photon with the following three equations:

$$E = h\nu$$

Equation 2-1 Planck's equation.

where E is the energy of the photon (in J or eV), h is Planck's constant (typically reported as 6.626×10^{-34} J Hz^{-1}, but when dealing with energy units of electron volts, eV, Planck's constant is $4.136... \times 10^{-15}$ eV Hz^{-1}), and ν is the frequency in Hz. Since frequency and wavelength are related by the equation:

$$\lambda = \frac{c}{\upsilon}$$

Equation 2-2 Wavelength - frequency relationship.

We can substitute Equation 2-2 into Equation 2-1 to get:

$$E = \frac{hc}{\lambda}$$

Equation 2-3 Relationship of wavelength to energy.

which allows much easier interconversion between energy and wavelength.

The visible range of light extends from wavelengths as long as ~700 nm, to as short as 400 nm[101] and such a spectrum is illustrated in Figure 2-1. As can be seen from Equation 2-3, the wavelength of light is inversely proportional to its energy. As such, photons with longer (larger) wavelengths actually have less energy than those with shorter wavelengths. Therefore, ultraviolet light is of higher energy than infrared.

The field of organic electronics deals with the emission and absorption of wavelengths ranging from 200 nm (during excitation), through the visible range (for standard devices) and into the infrared region for the application of IR OLEDs (of the order of 1000 nm). These equations therefore allow for the conversion from nm into eV for the discussion and elucidation of the physical energy transitions experienced by the molecules during their excitation and emissions (dealing in the range of 6.2 eV to 1.2 eV respectively).

A convenient means of converting from wavelengths in nanometre to energy in electron volts can be achieved with the equation:

$$E(eV) = \frac{1240}{\lambda(nm)}$$

Equation 2-4 The nanometre to electron volts conversion equation.

2.2 Band theory

The difference between a conductor, insulator and semiconductor is determined by the occupation of their valence and conduction bands and the energy gap between them[102].

Since the *Pauli Exclusion Principle* dictates that a quantum state may only be associated with a single electron, when many atoms are bound together in the same lattice the combined effect is to form 'bands'. This can be explained by examining the application of *linear combination of atomic orbital theory* (*LCAO*) to vast arrays of atoms. The metal *lithium* possesses three protons and, being of neutral charge, three electrons accordingly. The electrons inhabit two orbitals – 1s and 2s. Since electrons occupy orbitals in order of increasing energy (lowest energy first) as per the *Aufbau principle*, the 1s orbital contains its full complement of two electrons and the 2s orbital contains just the one electron. When one lithium atom bonds to a neighbouring lithium atom, the outermost electrons (the valence electrons) are involved in forming the bond. The two 2s electrons (one from each atom) form a *molecular bonding orbital* containing the two electrons[103]. This new orbital is lower in energy than the original orbitals, however when it forms, an additional unoccupied *antibonding orbital* forms as well; higher in energy than the original orbital. In this instance, the original 2s orbitals have combined by splitting in two.

The new *molecular bonding orbital* contains both electrons, both with opposite spins, as per *Hund's rule of maximum multiplicity*. If we were to take another lithium atom, the combined atomic orbitals will form three new orbitals, with the electrons filling them following the previously mentioned rules – one orbital at a time, increasing in energy, up to two electrons per orbital with opposite spins. In a metal, the atoms arrange in a repeating lattice with long range order, not individual molecules. This means that the number of atoms present will be extraordinarily vast, so electrons on each atom are influenced by the electrons on neighbouring atoms[104]. As this is repeated an inconceivably large number of times across the material's superstructure, the energy levels associated with individual atoms will widen into bands when considered en-masse in the bulk. Ergo, in the case of a metal, as in the example of lithium, electrical conductivity is possible as the electric field extends throughout

the crystalline lattice. Figure 2-2 illustrates the phenomena of band formation – as more and more atoms are added, a filled valence band forms as well as an empty conduction band.

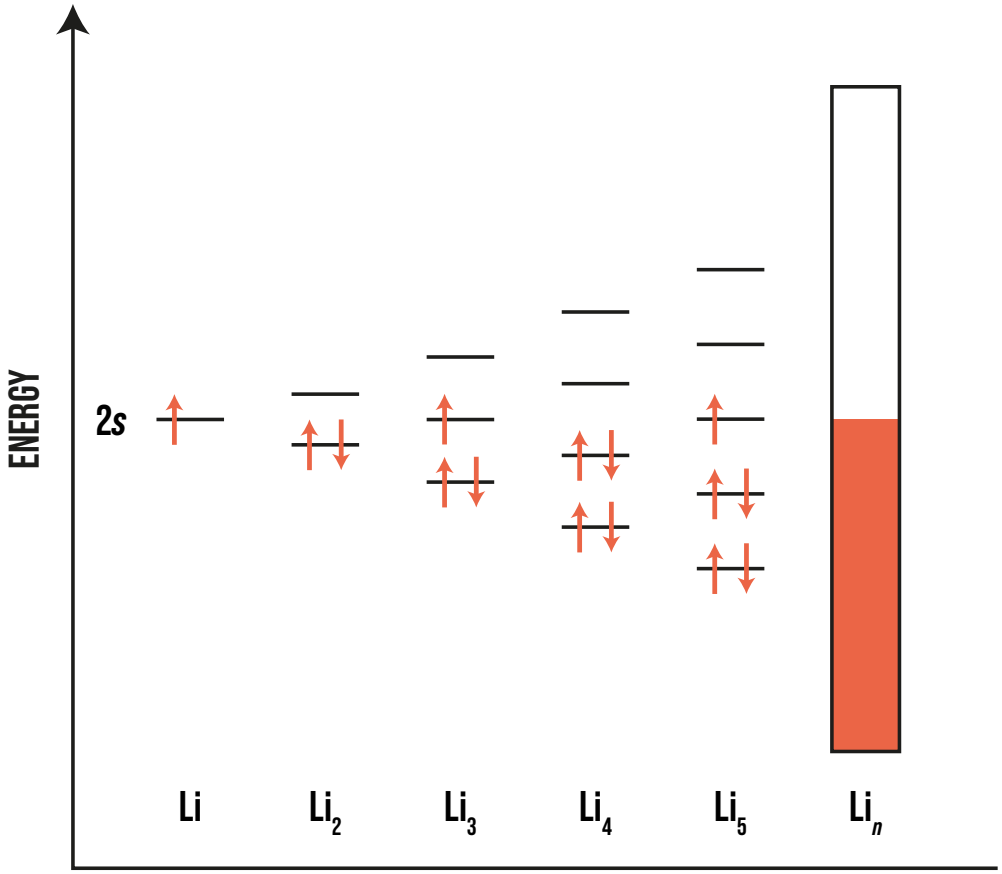


Figure 2-2 LCAO of Li. Adapted from Housecroft and Constable[103].

In conductors, there is no band gap between the valence band and the conduction band, resulting in electrical conductivity occurring with ease. In an insulator, the gap between the valence and conduction band is so large as to be insurmountable under normal conditions, and electrical conductivity is non-existent. Therefore, only the valence band possesses any electrons, the conduction band possesses no electrons at 0K[102], the valence band contains electrons as high as the material's Fermi level. Since the conduction band is 'off limits' it cannot conduct electricity, the only alternative method would require electrons to move into the quantum state of its neighbours in the valence band. Since those quantum states are also occupied, to do so would violate the *Pauli Principle.* The only place for it to go is into the conduction band which, while not impossible, is extraordinarily unlikely since an insulator has a band gap in excess of 4 eV[105]. The promotion of an electron into the conduction band in an insulator is possible only through dielectric breakdown which would necessitate an electric field of 10^{10} V/m.[102]

A semiconductor, whilst not as conductive as a pure metal, is able to overcome this obstacle. If the band gap is narrow enough, say "0.5-2.0 eV"[104] then, through thermal excitation, eliciting lattice vibrations which increase in intensity with temperature, travel across the band gap is possible. This kinetic energy is absorbed by some electrons - if enough energy is absorbed, then they will be able to cross the energy gap and inhabit the lowest levels of the conduction band. In this case, an electron-hole pair is formed. This charge may travel through the crystalline lattice thus enabling conductivity in the form of delocalised electrons. Since the electron-hole pair is formed through thermal excitation, it follows that the conductivity of a semiconductor is therefore proportional to temperature, as was first observed in 1833 by Michael Faraday[3].

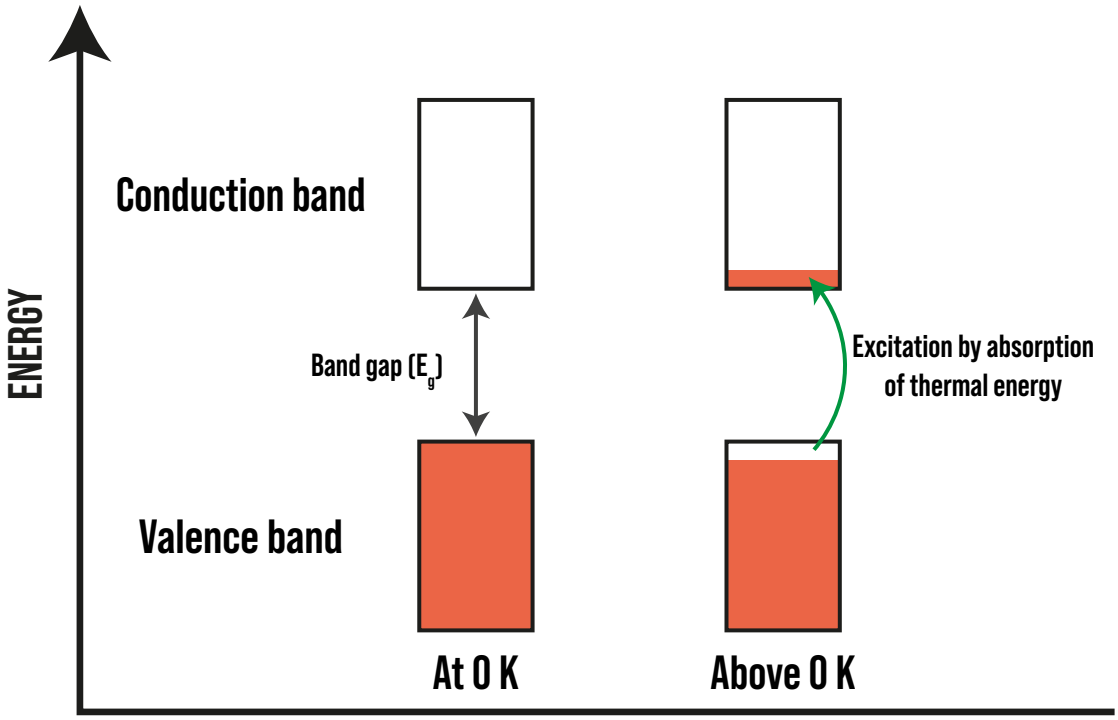


Figure 2-3 Thermal excitation of a semiconductor. At 0 K all electrons are in the valence band and there are none in the conduction band. Upon absorption of thermal energy, electrons are promoted across the band gap leaving behind holes. Electrons in the conduction band can now enable conductivity.

A material which exhibits pure semiconducting properties would appear at 0 K to be an insulator, owing to the presence of a band gap, with a full valence band and an empty conduction band. In comparison to insulators, the band gap of a semiconductor is much narrower, about 0.1-2 eV[105], though some can go up to 4 eV. As such, it is relatively easy to promote electrons across the band gap *via* thermal excitation. Normally at room temperature (298 K) a semiconductor will conduct electricity. Figure 2-3 illustrates the promotion of electrons across the band gap *via* thermal excitation.

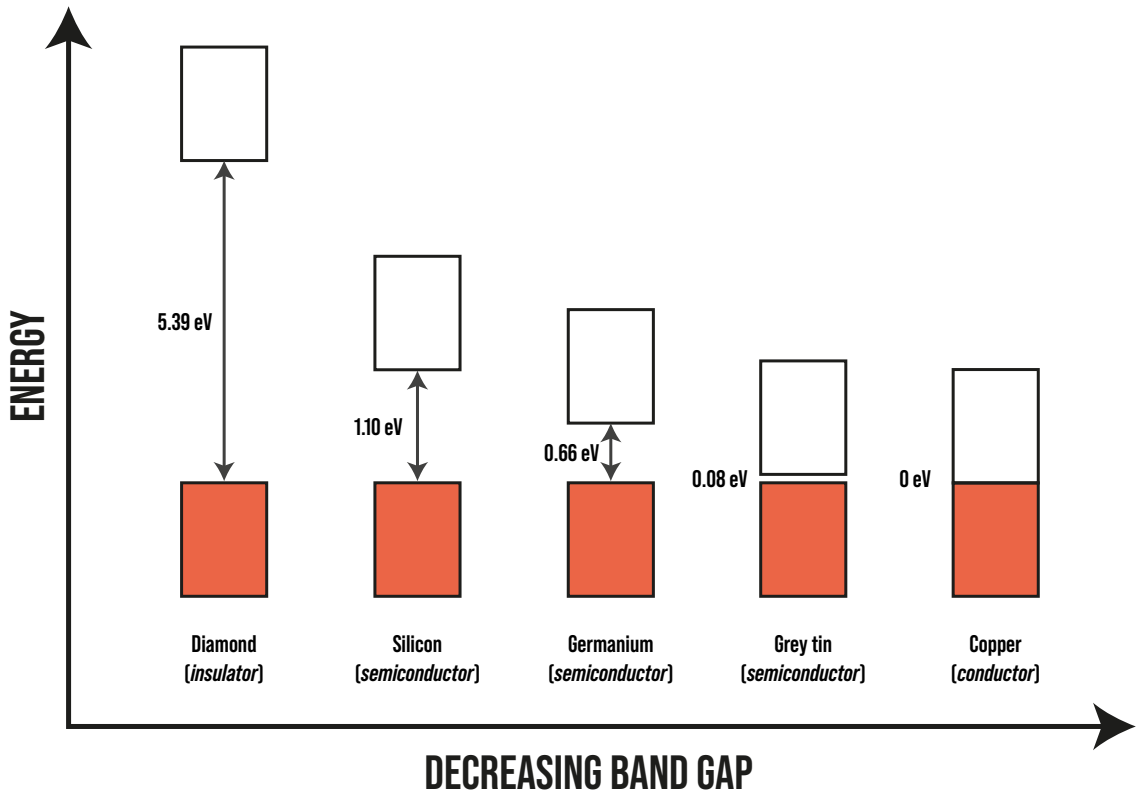


Figure 2-4 Comparison of the band gap between various conductors, insulators, and semiconductors. Adapted from Housecroft and Constable[103].

Figure 2-4 illustrates the difference in the band gap between a selection of insulators, conductors, and semiconductors. Converse to the positive correlation of temperature and conductivity of a semiconductor, a metal will exhibit negative correlation. This is a direct result of the vibrations in the lattice caused by the application of thermal energy (see Figure 2-5). In a metal, as the positive ions vibrate about their positions in the metal lattice, they distort the path of the electrons in a current. This increases the resistance of the metal. A semiconductor also exhibits this effect – vibration of atoms – however it reduces in resistance at higher temperature despite this effect because the gain in conductivity achieved by electrons traversing the band gap exceeds that of conductive retardation caused by lattice vibrations.

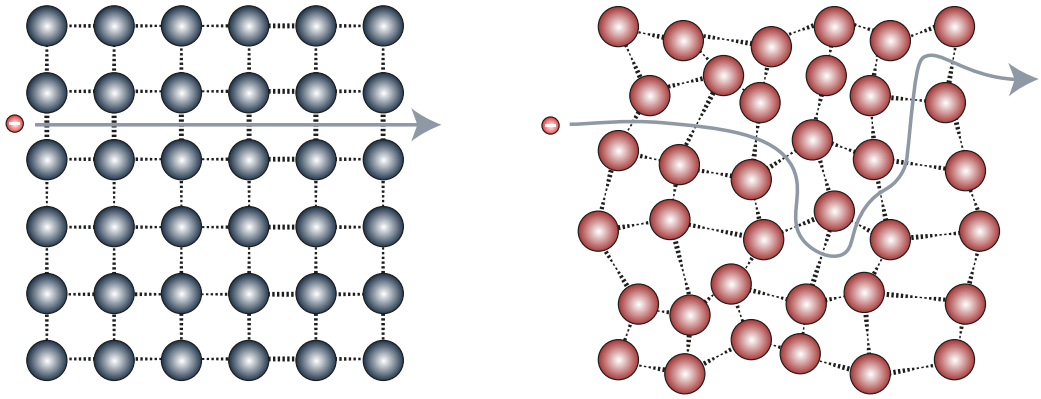


Figure 2-5 A 2-dimensional representation of how the path of electrons changes in a metal when heated. The same is true of semiconductors, but the negative impact up conductivity caused by the lattice distortions is negligible compared to the benefit of the electrons being able to traverse the band gap thanks to the heat energy applied.

2.3 Organic semiconductors

A vast quantity of research has focussed on inorganic-based semiconductor devices. Developments throughout the latter half of the twentieth century have demonstrated that organic compounds can be designed to demonstrate semiconducting properties as well[106–108]. Organic molecules and polymers have been incorporated into semiconductor devices such as organic field-effect transistors (OFETs), organic light-emitting diodes (OLEDs) and organic solar cells (OSCs)[109–111]. These have the advantage of being more flexible in terms of device design form factor[112,113], potentially biodegradable[114] and no longer require the use of toxic heavy metals or metals more difficult to access, thus improving safety and sustainability[114–116].

The key difference between inorganic and organic semiconductors is the use of *molecules* or *polymers* rather than elemental lattices (such as silicon). Organic molecules are arranged in a crystalline structure in semiconductors, sometimes without the regular long-range order associated with inorganic crystals. The molecules themselves contain conjugated π-bonds to allow electrons to delocalise across a molecule. This manifests in the form of carbon-to-carbon double bonds, but also aromatic rings. The wavefunction of the delocalised electron needs to be able to overlap with another molecule's electron wavefunction nearby to enable electronic conductivity similar to the aforementioned band structure of inorganic semiconductors or by electron hopping[117].

Organic semiconductors differ considerably from their inorganic counterparts. For starters, organic crystals have low melting points. This is a result of the difference in interactions between components of the crystal in each case. In an inorganic semiconductor, covalent bonds hold together the atoms in the lattice. In organic semiconductors, the covalent bonds are only *within* the molecules – since these are covalent molecules, there is no propensity to form bonds between molecules, so the only interactions between them are dipole-dipole interactions, hydrogen bonding and London Dispersion Forces. These intermolecular interactions are the only interactions to influence crystal structure in organic semiconductor materials. The massive difference in the strength of these interactions gives rise to the much-reduced melting points of organic semiconductors. The dominance of the intermolecular interactions can also result in deviation in the performance of organic semiconductors – slight temperature changes can cause significant changes to the crystal structure, resulting in distortions to the semiconductive character of the devices.

2.4 Band theory in organic semiconductors

The inorganic band theory method of describing semiconductors can be used for organic semiconductor compounds with a slight alteration. In this model, bands are replaced by frontier orbitals: the HOMO (highest occupied molecular orbital) replaces the valence band and the LUMO (lowest unoccupied molecular orbital) is analogous to the conduction band. The majority of optical transitions happen between the frontier molecular orbitals.

This can be illustrated with the simple molecular monomer, thiophene and its polymer, poly(thiophene)[118] (see Figure 2-6).

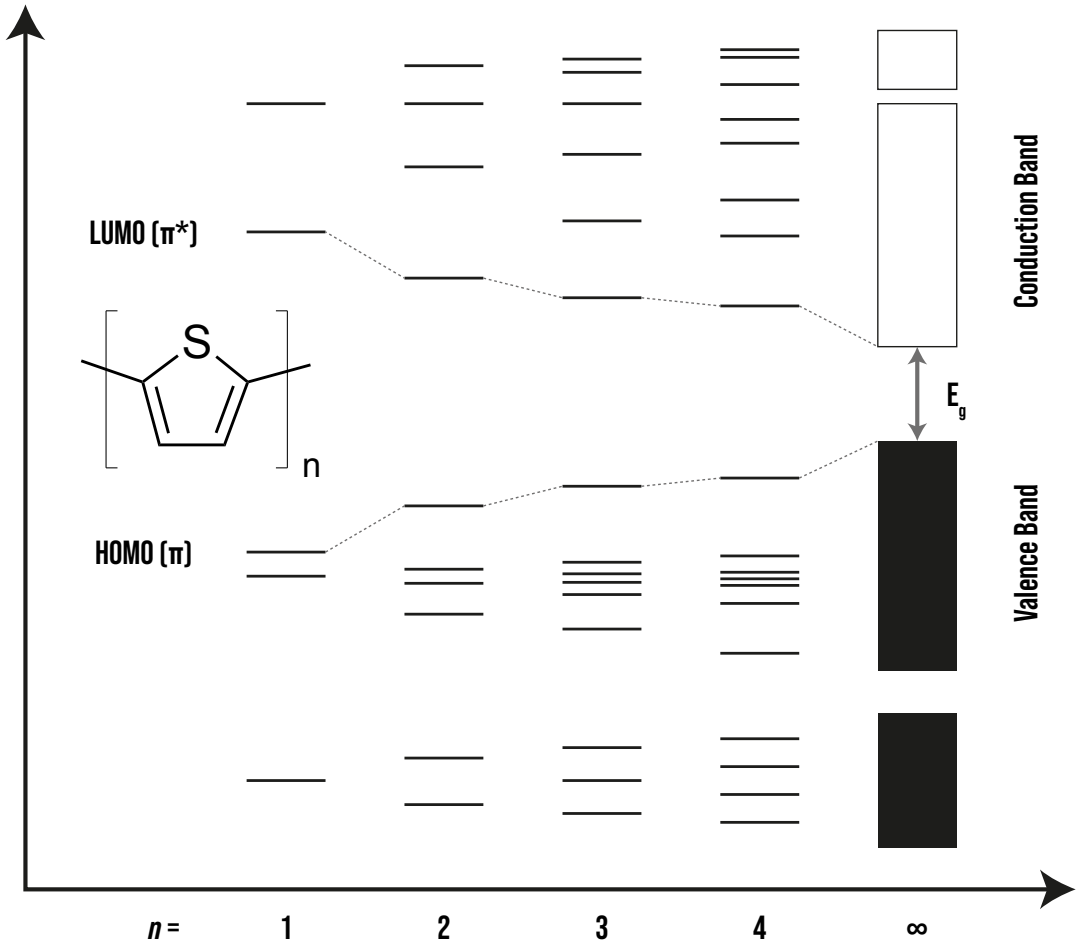


Figure 2-6 Relative energy levels for oligothiophenes with increasing number of repeat units. Based on Salzner *et al.*[118]

Organic semiconductors possess conjugated structures with alternating single and double bonds (be they aromatic or from C=C double bonds). Since carbon is exhibiting sp^2 hybridisation, once overlap of two sp^2 orbitals produces a σ-bond between two carbon atoms, the remaining two p-orbitals perpendicular to this plane overlap to form a π-bond between

the two atoms. There is not much difference in energy between the π and π* orbitals, so when many monomers are connected into a polymer system (or indeed when many molecules overlap in a crystalline system), the overlap between the molecular orbitals increases to such a degree that we can observe the formation of bands – valence bands where the π-orbitals have overlapped and conduction bands where the π*-orbitals have overlapped. See Figure 2-6 for a classic example of where this occurs in a an oligothiophene with increasing number of repeat units.

No more than one electron is permitted to occupy the same quantum state at one time (as per the *Pauli Exclusion Principle*). Electrons occupy orbitals in order of increasing energy, filling those of lower energy first (as per the *Aufbau Principle*). Each orbital can hold two electrons, each of opposing spin (+1/2 and -1/2)

When considering the HOMO and LUMO, there are 5 possible combinations of the orbitals, as described in Figure 2-7.

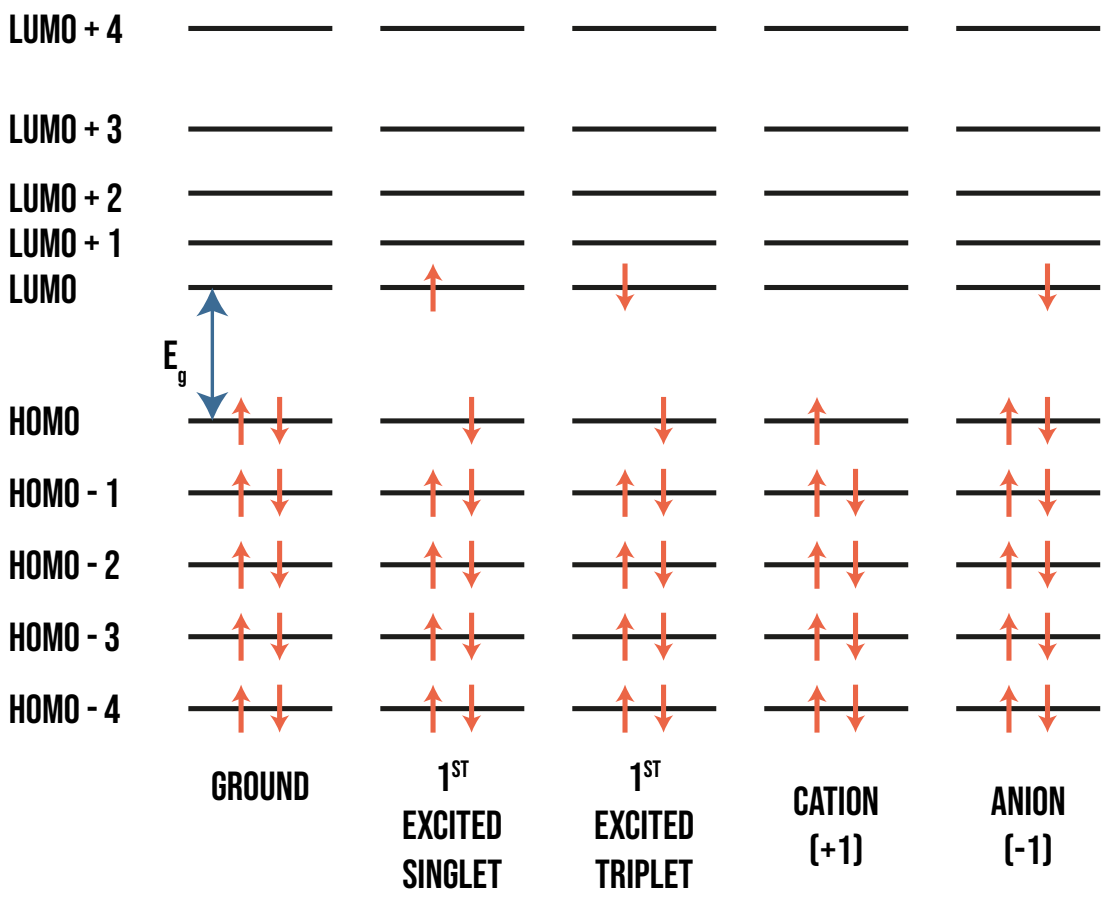


Figure 2-7 The five main combinations of molecular orbital excitations. Adapted from Forrest[34].

Rather than atoms and ions forming the superstructure, organic crystals consist of arrangements of molecules. Using the proximity approach, we can replace atomic orbitals in band theory with molecular orbitals. The HOMO consists of two π-electrons which results in the molecule being in the singlet ground state (S_0). These molecules can be excited to excited singlet (S_1) or triplet (T_1) states. Higher singlet and triplet states are possible, but their lifetimes are much shorter.

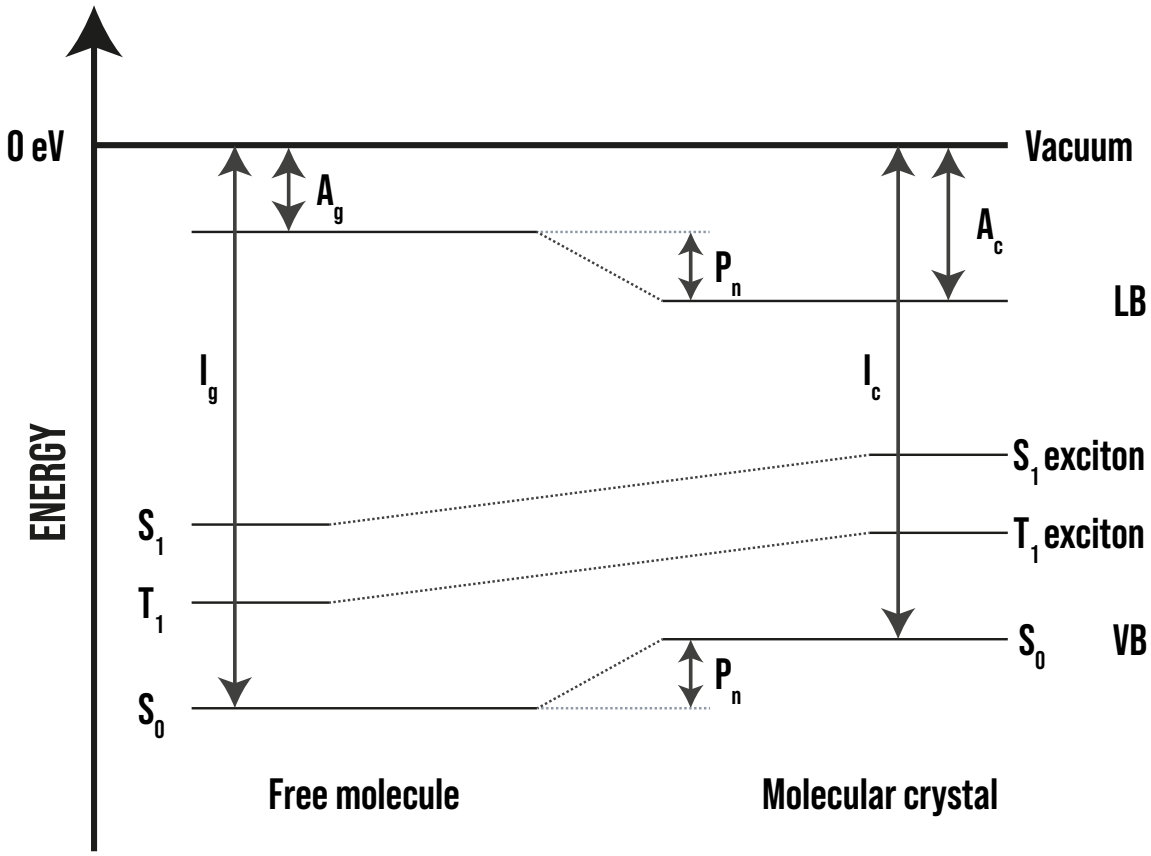


Figure 2-8 The excited states of free organic molecules and their crystalline form. Adapted from Pohl[119]. Here the ground state and excited states are labelled, as well as in the crystal lattice the valence band (VB) and the lower branch (LB) – the hole-based level of the valence band.

The **ground state** is characterised by all orbitals being filled with a pair of electrons up to and including the HOMO. Above this is the LUMO, separated from the HOMO by an energy gap E_g. The value of E_g is equal to the difference between the energy of the HOMO and LUMO as shown in Equation 2-5:

$$E_g = E_{LUMO} - E_{HOMO}$$

Equation 2-5 HOMO-LUMO energy gap equation.

When the orbitals are filled to this level and possess a pair of electrons each, it is referred to a *closed shell* system, where all electrons are paired such that N electrons fill N/2 number of orbitals.

Singlet states possess electrons with opposing spins ($+^1/_2$ and $-^1/_2$), with an overall spin of S = 0, whereas triplets have electrons with spins in the same direction, with an overall spin of S = 1.

The **first excited singlet state** (S_1) occurs when one of the HOMO electrons is promoted into the LUMO, whilst conserving its spin. This is an example of an *open shell* system. When a promoted electron relaxes back to the ground state (S_0) from the singlet state, light can be emitted *via* fluorescence.

The **first excited triplet state** (T_1) is formed when a HOMO electron is promoted into the LUMO, whilst changing its spin (+1/2 → -1/2 or -1/2 → +1/2).

Further states include **cations** and **anions**, where the system has lost or gained a single electron and is positively or negatively charged respectively. If an electron receives sufficient energy, it can be removed from the molecule *via* ionisation, the energy in the gas phase of which is I_g, from S_0 to the removal of electrons; A_c refers to the electron affinity – the addition of an electron to a molecule forming a negative ion. When an electron in a HOMO gains sufficient energy, it is promoted to just below the LUMO, leaving behind a positively charged hole. In a similar way to inorganic semiconductors, the LUMO behaves much like a conduction band and the HOMO like the valence band. The electron and hole are still bound to one another here and are effectively a quasi-particle known as an exciton (electron-hole pair).

When a molecule gains an electron in its LUMO, the negative charge will cause distortions to other molecules surrounding it. Electrons in the LUMO can travel across the semiconductor. As the LUMO electron travels through the crystal, the distortions in molecules surrounding it also travel with it. This distortion of its surroundings alters the *effective mass* of the electron, influencing its passage through the crystal. The electron in the LUMO and the distortion travel through the crystal together as a quasiparticle known as a *negative polaron*. Similarly, the hole in the HOMO distorts its surroundings and travels with that distortion as a *positive polaron*.

Polarons are the mobile quasi particle of cations and anions in the solid state. As charge from one ion passes to the neighbouring molecule (making a new ion and returning the original ion to the ground state) it appears that an ion is traveling throughout the solid - the polaron. When an ion's charge moves from one molecule to another, the state formed is referred to as a charge transfer state. The polarons' energy (see Figure 2-8) is given as follows[119] :

$$P_p = I_g - I_c$$

$$P_n = A_c - A_g$$

Where P_p = positive polaron; P_n = negative polaron; I_g and I_c refer to the ionisation energies of the molecule in the gas phase and crystal form respectively; A_g and A_c refer to the electron affinities of the molecule in the gas phase and the crystal lattice respectively.

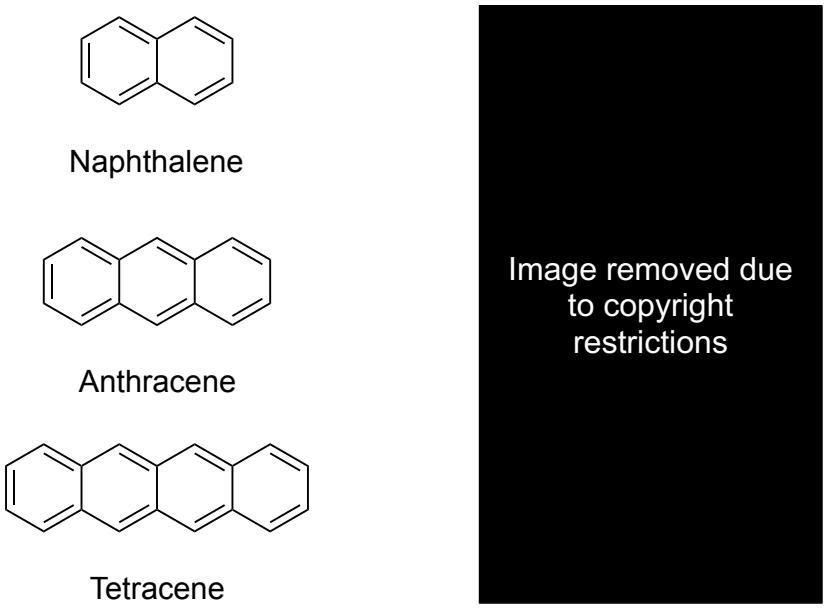


Figure 2-9 The width of the HOMO and LUMO in tetracene, anthracene and naphthalene crystals as temperature is increased. Taken from Hannewald *et al.*[120]

Normally the polarons are considered only as electrons and holes in descriptions of organic semiconductors. As the electrons and holes pass by a point in the lattice due to application of current, the lattice distortions will relax back to their original positions. This process is slower than their original distortions and it influences the band gap energy by lowering it (by 0.3 eV in anthracene[119]). When the lattice is distorted, the HOMO-LUMO gap is the "optical band gap" and when it has relaxed back to its original position it is the "adiabatic band gap".

The size of valence and conduction bands is controlled by the van der Waals forces, so they are smaller. At 0 K, the width of the HOMO and LUMO bands is at its largest. At higher temperatures these bands begin to narrow (see Figure 2-9) because the electrons and their respective distortional phonons are progressively more coupled together[120]. This traps the phonon-electron couples (much like soap micelles around grease). Movement of electrons proceeds *via* "hopping" at increased temperatures. The HOMO-LUMO gap (or strictly speaking the *transport* gap) is the difference in energy between the HOMO and the LUMO. To cross the band gap, Frenkel excitons (electron-hole pairs) are formed when electrons are injected *via* a current.

There are similarities between organic semiconductors and inorganic ones with amorphous structures. Both contain a significant degree of disorder in their structures, which results in band gaps not being as clear cut as those found in inorganic semiconductors with regular crystalline lattices. This distortion is caused by alterations to the positioning and angling of molecules in the lattice and its effects on bands referred to as band tailing, or Lifshitz tails[119]. Distortions also arise when a semiconductor is doped, however this can be a constructive distortion. Semiconductors with doping exceeding a density of 10^{17} cm^{-3} results in electron paths deviating when they encounter other electrons with a parallel spin to their own. Opposing spin electrons are attracted together. This process lowers the band gap.

2.5 The physics of phosphorescence and fluorescence in organic molecules

2.5.1 Excited states

When electricity or ultraviolet radiation is used to excite electrons, two paths are possible: the generation of a singlet, which decays by fluorescence or non-radiatively; or generation of a triplet from the excited singlet, which decays by phosphorescence or non-radiatively. The triplet formation pathway is three times more likely than the singlet formation pathway. Since only singlets can decay *via* fluorescence this limits the fluorescence quantum efficiency (the internal quantum efficiency, IQE) to 25% and the remaining excitons remain trapped as triplets which can decay non-radiatively. One of the main goals in the development of new emissive materials is to harvest the remaining 75% of excitons from the triplet states. An excited state is formed when an electron in the ground state (HOMO) is raised in energy to an orbital of higher energy, but absent of any electrons[121].

Transitions can occur from three orbital types :

σ – orbitals; π – orbitals; n – orbitals (non-bonding electrons of heteroatoms like N or O)

These transitions are:

$\sigma \rightarrow \sigma^*$ Transitions associated with the far UV

$n \rightarrow \pi^*$ } Absorption spectroscopy can see these

$\pi \rightarrow \pi^*$ } 200 nm → 700 nm

The type of excited state formed is dictated by quantum mechanics – the spin of the electron involved in the transition, S, which gives rise to the multiplicity of the molecule, M.

$S = \Sigma S_i$ $S_i = +1/2$ or $-1/2$

$M = 2S+1$

In a singlet, M = 1 $2(0)+ 1 = \underline{\mathbf{1}}$

Therefore, the spin of the electron remaining in the HOMO will be *anti-parallel* when compared to the excited electron in the LUMO[122].

In a triplet, M = 3

$2(1) + 1 = \underline{\mathbf{3}}$

The spin of the excited electron and the remaining electron are the same – meaning that they are parallel[122].

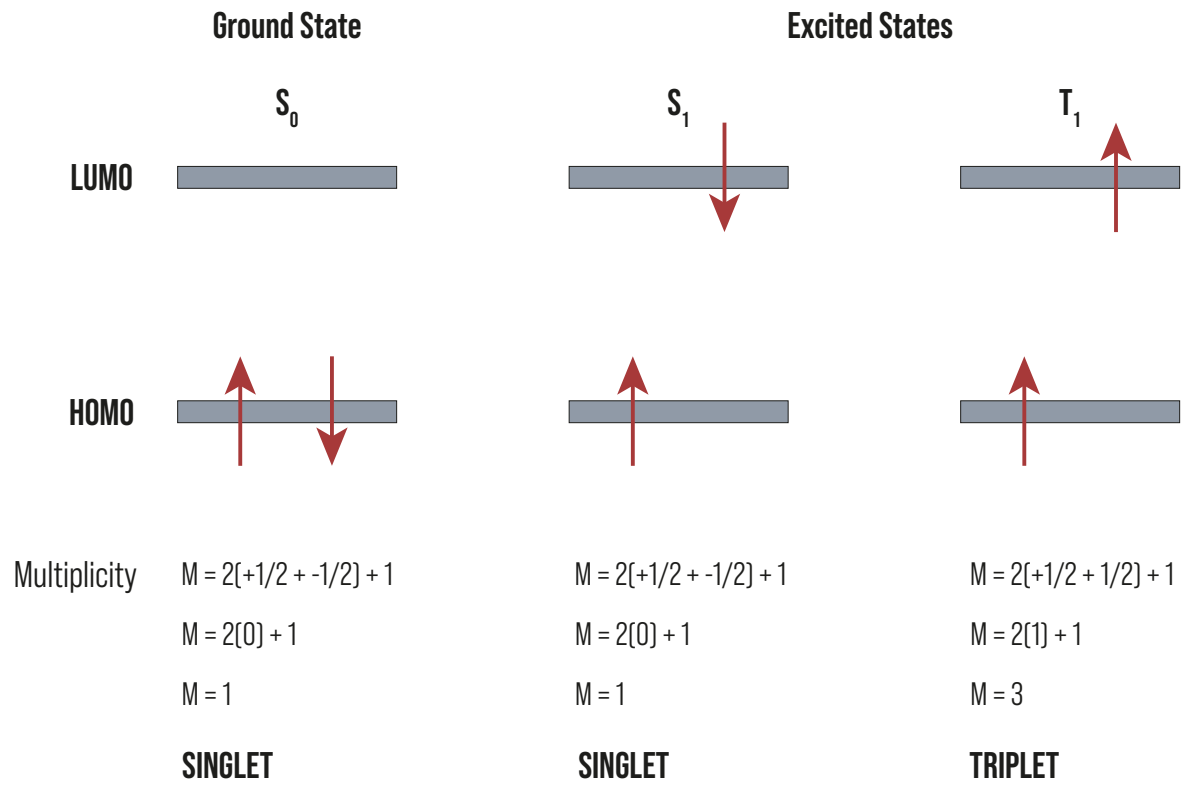


Figure 2-10 The multiplicity of the most commonly encountered ground and excited states.

Therefore, the terms *singlet* and *triplet* refer to the multiplicity of the electrons in accordance with *Hund's Rule of Maximum Multiplicity* – the system with spins in a more energetic orbital parallel to that of a lower orbital will have the lower energy, whereas opposing spin systems will have higher energy. This translates as singlets, with their *anti-parallel* spins, being higher in energy than the triplets, with their *parallel* spins (see the above Figure 2-10 for an illustration of the rationale behind spin and the state multiplicity).

This 1:3 ratio of multiplicity is also behind the distribution of excited states, namely that only 25% become singlets and 75% become triplets[123]. The processes associated with energy transformation of singlets and triplets can be visualised in a Jablonski diagram (see

Figure 2-11 and Figure 2-12) named after Polish physicist, Aleksander Jabłoński, who illustrated a letter to *Nature* in 1933[124] with a figure progenerating the diagram which today possesses his namesake.

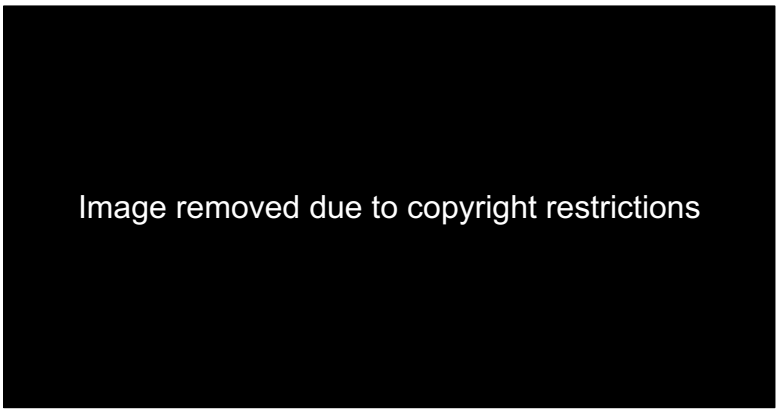


Figure 2-11 Jabłoński's original 1933 sketch illustrating the different photophysical processes in dyes. Taken directly from the letter to *Nature*[124].

A clearer and more detailed version of Jabłoński's original concept can be used to describe the transitions of materials of significance to this study. One such interpretation can be seen in Figure 2-12.

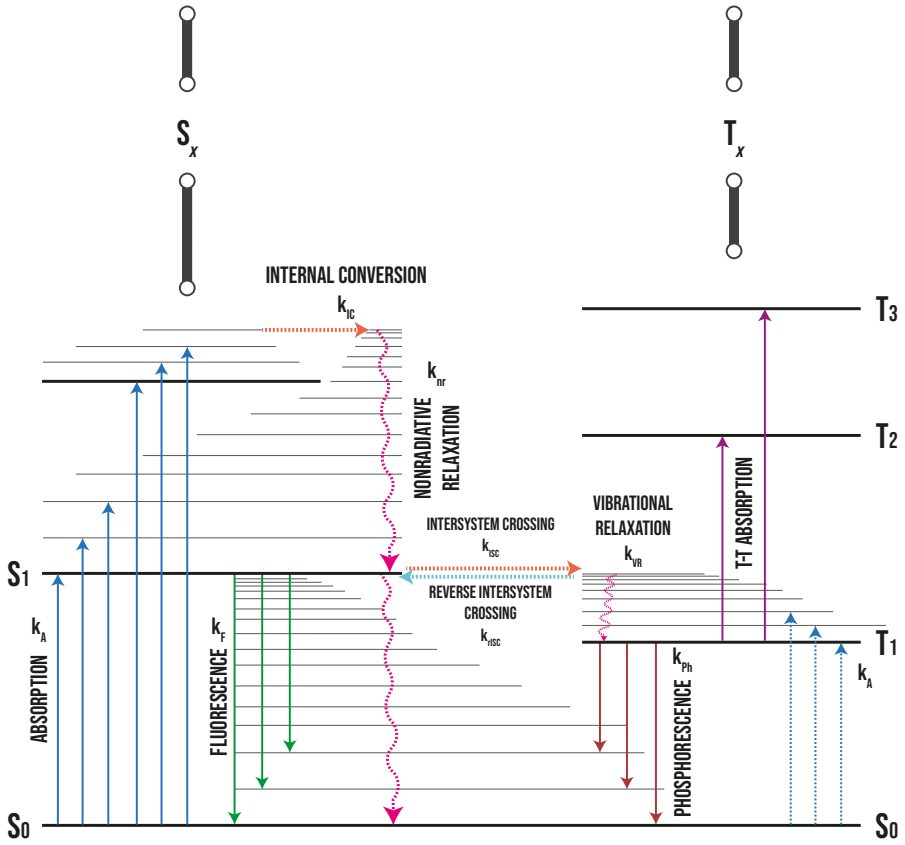


Figure 2-12 Jablonski diagram for the lower singlet and triplet states incorporating transitions relevant to fluorescence, phosphorescence and TADF. Curved arrows represent non-radiative transitions. Adapted from Forrest[34].

Fluorescence occurs from the excited singlet states (S_1 and S_2, *etc*.) to the ground state (S_0, which is almost exclusively a singlet state also). It can also occur between the T_2 and T_1 triplet states.

Phosphorescence is a much less common process since it is spin forbidden, so transitions between the singlet and triplet manifolds must first undergo intersystem crossing (ISC) to populate the singlet states. Depending on the energy of the destination vibrational triplet state, ISC can be an isoenergetic, exo- or endothermic process. Normally this process is facilitated by spin orbit coupling thanks to the heavy atom effect, necessitating the use of heavy atoms (such as metals) to convert singlets to triplets by spin flipping.

When a molecule's excited state decays to the ground state with no emission of radiation, the process is described as non-radiative decay. This occurs when energy is lost through vibrations, bond bending, heat release, *etc*. Design of molecules seeks to avoid this loss pathway wherever possible as it can significantly reduce a compound's photoluminescent efficiency.

Transitions between states of the same multiplicity (*i.e*. $S_2 \rightarrow S_1$, or $T_2 \rightarrow T_1$, *etc*.) occurs by a process known as internal conversion (IC). Between the excited states are multiple vibronic energy states - a molecule can transition between these states through energetic decay by a process known as vibronic relaxation (VR). This is accompanied by the release of energy in the form of vibrational modes. The opposite process is also possible, when a molecule gains energy to enter a higher vibrational state.

When a molecule is excited from the ground state (always a singlet, S_0, in the materials which we are concerned with), in both electroluminescence and photoluminescence, an electron absorbs energy and is promoted to the next singlet excited state, S_1, but if more energy is provided then the state is S_n (where n is any positive integer[125]) is reached. Following this, the electron can decay *via* vibrational relaxation within the same energy level, and internal conversion (IC) to the S_1 first excited singlet state (if excited to S_n first). Excited singlet states can decay radiatively (*via* emission of radiation) or non-radiatively (*via* internal conversion, IC, *via* vibrations and rotations), liberating heat. Internal conversion can only occur if multiplicity is conserved (*i.e*. to another singlet state – not to a triplet). If the emissive transition is from a singlet, then the process is known as *fluorescence* ($S_1 \rightarrow S_0$). The energy gap between S_1 and S_0 is commonly referred to as the *optical gap*[126].

In accordance with the Franck-Condon principle, if a fluorescent molecule is excited by absorption of light, then the light emitted *via* fluorescence will have wavelengths longer than the light absorbed, or, in the case of excitation by electric current, less energy than the energy absorbed, because some energy is lost *via* vibrational transitions prior to the remaining energy's emission – some is lost to the environment or surrounding molecules.

An alternative path to that of fluorescence is intersystem crossing (ISC) to the triplet excited state, which involves a change in electron spin multiplicity, followed by internal conversion to the T_1 triplet state. During the internal conversion, vibrational transitions also occur, lowering the molecule's energy through collisions and transfer to the environment, until the lower level of the triplet state is reached. At this point, further emission *via* transition to the singlet ground state is 'impossible' as it would violate the Pauli Principle and is thus spin forbidden. One cannot transfer directly from an excited triplet state to a singlet ground state. However, since ISC is possible, phosphorescence does in fact occur, but the process is weak and occurs over a prolonged time frame when compared to fluorescence. Heavy atoms are required to enable the flipping of electron spins in singlet to triplet and triplet to singlet transition, a process known as 'the heavy atom effect'[127]. The process of phosphorescence involves transition to the ground state ($T_1 \rightarrow S_0$).

Often mentioned in OLED research is the ΔE_{ST} gap energy, which is the difference in energy between the S_1 and T_1 states. This energy is closely linked to the rate of ISC and the opposite process, rISC, and is an important factor in the population of both excited states.

2.5.2 Electronic transitions and molecular spectra

Transition types

A chromophore is a functional group on a molecule which is associated with a specific colour, more specifically, associated with the electronic transition corresponding to the absorption of a specific wavelength. For example, carbonyl groups, C=O, are associated with n → π transitions, that is a non-bonding lone pair electron on the oxygen (n) is promoted into a vacant π^* antibonding orbital, through absorption of 290 nm, or 4 eV[128] (see Figure 2-13).

In a π non-conjugated bond, C=C, the transition is between a π-orbital and its antibonding π^*-orbital, π → π^* and is about 180 nm required to instigate the transition through a 7 eV energy gap[128]. In conjugated double bond systems, much less energy is required to jump the gap as the π and π^* energy levels are in closer proximity.

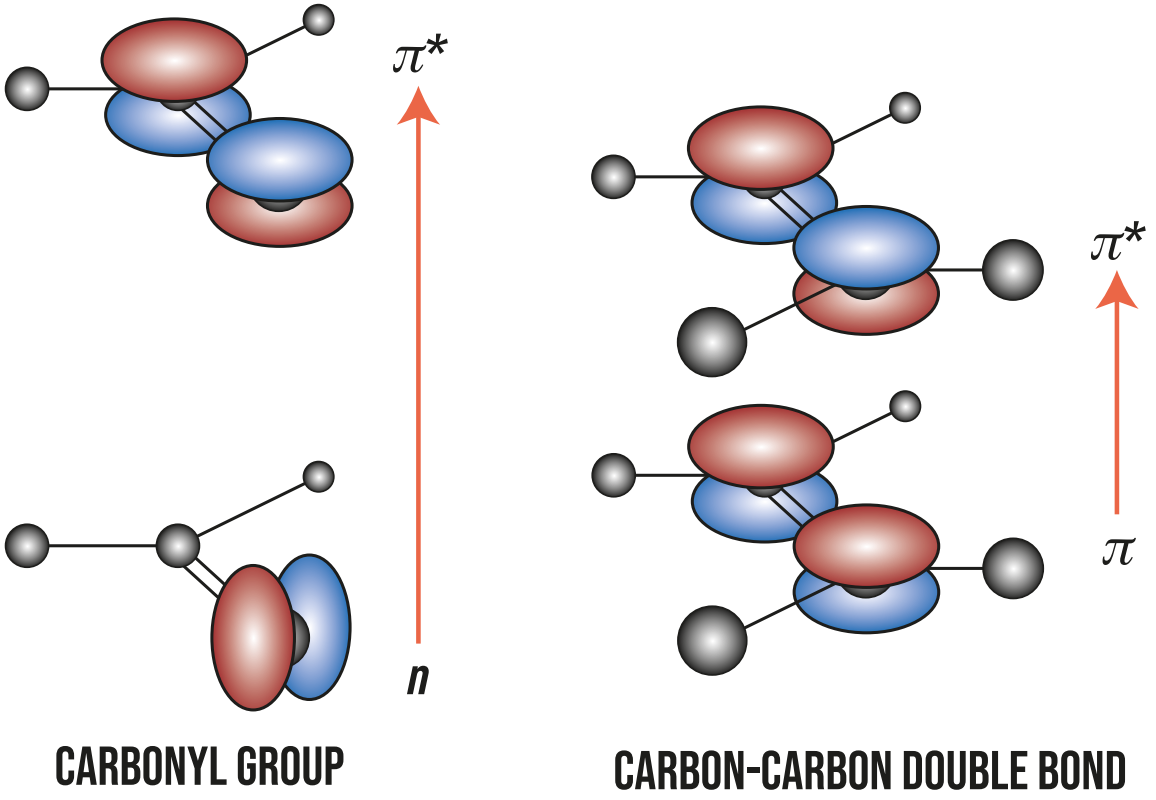


Figure 2-13 Illustration of the orbitals involved in the n - π* transition in a C=O carbonyl functional group (left) and in a C=C carbon – carbon double bond (right). Adapted from Atkins and de Paula.[128]

Molecular spectra

The vibronic energy levels of both the singlet ground state and the excited singlet state can be represented in the following diagrams:

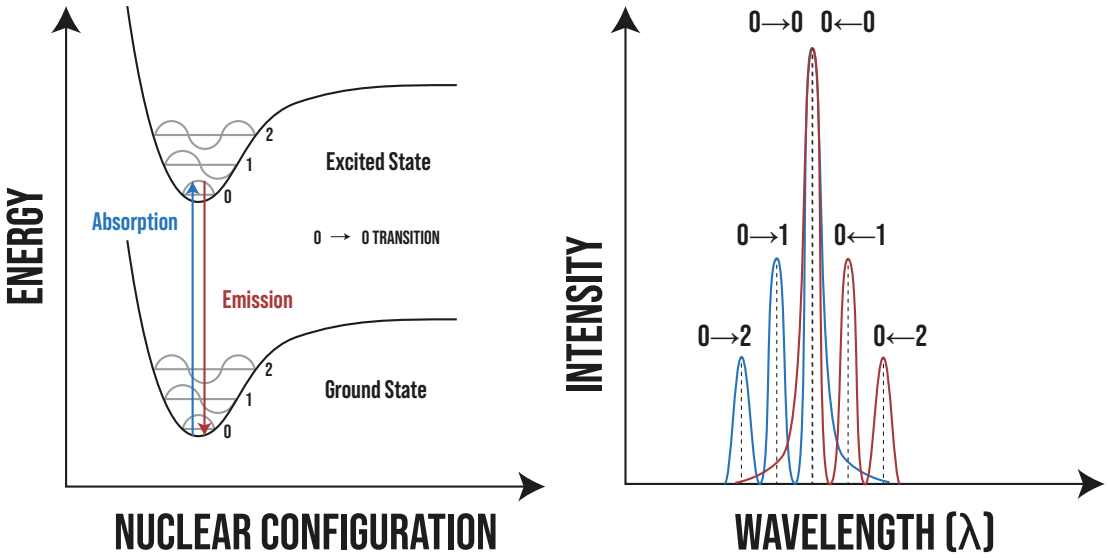


Figure 2-14 Illustration of the transitions in accordance to the Franck-Condon principle when the molecule undergoes no change to its geometry in the excited state.

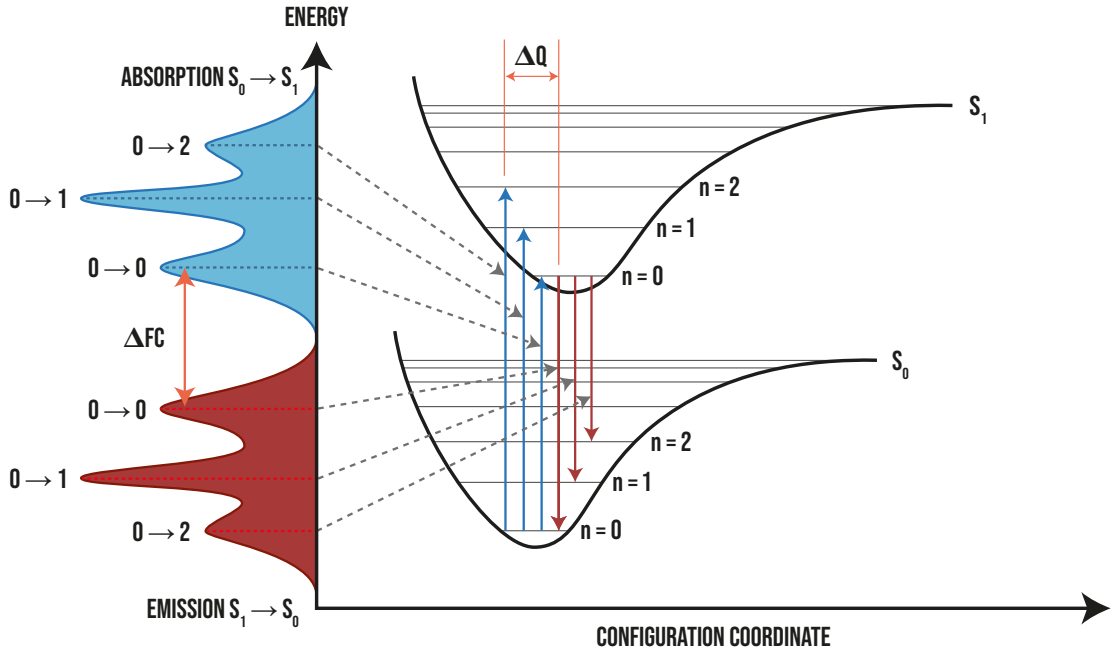


Figure 2-15 Singlet ground and first excited state potentials as a function of configurational coordinate (*Q*) when the geometry of the excited state changes relative to the ground state. Each grey line represents the vibronic level pertaining to quantum number *n*. The emission and absorption spectra are illustrated on the left, labelling the vibronic state transition to which each peak belongs (blue vertical lines and spectra represents absorption, red emissions). The Stokes shift is labelled as *ΔF*, representing the difference in wavelength between the first emission and absorption peak going from two *n=0* states. The change in configuration geometry caused by the $S_0 \rightarrow S_1$ transition is represented by *ΔQ*. Adapted from Forrest[34].

Since their structures differ slightly, their configuration coordinate (Q) is shifted by a small amount (ΔQ). The population of the vibronic states follows the Boltzman distribution via Equation 2-6:

$$N(n_i) = N(0)\exp\left(\frac{-n_i\hbar\omega_1}{k_B T}\right)$$

Equation 2-6 Boltzman distribution of electron population of vibronic states. From Forrest[34].

This relationship is called Kasha's rule, which effectively means that the greatest intensity of emission and absorption can be associated with transitions to or from (respectively) the lowest energy vibronic level in S_0 if the excited state and ground state geometries do not change (see Figure 2-14). This results in the absorption and emission spectra being mirror images of one another. In the event of the structure of the molecule changing in the excited state, the emission is shifted by wavelength ΔFC - the Stokes's or Franck-Condon Shift, as illustrated in Figure 2-15.

Absorption involves a transition from the ground state to a non-relaxed excited state, higher in energy than the original state. Following the transition, the molecule will relax into an equilibrium geometry, a process which takes between 10^{-14} and 10^{-12} s - *i.e.* the lifetime of a phonon.

On the other hand, the emission process, where one relaxed excited state loses energy to return to the ground state, the energy lost in the process is equal to the Frank-Condon shift - *i.e.* the difference in energy between the transition from the n = 0 vibronic state of the S_1 excited state to the n = 0 vibronic state of the S_0 ground state.

This process can be nicely illustrated by the work of Chen *et al.*[129], where transitions of the molecule FIPAC in methyltetrahydrofuran solvent were studied at different temperatures resulting in shifts in configuration coordinate. When excited at low temperatures, transitions to the LUMO result in a $S_0 \rightarrow S^*$ transition, with the geometry of the molecule adopting the S* conformation (see Figure 2-16). Emission from here back to the ground state occurs at 435 nm, with an energy gap of 2.85 eV. Warming the molecule up to room temperature provides sufficient energy that when in the excited state, the molecule undergoes a conformational change to the P* state, which is lower in energy than the S* state, resulting in emissions of 595 nm and an energy gap of 3.43 eV.

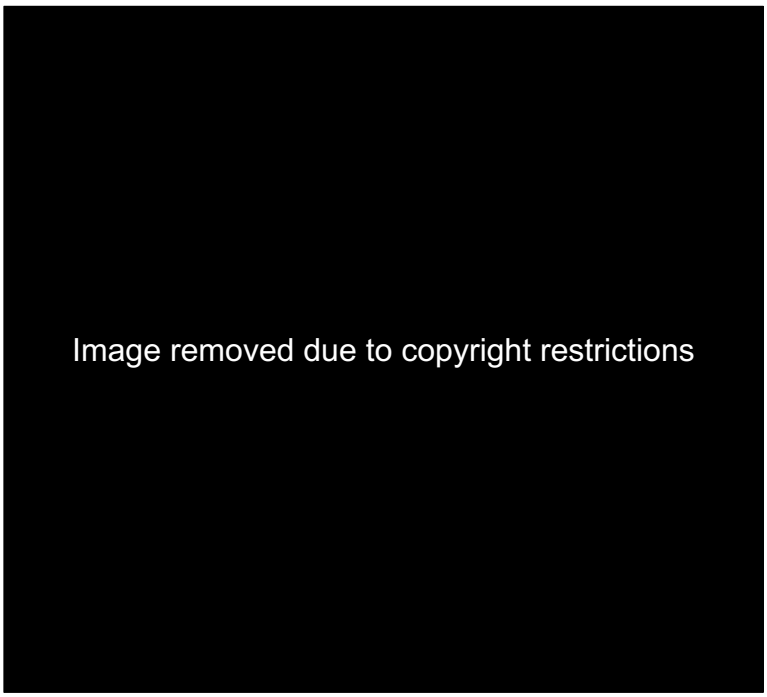


Figure 2-16 Thermally driven transition between the two conformers in Chen *et al.*'s[129] work. Diagram taken from Chen *et al.*'s paper[129].

2.5.3 HOMOs, LUMOs and states

One should be careful not to confuse the frontier orbitals with the electronic states.

An orbital is the region of probability where one may find an electron or hole in space bound to a molecule. They are referenced with respect to vacuum, so one can calculate the ionisation energy (IE) and the electron affinity (EA) of a molecule by first measuring the value of the molecule's HOMO and LUMO. The ionisation energy of a molecule is the energy required to remove an electron bound to an atom when in the gas phase; it can be ascertained from the HOMO energy by the equation:

$$IE = - E_{HOMO}$$

The electron affinity is the energy expelled when an electron is added to the system; it is obtained from the LUMO:

$$EA = - E_{LUMO}$$

A state differs in that it refers to the molecule, based upon configuration of electrons between the HOMO and the LUMO. An example is the singlet ground state, where the electrons are

both in the HOMO with opposite spin; the first excited singlet state, in which the HOMO's electrons are split up such that one is in the HOMO and the other is now in the LUMO (both with opposing spins); and the first excited triplet state, where once again one of the HOMO's original electrons remains in the HOMO and the other is in the LUMO, this time with parallel spins (see Figure 2-17). For clarity, this is not normally shown on Jablonski diagrams illustrating the change in states.

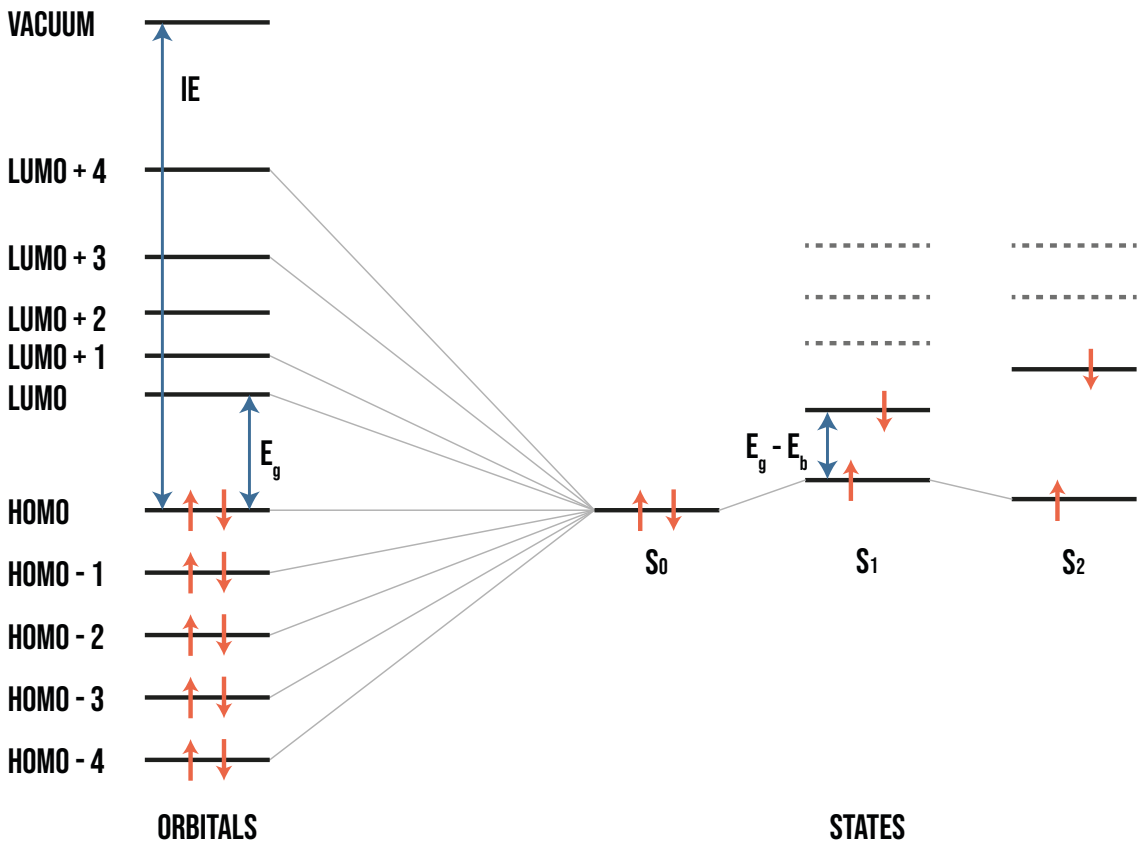


Figure 2-17 Illustration of the differences between orbitals and states with respect to electron spins. Adapted from Forrest[34].

The effects of the other orbitals (HOMO - 1, HOMO - 2… HOMO - n and LUMO + 1, LUMO + 2… LUMO + n) decrease as the orbital increases in distance from the band gap (*i.e.* as n increases).

2.5.4 Mobile excited quasiparticles - excitons

An exciton is an excited state in a solid state compound. The molecules themselves cannot travel across the bulk solid. However, they can pass their energy to one another, making it to all appearances seem as though the excited state itself is moving - a mobile quasi particle referred to as an exciton.

Electrical fields external to the compound have no influence on the exciton's travel because the exciton is chargeless.

2.5.5 Dimers, excimers and exciplexes

When two molecules agglomerate *via* aggregation, the result is known as a dimer. If the interactions are through van der Waals forces, it is called a physical dimer; however, if they chemically bond, it is a chemical dimer. Dimers cause the formation of band structure in the energy levels and bathochromic shifts in emissions, which can occur simultaneously with monomer emissions[34].

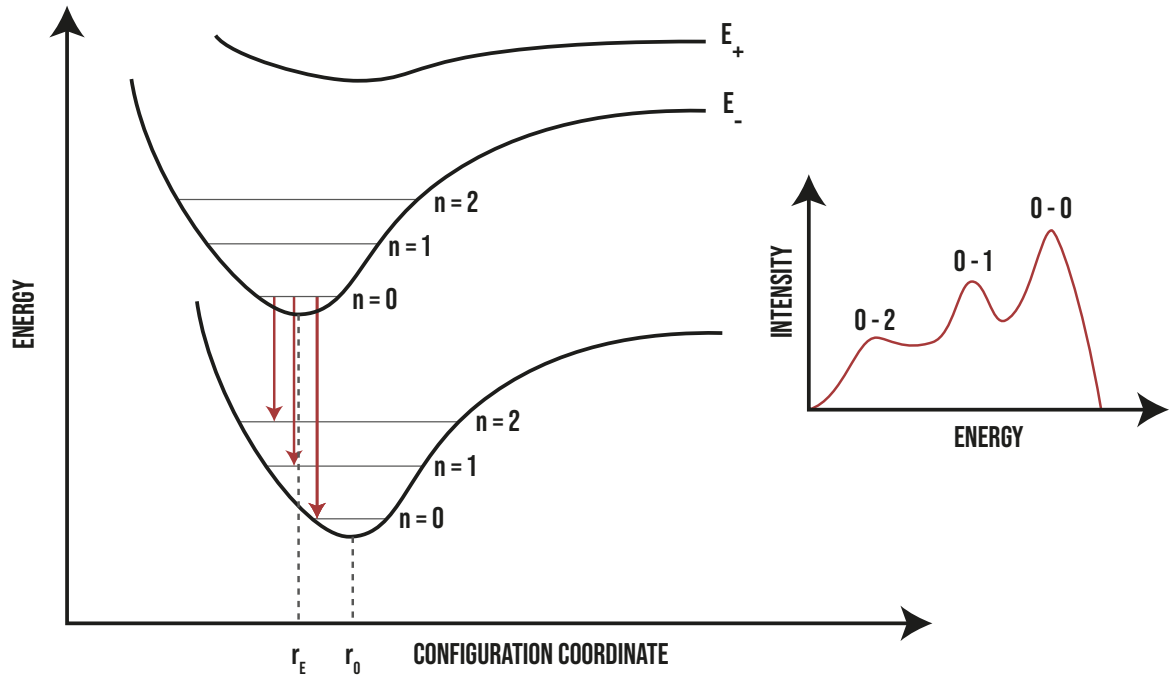


Figure 2-18 Configurational energy diagram illustrating the formation of a dimer. Vibronic structures are visible in the associated luminescence spectra. r_E and r_0 represent the equilibrium geometry in the excited state and the ground state geometry respectively. Adapted from Forrest[34].

An excimer is an excited state dimer, formed when two neighbouring molecules interact together when one is in an excited state, and the other initially the ground state[34]. When excited in this case, the dimers are bound to one another closely. If the two molecules are not identical, then the system is referred to as an exciplex. The terms excimer and exciplex are portmanteaux of excited-dimer and excited-complex, respectively.

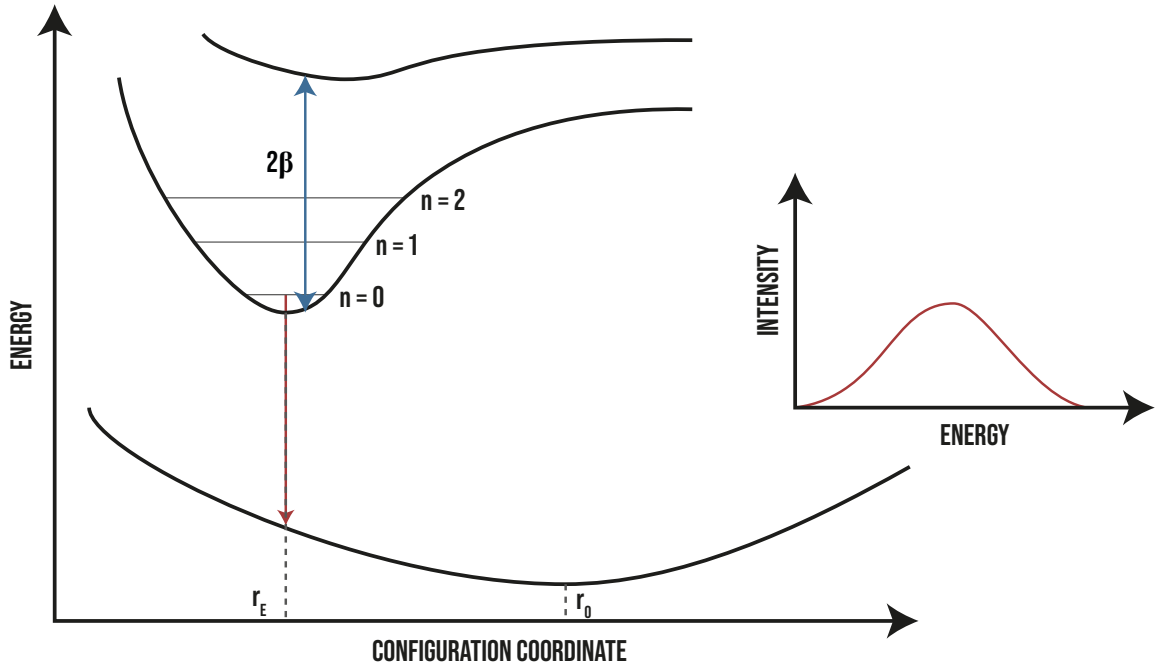


Figure 2-19 Configurational energy diagram illustrating an excimer. The accompanying luminescence spectra is featureless and broad. Adapted from Forrest[34].

Configurational energy diagrams of dimers and excimers (see Figure 2-18 and Figure 2-19) illustrate the excited state splitting in the dimer and the absence of a ground state for the excimer (since in this case the dimer can only exist when the molecules are excited). The vibronic transitions present in the dimer from the excited state to the ground state gives rise to peaks in the luminescence spectrum, whereas in excimers, the spectrum is broader. As such, analysis of the emission spectra allows one to ascertain whether dimerisation or excimer formation is occurring.

Excimers are often formed in solution where an excited molecule is able to come into contact with a ground state molecule and transfer its energy to form the excited dimer. Two pathways are possible after formation of the excimer - emission of radiation and relaxation of both molecules to the ground state, or non-radiative decay, resulting in the dimer falling apart back to the original two monomers.

Since in the solid state, the molecules are held in place by intermolecular forces, excimer formation is not possible as the excited state molecules cannot move to collide with their potential ground state partners. It is possible however, for molecules along the face of a crystal lattice to be in contact with a dimer partner directly opposite it in the lattice. In such circumstances, if one molecule becomes excited, lattice distortions can allow movement of the partner molecules closer to the excited molecules, compressing the lattice, sealing the generated exciton in place. When it relaxes back to the ground state when trapped, the crystal structure is considered *pre-excimeric*[34]. When pre-excimeric states are present in a host matrix, emission from both the monomers and excimers can be observed. At higher concentrations, more pre-excimeric states can be formed, leading to an increase in the intensity of excimer emissions at the expense of monomeric emissions.

Molecules with a planar structure are more likely to form excimers, pyrene being a good example. As the work of Birks and Christophorou (1963)[130] in Figure 2-20 shows, as the pyrene concentration is increased, the fluorescence intensity increases dramatically owing to dimer formation thanks to their closer molecular proximity.

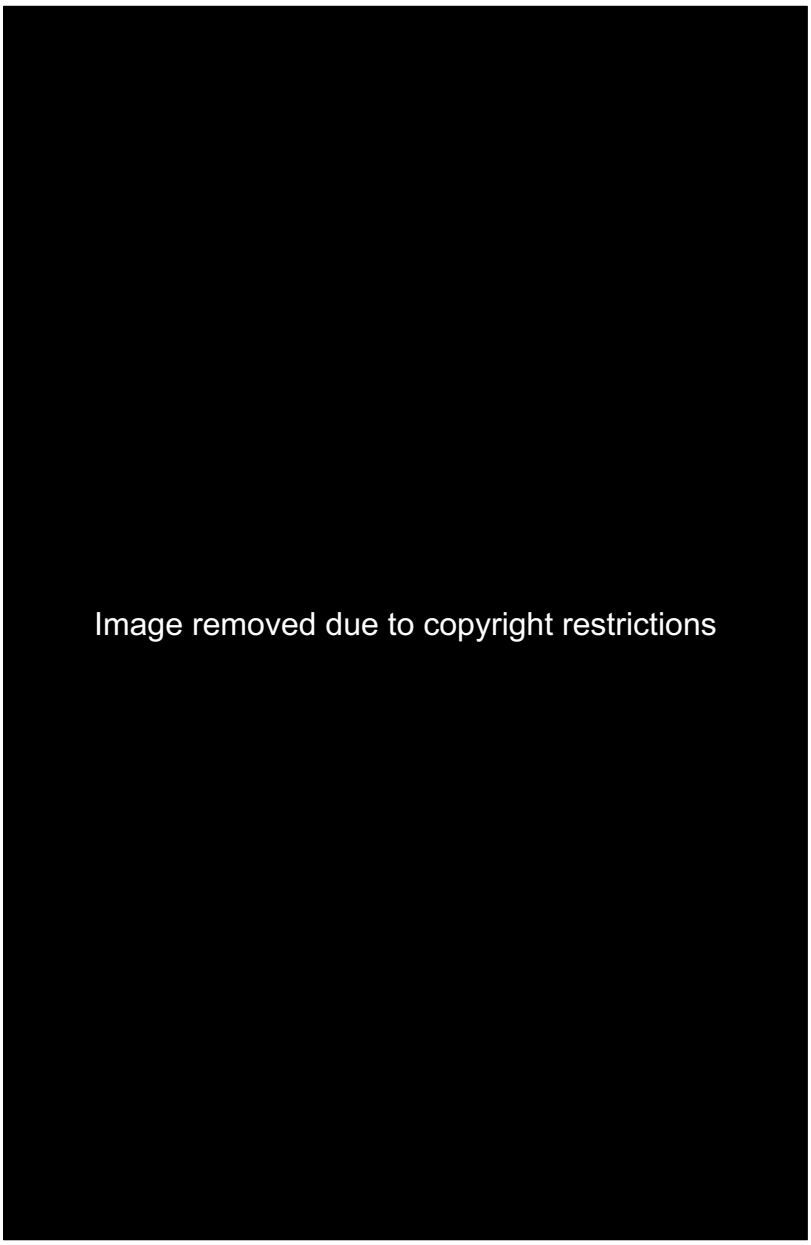


Figure 2-20 Fluorescence spectra of pyrene at different concentrations taken from the 1963 work of Birks and Christophorou[130].

An exciplex, as mentioned before, differs from regular dimers and excimers in that both molecules are different. This means that one molecule is necessarily an electron donor and the other an electron acceptor. In each case, the molecules ionise - the acceptor being an anion (since it receives electrons) and the donor being a cation (as it is the one giving away the electrons). Which molecule is which is determined by the HOMO and LUMO energies - the donor possesses a higher energy HOMO and the acceptor a lower energy LUMO. During the process, charge is redistributed from the donor to the acceptor thus:

$$D^* + A^0 \rightarrow [D^+ + A^-]$$

Equation 2-7 The charge transfer reaction[34].

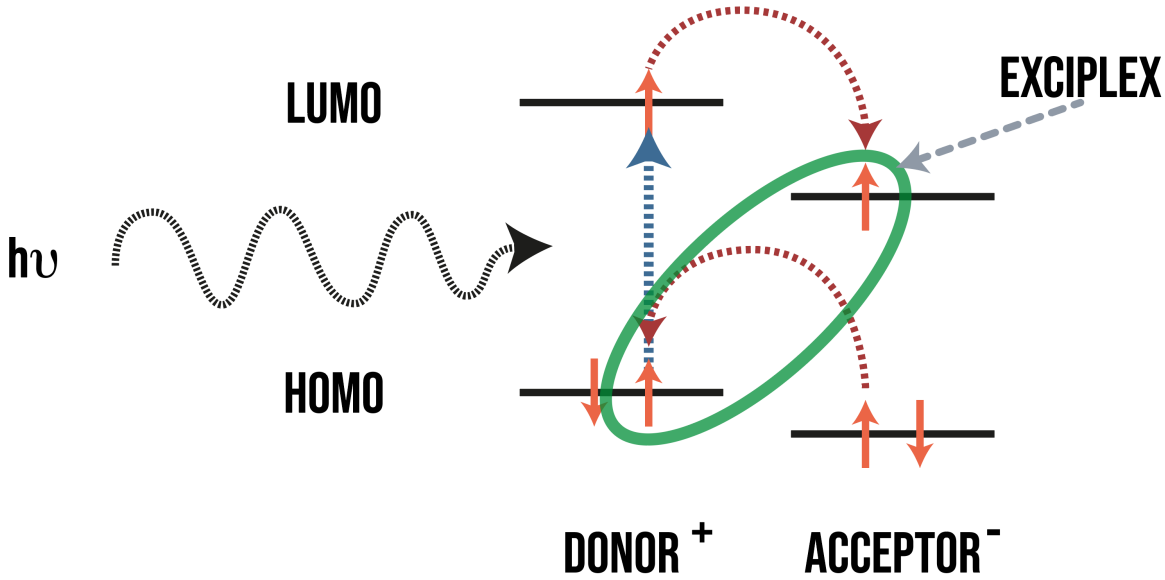


Figure 2-21 Energetics involved in exciplex formation. Adapted from Forrest[34].

Essentially this means that an excited donor molecule is bound to a ground state acceptor molecule to form the excited complex (see Figure 2-21). If transfer of charge occurs in the ground state, the complex is referred to as a charge transfer complex.

2.5.6 Types of excitons

Unlike their inorganic counterparts, organic semiconductors consist of individual molecules held together in crystalline lattices by intermolecular forces. As such, the dielectric constants and exciton radii are much smaller, and the binding energy of excitons are much larger.

There are three main types of semiconductor excitons and they are represented visually in Figure 2-22:

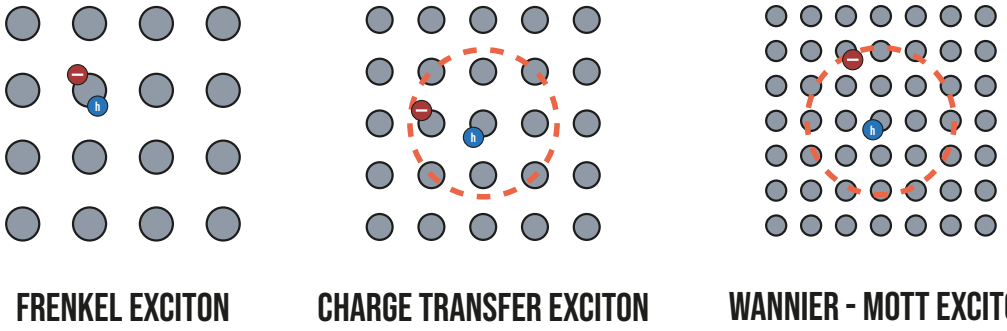


Figure 2-22 The three main types of excitons. The diagrams illustrate the locations of holes (blue circle) and electrons (red circle) with respect to the lattice at large. The orange dotted circle represents the effective Bohr radius. Adapted from Forrest[34].

Wannier-Mott excitons

In this case, the hole and electron are located many unit cells away from one another (up to 10-100 lattice constants)[34]. This is usually confined to inorganic semiconductors[34].

Charge transfer excitons

The electron and hole are located on closely neighbouring molecules in the lattice temporarily[34]. This can span across several molecules if they are stacked in close proximity to the electron and hole.

Frenkel excitons

The hole and electron are located on the same molecule in the lattice. The polarity of the environment influences the energy of the exciton, permitting observation of solvatochromism. 'Travel' of the exciton is achieved by the charge jumping from one molecule to the next. Since they are relatively stable at ambient conditions, this is the main exciton type considered in organic electronics[34].

2.6 Excited state decay kinetics

The time taken for electron transitions upon the absorption of UV-visible radiation (or indeed electrical energy) by a molecule is in the range of "10^{-16} – 10^{-15} s"[128]. In comparison, a first order chemical reaction instigated by photochemical means has a rate of "10^{16} s^{-1}"[128]. Fluorescence is a much slower process, between "10^{-12} – 10^{-16} s"[128], whereas phosphorescence is slower still – around "10^{-12} – 10^{-4} s"[128]. The key electronic transitions involved in photo- and electroluminescence and their rate equations are as follows in Table 2-1:

Table 2-1 Electrical transitions and their rate equations, adapted from Atkins and de Paula[128].

Process	Equation	Rate Equation
Absorption / Electronic excitation	$S_0 + h\nu_i \rightarrow S_1$ / $S_0 \rightarrow S_1$	I_{abs}
Fluorescence	$S_1 \rightarrow S_0 + h\nu_f$	$k_f[S_1]$
Phosphorescence	$T_1 \rightarrow S_0 + h\nu_p$	$k_p[T_1]$
Intersystem Crossing (ISC)	$S_1 \rightarrow T_1$	$k_{ISC}[S_1]$
Reverse Intersystem Crossing (rISC)	$T_1 \rightarrow S_1$	$k_{rISC}[T_1]$
Internal Conversion (IC)	$S_1 \rightarrow S_0$	$k_{IC}[S_1]$

When excitation ceases and excited states decay, the overall rate of decay of the excited singlet state is equal to the sum of all possible decay pathways from the excited singlet state:

$$Rate\ of\ decay\ of\ S_1 = k_f[S_1] + k_{ISC}[S_1] + k_{IC}[S_1]$$
$$= (k_f + k_{ISC} + k_{IC})[S_1]$$

Equation 2-8 Singlet rate of decay equation from Atkins and de Paula[128].

The typical rates of the various photophysical processes observed in this field are outlined in Figure 2-23.

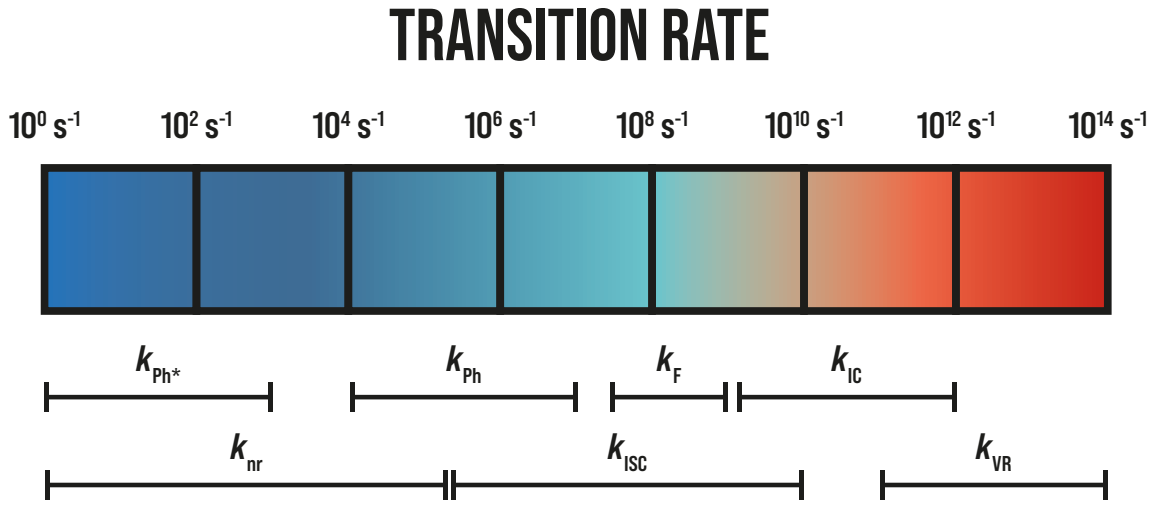


Figure 2-23 Typical transition rates experienced with photophysical processes. k_{Ph*} represents phosphorescence without heavy metals. Adapted from Forrest[34].

The process by which excited states decay back to the ground state is a first order one when excitation ceases:

$$[S_1]_t = [S_1]_0 e^{-(k_f + k_{ISC} + k_{IC})t/\tau_{obs}}$$

Equation 2-9 Describing the variance of the first excited singlet state as a function of time after excitation. From Atkins and Paula[128].

$$\tau_{obs} = Observed\ fluorescence\ time$$
$$\tau_{obs} = \frac{1}{k_f + k_{ISC} + k_{IC}}$$

Equation 2-10 Observed fluorescence lifetime equation. From Atkins and de Paula[128].

So, we can modify the above equations to focus on the quantum yield of fluorescence as:

$$\phi_f = \frac{k_f}{k_f + k_{ISC} + k_{IC}} = k_f \tau_{obs}$$

Equation 2-11 Fluorescence quantum yield equation. From Atkins and de Paula[128].

A more detailed examination of quantum yield now follows.

2.6.1 Quantum yield

When excited, not every molecule will go on to produce fluorescence or phosphorescence because some of the energy may be lost to other processes, such as deterioration of the molecule, chemical reactions, *etc*.

To measure the yield of the photoluminescent process, we use the *primary quantum yield*, ϕ[128].

$$\phi = \frac{number\ of\ events\ leading\ to\ desired\ emission}{number\ of\ photons\ absorbed}$$

Equation 2-12 Quantum yield of a photoluminescent process. Adapted from Atkins and de Paula[128].

This can be rephrased for electroluminescence as:

$$\phi = \frac{number\ of\ events\ leading\ to\ desired\ emission}{number\ of\ excitons\ promoted}$$

Equation 2-13 Quantum yield of an electroluminescent process.

If all photons absorbed, or all excitons promoted lead directly to emission of radiation, then $\phi = 1$. If no emission occurs after excitation, then $\phi = 0$. Sometimes the quantum yield is reported as a percentage.

If both parts of the above fraction are divided by the time they took to take place, then we get ν – the rate of radiation/electronically induced events and I_{abs}, the rate of photon absorbance/electron excitation.

$$\phi = \frac{\nu}{I_{abs}}$$

Equation 2-14 Quantum yield equation linking rate of excitation events to emission events. From Atkins and de Paula[128].

When excited, a molecule has to do one of two things – form a photochemical product, or eventually decay back to the ground state. All decay processes, be they radiative or non-radiative, must add up to the same number of excited states formed through the original excitation (*via* absorption of light or electrical energy).

The sum of primary quantum yields of all possible outcomes, known as channels, *i*, (where *i* is transitions, physical or photochemical processes) will always be equal to 1.

$$\sum_i \phi_i = \sum \frac{v_i}{I_{abs}} = 1$$

Equation 2-15 Equation for the sum of quantum yields of all possible outcomes. From Atkins and de Paula[128].

Where v_i = rate of formation of a product which could be light emission, number of molecules broken down, *etc*.

i.e. what energy goes in, must come out in one form or another – all energy is conserved.

When a molecule is excited, collisions with other molecules may remove the excitons from the process so we must consider the overall quantum yield, Φ. This is the quantity of molecules removed by the action of one excited molecule, excited initially by one photon or one initial excitation step (electrical).

This can be illustrated *via* a radical reaction such as the breaking down of hydrogen iodide by ultraviolet light[128]:

1. $HI + h\nu \rightarrow H^{\bullet} + I^{\bullet}$
2. $H^{\bullet} + HI \rightarrow H_2 + I^{\bullet}$
3. $I^{\bullet} + I^{\bullet} + M \rightarrow I_2 + M$

Here M represents a substance which removes energy from the system. In this 3-step process, one molecule of HI is broken down by a photon and the $H^{\bullet}$ fragment goes on to induce the breakdown of another HI molecule. Therefore, the initial photon was responsible for the breakdown of two molecules of HI. Thus, for this process, the overall quantum yield, Φ = 2. [128]

The observed fluorescence time (τ_{obs}) – *i.e*., the time taken for fluorescence to take place - can be measured experimentally by pulsing a laser at a sample and recording the intensity of the fluorescence[128]. The laser's wavelength corresponds to that which the $S_0 \rightarrow S_1$ transition best absorbs.

The faster of the two processes is fluorescence which involves a S_1 - S_0 transition. In phosphorescence, the slower spin forbidden T_1 - S_0 process, must occur *via* spin orbit coupling facilitated by the heavy atom effect.

The rate of phosphorescence is controlled by the size of the heavy atom (thanks to the aforementioned heavy atom effect) - strictly speaking its atomic number, and how strong the transitions are between the S_1 and S_0. The speed of phosphorescence is overall dictated by how swiftly singlets can be converted into triplets by ISC (with the rate constant being k_{ISC}) and then by how quickly the triplets can decay radiatively to the ground state, S_0 (with the rate constant of k_{Ph}). For phosphorescence to be the favoured process, all of these processes must have a rate which exceeds that of non-emissive processes, *i.e.* that:

$$k_{ISC} \text{ and } k_{Ph} >> k_{nr}$$

For effective phosphorescence, k_{ISC} must be much greater than k_F so that singlets are not lost, which in turn yields a large Φ_{ISC} (*i.e.* close to 1) and of course a low Φ_F.

The rates of the processes contribute to the quantum yields of fluorescence, phosphorescence and intersystem crossing:

$$\Phi_F = \frac{k_F}{k_F + k_{nrS} + k_{ISC}}$$

Equation 2-16 Fluorescence quantum yield.

$$\Phi_P = \frac{\Phi_{ISC} k_{Ph}}{k_{Ph} + k_{nrT}}$$

Equation 2-17 Phosphorescence quantum yield.

$$\Phi_{ISC} = \frac{k_{ISC}}{k_{ISC} + k_F + k_{nrS}}$$

Equation 2-18 Intersystem crossing (ISC) quantum yield.

2.7 Quenching of fluorescent molecules

Quenching occurs when the energy exciting a fluorescent molecule is removed *via* an interaction with another molecule. This will lower the fluorescence quantum yield of the device and must be considered when fabricating OLEDs.

The *Stern-Volmer Equation* describes the effects of a quencher on quantum yield[131,132]:

$$\frac{\phi_f}{\phi} = 1 + \tau_{obs} k_Q [Q]$$

Equation 2-19 Stern-Volmer equation.

Where, ϕ_f = Fluorescence Quantum Yield without a quencher

ϕ = Fluorescence Quantum Yield with a quencher

τ_{obs} = Observed fluorescence time

k_Q = Rate constant for quenching

$[Q]$ = Quencher concentration

This is based on a quenching action of the form:

$$S_1 + Q \rightarrow S_0 + Q$$

$$Rate\ of\ Quenching = k_Q [Q][S_1]$$

Equation 2-20 Quenching rate. From Atkins and de Paula[128].

With a quencher and when at a steady state, the rate of change of $[S_1]$ changes to:

$$Rate\ of\ change\ of\ [S_1] = I_{abs} - \left(k_f + k_{IC} + k_{ISC} + k_{IC} + k_Q[Q]\right)[S_1] = 0$$

Equation 2-21 Rate of change of the first excited singlet state. From Atkins and de Paula [128].

So, the quantum yield when quenched is :

$$\phi_f = \frac{k_f}{k_f + k_{ISC} + k_{IC} + k_Q[Q]}$$

Equation 2-22 Fluorescence quantum yield when the emitter is exposed to a quencher. From Atkins and de Paula[128].

The form of the Stern-Volmer equation lends itself to graphing, with $\frac{\phi_f}{\phi}$ on the *y-axis* (often labelled as I/I_0) and quencher concentration, [Q], on the *x-axis*, resulting in a straight-line graph. This is known as a *Stern-Volmer Plot* (see Figure 2-24).

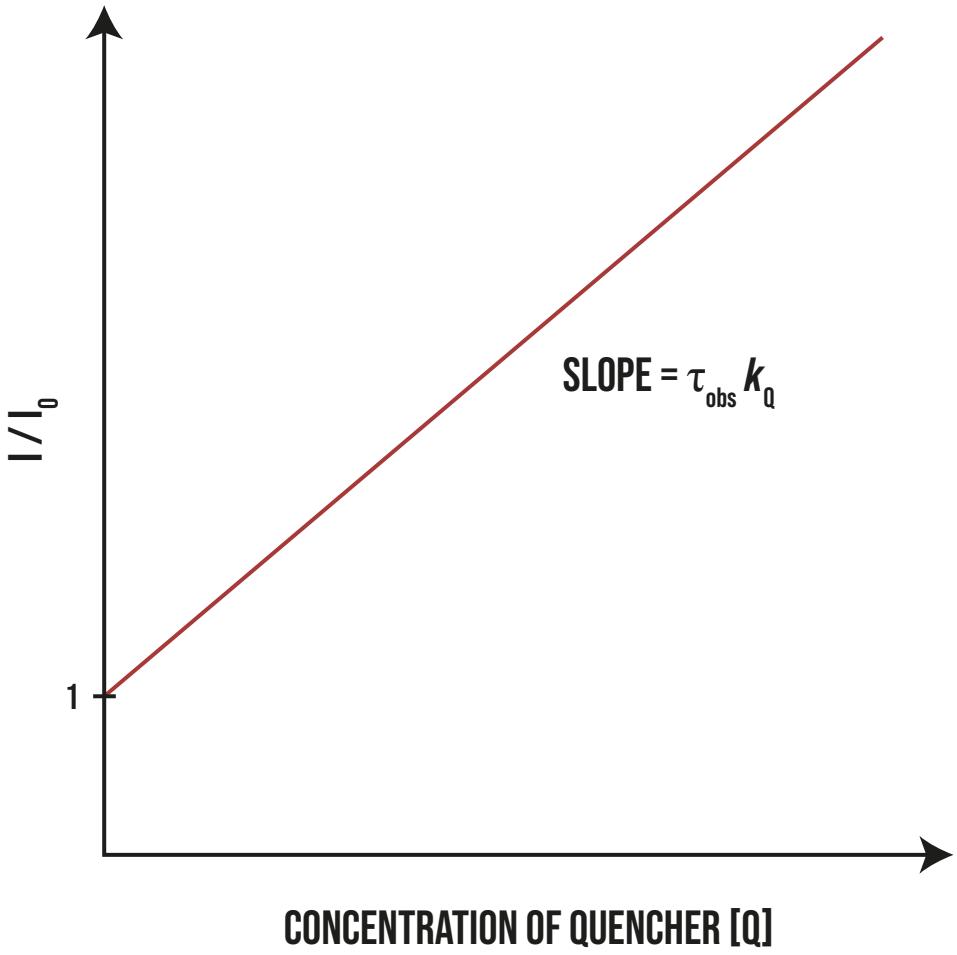


Figure 2-24 Stern-Volmer Plot relating quencher concentration [Q] to the ratio of fluorescence quantum yields with and without the quencher (I/I_0). Adapted from Atkins and de Paula[128].

The plot has a gradient of $\tau_{obs}k_Q$. Substituting $\frac{\phi_f}{\phi}$ for $\frac{\tau_{obs}}{\tau_{obs(Q)}}$, where τ_{obs}(Q) is the observed fluorescence lifetime with a quencher, we get the equation:

$$\frac{\tau_{obs}}{\tau_{obs}(Q)} = 1 + \tau_{obs} k_Q [Q]$$

Equation 2-23 From Atkins and de Paula[128].

Then, dividing by τ_{obs} gives:

$$\frac{1}{\tau_{obs}(Q)} = \frac{1}{\tau_{obs}} + k_Q [Q]$$

Equation 2-24 Stern equation, as described by Atkins and de Paula[128].

and can be plotted thus in Figure 2-25:

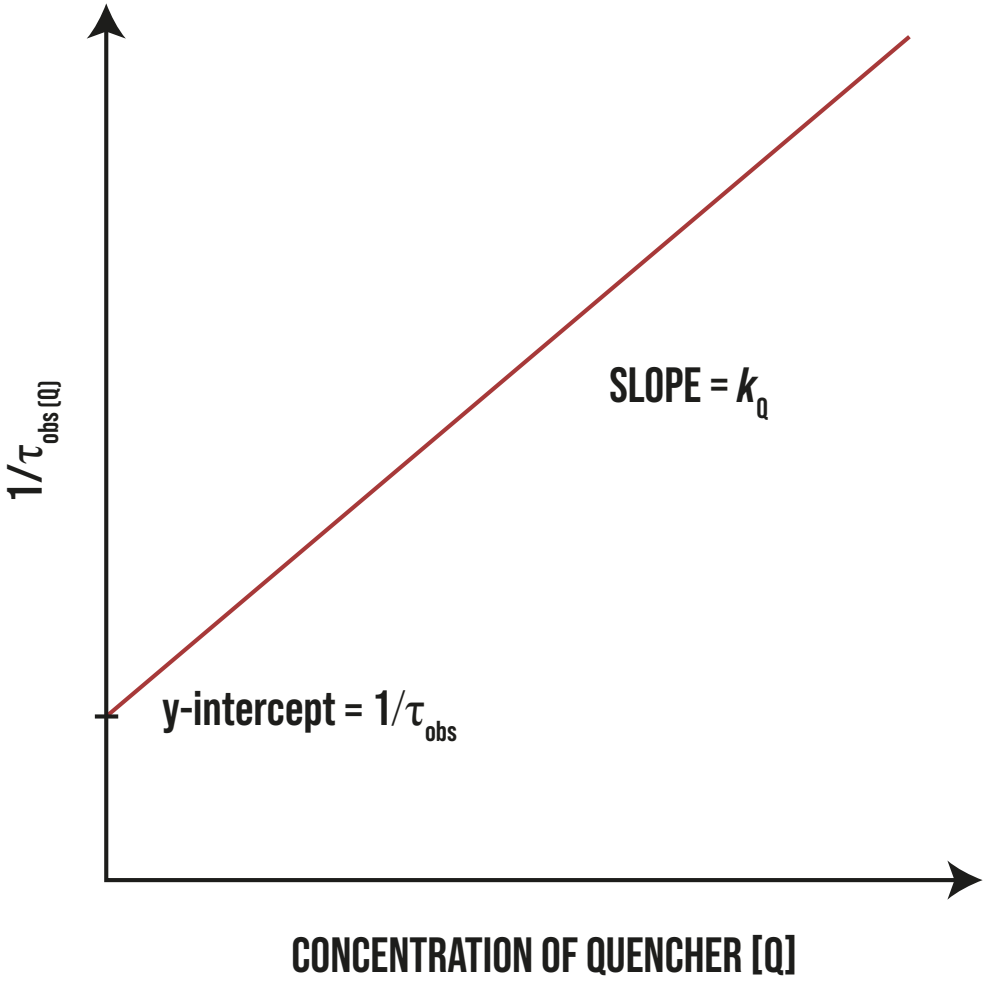


Figure 2-25 Stern-Volmer Plot comparing quencher concentration to the inverse lifetime of the material with a quencher. Adapted from Atkins and de Paula[128].

Where the *x-axis* represents the quencher's concentration [Q], *y-axis* represents the inverse lifetime $\frac{1}{\tau_{obs}(Q)}$ when quenched, the *y-intercept* the inverse lifetime without a quencher $\frac{1}{\tau_{obs}}$, and the gradient k_Q, the rate constant of quenching.

According to Atkins and de Paula[128], there are three major ways of quenching excited states, be they singlets or triplets:

Collisional deactivation

$$S_1 + Q \rightarrow S_0 + Q$$

This is where the excited species and a quencher molecule come into physical contact. The heavier the quencher molecule, the more efficient the process. The quencher absorbs energy from the excited species and then the quencher will decay in a non-radiative pathway.

Electron transfer

$$S_1 + Q \rightarrow S^+ + Q^- \; Or \; S^- + Q^+$$

This is based on the Marcus theory of electron transfer[128] which says that the closer the acceptor and donor species are to each other, the faster the rate.

The rate will be faster with more exergonic reactions (those with negative free energy), *i.e*. the reduction potential of the quencher must be higher than the reduction potential of the excited state species.

The closer the free energy (ΔG) is to the energy required to reorganise the molecules in response to electron transfer, the faster the rate of reaction.

The presence of electron transfer mechanisms can be established by "time-resolved spectroscopy"[128]. Observing the presence of the spectra of oxidised and reduced compounds when a laser is used to excite them indicated that an electron transfer quenching process is occurring.

Resonance energy transfer

$$S_1 + Q \rightarrow S_0 + Q_1$$

When excited, the electron density in a molecule shifts, resulting in a dipole. This dipole is lost when the molecule returns to the ground state. However, this change in electron density can induce a dipole in a quenching molecule nearby. The efficiency in this induction η_T, is

related to the fluorescence lifetimes of the molecule with and without a quenching molecule (shown in Equation 2-25):

$$\eta_T = \frac{\tau_{obs} - \tau_{obs}(Q)}{\tau_{obs}}$$

Equation 2-25 Resonance energy efficiency equation with respect to lifetimes. From Atkins and de Paula[128].

Förster Theory[133] states that if the excited species and the quenching molecule are in a structure which is rigid in character (*i.e.* they cannot move around) then the effect is much more efficient the greater the proximity to one another the excited species and quenching molecule are shown in Equation 2-26:

$$\eta_T = \frac{R_0^6}{R_0^6 + R^6}$$

Equation 2-26 Resonance energy efficiency equation. From Atkins and de Paula[128].

Where, R_0= Value unique to the excited species and quenching molecule pair

R = Distance between the excited species and the quenching molecule

We explore the implications of Förster Theory later in section 2.11.

2.8 Triplet harvesting

During the development of OLED devices, a number of methods have been used to improve the internal quantum efficiencies of devices. In standard fluorescence, 25% of all the excitons decay from excited singlet states *via* fluorescence, and the remaining 75% from non-radiative triplet decay. This severely limits the efficiency of fluorescent OLED devices. As such it is important that the triplet states be harvested to produce as close to 100% fluorescent emissive states as possible from the excitations.

Phosphorescent OLEDs

One way of getting 100% quantum efficiency is to convert the singlets (25%) into triplets, provided of course the triplet states are emissive. If they are made to be emissive then this would enable 100% quantum efficiency. Singlet to triplet conversion can occur *via* intersystem crossing (ISC) and is somewhat favourable since triplets are lower in energy than singlets. To promote ISC, heavy metals are incorporated into the structure of the molecule. This heavy metal also acts as the site where phosphorescence occurs.

Hot excitons

The hot exciton method involves exciting the electrons to upper high energy triplet states (T_n where n >1) and then using reverse intersystem crossing (rISC) to convert the triplets into a singlet state, S_n (where n >1). The excited singlet state, if it is higher in energy than S_1, will decay by internal conversion (IC) non-radiatively to the S_1 state, before decaying to the ground state in an emissive fashion *via* fluorescence.

Molecules that work well for this method need to have higher energy singlet and triplet states available and therefore a structure which allows for stability at such energies. Conversion from excited triplets (T_n) into excited singlets (S_n) needs to be efficient and be followed readily by internal conversion (IC) to the S_1 state to enable fluorescence, else energy is lost to non-radiative transitions.

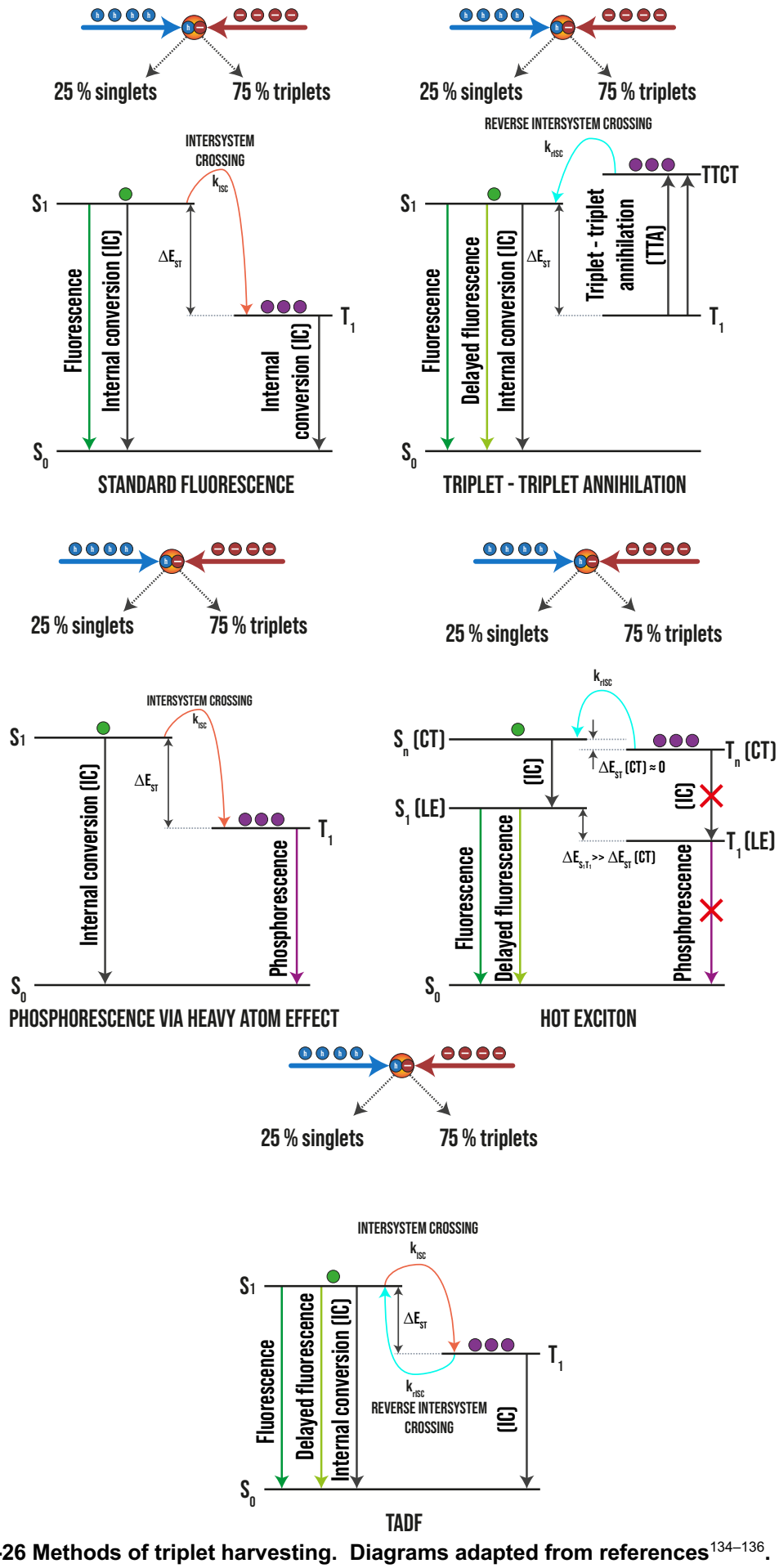


Figure 2-26 Methods of triplet harvesting. Diagrams adapted from references[134–136].

Since this technique can harvest the triplets to form singlets, the internal quantum efficiency (IQE) can theoretically be 100%[136]. It is important therefore that $T_n \rightarrow T_1$ internal conversions be reduced to prevent non-radiative quenching. The rate of IC ranges between 10^{10} and 10^9 s^{-1}, which means that $T_n \rightarrow T_1$ transitions are, unfortunately, more likely than rISC at elevated exciton levels which severely hinders its application in OLED devices.

Delayed fluorescence

The phenomena of delayed fluorescence can be divided into two main categories: Thermally Activated Delayed Fluorescence (TADF); and Triplet-Triplet Annihilation (TTA):

Thermally activated delayed fluorescence (TADF)

The application of TADF was limited for some time after its discovery (for a time referred to as E-type fluorescence after the material it was first observed in, eosin) in 1961[137], however since investigations by the Adachi group of Kyushu University in 2012[33] on a method of triplet harvesting, this method of luminescence has seen a massive resurgence. TADF is so called because heat energy is required to facilitate the rISC process – being endothermic in nature.

According to first order perturbation theory, the rate of intersystem crossing is at its largest when the energy gap between S_1 and T_1 (that of ΔE_{ST}) is at its smallest. At this point the two states are almost in resonance and the triplet states can be converted into singlets through application of thermal energy (since T_1 - S_1 is endothermic). After the singlet state is repopulated, it may undergo emissive decay back to the ground state *via* fluorescence. The rate of emission (k_F) in this case is restricted by rate of conversion of triplets into singlets - the reverse of ISC, reverse intersystem crossing (rISC), the rate constant of which is given by k_{rISC}.

Mixing between singlet and triplet states, while formally forbidden, can be achieved by use of heavy metals which facilitate spin-orbit coupling (SOC) and enable the triplet state decays to be emissive[138] *via* the heavy atom effect[127]. Heavy and transition metals are not ideal in devices, owing to their toxicity, economic cost and poor sustainability. Ergo, attempts are being made to replace these metals with cheaper, more widely available metals such as copper[139] or to design TADF emitting molecules entirely from organic materials.

TADF has similarities with hot-exciton rISC, however the excitons are only required to be in their first excited states – T_1 and S_1. $T_1 \rightarrow S_0$ emissive transitions are less likely as T_1 is much higher in energy than S_0, but its proximity to S_1 means that rISC from $T_1 \rightarrow S_1$ encounters very little competition from internal conversion (IC) and is thus more favourable[140]. Since the triplets are harvested to allow $S_1 \rightarrow S_0$ fluorescent transitions, the IQE of the process can be up to 100%. If the energy gap between S_1 and T_1 states is particularly narrow, then room temperature can be sufficient to provide thermal energy to enable up-conversion of T_1 states to S_1 states *via* rISC repopulating the singlet states with the remaining 75% triplet states, a process which takes longer, but also results in emissive $S_1 \rightarrow S_0$ transitions. This ultimately provides two forms of fluorescence: from the 25% of excitons already as singlets which decay to the ground state accompanied by emission of radiation promptly (in the range of nanoseconds after excitation – described as *prompt fluorescence*); and *delayed fluorescence*, when time is taken to convert triplets into singlets first before decaying to the ground state and emission of radiation (in the range of microseconds). One such illustration of this occurring is reported by Dias *et al.*[141] and shown in Figure 2-27. Here the molecule DBTZ-DBO2 decays first by prompt emissions lasting 15.2 ns (taken from the blue fit of the time resolved measurement). A later, delayed emission occurs with a lifetime of 5.48 μs (red fit). Phosphorescence lasts until at least 50 ms, as can be seen from the noisier green peak in the third figure – this comes from triplet – singlet decay, giving a different wavelength to that of the singlet – singlet delayed fluorescence (DF).



Figure 2-27 Plots of the prompt and delayed emissions from DPTZ-DBTO2 and their lifetimes (left most plot). Taken from Dias *et al.*[141]

One of the major goals in current TADF research is to develop a deep blue emitter which is stable and has a long lifetime. This necessitates a large excited singlet energy of over 2.65 eV[125], which presents difficulties in maintaining stability with a necessarily high energy

triplet state required. However red emitters also prove to be quite difficult to produce, owing to non-radiative $T_1 \rightarrow S_0$ decay occurring more readily when the necessarily low ΔE_{ST} value and low S_1 energy is attained. In order to keep S_1 high for blue emitters and the S_1-T_1 energy gap narrow enough to allow rISC, molecules are designed to have donor and acceptor moieties internally conjugated by possessing little or no conjugation to each section and arranged in different planes, often *via* steric hindrance.

Carbazole is attractive as a donor owing to its rigidity and good internal confinement of its HOMO and delocalisation across its structure. Acceptors include heterocycles, cyano, arylketones, diarylboryl groups, sulfones and phosphorous oxides[125]. It is now clearly entirely possible to only use organic chemicals, removing the necessity for unsustainable metal compounds.

TADF does not require heavy atoms to facilitate spin orbit coupling (SOC) as the singlet and triplet states are close to resonating with one another[34]. A cycle of S_1 - T_1 is set up and so long as the rate of non-radiative decay is less than that of phosphorescence, rISC is sustained until all excited states have fluoresced. The time take for this process (T_1 - S_1 - T_1) is equal to:

$$\frac{t}{\tau TADF} \approx k_{nr} + k_{\mathrm{Ph}}$$

Equation 2-27 The length of the T_1-S_1-T_1 cycle is related to the sum of the rates of non-radiative decay and phosphorescence. From Forrest[34].

The longer the lifetime of the triplet state (in so much as triplet states take longer before decaying non-radiatively), the greater the TADF efficiency, since it increases the chances that triplets will be harvested. This efficiency grows at higher temperatures as T_1 - S_1 conversion becomes more feasible[34].

The triplet and singlet quantum yields are as follows:

$$\Phi_T = \frac{k_{ISC}}{k_{ISC} + k_F + k_{nrS}}$$

$$\Phi_S = \frac{k_{rISC}}{k_{rISC} + k_{\mathrm{Ph}} + k_{nrS}}$$

Equation 2-28 Quantum yields for the formation of first excited triplet and singlet states respectively. From Forrest[34].

The process is cyclic - absorption or electrical stimulation promotes the molecule from the singlet ground state into the first excited singlet state, S_1, which can undergo ISC to the first excited triplet state, T_1, then rISC back to S_1, with a chance of radiative decay back to the ground state, with some excitons converting back into triplets, followed by rISC once again back to the singlet manifold, followed by emission of some, and ISC of others and so on (see Figure 2-28).

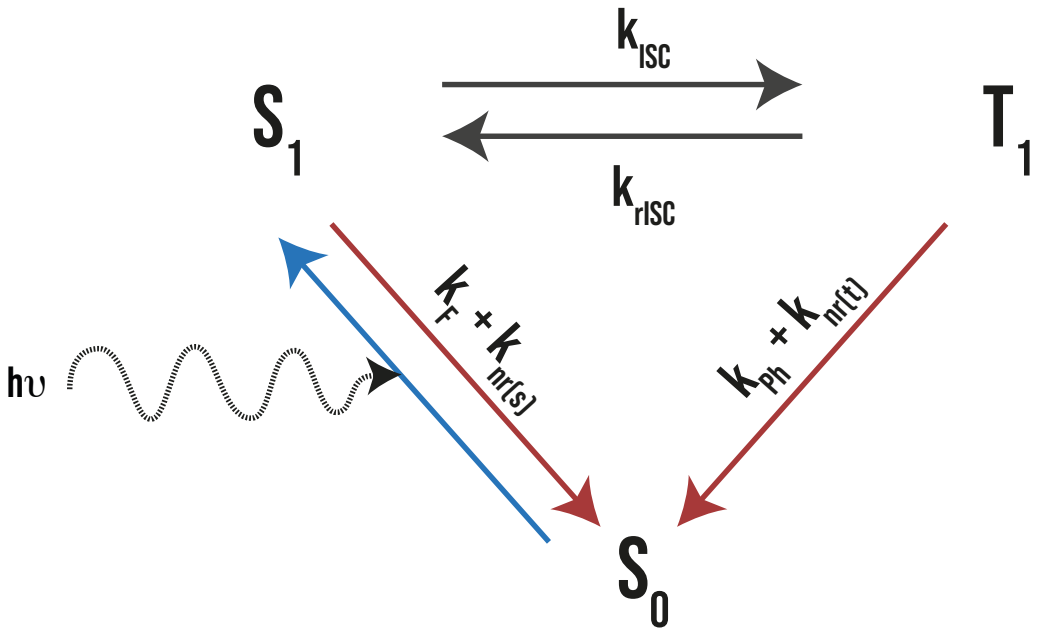


Figure 2-28 The cyclic TADF process. Adapted from Baleizão and Berberan-Santos[142].

Based on these equations, one can calculate the number of ISC - rISC cycles *via*:

$$\bar{n} = \frac{\Phi_T \Phi_S}{1 - \Phi_T \Phi_S}$$

Equation 2-29 The number of ISC-rISC cycles. From Forrest[34].

TADF emission spectra are devoid of overtone peaks associated with first excited singlet state fluorescence. This yields rather broad spectra with little in the way of characteristic peaks, caused mainly by the fact that effective TADF molecules have their HOMO and LUMO localised at separate regions on the same molecule with little or no orbital overlapping.

Triplet-triplet annihilation (TTA)

Another way of accessing the energy of triplets and converting it to emission of radiation *via* fluorescence, is to make use of *triplet-triplet annihilation*, which like TADF has a historical pseudonym – P-type delayed fluorescence - the P not to be confused with phosphorescence. It is so named as it was first observed in pyrene by Parker 1963[143].

This involves two molecules – a donor and an acceptor. The donor molecule is excited, producing a T_1 triplet after ISC from a S_1 singlet[125]. This exciton is relocated to another molecule's triplet state (the acceptor molecule). This acceptor molecule (also known as an annihilator) will interact with another excited acceptor. The energy from one molecule's triplet moves to the other and returns to the S_0 state. With the extra triplet energy, the second molecule now has a higher overall energy triplet state (T_n where $n>1$). Internal conversion (IC) converts this excited triplet into an S_1 singlet which can relax to the ground state *via* fluorescence.

The acceptor molecule is required to have a triplet state close in energy to that of the donor's triplet state but it needs to be more than half the energy of the acceptor's[125] singlet state energy. The acceptor's first triplet state must remain excited long enough to come into contact with an excited donor to achieve triplet-triplet annihilation. They will also need a high quantum yield for fluorescence or energy will be lost. The donor molecule needs to be easily able to form triplet states, so ISC needs to readily occur, and possess a similar ΔE_{ST} energy to that of the acceptor. It also needs to have a slow phosphorescence rate to increase the chances of triplet energy transferring to a neighbouring molecule to prevent energy loss – *i.e.* the time taken to phosphoresce must be longer than the molecule-to-molecule triplet transfer process.

Triplet-triplet annihilation has the disadvantage of the fact that its excited triplets are prone to exciting oxygen molecules in the air the device is exposed to, removing them entirely from the emissive process. Additionally, this is not a 100% efficient process, so the IQE is normally limited to 62.5%[144]. This limit comes from the fact that annihilation occurs in pairs, so the 75% triplet states must be divided by two (yielding 37.5%), then this is summed with the 25% original singlet states to yield 62.5%.

Spin-orbit coupling

Not all transitions from excited states are permissible. Some transitions are spin forbidden as they would effectively violate the Pauli exclusion principle. Electrons must not interconvert to different multiplicities when entering an excited state, nor when relaxing to a lower energy state. This process is said to be spin-forbidden. Therefore, electrons in a triplet state, may not transition to a singlet state and those in a singlet state may not become triplets[121]. However, transitions between singlets to singlets, or indeed triplets to triplets can occur.

Experimental observations reveal that the spin-forbidden process, which is crucial to TADF emissions, does actually occur[145–147]. The laws of physics are not broken here, rather the multiplicities are circumnavigating this rather inconvenient obstacle *via* another process.

The overall wavefunction for a molecule's triplet state, ψ , will be comprised of both the triplet's and a small degree of the singlet state's wavefunction.

$$\psi = \alpha^1\psi + \beta^3\psi$$

Equation 2-30 Taken from Valeur[121].

The same is true for the *vice versa* case of the singlet. This phenomena of wavefunction interaction is known as spin-orbit coupling (SOC), which gives rise to both intersystem crossing (ISC), when excited triplet states are populated by conversion from excited singlets, and the reverse process, rISC, which is crucial to triplet harvesting in TADF. For ISC, the atomic number (Z) of an element dictates the efficiency of SOC ($ISC_{efficiency} \propto Z^4$), so heavier atoms incorporated into its structure facilitates the population of triplet states and hence the ability of the molecule to undergo phosphorescence *via* the heavy atom effect.

2.9 The role of charge transfer states

In order to design TADF molecules, a comprehensive understanding of the physics involved in their transitions and the nature of their excited states is required.

Previously mentioned was the simplistic model of the TADF mechanism. However, photophysical and computational studies indicate that the process is slightly more complicated than just triplet to singlet conversion[148–153].

2.10 The physics of charge transfer

The TADF process was first described by Parker and Hachard in 1961[137], but its application in OLEDs was not fully realised until 2012 by Adachi *et al*. who described the TADF process as a thermal equilibrium which can be exploited to facilitate rISC[33]. The process of rISC was assumed to be facilitated by the proximity in energy of the S_1 and T_1 states - their energy gap, ΔE_{ST}, and their degree of mixing via spin-orbit coupling (α). This can be summarised in the following equation[154]:

$$\alpha \propto \frac{SOC_{S_1-T_1}}{\Delta E_{ST}}$$

Equation 2-31 from Cui *et al.*[154]

Where SOC_{S1-T1} represents the spin-orbit coupling between the first excited singlet and triplet states. This equation means that for rISC to be favourable, the singlet and triplet states need to have very similar energies, *i.e.*, a small ΔE_{ST} (ideally below 0.1 eV), whereas the spin-orbit coupling should be as strong as possible.

Spin orbit coupling is controlled by the size of the magnetic moments caused by the spin and orbital motion of electrons.[155] As the atomic number of atoms increases, so too does the magnitude of electrostatic attraction from the nucleus, meaning that electrons are accelerated to much greater velocities. This is known as the *heavy atom effect*. In these circumstances, rephasing of the electrons' spin can occur during transitions thanks to the coupling of the electron's spin magnetic moment (μ_S) and the orbital's magnetic moment (μ_L), which allows for spin flipping to occur – a process which would otherwise be forbidden. The orbital angular momentum drives the swapping of the spin vector into the other direction. Heavy atoms need not be metals – bromine and iodine are suitable for this effect. The process of

ISC is readily promoted by addition of heavier atoms to an aromatic molecule, as illustrated by the work of Mohan *et al*.[156]

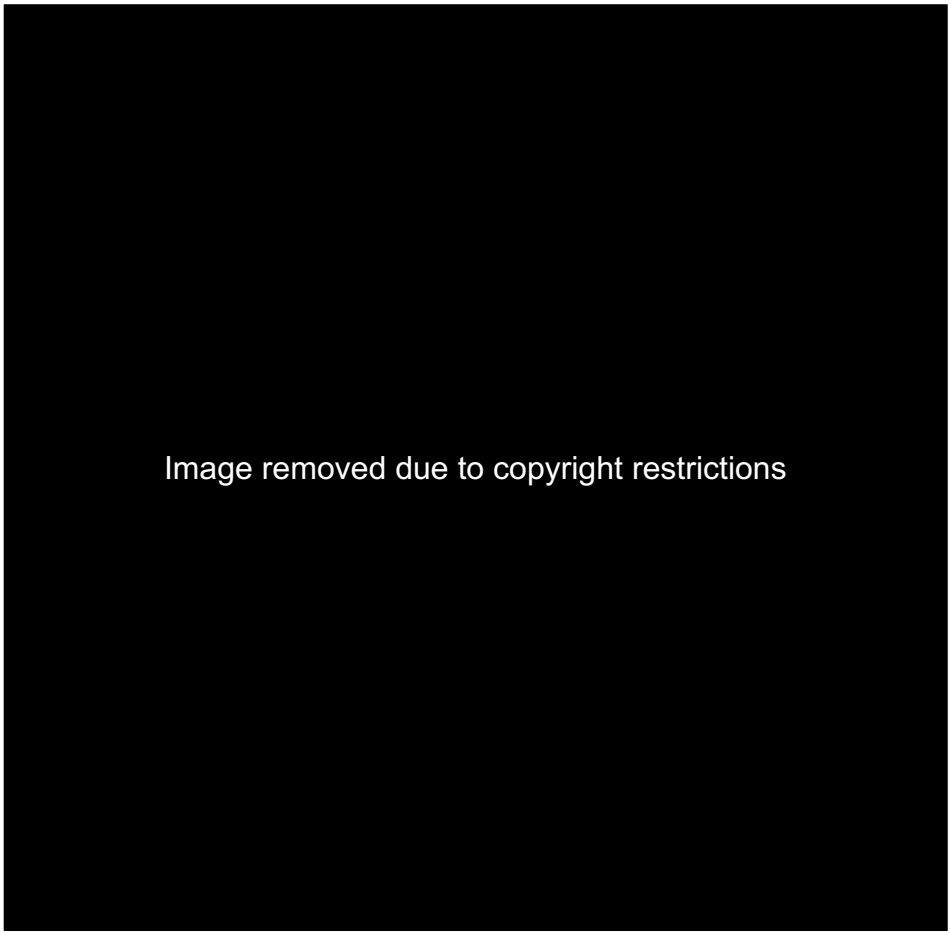


Figure 2-29 Illustration of the effect of the heavy atom effect on quantum yield. Taken from Mohan *et al*.[156]

The internal heavy atom effect involves heavy atoms bonded to π-conjugated systems[157], whereas the external heavy atom effect involves the π-orbitals of an organic system overlapping with the atomic orbitals of neighbouring heavy atoms. The greater the number of heavy atoms, the greater the degree of overlap and hence the better the SOC effect[158], which can result in increased photoluminescent quantum yield, as is illustrated nicely in Figure 2-29 (where Φ_f and Φ_T represent the fluorescent and triplet quantum yields respectively).

One major approach to exploiting Equation 2-31 is to keep the HOMO and LUMO localised on donor and acceptor moieties in a molecule, and to orientate them in such a way as to keep the HOMO and LUMO as far apart in space as possible. Unfortunately, when excited, molecules of this type will often exhibit charge transfer character, which works to suppress any spin-orbit coupling, running against the rISC effect, thus suppressing TADF. This

means that, even if ΔE_{ST} is very small, conversion from ^{3}CT to ^{1}CT is suppressed. Since triplet lifetime is therefore extended, annihilation effects and non-radiative decay are common and roll-off in OLEDs containing TADF emitters is pronounced.

However, more recently work by Monkman *et al*. sheds light on a more complicated process involved – that the rISC functions *via* a second-order vibronic-coupled spin-orbit coupling mechanism[159]. This process occurs *via* a ^{3}CT (triplet charge transfer) state to a ^{3}LE (locally excited) intermediate state, followed by transition to the ^{1}CT (singlet charge transfer) state[153,160] using a donor and acceptor moiety[161] and allows the issue of triplet to singlet rISC suppression to be avoided. They suggest that D-A-D structures can achieve 100% triplet harvesting[162,163] This mechanism was confirmed by utilising the concept to synthesise an efficient blue emitter by Dos Santos *et al*.[164]

The conformation of the donor and acceptor moiety has been shown to control the efficiency of the TADF effect.[165] Monkman *et al*. successfully demonstrated that the conformation could be further manipulated in order to control TADF efficiency[166] by observing that certain reorientations of conformation (ax- ax to ax-eq) in the excited state led to TADF, whereas suppression of that change prevented TADF. This more detailed model now supersedes that of the original process proposed by Adachi *et al*.[167]

There are two potential pathways after excitation for donor-acceptor type TADF molecules (illustrated in Figure 2-30):[153,168]

- A strong $\pi \rightarrow \pi^*$ transition of the donor or acceptor produces a ^{1}LE state (locally excited singlet). This is followed by a further three possible pathways:
    - Fluorescence *via* decay to S_0.
    - Electron transfer forming a charge transfer state (^{1}CT)
    - ISC to produce a locally excited triplet state (^{3}LE)
- A weak $n \rightarrow \pi^*$ excitation directly produces a singlet charge transfer state, ^{1}CT.

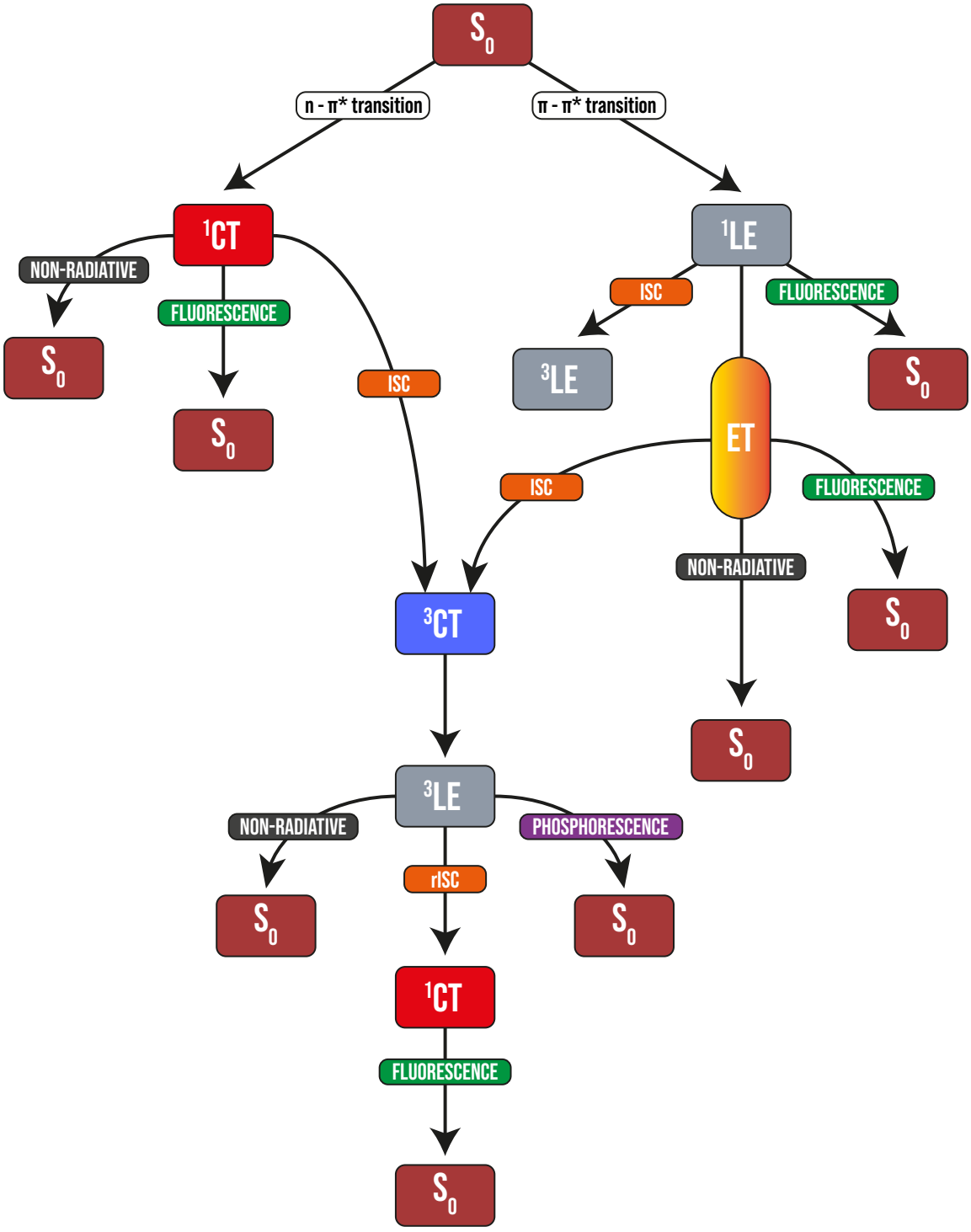


Figure 2-30 Flow diagram of all potential processes following the π → π* and n→ π* transitions from the singlet ground state.

Following a π → π* transition, one can detect locally excited singlet (^{1}LE) to ground state (S_0) transition within the initial few ns. However, most of the excited states are converted *via* slow electron transfer (ET) to the singlet charge transfer ^{1}CT manifold. The reason behind the slow ET lies in the orthogonal separation of the donor and acceptor moieties in space.

Once the ^{1}CT state is populated, three further transitions are possible:

- ISC from singlet ^{1}CT to a charge transfer triplet state, ^{3}CT then conversion to the lowest excited triplet state (^{3}LE), followed by either phosphorescence or non-radiative decay
- Prompt fluorescence, $^1CT \rightarrow S_0$ (this step is swift, with rate constant k_{PF})
- Non-radiative decay (rate is k_{nr})

rISC occurs when absorption of thermal energy causes the triplet state to become excited to a vibronic state at the same energy as the ^{1}CT state, permitting an adiabatic flip of the electron's spin. Since this process takes time, (μs to ms), the fluorescence fuelled from triplet harvesting, *i.e.*, $^1CT \rightarrow S_0$, is termed *delayed fluorescence*.

To promote rISC, ΔE_{ST} should be minimised (<100 meV, or for the most efficient ~<10 meV) so as to ensure that the rate constant for the rISC process is much larger than for non-radiative decay from the triplet state and phosphorescence combined.

The best way of reducing ΔE_{ST} is to ensure that the excited state's electron exchange energy is as small as possible. One method for achieving this is to use molecules incorporating donor – acceptor moieties capable of charge transfer. D-A type molecules are best suited to form charge transfer states,[169,170] with this further enhanced in D-A-D type molecules.[163]

Structures with a large dihedral angle between donor and acceptor moieties give rise to an incredible reduction to the electron exchange energy thanks to a significant reduction in the interactions between electrons situated on the donor and on the acceptor moieties.[163,168,171] A prime example of this is where the bridging atoms are nitrogen and carbon (N-C bond) from donor to acceptor.[172] This structure aids degeneracy in the ^{1}CT and ^{3}CT states, making SOC and thus rISC, spin forbidden.[168] To circumvent this problem, the nearest locally excited triplet state, ^{3}LE, of either an acceptor or donor must vibronically couple to the charge transfer states in order to facilitate a spin flipping mechanism, thereby permitting what would otherwise have been forbidden SOC and rISC processes between the ^{1}CT and ^{3}CT states *via* the ^{3}LE state as an intermediary[170] (see Figure 2-31).

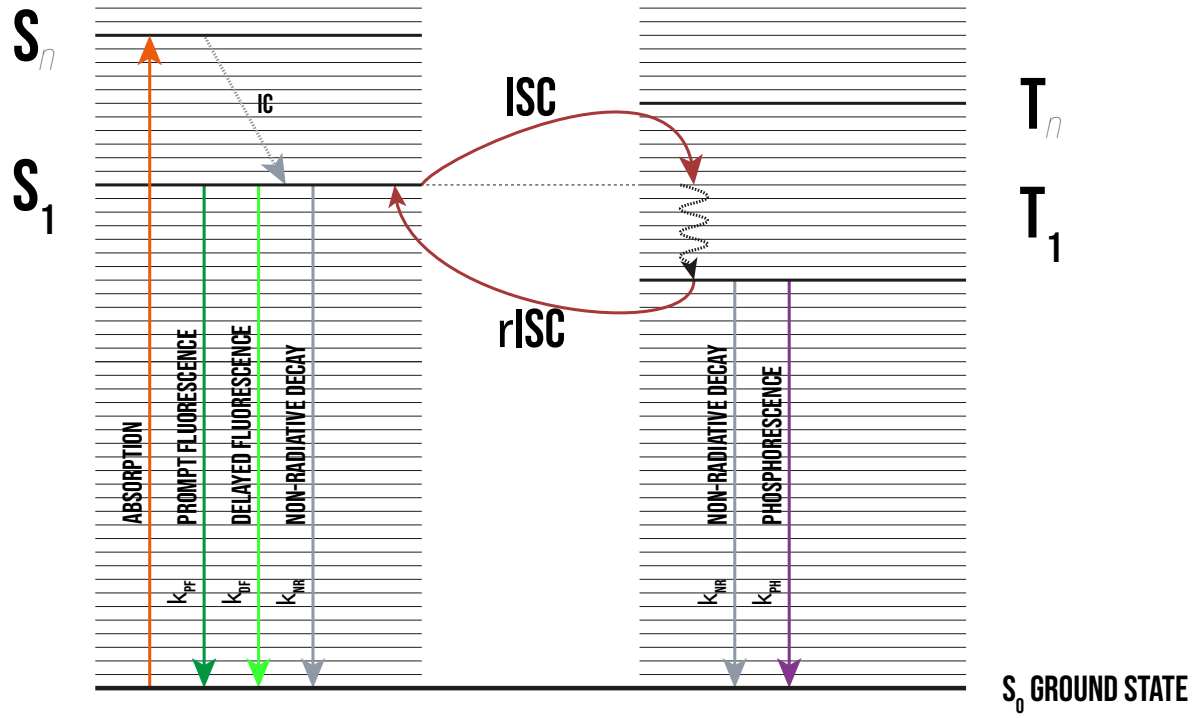


Figure 2-31 Jablonski diagram of absorption and emission and non-radiative processes in charge transfer type singlet and triplet excited states.

This feature of the TADF mechanism actually facilitates the photophysical detection and identification of the process in a device. To detect CT states, one must observe for solvatochromism – a phenomenon which is characterised by bathochromic or hypsochromic shifts in the emission wavelength depending on the polarity of the solvent or host medium in which the TADF molecule is held (which is discussed in more detail later). Owing to the pronounced dipoles CT states possess, molecules in an excited state are more prone to interactions with a polar solvent. A bathochromic shift arises as increased solvent polarity generates a greater attraction for the solvent molecules by the TADF molecule, forming a shell of solvent molecules around it, decreasing the TADF molecule's Coulomb energy[34]. Polarity has no influence on the ^{3}LE states, which are often localised upon the donor moiety. Another approach in analysing emissions is to investigate the vibronic structures of the emission spectra. ^{1}LE emission profiles will show detailed vibronic structure, however emissions from ^{1}CT do not possess vibronic features. The same is true when comparing emissions from ^{3}LE and ^{3}CT.

As a result of solvatochromism, environmental conditions (both from the solvent or host media) can be used to manipulate the ^{1}CT state's energy level, permitting the manipulation of ΔE_{ST}[163]. The optical ΔE_{ST} can be found from the difference between ^{1}CT and ^{3}LE energies obtained from emission spectra; states must pass through the ^{3}LE state to be harvested from the ^{3}CT state. One cannot go from ^{3}CT → ^{1}CT to perform ^{1}CT → S_0 fluorescence, instead

the process must be $^3CT \rightarrow {}^3LE \rightarrow {}^1CT \rightarrow S_0$ with the final step yielding delayed fluorescence.

Ogiwara *et al.*[123] suggest that rISC not only occurs *via* SOC, but utilises an additional mechanism *via* hyperfine coupling (HFC) facilitating ISC, *via* $^3CT \rightarrow {}^1CT$. This was determined *via* electron paramagnetic resonance spectroscopy (EPR). However, this is disputed. Gibson *et al.*[160] suggest that the rate of rISC cannot be elucidated by both of these theories. Instead, Gibson *et al.* suggest both the triplet charge transfer and lowest excited states are of paramount significance in the rISC. Furthermore, one should concern oneself with two energy gaps during molecular design: ΔE_{ST} and E_a (see Figure 2-32).

$\Delta E_{ST} = {}^1CT - {}^3LE$
$E_a = {}^1CT - {}^3CT$

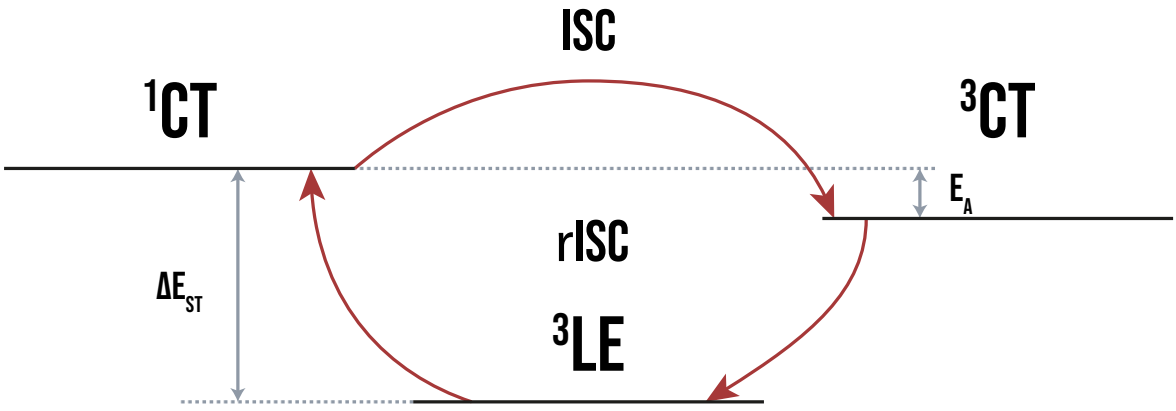


Figure 2-32 Closer inspection of the charge transfer Jablonksi diagram for the ISC and rISC processes.

In all, thermal equilibrium is attained between ^3LE and ^3CT by absorption of heat energy, resulting in the two states being mixed together: in other words, being vibronically coupled.

Once mixed, the ^3CT state undergoes SOC to ^1CT adiabatically (no loss or gain of energy overall) with the ^3LE state acting as the mediator for the process.

$$k_{rISC} = \frac{2\pi}{\hbar}\left|\frac{< {}^1\psi_{CT}|\hat{H}_{SOC}|{}^3\psi_{LE} >< {}^3\psi_{LE}|\hat{H}_{Vib}|{}^3\psi_{CT} >}{\delta({}^3E_{LE} - {}^3E_{CT})}\right|^2 \delta({}^3E_{CT} - {}^1E_{CT})$$

Equation 2-32 from Dias *et al.*[173]

Equation 2-32 describes the rate constant for rISC involving vibronic coupling of ^3CT and ^1CT *via* mediation by ^3LE (the locally excited triplet state mediator)[173]. The coupling between ^3LE and ^3CT is non-adiabatic; meaning that energy is needed to enter the system to power the conversion. The coupling generates an equilibrium between ^3LE and ^3CT which

results in less energy required to permit rISC. Second order perturbation theory states that E_a is controlled by the difference in energy between the ^1CT – ^3CT states.

Lim *et al.*[174] established that ISC from singlets to a triplet state is not an efficient process owing to a lack of mixing (SOC) between ^1CT and ^3CT; however, conversion from one to the other can be made more efficient by introduction of a locally excited state, ^3LE, so long as that state is lower in energy than the ^1CT state. This applies as well to rISC. It turns out however, from more recent studies[159] with molecules with orthogonal donor and acceptor moieties, that it does not actually matter whether ^1CT is above or below ^3LE_D, only that they are in close proximity: ΔE_{ST} can be positive or negative, so long as it is small; rISC can be promoted by the locally excited state acting as an intermediate to conversion from the triplet to the singlet state $^3CT \rightarrow {}^3LE \rightarrow {}^1CT$, with ^3LE and ^1CT being close in energy. The ^3CT state cannot be seen spectroscopically if it has the same energy as ^1CT since telling the difference between their emissions would be impossible. If donor and acceptor moieties are orthogonal, then the exchange energy between ^3CT and ^1CT will be negligible, for they are isoenergetic.

So, in order to go from ^1CT to ^3CT and vice versa, the ^3LE state must act as a mediator to perform the SOC, hence ^3LE can be above or below the energy of the CT state, so long as they are close in energy, they will couple and form a thermal equilibrium and their populations allowed to mix. It is the resulting mixed ^3CT – ^3LE state that spin orbit couples to ^1CT.

2.10.1 Investigating the SOC mechanism

Just how spin-orbit coupling is generated was investigated by Wang *et al.*[175] through use of magneto-EL and magneto-PL spectroscopy. In phosphorescent materials, spin flipping is achieved *via* the heavy atom effect. In all-organic TADF molecules, no such heavy atom is present to facilitate this, so another mechanism must drive it. Wang *et al*. demonstrated that SOC is formed in CT states with D-A type structural motifs.

The degree of mixing (and hence degree of TADF) between the S_1 and T_1 states is dependent upon both SOC (as the SOC constant, H_{SO}) and inversely proportional to ΔE_{ST} thus:

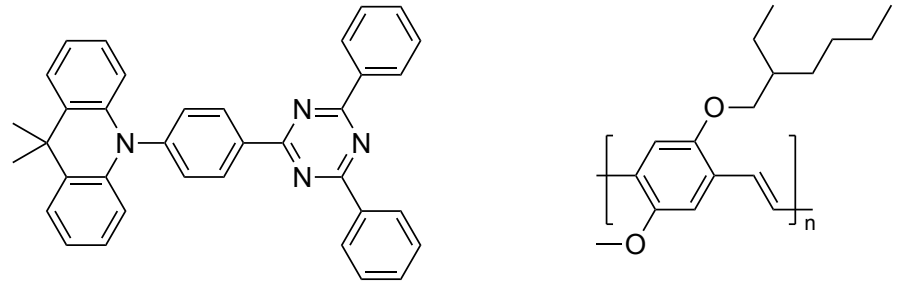
$$\lambda = \frac{H_{SO}}{\Delta E_{ST}}$$

Equation 2-33 The spin mixing rate equation from Wang *et al*. [175]

Where λ represents the spin-mixing rate. Indeed, Equation 2-33 illustrates that a narrower ΔE_{ST} results in a larger value of λ (as expected), however if ΔE_{ST} is wide, a higher rate of spin-mixing can still be achieved if HSO is large.

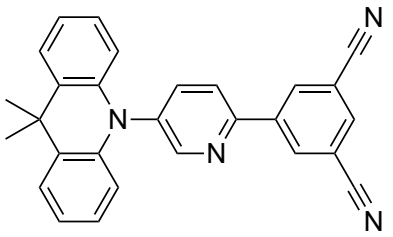
To explore this concept, the authors used magneto-electroluminescence (MEL) spectroscopy to directly observe the presence of the SOC effect. By comparing a well-established, purely fluorescent emitter (MEH-PPV) to that of a well-studied TADF emitter (DMAC-TRZ), they were able to observe strong SOC between donor and acceptor moieties when an electric dipole is produced. Under magneto-EL analysis, magnetic effects were only observed when CT states (from TADF molecules) are excited, not the LE states. This means that SOC only occurs with the CT states of the molecule.

Extending this study to two further TADF molecules, a weakly TADF molecule (DMAC-PymCN) and a stronger TADF molecule (DMAC-PmmCN), a stronger magnetic signal was observed associated with SOC was observed for DMAC-PmmCN, whereas it was reduced in DMAC-PymCN, further confirming the role of SOC in determining the effectiveness of TADF in a molecule.

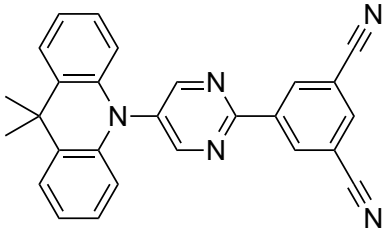


DMAC-Trz

MEH-PPV



DMAC-PymCN



DMAC-PmmCN

Figure 2-33 Structures used in Wang *et al.*'s[175] study.

The authors propose that SOC must be generated by the CT states somehow. They suggest that an optically induced dipole is set up in the CT state when the donor becomes positively charged, and the acceptor is negatively charged:

$$D + A \rightarrow D^{+} + A^{-}$$

In the ground state, there is no SOC since the orbitals of the donor and acceptor are isotropically distributed. Upon excitation, these orbitals become asymmetrically distributed and can now interact with the spins of the now charged donor (D^{+}) and acceptor (A^{-}) which forms SOC within the CT state.

Further confirmation was achieved by exposing the compound to oxygen. Since oxygen quenching predominantly affects the triplet state, but also both ^{1}CT and ^{3}CT, quenching of the CT states yielded a reduced magneto-EL signal alongside that of reduced TADF, indicating that spin-mixing is retarded. Repeating in a nitrogen atmosphere yielded no such change – clearly highlighting that the CT states are instrumental to the function of the CT process.

The same study showed that $^3CT \rightarrow {}^1CT$ direct conversion does not occur, since quenching just the ^3LE intermediary state retarded TADF. Thus, the process must occur *via* $^3CT \rightarrow {}^3LE \rightarrow {}^1CT$. Using magneto-PL analysis, they showed that this process is driven by the SOC of the CT states causing the spin flipping in the ^3LE state.

Further analysis involved solvatochromism studies. Since solvatochromism does not influence the LE states, only the CT states, the influence of solvent polarity on the emitted light illustrates the change in the CT state energy only. As solvent polarity is increased and emissions redshift, the magneto-PL spectra indicate SOC is reduced, as is the TADF effect. Wang *et al*. argue that this shows that spin-mixing, permitting rISC, is enabled by SOC, enhanced as the difference in ^3LE and ^1CT energies are reduced.

2.10.2 Charge transfer and additional donors

The work of Cui *et al*.[154] gives a good example of keeping the HOMO and LUMO separated on different moieties, however when separation is too far, CT character suppresses spin orbit coupling, retarding rISC, meaning that minimising ΔE_{ST} is required to enable rISC. This group worked around this obstacle by making use of locally excited states. They synthesised a TADF molecule based on a triazine acceptor moiety, and several carbazole donor moieties. This structure led to strong spin-orbit coupling and to formation of hybrid triplet states, permitting them to be closer in energy to the first excited singlet state, thereby enhancing the rISC process.

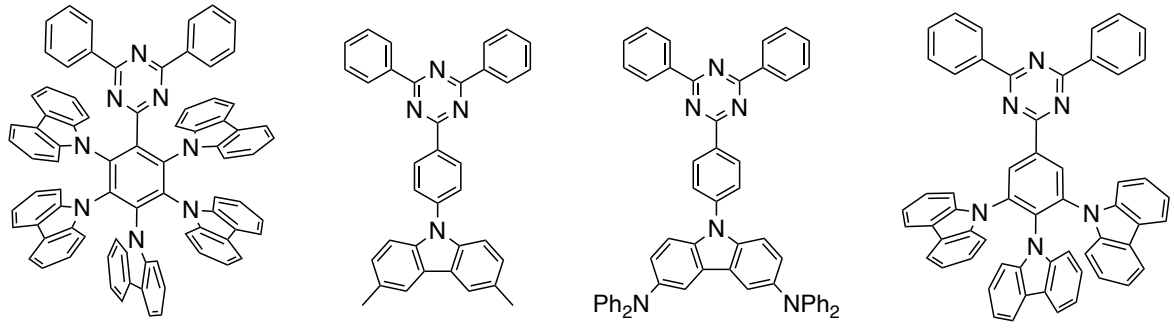


Figure 2-34 Examples of triazine-based TADF molecules with effective HOMO and LUMO separation - adapted from Cui *et al*.[154]

The structures of these molecules introduce additional moieties into molecules where the first excited triplet state is confined to the donor moiety. These extra donor moieties work

to narrow the overall energy between the singlet and triplet states (ΔE_{ST}), but also to not affect the nature of the triplet states. This gives different excitation characters to both the singlet and triplet states, as well as the potential for higher triplet states (T_2) from which conversion to the singlet state by second order spin-vibronic pathways are possible to enable rISC.

The group synthesised a range of molecules (see Figure 2-34) to compare, however they are all based on varying the number and type of donor moieties of 5Cz-Trz (full name: 9,9′,9″,9‴,9⁗-(6-(4,6-diphenyl-1,3,5-triazine-2-yl)benzene-1,2,3,4,5-pentayl) pentakis(9H-carbazole)).

In 5Cz-TRZ, the S_1 state exhibits charge transfer properties, making it strictly a ^{1}CT state. The triplet state possesses hybrid properties, giving both a ^{3}CT state and a ^{3}LE state. The stability of the first excited singlet state is enhanced by the presence of the five carbazole moieties, providing enhanced electron delocalisation, resulting in strong spin-orbit coupling and a very small ΔE_{ST}. The triplet states are within a dense manifold thanks to the multiple donor moieties, which provides a second excited triplet state with energy very close to that of the first excited triplet state. Additionally, the spin-orbit coupling between the two triplet states (T_1 and T_2) is much stronger than that observed between the first excited singlet and triplet states (S_1 and T_1), owing to the locations of the T_1 and T_2. Transitions from T_2 to S_1 are much quicker than from T_1 to S_1 in this case, so with a narrow enough gap between the T_1 and T_2 states, this alternative pathway to harvest triplets through mixing of the triplet states followed by spin flipping, becomes favourable.

Enhanced rISC rate occurs with this molecule because two rISC pathways are occurring: ^{3}CT $\rightarrow$ ^{3}LE $\rightarrow$ ^{1}CT and $T_1 \rightarrow T_2 \rightarrow S_1$. Extra carbazole donors lowers the first excited singlet state energy, narrowing ΔE_{ST}; a localised T_1 state results in a locally excited state (^{3}LE), which can mediate transitions from ^{3}CT to ^{1}CT as ^{3}LE exhibits strong SOC with ^{1}CT; the dense triplet manifold enables promotion of T_1 triplets to T_2 triplets which in this case can more readily undergo conversion to S_1 through a separate rISC pathway.

The strong ^{1}CT character is confirmed by redshifts observed when the emission spectrum is observed in a non-polar, followed by a polar, solvent (solvatochromism indicating the presence of a charge transfer state). The ^{3}LE state is proven when the molecule is frozen in a toluene matrix at 77K, revealing the vibrational structure concomitant with a locally

excited state. Transient electron spin resonance (TrESR) analysis reveals that SOC is used to form the T_1 states from the S_1 states. A narrow ΔE_{ST} of 0.06 eV is confirmed, as well as the differing excitation character of the singlets and triplets.

2.10.3 Solvatochromism and CT states

Molecules with conjugated π-bonding are prone to interactions with the environment around them if they themselves possess a dipole, such that their spectra shifts when in polar solvents.[176]

Normally, a dipole in the excited state of the molecule will attract polar solvent molecules which results in a reduction in the energy of the molecule, resulting in a bathochromic shift in emissions, also known as positive solvatochromism (see Figure 2-35). In rare cases the opposite can happen and a hypsochromic shift is observed (such as in vinylogues like 1,3-dibutyl-5-[2-(1,3-dibutyl-1,3-dihydro-2H-benzimidazol-2-ylidene)ethylidene]-2-thioxodihydropyrimidine-4,6(1H,5H)-dione[177]), referred to as negative solvatochromism.[176]

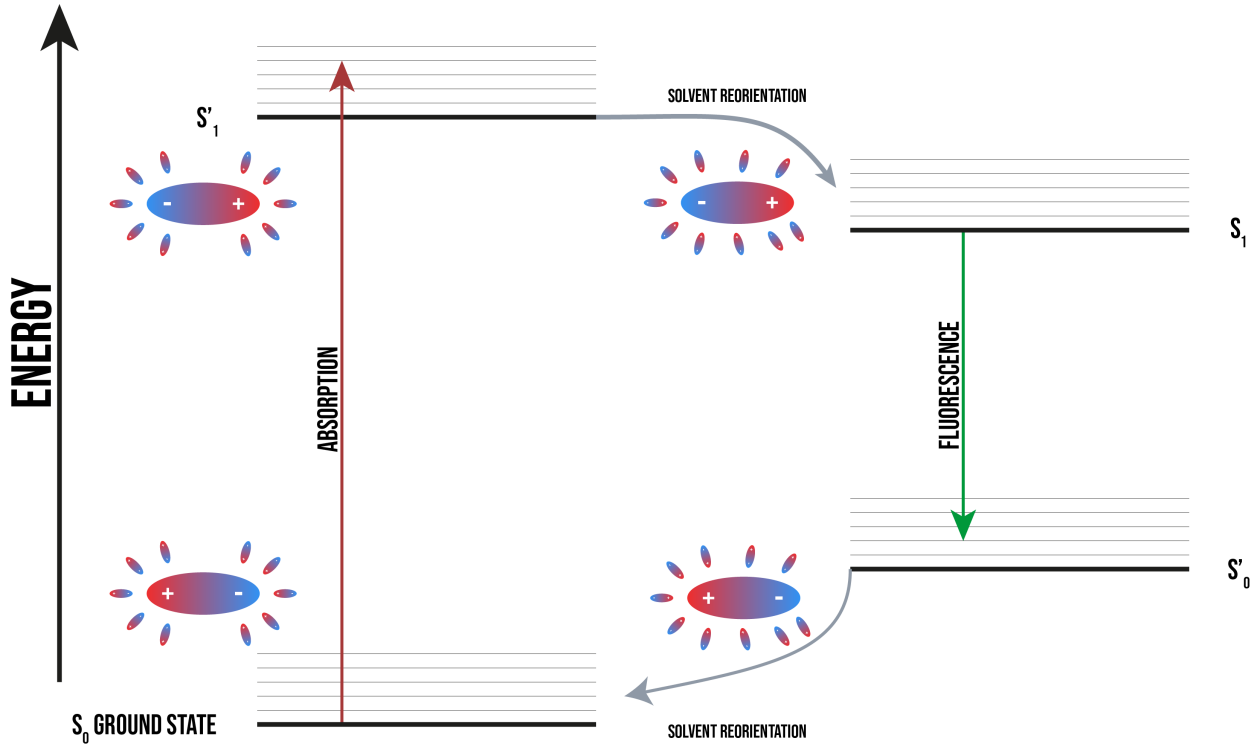


Figure 2-35 Jablonski diagram illustrating the relationship of excited states and solvatochromism. The large ellipses represent fluorescent molecules with a dipole, and the smaller ellipses represent polar solvents. As the fluorescent molecule's dipole changes, the orientation of the solvent molecules changes to accommodate it. Adapted from Forrest[34].

The cause of solvatochromism in molecules arises from three sources:

- In the case where one of the molecules (either the molecule in question or the solvent) possess a permanent dipole in the ground state, then long-range permanent-dipole - induced-dipole forces dominate;

- where the is no permanent dipole in either the solvent or the molecule, then weak intermolecular forces such as London-dispersion forces or van der Waals forces control the solvatochromism, which only take effect at short distances, so their impact on the emission spectra is minimal;

- where both the solvent and the solute are both polar, the molecules of solvent will surround the solute molecule acting as a screen against the electric field.

The polarity of solvent can have enormous effects on the TADF component of emissions thanks to the interaction between the solvent and CT states. An example of this can be found with the molecule DPO-TXO2 when made into a solution with methylcyclohexane (non-polar) and toluene (slightly polar).[163]

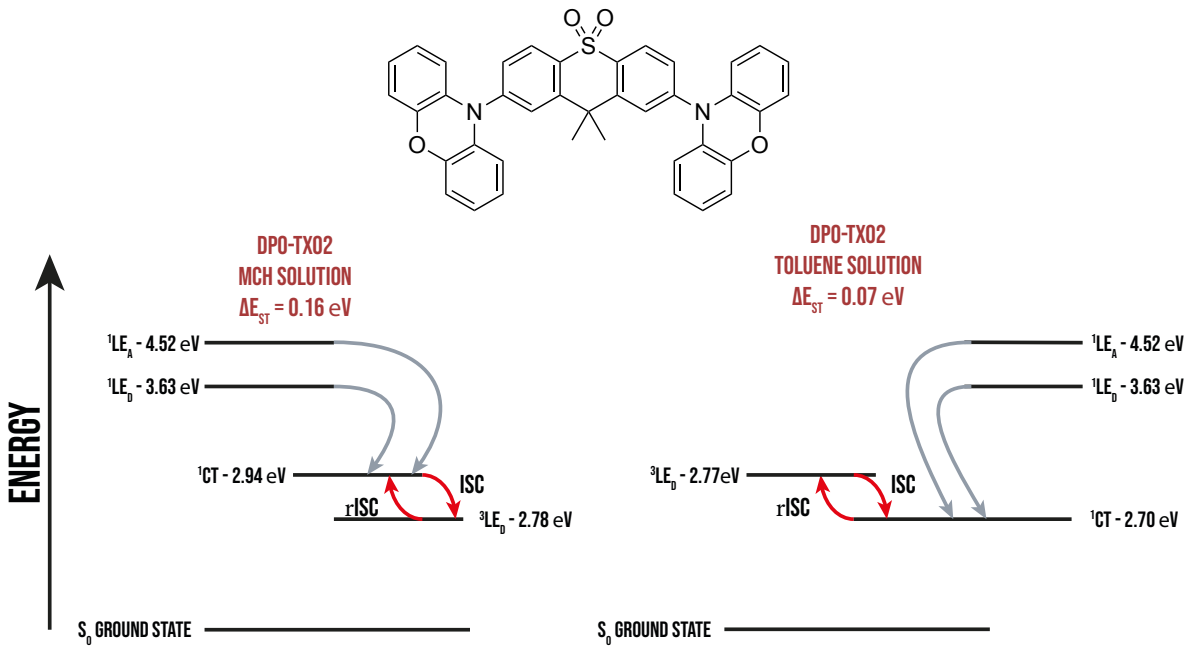


Figure 2-36 Structure and Jablonski diagrams of the charge transfer and locally excited states of DPO-TXO2 in two different solvents - methylcyclohexane (MCH) and Toluene. Adapted from P.L. Santos *et al.*[163]

^3LE_D triplet states (those located on the donor moieties of DPO-TXO2) are independent of solvent polarities (as mentioned earlier), however the ^1CT state decreases in energy when in

a polar solvent (see Figure 2-36). The CT state is pushed closer to the locally excited triplet state (below it now in toluene) and TADF increases dramatically.

More recent work by Monkman *et al*. investigated the effects of solvatochromism on charge transfer states[153]. In this work, polyethylene oxide (PEO) is used as a host matrix, which has a dielectric coefficient which is temperature dependent. Essentially, the polarity of the medium changes as a function of its temperature. The emitter molecule, PTZ-DBTO2 was chosen since it has orthogonality between the donor and acceptor and a strong CT state, but does not require the polarity of a solvent to stabilise the charge transfer state. In D-A-D molecules, one can observe dual phosphorescence - that is both phosphorescence from the low energy D or A and from the high energy state D or A. One needs to look at the emission wavelengths of the individual D and A molecules as well as D-A-D molecule to work out where the emissions are coming from.

The lowest energy triplet is the one needed to work out the ^{1}CT - Triplet energy gap (with the triplet being ^3LE_D or ^3LE_A). In Monkman's work, the vibrionic coupling was investigated by using solid-state solvatochromism (see Figure 2-37). In this case, PTZ-DBTO2 was suspended in a polyethylene oxide host, which changes its polarity with changes to temperature, allowing them to vary the polarity to observe solvatochromism. As the polarity changes with temperature, the energy of the CT state is altered, whilst the ^{3}LE local triplet state's energy remains unchanged because it has no dipole moment. This causes changes to the ΔE_{ST} and so allowing exploration of the mechanism.

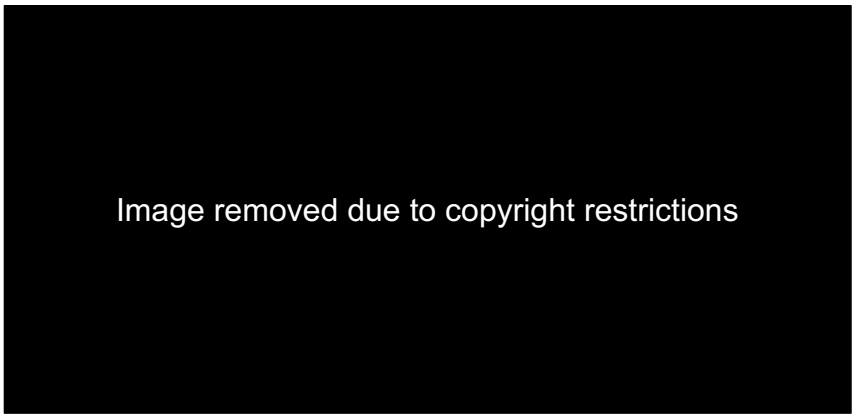


Figure 2-37 The effect of temperature on solvatochromism using a polyethylene oxide host matrix. The optimal temperature for enhanced rISC is around 225 K. Reproduced from Monkman *et al*.[153]

Normally, increasing the temperature will increase the efficiency of TADF as it is a thermally activated process. However, when in the polyethylene oxide host, what is seen is

that TADF increases as temperature decreases. This is because even at the lower temperature, there is sufficient thermal energy to enable TADF, but more to the point, in this host matrix, the lower temperature promotes an increase of the energy of the ^{1}CT state to that of the ^{3}LE state (at resonance) thanks to solid state solvent effects of the matrix - thereby promoting rISC.

The efficiency of TADF is linked directly to the splitting of the ^{1}CT and ^{3}LE states which is the greatest contributor to rISC, rather than the non-adiabatic coupling between ^{3}CT and ^{3}LE. When ^{1}CT and ^{3}LE are in resonance, the delayed fluorescence is at its maximum intensity. In donor - acceptor systems with narrow energy gaps, spin orbit coupling (SOC) is not accessible because the donor and acceptor, being orthogonal, would have identical orbitals - the electrons could not transition because there is no way to change the spin angular momentum of the electron - flipping of the electron's spin during the transition is not possible[174].

This boils down to the fact that SOC is not possible between the ^{1}CT and ^{3}CT states. A intermediate mediator state close in energy to the CT states which enables the spin flipping is required. This can be a singlet or triplet LE or CT, though normally it is the locally excited triplet state (^{3}LE) – as the molecules vibrate, coupling occurs between the ^{3}CT state and this locally excited intermediate state their respective geometries match, allowing them to mix, thereby allowing rISC (see Figure 2-32).

All three energy levels need to be taken into consideration when designing a potential TADF molecule. ^{1}CT and ^{3}CT should be as close together in energy as feasible as well as both being very close in energy to the intermediate state (^{3}LE).

For efficient rISC, molecules should have a large dihedral angle between donor and acceptor moieties to reduce HOMO and LUMO overlap, and a structural means of forming a locally excited triplet state to permit transfer of energy from ^{3}CT to ^{1}CT. All this must be done whilst limiting the opportunity for triplet states to be quenched, so the rate of the rISC process must be as high as possible under as wide a range of conditions to prevent efficiency roll-off.

2.11 Förster and Dexter energy transfer

Energy can be imparted from an excited state donor to a ground state acceptor species *via* three major mechanisms: Trivial Energy Transfer (through the mechanism of emission of electromagnetic radiation by the donor, which is received *via* absorption of the acceptor species); Förster energy transfer (a non-contact means of *inducing* excitation); and Dexter Energy Transfer (electron *transfer via* collisions).

2.11.1 Trivial energy transfer

An excited state donor species emits a photon of electromagnetic radiation thus:

$$^{*}D \rightarrow D + h\nu$$

Where D and D* are the ground state and excited state donor respectively. After travelling through space, if the photon comes into contact with a ground state acceptor species, excitation proceeds thus:

$$A + h\nu \rightarrow {}^{*}A$$

Where A and A* are the ground state and excited state respectively. We consider this process to be *trivial* since it is only driven by the emissions and reabsorption of photons between two molecules and does not directly involve the changes of spin during an interaction[121].

The rate of such trivial processes is dictated by the rates at which emission and absorption occurs. As such, the system's quantum yield Φ_e, depends on the concentration of the acceptor species [121]. This is because as the concentration increases, so too do the chances of the donor's photon being absorbed by another molecule. The acceptor's molar absorption coefficient ε_A should be as high as possible to also increase the likelihood of absorption occurring. Furthermore, owing to the law of conservation of energy, there must be enough overlap between the absorption profile and emission profile to minimise the loss of energy.

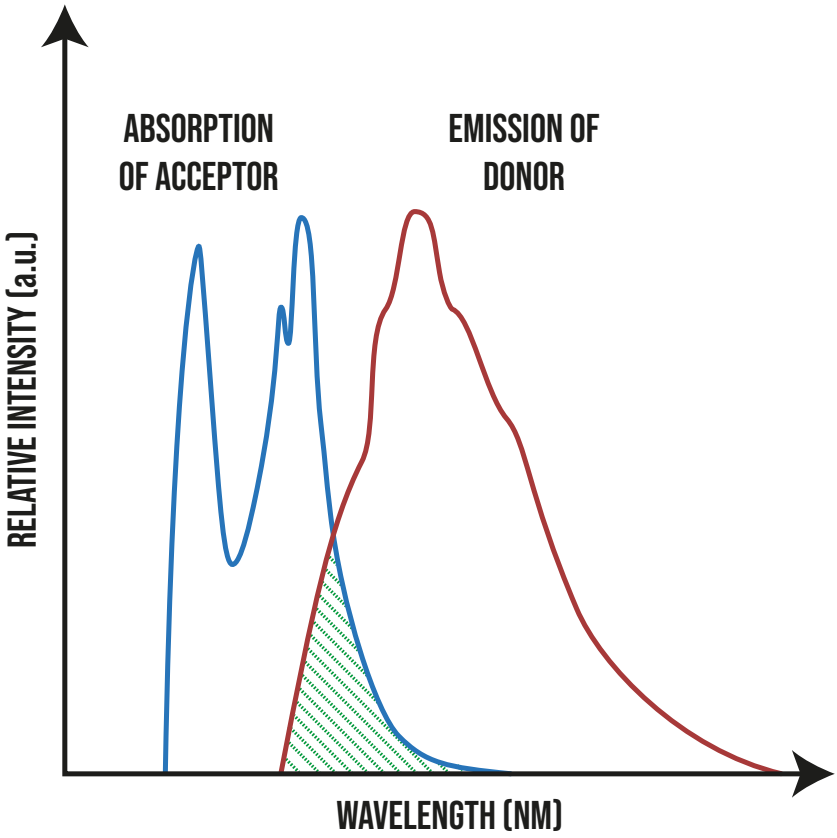


Figure 2-38 Spectral overlap required for the transfer of energy *via* trivial energy transfer.

In Figure 2-38 above, the emission wavelengths from the donor which are suitable for exciting the acceptor are found in the green hatched region. The larger the area of this region, the greater the energy transfer. This process is illustrated in terms of the excited states in Figure 2-39.

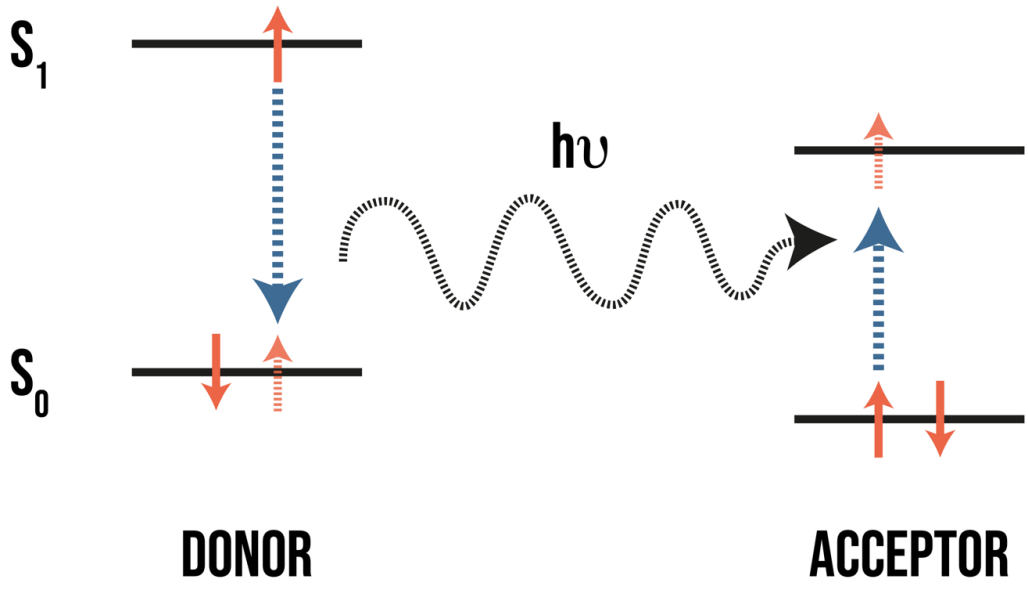


Figure 2-39 Excitation *via* trivial energy transfer. The excited singlet state of the donor decays radiatively to the ground state releasing a photon. This photon is then absorbed by the acceptor forming and excited state. Adapted from Forrest[34].

2.11.2 Förster resonance energy transfer (FRET)

Förster Resonance Energy Transfer (FRET) is facilitated by a means reminiscent of van der Waals forces. It is driven by inductive effects, namely dipole-dipole interactions[34]. When an excited state donor (be it a moiety or molecule) decays back to the ground state, and electron is transferred from the LUMO to the HOMO. This causes a change in the dipole of the molecule, which can affect the neighbouring acceptor molecules such that their electrons in their HOMOs get promoted into their LUMOs. Thus, the oscillating dipole of the donor sets up an oscillating dipole in the acceptor, promoting it to an excited state, and energy is transferred. Unlike *trivial* energy transfer, no photon is released in the process – it is instead driven by an electric field set up by the change in dipole moment. This electric field can be considered a *virtual photon* for all intents and purposes.

This is a *coulombic mechanism of energy transfer* because it is the charge interactions of the electrons driving the energy transfer *via* changes in dipoles, rather than physical collisions[121].

The oscillation of the excited donor (*D) induces a dipole in the acceptor (A), exciting the acceptor to *A as *D relaxed to D. Therefore, assuming energy is conserved:

$$\Delta E = ({}^{*}D \rightarrow D) = \Delta E = (A \rightarrow {}^{*}A)$$

FRET is distance dependent. If the donor and acceptor molecules are too far apart, no FRET can occur. Similarly, if they are too close, then Dexter interactions will instead dominate. The distance between donor and acceptor is r_{DA}.

When excited, *D can do the following:

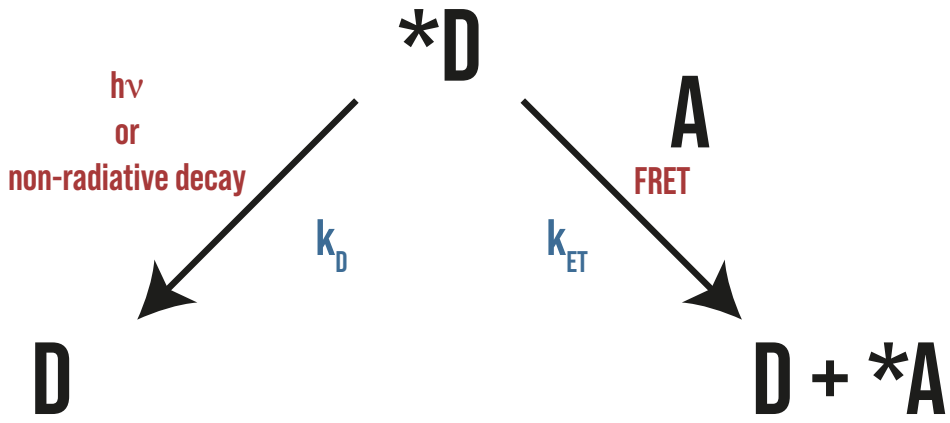


Figure 2-40 Pathways of decay for an excited state donor. Either *via* light emission/non-radiative decay, or *via* FRET. Adapted from Evan's lecture[178].

Where in Figure 2-40, k_D is the rate of radiative decay of the donor, k_{ET} is the rate of energy transfer from *D to nearby A. At the point where FRET is 50% efficient, the distance between the donors and acceptors is the Förster radius, r_0, the critical separation distance for energy transfer.

Förster's equation can be used to describe this situation[121]:

$$k_T^{dd} = k_D \left(\frac{R_0}{r}\right)^6 = \left(\frac{1}{\tau_D^0}\right)\left(\frac{R_0}{r}\right)^6$$

Equation 2-34 Förster's rate of transfer equation[121].

Where k_T^{dd} is the rate of transfer *via* FRET and τ_D^0 is the lifetime of the donor's emission when no acceptor is present to quench it. r is the intermolecular distance between the donor and acceptor.

FRET can still operate even if the van der Waals spheres are far from overlapping (up to ~10 nm).

2.11.3 Dexter energy transfer

Where Förster Resonance Energy Transfer transfers energy from one molecule to another at a distance, Dexter Energy Transfer requires molecules to make physical contact to facilitate the transfer of energy.

This process involves an electron from the molecule in the excited state (the donor), transferring from the LUMO into the LUMO of a ground state molecule (the acceptor). All the while one of the two electrons in the ground state acceptor's HOMO is simultaneously transferred into the singly occupied HOMO of the excited state donor. This gives (diagrammatically at least) the illusion of a simple conversion of an excited state into a ground state and vice versa[179].

Dexter energy transfer comes in two forms: *Singlet-Singlet Dexter Energy Transfer* and *Triplet – Triplet Dexter Energy Transfer*, shown in Figure 2-41and Figure 2-42, respectively.

2.11.3.1 Single – singlet Dexter energy transfer

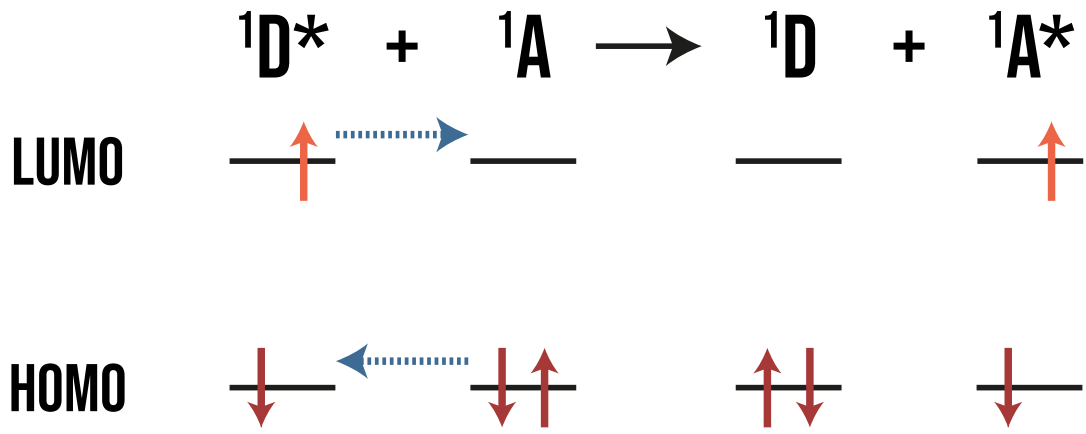


Figure 2-41 Singlet-singlet dexter energy transfer. Here the excited donor's lone electron in the LUMO is transfered to the acceptor's LUMO, whilst the electron in the acceptor's HOMO of opposite spin to the donor's is transferred to the opposing spin space in the donor's HOMO. Adapted from Forrest and Evans[34,179].

In this case, the initial acceptor and donor are both in the singlet state - be it excited, in the case of the donor (S_1) or ground state (S_0) in the case of the acceptor. As such, the singly occupied HOMO and LUMO remain with opposing spins throughout the process[179].

2.11.3.2 Triplet – triplet dexter energy transfer

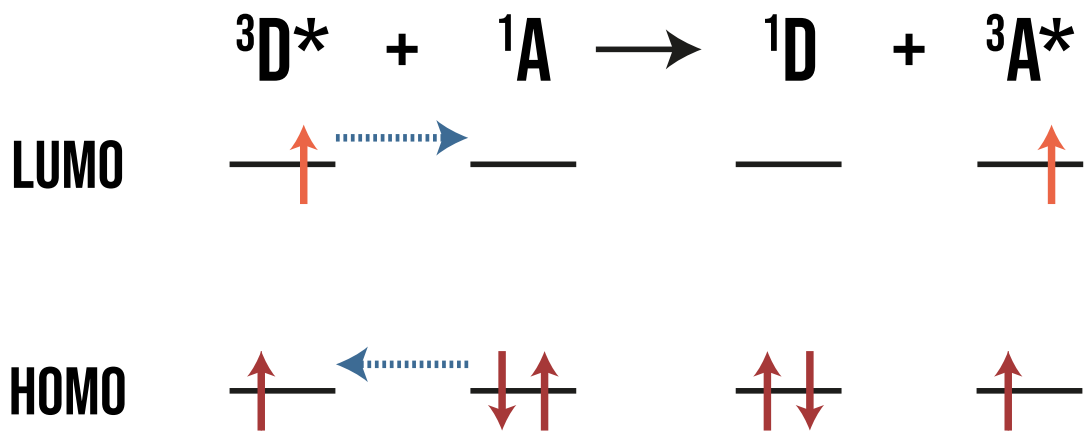


Figure 2-42 Triplet-triplet dexter energy transfer. Here the excited donor in the triplet state loses it lone electron in the to the acceptor's LUMO, whilst the electron in the acceptor's HOMO of opposite spin to the donor's is transferred to the opposing spin space in the donor's HOMO. Adapted from Forrest and Evans[34,179].

This process differs in that the spins of the electron in the HOMO and LUMO in the excited molecule remain identical to one another even after transfer, meaning that the excited states involved are triplets.

Regardless of whether the Dexter mechanism is singlet-singlet or triplet-triplet, a collision must occur between the two molecules so that energy can be transferred. As the excited donor and ground state acceptor approach one another, delocalisation of the excitation energy is manifest across both donor and acceptor. Visualising this on a potential energy surface (see Figure 2-43), we see a minimum (or *well*) forming as D* and A get closer together. At this point, an exciplex forms where the energy is delocalised across both donor and acceptor [D-A]*.

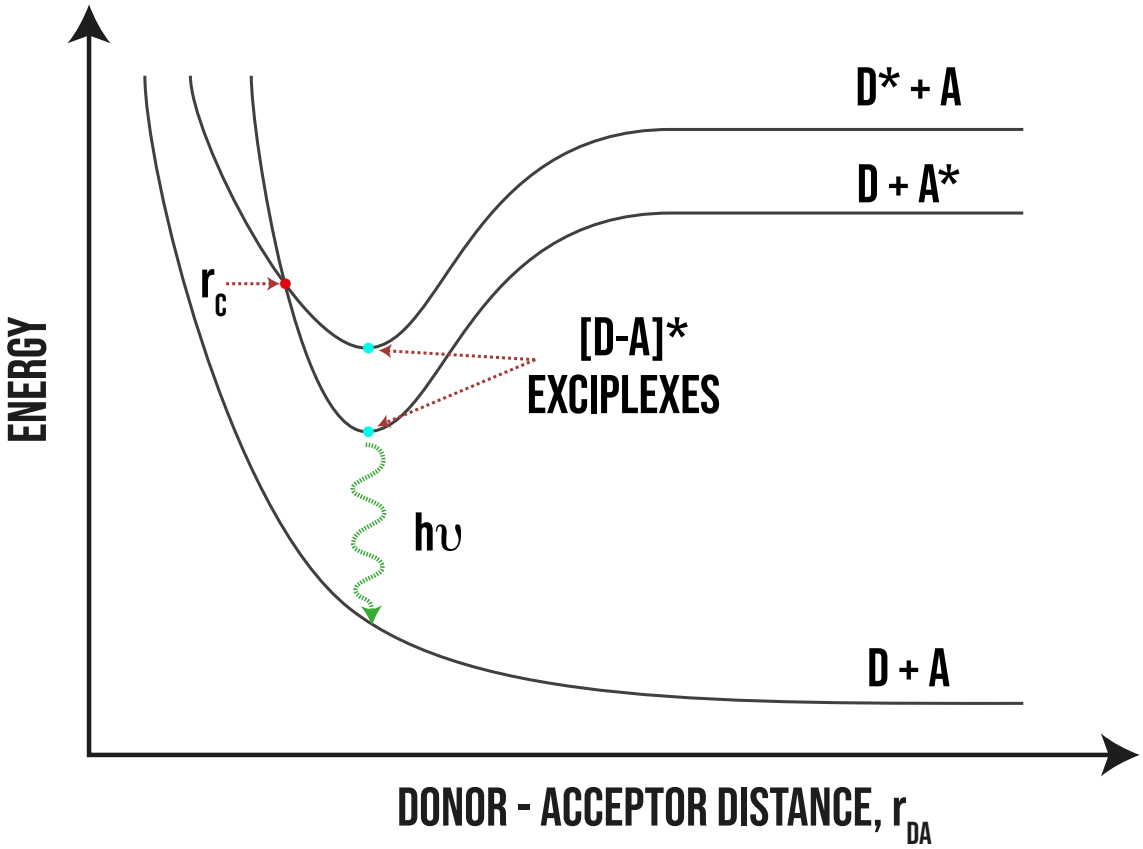


Figure 2-43 Potential energy surfaces for the dexter process between an excited donor and ground state acceptor (starting products); excited acceptor and ground state donor (products); giving rise to emission from the acceptor yielding the PES of the donor and acceptor both in the ground state. Adapted from Evans' lecture[179].

In the above diagram, r_C (where the potential energy surfaces for the D* + A and D + A* systems intersect) represents the distance at which the donor and acceptor are pushed even closer together to a point where it becomes favourable for the excitation energy to pass over from one molecule to the other – *i.e.*, the point at which D* + A → D + A* happens[179]. At this point, we shift from the "reactant's" potential energy surface (with the excited donor and ground state acceptor) to the "product's" potential energy surface and the exciplex adopts a form where slightly more energy is localised on the former acceptor rather than the donor.

Following this transfer, we either observe separation of the donor and acceptor species with non-radiative losses or emission of radiation as the acceptor returns to the ground state. In an ideal situation, the donor and excited acceptor should separate first so that A* can decay radiatively on its own[179].

Quantum mechanically, the initial state is described thus:

$$\psi(^{*}D)\psi(A)$$

Where localisation of the excitation energy wavefunction is entirely upon the donor.

And the final state thus:

$$\psi(D)\psi(^{*}A)$$

Where the localisation of excitation energy is upon only the acceptor.

Since singlet to triplet and vice versa transitions are spin forbidden, singlet-triplet Dexter transitions are not possible. Additionally, the wavefunctions are orthogonal in this case, which prevents any energy exchange between triplet and singlet states *via* Dexter Energy Transfer[179].

However, it is possible through Dexter interactions for oxidative and reductive mechanisms to occur. In a simplistic sense, we can consider electrons transferring from LUMO to LUMO and HOMO to HOMO without any energy lost (if the donor's HOMO is the same energy as the acceptors, and the same being true for the LUMOs). However, in reality, the respective HOMOs and respective LUMOs will differ in energy, so it is useful to consider oxidative and reductive mechanisms in the excited states.

2.11.4 Oxidative mechanism

This is when the LUMO of the donor *loses* its electron to the acceptor's LUMO *via* electron transfer, with this occurring prior to the acceptor's HOMO losing its electron to the donor's HOMO. This results in an intermediate state composed of a radical ion[179] (see Figure 2-44).

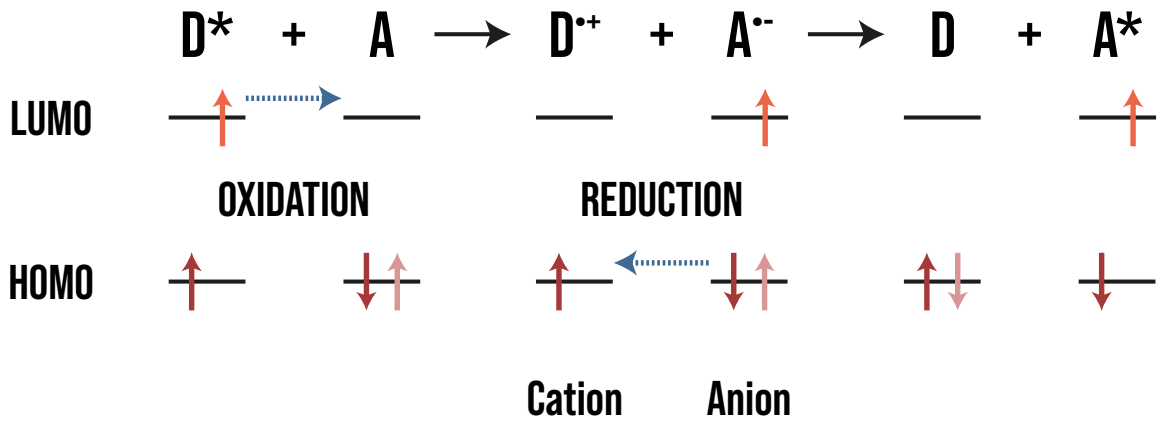


Figure 2-44 Oxidative dexter mechanism. Here oxidation of the excited state donor occurs *via* the LUMOs first, followed by reduction of the acceptor anion *via* its HOMO to yield and excited state acceptor and ground state donor. Adapted from Evan's lecture [179].

A cation is formed by the donor since it has lost an electron, whereas the acceptor becomes an anion. We see this process occurring if the acceptor molecule's orbital energies are lower than the donor's [179].

2.11.5 Reductive mechanism

In the case of an excited state donor molecule possessing lower HOMO orbital energies than a potential acceptor molecule instead, then reduction occurs. This involves the *gain* of electrons with respect to the donor's HOMO – the acceptor transfers its electrons from its HOMO to the donor's first. This is then followed later by electrons from the donor's LUMO going to the acceptor's LUMO. Following reduction, a radical ion is formed. Unlike the oxidative mechanism, in reduction, the donor becomes the anion as it gains an electron, and the acceptor becomes a cation [179] (see Figure 2-45).

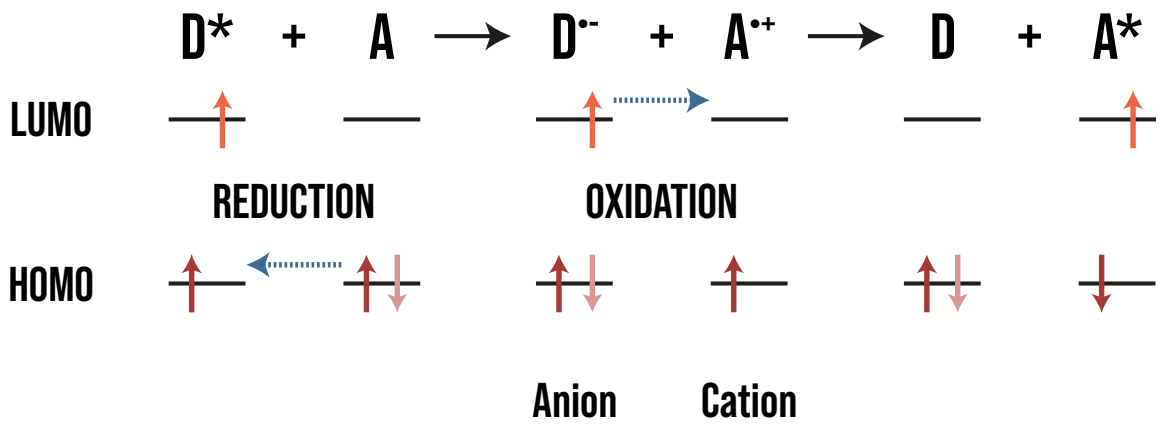


Figure 2-45 Reductive dexter mechanism. Here reduction of the excited state donor occurs through the HOMOs first, followed by oxidation of the acceptor anion *via* the LUMOs to yield and excited state acceptor and ground state donor. Adapted from Evan's lecture [179].

Simplified, the intermediates would look like the following:

Reduction mechanism intermediate:

$$^{*}[D^{\delta-} \cdots A^{\delta+}]$$

Oxidative mechanism intermediate:

$$^{*}[D^{\delta+} \cdots A^{\delta-}]$$

The reason for Dexter interactions requiring a molecular collision lies in the fact that it requires orbital overlap, and is hence dependent upon distance[121]:

$$k_T = \frac{2\pi}{h} KJ' \exp\left(\frac{-2r}{L}\right)$$

Equation 2-35 Dexter equation for energy transfer. Taken from Valeur and Berberan-Santos[121].

Where *r* is the distance between the donor and acceptor, L is the average Bohr radius, K is a constant and J is the integral of spectral overlap between the donor's emission spectrum normalised to unity, and the acceptor's absorption spectrum normalised to its molar absorption coefficient[121].

This equation highlights the collisional importance for Dexter interactions to work. If the distances between the donor and acceptor (*r*) exceeds that of the radii of the combined donor and acceptor molecules (with the van der Waals radii no longer overlapping), then the rate of exchange, k_T becomes negligible and so energy transfer completely ceases to occur.

2.12 Efficiency roll-off

2.12.1 What is it?

Whilst OLEDs offer an attractive alternative to conventional lighting technologies in terms of their efficiencies and tuneable output wavelengths (with the ability to select comfortable CCT for the device's usage situation and high CRI), they suffer from degradation of their efficiencies when used at high brightness - a process referred to as "efficiency roll-off". In order to be successfully implemented as a lighting technology, OLEDs must overcome this limitation. The exact mechanism for efficiency roll-off is hotly debated, however there are two main culprits: namely, exciton quenching and alterations to the charge carrier barrier. Exciton quenching has three different forms: triplet – triplet annihilation; polaron mitigated quenching; and field-induced quenching.

For use in lighting applications, OLEDs will need to have a brightness of around 5,000 cd/m^2 at least.[180] Owing to the structure of OLEDs, the form factor of a space illuminating OLED device will take up a large area. As such the devices will need to have a large current density to function to these demands; some suggest[181] that it could be as a large as 600 A/cm^2. For use in novel applications, such as biomedical devices, projectors and lasers,[182] the brightness of the OLED must be significantly greater than that of current commercial OLED based devices. In order to meet these demands, efficiency roll-off and degradation of the devices at high brightnesses and current densities must be overcome. The lifetime (LT) of OLED devices is roughly related to the current density (J) raised to the negative power of β (which is a fitting parameter between 1.5 and 3):[183]

$$LT \propto J^{-\beta}$$

Equation 2-36 Lifetime varies with current density. From Murawski *et al.*[183]

In a hand-waving summary, in order to make OLEDs operate at a practically useful brightness intensity, they will need to increase their luminosity output by a factor of 10, however, currently this will result in a 100 × reduction in the lifetime of the OLED device.

The critical current density, J_0, is the point at which the current density causes the EQE of the device to be reduced to 50% of its original value. A device is said to have a high, or strong roll-off if the critical current density is low, since only a small amount of current

would be needed to reduce its efficiency to 50%. Normally, it is difficult to achieve J_0 under standard operating conditions if the device is efficient - it is more likely that in trying to reach J_0, the device will degrade beforehand. A better measure of the roll-off of the device is the $J_{90\%}$ - the current density required to reduce the EQE to 90% of the starting point. Murawski *et al*.[183] surveyed multiple fluorescent, phosphorescent, TADF, flat outcoupling, and tandem devices and demonstrated that most high efficiencies, *i.e*. those with EQEs above 15%, function *via* phosphorescence. However, these devices had very poor performance in that they possessed very high efficiency roll-off: $J_{90\%}$ of between 1 and 30 mA/cm^2 between 1,000 and 10,000 cd/m^2. Conversely, they showed that fluorescent devices, while having low EQEs (in the sub 10% region) possessed much improved, low efficiency roll-off (between 50 and 1,000 mA/cm^2). Making use of hybrid structures aids the decreasing of roll-off, however fluorescent devices are so far the best performers with low roll-off, making them ideal candidates for consumer electronics where roll-off must be minimised.

Fluorescent devices differ negligibly between red, green, and blue where roll-off is concerned, however the phosphorescent emitters have the largest roll-off in their blue emitters. This is caused by the high energy triplet state needed to achieve blue emissions by phosphorescence, which leads to poor stability chemically, as it readily undergoes triplet quenching. This enhances the rate of degradation when exposed to high currents. This same disadvantage plagues TADF type emitters since the triplet state is initially populated prior to rISC. In terms of luminance, the $L_{90\%}$ measurement gives the luminance range at which a reduction to 90% of the EQE is observed. For purely fluorescent emitters, $L_{90\%}$ is between 1,000 and 10,000 cd/m^2

Organic molecules exhibit weaker spin orbit coupling between their singlet and triplet states. This can give rise to the rISC process being slow in TADF devices, taking milliseconds to proceed. As a result of this, when devices are operated at higher current densities, their efficiencies rapidly and irreversibly deteriorate.[184]

2.12.2 The causes of efficiency roll-off

Murawski *et al*.[183] suggest several processes that result in roll-off: annihilation of excited states (be it singlet-singlet, singlet-triplet or triplet-triplet), exciton-polaron interactions, field induced quenching, imbalance of charge carrier balance, and a combination of these processes.

Increasing the current density in an OLED can result in the recombination zone relocating its position in the active layer, which in turn can alter the outcoupling efficiency, η_{out}, of the device; the charge balance (ratio of holes to electrons) may even shift, resulting in an alteration to the electric efficiency of exciton formation, γ. If bimolecular annihilation occurs, excitons will be quenched and thus prevented from emitting. This negatively affects the radiative efficiency, η_{rad}, of the device. Since the roll-off effect impacts the EQE of the device, a look at the EQE equation reveals just how significant the aforementioned factors are as potential pathways to roll-off:

$$EQE = \gamma \chi \eta_{rad} \eta_{out} = IQE \ \eta_{out}$$

Equation 2-37 from Murawski *et al.*[183]

Since the ratio of singlets to triplets, χ, (or more precisely the spin factor) stays mostly constant, then the culprits behind roll-off are likely to be any of the other variables.

Quenching can be facilitated by a number of pathways. Singlets can be returned to the ground state by interaction with neighbouring singlet states or triplet states, and the same is true of excited triplets. Singlets can also be removed from radiative emission pathways by conversion into triplet states *via* intersystem crossing (ISC). It is also possible for polarons to quench both singlets and triplets in singlet-polaron or triplet-polaron annihilation (SPA and TPA respectively). Additionally, it is possible for exciton molecules to be physically degraded irreversibly by the effects of heat, or an excessively large current, or chemically by reaction with neighbouring molecules, or radicals.

TTA - Triplet-triplet annihilation

$$T_1 + T_1 \xrightarrow{3/4k_{TT}} T_1 + S_0$$
$$T_1 + T_1 \xrightarrow{1/4k_{TT}} S_1 + S_0$$

Equation 2-38 Pathways from TTA. From Kasemann *et al.*[185]

When excited molecules are quenched by interactions with other excited state molecules, the process is referred to as "bimolecular quenching". Triplet states have lifetimes in the microsecond region - much longer than singlet states. Naturally, being in existence for a longer period increases the likelihood of interactions with other molecules and subsequent quenching. It is possible for triplets to annihilate other triplets in the triplet-triplet annihilation process. Here, once they interact, one triplet loses energy and returns to the

ground state, and the other is energised to a higher energy intermediate state. This could be a triplet or a singlet. In the case of higher energy singlet states, this can be advantageous, as it can eventually internally convert to the S_1 state, then to the ground state *via* fluorescence. Additionally, interactions of two triplet states can produce an excited singlet state in addition to a ground singlet state. The share of these two processes is 75% for T_1 + S_0 formation, and 25% for S_1 and S_0 production. However, it is also possible that the singlet will once again undergo intersystem crossing back to the triplet state, this time with fewer triplets to interact with, and decay non-radiatively. As such, triplet-triplet annihilation has the potential to significantly reduce the efficiency of a device.

Devices have been developed based entirely on this principle, however TTA emitters are restricted to a total overall efficiency of well below 100%. This is due to phosphorescence from the 75% triplets really only reaching 50% of this value thanks to it being a bimolecular process, so the phosphorescence is actually 37.5% efficient. The 25% singlets, assuming they are all emissive *via* fluorescence, combines with phosphorescence to yield only 62.5% efficiency in total.

STA - Singlet-triplet annihilation

$$S_1 + T_1 \xrightarrow{k_{ST}} T_1 + S_0$$

Equation 2-39 STA pathway. From Kasemann *et al.*[185]

Interaction between a singlet and a triplet can also occur, particularly at elevated current density. Here an excited electron donating singlet species interacts with an excited triplet state, causing the singlet to decay to the ground state and elevation of the triplet to a higher triplet state. This elevated triplet decays back to the first excited triplet state, and energy from the pair is lost overall. When the current density is lower, the triplet population is below the threshold required to enable STA. Above this point, increased triplet population density will increase the likelihood of singlet-triplet annihilation.[185]

SSA - Singlet-singlet annihilation

$$S_1 + S_1 \xrightarrow{k_{SS}} S_1 + S_0$$

Equation 2-40 SSA Pathway. From Kasemann *et al.*[185]

This process between two excited singlet states, has its roots in their dipole-dipole interactions and occurs more often in crystalline structures such as anthracene[186]. When the two singlet states interact, the resultant intermediate state is still a singlet, with no conversion to a triplet state. This intermediate state decays to produce one singlet excited state at a higher vibronic energy and one singlet ground state, with an overall loss of energy.

Exciton–polaron interactions

$$S_1 + n \xrightarrow{k_{SP}} S_0 + n$$

Equation 2-41 Exciton-polaron interaction. From Kasemann *et al.*[185]

It is also possible for excitons to interact with polarons or charge carriers in devices. Interaction of holes or electrons with excited singlet or triplet states results in the conversion of the excited state to the ground state and absorption of the excited state's energy by the holes and electrons - increasing their respective potential energy[185].

Shifting of the recombination zone

When current density is low, there are likely to be imbalances of charge carriers, yielding reduced efficiency[185]. However, increasing the currents, the charge carrier populations tend towards balancing each other out, leading to decreased roll-off. If charge balance changes when the current density is changed (such as more holes than electrons, or vice versa), then the recombination region in the active layer can be shifted to a less efficient location (partially covering the hole or electron injection layer for example) significantly increasing the efficiency roll-off. This would lead to significant reductions in emissions, as the electric efficiency of exciton formation, γ, is reduced.

Field-induced quenching

Higher voltages may lead to field-induced quenching, where excited state molecules dissociate forming free charges and are capable of leaving the active layer, thereby reducing overall emissions by again reducing the value of γ[185].

Joule heating

Joule heating is caused by the inherent resistivity of the layers of the device, which can result in dissociation of excited singlet states before they are able to fluoresce (or undergo ISC to phosphorescence)[185].

2.12.3 How to prevent roll-off

Molecules incorporating donor and acceptor moieties, such as TAT-3DBTO2 (Figure 2-46), which permit significant spin and electronic coupling, have been shown to supress efficiency roll-off thanks to multiple routes for triplet harvesting.[187]

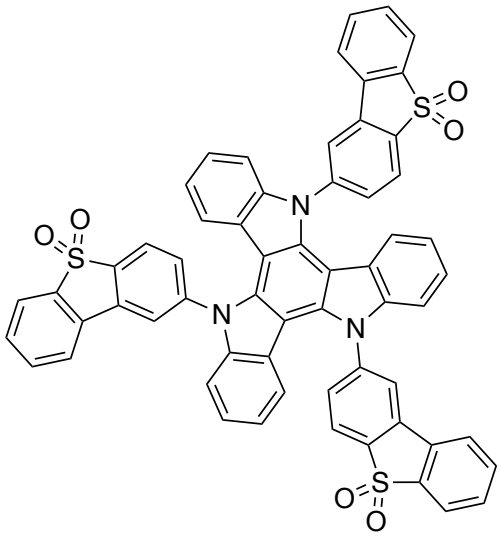


Figure 2-46 Structure of TAT-3DBTO2 from Eng *et al.*[187]

Work by Monkman *et al*. involving D-A type molecules with multiple carbazole based donors, produced non-equivalent triplet states thanks to a crowded geometry. Differing dihedral bond angles between donors and acceptors gave rise to multiple rISC pathways, all with significantly different rates,[188] which helps to decrease the likelihood of quenching.

Murawski *et al*.[183] go further to suggest a number of methods for preventing roll-off at high brightness, based largely on three principles:

- Decrease field-induced quenching
- Decrease the likelihood of exciton annihilation
- Sustain an ideal charge balance

These can be further exploited as five key considerations:

Preventing molecular aggregation

The distance between the emissive molecules should be maximised. When excited, they can migrate together to form clusters of molecules. The lower the dipole of the molecule, the weaker their electrostatic interactions - this results in reduced clustering. Incorporating this consideration into the molecular design stage will aid with development of devices with reduced roll-off and keep dipoles to an absolute minimum. A clue as to whether a device suffering from efficiency roll-off has its roots in molecular aggregation can be found by exploring the photoluminescence spectra of the molecule. At increased concentrations of a dipolar molecule in the active layer, the emission spectra will begin to broaden, as observed by Kawamura *et al*.[189], in their 2006 work with Ir(III) complexes (see Figure 2-47). They observed that with increased dopant concentration, the wavelength of emissions widened.

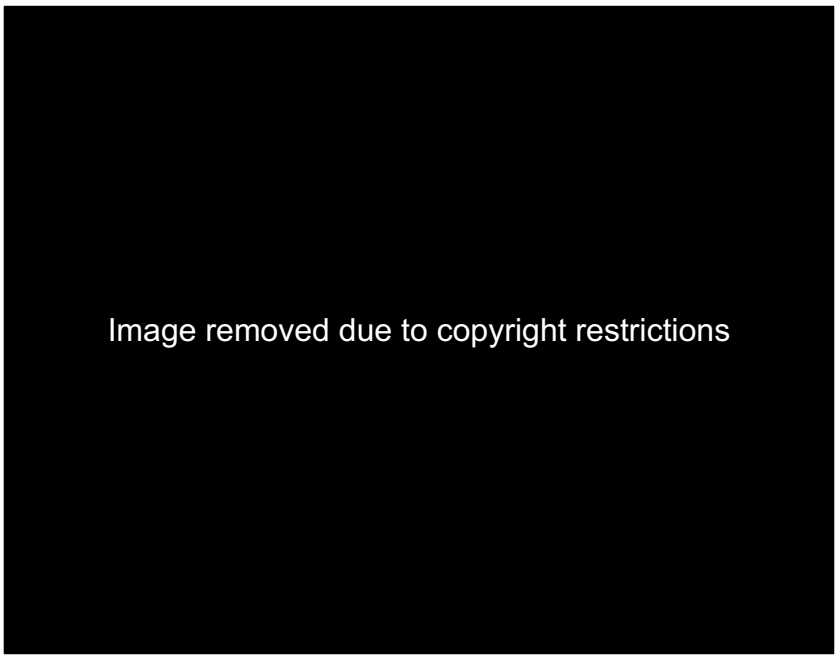


Figure 2-47 Influence of dopant concentration on photoluminescence intensity. Reproduced from Kawamura *et al*.[189]

Adding dendrons to the emitter molecule's structure helps with spacing molecules out, which leads to suppression of triplet-triplet annihilation as well as preventing aggregation[190]. If the dendrimers are sufficiently large enough to exceed that of the molecule's Dexter transfer radius (the maximum distance within which electrons can be transferred from a donor to an acceptor by contact), it can lead to reductions in roll-off.[190,191]

Reducing the lifetimes of excitons

Singlet lifetimes are too short (nanoseconds) to contribute to roll-off by themselves. Polarons and triplets on the other hand, have lifetimes long enough (microseconds) to allow them to persist such that triplet and polaron densities can become high enough to influence roll-off *via* such processes as triplet-triplet annihilation. Use of "active hydrogen" by Han *et al*.[192] (to all intents and purposes, hydrogen bonding) in an $Ir(ppi)_2acac$ based emitter (see Figure 2-48), enhanced intermolecular forces *via* interactions between C=O (acetylacetone) and N-H (imidazole) and thus enabled molecular aggregation. This in turn yielded much reduced triplet lifetimes (3.72 ns). However, when $Ir(ppi)_2acac$ is doped beyond 7%, further enhancement of EQE is suppressed by the aforementioned molecular aggregation effects, effectively stunting any practical reduction in efficiency roll-off beyond this point. Han *et al*.'s work points to reduction in triplet lifetimes being a highly important consideration when attempting to suppress efficiency roll-off.

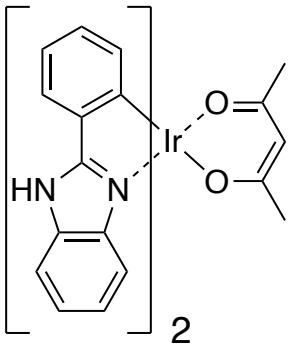


Figure 2-48 Structure of Ir(ppi)$_2$ acac adapted from Han *et al.*[192]

Manipulation of the host matrix

The host matrix in an OLED is the material in which the emissive molecule is held. They are ideally transparent to charge, meaning they should have little resistance, and divert the majority of charge carriers to the emitter molecule. The host matrix can also influence the roll-off. If the triplet lifetime of the host matrix is too long, then the chances of roll-off occurring are enhanced. Replacing the host matrix with one that possesses a shorter triplet lifetime has been shown to significantly reduce roll-off,[193] as it can pass on triplets to the emissive molecule.

Use of gold nanoparticles in the emitter layer has also been shown to reduce roll-off. Work by Ji *et al*.[194] revealed that interactions between surface plasmons on gold nanoparticles and the emitter molecule in the triplet state result in suppressing the lifetime of excited states, reducing roll-off. They also found that the closer a phosphorescent molecule is to the gold nanoparticle, the rate of radiative decay increases. Although this approach has a disadvantage of complicated considerations with respect to needing to be coupled to the emitter molecule effectively (how the size and locations of the emitter molecules relate to that of the nanoparticles), as well as effects the presence of a metal may have chemically and electrically on the emissive molecules.

Have a larger hole-electron recombination region in the device

Most emission occurs within a region of the active layer known as the recombination zone (where holes and electrons recombine and release photons). If this region is increased in size, it will result in the density of excitons being reduced, which will have the effect of reducing the chances of annihilations occurring.[195]

One way of broadening the recombination zone is to have two emissive layers stacked next to one another (see Figure 2-49). Under normal conditions with a single emissive layer, the recombination zone is restricted to a narrow space on one side of the layer (which side depends on whether the layer's matrix is mainly electron or hole transporting). Applying a double layered structure (one with an electron transporting, and one with a hole transporting matrix) extends the recombination zone into both layers, broadening it[196]. Broadening it further can be achieved by using a single layer, but with a mixture of hole and electron transporting matrix materials[183]. This can be further enhanced by introducing a gradient across the emissive layer's matrix mix - higher concentration of one matrix material at one side, gradually decreasing across the structure as the other matrix material's concentration increases[197] – in order to achieve the optimal balance of, and increase the mobilities of the holes and electrons. The previous two methods suffer from slightly complex manufacturing processes, however, use of a bipolar/ambipolar[198] matrix, which aids the transport of both holes and electrons, achieves a similar broadening of the recombination zone - though one must consider the size HOMO and LUMO energies of the ambipolar material with respect to one's emissive molecule and neighbouring electron and hole injection layers.

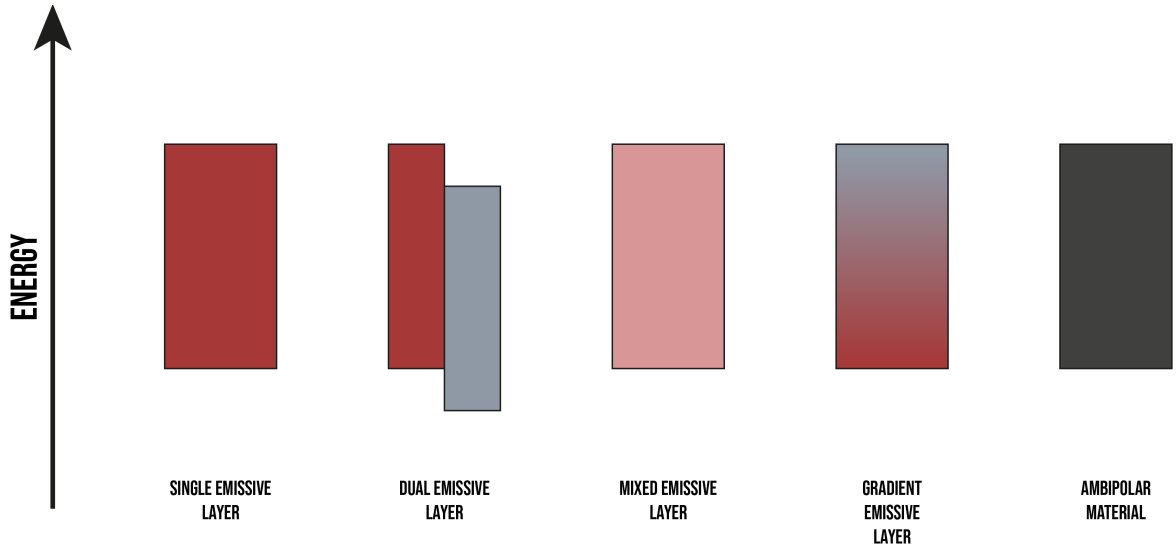


Figure 2-49 Emissive layer modifications for controlling the location of recombination zone. Adapted from Muraski *et al.*[183] Colours signify separate materials.

Use device layers to control triplets

If the point at which singlet emission coincides with that of the triplet absorption, then singlet-triplet annihilation (STA) is exceedingly more likely.[199] To combat this, use of an additional dopant in the matrix known as a "triplet manager"[200] is suggested. This functions

by having a triplet energy which is less than the rest of the matrix or emitter molecule, which enables the emitter's triplet states to be removed. Effectively, this means that the triplet energy is lower than the singlet energy of the emitter and means that STA is suppressed. The goal is to prevent triplet population on the active molecule from being sufficiently high that interaction with singlets can occur. Quenching the triplets in the matrix aids this, as it takes the triplet states out of play; leaving the singlets to decay radiatively and undisturbed by potential quenchers. However, in TADF emitters this will of course yield reduced efficiency.

2.12.3.1 Impact of interlayers on roll-off

Standard multilayer OLED device structures present effective methods for hole and electron transportation into the active material. However, additional layers introduce the issue of energy loss due to resistance to charge transport. It has been shown that with careful consideration of the properties of the emissive material, it is possible to simplify OLED devices to effectively consist of a single layer, without the need for a host matrix.

Under normal circumstances, multilayer devices are required so that the recombination zone can be centred in the emissive molecule region. Kotadiya *et al.*[201] have recently shown that total replacement of the hole injection, hole transport, electron transport and electron injection layers (HIL, HTL, ETL and EIL) can be achieved by coating the anode and cathode in specific interlayers (significantly thinner than the usual HIL and EIL). However, it could be argued that these so called 'interlayers' are in fact hole and electron transport layers in all but name on a much smaller scale. The group utilised the molecule CzDBA (see Figure 6-1, a molecule of interest to us as it is the molecule on which our work in chapter 6 is based), which possesses a HOMO and LUMO of sufficiently low energy to prevent the trapping of electrons in the EML; as well as efficient charge transport properties (thanks to its high electron and hole mobilities) permitting the lack of transport layers. Holes were pumped in from a molybdenum oxide anode and electrons from an aluminium cathode. Interestingly molybdenum oxide is not conductive enough to be an anode, so it is likely that the authors have coated this on the surface of an anode and not specified this. The anode was coated with a C_{60} interlayer, whereas the cathode was coated with a 1,3,5-tris(N-phenylbenzimidazol-2-yl)benzene (TPBi) interlayer. The interlayers are transparent to charge, meaning that electron and hole injection is facilitated easily into the active layer.

Additionally, the interlayers aid with widening the region in which recombination occurs, improving device efficiency and reducing roll-off. The result of this was a single layer device yielding excellent efficiencies and brightness, surpassing that of the best phosphorescent equivalent devices, giving 1,000 cd m^{-2} with an operating voltage of 2.41 V and 10,000 cd m^{-2} with 2.89 V; they also demonstrated prolonged lifetimes compared to similar devices.

More recent studies by Tang *et al.*[202] incorporated tris(4-carbazoyl-9-ylphenyl)amine (TCTA) as an interlayer type hole injection layer between the NPB based HTL and a CzDBA active layer in a multilayer device (NPB being N,N′-Di(1-naphthyl)-N,N′-diphenyl-(1,1′-biphenyl)-4,4′-diamine). Here they investigated how the balance of charge in the active layer could be enhanced. The very high carrier mobility (3×10^{-4} $cm^2/V\ s$) and IE of 5.7 eV of the TCTA interlayer permits efficient hole injection from the HTL into CzDBA (IE – 5.9 eV). The group observed the ISC and rISC processes at the contact between the hole injection interlayer and the emissive layer. Without the interlayer, the rate of ISC decreases with increasing current, but rapidly increases at much higher currents: this can be explained by exciplexes forming at the EML-HTL interface. Adding the hole injection interlayer resulted in prevention of non-radiative decay and reduced triplet quenching, allowing the triplet states to persist long enough to undergo rISC. As with Kotadiya's work, Tang *et al*. observed a reduction in the operating voltage with an interlayer – reduced to 2.9 V down from 3.1 V. Using the EQE equation in the form:

$$EQE = \chi_S \times \eta_r \times \eta_{PL} \times \eta_{out}$$

Equation 2-42 from Tang *et al.*[202]

and all else being equal, the authors were able to deduce that the differences in efficiency with and without the interlayer lies in the charge combination efficiency, η_r – the balance of charge in the active layer is enhanced with the presence of an interlayer. The interlayer device exhibits unorthodox behaviour at higher currents, that the process is not reduced. Results from magneto electroluminescence analysis reveal that rISC and ISC are occurring together in the interlayer device (see Figure 2-50). The abnormal dependency on current in the interlayer device means that it is less predisposed to undergo ISC at low currents, thanks to the charge transfer states. The interlayer helps to facilitate ^{3}CT to ^{1}CT spin conversion, allowing rISC. The reason for rISC occurring more readily than ISC in the interlayer devices is because the ^{3}CT state is longer lived than the ^{1}CT state, coupled with the fact that non-radiative decay from the ^{3}CT state is suppressed – allowing it to persist long enough to

undergo rISC. The narrow energy gap between these two states also serves to provide sufficiently ripe conditions to allow both ISC and rISC.

Mentioned earlier was the formation of exciplexes at the HTL-EML interface. The evidence for this lies in the observed emissions. Closer inspection of the emission spectrum of both devices reveals that there are two emission peaks in the device without the interlayer and only the one in the device containing the interlayer. There are two reasons for this: first, that the normal ^{1}CT state decays *via* fluorescence, giving rise to the first peak; and the second reason lies in the formation of singlet exciplexes at the interface between the active layer and the HTL, yielding an additional emission from the exciplex singlet state. The ^{1}CT peak has undergone a bathochromic shift when compared to the interlayer device (λ_{EL} = 569 nm interlayer; 572 nm non-interlayer). Evidence for the second peak coming from an exciplex are that its energy (1.95 eV) is very similar to that of the HOMO-LUMO gap between the CzDBA and NPB based HTL layer respectively (which is around 1.9 eV).

Overall, the authors propose that competition between the CzDBA CT state processes (rISC) and formation of exciplexes (the TQA process - triplet quenching annihilation) thanks to interactions of the active layer with the hole transport layer, are to blame for lower efficiencies in non-interlayered devices. They suggest that use of an interlayer suppresses the formation of exciplexes and enables the enhancement of the CT rISC process by permitting isoenergetic ^{1}CT and ^{3}CT states activating the route to delayed emission (see Figure **2-50**).

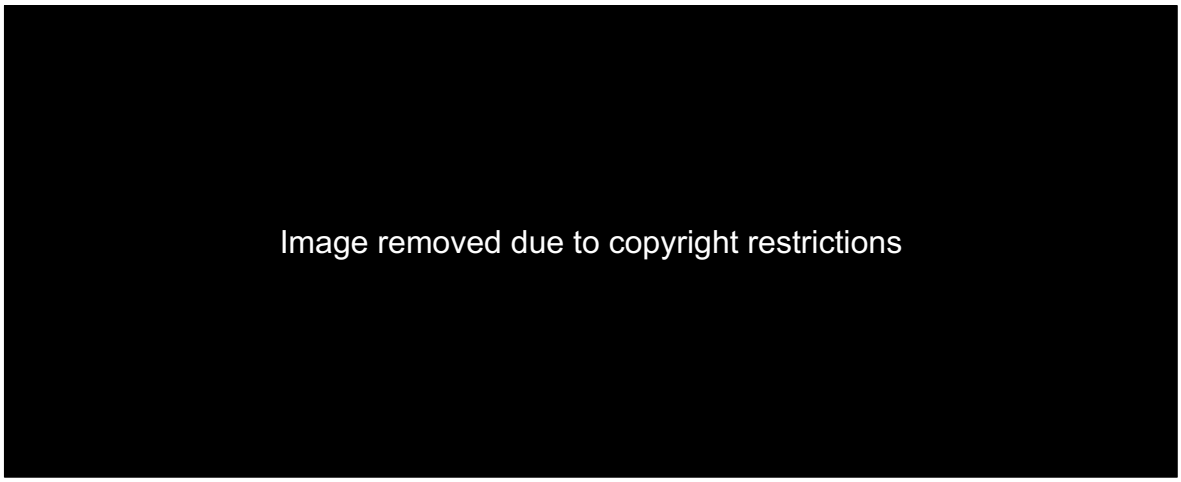


Figure 2-50 Magneto electroluminescence analysis of OLEDs incorporating the interlayer and without. The presence of the interlayer facilitated rISC, whereas without it only prompt fluorescence was observed. Taken from Tang *et al.*[202] a) refers to the interlayer device, whereas b) is the reference device. c) and d) show the magneto electroluminescence plots.

2.13 Summary

The properties of organic semiconductors originate in their ability to form excitonic states. These properties arise because of no direct bonding between molecules in the structure - intermolecular forces are dominant - and low dielectric constants. This means that when excited states form, the binding energy of the electron and hole associated with them is much greater than the energy supplied from room temperature (around 0.5 eV, compared to the room temperature giving only 0.025eV). This allows the exciton to be highly stable and to persist in the device, and 'travel' across its structure - enabling effective energy transfer.

The use of band theory from inorganic semiconductors, is analogous to the HOMO and LUMO in organic compounds when in the bulk. Engineering of device properties can be achieved through consideration of the HOMOs and LUMOs of the materials used to make them. Careful selection of materials enables fine control of the recombination zone in the EML to enable more efficient devices and reduce roll-off.

Of great importance when designing TADF molecules, is the engineering of the singlet and triplet state energies. In order to drive rISC and hence TADF, the singlet and triplet states must be in close proximity energetically. To facilitate the spin forbidden process of rISC whilst avoiding the use of toxic heavy metals, molecules must be designed to possess charge transfer singlet and triplet states (^{1}CT and ^{3}CT) as well as a locally excited triplet state (^{3}LE) to act as an intermediate between the two charge transfer states to allow for triplet harvesting. The rate of rISC must exceed that of non-radiative decay of the triplet states so as to enhance quantum yields.

The environment around the TADF molecules influences the nature of the emissions since emission comes from a polarity sensitive CT state. This can have a detrimental effect on colour purity in devices and must be considered when selecting host matrices. Potential losses *via* quenching or chemical reactions causing irreparable damage upon the emitter molecule, must also be taken into consideration when designing OLEDs with TADF molecules.

A thorough understanding of the photophysical pathways that excited organic luminophores can undergo, is of fundamental importance to the design of emitter molecules. Understanding the decay routes available to a given structure can help in the effective pairing

of donor and acceptor moieties and also what chemical modifications to make to the respective moieties' structures, to obtain the desired emission wavelengths, high PLQYs, narrow full width at half maximum (FWHM – how broad the emission peaks are at half their intensity) and physical properties. The design of molecules, once all of this is taken into consideration, is explored in the following chapter.

Chapter 3 Design of TADF molecules

3.1 General concepts

As established in Chapter 2, molecules that exhibit TADF need to have a very small energy gap between S_1 and T_1 states (a small ΔE_{ST}) and prevent non-radiative transitions to S_0, thereby allowing excited triplet states to persist for a period long enough for rISC to occur through thermal activation.

For effective and efficient TADF properties, potential molecules must fulfil various requirements:

- The gap in energy between T_1 and S_1 must be narrow in order to promote rISC.
- IC (internal conversion) permitting nonradiative energy loss needs to be minimised.
- The molecules must provide good fluorescent yields.
- The molecules need to possess regions or moieties covalently bonded, but distinctly separate in space, with electron donating and accepting properties so as to separate the HOMO and LUMO as much as possible as a means of narrowing the T_1 and S_1 energy gap. This provides S_1 and T_1 states which have strong charge transfer character[140].
- Possess a structure and properties to minimise issues that arise resulting from the "dielectric medium"[140] of the host material – *i.e.* triplets too low in energy trapped in an acceptor or donor unit, or by a less-than-ideal orientation.

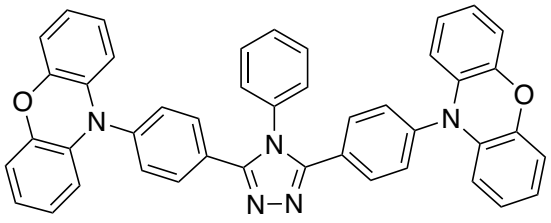
To enhance TADF in emitter molecules, the radiative rate constant (k_r) needs to be high and there needs to be a narrow energy gap between the first excited singlet and triplet states (*i.e.* a low ΔE_{ST}). The latter often coincides with minimal HOMO and LUMO overlap in space. This is best accommodated in molecules where there is enhanced reverse intersystem crossing (rISC) aided by local triplet excited states and singlet charge transfer excitations, aided further by separate moieties displaying electron accepting and electron donating character – acceptors (A) and donors (D). This is further promoted *via* a number of factors: donor-acceptor connection twisting, where the angle between the donor moiety and acceptor

moiety is increased *via* steric hindrance such that they are no longer in the same plane[203], π-bridging between the donor and acceptor moieties, such that the connection is Donor – π-rich group – Acceptor (or D-π-A)[204]; or by connecting moieties though a single carbon atom on a ring, known as *spiro-linking*[205].

The quest to obtain efficient rISC has the unfortunate side effect of causing the excited singlet states to become less electronically coupled to their ground states, owing to the need to confine HOMO and LUMO to separate regions on the molecule. This leads to a reduction in the rate of $S_1 \rightarrow S_0$ transitions and hence reduces the overall PLQY. This trade-off necessitates that the pursuit of rISC efficiency in TADF molecules is accompanied simultaneously by a pursuit of good fluorescence efficiency.

3.2 *Donor – acceptor* and *donor – acceptor – donor structures*

As mentioned previously, TADF molecules often involve structures involving a donor moiety bonded to an acceptor moiety, or a central acceptor moiety bonded to two or more surrounding donor moieties. The HOMO is confined to the electron donating moiety, whilst the receiving electron accepting moiety is where the molecule's LUMO is localised. The positions of substitution, conformation, bond angles and twisting of the connecting bonds, play a vital role in the overall function of the TADF molecule. One such example of a D-A-D type TADF emitter is Trz-2[206] in Figure 3-1.



ΔE_{ST} = 0.23 eV
EQE = 6.4%

Figure 3-1 Triazole based emitter Trz-2 from Bui *et al.*[206]

Here the HOMO is located upon the two phenoxazine donor moieties, whereas the LUMO is located upon the triazole acceptor core. Both donor and acceptor are separated by the two phenyl π-bridges.

3.3 Isomerism

Conformational isomers can differ significantly in their ability to display TADF properties. This is partially due to changes in the geometry of a molecule in the excited state interrupting π-conjugation or the structure of the HOMO and LUMO, for example, if the molecule were to bend[165].

TADF can be promoted if a D-A-D structure is used, provided that the molecule has good charge transfer (CT) character. Changes in conformation could yield a significant drop in performance, so it is important to consider vibrational and rotational degrees of freedom in moieties at the molecular design stage. One should steer clear of donors and acceptors with many possible conformations and opt instead for planar geometries to promote delocalisation. Regioisomerism also causes significant changes to TADF properties. In changing the positions of the donor moieties in 2,8-DPTZ-$DBTO_2$ from the *ortho* to the *meta* positions, giving 3,7-DPTZ-$DBTO_2$ (see Figure 3-2), leads to red-shifting and additional and increased energy charge transfer states arising due to mixed rotational conformations arising with the greater degree of rotational freedom in 3,6-DPTZ-DBO_2, and prevents the rISC and therefore the TADF process[165].

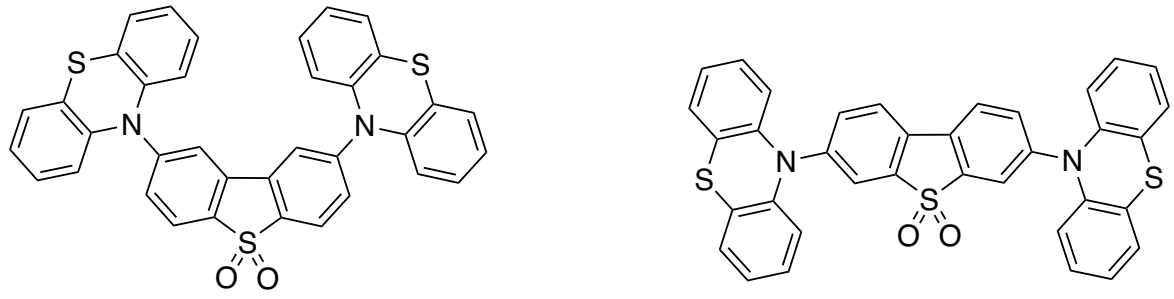
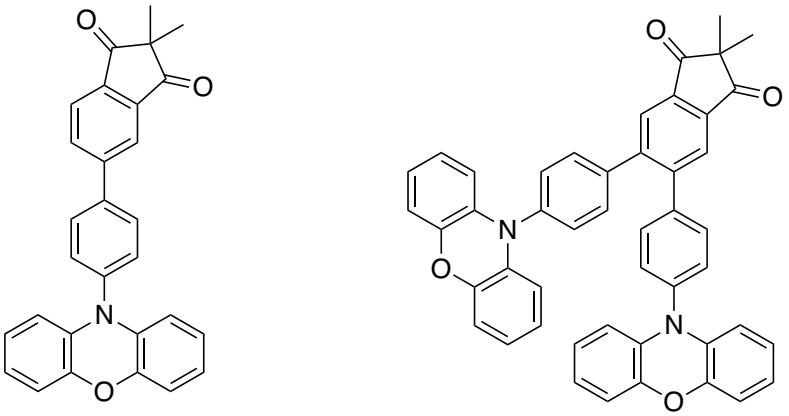


Figure 3-2 Structures of the two regioisomers 2,8-DPTZ-DBTO2 and 3,7-DPTZ-DBTO2 from Etherington *et al.*[165]

3.4 π-bridging

Π-bridging involves separating the donor and acceptor moieties *via* the placement of a phenylene ring inbetween them. Often the HOMO of the donor can spread onto this ring[204]. The carbon-donor bond at one end of the ring enables some degree of rotation of the donor moiety, however branches added to the donor side of the phenylene ring have been shown to aid maintaining twisting angles of the donor moiety with respect to the acceptor moiety[204]. One such example is 5PXZ-PIDO (see Figure 3-3) where an indandione acceptor is connected to a phenoxazine donor *via* a phenylene π-bridge, and in 5,6PXZ-PIDO, where two phenoxazine donors are connected to the acceptor *via* π-bridges[207]. Both molecules exhibit TADF properties, though the D-A-D 5,6PXZ-PIDO possesses greater k_{rISC} and a lower ΔE_{ST}.



5PXZ-PIDO
ΔE_{ST} = 0.04 eV,
k_{rISC} = 4.06x10^5 s^{-1}

5,6PXZ-PIDO
ΔE_{ST} = 0.02 eV,
k_{rISC} = 5.89x10^5 s^{-1}

Figure 3-3 Structures of indandione emitters from Etherington *et al.*[165]

Single π-bridging phenyl rings help the rISC process and prevent non-radiative decay, improving the molecule's EQE. However, longer π-bridges give rise to more degrees of rotational freedom, being subject to conformational change when the molecule is excited, reducing the localisation of the HOMO and LUMO.

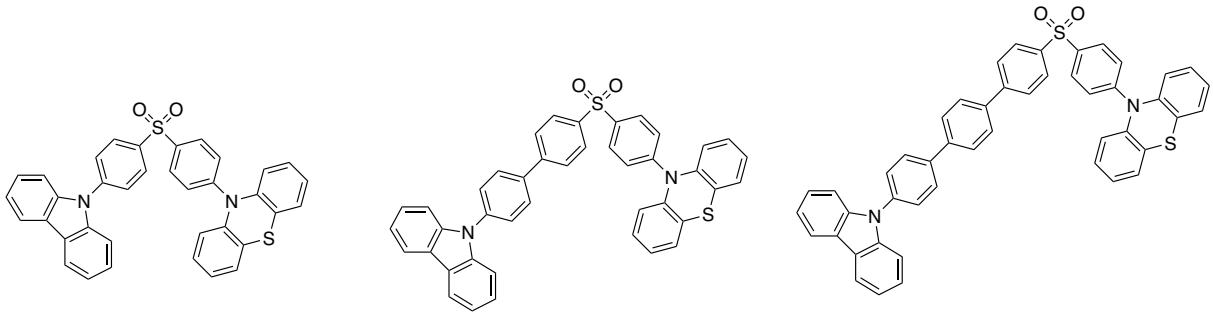
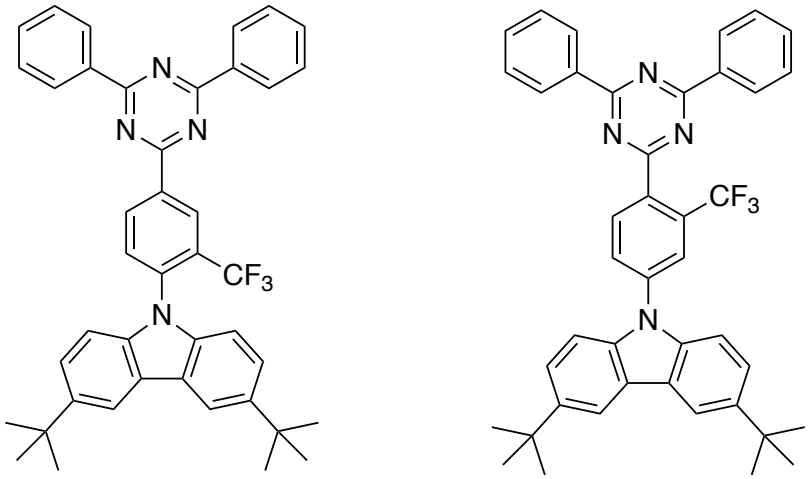


Figure 3-4 π-bridge length. The structures of asymmetric SCP based TADF molecules with varying π-bridge length and positions from Wei *et al*.[208]

Clearly the use of π-bridges can yield narrower $S_1 - T_1$ gaps, though in the case of Wei *et al*.'s[208] work (shown in Figure 3-4) it can result in lower photoluminescent quantum yields if the length of the π-spacing is too great. Additional π-bridges are accompanied by further reduction in PLQY, as well as widening the $S_1 - T_1$ gaps. This is rationalised when one considers the ability of the C-C bonds to rotate more freely between the phenylene rings and the donor groups.

Going further, Figure 3-5 illustrates the work of Li *et al*.[209] which shows the effects of bulky substituents on the π-bridge *and* bulky substituents on the donor moiety – in this case two tert-butyl groups. Li *et al*.[209] demonstrate that by adding a bulky group (methyl or trifluoromethane) on the phenylene ring positioned ortho to the donor group helps maintain a high dihedral angle, enhancing HOMO-LUMO separation. However, when the substitution is in the position ortho to the acceptor, ΔE_{ST} widens significantly, but is accompanied by a large increase in PLQY (likely due to reduced losses *via* rotational motion). Additionally, these structural features in TrzBuCz-CF_3 work in concert to increase the overall EQE of the molecules in devices significantly.



TrzBuCz-CF_3

ΔE_{ST} = 0.02 eV,
$\lambda_{emission}$ = 476 nm
$\theta_{dihedral}$ = 83.83°
PLQY = 72%

TrzBuCz-CF_3-1

ΔE_{ST} =0.14 eV
$\lambda_{emission}$ = 466 nm
$\theta_{dihedral}$ = 47.04°
PLQY = 99%

Figure 3-5 π-bridge modifications. Structures of trifluoromethyl substituted variants of TrzCz with additional tert-butyl substituents on the carbazole donor moieties. Structures from Li *et al*.[209]

The extent of the HOMO dispersing onto the π-bridge from the carbazole donor and subsequent HOMO-LUMO overlap is dependent upon the position of the methyl and trifluoromethyl groups on the π-bridge.

If bulky groups are positioned ortho with respect to the donor (see Figure 3-6, structure 1) then steric hindrance twists the donor – π-bridge bond, increasing the dihedral angle. This reduces the donor and acceptor HOMO-LUMO overlap, thus decreasing ΔE_{ST}. The bulkier the substituent group, the greater the distortion. Groups positioned closer to the acceptor moiety (Figure 3-6, structure 2) exhibit less steric hindrance upon the donor group, thereby allowing for the donor-π bond to possess a greater degree of rotational freedom, permitting conformational change.

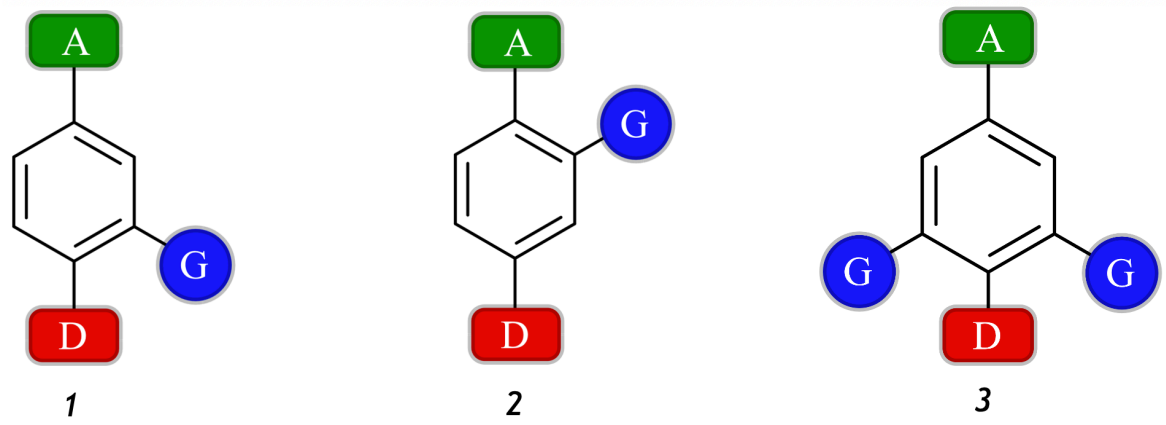


Figure 3-6 Position of substituent groups on π-bridges. Substituent group (G) positioning on a π-bridge with respect to the donor (D) and acceptor (A) moieties. Structure 1 represents a group ortho- with respect to the donor, 2 positions the substituent group meta- with respect to the donor, and 3 possesses two substituent groups both ortho- with respect to the donor.

Here the HOMO and LUMO of the donor and acceptor are more able to overlap, reducing the rate of rISC. In the case of doubly substituted π-bridges, steric hindrance can be more pronounced. In Figure 3-6, structure 3, the two substituent groups trap the donor at almost 90° to the acceptor moiety. This allows for particularly good separation of the HOMO and LUMO. Good HOMO and LUMO separation aids a decrease in exchange energy and improves charge transfer character of the first excited singlet state, enabling more efficient TADF emission.

It is clear therefore, that the presence of a π-bridge, while beneficial, is not sufficient on its own to increase the rate of rISC and TADF efficiency in donor-acceptor type molecules. Required is a combination of methods:

- A geometrical character to separate the HOMO and LUMO, however, not so much so as to totally eliminate interactions, such as a twist along the bond axis relative to the donor-acceptor axis.

- The avoidance of strain across each moiety – ensuring that both the donor and acceptor are planar (but angled against one another) to allow internal delocalisation upon each.

- A bulky substituent, or pair of substituents, on the π-bridge (if present) in order to constrain the conformation of the molecule such as to maintain a large angle down

the donor-acceptor bond, as well as to prevent HOMO – LUMO mixing, particularly across the π-bridge itself.

- Bulky or electron donating substituents on the donor moiety to increase its electron donating character and delocalisation of the HOMO across the donor moiety.

3.5 Spiro compounds

3.5.1 General background

A spiro compound is one in which two rings are fused *via* a single carbon atom, shared between both rings[210]. Examples include the two connected cyclohexane rings in spiro[5.5]undecane, and S-(+)-spiro[3,3]hepta-1,5-diene[211] in Figure 3-7.

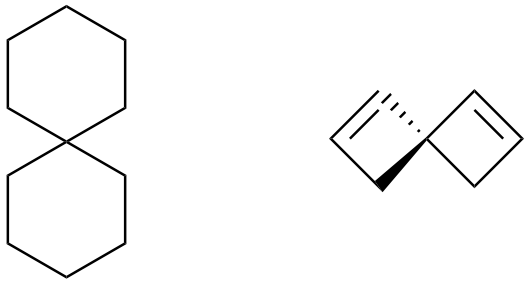


Figure 3-7 Examples of spiro compounds: spiro[5,5]undecane (left) and S-(+)-spiro[3,3]hepta-1,5-diene (right).

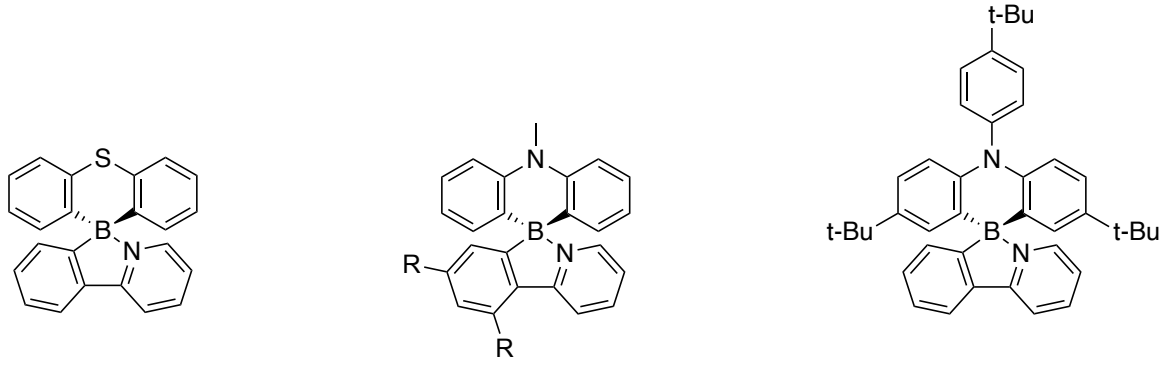
Spiro-bifluorenes are suitable for OLEDs since they remain stable when subjected to varying temperatures in devices and have elevated glass-transition temperatures[205]. Essentially, these consist of a moiety where two fluorene molecules are bonded through the central sp^3 hybridised carbon atom. One such example of a spiro-based TADF emitter is Spiro-CN (Figure 3-8), which is based on a D-A-D arrangement with the di-*p*-tolylamino donor moieties and a cyano-spirobifluorene acceptor moiety[205]. Spiro-compounds can exhibit TADF, with high triplet energies and high stabilities, allowing long lifetime emissions and high efficiency[212]. The quaternary carbon at the spiro linkage essentially locks the donor and acceptor moieites at ~90° to one another since rotation between them is impossible through this type of linkage.



Figure 3-8 Spiro-CN structure and HOMO and LUMO localisation from the work of Nakagawa *et al*[205].

Interestingly, in Nakagawa *et al*.'s work[205] exploring the electroluminescent properties of Spiro-CN, the HOMO of the donor is demonstrated to spread onto the top two phenyl rings of the spiro-bifluorene, but is prevented from merging with the LUMO by the spiro-bridge. This isolates the LUMO on the bottom two phenyl rings and cyano groups. The molecule exhibited yellow coloured TADF emission, but lower external quantum efficiency in devices than an equivalent yellow phosphorescent molecule. It was found that control of colour could be achieved *via* altering the π-conjugation of the donor and acceptor moieties.

Spiro molecules can also be formed from compounds where the central shared atom at the spiro-link between two rings is another element than carbon. 4-Coordinate boron has been used as the spiro-centre to some effect[213,214,215]. In the case of work by Stanoppi and Lorbach[213], different donor moieties were investigated using borylated 2-phenylpyridines for an acceptor moiety (see Figure 3-9).



Φ = 11%
$\lambda_{emission}$ = 526 nm
θ = 89°

R = H
Φ = 33%
$\lambda_{emission}$ = 599 nm
θ = 87°

R = F
Φ = 28%
$\lambda_{emission}$ = 604 nm
θ = 86°

Φ = 25%
$\lambda_{emission}$ = 540 nm

Figure 3-9 Structures of 4-coordinate borylated 2-phenylpyridines from Stanoppi and Lorback[213] (R = H or F).

As with standard D-A type emitters, addition of branches to the donor aids TADF, however bulkier substituents on the acceptor moiety leads to a reduction in TADF efficiency. The addition of t-Bu groups to the donor was found to raise the HOMO energy levels[213]. The angle between the donor and acceptor, caused by the twist at the spiro-centre controlled by the geometry of the phenylpyridine acceptor, causes major changes to the HOMO and LUMO energy levels, regardless of the fact that HOMO and LUMOs are distinctly separate in space in these molecules. It appears that the length of the B-N coordinate bond, influenced by the acceptor moiety and the donor moiety (especially going from S to N-CH_3 and N-Ph), is key to the torsional angle exhibited[213].

3.5.2 Varying substituent groups on spiro-compounds

Changing branches on the acceptor moiety on a spiro-link compound also influences TADF behaviour. Ganesan *et al*.[216] investigated changing the phenyl rings on the acceptor moiety of PhPMAD with various isomers of pyridyl groups (see Figure 3-10 for the structures and Table 3-1 for the properties).

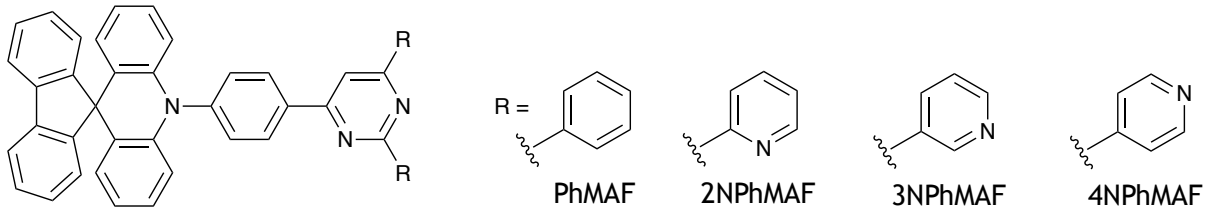


Figure 3-10 Varying substituent groups on spiro-compounds from[216].

In the para-isomer of the pyridyl groups, the horizontal dipole ratio (the ratio between the horizontal dipole to that of the total transition dipole of the emitter) is much higher (0.91) compared to ortho or meta (0.87 and 0.86 respectively). The dipole moment is related to the molecular geometry and is reflected in the lower value for ΔE_{ST} in the para isomer based 4PhPMAF.

Table 3-1 Table of TADF properties of PhPMAF and derivatives from Ganesan *et al*[216].

Molecule	Horizontal dipole ratio (θ)	$\lambda_{emission}$ (nm)	PLQY (%)	ΔE_{ST} (kcal/mol)
PhPMAF	0.90	457	47	-3.95
2NPMAF	0.87	482	73	-2.59
3NPMAF	0.86	486	86	-2.95
4NPMAF	0.91	488	75	-2.43

Clearly, addition of pyridyl branches to the acceptor moiety increases the PLQY and lowers the ΔE_{ST}, however the dipole moment produced by the heterocycle added must be considered in order to optimise the EQEs in TADF based OLEDs. Ganesan *et al*. propose that the better electron mobilities caused by the pyridyl functional groups aids device efficiency and reduces aggregation induced quenching.

Spiro-linked compounds provide an attractive field of research owing to their versatility and flexibility of choice for donor and acceptor moieties. The angle between the donor and acceptor (and separation of HOMO and LUMO) can be controlled by altering the bond lengths of the bonds connecting to the central spiro atom, which leads to an overall twist of a moiety. This can be achieved though changing the groups or heteroatoms adjacent to it.

3.6 TADF design methodology

When designing molecules intended to exhibit TADF emission, it is important to take into consideration factors which will influence the rate of fluorescence and wavelength of light produced. There are certain key parameters that need to be controlled when developing TADF molecules. As mentioned previously, the ΔE_{ST} energy gap between the first excited singlet and triplet states needs to be narrowed as far as possible. The importance of this notwithstanding, other variables can be neglected or negatively influenced in the pursuit of this particular goal. Whilst a smaller energy gap does allow for triplet states to be up-converted to singlet states much more readily, it is not the sole principle behind the TADF process.

When developing new TADF molecules, efficiency is enhanced when the following two criteria are met:

- Narrow the $S_1 – T_1$ energy gap to lower ΔE_{ST} to enhance the rate of the rISC.
    - This means that the adiabatic ^{1}CT and ^{3}CT states should be close in energy to ^{3}LE (see section 2.9 in chapter 2).
    - A good way of doing this is by lowering the electron exchange energy, *J*, by use of donor – acceptor moieties to separate the HOMO and LUMO in space by a dihedral angle or steric hindrance. The molecules should exhibit strong charge transfer character in the excited state.

$$J = \iint \Phi(1)\psi(2)\left(\frac{e^2}{r_1 - r_2}\right)\Phi(2)\psi(1)dr_1 dr_2$$

Equation 3-1 Exchange energy.

    - Equation 3-1 illustrates that the exchange energy, *J*, varies as a function of the integrals of the overlap of the HOMO and LUMO of a compound.

- Prevent non-radiative decay from excited states and ensure that all decay is emissive.
    - Reducing internal conversion whilst simultaneously enhancing CT is difficult. ^{1}CT must be well coupled to the S_0 ground state to enhance

fluorescence yields, however the orthogonal structures required to promote rISC by narrowing the $^3CT - {}^1CT$ energy gap have a tendency to reduce the $^1CT - S_0$ ground state coupling.

Balancing both of these requirements, when one undermines the work of the other, is a significant challenge in the design of novel and efficient TADF molecules.

Blue emitters are particularly difficult to synthesise because they require larger $S_0 - S_1$ optical energy-gaps (larger than 3 eV) which complicates matters when fabricating devices since this energy needs to pass from other layers in the device to the emitter layer, necessitating less than ideal high voltages. Statistically, given a large optical-gap, it is less likely for an electron to cross the gap into an excited state, lowering the external quantum efficiency (EQE) of blue TADF devices. Often when used in OLEDs it results in blue devices red shifting relatively quickly if the radiative rate constant (k_r) is too low and intramolecular charge transfer (ICT) is permitted to reduce quantum yields[217].

For TADF to function, we harvest non-emissive triplet states and convert them endothermically into singlet states which emit radiation *via* fluorescence upon relaxing to the ground state. Minimising the ΔE_{ST} alone is not sufficient a practice to improve TADF emissions, as spin-orbit-coupling (SOC) must also be taken into consideration in order to allow triplets to be converted into singlets – a process which is technically spin forbidden. The propensity for this transformation must be maximised in conjunction with lowering ΔE_{ST}.

In order to simplify the design process, a comprehensive review of the structure of TADF molecules was undertaken by Bui *et al*.[206] who suggested a six-step process to keep in mind when designing TADF emitters:

- Do not allow donors and acceptors to be directly conjugated to one another

  Π-conjugation between a donor and acceptor moiety can be prevented through application of orthogonal character at their connection, such as a geometric twist or bend to minimise HOMO – LUMO overlap.

- Allow proximity for charge transfer to take place

  Segregation between the donor and acceptor must not be absolute, thus they must be located in close proximity to one another.

- Enhance π-conjugation within the donors and acceptors

  The π-conjugation within the donor moiety or within the acceptor moiety should be enhanced across its respective structure to further promote oscillator strength to enhance PLQY.

- Keep ΔE_{ST} very low

  ΔE_{ST} should be as small as possible, *i.e.* S_1 and T_1 states should have energies as close together as possible, but S_1 should be at an energy level pertaining to the desired wavelength of emission. The low ΔE_{ST} is required to promote the occurrence of rISC by increasing its rate constant, k_{rISC}.

- Prevent excited state quenching

  As a means of preventing TTA (triplet-triplet annihilation) and thus preventing the unwanted removal of excited states from the TADF process, the time taken for delayed emissions should be minimised by promoting efficient rISC.

- Plan bonding location

  The position at which moieties are bonded must be considered such to maximise the likelihood of emissions. Some structural isomers are more dispositioned to bend or twist during excitation, which reduces the overall emission efficiency, in some cases stopping it entirely. Molecular design must ensure minimum chance of distortion during operation.

3.7 Boron-based TADF

3.7.1 Why is boron suitable?

For viable implementation into commercial applications, TADF emitters need to be found that can encompass red, green and blue wavelengths, such as with single molecule white light emitters (SMWLE)[218] to be combined with filters or, better still, a combination of each colour emitter separately. So far red and green emitters have been developed successfully, however satisfactorily efficient long-lasting blue emitters have yet to be developed.[219] For blue emitters, one requires a large HOMO – LUMO gap. This would normally yield unstable excitons and poor-quality emitters.[220]

Donor and acceptor moiety-based structures are selected to promote triplet harvesting *via* rISC by lowering the ΔE_{ST}.[221] Acceptor moieties need to be electron deficient, such as polycyclic borazine, sulfone and triazine.[220] Boron-based acceptors are becoming increasingly popular for TADF devices,[214,222] owing to the electron deficiency of the boron atom's p-orbital.

Whilst it is a finite resource, boron is highly abundant in the Earth's crust with a relative supply risk factor of 4.5 (which is the same as carbon).[223] It is often found in the form of the minerals borax and rasorite, with the three major producers being Turkey, the United States of America, followed by Chile.

There are two major categories of boron emitters – those that are based around three or four, or even five coordinate boron atoms[224,225] and where boron is used to fuse together aromatic or heteroaromatic groups.[226] 3-Coordinate boron forms a trigonal planar environment with sp^2 type hybridisation of the boron bonding orbitals.[103] Σ-bonds form with neighbouring atoms, and the remaining 2p orbital orients above and below the plane of the bonds. In some cases (such as with the halogens), neighbouring atoms can contribute π-electrons into the empty p-orbitals, providing π-character to the bonds and the added stability associated with this. In this configuration, boron compounds can behave as a Lewis acid, permitting attack in the empty p-orbital by the lone pair of electrons on a Lewis base (see Figure 3-11). In this case, the boron can form an ionic bond with the Lewis base, having a negative formal charge, or alternatively, form a dative bond to the Lewis base - both cases result in a tetrahedral sp^3 hybridised boron - 4-coordinate boron.

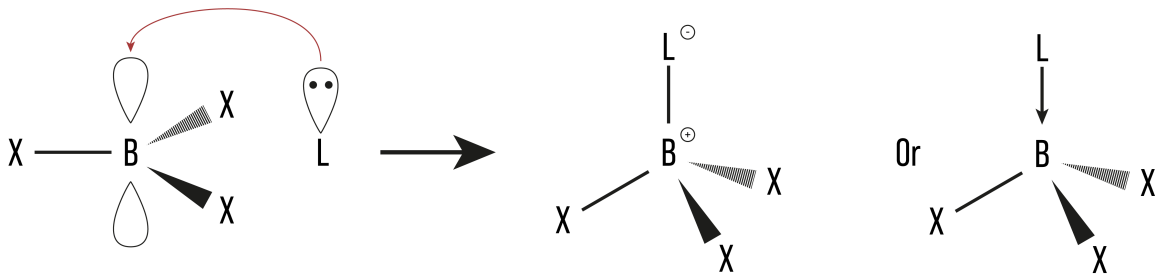


Figure 3-11 Action of boron as a Lewis base. Boron's empty p-orbital allows it to readily accept electrons in bonding. This can be exploited in 3-coordinate boron-based acceptor moieties.

Owing to the nature of 3-coordinate boron's empty p-orbital, it is an effective "electron acceptor". This allows for charge transfer from the donor to the acceptor moieties when boron is a component of the electron deficient moiety and is connected to an electron rich donor moiety,[225] making it highly suited to incorporation into acceptor moieties for TADF molecules. A π-bridge is often used to separate 3-coordinate boron acceptors from the donor. In some cases, para-substituted π-bridges result in only fluorescence, whereas having substituents in the ortho positions, allows for TADF to occur, owing to the increased steric hindrance in this position, narrowing the ΔE_{ST}.[227]

The degree of acceptor character of the boron's empty p-orbital depends on how much π-character is fed into it by the neighbouring atoms in its moiety. If there is poor donation thanks to poor matching of orbitals (such as with iodine's 5p orbital in BI_3), then the empty p-orbital will be more accepting in character. In the case of good orbital matching (such as fluorine's 2p orbital) then the π-character is stronger, meaning that the orbital is less likely to accept further electrons, and the compound is a poorer electron acceptor. This phenomenon must be taken into consideration in boron-based emitters where the halides are replaced with the structure of the acceptor moieties or connections to other moieties – allowing one to tune the boron moiety's accepting character – stronger electron donation into the conjugation region of the boron acceptor moiety will result in reduced acceptor character and vice versa.

3.7.2 Boron moiety structural types

Lee *et al.*[228] suggest that boron-based emitters can be categorised into four key structural features. Example molecules are shown in Figure 3-12 and are described herein:

Unbridged - such as with DMBP-Ac[228], where groups attached to boron are not connected to one another and boron bonds directly to the donor moiety or to a π-bridge connected to the donor. The efficiency of these structures can be improved by using steric hindrance between donor and acceptor *via* the ortho position (narrowing the ΔE_{ST}). Ortho-carbazole based triarylboron emitters prove to be suitable for blue emission *via* TADF[228]. Modification by adding substituent groups to either or both the donor and acceptor moieties allows one to control wavelengths of emission or even photoluminescent quantum yield (PLQY).

Partially bridged - such as PXB-Sac[228], where at least two of the boron bonds are linked to the same structure.

Fully/oxygen bridged - such as TDBA-Ac[228], where boron is surrounded by a structure which connects to the donor moiety – oxygen bridged structures incorporate oxygen into the aromatic system, preventing rotation around the boron – carbon bonds, aiding rigidity and planarity. Oxygen bridging has been demonstrated to narrow the full width half maximum (FWHM) and improve TADF deep blue emitters[228], making excellent and stable emitters. Good conjugation within donor and acceptor moieties and good separation of the HOMO and LUMOs in space, yields very high PLQY and sharp emission spectra.

Multiple resonance structures – which often resemble analogues to fully or oxygen bridged structures such as TBN-TPA[228]. Their structures are rigid, planar and have a high degree of symmetry. Their HOMO and LUMOs are separated upon the nitrogen and boron's positions within the same conjugated structure as opposed to the regular donor – acceptor structures. A collection of MR-TADF-type structures is shown in Figure 3-12. Their rigidity gives rise to narrow FWHM and pure emission colours and very deep blue emissions, but slight modification to their structures can result in significant reductions in efficiencies, and the synthetic schemes used to produce them are convoluted and inefficient, making them challenging candidates for research. Additionally, multiple resonance TADF (MR-TADF) molecules possess low ΔE_{ST} in conjunction with high oscillator strength (the details of the process of which remains somewhat elusive[228]), the combination of which is not common in

standard donor-acceptor type structures. However, this benefit is offset by poor efficiency roll-off[228]. Additionally, dopants like DMAC-DPS can be added to improve (decrease) the efficiency roll-off and adding carbazole donor moieties has been shown to increase the PLQY,[229] as well as decreasing the ΔE_{ST} further. MR-TADF structures also include nanographenes, extended DABNA based cores further doped with boron and nitrogen (such as TBN-TPA). Dimers of DABNA-1 cores with doping have been shown to yield an excellent ΔE_{ST} of 17 meV in the compound DOBNA-OAr[230] and possess very low efficiency roll-off when compared to monomer MR-TADF structures. This is the best efficiency of a MR-TADF structure to date.

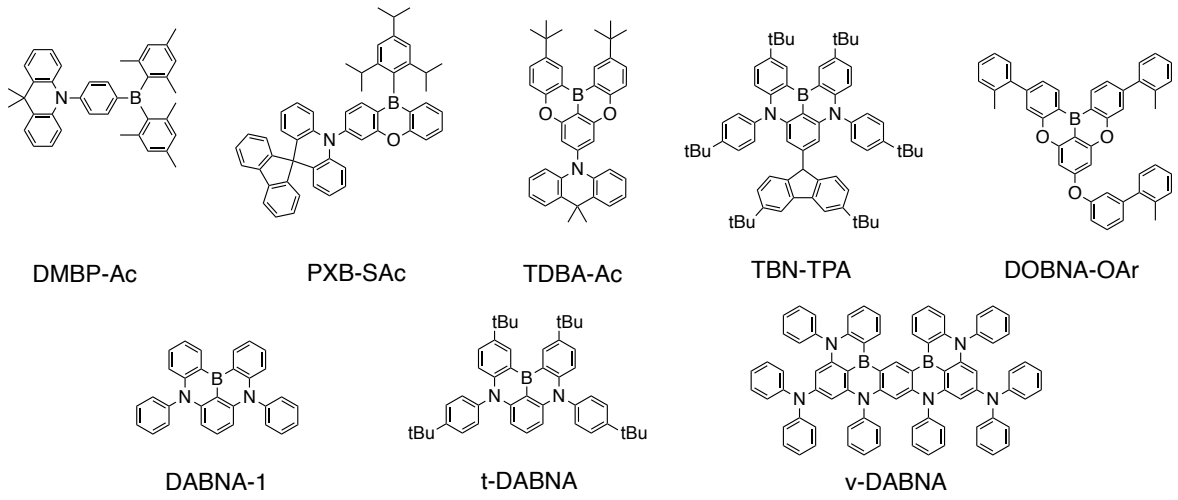


Figure 3-12 Examples of MR-TADF type molecules. Structures adapted from Lee *et al.*[228] and Kondo *et al.*[230] (for DOBNA-OAr) and the structures of DABNA-1, t-DABNA and v-DABNA for comparison.

Compounds containing boron incorporated into polycyclic aromatic structures have sparked significant interest owing to their desirable electronic properties and increased stability at blue wavelengths[1]. Here follows a few examples of boron polyaromatic structures (all of which are described in detail in the work of Escande and Ingleson[231]):

Fused borole moieties

A 5-membered ring with one atom being a boron. Often bonded to aromatic or heterocyclic groups but is itself non-aromatic. Some examples are shown in Figure 3-13 and Figure 3-14.

Ladder structures

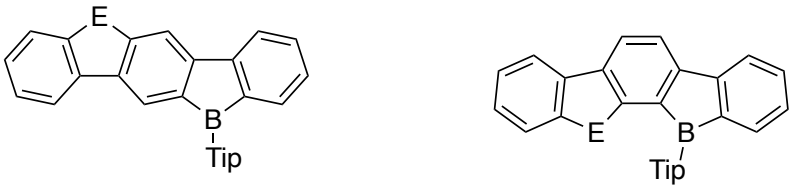


Figure 3-13 Examples of ladder-type structures adapted from Escande and Ingleson[231].

Boracycles

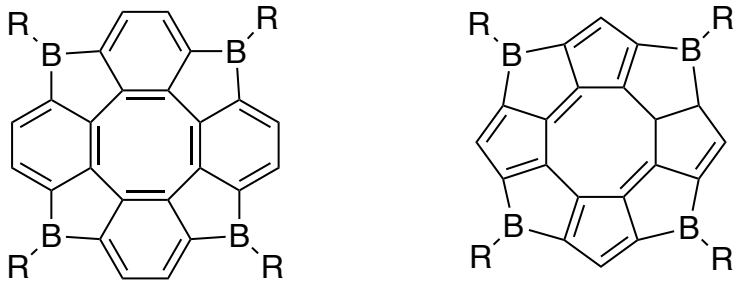


Figure 3-14 Examples of boracycle type structures, adapted from Escande and Ingleson[231].

Diboraanthracene

9,10-Dihydro-9,10-diboraanthacene (DBA) provides a platform from which luminescence can be obtained[231] (see Figure 3-15).

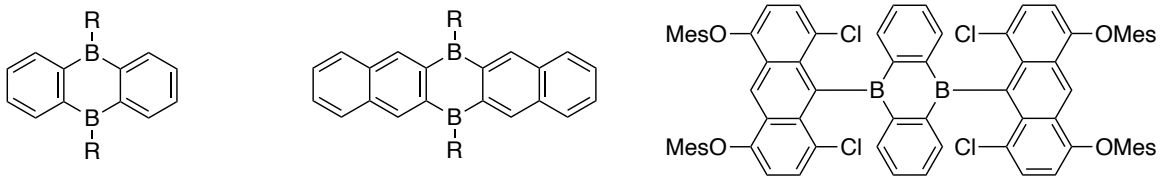


Figure 3-15 Three forms of diboroanthracene type structures with Pi conjugation extension and anthracene substitution. Adapted from Escande and Ingleson[231].

Compared to pure carbon analogues, including boron in their structure results in a lowered band gap[231]. As such, electron donating substituents attached to donors bonded to the boron atoms can permit significant bathochromic shift into the orange wavelengths. Substituent groups on the donor moieties (or a π-bridge separating the donor and acceptor) can interact with the empty p-orbital on the boron atom such that the system is pentacoordinate[231].

Work by Dou *et al*.[232] shows that the chlorine atoms in donor moieties can coordinate as ligands to the boron atoms which result in blue shifted emissions. Escande and Ingleson[231] describe this behaviour thus:

> "*The theoretical calculations highlighted that an antibonding interaction on chlorination of the anthracene moieties elevates the p–π* molecular orbital of the DBA core and is the dominant cause of the changes in the photophysical and electrochemical behaviour*"

This is of particular interest since our work in Chapter 6 is based on a DBA core. Manipulation of the energy levels of the target molecule could be achieved with additional modifications to the DBA acceptor moiety by addition of electron withdrawing (or donating) groups in future work.

Fused diboraanthacenes (trapped boron)

In this case, the "donor moiety" bonded to the boron is also bonded to other parts of the "acceptor moiety" (see Figure 3-16).

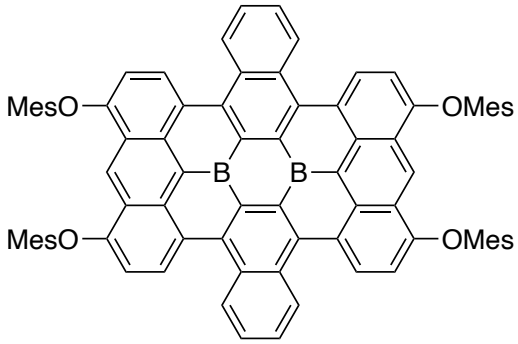


Figure 3-16 A fused diboraanthacene - forming a nanographene type structure. Adapted from Dou *et al*.[233]

This maintains a planar structure which prevents nucleophilic attack at the boron and will also allow for improved intermolecular interactions which enhance charge transport (CT).

In the case where non-aromatic carbons are incorporated into the structure, there is a degree of flexibility, which can lead to different shaped excited states and therefore multiple emission wavelengths[233].

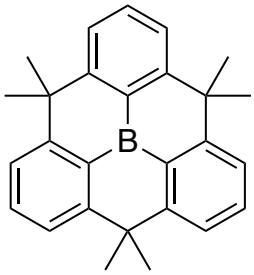
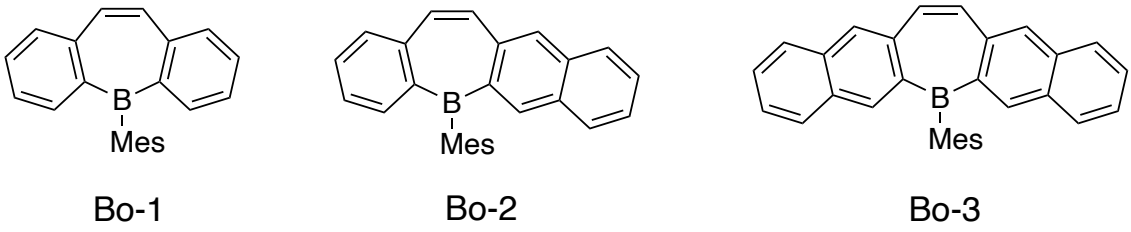


Figure 3-17 A planarised structurally constrained triarylborane. Adapted from Zhou *et al.*[234]

When planar and excited, the molecule in Figure 3-17 emits at 337 nm, however when its structure is distorted into a bowl-shaped form and is excited, it emits at 407 nm[234].

Fused borepin moieties

Borepin contains a 7 membered ring with one boron atom in it, and essentially resembles a boron analogue to iminostilbene (see Figure 3-18).



Bo-1 Bo-2 Bo-3

Figure 3-18 Three simple examples of aryl substituted borepins. Adapted from Escande and Ingleson[231].

As the systems get longer and more π-conjugated, so the absorption is red shifted (here it is 260 nm in **Bo-1**, 280 nm, in **Bo-2** and 314 nm in **Bo-3**[231]). The band gap decreases upon increased π-conjugated. However, the intensity of emissions is reduced for the larger molecules. The HOMO resides on the aromatic rings and the LUMO is located nearer the boron in the larger systems. It has been found that with the right substituent groups, one can tune the HOMOs and LUMO energies[231] – narrowing the band gap by conjugation, or blue-shifting *via* meta-substitution and raising electron affinity *via* para-substitution (see Figure 3-19).

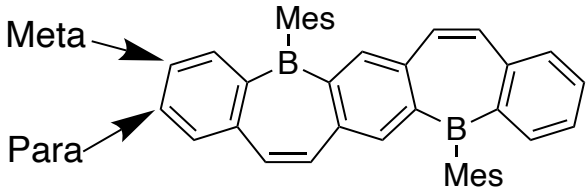


Figure 3-19 Meta and para substitution on dibenzoborepinobenzene systems. Adapted from Escande and Ingleson[231].

Rigid structures help to prevent non-radiative decay since they have fewer degrees of rotational and vibrational freedom.

Fused heteroborins

In boron ladder like structures, it is possible to add an electron donating heteroatom into the same ring as the boron atom. This could be oxygen, nitrogen, or sulfur. This leads to a rise in the energy of the HOMO, whereas boron lowers the LUMO's energy. The LUMOs tend to be located around the boron atoms. Use of amino groups lead to a red shift in emissions. Sulfur heteroatoms give the structure a slight twist (12.4°), which leads to a blue shift when compared to nitrogen heteroatoms (9.1°). Phosphorous provides an even greater distortion (15.7°). If the structure is rigid it tends to present a better quantum yield as there are fewer non-radiative decay pathways.

In summary, thus far boron-based acceptor moieties used in TADF emitters make for promising solutions to finding efficient blue emitters. As of the time of writing, the highest EQE achieved with a boron-based compound is 38.15%,[235] outperforming non-boron-based blue emitters. For efficient emitters with high PLQY, low ΔE_{ST} and pure emission colour, the ranking of boron-based molecular structures goes: *fully bridged boron compounds > partially bridged boron compounds > unbridged boron compounds*.

When full bridging is achieved *via* oxygen bridges in the acceptor moiety, efficiency is enhanced because horizontal dipole orientation is favoured with these structures. Fully bridged oxygen-boron acceptors are ideal for deep blue emitters which are very efficient. In the case of MR-TADF molecules, their ΔE_{ST}, efficiency and PLQY can be enhanced through addition of a donor moiety para to the boron.

3.8 Carbazole based TADF

Carbazole is a heteroaromatic, biphenyl compound based on a pyrrole centre, bonded to two benzene rings. It could be considered an indole molecule bonded to a single benzene ring at indole's 2 and 3 positions (see Figure 3-20).

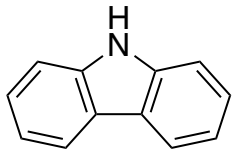


Figure 3-20 The chemical structure of carbazole.

Carbazole has several attractive qualities as a building block for TADF emitters:[236]

- It is relatively cheap and readily available from chemical suppliers.
- Its aromaticity aids conjugation of the moiety in which it is a component, as well as overall molecular stability.
- It possesses multiple locations which can hold substituent groups to tune its electron donating character (such as with methoxy groups[237]), or enhance overall solubility of the target molecule for solvent based OLED fabrication techniques (such as tert-butyl substituents[238]).
- It is easy to connect it to other functional groups or moieties from its nitrogen atom.
- It possesses a high triplet energy of 3.02 eV,[239] which is high when compared to similar donor molecules.

3.8.1 Structure of carbazole – why is it a donor?

Carbazole's photonic properties reveal $\pi \rightarrow \pi^*$ transition character in both fluorescence and absorption. This is because of the availability of the electron lone pair on the nitrogen atom, which, owing to their perpendicular orientation relative to the aromatic rings on the carbazole proper, are capable of delocalising into the aromatic system in the excited state *via* n – π-orbital overlap.[121]

The conjugation across the structure, along with the availability of the nitrogen's lone pair, results in carbazole being an effective electron donor. Inductive effects of tert-butyl and methoxy derivatives have been shown to further enhance the electron donating ability of carbazole – the 3 and 6 positions having been demonstrated to provide bathochromic shifts in emissions, whereas positions 2 and 7 yield hypsochromic shifts[240] (see Figure 3-21). In addition to this, narrowing of the HOMO and LUMO, as well as the ΔE_{ST} occurs upon increased substitution on positions 3 and 6.[237] Steric hindrance can be exploited from positions 1 and 8 to prevent rotation along the dihedral of TADF molecules to maintain HOMO and LUMO separation and minimise energy loss.[220]

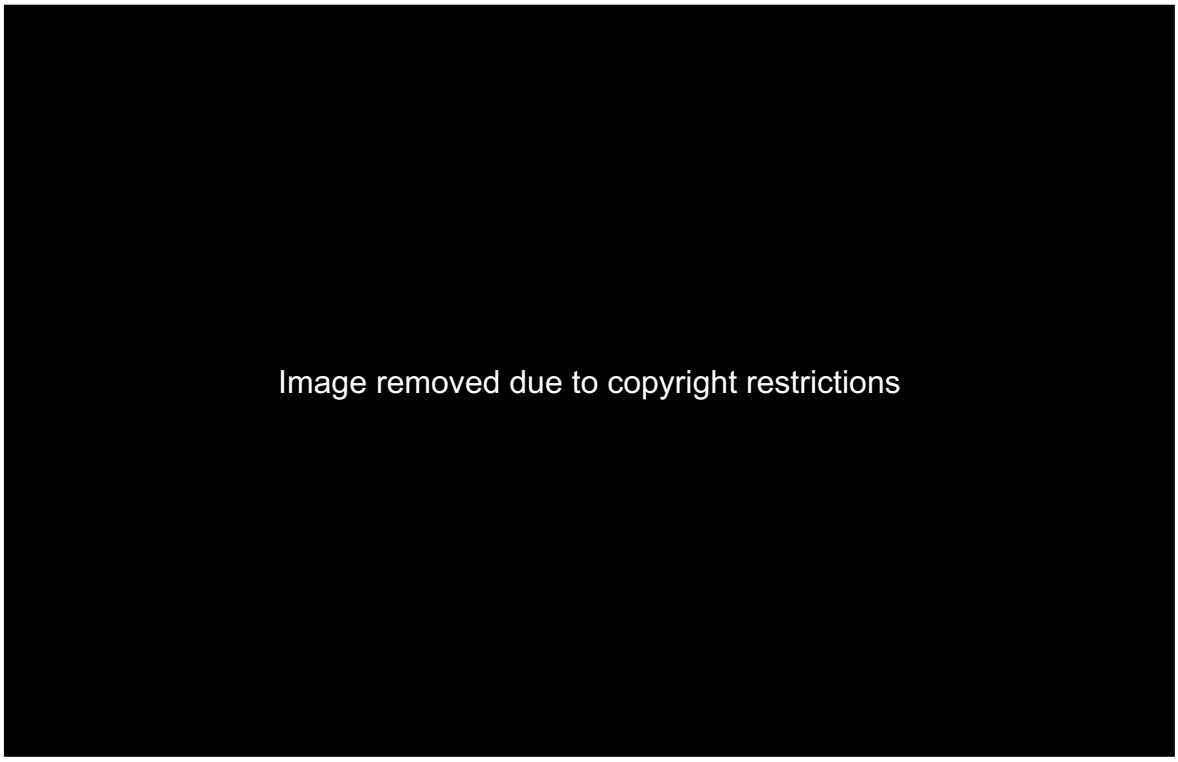


Figure 3-21 Structures and excited states of the molecules made by Liu *et al*.[237] Adding methoxy groups narrows the HOMO and LUMO gaps well as ΔE_{ST}. Diagram is reproduced from Liu *et al*.[237]

3.9 Conformational effects

The nature of excited states can be manipulated by changing the molecular conformation adopted by a molecule. This can lead to enhancement of the TADF process if correctly understood, however it can also serve to suppress emissions if during excited states, distortions to molecular geometry occur, preventing radiative decay, or increasing the rate of non-radiative decay pathways.

In addition to this, different conformations can yield entirely different emission wavelengths of the same molecule - interconversion between each conformation can be achieved *via* careful control of temperature, mechanical grinding force or the nature of the solvent used.[241]

In the work of Data *et al*.[242] the authors took the molecule PTZ-DBPHZ (see Figure 3-22) and recrystallised it from two different solvents (chloroform/hexane, dichloromethane), as well as simply grinding it up. The chloroform/hexane mix produced a conformer in the ax - ax form; dichloromethane yielded an eq - eq conformer and use of a pestle and mortar resulted in a hybrid conformer ax - eq. It was found that greater equatorial character in a molecule gave a higher magnitude of bathochromic shift in all emissions (fluorescent and phosphorescent). See Figure 3-22 and Figure 3-23 for illustrations. The ax - ax conformer yielded predominantly prompt fluorescence in its emission profile, from the ^{1}LE state along with room temperature phosphorescence from the ^{3}LE state, which is populated *via* ISC from the slightly lower in energy (relative to the ^{1}LE state) ^{1}CT state. The ^{1}CT state is much higher in energy than the ^{3}LE state, which makes rISC (and thus TADF) less energetically favourable. The eq - eq conformer exhibited TADF, with the ^{1}CT and ^{3}LE states being in much closer proximity, and the HOMO and LUMO effectively separated in space thanks to the geometric structure of the eq - eq conformer. The ax - eq conformer sits somewhere between both pure ax and eq conformers in terms of its emission character, having both prompt fluorescence like the ax - ax conformer, and delayed fluorescence. Its ΔE_{ST} is slightly larger than the purely equatorial conformer, so the rISC process is much less favourable, though still achievable.

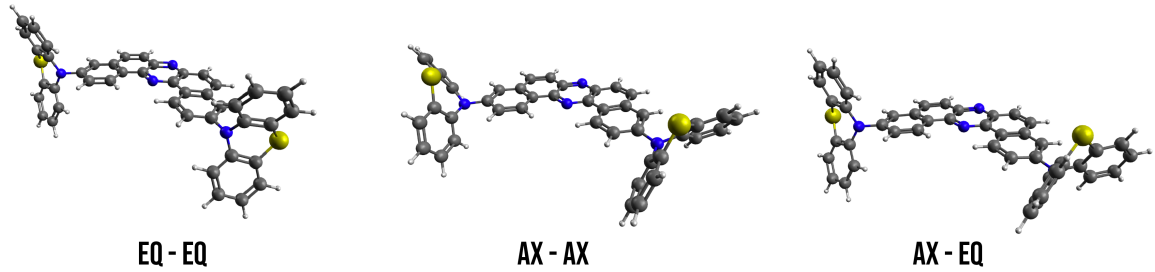


Figure 3-22 Structures of the three conformers of PTZ-DBPHZ. Based on the work of Data *et al.*[242]

Alteration to the energy of the singlet state is much more pronounced than the triplet state, owing to the enhanced spin orbit coupling exhibited in the equatorial conformation for the singlet charge transfer state.

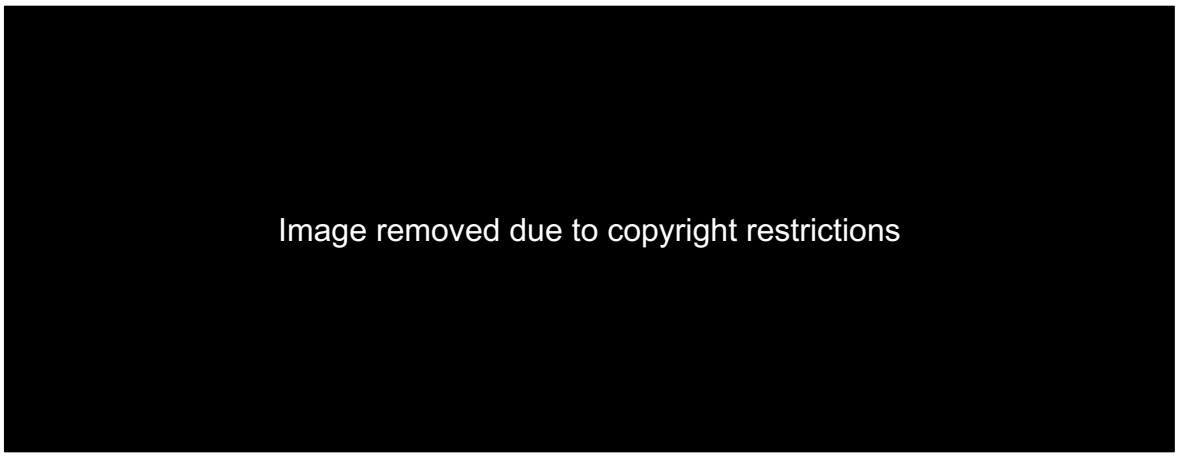


Figure 3-23 Jablonski diagram showing the different photophysical processes in the three conformers of PTZ-DBPHZ. Taken from Data *et al.*[242]

From this work, the authors demonstrate it is therefore important both in the molecular design stage and in device fabrication, to either minimise the degree of conformational freedom in molecule or select the optimum solvent or device design for maximising the abundance of the most effective conformer – depending on the solvent used in the thin layer deposition stage, radically different results from OLED devices can be observed.

3.10 Non-covalent interactions

Non-covalent interactions provide a means of controlling the conformation of TADF molecules; this allows one to precisely control the properties of a semiconducting material.[243,244]

These interactions come in five main forms: molecules with intramolecular n···π (lone pair), π···π non-covalent interactions, n - σ* interactions, n - π* interactions, along with electrostatic interactions. The first two have been suggested as a suitable structural feature to exploit a fast rISC rate, as well swift radiative S_1 to S_0 fluorescence decay.[245] Molecules whose structure results in folds or twists can result in interactions between π-orbitals and *n*-lone pairs, which can aid the spin orbit coupling between the triplet and singlet states thanks to $n \rightarrow \pi^*$ character.

In order for efficient mixing of singlet and triplet states, ΔE_{ST} should be as narrow as possible, whilst the spin orbit coupling, $H_{SO}^{S_1T_1}$, should be as large as possible, as described by the equation:

$$c_{S_1T_1} = \frac{H_{SO}^{S_1T_1}}{\Delta E_{ST}}$$

Equation 3-2 from Chen *et al.*[245]

where $c_{S_1T_1}$ is the mixing coefficient between the first excited singlet and triplet states.

Previously, attempts to enhance TADF were concerned mainly with narrowing ΔE_{ST} by separating the HOMO and LUMO in space, utilising donor and acceptor moieties separated by structural features such as spiro linkages, or dihedral twists. When the HOMO and LUMO are confined to the donor and acceptor moieties respectively, charge transfer excitation character is introduced in these regions. Unfortunately, as mentioned previously, this works against the rISC process, since separation of the HOMO and LUMO in space gives rise to small transition dipole moments between the S_1 and S_0 states, suppressing the radiative decay rates and promoting non-radiative decay. Also, separate singlet and triplet states which form on each moiety will have the same charge transfer character (^{1}CT and ^{3}CT), making interconversion unfavourable.

In order to achieve efficient TADF character, a fine balance must be struck between all the variables involved in the process: spin orbit coupling; ΔE_{ST}; and the transition dipole between the S_1 and S_0 states. Use of non-covalent interactions has recently shown promise with achieving this.

The molecule B-oTC[245] (Figure 3-24) incorporates a triarylboron-based acceptor moiety bonded to a tert-butylcarbazole donor. The structure of this molecule orients the donor moiety at 83.3° from planarity with the phenyl ring of the acceptor to which it bonds. This causes it to stack with the neighbouring phenyl ring of the acceptor, facilitating charge transfer through space *via* the aryl linker potentially by way of π···π interactions. This results in a very efficient blue emitter, with extremely narrow ΔE_{ST} of 0.05 eV and PLQY of 94%. Evidence of this cofacial internal packing has been observed in other molecules too, such as TRZ-oCZ,[246] where instead of a π···π interaction, a lone pair *n*···π interaction is suggested.

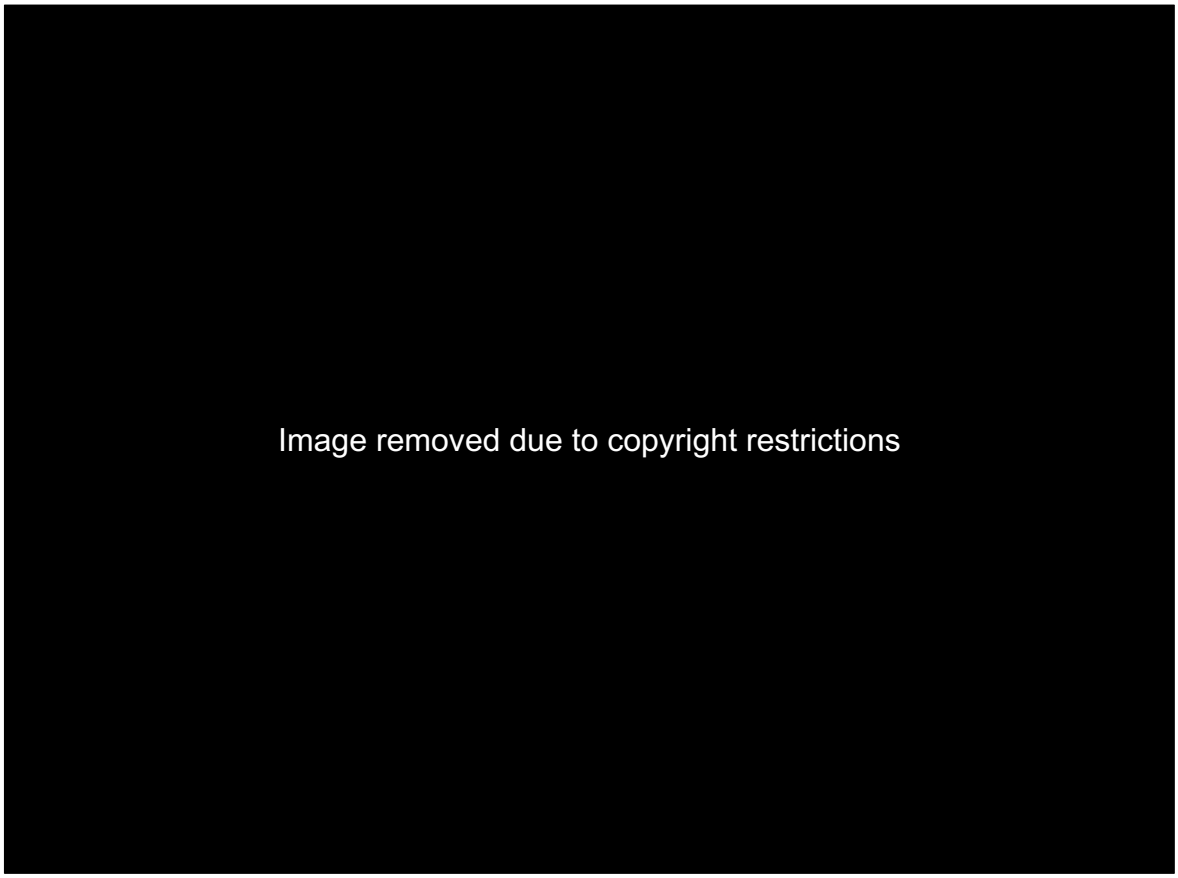


Figure 3-24 A collection of TADF molecules exhibiting through space non-covalent interactions and their linear analogues which do not exhibit non-covalent interactions. Taken from Chen *et al.*[245]

Through a series of quantum chemical calculations, Chen *et al*.[245] explored the non-covalent interactions in a series of molecules and examined how geometries of such molecules impact the TADF process (see Figure 3-25). Their findings provide significant insights as to the impact of lone-pair n···π interactions. They indicate that for π···π interactions, cofacial arrangement of aromatic components should be within the 3 - 4 Å range. Steric hindrance caused by structural features can result in reduction in the strength of interactions, so design of such molecules should take into account the ability of the molecules to fold into a suitable arrangement for non-covalent interactions to take place (the phenlyene ring in the para-connecting orientation of B-pTC significantly hindering stacking for example, as well as a significantly greater degree of rotational freedom).

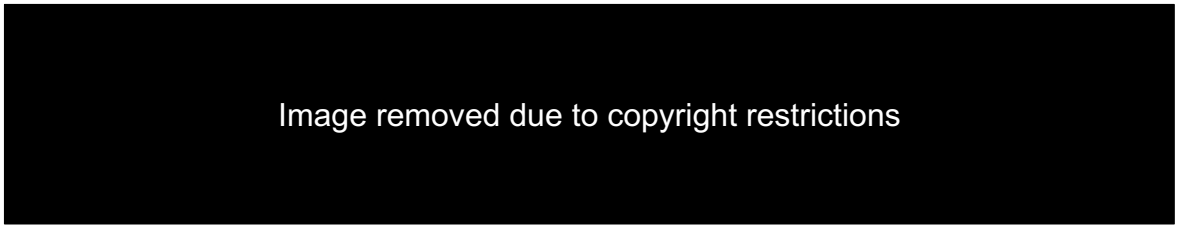


Figure 3-25 3D structures of Chen *et al*.'s molecules. Key to note is the proximities and angles of the n···π and π···π interactions. Images taken from Chen *et al*.[245]

The group focussed on investigating B-oTC and TRZ-oCz for comparison. In the case of TRZ-oCz, the proximity of the nitrogen atoms in the donor and acceptor conspired to destabilise the molecule, however this was countered by the overall dense structure formed from the ortho-position maintaining a short intramolecular distance which facilitates the *n*···π interactions.

Additionally, TRZ-oCz possesses a HOMO confined to the donor moiety and the π-bridge to which it is bonded, but it also creeps onto the nearest nitrogen atom of the acceptor moiety (triazine). This spreading of the HOMO is behind the *n*···π interaction - the lone pair from the nitrogen of the triazine, and the π-orbitals from the carbazole. As such, in this *n*···π type molecule, the wavefunction of the HOMO is a combination of the π-bridge, lone pair and π-orbitals. Since the LUMO of this molecule is confined to just the acceptor and the π-bridge, its wavefunction is a combination of their π-orbitals.

With molecules possessing sufficient folds that are of firm structure - *i.e*. with little in the way of rotational freedom – the intramolecular π···π interactions serve to prevent distortions to their structures in the S_1 state, enhancing CT character and the rISC process. On the other hand, increasing the flexibility of the molecule, or indeed diverging to a linear molecular

structure, significantly increases rotational freedom, resulting in an increased likelihood of non-radiative decay. In the more congested structures, the triplet state takes on a more hybridised form, giving rise to ^{3}CT and ^{3}LE states which permit small ΔE_{ST} values (calculated as 0.06 eV in B-oTC which is congested, and 0.15 eV in B-pTC which is linear).

For molecules exhibiting $n\cdots\pi$ interactions, the transition from a *n* orbital to a π^* orbital involves spin orbit coupling and occurs from transition from the HOMO to LUMO[245]. The HOMO and LUMO are separated on the donor and acceptor respectively, however the nitrogen lone pair on the acceptor is orientated out of plane with the LUMO, meaning that its *n*-orbital actually interacts with the HOMO instead. This gives rise to a very fast rISC rate. The group investigated the orientation of the triazine acceptor moiety with respect to the donor to assess the excited state singlet and triplet spin orbit coupling and the effects on dihedral angles and the ΔE_{ST} (see Figure 3-26).



Figure 3-26 Chen *et al.*'s work illustrates the optimal angle at which non-covalent interactions reaches a maximum intensity. The optimal angle is 43°. Taken from Chen *et al.*[245]

As the angle between the acceptor and the π-bridge is increased, the distance between the carbazole and *n*-orbital increases, reducing the strength of the $n\cdots\pi$ interactions. The optimal structural angle for the ground state singlet is 43°. As the moiety is rotated, the ΔE_{ST} appears to reach a minimum at 60°. However, the spin orbit coupling is reduced from ~0.18 cm^{-1} to 0.03 cm^{-1} at this point, which would significantly restrict the rISC process despite the reduction in ΔE_{ST}[245]. This highlights the significant contribution of non-covalent interactions to spin orbit coupling, and spin orbit coupling's significant contribution itself to the efficiency of the rISC process.

The authors suggest three key considerations to be made when exploiting non-covalent interactions to enhance TADF[245]:

- Molecules can be made to possess congested geometries - orientating moieties such that structural folding permits the stacking of aromatic regions allows for π···π interactions, or orientation of atoms with lone pairs to aromatic regions such that *n*···π interactions may occur - through use of ortho-position substitution of donor moieties to acceptor moieties.

- The π···π interactions can be utilised to promote $^3CT \rightarrow {}^3LE \rightarrow {}^1CT$ transitions, spin orbit coupling, as well as allow some HOMO – LUMO overlap without detriment to ΔE_{ST}, and increased differences in the dipole moments of the S_0 and S_1 states to enhance the rate of fluorescent decay.

- First excited singlet and triplet spin orbit coupling can be promoted *via* *n* – π interactions, allowing for a $n \rightarrow \pi^*$ character to the transitions.

A fine example of this phenomenon in practice is in the work of Peng *et al*.[247] where a 2,4,6-triphenyl-1,3,5-triazine (TPZ) acceptor moiety is bonded to a fluorene spacer group, bonded to a spiro-acridine based donor moiety, with varying numbers of tert-butyl substituents attached to the donor (see Figure 3-27).



Figure 3-27 Peng *et al*.'s two molecules exhibit face-to-face interactions between a donor moiety (purple) and an acceptor moiety (orange) linked and orientated by a rigid fluorene spacer group. Reproduced from Peng *et al*.[247]

These molecules remove all conjugation effects owing to the fluorene spacer group, meaning that any charge transfer occurs through space *via* the aligned donor and acceptor moieties.

The authors pose that in donor - acceptor systems, often the bond between the donor and acceptor presents a mode of rotational freedom, with which energy can be lost. Structures that fix the geometry of the donor and acceptor with respect to one another yield more efficient transfer of charge to the donor and acceptor, as well as increased PLQY. In the case of their work, OLEDs containing the molecules produced very high EQEs - 2tDMG giving 30.8%, and 3tDMG producing 20.2%.

Fixing the geometry here is achieved by the spiro linkage – the quaternary carbon having no rotational degrees of motion, and significantly minimising vibration. The proximities of the donor and acceptor faces are around 3.09 Å for 2tDMG and 3.11 Å for 3tDMG - cofacial distances which are more than suitable for intramolecular charge transfer. Computational studies reveal that the additional tert-butyl group on 3tDMG results in increased donor character, meaning that its HOMO energy is higher, which most likely accounts for the larger distance between the moieties and reduced EQE.

Another example of non-covalent interactions enhancing TADF is with the molecule 2Cz-DPS. Work by Yang *et al*.[248] compared this contorted ortho-linked structure to its para-linked linear analogue, 4Cz-DPS (see Figure 3-28).

Image removed due to copyright restrictions

Figure 3-28 Left - Comparison of the structures of 4Cz-DPS and 2Cz-DPC comparing the through space charge transfer of the latter. Right - Comparison of the excited state energy levels for 4Cz-DPS and 2Cz-DPS. Note the narrowing of the 3LE and 3CT energy gap in 2Cz-DPS thanks to the through space non-covalent interactions. Both taken from Yang *et al*.[248]

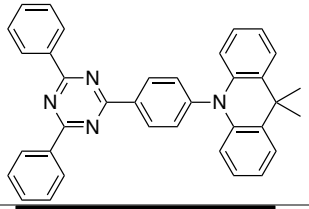
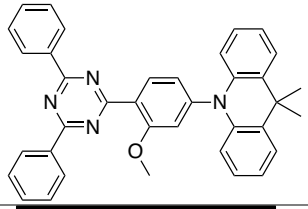
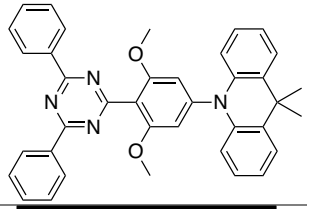
Both molecules incorporate a diphenylsulfone acceptor moiety bonded to two donors - carbazole and phenothiazine. The phenothiazine is connected to the acceptor *via* the para-position, as is the carbazole on the opposite side in 4Cz-DPS, whereas in 2Cz-DPS, carbazole bonds to the ortho-position of the acceptor. Interestingly here, no spacer groups are included, which gives rise to two charge transfer mechanisms: one through the bond (conjugated, $n - \pi^*$) and the other through space ($\pi - \pi^*$). The through space charge transfer

only occurs in 2Cz-DPS owing to its more congested structure which orients the carbazole aromatic rings to be cofacial with the opposite phenyl ring on the acceptor to the one which it is bonded. The V-shaped structure of 4Cz-DPS prevents any orientation which would permit through-space charge transfer. The carbazole in 2Cz-DPS orients such that its face is around 3.1 - 3.8 Å from that of the face of the acceptor's opposing phenyl ring, which itself rotates out of plane with the rest of the acceptor moiety so that there is only 14.2° between the phenyl ring and the carbazole. This results in a hypsochromic shift of 10 nm between the two molecules' emissions, the through-space charge transfer molecule's being at 520 nm, and the single CT molecule's at 530 nm. The rate of rISC almost doubles between 4Cz-DPS and 2Cz-DPS - going from 0.89×10^5 s^{-1} to 1.74×10^5 s^{-1} respectively thanks to the non-adiabatic coupling afforded by the non-covalent interactions. This is despite an increase in the value of ΔE_{ST} of about 0.07 eV. The non-adiabatic coupling effect arises because of additional triplet states existing below the S_1 state in both molecules. In 2Cz-DPS, the energy gap between the T_2 and T_1 levels, corresponds to a gap between ^{3}CT and ^{3}LE and is 0.16 eV, which is narrower than the ^{3}CT and ^{3}LE gap in 4Cz-DPS, which is 0.33 eV (and between the T_4 and T_1 states respectively). The narrower gap between ^{3}CT and ^{3}LE in 2Cz-DPS gives rise to a faster rISC process, despite it having the larger ΔE_{ST} value.

3.11 Modification to π-bridges

Π-bridges in the form of a phenylene spacer group serve to maintain spatial separation of the donor-based HOMO and the acceptor based LUMO and can aid the production of a dihedral angle between the two moieties. The bridge also serves as a site where both the HOMO and LUMO can both be present, meaning that modification to the bridge will affect the properties of both the HOMO and LUMO. A useful illustration of the effects of modifying substituents on a π-bridge can be found in the work by Oh *et al*.[249] (see Table 3-2). They investigated modification to the π-bridge by addition of electron donating methoxy groups. Three molecules were studied, AcTrZ, 1mAcTrz and 2mAcTrz, containing no, one and two methoxy groups respectively.

Table 3-2 Structures, HOMO/LUMO and excited state properties of π Bridged based molecules from Oh *et al*.[249] The HOMO/LUMO images are reproduced from this paper.

	AcTrz	1mAcTrz	2mAcTrz
Structure			
LUMO	Image removed due to copyright restrictions	Image removed due to copyright restrictions	Image removed due to copyright restrictions
HOMO	Image removed due to copyright restrictions	Image removed due to copyright restrictions	Image removed due to copyright restrictions
S_1 (eV)	2.94	3.03	3.30
T_1 (eV)	2.70	2.76	2.85
ΔE_{ST} (eV)	0.24	0.27	0.45
EL peak (nm)	508	496	488
EQE (%)	21.3	21.2	13.5

In all three molecules (see Table 3-2), the HOMOs and LUMOs were spatially separated, however in AcTrz and 1mAcTrz, overlapping of the HOMO and LUMO was predicted to occur on the π-bridge, but not at all in 2mAcTrz. The first two molecules are closer to planarity across the dihedral owing to hydrogen bonding between the nitrogen atom and the π-bridge's nearest hydrogen atom. This is not present in 2mAcTrz owing to the positioning of the methoxy groups, as well as the steric hindrance brought on by the larger methoxy

groups compared to hydrogen. This keeps the HOMO and LUMO completely disconnected through twisted geometry. In all cases however, the addition of methoxy groups increases both the singlet and triplet energies, weakening the strength of the acceptor moiety - most prominent in 2mAcTrz where two methoxy groups are present. In the single methoxy derivative (1mAcTrz) this permits hypsochromic shifts in emissions without compromising EQE (with only a 0.1% reduction). Increasing methoxy substitution further with a second group widens the ΔE_{ST} gap significantly, yielding a reduction in the EQE.

This paper clearly demonstrates the usefulness of a π-bridge (that of spatial separation of the bulk of the HOMO and LUMO but permitting a small degree of mixing), as well as the electron donating effects of methoxy groups on said π-bridge, where both the HOMO and LUMO are present. This can be utilised to effectively raise both the singlet and triplet energies (and presumably lower them should an electron withdrawing group be used in place of the methoxy groups). Whilst steric hindrance of two methoxy groups maximises the dihedral angle in 2mAcTrz, TADF is suppressed because of total absence of π-bridge mediated HOMO and LUMO mixing. Without this suppression, the double methoxy derivative would likely be of significantly greater TADF character. This is important for our work, as we shall be exploiting the 'double methoxy substitution on a π-bridge' effect, along with non-covalent interactions designed to mediate interactions between the HOMO extending onto the π-bridge and the boron of the acceptor moiety in Chapters 5 and 6.

3.12 Broad emission profiles in TADF molecules

In order for TADF molecules to find successful use in display applications, they are required to have very narrow full width at half maximums (FWHM) in their emission profiles.

The reverse intersystem crossing process requires structures with large dihedral angles between the donor and acceptor moieties. This separates the HOMO and LUMO in space as much as possible, meaning that any transition to an excited state must be *via* a charge transfer process (rather than a locally excited state as found when the HOMO and LUMO overlap significantly). This design methodology results in large FWHM of the emission profiles (typically between 70 and 100 nm). One cause for this broadening is suggested to be the increased degree of rotational motion between the donor and acceptor moieties in such molecules. These degrees of freedom give rise to multiple conformations in the excited state, allowing for multiple radiative decay pathways with differing emission wavelengths, producing a broader emission profile.

However, more recent work by Ansari *et al*.[250], argues that the impact of rotation freedom is actually a negligible contributor to the broad FWHM, and that the charge transfer character of the molecule is the root cause of the broadening.

When designing TADF molecules, the primary factor to control is the energy difference between the first excited singlet and triplet states, ΔE_{ST}. The dominant approach to this is separating the HOMO and LUMO in space *via* a large dihedral angle between the donor and acceptor moieties. As Equation 3-1 shows, ΔE_{ST} is strongly linked to the electron exchange energy, J, which is half that of ΔE_{ST}. J is in turn controlled by the degree of spatial overlap between the HOMO and LUMO. Reducing this spatial overlap therefore minimises the difference in energy between the S_1 and T_1 states, producing a small ΔE_{ST}.

With good separation of the HOMO and LUMO, excited states will be charge transfer (CT) in character, as opposed to locally excited (LE) when there is good HOMO and LUMO overlap. The rotational freedom of the D-A bond is the root cause of CT emission broadening as the rotation leads to a greater Stokes shift due to multiple radiative decay pathways. To counter this, colour filters are required in devices which cut out light of undesired wavelengths, effectively defeating the object of enhanced efficiency provided by the TADF principle.

To obtain TADF from twisted structures separating the HOMO and LUMO, the so-called twisted intermolecular charge transfer (TICT) locks the D-A dihedral in place with bulky groups, causing steric hindrance[250].

Originally it was thought that steric hindrance preventing D-A rotations resulted in narrowed FWHM[251] such as in the work of Chen *et al*., where two similar molecules, oPTC and mPTC differ in the position of the phenyl rings (see Figure 3-29). The meta-derivative is said to prevent rotation along the C-N bond due to steric hindrance blocking any rotation, thus yielding narrower FWHM. However, Ansari *et al*.[250] performed computational studies on these same molecules, the results of which suggest that the change in structure is actually reducing the CT character thanks to reduced spread of the LUMO in mPTC, yielding the narrower FWHM. They conclude that, in reality, the actual cause of the narrower emission profile is ambiguous.

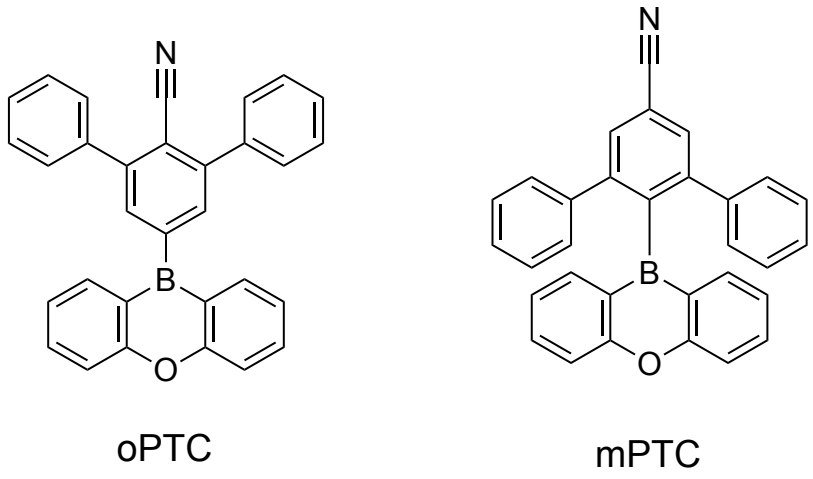
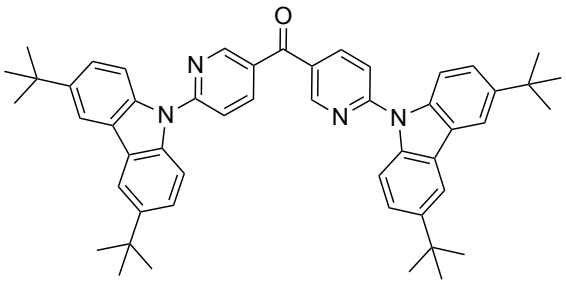
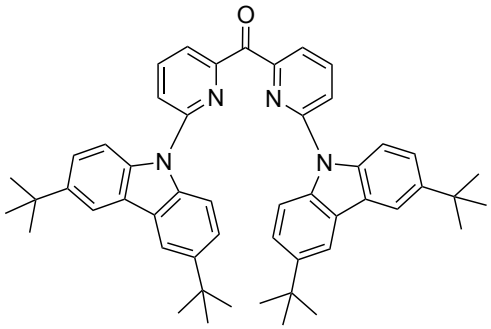


Figure 3-29 Molecules oPTC and mPTC from Chen *et al*.'s[251] study. The meta-substituted derivative is suggested to prevent broadening of the emission profile by locking the dihedral angle in place, whereas oPTC has a greater degree of rotational freedom, however Ansari *et al*.[250] disagree.

Ansari *et al*. go further[250], and criticise the work of Rajamalli *et al*.[252] Rajimalli *et al*. observed the molecule 3DPyM-pDTC possessing a FWHM of 62 nm, and the molecule with greater rotational freedom, 2DPyM-mDTC possessing a FWHM of 89 nm. They explain this difference as "due to the more flexible structure" permitting the D-A rotation, whereas it is restricted in the former molecule (see Figure 3-30). Ansari *et al*.[250] on the other hand, propose that this is not true. They say that the CH···N hydrogen bonding in their structures should be similar and therefore any difference in steric hindrance that would reduce the donor – acceptor rotation to be altered, should not be at all that different between both molecules.



3DPyM-pDTC



2DPyM-mDTC

Figure 3-30 Structures of 3DPyM-pDTC and 2DPyM-mDTC as synthesised by Rajamalli *et al.*[252] Once again Ansari *et al.*[250] disagree with the author's explanation for the narrower FWHM of the allegedly more restricted D-A rotations.

Ansari *et al.*[250] continue to compare molecules from a survey of the literature which possess more sterically restricted derivatives and they posit that the argument for increased resistance to D-A rotation does not stand up since the energy barriers have very little difference between the molecules, regardless of the substituent groups used to obstruct D-A rotations. Their DFT calculations show little difference between the HOMO and LUMO overlap coefficients for these molecules as well.

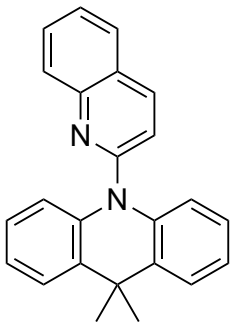
Ansari *et al.*[250] further suggest that FWHM should be reported in eV as they feel this reveals the true difference between the molecules – that in their survey, there is little difference between the FWHM when converted to eV. They highlight the two molecules FBPCNAc and FDQCNAc, which possess FWHMs of 96 nm and 86 nm respectively. Converting this to eV gives 0.325 eV and 0.346 eV respectively. This suggests the 10 nm difference between the FWHM of the molecules (which one might suggest is significant enough to be noticeable, despite it actually being opposite to the trend since the broader emitter is more restricted in rotation) is only 0.021 eV, which they consider to be negligible.

This approach seems flawed, however. Whilst indeed, if one compares two molecules with ΔE_{ST} values differing by 0.021 eV, or indeed S_1 energies differing between two molecules by only 0.021 eV, one would be well within one's right to suggest that the difference between two molecules was negligible. However, a 10 nm broader emission profile is much more noticeable.

3.13 Aggregation induced emission

Many luminescent molecules emit strongly in solution, but the emissions are quenched upon aggregation in the solid state[253,254], a physical phenomenon known as aggregation caused quenching (ACQ). In donor – acceptor type molecules, where the electron rich and electron poor moieties are linked by a single σ-bond, the molecule possesses a high degree of rotational freedom[255]. Naturally, this presents a potentially significant route for non-radiative decay, and in solution these types of molecules can present very low emission quantum yields. However, introducing aggregation by means of a poorer solvent or formation of a thin film of the material in question, results in a restriction of this rotation, along with reduced vibrational motions[256]. Since the major route for non-radiative decay is therefore prevented, the rate of radiative decay now outcompetes that of what would be expected by aggregational quenching and thus luminescence is significantly enhanced. This physical property is known as aggregation induced emission (AIE).

A typical procedure for investigating the presence of ACQ or AIE involves varying the fraction volume of aliquots of the material in solution with a poorer solvent. This involves dissolving the compound to be analysed in a good solvent, then gradually adding a poor solvent to aliquots such that the overall concentration in the volume being analysed remains the same. A good example of this procedure can be found in the of the work of Shen *et al*.[257] who investigated AIE in quinoline-based TADF molecules such as DMAC-QL (see Figure 3-31).



DMAC-QL

Image removed due to copyright restrictions

Figure 3-31 Structure of DMAC-QL and PL spectra from various different water fractions of the compound in solution. Taken from Shen *et al.'s*[257] work.

When AIE is present, the PL intensity increases at much higher water fractions (typically above 90% vol). Materials with AIE are particularly attractive for OLEDs since quenching

in the solid state is suppressed, they therefore present the opportunity for neat film EMLs avoiding the need for host matrices to quell ACQ effects, which also enhances device stability and makes the fabrication much simpler[258].

3.14 Summary

In short, TADF molecules should be designed incorporating electron rich moieties (the donor) and electron deficient moieties (the acceptor). They should be orientated such that a large dihedral angle between the different moieties affords excellent separation of the HOMO and LUMO. This can be further aided by use of π-bridges or spiro-linkages. Further modification to the donor, acceptor or π-bridge can aid both steric hindrance (maintaining the dihedral angle) and can influence the electronic properties of the respective donor or acceptor (making their electron donating or receiving character stronger or weaker). This also permits the fine turning of the emissive and solvation properties of the molecule.

When structural features are orientated in close proximity (such as π- π face contacts), non-covalent interactions *within* the TADF molecule are possible, influencing the stability of the molecule in the excited state, and its resulting emissive properties.

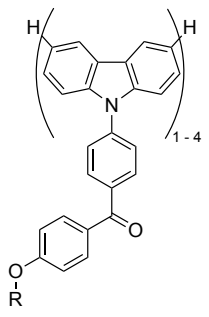
Owing to its empty p-orbital, boron is becoming an increasingly attractive component for electron deficient acceptors and further research into its application into highly efficient, deep blue devices with low efficiency roll-off is a fast growing area of OLED research.

Chapter 4 An investigation into novel small molecule donor-acceptor-type TADF molecules

4.1 Introduction

As the field of organic luminescent materials continues to grow, structures of emissive materials get more and more complicated in the drive to find novel, highly efficient emitters. As such, many of these materials require multiple synthetic steps and numerous intermediates, with long-winded and sometimes inefficient purification methods. To aid sustainability and keep costs down, materials for devices should ideally require as few synthetic steps as feasible and require as simple a purification method as possible. As such, aiming for small donor-acceptor (D-A) type molecules, synthesised from already commercially available material (which should typically have well understood and optimised synthetic pathways themselves), presents an ideal solution for the long-term sustainability and cost effectiveness of the OLED fabrication industry.

Dimesityl boron is one such acceptor which fits this requirement, and derivatives of the well-known electron-rich molecule, carbazole, are a similarly suitable selection of donor materials. Studies have shown that TADF can be achieved with simple D-A type compounds synthesised in a single step with carbazole-like donors and dimesityl boron as an acceptor.[259] Altering the strength of the donor by addition of substituent groups (such as methoxy groups) can also help tune non-TADF active material to enable rISC and switch on TADF [259] and alter the emissive properties of established TADF structures.[260] Increasing the conjugation of aromatic donors can also contribute to aiding TADF by narrowing the ΔE_{ST}. When bonding through multiple carbazole units together into a conjugated chain in the donor, Wei *et al*.[261] observed a substantial narrowing of ΔE_{ST} by 100 meV, simply by coupling two carbazole units in their structure (see Figure 4-1). Extending the conjugation to four units realised a 16% increase in the PLQY, despite the slight twisting between each carbazole unit potentially rupturing the conjugation of the HOMO.



R' = n-$C_{12}H_{25}$

Figure 4-1 General structure of Wei *et al*.'s[261] oligomers. Several repeating units of the molecule are connected through conjugated carbazole units.

In order to explore the impact of conjugation in a single carbazole-like moiety and their steric hindrance around the B-N bond, four novel D-A type molecules were successfully synthesised (see Figure 4-2). These use dimesityl boron as the acceptor unit and varying the donor unit to change HOMO conjugation. Iminostilbene (also known as dibenzazepine), 7H-benzo[c]carbazole, 7H-dibenzo[c,g]carbazole, and 3,6-diphenyl-9H-carbazole were selected as the donor moieties.

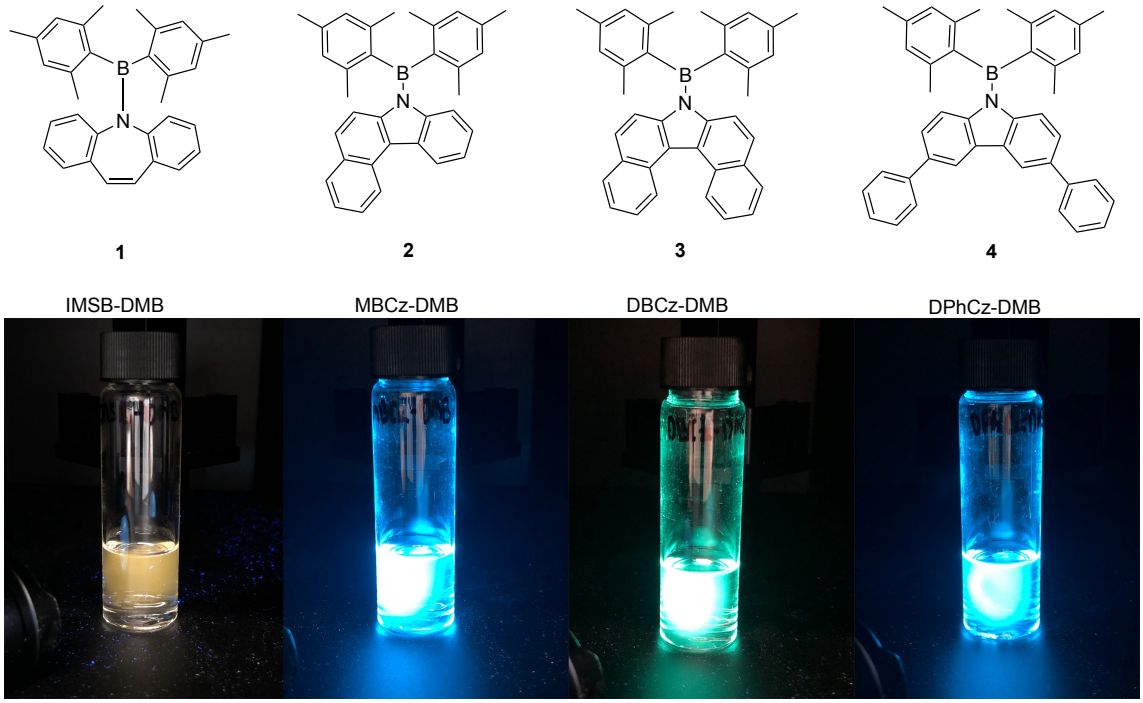
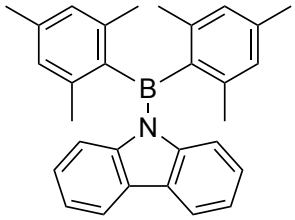


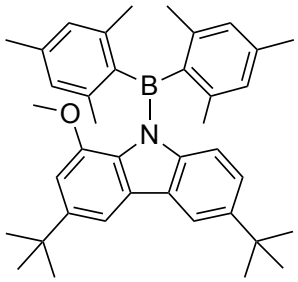
Figure 4-2 Structures of compounds 1 - 4 accompanied by samples in THF excited with a 365 nm UV torch showing their variation in photoluminescence properties.

To gain an understanding of the different factors influencing the photophysical properties of dimesitylboron-based donor-acceptor molecules, compounds **1** – **4** were compared with the literature compound **5**[262] and compounds **6** – **9**, synthesised by Dr Joseph Cameron. These are based on a similar design motif and permit the exploration of steric effects, altering the donor character, and investigating the possibility of non-covalent interactions between methoxy groups and the empty p-orbital of the boron. The structures of these compounds are shown in Figure 4-3.



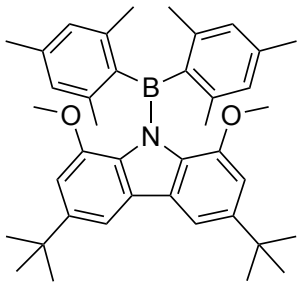
5

Cz-$BMes_2$



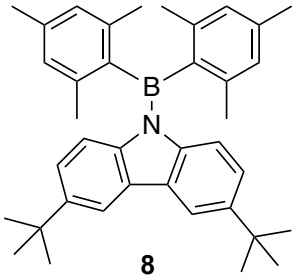
6

tBu_2-CzOMe-$BMes_2$



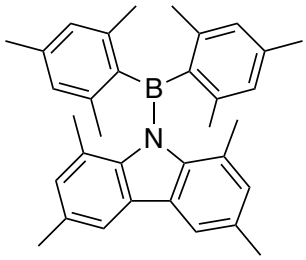
7

tBu_2-$CzOMe_2$-$BMes_2$



8

tBu_2-Cz-$BMes_2$



9

Me_4-Cz-$BMes_2$

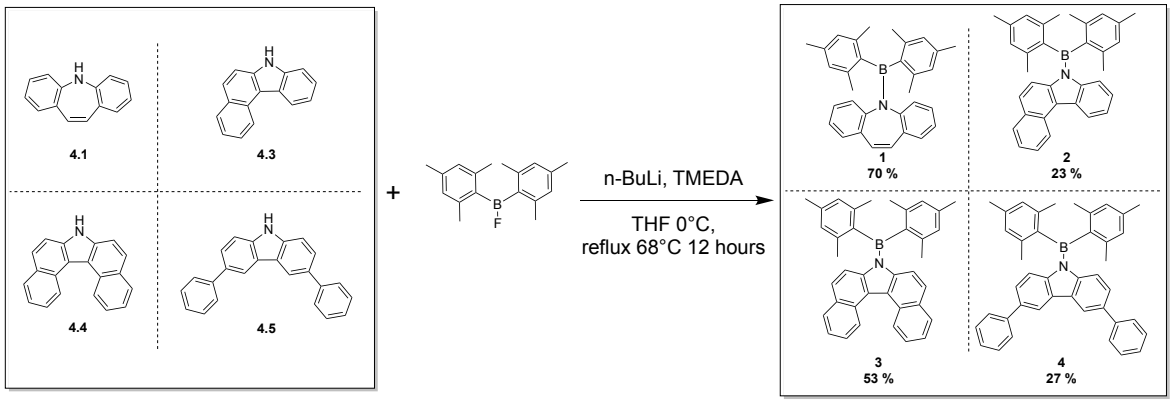
Figure 4-3 Structures of compounds 5 - 9 synthesised by Dr Joseph Cameron

Compounds **5**[262] and the non-tert-butyl derivative of **6**[259] were previously reported in the literature.

4.2 Results and Discussion

4.2.1 Synthesis

All four molecules exploring conjugation were synthesised *via* lithiated deprotonation of the central nitrogen atom, followed by coupling directly to dimesitylboron fluoride (see Scheme 4-1).



Scheme 4-1 Synthesis of compounds 1 - 4.

The iminostilbene derivative, IMSB-DMB (**1**), was successfully synthesised using an aqueous workup with high yield (70%), however upon aqueous workup, the dibenzo carbazole derivative, DBCz-DMB (**3**), went from exhibiting green fluorescence in the crude form to purple fluorescence in the organic layer. Completing the workup yielded none of the expected product, only the starting materials (7H-dibenzo[c,g]carbazole having a purple fluorescence in solution). This suggested that this compound readily undergoes hydrolysis and is explored further in section 4.2.14. Following this, the reaction was repeated, replacing the aqueous workup with a non-aqueous workup *via* filtering through celite. This resulted in a successful yield (53%). A small aliquot was taken, and water added, yielding almost immediate hydrolysis of the B-N bond. For the diphenyl carbazole derivative, a similar hydrolysis was noted, albeit at a slightly slower rate. As such, a non-aqueous workup was used for this compound, as well as for all further compounds with a B-N bond.

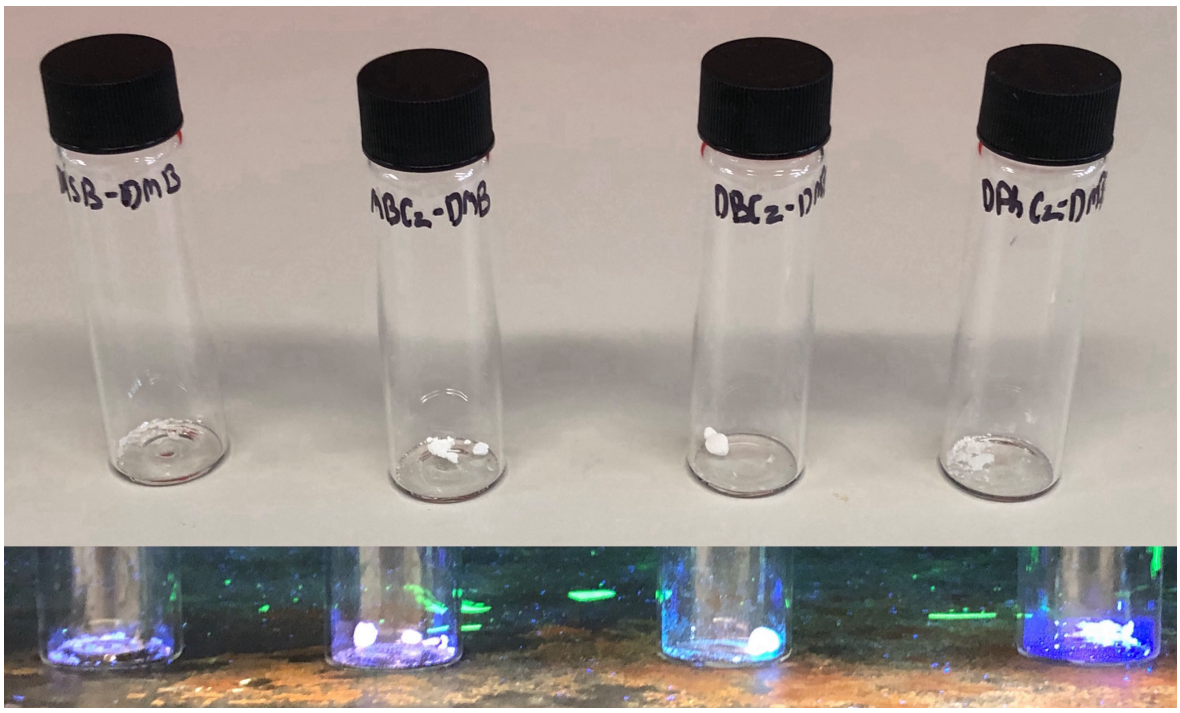


Figure 4-4 Samples of solids of compounds 1 - 4.

The monobenzocarbazole derivative, MBCz-DMB (**2**) was obtained in an even lower yield (23%), whereas the more stable DPhCz-DMB (**4**) was only obtained at 27% yield.

The four compounds in this study yielded white solids, with compounds **1** and **4** being more crystalline in appearance (see Figure 4-4). In the solid state, their fluorescence is a purple-blue with the exception of compound **3**, which has a cyan fluorescence, visually suggesting more bathochromic emissions.

4.2.2 Computational chemistry

Computational calculations were performed on the structures of the three molecules. Optimisation was performed at the DFT-B3LYP level of theory using the 6-31+G (d) basis set. Confirmation that the optimised structured was at a minimum on the potential energy surface was determined by the absence of negative frequencies. Energy calculations were performed *via* TD-DFT PBE0 6-31+G (d).

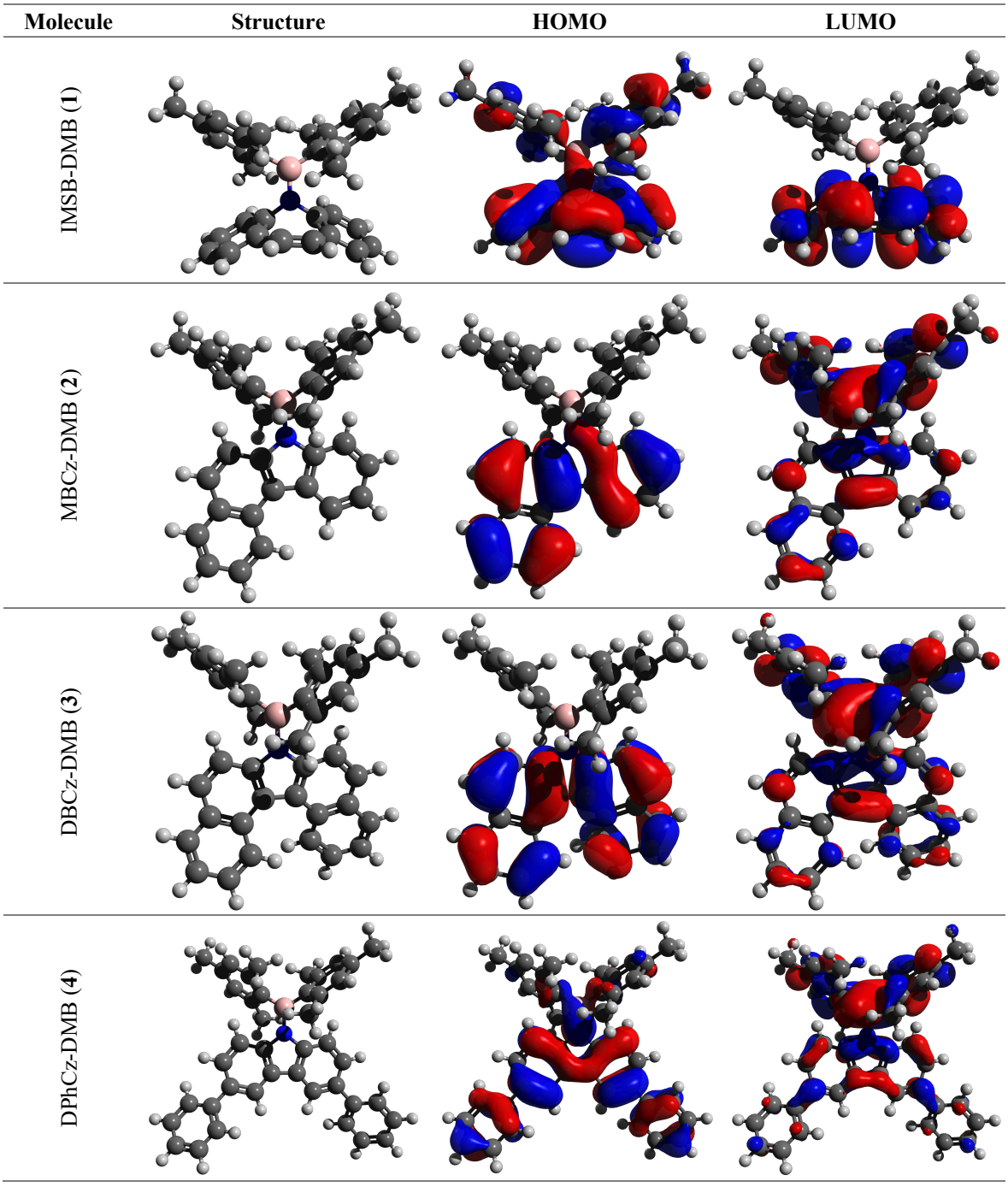


Figure 4-5 Optimised structures and HOMO and LUMOs calculated *via* TD-DFT.

Figure 4-5 shows the DFT optimised structures of compounds **1** – **4** as well as their TD-DFT calculated HOMOs and LUMOs. The calculated photophysical and HOMO-LUMO energies are summarised in Table 4-1.

Table 4-1 Summary of TD-DFT results for compounds 1 - 4. Italics represent experimental results from this chapter.

Molecule	S_1 (eV)	T_1 (eV)	ΔE_{ST} (eV)	HOMO (eV)	LUMO (eV)	Eg (eV)
IMSB-DMB (1)	3.97 *3.40*	2.53	1.44	-6.13 *-5.90*	-1.38 *-2.17*	4.75
MBCz-DMB (2)	3.48 *3.11*	2.44 *1.96*	1.01	-5.81 *-5.62*	-1.594 *-2.31*	4.21
DBCz-DMB (3)	3.19 *3.15*	2.27 *2.42*	0.92	-5.58 *-5.69*	-1.659 *-2.24*	3.92
DPhCz-DMB (4)	3.59 *3.28*	2.86 *3.18*	0.73	-5.92 *-5.90*	-1.551 *-2.09*	4.37

The optimised structures suggest significant buckling of the iminostilbene unit in compound **1**, with a slight deviation from planarity of the benzene rings of the dibenzo carbazole in compound **3**. The significant distortion of iminostilbene suggests incredibly poor conjugation across its HOMO, which explains why no TADF was observed. The excellent conjugation of the HOMO across dibenzocarbazole, despite its non-planar nature means the red shifting of its delayed emissions could be a result of potential 'flapping' motions of the donor moiety in the excited state.

In compound **1** the B-N bond is calculated as 1.44 Å, with the two B-C_{endo} bonds being 1.61 Å. In compound **2**, the B-N bond increases to 1.46 Å, whereas the two B-C_{endo} bonds shorten to 1.58 Å. With the more carbazole-like diphenyl-carbazole in compound **4**, the B-N bond is intermediate in length at 1.45 Å. The B-C_{endo} bonds are again intermediate in length, much closer to the dibenzo carbazole derivative at 1.59 Å. The longer B-N bond lengths would explain the reduced stability in compounds **3** and **4**, which both readily undergo hydrolysis, whereas compound **1** (with the shortest B-N bond length) survives intact (see Section 4.2.14).

The bond angles in the IMSB-DMB (**1**) acceptor moiety are C-B-C = 120.5°, C-B-N = 119.4 and 119.9° (C-B-N for each mesityl ring). In DBCz-DMB (**3**) the acceptor's angle remains much the same at 120.7°, as do the two C-B-N angles at 119.7° and 119.6°. In DPhCz-DMB (**4**) the C-B-C angle widens by a degree to 121.0°, with no change to the N-B-C angles, both being 119.5° in this molecule.

The donor environments differ significantly, with compound **1** seeming to buckle such that the central heterocycle has an envelope-type structure with an almost 110° kink. Compound **2** remains undistorted with a completely planar donor environment, whereas compound **3** has an almost helical-like quality with the benzo groups deviating from planarity by 30.3° (using the carbons furthest from the nitrogen, and the two carbons making up the 5-membered ring as reference). The carbazole moiety in compound **4** remains planar, however the two phenyl rings exhibit a slight twisting and deviate from the planarity of the heterocycle by 37.7° and 37.2°, interrupting the conjugation of the HOMO across the whole donor.

What is fascinating with the monobenzo- and dibenzocarbazole donors is that the HOMO spreads well across the donor moieties without any spread into the acceptor moiety whatsoever, suggesting they will be of greater charge transfer character to the other two compounds, owing to reduced HOMO-LUMO overlap. Interestingly, the HOMO in compound **1** spreads across both the donor and acceptor moieties and the LUMO locates itself upon the donor, not the acceptor. This could go somewhere in explaining the unusual UV-vis spectrum obtained in Figure 4-23, and that the typical D-A nature of this compound has broken down, perhaps as a result of the significant buckling of the iminostilbene moiety.

The dihedral angles between donor and acceptor (with respect to both mesityl rings) are calculated to be 8.0°/11.6°, 31.5°/31.7°, 34.2°/34.3° and 28.5°/28.5° for compounds **1**, **2**, **3**, and **4**, respectively. Note that since there are two mesityl rings in the acceptor moiety, we consider two values for the dihedral to account for the two unconnected B-C bonds.

The electronic properties calculated suggest that the more conjugated molecules have redder emissions, with narrower ΔE_{ST} values. It is interesting that the ΔE_{ST} value calculated for IMDB-DMB (**1**) is quite wide, in-keeping with the observed lack of TADF character. The S_1 values for DBCz-DMB (**2**) and DPhCz-DMB (**4**), whilst different from the experimental values, also exhibit the same trend, with the dibenzocarbazole having the most potential for red-shifted emissions.

Despite having greater degrees of rotational freedom, compound **4** is a relatively blue emitter (both suggested by the calculations and observed experimentally). Compound **2** has extended conjugation compared to compound **4** and is a bluer emitter still. Despite this, adding another benzene ring to the donor in compound **3** to further increase conjugation, the

emission red-shifts significantly instead. This suggests that rotational freedom of the diphenyl groups in compound **4** contributes less to red-shifting of emissions than the potential flapping motion of the donor in compound **3**.

The trend in the PBE0 calculated singlet state energies correctly match the trend observed experimentally for compounds **2**, **3** and **4**, with compound **1** significantly more red-shifted in reality. In the solid state however, this degree of inaccuracy is reduced, since crystals of compound **1** are bright blue emitters. This suggests that the impact on the environment surrounding IMSB-DMB (**1**) is not taken into account in our calculations.

Of significant note is the localisation of the LUMO upon the supposed iminostilbene donor moiety in compound **1**. Whilst the HOMO is mostly on the iminostilbene unit, it still spreads into the supposed acceptor (dimesityl boron) region. The fact that there is no LUMO localisation upon the dimesityl boron moiety, and only on iminostilbene suggests that the photophysics is likely to be much more complicated for this molecule, with first appearance suggesting that the iminostilbene unit is in fact an acceptor moiety in this case despite the literature reporting iminostilbene as a donor[263]. Alternatively, the much more likely case is that the extension of the acceptor's conjugation may in fact be raising the HOMO and lowering the LUMO, meaning that in this case, the iminostilbene is actually too strong a donor to be paired with dimesityl boron effectively.

4.2.3 Crystal structures

Single crystals of compounds **1**, **3** and **4** were grown *via* CH_2Cl_2 : MeOH vapour diffusion. Despite using an array of different solvents and techniques, preparing crystals of compound **2** has thus far been unsuccessful. Single crystal XRD was performed at the University of Southampton by Dr Laura McCormick. The .cif files were processed in Mercury software for rendering and structural measurements.

The crystal structures provide an understanding of the structural conformation and packing in the solid state – allowing for the observation of steric effects, donor contortions and potential interactions.

Table 4-2 Summary of key bond distances from single crystal XRD structures of compounds in this study.

Compound	B – O/H distance (Å)	N – B bond length (Å)	B – C_{endo} bond lengths (Å)
IMSB-DMB (1)	2.96 / 3.17 (B-H)	1.42	1.60/ 1.60
DBCz-DMB (3)	2.89 / 2.91 (B-H)	1.45	1.58 /1.58
DPhCz-DMB (4)	2.97 / 2.99 (B-H)	1.45	1.57 / 1.58
Cz-$BMes_2$ (5)	2.98 / 2.98 (B-H)	1.44	1.58 / 1.58
tBu_2-CzOMe-$BMes_2$ (6)	2.99 (B-H) 3.02 (B-O)	1.46	1.58 / 1.58
tBu_2-$CzOMe_2$-$BMes_2$ (7)	2.91 / 2.97 (B-O)	1.48	1.57 / 1.57
Me_4-Cz-$BMes_2$ (9)	2.87 / 2.67 (B-H)	1.47	1.58 / 1.58

Table 4-3 Summary of key bond angles from single crystal XRD structures of compounds in this study.

Compound	D – A dihedral (°)	C-B-C angle (°)
IMSB-DMB (1)	0.98 / 9.5	119.2
DBCz-DMB (3)	33.2 / 37.5	122.2
DPhCz-DMB (4)	26.8 / 26.0	121.4
Cz-$BMes_2$ (5)	23.1 / 23.1	119.6
tBu_2-CzOMe-$BMes_2$ (6)	26.5 / 44.1	121.1
tBu_2-$CzOMe_2$-$BMes_2$ (7)	49.6 / 54.0	121.4
Me_4-Cz-$BMes_2$ (9)	50.4 / 38	123.8

The main measurements of consideration of compounds in this study are summarised in Table 4-2 and Table 4-3, and their structures displayed in Figure 4-6, Figure 4-7 and Figure 4-8.

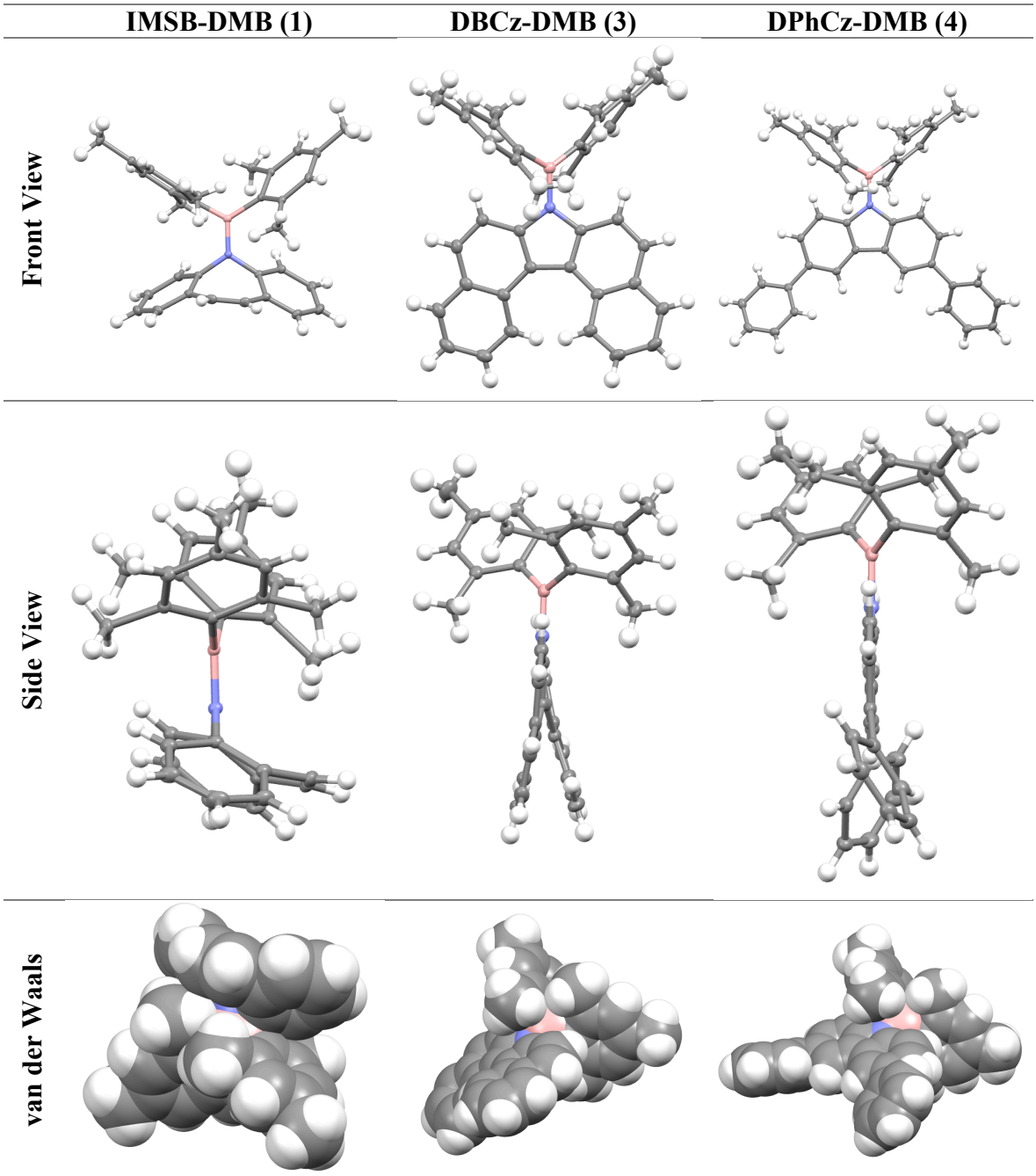


Figure 4-6 Structures of compounds 1, 3 and 4 derived from single crystal XRD studies.

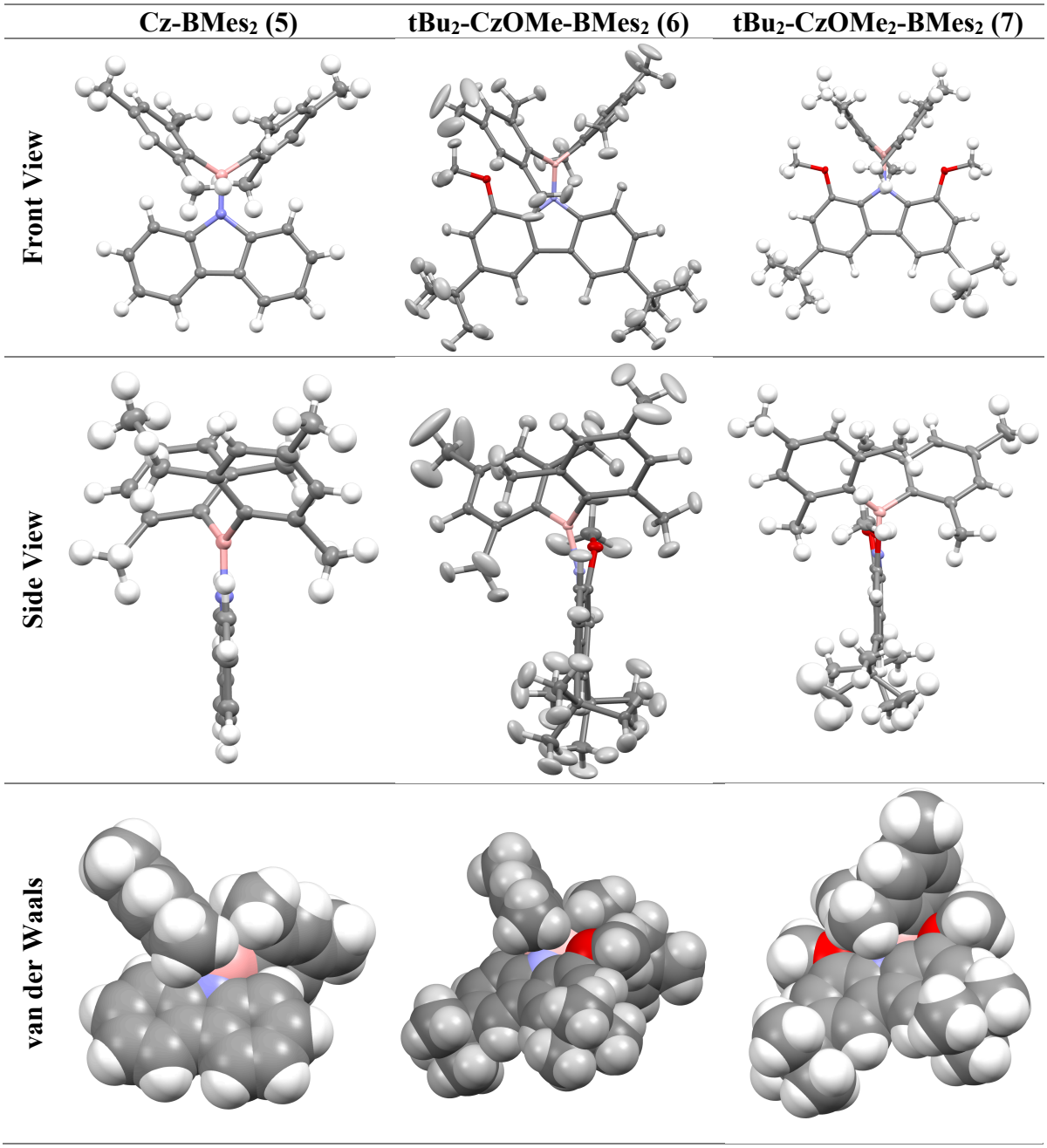


Figure 4-7 Structures of compounds 5, 6 and 7 derived from single crystal XRD studies, kindly provided by Dr Joseph Cameron.

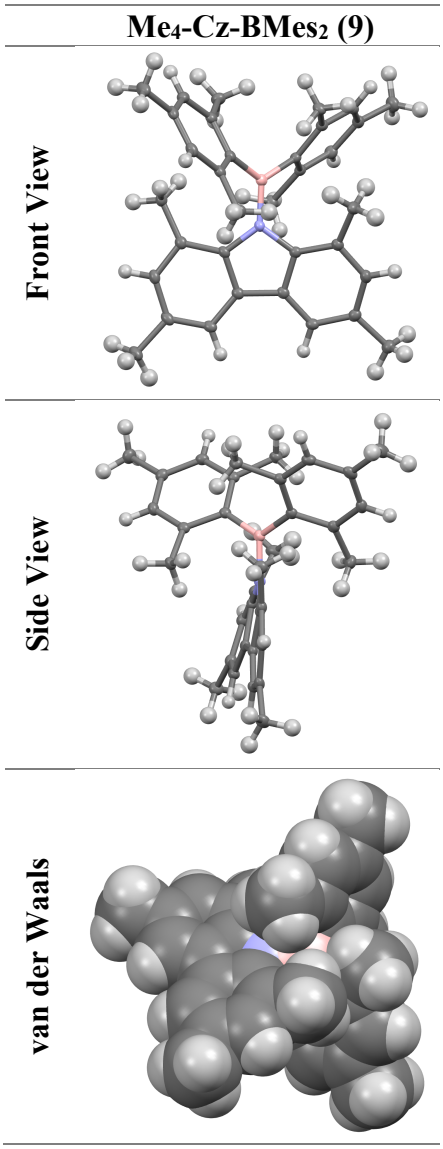


Figure 4-8 Structures of compound 9 derived from single crystal XRD studies, kindly provided by Dr Joseph Cameron.

Compounds **1**, **3** and **4** produced good quality single crystals from chloroform : methanol vapour diffusion. The molecular structures were revealed *via* single crystal X-ray diffraction studies. IMSB-DMB (**1**) shows a very congested structure, with significant buckling of the iminostilbene donor moiety, in keeping with the DFT calculations. The B-N bond is 1.42 Å, with the two B-C_{endo} bonds being 1.61 Å and 1.60 Å. Whilst the B-N bond is slightly shorter, the B-C bond lengths are in good accordance with those calculated. In DBCz-DMB (**3**), the B-N bond increases to 1.45 Å, whereas the two B-C_{endo} bonds shorten to 1.58 Å and 1.58 Å accordingly. With the more carbazole like diphenyl-carbazole in DPhCz-DMB (**4**), the B-N bond is intermediate in length at 1.45 Å. The B-C_{endo} bonds are again intermediate in length, much close to the dibenzo carbazole derivative at 1.57 Å / 1.58 Å. The observed bond distances and angles are in very good accordance with the optimised structures that were calculated.

The bond angles in the IMSB-DMB (**1**) acceptor moiety are C-B-C =119.2°, C-B-N = 124.0°/123.3°. This differs from the more evenly spaced trigonal planar environment calculated previously. In DBCz-DMB (**3**) the acceptor's C-B-C angle increases to 122.2°, 1.5° wider than calculated, whereas the C-B-N angles narrow to 117.8° and 119.9°. In DPhCz-DMB (**4**) the C-B-C angle remains similar to the dibenzo carbazole compound at 121.4°, with slightly more evenly spaced N-B-C angles, both being 119.3° in this molecule, both in good accordance with the computationally calculated measurements.

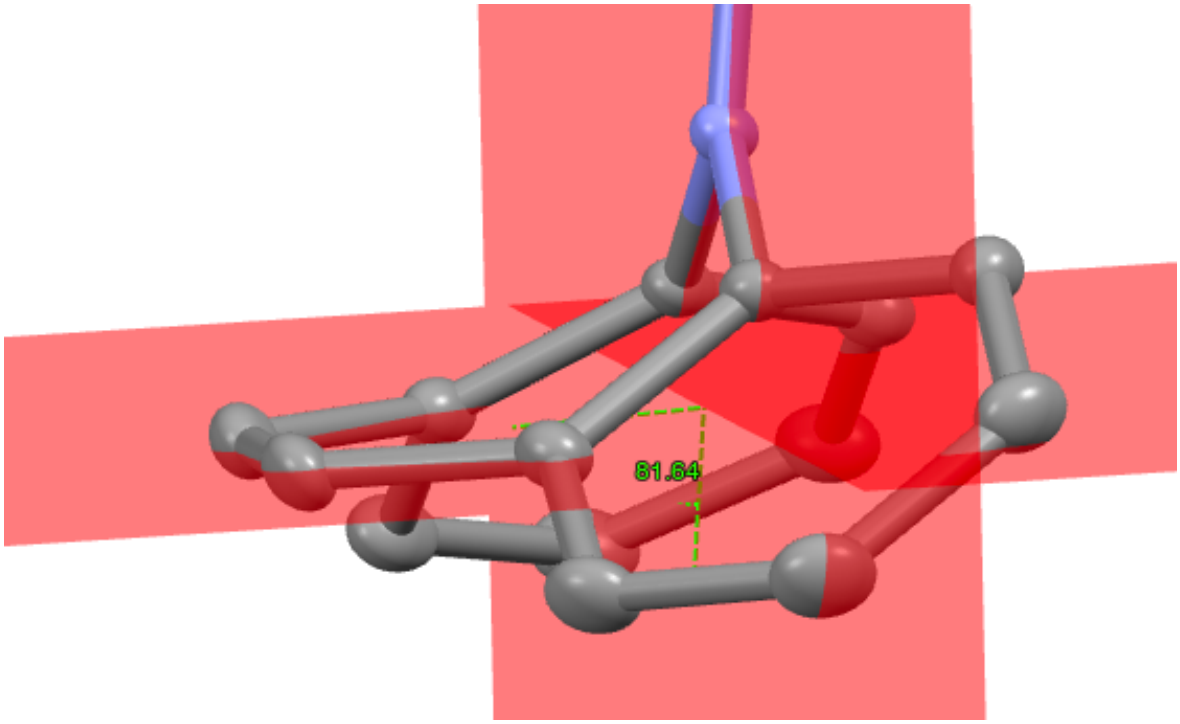


Figure 4-9 Close up of the buckling the olefin bond in the iminostilbene moiety of IMSB-DMB (1). Red boxes indicate the planes made by the -C-C=C-C- region and the C-N-C region with the 81.6° angle at the two planes intersection.

The donor moieties show widely differing structures. In IMSB-DMB (**1**), the entire moiety is buckled with the central cycloheptene ring deviating from planarity by 98.4° from nitrogen to the double bond (see Figure 4-9). The C-N-C bond is 112.7° suggesting little in the way of strain. The dihedral between the acceptor and donor is difficult to assess owing to the twisting of the dimesityl rings resulting in the boron centre deviating slightly from planarity, however the C-N-B-C dihedrals with respect to the donor and two mesityl rings ranges from 1.0° to 9.5°. This lack of dihedral twist suggests good mixing of the HOMO and LUMO, which would work to prevent any TADF character.

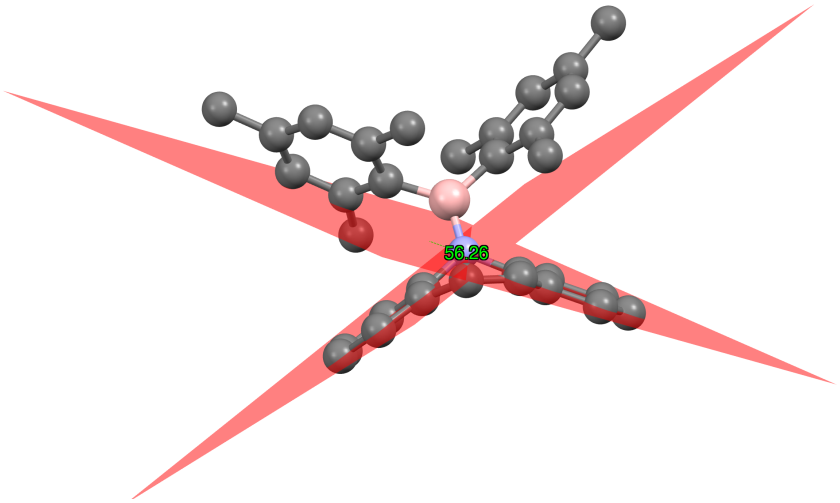


Figure 4-10 Angle between phenyl rings in iminostilbene moiety of IMSB-DMB (1).

Furthermore, an additional buckling of the iminostilbene moiety manifests at 56.3° between the two aromatic rings (see Figure 4-10).

In DBCz-DMB (**3**) the donor's C-N-C angle decreases to 105.9° owing to the transition from a heptagonal to pentagonal structure, naturally. This change in donor also results in an increase in the relative dihedral angle between the donor and acceptor moieties to 33.2°/37.5°, very similar to that which was predicted in calculations. Interestingly, the entire dibenzocarbazole moiety appears to twist along the aromatic region in a quasi-helical manner, resulting in a 29.1° deviancy between the pentagonal region and furthest central carbon atoms (once again using the carbons furthest from the nitrogen, and the two carbons making up the 5-membered ring as reference), which matches what was observed in the calculations. With DPhCz-DMB (**4**) the dihedral is at 26.8° and 26.0° with respect to the B-(mes) bonds. Unlike DBCz-DMB (**3**), DPhCz-DMB (**4**) exhibits no distortion to the planar carbazole moiety, however the two phenyl rings in the 3 and 6 positions twist with respect to the carbazole by 36.1° (C4 – C13) and 33.2° (C9 – C19), with C-C bonds between the rings and the carbazole being 1.49 Å and 1.45 Å, respectively.

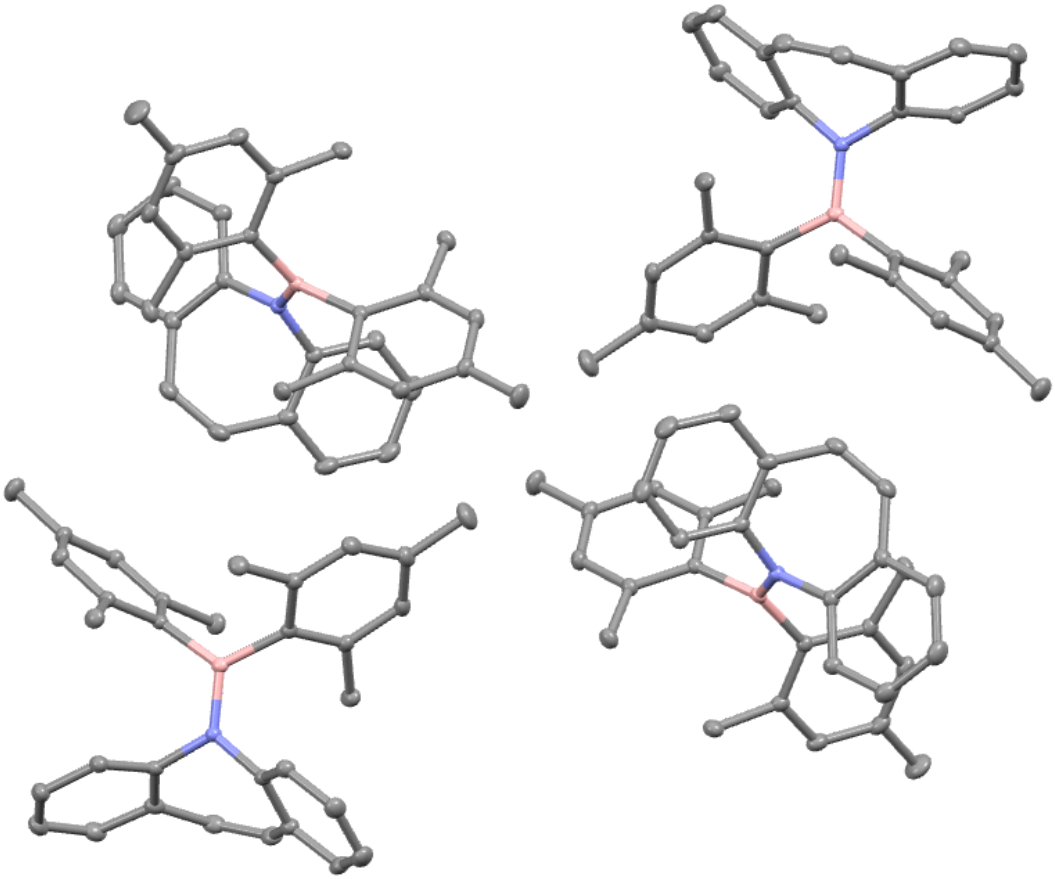


Figure 4-11 Packing of four IMSB-DMB (1) molecules (hydrogens omitted for clarity).

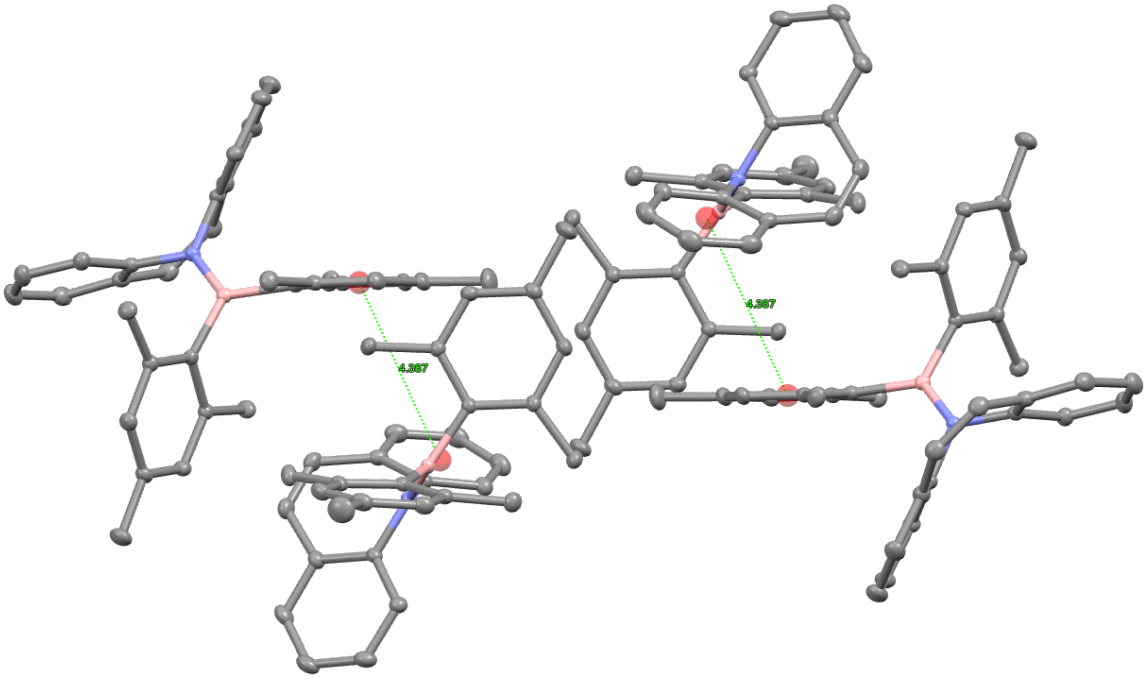


Figure 4-12 View showing the centroidal close contacts between IMSB-DMB (1) molecules.

Centroidal π-π distances in IMSB-DMB (**1**) are 4.37Å, which are beyond the potential for π-π interactions (see Figure 4-12).

In DBCz-DMB (**3**) these distances are largely similar at 4.38 Å at their closest centroidal close-packing (see Figure 4-13).

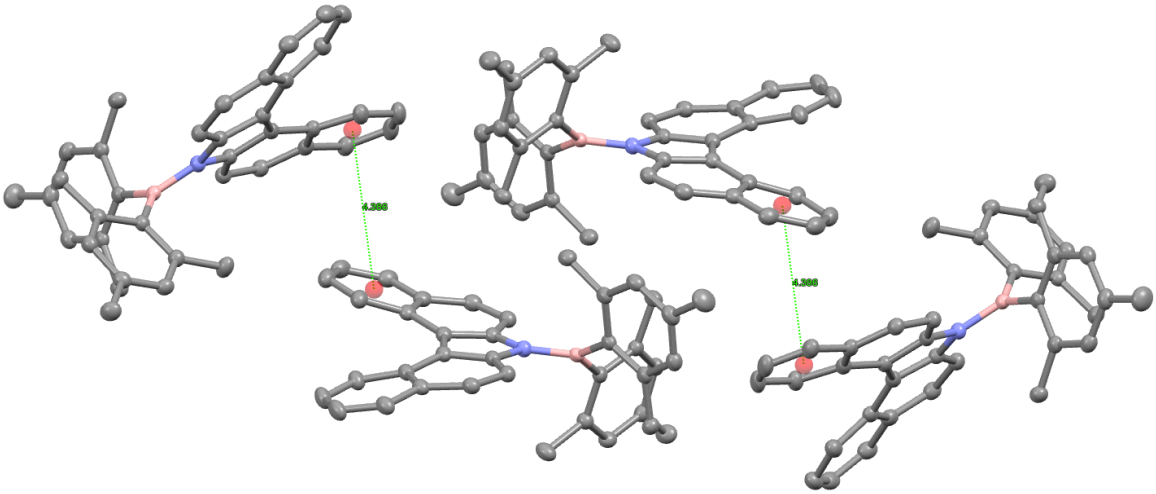


Figure 4-13 View showing the centroidal close contacts between DBCz-DMB (3) molecules.

Centroidal close contacts in DPhCz-DMB (**4**) are at their narrowest at 4.69 Å (see Figure 4-14).

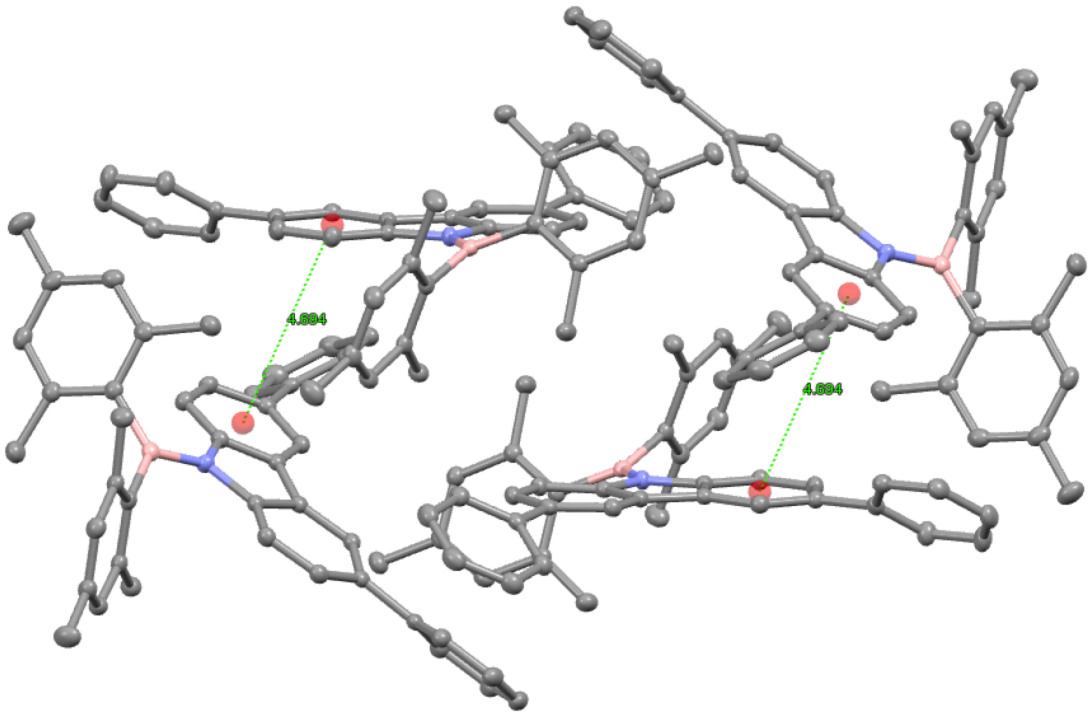


Figure 4-14 View showing the centroidal close contacts between DPhCz-DMB molecules.

Interestingly, the monomethoxy carbazole introduces a distortion to the structure in $tBu_2CzOMe\text{-}BMes_2$ (**6**) of 23.7° between the methoxy group's oxygen atom and the central boron atom with respect to the carbazole donor moiety (see Figure 4-15).

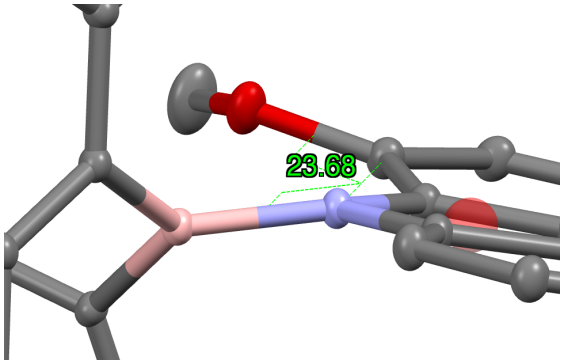


Figure 4-15 Distortion in $tBu_2CzOMe\text{-}BMes_2$ (6) across the methoxy - nitrogen - boron region.

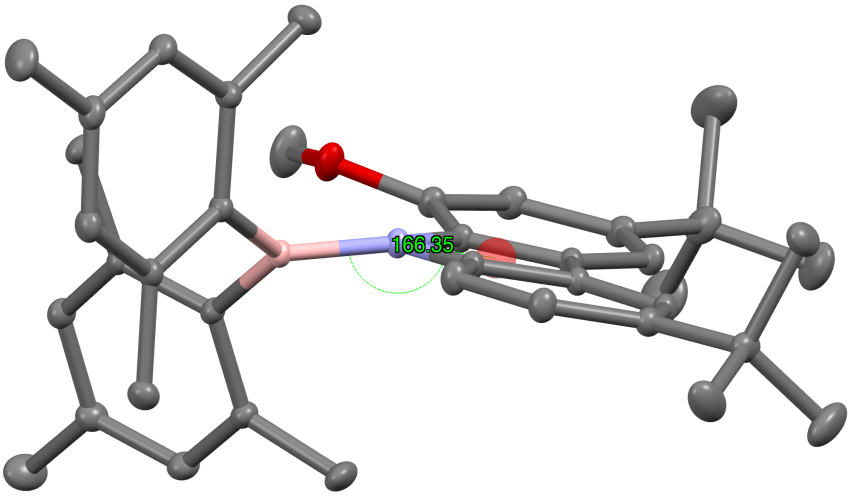


Figure 4-16 Kink across $tBu_2CzOMe\text{-}BMes_2$ (6). Hydrogens omitted for clarity.

Compound **6** also exhibits a 13.7° kink across the carbazole to boron structure, as seen in Figure 4-16. This is likely a result of steric hindrance caused by the nearest mesityl ring upon the methoxy group (see Figure 4-17), thereby forcing the carbazole moiety away from planarity with respect to the acceptor's boron core.

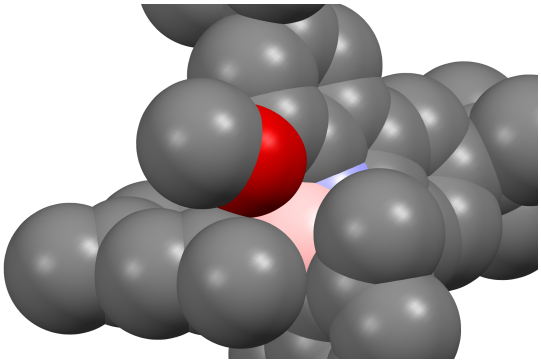


Figure 4-17 Van der Waals sphere view of $tBu_2CzOMe\text{-}BMes_2$ (6).

A structural distortion is also observed in Me_4-Cz-$BMes_2$ (**9**) which manifests as a 4.3° kink to the benzene rings of the carbazole (Figure 4-18).

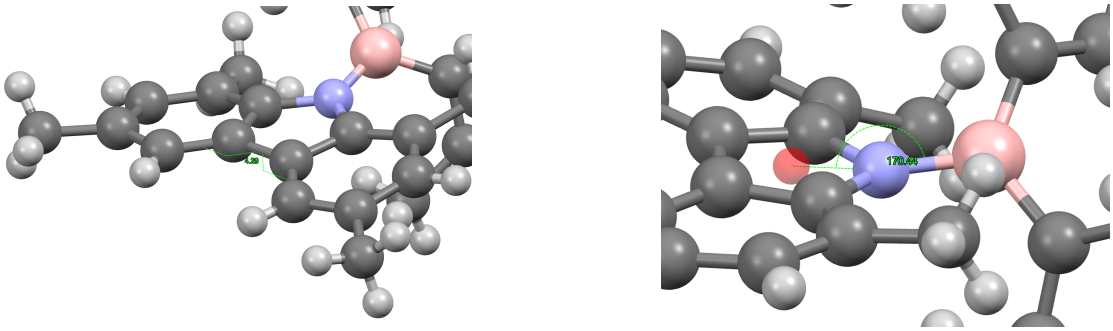


Figure 4-18 Deviation from planarity in Me_4-Cz-$BMes_2$ (9). Left shows the buckling between the two aromatic regions across the linking C-C bond. Right shows the bend across the over donor - nitrogen - boron linkage.

This results in a 9.6° deviation from planarity of the carbazole central ring through the nitrogen with respect to boron. This is likely a result of the steric hindrance brought about by the methyl groups in positions 1 and 8 pushing back against the dimesityl groups.

Potential interactions due to the proximity between the boron and oxygen atoms in compounds **6** and **7** is of great interest. Non-covalent interactions have been demonstrated to be of great importance to various biological processes[264–266], as well as in driving attractively efficient reaction pathways in organic synthesis[267] and have found usage in improving performance in organic perovskite solar cells owing to their ability to enhance molecular stacking[268]. More recently, it has been shown that boron-based materials have a propensity to act as a receptor for non-covalent interactions[269,270].

Such interactions are not limited to intermolecular interactions but can be intramolecular as well. According to Conboy *et al.*[243], when two heteroatoms are in close enough proximity such that they are closer than the sum of their individual van der Waals radii, the presence of non-covalent interactions between the two heteroatoms is permitted. In comparing the structure of various organic polymers (such as PEDOT, PEDRR, POSO and PSOS, shown in Figure 4-19), with and without varying degrees of non-covalent interactions, Conboy *et al*. make a compelling argument that these heteroatom non-covalent interactions play a key role in dictating the conformation of organic structures and locking different structural moieties at specific conformational orientations.



Figure 4-19 Structures of PEDOT, PEDTT, POSO and PSOS. Taken from Conboy *et al*.[243]

Further work by Kharandiuk *et al*.[244] illustrates the synergetic influence of attractive hydrogen bonding and S – F non-covalent interactions and repulsive O – F interactions can conspire to control the conformation of conjugated moieties, the degree of which depends on the strength of the dominant force at that structural locality (see Figure 4-20).

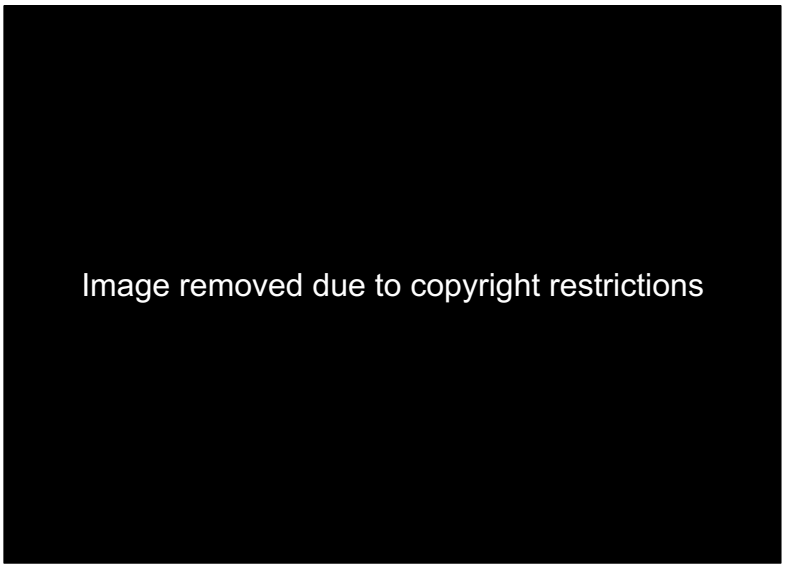


Figure 4-20 Structures exhibiting S - F non-covalent interactions and O - F repulsions. Taken from Kharandiuk *et al*.[244]

There are three structural interactions that can control the conformation of donor – acceptor materials: steric repulsions, non-covalent interactions (hydrogen bonds, lone pair – empty orbital interactions), and van der Waals type interactions (such as π-π interactions between aromatic rings)[271].

Separation of the HOMO and LUMO by a large dihedral angle is a well-established means of activating TADF in donor – acceptor type molecules[243,244]. The potential for achieving this with boron and methoxy type substituents upon a donor moiety is therefore an attractive proposition since locking specific conformations *via* non-covalent interactions is well established[272].

From the crystal structure of the compounds in this chapter, the two compounds with methoxy groups in close proximity to boron (**6** and **7**) have respectable D-A dihedral angles and B-O distances below that of the sum of the van der Waals radii of the individual boron and oxygen atoms (2.00 Å and 1.53 Å respectively[273], yielding a limit of 3.53 Å for this B-O interaction) implying the presence of non-covalent interactions.

Comparing compounds **5**, **6** and **7**, (*i.e*. those with zero, one and two methoxy groups), the boron – oxygen intramolecular distance gets shorter as more methoxy groups are added. The non-covalent interactions involve the electron density of the lone pair on the oxygen donating into the boron's empty p-orbital. This is evidenced by the large increase in the boron – nitrogen bond lengths, 1.44 Å in **5** with no methoxy groups, increasing in length to 1.46 Å in **6** and 1.48 Å in **7**.

An explanation of this lies in the fact that the lone pair on the nitrogen can donate into the boron's empty p-orbital as well. If successfully donating, this means the B-N bond would have partial double bond character (B=N) and be shorter (which is nicely illustrated in an extensive study into boron – nitrogen single, double and triple bond length character by Mierzwa *et al*.[274]). However, if the lone pairs on the methoxy groups are also donating into the boron's p-orbital, then the electron accepting nature of boron will decrease, and nitrogen's lone pair is less likely to donate as much, meaning the B-N bond will be more σ-bond in character and hence longer. According to an earlier study by Berski *et al*.[275], typical single B-N bonds can range from 1.67 Å to 1.70 Å, partial single-double bonds between 1.41 Å and 1.44 Å, fully double boron-boron double bonds (B=B) at around 1.39 Å – 1.37 Å, whereas the triple boron-boron bond (B≡B) is around 1.23 Å – 1.25 Å.

This is represented in our XRD data, where increasing the number of methoxy groups in **6** and **7** both decreases the B-O intramolecular distances, as well as elongating the boron-nitrogen bond length, increasing the single-bond character, thereby evidencing the methoxy – boron non-covalent interaction being present.

Unfortunately, crystals of sufficient quality for XRD study for the remaining compounds (**2** and **8**) in this study were not forthcoming in time for the completion of this project, however, attempts at growing them are still ongoing.

4.2.4 Thermal properties

4.2.4.1 Thermogravimetric analysis and differential scanning calorimetry

The thermal stability and thermal properties of emissive materials are of great importance when deciding their suitability to use in OLED devices. The thermal properties of the compounds in this study were analysed *via* thermogravimetric analysis (see Figure 4-21) and differential scanning calorimetry (see Figure 4-22). Their key properties are summarised in Table 4-4.

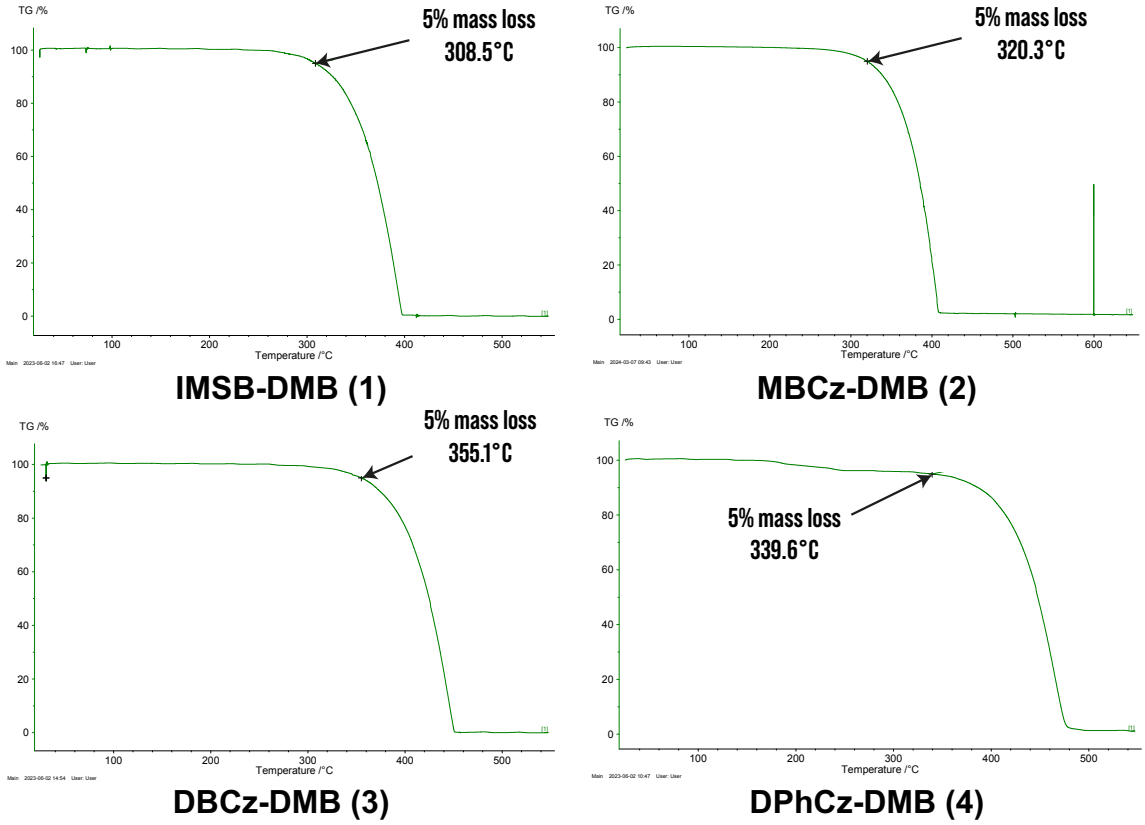


Figure 4-21 TGA plots for the main compounds in this study.

All four molecules exhibit good thermal stability with temperatures >300°C required before 5% mass loss. There does not appear to be a link to donor conjugation and melting point, however the quasi-helical DBCz-DMB has a significantly lower melting point than the rest of the compounds. This may be due to poorer π-stacking in the solid state owing to deviation from planarity of the donor since the similar, but non-quasi-helical MBCz-DMB has a significantly higher melting point. Comparing the work of Arivazhagan, *et al.*[276] where they used very contorted phenothiazinyl donors, to other more planar donors (such as Taniguchi *et al.*'s[262] work) and bonding with dimesityl boron acceptors, it can be seen that they typically have lower melting points when the donor deviates from planarity.

Interestingly, despite the ease of which the B-N bond is broken during hydrolysis in DBCz-DMB compared to the rest, it possesses the highest 5% mass loss temperature, 355.1°C, suggesting excellent thermal stability.

MBCz-DMB's thermal stability is significantly lower than DBCz-DMB, whereas IMSB-DMB is even poorer.

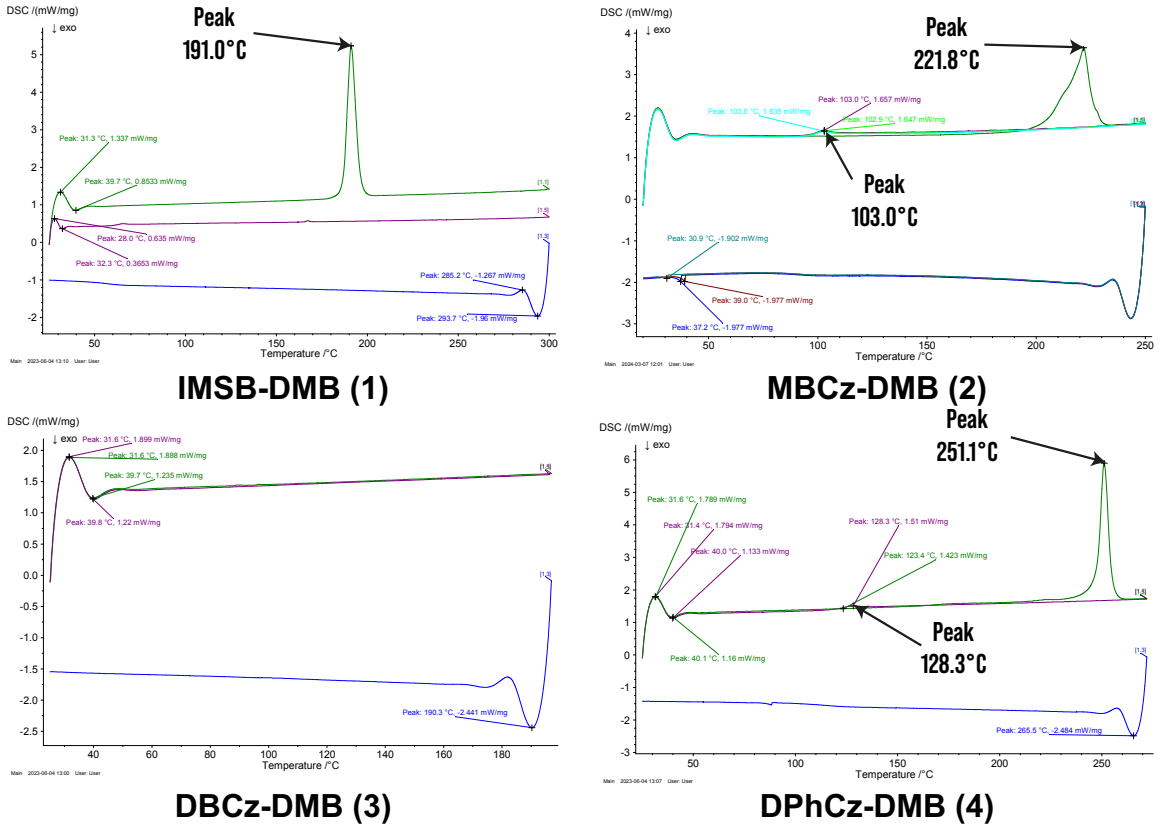


Figure 4-22 DSC plots for the four main compounds in this study. Dark green = First heating; blue = first cooling; purple = second heating; black = second cooling; light green = third heating; teal = third cooling; cyan = fourth heating. Peaks at the beginning and end of each plot are artefacts of the instrument.

Table 4-4 Summary of key thermal properties of compounds 1 - 4.

Compound	Melting point (°C)	Structural transition temperature (°C)	5% mass loss (°C)
IMSB-DMB (1)	191.0	-	308.5
MBCz-DMB (2)	221.8	103.1	320.3
DBCz-DMB (3)	176-178	-	355.1
DPhCz-DMB (4)	251.1	128.3	339.6

IMSB-DMB exhibits a melting point of 191.0°C, with the lowest 5% mass loss temperature observed at 308.5°C, despite it being the most chemically stable.

After the initial melting of MBCz-DMB (**2**), a lower temperature peak at 103.1°C, with a potential crystallising peak at 37-39°C upon cooling is observed in the DSC plot. The peak at 103.1°C was thought to be associated with a different polymorph compared to the original unheated material, so photoluminescence spectra were measured of the solid in the DSC pan prior and post heating (see Section 4.2.9).

4.2.5 Optical and electrochemical properties

To determine the impact of varying the donor in D-A compounds on the optical and electrochemical properties, UV-vis, photoluminescence spectroscopy and cyclic voltammetry experiments were carried out. A condensed summary of the key photophysical and properties of compounds **1** – **4** is compiled in Table 4-5 and the electrochemical properties are summarised in Table 4-6, with Dr Joseph Cameron's data for compounds **6** – **9** in Table 4-8.

Table 4-5 Solution-based optical properties of compounds 1 – 4.

Molecule	λ_{abs} (nm)[a]	λ_{pl} (nm)[a]	FWHM (nm)	$E_{g\ opt}$* (eV)	Φ_{PL} (air/argon) (%)[b]	S_1 (eV)	T_1 (eV)+	ΔE_{ST} (eV)
IMSB-DMB (1)	285 (sh)	574	131	3.67	1 / 0.7	3.40	-	-
MBzCz-DMB (2)	349, 333(sh), 326, 318(sh), 304(sh), 279, 256, 213	440	32	3.33	19 / 28	3.11	1.96**	1.15 **
DBCz-DMB (3)	358, 341, 325, 307, 293, 273	474	83	3.20	8 / 11	3.15	2.42	0.73
DPhCz-DMB (4)	334, 275(sh) 257	449	62	3.33 (3.92)	32 / 40	3.28	3.18	0.10

[a] Measured in methylcyclohexane; [b] measured in toluene; *Taken from onset of main λ_{abs} peak in methylcyclohexane (in brackets from most intense peak); ✢ indicates measurements performed at the University of Durham by Dr Suman Kuila measured in 1% w.t. Zeonex thin films; **measured in Glasgow using degassed glass cuvette and 1% w.t. Zeonex thin films.

Table 4-6 Summary of electrochemical properties of compounds 1 - 4.

Molecule	E_{ox} (V)	E_{red} (V)	HOMO (eV)	LUMO (eV)	$E_{g\ chem}$ (eV)
IMSB-DMB (1)	1.10 irr	-2.63	-5.90	-2.17	3.73
MBzCz-DMB (2)	0.82 irr	-2.49	-5.62	-2.31	3.31
DBCz-DMB (3)	0.89 irr	-2.56	-5.69	-2.24	3.45
DPhCz-DMB (4)	1.10 irr	-2.71	-5.90	-2.09	3.81

Irr refers to an irreversible oxidation. HOMO and LUMO energies are calculated from the corresponding redox peak wave with reference to ferrocene.

IMSB-DMB possesses the deepest UV absorption peak of the first family of compounds in this study. The PLQY is also very low, and the PL considerably red-shifted and broad in solution. Returning to more carbazole-like conjugation in MBCz-DMB, additional red-shifted UV absorption peaks are noticeable, along with an increase in PLQY and the narrowest and most blue-shifted emissions observed in this study. Extending the carbazole conjugation further with DBCz-DMB, the emissions red shift and broaden. The PLQY also decreases to almost a third of that of MBCz-DMB, presumably owing to the increased degree of motion afforded to the donor by the quasi-helical dibenzocarbazole moiety. DPhCz-DMB most closely resembles that of carbazole, albeit with two phenyl rings bonded to the 3 and 6 positions. This compound has the highest PLQY, suggesting that energy loss by their rotation is less than any potential flapping motion of the dibenzocarbazole in DBCz-DMB.

To further explore the origins of the UV peaks, samples of the pure, disconnected donor and acceptor moieties were prepared in toluene solution for compounds **1** – **4** and the spectra plotted in Figure 4-23 and are summarised in Table 4-7. Monkman (in Yersin's 2018 book[277]) argues that one can observe how well conjugated the HOMO and LUMO are, or how decoupled they are in a D-A type compound, simply by observing the UV-vis spectra of the free donor and acceptor molecules in solution and comparing it to the UV spectra of the final product molecule. Weak coupling is typified by the target molecule's UV spectra being an almost perfect representation of the superimposition of both the free donor and acceptor's respective UV spectra. Deviancy from the progenitor compounds' UV spectrum is a sign that strong HOMO and LUMO mixing is occurring. So, an effective CT molecule that would be a good candidate for TADF will have UV-vis spectra that resembles the sum of the plots of the individual donor and acceptor.

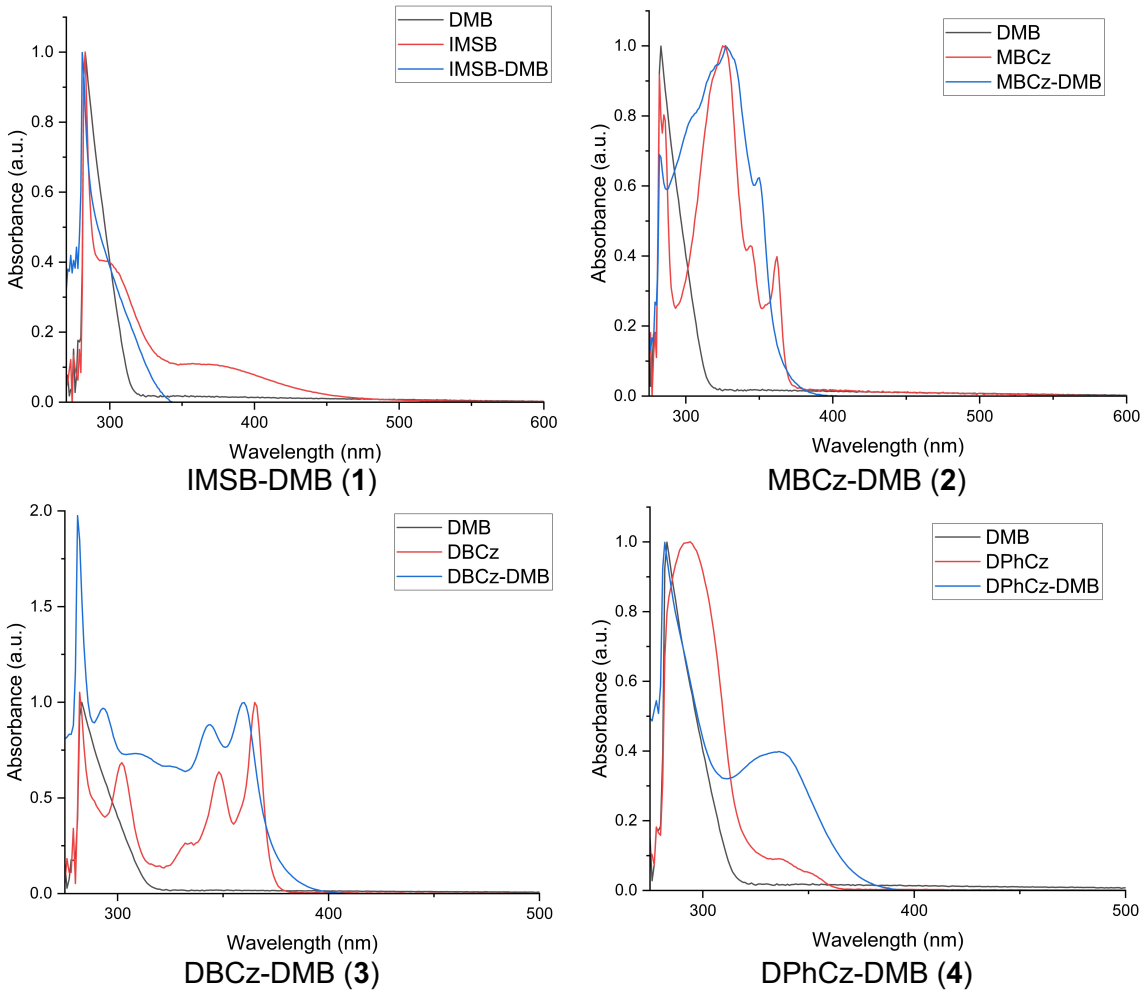


Figure 4-23 UV-vis spectra of free donors and acceptors in dry toluene compared with the spectra of the target compounds.

Table 4-7 Summary of the UV-vis spectra of free donors and acceptors in dry toluene compared with the spectra of the target compounds.

Molecule	Acceptor λ_{abs} (nm)	Donor λ_{abs} (nm)	Product λ_{abs} (nm)*
IMSB-DMB (1)	283	283, 297, 358(CT)	281
MBzCz-DMB (2)	283	362, 355, 344, 326, 285, 282	350, 322(sh), 327, 320(sh), 304(sh), 283
DBCz-DMB (3)	283	365, 348, 333, 302, 282	359, 343, 325, 310, 293, 281
DPhCz-DMB (4)	283	349(sh), 294	336, 327(sh), 282

All four compounds exhibit a sharp peak at 281 nm – 283 nm which coincides with the sole absorption peak of dimesitylboron fluoride (**4.2**) in toluene. Despite three absorption peaks being present in pure iminostilbene (**4.1**), including the broad, possibly CT absorption centred at 358 nm, only one peak is present in the compound IMSB-DMB (**1**) – most likely the absorption associated with the dimesityl boron acceptor. This major difference in the donor absorption suggests a major change to the HOMO – LUMO structure, but not one consistent with TADF (see the computational calculations in section 4.2.2). This gives

further credence to the notion that iminostilbene is a much stronger donor than previously thought, when bonded to dimesityl boron. Increased donor strength in the IMSB unit means that the lone pairs of the nitrogen will be better able to donate towards the boron atom. In so doing, the antiaromatic character of the IMSB unit is reduced, yielding a deeper UV absorption peak. This is further supported by the fact that the boron – nitrogen bond length is demonstrated to be shorter than the rest of the compounds in the single crystal XRD data (see Table 4-2). This reveals that the B-N bond in IMSB-DMB (**1**) has increased double bond character, which would be expected of a stronger donor moiety.

Both MBCz-DMB (**2**) and DBCz-DMB (**3**) show rather complex absorption profiles, with the 350 nm and 327 nm peaks in MBCz-DMB (**2**) clearly being slightly blue-shifted analogues of the 344 nm and 326 nm peaks of the free MBCz donor (**4.3**). Similar, blue-shifted peaks are seen in the case of DBCz-DMB (**3**) for the donor's 365, 348, 333 and 302 nm peaks becoming 359, 343, 325, and 293 nm, respectively. In both cases, the 283 nm peak of dimesitylboron fluoride (**4.2**) remains present – unchanged at 283 nm in MBCz-DMB (**2**), but slightly blue-shifted to 281 nm in DBCz-DMB (**3**).

In the more carbazole-esque DPhCz-DMB (**4**), the acceptor peak is clearly present (blue-shifted to 282 nm) but the 349 nm shoulder seen in the 3,6-diphenyl-9H-carbazole donor (**4.5**) increases in intensity significantly with the major 284 nm peak of the donor disappearing completely when bonded to dimesityl boron.

In compounds **2**, **3** and **4**, the UV-vis absorption spectra are largely superpositions of the absorption spectra of their respective donor and acceptor molecules. This strongly suggests reduced conjugation between the donor and acceptor units, meaning the HOMO and LUMO are (partly at least) decoupled in each case. The fact that the additional shoulder and hump peaks of iminostilbene is not present in the absorption spectra of IMSB-DMB (**1**), we can safely say that the donor and acceptor are not adequately decoupled and HOMO-LUMO mixing is likely extensive (as the DFT calculations in section 4.2.2 confirm).

Table 4-8 Solution optical properties of materials in this study measured by Dr Joseph Cameron.

Molecule		λ_{abs} (nm)	λ_{pl} (nm)	FWHM (nm)	$E_{g\ opt}$ (eV)	S_1 (eV)
tBu_2-Cz-$BMes_2$ (8)	Methylcyclohexane	323, 314, 289	455, 378, 361	70	3.45	3.16
	Toluene	325	470	75	3.40	3.05
	Dichloromethane	325, 288	496	91	3.40	2.95
	Acetonitrile	325	501	97	3.40	2.91
tBu_2-CzOMe-$BMes_2$ (6)	Methylcyclohexane	-	461	69	-	2.99
	Toluene	-	478	80	-	2.92
	Dichloromethane	340, 286	502	97	3.27	2.86
	Acetonitrile	-	516	104	-	2.78
tBu_2-$CzOMe_2$-$BMes_2$ (7)	Methylcyclohexane	364, 304, 290	451	65	3.03	3.00
	Toluene	368	467	72	2.99	2.92
	Dichloromethane	368	496	89	2.99	2.83
	Acetonitrile	368	503	94	2.99	2.81
Me_4-Cz-$BMes_2$(9)	Methylcyclohexane	371, 299	479	64	2.90	2.82
	Toluene	373, 299	499	76	2.91	2.78
	Dichloromethane	374, 299, 288	518	92	2.90	2.72
	Acetonitrile	368, 299	530	98	2.93	2.70

$E_{g\ opt}$ calculated from the onset of the main UV-vis absorption peak *via* 1240/λ, S_1 energy calculated from the onset of the main PL peak.

Going from no methoxy groups in **8**, one in **6**, and two in **7**, we see a narrowing of the FWHM, going from 70 nm > 69 nm > 65 nm in methylcyclohexane, respectively. This trend is accompanied by an initial red-shifting in emissions going from zero to one methoxy group (455 nm to 461 nm), but adding a second methoxy group blue-shifts the main emission wavelength (451 nm).

It is possible that the methoxy groups aid in the narrowing of the emissions due to interactions with the boron's empty p-orbital. The redder emission in the monomethoxy compound could be due to a more flexible structure – or at least one in which the dihedral is further from 90° than either **6** or **8**. Whilst no XRD data is present for **8**, the structure of **5** would presumably be similar (since the only difference are the two tert-butyl groups). In this compound a dihedral of 23° is observed.[262] Compounds **6** and **7** have dihedrals of 44° and 54°, respectively. However, sterically, compound **6** has much more freedom to rotate

along the B-N bond than **7**, suggesting that this could give rise to its redder and broader emissions.

The two methoxy groups in **7** prevent the broader emissions caused by CT states as there are fewer degrees of rotational freedom.

To explore the steric hypothesis further, compound **9** was synthesised by Dr Joseph Cameron. The methyl groups in positions 1 and 8 are analogous to the methoxy groups in compound **7**, but do not have substituents with lone pairs capable of facilitating donation into the empty p-orbitals of boron. Compound **9** has the reddest emission of this family, but comparable FWHM to the dimethoxy compound. This suggests that the methoxy groups provide a narrowing of the FWHM mainly because of their steric effects. The blue shift in emissions would be down to the stronger donor character that the methoxy groups provide. However, non-covalent interactions between the methoxy and boron atoms cannot be ruled out. In these structures, they may not be orientated in an optimal orientation to function to their fullest potential, so compounds with the oxygen atoms positioned closer to the boron atom are explored in Chapter 5. The increased PLQY when **7** is in Zeonex (Table 4-11) compared to the rest of this series also gives credence to the idea of enhanced rISC possibly induced by B-O interactions, as none of the other compounds in this series reaches such a high value (87%).

4.2.6 Molar absorption coefficient

Molar absorption coefficients of each UV-vis peak help to assign the nature of the transition which caused it (such as n → π*, π → π* , or a CT state, *etc*.). The measurement of the molar absorption coefficients was performed in dry toluene at various concentrations for each compound and are reported as follows:

IMSB-DMB (1)

The single UV peak of compound **1** has an absorption coefficient of just 9.1323×10^3 cm^{-1} M^{-1} (see Figure 9-1 in Appendix 1). Combined with the deep UV wavelength required to perform the excitation, this suggests that it is a π → π* transition, but being towards the low end of the absorptions in this family of compounds, it is the least efficient absorber.

MBCz-DMB (2)

The first peak at 349 nm for compound **2** has a molar absorption coefficient of 1.6969×10^4 cm^{-1} M^{-1}, however the larger, more dominant peak at 328 nm doubles its absorption coefficient to 2.7108×10^4 cm^{-1} M^{-1} (see Figure 9-2 in Appendix 1). This suggests much better absorption potential for this wavelength. All the peaks observed represent π → π* transitions.

DBCz-DMB (3)

The absorptions seen for compound **3** (see Figure 9-3 in Appendix 1) are once again representative of π → π* transitions, but are on average stronger than compound **2**, suggesting the additional aromatic ring in the donor is aiding with energy absorption.

DPhCz-DMB (4)

The broad peak at 335 nm in compound **4** (see Figure 9-4 in Appendix 1) suggests CT character, with a π → π* transition. The slightly higher absorption coefficient for compound **4** (at 284 nm) suggests a much stronger absorption.

4.2.7 Electrochemical analysis

Dilute solutions were prepared in dry tetrahydrofuran or acetonitrile and cyclic voltammetry performed to ascertain the oxidation and reduction properties.

Cyclic voltammetry studies of all four molecules of the first series were performed, with a scan rate of 0.1 V s^{-1}, using glassy carbon, platinum wire and silver wire as the working, counter and quasi-reference electrodes, respectively. The analyte solution was prepared at 10^{-4} M concentration using 0.1 M tetra-n-butylammonium hexafluorophosphate as the electrolyte. Tetrahydrofuran was used as the solvent for **3** and **4**, switching to acetonitrile for **1** owing to its poor solubility in tetrahydrofuran. Acetonitrile was used for **2** owing to its convenient solubility and ability to cover the range of voltages used. All molecules exhibit reversible reduction peaks, which can be attributed to the dimesityl boron acceptor unit, while oxidation of the donors results in irreversible oxidation peaks as can be seen in Figure 4-24. This is likely due to the weak nature of the B-N bond and resulting hydrolysis which is explored further later in this article. In the case of **1**, the oxidation peak, E_{ox} occurs at 1.10 V, and E_{red} at -2.63 V. Compound **2** (monobenzocarbazole) shows an oxidation peak at 0.82 V and reduction at -2.49 V, whereas the dibenzocarbazole based **3** exhibits a similar voltage E_{ox} at 0.89 V and slightly lower voltage E_{red} at -2.56 V. In **4**, the oxidation and reduction peaks are more comparable to those of **1** with E_{ox} at 1.10 V and E_{red} at -2.71 V. This results in the HOMO and LUMO energies of the molecule being -5.90 eV / -2.17eV, -5.62 eV / -2.31 eV, -5.69 eV / -2.24 eV and -5.90 eV / -2.08 eV for **1**, **2**, **3**, and **4**, respectively. The irreversibility of the oxidation peaks highlights the fragility of the B-N bond which was observed for each molecule.

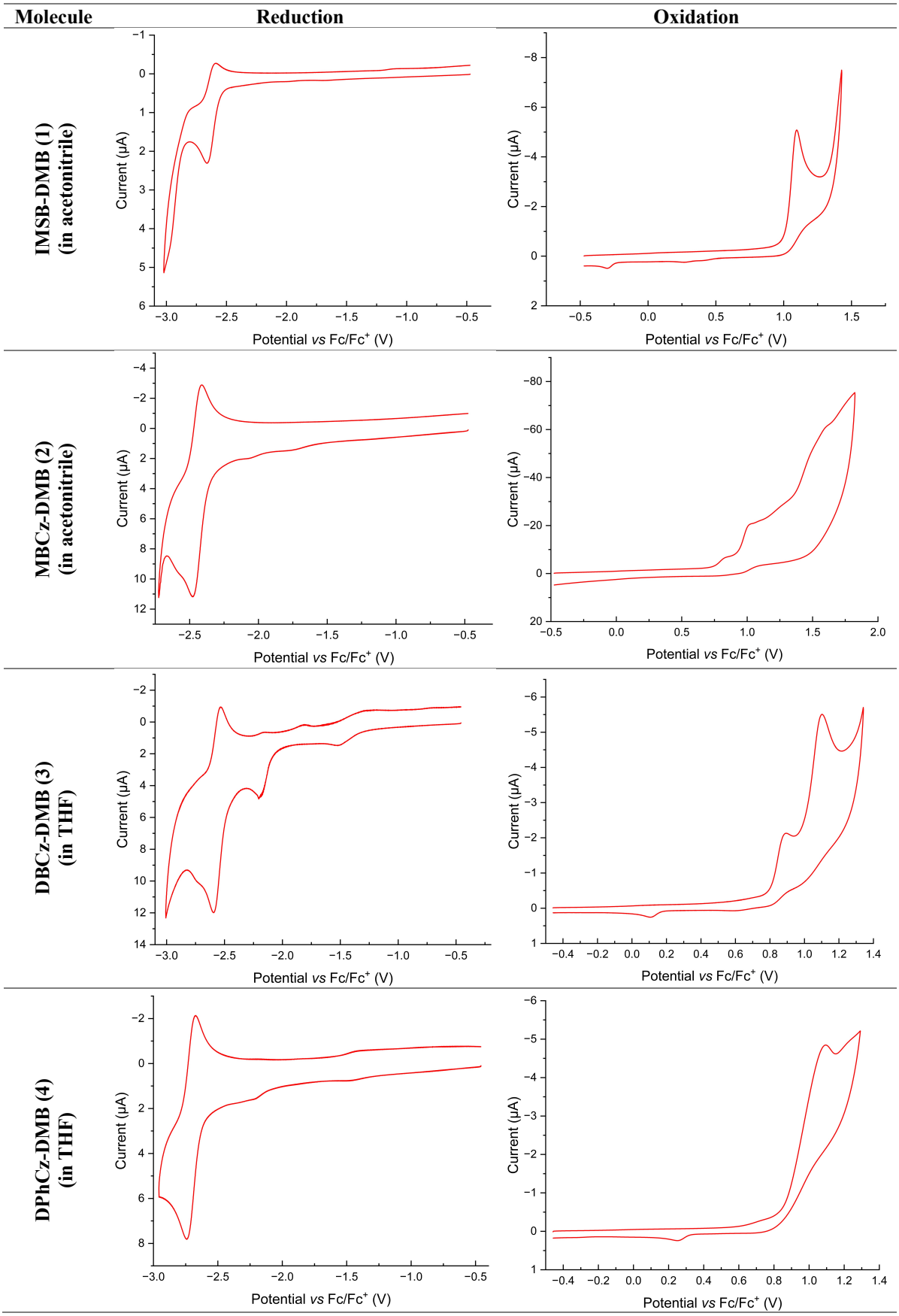


Figure 4-24 Cyclic voltammetry plots of the compounds in this study. Each measured in either tetrahydrofuran or acetonitrile as the solvent. A solution of 0.1 M tetrabutylammonium hexafluorophosphate was used as the electrolyte. EA, IP, HOMO and LUMO energies were calculated referenced against the $E_{1/2}$ of the Fc/Fc^+ redox couple.

DPhCz-DMB (**4**) interestingly, has an identical HOMO energy to that of IMSB-DMB (**1**). MBCz-DMB (**2**) and DBCz-DMB (**3**) have shallower HOMO energies, suggesting monobenzocarbazole and dibenzocarbazole are the stronger donors, with monobenzocarbazole being the strongest of the four. In terms of the LUMO energies, the weaker accepting character caused by dimesityl boron (DMB) being bonded to diphenylcarbazole yields the weakest acceptor. The equally weak donor in this case gives rise to the widest energy gap between the HOMO and LUMO in **4**. The strength of the accepting character increases going through **1**, **3** and **2**.

Interestingly, the two benzocarbazole structures seem to have the greatest deviance in their electronic properties – both having shallower HOMOs and deeper LUMOs than **1** and **4** (with correspondingly narrowest energy gap between the two). The properties of **2** are also well represented in the calculated HOMO and LUMO energies and are perhaps due to the much better-defined conjugation for the HOMO across the surface of the donor. The HOMO-LUMO gap decrease in energy following the order **4** > **1** > **3** > **2**. This differs with the optically measured gap which follows the order **4** > **1** > **2** > **3**. The inversion of compounds **2** and **3** may be due to their structural similarity and the fact that different solvents were used in the cyclic voltammetry scans. However, it has been shown that the error between different methods of measuring the HOMO – LUMO gaps can be as large as 0.5 – 1.0 eV[278] owing to differences in solvent-solute interactions impacting the lower excited state energies of the analytes.

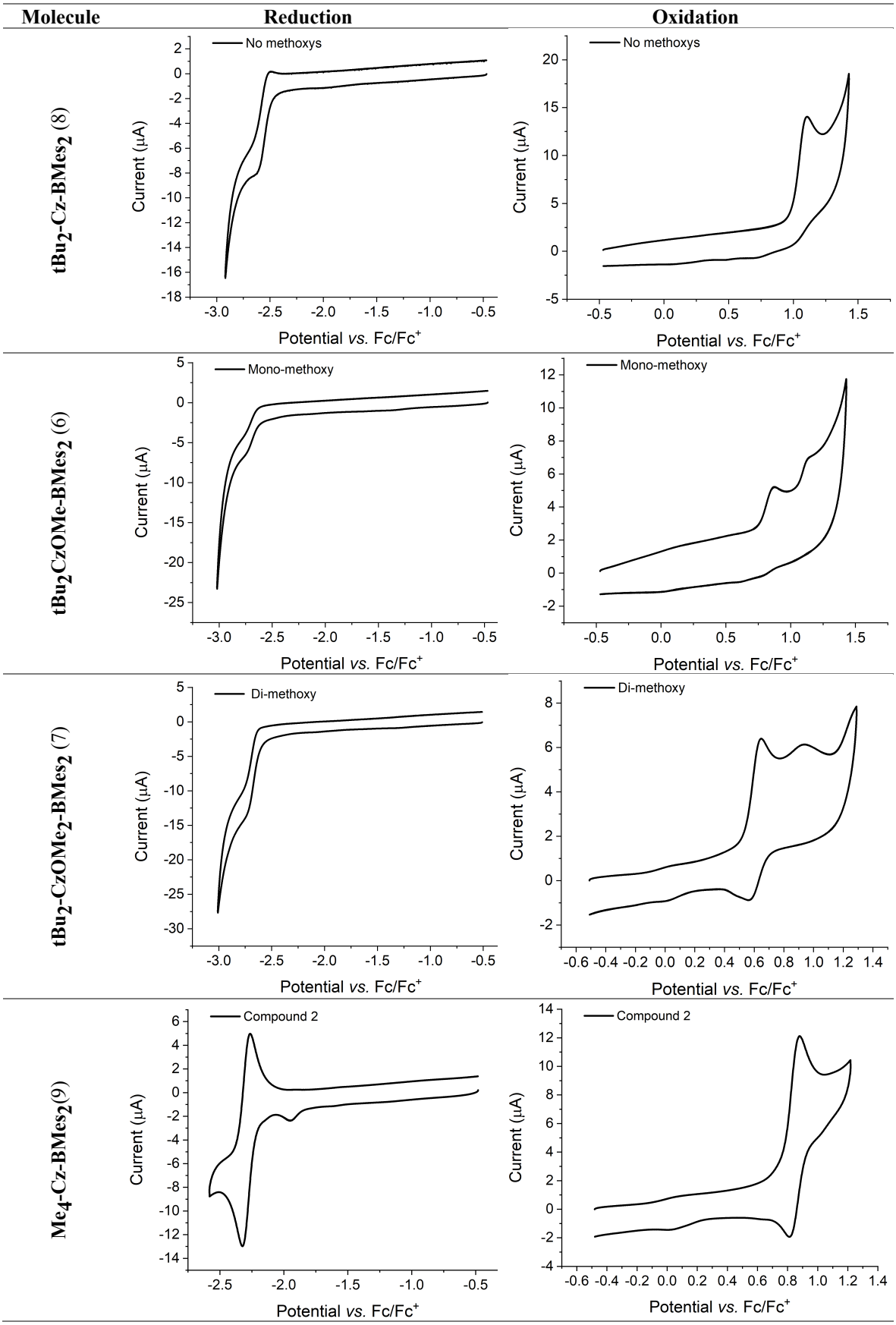


Figure 4-25 Cyclic voltammetry plots of the compounds in this study measured by Dr Joseph Cameron. Each measured at a concentration of 10^{-4} M in dry acetonitrile. A solution of 0.1 M tetrabutylammonium hexafluorophosphate was used as the electrolyte. EA, IP, HOMO and LUMO energies were calculated referenced against the $E_{1/2}$ of the Fc/Fc^+ redox couple.

The four carbazole based compounds from Dr Joseph Cameron on the other hand show materials with HOMOs and LUMOs in a comparable range to those of compounds **1** – **4**. The cyclic voltammetry plots for these compounds are shown in Figure 4-25 and the electrochemistry data for these compounds is summarised in Table 4-9. Compounds **7** and **9** show quasi-reversible and reversible oxidation curves as well, suggesting they have increased chemical stability compared to the rest of the compounds in this chapter.

Table 4-9 Solution electrochemical properties of materials in this study measured by Dr Joseph Cameron.

Molecule	E_{ox} (V)	E_{red} (V)	HOMO (eV)	LUMO (eV)	$E_{g\ chem}$ (eV)
tBu_2-Cz-$BMes_2$ (8)	1.11/1.01, qr	-2.62/-2.50	-5.9	-2.2	3.7
tBu_2-CzOMe-$BMes_2$ (6)	0.86/0.77, qr 1.14,4 irr	-2.65/-2.55	-5.6	-2.2	3.4
tBu_2-$CzOMe_2$-$BMes_2$ (7)	0.65/0.57, qr 0.94, irr	-2.74/-2.62	-5.4	-2.1	3.3
Me_4-Cz-$BMes_2$(9)	0.88/0.82	-2.32/-2.26	-5.7	-2.5	3.2

Irr refers to an irreversible oxidation, *qr* refers to quasi-reversible oxidation. HOMO and LUMO energies are calculated from the corresponding redox peak wave with reference to ferrocene.

Addition of a single methoxy group in tBu_2CzOMe-$BMes_2$ (**6**) yields a shallower HOMO by 0.3 eV (going from -5.9 eV to -5.6 eV), with no change to the LUMO energy (remaining at -2.2 eV). Adding a second methoxy group raises the HOMO by a further 0.2 eV to -5.4 eV, and the LUMO increases by 0.1 eV. This results in a corresponding narrowing of the HOMO-LUMO band gap by addition of methoxy groups to the donor in positions in close proximity to the boron atom. Increasing the number of methoxy groups raised the HOMO and LUMO energies but has a greater impact upon the energy of the HOMO. This suggests evidence that the lone pairs on the methoxy groups are donating into the empty p-orbital of boron.

Swapping the two methoxy groups for methyl groups allows for a comparison of the effects of similar steric hindrance and differing electron donating potential on the properties of the molecules. Comparing tBu_2-$CzOMe_2$-$BMes_2$ to that of a similarly sterically congested Me_4-Cz-$BMes_2$, we can see a significant deepening of the HOMO by 0.3 eV (-5.4 eV in the methoxy case to -5.7 in the methyl case) suggesting a weakening of the donor when swapping methoxy for methyl and a deepening of the LUMO by 0.4 eV as well (-2.1 eV dropping to -2.5 eV). This results in only a slight narrowing of the HOMO – LUMO bandgap

from 3.3 eV to 3.2 eV. Nevertheless, a red-shifting of the emissions by 28 nm (479 nm from 451 nm) in methylcyclohexane when methoxy groups are replaced by methyl groups, is observed. The change in HOMO energies between tBu_2-$CzOMe_2$-$BMes_2$ (**7**) and Me_4-Cz-$BMes_2$ (**9**) suggests a substantial increase in donor character in the dimethoxy compound, but almost negligible change in the HOMO-LUMO gap, which suggests another mechanism is at play for the difference in emission wavelength. Additionally, the structures of **7** and **9** offer more steric protection around the boron atom, which would mean the boron is less exposed to chemical attack, making these compounds more stable, enhancing the reversibility of their redox processes. Interestingly, Section 4.2.3 shows that the B-N bond lengths of **7** and **9** are slightly longer, whereas the C-B bond lengths to the mesityl groups are shorter when compared to the rest of the compounds in this study. This also suggests enhanced stability, making compounds **7** and **9** superior candidates for application in OLEDs compared to the rest of the family.

Based on the calculated HOMO energies from the cyclic voltammetry, the strength of the donors in compounds **6** – **9** follow the trend of increasing strength: **8** < **9** < **6** < **7**. It is clear that adding increasing numbers of methoxy groups to the donor moiety increases electron donating character.

4.2.8 Photoluminescence and UV-vis spectroscopy

UV-vis absorption spectroscopy in solution and the solid-state provides insights into the photophysical character of materials.

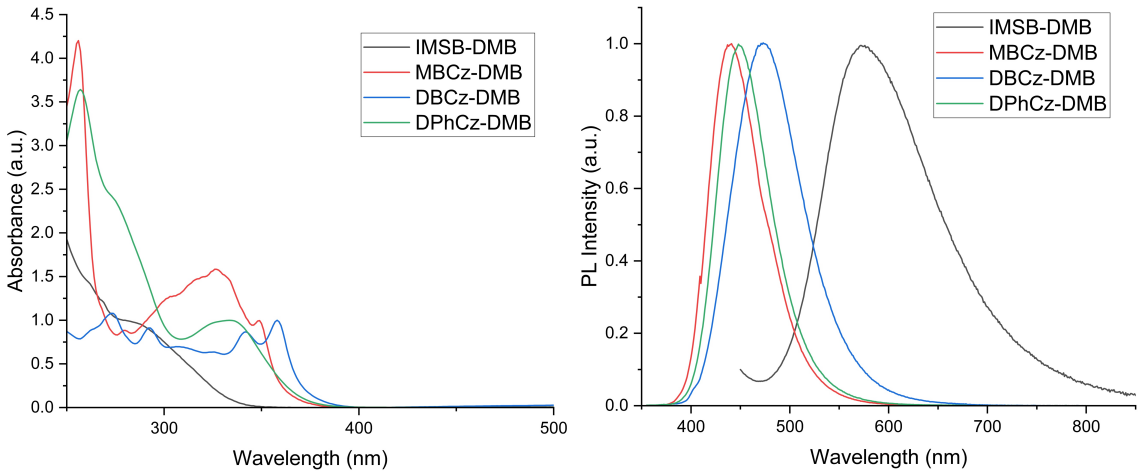


Figure 4-26 UV-vis absorption and photoluminescence spectra in methylcyclohexane (1×10^{-5} M) for compounds 1 - 4. All samples excited at the main absorption wavelength for that compound.

In non-polar methylcyclohexane, compounds **2**, **3** and **4** each possess relatively pale blue emissions, with **2** and **4** having the bluest emissions at 440 nm and 449 nm, respectively, with quasi-helical DBCz-DMB (**3**) being redshifted to 473 nm (see Figure 4-26). Even in this very non-polar solvent, IMSB-DMB (**1**) differs to the rest of the family by emitting at 574 nm.

Unlike in solution, the solid state pure-film photoluminescence spectra of compounds **1** – **4** all emit around 447 nm – 468 nm, with compound **1** no longer the most red-shifted of the four – suggesting aggregation effects influencing its emissions (see Figure 4-27).

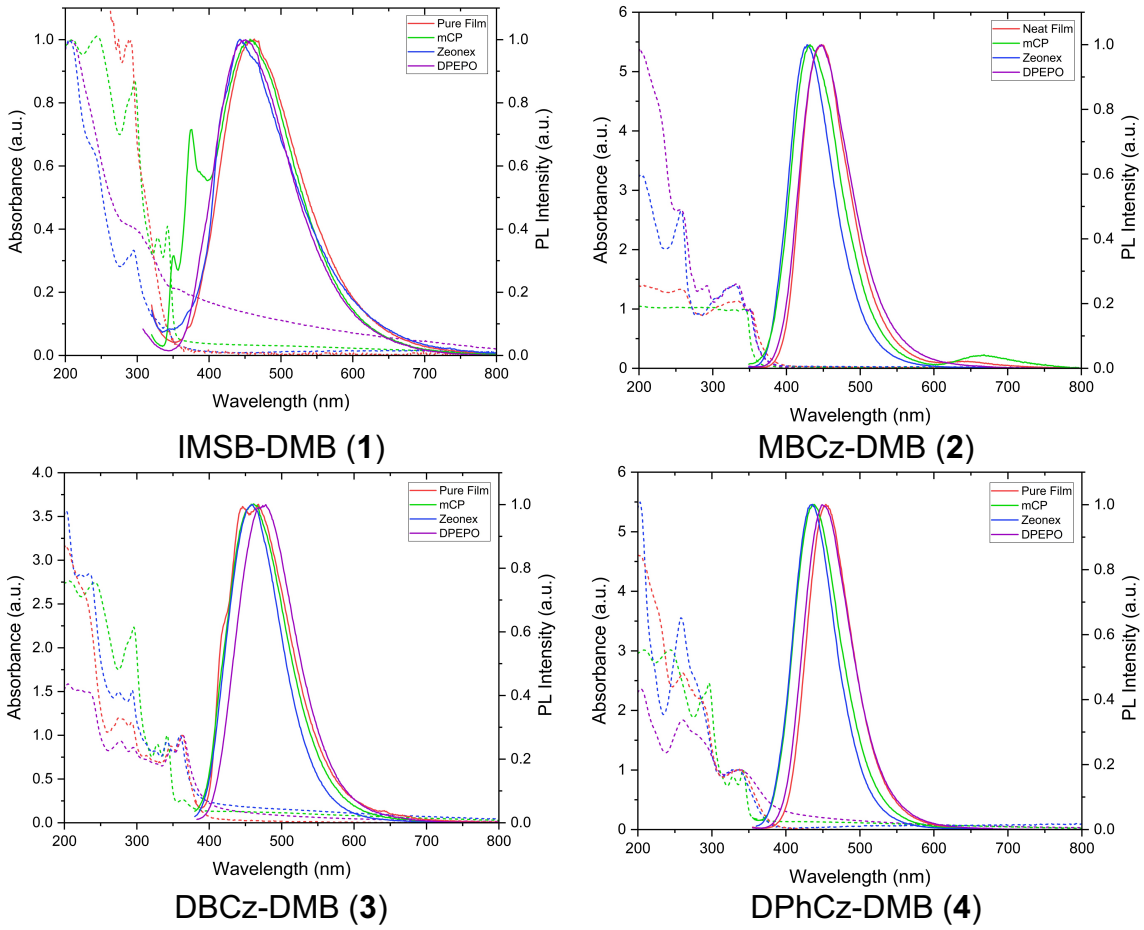


Figure 4-27 UV-vis absorption and photoluminescence spectra of compounds prepared as thin films both neat and in host matrices (5 % w.t.).

Slight solid-state solvatochromism is observed in all four compounds when the host is changed from non-polar Zeonex, to much more polar DPEPO. For the most part, the PL spectra are featureless in the solid state, however mCP appears to result in exciplex emissions in MBCz-DMB at 663 nm, and potentially blue-shifted exciplex emissions in IMSB-DMB at 375 nm and 350 nm. This is of important consideration since when applied as emitter layers (EML) in OLEDs, the polarity of different hosts will influence the colour of electroluminescence produced.

Photoluminescence properties of the second family

The PL and UV-vis absorption plots for the second family have been provided by Dr Joseph Cameron and are shown in Figure 4-28.

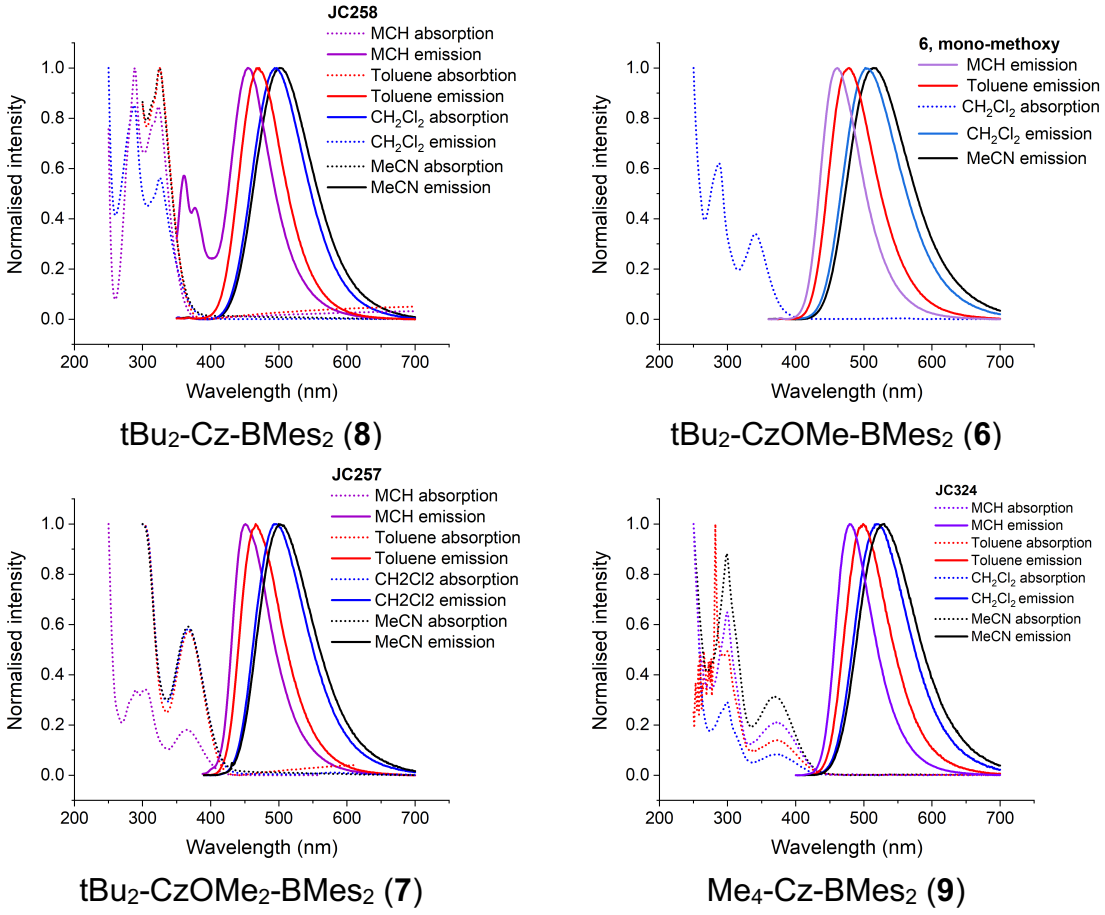


Figure 4-28 Solution PL and UV spectra provided by Dr Joseph Cameron for compounds 6 - 9.

Compounds **6** – **9** all exhibit some solvatochromism, suggesting the presence of CT states as the source of their emission. An assumed CT peak is seen in compound **7** and **9**'s UV-vis spectra at around 375 nm. A similar CT peak is seen in compound **6** at ~340 nm.

Table 4-10 Solid-state photophysical properties of materials in this study.

Molecule	Host	λ_{abs} (nm)	λ_{pl} (nm)	FWHM (nm)	S_1 (eV)
IMSB-DMB (1)	Pure Film	294(sh), 348(sh), 207	461, 476(sh)	128	3.38
	mCP	342, 328, 296, 244, 208	457, 471(sh), 375(mCP), 350(mCP)	163	3.65
	Zeonex	341, 322(sh), 293, 286(sh), 236(sh), 205	443, 462(sh), 422(sh)	123	3.40
	DPEPO	291, 316(sh)	449	124	3.80
MBCz-DMB (2)	Pure Film	352, 334, 257	447, 641	75	3.15
	mCP	342	431, 663	77	3.33
	Zeonex	350, 330, 318(sh), 304(sh), 281, 257	428	69	3.11
	DPEPO	351, 332, 318(sh), 292, 256	445	81	3.19
DBCz-DMB (3)	Pure Film	364, 347, 326(sh), 310(sh), 294, 277, 234, 221, 205	468, 446, 422(sh)	106	3.10
	mCP	363, 342, 328, 296, 288(sh), 242, 206	461	97	3.14
	Zeonex	360, 342, 324, 293, 274, 235, 221, 202	459	86	3.15
	DPEPO	363, 345, 312, 293, 274	475	95	3.07
DPhCz-DMB (4)	Pure Film	340, 279(sh), 260, 205	454	69	3.08
	mCP	342, 329, 295, 286(sh), 242, 207	438	73	3.27
	Zeonex	332, 274(sh), 258, 203	434	66	3.28
	DPEPO	336,284(sh), 273, 261	450	75	3.12
t*Bu$_2$-Cz-BMes$_2$ (5)	Zeonex	325	445	-	-
t*Bu$_2$CzOMe-BMes$_2$ (6)	Zeonex	340	455	-	-
t*Bu$_2$CzOMe$_2$-BMes$_2$ (7)	Zeonex	368	460	-	-

*Indicates measurements performed by Dr Joseph Cameron

Table 4-11 PLQYs of solid-state samples of the compounds in this chapter.

Molecule	Host	Φ_{PL} (air)	Φ_{PL} (argon)
IMSB-DMB (1)	Pure Film	20	11
	mCP	35	37
	Zeonex	11	7
	DPEPO	34	32
MBCz-DMB (2)	Pure Film	33	44
	mCP	27	40
	Zeonex	44	31
	DPEPO	40	43
DBCz-DMB (3)	Pure Film	11	7
	mCP	37	27
	Zeonex	19	18
	DPEPO	23	28
DPhCz-DMB (4)	Pure Film	47	40
	mCP	43	44
	Zeonex	25	21
	DPEPO	60	61
t*Bu$_2$-Cz-BMes$_2$ (5)	Zeonex	-	42
t*Bu$_2$-Cz-BMes$_2$ (8)	Zeonex	41	42
	mCP	31	31
	DPEPO	26	25
t*Bu$_2$CzOMe-BMes$_2$ (6)	Zeonex	47	51
	mCP	42	41
	DPEPO	34	37
t*Bu$_2$CzOMe$_2$-BMes$_2$ (7)	Zeonex	75	87
	mCP	43	54
	DPEPO	46	45
	Neat Film	65	83

*Indicates measurements performed by Dr Joseph Cameron

Table 4-10 summarises the solid-state UV-vis and photoluminescence properties of the compounds in this study and Table 4-11 summarises the PLQYs of the same compounds. For compounds **1** – **4**, the PLQYs are mostly rather low, with inconsistent changes when degassed. This suggests that they are not TADF active. On the other hand, compounds **6** and **7** have clear increases in their already respectable PLQYs when degassed, suggesting triplet state involvement in their photophysics, and the possibility for TADF.

4.2.9 Thermochromism in MBCz-DMB

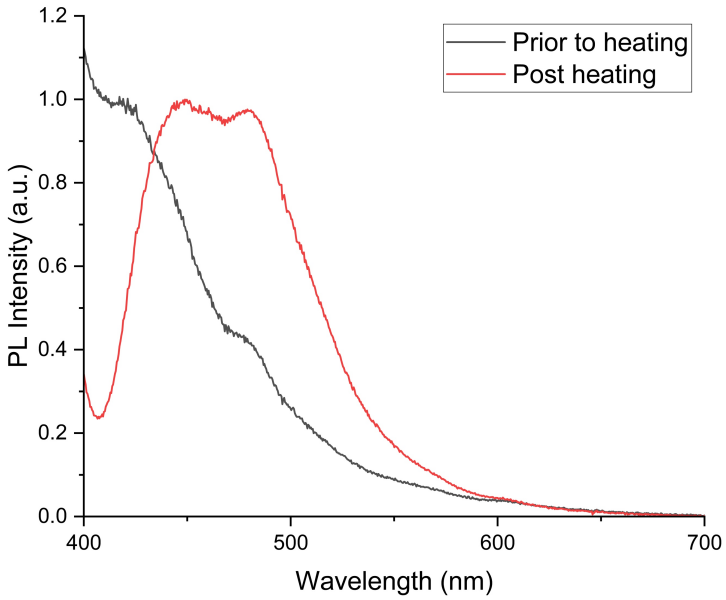


Figure 4-29 Photoluminescence spectra of solid MBCz-DMB (2) powder in aluminium pans, before and after four heating cycles to 250°C in the DSC instrument. Excited with a 365 nm UV torch.

The initial PL peak for solid MBCz-DMB (**2**) is far too deep blue to be fully resolved using the fibreoptic spectrometer (see Figure 4-29), as the excitation source was a UV torch (365 nm) with a rather board and uncontrollable bandwidth (reaching 400 nm). What is clear however, is that there is a PL peak at ~417 nm, with a shoulder at ~477 nm. Upon removal from the DSC instrument after 4 heating cycles (up to 250°C) there is a substantial red-shift of the main emission peak to ~449 nm, with the shoulder increasing in intensity and becoming a peak in its own right at ~477 nm. To the naked eye, the intensity of the sample's emission appears to increase as well (see Figure 4-30).

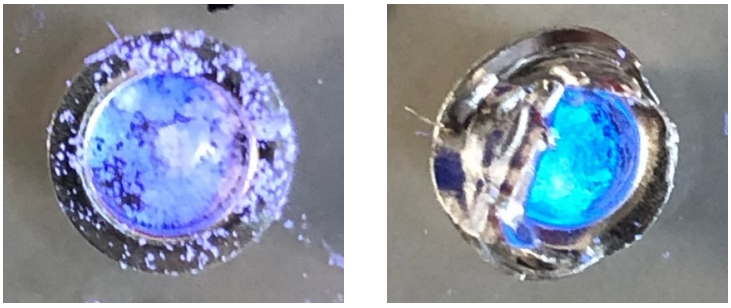


Figure 4-30 Fluorescence of MBCz-DMB (2) in aluminium DSC pans under illumination of a 365 nm UV torch. Left is prior to heating; right is after heating.

4.2.10 Phosphorescence

TADF materials function by harvesting triplet states in order to repopulate emissive singlet states. As such, the triplet state should decay radiatively (by phosphorescence) or non-radiatively at a rate which is slower than the rate of reverse intersystem crossing (k_{rISC}) to the singlet manifold. Simply, we need rISC followed by fluorescence to occur quicker than phosphorescence or non-radiative decay can occur from the triplet state.

Compounds **2** and **3** appear to possess room temperature phosphorescence in the solid state when degassed. Compound **2** shows a red peak only in the neat film and mCP initially under air or degassed, suggesting exciplex formation (see Figure 4-27 for air exposed thin films and Figure 4-31 for PL plots from a degassed integrating sphere).

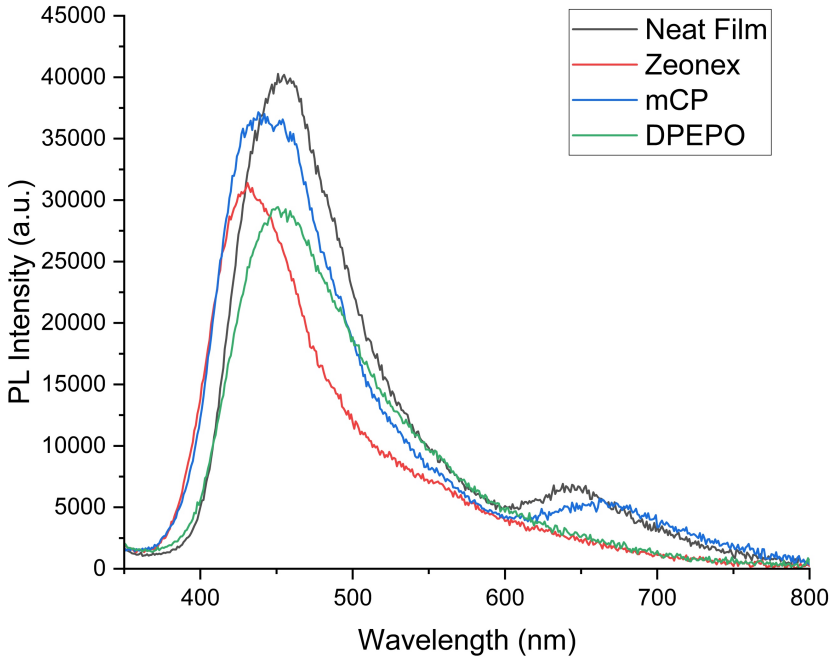


Figure 4-31 Photoluminescence spectra of thin films of MBCz-DMB (2) in a degassed integrating sphere.

However, using a microsecond flash bulb excitation source, gated to measure between 20 µs and 40 µs allows exploration of delayed emissions (see Figure 4-32). This provides confirmation that energy loss is occurring from the $T_1 \rightarrow S_0$ phosphorescent route, which is competing with the potential for rISC.

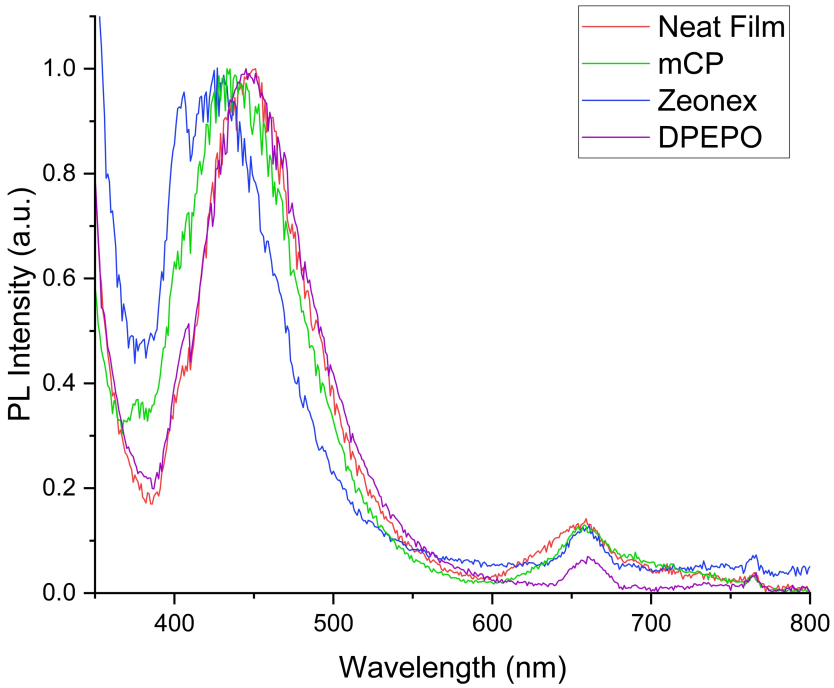


Figure 4-32 Photoluminescence spectra for MBCz-DMB (2) excited using a microsecond flash bulb excitation source, gated to measure between 20 µs and 40 µs.

Figure 4-33 shows that the neat film and mCP both exhibit weak red emission, however in this timeframe so too do DPEPO and Zeonex (to a lesser degree). Since exciplex emission is less likely in these hosts, it is possible that room temperature phosphorescence is occurring.

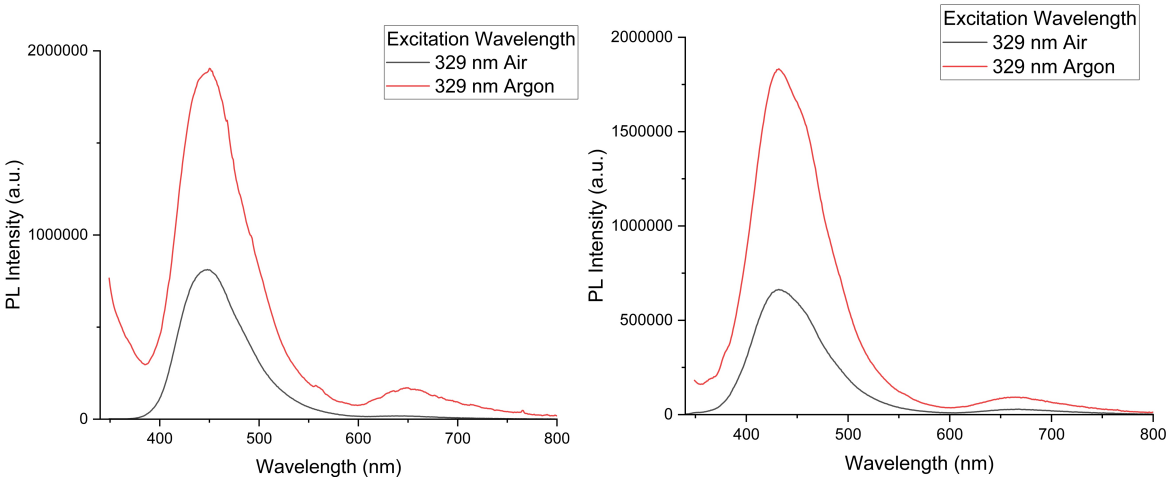


Figure 4-33 Photoluminescence plots of MBCz-DMB (2) in neat films (left) and mCP host (right).

When degassed, the longer wavelength peak increases in intensity in neat films and mCP suggesting it arises from emission from a triplet state.

Compound **3** was observed by Dr Suman Kuila at Durham University to also have room temperature phosphorescence in the deep orange. In our spectrometer, this can possibly be

glimpsed as a red peak between 20 μs to 40 μs as well as in DPEPO (see Figure 4-34), though seemingly less intense than with compound **2**.

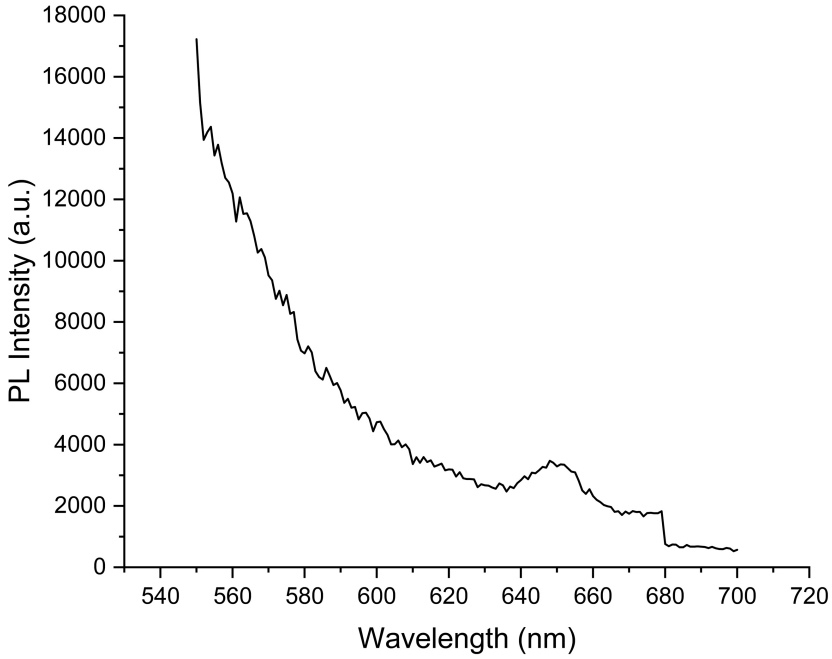


Figure 4-34 Time dependant PL of DBCz-DMB (3) in DPEPO (degassed) excited using a microsecond flash bulb excitation source, gated to measure between 20 μs and 40 μs.

4.2.11 Solvatochromism

Since TADF molecules possess CT states, their photoluminescence properties are highly influenced by the polarity of the solvent in which they are dissolved. As such, measuring the PL spectra in a variety of solvents helps to provide evidence of the presence of a CT state involved in fluorescence (^{1}CT). Compounds **1** – **4** were dissolved in a variety of solvents and their UV-vis absorption and photoluminescence spectra are reported in Figure 4-35).

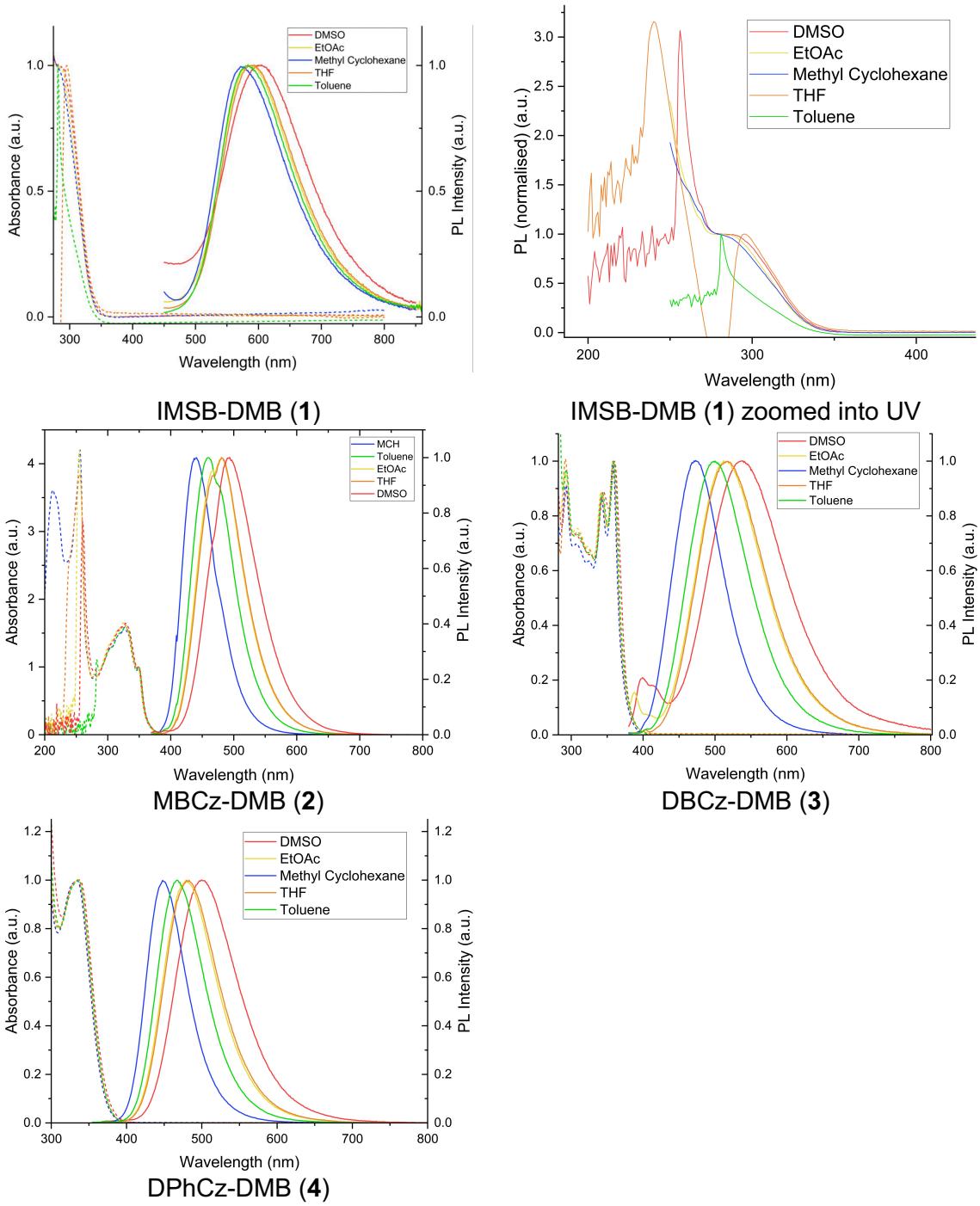


Figure 4-35 UV-vis absorption and PL spectra plots for the compounds demonstrating solvatochromism.

Each compound in this series exhibits solvatochromism, with DBCz-DMB (**3**) exhibiting this phenomenon to the greatest effect (see Figure 4-35). Compound **3** also shows some additional emission peaks in more polar solvents centred at ~400 nm, which also vary with polarity, suggesting the presence of at least two charge transfer states emitting.

Compounds **2** and **3** exhibited shoulder peaks and seemingly additional CT peaks too (see Table 4-12). Of note is that the FWHM of the diphenyl-carbazole compound is not excessive. In fact, the emissions of the dibenzocarbazole compound are significantly broader. This suggests that, whilst the extra phenyl rings on the diphenylcarbazole moiety have the potential for increased non-radiative decay pathways by fortune of the increased degree of rotational freedom that they afford the molecule, this appears to be of minimal significance (indeed the FWHM of compounds **2** and **4** are virtually identical!).

Table 4-12 Summary of the secondary peaks or shoulders in the solvatochromism emissions of MBCz-DMB (2) and DBCz-DMB (3).

	MBCz-DMB (2) (shoulder)	DBCz-DMB (3) (second peak)
Toluene	475	404(sh)
Tetrahydrofuran	468	404
Methylcyclohexane	474	404(sh)
Ethyl acetate	465	388, 405(sh)
Dimethyl sulfoxide	468	398, 413(sh)

In MBCz-DMB (**2**), it is almost as if the emission peak consists of two peaks, each swapping place with the other as the peak of maximum emission intensity depending on the solvent. Since this shoulder stays more or less the same, regardless of solvent polarity, it likely that this originates from co-emission of a locally excited (LE) state (since LE states are solvent independent). In DBCz-DMB (**3**) the additional peak is only visible in the more polar solvents.

4.2.11.1 Lippert–Mataga analysis for solvatochromism

Using the Stokes-shifts of compounds in various solvents, it is possible to perform Lippert-Mataga analysis to determine the strength of the dipole in the excited state. The data required for this are presented in Table 4-13 and Table 4-14, and the Lippert-Mataga plots are illustrated in Figure 4-36.

Table 4-13 Dielectric constants and refractive indices for solvents used in this thesis.

Solvent	$\varepsilon^{[a]}$	$n^{[a]}$	$f(\varepsilon,n)$
Toluene	2.38	1.4969	0.0132
Tetrahydrofuran	7.58	1.4072	0.2096
Methylcyclohexane	2.02	1.4230	-0.0006
Ethyl acetate	6.40	1.3724	0.2060
Dichloromethane	8.93	1.4241	0.2171
Dimethyl sulfoxide	46.68	1.4793	0.2631

[a] The values for ε and n were obtained from Stenutz Chemistry Tables.[279]

Table 4-14 Summary of solvatochromism UV-vis and photoluminescence data and corresponding Lippert-Mataga calculations for compounds 1 - 4.

	IMSB-DMB				**MBCz-DMB**			
Solvent [~1x10^{-5} M]	Abs_{max} (nm)	PL_{max} (nm)	FWHM (nm)	$\nu_a - \nu_p$ (cm^{-1})	Abs_{max} (nm)	PL_{max} (nm)	FWHM (nm)	$\nu_a - \nu_p$ (cm^{-1})
Toluene	281	582	132	18405	350	459	77	6785
Tetrahydrofuran	295	590	139	16949	349	481	83	7863
Methylcyclohexane	280	574	131	18293	349	440	32	5926
Ethyl acetate	282	586	137	18396	348	481	83	7946
Dimethyl sulfoxide	287	601	156	18204	349	493	89	8369

	DBCz-DMB				**DPhCz-DMB**			
Solvent [~1x10^{-5} M]	Abs_{max} (nm)	PL_{max} (nm)	FWHM (nm)	$\nu_a - \nu_p$ (cm^{-1})	Abs_{max} (nm)	PL_{max} (nm)	FWHM (nm)	$\nu_a - \nu_p$ (cm^{-1})
Toluene	359	499	99	7815	336	467	73	8349
Tetrahydrofuran	358	518	110	8628	335	482	83	9104
Methylcyclohexane	358	473	83	6791	333	449	62	7758
Ethyl acetate	357	514	110	8556	334	480	82	9107
Dimethyl sulfoxide	360	537	127	9156	337	501	95	9714

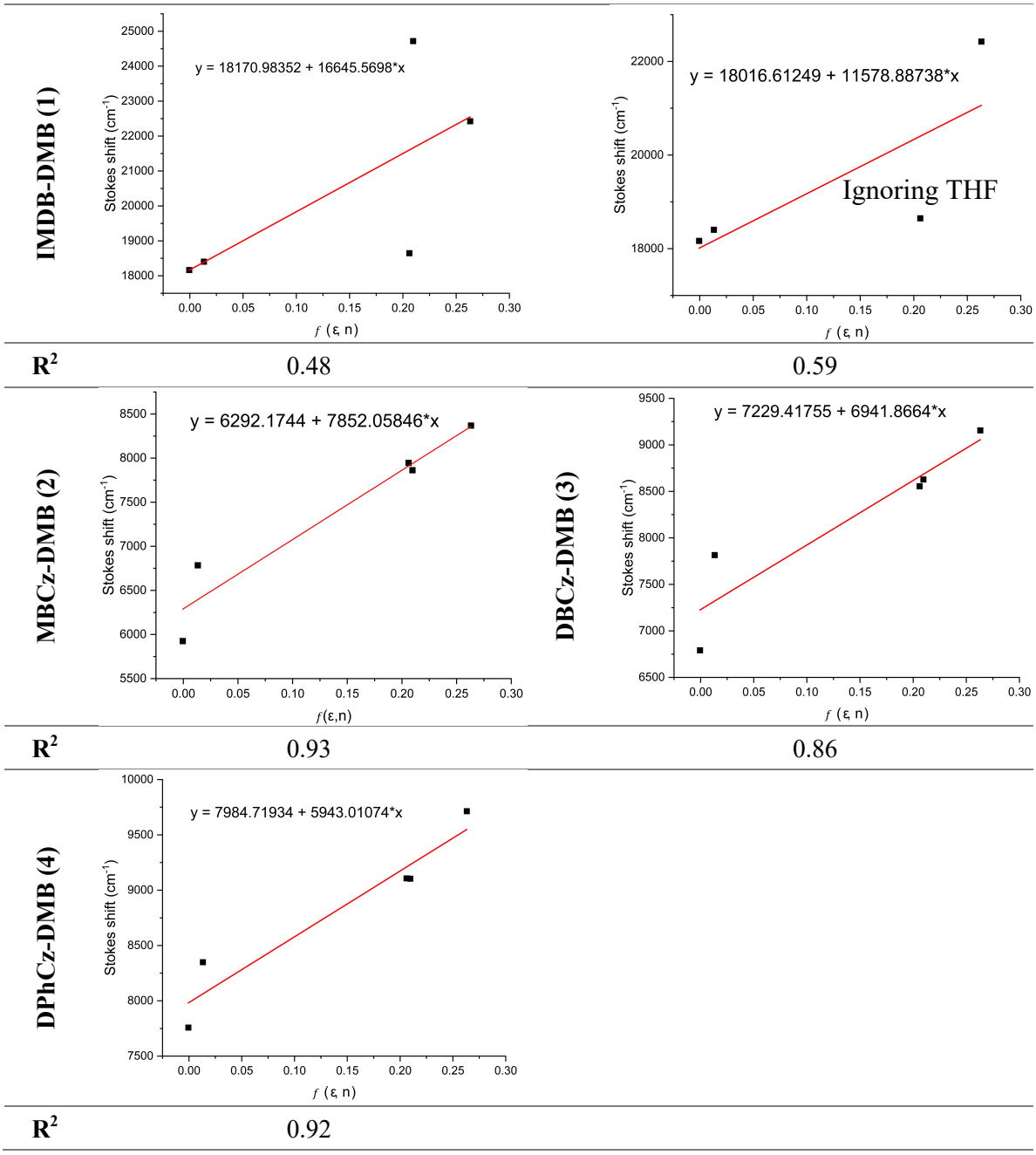


Figure 4-36 Lippert-Mataga plots for the first four compounds in this study.

The change in dipole moment going from the ground to excited state, *i.e.* :

$$\Delta\mu = \mu_e - \mu_g$$

Equation 4-1 Change in dipole moment upon excitation.

can be estimated from the slope of the Lippert–Mataga plots.

Table 4-15 Calculated dipole moments for compounds 1 - 4.

Molecule	$\Delta\mu$ (cm^{-1})	a (Å)[a]	(μ_e -μ_g)D
IMSB-DMB (1)	16645 / 11579	7.53	27 / 22
MBCz-DMB (2)	7852	7.35	18
DBCz-DMB (3)	6942	8.42	20
DPhCz-DMB (4)	5943	9.49	22

[a] Onsager cavity radius, calculated *via* DFT-B3LYP-6-31G(d) as the largest diameter across the whole molecule.

Table 4-15 shows fitted slopes, Onsager cavity radii and dipole moments for compounds **1** – **4**. Comparing the diphenyl to dibenzo-carbazole, the presence of the diphenyl groups seems to significantly increase the dipole moment of the molecule in the excited state. The presence of this dipole in the excited state suggests the excited states being charge transfer in nature. This may be due to increased rotational freedom in the donor (phenyl) compared to the potential for flapping motion of the dibenzocarbazole. The dipole is less for mono-benzocarbazole as it presents a much more rigid donor structure. When compared to the unsubstituted carbazole analogue reported by Taniguchi *et al*.[262] these compounds possess weaker dipole moments (on the basis of Taniguchi *et al*.'s [262] compound possessing a Stokes shift of 8500 cm^{-1}).

4.2.12 Lifetime measurements

Time-correlated single photon counting (TCSPC) involves exciting samples of emissive materials with a pulsed laser source, and measuring the number of photons released after the laser is switched off. In order to build up a good signal-to-noise ratio, the process is repeated many thousands of times to build up a dataset revealing the kinetics of the emissive decay processes at a specifically monitored emission wavelength. This allows the determination of the lifetimes of the prompt decay (τ_p) and delayed decay (τ_d) by performing mathematical exponential fittings upon the decay plots with reference to the instrument response factor.

IMSB-DMB (**1**), MBCz-DMB (**2**), DBCz-DMB (**3**), DPhCz-DMB (**4**) were characterised by myself and compounds Cz-$BMes_2$ (**5**), tBu_2CzOMe-$BMes_2$ (**6**), tBu_2CzOMe_2-$BMes_2$ (**7**), tBu_2-CzBMes_2 (**8**) and Me_4-Cz-$BMes_2$ (**9**) were characterised by Dr Joseph Cameron from the University of Glasgow.

Unfortunately, the excitation wavelength of compound **1** was far too short to be excited *via* our laser source, however, TCSPC measurements were obtained for **2**, **3** and **4**. A slight delayed component was observed for **2**, **3** and **4** in solution, however this increased the most for compound **3** under argon.

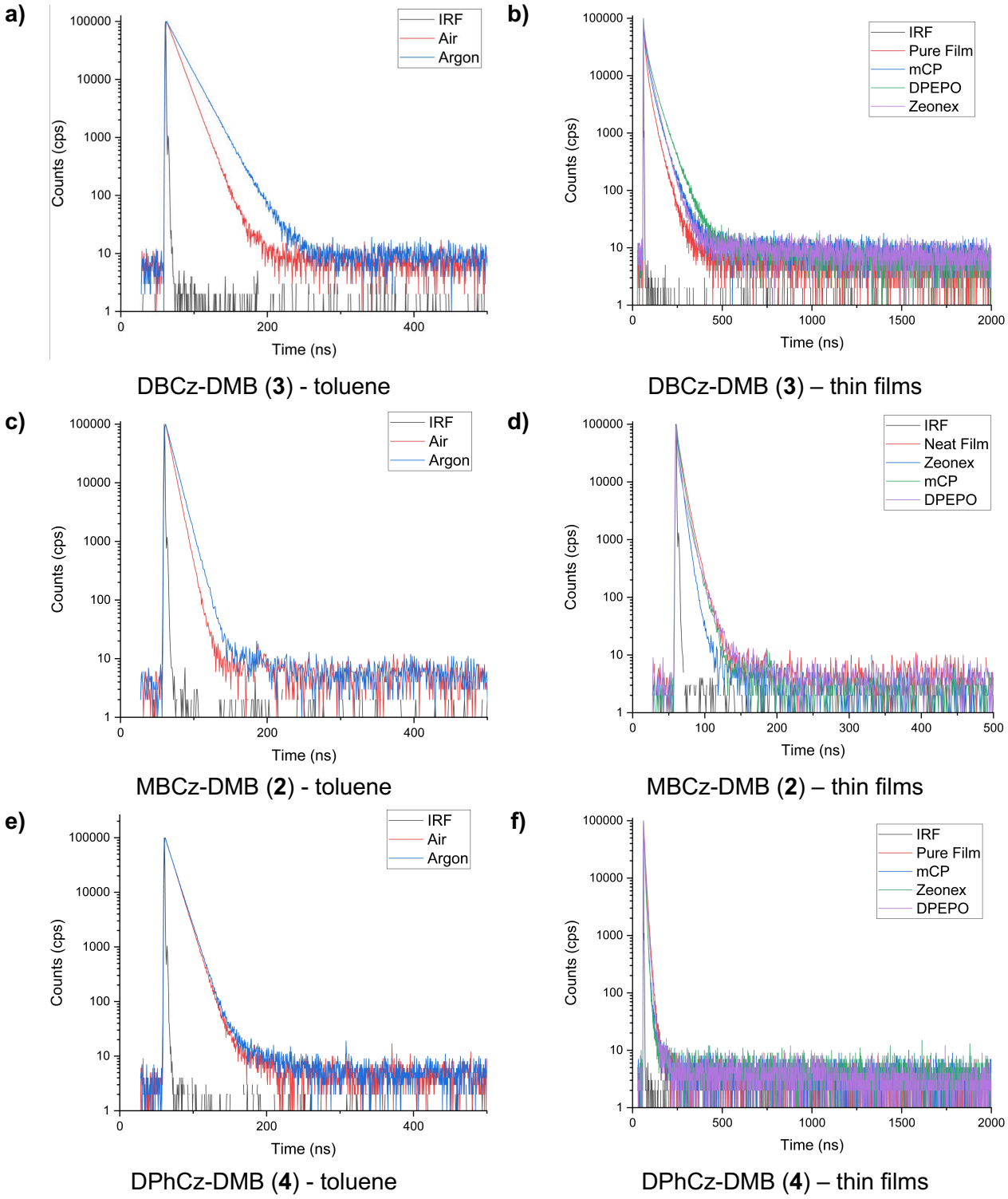


Figure 4-37 TCSPC plots for compounds in toluene (a, c, e), and thin films (b, d, f). All excited with a 365 nm 5µs pulsed laser and measured over 2µs.

Closer inspection of the degassed solid-state lifetime measurements for the orange peak in compound **2** reveals a slight delayed component with a lifetime of 200 ns in a mCP host. Extending the window of measurement (using 40 µs pulses and 20 µs window instead of 5 µs and 2 µs) shows that indeed in mCP the lifetime of the delayed component of the

emissions of the red luminescence is indeed longer (815 ns, see Figure 4-38) though too short in this instance to be confidently assigned to phosphorescence.

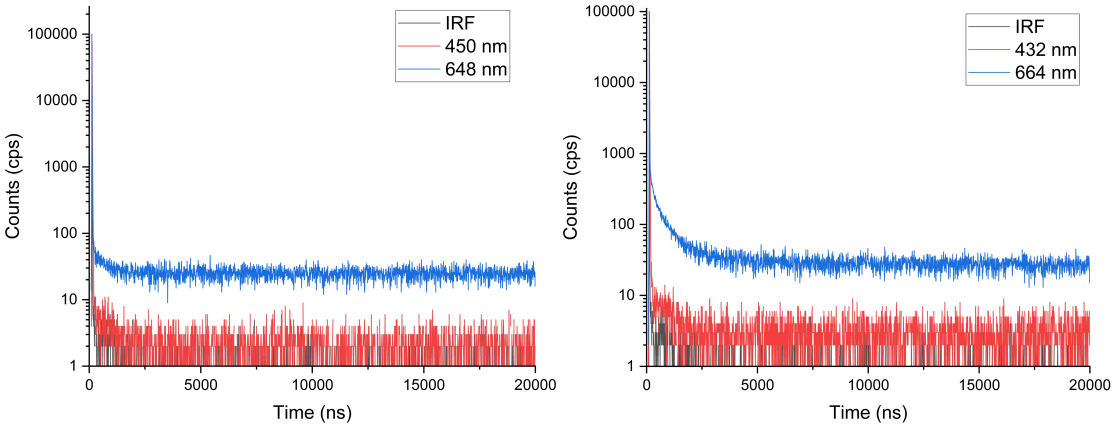


Figure 4-38 Degassed TCSPC of MBCz-DMB (2) extended to a 40 µs / 20 µs measurement. Left is neat film, right is in mCP. The red peak is significantly long lived in comparison to the blue prompt emission.

The increased lifetime in mCP, along with the red-shifted peak, suggests the formation of an exciplex giving rise to the red emission. However, mCP exciplexes do not explain the observed red emission in the neat film. In this instance, it is possible that there is excimer formation between neighbouring MBCz-DMB (**2**) molecules.

Table 4-16 Summary of solution and solid-state TCSPC lifetimes for the molecules in this study. All were excited with a 365 nm diode laser. τ_p refers to the prompt lifetime and τd the delayed lifetime.

Molecule	Sample	τ_p (ns)	τ_d (ns)
MBCz-DMB	Toluene (air)	6.9	33.0
	Toluene (degassed)	9.0	32.1
	Pure film	4.9	9.0
	(orange peak)	(4.3)	(9.8)
	mCP	4.0	8.4
	(orange peak)	(4.0)	(200.0)
	mCP Long lifetime	21.6	701.2
	(orange peak)	(26.1)	(814.7)
	Zeonex	3.7	6.8
	DPEPO	5.1	10.8
DBCz-DMB	Toluene (air)	5.3	12.8
	Toluene (degassed)	15.0	19.2
	Pure film	7.9	28.1
	mCP	8.5	32.4
	Zeonex	9.1	31.1
	DPEPO	8.2	38.1
DPhCz-DMB	Toluene (air)	9.9	13.9
	Toluene (degassed)	10.3	41.0
	Pure film	5.6	11.2
	mCP	4.7	10.3
	Zeonex	4.4	8.8
	DPEPO	4.1	8.6

Dr Joseph Cameron provided the TCSPC data for his compounds:

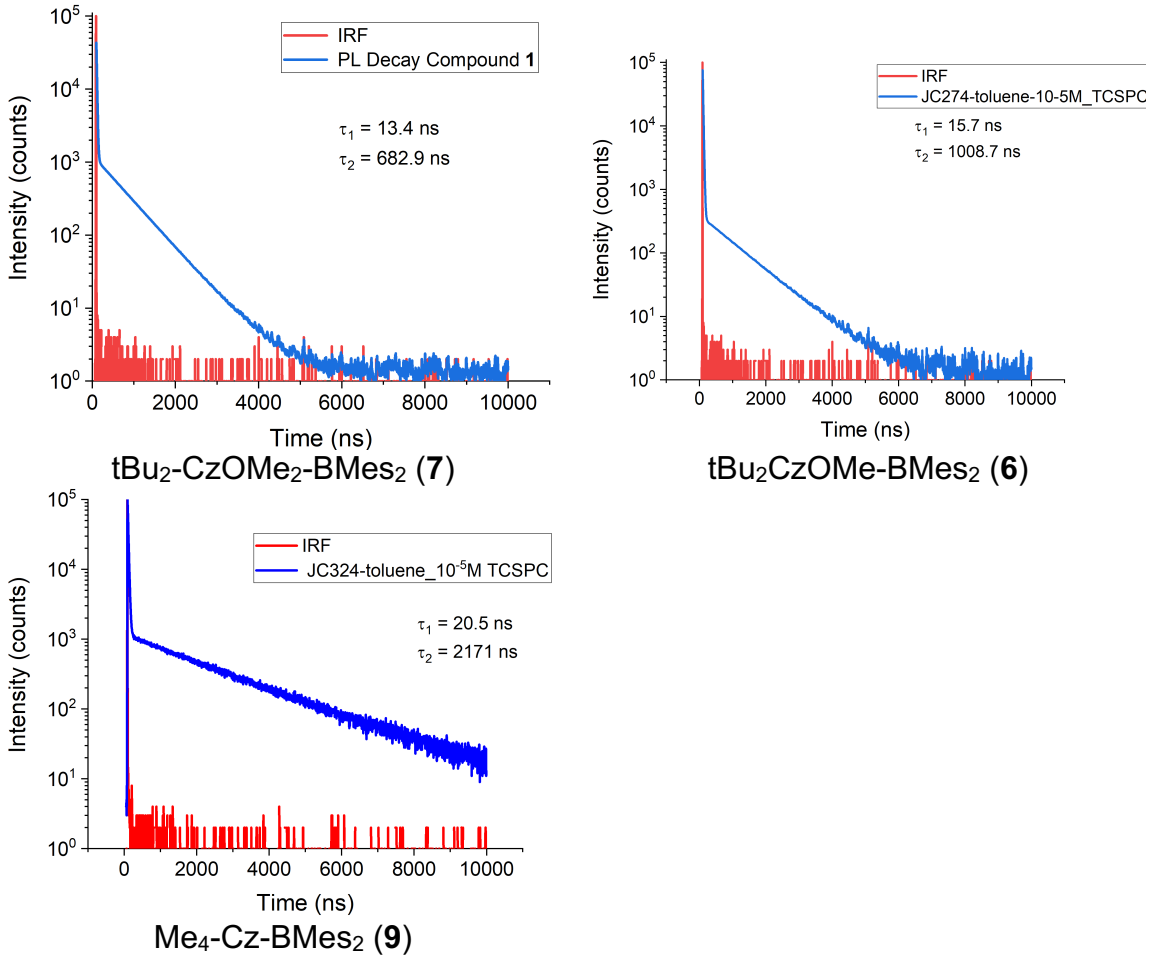


Figure 4-39 TCSPC plots in degassed toluene for compounds 6, 7 and 9. Plots produced by Dr Joseph Cameron and used with permission.

Use of methoxy groups significantly enhances emission lifetimes when compared to unsubstituted carbazole for **5** in the literature.[262] Interestingly, emission lifetimes are much longer when an unsubstituted carbazole unit is used. However, the lifetimes more than double when the two methoxy groups are replaced by methyl units, suggesting that steric effects in this case make a significant contribution to the rISC process in this particular structure. The short lifetimes mean that in blue OLEDs these compounds are attractive as they exhibit high intensity of the blue emissions, whilst the fact that non-radiative deactivation is likely to be suppressed further adds to their suitability for devices.

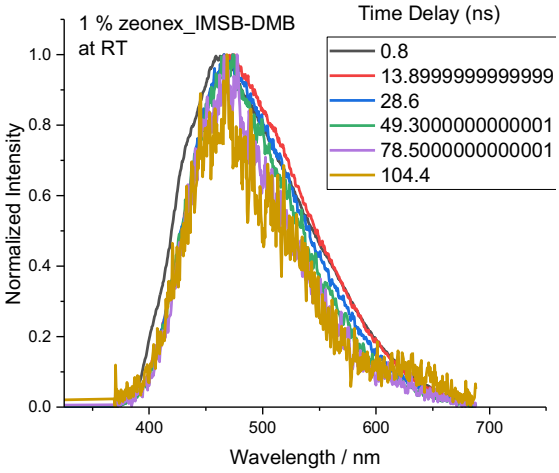
4.2.13 CCD time-resolved measurements

Whilst TCSPC measurements present a highly suitable method of measuring the decay lifetime for emissive materials, they are only able to measure the decay of a single emissive wavelength (with specified bandwidth) at a time. During decay of compounds with more complicated photophysics than simple fluorescence, the photoluminescence can vary over time. As such, being able to record the emissive spectrum over known time intervals gives a much more detailed picture as to which excited state is involved with the emissions at a particular point in time after excitation.

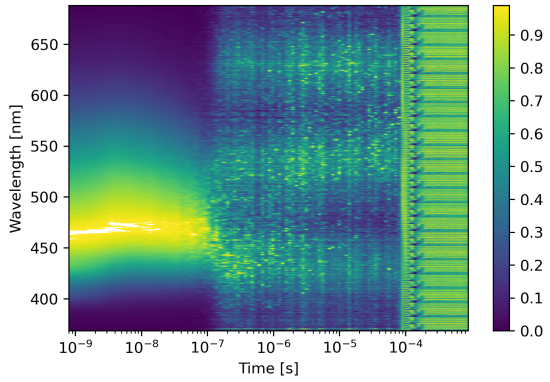
In the OEM group of Professor Andy Monkman at Durham University, a custom-made laser table uses a femtosecond laser excitation source which excites the material at regular pulses. A charged-coupled device (CCD) camera monitors emissions at an angle out of the laser beam's path. The CCD's camera shutter (digital) is synchronised with the pulsed laser source and captures a photoluminescence spectrum at regular intervals along the duration of the emitter material's decay.

All measurements in this section were performed by Dr Suman Kuila at Durham University.

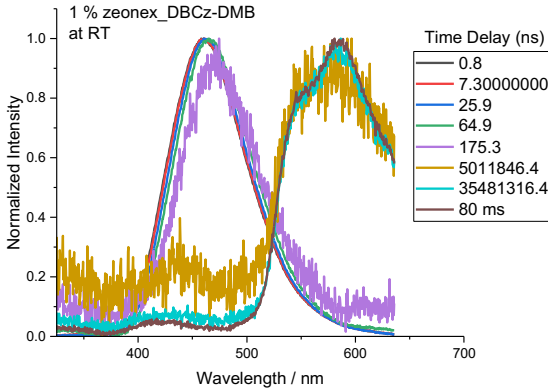
Samples of compounds **1**, **3** and **4** were prepared at 1% w.t. concentration to minimise intermolecular interactions and the resulting heat maps and time-resolved photoluminescence spectra are reported in Figure 4-40. MBCz-DMB (**2**) is not included as it was synthesised much later in the project.



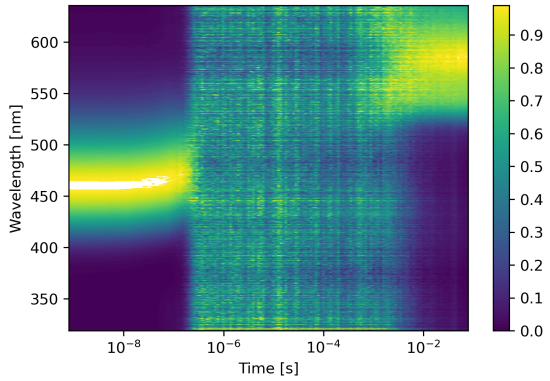
IMSB-DMB (**1**) 1% w.t. in Zeonex time-resolved PL



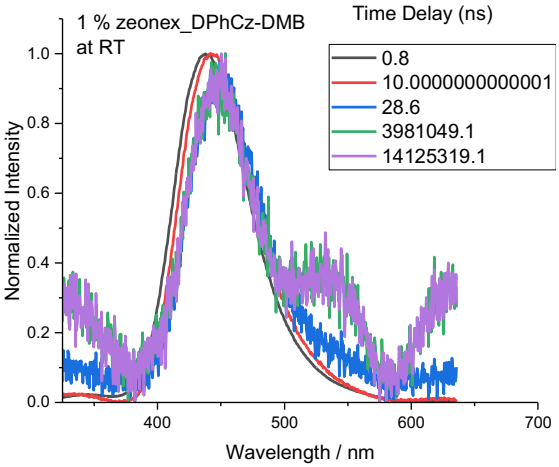
IMSB-DMB (**1**) delayed emission heatmap



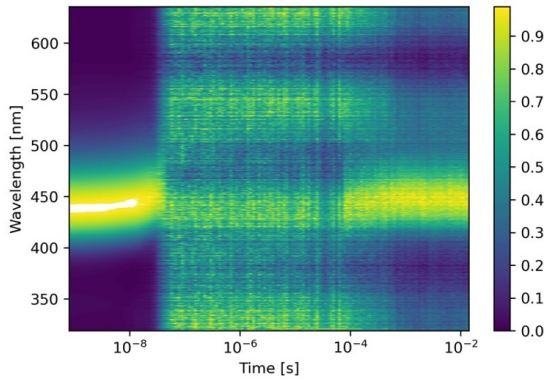
DBCz-DMB (**3**) 1% w.t. in Zeonex time-resolved PL



DBCz-DMB (**3**) delayed emission heatmap



DPhCz-DMB (**4**) 1% w.t. in Zeonex time-resolved PL



DPhCz-DMB (**4**) delayed emission heatmap

Figure 4-40 Time-resolved spectra and heat maps of compounds 1, 3 and 4 in Zeonex hosts.

As was observed in our attempts to measure TCSPC for compound **1**, there are no delayed emissions from this compound, with the entirety being prompt emissions, completely finishing by 10^{-7} s with a τ_{PF} of just 5.31 ns. Compound **3** on the other hand exhibits initially prompt blue emissions (~460 nm for around 10^{-7}s) followed by a significantly red-shifted room temperature phosphorescence at 586 nm with a lifetime of 80 ms. The more carbazole reminiscent compound **4** emits mostly *via* prompt blue emissions (~440 nm) for just over

10^{-8} s, but this too is followed by a slight room temperature phosphorescence at ~450 nm after around 14 ms – representing a significant reduction in the red-shift compared to dibenzocarbazole, which can be seen in the contour plot to change significantly in this timeframe.

For compounds **3** and **4**, the T_1 energies in Table 4-5 were determined from the onset of the phosphorescence peaks respectively from this data. The prompt and delayed lifetimes were obtained from the bi-exponential fittings of the decay curves in Figure 4-41, and are summarised in Table 4-17.

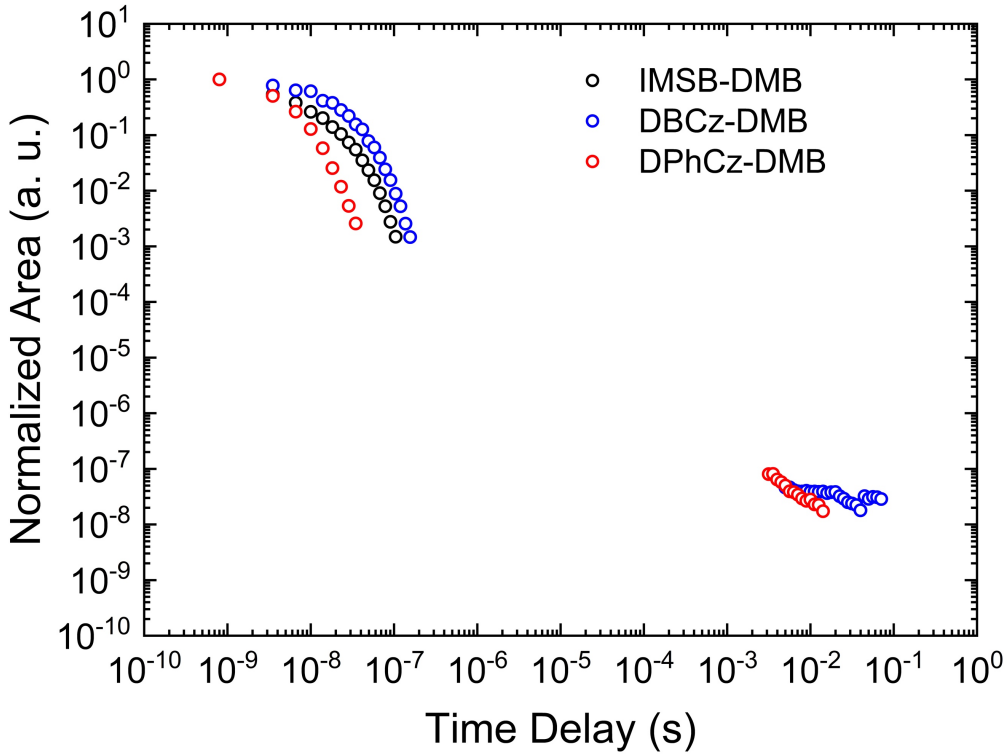


Figure 4-41 Time-resolved emission decays of compounds 1, 3 and 4 in 1% w.t. Zeonex.

Table 4-17 Summary of time-resolved emission decays. Values are from mono-, bi- or tri-exponential fittings of the prompt fluorescence (PF) or delayed fluorescent (DF) emission regions and are weighted averages.

	τ_p (av)	τ_d (av)
Compound in Zeonex host	(ns)	(μs)
IMSB-DMB (1)	12.4	-
DBCz-DMB (3)	19.9	12870
DPhCz-DMB (4)	4.64	20249

From the CCD data, it is clear that IMSB-DMB (**1**) only possesses prompt fluorescence (with an average τ_p of 12.4 ns. DBCz-DMB (**3**) and DPhCz-DMB (**4**) both have prompt components of 19.9 ns and 4.6 ns, respectively, but with vastly differing delayed

components, at 12.9 ms and 20.2 ms, respectively, likely coming from weak TADF emissions. Further low temperature measurements are now required to determine whether these delayed emissions are RTP or TADF.

The difference in wavelength of DBCz-DMB's (**3**) prompt and delayed emissions (~200 nm) highlight the advantage of CCD measurements compared to TCSPC – without being able to measure PL spectra at delayed intervals, this emission would have gone unnoticed.

4.2.14 Hydrolysis of the B-N bond in DBCz-DMB (3)

Boron is an electron deficient Lewis acid, due to its empty p-orbital. This presents an avenue of attack for electron-rich reagents. As such, the B-N bond is susceptible to cleavage through hydrolysis by water molecules.

Following on from the realisation of DBCz-DMB's (**3**) sensitivity to water during the first aqueous workup, a sample of compound (**3**) in methanol (5.2×10^{-4} M) was prepared. This was spiked with 20 µL of deionised water. The solution was sonicated for 1 min and stirred for 30 s. Using a 360 nm excitation beam, the fluorescence spectra of the solution were taken multiple times over the course of 7.1 hours and are shown in Figure 4-42.

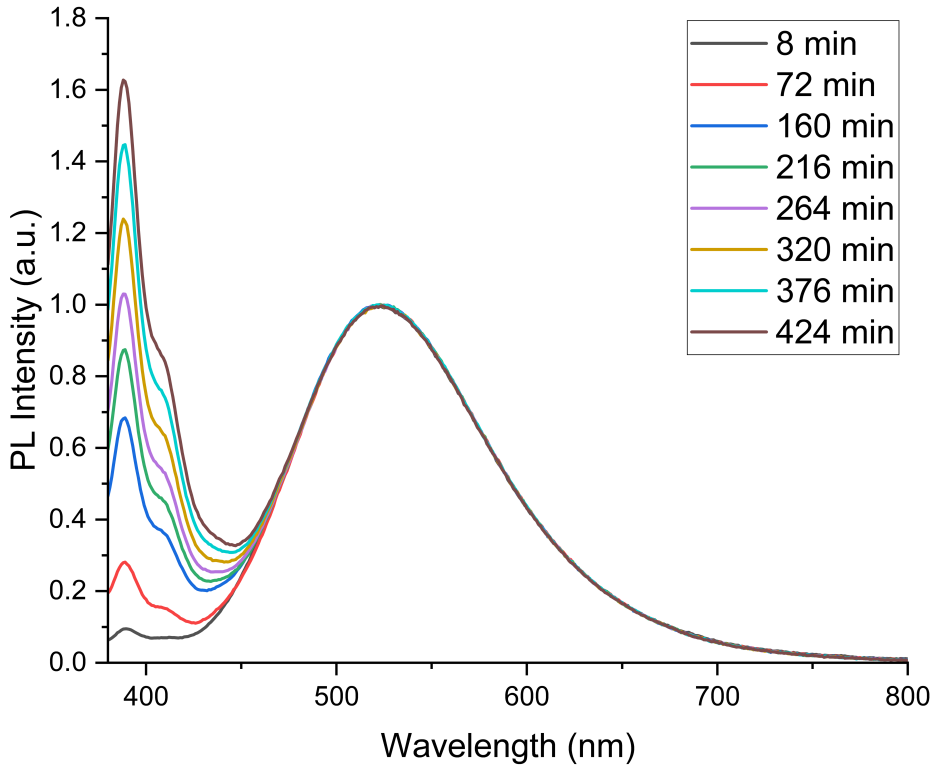
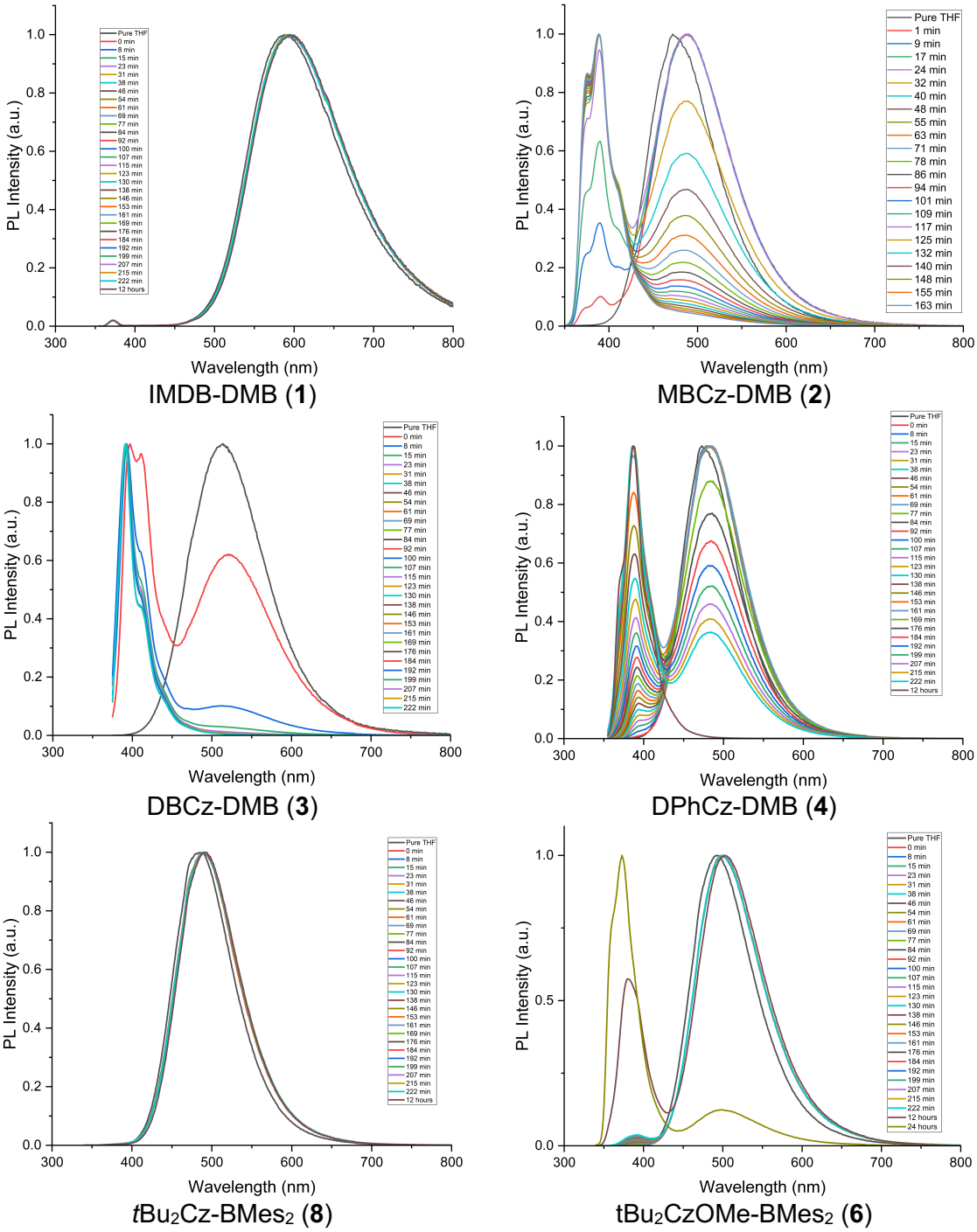


Figure 4-42 Normalised PL spectra of a methanol solution of DBCz-DMB (3) spiked with 20 µL of deionised water.

A peak at 518 nm is clearly visible throughout, but over time an additional peak appears at 389 nm and increases in intensity dramatically. A separate sample of pure 7H-dibenzo[c,g]carbazole in solution reveals that this molecule is the origin of the new peak. As such, it is clear that exposure to water results in cleavage of the B-N bond *via* hydrolysis, yielding the starting materials.

Further exploration of the strength of the B-N bond in each compound was performed in dry tetrahydrofuran, spiking with 300 µL deionised water, shaking, and measuring immediately thereafter, exciting at that particular molecule's main absorption wavelength. The resulting photoluminescence spectra are shown in Figure 4-43.



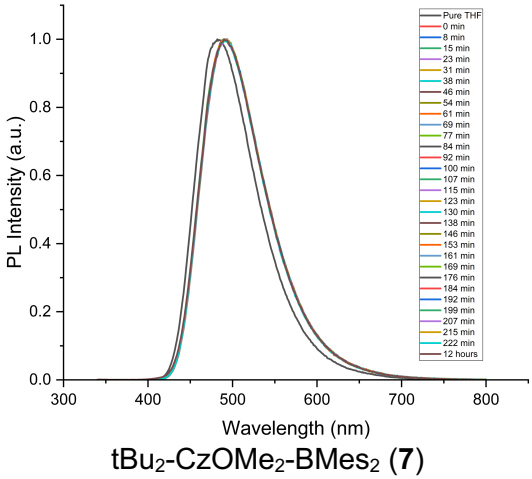


Figure 4-43 Fluorescence spectra of compounds in this study in tetrahydrofuran showing the impact of water exposure.

Measurements were performed on pure samples of the analytes in tetrahydrofuran (~1E-4 M). After initially adding the deionised water, a red shift is observed in each sample. This is due to the more polar water molecule imparting solvatochromic effects upon the analytes. Pure samples of each material's carbazole donor were prepared in dry tetrahydrofuran and confirmed that the new peaks that form over time were from the products of hydrolysis (see Figure 4-44).

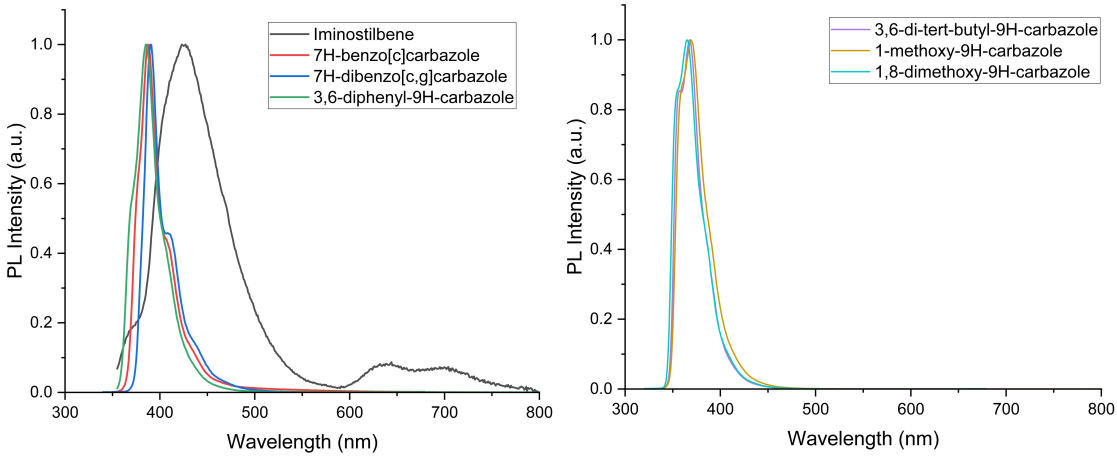


Figure 4-44 PL Spectra of pure donors in dry THF. Donors of compounds 1 - 4 (left), donors of compounds 6-8 (right).

Compound (**1**) exhibits no change in PL properties after exposure to water. Even after 12 hours of exposure and an additional 1 mL water added, no change in wavelength was noticed. The DFT and single crystal XRD data of compound (**1**) reveals that the buckling of the iminostilbene donor moiety and twisting of the mesityl groups attached to the boron, introduces a highly congested environment around the central boron atom. Examining the van der Waals spheres of these structural configurations using single crystal XRD and density functional theory shows that the boron's empty p-orbital is highly sterically protected

from potential attack by water molecules, which undoubtedly gives rise to the excellent chemical stability of IMSB-DMB (**1**).

The B-N bond length is shortest with compound (**1**) due, as outlined previously, to iminostilbene being a stronger donor and the B-N bond therefore having increased double bond character. This allows for a distortion in the iminostilbene moiety allowing the bulky dimesityl boron moiety to be drawn closer to the donor and forming an X-shaped conformation. The bond length increases for the more conjugated **2**, **3** and **4**, which also have poorer stability. Compound **3** is so unstable that it had already begun to hydrolyse before the first measurement could be made and had converted to the original starting materials by 23 minutes. By comparison, the sample of compound **2** required 163 minutes to convert back to mostly the starting material. Compound **4** still possessed emissions from intact DPhCz-DMB (**4**) after 222 minutes (it had to be left 12 hours overnight for complete hydrolysis to be observed). Since both these molecules have almost the same B-N bond length, the rate of hydrolysis must be influenced by other factors as well, however the order of reactivity **3** > **2** > **4** > **1**, matches the order of B-N bond lengths in these molecules from the DFT calculations (1.437 Å for **1**, 1.458 Å for **2**, 1.460 Å for **3** and 1.452 Å for **4**, respectively).

The pure carbazole donor in Cz-$BMes_2$ (**5**) possesses a slightly shorter B-N bond (by 0.01 Å) than its dibenzo- and diphenylcarbazole analogues DBCz-DMB (**3**) and DPhCz-DMB (**4**) and is highly stable in the water spiked THF solution. After 12 hours, there is no component in the PL spectra of any product of hydrolysis. Initially, this might suggest that the stability of these compounds is related to the length of the B-N bond. Indeed, tBu_2CzOMe-$BMes_2$ (**6**) hydrolyses in the water-spiked solution, and its B-N length is 0.02 Å longer than Cz-$BMes_2$ (**5**). However, it takes considerably longer for the dominant component of the PL spectra to be the hydrolysis product than DBCz-DMB, despite the B-N length of tBu_2CzOMe-$BMes_2$ (**6**) being longer still.

Further evidence to discount B-N length alone leading to hydrolysis is the dimethoxy derivative, tBu_2-$CzOMe_2$-$BMes_2$ (**7**), where the B-N bond length extends by a further 0.02 Å. In this compound, there appears to be absolutely no hydrolysis occurring, despite it having the longest distance between the donor and acceptor.

An overall examination of the structure of the molecule is therefore key to understanding the water stability. Viewing the van der Waals radii of the structures shows how exposed the central boron atom is. In highly congested structures such as IMDB-DMB (**1**), the boron atom is almost completely hidden by the cluttered environment around it. This would prevent any nearby water molecules from attacking its empty p-orbital. In MBCz-DMB (**2**), DBCz-DMB (**3**) and DPhCz-DMB (**4**), the boron atom is much more exposed, which would suggest it can be more readily attacked by a passing water molecule, leading to B-N bond cleavage. Despite its increased B-N bond length, the central boron core of tBu_2-$CzOMe_2$-$BMes_2$ (**7**) is completely shielded from attack, due to the two methoxy groups. Potential coordination of the oxygen atoms also helps this molecule to have a significantly larger dihedral angle, further blocking off attack (and switching on TADF). In the monomethoxy derivative, tBu_2CzOMe-$BMes_2$ (**6**), a slight kink to the D-A link is introduced owing to the coordination of the methoxy group. This makes the opposite side of the carbazole orientate slightly further away from the boron atom, further exposing the boron's empty p-orbital to attack.

Taking the above into account, it might seem somewhat counterintuitive that the tert-butyl carbazole derivative, *t*Bu_2Cz-$BMes_2$ (**8**), would be stable, considering that it's smaller analogue, Cz-$BMes_2$ (**5**), has the least protection of the boron, and supposedly a central environment that would be very similar to that of compound **4**. However, the lack of any conjugated or significantly electron-donating substituents on the carbazole donor most likely results in it having increased donating character, leading to the slightly shorter B-N bond length making cleavage more difficult. Confirmation of this theory requires single crystal XRD of this compound, but the growth of suitable crystals has thus far been unsuccessful

Interestingly, the van der Waals structure of tBu_2CzOMe-$BMes_2$ (**6**), shows increased protection of the boron atom compared to other more stable compounds. However, it still exhibits distinct hydrolysis. A reason for this most likely lies in the distortion to the structure caused by the single methoxy group. Unbalanced in symmetry as it is, attack by water presumably requires less energy to overcome the steric hinderance because of the structural distortion (B-O interactions on one side and the 23.7° kink making access to the empty p-orbital of the boron atom to a water molecule owing to a more exposed opposite side).

Furthermore, the thermal stability of the molecules as determined by TGA reveals that the first four molecules increase in thermal stability in the order **1** < **2** < **4** < **3**. This is completely

at odds with their observed chemical stability, which goes in the order of increasing stability **3** < **2** < **4** < **1**. Assuming that the thermal degradation arises from the cleavage of the B-N bond, this suggests that the strength of the B-N bond as a function of its length is less important with regards to chemical stability in these types of molecules, than that of steric effects, which according to the XRD data, follows the increasing obscuration of the boron atom by **3** < **4** < **1**. This matches the chemical stability, and therefore suggests that this is the main reason for B-N cleavage in this family of molecules. Unfortunately, owing to the lack of XRD data for compound **2**, we cannot fully confirm where it would fit on this sequence. However, comparing the XRD data of the other three compounds to that of the DFT calculated structures shows very similar trends in how exposed the boron atom is in each case. Using both the optimised structure for compound **2** and the observed chemical reactivity, we can infer that it should have intermediate obscuration of the boron to that of compounds **3** and **4**.

4.2.15 Aggregation induced emission of IMSB-DMB

Work by Wang *et al*.[255] demonstrated that iminostilbene bonded to a benzothiadiazole-based acceptor unit yields material that exhibits aggregation induced emission (AIE), a feature of some fluorescent organic molecules the name of which was coined in 2001 by Luo *et al*.[253], but has been reported in various forms throughout the twentieth century[280] since its observation in J-aggregates in 1936 by Edwin Jelly[281]. The above computational structural optimisations and XRD crystal structures suggest that the IMSB-DMB molecule adopts an X-/Z-shaped conformation, which could potentially lead to interesting aggregation properties.

It was noted that IMSB-DMB (**1**) exhibited dim yellow fluorescence in solution, but bright blue fluorescence in the solid state (see Figure 4-45), so an attempt was made to observe aggregation effects experimentally. A solution of compound **1** in THF (1.38×10^{-3} M) was prepared, and several 0.5 mL aliquots taken and diluted with a 10 mL mixture of THF and deionised water with a range of compositions (10% water, all the way up to 99% water).

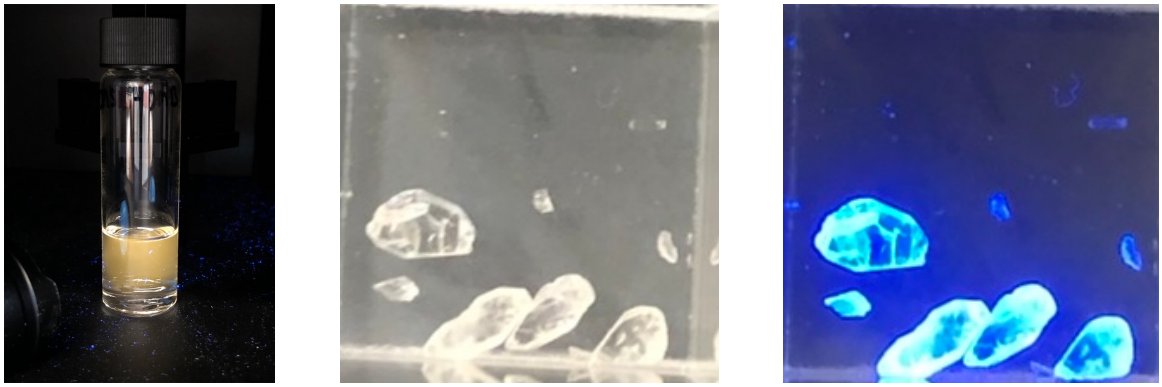


Figure 4-45 IMSB-DMB (1) fluoresces yellow in solution, but blue in the crystalline form.

The resulting UV-vis absorption spectra and photoluminescence spectra are reported in Figure 4-46, along with a comparison of the water volume fraction to the change in intensity from the untreated tetrahydrofuran sample.

It was observed that all samples up to 95% water content exhibited broad and dim yellow emissions. However, at 96% water : 4% tetrahydrofuran, the emission spectra begin to blue-shift from 582 nm down to 464 nm, accompanied by an approximately 430,000-fold increase in emission intensity (91% vol *vs* 98% vol). This begins to drop off after 98% vol. Since water is more polar than methanol, this cannot be due to solvatochromism.

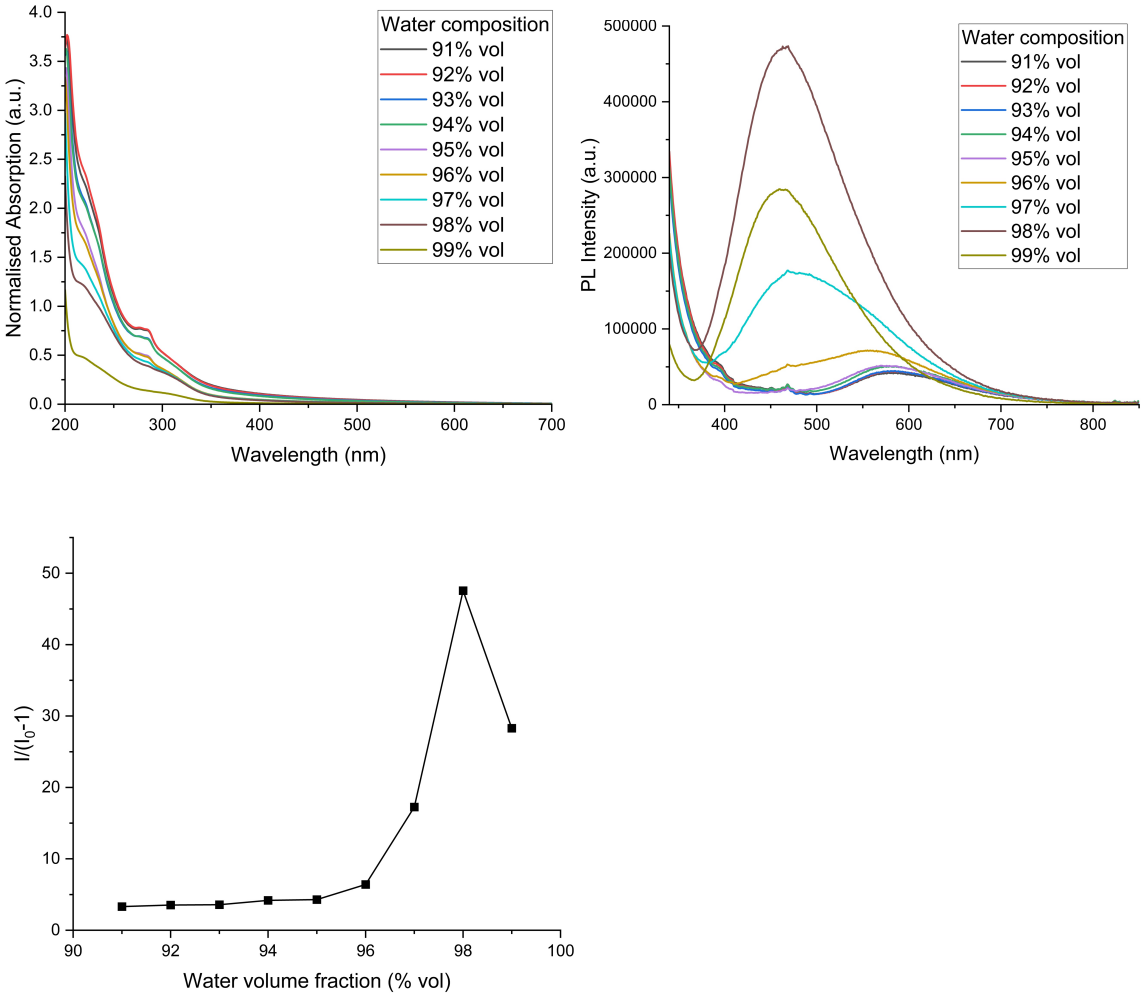


Figure 4-46 PL spectra of IMSB-DMB (1) in tetrahydrofuran spiked with varying volumes of water. Plot of normalised $(I/I_0)-1$ against water volume fraction (f_W) (bottom left), where I and I_0 are the intensities of emission with and without water spiking.

Rather, it is likely due to the formation of nanoparticles of solid IMSB-DMB (**1**) which emit in the blue region. The fact that the emission intensity drops off at higher water fractions also supports the likelihood of nanoparticle formation[282]. The UV-vis absorption plots decrease in intensity with increased water content, which suggests the formation of aggregates since the overall concentration is kept the same with each sample.

The reason for enhanced emissions *via* AIE is that in the well dispersed form in solution, compound **1** emits weakly, but has many effective non-radiative decay pathways to rapidly quench emissions. Upon formation of clusters of nanoparticles at high water content, the molecules are forced closer together and their motions, vibrations and rotations severely restricted, thereby permitting emission to outcompete non-radiative decay[283,284].

A similar phenomenon was observed by Neena *et al.*[285] in a similarly structured phenothiazine derivative. The kink in Neena *et al.*'s donor, along with the conformation of their dimesityl boron acceptor yielded a similar X-shaped molecule in the XRD data.

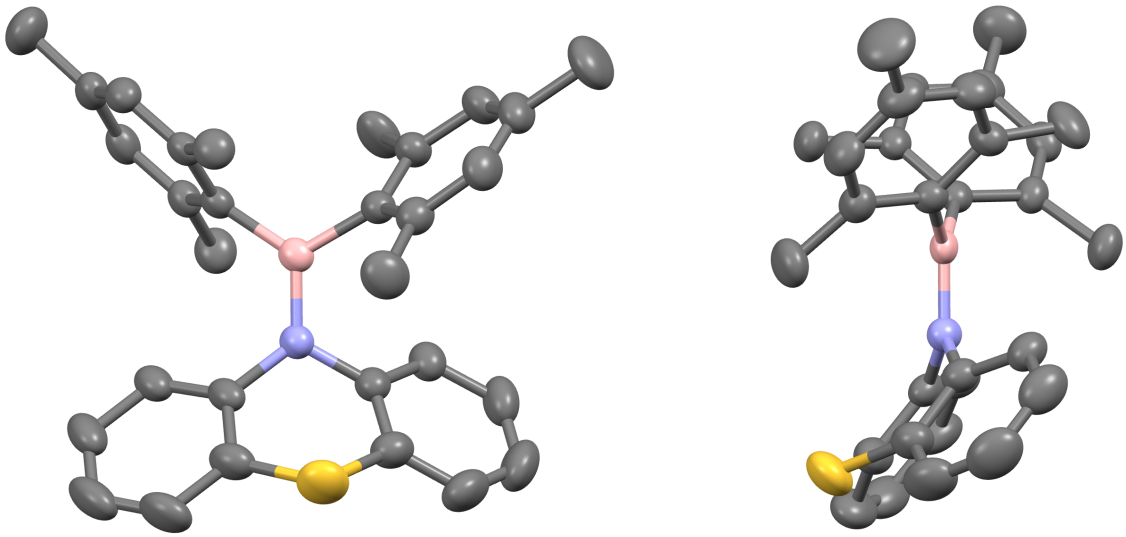


Figure 4-47 XRD crystal structure of Neena *et al.*'s[285] phenothiazine derivative.

In addition to this, the face-to-face contacts are skewed, but only as close as 3.68 Å, but still reported to demonstrate aggregation induced emission (see Figure 4-48).

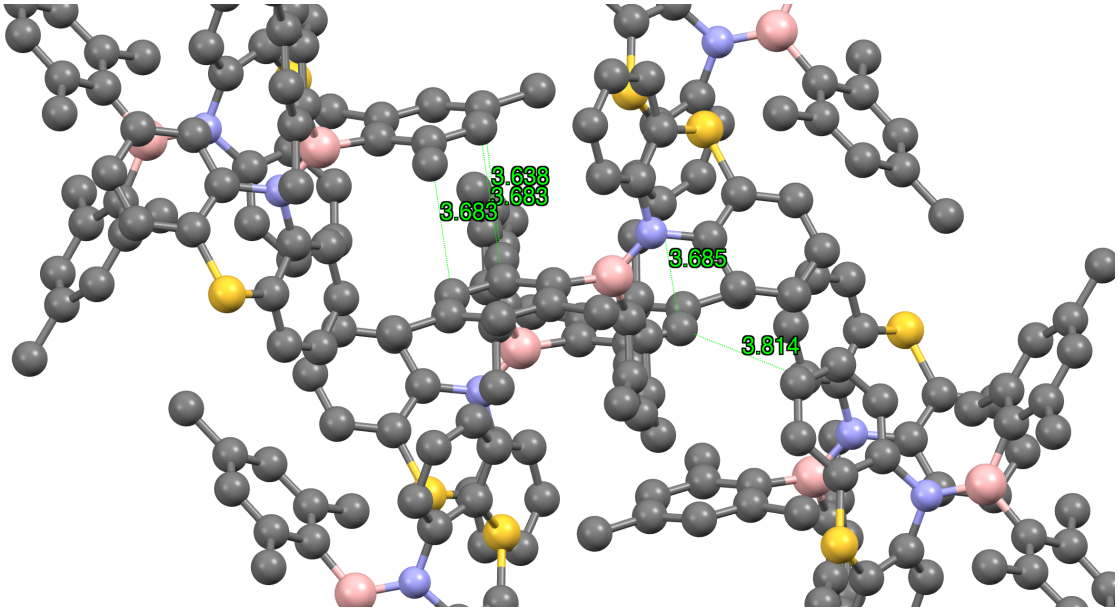


Figure 4-48 Face-to-face contacts from Neena *et al.*'s[285] phenothiazine derivative.

In comparison, the closest face-to-face contacts in IMSB-DMB (**1**) was measured to be 3.36 Å (see section 4.2.3).

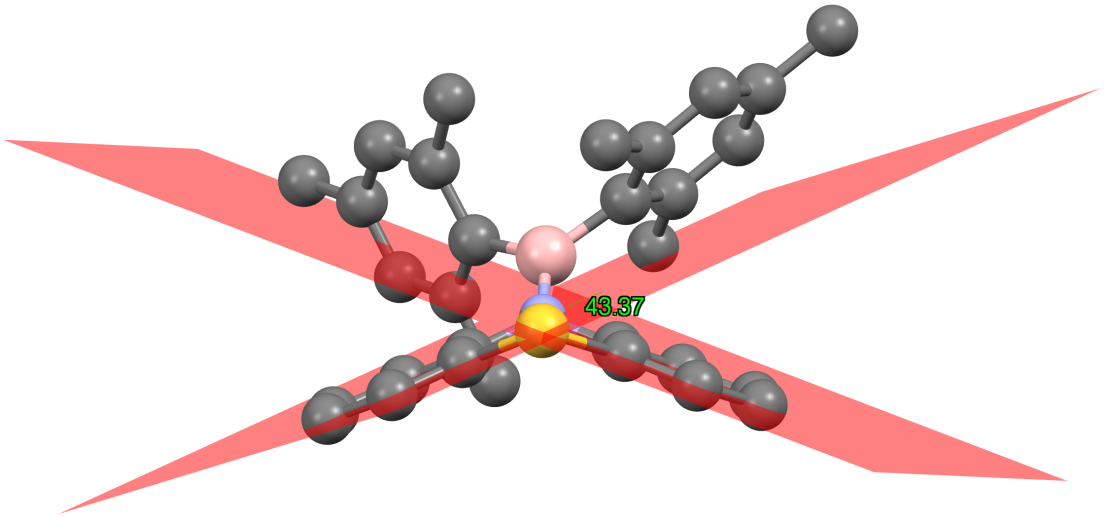


Figure 4-49 Kink in Neena *et al.*'s[285] donor moiety.

Furthermore, the kink in the donor moiety reaches 43.4° (see Figure 4-49), which is 12.9° less than in compound **1** (Figure 4-10). This increased contortion in the molecular structure of compound **1** gives rise to easier packing than in the literature compound.

4.3 Conclusions

This initial study reveals that boron-based acceptors have potential for application in small molecules with simple synthetic strategies designed to exhibit TADF. Special consideration must be taken during synthesis of boron-based TADF compounds, as a poorly shielded boron atom may permit cleavage of the B-N bond during aqueous work up. Presumably, this weakness in their structure would also apply to B-C bonds in D-π-A type structures where the boron atom bonds to a carbon on a π-bridge. It is therefore highly recommended that use of a non-aqueous workup during synthesis is adopted, and the use of anhydrous and non-protic solvents employed wherever possible for photophysical studies of boron based D-A small molecules.

To further enhance chemical stability in boron based TADF molecules, it is clear from this study that sterically shielding the boron's empty p-orbital is vital. This can be achieved through use of a congested donor or acceptor, which gives rise to a more twisted conformation, blocking off the boron atom from attack, or by using additional functional groups on the donor, orientated to help block the boron from attack. This would also serve the double function of increasing the dihedral angle between the donor and acceptor, enhancing the ease of rISC.

Use of methoxy groups bonded to the donor moiety can serve as a means of lowering the energy of the first excited singlet state and raising the first excited triplet state, thereby narrowing the ΔE_{ST}, permitting the activation of the rISC process when compared to molecules without methoxy groups. This is due to the enhanced electron donating ability of methoxy-derived aromatic systems.

The proximity of the methoxy groups' oxygen atoms and boron, and the overlap of their van der Waals radii, suggests the possibility of non-covalent interactions between the oxygen's lone pair and boron's empty p-orbital. This could be giving rise to the increased dihedral angle, without total decoupling of the HOMO and LUMO. Increasing the number of methoxy groups bonded to the carbazole moiety also leads to enhanced electron density in the donor, due to the resonance effect of the methoxy groups. This in turn leads to a lengthening of the B-N bond.

Of special mention is the 7H-dibenzo[c,g]carbazole donor in DBCz-DMB (**3**). Despite its quasi-helical nature, where one would expect deviation from planarity to introduce interruption to HOMO conjugation across the donor, we observe (*via* DFT calculations), a rather interesting uniformity in the localisation of the HOMO upon the donor moiety, with absolutely no spreading into the acceptor moiety. The LUMO still mixes a little with the HOMO on the donor, but this presents an interesting potential for enhanced HOMO-LUMO separation if the same phenomenon is replicated when 7H-dibenzo[c,g]carbazole is coupled with other acceptors (providing, of course, that the calculation results are accurate). In the series of molecules exploring conjugation effects, the 7H-dibenzo[c,g]carbazole compound, DBCz-DMB (**3**) is the only one to exhibit any form of delayed emissions, in this case as room temperature phosphorescence. The marginal increase in emission lifetime when degassed suggests potential for delayed character. Therefore, we shall explore this donor further in Chapter 7.

From this study, DPhCz-DMB (**4**) would seemingly make for a better EML than DBCz-DMB (**3**) in a TADF OLED, since delayed emissions are of the same wavelength as prompt emission (whereas DBCz-DMB's (**3**) delayed emissions shift by ~200 nm). Unfortunately, the poor chemical and thermal stability precludes its use in devices. The enhanced TADF character of tBu_2-CzOMe-$BMes_2$ (**6**) and tBu_2-$CzOMe_2$-$BMes_2$ (**7**) makes them much better OLED candidates – with the significantly higher PLQYs of tBu_2-$CzOMe_2$-$BMes_2$ (**7**) in the solid state making it particularly attractive.

Chapter 5 Novel carbazole - boron molecules and the impact of methoxy groups on non-covalent interactions

5.1 Introduction

Boron has been reported as a suitable component of electron-accepting moieties. Lee *et al*.[260] demonstrated that combining carbazole-based donors with dimesityl boron, separated by means of an ortho-substituted π-bridge, can yield blue emitters with high PLQYs and attractively high EQEs. In their work, Lee *et al*.[260] found tert-butyl carbazole to be particularly effective as a donor moiety when creating highly efficient TADF blue devices, with exceedingly narrow ΔE_{ST} energy gaps of just 82 meV and with an EQE of 26.1%. The emissions were 485 nm, with a PLQY of 92% under inert atmosphere when doped in DPEPO. Their XRD data suggests that, whilst the boron and nitrogen are orientated in close proximity to one another, they are too far apart to facilitate any interactions. Conversely, in a similar study using planar diboraanthacene (DBA) acceptor moieties and ortho-substituted carbazole based donors, Kumar *et al*.[227] suggest N-B interactions can occur at 2.87 – 2.93Å thanks to the overlapping of the nitrogen and boron's van der Waals radii. Kumar *et al*.'s carbazole based compounds, Cz2oDBA and the tert-butyl derivative BuCz2oDBA, exhibited photoluminescent emissions at 536 nm and 550 nm respectively, with FWHM of 79 nm in both cases when doped at 20% w.t. in CBP host films. The PLQY in these samples were 100% and 99%, respectively, when degassed. Devices incorporating Cz2oDBA reached an EQE of 26.6%, whereas the BuCz2oDBA devices reached 21.6 %.

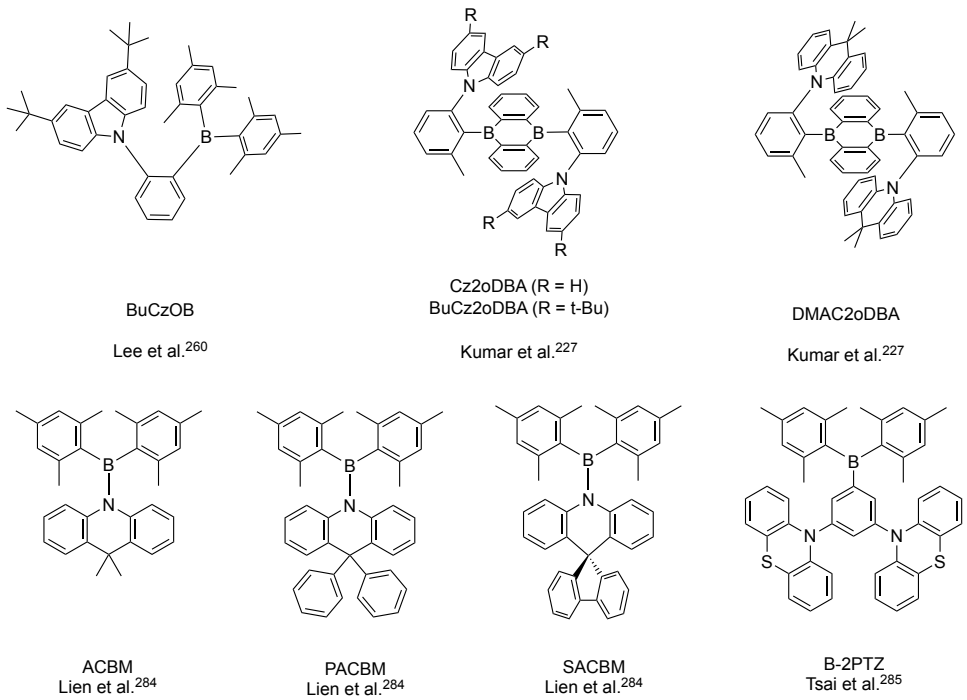


Figure 5-1 Boron-based structures supporting the potential for non-covalent interaction involving boron (top) and supporting simple donor to dimesitylboron acceptor structures (bottom).

On the basis that dimesityl boron can be coupled to acridine[286] and phenothiazine[287] to yield TADF (see Figure 5-1), whilst carbazole bonded to this acceptor lacks TADF, Ganesan *et al.*[220] sought to modify carbazole moieties with methoxy groups and a π-bridge in order to further separate the HOMO and LUMO and make carbazole a stronger donor moiety (by making its HOMO level shallower) to turn on the rISC mechanism (see Figure 5-2). Interestingly, they found TADF could be turned on simply by adding a single methoxy group to the carbazole moiety. Ganesan *et al.*'s[220] materials exhibited red-shifting of emissions upon addition of methoxy groups (in neat films, emissions are observed at 442 nm in CzBM-0, shifting to 481 nm in CzBM-1 where one methoxy group is added to the position adjacent to the nitrogen atom, PLQYs go from 30% to 32%, respectively). In devices, the same two molecules showed EQEs of 1.8% and 12.5%, respectively, demonstrating the interesting potential for methoxy groups on enhancing device properties.

Ganesan *et al.*'s[220] DFT calculations reveal good HOMO and LUMO separation, with a small degree of mixing on the π-bridge. It is well established that bulky groups attached to a π-bridge can further aid HOMO-LUMO decoupling[238], and in many cases, the π-bridge can be considered an extension of the donor moiety, with the HOMO often bleeding into this region. The π-bridge also increases donor strength by making the HOMO shallower.

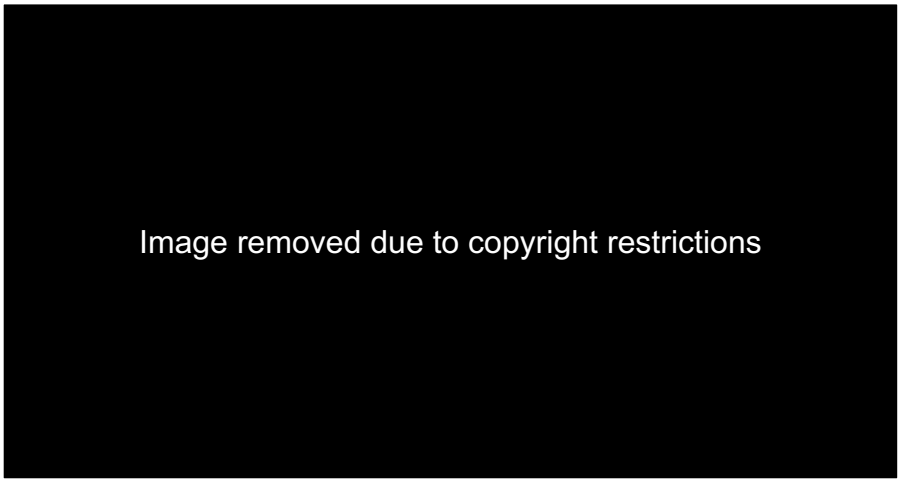


Figure 5-2 Dimesityl boron - carbazole derivatives synthesised by Ganesan *et al.*[220] incorporating methoxy groups in various positions upon the donor moiety (image reproduced from the 2020 paper).

With this in mind, it is likely that addition of methoxy groups directly to the π-bridge attached to a carbazole donor instead will have a three-fold benefit: namely, enhancing donor strength (potentially switching TADF on), applying a steric lock between the donor and acceptor (yielding a high dihedral angle and HOMO-LUMO separation), and potentially yielding non-covalent interactions with the boron (based on the findings of Chapter 4, with

the methoxy substituents on Dr Joseph Cameron's molecules, being here instead on a π-bridge, oriented at a more compatible angle towards the boron atom), thereby facilitating more effective charge transfer.

Kitamoto *et al*.[288] developed three, π-bridged emitters with 10H-phenoxaborin, a 3-coordinate boron acceptor, and carbazole, phenoxazine and dimethylacridine as the donors (see Figure 5-3 top). Their hypothesis was that steric repulsion of the hydrogens on the donors, would cause large dihedral angles with the π-bridge, as would the hydrogens on the acceptor. This is seemingly true in their DFT calculations for phenoxazine and dimethylacridine, however, the pentagonal centre of the carbazole moiety orients the 1 and 8 positioned hydrogens ever so slightly wide of any interaction with the π-bridge, yielding a reduced dihedral angle compared to the other two molecules.

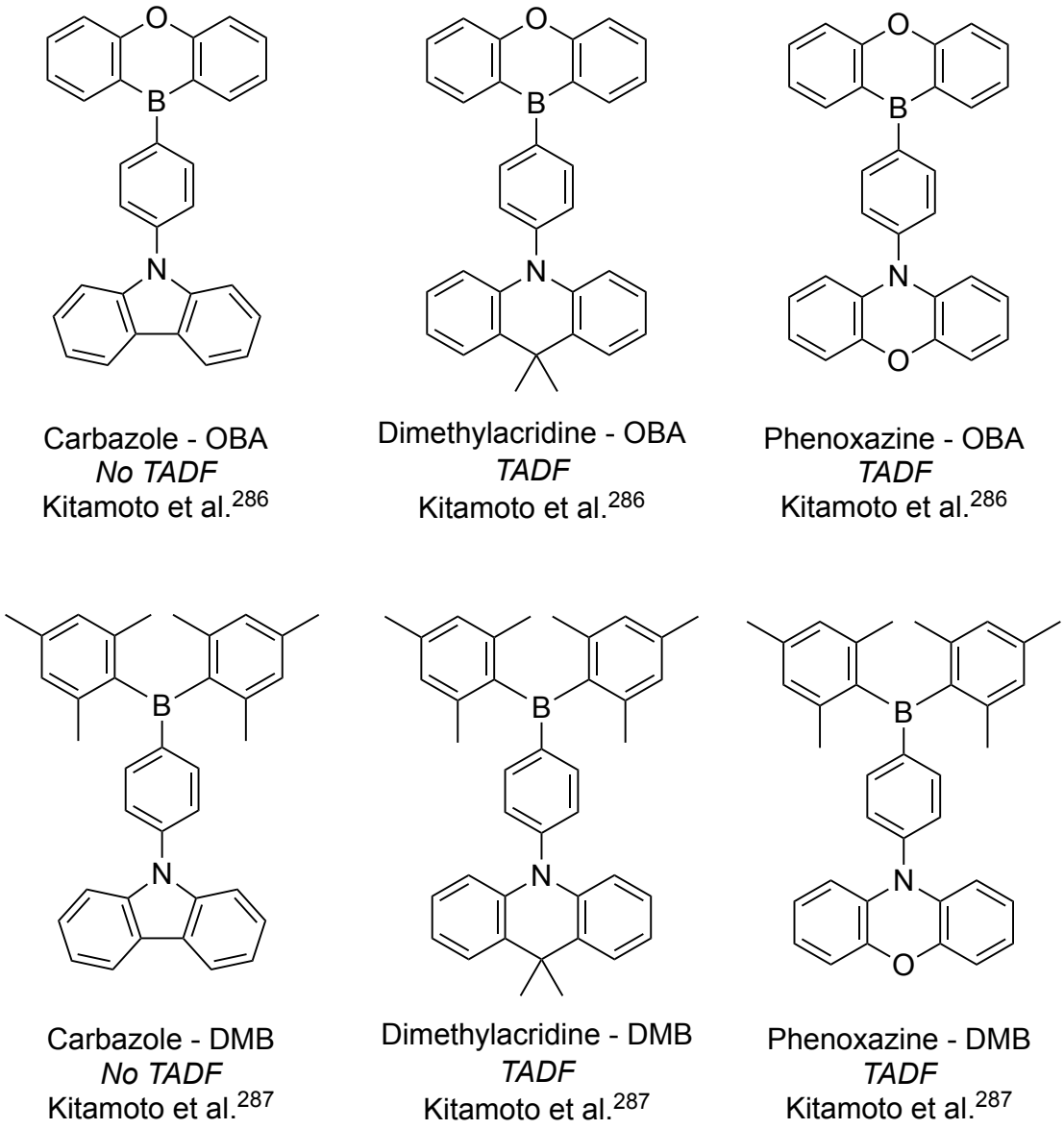
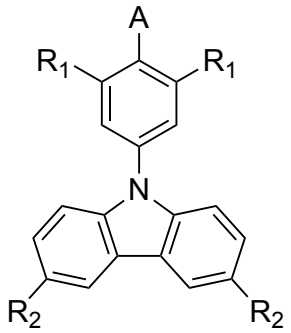


Figure 5-3 Structures of the boron-based emitters from Kitamoto *et al*.'s two papers[288,289].

Kitamoto *et al*.[289] returned to this a year later, this time swapping the acceptor moiety for the much more readily available dimesityl boron (see Figure 5-3, bottom). They observed strong solvatochromism in all three compounds (using the same donors as before), however it was less pronounced in the carbazole derivative, and the UV-spectra lacked the CT peak of the others. Furthermore, TCSPC studies revealed only prompt decay from the emissions with carbazole, with impressive TADF in the phenoxazine and dimethylacridine compounds.

Based on the success of the dimethylphenyl π-bridge used by Wu *et al*.[238], we propose that the separation of the HOMO and LUMO will be similarly enhanced by the incorporation of this donor in place of Kitamoto's choice, therefore leading to increased charge transfer character. Simultaneously, thanks to steric hindrance, this will potentially open up Kitamoto's choice of acceptors to TADF compatibility with carbazole derivatives.



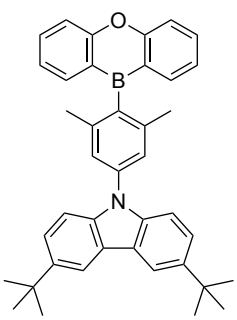
Adaption of Wu et al.'s donor

R_1 = Methyl / methoxy / phenoxy
R_2 = H / tert-butyl

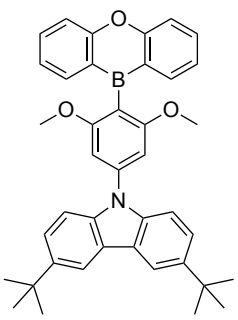
Figure 5-4 Generic structure of the Wu *et al*.[238] donor.

Incorporating bulky groups (such as methyl, methoxy and phenoxy) onto the π-bridge should support a larger dihedral angle between the donor and acceptor moieties (something that Kitamoto *et al*.'s work was lacking[288, 289]). Additionally, substitution of the methyl groups for methoxy should further aid charge transfer, increase the electron donating character of the donor as well as the steric hindrance between π-bridge and acceptor. At the very least this design should make the HOMO shallower in order to make the carbazole based donor comparable to Ganesan *et al*.'s[220] to facilitate TADF. On the bases of this, six molecules were planned for synthesis, tBu-DMP-Cz-OBA (**10**), tBu-DMeOP-Cz-OBA (**11**), tBu-DMP-Cz-DMB (**12**), tBu-DMeOP-Cz-DMB (**13**), and the phenoxy derivatives tBu-MPhOP-Cz-DMB (**14**) and tBu-DPhOP-Cz-DMB (**15**), the structures of which are shown in Scheme 5-1. The tert-butyl modification to carbazole was chosen for two reasons – firstly tert-butyl

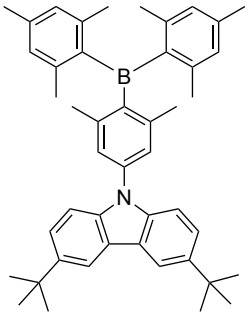
groups further enhance electron donating character of the donors to which they are bonded, and secondly, they aid solubility.



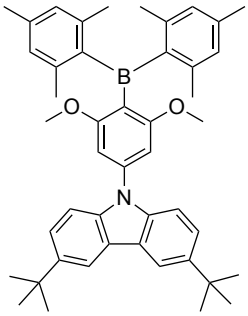
tBu-DMP-Cz-OBA
10



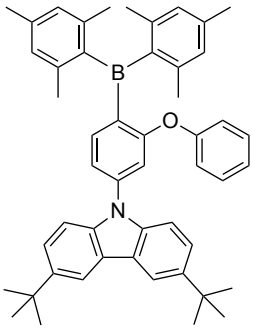
tBu-DMeOP-Cz-OBA
11



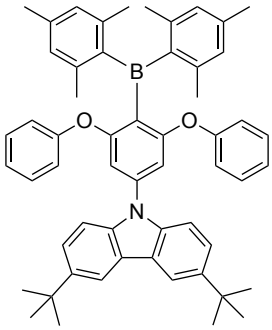
tBu-DMP-Cz-DMB
12



tBu-DMeOP-Cz-DMB
13



tBu-MPhOP-Cz-DMB
14



tBu-DPhOP-Cz-DMB
15

Scheme 5-1 Structure of all the compounds involved in this study. All were successfully synthesised and isolated, with the exception of tBu-DMeOP-Cz-OBA (11), which proved impossible to fully purify.

All molecules, with the exception of tBu-DMeOP-Cz-OBA (**11**), were successfully synthesised by myself, with the additional exceptions of tBu-MPhOP-Cz-DMB (**14**) and tBu-DPhOP-Cz-DMB (**15**), which were prepared by Dr Andrea Pinto. Additionally, approximately 10 mg of tBu-DMeOP-Cz-OBA (**11**) was eventually obtained by Dr Andrea Pinto, however further purification was unsuccessful. Nevertheless, it was pure enough for rudimentary solution photophysics to be performed to provide a rough idea as to how it compares to the rest of the series.

5.2 Experimental

5.2.1 General

All compounds were successfully synthesised with acceptable yields, with the noted exception of compound **11**. A possible reason for this is the nature of the environment surrounding boron being too rigid to accommodate the methoxy groups. The dimesityl rings in compound **13** have much greater degrees of rotational and translational freedom compared to the anthracene-like case of compound **11**. Lithiation of the methoxy donor was successful, as evidenced by the significant blue fluorescence upon addition of n-butyllithium to the solvated donor and the fact that the synthesis of compound **13** is demonstrably possible. Therefore, stability of the product of the coupling step is likely the cause of low yield, although 10-bromo-10H-dibenzo[b,e][1,4]oxaborinine is very air sensitive, so degradation of this material prior to the coupling step may also have hampered synthesis.

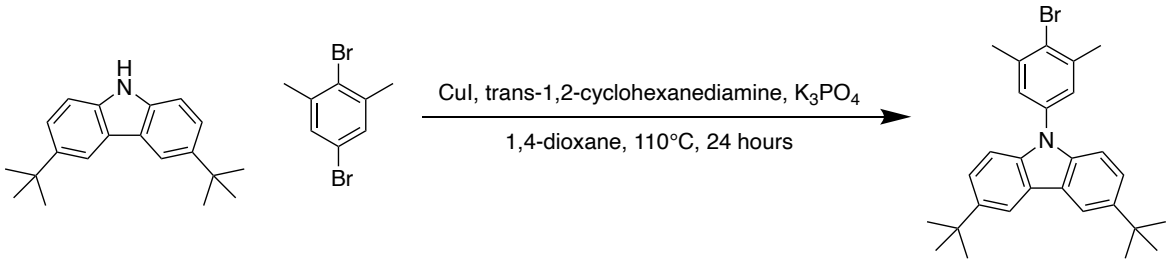
Further attempts were made to synthesise novel monomethoxy donor molecules, however their synthesis failed, possibly due to the influence of the methoxy group, despite numerous attempts to produce the material under different conditions.

5.2.2 Synthesis

Synthesis for the six molecules is divided into four stages:

- Synthesis of dimethyl donor
- Synthesis of dimethoxy donor
- Synthesis of B-O acceptor (10-bromo-10H-dibenzo[b,e][1,4]oxaborinine)
- Coupling of respective donors to their acceptors

The dimethyl donor was synthesised trivially using commercially available starting material, based on a procedure from the work of Stahl *et al*.[290] (see Scheme 5-2).

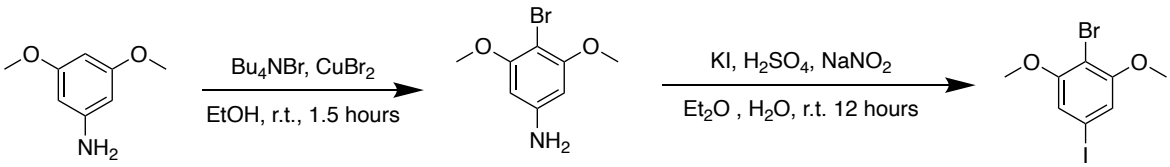


5.1 **5.2** **5.3**

40%

Scheme 5-2 Synthesis of 9-(4-bromo-3,5-dimethylphenyl)-9H-3,6-di-tert-butylcarbazole based on the work of Stahl *et al.*[290]

The methoxy donor proved somewhat more challenging to produce. A similar π-bridge to **5.2**, with a potential bromine leaving group for coupling to boron was not available, so a more long-winded approach was necessary.

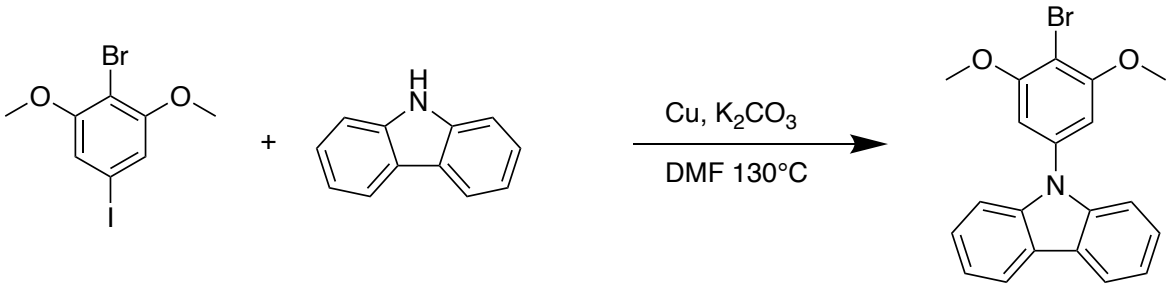


5.4 **5.5** **5.6**

40% **52%**

Scheme 5-3 Original synthesis of the methoxy π-bridge by adapting the work of Zhao *et al.*[291] and Fujihara *et al.*[292]

The π-bridge was synthesised using a modification on the approach reported by Zhao *et al*.[291] for the bromination of **5.4** to yield the intermediate **5.5**. This was followed by adapting an iodination procedure by Fujihara *et al*.[292] to yield the intermediate **5.6**. Both steps are illustrated in Scheme 5-3.



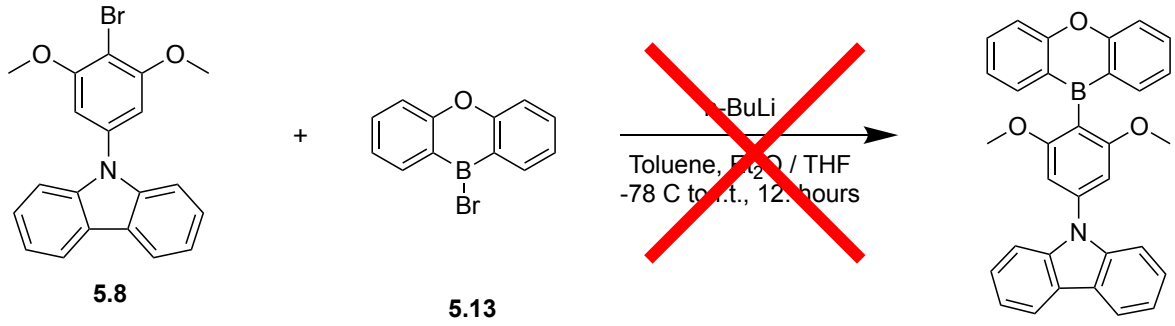
5.6 **5.7** **5.8**

49%

Scheme 5-4 Synthesis of the original methoxy donor achieved by trivially adapting Wu *et al.*'s copper catalysed amination method.[238]

Final assembly of the initial donor, **5.8** was completed *via* copper catalysed amination as performed in the original Wu *et al*.[238] paper (see Scheme 5-4).

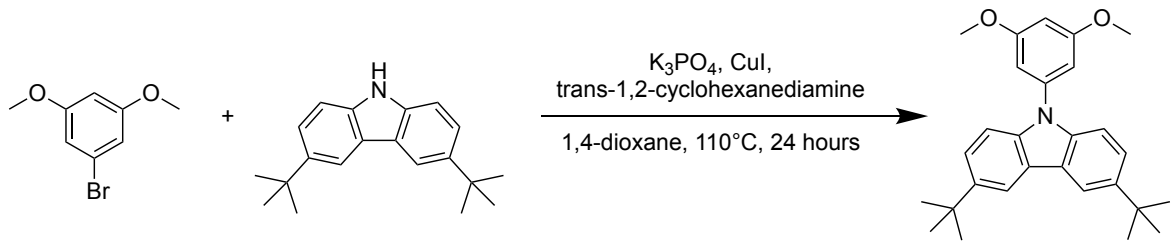
Whilst the yields in this three-step process were tolerable, compound depreciation was found to a significant obstacle, with low intermediate yields giving way to even smaller quantities of targets. Purification of **5.5** and **5.6** required exceptionally long column chromatography, with the product sticking to the silica gel well beyond the retention indicated by TLC.



5.8 **5.13** **5.14 b**

Scheme 5-5 Failed coupling of the methoxy donor to the 10-bromo-10H-dibenzo[b,e][1,4]oxaborinine acceptor.

Following this, lithiation or **5.8** and coupling to **5.13** (see Scheme 5-5) yielded a cloudy suspension owing to poor solubility, causing the synthesis to fail, regardless of whether a diethyl ether : toluene solvent mix was used, or the reaction carried out entirely in tetrahydrofuran.



5.9 **5.1** **5.10**

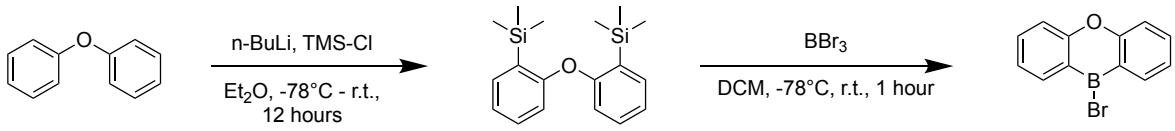
36%

Scheme 5-6 Synthesis of the tert-butyl derivative of the novel methoxy donor. Once again, using Stahl *et al*'s.[290] method.

An alternative approach was adopted adding tert-butyl groups to the 3 and 6 positions on the carbazole (see Scheme 5-6). This aids solubility and also reduces the number of potential additional lithiation sites (thereby allowing us to avoid multiple side products complicating the coupling step). In addition to this consideration, so as to reduce the long synthesis

process (and excessive quantities of solvent required for the column chromatography), an alternative commercially available π-bridge was sought. Compound **5.9** was obtained from Fluorochem at a reasonable price (£18 for 25g as of August 2024[293]) and coupling to 3,6-di-tert-butyl-9H-carbazole (**5.1**) was trivial *via* Ullmann coupling. As such, for subsequent coupling to boron, lithiation occurs *via* deprotonation on the central hydrogen on the π-bridge instead of lithium-halogen exchange. The initial reason for adopting this bromide free π-bridge is outlined further in Chapter 6, but suffice it to say its effectiveness was a serendipitous discovery when recycling the starting material from a similar failed coupling step.

The anthracene-like B-O acceptor unit (**5.13**) was synthesised in a two-step process from diphenyl ether (see Scheme 5-7).



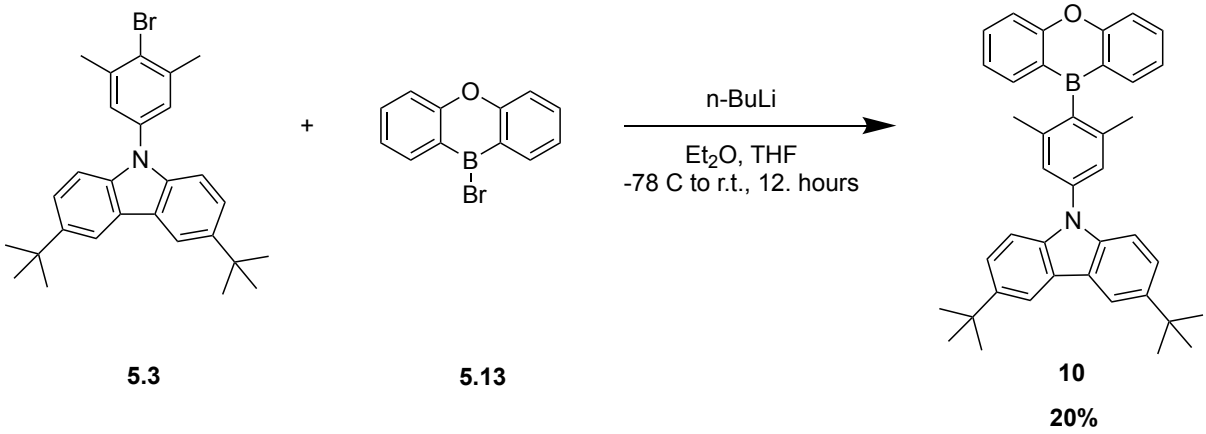
5.11 **5.12** **5.13**

53%

Scheme 5-7 Synthesis steps to the B-O acceptor moiety.

The silylation step was based on the work of Solé and Gabbaï[294], replacing their use of diphenyl sulfide with diphenyl ether. This yielded an oil which required no further purification after aqueous workup. Continuing to adapt Solé and Gabbaï's[294] work yielded **5.13** upon treatment of **5.12** with boron tribromide (also shown in Scheme 5-7). Compound **5.13** was found to be highly air and moisture sensitive (though not as sensitive as DBDBA in Chapter 6), so purification was attempted only by washing with dry hexane and filtration *via* a custom-built fritted filter stick to remove excess boron tribromide and hydrogen bromide, prior to use in the donor-acceptor coupling step (see Scheme 5-8) to form tBu-DMP-Cz-OBA (**10**).

Attempts to produce a methoxy derivative of compound **10** were, initially, unsuccessful, but was later achieved by Dr Andrea Pinto in ~10 mg, impure yield.

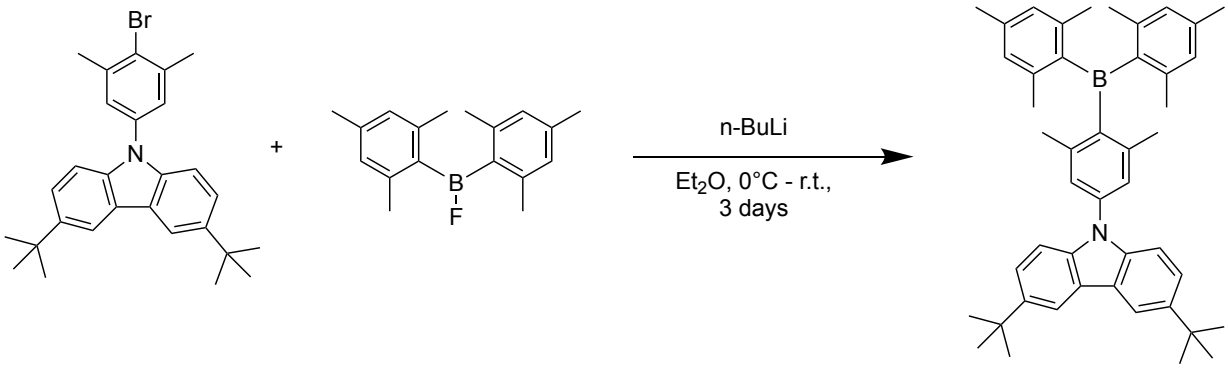


5.3 **5.13** **10**

20%

Scheme 5-8 Successful coupling of 5.3 to 5.13 to yield the B-O target compound 10. The lithium-halide exchange is based on Wu *et al*'s. [238] **procedure.**

The dimesityl boron compound, tBu-DMP-Cz-DMB (**12**) was synthesised by coupling the halogenated **5.3** to the commercially available acceptor, dimesitylboron fluoride (**4.2**) *via* lithium-halogen exchange (see Scheme 5-9).

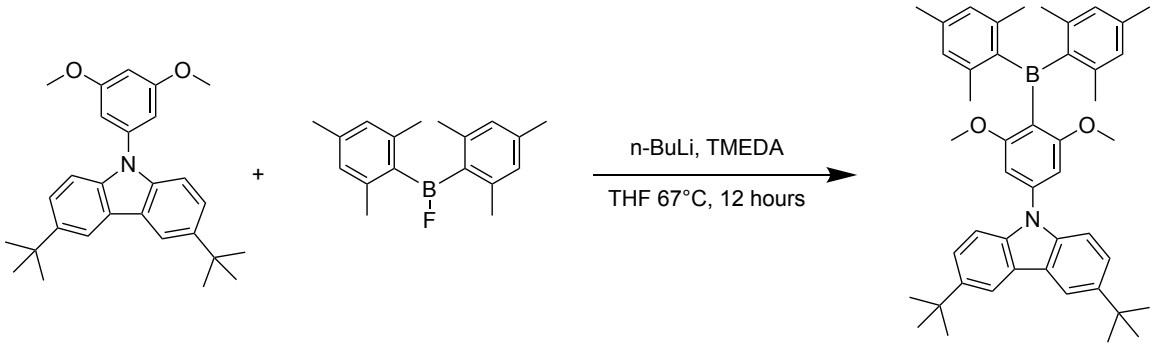


5.3 **4.2** **12**

31%

Scheme 5-9 Synthesis of tBu-DMP-Cz-DMB *via* lithium-halogen exchange.

Synthesis was successful, and a similar reaction, employing lithium-mediated deprotonation was adopted for the synthesis of the methoxy derivative, tBu-DMeOP-Cz-DMB (**13**) and is shown in Scheme 5-10.



5.10 **4.2** **13**

8.2%

Scheme 5-10 Synthesis of tBu-DMeOP-Cz-DMB *via* lithium mediated deprotonation of the methoxy donor, 5.10.

5.3 Results and discussion

5.3.1 Thermal properties

Since the thermal properties of organic molecules greatly influence OLED device lifetimes, as well as determine whether evaporation or solution-processing methods are best suited to device fabrication, thermogravimetric analysis (TGA) and differential scanning calorimetry (DSC) analysis was performed on the molecules in this study.

5.3.1.1 Thermogravimetric analysis and differential scanning calorimetry

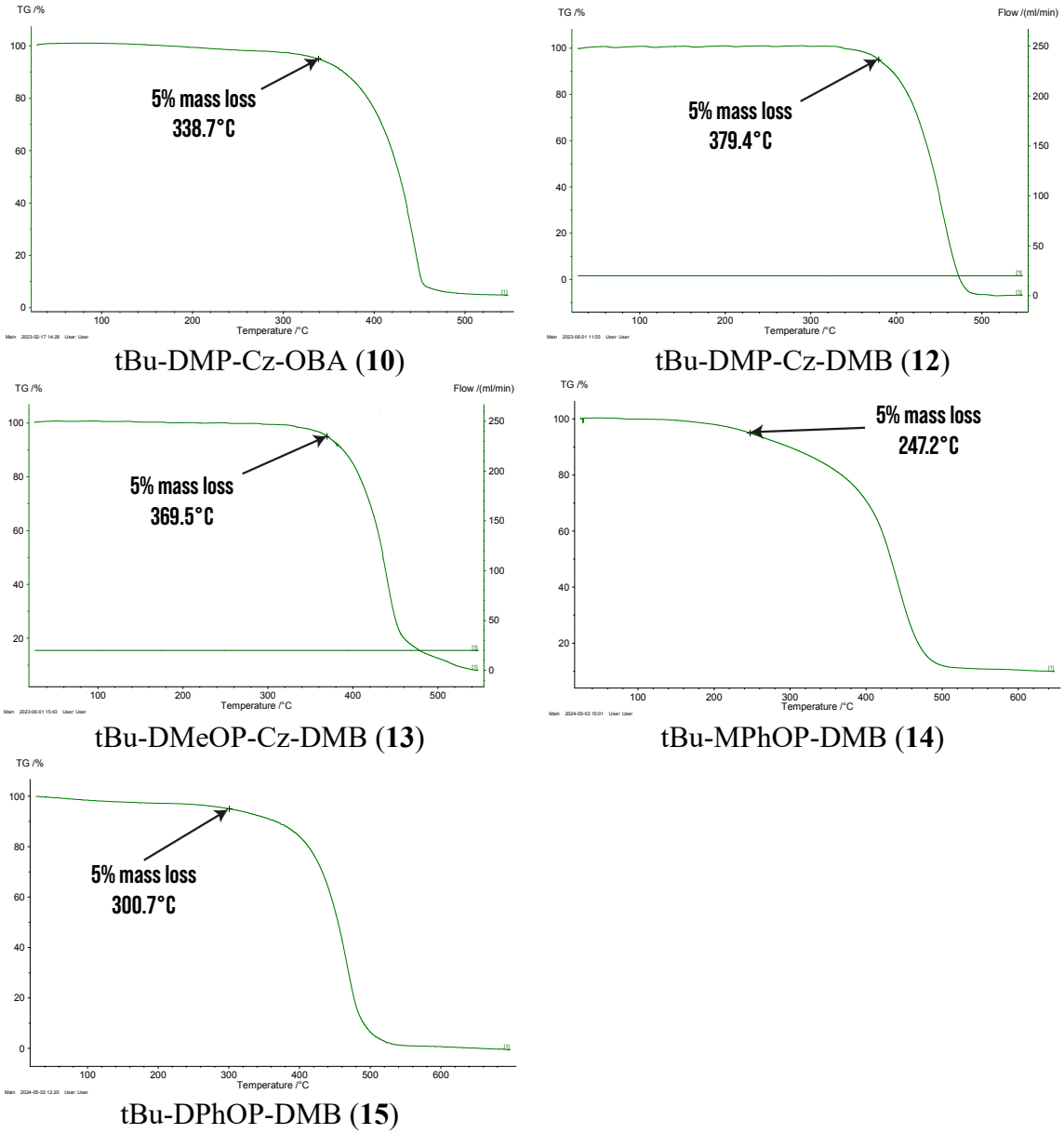
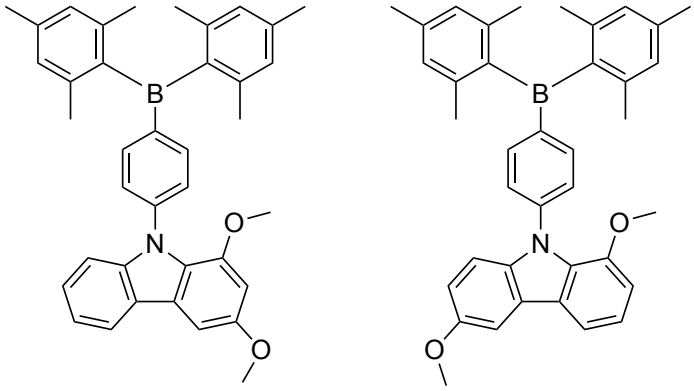


Figure 5-5 TGA plots for the purified compounds in this study.

Figure 5-5 shows the TGA plots for compounds **10** and **12**-**15**. Compound **11** was not analysed owing to its lack of purity and low quantity. The 5% mass loss for the three methyl and methoxy materials (compounds **10**, **12** and **13**) are 338.7°C, 379.4°C and 369.5°C, respectively. All three degradation temperatures are similarly high, however there is a 30.8°C increase when *9-oxa-10-boraanthracene* is switched for *dimesityl boron*, suggesting this acceptor yields more thermally stable materials. When the π-bridge is modified to incorporate methoxy groups in place of methyl, the degradation temperature decreases by 9.9°C. This slight change suggests that methoxy groups cause a slight decrease in stability, perhaps by steric effects, or resonance effects into the π-bridge making the boron-carbon bond easier to break (however, XRD data in Section 5.3.11 would appear to refute this owing to no appreciable change in the B-C bond length). Interestingly, the degradation temperature drops significantly by 68.8°C when the two methoxy groups are replaced by two phenoxy groups in compound **15**. With only one phenoxy group, a further drop in degradation temperature by 53.5°C is observed. Additional bulk by the peripheral phenoxy benzene rings would be causing steric hindrance with the mesityl rings on the acceptor moiety, leading to increased strain on the B-C bond connecting the donor's π-bridge to the acceptor, which leads to the lower temperature required to cause decomposition. Interestingly, the even bigger reduction in the temperature required to instigate decomposition for the mono-phenoxy compound suggests this compound is even less stable – despite the reduced steric hindrance. However, this can be explained by the additional room the dimesityl boron moiety has to reorient to accommodate the single bulky phenoxy group. In compound **10** and **13**, the single crystal XRD data suggest a slight kink to the B-π-bridge bond. This raises the probability that this would also be the case in compound **14**, but to a much greater degree, making the B-C connection much less stable, particularly with additional rotational degrees of freedom at higher temperatures. However, the XRD data discussed later in section 5.3.11, suggests that the kink to the structure of compound **14** is not noticeably different than for compound **10** or **13**, and is not present at all in compound **15**. This suggests that the thermal instability being greater in compound **14** is likely due to a combination of steric hindrance with the mesityl groups coupled with the kink across the molecule, and not down to one structural feature alone.



CzPMB-2 CzPMB-3

Figure 5-6 For comparison, Ganesan *et al.*'s[220] compounds CzPBM-2 and CzPBM-3 had lower decomposition temperatures.

For comparison, Ganesan *et al.*'s[220] compounds with no substituents on the π-bridge, CzPBM-2 and CzPBM-3, reached 5% mass loss at 287°C and 308°C, respectively. Since our molecules differ in that they possess no methoxy groups on the carbazole itself, only the π-bridge, it is clear that addition of steric hindrance on the π-bridge yields significantly greater thermal stability than afforded by increased donor character, since changing from methyl to methoxy yields minimal change.

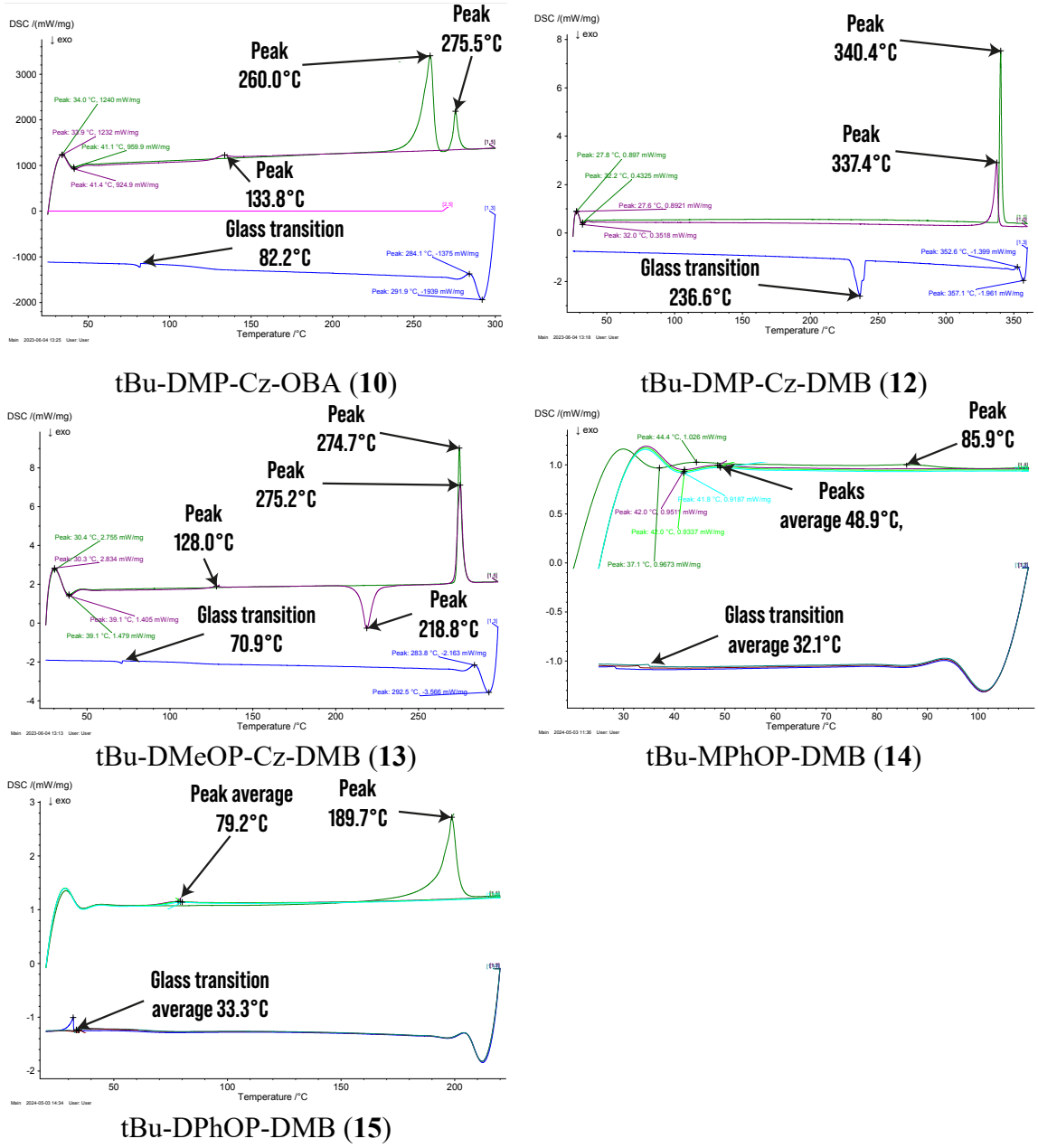


Figure 5-7 DSC plots for the four main compounds in this study. Dark green = First heating; blue = first cooling; purple = second heating. Peaks at the beginning and end of each plot are artefacts of the instrument.

Heat-cool cycles were performed for DSC analysis on the five compounds and are shown in Figure 5-7, with the first cycle to remove thermal history. We observe three processes in the plots – the melting point of the five materials: 260°C for compound **10** and 340.4°C and 274.7°C for compounds **12** and **13**, respectively, with 198.7°C seen clearly for compound **15**. Interestingly, the melting point peak for compound **14** is much shorter and broader than the other compounds at 85.9°C, which is slightly higher than the 76°C observed with the manual melting point instrument. This discrepancy may be more to do with the way the software detects peaks. In addition to melting points, the glass transition point is observed for the first three compounds: a small peak at 82.2°C for compound **10**, and more prominent

peaks at 236.6°C and 70.9°C for compound **12** and **13**, respectively. For compound **10** and **13** there is an additional transition peak at 133.8°C and 128.0°C, respectively, which is completely absent in compound **12**. Also seen are glass transition peaks for the phenoxy compounds - compound **14** has an average at 32.1°C, with compound **15** having an average of 33.3°C. In both these compounds, a small hump is seen at 48.9°C and 79.2°C for the monophenoxy and diphenoxy compound, respectively. This most likely come from polymorphic structural transitions in the solid state.

It is interesting how similar compounds **10** and **13** are with their glass transition temperatures and the presence of another transition peak. The aromatic rings of the anthracene-like acceptor in compound **10** are locked in a planar configuration owing to covalent bonding to the boron and oxygen atom. As such, any structural changes to the crystal structure *via* application of heat cannot rotate the aromatic rings in the acceptor moiety. This restriction could give rise to polymorphism as a lack of rotation of the benzene rings permits a stronger possibility of aromatic intermolecular interactions instead. The methoxy groups on compound **13** are orientated close enough such that non-covalent interactions with the boron atom are possible (see Section 5.3.11). Therefore, rotation of the dimesityl boron acceptor moiety is likely to be much more restricted when compared to compound **12**. This rigidity could give rise to an increased chance of polymorphism in the crystal state[295], hence the 128.0°C peak for compound **13**, which is absent in compound **12**.

Table 5-1 Summary of key thermal properties.

Compound	Melting point (°C)	Glass transition temperature (°C)	Structural transition temperature (°C)	5% mass loss (°C)
tBu-DMP-Cz-OBA (10)	260.0	82.2	133.8	338.7
tBu-DMP-Cz-DMB (12)	340.4	236.6	-	379.4
tBu-DMeOP-Cz-DMB (13)	274.7	70.9	128.0	369.5
tBu-MPhOP-Cz-DMB (14)	76 / 85.9	32.1	48.9	247.2
tBu-DPhOP-Cz-DMB (15)	198.7	33.3	79.2	300.7

The dip in stability by applying methoxy groups to the π-bridge structure must therefore be taken into consideration when designing molecules to exploit potential B-O non-covalent interactions, so as to avoid the risk of developing issues with device lifetimes. The bulkiness of the phenoxy groups suggests a potential limit in the scale of functional groups one can

exploit for non-covalent interactions with boron acceptor cores and that care must be taken in the design phase not to risk using substituent groups that may result in easier molecular decomposition.

5.3.2 Optical and electrochemical properties

To determine the influence of methoxy or phenoxy groups potential non-covalent interactions, as well as changing the acceptor moiety, on the optical and electrochemical properties of the compounds, the UV-vis absorption, photoluminescence, cyclic voltammetry, quantum yield and TCSPC lifetime measurements were performed on all five compounds. The main UV-vis absorption and photoluminescence results are shown in Table 5-2 and a summary of the electrochemical properties can be found in Table 5-3, with sections 5.3.4 and 5.3.8 for cyclic voltammetry and TCSPC studies respectively.

Table 5-2 Summary of optical properties.

Molecule	λ_{abs} (nm)[a]	λ_{pl} (nm) [a]	FWHM (nm)	$E_{g\ opt}$* (eV)	S_1** (eV)
tBu-DMP-Cz-OBA (10)	346, 334(sh)	388, 405(sh)	32	3.45	3.35
tBu-DMP-Cz-DMB (12)	372, 346, 334, 297	402	28	3.15	3.17
tBu-DMeOP-Cz-DMB (13)	348, 335, 298	386	29	3.45	3.38
tBu-MPhOP-Cz-DMB (14)	366, 347, 330, 296, 290(sh)	398, 415(sh)	29	3.13	3.26
tBu-DPhOP-Cz-DMB (15)	348, 335(sh), 297, 285, 261	404, 422(sh)	29	3.29	3.22

[a] Measured in methylcyclohexane, *taken from onset of main λ_{abs} peak in methylcyclohexane (hexane for tBu-DMP-Cz-OBA), (in brackets from most intense peak), **taken from onset of λ_{PL} peak in methylcyclohexane (hexane for tBu-DMP-Cz-OBA), † from CT shoulder.

Table 5-3 Summary of electrochemical properties.

Molecule	E_{ox} (V)	E_{red} (V)	HOMO (eV)	LUMO (eV)	$E_{g\ chem}$ (eV)
tBu-DMP-Cz-OBA (10)	0.75	-2.43	-5.55	-2.37	3.18
tBu-DMP-Cz-DMB (12)	0.73	-2.57	-5.53	-2.24	3.29
tBu-DMeOP-Cz-DMB (13)	0.76	-2.73	-5.56	-2.07	3.49
tBu-MPhOP-Cz-DMB (14)	0.81	-2.26	-5.61	-2.54	3.07
tBu-DPhOP-Cz-DMB (15)	0.80	-2.33	-5.60	-2.47	3.13

Solution PLQY measurements were performed in dry toluene, both exposed to air and degassed by bubbling argon through it for twenty minutes. Thin films were prepared in a variety of polar and non-polar hosts, as well as neat films, to observe the influence on molecular environment on quantum yield. The combined results of which are shown in Table 5-4.

Table 5-4 Summary of solution and solid-state PLQY measurements.

Molecule	Host/Solvent	PLQY Air (%)	PLQY Argon (%)
tBu-DMP-Cz-OBA (10)	Toluene	18	26
	(298 nm)	33	79
	Thin Film	47	57
	(298 nm)	50	58
	Zeonex	30	21
	mCP	46	61
	DPEPO	63	80
	PVK	38	58
	CPB	56	65
tBu-DMP-Cz-DMB (12)	Toluene	47	43
	Pure film	39	27
	Zeonex	20	22
	mCP	21	20
	DPEPO	37	38
tBu-DMeOP-Cz-DMB (13)	Toluene	27	30
	Pure film	20	15
	Zeonex	18	13
	mCP	28	32
	DPEPO	24	31
tBu-MPhOP-Cz-DMB (14)	Toluene	56	70
	Pure film	70	77
	Zeonex	38	55
	mCP	69	70
	DPEPO	39	59
tBu-DPhOP-Cz-DMB (15)	Toluene	48	69
	Pure film	37	41
	Zeonex	37	34
	mCP	43	43
	DPEPO	37	42

In the methyl and methoxy dimesityl boron compounds tBu-DMP-Cz-DMB (**12**) and tBu-DMeOP-Cz-DMB (**13**), the solution PLQYs are moderate, with no significant changes when degassed with argon. The same lack of change is also present in the solid state thin films, all of which demonstrate poorer PLQYs in comparison to the solution measurements. This suggests a lack of TADF in these two compounds and that emissions are only from prompt fluorescence.

The PLQYs of the derivatives with phenoxy groups attached to the π-spacer, tBu-MPhOP-Cz-DMB (**14**) and tBu-DPhOP-Cz-DMB (**15**), are much higher in solution, with noticeable increases in intensity when degassed. This suggests the operation of photophysical processes susceptible to oxygen quenching. In the pure film and host matrix samples, this oxygen sensitivity is also observed. Interestingly, in all cases the monophenoxy compound presents marginally better performance when degassed compared to the diphenoxy compound. This suggests the potential for TADF, or indeed at the very least, triplet states being used in the photophysical process.

Swapping the acceptor in the dimethyl π-spacer compound with a boron-bridged anthracene-like moiety, tBu-DMP-Cz-OBA (**10**), results in a drop in PLQY in toluene when excited at the main absorption wavelength (with an increase when degassed). However, using a higher energy wavelength excitation source yields a higher PLQY, with dramatically increased quantum yield when degassed. In the solid state the degassed PLQYs are significantly higher than all other compounds in this study. This suggests the B-O acceptor is a much better match for the donor for making highly efficient emitters. The distinct impact of oxygen quenching on this compound also suggests that triplet states are involved in its photophysics.

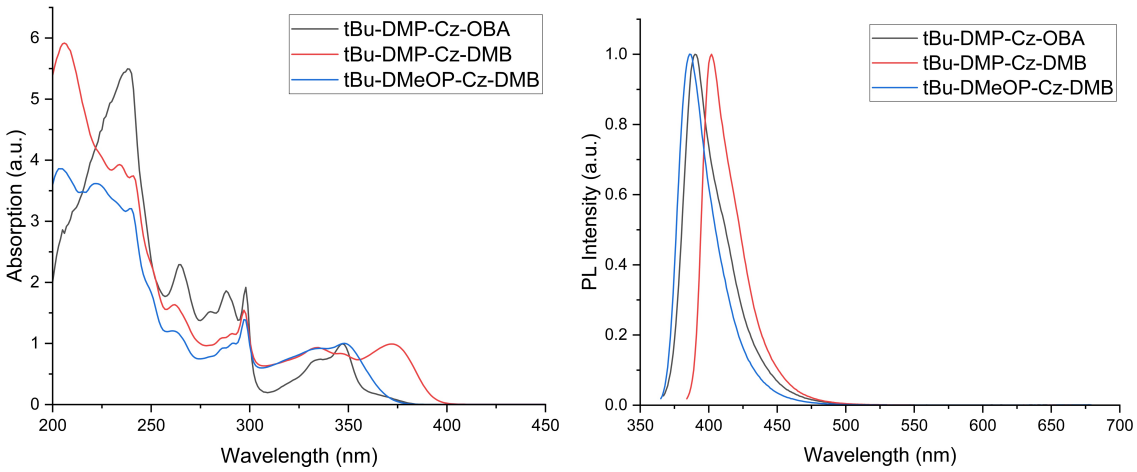


Figure 5-8 UV-vis absorption (left) and photoluminescence (right) of compounds 10, 12 and 13 in methylcyclohexane.

The photoluminescence properties of **10**, **12**, and **13** are particularly interesting (see Figure 5-8). Their PL wavelengths in methylcyclohexane are 386 nm, 388 nm and 402 nm, respectively, with FWHMs of 29 nm, 32 nm and 28 nm respectively (see Figure 5-8). If truly TADF, these would represent some of the bluest and narrowest non-MR-TADF emitters reported to date[296,297]. This is likely due to high dihedral angles between the donor and acceptor moieties being maintained by steric hindrance from the substituents of the π-

bridges, preventing rotational freedom. The broad absorption peaks at 348 nm, 346 nm and 372 nm in **10**, **12** and **13**, respectively, suggest charge transfer character in all three compounds[277].

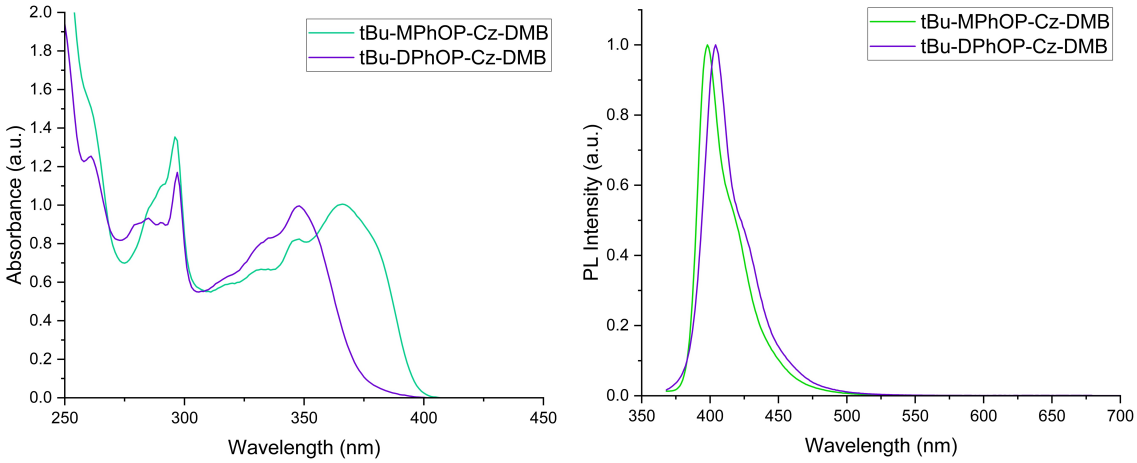


Figure 5-9 UV-vis absorption (left) and photoluminescence (right) spectra of compounds 14 and 15 in methylcyclohexane.

Comparing the phenoxy compounds in the non-polar solvent, methylcyclohexane, we see very blue emission peaks at 404 nm for the diphenoxy compound and 398 nm for the monophenoxy compound (see Figure 5-9). Despite the bulky phenoxy groups, and the added degree of rotational freedom that they present, the FWHM of the emission is identical to that of the dimethoxy compound **13** at 29 nm. The broad absorption at 366 nm for the monophenoxy compound and 348 nm for dimethoxy compound also suggests CT character. In both compounds, there is an appearance of vibronic character in the emissions with shoulders at 415 nm and 422 nm for the monophenoxy and diphenoxy compounds, respectively, which is not visible in the more polar solvents (see Figure 5-16). As with the methyl and methoxy compounds in solution monophenoxy and diphenoxy compounds have the potential of being among the bluest and narrowest FWHM, non-MR-TADF, TADF emitters to date.

The free donors and acceptors were dissolved in dry toluene in order to compare their UV-vis absorption to that of the target compounds. Owing to the air and moisture sensitivity of the 10-bromo-10H-dibenzo[b,e][1,4]oxaborinine (**5.13**) acceptor unit, UV-vis was not obtained for the acceptor of compound **10**.

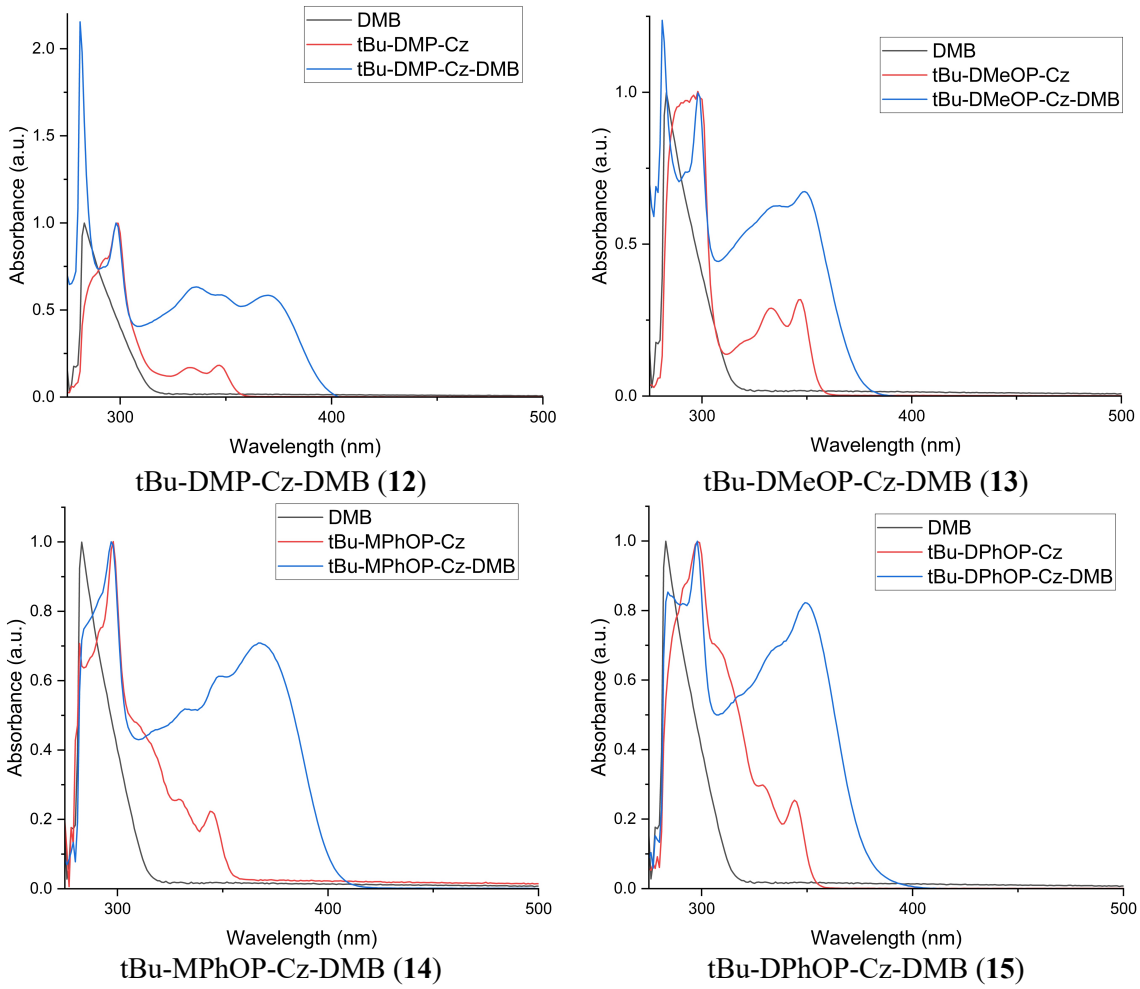


Figure 5-10 UV-vis spectra of tBu-DMP-Cz-DMB (12), tBu-DMeOP-Cz-DMB (13), tBu-MPhOP-Cz-DMB (14) and tBu-DPhOP-Cz-DMB (15) and their respective donor- and acceptor-free molecules in dry toluene.

Each of the compounds studied shows the characteristic 283 nm peak associated with the sample of dimesitylboron fluoride (albeit ranging from 281-284 nm). In compound **14**, this peak is just about visible as a shoulder, being dwarfed somewhat by the neighbouring 297 nm peak and 291 nm shoulder.

Table 5-5 Summary of the UV-vis spectra of free donors and acceptors in dry toluene compared with the spectra of the target compounds.

Molecule	Acceptor λ_{abs} (nm)	Donor λ_{abs} (nm)	Product λ_{abs} (nm)*
tBu-DMP-Cz-DMB (12)	283	347, 333, 298, 293,288(sh)	370, 347, 336, 298, 281
tBu-DMeOP-Cz-DMB (13)	283	347, 333, 320(sh), 298	349, 334, 320(sh), 298, 281
tBu-MPhOP-Cz-DMB (14)	283	345, 329, 310(sh), 298, 292(sh), 282	368, 348, 333, 318(sh), 297, 291(sh), 284(sh)
tBu-DPhOP-Cz-DMB (15)	283	344, 329, 307(sh), 298, 292(sh), 288(sh)	350, 336(sh), 317(sh), 298, 291(sh), 284

In compounds **12** and **13**, their respective donor compounds are superimposed upon the product molecule's absorption. In the dimethyl compound, the absorption wavelengths in the free donor at 347, 333 and 298 nm shift to 347, 336 and 298 nm. Compound **13** has a very similar absorption profile to its free donor with peaks at 349, 334, 320(sh), 298 nm for the product and the same four remaining identical, save for a minor blue shift of the 334 nm peak to 333 nm. Both compounds also have the distinct peak from dimesityl boron (281 nm in both cases, blue shifted from 283 nm). The presence of these peaks closely associated with the pure donor and acceptors suggests good decoupling of the HOMO and LUMO in both molecules[277]. Interestingly, compound **12** possesses an additional peak at 370 nm, which may be of CT nature, further supporting the good HOMO and LUMO separation. This peak is also dependent on solvent polarity, *i.e*. solvatochromic, as is shown in section 5.3.6, which further supports this designation of that peak as being charge transfer in nature. Indeed, the large solvatochromic shifts seen in section 5.3.6 further support the suggestion of HOMO-LUMO separation giving rise to CT character.

Looking at the phenoxy compounds, the dimesityl boron peak is less visible, appearing as more of a shoulder at 284 nm in both cases. Again, superimposition of the donor peaks is clear for the monophenoxy compound **14**, with the donor showing 345, 329, 310(sh), 298, 292 nm (sh) and the product showing 348, 333, 318(sh), 297, 291 nm (sh), suggesting good HOMO and LUMO separation[277]. These all red-shift by ~1-8 nm, along with an additional, large peak showing up at 368 nm. The diphenoxy compound **15**, on the other hand, shows only one superimposed peak from the donor at 298 nm and from the acceptor moiety at 288 nm, and is therefore likely to have more mixing of the HOMO and LUMO[277]. (although it is possible that the large, long wavelength CT peak may be concealing the donor's other peaks).

5.3.3 Solid-state photoluminescence properties

To further explore the photophysical properties of the compounds in this study, solid-state pure film and host-matrix samples were prepared upon quartz substrates *via* drop-casting from toluene and their UV-vis absorption and photoluminescence spectra are reported in Figure 5-11.

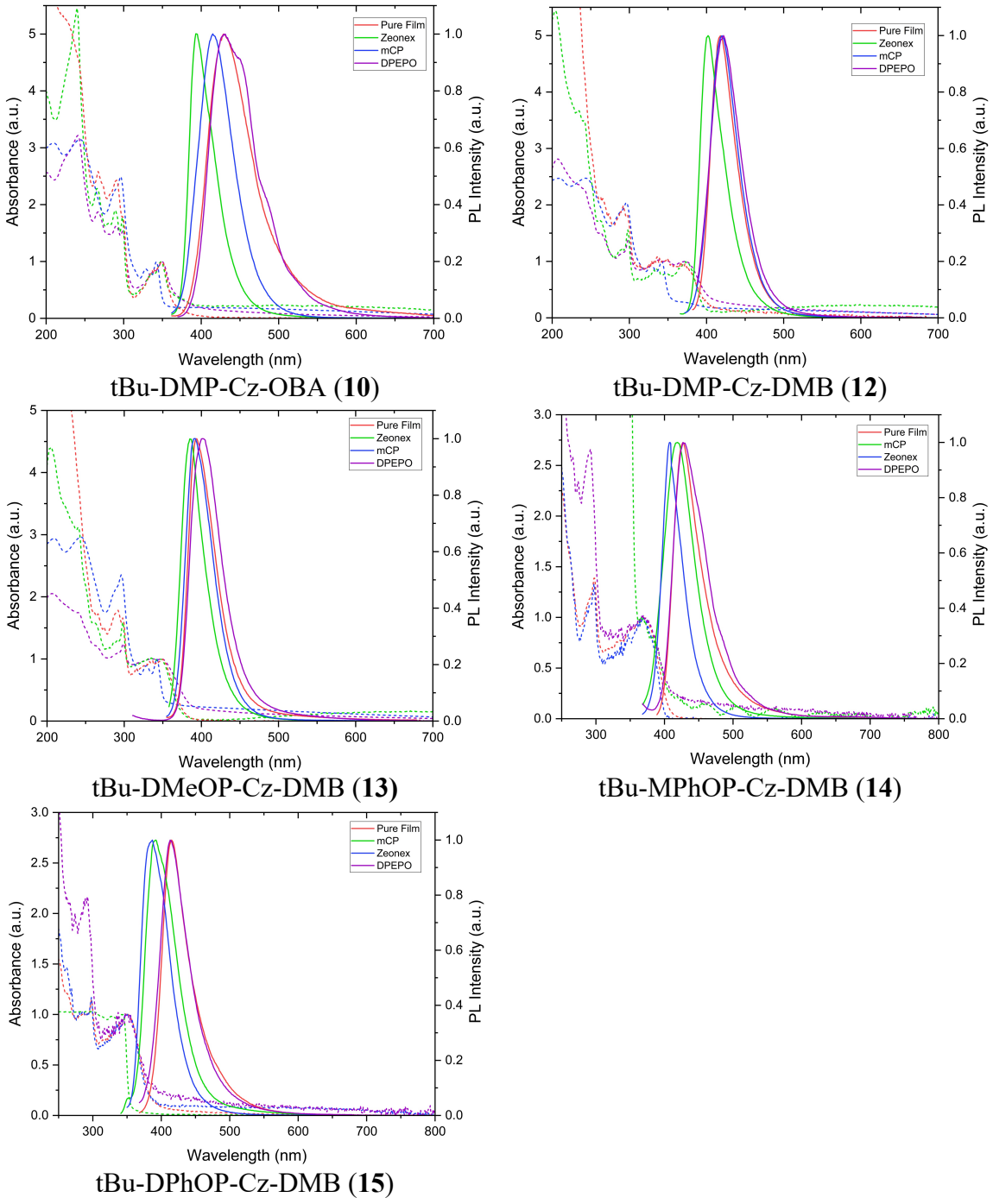


Figure 5-11 Solid-state UV-vis absorbance and PL spectra in 5% w.t. doped films and pure films.

All compounds exhibit deep blue/purple photoluminescence in the solid state – both as neat films and in host matrices. The polarity of the host matrices has a solvatochromic influence on emissions (with red-shifts in the more polar solvents), but this is most pronounced in compound **10**. The UV-vis absorption and photoluminescence properties are summarised in Table 5-6.

In the solid state (neat film), compound **13** is the bluest emitter with a λ_{PL} of 393 nm, followed by compounds **15**, **12**, **10** and **14**, with 415 nm, 419 nm, 421 nm and 427 nm, respectively. The absorption spectra follow a seemingly unrelated order of increasing absorbance: **13** = **10** > **15** > **14** > **12**. This trend in solid-state absorbance is almost identical to that observed in methylcyclohexane, albeit with compound **10** being the lowest in solution measurements.

Despite varying solvatochromism, the spectral features of compounds **12** and **13** are largely similar. However, for compound **10** we observe additional vibronic characteristics appearing in the PL of the DPEPO samples. This is also visible in compound **14** (and to a much lesser extent, compound **15**), despite the different acceptor moieties.

The lack of bulky mesityl groups around the boron atom in compound **10** means increased intermolecular interactions are possible between the molecules in the solid state, hence much broader emissions compared to the dimesityl boron compounds. The same is true when comparing compound **13** to its diphenoxy counterpart, compound **15**. The thin film emissions increase in their FWHM by 5, 12, 3 and 12 nm for pure films, Zeonex, DPEPO and mCP, respectively, and the λ_{PL} red-shifts by 22, 1, 12 and 4 nm, respectively. These alterations in PL properties are larger in the diphenoxy compound and suggests that it is interacting slightly more with its surroundings than its dimethoxy counterpart[298]. This could be due to π-π interactions between the host material and the phenoxy rings.

Table 5-6 Summary of solid-state PL properties.

Molecule	Host matrix	Abs (nm)	PL (nm)	FWHM (nm)	S_1 (eV)
tBu-DMP-Cz-OBA (10)	**Pure Film**	349, 337(sh)	421	46	3.19
	Zeonex	348, 335(sh) 297, 289, 265, 239	394	38	3.33
	DPEPO	349, 338(sh), 298(sh), 291, 267	430, 449(sh), 481(sh), 517 (sh)	67	3.20
	mCP	342, 328, 295, 289(sh), 244, 209	415	53	3.30
	PVK	345	421	53	3.22
	CPB	344, 331	421	51	3.22
tBu-DMP-Cz-DMB (12)	**Pure Film**	373, 349, 337, 299, 290(sh), 263, 240(sh), 233, 206	419	39	3.18
	Zeonex	373, 348, 335, 298, 262, 241, 235, 204	402	36	3.28
	DPEPO	370, 336, 292, 261(sh)	422	46	3.23
	mCP	367(CT), 341, 328, 296, 287(sh), 244, 207	420	42	3.25
tBu-DMeOP-Cz-DMB (13)	**Pure Film**	349, 336, 299, 290(sh), 263(sh), 240, 206	393	41	3.37
	Zeonex	348, 334, 298, 261, 240, 205	386	35	3.47
	DPEPO	349, 333, 291, 263(sh)	402	45	3.36
	mCP	343, 328, 296, 287(sh), 244, 209	391	40	3.36
tBu-MPhOP-Cz-DMB (14)	**Pure Film**	369, 348, 334, 298	427	46	3.12
	Zeonex	369, 346, 296	408	35	3.26
	DPEPO	369, 336, 292, 275, 265	429, 450(sh), 483(sh)	56	3.15
	mCP	368, 342	418	53	3.32
tBu-DPhOP-Cz-DMB (15)	**Pure Film**	351, 337(sh), 298, 261(sh)	415	46	3.23
	Zeonex	352, 337(sh), 298, 262	387	47	3.48
	DPEPO	349, 337, 291, 264(sh)	414	48	3.29
	mCP	343, 328	392, 403(sh)	52	3.45

5.3.4 Electrochemical properties

In order to ascertain the oxidation and reduction potentials and hence HOMO and LUMO energies, cyclic voltammetry was performed on each compound in anhydrous tetrahydrofuran or acetonitrile at a concentration of ~1×10^{-4} M with 0.1 M tetrabutylammonium hexafluorophosphate used as the electrolyte. They provided estimates for the electron affinity from the reduction plot and ionisation energy from the oxidation plot after reference to a ferrocene external standard (see Figure 5-12). Electrochemical studies of all five purified molecules were performed, with a scan rate of 0.1 V s^{-1} and sensitivity varying between 1E-5 and 1E-6.

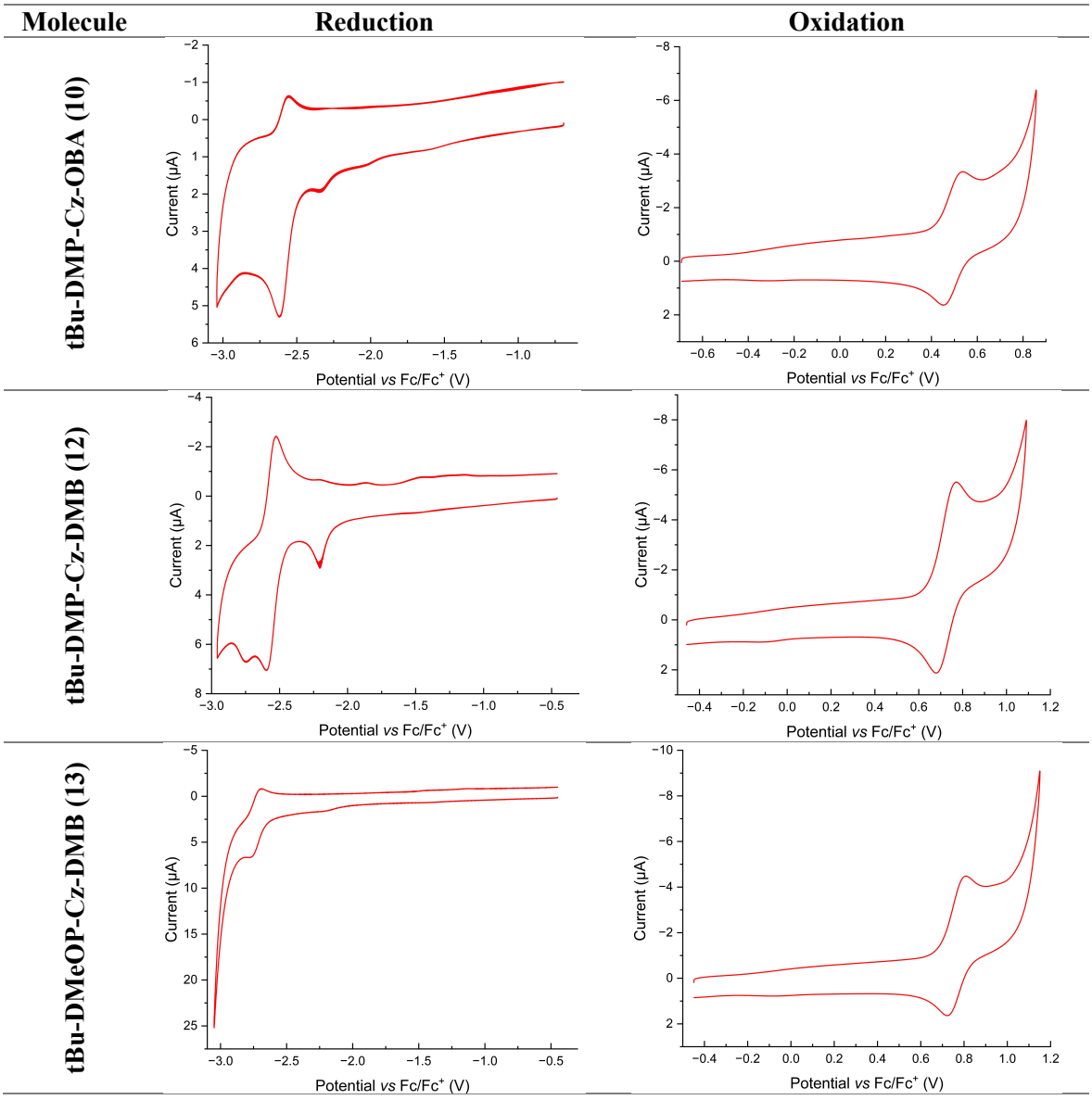


Figure 5-12 Cyclic voltammograms of the compounds 10, 12 and 13. Each measured in dry THF and 0.1M tetrabutylammonium hexafluorophosphate was used as the electrolyte. EA, IP, HOMO / LUMO energies were calculated referenced against the $E_{1/2}$ of the Fc/Fc^+ redox couple.

Compounds **10** and **12** exhibited irreversible reduction waves at -2.4 V and -2.6 V, respectively, with compound **13**'s reduction being reversible at -2.7 V. All three compounds exhibited oxidation waves between at 0.75 V, 0.73 V and 0.76 V for **10**, **12** and **13**, respectively. Changing the acceptor from OBA to DMB results in a negligible change in HOMO (0.02 eV), however the LUMO increases by 0.13 eV. Since the overall structure of the donor moiety isn't changing in all three of the molecules, it stands to reason that the overall energy of the HOMO would remain largely unchanged (since it is mostly upon the donor where the HOMO is located). The electron-donating character of the methoxy groups do make the donor more electron donating, however since they are only really donating into the π-bridge, and the dihedral twist between the donor and π-bridge serves to decouple the two regions somewhat, the change in HOMO energy is only minimal (0.03 eV). On the other hand, we observe a raising of the LUMO energy between compounds **12** and **13** (0.17 eV). Since their acceptor moieties are the same, this raising of the LUMO energy can be explained by the fact that the LUMO may be extending into the π-bridge somewhat, as Wu *et al*.[238] observed in their donor moiety π-bridges (see section 5.3.10 for our work). In this case, the methoxy groups would make the acceptor a poorer acceptor and raise its LUMO energy. These trends (with the exception of compound **10**) are reflected in the HOMO and LUMO energies from the DFT calculations in section 5.3.10.

Swapping the acceptor moiety however, comparing compounds **12** and **10**, we observe, once again, very little impact upon the HOMO energy (0.02 eV), owing to identical donors in each molecule. However, this time the LUMO energy drops by 0.13 eV. In this instance, the difference is undoubtedly due to OBA being a stronger acceptor moiety than dimesityl boron.

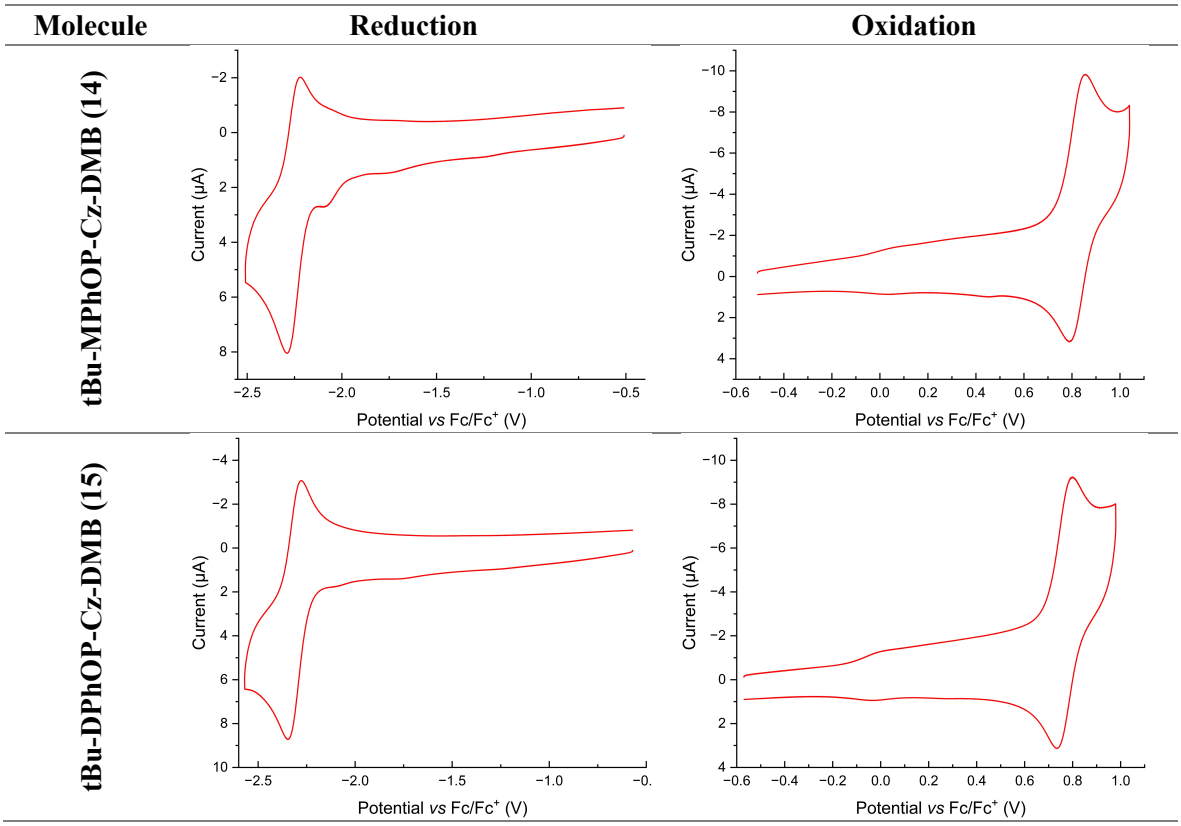


Figure 5-13 Cyclic voltammograms of the phenoxy compounds in this study. Each measured in THF with tetrabutylammonium hexafluorophosphate as the electrolyte. EA, IP, HOMO and LUMO energies calculated with reference to a ferrocene external standard.

Swapping the dimethoxy groups for diphenoxy results in the HOMO energy deepening by 0.04 eV and the LUMO lowering by a larger degree by 0.40 eV (see Figure 5-13). This results in the E_g narrowing by 0.36 eV. This can be explained by the TD-DFT calculations in section 5.3.10, where the HOMO is shown to be located upon the donor and π-bridge but does not spread into either of the phenoxy groups at all. However, the LUMO does spread into the available space of the phenoxy groups, which are not present in the dimethoxy compound, thus lowering the LUMO energy by stabilising this molecular orbital. Interestingly, going from two to one phenoxy group deepens the HOMO by just 0.01 eV but deepens the LUMO further still by 0.07 eV. These observations are in good agreement with the trends observed in the TD-DFT calculations in section 5.3.10. The same trend is observed for the optical gap too, going from 3.45 eV with two methoxy groups to 3.29 eV with two phenoxy groups, and narrowing further to 3.13 eV when just one phenoxy group is present.

5.3.5 Molar absorption coefficient

In order to explore the origins of the transitions associated with the UV-vis peaks of the five compounds, each compound was dissolved in dry toluene and several dilute concentrations made up to produce UV-spectra at each concentration. This was used to determine the molar absorption coefficients of each wavelength.

tBu-DMP-Cz-OBA (10)

tBu-DMP-Cz-OBA (**10**) exhibits a broad initial peak at 347 nm, the tail on the long wavelength side of which extends into longer wavelengths with more polar solvent, suggesting CT character, albeit with a somewhat low molar absorption coefficient, more in keeping with a $\pi \rightarrow \pi^*$ transition (see Figure 9-5 in Appendix 1). The remainder of the absorption peaks are clearly also from $\pi \rightarrow \pi^*$ transitions.

tBu-DMP-Cz-DMB (12)

tBu-DMP-Cz-DMB (**12**) (see Figure 9-6 in Appendix 1) possesses a series of three rather broad absorption peaks at 370, 348 and 335 nm, each of which the absorption coefficient suggests is associated with relatively weak $\pi \rightarrow \pi^*$ transitions.

tBu-DMeOP-Cz-DMB (13)

Whilst tBu-DMeOP-Cz-DMB (**13**) is similar to its dimethyl counterpart, the 370 nm peak is missing, leaving only 349 nm and 335 nm above 300 nm, although they are marginally stronger $\pi \rightarrow \pi^*$ transitions based on their molar absorption coefficients (see Figure 9-7 in Appendix 1).

tBu-MPhOP-Cz-DMB (14)

Switching to one phenoxy group in tBu-MPhOP-Cz-DMB (**14**) (see Figure 9-8 in Appendix 1), a third post 300 nm absorption peak is returned at 368 nm. In this molecule the strength of the $\pi \rightarrow \pi^*$ transitions are much less than the diphenoxy compound based on the molar absorption coefficients.

tBu-DPhOP-Cz-DMB (15)

As with the dimethoxy derivative, tBu-DPhOP-Cz-DMB (**15**) has just 2 peaks beyond 300 nm, both once again at 349 nm and 335 nm (see Figure 9-9 in Appendix 1). Here the molar absorption coefficients are slightly weaker (though at the same order of magnitude) $\pi \rightarrow \pi^*$ transitions.

5.3.6 Solvatochromism

Charge transfer states are the driving force of emissions in TADF molecules. Since these excited states are heavily influenced by the polarity of the solvent in which the material is dissolved, solvatochromism studies were performed on the molecules in this study to ascertain the strength of their solvatochromic character.

tBu-DMP-Cz-OBA (10)

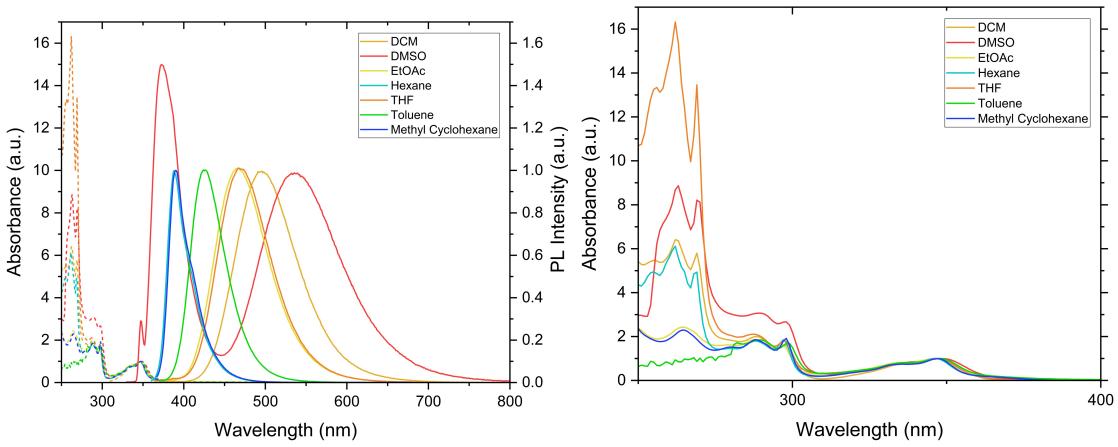


Figure 5-14 Solvatochromism of tBu-DMP-Cz-OBA (10) (left). A zoomed in plot of the absorbances in different solvents is shown (right) for clarity.

tBu-DMP-Cz-OBA (**10**), with its *9-oxa-10-boraanthracene* acceptor moiety demonstrates very strong solvatochromism in its photoluminescence spectrum, with a slight red-shift with stronger polarity solvents in its longest wavelength UV-spectrum. The emission wavelengths range from 388 nm in non-polar methylcylclohexane, to 536 nm in polar dimethyl sulfoxide. In the most polar solvent, an additional peak at 373 nm appears, suggesting an additional emissive decay pathway at this point. The overall range of solvatochromism is 148 nm.

Dimesityl boron compounds

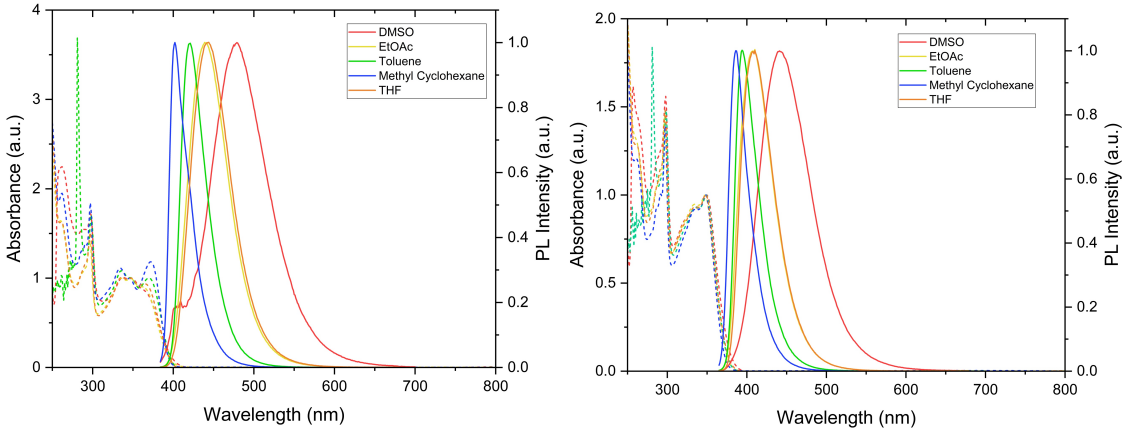


Figure 5-15 Solvatochromism plots of tBu-DMP-Cz-DMB (12) (left) and tBu-DMeOP-Cz-DMB (13) (right).

Switching to the dimesityl boron acceptor moieties, the compounds with the methyl and methoxy substituted π-bridges exhibit prominent solvatochromism, with the extremes of tBu-DMP-Cz-DMB (**12**) being 402 nm and 478 nm in methylcyclohexane and dimethyl sulfoxide, respectively – a range of 76 nm. Switching to methoxy groups, tBu-DMeOP-Cz-DMB (**13**) ranges from the much more blue-shifted 386 nm in non-polar methylcyclohexane, to 441 nm in dimethyl sulfoxide – representing a range of just 55 nm. Clearly, it appears that methoxy groups have a stark effect on blue-shifting emissions, but they also contribute to reduced solvatochromism in solution at least.

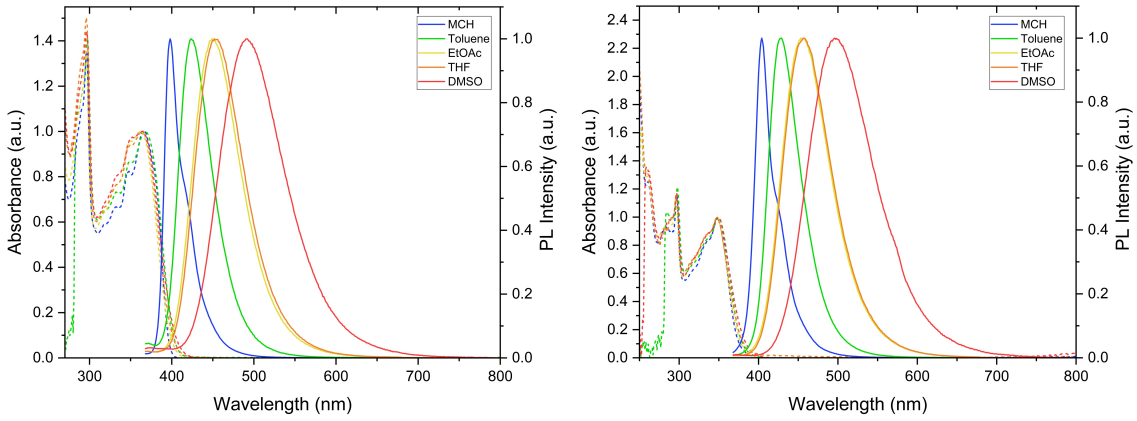


Figure 5-16 Solvatochromism plots of tBu-MPhOP-Cz-DMB (14) (left) and tBu-DPhOP-Cz-DMB (15) (right).

The phenoxy derivatives show slightly increased solvatochromism compared to their methyl and methoxy counterparts. A slight shoulder to the emission peak in methylcyclohexane at 422 nm and 415 nm in tBu-DPhOP-Cz-DMB (**15**) and tBu-MPhOP-Cz-DMB (**14**) suggests vibronic character and is a mirror image of the corresponding absorption spectra. For the

singly substituted compound **14**, emission range from 398 nm in methylcyclohexane to 491 nm in dimethyl sulfoxide, a range of 93 nm, whereas with two phenoxy groups, the range remains the same.

5.3.7 Lippert-Mataga analysis for solvatochromism

As outlined in Chapter 4, taking the Stokes shift from solvatochromism studies allows one to determine the strength of a molecule's dipole in the excited state. In order to perform Lippert-Mataga analysis upon the compounds in this chapter, the dielectric constants and refractive indices for the various solvents shown in Table 4-13 in Chapter 4 were used.

Table 5-7 Summary of solvatochromism for Lippert-Mataga calculations from UV-vis absorption and photoluminescence spectra for compounds in this chapter.

	tBu-DMP-Cz-OBA (10)				
Solvent [~1x10^{-5} M]	λAbs_{max} (nm)	λPL_{max} (nm)	S_1 (nm)	FWHM (nm)	$\nu_a - \nu_p$ (cm^{-1})
Toluene	348	425	3.20	50	5206
Tetrahydrofuran	347	467	3.02	76	7405
Methylcyclohexane	346	388 (405sh)	3.35	32	3129
Ethyl acetate	346	466	3.05	76	7443
Dimethyl sulfoxide	348	373(LE), 536(CT)	2.75	39 (LE), 114 (LE)	10079

	tBu-DMP-Cz-DMB (12)				
Solvent [~1x10^{-5} M]	λAbs_{max} (nm)	λPL_{max} (nm)	S_1 (nm)	FWHM (nm)	$\nu_a - \nu_p$ (cm^{-1})
Toluene	370	420	3.10	37	3218
Tetrahydrofuran	365	443	3.08	58	4824
Methylcyclohexane	372	402	3.20	28	2006
Ethyl acetate	366	420	3.12	37	3513
Dimethyl sulfoxide	360	478	2.99	81	6857

	tBu-DMeOP-Cz-DMB (13)				
Solvent [~1x10^{-5} M]	λAbs_{max} (nm)	λPL_{max} (nm)	S_1 (nm)	FWHM (nm)	$\nu_a - \nu_p$ (cm^{-1})
Toluene	349	394	3.30	34	3273
Tetrahydrofuran	348	409	3.27	48	4286
Methylcyclohexane	348	386	3.38	29	2829
Ethyl acetate	348	408	3.30	50	4226
Dimethyl sulfoxide	349	441	3.19	73	5978

	tBu-MPhOP-Cz-DMB (14)				
Solvent [~1x10^{-5} M]	λAbs_{max} (nm)	λPL_{max} (nm)	S_1 (nm)	FWHM (nm)	$\nu_a - \nu_p$ (cm^{-1})
Toluene	368	424	3.16	46	3589
Tetrahydrofuran	364	453	3.06	70	5397
Methylcyclohexane	366	398, 415(sh)	3.26	29	2197
Ethyl acetate	362	450	3.10	68	5402
Dimethyl sulfoxide	365	491	2.93	94	7031

	tBu-DPhOP-Cz-DMB (15)				
Solvent [~1x10^{-5} M]	λAbs_{max} (nm)	λPL_{max} (nm)	S_1 (nm)	FWHM (nm)	$\nu_a - \nu_p$ (cm^{-1})
Toluene	350	428	3.13	48	5207
Tetrahydrofuran	348	457	3.07	72	6854
Methylcyclohexane	348	404, 422(sh)	3.22	29	3983
Ethyl acetate	348	455	3.07	72	6758
Dimethyl sulfoxide	349	497	2.92	98	8533

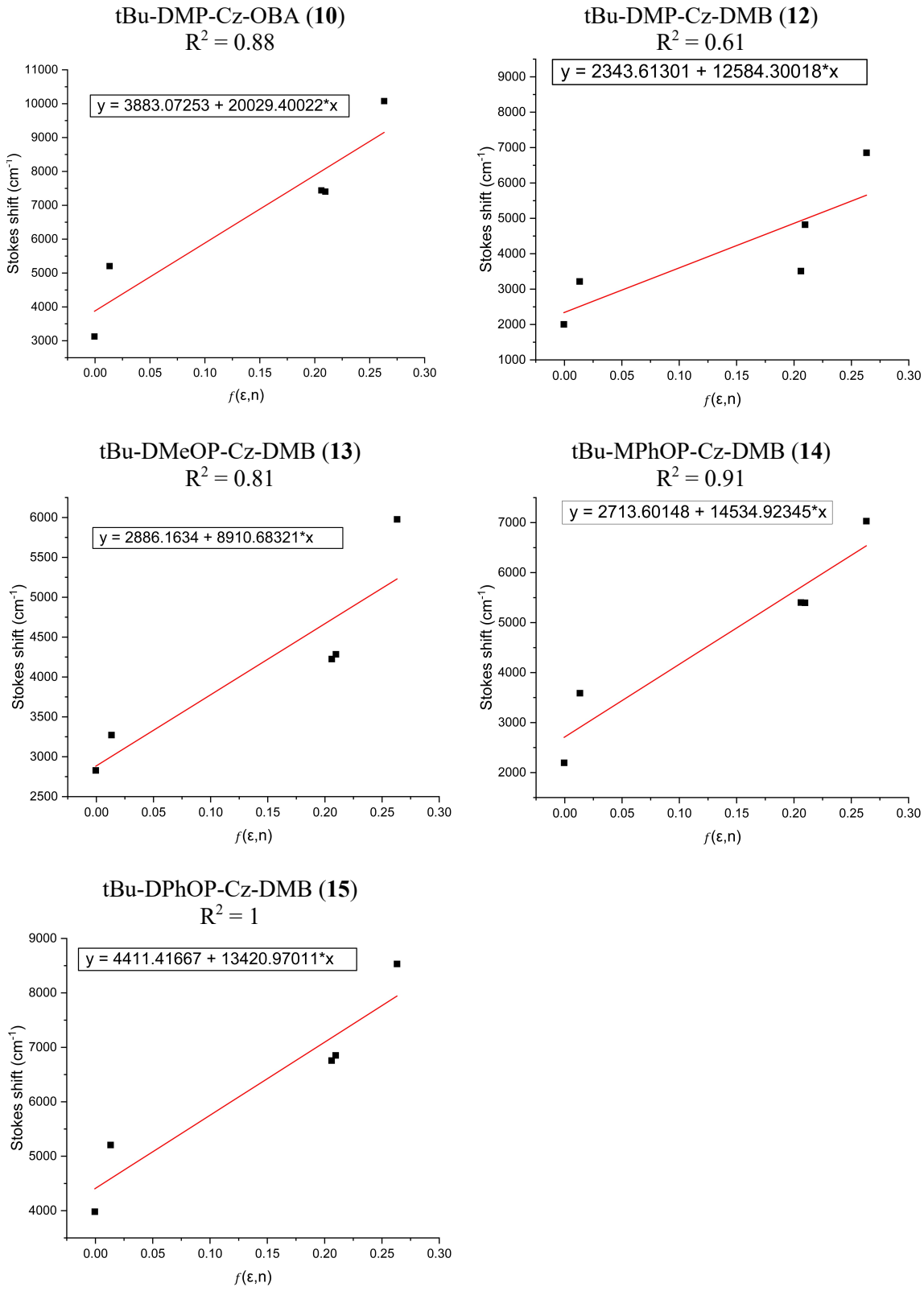


Figure 5-17 Lippert-Mataga plots of the compounds in this study.

As with Chapter 4, using Equation 4-1 permits the use of the slope of the Lippert–Mataga plots from Figure 5-17, and Divac *et al.*'s[299] method to yield the dipole moments of the compounds (see Table 5-8).

Table 5-8 Dipole moments of the compounds in this study.

Molecule	$\Delta\mu$ (cm^{-1})	a (Å)[a]	(μ_e -μ_g)D
tBu-DMP-Cz-OBA (10)	20029	8.69	36
tBu-DMP-Cz-DMB (12)	12584	9.20	31
tBu-DMeOP-Cz-DMB (13)	8911	9.21	26
tBu-DPhOP-Cz-DMB (15)	13421	9.26	33
tBu-MPhOP-Cz-DMB (14)	14535	9.25	34

[a] Onsager cavity radius, calculated *via* DFT-B3LYP-6-31G(d) as half the largest diameter plus van der Waals radii of the most distant atoms, across the whole molecule.

The dipole moment of each compound changes very little, with the dimethoxy compound having the weakest dipole moment. This may be due to enhanced symmetry afforded by B-O interactions maintaining a large dihedral between the donor and acceptor moiety.

5.3.8 TCSPC Lifetime measurements

As outlined in Chapter 4, TCSPC allows one to determine the prompt and delayed lifetime components of an emission decay. This helps to distinguish between simple prompt fluorescence and phosphorescence or TADF. The TCSPC measurements of compounds **10** and **12** – **15** are reported herein as solution measurements in toluene and in the solid state using a variety of host matrices. A 365 nm diode laser using a 5 µs pulse was used to excite the samples and a 2 µs gate used for the measurements.

tBu-DMP-Cz-OBA (10)

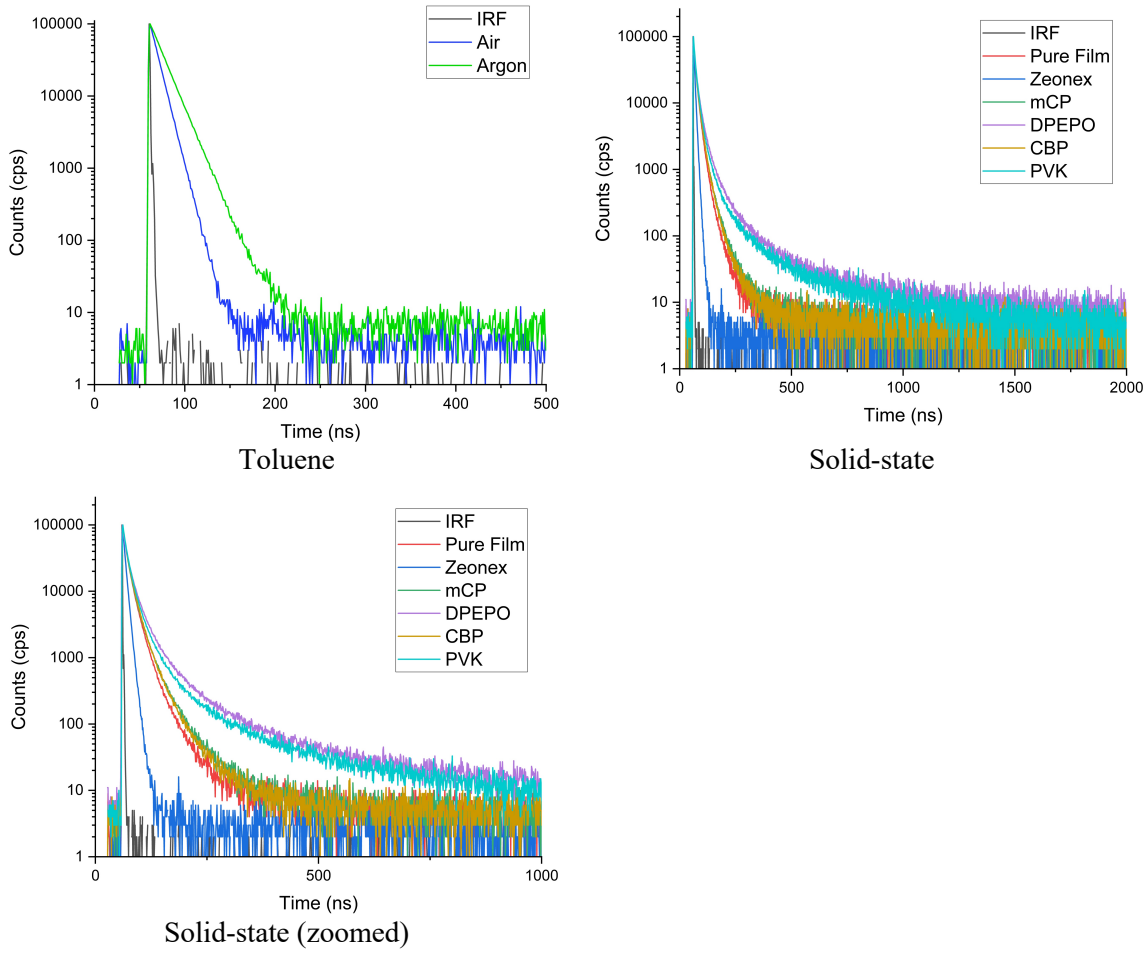


Figure 5-18 TCSPC plots for tBu-DMP-Cz-OBA (10). All excited at 365 nm with 5 µs pulse and 2 µs measurement.

Compound **10** exhibits prompt emissions in solution with a lifetime of 8.52 ns. Degassing introduces a slight delayed component of 15.03 ns for the 425 nm emission in toluene. Switching to solid-state and host matrices, non-polar Zeonex results in prompt emission,

which is extended in more polar hosts, reaching a maximum in DPEPO with τ_p of 17.93 ns and τ_d of 115.29 ns.

Dimesityl boron compounds

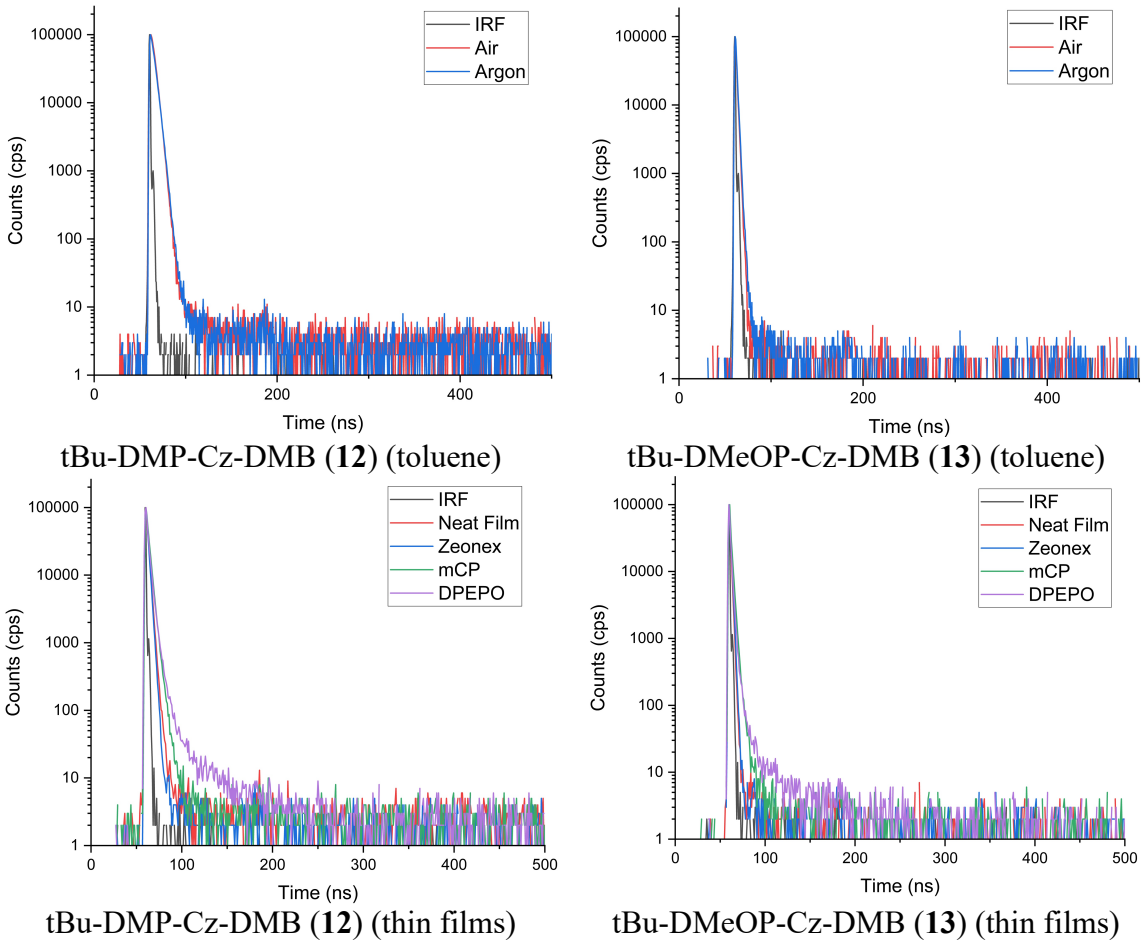


Figure 5-19 TCSPC plots for tBu-DMP-Cz-DMB (12) (left) and tBu-DMeOP-Cz-DMB (13) (right). All excited at 365 nm with 5 µs pulse and 2 µs measurement.

In both the dimethyl and dimethoxy donor - dimesityl boron compounds, emission is prompt, with negligible change to emission lifetimes upon degassing in toluene. In DPEPO (a polar host) there is a slight increase in a delayed component to the emission.

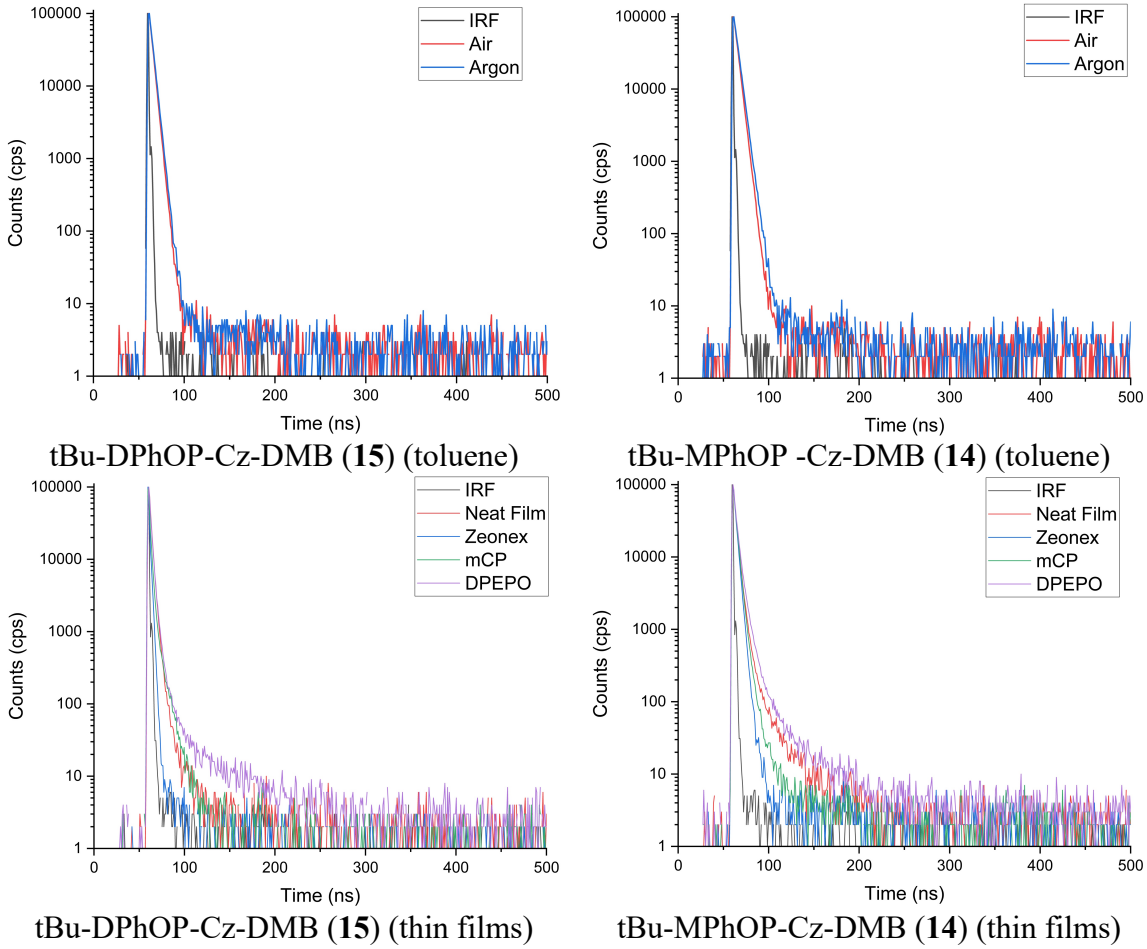


Figure 5-20 TCSPC plots for tBu-DPhOP-Cz-DMB (15) (left) and tBu-MPhOP-Cz-DMB (14) (right). All excited at 365 nm with 5 µs pulse and 2 µs measurement.

Both phenoxy compounds exhibit prompt decays with exceedingly short delayed components to the fittings. However, more polar hosts such as DPEPO do increase the lifetimes very slightly.

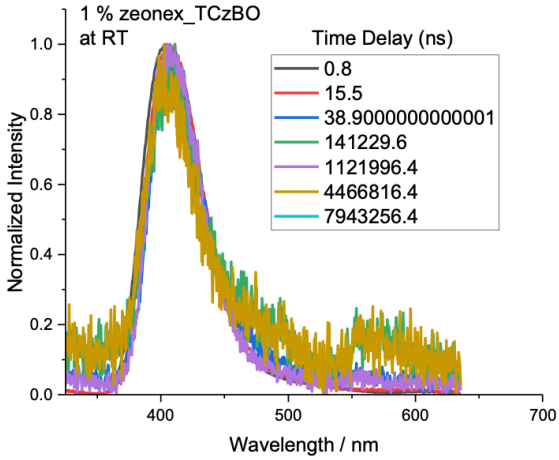
Table 5-9 Summary of lifetime measurements.

Molecule	Sample	τ_p (ns)	τ_d (ns)
tBu-DMP-Cz-OBA (10)	Toluene (air)	8.52	-
	Toluene (degassed)	7.52	15.03
	Pure film	8.82	22.10
	mCP	9.23	26.94
	Zeonex	4.40	7.36
	DPEPO	17.93	115.29
	CBP	9.63	24.04
	PVK	10.51	53.69
tBu-DMP-Cz-DMB (12)	Toluene (air)	2.39	2.89
	Toluene (degassed)	2.56	3.23
	Pure film	2.20	5.06
	mCP	2.48	4.38
	Zeonex	0.41	2.06
	DPEPO	2.59	8.19
tBu-DMeOP-Cz-DMB (13)	Toluene (air)	1.23	3.08
	Toluene (degassed)	1.29	2.80
	Pure film	1.16	12.42
	mCP	1.88	4.85
	Zeonex	1.38	-
	DPEPO	1.97	8.53
tBu-MPhOP-Cz-DMB (14)	Toluene (air)	3.99	16.01
	Toluene (degassed)	4.47	26.82
	Pure film	2.87	8.65
	mCP	2.53	5.73
	Zeonex	2.67	5.53
	DPEPO	3.22	9.52
tBu-DPhOP-Cz-DMB (15)	Toluene (air)	3.34	19.06
	Toluene (degassed)	3.62	58.32
	Pure film	2.19	5.22
	mCP	1.95	7.91
	Zeonex	1.69	-
	DPEPO	2.30	14.25

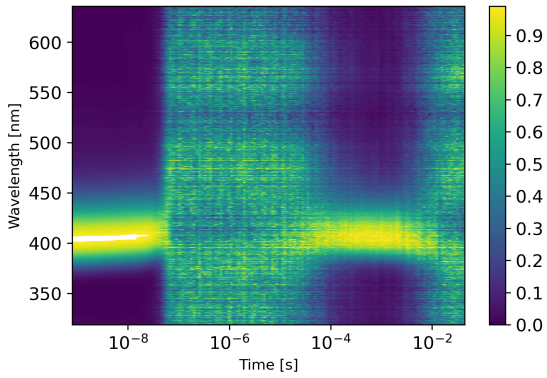
5.3.9 CCD Time-resolved measurements

All measurements in this section were performed by Dr Suman Kuila of Durham University, with the exception of compounds **14** and **15**, which were performed by myself.

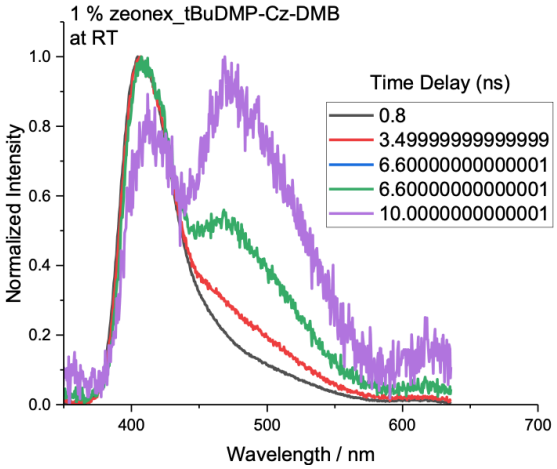
The observations made from CCD time-resolved measurements confirm our TCSPC results in that compound **10** possesses a delayed component (see Figure 5-21) – though much greater than our system was able to observe. As demonstrated in Chapter 4, the system in Durham is able to perform the measurements under vacuum, and at the time of writing our fluorimeter in Glasgow could only perform TCSPC in air. The fact that the delayed emission in compound **10** was missed in our air-exposed fluorimeter strongly suggests that this component of the emission comes from an oxygen sensitive source such as a triplet state.



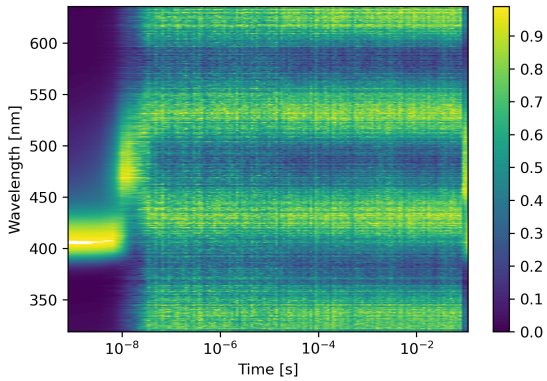
tBu-DMP-Cz-OBA 1% w.t. in Zeonex time resolved PL



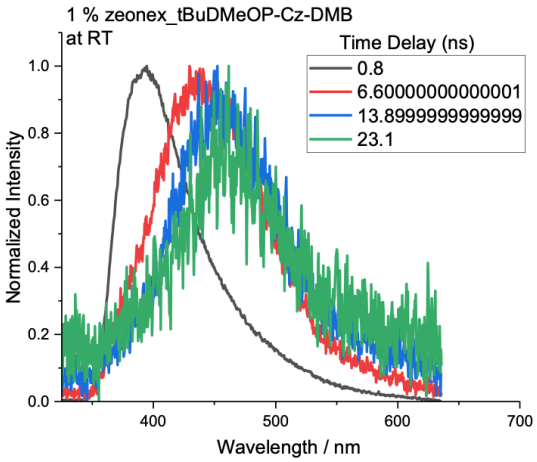
tBu-DMP-Cz-OBA delayed emission heatmap



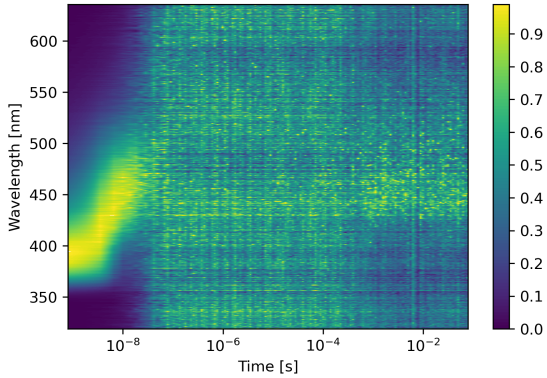
tBu-DMP-Cz-DMB 1% w.t. in Zeonex time resolved PL



tBu-DMP-Cz-DMB delayed emission heatmap



tBu-DMeOP-Cz-DMB 1% w.t. in Zeonex time resolved PL



tBu-DMeOP-Cz-DMB delayed emission heatmap

Figure 5-21 Time-resolved emission spectra and heat maps for tBu-DMP-Cz-OBA (10), tBu-DMP-DMB (12) and tBu-DMeOP-Cz-DMB (13) in Zeonex as a host matrix at 1% w.t. concentration.

Emissions from compounds **12** and **13** are only prompt (see Figure 5-21), with decays reaching 10 ns and 23.1 ns, respectively, however during this time a large red-shift in emissions are observed (see Figure 5-21 for the heat maps and time-dependent PL spectra highlighting this, as well as Table 5-10 which shows the wavelength of the PL spectra peaks at a specific time delay).

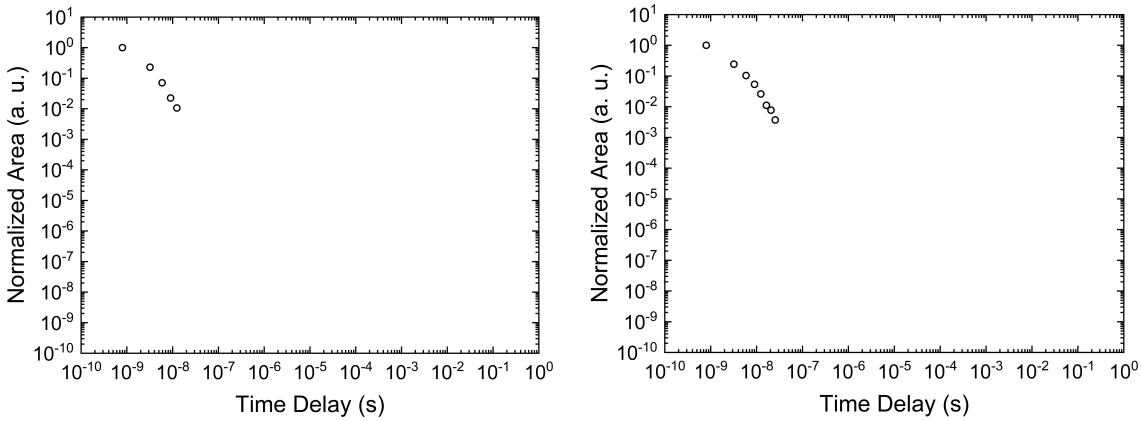
Table 5-10 Summary of PL properties at different times after excitation.

Molecule	PL (nm)	Time delay (ns)
tBu-DMP-Cz-OBA (10)	404	0.8
	406	15.5
	410	38.9
	406	141229.6
	406	1121996.4
	404	4466816.4
	N/A	7943256.4
tBu-DMP-Cz-DMB (12)	406	0.8
	406	3.5
	408, 467	6.6
	473, 411	10.0
tBu-DMeOP-Cz-DMB (13)	393	0.8
	437	6.6
	453	13.9
	462	23.1

Compound **12** emits promptly at 406 nm at 0.8 ns, with a shoulder at ~465 nm. By 6.6 ns, this has developed into a second peak at 467 nm, before becoming the dominant peak at 10 ns, red-shifting further to 473 nm. This suggests a second excited state decaying weakly after a brief delay. From the fact that the bluer peak is shortly extinguished after 10^{-8} s, we

can rule out any efficient rISC occurring, and that any further decay pathways are non-radiative.

After the initial 0.8 ns emission at 393 nm for compound **13**, the prompt emission ceases, being entirely replaced with a delayed component at 437 nm at 6.6 ns, shifting to 462 nm by 23.1 ns. All emission ceases shortly after 10^{-8} s, suggesting no efficient rISC.



tBu-DMP-Cz-DMB (**12**) tBu-DMeOP-Cz-DMB (**13**)

Figure 5-22 Time resolved decay plots from Durham. Samples of tBu-DMP-Cz-DMB (12) (left) and tBu-DMeOP-Cz-DMB (13) (right) in 1% w.t. Zeonex.

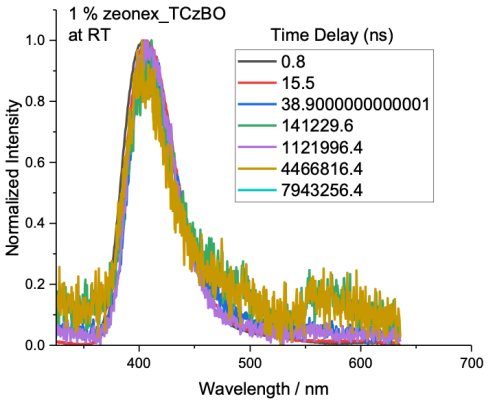
Compound **10** on the other hand, continues to emit up to 44.7 ms with very little shifting, just from 404 nm at 0.8 ns, shifting to 410 nm by 38.9 ns, then back to 404 nm by 44.7 ms. Interestingly, the heat map plot shows an absence of any emissions between 10^{-7} ns and 10^{-4} ns. This suggests that rISC is occurring, albeit with quite a slow rate, with no competing phosphorescence occurring. The relatively low PLQY of compound **10** in Zeonex would indicate competing non-radiative processes outcompeting the rISC process.

Table 5-11 Summary of fittings for time resolved data from Durham. Samples in 1% w.t. Zeonex.

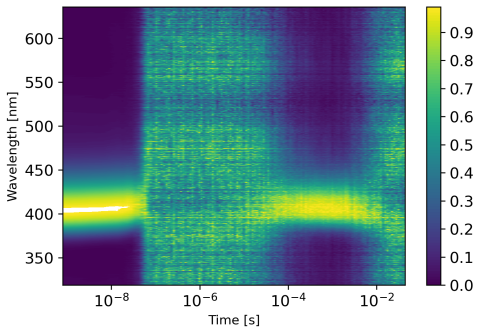
	τ_{PF} (av)	τ_{DF} (av)
Compound in Zeonex host	**(ns)**	**(µs)**
tBu-DMP-Cz-OBA (10)	7.34	31647
tBu-DMP-Cz-DMB (12)	2.19	-
tBu-DMeOP-Cz-DMB (13)	1.49	-
tBu-MPhOP-Cz-DMB (14) (r.t.)	4.67	20467
tBu-MPhOP-Cz-DMB (14) (80 K)	13.49	59476
tBu-DPhOP-Cz-DMB (15) (r.t.)	4.14	10.99 / 12100
tBu-DPhOP-Cz-DMB (15) (80 K)	5.61	136281

Examining the weighted fittings for the decay plots (see Table 5-11), it is clear that the dimesityl boron acceptor yields only prompt emissions when paired with the methyl or

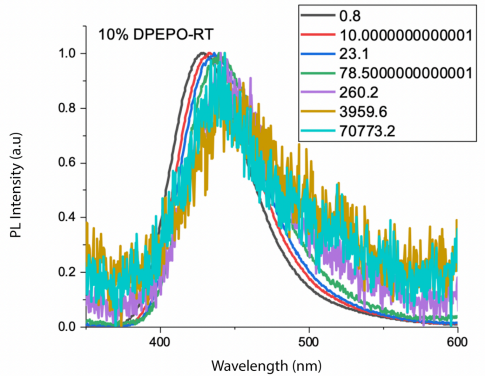
methoxy π-bridged tert-butyl carbazole donor moieties. The 10-bromo-10H-dibenzo[b,e][1,4]oxaborinine acceptor, however, yields a delayed component of ~32 ms, providing weak TADF in 1% w.t. non-polar Zeonex films. These fittings were obtained from the time resolved decay plots of Figure 5-22, Figure 5-25 and Figure 5-28.



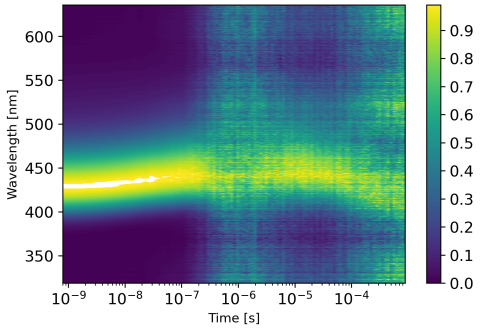
tBu-DMP-Cz-OBA 1% w.t. in Zeonex time resolved PL



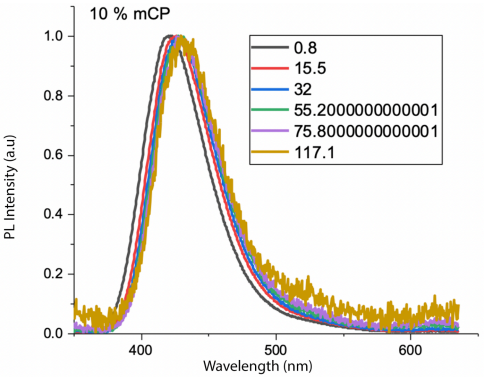
tBu-DMP-Cz-OBA 1% w.t. in Zeonex delayed emission heatmap



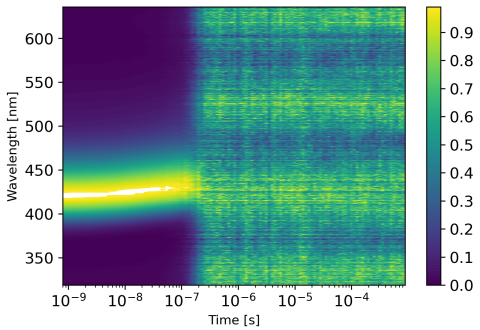
tBu-DMP-Cz-OBA 10% w.t. in DPEPO time resolved PL



tBu-DMP-Cz-OBA 10% w.t. in DPEPO delayed emission heatmap

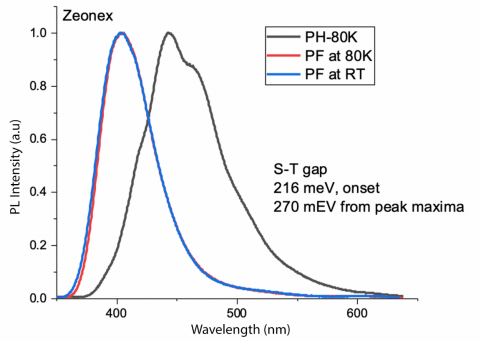


tBu-DMP-Cz-OBA 1% w.t. in mCP time resolved PL

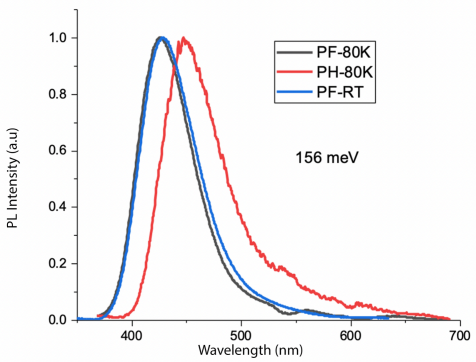


tBu-DMP-Cz-OBA 1% mCP delayed emission heatmap

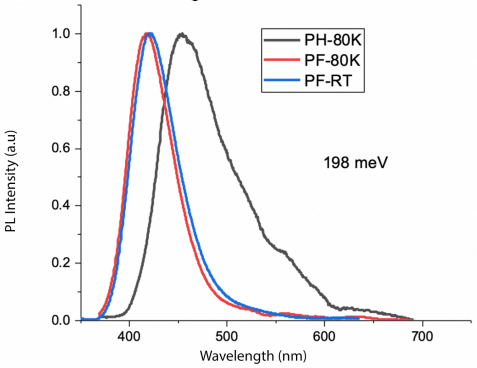
Figure 5-23 Time resolved emission spectra and heat maps for tBu-DMP-Cz-OBA (10) in different host matrices.



tBu-DMP-Cz-OBA 1% w.t. in Zeonex
Prompt fluorescence and phosphoresce at room temperature and 80 K



tBu-DMP-Cz-OBA 10% w.t. in DPEPO
Prompt fluorescence and phosphoresce at room temperature and 80 K



tBu-DMP-Cz-OBA 1% w.t. in mCP
Prompt fluorescence and phosphoresce at room temperature and 80 K

Figure 5-24 Comparison of prompt, steady-state fluorescence (PF) of tBu-DMP-Cz-OBA (10) at room temperature and 80 K, and phosphorescence at 80 K in a variety of host matrices.

Switching to more polar host matrices, higher PLQYs were obtained. However, the long-lived emission, whilst still not shifting much in wavelength (suggesting delayed fluorescence emission), is reduced in intensity (see Figure 5-23 and Figure 5-24). mCP on the other hand completely quenches the delayed emission. This is reflected in the fitted decay lifetimes in Table 5-12 and illustrated in the decay curves in Figure 5-25.

Using emission onsets in different hosts, the ΔE_{ST} for compound **10** was found to be 216 meV for Zeonex, 156 meV for DPEPO and 198 meV for mCP. In the non-polar Zeonex host, the emission lifetime of the phosphorescent peak stretched to 4.47 ms. In polar hosts, the emission lasted 70 µs and 117.1 ns in DPEPO and mCP, respectively.

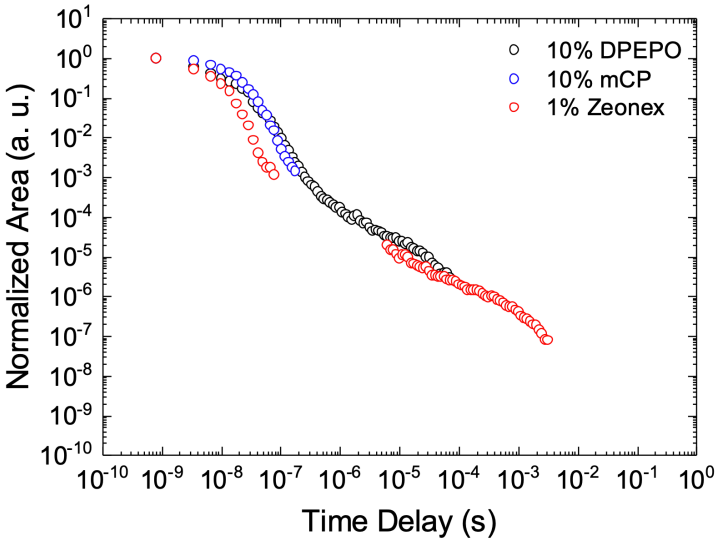
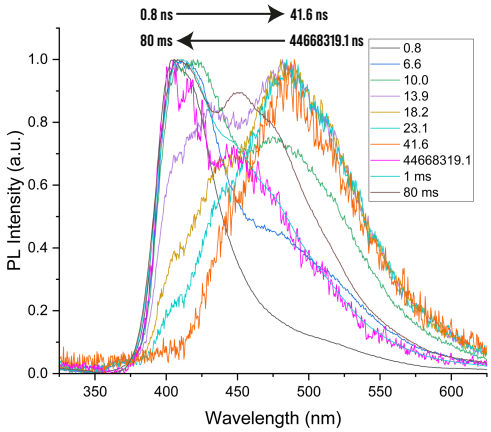


Figure 5-25 Time-resolved decay plot from Durham for tBu-DMP-Cz-OBA (10) in various hosts.

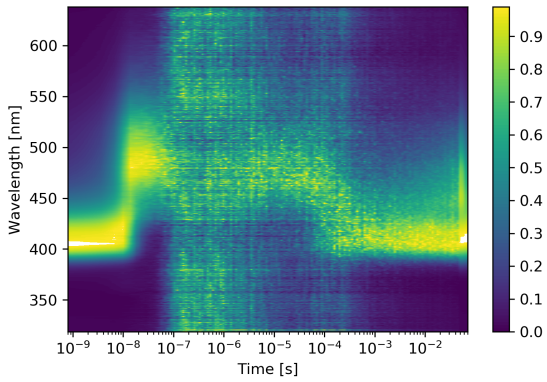
Table 5-12 Summary of fittings for time-resolved data for tBu-DMP-Cz-OBA (10) in Zeonex, mCP and DPEPO hosts from Durham.

	τ_{PF} (av)	τ_{DF} (av)
Compound in Zeonex host	**(ns)**	**(µs)**
1% w.t. Zeonex	7.34	31647
10% w.t. mCP	18.67	-
10% w.t. DPEPO	18.24	22.59

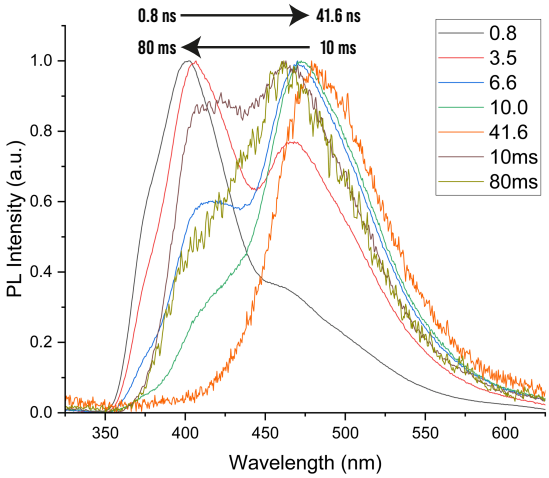
Samples of tBu-MPhOP-Cz-DMB (**14**) and tBu-DPhOP-Cz-DMB (**15**) were similarly prepared at a concentration of 1% w.t. in Zeonex host matrices. The resulting decays are a stark contrast to their dimethyl and dimethoxy brethren.



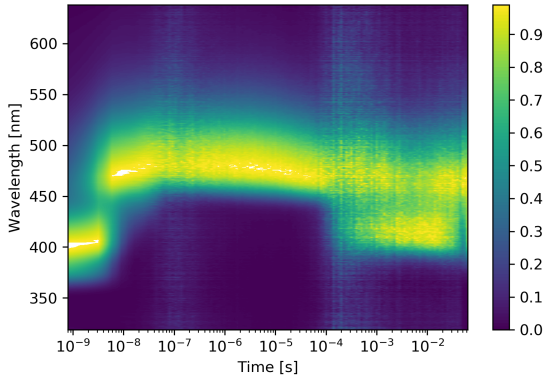
tBu-MPhOP-Cz-DMB 1% w.t. in Zeonex time resolved PL



tBu-MPhOP-Cz-DMB delayed emission heatmap



tBu-DPhOP-Cz-DMB 1% w.t. in Zeonex time resolved PL



tBu-DPhOP-Cz-DMB delayed emission heatmap

Figure 5-26 Time-resolved emission spectra and heat maps for tBu-MPhOP-Cz-DMB (14) and tBu-DPhOP-Cz-DMB (15) in Zeonex at room temperature under vacuum.

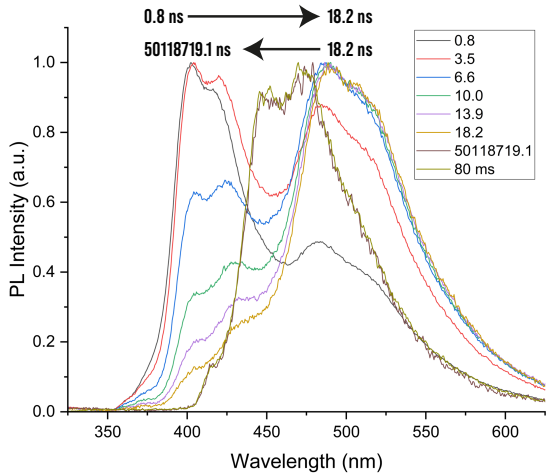
Figure 5-26 illustrates the time-dependent emissions of compounds **14** and **15** at room temperature. At room temperature and under vacuum, prompt emissions are observed at 405 nm for compound **14**, with shoulders at 417 nm and 509 nm. After ~40 ns, this red-shifts to 486 nm, and broadens from a FWHM of 48 nm to 94 nm. Emission intensity decreases for a period of 0.1 µs to 0.1 ms, before returning as blue-shifted room temperature phosphorescence with two peaks at 408 nm and 450 nm, with a 476 nm shoulder by 10 ms. At 80 ms, the 408 nm peak diminishes to a shoulder and the peak remains at 476 nm. Emissions at this point widen to a FWHM of 113 nm.

For the diphenoxy derivative, compound **15**, a similar room temperature phosphorescence is observed. Initially, prompt emissions occur at 401 nm, with 376 nm and 456 nm shoulders and FWHM of 64 nm. By 40 ns, the emissions red-shift to 481 nm and widen to a FWHM of 78 nm. This delayed component continues until ~ 0.1 ms and by 10 ms there are two blue-shifted emission peaks at 462 nm and 419 nm, with the 419 nm peak becoming a shoulder by 80 ms.

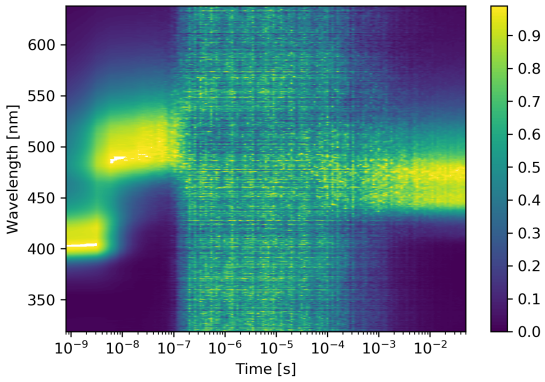
Table 5-13 Summary of the prompt and delayed emissions from the Zeonex thin films of tBu-MPhOP-Cz-DMB (14) and tBu-DPhOP-Cz-DMB (15) at room temperature and 80 K.

Sample	Prompt emission (nm)	Prompt FWHM (nm)	Secondary prompt emission (nm)	Secondary prompt FWHM (nm)	Delayed emission (nm)	Delayed FWHM (nm)
tBu-MPhOP-Cz-DMB (14) (r.t.)	405, 417sh, 509sh	48	486 (*41.6 ns*)	94	408, 450, 476sh (*80 ms*)	113
tBu-MPhOP-Cz-DMB (14) (80 K)	402, 416sh, 483, 511sh	57	490, 405sh, 435sh, 508sh (*18.2 ns*)	83	452, 470, 418sh (*80 ms*)	79
tBu-DPhOP-Cz-DMB (15) (r.t.)	401, 376sh, 456sh	64	481 (*41.6 ns*)	78	462, 419sh (*80 ms*)	109
tBu-DPhOP-Cz-DMB (15) (80 K)	400, 379sh, 464, 487sh	123	485 (*41.6 ns*)	78	476 (*80 ms*)	92

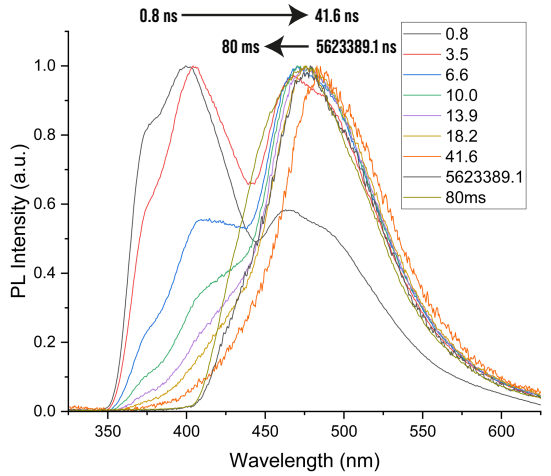
When cooled to 80 K, the rISC process should be switched off, and all emissions considered phosphorescent. These emissions are shown in Figure 5-27.



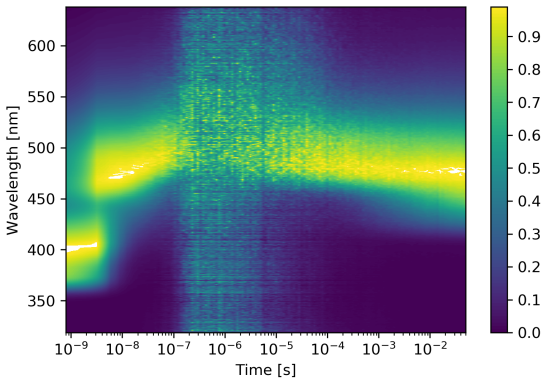
tBu-MPhOP-Cz-DMB 1% w.t. in Zeonex time resolved PL



tBu-MPhOP-Cz-DMB delayed emission heatmap



tBu-DPhOP-Cz-DMB 1% w.t. in Zeonex time resolved PL



tBu-DPhOP-Cz-DMB delayed emission heatmap

Figure 5-27 Time-resolved emission spectra and heat maps for tBu-MPhOP-Cz-DMB (14) and tBu-DPhOP-Cz-DMB (15) in Zeonex at 80 K under vacuum.

Initial prompt emissions from compound **14** at 80 K occur at 402 nm and 483 nm, with shoulders at 416 nm and 511 nm. The dual emission here is noticeably absent at room temperature. As time passes, the 402 nm peak decreases in intensity as the 483 nm peak increases, simultaneously red-shifting to 490 nm by 18 ns (significantly quicker than at room temperature) with the remains of the blue peak now just a shoulder. Between 0.1 µs and 0.1 ms, emissions diminish at all wavelengths, before once again returning by 5.6 ms to yield a blue-shifted double peak at 419 nm and 462 nm, with the 419 nm peak decreasing in intensity slightly by 80 ms and becoming a prominent shoulder.

This represents a different, redder decay pathway at the later time compared to the measurements at room temperature. It would suggest that the later 408 nm decay pathway is thermally activated. Since the ~ 450 nm decay occurs both at room temperature and at 80

K, we can confidently label this as room temperature phosphorescence. Ergo, compound **14** emits *via* RTP and TADF.

At 80 K the diphenoxy compound **15** decays promptly, also with dual emission, at 400 nm and 464 nm, with shoulders at 379 nm and 487 nm. Emission red-shifts to 485 nm by ~ 40 ns and narrows from the initial 123 nm FWHM to 78 nm. This emission is cut off by 0.1 µs but returns by 40 µs as a weakly blue shifted peak at 476 nm, widening to 92 nm. The fact that compound **15** displays a period of inactivity in its delayed component suggests that its bulky structure gives way to both room temperature phosphorescence pathways and TADF mechanism, giving a much more complicated display of emissions than the dimethyl and dimethoxy compounds.

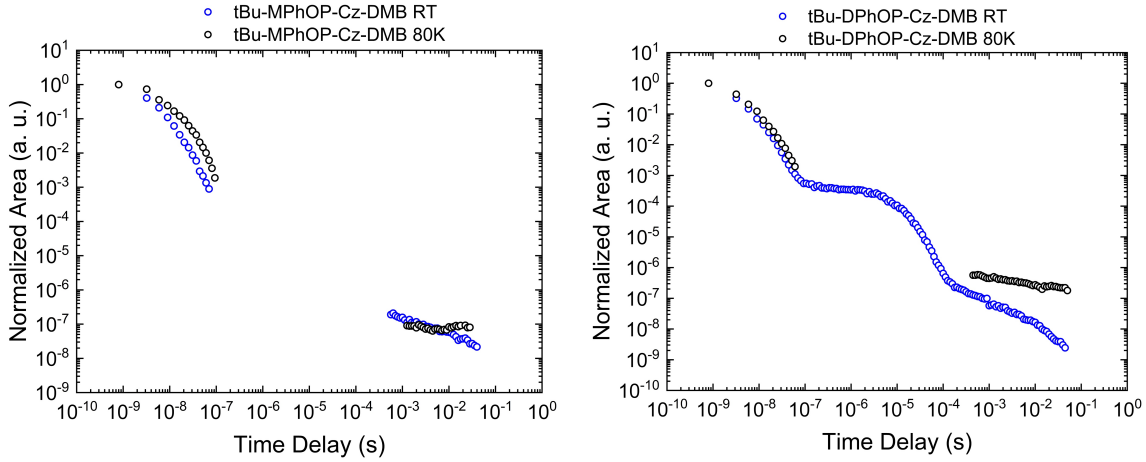


Figure 5-28 Time-resolved decay plots for thin film samples of tBu-MPhOP-Cz-DMB (14) (left) and tBu-DPhOP-Cz-DMB (15) (right) in 1% w.t. Zeonex.

In Table 5-11, the fitted lifetimes from the time-resolved plots in Figure 5-28 reveal significantly increased lifetimes when methyl / methoxy groups are replaced with phenoxy groups. Prompt emissions at ~4 ns are followed by delayed components of 20 ms for compound **14** and 11 µs and 12 ms for compound **15**, respectively. The diphenoxy compound has dual delayed emissions at room temperature, suggesting both RTP and TADF. The prompt emission increases slightly to 13.5 and 5.6 ns for compounds **14** and **15**, respectively, with significantly increased delayed lifetimes of 59 ms and 136 ms for compounds **14** and **15**, respectively at 80 K where phosphorescence emissions dominate.

Further exploration of the emission peaks in the steady-state and at the various time intervals for compound **14** in Table 5-14, reveals an S_1 energy state at 3.23 eV and a triplet state capable of room temperature phosphorescence at 3.01 eV, with a further two triplet states

present at 2.95 eV and 2.88 eV (assigned as triplets owing to their clear presence at 80 K). Compound **15** on the other hand has a S_1 state at 3.49 eV, with a secondary prompt peak at 2.91 eV. A main triplet state (possibly ^{3}CT) is present at 3.04 eV. The delayed emission at 3.35 eV is not present at 80 K and can therefore be associated with the S_1 TADF decay. It differs from the prompt decay by 0.12 eV, which could be due to interactions between the phenoxy rings and dimesityl rings causing a shift in the conformation of the molecule by the time the delayed S_1 decay occurs and is supported by the distinct drifting of this emission in Figure 5-26. This drifting (red-shifting followed by blue-shifting) is indicative of non-homogeneity of conformations of the emitter molecule suspended in the host matrix[300]. The fact that the drifting is still present in compound **15** at 80 K (where the Zeonex chain motion should be negligible and the conformations of the emitter should be homogeneous[300]) suggests that through-space interactions between the donor and acceptor moieties can influence conformational change in the excited state quite significantly, even at cryogenic temperatures. It is therefore likely that there is a complex interchange between the energy states involved in the RTP and TADF processes in the phenoxy compounds due to conformational effects[242,301].

Table 5-14 Singlet (steady-state in bold) and triplet energies of tBu-MPhOP-Cz-DMB (14) and tBu-DPhOP-Cz-DMB (15) taken from the onset of the emission peaks at the stated delay time.

Compound	S_1 (eV)	Secondary prompt peak (eV)	T_1 (eV)	Secondary delayed peak (eV)
tBu-MPhOP-Cz-DMB (14) (r.t.)	**3.23** 3.26 (0.8ns)	3.01 (41.6 ns)	3.26 (44.7 ms) (S_1 TADF)	3.26 / 3.28 (from fitting) (80 ms) TADF / RTP
tBu-MPhOP-Cz-DMB (14) (80 K)	3.28 / 2.86 (0.8ns)	2.81 (18.2 ns)	2.95 / 2.88 (50 ms) (Alternative pathway) T_1	2.95 / 2.88 (80 ms)
tBu-DPhOP-Cz-DMB (15) (r.t.)	**3.49** 3.47 (0.8ns)	2.91 (41.6 ns)	3.35 / 3.03 (80 ms) TADF / RTP	-
tBu-DPhOP-Cz-DMB (15) (80 K)	3.50 / 3.03 (0.8ns)	2.89 (41.6 ns)	3.04 (T_1) (80 ms)	-

Whilst dual TADF and RTP caused by structures with multiple moieties or *via* intermolecular interactions is represented in the literature[302,303], the work of Bhatia and Ray[304] demonstrates it in molecules involving carbazole and phenoxy groups, the latter of which were described as donors in their own right, and demonstrating intramolecular interactions. When combined with an additional carbazole donor (in what the authors

describe as a (D_2D_2') – acceptor type compound), they also observed internal π-π interactions from the phenoxy rings (this time interacting with the other donor), as well as dual TADF and RTP. Their hypothesis also cited a complicated mix of excited states, with triplets forming on both the phenoxy moieties (producing decay *via* RTP), and upon the carbazole moiety (undergoing rISC to yield TADF). They suggest that both the ^{1}CT and ^{3}CT states form upon the carbazole, and the ^{3}LE state forms on the phenoxy groups. The crystal structures obtained *via* XRD of compounds **14** and **15** in section 5.3.11 bear a striking resemblance to Bhatia and Ray's[304] findings which strongly suggests a similar mechanism is at play here.

Following from this fascinating observation, the advantages of using a femtosecond pulsed laser and CCD camera for performing time-resolved measurements over using just TCSPC measurements are abundantly clear. Our TCSPC instrument could monitor the lifetime of the decay from a single wavelength. The CCD system in Durham monitors all wavelengths by recording full photoluminescence spectra at each recorded time interval using a femtosecond laser as the excitation source. This allows the observation of additional emission wavelengths at different time intervals which would otherwise have been missed since they would have been drowned out by the dominant prompt emission peak in the initial fluorescence spectroscopy used to select the wavelength to be monitored by TCSPC, meaning that the later peaks would have remained unobserved.

5.3.10 Computational chemistry

In order to explore shapes and locations of the HOMOs and LUMOs of the compounds in this study, computational studies were performed on their structures.

Table 5-15 Distance and bond length measurements from DFT-B3LYP 6-31+G (d) calculations.

Compound	B – π (O/C/H) distance (Å)	B – π (O/C/H) distance (Å	N – C bond length (Å)	B – C bond length (Å)
tBu-DMP-Cz-OBA (10)	2.94 (B-H) 2.99 (B-C)	2.94 (B-H) 2.99 (B-C)	1.43	1.58
tBu-DMP-Cz-DMB (12)	2.93 (B-H) 3.07 (B-C)	2.93 (B-H) 3.07 (B-C)	1.42	1.59
tBu-DMeOP-Cz-DMB (13)	2.82 (B-O)	2.82 (B-O)	1.42	1.58
tBu-MPhOP-Cz-DMB (14)	2.92 (B-O)	2.74 (B-H)	1.42	1.58
tBu-DPhOP-Cz-DMB (15)	2.86 (B-O)	2.86 (B-O)	1.42	1.59

Table 5-16 Angular measurements from DFT-B3LYP 6-31+G (d) calculations.

Compound	D – A dihedral (°)	D – π-bridge dihedral (°)	A – π-bridge dihedral (°)
tBu-DMP-Cz-OBA (10)	27.6	61.7	89.0
tBu-DMP-Cz-DMB (12)	1.6	52.9	50.0
tBu-DMeOP-Cz-DMB (13)	5.30	51.9	56.6
tBu-MPhOP-Cz-DMB (14)	13.9	54.2	41.3
tBu-DPhOP-Cz-DMB (15)	7.1	50.3	56.5

The structures of all five purified synthesised compounds were optimised in Gaussian 09 *via* DFT-B3LYP 6-31+G (d). Confirmation that the optimised structure was at a minimum on the potential energy surface was determined by the absence of negative frequencies. The key structural properties are summarised in Table 5-15 for structural distances and bond lengths and Table 5-16 for key angular measurements. Table 5-17 shows the DFT optimised structures of the molecules and Table 5-18 shows the structures of their calculated HOMOs and LUMOs. According to the DFT optimisations, the methoxy and phenoxy compounds all have oxygen and boron atoms in close enough proximity to facilitate non-covalent interactions (their distances being less than the sum of the van der Waals radii of the atoms involved), with the monophenoxy compound having the largest distance – most likely due to the free space afforded by the solitary hydrogen atom on the position meta to the phenoxy group on the π-bridge, adjacent to the C-B bond.

Table 5-17 DFT optimised structures of the purified compounds in this study.

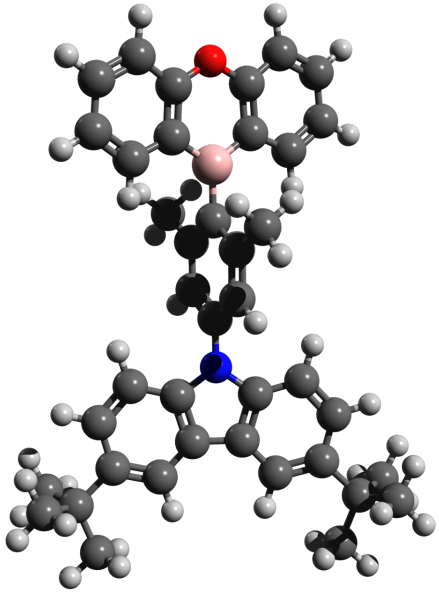
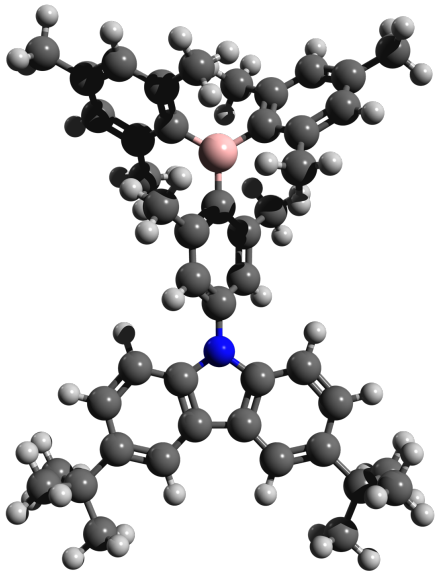
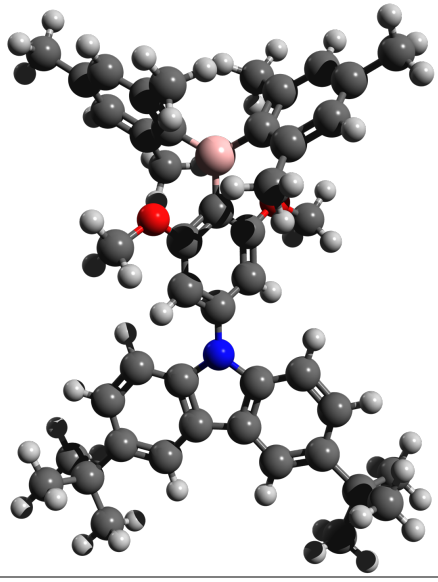
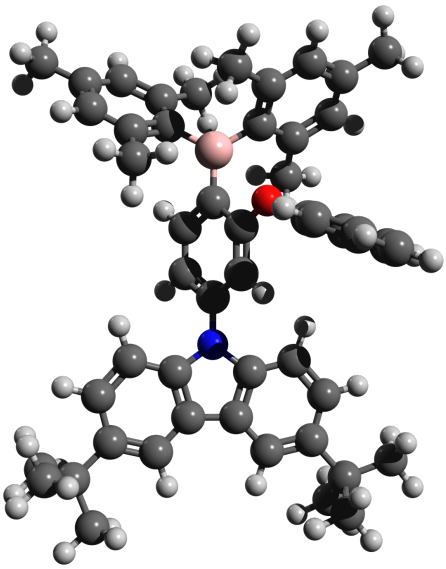
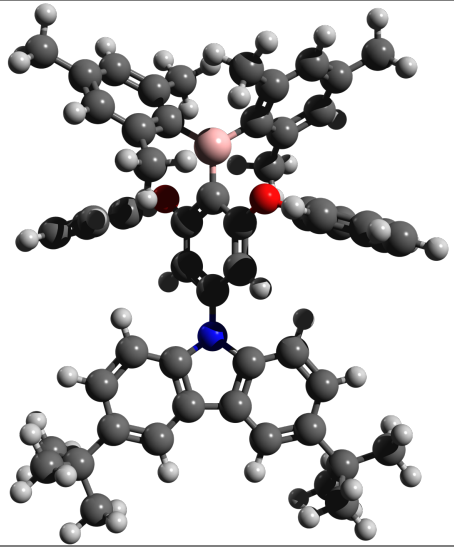
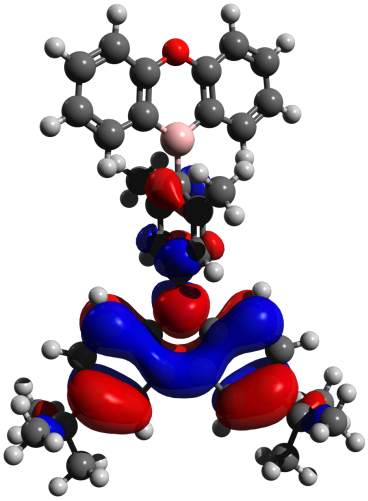
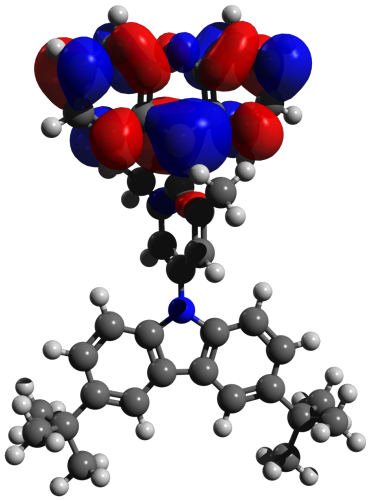
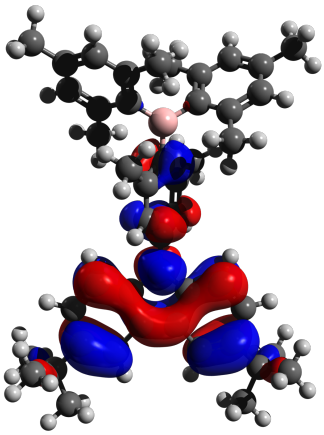
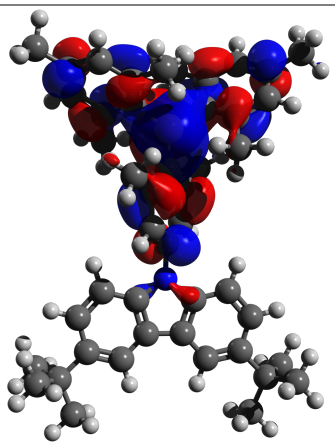
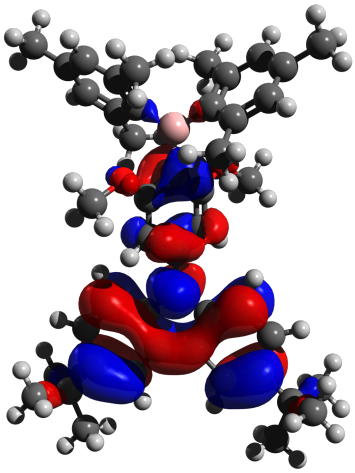
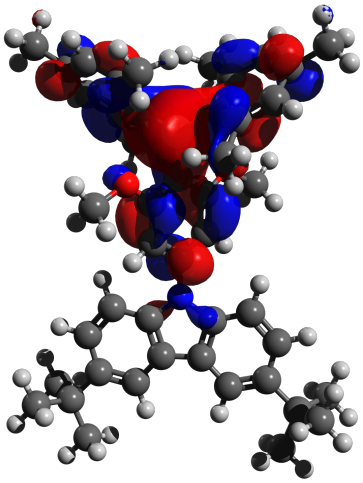
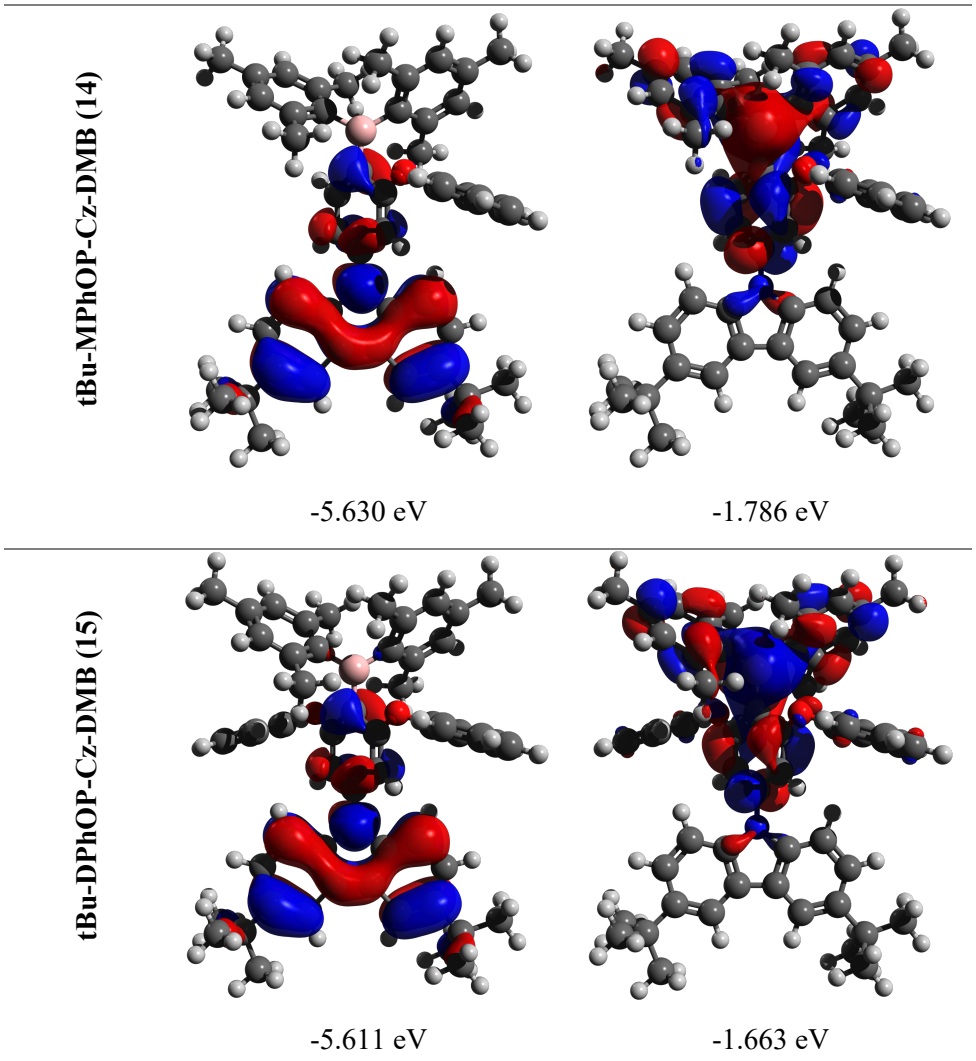
	
tBu-DMP-Cz-OBA (10)	**tBu-DMP-Cz-DMB (12)**
	
tBu-DMeOP-Cz-DMB (13)	**tBu-MPhOP-Cz-DMB (14)**
	
tBu-DPhOP-Cz-DMB (15)	

Table 5-18 DFT calculated HOMOs and LUMOs.

Molecule	HOMO	LUMO
tBu-DMP-Cz-OBA (10)		
	-5.506 eV	-1.992 eV
tBu-DMP-Cz-DMB (12)		
	-5.535 eV	-1.884 eV
tBu-DMeOP-Cz-DMB (13)		
	-5.618 eV	-1.516 eV



The lack of TADF and reduced solvatochromism in tBu-DMP-Cz-DMB (**12**) and tBu-DMeO-Cz-DMB (**13**) compared to tBu-DMP-Cz-OBA (**10**) can be explained by examination of the HOMO and LUMO locations on the molecules *via* TD-DFT calculations.

In compound **10**, the HOMO and LUMO are well-separated, with the HOMO localised over the donor moiety and to a lesser extent the π-bridge. The LUMO on the other hand, remains entirely located upon the 10-bromo-10H-dibenzo[b,e][1,4]oxaborinine acceptor, with only a tiny component entering the π-bridge. The high dihedral of 89° gives rise to excellent HOMO-LUMO separation, but the small degree of mixing upon the π-bridge prevents total decoupling, permitting the observed CT character of the emissions in the solvatochromism study.

For the other two compounds, the donor's HOMO is spread well across the tert-butyl carbazole and π-bridge, however in compound **12**, this extends further into the acceptor

moiety. The LUMO extends much further into the π-bridge, which contributes to significant mixing. With the much-reduced dihedral angles as well, the CT nature of the emissions is less, and is observed with the much-reduced solvatochromism and narrower emission FWHM in both cases.

What is perhaps surprising with the HOMO and LUMO of tBu-MPhOP-Cz-DMB (**14**) and tBu-DPhOP-Cz-DMB (**15**) is that they appear to be much more mixed upon the π-bridge than the other molecules in this series, yet their emissions show slight TADF character. However, it could be the case that in the excited state the phenoxy groups add additional steric hindrance, permitting better HOMO-LUMO separation than the calculations at this level of theory would suggest. Furthermore, interactions between the oxygens of the phenoxy groups and the boron's empty p-orbital may be having a greater effect on rISC than the mixing of the HOMO and LUMOs are able to quench. Further exploration of the proximity of the oxygen to the boron *via* single crystal XRD is required to understand this better.

5.3.11 Crystal structures

Single crystals of compounds **10** and **12**-**15** were grown from chloroform : methanol vapour diffusion and single crystal XRD was performed at the University of Southampton by Dr Laura McCormick. The .cif files were processed in Mercury software for rendering and structural measurements. This data aids in the exploration of the conformations of the molecules, as well as the potential for non-covalent interactions and yielded interesting and unexpected results for compounds **14** and **15**.

Table 5-19 Key distances and bond lengths from single crystal XRD. The B-O/C/H distances refer to the distances between boron and the nearest atoms on the substituent groups of the π-bridge.

Compound	B – O/C/H distance (Å)	B – O/C/H distance (Å)	N – C bond length (Å)	B – C bond length (Å)
tBu-DMP-Cz-OBA (10)	2.60 (B-H) 2.95 (B-C)	2.61 (B-H) 3.04 (B-C)	1.42	1.58
tBu-DMP-Cz-DMB (12)	2.84 (B-H) 3.03 (B-C)	2.90 (B-H) 3.03 (B-C)	1.42	1.58
tBu-DMeOP-Cz-DMB (13)	2.77 (B-O)	2.82 (B-O)	1.42	1.58
tBu-MPhOP-Cz-DMB (14)	2.93 (B-O)	2.72 (B-H)	1.42	1.57
tBu-DPhOP-Cz-DMB (15)	2.91 (B-O)	2.88 (B-O)	1.41	1.58

Table 5-20 Key angular measurements from single crystal XRD. The B-O/C/H distances refer to the distances between boron and the nearest atoms on the substituent groups of the π-bridge.

Compound	D – A dihedral (°)	D – π-bridge dihedral (°)	A – π-bridge dihedral (°)
tBu-DMP-Cz-OBA (10)	15.1	53.36	67.06
tBu-DMP-Cz-DMB (12)	2.48 / 2.37	52.20	49.55 / 49.98
tBu-DMeOP-Cz-DMB (13)	12.38 / 2.76	46.48	54.24 / 57.70
tBu-MPhOP-Cz-DMB (14)	18.65 / 2.58	30.17	48.59 / 42.95
tBu-DPhOP-Cz-DMB (15)	0.38 / 15	46.41	48.79 / 46.77

The single crystal XRD structures are shown for compounds **10**, **12** and **13** in Figure 5-29 and the structures for **14** and **15** are shown in Figure 5-30, with the key structural features for all five molecules recorded in Table 5-19 and Table 5-20.

In all cases, a dihedral exists between the donor's π-bridge and the acceptor, suggesting scope for HOMO-LUMO separation. The rigidity of the anthracene-like acceptor in compound **10** affords this the best HOMO-LUMO separation, with the remaining dimesityl boron compounds being less well separated. Interestingly, the dimethoxy compound **13** has a larger dihedral angle than its dimethyl analogue by 4.7° / 7.7°, which suggests the methoxy

groups contribute to increasing the dihedral angle more than methyl groups are capable of. Conversely, phenoxy groups have slightly reduced dihedrals. This is most likely due to steric effects of their bulk impacting upon the two mesityl groups, making the π – A twist more difficult to attain despite any non-covalent benefits the oxygen atoms may be capable of.

The XRD data is in good agreement with the DFT calculations with regards to N – C and B – C bond lengths. The D-A dihedral angles differ somewhat, but the trends observed (the dimethoxy and diphenoxy compounds have slightly larger dihedrals than their dimethyl and monophenoxy counterparts) are present. Whilst significantly different in value, the DFT calculations correctly predicted that the compound with the 10-bromo-10H-dibenzo[b,e][1,4]oxaborinine acceptor (compound **10**) would have a significantly larger acceptor – π-bridge dihedral angle compared to dimesityl boron.

Interestingly, none of the kinks to the D-π-A structures (shown in Figure 5-31) nor the face-to-face orientation of the phenoxy and dimesityl rings, were predicted at the particular level of theory used in the calculations. This suggests its limitation for predicting the presence of non-covalent interactions of this nature.

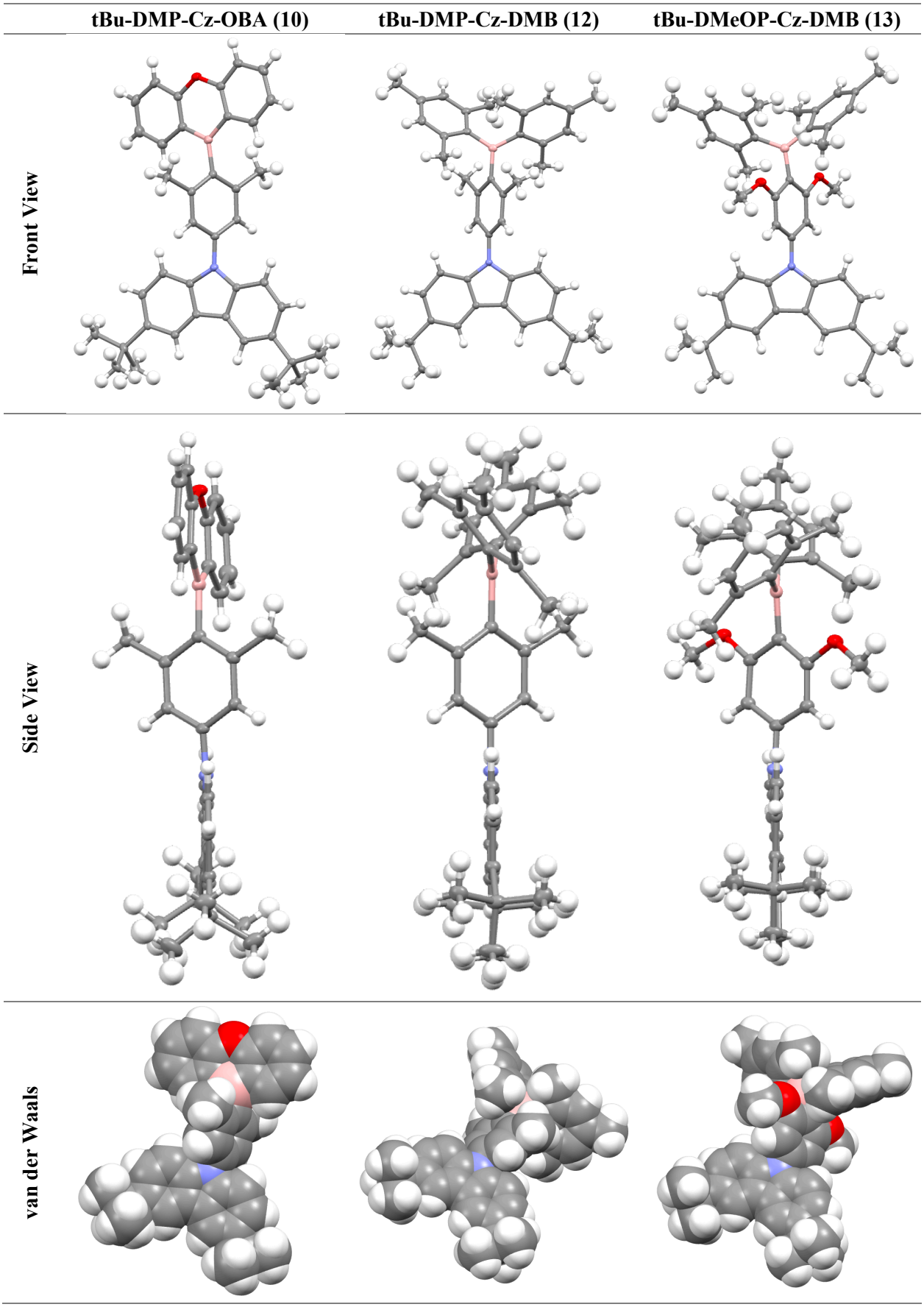


Figure 5-29 Single crystal XRD structures for compounds 10, 12 and 13.

In compound **10** the XRD data shows the methyl groups orient such that the hydrogen atoms are closer to boron than the methyl carbon is in the DFT calculations.

Twisting of the dimesityl groups, combined with steric hindrance of the methyl groups on the π-bridge on compound **12**, and the methoxy groups on compound **13**, conspire to offer protection of the boron atom from potential chemical attack (see van der Waals diagrams in Figure 5-29). The boron atom in compound **10** is much more exposed owing to the more planar anthracene-like acceptor unit.

Interestingly, in compound **13** the oxygen atoms on the π-bridge are orientated to potentially interact with the boron atom's empty p-orbital. Indeed, the distance between boron and oxygen in this case is just 2.77 Å on one side and 2.82 Å on the other. All three molecules have a slight kink across their centre between the donor π-bridge and acceptor (N – π – B). This is most likely an artefact of steric congestion around the π-bridge.

In addition, the B-C bond length is identical between each molecule. This suggests that the poorer stability observed in the TGA measurements is perhaps not related to the strength of this bond.

The phenoxy compounds' XRD structures paint a very different picture, as can be seen in Figure 5-30.

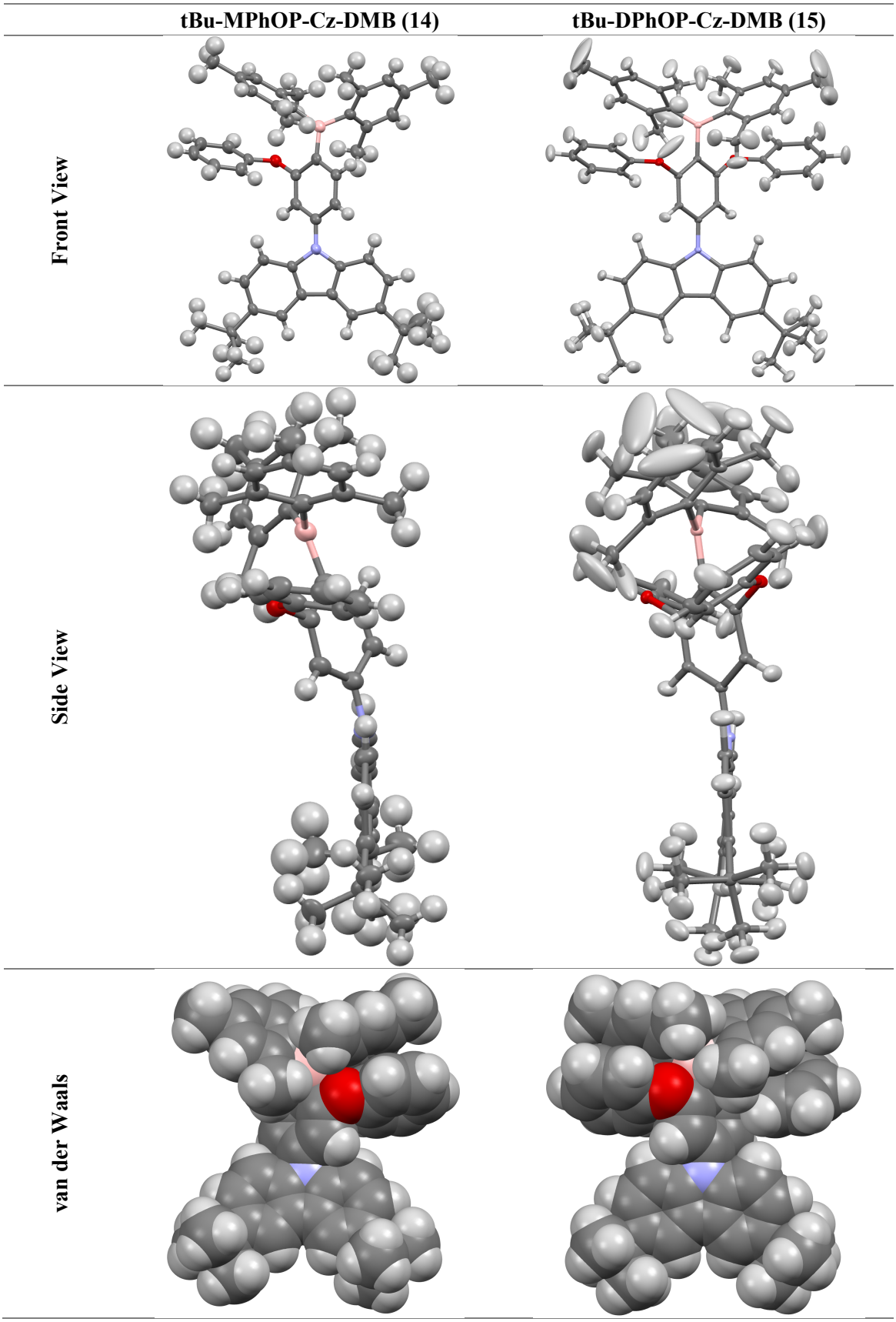


Figure 5-30 Single crystal XRD structures of the phenoxy compounds.

Compound **15** exhibits a 4.51° kink across the carbazole unit across the lower C-C bridging bond. This compares to the monophenoxy derivative which exhibits a 0.09° kink, resulting in reduced distortion to the carbazole's planarity.

Across the π-bridge (boron to π-bridge centroid to nitrogen) can be observed a slight distortion to the supposedly linear rod-like structure. This is illustrated in Figure 5-31.

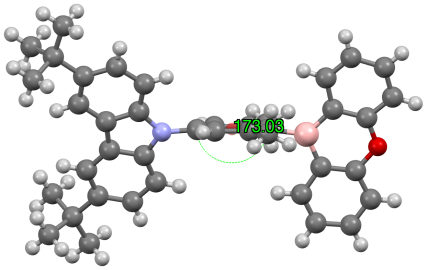
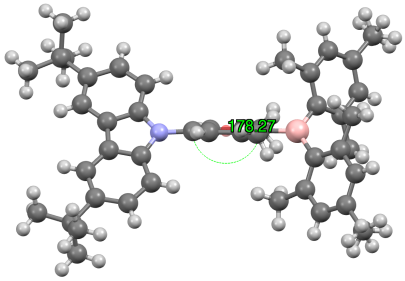
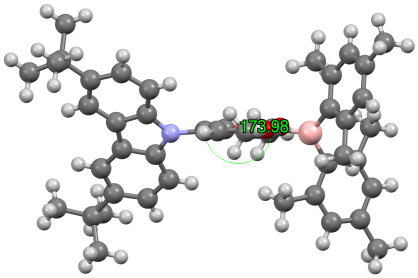
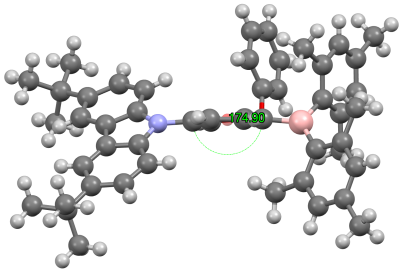
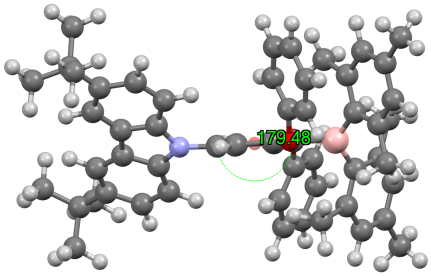
	Structure	Deviation from planarity
tBu-DMP-Cz-OBA (10)		6.97°
tBu-DMP-Cz-DMB (12)		1.73°
tBu-DMeOP-Cz-DMB (13)		6.02°
tBu-MPhOP-Cz-DMB (14)		5.10°
tBu-DPhOP-Cz-DMB (15)		0.52°

Figure 5-31 Illustration of D-π-A kinks centred on the π-bridge centroid.

In compound **10**, the molecule buckles by 6.97° across the D – π – A chain. Swapping the acceptor for dimesityl boron in compound **12** the buckling is negligible – just 1.73°. This increases upon substitution of the methyl groups for methoxy groups in compound **13** to 6.02°, which is comparable to compound **10**.

The bulky phenoxy group in compound **14** yields a kink of 5.10° but adding a second in compound **15** reduces this to 0.52°. Interactions between the phenoxy rings and the dimesityl rings may be contributing to this.

In all the compounds featuring a methoxy or phenoxy group, the boron – oxygen distances are less than the sum of the respective van der Waals radii of boron and oxygen atoms (2.00 Å and 1.53 Å, respectively[273], yielding a limit of 3.53 Å for this B-O interaction). Furthermore, Conboy *et al*.[243] demonstrate that enhanced conjugation (planarity) caused by non-covalent interactions leads to narrower optical HOMO-LUMO energy gaps. Conversely, therefore, if non-covalent interactions lead to enhanced HOMO-LUMO separation, then the energy of the optical HOMO-LUMO energy gap will increase. Indeed, this is observed when comparing the methyl derivative, compound **12**, to that of compound **13** and **15**, where the optical HOMO-LUMO gap clearly increases in energy by 0.3 eV and 0.14 eV, respectively, suggesting better HOMO-LUMO separation.

An additional consideration to the interactions between the phenoxy rings and mesityl rings in tBu-MPhOP-Cz-DMB (**14**) and tBu-DPhOP-Cz-DMB (**15**) is that boron, being electron deficient, will make the whole dimesityl boron moiety electron deficient, thereby drawing electron density away from the mesityl rings. Further to this, the oxygen will be less likely to induce electron density into the π-bridge through resonance effects, owing to the nearby nitrogen with its n-orbital. As such, it is likely to induce at least some of its potential electron density into the phenoxy rings instead, making them slightly more electron rich. These electron rich phenoxy rings are therefore able to draw the electron deficient mesityl rings into better alignment, maintaining the conformation seen in the XRD structures through face-to-face π stacking[305].

5.3.12 Crystal packing

tBu-DMP-Cz-OBA (10)

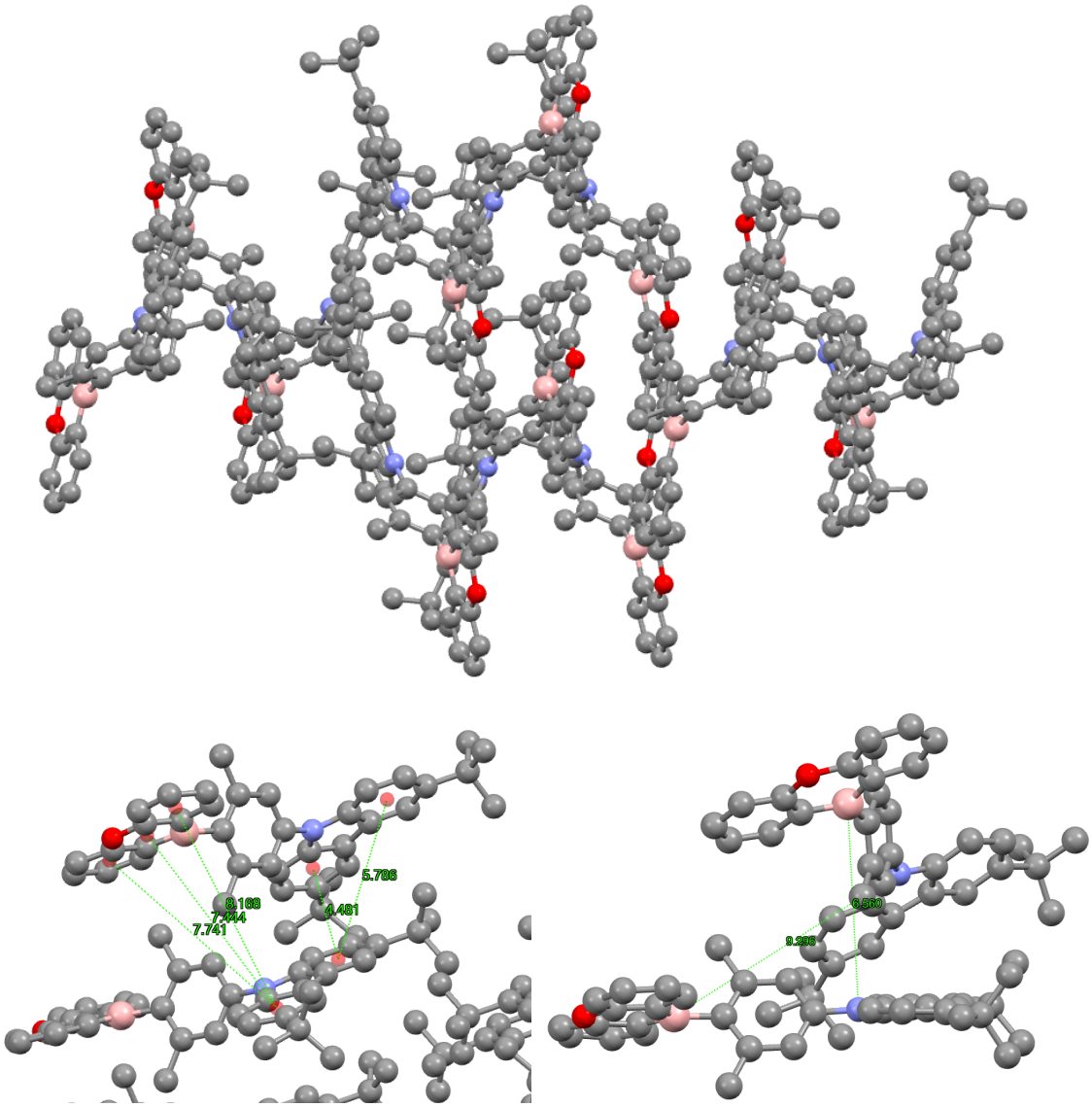


Figure 5-32 Packing and centroidal and B-N close contacts in tBu-DMP-Cz-OBA (10).

According to Janiak's 2001 study[306], π-π interactions from perfectly aligned aromatic systems, typically operate in the range of 3.3 Å to 3.8 Å. However, this can extend up to a far as 4 Å according to Chen *et al.*[245,307] for intramolecular π-π interactions.

Compound **10** packs with aromatic ring distances from 4.48 Å to 8.17 Å which is therefore far too distant to give rise to aggregation effects (see Figure 5-32). Neighbouring boron and nitrogen atoms are at their closest point 6.56 Å from one another, meaning that any interactions between lone pair electrons and empty p-orbitals cannot be occurring between molecules, so any CT character must be arising from internal effects on each molecule.

tBu-DMP-Cz-DMB (12)

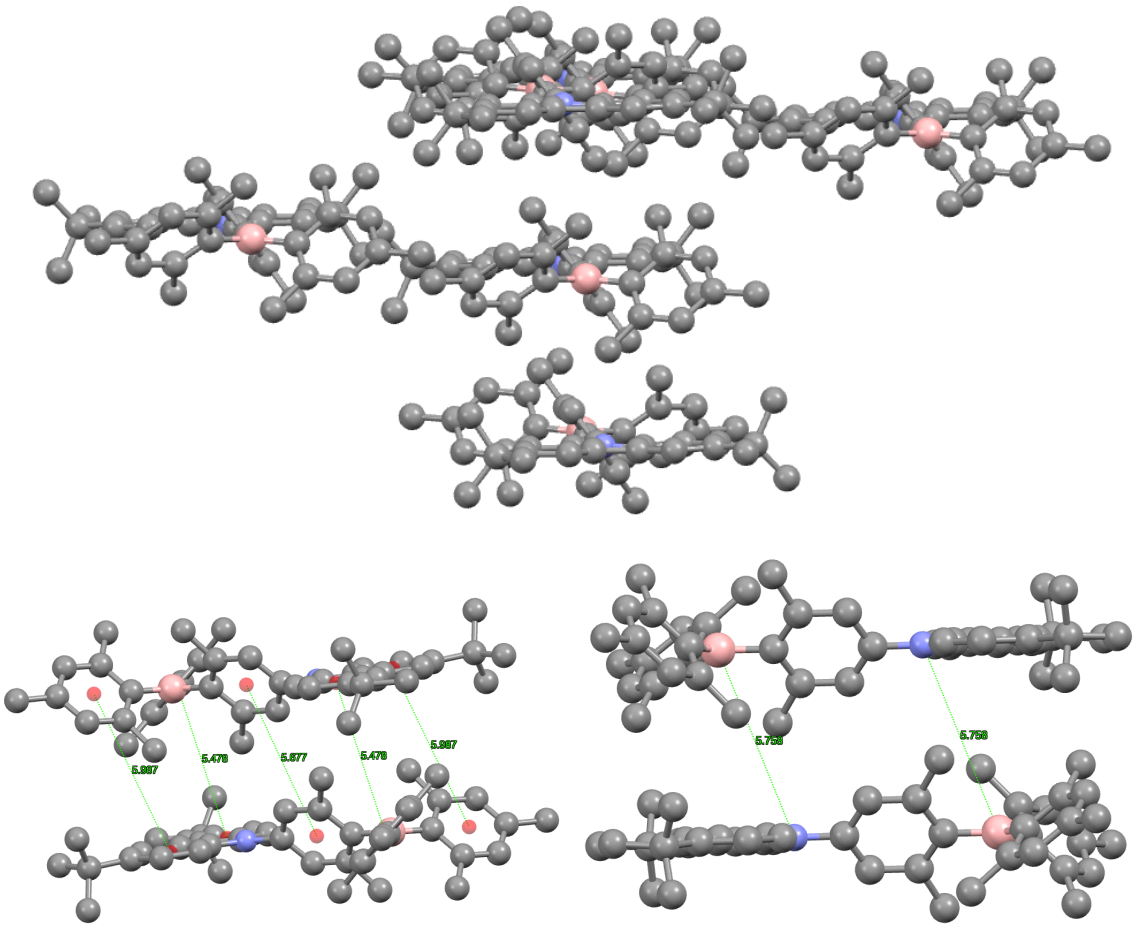


Figure 5-33 Packing and centroidal and B-N close contacts in tBu-DMP-Cz-DMB (12).

Compound **12** stacks with intermolecular aromatic distances of as little as 5.48 Å, which again is too far for non-covalent interactions to be occurring between individual molecules (see Figure 5-33). Intermolecular boron-nitrogen distances are on the order of 5.76 Å, which also will result in no donation to the boron atom from a neighbouring molecule's nitrogen atom.

tBu-DMeOP-Cz-DMB (13)

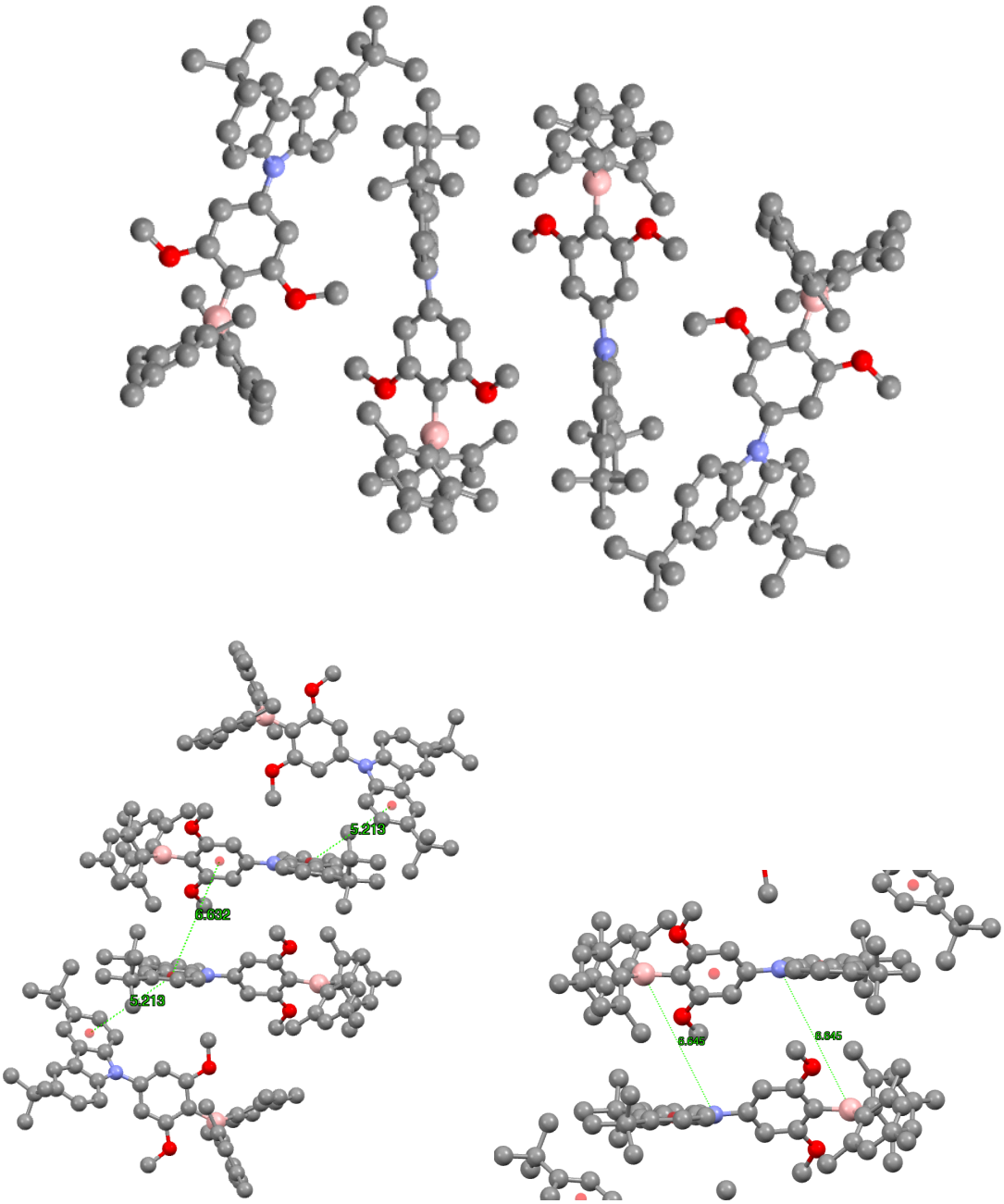


Figure 5-34 Packing and centroidal and B-N close contacts in tBu-DMeOP-Cz-DMB (13).

The closest aromatic distance in compound **13** is 5.21 Å, preventing any meaningful interactions (see Figure 5-34). The intermolecular boron-nitrogen distances are 6.65 Å, which is 0.89 Å greater than the non-methoxy derivative, owing to the greater steric bulk of methoxy substituent groups compared to methyl on the π-bridge.

tBu-MPhOP-Cz-DMB (14)

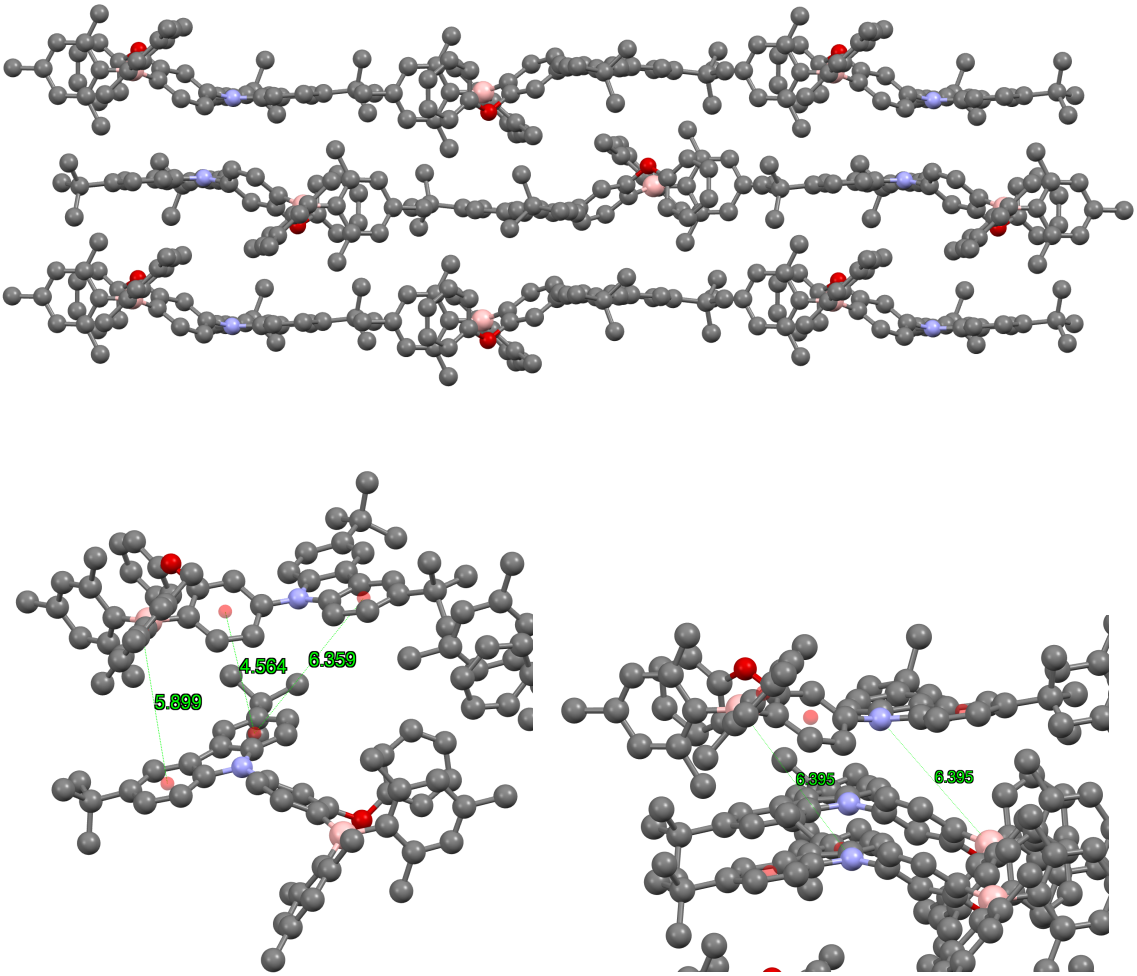


Figure 5-35 Packing and centroidal and B-N close contacts in tBu-MPhOP-Cz-DMB (14).

Compound **14** packs in layers, however their face-to-face aromatic contacts are misalligned and in excess of 5.90 Å for the most part (with a slightly closer distance between one donor's π-bridge and neighbouring carbazole at ~4.6 Å), with interactions still being unlikely (see Figure 5-35). Neighbouring donor and acceptor borons and nitrogens from adjacent molecules are too far apart to facilitate interactions here too.

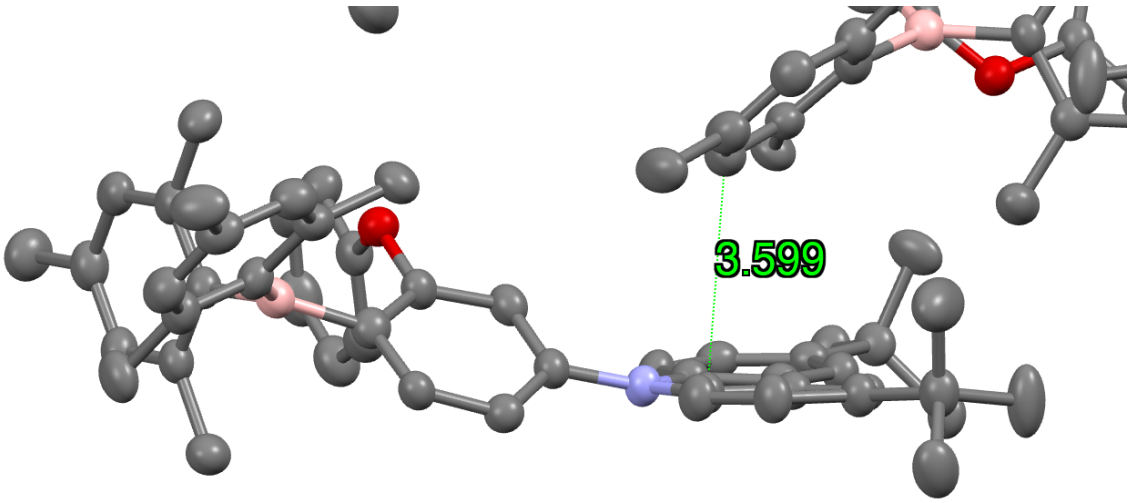


Figure 5-36 Closest atom-by-atom close contact in the crystal structure for tBu-MPhOP-Cz-DMB (14).

However, Figure 5-36 reveals that on an atom-by-atom basis, the proximities between the aromatic rings on neighbouring tBu-MPhOP-Cz-DMB (**14**) molecules get as close as 3.6 Å, suggesting potential for weak aggregation effects.

tBu-DPhOP-Cz-DMB (15)

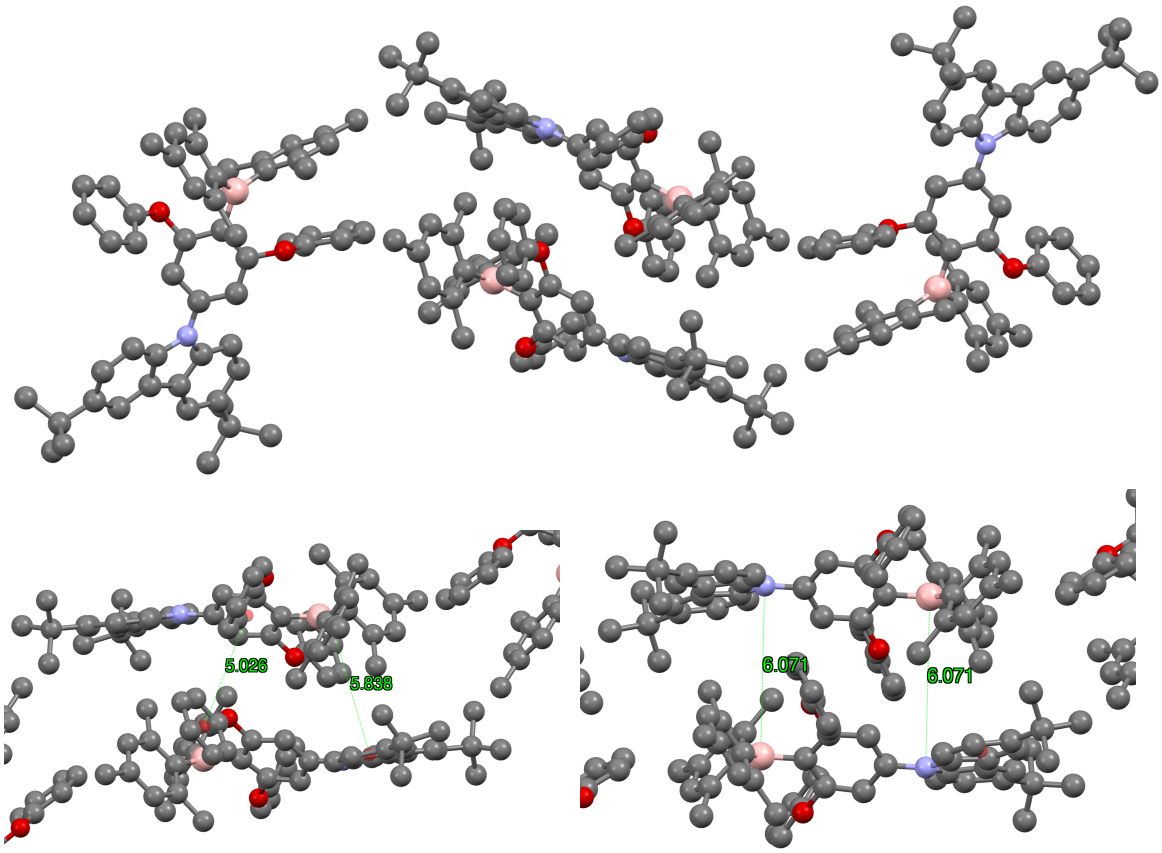


Figure 5-37 Packing and centroidal and B-N close contacts in tBu-DPhOP-Cz-DMB (15).

The distances between molecules of compound **15** are still too large to facilitate interactions (see Figure 5-37). Additionally, the borons and nitrogens of adjacent molecules are too far apart for intermolecular charge transfer to occur, despite good alignment.

On an atom-by-atom basis, there are no face-to-face rings at close enough proximity to facilitate interactions either.

5.3.13 Intramolecular phenoxy interactions

The two phenoxy compounds (**14** and **15**) demonstrate interesting co-facial orientations of their phenoxy and mesityl rings, which may give rise to intramolecular π-π interactions[308–311].

tBu-MPhOP-Cz-DMB (14)

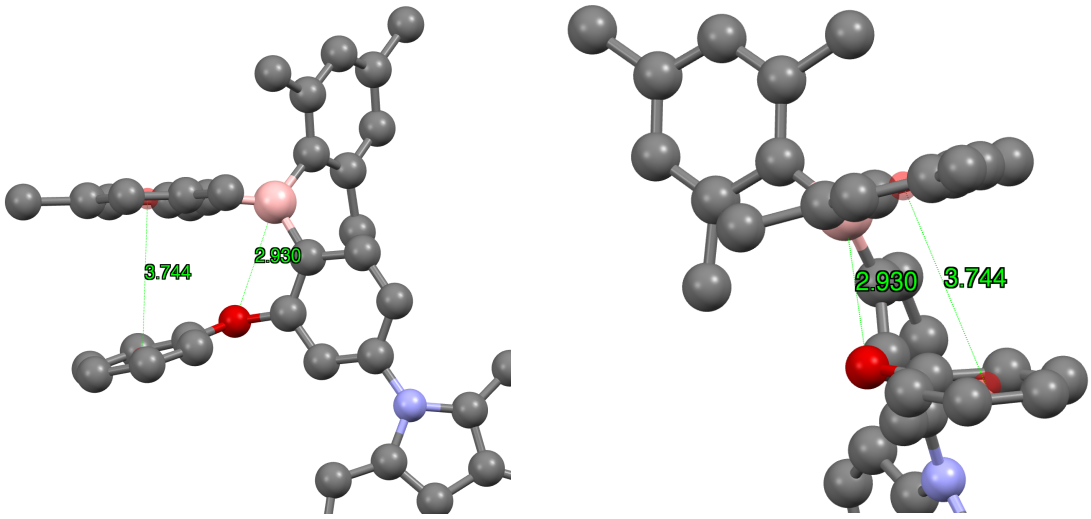


Figure 5-38 Internal π-π centroidal distances between phenoxy rings and dimesityl rings in tBu-MPhOP-Cz-DMB (14).

In compound **14**, the phenoxy group orientates to be coplanar with the nearest mesityl ring on the acceptor moiety with a distance of 3.74 Å. This orientates the oxygen away from the boron, but at a close enough distance for non-covalent intearactions at 2.93 Å. However, the cofacial alignment between phenoxy and mesityl rings is well within the 3-4 Å range for permitting donor – acceptor through-space π-π interactions[245,307].

tBu-DPhOP-Cz-DMB (15)

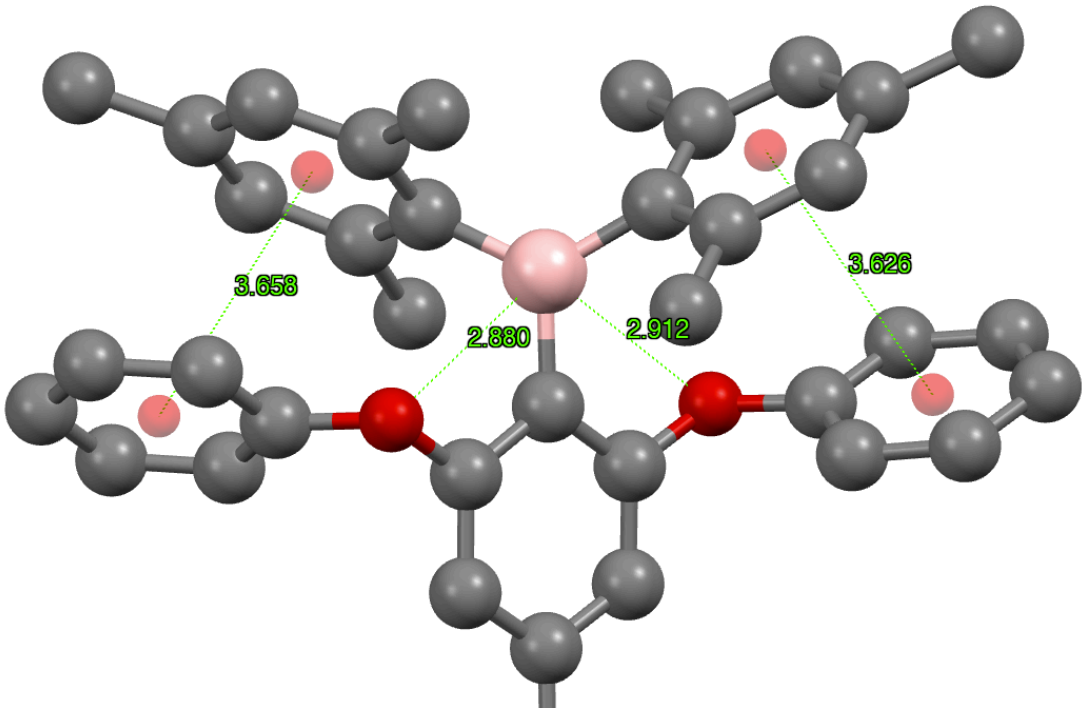


Figure 5-39 Internal π-π centroidal distances between phenoxy rings and dimesityl rings in tBu-DPhOP-Cz-DMB (15).

The additional phenoxy group in compound **15** adds extra steric bulk and yields boron – oxygen distances as little as 2.88 Å, suggesting the potential for B-O non-covalent interactions. An additional effect of the two phenoxy groups is that they orient co-facially with the mesityl groups to permit face-to-face π-π interactions at 3.63 Å and 3.66 Å centroidal distances, also within permissible proximity [245,307]. Interestingly, the whole dimesityl boron acceptor moiety reorients such that both phenoxy rings are interacting with both mesityl rings at very similar distances.

Tsujimoto *et al.*[312] observed non-covalent π-π interactions yielding TADF in three molecules: XPT, XCT and XtBuCT. In their study, they reported the close contact distances as being from the closest atom-to-atom distances (as opposed to centroidal – see Figure 5-40). Whilst centroidal close contacts is the dominant method of reporting interactions in the literature (owing to it illustrating an average of the orbital overlap between neighbouring aromatic systems), measurements of the closest contact distance for interactions have been adopted in some cases to provide some information as to the orientation preference of neighbouring rings[313]. As there is naturally some flexibility in the moieties' orientations, this measurement is adopted herein to illustrate the potential for at least partial π-π interactions in the same manner as Tsujimoto *et al.*'s [312] work for consistency.

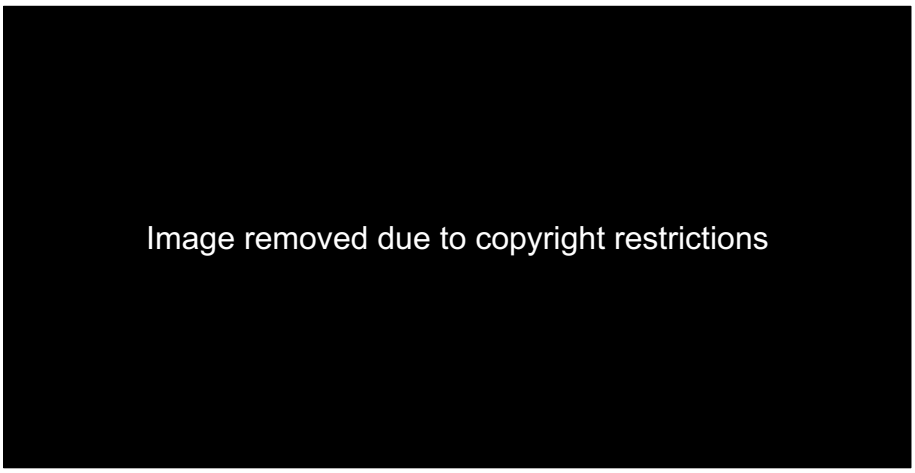


Figure 5-40 Tsujimoto *et al.*[312] reported crystal structures and close contact distances. a) d = 3.42 Å, b) d = 3.38 Å, c) d = 3.30 Å.

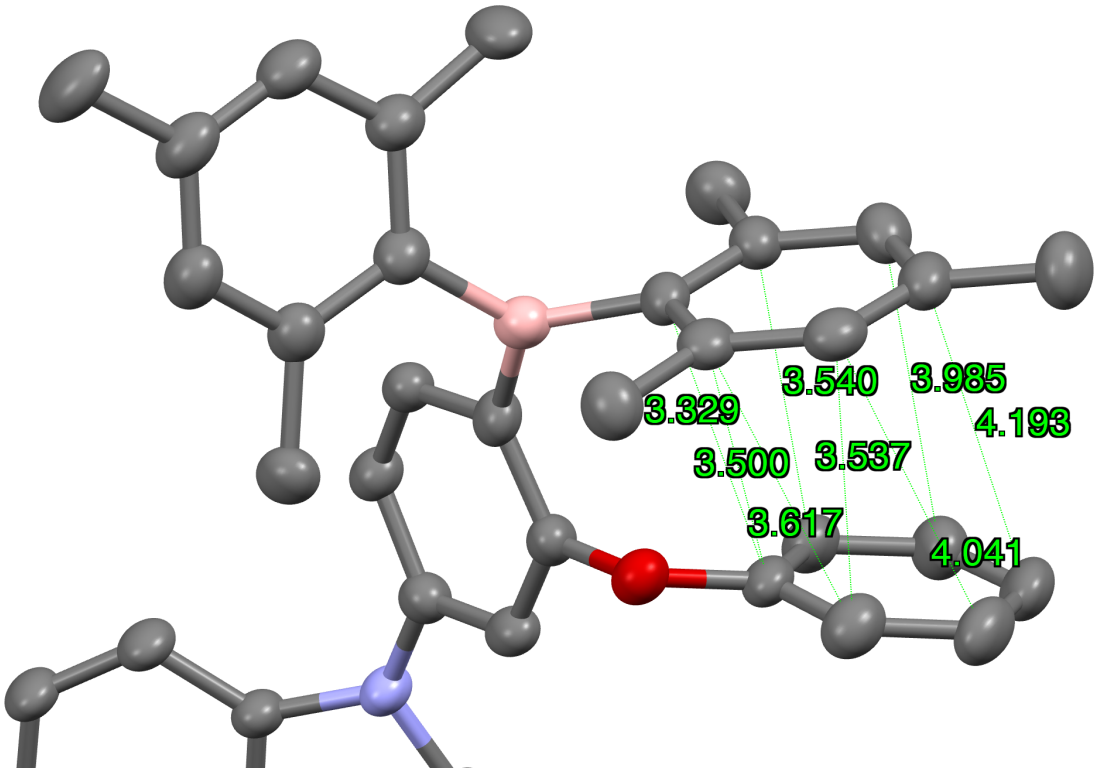


Figure 5-41 Internal π-π atom-by-atom distances between phenoxy rings and dimesityl rings in tBu-MPhOP-Cz-DMB (14).

In compound **14**, the closest contact between the phenoxy and mesityl rings using this approach is 3.33 Å, which is of the same order as Tsujimoto *et al.*'s[312] work and permits non-covalent intramolecular interactions in this compound.

In compound **15**, thanks to the steric hindrance of two phenoxy rings contorting the dimesityl boron acceptor moiety, we actually have contacts slightly closer than Tsujimoto *et al.*[312]

reported – reaching as narrow a gap as 3.27 Å, further confirming the presence of intramolecular non-covalent interactions in this molecule.

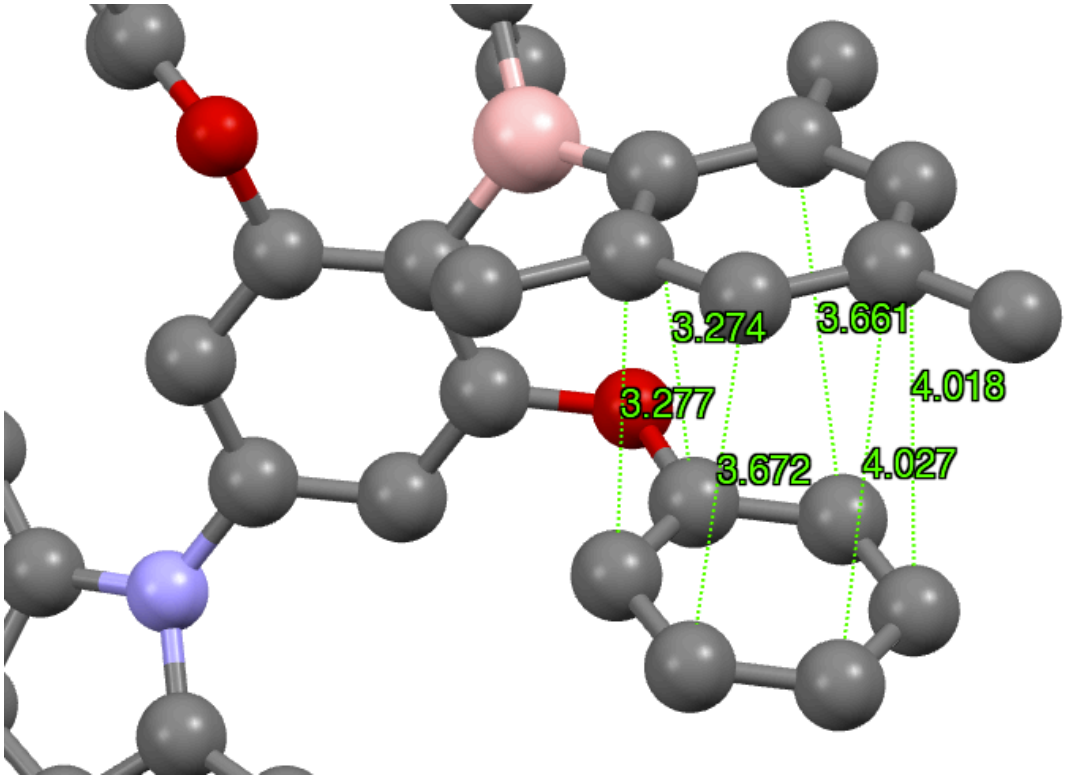


Figure 5-42 Internal π-π atom-by-atom distances between phenoxy rings and dimesityl rings in tBu-DPhOP-Cz-DMB (15).

Caution should be taken with this approach however, as it can misleadingly result in the assumption of interactions when the rings are in fact only partially aligned, which diagram c) from Tsujimoto *et al.*'s [312] work in Figure 5-40 clearly is. Nevertheless, as mentioned previously, the centroidal close contacts for tBu-MPhOP-Cz-DMB and tBu-DPhOP-Cz-DMB are in good agreement with accepted π-π interactions distances in the literature, and we can therefore conclude that interactions between the phenoxy rings and mesityl rings are occurring (however weak they may in fact be).

5.3.14 Chemical stability

In Chapter 4, the chemical stabilities of the boron-based emitter compounds were found to be highly sensitive to the steric congestion around the boron – nitrogen bond. In this chapter, the six molecules were designed to avoid B-N bonds and incorporate π-bridges with substituents designed to offer some protection to the boron's empty p-orbital.

To investigate the impact of these design considerations, 1E-4 M solutions of each (excluding compound **11**) were prepared in dry tetrahydrofuran and the solutions spiked with 1 mL deionised water, shaken vigorously and the PL spectra recorded over a period of time (shown in Figure 5-43 and Figure 5-44).

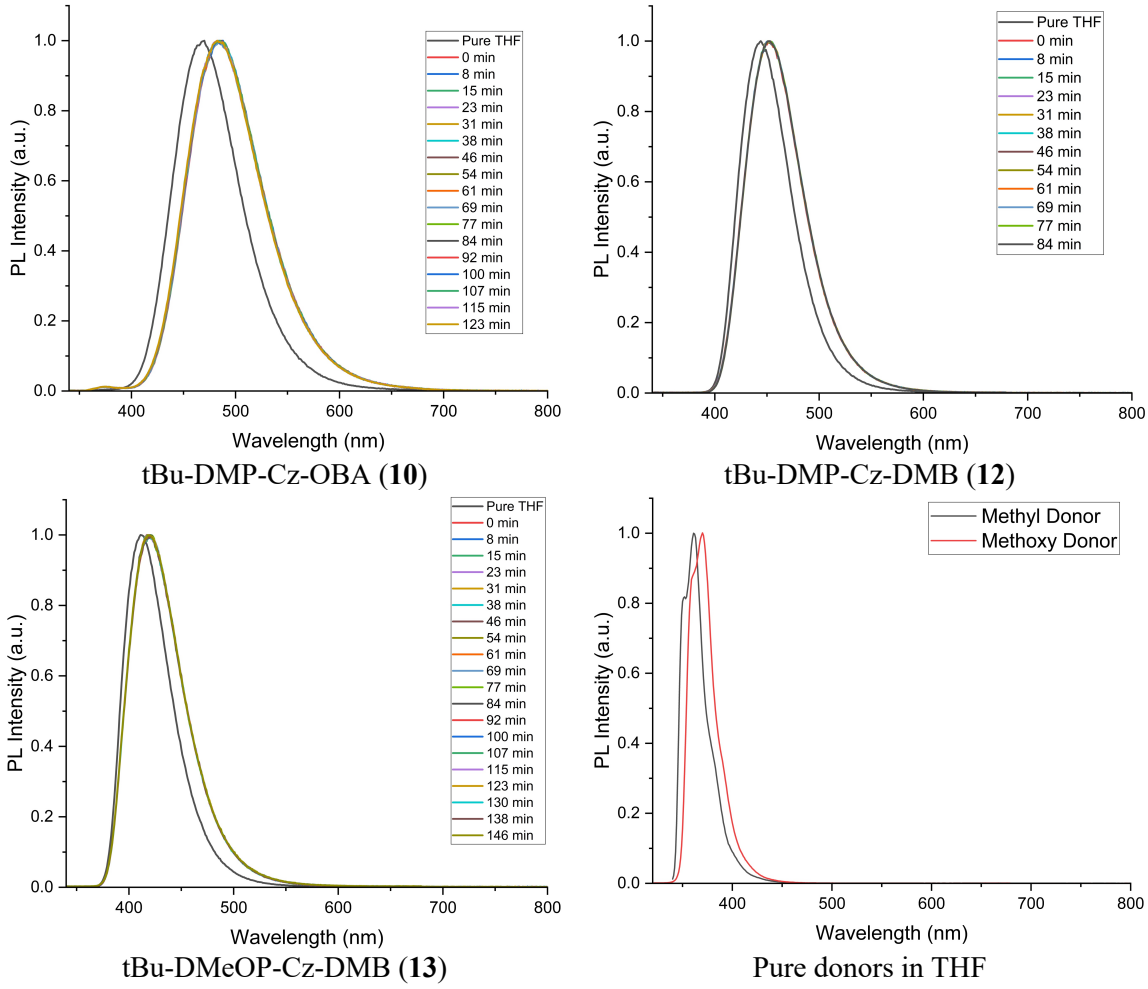
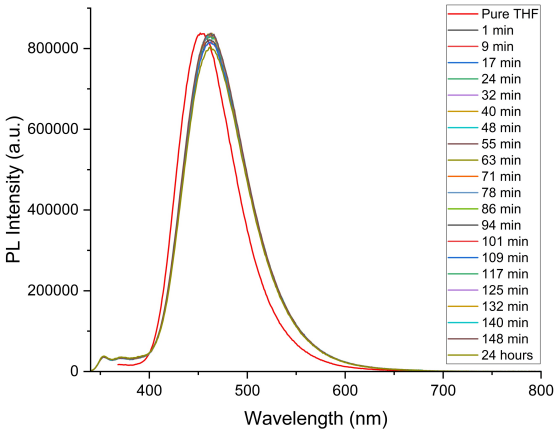


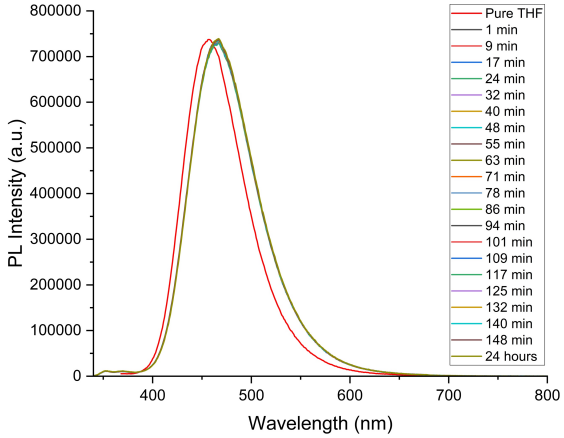
Figure 5-43 PL Spectra of compounds 10, 12 and 13 in dry tetrahydrofuran, spiked with 1 mL of deionised water. Included are the recorded emissions prior and post spiking for comparison, along with the PL of the pure donor material in tetrahydrofuran.

After being spiked with a substantial quantity of water and left for more than an hour, no changes to the emission spectra were observed, other than the corresponding solvatochromic

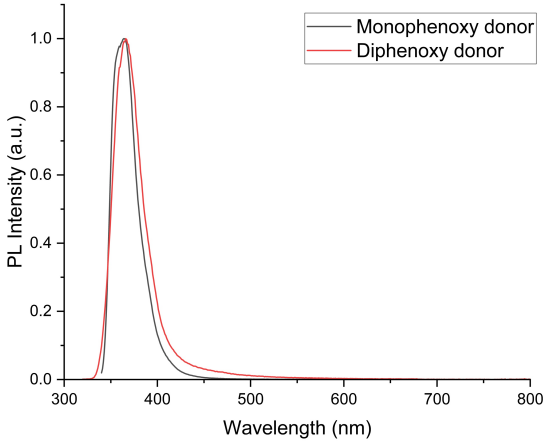
red-shift associated with exposure to more polar water than tetrahydrofuran. Comparison to the pure donor molecules in tetrahydrofuran clearly shows no presence of emissions associated with that free compound which would be expected if hydrolysis occurs.



tBu-MPhOP-Cz-DMB (**14**)



tBu-DPhOP-Cz-DMB (**15**)



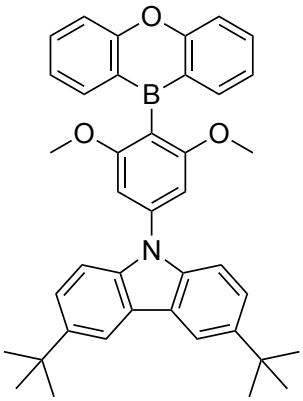
Pure Donors in THF

Figure 5-44 PL Spectra of the phenoxy derivatives in this study in dry tetrahydrofuran, spiked with 1 mL of deionised water, as well as the pure donors in tetrahydrofuran.

Therefore, it is concluded that these compounds with π-bridges exhibit much greater chemical stability thanks to steric hindrance around the boron atom's empty p-orbital.

5.4 tBu-DMeOP-Cz-OBA (11)

The dimethoxy derivative of tBu-DMP-Cz-OBA (**10**), tBu-DMeOP-Cz-OBA (**11**) was prepared by Dr Andrea Pinto and the structure is shown in Figure 5-45. However, only 10 mg was obtained, and the purity was not 100% (though still of a decent quality). As such, only basic photophysical measurements were attempted to observe how it compared to compound **10** since traces of the free donor or acceptor would skew any CV measurements, and there was not enough material for TGA or DSC measurements. The UV-vis absorption, PL and TCSPC spectra are shown in Figure 5-46.



tBu-DMeOP-Cz-OBA

Figure 5-45 Structure of tBu-DMeOP-Cz-OBA (11).

In toluene, the PLQY under air was found to be 41% and 72% when degassed with argon. Whilst the degassed measurement is slightly less than the 79% observed for the dimethyl derivative, the air-exposed measurement increased by 8%. Whilst this may suggest that the addition of the methoxy groups reduces the impact of oxygen quenching, this is unlikely to be the case since the opposite effect is noticed with the dimesityl boron compounds. As such, it is likely to be a combined artefact of the contaminated sample and measurement error.

The UV-vis absorption spectra reveal a sharp peak at 348 nm, with a shoulder at 337 nm (being less prominent in dimethyl sulfoxide than it is in toluene). In toluene, emission occurs at 400 nm, with a FWHM of 45 nm. In more polar dimethyl sulfoxide, emission occurs at 500 nm, with a FWHM of 95 nm. This large solvatochromic red-shift (100 nm) going from toluene to dimethyl sulfoxide, along with an increase in PLQY upon degassing (72% degassed versus 41% when exposed to oxygen), suggests that the key emission pathway is from a singlet charge transfer state.

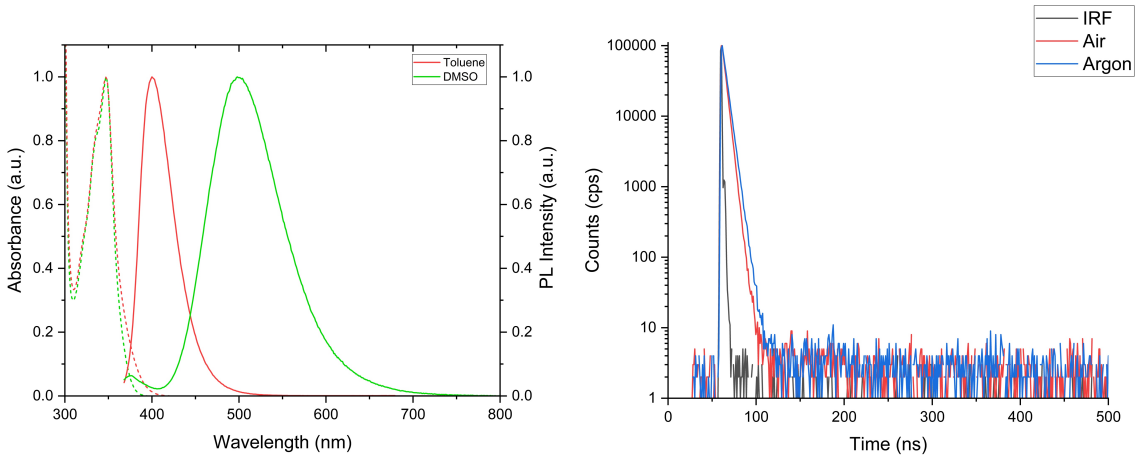


Figure 5-46 UV-vis and PL spectra (left) for tBu-DMeOP-Cz-OBA (11) in non-polar toluene and polar DMSO revealing very strong solvatochromism. TCSPC plot (right) in toluene under oxygen (red) and degassed (blue). A 365 nm laser was used as the excitation source with pulses at 5 µs intervals and gated at 2 µs.

This stands in stark contrast to the dimethyl derivative, compound **10**, which has a solvatochromic shift of 111 nm (slightly larger), but the dimethoxy derivative lacks the double emission peaks in DMSO at 373 and 536 nm (only 500 nm). However, the emission peak in toluene is 25 nm blue-shifted relative to the dimethyl derivative, and its FWHM is 5 nm narrower, further supporting the idea of methoxy groups aiding the production of blue emitters with narrower FWHMs. It should be stressed that the sample of compound **11** used was slightly impure, but the dominant emissions are from the target compound.

The TCSPC measurements performed on compound **11** in toluene, under oxygen and degassed, reveal prompt emissions, with τ_p in oxygen being 3.8 ns, with degassing extending this slightly to a τ_p of 4.59 ns. This contrasts with the methyl derivative in that the emissions remain significantly prompter with much less difference when oxygen is removed.

Whilst emissions from this compound are certainly of a CT nature, and are partially quenched by exposure to oxygen, it is unlikely to be of TADF nature owing to the lack of any delayed emission based on the TCSPC data.

However, owing to the CCD measurements in Durham revealing TADF in compounds **14** and **15** where the TCSPC did not, TADF in compound **11** should not be completely ruled out. Further studies of this compound are required, and a new synthesis is required to obtain a better-quality sample to explore its time-dependent decay and remaining physical and electrochemical properties.

5.5 Conclusions

In conclusion, the synthesis and photophysical characterisation of five novel boron-based D-π-A molecules has been reported, along with preliminary studies of a crude sample of a sixth. It was shown that the introduction of steric crowding around the donor – boron bond has led to enhanced thermal and chemical stability. Single crystal XRD studies reveal enhanced shielding around the boron atom preventing chemical attack *via* the empty p-orbital. However, the thermal stability is lost if the ortho-substituted groups upon the π-bridge are too bulky, as is the case with phenoxy groups.

Whilst Wu *et al*.[238] used our tert-butyl carbazole donor to effectively produce highly efficient green emissions when paired with a dibroaanthracene acceptor core in a D-π-A-π-D type structure, we have observed deep blue, weak TADF emissions in simpler D-π-A type structures with moderately weaker acceptor character in tBu-DMP-Cz-OBA (**10**) with 10-bromo-10H-dibenzo[b,e][1,4]oxaborinine as the acceptor. The use of phenoxy compounds yielded internal non-covalent π- π interactions as well as possibly B-O non-covalent interactions, effectively switching on delayed emissions in the form of dual room temperature phosphorescence and TADF, in stark contrast to the methyl and methoxy derivative which only exhibit prompt decay. This may well be the result of compounds **14** and **15** possessing (DD') - π - A and (DD_2') - π - A type structure, respectively, instead of the previously assumed D – π – A type structures, giving rise to distinctly separate ^{3}LE excited states upon the phenoxy groups.

Whilst O-B non-covalent interactions between the phenoxy groups and the boron atoms cannot be ruled out, the XRD data strongly suggests that π- π interactions between phenoxy aromatic rings and the aromatic mesityl rings are the dominant mechanism present in tBu-MPhOP-Cz-DMB (**14**) and tBu-DPhOP-Cz-DMB (**15**).

After an extended period with exposure to water, all five molecules in this chapter exhibited no sign of chemical degradation, suggesting that they are far more chemically stable than their counterparts in Chapter 4. This could be due to a combination of stronger C-B bonds and steric effects protecting the boron atom's empty p-orbital.

Expanding upon the work of Dr Joseph Cameron in Chapter 4, we see here that the presence of methoxy groups provides the potential for non-covalent interactions from the donor

moiety to the acceptor moiety from oxygen – boron interactions. Indeed, the methoxy compound exhibited a staggeringly deep blue, well into the ultraviolet emission range. A narrowing of emission FWHM accompanying the two dimesityl boron compounds suggests a loss of CT character compared to the boron-oxygen anthracene type donor. CT character is slightly enhanced with phenoxy groups, with additional numbers attached to the π-bridge, surprisingly causing no change in FWHM. A single phenoxy group permits bluer emissions with enhanced PLQY, likely due to reduced decay pathways permitted by the additional groups.

Further work on elucidating a higher yield reaction pathway to the dimethoxy compound, tBu-DMeOP-Cz-OBA (**11**) would be highly desirable, since that particular acceptor may unlock stronger CT character in the emissions, due to better HOMO-LUMO decoupling with such a rigid acceptor framework. Additionally, phenoxy analogues of this compound would be of great interest for further study as the phenoxy – mesityl effect may prove to yield more effective rISC than methoxy groups are capable, based on this study.

Chapter 6 Rod-like donor-acceptor-donor π-bridged boron-based TADF molecules exploiting non-covalent interactions to improve the rate of rISC

The work in this chapter encompasses a collaborative project investigating non-covalent interactions between methoxy groups upon a donor moiety's π-bridge and boron's empty p-orbital as part of a diboraanthracene acceptor moiety. Work was performed between myself, the University of Newcastle and Durham University. The entirety of the synthesis and the bulk of the photophysics herein was performed by myself, with additional quantities of precursors later provided by Dr Joseph Cameron and Dr Andrea Pinto, however the lifetime measurements and low temperature photophysics were performed at Durham University when I visited there. The Durham work was performed jointly by myself and Kamile Bareikaite who supervised me on my visits. The work in Durham is herein indicated with a δ symbol. I presented the results of this chapter as a poster at ICEL 2024 in Kyoto, Japan in November 2024.

6.1 Introduction

D-A-D type molecules provide the advantage of having the donor and acceptor units confined to a single molecule. In principle, synthesis of such structures can be simplified to a minimal number of steps[238].

Diboraanthracene (DBA)-based emitters have been shown to have high quantum yields when solid[227,238,314]. The colour of their emission wavelengths can also be tuneable, depending on substituent groups and donor moieties attached[238]. The empty p-orbital of 3-coordinate boron atoms provides enhanced electron acceptor character for DBA based moieties.

Boron-based, phenylene π-bridged D-A-D TADF emitters have recently been synthesised by Wu *et al*.[238] The group synthesised two molecules of this type, 9,10-bis(4-(9H-carbazol-9-yl)-2,6-dimethylphenyl)-9,10-diboraanthracene (or CzDBA) and 9,10-bis(4-(3,6-ditertbutyl-9H-carbazol-9-yl)-2,6-dimethylphenyl)-9,10-diboraanthracene (or tBuCzDBA).

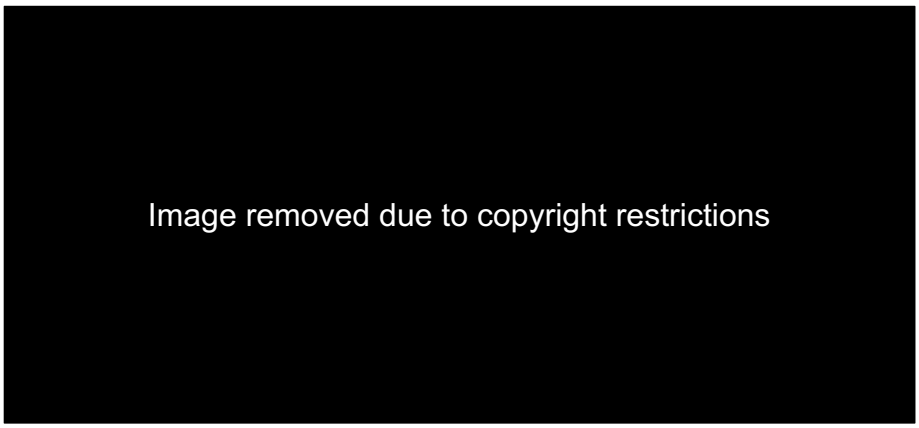


Figure 6-1 Structures and HOMOs and LUMOs of CzDBA (top) and tBuCzDBA (bottom), taken directly from Wu *et al*.[238]

Carbazole possesses a high triplet energy[315] which helps to promote rISC (and therefore TADF) and this moiety's planar geometry aids the confinement of the HOMO upon it.

In these structures, a carbazole based donor moiety (carbazole in CzDBA, tert-butyl carbazole in tBuCzDBA) is connected to the central diboraanthracene (DBA) acceptor moiety *via* a 2,6-dimethylphenyl π-bridge, which is orientated at a plane out-with that of the DBA acceptor moiety. The HOMO spreads partly onto the π-bridge, but remains largely over the carbazole moiety, whereas the LUMO spreads across the DBA acceptor moiety and only to a small degree, onto the π-bridge. The two methyl groups on the π-bridge maintain steric hindrance, enabling spatial separation of the carbazole centralised HOMO from the DBA centralised LUMO *via* a large dihedral angle, as well as shielding the boron's empty p-orbital from chemical attack (an attractive quality as demonstrated by the previous two chapters). Π-conjugation across the carbazole and across the DBA moiety is significantly aided by their planar structures and π-bond character, however the twist with respect to the π-bridge reduces π-conjugation between the donor and acceptor – keeping the HOMO and LUMO separate in space – the small degree of mixing still occurring on the π-bridge enabling spin-orbit coupling[121]. The overall structure is inflexible and rod-like, with only the carbazole moieties having any rotational degrees of freedom. This is reflected in the narrow fluorescence emission bands (524 nm with 77 nm FWHM for CzDBA and 553 nm with 78 nm FWHM for tBuCzDBA[238]) observed for the molecules. Additionally, the colour of devices fabricated involving CzDBA produced green emission CIE 1931 coordinates of 0.31, 0.61, making it the third best example of a pure green OLED emitter, with an EQE of 37.8%[238] at the time of their publication. Both molecules exhibited very low efficiency roll-off (some of the lowest of TADF molecules synthesised at that point) due to the short TADF lifetime, suppressing triplet-triplet annihilation, and reduced rotational and collisional

quenching. The significant horizontal dipole of the molecules contributed to their very high PLQY.

It has also been found that the steric effects of the molecule's π-bridge aids defence against water and oxygen reacting with the acceptor moiety. Previous work has indicated impressive tunability of DBA-based molecules. For example, use of 2-thienyl substituents allows for shifting blue emissions to the green region of the visible spectrum, whereas p-aminophenyl substituents have been shown to extend this shift into the red region[316].

6.2 Modifications

Use of tert-butyl substituent groups on the donor moiety in the original work of Wu *et al*.[238] enhances the carbazole's electron donating character, allowing for a 20 nm red shift in the emission. The tert-butyl groups also reduce the gap between singlet and triplet energy levels, ΔE_{ST} being 33 meV in CzDBA and 22 meV in tBuCzDBA. The narrow ΔE_{ST} in both cases allows for TADF to occur and is reflected in the lifetimes of prompt and delayed fluorescence reported, as well as the temperature dependence of the emissions – being greater at higher temperatures, reflecting the enhanced thermally activated rISC process and respective rates of rISC ($k_{rISC} = 3.13 \times 10^5\ s^{-1}$ in CzDBA and $k_{rISC} = 3.52 \times 10^5\ s^{-1}$ in tBuCzDBA). It was also observed that the PLQY is exceptionally high in thin films (100% for CzDBA and 86% for tBuCzDBA), likely enhanced in the thin film form due to a reduction in rotational and collisional quenching between molecules. However, the PLQY is significantly lower in toluene solution: 8.7% in air and 14% when degassed for CzDBA and 7.4% in air and 11.9% when degassed for tBuCzDBA. This suggests a limit to the effectiveness of steric hindrance from the methyl groups. Both molecules remained thermally stable at elevated temperatures – CzDBA exhibited a 5% weight loss at 418°C and tBuCzDBA at 402°C making them suitable for vapour deposition in OLEDs.

6.3 Recent advancements with CzDBA-type molecules

In 2020, Hsieh *et al*.[314] followed up on their group's previous paper on CzDBA with a paper reporting the synthesis of three additional derivatives, dPhADBA, dmAcDBA and SpAcDBA with orange to red emissions (see Figure 6-2 and Table 6-1).

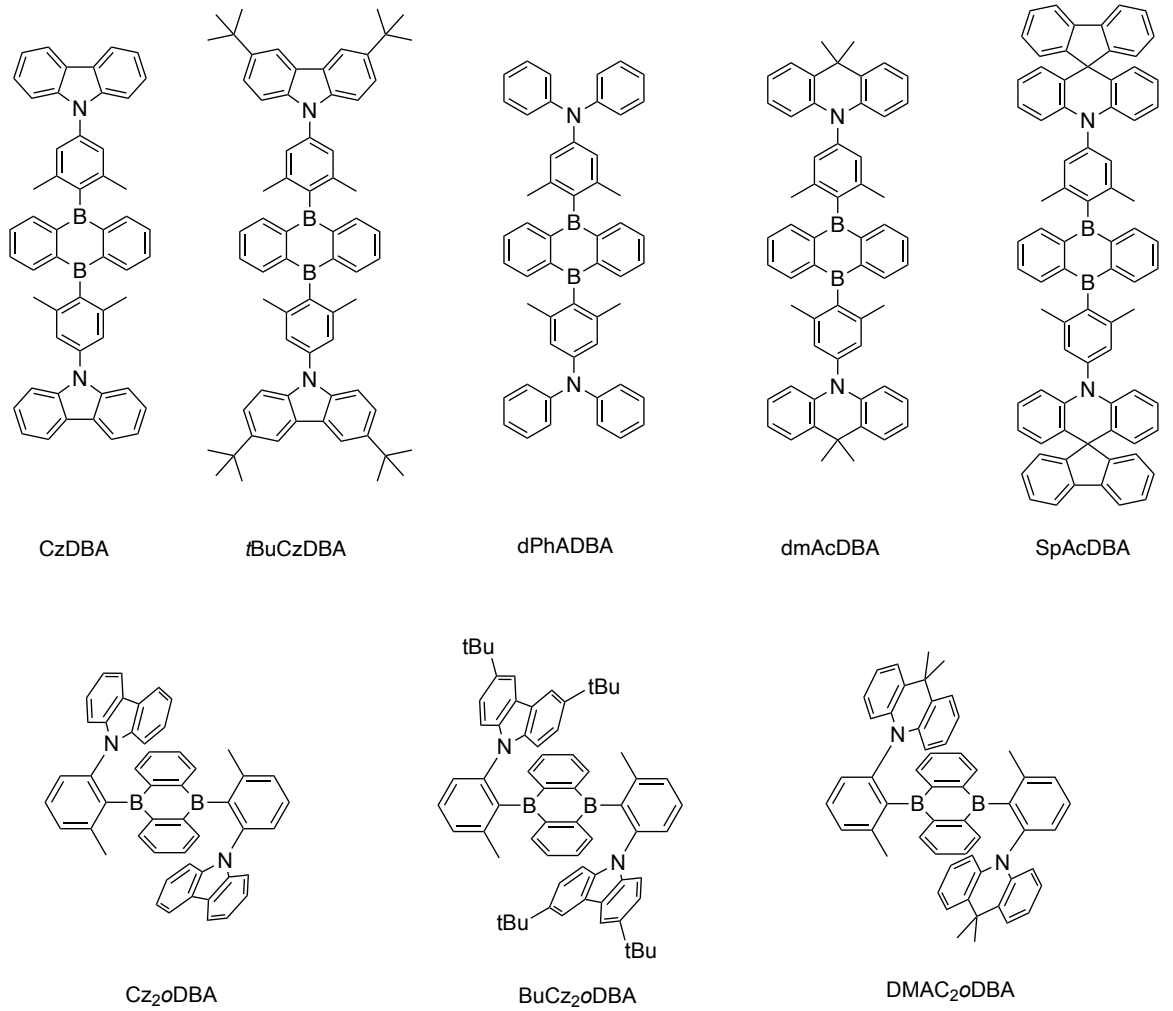


Figure 6-2 Structures of linear CzDBA derivatives adapted from Wu *et al*.[238], Hsieh *et al*.[314] (top); and ortho substituted derivatives reproduced from Kumar *et al*.[227] (bottom).

The structures differ from their progenitor, CzDBA, in that they used donor moieties with stronger donor character than carbazole. The donors were replaced with diphenylamine, dimethylacridine and 10H-spiro[acridine-9,9'-fluorene] bonded to a phenylene π-bridge in place of the carbazole used previously. The greater donor strength yielded bathochromic shifts in emissions.

Table 6-1 Photophysical properties of linear CzDBA derivatives from Wu *et al.*[238] and Hsieh *et al.*[314]

Molecule	PL_{fl} (nm)	S_1 (eV)	T_1 (eV)	ΔE_{ST} (eV)	PLQY*(%)
CzDBA†	524	2.629	2.596	0.033	100
t-BuCzDBA†	553	2.486	2.464	0.022	86.0
dPhADBA‡	614	2.30	2.26	0.04	53
dmAcDBA‡	587	2.52	2.46	0.06	71
SpAcDBA‡	570	2.57	2.49	0.08	85

† From Wu *et al.*[238]; k_{rISC} measured at 300K in 30nm CBP film; *thin film measurements; ‡ From Hsieh *et al.*[314]

Table 6-2 Photophysical properties of linear CzDBA derivatives from Wu *et al.*[238] and Hsieh *et al.*[314]

Molecule	k_{rISC} (10^5 s^{-1})	HOMO / LUMO (eV)	E_g (eV)	EQE (%)
CzDBA†	3.13	-5.93 / -3.45	2.48	37.8
t-BuCzDBA†	3.52	-5.88 / -3.49	2.39	32.4
dPhADBA‡	2.42	-5.52 / -3.34	2.18	11.1
dmAcDBA‡	1.32	-5.56 / -3.25	2.31	24.9
SpAcDBA‡	2.16	-5.56 / -3.27	2.38	30.0

† From Wu *et al.*[238]; k_{rISC} measured at 300K in 30nm CBP film; *thin film measurements; ‡ From Hsieh *et al.*[314]

Comparing the findings in Table 6-1 and Table 6-2, it is notable that, for the compounds containing carbazole and tBu-carbazole, the molecules exhibit a greater PLQY and narrower ΔE_{ST}, as well as higher k_{rISC}. Clearly the more rigid the structures (the fewer degrees of rotational freedom), the more enhanced the PLQY is. Taking a comparison of dPhADBA and CzDBA, the aromatic rings bonded to the nitrogen on the donor in dPhADAB are free to rotate, providing a means of non-radiative decay from the excited state, whereas in CzDBA, the C-C bond between the two rings prevents such a loss. This is reflected too in dmAcDBA and SpAcDBA, both of which have no means of rotation due to an additional sp^3 quaternary carbon and spiro-linkage respectively. The molecules were determined *via* DSC and TGA to possess very good thermal stability, decomposing at temperatures in excess of 350°C, making them highly suited to manufacturing devices *via* vacuum deposition. As with CzDBA, these molecules maintain a high dihedral angle between the donor and acceptor moieties due to the methyl groups on their π-bridge. Use of DBA as the acceptor moiety makes the TADF emitter molecule a '*doubly boron-doped*'[227] emitter owing to the two boron atoms in its structure.

Going further, Kumar *et al.*[227] took a diboraanthracene acceptor moiety with two methyl π-bridges much like Wu *et al.*[238] and Hsieh *et al.*'s[314] work, but instead of linear rod-like structures, introduced steric hindrance *via* a more contorted ortho-substituted structure (see the bottom of Figure 6-2). Their photophysical properties and EQEs are summarised in Table 6-3). A phenylene π-bridge is inserted between the DBA acceptor and the carbazole,

tBu-carbazole and DMAC donor moieties where the donors are bonded to the phenylene π-bridge in the *ortho* position instead of the *para* position previously. The D – A – D type structure is significantly twisted, giving rise to a narrow ΔE_{ST} gap of less than 0.08 eV due to minimal HOMO - LUMO overlap, locating their positions respectively on the donor and acceptor moieties. This enables efficient rISC and pronounced TADF. It was possible to control the emitted wavelength by changing the donor moiety. Weaker donors like carbazole giving shorter wavelengths (green) with bathochromic shifts observed for stronger donors such as DMAC. DMAC produced a poorer PLQY at around 44%, with carbazole being close to 100%. The two carbazole emitters demonstrated very good external quantum efficiencies (26.6% in the case of the carbazole donor and 21.6% for the tBu-carbazole donor). As with the aforementioned molecules, these structures exhibited excellent thermal stability, making them well-suited to vacuum deposition methods.

Interactions between the boron's p-orbital and the π-orbitals on the DBA rings are indicated by the shortened B-C bond lengths within them, whereas the C-B bond lengths to the π-rings are longer in comparison[227]. It seems that the B - N through-space non-covalent interactions narrows the ΔE_{ST} gap and facilitates rISC even for red emitters. The distances between the acceptor moiety's boron atom and the donor moiety's nitrogen atom in space is rather small, with X-ray crystallography indicating that the nitrogen and boron atom's van der Waals spheres overlapped (being between 2.87 Å and 2.93 Å apart), meaning that it is possible that there is interaction between the lone pair on the nitrogen and the empty p-orbital on the boron. This is further supported by the 24 nm shift in emission. When compared to the use of differing strength of donor moiety, the weaker electron donating moiety (carbazole) yielded longer N - B spatial distances. This property is of interest to our work - which involves a stronger donor causing ideally shorter methoxy - boron interatomic distances. However, whether the lone pair of the nitrogen atoms actually orients to interact with the boron atoms in this case is debatable owing to the subtle twisting of the carbazole moieties with respect to the π-bridge. Closer inspection of the structure held in the CCDC database (accompanying Kumar *et al.*'s[227] paper – see Figure 6-3) reveals a 54.9° donor twist with respect to the π-bridge, which could result in the n-orbital and empty p-orbitals being misaligned. In such a case, it is more likely that the enhancement they observe is more a result of structural hindrance preventing lossy pathways due to the sheer bulk of the donor moieties at such a contortion.

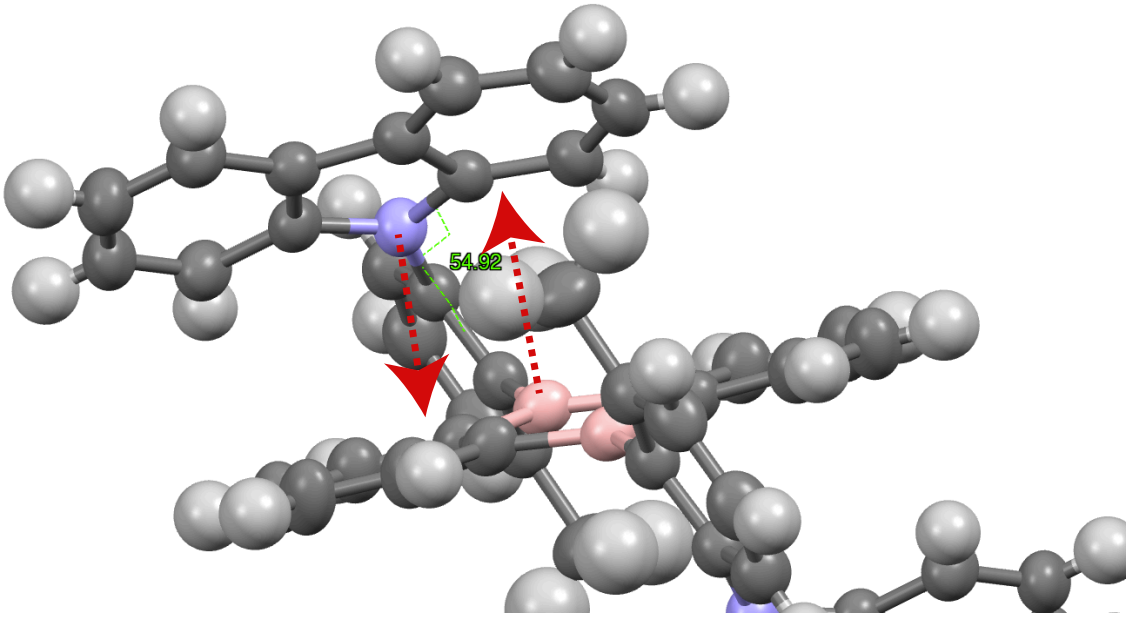


Figure 6-3 Misalignment of the n-orbital and empty p-orbital in Cz2oDBA from Kumar *et al.*'s work[227]. Image produced from the publicly available XRD data provided in their supporting information.

In addition, as the electron donating properties of the donor increases (greater donor strength), so too does the narrowing of the ΔE_{ST} and of the HOMO - LUMO gap, E_g, and increased bathochromic shift of emissions, as with Hsieh *et al.*'s work[314] (see Table 6-3 and Table 6-4 for a comparison of the photophysical properties).

Table 6-3 Photophysical properties and EQEs of ortho substituted CzDBA derivatives from Kumar *et al.*[227]

Molecule	E_g (eV)	ΔE_{ST} (eV)*	HOMO / LUMO (eV)	λ_{PL} (nm)
Cz2oDBA	2.65	0.029	-5.61 / -2.96	538
BuCz2oDBA	2.60	0.017	-5.60 / -2.99	558
DMAC2oDBA	2.39	0.010	-5.37 / -2.98	626

*Measured in toluene

Table 6-4 Photophysical properties and EQEs of ortho substituted CzDBA derivatives from Kumar *et al.*[227]

Molecule	$PLQY_{N2}$ Thin film (%)	$PLQY_{N2}$* (%)	$PLQY_{O2}$* (%)	k_{rISC} (10^5 s^{-1})	EQE (%)
Cz2oDBA	100	99	10	1.56	26.6
BuCz2oDBA	99	83	12	2.26	21.6
DMAC2oDBA	44	19	8	2.74	10.1

*Measured in toluene

The PLQY decreases going from least electron donating to greatest electron donating character, however when compared to para-substituted equivalents, these represent a good improvement owing to the more rigid ortho donor-acceptor structure. The significant drop

in PLQY when in oxygen saturated solution indicates oxygen-facilitated triplet state quenching, meaning that very efficient rISC occurs between S_1 and T_1 states when degassed. Furthermore, the significantly higher solution PLQYs of Cz2oDBA and BuCz2oDBA compared to Wu *et al.*'s[238] CzDBA and tBuCzDBA, suggests π-bridge rotational losses are reduced due to the possible nitrogen – boron interactions in the excited state.

The delayed lifetime also decreases with increased electron-donating character, further supporting the case for a narrower ΔE_{ST}. Despite DMAC2oDBA possessing a narrow ΔE_{ST} gap, its delayed emission quantum yield is relatively low (6.3%), which is likely caused by nonradiative decay from the excited triplet state T_1 occurring at a more rapid rate than rISC. The authors suggest that having donor moieties connected in the ortho position to a phenylene ring on diboraanthracene systems is key to improving solution TADF.

9,10-Diboraanthracene acceptor-based TADF molecules show promising potential as highly efficient organic light emitting molecules. The tuneability of emission wavelength by modification of the substituent groups bonded to the carbazole moiety makes them attractive building blocks for OLED devices. Protection from oxygen and water attack by a sterically hindered π-bridge bonded to the boron atoms provides a great advantage to their versatility. Investigation into modification of the substituents on the carbazole donor moiety (and perhaps even alternatives to carbazole), and replacement of the methyl groups bonded to the phenylene π-bridge is an exciting area for further research.

Functional groups possessing lone pairs to induce weak interactions with boron have been demonstrated to aid stability, as well as making effective molecular sensors[317–321]. Functional groups involving oxygen atoms have also been shown to be quite effective in interacting with boron through-space from a neighbouring moiety[318–323], which raises the question – could such an interaction aid steric separation of the HOMO and LUMO (increasing CT character) but be soft enough to prevent total decoupling of the frontier orbitals?

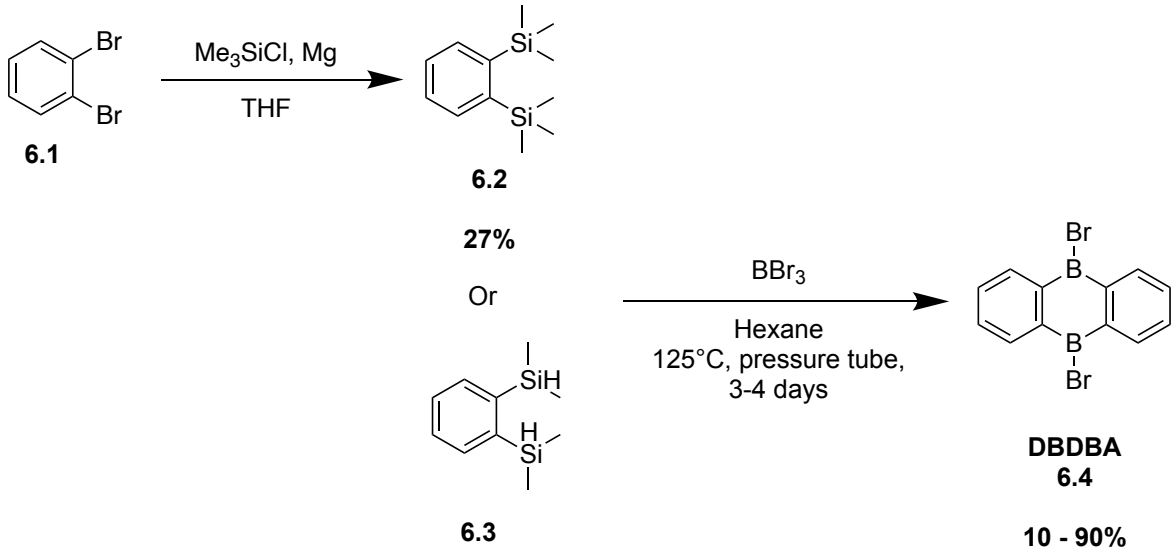
The aim of this chapter is to utilise the 9,10-diboroaanthracene acceptor moiety, bonded to two carbazole based donor moieties and investigate the effects of modifying substituent groups. The methyl groups on the π-bridges are replaced with methoxy groups with the intention to facilitate through-space non-covalent interactions from the oxygens' lone pairs

to the empty p-orbital of the boron atoms. This should provide the benefit of enhanced charge transfer and fast rISC rate observed with the aforementioned ortho-derivative molecules (albeit here with potential for better n-orbital to empty p-orbital alignment due to them being less bulky than Kumar *et al*.'s[227] carbazoles), as well as maintaining a high dihedral angle between donor and acceptor moieties, with the added steric protection afforded to the boron atom due to substituents on the π-bridges. Additionally, with respect to Kumar *et al*.'s[227] suggestion that their non-covalent interactions improve solution TADF, we anticipate that non-covalent interactions *via* methoxy – boron interactions should facilitate this as well.

6.4 Results

6.4.1 Synthesis

Initial attempts were made to synthesise CzDBA using previously reported methods. Both target compounds (CzDBA and tBu-MeOCzDBA) require the same acceptor molecule to be synthesised prior to donor-acceptor assembly, which is outlined in Scheme 6-1.



Scheme 6-1 Synthesis pathways to the acceptor molecule, DBDBA (6.4).

6.4.1.1 1,2-Bis-(trimethylsilyl)benzene

The acceptor core, dibromodiboraanthracene (DBDBA, **6.4**), requires a bis-silylated benzene as the precursor for its synthesis. Previous reported methods use 1,2-bis-(trimethylsilyl)benzene (**6.2**) as the precursor.

Synthesis of this compound is achieved *via* a Grignard reaction replacing the bromine groups in 1,2-dibromobenzene (**6.1**) with the trimethylsilane groups and is illustrated in Scheme 6-1. Yields from this reaction were found to be reproducibly low (reaching only as much as 27% in our attempts).

6.4.1.2 9,10-Dibromo-9,10-diboraanthracene (DBDBA)

There are several papers involving the synthesis of 9,10-dibromo-9,10-diboraanthracene (DBDBA), each using slightly different conditions and some reporting wildly different physical appearances of the product material![238,314,324,325] What unites all the methods

however is the fact that DBDBA is highly air and moisture sensitive – so much so in fact that Bieller *et al*.[325] state they were unable to even produce elemental analysis or mass spectrum analysis owing to its rapid degradation (although all the cited papers are devoid of any characterisation more than ^{1}H and ^{13}C NMR spectra, with Wu *et al*.[238] skipping this entirely!). Most papers reporting the compound use it as an intermediate for a following step and often state that it is used "as-is" without any additional purification. Confusingly, Januszewski *et al*.[324] report DBDBA as "pale orange crystals" in their supporting information[324], whereas Wu *et al*. describe it as "white crystals"[238].

Novel method of DBDBA synthesis

Initial attempts to synthesise DBDBA were made using reflux, as detailed by Bieller *et al*.[325], thus avoiding the potential explosion risk associated with heating toluene in sealed glassware. However, when we attempted to replicate the methodology, it was found to be impossible to adequately seal the glassware, with BBr_3 and resultant HBr escaping through the glass joints, and the solid that formed there causing even more exposure to air as the joints were prised open.

This particular method was compounded by the post-coronavirus lockdown restrictions of 2020-2021, meaning that the six-day reaction was left unattended for several days (since I was strictly only allowed on campus two days a week), and each attempt required a full week before observations of the outcome could be performed (mitigating leakage was therefore impossible).

Additional methods of protection were attempted (silicone grease, Teflon tape, Parafilm, keck grips, *etc*.) but each method failed to prevent the escape of the aggressively reactive Lewis acid.

Following on from Januszewski *et al*.'s[324] sealed glass ampule method, we attempted to use a Biotage microwave reaction vial (designed to be heated for long periods) as a safer alternative. This was clamped in place in a paraffin oil bath and heated to 120°C. After 6 days, the boron tribromide had reacted with the Reseal septum and leaked out yet again.

Eventually, after correspondence with Dr Deborah Kays from the University of Nottingham (who has extensive experience with working with boron Lewis acids under inert conditions), in 2021 a pressure tube was purchased (Ace Glass) to better seal the reactants, which has

since yielded much more successful results. It was noted that even with the pressure tube, after six days, the paraffin oil would take on an orange discolouration from boron tribromide exposure.

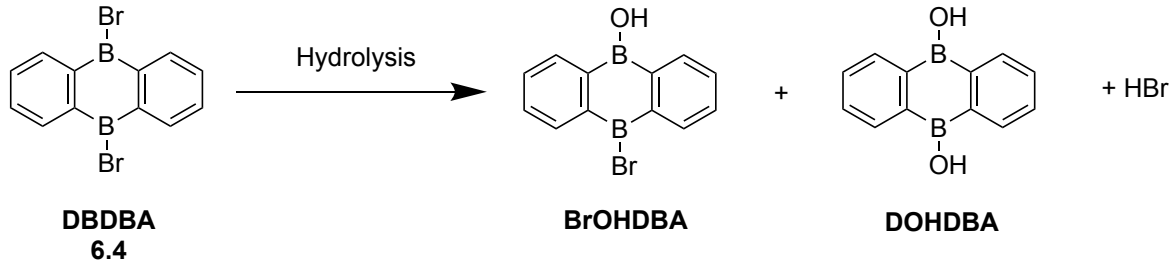
The pressure tube is fitted with a PTFE screw-fit three-way tap and screw-fit plug to its side arm. When preparing for the DBDBA synthesis, the side arm plug is replaced with a rubber septum. A plastic tubing is connected to the three-way tap and linked to a cold trap with standard rubber Schlenk tubing, which is in turn connected to the Schlenk line. The pressure tube is then purged several times with a vacuum – argon cycle (later attempts used twenty such cycles to ensure as little oxygen or moisture remained). The bis-silylbenzene is then transferred to the pressure tube *via* a syringe, which is then purged a further 20 times, and left under vacuum for one hour with stirring to remove residual air in the oil. Dry toluene or hexane is then added *via* a syringe, followed by quick purging several times, then the boron tribromide is added as quickly as possible with stirring. This usually results in the white smoke of hydrogen bromide forming upon contact with residual moisture. This is purged quickly again, and the rubber septum swiftly replaced with the PTFE screw-plug with a strong argon flow to minimise air entering the pressure tube. Following this, the pressure tube is quick-purged a final twenty times, filled with argon and sealed by means of closing the three-way tap. From this point, the pressure tube is heated to 120°C with stirring for the reaction period.

When using 1,2-bis-(trimethylsilyl)benzene (**6.2**) as the precursor and toluene as the solvent, a period of six days was initially required. Upon cooling to 70°C, the product began to precipitate. However, Kirschner *et al*.[326] made use of hexane as the solvent for a very similar reaction, for less than half the reaction time of Wu *et al*.[238], so we attempted this. Interestingly, the product began to precipitate out at 90°C upon cooling. Our yields were slightly better using hexane.

Upon returning to room temperature, the pressure tube is submerged in petroleum ether cooled to -78°C with liquid nitrogen for a period of 30 minutes to complete the crystallisation/precipitation of the product material. When returned to room temperature, the pressure tube is reconnected to the cold trap by opening the three-way tap and the screw-plug is quickly replaced under positive argon flow with a rubber septum connected to a cannula fitted with a filter (five layers of standard filter paper held in place with Teflon tape). The solvent and any excess liquid reactants or side products are then crudely removed by

connecting the other end of the cannula to a round-bottom flask under reduced pressure and siphoned off. The solid material is then washed with anhydrous hexane three times and chilled, with the hexane being siphoned off each time. The screw-plug is then replaced, and the cold trap connected to a high-vacuum (10^{-2} bar) and the pressure tube dried over the course of three hours.

The solid material of DBDBA is a beige or off-white solid – the differences noticed between batches is presumably a result of residual boron tribromide, as it fumes white smoke of hydrogen bromide upon exposure to air, however this could also be a result of debromination of DBDBA also yielding hydrogen bromide *via* hydrolysis (see Scheme 6-2).

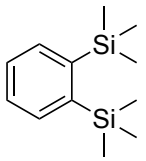


Scheme 6-2 Potential hydrolysis side products of DBDBA.

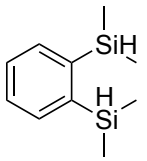
Unfortunately, in terms of the precursor material, we found that 1,2-bis-(trimethylsilyl)benzene takes up to a week to synthesise. In theory it should only take a couple of days, but after reacting overnight, the workup often takes a few hours owing to the not insignificant exotherm, often yielding a mix of side products. Column chromatography always yielded elution of the product and the mono-substituted half product at the same time, regardless of eluent used. The solution to this is to repeat the Grignard reaction again with the product mixture as the starting material in order to fully silylate the compound. This is not ideal as it requires yet another chromatography column and associated loss of yield. During the two-day-a-week post-lockdown restriction, this was a particularly infuriating synthesis (particularly as only enough product was produced for a single attempt at the following DBDBA synthesis step).

An ideal solution would be to purchase 1,2-bis-(trimethylsilyl)benzene from a chemical supplier, providing a purer starting material. Unfortunately, this was unavailable for the duration of this PhD, although it is now available at Fluorochem for £388 per 5g[327]. On the other hand, 1,2-bis-(dimethylsilyl)benzene (**6.3**), illustrated in Figure 6-4, is much cheaper and readily available from several providers (£45 per 5g on Fluorochem[328]). It is reasonable to think that, whilst each silicon is a methyl short compared to the original compound, it

should not be that much poorer of a leaving group. As such, we sought to attempt to perform the synthesis of DBDBA with this far cheaper and more readily commercially available compound.



1,2-bis(trimethylsilyl)benzene
(**6.2**)



1,2-bis(dimethylsilyl)benzene
(**6.3**)

Figure 6-4 Two alternative starting materials for the synthesis of DBDBA.

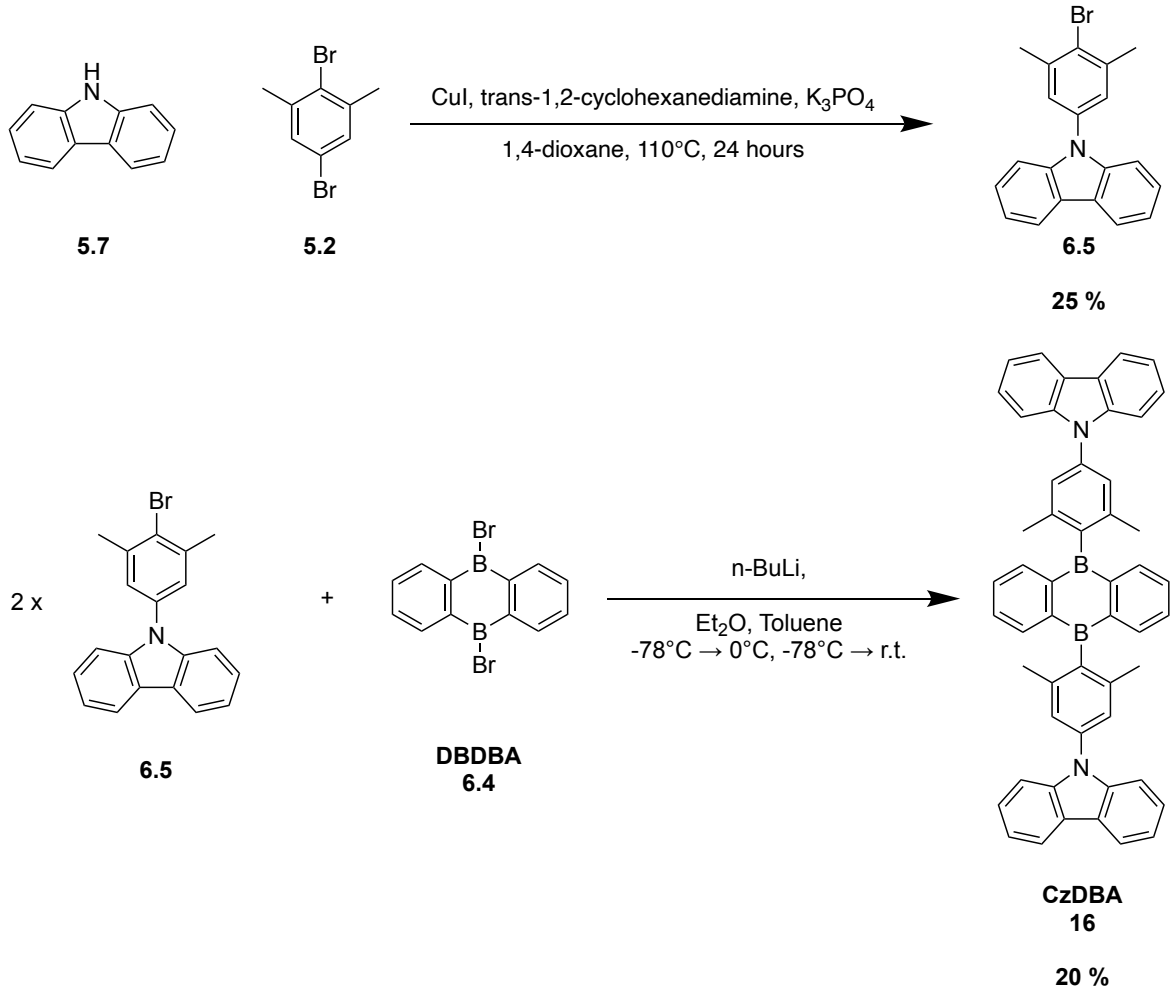
Using anhydrous hexane as the solvent, 1,2-bis-(trimethylsilyl)benzene (**6.2**) was replaced with 1,2-bis-(dimethylsilyl)benzene (**6.3**), maintaining the same molar ratios of the reactants. Surprisingly, upon addition of boron tribromide to the fully purged pressure tube of **6.3** and hexane, white crystals of product material formed within seconds, without even heating the reaction mixture. In the interest of prudence and to maximise the yield, the reaction was performed at 125°C for three days, resulting in an exceptional yield of 90%. The proton NMR spectrum reveals that DBDBA is the only product of this reaction post filtration (with traces of solvent and some non-aromatic material). This contrasts significantly with our previous attempts at DBDBA synthesis starting with **6.2**, with yields ranging between 25% and 39%, and compares very favourably with the literature reported yields using traditional methods. The yields of this work and major published works are summarised in Table 6-5.

Table 6-5 Summary of 5 different DBDBA synthesis methods and their respective yields.

Method	Yield (%)	Reference
1,2-bis-(trimethylsilyl)benzene, toluene, pressure tube	25 - 39	This work
1,2-bis-(trimethylsilyl)benzene, hexane, pressure tube	10	This work (no NMR obtained owing to prudence for next step).
1,2-bis-(dimethylsilyl)benzene, hexane, pressure tube	**90**	This work
1,2-bis-(trimethylsilyl)benzene, toluene, flame sealed glass ampoule	54	Januszewski *et al.*[324]
1,2-bis-(trimethylsilyl)benzene, toluene, refluxed overnight	58	Bieller *et al.*[325]

6.4.1.3 CzDBA

The donor for 9,10-bis(4-(9H-car-bazol-9-yl)-2,6-dimethylphenyl)-9,10-diboraanthracene (CzDBA) was synthesised according to a procedure reported by Stahl *et al*.[290] This is followed by the same lithium-halogen exchange used by Wu *et al*.[238] Both methods are shown in Scheme 6-3.



Scheme 6-3 Synthesis of CzDBA based on Stahl *et al*.'s [290] donor synthesis and lithiation step as outlined by Wu *et al*.[238]

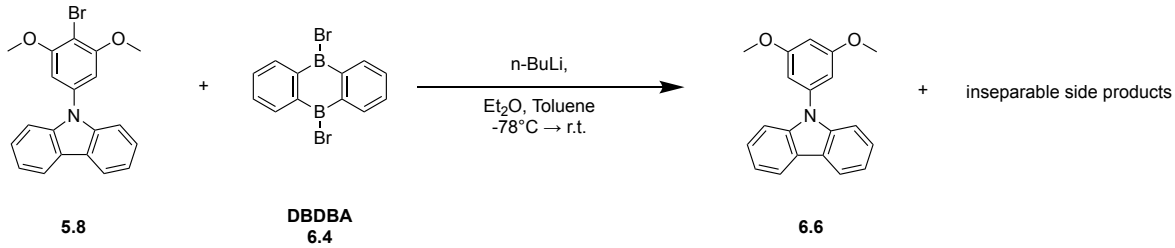
Initial attempts were made to synthesise CzDBA following the work of Wu *et al*.[238] Yields were disappointingly low (< 20% compared to the 76% reported in the original paper). Despite a promising quantity of crude material, use of a chromatography column always yielded a bright blue-green streak and minimal yield obtained. It was suspected that interactions with silica gel was causing decomposition of CzDBA. After numerous failed attempts to purify the crude material, I reached out to the authors in case they used a specific grade of silica gel, and they informed me that they only used a very short column to minimise decomposition, but also that the solvent mix they used was 1 : 10 hexane : dichloromethane

(the complete opposite of the 10 : 1 they report in their Nature Photonics paper). Despite this giving exceedingly poor separation, this approach was effective for isolating a sufficient quantity for characterisation, provided one collected exceedingly small fractions.

tBuMeOCzDBA

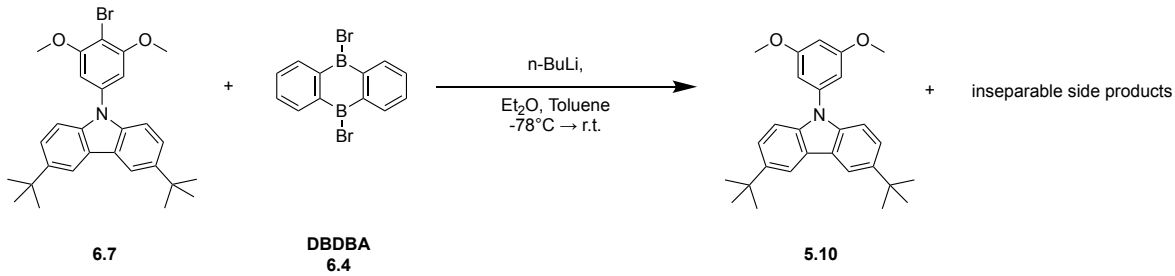
Initially, attempts to make tBuMeOCzDBA were impeded by rapidly degrading DBDBA. Wu *et al.*'s[238] work demonstrated that lithium-halogen exchange is required to synthesise the target compound. The synthesis pathway to the bromide variant of the methoxy donor molecule takes multiple steps, each with relatively low yields as was outlined in Chapter 5 in scheme 5-3.

During the lithiation, the lithiated donor material would form an insoluble precipitate upon returning to room temperature, irrespective of the solvent used. The donor – acceptor coupling was attempted regardless, yielding no desired product (see Scheme 6-4).



Scheme 6-4 Failed coupling attempt of donor to acceptor.

To avoid the poor solubility in the lithiation step, a derivative of the donor with tert-butyl groups added to the 3 and 6 position of the carbazole was synthesised and the reaction repeated. Compound **6.7** was kindly synthesised by Dr Andrea Pinto. Whilst the lithiated product was much more soluble, the reaction continued to fail.



Scheme 6-5 Failed coupling of tert-butyl donor and acceptor.

However, post column chromatography, it was possible to isolate the hydrolysed donor molecule, **6.6** as outlined in Scheme 6-4 and also of **5.10** as seen in Scheme 6-5 (albeit with

some impurities – see Figure 6-5 for an example of the proton NMR obtained when **6.6** was isolated).

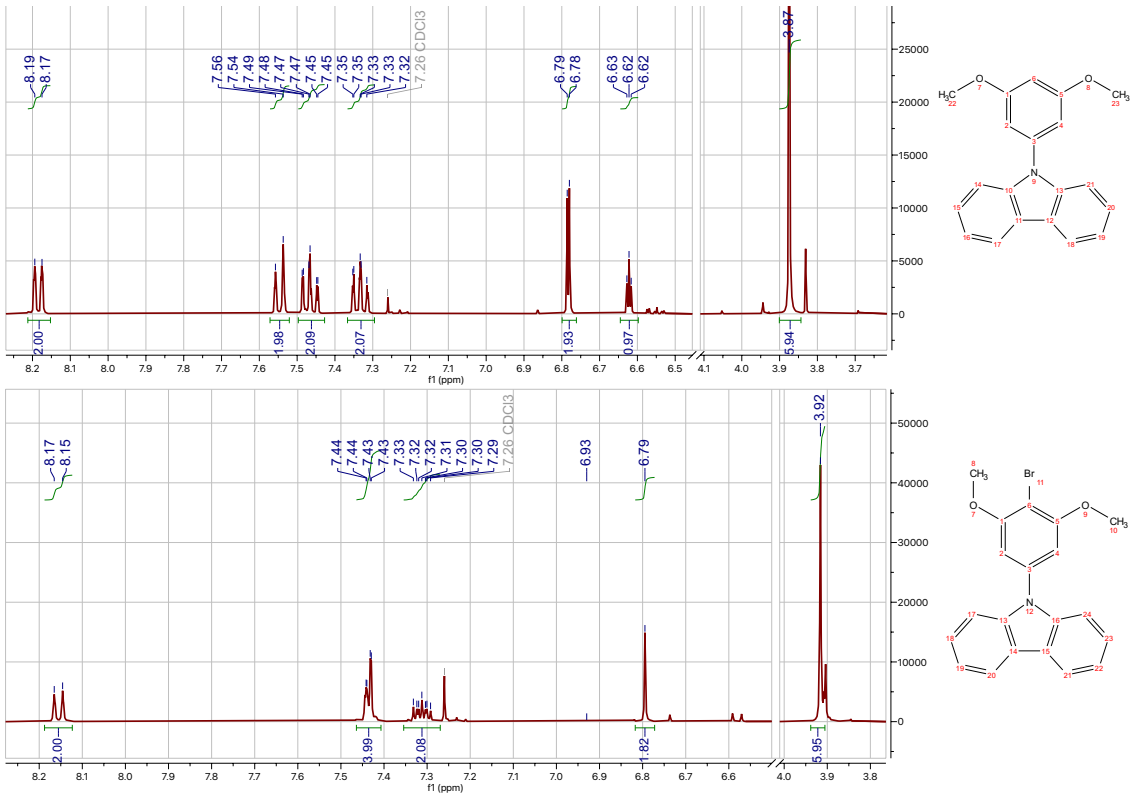
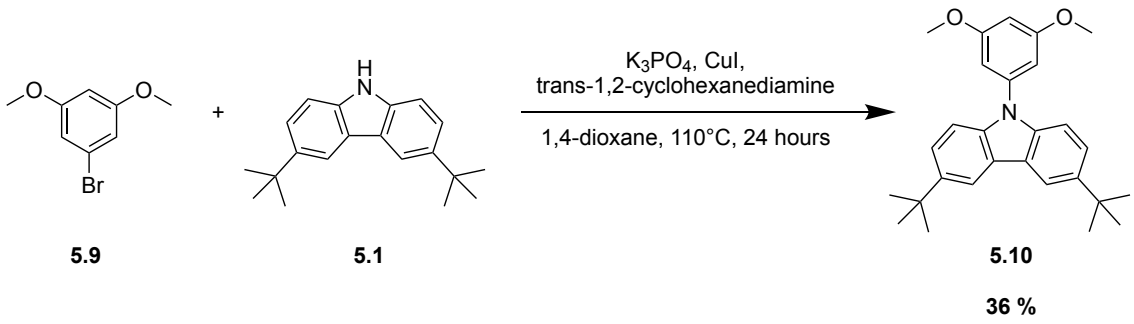


Figure 6-5 ^{1}H NMR of brominated donor and hydrolysed donor.

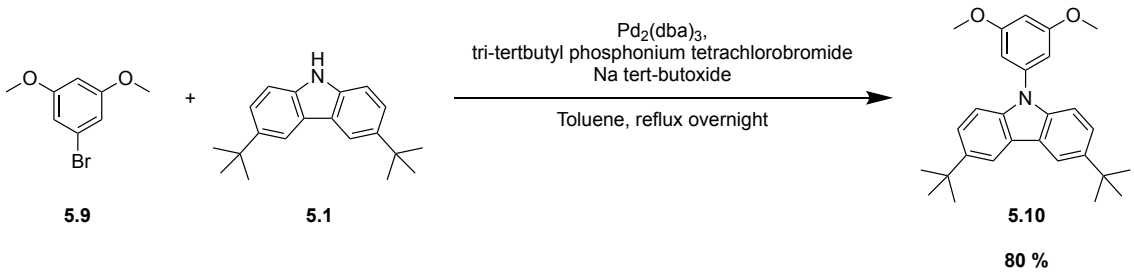
Since a large quantity of the tert-butyl donor was isolated, in that attempt, a further attempt was made at lithiating it in the synthesis of compound **13** (described in detail in Chapter 5) in place of the bromide compound. This reaction demonstrated the successful coupling of the dimethoxy donor to a boron-based acceptor in Chapter 5.

Buoyed by the success of this reaction, we sought an alternative and quicker synthesis pathway to a non-brominated derivative of the methoxy donor (see Scheme 6-6). This significantly reduced synthesis time, as well as permitting the use of cheaper starting material. Using 3,5-dimethoxy-1-bromobenzene (**5.9**) as the starting material, coupling to 3,6-tert-butyl-9H-carbazole (**5.1**) was trivial.



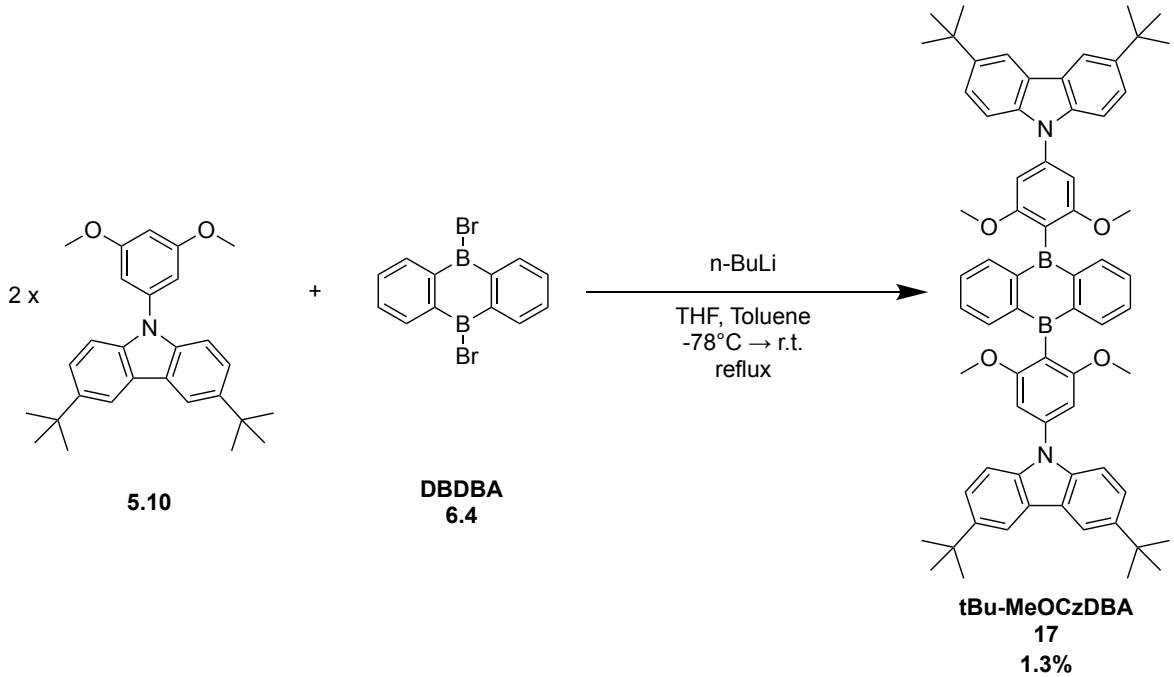
Scheme 6-6 Direct synthesis of non-brominated donor from more readily available starting material in a single step. From section 5.6.5 in Chapter 5.

An alternative, Ullman-coupling was also attempted by Dr Joseph Cameron, providing a much higher yield (illustrated in Scheme 6-7) for later synthesis attempts.



Scheme 6-7 Dr Joseph Cameron's method of synthesis of non-brominated methoxy donor.

Coupling of this donor to DBDBA was then achieved *via* lithium facilitated deprotonation of the donor (shown in Scheme 6-8).



Scheme 6-8 Successful method of coupling the methoxy donor to the DBDBA acceptor.

6.4.2 Thermal properties

As thermal stability is important for device fabrication, TGA and DSC studies were performed on tBu-MeOCzDBA.

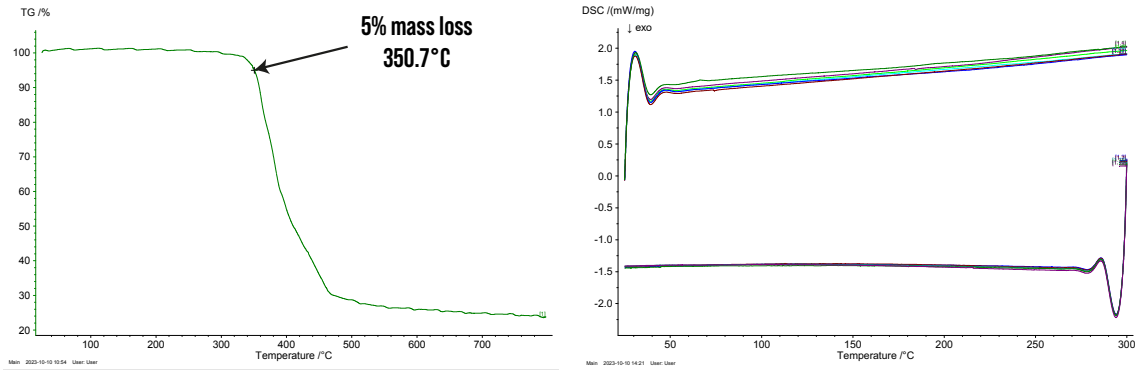


Figure 6-6 TGA (left) and DSC (right) plots for tBu-MeOCzDBA.

The thermogravimetric analysis plot in Figure 6-6 shows that tBu-MeOCzDBA exhibits good thermal stability, with a 5% mass loss at 350.7°C. However, this indicates that it is less stable than both compounds reported by Wu *et al.*[238] The 5% mass loss is 67°C lower than that which Wu *et al.*[238] reported for CzDBA and 51.3°C lower than tBuCzDBA, which is consistent (though slightly greater) with the impact of methoxy groups observed in Chapter 5.

The differential scanning calorimetry in Figure 6-6 reveals no distinct melting point or crystallisation temperatures. This was reflected in the failed attempt to manually obtain a melting point, where decomposition or sublimation was observed. Wu *et al.*[238] also observed no distinct melting point, but did see a glass transition temperature for CzDBA at 108°C. Interestingly, they saw no such transition in tBuCzDBA, which is also absent for our tBu-MeOCzDBA.

6.4.3 Electrochemical properties

In order to explore the redox properties and HOMO and LUMO energies of tBu-MeOCzDBA, cyclic voltammetry was performed at 1×10^{-3} M in tetrahydrofuran, 2×10^{-4} M in dichloromethane.

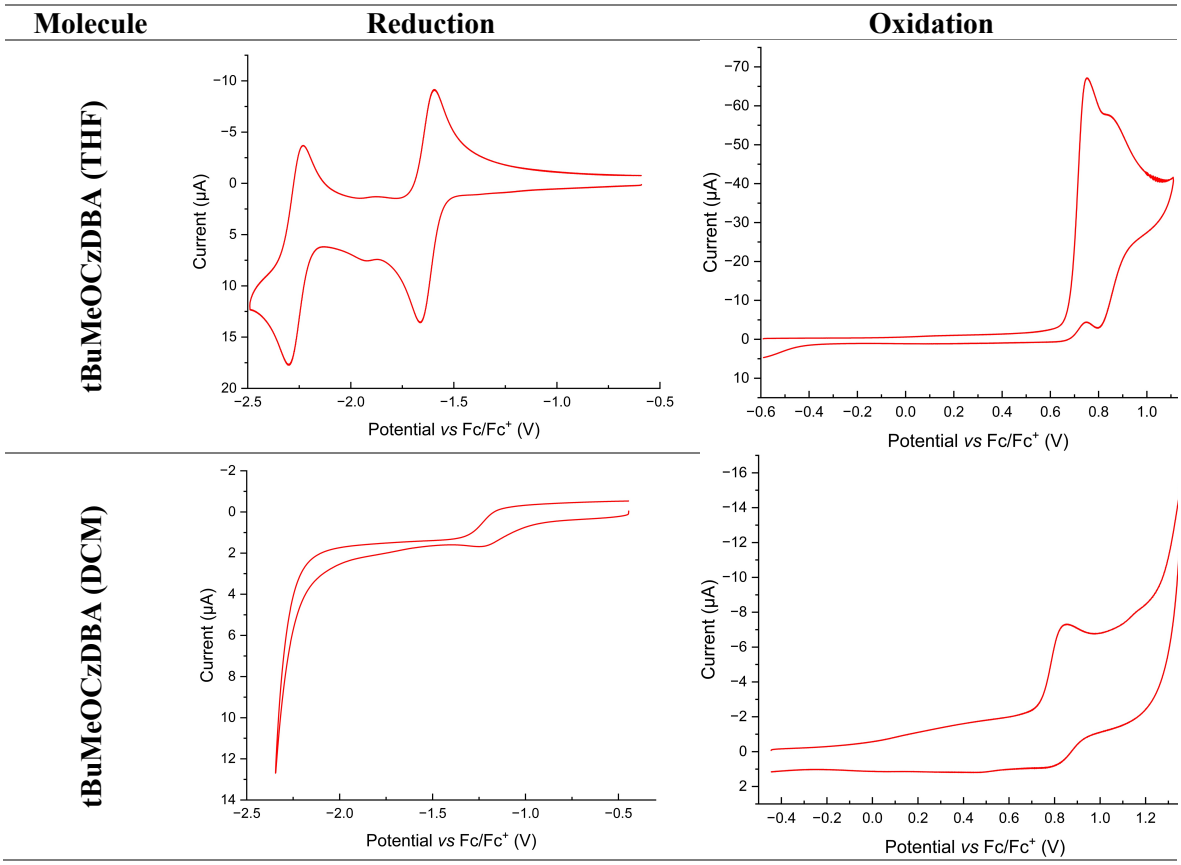


Figure 6-7 CV Plots of tBuMeOCzDBA measured in dry tetrahydrofuran (top) and dry dichloromethane (bottom). All were referenced against the $E_{1/2}$ of the Fc/Fc^+ redox couple in ~1 × 10^{-3} M solution for tetrahydrofuran and ~2 × 10^{-4} M solution for dichloromethane, both with 0.1 M tetrabutylammonium hexafluorophosphate as the electrolyte.

All CV cycles were performed with 0.1 M tetrabutylammonium hexafluorophosphate as the electrolyte and corrected against ferrocene Fc/Fc^+ redox couple as an external standard in the separate reduction/oxidation scans, and as an internal standard for the full cycle measurements.

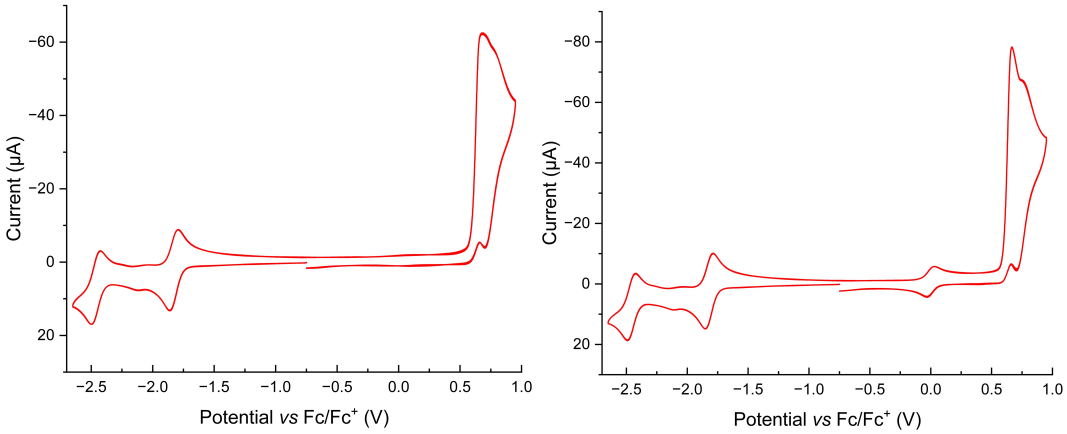


Figure 6-8 Full cycle CV plots of tBu-MeOCzDBA in dry tetrahydrofuran (~1 × 10^{-3} M). No internal standard (left), including ferrocene internal standard (right). Both with 0.1 M tetrabutylammonium hexafluorophosphate as the electrolyte.

For tBu-MeOCzDBA, tetrahydrofuran permits the observation of two reversible reduction peaks at -1.82 V and -2.43 V, with two irreversible oxidation peaks at 0.67 V and 0.73 V (from full cycle). This equates to HOMO and LUMO energies of -5.47 eV and -2.98 eV respectively, yielding an electrochemical energy gap, E_g, of 2.49 eV.

This is comparable to the tert-butyl derivative of CzDBA, tBuCzDBA, synthesised by Wu *et al.*[238], which has a HOMO-LUMO gap of 2.37 eV, but is closer to the energy gap they report for the standard CzDBA, being 2.43 eV (based on the CV data in Wu *et al.*'s[238] supplemental information). Interestingly, in Wu *et al.*'s[238] work, the oxidation curves are reversible for both CzDBA and tBuCzDBA, suggesting decreased chemical stability for tBu-MeOCzDBA.

Compared to tBuCzDBA, the exchange of methyl groups for methoxy raises the HOMO by 0.01 eV (from -5.48 eV) and raises the LUMO by 0.13 eV from -3.11 eV. This suggests that the methoxy groups are inducing electron density into the boron's empty p-orbital, making diboraanthracene a weaker acceptor, rather than strengthening the donor's character.

6.4.4 Molar absorption coefficient

To investigate the strength of the absorption bands, tBu-MeOCzDBA was dissolved in dry toluene at varying concentrations. The obtained UV-vis spectra are illustrated in Figure 9-10 in Appendix 1.

In toluene, the UV-vis absorption spectra reveal a broad peak at 416 nm, followed by two sharp peaks at 348 nm and 335 nm, and a much more intense peak at 298 nm. The molar absorption coefficients of the aforementioned peaks (calculated from the fittings of the absorption plots in Figure 9-10 in Appendix 1), reveal that the 416 nm peak is likely to be from an intense $\pi \rightarrow \pi^*$ transition or CT state, with the other three much more intense absorptions being associated with CT D-A transitions.

6.4.5 Photophysical properties

Table 6-6 summarises the photophysical and Table 6-7 summarises the electrochemical properties of CzDBA (from our sample for all measurements except S_1 and T_1 energies and electrochemistry) and tBu-MeOCzDBA.

Table 6-6 Summary of photophysical properties of CzDBA and tBu-MeOCzDBA.

Molecule	λ_{abs} (nm)[a]	λ_{pl} (nm) [a]	FWHM (nm)	$E_{g\ opt}$* (eV)	Φ_{PL}[a]	S_1** (eV)	S_1^{δ} (eV)	T_1^{δ} (eV)	ΔE_{ST} (eV)
CzDBA	426(CT), 356sh, **344**, 330, 318sh, 294, 287, 283	542, 417sh, 382sh, 365, 350	94 (CT) 34 (LE)	2.55 (CT) 3.47 (LE)	14 (Ar) 8.7 (Air)	2.56 (CT) 3.67 (LE)	2.72^{+}	2.73^{+}	0.01
tBu-MeOCzDBA	416(CT), **348**, 335, 320sh, 298, 292, 282	515, 390sh, 370, 356	86 (CT) 33 (LE)	2.58 (CT) 3.41 (LE)	91 (Ar) 17 (Air)	2.69 (CT) 3.62 (LE)	2.86^{+} (CT) 3.62^{+} (LE)	2.93^{+}	0.07

[a] Measured in toluene, *Taken from onset of main λ_{abs} peak in toluene as 1240/ $\lambda_{max\ abs}$, **Taken from onset of λ_{PL} peak in methylcyclohexane, $^{+}$Taken from onset of λ_{PL} peak in Zeonex thin film, † from CT shoulder. Absorbance λ_{max} shown in **bold**. $^{\delta}$Measurements performed at the University of Durham.

Table 6-7 Summary of electrochemical properties of CzDBA and tBu-MeOCzDBA.

Molecule	E_{ox} (V)	E_{red} (V)	HOMO (eV)[a]	LUMO (eV)[a]	$E_{g\ chem}$ (eV)	τ_p (ns)	τ_d (ns)
CzDBA	-	-	-5.93*	-3.45*	2.48*	26 (Air) 82 (Argon)	271 (Air) 1831 (Argon)
tBu-MeOCzDBA	0.67 (0.73)	-1.82 (-2.43)	-5.47	-2.98	2.49	17 (Air) 28 (Argon)	226 (Air) 2912 (Argon)

[a] from CV measurements performed in THF in the case of tBu-MeOCzDBA, *Taken from original Wu *et al.*[238] paper. Absorbance λ_{max} shown in **bold**.

CzDBA

Photoluminescence spectra of CzDBA were recorded in dry toluene to compare as our control sample.

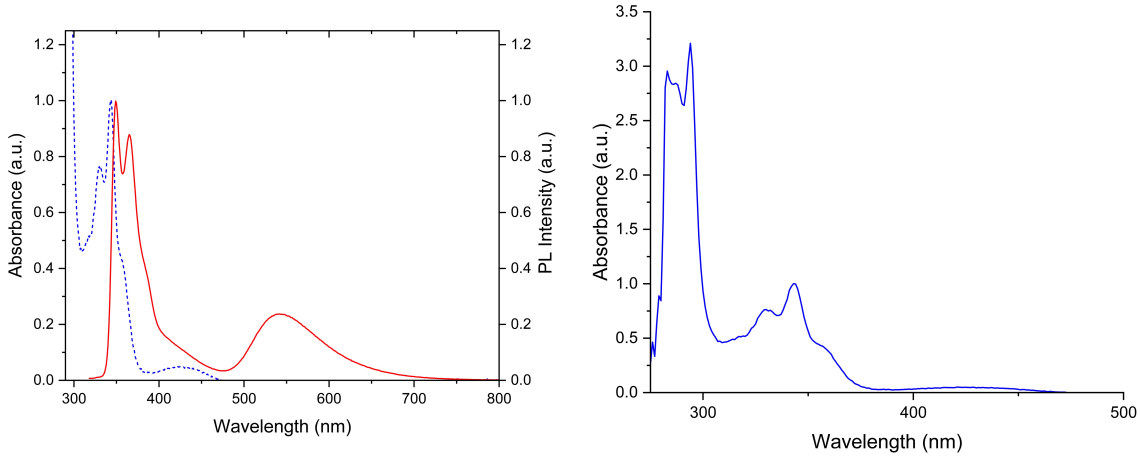


Figure 6-9 PL and UV-vis absorption spectra of CzDBA in toluene (left), expanded UV-vis absorption spectra (right) scaled to show full range.

In toluene, CzDBA is revealed to possess two emission peaks. In Wu *et al.*'s original paper,[238] the PL spectrum is cut off at 450 nm, meaning this peak is completely hidden. As such it sheds light on the potential for the presence of a locally excited state being present in this molecule's rISC process, being as yet unexplored.

tBu-MeOCzDBA

The photoluminescence spectrum of tBu-MeOCzDBA was recorded initially in dry toluene.

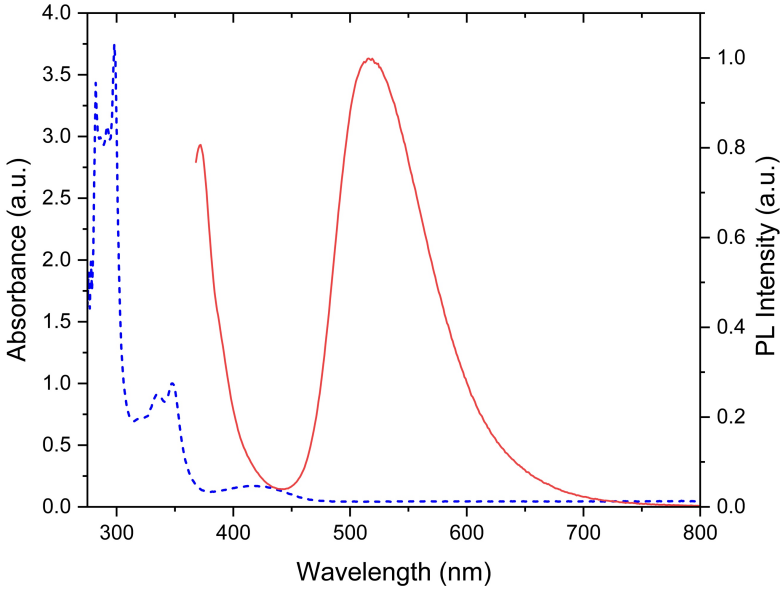


Figure 6-10 PL and UV-vis absorption spectra of tBu-MeOCzDBA in toluene showing the full UV range. Excited at main absorption peak.

tBu-MeOCzDBA possesses two emissions peaks in toluene. In our spectrometer, the shorter wavelength peak is partially cut off when excited at the main excitation wavelength. Exciting at different wavelengths in toluene allows for resolution of the second emission peak, as the cutoff region can be moved to compensate.

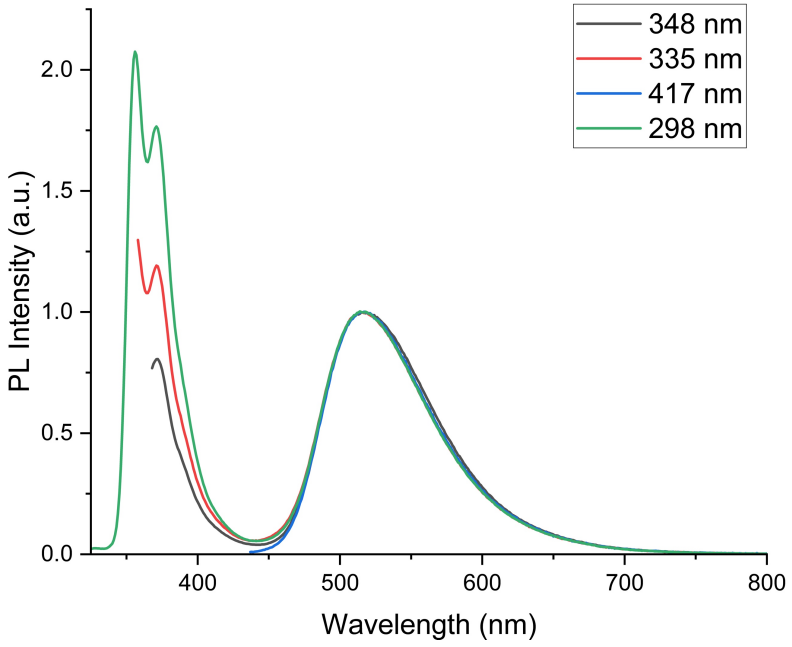


Figure 6-11 PL spectra at varying excitation wavelengths to fully resolve the LE peak of tBu-MeOCzDBA.

When excited at 298 nm, the extra peaks at 371 nm and 355 nm are better resolved on the spectrometer, showing a FWHM of the blue peaks being 31.44 nm. Since the shorter wavelength peak does not change in wavelength when excited at different wavelengths, this implies that the emission comes from the same material and is not an artefact of impurities[323] (such as leftover donor material or from degradation products).

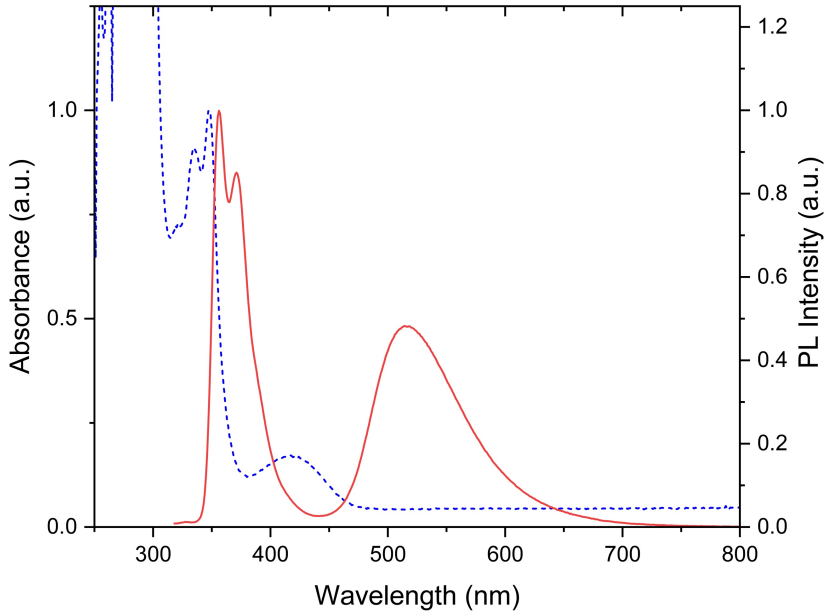


Figure 6-12 UV-vis absorption and PL spectra showing main UV peaks and full emission profile of tBu-MeOCzDBA. Excited at 298 nm.

The onset of the main absorption peak reveals the optical E_g value of 3.41 eV, which is wider than the electrochemical energy gap. This suggests it is the energy of the transition between the orbitals involved in producing the locally excited state. However, applying this process to the onset of the CT peak (416 nm peak), the value obtained, 2.58 eV, is much more comparable to the value obtained *via* cyclic voltammetry and can therefore be assigned to the HOMO – LUMO energy gap for the compound.

Figure 6-13 allows for comparison of the UV-vis spectra of the donor and tBu-MeOCzDBA reveals good alignment of peaks associated with the donor and the product. Here the free donor molecule's UV-vis absorption spectrum in toluene is compared with that of tBu-MeOCzDBA (the peaks are summarised in Table 6-8).

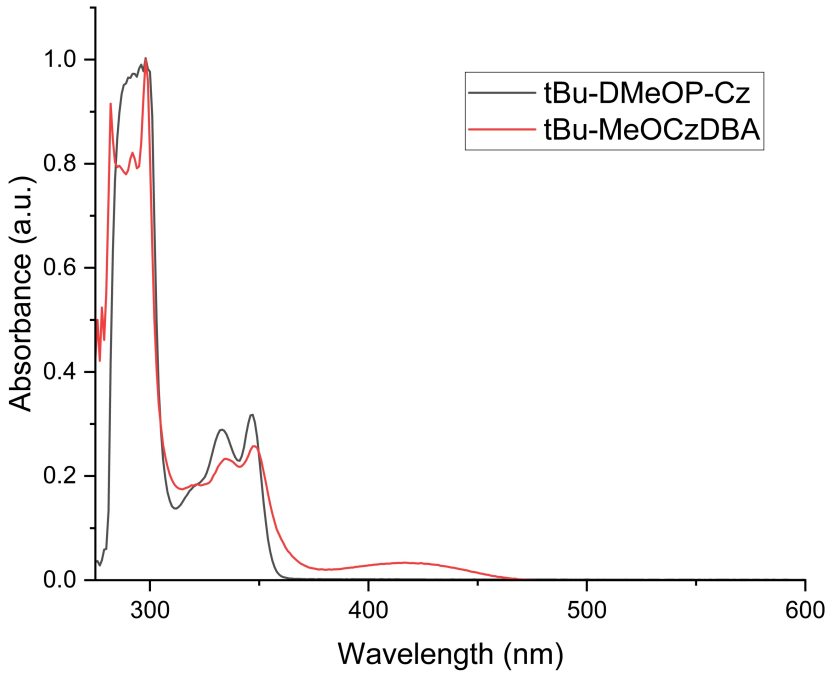


Figure 6-13 UV-vis absorption spectra of the donor tBu-DMeOP-Cz and the target compound tBu-MeOCzDBA in toluene.

Unfortunately, the DBDBA acceptor was too air and moisture sensitive to record a UV-vis absorption spectrum, however the good superimposition of the donor on the product spectra suggests a highly decoupled HOMO and LUMO[277] due to the large dihedral angle across the donor and acceptor moieties.

Table 6-8 Summary of the absorption peaks from the free donor molecule and tBu-MeOCzDBA in toluene.

Donor λ_{abs} (nm)	Product λ_{abs} (nm)
347, 333, 320(sh), 298	348, 335, 320, 298, 292, 286, 282, 416(CT)

The solution PLQY in toluene for tBu-MeOCzDBA is significantly greater compared to Wu *et al.*'s[238] reported value for CzDBA and tBuCzDBA (14% and 11.9% when degassed respectively, and 8.7% and 7.4% under oxygen, respectively); for our methoxy derivative, were observed 91% degassed and 17% under air. This is likely evidence of enhanced rigidity caused by O-B non-covalent interactions, similar to that which was observed by Kumar *et al.*[227] in their 2020 study into ortho-substituted derivatives of CzDBA analogues. Their work showed that the close proximity and van der Waals sphere contact between nitrogen and boron meant that interactions of this nature were suspected. Regardless, their structures possessed enhanced rigidity in the excited state compared to CzDBA and tBuCzDBA, which was reflected in their enhanced PLQYs (jumping to 99% and 83% for the carbazole and tertbutyl carbazole derivatives when degassed respectively). To confirm the presence of

non-covalent interactions in tBu-MeOCzDBA however, single crystal XRD studies will be required. The growth of sufficient quality crystals has so far proved elusive, owing to tBu-MeOCzDBA's propensity to rapidly decompose, even with non-polar, aprotic and ultra-dry solvents.

As such, it seems that methoxy – boron interactions are occurring here and are highly effective at substantially improving PLQYs in solution.

Solid-state

To further explore the photoluminescence properties of tBu-MeOCzDBA, thin films were prepared in host matrices of varying polarity, along with samples of CzDBA for comparison (see Figure 6-14).

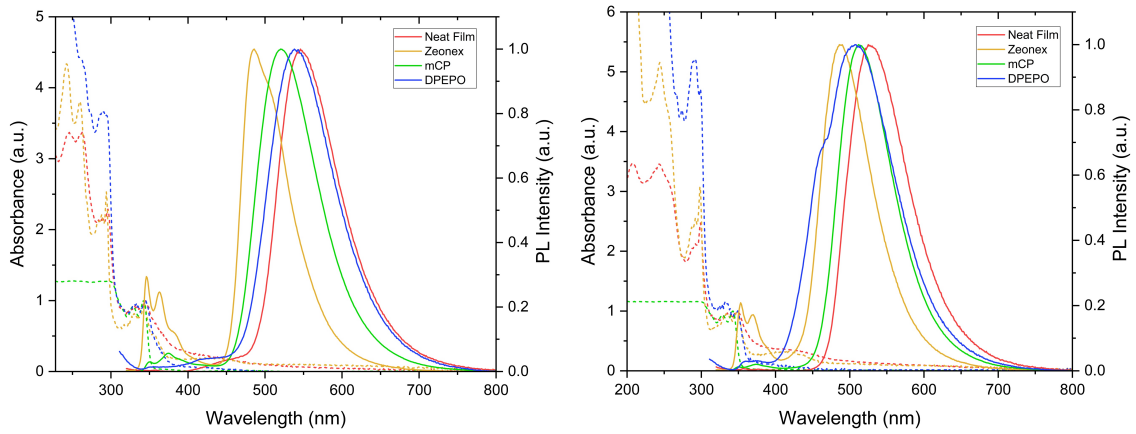


Figure 6-14 Solid-state UV-vis absorption and PL of CzDBA (left) and tBu-MeOCzDBA (right) in various host matrices.

Doped films (1% w.t.) were drop-cast onto quartz substrates. In polar matrices and neat films, the CT emissions are red-shifted in both CzDBA and tBu-MeOCzDBA, and the double LE peak at 356 nm and 370 nm is suppressed. In non-polar Zeonex hosts, the main emission peak blue-shifts and the emission from the double peak increases in intensity.

6.4.6 Lifetimes

The lifetimes of the excited states of CzDBA and tBu-MeOCzDBA in solution, neat film and host matrices, were measured using time correlated single-photon counting (TCSPC).

6.4.6.1 Solution-state measurements

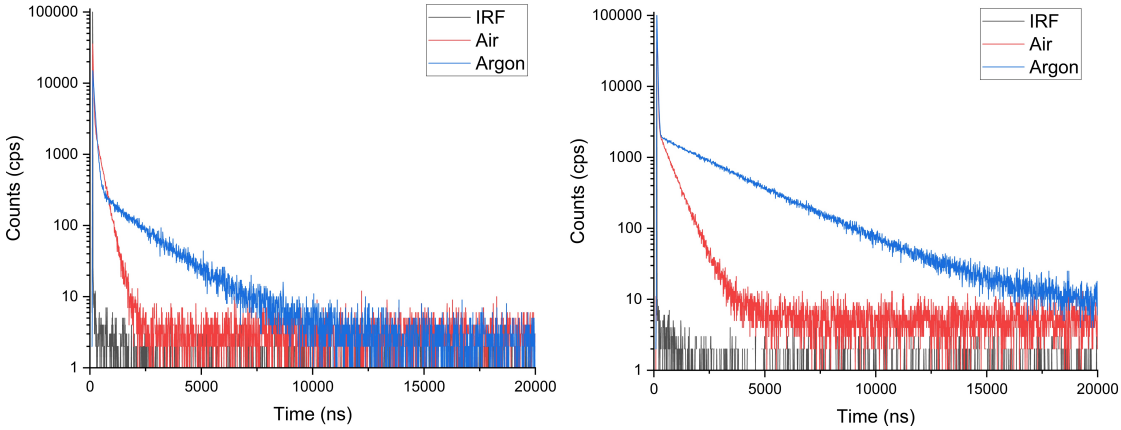


Figure 6-15 Emission lifetime of main emission peak of CzDBA (left) and tBu-MeOCzDBA (right). All measurements were performed in dry toluene under air exposure and degassed by bubbling argon for 20 minutes. Excitation source was a 365 nm laser pulsed at 40 µs and gated at 20 µs.

In air-saturated toluene solution, the main emission peak of tBu-MeOCzDBA emits for roughly twice as long as CzDBA, however when degassed, this lifetime increases dramatically (see Figure 6-15 and Table 6-9). It was not possible to monitor the lifetime of the shorter wavelength peak owing to its close proximity to the wavelength of the laser excitation source – as such, more detailed exploration of the lifetime of the emissions is explored with the CCD-time resolved experiments in section 6.4.8.

Table 6-9 Summary of the prompt and delayed lifetimes for the TCSPC studies of CzDBA and tBu-MeOCzDBA.

Molecule	Sample	τ_p (ns) air / argon	τ_d (µs) air / argon
CzDBA	Toluene	26 / 82	0.26 / 1.18
	Pure film	69 / 53	0.42 / 0.77
	mCP	49 / 31	2.04 / 3.06
	Zeonex	22 / 28	3.69 / 2.44
	DPEPO	69 / 86	3.41 / 3.56
tBu-MeOCzDBA	Toluene	23 / 28	0.42 / 2.87
	Pure film	36 / 38	1.12 / 2.27
	mCP	41 / 23	2.89 / 4.13
	Zeonex	21 / 22	3.89 / 7.75
	DPEPO	36 / 40	0.98 / 1.72

The prompt component of the emissions for tBu-MeOCzDBA is seemingly host and solvent independent – suggesting that the rate of population of the locally excited state remains unchanged regardless of whether it is degassed or not. On the other hand, the delayed component is clearly air sensitive – doubling in its lifetime when degassed.

6.4.6.2 Solid-state measurements

TCSPC studies were also performed on both compounds in a variety of host matrices to ascertain the impact of the solid-state environment on emission lifetimes.

CzDBA

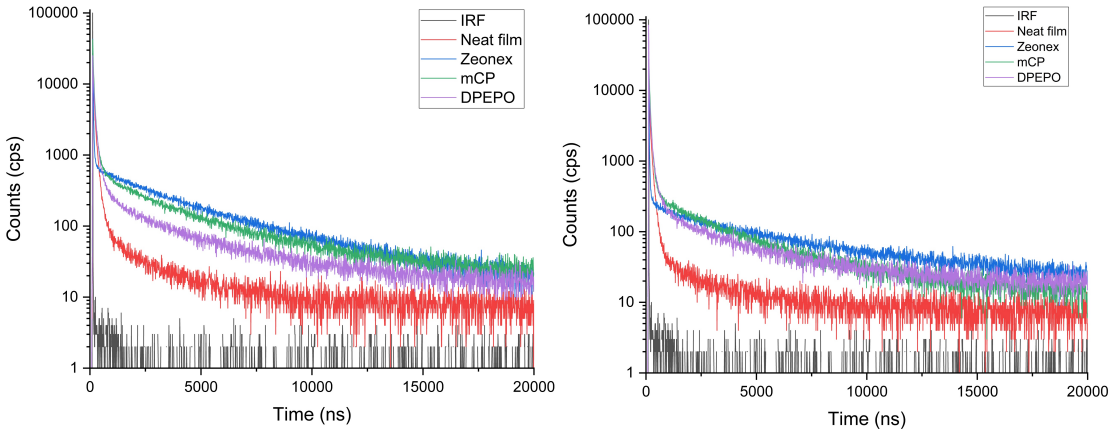


Figure 6-16 TCSPC plots of CzDBA thin films in air (left) and under argon atmosphere (right). All excited at 365 nm.

tBu-MeOCzDBA

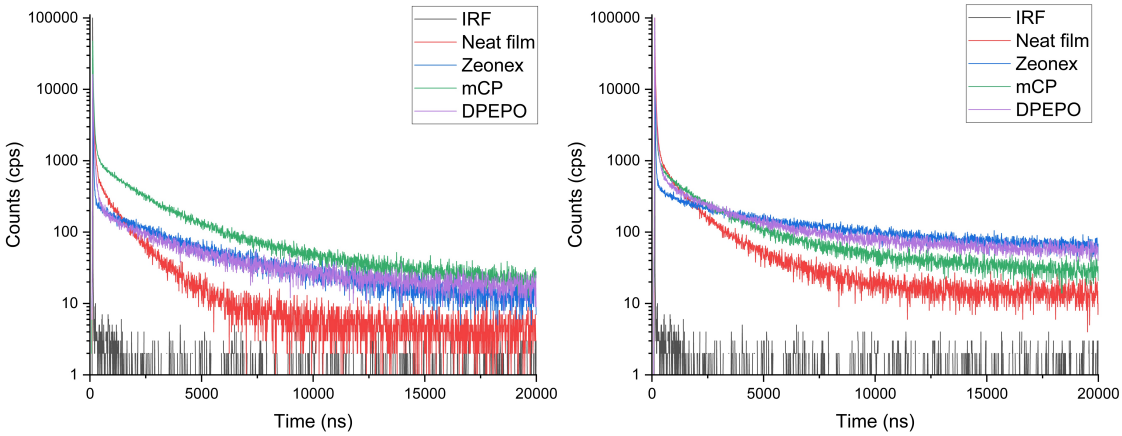


Figure 6-17 TCSPC plots of tBu-MeOCzDBA thin films in air (left) and under argon atmosphere (right). All excited at 365 nm.

In the solid-state, lifetimes are much longer than in solution, even when exposed to air, for both CzDBA and tBuMeOCzDBA (see Figure 6-16, Figure 6-17 and Table 6-9). Owing to our spectrometer having no means of providing inert atmosphere for performing TCSPC measurements, a crude modification was performed. This involved configuring the fluorimeter chamber for holding a quartz cuvette instead of the usual quartz substrate holder. Into the cuvette was placed one 1 cm diameter quartz substrate to serve as a base on top of which a second quartz substrate coated with the sample was placed. This arrangement afforded the second substrate to be placed in direct line of fire of the pulse source at a 45° angle. Whilst not ideal, owing to the risk of scattering by the cuvette (the detector is at 45° to the substrate in this set up too), it provided acceptable data collection. The cuvette was sealed with a rubber septum and was quickly purged five times *via* vacuum – argon cycling on a Schlenk line. Once under inert atmosphere, a balloon filled with argon was attached *via* a needle to maintain positive argon pressure during the measurement, and the cuvette and balloon were placed in the spectrometer for the measurement. For the most part, this methodology appears to be effective.

Overall, the prompt emissions are only slightly longer for each compound when degassed, however the delayed component increases by a factor up to 2.29 in Zeonex for tBu-MeOCzDBA. The photophysical properties for the two compounds are summarised in Table 6-10.

Table 6-10 Summary of the solid-state photophysical properties of both CzDBA and tBu-MeOCzDBA. All measurements performed with our material in Glasgow and not from the Wu *et al.*[238] paper.

Molecule	Host	λ_{abs} (nm)	λ_{pl} (nm)	FWHM (nm)	Φ_{PL} (air)	Φ_{PL} (argon)	S_1^* (eV)
CzDBA	Pure film	345, 331, 296, 263, 244, 426(CT)	546, 459sh	92	27	45	2.56 (^{1}CT)
	mCP	365(CT), 342, 328	521, 349, 374	91	100	100	2.69 (^{1}CT) 3.65 (^{3}LE)
	Zeonex	355sh, 343, 330, 294, 287, 241, 426(CT)	485, 504sh, 380sh, 363, 346	69	57	100	2.74 (^{1}CT) 3.67 (^{3}LE)
	DPEPO	360sh, 344, 331, 288	539, 424sh, 354	101	46	81	2.63 (^{1}CT) 3.69 (^{3}LE)
tBu-MeOCzDBA	Pure film	350, 335, 299, 288, 255sh, 244, 208, 417(CT)	529, 377, 357	95	38	59	2.65 (^{1}CT) 3.57 (^{3}LE)
	mCP	342, 329	512, 374, 350	86	100	100	2.71 (^{1}CT) 3.64 (^{3}LE)
	Zeonex	348, 335, 298, 291, 255sh, 244, 207, 417(CT)	487, 386sh, 369, 353	79	49	100	2.86 (^{1}CT) 3.62 (^{3}LE)
	DPEPO	349, 331, 299, 291, 273, 394(CT)	506, 466sh, 375, 360	122	33	61	3.02 (^{1}CT) 3.58 (^{3}LE)

* Taken from the onset of the short wavelength emission for the LE state and from the long wavelength peak for CT.

Both compounds exhibited increases in PLQY in thin films when held under argon atmosphere compared to when they were exposed to air. This once again implies that a triplet state is involved and that rISC is possible in tBu-MeOCzDBA.

From the TCSPC derived lifetimes and PLQYs, it was possible to calculate the rate constants of the photophysical processes in the two molecules (see Table 6-11). From the results, it appears that tBu-MeOCzDBA possesses a higher rate of rISC in polar hosts than CzDBA,

although this process is poorer than CzDBA in non-polar hosts. This could be due to polar media assisting with the stabilising of the molecule's conformation to drive CT emissions, owing to a narrowing of the time-dependent energy gap between the excited states involved in rISC[329].

Table 6-11 Summary of photophysical rate constants calculated from fittings of time dependent photoluminescence decays using a method outlined by Dias *et al*.[173]

		k_F	k_{ISC}	k_{rISC}
		(s^{-1})	(s^{-1})	(s^{-1})
CzDBA	Toluene	1.06E+06	4.62E+06	1.36E+06
	Pure film	5.09E+06	7.55E+06	2.15E+06
	mCP	3.23E+07	0.00E+00	3.27E+05
	Zeonex	2.04E+07	1.54E+07	7.19E+05
	DPEPO	5.35E+06	5.02E+06	4.94E+05
tBu-MeOCzDBA	Toluene	6.18E+06	2.89E+07	1.83E+06
	Pure film	1.00E+07	9.37E+06	6.84E+05
	mCP	4.35E+07	0.00E+00	2.42E+05
	Zeonex	2.23E+07	2.32E+07	2.63E+05
	DPEPO	8.25E+06	1.15E+07	1.07E+06

To determine if the peaks at 371 nm and 355 nm were a result of dual emission or B-C bond cleavage from traces of water in the solvent, a sample was prepared in tetrahydrofuran and the PL measured. This was then spiked with 20 μL of water. Additionally, a sample of the donor molecule was prepared in dry tetrahydrofuran for comparison. The resulting photoluminescence spectra are reported in Figure 6-18.

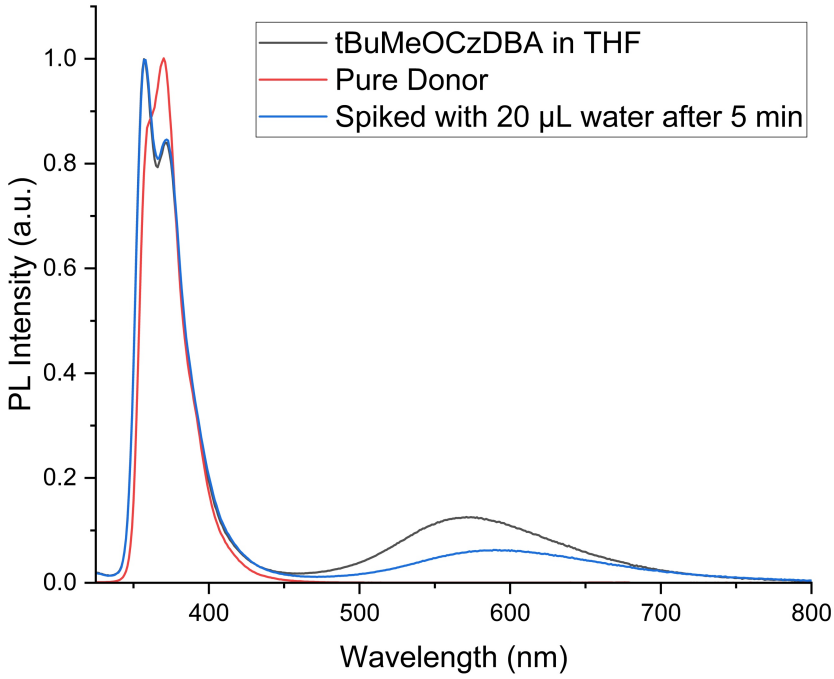


Figure 6-18 PL spectra of tBu-MeOCzDBA and its respective donor in tetrahydrofuran, compared to a sample of tBu-MeOCzDBA in tetrahydrofuran spiked with 20 µL of deionised water after 5 minutes.

Addition of water blue-shifts the main emission peak, suggesting the potential for solvatochromism, however the nature of the dual emission peak remains the same. This suggests that shorter wavelength peaks are the result of an LE state in the molecule and not CT. The PL spectra for the pure donor in tetrahydrofuran, whilst of a similar wavelength, differs significantly in appearance. This suggests that the molecule is not breaking down *via* hydrolysis due to traces of water initially, rather this dual peak is in fact emission from a locally excited state situated on the donor moieties.

6.4.7 Solvatochromism

The molecule exhibits pronounced positive solvatochromism in a variety of solvents when excited at 348 nm and the data are reported in Figure 6-19.

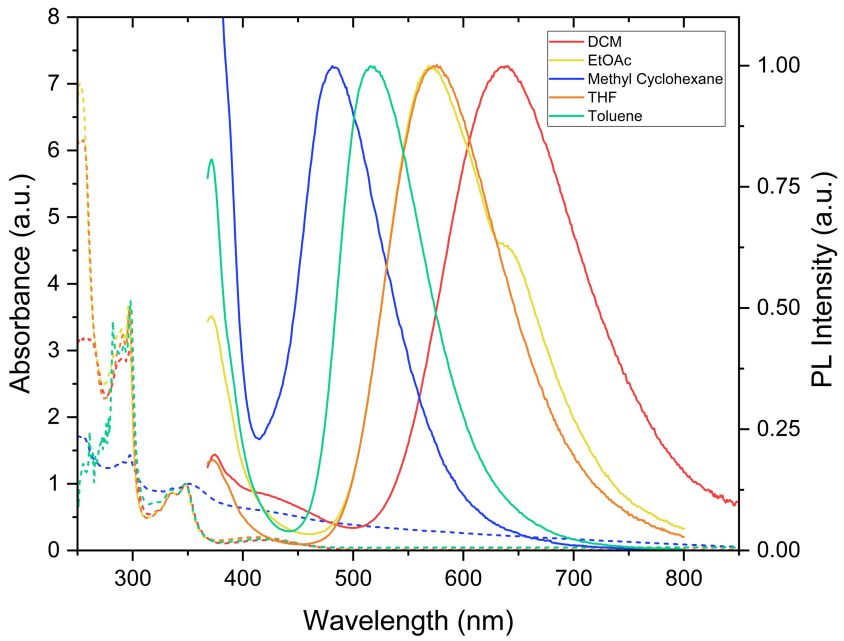


Figure 6-19 Normalised UV-vis absorption and PL spectra of tBu-MeOCzDBA when excited a 348 nm in various solvents. Note a blue-shifted LE emission appearing at lower wavelengths. This is cut off as it overlaps with the spectrometer excitation wavelength.

There is very little change when excited at 298 nm, except for the loss of the shoulder in the ethyl acetate sample, but this allows us a clearer exploration of the bluer dual emission which was previously hidden by cutting off for the spectrometer's excitation wavelengths (see Figure 6-20).

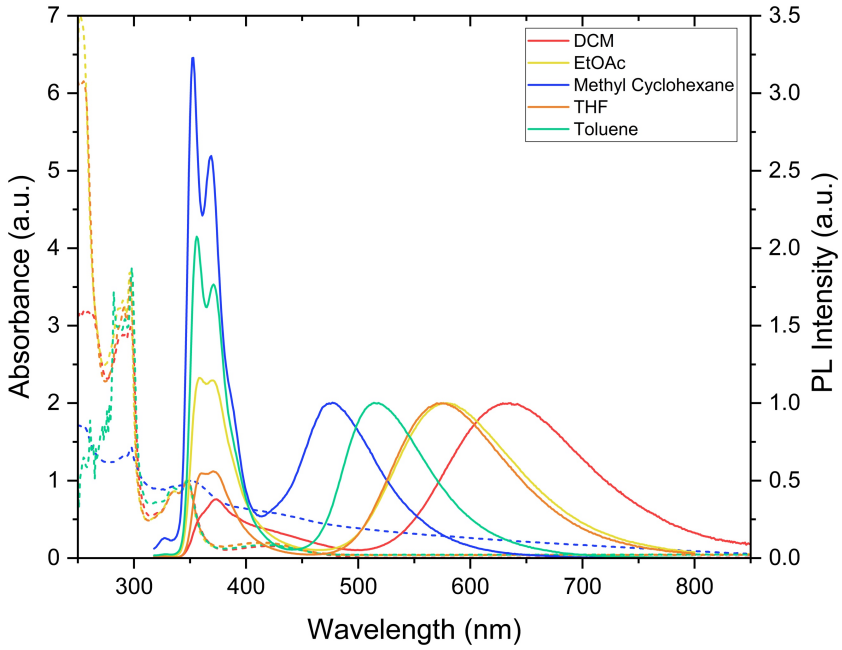


Figure 6-20 Normalised UV-vis absorption and PL spectra of tBu-MeOCzDBA excited at 298 nm. At this wavelength, the LE emission peak is no longer cut off by the spectrometer.

A detailed breakdown of the UV-vis absorption and PL data (using 298 nm as the excitation wavelength), are reported in Table 6-12 and the details pertinent to Lipper-Mataga calculations are shown in Table 6-13.

Table 6-12 Comparison of UV-vis absorption and PL spectra and the corresponding CT and LE emission in different solvents.

	λAbs (nm)	**λPL_{CT} (nm)**	**$FWHM_{CT}$ (nm)**	**λPL_{LE} (nm)**	**$FWHM_{LE}$ (nm)**
Toluene	416(CT), 348, 335, 320, 298, 292, 286, 282	516	88	371, 356	31
Tetrahydrofuran	413(CT), 348, 335, 297, 291, 285sh, 255, 242	573	121	371, 360	40
Methylcyclohexane	352, 337, 297, 291	477	83	369, 353, 387sh	31
Ethyl acetate	413(CT), 347, 335, 296, 290, 285sh, 251	578	126	370, 359	40
Dichloromethane	420(CT), 348, 335, 297, 290	634	149	373, 362sh	28

The 371 nm and 355 nm peaks remain largely unaffected by the solvent polarity, strongly supporting the suggestion that they are the result of a locally excited emission, with the redder peak which shifts from 477 nm in methylcyclohexane to 634 nm in dichloromethane, as well as broadening with increased solvent polarity, being clearly charge transfer in nature. Interestingly, the LE peaks increase in intensity relative to the CT peaks as the solvent used is replaced with one less polar.

In order to perform Lippert-Mataga analysis on tBu-MeOCzDBA, the dielectric constants and refractive indices for the various solvents shown in Table 4-10 in Chapter 4 were used.

Table 6-13 The UV-vis absorption, PL data and Stokes shift for the CT emission peak of tBu-MeOCzDBA in different solvents when excited at λAbs_{max}.

Solvent [~1 × 10^{-5} M]	λAbs_{max} (nm)	λPL_{max} (nm)	FWHM (nm)	$\nu_a - \nu_p$ (cm^{-1})
Toluene	348	517	90	9393
Tetrahydrofuran	348	575	122	11344
Methylcyclohexane	352	482	93	7662
Ethyl acetate	347	570	139	11275
Dichloromethane	348	637	147	13037

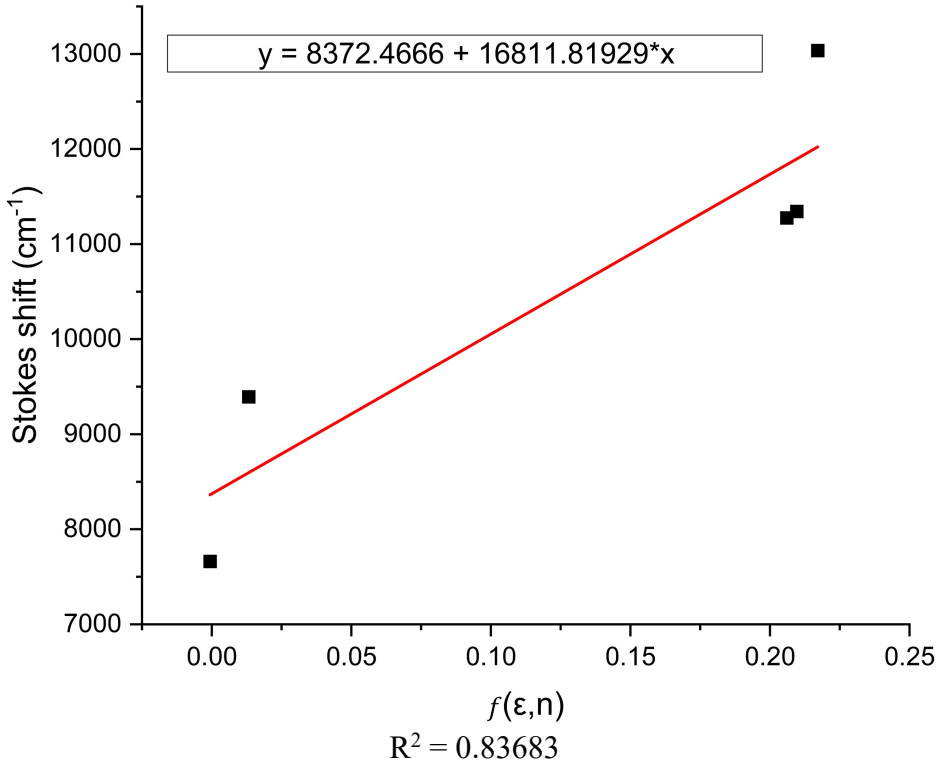


Figure 6-21 Lippert–Mataga plot for tBu-MeOCzDBA. *f*(ε,n) is the orientation polarisability of the solvent.

As with Chapter 4, using Equation 4-1 permits the use of the slope of the Lippert–Mataga plots from Figure 6-21, and Divac *et al.*'s[299] method to yield the dipole moments of the CzDBA and tBu-MeOCzDBA in Table 6-14.

Table 6-14 Dipole moment of CzDBA and tBu-MeOCzDBA. CzDBA data taken from Wu *et al*.[238]

Molecule	$\Delta\mu$ (cm^{-1})	a (Å)	$(\mu_e - \mu_g)D$
CzDBA	9240.7[b]	12.1[c]	40
tBu-MeOCzDBA	16811.82	15.4[a]	78

[a] Onsager cavity radius, calculated *via* DFT-B3LYP-6-31+G(d) as the half largest diameter across the whole molecule plus the van der Waals radii of the two furthest atoms. [b] Value taken from Wu *et al*.'s paper [238]. [c] measured from CCDC single crystal XRD structure reported by Wu *et al*.[238]

From the Lippert–Mataga plot, it can be seen that the change in dipole moment when tBu-MeOCzDBA is excited is significantly greater than that of CzDBA. From Table 6-13, we observe quite a large Stokes shift for tBu-MeOCzDBA, reaching 13037 cm^{-1} in dichloromethane. Whilst not as large as that reported by Cassidy *et al*.[323] (who also incorporated boron-based heterocycles as acceptors), they ascribe their significant Stokes shifts to interactions between the ethoxy groups bonded to their donor moiety and the empty p-orbital of boron, which is highly likely what is happening with tBu-MeOCzDBA (although single crystal XRD studies are required to confirm this). Interestingly, they suggest bond-cleavage-induced charge transfer (BICT) as the mechanism behind the interactions. This involves dative bonds forming between boron and an electron lone pair in a nearby atom which is cleaved in the excited state by photodissociation, yielding two major emission bands[317]. The dual emission bands being a potential indicator of BICT is further supported by the work of Kawashiro *et al*.[330] and they bear a striking similarity to our own spectra (see



Figure 6-22).



Figure 6-22 Structure of BMMP-BF-(2T)$_2$ and its UV-vis and photoluminescence spectra (spectra reproduced from Cassidy *et al*.[323]).

The impact of solvatochromism on PLQY, both in solution and the solid-state, was also explored in order to see how the LE and CT peaks contributed to the overall emissions. The PLQYs of CzDBA and tBu-MeOCzDBA were measured in two solvents of differing polarity, as well as a variety of host matrices and as a neat film (see Table 6-15). Where possible, the PLQY was recorded for both the CT and LE emissions individually.

Table 6-15 Degassed PLQYs of LE and CT peaks for both compounds.

		LE	CT	Total
CzDBA	MCH	7.8	41.4	49.2
	DCM	2.9	22.9	25.8
	Pure film	-	45	45
	mCP	0.4	99.6	100
	Zeonex	4	96	100
	DPEPO	-	81	81
tBu-MeOCzDBA	MCH	16.1	16.7	32.8
	DCM	0.4	27.2	27.6
	Pure film	-	59	59
	mCP	1	99	100
	Zeonex	1.3	98.7	100
	DPEPO	-	61	61

In more polar solvents and hosts, the contribution to emissions from the LE peak is significantly reduced, and the CT emission dominates (see Figure 6-20). This suggests the LE state is stabilised in non-polar media, perhaps by near total decoupling of the HOMO and LUMO by a large dihedral angle. In polar media, decay from the LE is suppressed in favour of CT emissions (see Figure 6-20). In the non-polar solvent, methylcyclohexane, the contribution of the LE is almost identical to the CT peak. This suggests that in non-polar media, the losses caused by rotational motion at the donors is reduced, due to interactions between the methoxy groups and the boron atoms. The fact that the overall PLQYs are very high shows that non-radiative decay pathways are suppressed. Note that the DCM and MCH samples were prepared with the last remaining traces of tBu-MeOCzDBA in Glasgow, and therefore lower concentrations than ideal were used giving lower than expected PLQYs – nevertheless, the differences in the PLQY ratios between the LE and CT peaks are clear.

6.4.8 CCD time-resolved measurements$^{\delta}$

All measurements in this section were performed jointly by Kamile Bareikaite of Durham University and myself.

6.4.8.1 Solution-state measurements$^{\delta}$

Solutions of CzDBA and tBu-MeOCzDBA were prepared in dry toluene and dry dichloromethane to assess the impact of solvatochromism on time-resolved emissions.

A specialist quartz cuvette with attached vacuum adaptor was used to degas the samples *via* five cycles of freeze-thaw purging. The data obtained from the femtosecond-pulsed laser – CCD camera are shown in Figure 6-23 through to Figure 6-30 and are summarised in Table 6-16 and Table 6-17 followed by the photophysical rate constants in Table 6-18.

Toluene

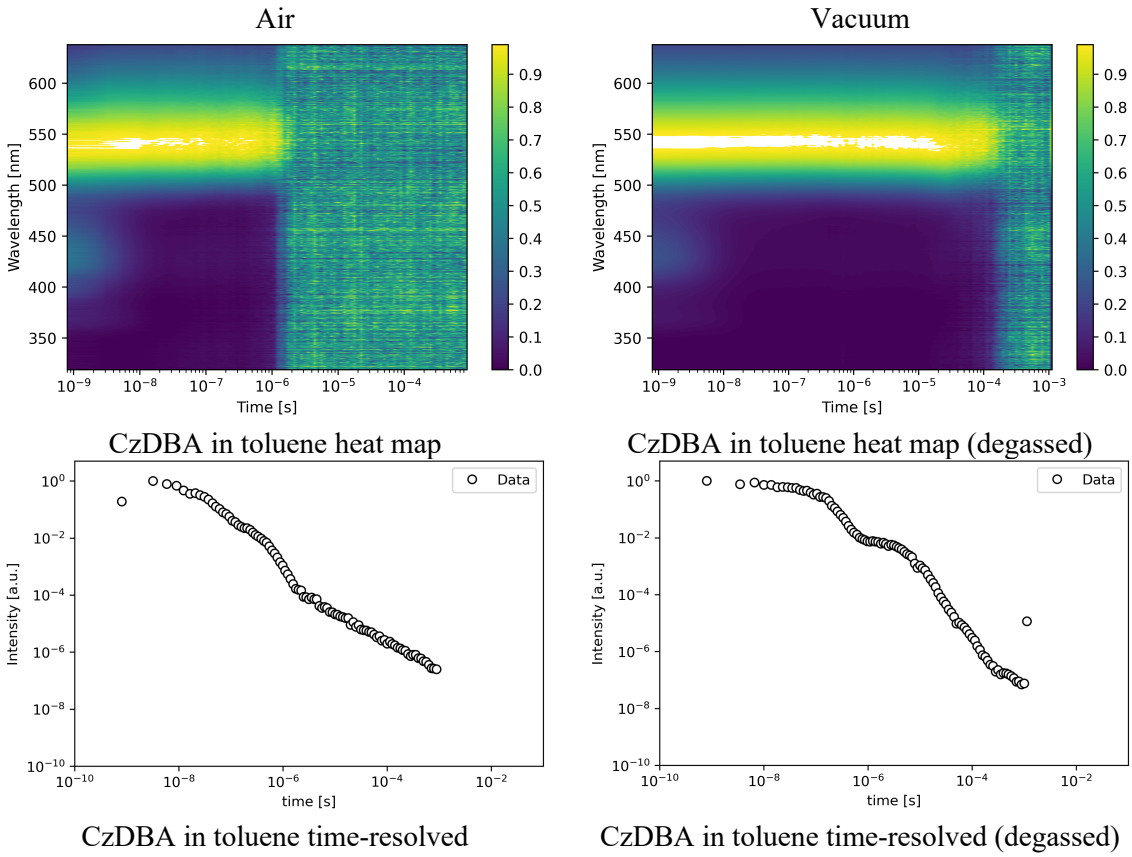


Figure 6-23 Time-resolved measurements for CzDBA in toluene.

In toluene, CzDBA primarily emits in the green region (540 nm) with a small peak in the blue (429 nm), which disappears after the first few nanoseconds. Emission lifetimes become longer upon degassing with no change to the emission wavelength.

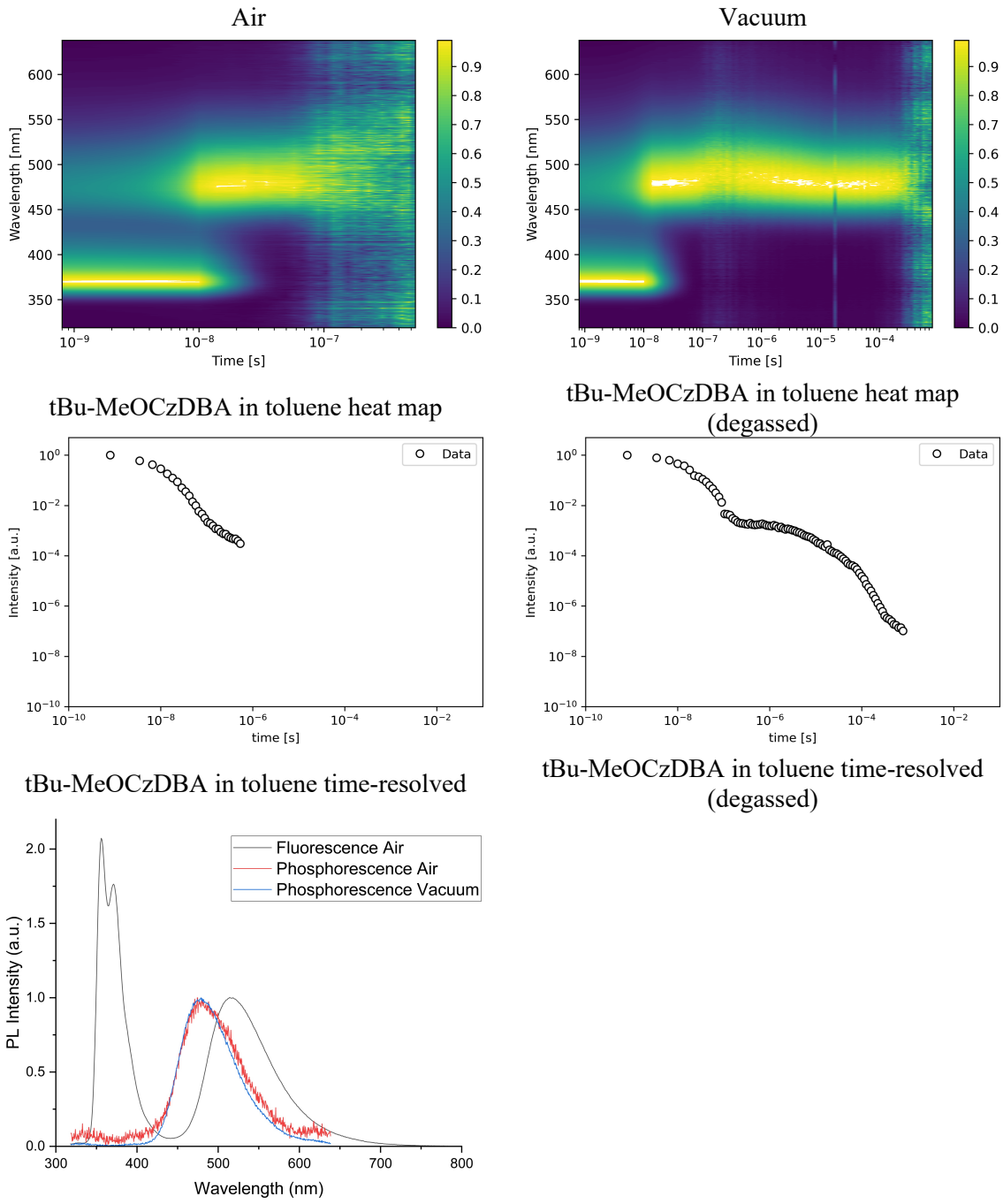


Figure 6-24 Time-resolved measurements for tBu-MeOCzDBA in toluene.

In toluene, tBu-MeOCzDBA emits initially at 478 nm and 371 nm. The bluer peak ceases to emit by ~10 ns and emission is dominated by the 478 nm peak. The lifetime of this peak is extended significantly with degassing.

Dichloromethane

Owing to the red-shifted emissions of the dichloromethane samples, the CCD detector was adjusted to compensate. This requires two separate measurements up to 550 nm and 750 nm, respectively.

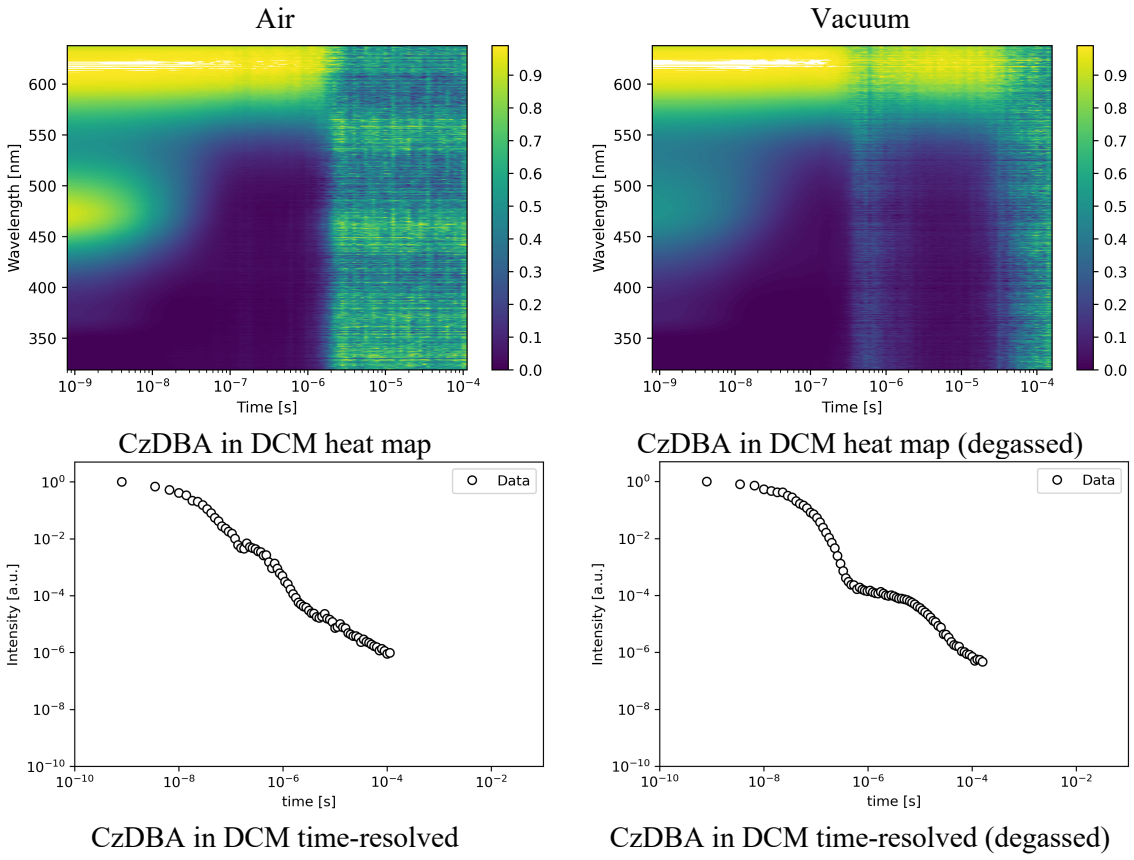


Figure 6-25 Time-resolved measurements for CzDBA in DCM, 550 nm region.

The intensity of the LE emission in the first few nanoseconds appears greater when exposed to air (see Figure 6-25). The experiment was repeated with a fresh sample only to obtain the same result. This unexpected increased intensity could be the result of chemical degradation as chlorinated solvents were observed to readily degrade both CzDBA and tBu-MeOCzDBA. The fact that this is mainly observed in air suggests that oxygen reacting with CzDBA in the excited triplet state could be resulting in unintended bond cleavage.

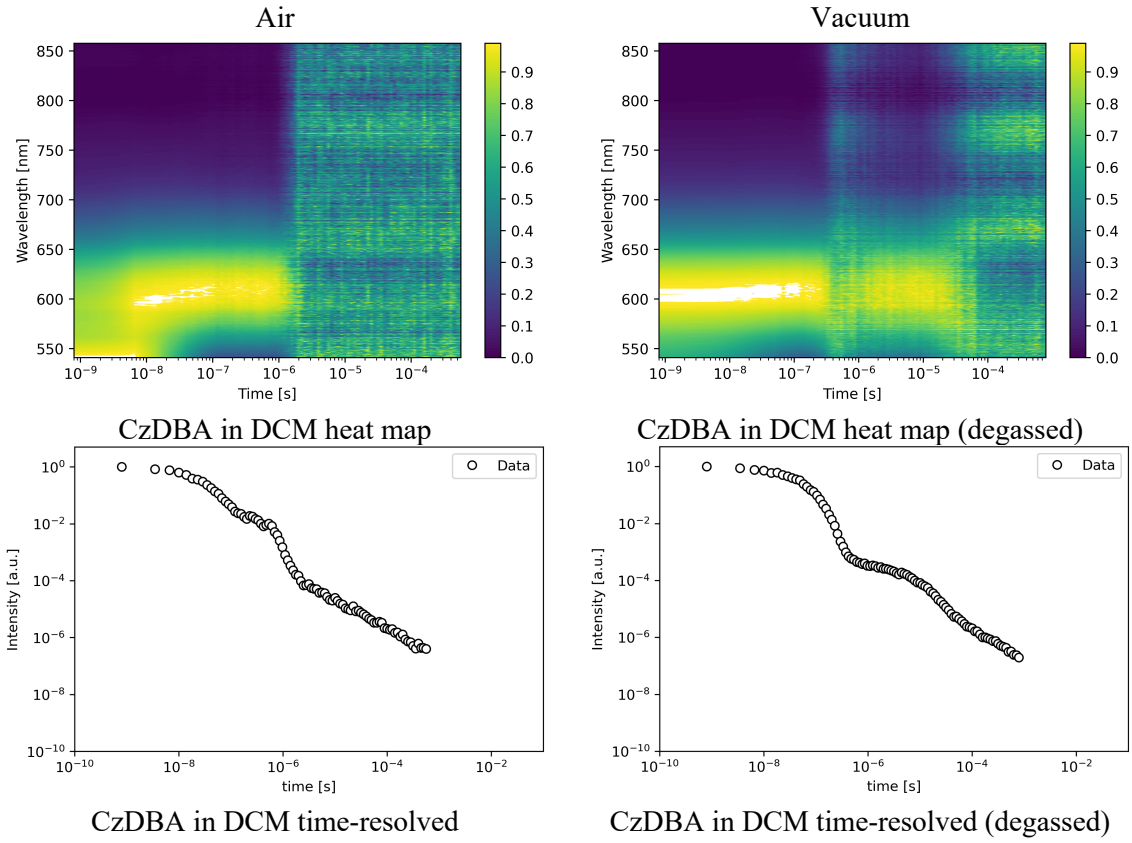


Figure 6-26 Time-resolved measurements for CzDBA in DCM, 750 nm region.

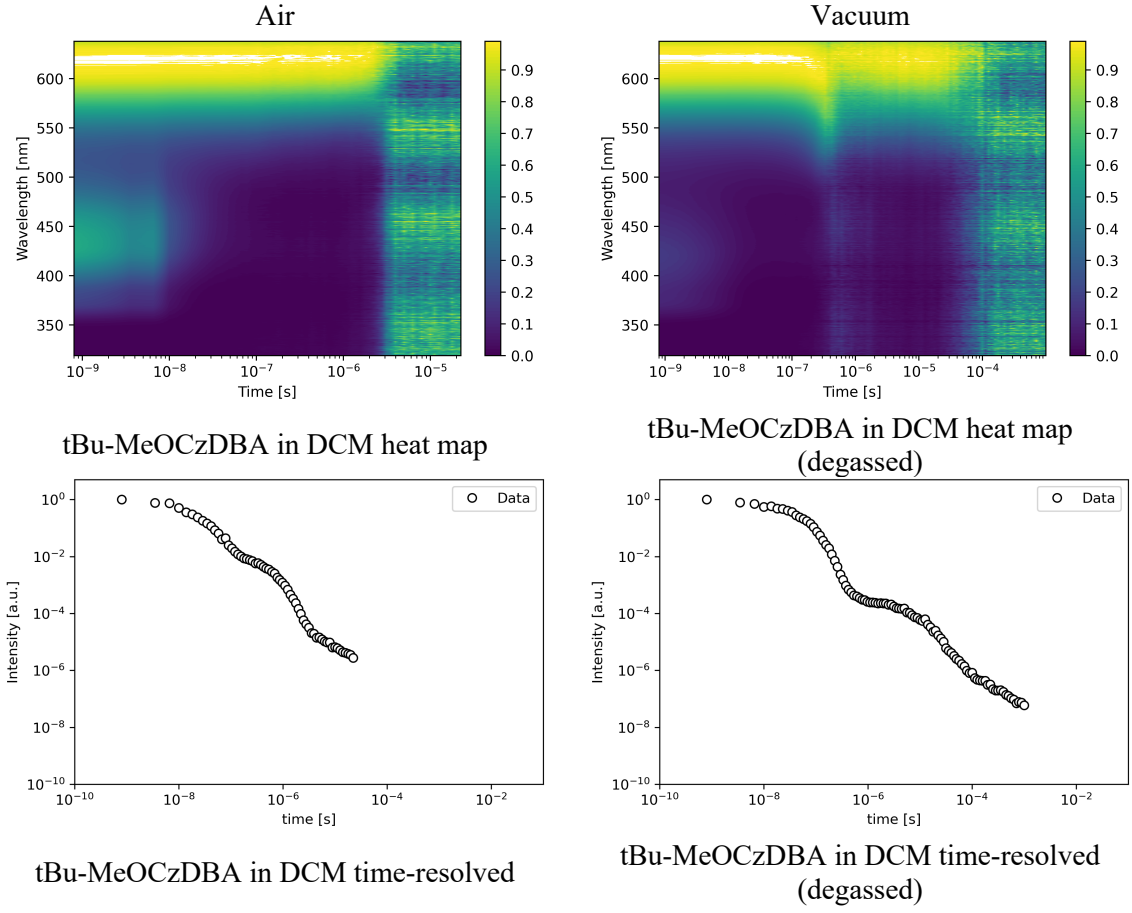


Figure 6-27 Time-resolved measurements for tBu-MeOCzDBA in DCM, 550 nm region.

In DCM, tBu-MeOCzDBA's LE emissions cease even sooner than when degassed (see Figure 6-27), with all emissions being from the CT state throughout the decay after the first few nanoseconds. This suggests better stabilisation of the CT state and enhancement of rISC rate in more polar solvents.

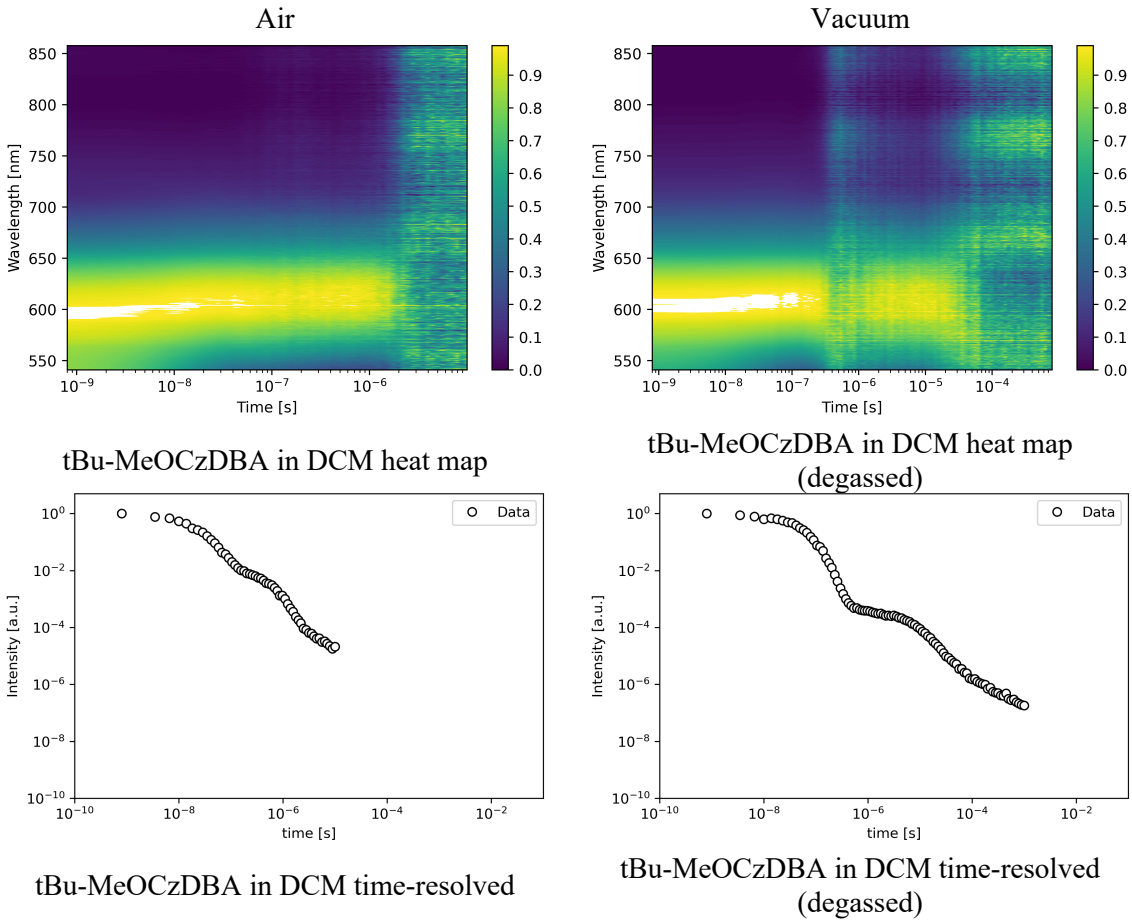


Figure 6-28 Time-resolved measurements for tBu-MeOCzDBA in DCM, 750 nm region.

6.4.8.2 Solid-state time-resolved measurements[δ]

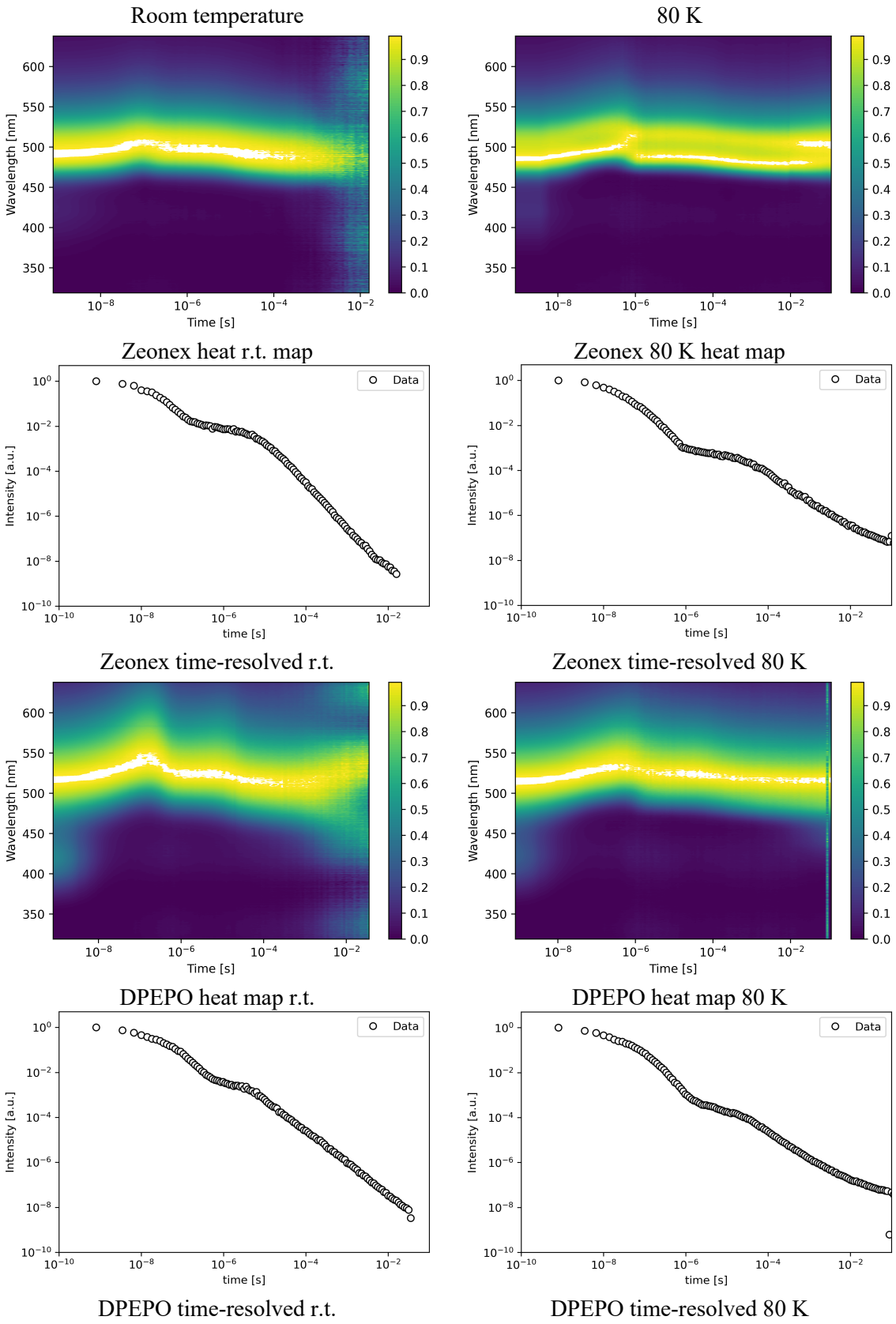


Figure 6-29 Solid-state time resolved measurements for CzDBA.

In non-polar Zeonex, CzDBA emits initially at 490 nm, with a slight shoulder at 419 nm. This emission persists for a significant length of time and is extended when cooled to 80 K when emissions will be dominated by the first excited triplet state.

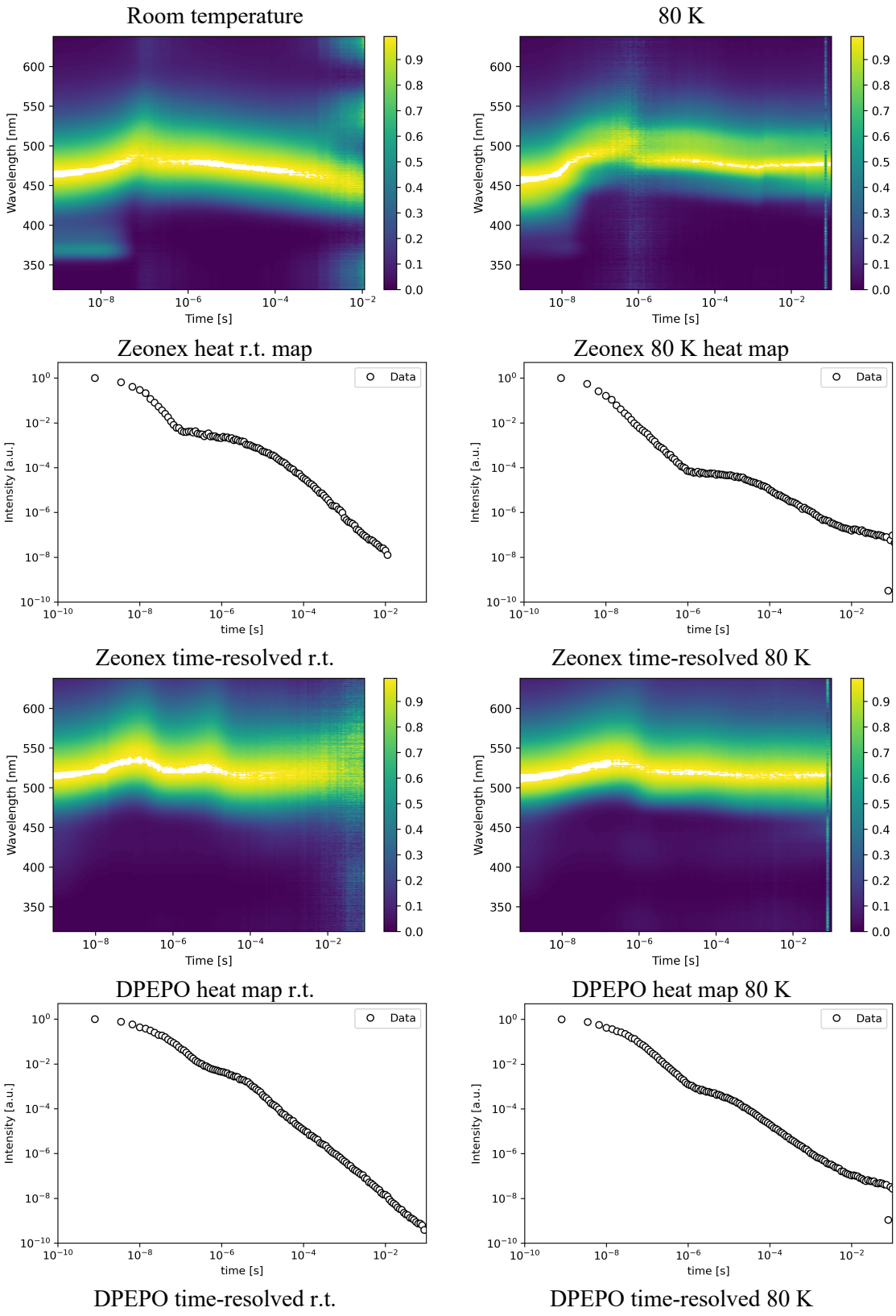


Figure 6-30 Solid-state time-resolved measurements for tBu-MeOCzDBA.

The first few nanoseconds of emission in DPEPO exhibits two emission peaks – a short lifetime 419 nm peak and a very long-lived emission at 517 nm. This peak red-shifts to ~525 nm after ~10^{-7} s (more pronounced at 80 K), before quickly returning to 517 nm.

For tBu-MeOCzDBA, Zeonex yields very long-lived emission at 465 nm, with a short-lived emission at 370 nm for the first few nanoseconds. Between 10^{-7} and 10^{-8} s, the main emissions red-shift to ~483 nm. At room temperature, the emissions gradually return to 465 nm by 10^{-3} s, however the return is much sharper at 80 K, blue-shifting to 474 nm by 10^{-6} s.

In DPEPO, emission begins at 514 nm, with no LE emission peak. This shifts to 527 nm by 10^{-7} s, before returning to 514 nm by 10^{-6} s. The drifting of emissions by 10^{-6} s is much less prominent in DPEPO, suggesting that the triplet emitting at this point is polarity sensitive.

Table 6-16 Summary of time resolved PL of CzDBA from mono-, bi-, or tri-exponential fittings.

	τ_{PF}	τ_{DF}
Sample	**(ns)**	**(µs)**
DCM Vacuum	33.4	7.06
DCM Air	19.3	0.27
Toluene Vacuum	126.3	4.41
Toluene Air	39.4	0.26
Zeonex RT	21.9	10.6
Zeonex 80 K	19.4	214.8
DPEPO RT	16.7	15.3
DPEPO 80 K	27.0	83.1

Table 6-17 Summary of time resolved PL of tBu-MeOCzDBA from mono-, bi-, or tri-exponential fittings.

	τ_{PF}	τ_{DF}
Sample	**(ns)**	**(µs)**
DCM Vacuum	42.9	8.20
DCM Air	19.9	0.41
Toluene Vacuum	20.8	420.0
Toluene Air	10.3	-
Zeonex RT	9.22	21.0
Zeonex 80 K	8.53	325.0
DPEPO RT	28.5	6.00
DPEPO 80 K	27.3	29.1

Table 6-18 Summary of photophysical rate constants calculated from fittings of time-dependent photoluminescent decays using a method outlined by Dias *et al.*[173]

		k_F	k_{ISC}	k_{rISC}
	Sample	**(s^{-1})**	**(s^{-1})**	**(s^{-1})**
CzDBA	Toluene Vacuum	1.32E+07	7.57E+07	1.65E+05
	Zeonex RT	1.00E+08	7.57E+07	1.65E+05
	Zeonex 80 K	7.60E+07	5.73E+07	8.16E+03
	DPEPO RT	9.49E+07	8.48E+07	1.13E+05
	DPEPO 80 K	8.08E+07	7.21E+07	2.88E+04
tBu-MeOCzDBA	Toluene Vacuum	1.75E+07	8.17E+07	2.06E+05
	Zeonex RT	1.54E+08	1.60E+08	9.75E+04
	Zeonex 80 K	1.32E+08	1.38E+08	6.28E+03
	DPEPO RT	6.26E+07	8.71E+07	3.09E+05
	DPEPO 80 K	6.27E+07	8.73E+07	6.35E+04

Table 6-18 describes the various photophysical rates calculated from the experimental data in Table 6-16 and Table 6-17. As can be seen here, the rate of rISC is significantly reduced at lower temperatures, highlighting its temperature dependence. The rISC rate of tBu-MeOCzDBA is poorer than CzDBA in the non-polar host but is enhanced compared to CzDBA in the polar DPEPO host.

6.4.8.3 Solvatochromic host[δ]

Polyethylene oxide exhibits a substantial change in its dipole moment at low temperatures[153]. It therefore makes for an excellent solid-state host for investigating solvatochromism of materials in the solid-state. Drop casting 1% w.t. tBu-MeOCzDBA in PEO permitted exploration of the impact of the host environment on the emissions in the solid-state (see Figure 6-31).

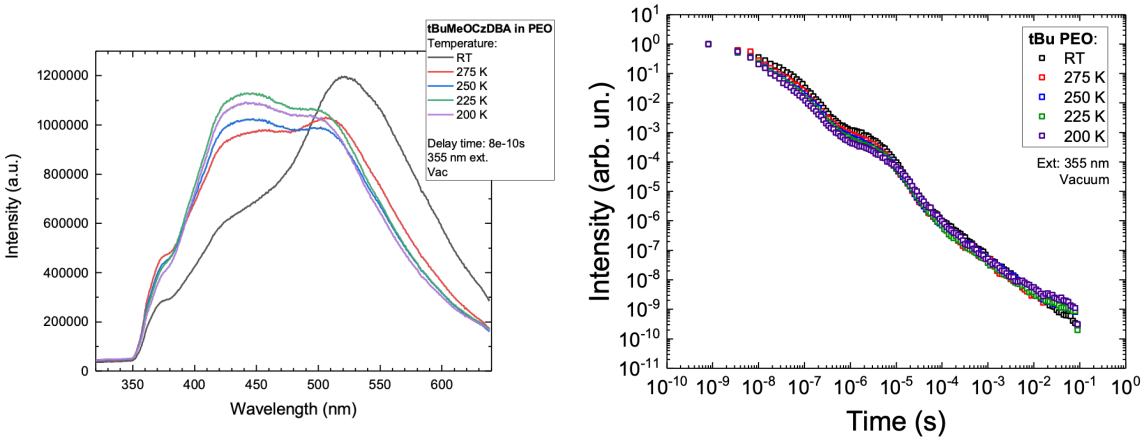


Figure 6-31 Time-resolved luminescent properties of tBu-MeOCzDBA in PEO.

Taking the PL intensities at various temperatures, along with the onset of the CT emission peak (fitted using a bi-gaussian fitting), the impact of polarity as a function of temperature upon the CT energy can be visualised as compared to the ^{3}LE energy.

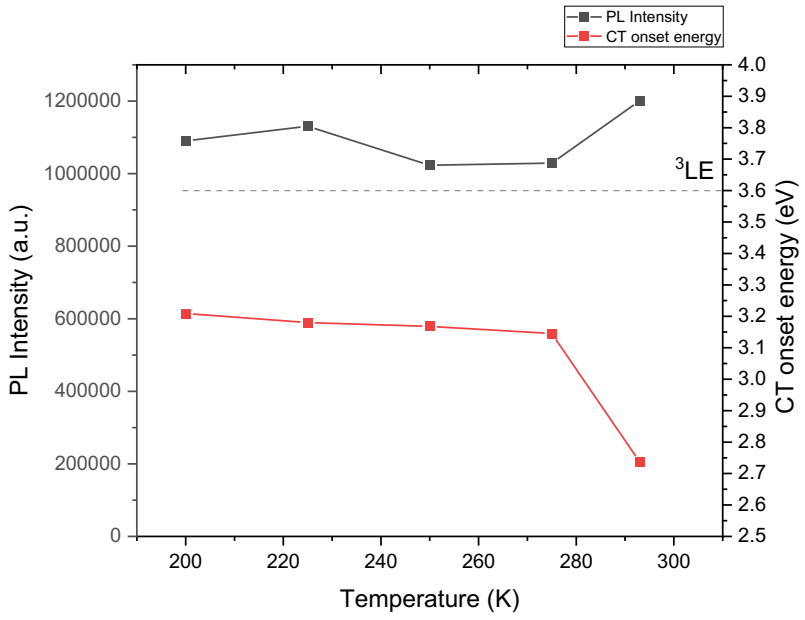


Figure 6-32 Change in emission intensity as CT state energy changes as a function of temperature in PEO host matrix. The dashed line represents the energy of the ^{3}LE state (based on the Zeonex and DPEPO samples).

At room temperature, the PEO host's dielectric constant is close to that of toluene, becoming increasingly non-polar at lower temperatures[153]. This is reflected in Figure 6-31 and Figure 6-32 as the CT peak blue-shifts as the temperature is decreased.

6.4.9 Fluorescence and phosphorescence[δ]

Using a combination of fluorescence spectroscopy and the 80 K CCD measurements, the energies of the singlet and triplet states could be determined by the PL onsets for the solid-state samples. For solutions, the same approach was used, but at room temperature and using degassed solutions.

CzDBA

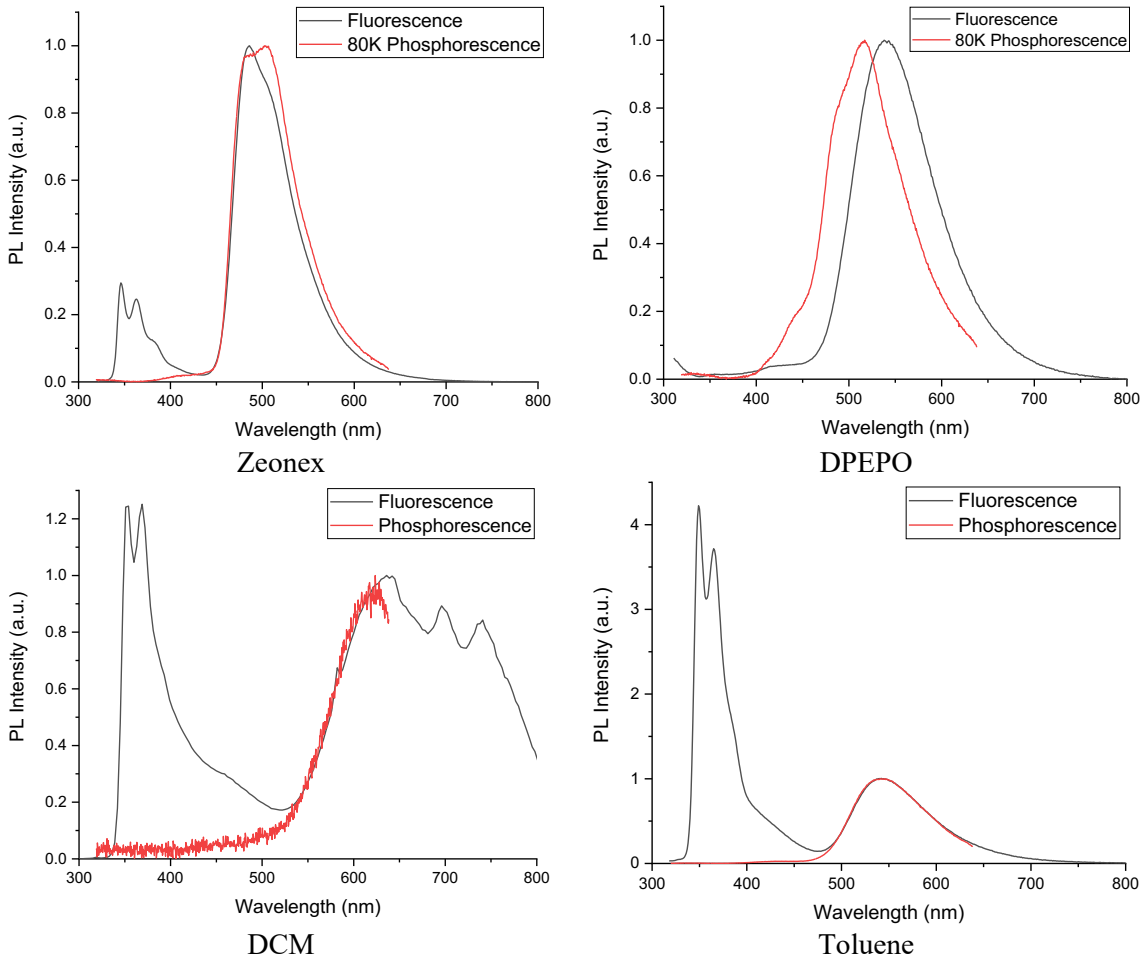


Figure 6-33 PL spectra of fluorescence and phosphorescence of CzDBA in solid-state hosts and solution.

In the non-polar host matrix, Zeonex, the onset of CT fluorescence for CzDBA is very close to that of CT phosphorescence, yielding narrow ΔE_{ST} of 0.0082 eV (see Figure 6-33 and Figure 6-34). Switching to DPEPO (a polar host) the ΔE_{ST} widens to 0.2 eV. A similar effect is noticed in solution, to a lesser degree – widening from 0.011 eV in non-polar toluene to 0.019 eV in polar dichloromethane.

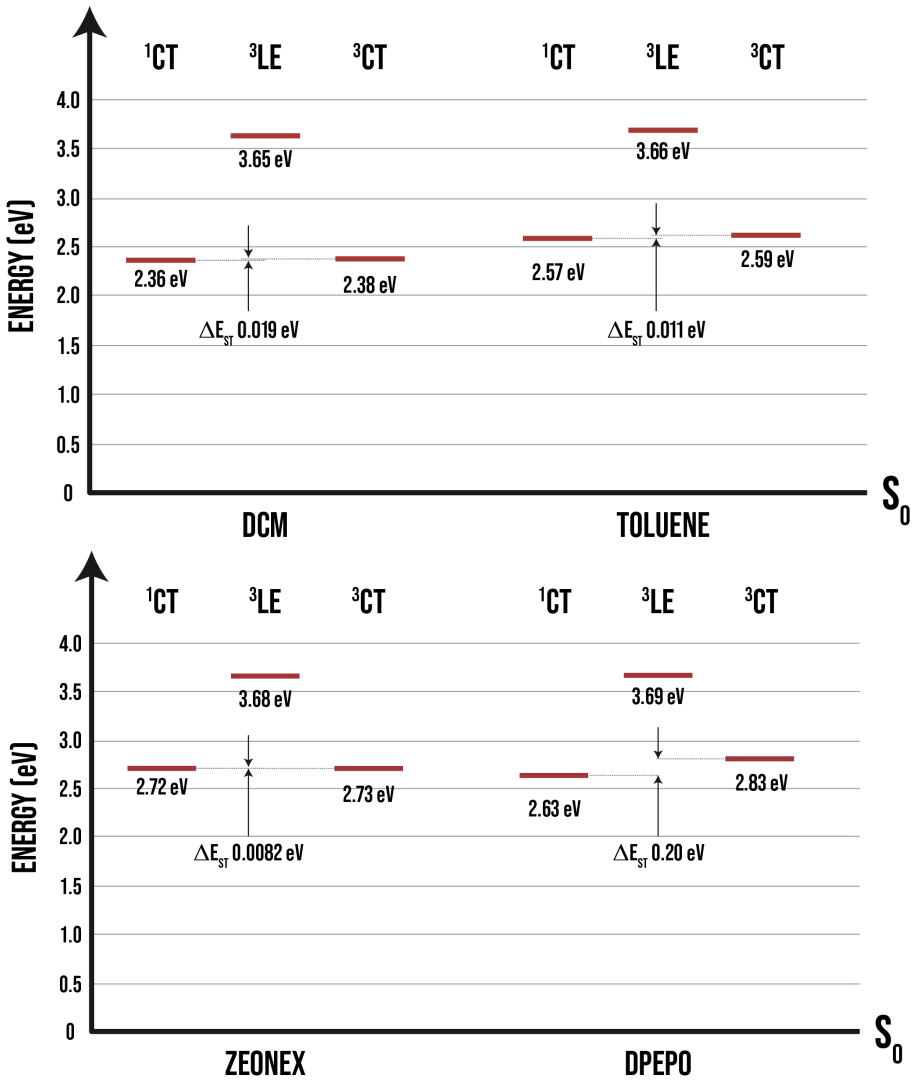


Figure 6-34 Energy state diagrams for CzDBA in different hosts and solvents.

In all cases, the locally excited emission remains largely unchanged, both in the solid-state, and is solvent independent in solution.

tBu-MeOCzDBA

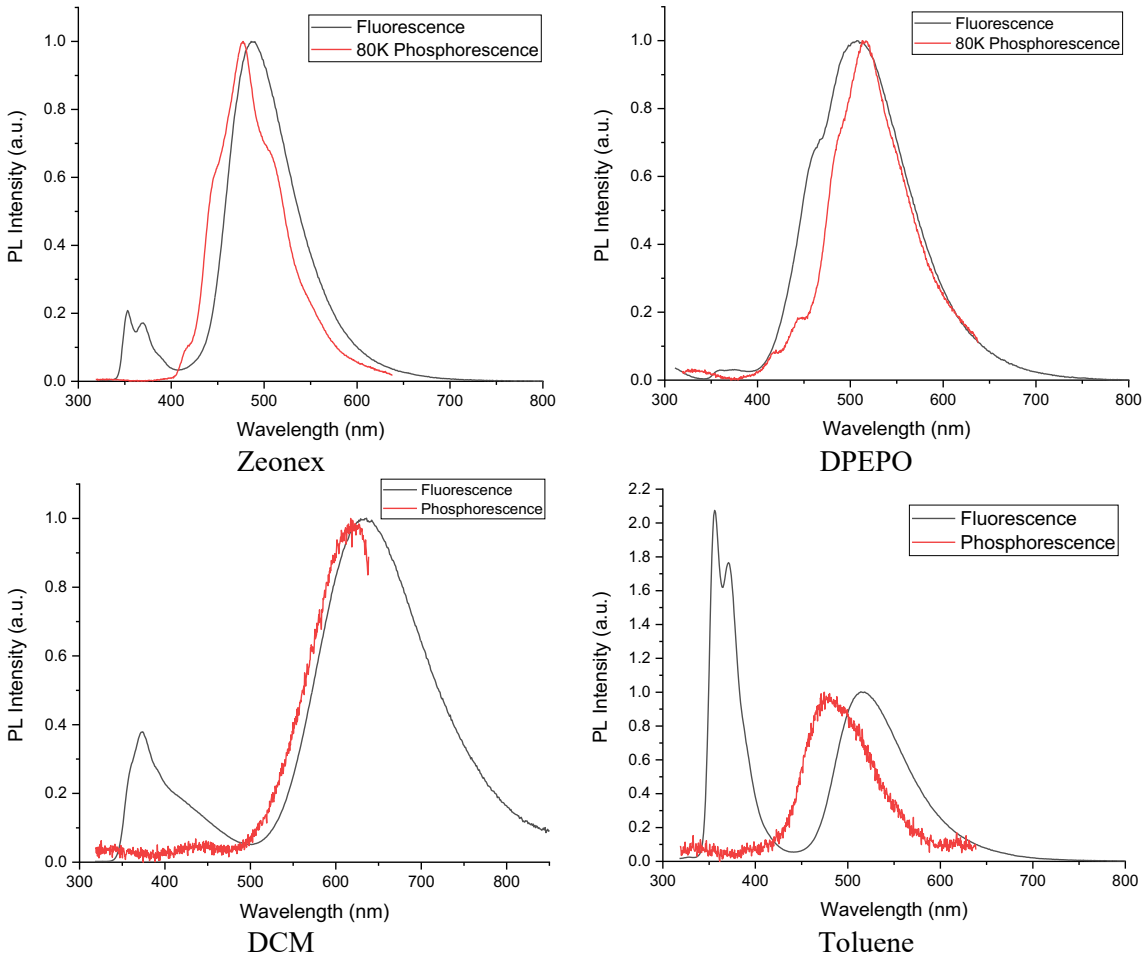


Figure 6-35 PL spectra of fluorescence and phosphorescence of tBu-MeOCzDBA in solid-state hosts and solution.

For tBu-MeOCzDBA in host matrices, the ΔE_{ST} widens from 0.068 eV in Zeonex to 0.25 eV in DPEPO (see Figure 6-35 and Figure 6-36). This 0.182 eV difference compares to the 0.192 eV difference in CzDBA. In solution, the energy gap is much greater, with ΔE_{ST} in toluene and dichloromethane being 0.23 eV and 0.10 eV, respectively, a difference of 0.13 eV compared to the difference of 0.008 eV in CzDBA. This difference in solution reflects the large dipole moment calculated for tBu-MeOCzDBA in Table 6-14.

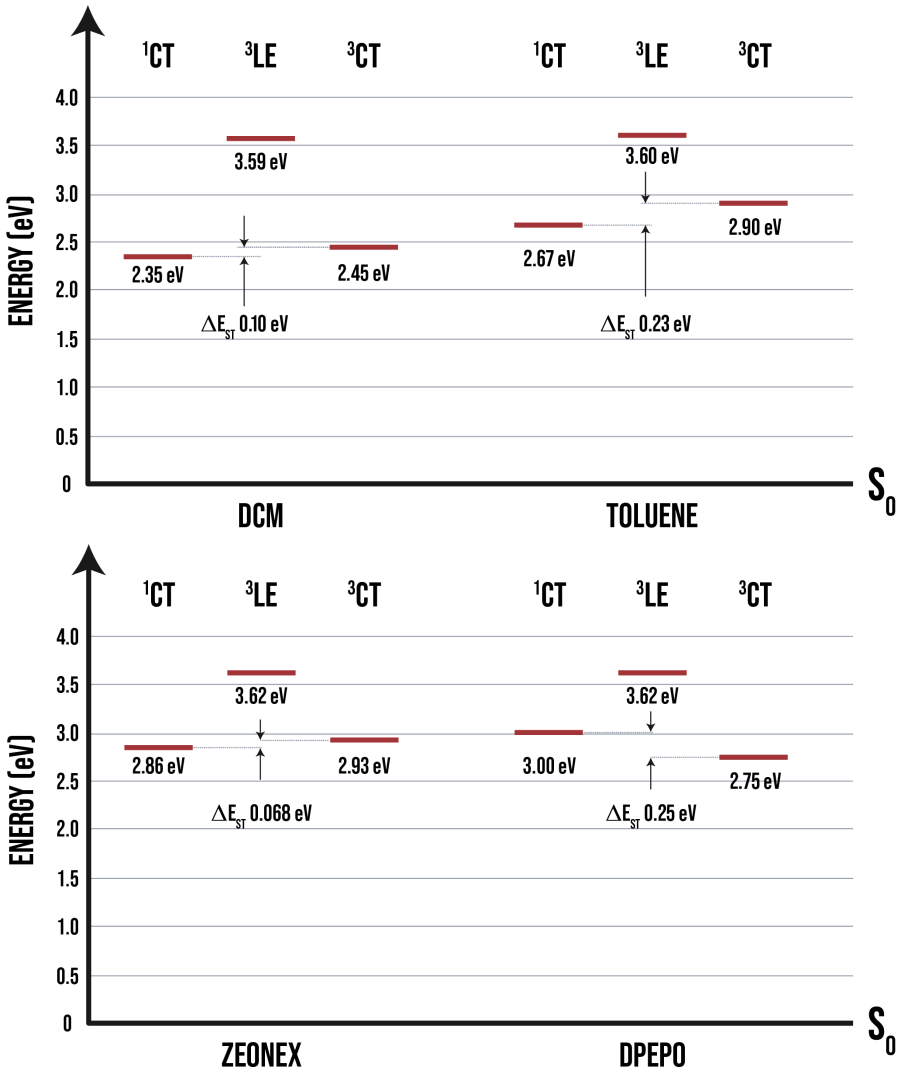


Figure 6-36 Energy state diagrams for tBu-MeOCzDBA in different hosts and solvents.

As with CzDBA, the locally excited state of tBu-MeOCzDBA is solvent independent (differing by only 0.01 eV) and is not affected by the host matrix.

The lack of solvatochromism supports the blue peak in both molecules being from a locally excited state, and the cutting off of emissions at low temperatures suggests that the population of it is driven by rISC.

In both molecules, the energy states are of the order:

$$E\,^3{}_{LE} > E_{CT}$$

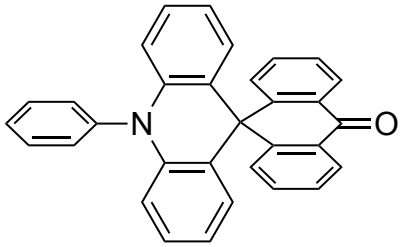
Which means both compounds possess type III TADF, where the locally excited intermediary state is higher in energy than the charge transfer states[300].

In summary, for tBu-MeOCzDBA, it would appear that the methoxy groups present significant steric hindrance, yielding a large dihedral angle between the donor and acceptor moiety. This results in almost total decoupling of the HOMO and LUMO in non-polar solvents and hosts. The locally excited state is situated (and almost isolated in non-polar conditions), upon the tert-butyl carbazole donor moiety (based on the wavelengths of its emissions). More polar hosts and solvents permit greater mixing of the HOMO and LUMO. Therefore, purely steric hindrance cannot be behind this alone. It is highly likely that non-covalent interactions between the methoxy groups and the acceptor moiety allow a certain degree of 'give' in more polar conditions to allow for increased mixing, however, based on the significantly higher PLQYs compared to CzDBA, methoxy – boron interactions appear to substantially quell non-radiative decay in solution by enhancing rigidity. Single crystal XRD studies are required to confirm this.

In section 6.4.7, we tentatively speculate that BICT can provide an explanation for the dual emission bands seen in tBu-MeOCzDBA. However, as we have shown in our other photophysical studies, expanded to include CzDBA, this dual emission nature is also present in the methyl compound. Since methyl groups will not be able to undergo the same type of interactions with boron, the dual emission must come from another source. Additionally, compounds exhibiting a ligand group acting as a Lewis base in forming a dative bond with boron, exhibit distinctive UV-vis absorption spectra with a major band in the narrow wavelength UV and little else beyond 300 nm[323,331]. Since the absorption spectrum has clear additional peaks at 416 nm, 348 nm and 335 nm, in addition to the 298 nm peak (see sections 6.4.4 and 6.4.5), this explanation can be ruled out. Instead, we propose that the methoxy groups help to sustain a large dihedral angle between the donor and acceptor units in the same way Wu *et al*.[238] observed with CzDBA and tBuCzDBA. However, the response of tBu-MeOCzDBA to solvent polarity suggests that in non-polar solvents, a complete decoupling of the HOMO and LUMO is achieved, yielding purely fluorescent emissions from a locally excited state upon the donor moiety (assigned LE owing to the lack of influence from polarity on its emission wavelength, and assigned to being upon the donor moiety owing to the proximity of the emissions peaks to those seen for the pure donor material). Therefore, the solvent-dependent emission comes from a mix of singlet and triplet CT states.

The decoupling of the HOMO and LUMO is evidenced by the significantly reduced CT emissions relative to the LE emissions in non-polar media. This is similar to the effect of

significant spiro-centre-based decoupling observed by Franca *et al.*[151] when 10-phenyl-10H,10′H-spiro[acridine-9,9′-anthracen]-10′-one (ACRSA) was observed to appear to completely separate emissions from the donor and acceptor subunits (see Figure 6-37 for the structure of ACRSA).



ACRSA

Figure 6-37 Chemical structure of ACRSA from Franca *et al.*'s study.

Furthermore, Franca *et al.*[151] observed a dependence upon the excitation wavelength used on the emission properties, with 330 nm excitations giving rise to greater emissions from the acceptor unit, and 350 nm promoting more emissions from the donor moiety. The significant decoupling allows ACRSA to be treated as though it is composed of three different emissive molecules in one. Figure 6-11 illustrates that this is somewhat true of tBu-MeOCzDBA as well – when deep UV excitation wavelengths are used. With this in mind, the LE peak's emission intensity increases relative to the CT emissions, representing distinct decoupling of the HOMO and LUMO and allowing increased donor-originated emissions when excited at shorter wavelengths, and more acceptor-based emissions at longer wavelength excitations. It should be noted, however, that we do not possess any photoluminescence measurements for the pure acceptor molecule DBDBA, owing to its significant instability. Nevertheless, when synthesised, holding a UV-torch up to the pressure tube revealed it to fluoresce with yellow emission.

6.4.10 Chemical stability

Use of steric hindrance around boron centres has been shown to aid protection of boron compounds from chemical attack[332]. Interestingly, after being left in deuterated chloroform for 24 hours during the NMR analysis, the collected NMR tube no longer contained the yellow-green solution with yellow fluorescence of tBu-MeOCzDBA as it was the day before. Instead, the solution inside had turned red and lost all of its fluorescence.

The solution was placed back into the spectrometer and another spectrum was run.

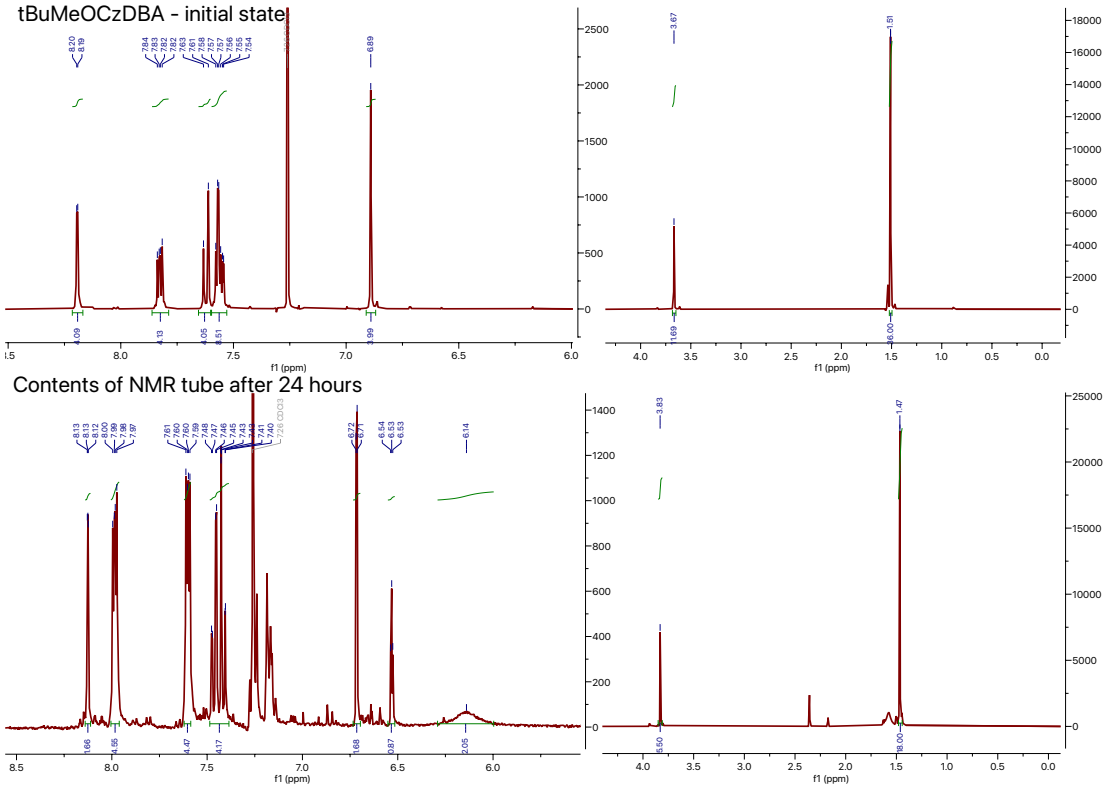


Figure 6-38 Comparison of the ^{1}H NMR in d-chloroform 10 minutes after solvation (top) and 24 hours later (bottom).

Substantial changes to the ^{1}H NMR are clearly visible in Figure 6-38. The singlet from the two aromatic protons on the π-bridge has been replaced with a doublet and triplet integrating to 2 and 1 respectively. This is indicative of the region of the molecule with the carbon-to-boron bond having undergone hydrolysis, to be replaced with a hydrogen atom and giving rise to the triplet signal. Additionally, the two doublets of doublets associated with the DBA core (7.84 ppm and 7.54 ppm) have shifted considerably, with the upfield peak more clearly visible after both peaks have shifted downfield (now at 8.00 ppm and 7.59 ppm). The peaks associated with the carbazole rings have also shifted, indicating a significantly different

environment. Additionally, a broad singlet has appeared integrating to 2 protons at 6.14 ppm, which undoubtedly is due to the protonation of the boron during hydrolysis (B-H bonds forming). This is confirmed by the observations of von Grotthus *et al.*[333], who successfully synthesised diboraanthracene in their work (essentially dibromodiboraanthracene without bromine).

This suggests that the slightly acidic nature of d-chloroform results in successful attack on the boron's empty p-orbital, yielding cleavage of the B-C donor-to-acceptor bond. Additionally, attempts were made to crystallise tBuMeOCzDBA *via* vapour diffusion from chloroform : methanol and dichloromethane : methanol. Both methods yielded a colourless solution after two days and a loss of fluorescence, suggesting that analytical grade chloroform and dichloromethane are sufficiently acidic to hydrolyse this molecule.

In order to assess the susceptibility of the boron-carbon bond to chemical attack, samples of CzDBA and tBuMeOCzDBA in tetrahydrofuran were spiked with 100 µL deionised water and their photoluminescence spectra recorded repeatedly over time and are shown in Figure 6-39 and Figure 6-40, respectively.

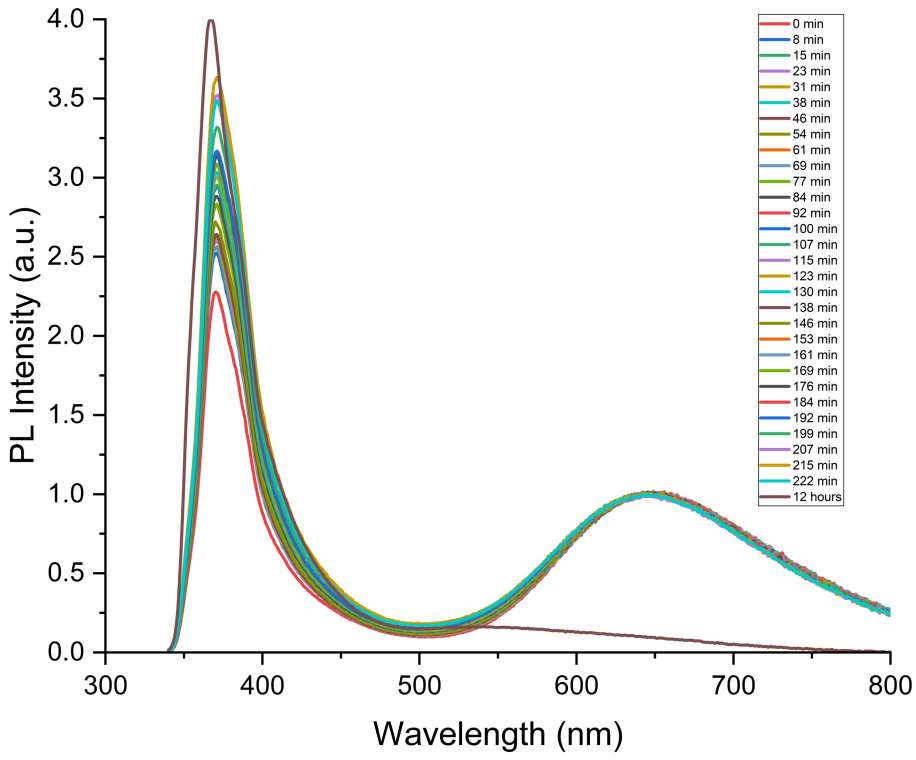


Figure 6-39 PL plot of CzDBA in THF spiked with 100 µL deionised water.

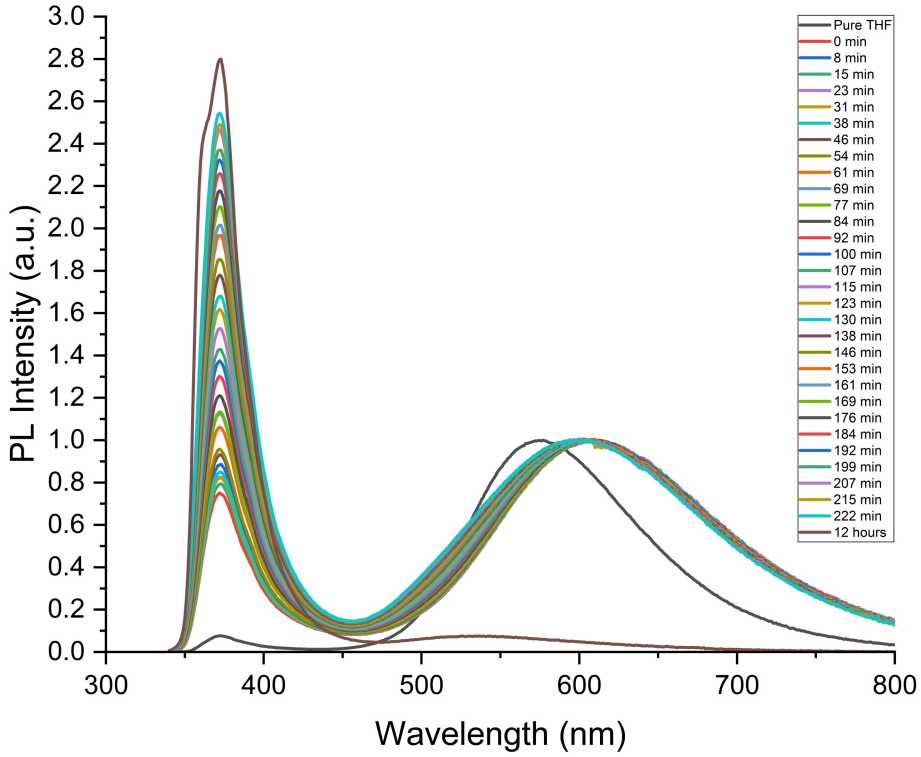


Figure 6-40 PL plot of tBuMeOCzDBA in THF spiked with 100 µL deionised water.

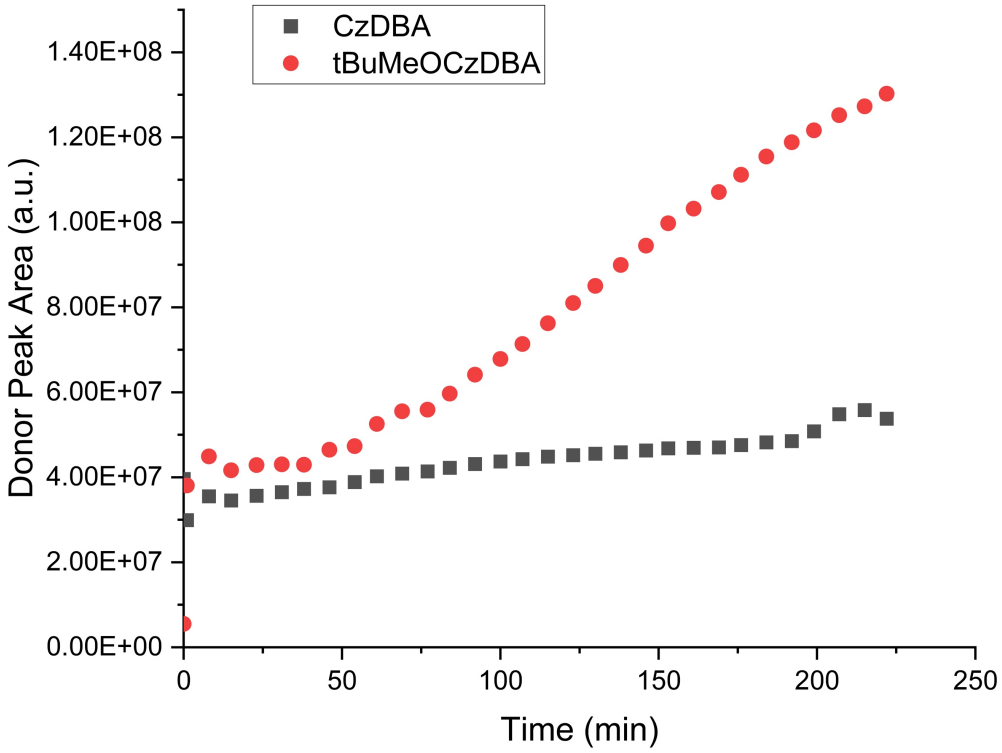


Figure 6-41 Comparing the peak integral of the free donor molecule peak during hydrolysis values taken from raw, non-normalised data with the same spectrometer conditions and exposure / excitation parameters.

The hydrolysis of both compounds can be compared in Figure 6-41. tBu-MeOCzDBA is significantly more sensitive to chemical attack compared to CzDBA, despite the protection the slightly bulkier methoxy groups would be expected to afford compared to CzDBA's

methyl groups. Despite BICT being effectively ruled out in section 6.4.9, this may still be explained as a result of dative bond formation in the ground state between the methoxy groups oxygen atoms and boron (as explained in section 6.4.7) which could give rise to slight kinks to the π-bridge – acceptor structure (as seen in Chapter 5), thereby making one side of the boron atom more exposed to chemical attack. Regardless of this, however, unlike the compounds explored in Chapter 4, both of these diboraanthracene compounds are slightly more stable.

6.5 Conclusions

A novel and convenient single-step synthesis has been developed for the preparation of 9,10-dibromo-9,10-diboraanthracene (DBDBA), beginning with commercially available starting material and producing exceptional yields.

tBu-MeOCzDBA demonstrates a very large, excited state dipole, very high PLQYs and excellent TADF character in both solution and solid-state, rivalling that of its 2018 progenitor, CzDBA[238]. A narrow ΔE_{ST} energy gap was observed, along with good thermal stability, making tBu-MeOCzDBA attractive for either solution processing or vapour deposition in TADF OLED devices. Unfortunately, the chemical instability associated with the diboraanthracene acceptor core limits the range of solvents available for preparing high quality OLEDs, and the unexpectedly ultra long-lived emissions makes it of questionable use for display applications.

Based on the findings of Chapters 4 and 5, we can posit that non-covalent interactions from the lone pairs on the oxygens of the methoxy groups in tBu-MeOCzDBA have the potential to interact with the empty p-orbitals of the boron atoms of the acceptor core. This acts to facilitate donor-to-acceptor intramolecular charge transfer, as well as providing a secure lock to the donor-acceptor dihedral. This is evidenced by the prominent LE emission peak in non-polar solvents, giving way to purely CT emissions in polar solvents, as well as the very high PLQY in degassed solution compared to CzDBA.

However, in order to fully confirm the presence of non-covalent O-B interactions, single crystal XRD measurements must be performed. As yet, the crystals grown from non-polar solvents have been of too poor quality for XRD analysis and, owing to the demonstrated sensitivity of the B-C bond, the range of appropriate solvents for crystal growth are severely limited. Growth by sublimation (as performed in the original CzDBA paper by Wu *et al*.[238]), is currently being attempted at Durham University with the goal of obtaining higher quality crystals to explore their structural properties.

Ongoing work as part of my post-doctoral position at Durham University is in fabricating OLEDs from tBu-MeOCzDBA and CzDBA for comparison. Optimisation and characterisation will shed light on how the methoxy groups impact device properties.

Chapter 7 An investigation into novel application of dibenzocarbazole as a quasi-helical donor for D-A type TADF molecules

7.1 Introduction

Dicyanobenzene, diphenyl sulfone and dibenzophenone have been well established as effective electron acceptor moieties[295,334–339]. Coupling multiple planar donor moieties to them allows for distortion from overall planarity of the entire molecule due to steric hindrance *via* twisted dihedral angles. This enables excellent separation of the HOMO and LUMO in space, and a narrowing of ΔE_{ST}.

In Chapter 4, 7H-dibenzo[c,g]carbazole was shown to produce a well-defined HOMO across the donor moiety, despite its quasi-helical structure causing deviation from the planar conjugation usually associated with ideal donors for TADF. This material seems underrepresented in the literature, with only 23 journal articles published with it as a reactant (according to SciFinder in July 2024, excluding patents) and only one paper actually incorporates it as a donor in an OLED device[340].

Whilst the B-N bond appears to be relatively unstable when the dimesityl boron acceptor is coupled with 7H-dibenzo[c,g]carbazole in DBCz-DMB (**3**) in Chapter 4, this is unlikely to be the case when coupled to an aromatic carbon system such as a dicyanobenzene, given our success with attaching π-bridges to 3,6-di-tert-butyl-9H-carbazole in Chapter 5.

Like carbazole in the aforementioned molecules, the structure of 7H-dibenzo[c,g]carbazole should give rise to steric hindrance to yield good separation of the HOMO and LUMO, whilst the quasi-helical nature observed in the XRD data of DBCz-DMB in Chapter 4 should also enhance this further due to increased steric bulk.

Further supporting the excellent HOMO confinement observed in our DFT calculations in Chapter 4, is the work of Gridneva *et al.*[341]. When exploring mechanochromic copper complexes with dibenzocarbazole donors, their DFT calculations (in the supplemental information) also show their dibenzocarbazole moieties demonstrating good confinement of the HOMO to the donor regions. This is seemingly better still than their carbazole derivatives.

Whilst dibenzocarbazole has been reported to produce relatively low PLQYs[342], Patil *et al.*[343] found that 7H-dibenzo[c,g]carbazole could be modified to become significantly more rigid, substantially enhancing PLQYs. In a heavily congested environment such as 4CzIPN, we

investigate whether such intramolecular steric hindrance can be utilised to enable TADF to be achieved from this particular donor moiety without any chemical modifications.

Recently, Matsuda *et al*.[344] observed that dibenzocarbazole, when used as a donor in a TTM luminescent radical, caused significantly red-shifted and broadened CT emissions when compared to both carbazole and monobenzocarbazole (see Figure 7-1). They ascribe this broadness to the quasi-helical nature of dibenzocarbazole that may give rise to "*intramolecular excimer-like*" structures [344].

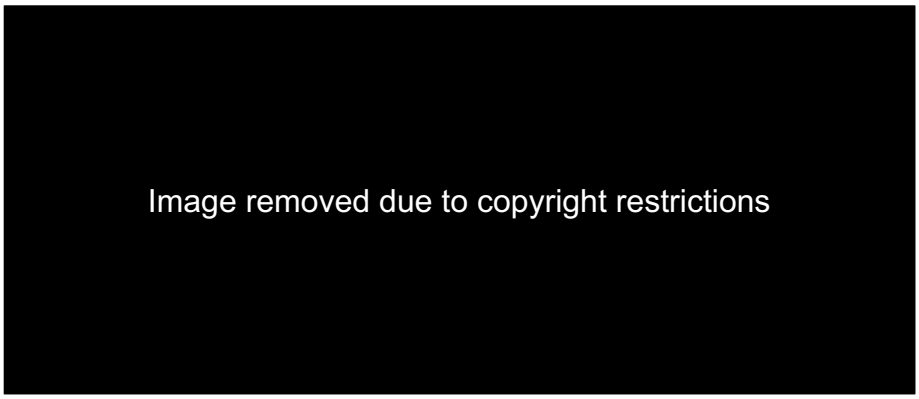


Figure 7-1 Structures of the carbazole based TTM radicals. Taken from Matsuda *et al*.'s paper[344].

When organic molecules are able to interact in the solid state, additional properties such as mechanochromism or thermochromism can arise. Thermochromism involves materials undergoing photophysical changes when subjected to temperature changes. These can manifest as enhanced or decreased PLQY, or shifting of the emission wavelength, as well as changes to the physical colour of the material when not subject to ultraviolet excitation[345]. Thermochromism can be irreversible when a chemical change to the fluorophore occurs[346], but can be reversible if intermolecular interactions are driving the changes[347,348]. Thermochromic materials can find application as temperature sensors, but also in encryption[348] and anticounterfeiting[349]. Thermochromism can shift fluorescence by as much as 250 nm in some metal carboranes[350], with 4CzIPN demonstrating a 510 nm to 549 nm shifting for its CT emission when annealed[351] due to thermally induced alterations to the 4CzIPN crystal structure giving rise to dimer formation.

Furthermore, when external forces such as grinding are applied to materials, colour changes (both physical and luminescent) can be observed – a process which is known as mechanochromism. This process often involves irreversible chemical changes[352], however full reversibility is possible through thermal action or chemical fuming, depending on the

cause of the photoluminescent changes[353,354]. Mechanochromism finds application in smart-materials used for damage detection, as well as indicating structural stresses[341].

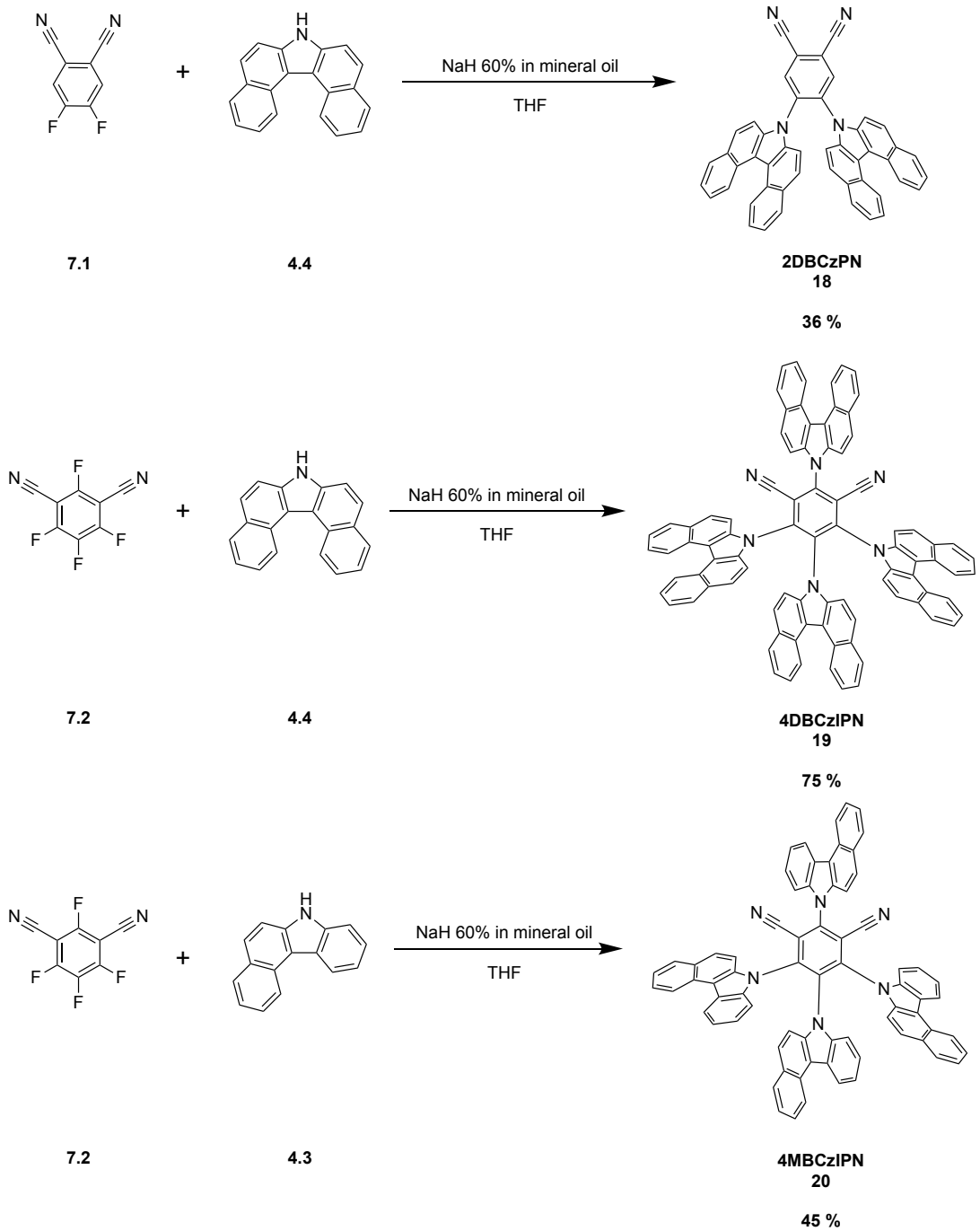
Some materials exhibit both mechanochromism and thermochromism simultaneously, permitting emission shifting of around 128 nm with a combination of heating and grinding[241].

In the dimesityl boron derivative, DBCz-DMB (**3**) in Chapter 4, orange room temperature phosphorescence was observed. In an attempt to suppress non-radiative decay, and possible structural changes in the excited state, we herein utilise cyano- groups in the acceptor moiety, which have been demonstrated to prevent such losses[33] and improve IQE. The congested nature of the well-studied 4CzIPN is also explored – given the bulk of the dibenzocarbazole donors, we anticipate good HOMO-LUMO separation due to steric effects. Further exploration with diphenyl sulfone and benzophenone is also attempted. In addition to this, a monobenzocarbazole derivative of 4CzIPN was synthesised to assess the impact of removing the quasi-helical nature of the dibenzocarbazole donor on photoluminescent properties.

7.2 Experimental

7.2.1 Synthesis

A modified literature procedure was used for the preparation of both 2DBCzPN (**18**), 4DBCzIPN (**19**) and 4MBCzIPN (**20**), replacing the carbazoles with 7H-dibenzo[c,g]carbazole or 7H-benzo[c]carbazole and adapting the mass ratio appropriately[355,356]. The syntheses are summarised in Scheme 7-1.

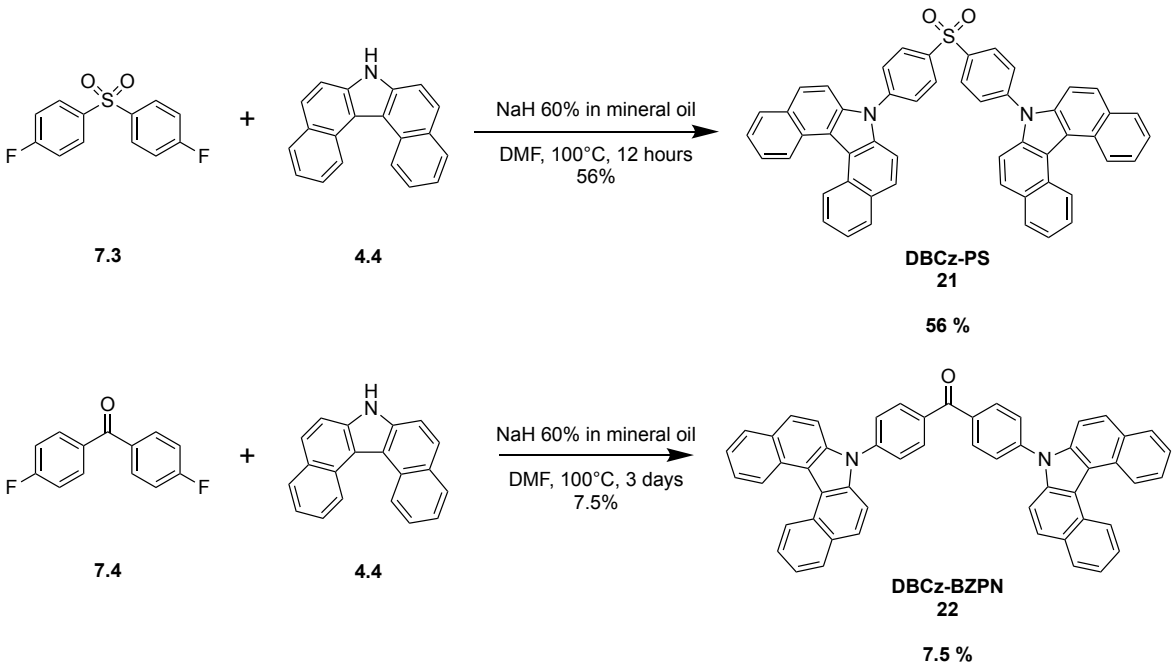


Scheme 7-1 Synthesis of mono- and dibenzocarbazole – dicyanobenzene derivatives.

In all cases, the dibenzocarbazole (**4.4**) or monobenzocarbazole (**4.3**) donors were deprotonated in tetrahydrofuran using sodium hydride. The purple fluorescence of **4.3** and **4.4** was almost immediately lost and replaced with an intense blue fluorescence upon coordination of the sodium ion to the central nitrogen. Once successfully deprotonated, the dicyanobenzene (**7.1** or **7.3**) was added in small portions in the solid state, which leads to nucleophilic aromatic substitution of the dibenzocarbazole anion. A significant red-shifting in solution colour and fluorescence was noticed in both cases as the bonding to the dicyanobenzene acceptor unit proceeded.

All three materials were easily purified *via* precipitation from hot dichloromethane : methanol, highlighting the ease of synthesis for these new compounds. The molecular structures of **18**, **19** and **20** were confirmed *via* ^{1}H NMR and ^{13}C NMR as well as high-resolution mass spectrometry.

The additional two members of this family of molecules, DBCz-PS (bis-7H-dibenzo[c,g]carbazole diphenyl sulfone) (**21**) and DBCz-BZPN (bis-7H-dibenzo[c,g]carbazole benzophenone) (**22**) are based on the structures of two well studied TADF molecules Cz-PS (bis-(4-(3,6-di-tert-butylcarbazole)phenyl)sulfone)[336,337,357–359] and Cz_2BP (4,4'-bis(9H-carbazol-9-yl)methanone)[334], both prepared using a similar synthesis protocol, shown in Scheme 7-2.



Scheme 7-2 Synthesis of dibenzocarbazole – diphenyl sulfone and benzophenone derivatives.

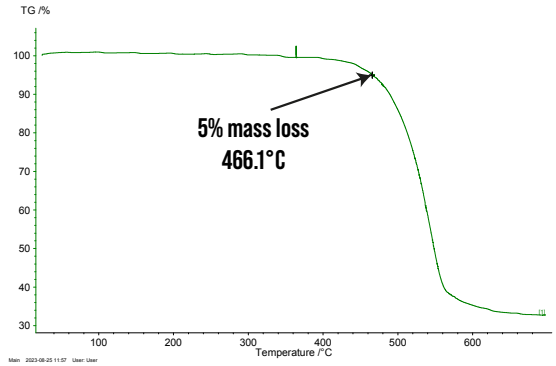
7.3 Results and discussion

7.3.1 Thermal properties

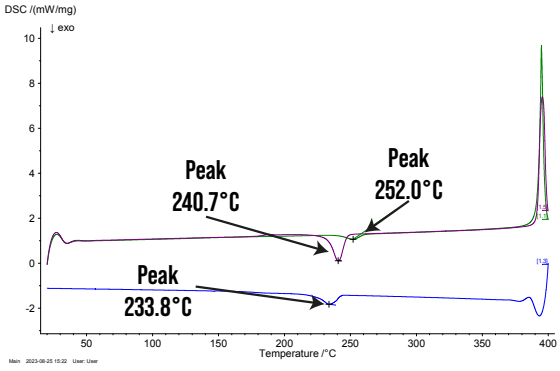
7.3.1.1 Thermogravimetric analysis and differential scanning calorimetry

For use in OLEDs, an understanding of the material's thermal properties is of great importance. As such, the thermal properties of all the compounds in this chapter are explored *via* thermogravimetric analysis (TGA) and differential scanning calorimetry (DSC). The data for these experiments are reported in Figure 7-2 to Figure 7-6 and the key thermal properties summarised in Table 7-1.

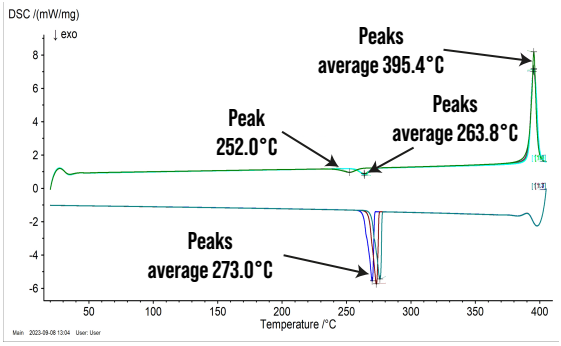
2DBCzPN (18)



TGA



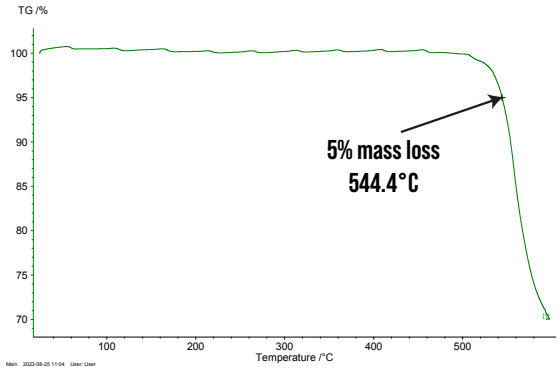
DSC – 2 heating cycles



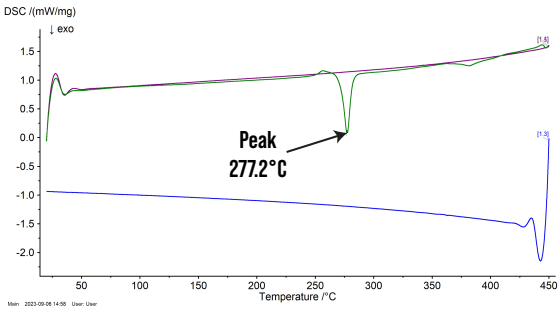
DSC 4 heating cycles

Figure 7-2 TGA and DSC plots of compound 18 ***Dark green = First heating; blue = first cooling; purple = second heating; black = second cooling; light green = third heating; teal = third cooling; cyan = fourth heating.***

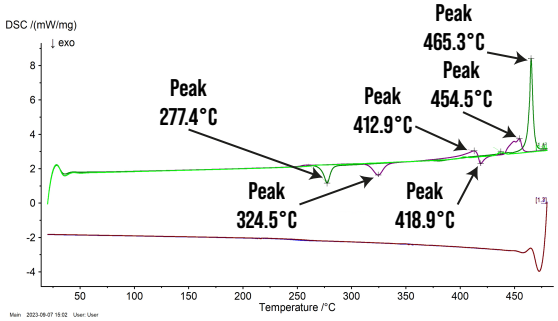
4DBCzIPN (19)



TGA



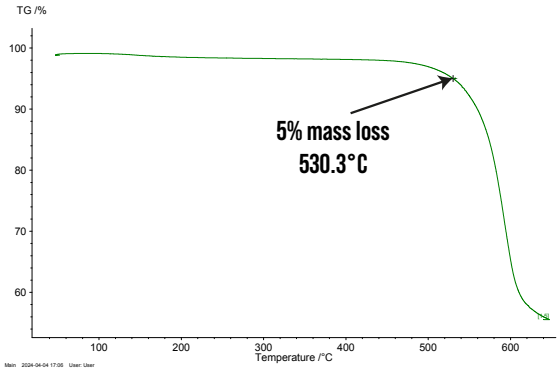
DSC – 2 heating cycles



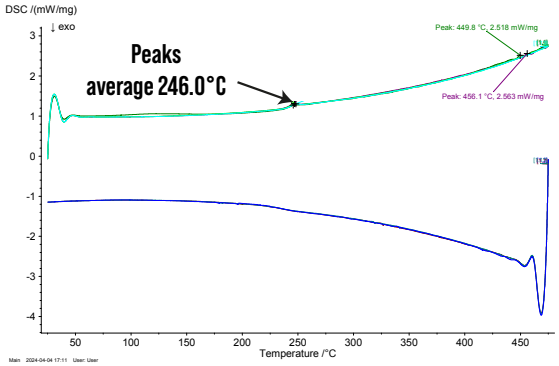
DSC – 3 heating cycles

Figure 7-3 TGA and DSC plots of compound 19 ***Dark green = First heating; blue = first cooling; purple = second heating; black = second cooling; Light green = third heating.***

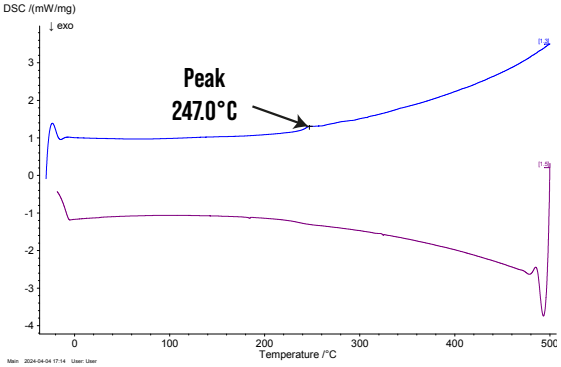
4MBCzIPN (20)



TGA



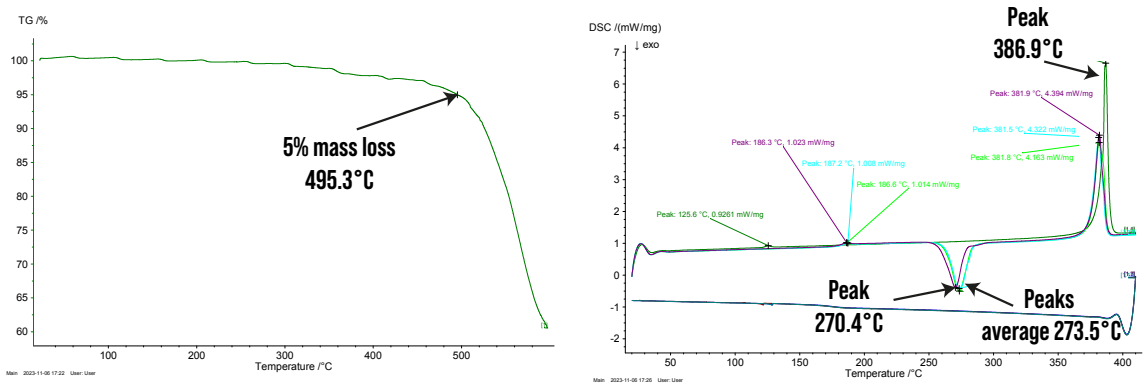
DSC – 4 heating cycles



DSC – 1 heating cycles -20°C to 500°C

Figure 7-4 TGA and DSC plots of compound 20 Dark green = First heating; blue = first cooling; purple = second heating; black = second cooling; light green = third heating; teal = third cooling; cyan = fourth heating. Owing to a mostly featureless DSC plot, an additional scan was run from -20°C to 500°C in case the melting point was close to the degradation point.

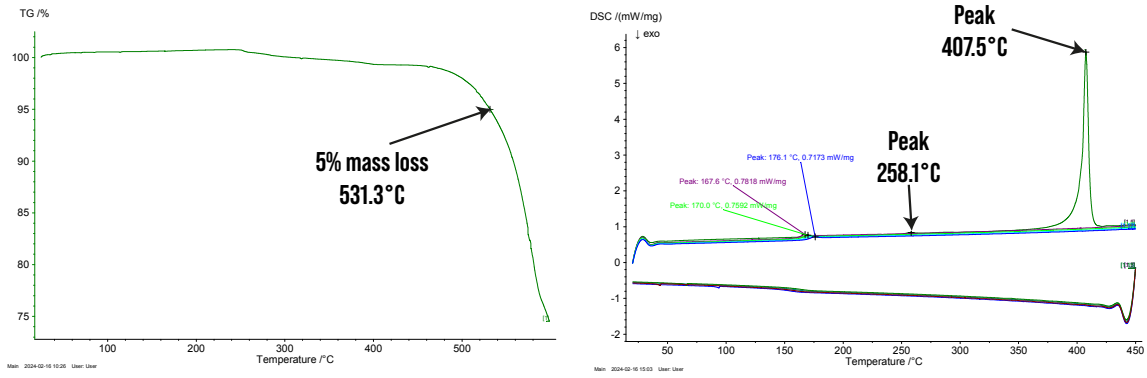
DBCz-PS (21)



TGA **DSC – 4 heating cycles**

Figure 7-5 TGA and DSC plots of compound 21 Dark green = First heating; blue = first cooling; purple = second heating; black = second cooling; light green = third heating; teal = third cooling; cyan = fourth heating.

DBCz-BZPN (22)



TGA **DSC – 4 heating cycles**

Figure 7-6 TGA and DSC plots of compound 22 Dark green = First heating; blue = first cooling; purple = second heating; black = second cooling; light green = third heating; teal = third cooling; cyan = fourth heating.

Compounds **18**, **19** and **20** are all extremely thermally stable, requiring 466°C, 544°C and 530°C to cause 5% mass loss respectively, as well as accordingly high melting points of 395°C, 465°C and 456°C respectively.

Table 7-1 Transition temperatures determined by TGA and DSC measurements.

Compound	Melting point (°C)	Thermochromic transition temperature (°C)	5% mass loss (°C)
2DBCzPN (18)	395.4	252	466.1
4DBCzIPN (19)	465.3	277	544.1
4MBCzIPN (20)	456.0	246	530.3
DBCz-PS (21)	386.9	270	495.3
DBCz-BZPN (22)	407.5	258	531.3

At 277°C there is what appears to be a crystallisation point, well below the melting point of compound **19**. Since there is no such peak in the second thermal run, it is likely thermally irreversible.

Later studies in section 7.4 demonstrate the chemical reversibility of this by exposing heated solids of compound **19** to dichloromethane fumes, whereupon after several hours the PL returned to its original state prior to vapour treatment.

To further explore the crystallisation peak in compound **19**, a further DSC experiment was run with three heating cycles, to assess whether the material is decomposing as the crystallisation peak diminishes. The DSC pans were opened after both DSC experiments and the glassy residue was washed with deuterated chloroform and ^{1}H NMR spectra were measured (see Figure 7-7). In both cases, they perfectly match that obtained with the original proton NMR spectra, indicating that, despite the repeated heating, only compound **19** is present, with no observable degradation products.

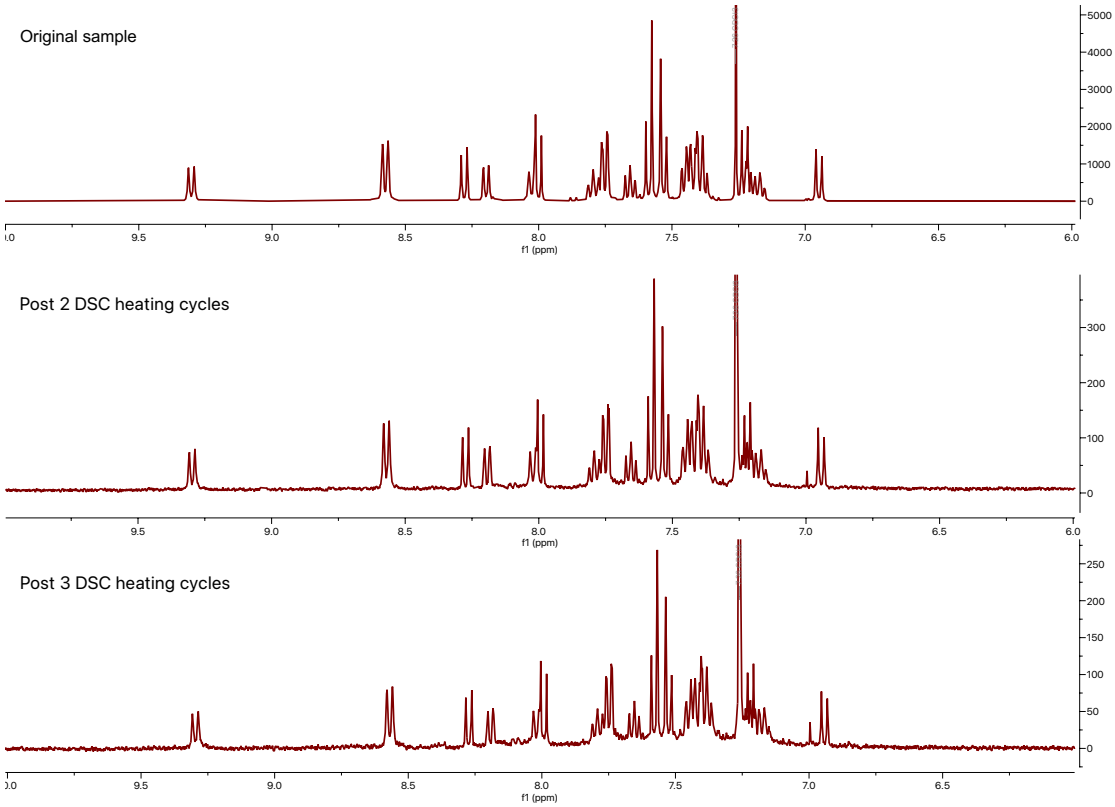


Figure 7-7 ^{1}H NMR spectra of the compound 19 sample - prior to heating; post 2 heating cycles; post 3 heating cycles. Note that there is no change in the molecular structure during the heating cycles, suggesting the presence of different polymorphs in the solid state.

There are, however, some very minor peaks appearing at 8.1 ppm and 8.4 ppm in the post-DSC ^{1}H NMR spectra, which could be due to some degradation, although overall compound **19** is demonstrating good stability.

In compound **18**, there is a peak in the DSC at 252°C in the first run, then upon the removal of thermal history, it returns at 240.7°C in the second heating ramp. This cannot be a melting point since this occurs well beyond 360°C (if at all) as the compound did not melt by this temperature in the melting point assessment. It is likely therefore crystallisation since it is exothermic. A sample of compound **18** was subjected to four DSC heating runs to assess reproducibility. After heating to 405°C four times, the DSC pan was rinsed with deuterated chloroform and a proton NMR spectrum obtained (see Figure 7-8).

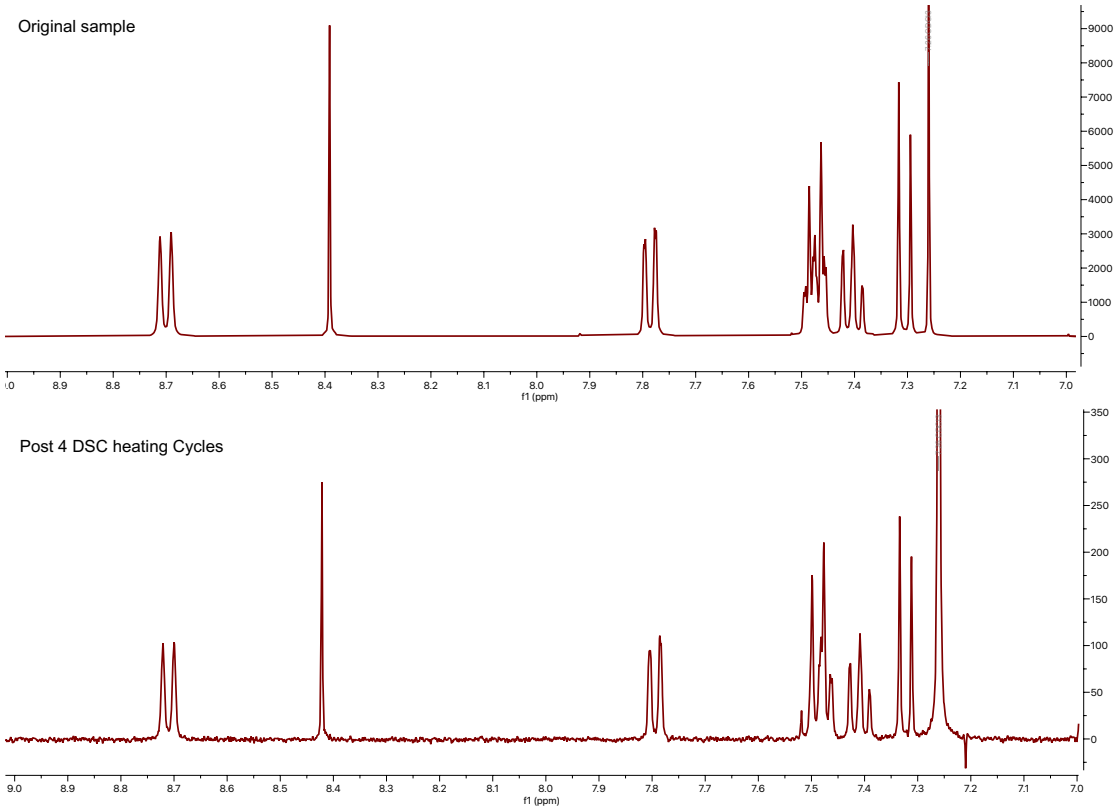


Figure 7-8 ^{1}H NMR spectra of compound 18 prior to DSC heating, and after 4 heating cycles. Note the lack of change in molecular structure, suggesting the presence of different polymorphs in the solid state.

Despite repeated heating and cooling the material was clearly the same molecule before and after, with no noticeable degradation, highlighting its superb thermal stability.

The monobenzocarbazole derivative of 4BDCzIPN (**19**), 4MBCzIPN (**20**) was heated 4 times *via* DSC and proton NMR spectra were recorded (see Figure 7-9).

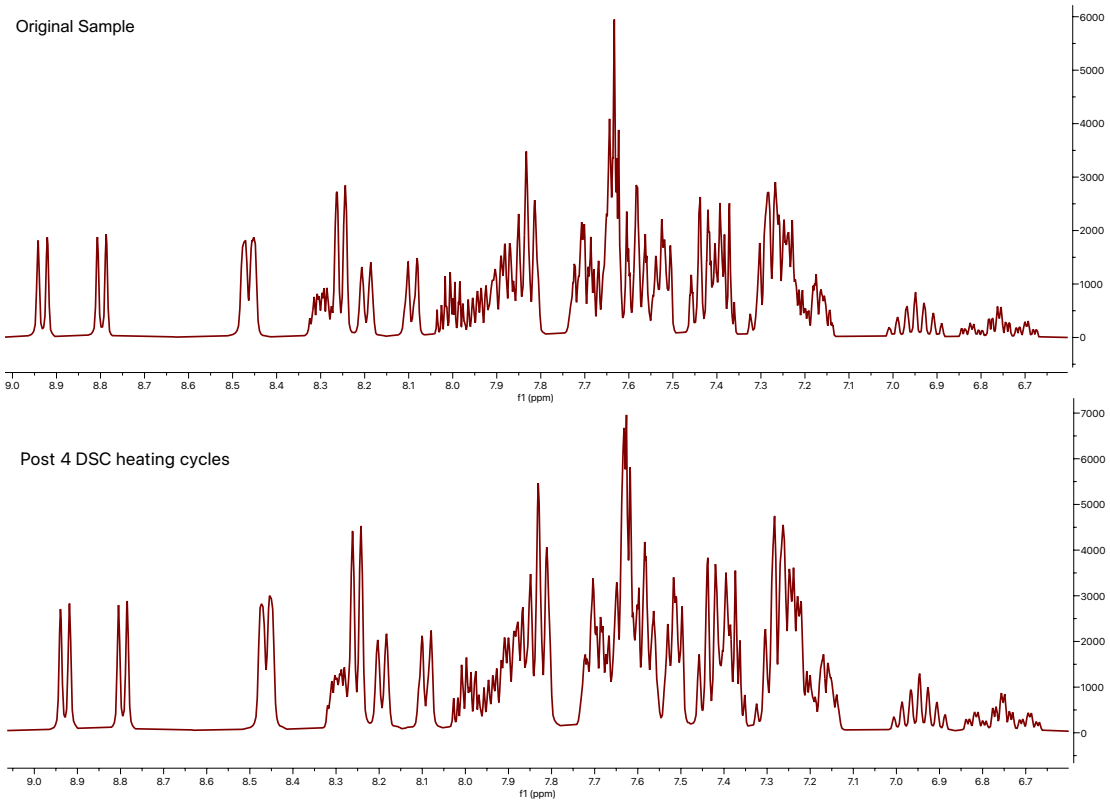


Figure 7-9 ^{1}H NMR spectra of compound 20 prior to DSC heating, and after 4 heating cycles. Note once again the lack of change in molecular structure, suggesting the presence of different polymorphs in the solid state.

Once again, despite the physical change, there is no chemical change occurring.

DBCz-PS (**21**) and DBCz-BZPN (**22**) also both exhibit excellent thermal stability, with 5% mass loss observed at 387°C and 408°C respectively.

A clear melting point occurs at 387°C for compound **21**. An additional peak at 126°C is also observed. This is unlikely to be a melting point, but like the other compounds in this family, potentially related to polymorphism. In repeated cycles removing thermal history, this peak moves to and remains at ~186°C. This is possibly a minor polymorph however, as a substantially larger endothermic peak is present at 270°C (which is explored further in section 7.3.12).

A potentially polymorphic transition peak is present in compound **22** as well at 258°C, shifting to 167- 176°C upon removal of thermal history.

7.3.2 Optical and electrochemical properties

The photophysics of all four compounds was studied extensively in the solid state and in solution. Compounds 2DBCzPN (**18**) and 4DBCzIPN (**19**) are yellow and red solids, respectively, with yellow and red fluorescence. They possess very broad emissions, even in non-polar solvents, and very strong solvatochromism. This suggests the presence of charge-transfer states, which is unsurprising owing to the carbazole-like nature of 7H-dibenzo[c,g]carbazole and the densely packed arrangement of donors in their structures (particularly compound **19**). Prompt emissions are enhanced in efficiency in degassed environments, suggesting triplet states are involved in the emissions process. The monobenzocarbazole derivative, 4MBCzIPN (**20**) demonstrates emissions significantly blue-shifted with much narrower FWHM and substantially increased PLQY owing to reduced degree of motion in the planar donor moieties. Both compounds **19** and **20** have significantly red-shifted emission onsets compared to their progenitor 4CzIPN which confirms that extending the conjugation of the carbazole-like donor moiety in this way leads to stronger electron donating character[360]. The key photophysical and electrochemical properties of the compounds in this study are summarised in Table 7-2 and Table 7-3, respectively.

Table 7-2 Summarised optical properties of compounds 19 – 22.

Molecule	λ_{abs} (nm)[a]	λ_{pl} (nm) [a]	FWHM (nm)	$E_{g\ opt}$* (eV)	Φ_{PL} [b]	S_1** (eV)	τ_p (ns)	τ_d (ns)
2DBCzPN (18)	361, 344, 300, 273, 226, 204, 395†, 329†, 288†, 267†, 250†, 240†	546	107	2.83	3.82 (Air) 10.07 (Ar)	2.60	7.33 (Air) 10.3 (Ar)	24.7 (Air) 33.8 (Ar)
4DBCzIPN (19)	358, 343, 301, 272, 238, 205, 448†, 397†, 328†, 290†, 265†. 225†	626	145	2.52	1.81 (Air) 4.37 (Ar)	2.38	8.35 (Air) 9.59 (Ar)	296 (Air) 2724 (Ar)
4MBCzIPN (20)	465(sh), 379(sh), 355, 322, 315, 287	520	94	2.56	24.1 (Air) 54.8 (Ar)	2.63	18.10 (Air) 25.08 (Ar)	299 (Air) 1554 (Ar)
DBCz-PS (21)	367, 349, 333, 303, 282	442	92	3.27	7.03 (Air) 23.3 (Ar)	3.32	7.45 (Air) 8.98 (Ar)	14.5 (Air) 62.6 (Ar)
DBCz-BZPN (22)	366, 349, 335(sh), 304, 282	491 390 373	86	3.14	2.64 (Air) 3.48 (Ar)	3.01 3.43 (LE)	3.83 (Air) 4.33 (Ar)	8.55 (Air) 9.82 (Ar)

[a] Measured in methylcyclohexane for compounds **18**, **19** and **20**, toluene for compounds **21** and **22** owing to poor solubility, [b] measured in toluene, *Taken from onset of main λ_{abs} peak in methylcyclohexane or toluene for compounds **21** and **22** (in brackets from most intense peak), **Taken from onset of λ_{PL} peak in methylcyclohexane, † from CT shoulder, [z] zeonex host, [m] mCBP host

Table 7-3 Summarised electrochemical properties of compounds 19 – 22 from CV measurements performed in acetonitrile.

Molecule	E_{ox} (V)	E_{red} (V)	HOMO (eV)	LUMO (eV)	$E_{g\ chem}$ (eV)
2DBCzPN (18)	0.84	-1.65	-5.64	-3.15	2.49
4DBCzIPN (19)	0.75	-1.41	-5.55	-3.39	2.16
4MBCzIPN (20)	1.11	-1.42	-5.91	-3.39	2.52
DBCz-PS (21)	0.97	-1.34	-5.77	-3.46	2.31
DBCz-BZPN (22)	0.85	-1.26	-5.65	-3.54	2.11

Compounds DBCz-PS (**21**) and DBCz-BZPN (**22**) are white powders with bright blue fluorescence – a significant difference to compounds **18** – **20**. This is also reflected in their solution and thin film measurements.

The donors and acceptors for each target compound were dissolved in dry toluene and the UV-vis absorption spectra recorded for each in order to compare to the products' absorption profiles, which can be seen in Figure 7-10.

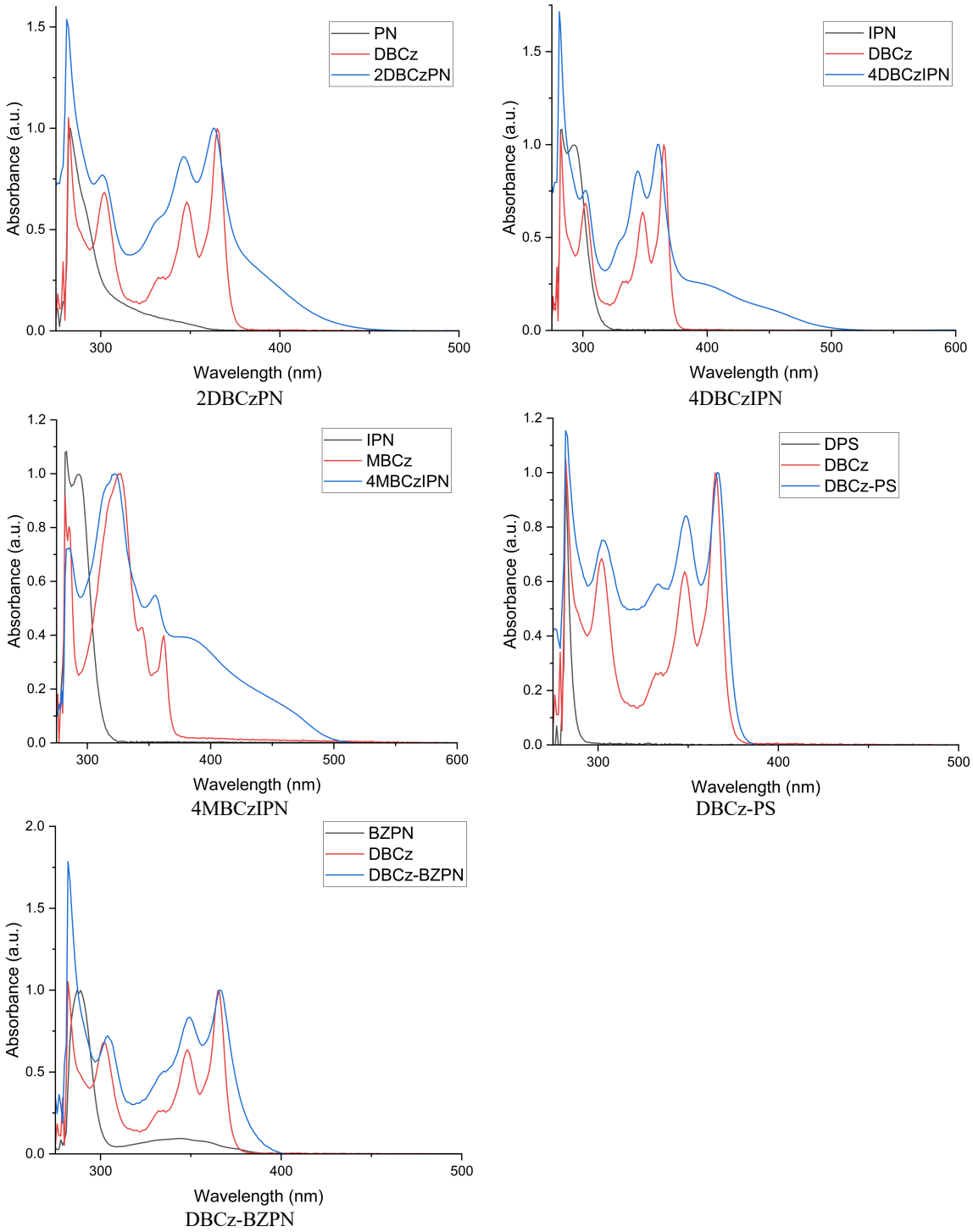


Figure 7-10 UV-vis absorption spectra for the products and their constituent donor and acceptor molecules dissolved in toluene.

All the compounds using dibenzocarbazole as the donor exhibit strikingly accurate superimposition of the UV-vis absorption spectra of the donor onto the UV-vis absorption spectra of the corresponding target compounds. This suggests very good separation of the HOMO, with this preserved in each molecule regardless of the attached acceptor moiety. Very slight blue-shifting (~1-2 nm) is observed for compound **18**, **21** and **22** with this extending to ~5 nm for compound **19**.

Table 7-4 Summary of the UV-vis absorption spectra of free donors and acceptors in dry toluene compared with the spectra of the target compounds.

Molecule	Acceptor λ_{abs} (nm)	Donor λ_{abs} (nm)	Product λ_{abs} (nm)
2DBCzPN (18)	283, 292(sh)	365, 348, 333, 302, 282	363, 346, 333(sh), 301, 290(sh), 281, 393(CT)
4DBCzIPN (19)	293, 283	365, 348, 333, 302, 282	360, 344, 330(sh), 302, 281 450(CT), 393(CT)
4MBCzIPN (20)	293, 283	362, 355, 344, 326, 285, 282	355, 322, 284, 453(CT), 379(CT)
DBCz-PS (21)	282	365, 348, 333, 302, 282	367,349, 333, 303, 282
DBCz-BZPN (22)	344(broad), 288	365, 348, 333, 302, 282	366, 349, 334, 304, 288(sh), 282

It is difficult to accurately determine whether the shortest wavelength peak in each case comes from the donor or acceptor, since they all have a distinct peak at 283 nm, however the presence of the 293 nm shoulder or second peak in PN, IPN and PS is potentially visible as a subtle broadening of the shortest wavelength peak in all cases (see Table 7-4 for a summary of the donor, acceptor and product UV-vis absorption properties). As such, the donor and acceptor's corresponding HOMO and LUMO appear to possess good separation, as the twisted dihedrals in the DFT and single crystal XRD supports in sections 7.3.11 and 7.3.12. The strong localisation of the HOMO upon dibenzocarbazole could be a strong contributor to the separation as the DFT calculations reveal it does not spread onto the acceptor at all. The broad charge-transfer bands in 2DBCzPN, 4DBCzIPN and DBCz-PS further support the presence of good HOMO and LUMO separation.

With the monobenzocarbazole compound, 4MBCzIPN (**20**), the acceptor peak at 288 nm aligns (albeit as a shoulder in the product molecule), but the donor moiety peaks seem to differ quite considerably in intensity, however the alignment of the 355 nm peaks are in good agreement, and the donor's 326 and 285 nm peaks are comparable to the product's 322 nm and 284 nm peaks. This is accompanied by a very broad CT shoulders at 379 nm and 453 nm, supporting good HOMO and LUMO separation.

7.3.3 Solid-state photophysics

Three host matrices were selected owing to their differing polarity. Zeonex, being non-polar, and yielding dopant spectra similar to those observed in methylcyclohexane[300], mCP (being weakly polar but a compatible host for devices[361–363]) and DPEPO[364,365] (being a both polar and a well-established EML host for devices).

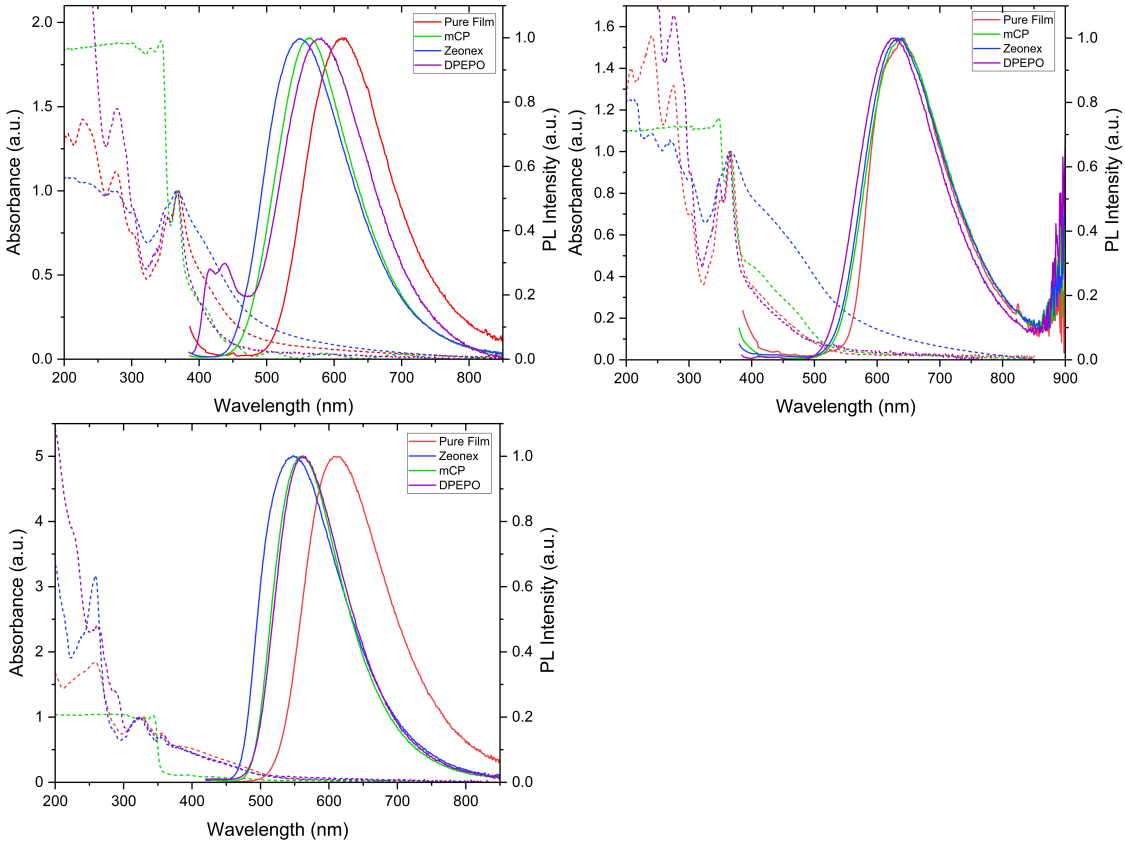


Figure 7-11 Solid-state PL and UV-vis absorption plots of compounds 18 (left), 19 (right) and 20 (bottom). Excited at 366 nm, 360 nm and 355 nm, respectively.

Pure films and doped films of compounds **18**, **19** and **20** were prepared *via* drop-casting from toluene solution and the photoluminescence and UV-vis absorption data are shown in Figure 7-11.

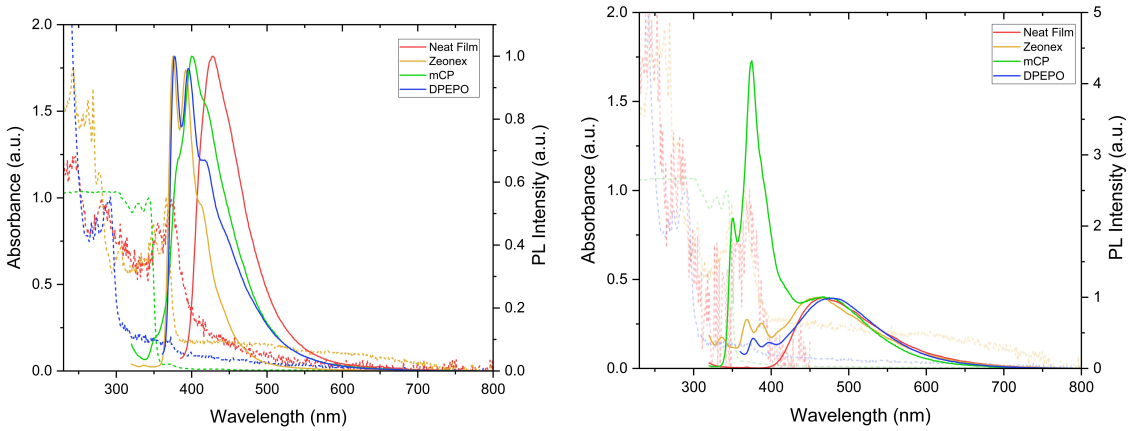


Figure 7-12 Solid-state PL and UV-vis absorption plots of compounds 21 (left) and 22 (right), excited at 329 nm. Note the absorbance spectra for compound 22 has been rendered transparent so as to make the PL spectra visible owing to significant scattering as a result of very poor solubility yielding poor quality thin films.

Thin films of compounds **21** and **22** were prepared in various hosts and as pure films using the same approach as for the other two compounds and the photoluminescence and UV-vis absorption spectra are shown above in Figure 7-12. Unfortunately, these two molecules have significantly poor solubility in most solvents and the UV-vis absorption spectra are particularly poor owing to scattering effects (most prominently in compound **22**). The photoluminescence properties of the five molecules are outlined in Table 7-5.

Table 7-5 PL and UV-vis absorption properties of compounds 18 - 22 in thin films.

Molecule	Host	λ_{abs} (nm)	λ_{pl} (nm)	FWHM (nm)	S_1^* (eV)
2DBCzPN (18)	Pure film	450sh, **370(main)**, 354sh, 300sh, 276, 288, 206	612	145	2.45
	mCP	442 sh, **367(main)**, 343,	564	134	2.66
	Zeonex	412sh, **368(main)**, 352sh, 302, 275	549	145	2.75
	DPEPO	367, 351, 300(sh), 278, 222(sh)	578, (438, 416)	129	2.61 (3.12)
4DBCzIPN (19)	Pure film	450sh, **367(main)**, 351, 303sh, 275, 241, 208	642 618sh	142	2.27
	mCP	456sh, 408sh, **365(main)**, 347	639	153	2.35
	Zeonex	450sh, 406sh, **366nm(main)**, 351sh, 304, 270, 240	633	155	2.28
	DPEPO	364, 348, 302(sh), 289(sh), 276	626	151	2.37
4MBCzIPN (20)	Pure film	355, 326, 258, 465(CT), 385(CT)	611	142	2.38
	mCP	474(CT), 426(CT), 390(CT), 343(max), 328	560	118	2.54
	Zeonex	355, 322, 258, 381(CT), 440(CT)	548	139	2.64
	DPEPO	357, 325, 286(sh), 262, 380(CT), 440(CT)	562	120	2.52
DBCz-PS (21)	Pure film	373, 355, 282, 244	428	66	3.15
	mCP	343, 368 (CT), 328	400, 353sh, 382sh, 414sh	74	3.50
	Zeonex	366, 349, 306, 278, 269, 242	375, 392, 412sh	47	3.42
	DPEPO	369, 310, 290	377 396 415sh 442sh	62	3.38
DBCz-BZPN (22)	Pure film	371, 280, 242	466, 366	114	3.03
	mCP	342, 328, 368 (CT)	467, 391sh, 375, 350	34 (blue peak normalised), 190 (green peak normalised)	3.65, 3.58
	Zeonex	365, 345, 305, 262, 242	458, 412sh, 387, 369, 356	157	3.20 / 3.50 Main / minor
	DPEPO	371, 290, 274, 266	478 (397) (377)	123	3.20

(sh) refers to shoulder of peaks; *Taken from onset of λ_{PL} peak

Table 7-6 PLQYs of compounds 18 - 22 in the solid state.

Molecule	Host	Φ_{PL} (air)	Φ_{PL} (argon)
2DBCzPN (18)	Pure film	3.3	4.0
	mCP	17.6	36.2
	Zeonex	6.4	8.7
	DPEPO	4.3	7.9
4DBCzIPN (19)	Pure film	3.9	5.5
	mCP	10.3	10.9
	Zeonex	2.7	7.2
	DPEPO	3.6	8.1
4MBCzIPN (20)	Pure film	6.7	10
	mCP	59	90
	Zeonex	31	58
	DPEPO	40	47
DBCz-PS (21)	Pure film	9.5	9.1
	mCP	36	30.9
	Zeonex	38	30.7
	DPEPO	15.5	21.3
DBCz-BZPN (22)	Pure film	2.6	3.4
	mCP	26	13.6
	Zeonex	1.3	2.7
	DPEPO	6.0	7.2

Table 7-6 shows that the PLQYs increase in the solid state in most cases, suggesting the potential for aggregation effects. Interestingly, comparing the monobenzocarbazole and dibenzocarbazole derivatives, 4MBCzIPN (**20**) and 4DBCzIPN (**19**), a significant jump in PLQY is observed going from dibenzocarbazole to monobenzocarbazole. This is likely owing to the lack of lossy non-radiative pathways caused by potential flapping motions from the dibenzocarbazole moieties.

7.3.4 TCSPC Lifetime measurements

Time correlated single photon counting spectroscopy (TCSPC) measurements were performed for all five compounds in toluene and in various host matrices to explore the lifetimes of the emissions.

7.3.4.1 Lifetimes in solution

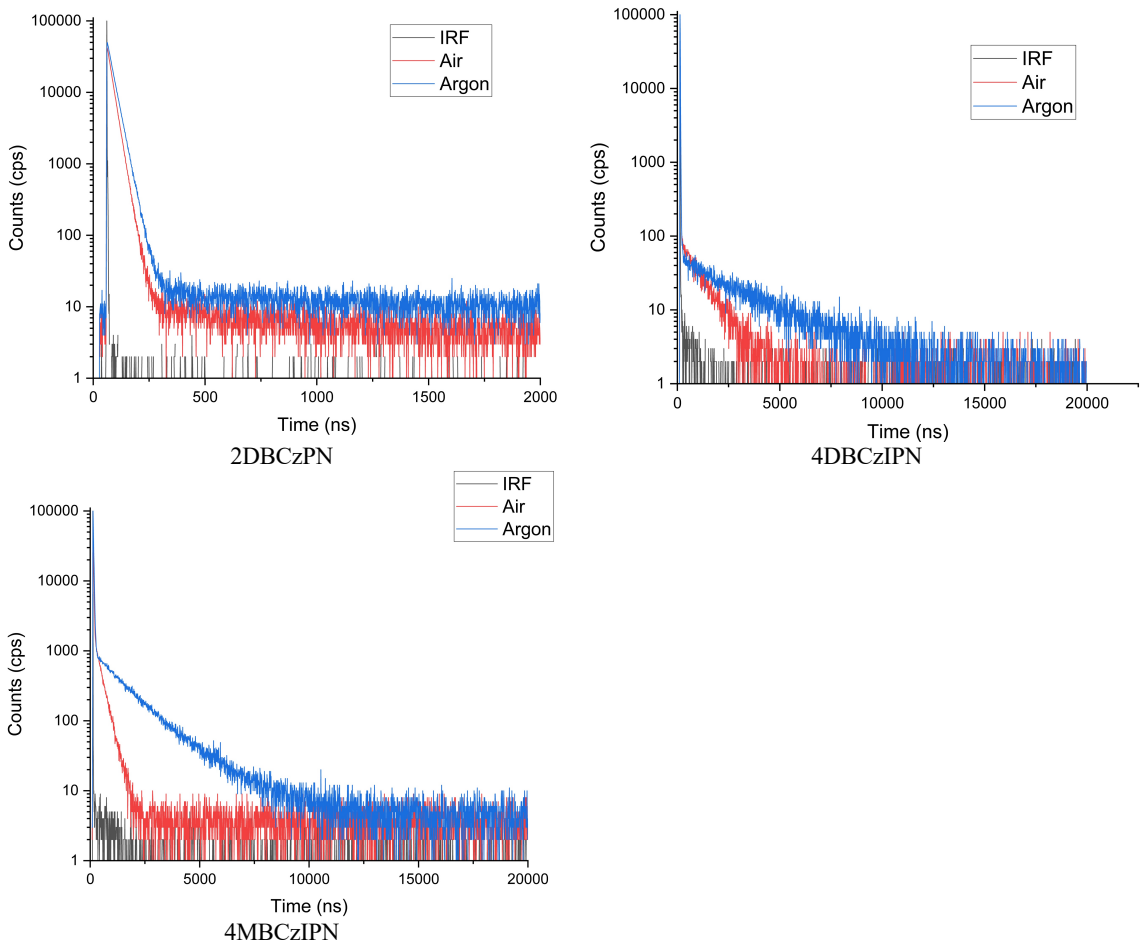


Figure 7-13 TCSPC plots of compounds 18, 19 and 20 in toluene solution, under oxygen and degassed with argon for 20 minutes. Compound 18 is excited with a 365 nm laser, close to its main excitation peak, whereas compounds 19 and 20 were excited at 450 nm, at their CT peak.

As with their well-studied TADF progenitor, 4CzIPN, compounds **19** and **20** both exhibit pronounced elongated lifetimes when degassed in toluene, suggesting the potentially for rISC to be occurring (see Figure 7-13). This is significantly less so for compound **18.**

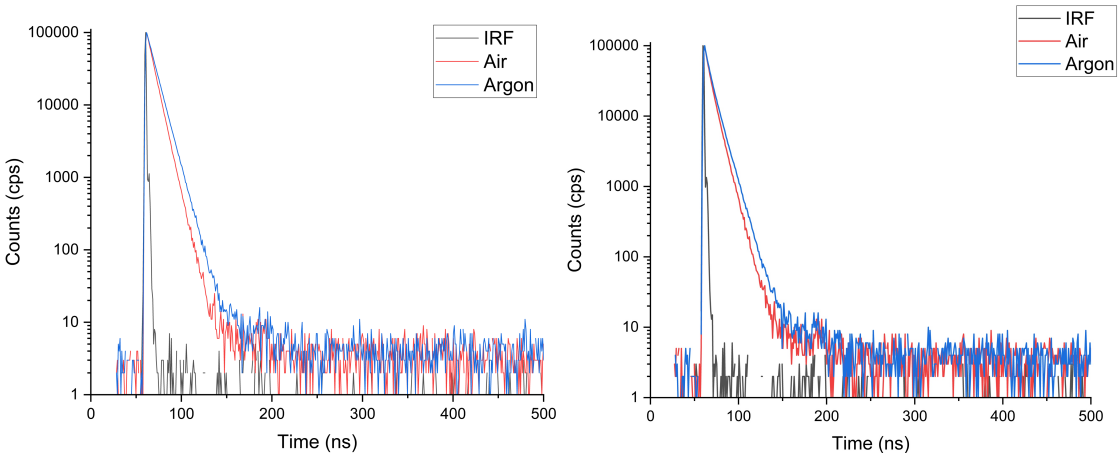


Figure 7-14 TCSPC plots of compounds 21 (left) and 22 (right) in toluene solution, under oxygen and degassed with argon for 20 minutes.

Much shorter lifetimes for compounds **21** and **22** are observed (see Figure 7-14). Compound **21** increases its delayed component in toluene from 14.5 ns to 62.7 ns when degassed. This is similar to observations made with its progenitor Cz-PS, which although a fairly prompt emitter, still possesses TADF[337]. Compound **22** has much prompter emissions in solution however, only increasing by 1.3 ns when degassed in toluene.

7.3.4.2 Lifetimes in the solid state

Solid-state thin films were prepared from 5% w.t. toluene solutions. Compound **18** shows a slight delayed component to its emissions (up to 96 ns), with the formation of exciplexes with mCP obvious by its extended lifetime. Compound **19** on the other hand shows long lived delayed emissions, up to 5 µs in our TCSPC studies. TCSPC plots for compounds **18** and **19** in variety of host matrices are shown in Figure 7-15 and compound **20** in Figure 7-16.

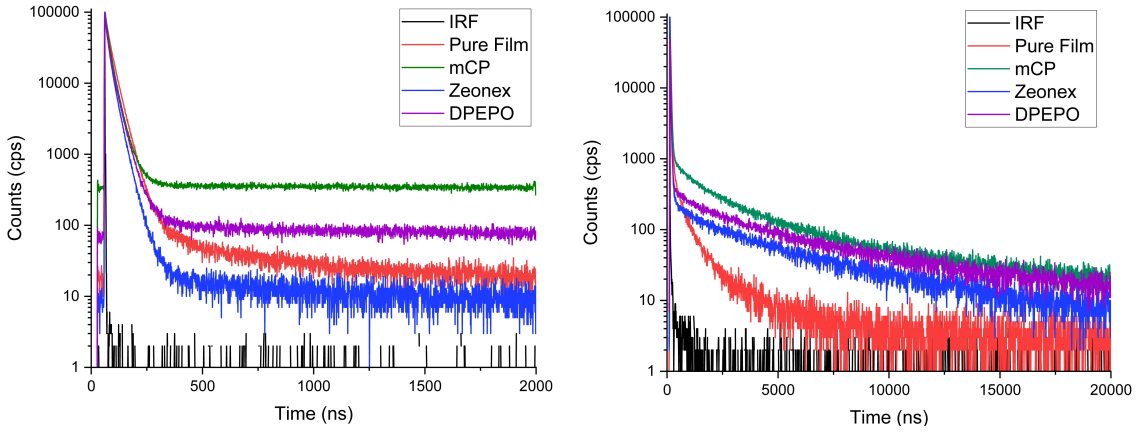


Figure 7-15 TCSPC plots of compounds 18 (left) and 19 (right) from thin films. Both excited at 365 nm.

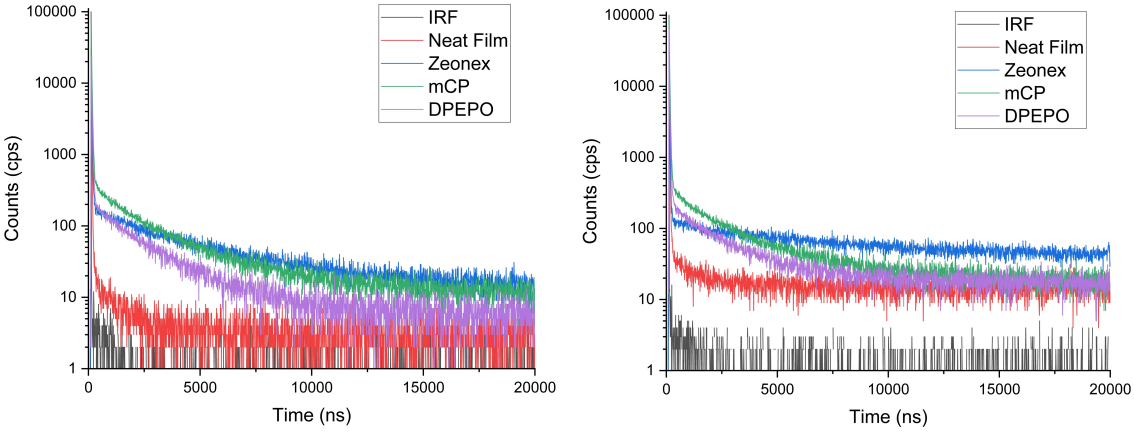


Figure 7-16 TCSPC plots of compound 20 in air (left) and argon (right) from thin films. All excited at 365 nm. Our method of inert measurements was designed after all other molecules in this study were measured, and the CCD method from the University of Durham was used instead.

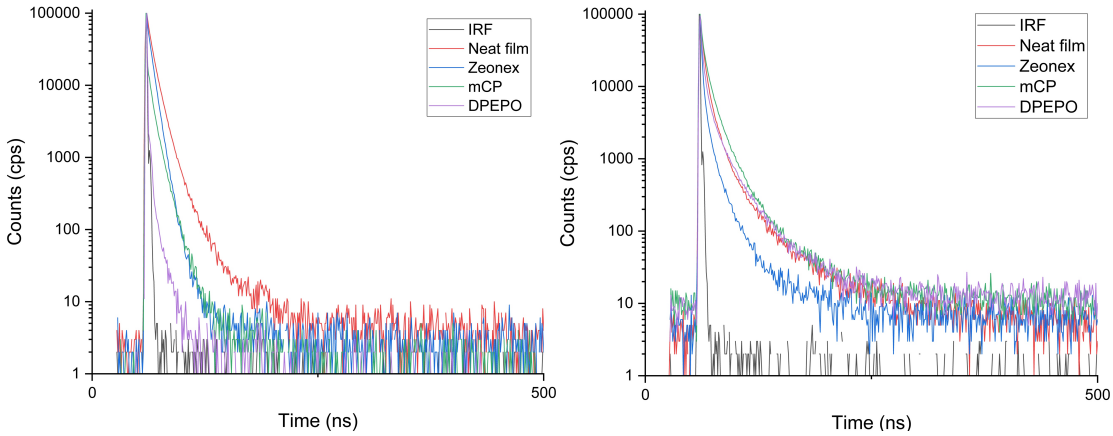


Figure 7-17 TCSPC plots of compounds 21 (left) and 22 (right) from thin films. Both excited at 365 nm and viewing the main emission peaks.

The solid-state TCSPC decays for compounds **21** and **22** (see Figure 7-17) are fairly prompt, but the delayed components of compound **22** are nearly double those of compound **21**, regardless of host media.

The fitted prompt and delayed lifetimes for all of the compounds in this study in both air-exposed and degassed toluene, as well as thin films (neat and in host matrices), are summarised in Table 7-7.

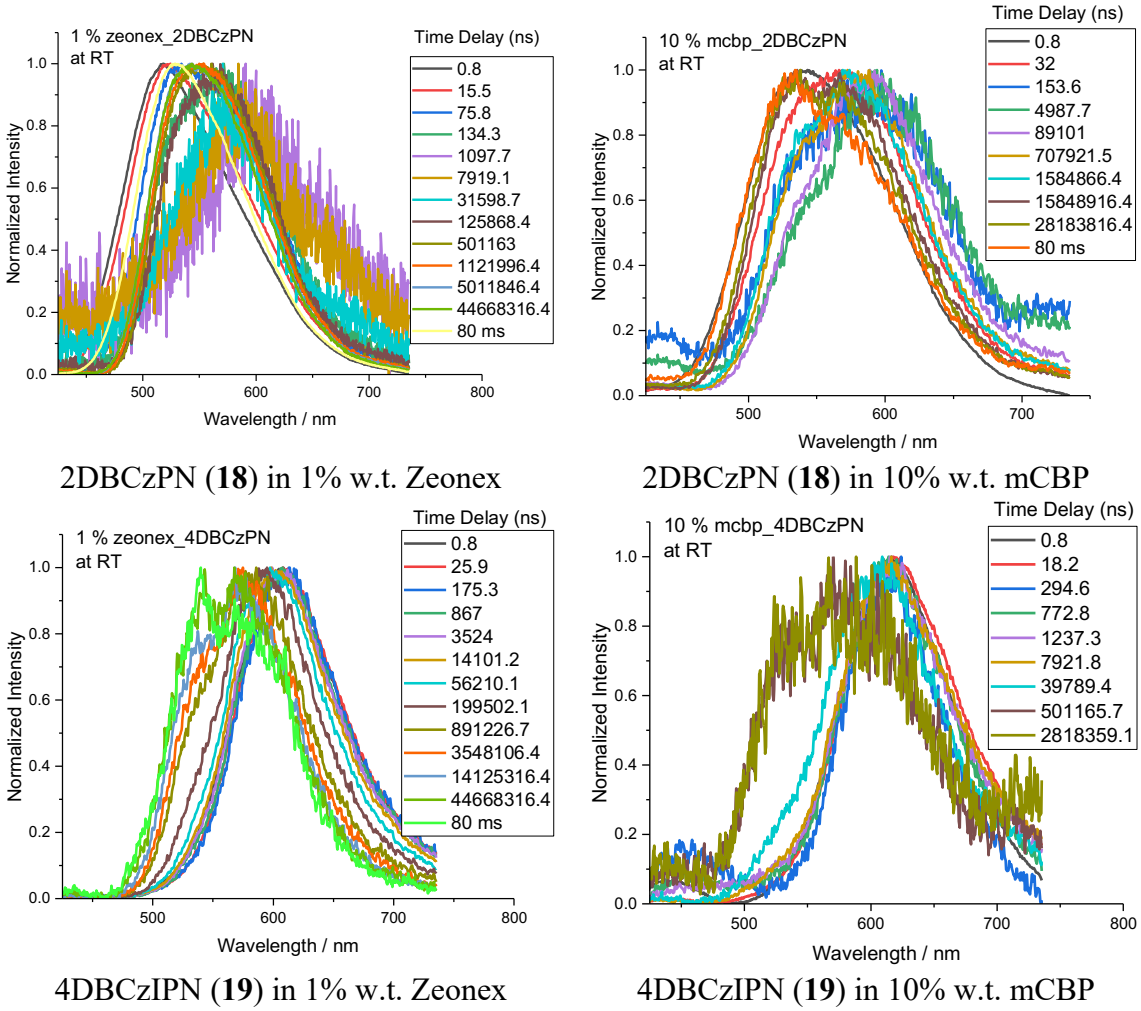
Table 7-7 Summary of the lifetime measurements prompt and delayed components from TCSPC measurements for compounds 18 - 22.

Molecule	Sample	τ_p (ns)	τ_d (ns)
2DBCzPN (18)	Toluene (air)	5.43	22.37
	Toluene (degassed)	2.49	48.19
	Pure film	26.54	96.06
	mCP	26.82	565600
	Zeonex	14.25	40.64
	DPEPO	11.80	34.38
4DBCzPN (19)	Toluene (air)	8.86	529.87
	Toluene (degassed)	9.45	2277.2
	Pure film	31.37	938.5
	mCP	34.66	5019.9
	Zeonex	31.07	3607.3
	DPEPO	27.31	4978.5
4MBCzIPN (20)	Toluene (air)	18.10	298.92
	Toluene (degassed)	25.08	1553.7
	Pure film	16.64	1102.7
	mCP	25.41	2419.6
	Zeonex	22.69	6259.7
	DPEPO	28.05	1989.10
DBCz-PS (21)	Toluene (air)	7.45	14.54
	Toluene (degassed)	8.98	62.65
	Pure film	3.36	8.91
	mCP	3.64	9.14
	Zeonex	3.77	6.22
	DPEPO	1.55	8.69
DBCz-BZPN (22)	Toluene (air)	3.83	8.55
	Toluene (degassed)	4.33	9.82
	Pure film	4.28	19.04
	mCP	3.51	14.24
	Zeonex	1.90	10.91
	DPEPO	3.64	15.54

From this, we can conclude that, whilst dibenzocarbazole is a poor donor match for diphenyl sulfone and dibenzophenone acceptors when looking for TADF, there is a clear delayed component associated with the dicyanobenzene acceptors when paired to dibenzo and monobenzocarbazole donors.

7.3.5 CCD time-resolved measurements

Using Durham University's ultrafast time dependent PL spectrometer, more detail of the delayed components of the two cycanobenzene molecules can be observed.



2DBCzPN (**18**) in 1% w.t. Zeonex

2DBCzPN (**18**) in 10% w.t. mCBP

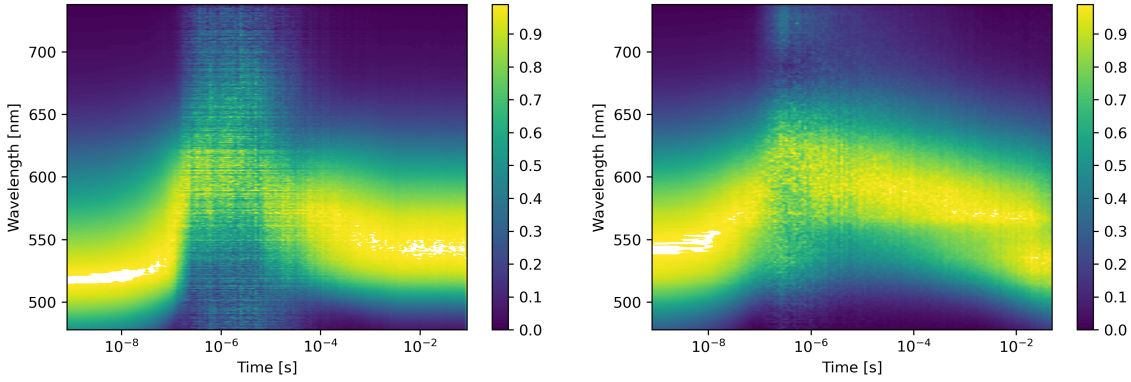
4DBCzIPN (**19**) in 1% w.t. Zeonex

4DBCzIPN (**19**) in 10% w.t. mCBP

Figure 7-18 Time-resolved spectra of compounds 18 (top) and 19 (bottom) in Zeonex (left) and mCBP (right).

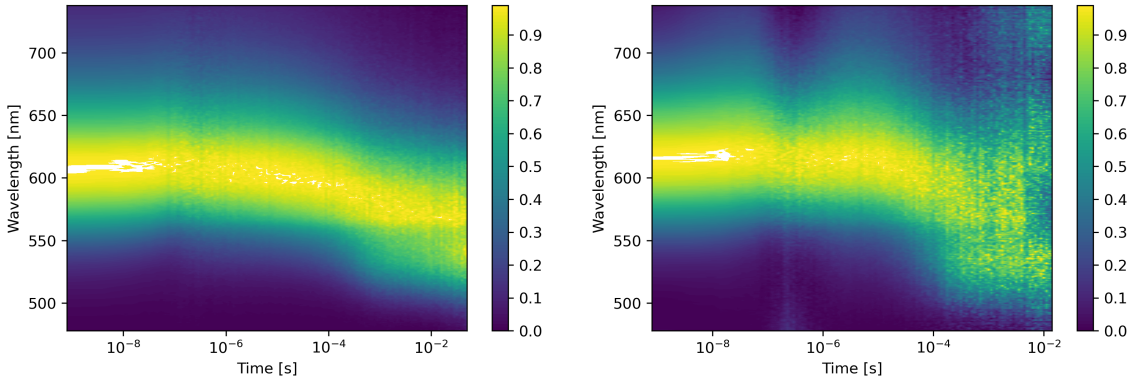
In Zeonex, compound **18**'s prompt emission occurs at 518 nm. By 1 ms, this shifts to 597 nm, returning to 529 nm by 89 ms. A similar shifting is observed in the more polar host, mCBP. In this host, compound **18** exhibits an initial emission wavelength of 542 nm, with a transition to 594 nm by 5 ms, with a gradual shift back to 532 nm by 80 ms.

For compound **19**, prompt emissions were observed in Zeonex at 607 nm, followed by a shift to 653 nm by 50 ms. In the more polar host, mCBP, prompt emission is observed at 616 nm before shifting only very slightly to 588 nm, with a large shoulder at 540 nm by 28 ms.



1 % w.t. Zeonex 10 % mCBP

Figure 7-19 Contour plots of 2DBCzPN (18) doped thin films.



1 % w.t. Zeonex 10 % mCBP

Figure 7-20 Contour plots of 4DBCzIPN (19) doped thin films.

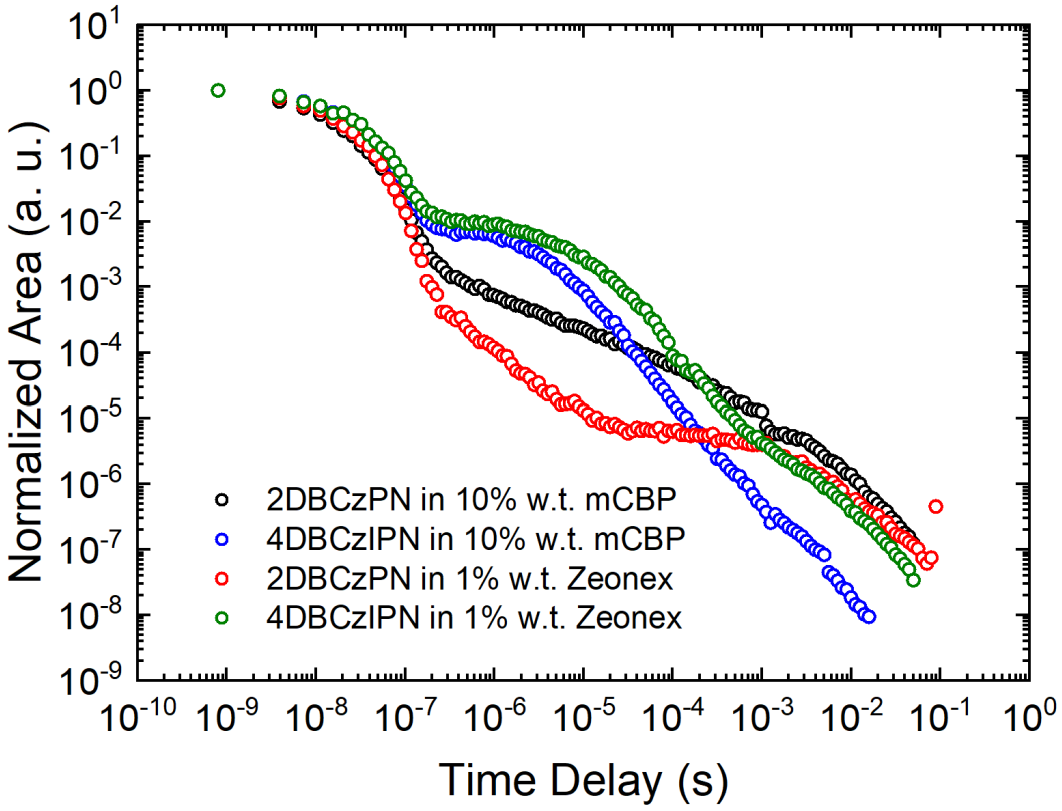


Figure 7-21 Photoluminescence decay of 2DBCzPN (18) and 4DBCzIPN (19) in 1% w.t. Zeonex and 10% w.t. mCBP.

Both compounds clearly have delayed fluorescence (observed by the second curve in each transient decay plot in Figure 7-21 and summarised in Table 7-8), reaching 21.4 ms in Zeonex and 13.6 ms in mCBP for compound **18**, and extending to 71.4 ms and 14.9 ms in Zeonex and mCBP for compound **19**. However, further low temperature time-resolved measurements should be performed prior to publication to completely isolate $T_1 - S_0$ decay to confirm.

Table 7-8 Summary of time-resolved PL of compounds 18 and 19 from mono-, bi-, or tri-exponential fittings.

	Host	τ_{PF} (av) (ns)	τ_{DF} (av) (µs)
2DBCzPN (18)	Zeonex	22.15	21351
	mCBP	20.82	13653
4DBCzIPN (19)	Zeonex	31.2	71364
	mCBP	31.2	14889

Table 7-9 Summary of photophysical rate constants calculated from fittings of time-dependent photoluminescence decays from Zeonex host matrices using a method outlined by Dias *et al.*[173]

	k_F (s^{-1})	k_{ISC} (s^{-1})	k_{rISC} (s^{-1})
2DBCzPN (18)	2.89×10^6	1.19×10^7	6.37×10^1
4DBCzIPN (19)	8.65×10^5	2.00×10^7	3.74×10^1

Using the onset of the prompt decays and delayed emission under vacuum, it is possible to use the time-dependent camera spectra to determine the S_1 and T_1 energies, and hence ΔE_{ST} for the two materials studied in host matrices. The resulting values are shown in Table 7-10.

Table 7-10 Excited state energies calculated from prompt and delayed emissions for compounds 18 and 19 in Zeonex and mCBP hosts.

Sample and host	S_1 (eV)	T_1 (eV)	ΔE_{ST} (eV)
2DBCzPN (18) Zeonex	2.81	2.61	0.2
2DBCzPN (18) mCBP	2.72	2.57	0.15
4DBCzIPN (19) Zeonex	2.38	2.59	-0.21
4DBCzIPN (19) mCBP	2.34	2.60	-0.26

Interestingly, the ΔE_{ST} is quite wide for both molecules, so if emissions are indeed TADF, it will be relatively poor by modern standards, especially so in Zeonex based on the disappointingly slow calculated rISC rates in Table 7-9.

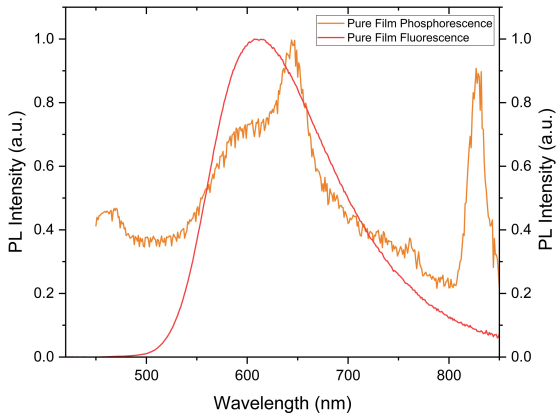
Strangely, owing to the blue-shifted delayed emissions relative to the prompt decay, compound **19** appears to possess a negative ΔE_{ST} in both polar and non-polar host matrices. This implies its triplet state is higher in energy than the emissive singlet state.

One potential explanation would be that there is in fact only room temperature phosphorescence occurring – from a higher energy triplet state as time goes by. The measurements were performed by our colleagues in Durham shortly before the post-doc assigned to the project there leaving the research group, so further measurements were not performed. Further studies at low temperature (80 K) will deactivate any delayed emission from the singlet state, thereby permitting only $T_1 \rightarrow S_0$ decay. If there is no change in the observed emission lifetimes and delayed wavelengths, then RTP can be confirmed, rationalising the seemingly larger ΔE_{ST} (being from two separate decay pathways, and not involving rISC).

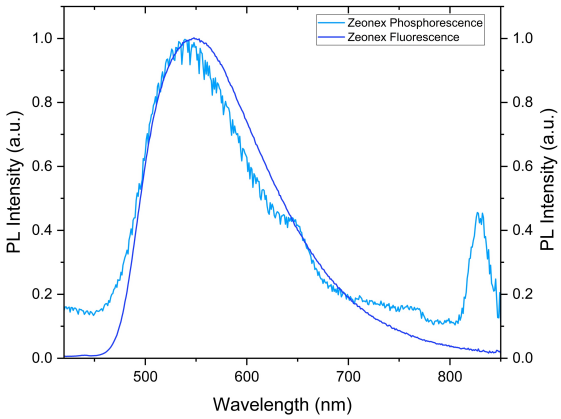
Overall, taking into consideration both the UV-vis absorption and PL emission data of the three compounds, they possess CT absorption bands, with broad, solvent sensitive emission peaks, also characteristic of being CT in nature. Their prompt and delayed emission components in the photoluminescence decay are in-line with those typically observed with TADF emitters[366], as well as their PLQY sensitivity to oxygen. Whilst their significant thermal stability makes them ideal for vapour deposition in OLEDs, the low PLQYs of compounds **18** and **19** (and as explored in section 7.4, their thermochromism also), make them poorly suited to device applications. Compound **20** on the other hand has far greater PLQYs in both solution and in the solid state, meaning its application to red-emitting OLEDs may yet prove attractive (if further photophysics in Durham is promising).

7.3.6 Room temperature phosphorescence of 4MBCzIPN (20)

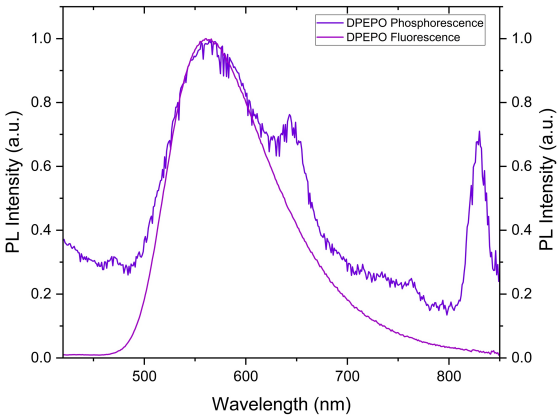
A crude methodology was adopted for performing delayed PL emission measurements on compound **20** (the compound synthesised most recently at the end of this PhD since there was not enough time to obtain results for this compound from our collaborators at Durham University). This involves supporting a quartz substrate coated with the analyte, on top of another blank quartz substrate held inside a quartz cuvette. Due to the diameters of the substrates, these fit perfectly in standard 10 mm cuvettes used in our spectrometer, and the analyte substrate is perfectly held indirect line of the *excitation* source and detector. A rubber septum is stretched over the top of the cuvette and the atmosphere in the cuvette purged five times by means of a standard argon – vacuum Schlenk setup. An argon filled balloon connected to a needle was inserted into the septum, replacing the Schlenk line, and the setup transferred into the spectrometer. Using the 250 blaze flash bulb the spectrometer is equipped with, the samples were excited and measurements performed after a 20 µs delay for a 20 µs period (*i.e.* from 20 µs after excitation until 40 µs).



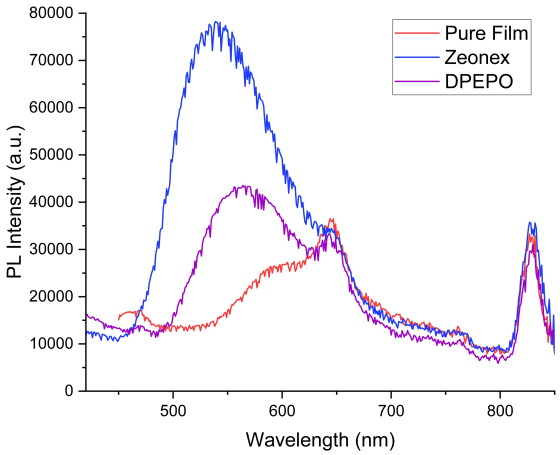
Pure film prompt and delayed components



Zeonex film prompt and delayed components



DPEPO film prompt and delayed components



Delayed emission for all three thin films

Figure 7-22 Comparing prompt and delayed emissions from compound 20 in neat thin films, and in films with Zeonex and DPEPO. Delayed emissions recorded using 355 nm flash bulb.

After 20 μs, the main emission comes from the same source as the prompt emission. However, by this time an additional peak can be seen in the pure film and DPEPO at 644 nm. This peak is present as a shoulder in the Zeonex sample, suggesting it is stabilised by more a more polar host matrix, and that the polarity of compound **20** is sufficiently strong enough that it is emitting here in the neat film too.

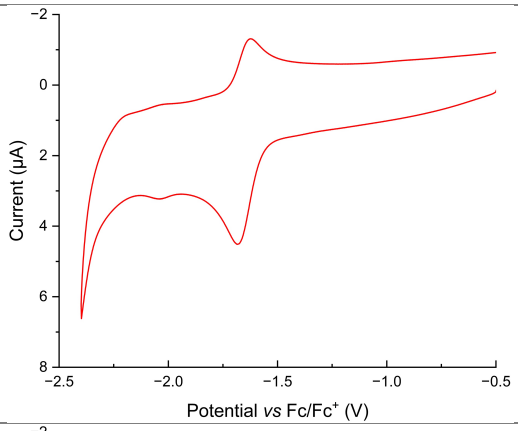
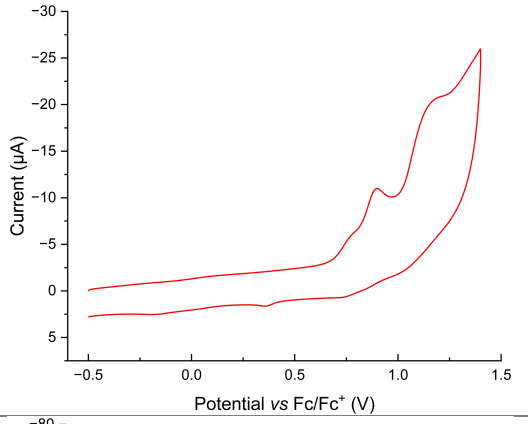
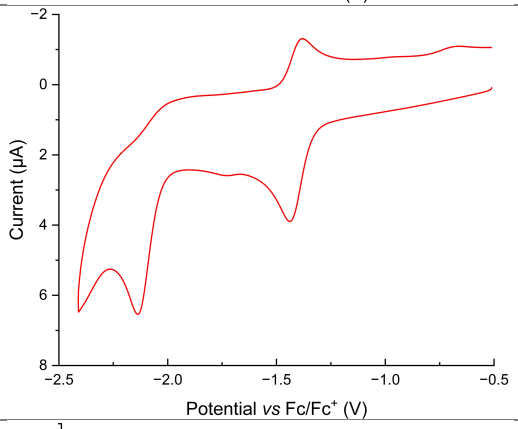
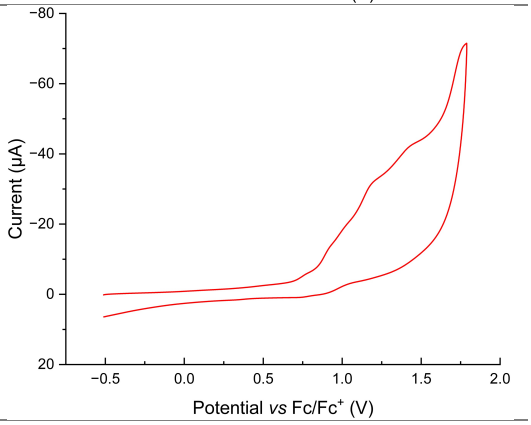
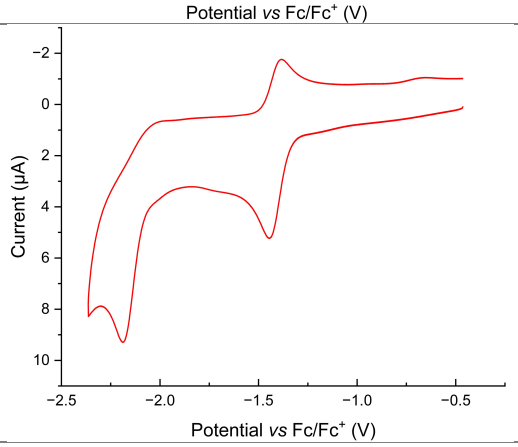
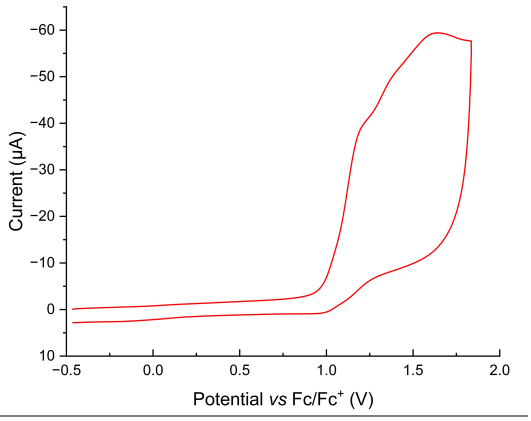
Table 7-11 Summary of the thin film delayed emissions compared to fluorescence. Fluorescence data is reproduced from Table 7-4.

Sample	Fluorescence (nm)	Fluorescence FWHM (nm)	Delayed PL (nm)	Delayed PL FWHM (nm)
Pure film	611	142	615, 644, 826	156
Zeonex	548	139	539, 644(sh), 829	128
DPEPO	562	120	564, 644, 828	169

Since the peak at 826 – 829 nm is not a multiple of the excitation wavelength (355 nm) it is safe to assume that this is not a result of harmonics and is genuinely being emitted by the samples. Its intensity is independent of the host (as seen in Figure 7-22), suggesting that the emission is from a locally excited state, unaffected by polarity. Its absence in the prompt emissions shows that this is the result of deep-red room temperature phosphorescence in compound **20** from a ^{3}LE state.

7.3.7 Electrochemical properties

To explore the electrochemical properties of the compounds in this study, cyclic voltammetry was performed. All five compounds exhibited reversible oxidation waves with irreversible oxidation waves.

Molecule	Reduction	Oxidation
2DBCzPN (18)		
4DBCzIPN (19)		
4MBCzIPN (20)		

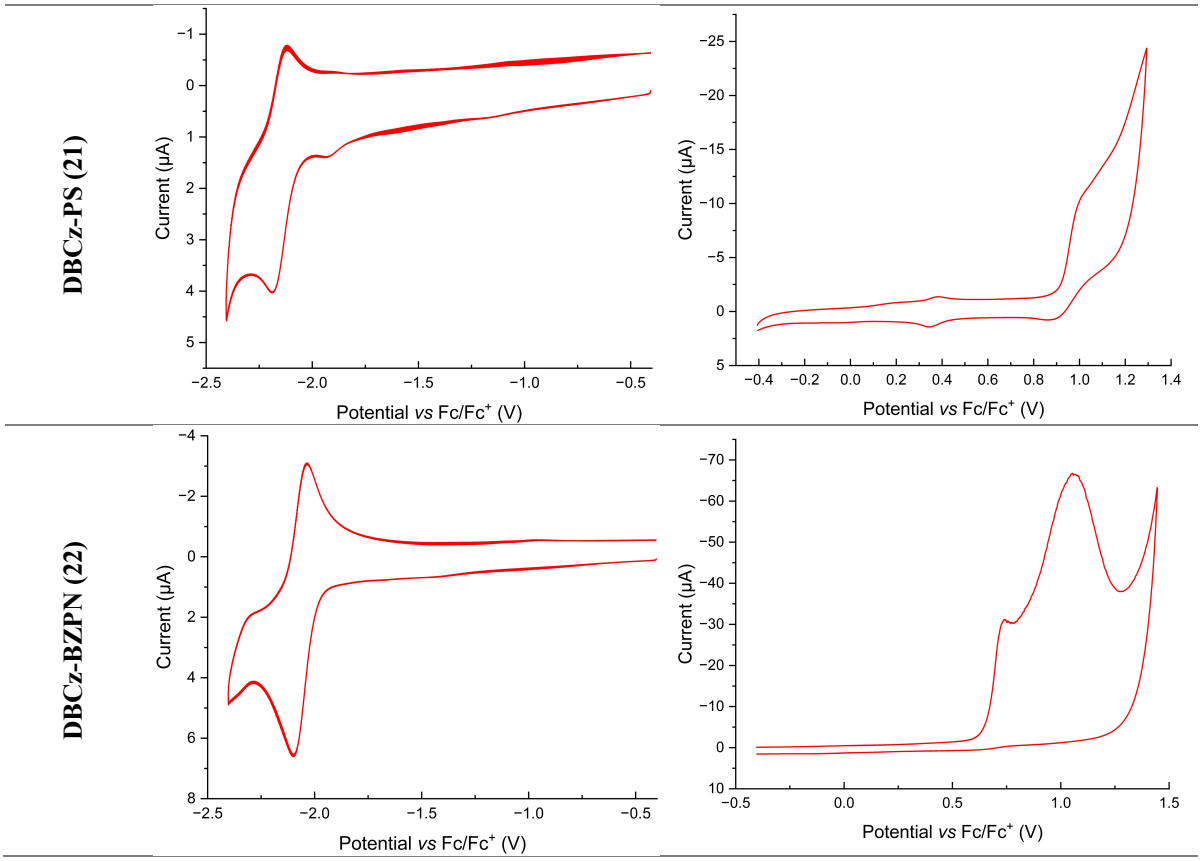


Figure 7-23 Cyclic voltammograms of compounds 18 to 22. Compounds 18 – 20 were measured in dry acetonitrile, and compounds 21 and 22 were measured in dry THF, owing to poor solubility. All were referenced against the $E_{1/2}$ of the Fc/Fc^+ redox couple in ~1 x 10^{-4} M solutions in 0.1 M tetrabutylammonium hexafluorophosphate.

Cyclic voltammetry of the five compounds reveals that the extra dibenzo-carbazole groups bonded to a dicyanobenzene acceptor core narrows the HOMO-LUMO energy gap by raising the HOMO energy slightly by 0.09 eV, whilst also deepening the LUMO by 0.24 eV, which narrows the energy gap by 0.33 eV.

Swapping the acceptor core for diphenyl sulfone and benzophenone results in a deepening of the HOMO by 0.13 eV in the case of compound **21** and just 0.01 eV for compound **22**. The LUMO becomes deeper as well by 0.31 eV in the case of compound **21** and 0.39 eV in compound **22**. Despite this, the HOMO-LUMO energy gap decreases in the order 2DBCzPN (**18**) > DBCz-PS (**21**) > DBCz-BZPN (**22**). This is likely owing to the donor moieties being identical in each of these three molecules (and the quantity remaining the same). The only difference is the shallower LUMO energies going from dicyanobenzene < diphenyl sulfone < benzophenone.

7.3.8 Molar absorption coefficients

The measurement of molar absorption coefficients is reported as follows, permitting the exploration of the origin of the electronic transitions.

2DBCzPN (18)

Several solutions at different concentrations of compound **18** were prepared in dry toluene solution from a stock of 1×10^{-4} M. For the λ_{max} absorbance peak at 363 nm, the molar absorption coefficient was calculated to be $\varepsilon = 4.28 \times 10^4$ cm^{-1} M^{-1}, with the peaks at 346 nm, 301 nm and 283 nm giving molar absorption coefficients of $\varepsilon = 3.68 \times 10^4$ cm^{-1} M^{-1}, 3.13×10^4 cm^{-1} M^{-1}, and 3.93×10^4 cm^{-1} M^{-1} respectively (see Figure 9-11 in Appendix 1). These are once again likely to be associated with moderate $\pi \rightarrow \pi^*$ transitions, although no peak appears to be strong enough to be related to CT transitions, which suggests compound **18** is less likely to be a TADF emitter.

In comparison to compound **19**, the absorption peaks red-shift by 3 nm, 2 nm, and 1 nm for the first two and fourth peaks, but the third peaks blue-shifts by 2 nm in compound **18**, however these are within experimental error for the instrument. The absorption coefficient for the 360 / 363 nm peak is 5.06×10^4 cm^{-1} M^{-1} greater in compound **19** than in compound **18**; the 344 / 346 nm peak is 2.72×10^4 cm^{-1} M^{-1} greater; 303 / 301 nm is 2.17×10^4 cm^{-1} M^{-1} greater; and the shortest wavelength peak is 1.44×10^4 cm^{-1} M^{-1} greater. In all cases compound **19** possesses the greatest absorption coefficient in toluene compared to compound **18**.

4DBCzIPN (19)

Solutions of compound **19** were prepared in the same manner as compound **18**, from a 1×10^{-4} M stock solution in toluene. For the λ_{max} absorbance peak at 360 nm, the molar absorption coefficient was calculated to be $\varepsilon = 9.34 \times 10^4$ cm^{-1} M^{-1}, with the peaks at 344 nm, 303 nm and 281 nm giving molar absorption coefficients of $\varepsilon = 6.39 \times 10^4$ cm^{-1} M^{-1}, 5.30×10^4 cm^{-1} M^{-1}, and 5.37×10^4 cm^{-1} M^{-1} respectively (see Figure 9-12 in Appendix 1). These represent strong absorptions, most likely of $\pi \rightarrow \pi^*$ character, although the 360 nm peak could be CT in nature owing to its high molar absorption coefficient.

4MBCzIPN (20)

The broad shoulder at ~465 nm only has a molar absorption coefficient of 5.84×10^3 cm^{-1} M^{-1}, so unlike compound **19**, this is not likely to be CT in nature, it is most likely to be a $\pi \rightarrow \pi^*$ or $n \rightarrow \pi^*$ transition (see Figure 9-13 in Appendix 1). The remainder of the absorption peaks are clearly from $\pi \rightarrow \pi^*$ transitions.

DBCz-PS (21)

For compound **21**, the λ_{max} absorbance in toluene was found to be 366 nm, with an absorption coefficient of $\varepsilon = 3.41 \times 10^4$ cm^{-1} M^{-1} (see Figure 9-14 in Appendix 1). Additional absorption peaks of 349 nm, 333 nm, 303 nm and 282 nm gave absorption coefficients of $\varepsilon = 2.85 \times 10^4$ cm^{-1} M^{-1}, 2.0179×10^4 cm^{-1} M^{-1}, 2.53×10^4 cm^{-1} M^{-1} and 2.98×10^4 cm^{-1} M^{-1} respectively. All of these are of the order typical of $\pi \rightarrow \pi^*$ transitions.

DBCz-BZPN (22)

Compound **22** possesses an identical λ_{max} absorbance in toluene to compound **21** at 366 nm. The absorption coefficient is an order of magnitude smaller however, at 4.25×10^3 cm^{-1} M^{-1} (see Figure 9-15 in Appendix 1). For the other absorption peaks (again at very similar wavelengths to compound **21**) at 349 nm, 355 nm (albeit a shoulder), 304 nm and 283 nm, the absorption coefficients are : $\varepsilon = 3.59 \times 10^3$ cm^{-1} M^{-1}, 2.20×10^3 cm^{-1} M^{-1}, 3.10×10^3 cm^{-1} M^{-1} and 4.70×10^3 cm^{-1} M^{-1}. These very weak transitions suggest compound **22** is unlikely to possess any charge-transfer states in toluene. These peaks are likely to be from $\pi \rightarrow \pi^*$ transitions, however the 335 nm peak may come from a $n \rightarrow \pi^*$ transition. It should however be stressed that compound **22** has exceedingly low solubility in most solvents, so it is possible that the intensities of the peaks are misleading.

7.3.9 Solvatochromism

As mentioned previously, all five compounds exhibit broad emission and highly pronounced solvatochromism. The UV-vis absorption and photoluminescence spectra of compounds **18**, **19** and **20** in a variety of solvents are shown in Figure 7-24 and those for compounds **21** and **22** are shown in Figure 7-25. Interestingly, compound **19** shows a peak at 445 nm which does not change with solvent polarity, suggesting it is LE emission, whereas a clear solvatochromic shift occurs with the second peak from 627 nm in methylcyclohexane to 715 nm in dimethyl sulfoxide, indicating the presence of a CT state. A LE emission peak is absent in any solvent for compound **18**, however solvatochromism in emissions is clearly visible, ranging from 546 nm to 705 nm, almost double the solvatochromic shift of that of compound **19**, suggesting a much stronger charge-transfer state in compound **18**. This is because the molecule is a non-linear D-A-D system, whereas compound **19** has multiple donor moieties reducing the overall magnitude of the dipole. This results in an increased dipole in the excited state for compound **18** making it much more susceptible to the influence of surrounding solvent molecules[176].

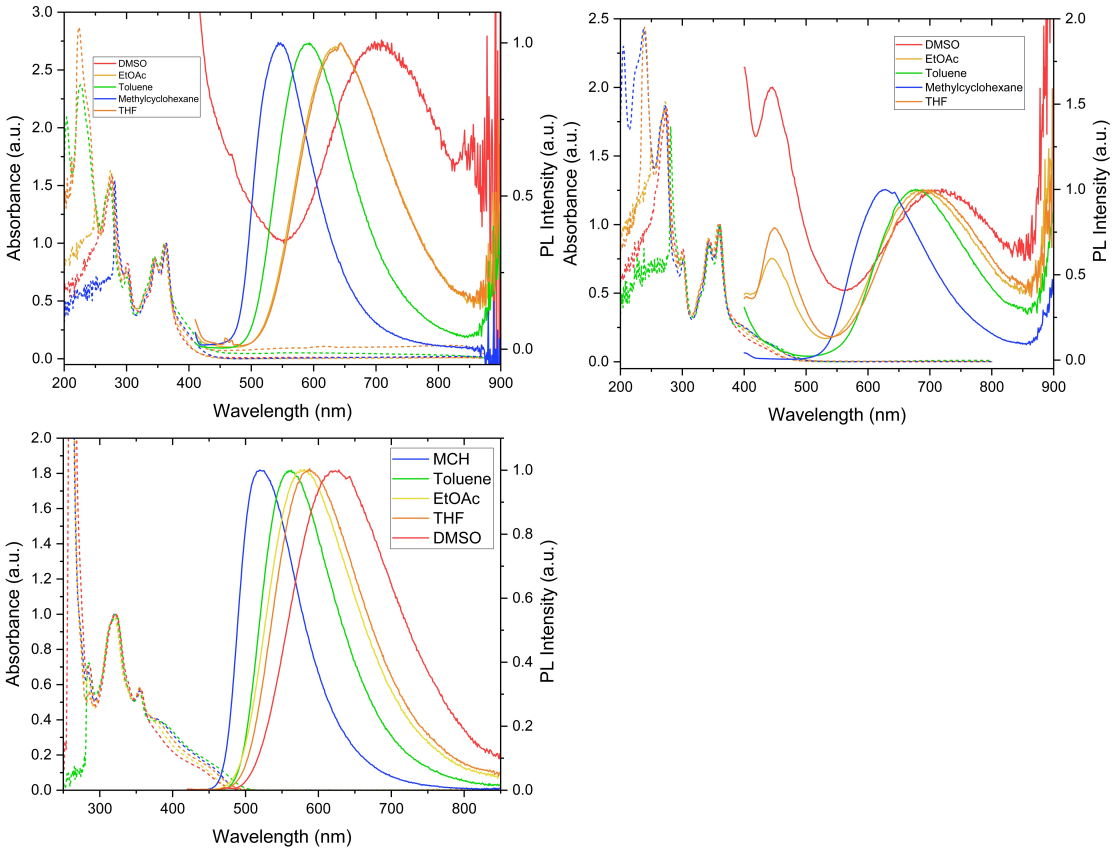


Figure 7-24 Solvatochromism UV-vis and PL plots of compound 18 (left), 19 (right), 20 (bottom) from ~1 x 10^{-5} M solutions.

The nature of the excited states driving the emissions can be determined by measuring the PLQY of the compound when exposed to O_2 and when purged of O_2 through bubbling with an inert gas such as argon (see Table 7-7). In toluene solution, the PLQY of both molecules increases when degassed (1.8% in air for compound **19**, then 4.4% under argon; 3.8% for compound **18** in air, 10.1% in argon). This quenching by oxygen strongly suggests that the triplet states are involved in the photophysical process, either as phosphorescent emission, or TADF.

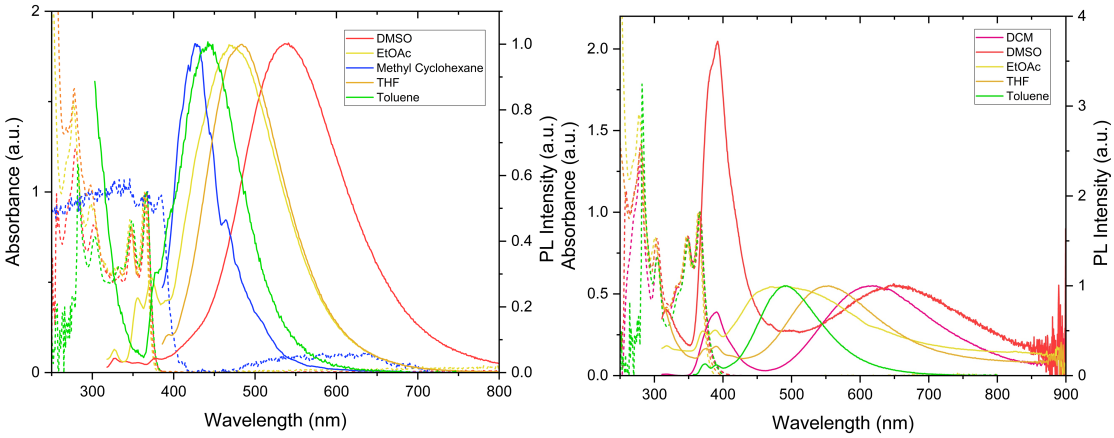


Figure 7-25 Solvatochromism UV-vis and PL plots of compounds 21 (left) and 22 (right) from ~1 x 10-5 M solutions. Owing to poor solubility, methylcyclohexane is omitted and an additional polar solvent, DCM used instead to enhance LE peak intensity.

Solvatochromism of CT peaks is present in both compounds **21** and **22** as well, along with seemingly LE emissions which are solvent independent in terms of their wavelength but increase in intensity with solvent polarity for compound **22**. The solvatochromism in compound **22** is dramatic, shifting 160 nm from 491 nm in toluene, up to 651 nm in dimethyl sulfoxide. Toluene was used as the most non-polar solvent for compound **22** owing to its insolubility in methylcyclohexane. The CT nature of the emissions in compound **22** suggests the molar absorption coefficient reported above may be misleading owing to poor solubility.

For compound **22**, the massive increase in intensity of the LE emission peak in dimethyl sulfoxide suggests that in more polar environments, a decoupling of the HOMO and LUMO is occurring, ensuring mostly locally excited emissions from the dibenzocarbazole donors is occurring, with limited energy transfer to the benzophenone core.

Of special note is the difference between the solvatochromism photoluminescence spectra of compounds **19** and **20**. Compound **19** shows a strong LE emission peak (assigned so because of the lack of shifting in wavelength as a function of solvent polarity) in a variety

of solvents, whereas this emission is completely absent in compound **20**. This is most likely due to enhanced steric crowding of the donor moieties due to the additional benzo group in compound **19**, maintaining D-A orthogonality, whereas the smaller donors in compound **20** have more flexibility[367,368].

7.3.9.1 Lippert–Mataga analysis for solvatochromism

The solvatochromism effect on compounds **18** and **19** is more visible in the absorption spectra closeup and is show in Figure 7-26.

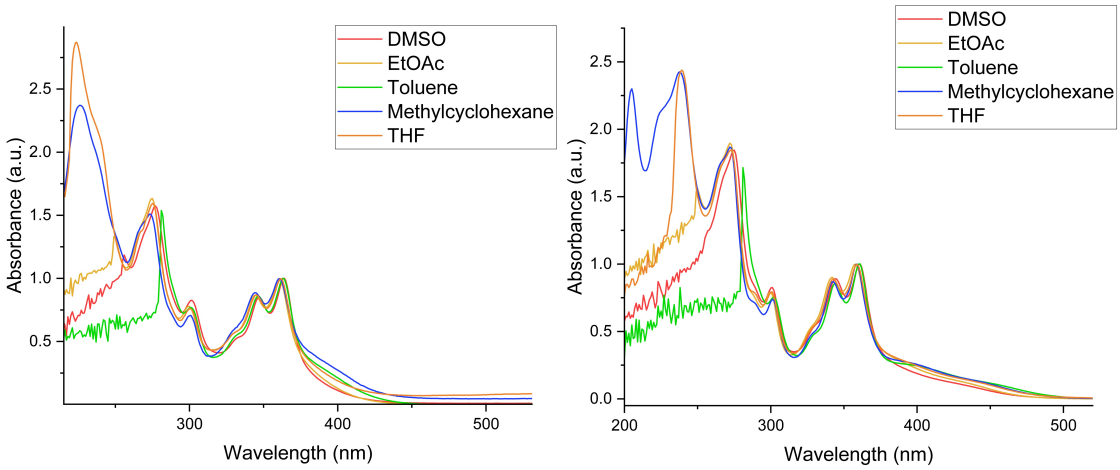


Figure 7-26 Close-up UV-vis absorption plots of compounds 18 (left) and 19 (right) in 1 x 10-5 M solutions for solvatochromism studies.

In order to perform Lippert-Mataga analysis upon the compounds in this chapter, the dielectric constants and refractive indices for the various solvents shown in Table 4-10 in Chapter 4 were used. The Stokes shift (ν_a - ν_p) for each compound in different solutions was calculated by calculating the difference between λ_{max} for both absorbance and PL.

Table 7-12 The UV-vis, PL data and Stokes shift for the dibenzocarbazole compounds in different solvents.

	2DBCzPN (18)				**4DBCzIPN (19)**			
Solvent [~1x10^{-5} M]	λAbs_{max} (nm)	λPL_{max} (nm)	FWHM (nm)	$\nu_a - \nu_p$ (cm^{-1})	λAbs_{max} (nm)	λPL_{max} (nm)	FWHM (nm)	$\nu_a - \nu_p$ (cm^{-1})
Toluene	363	590	137	10599	360	678	178	13029
Tetrahydrofuran	362	636	170	11901	359	698	209	13529
Methylcyclohexane	361	546	107	9386	358	626	145	11959
Ethyl acetate	361	636	173	11978	357	688	204	13476
Dimethyl sulfoxide	364	705	256	13288	361	715	268	13715
	4MBCzIPN (20)				**DBCz-PS (21)**			
Solvent [~1x10^{-5} M]	λAbs_{max} (nm)	λPL_{max} (nm)	FWHM (nm)	$\nu_a - \nu_p$ (cm^{-1})	λAbs_{max} (nm)	λPL_{max} (nm)	FWHM (nm)	$\nu_a - \nu_p$ (cm^{-1})
Toluene	355	561	117	10344	367	442	90	4624
Tetrahydrofuran	355	588	141	11162	365	483	109	6693
Methylcyclohexane	355	520	94	8938	383	428	56	2745
Ethyl acetate	355	580	140	10928	364	470	121	6196
Dimethyl sulfoxide	356	622	169	12013	366	538	144	8735
	DBCz-BZPN (22)							
Solvent [~1x10^{-5} M]	λAbs_{max} (nm)	λPL_{max} (nm)	FWHM (nm)	$\nu_a - \nu_p$ (cm^{-1})				
Toluene	366	491, (391, 373)	105	6956				
Tetrahydrofuran	365	553, (390, 373)	167	9314				
Methylcyclohexane	-	-	-	-				
Ethyl acetate	364	492, (389, 370)	227	7147				
Dichloromethane	366	617, (390)	193, (27)	11115				
Dimethyl sulfoxide	367	651, (392)	268, (119)	11887				

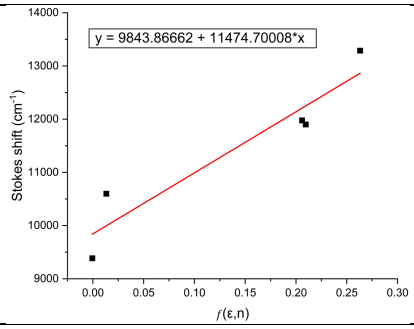
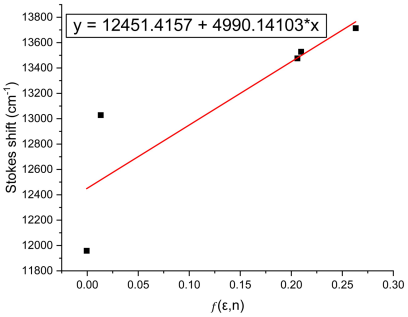
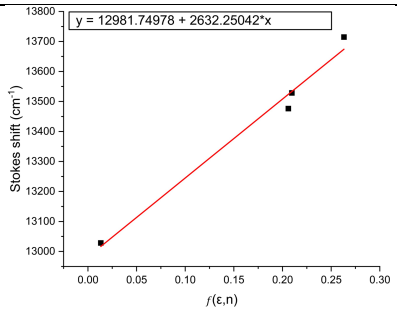
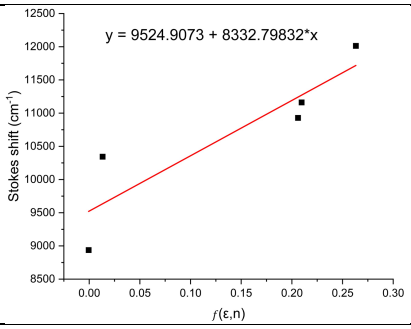
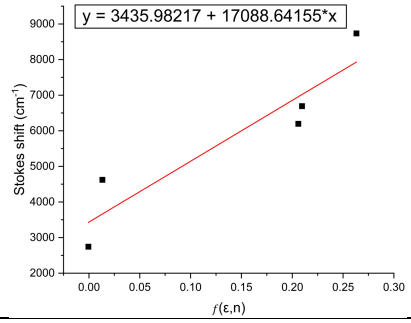
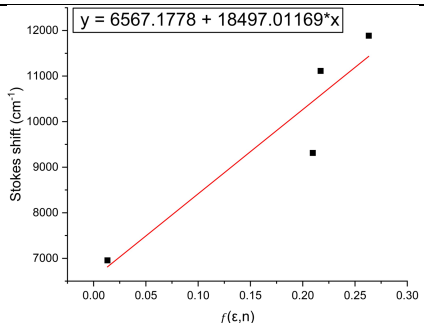
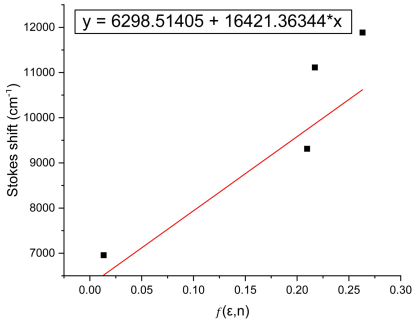
2DBCzPN (18)		
$R^2 = 0.8957$		
4DBCzIPN (19)		 Ignoring MCH
$R^2 = 0.748$		$R^2 = 0.98395$
4MBCzIPN (20)		
$R^2 = 0.80086$		
DBCz-PS (21)		
$R^2 = 0.86608$		
DBCz-BZPN (22)	 Ignoring EtOAc	
$R^2 = 0.87607$		$R^2 = 0.50437$

Figure 7-27 (*previous page)* Lippert–Mataga plots for both the compounds studied. Where poor solubility was an issue, that particular solvent is omitted and the plot with the best fit used for the following dipole moment calculation.

As with Chapter 4, using Equation 4-1 permits the use of the slope of the Lippert–Mataga plots from Figure 7-27, and Divac *et al.*'s[299] method to yield the dipole moments of the CzDBA and tBu-MeOCzDBA in Table 7-13.

Table 7-13 Dipole moments of compounds 18 – 22.

Molecule	$\Delta\mu$ (cm^{-1})	a (Å)[a]	$(\mu_e - \mu_g)D$
2DBCzPN (18)	11475	8.78	28
4DBCzIPN (19)	2632	10.9	18
4MBCzIPN (20)	8333	9.43	26
DBCz-PS (21)	17089	13.2	63
DBCz-BZPN (22)	18497	12.7	62

[a] Onsager cavity radius, calculated *via* DFT-B3LYP-6-31G(d) as half of the largest diameter across the whole molecule plus the van der Waals radii of the atoms measured.

Comparing the dicyano-benzene acceptor molecules (compounds **18** – **20**) to the stronger diphenyl sulfone and dibenzophenone acceptors (compounds **21** and **22** respectively), the presence of the diphenyl groups seems to significantly increase the dipole moment of the molecule in the excited state (presumably acting as an internal π-spacer in the acceptor system). The presence of this dipole in the excited state suggests the excited states being charge-transfer in nature.

7.3.10 Investigating CT Peaks

In an effort to understand the origin of the second, blue-shifted peak for 4DBCzIPN (**19)** in the more polar solvents, a sample was prepared in diethyl ether and excited at the wavelengths of each of the absorption peaks of compound **19**. It is not present in any of the non-polar solvents (toluene and methylcyclohexane), suggesting that it is an artefact of CT states, which are well known to be influenced by more polar solvents. However, since its intensity is dependent upon excitation source wavelength (see Figure 7-28), it can more likely be assigned to the local excitation emission from one of the donor moieties, possibly with its HOMO decoupled from the LUMO under polar conditions, due to the bulk of the dibenzocarbazole donor.

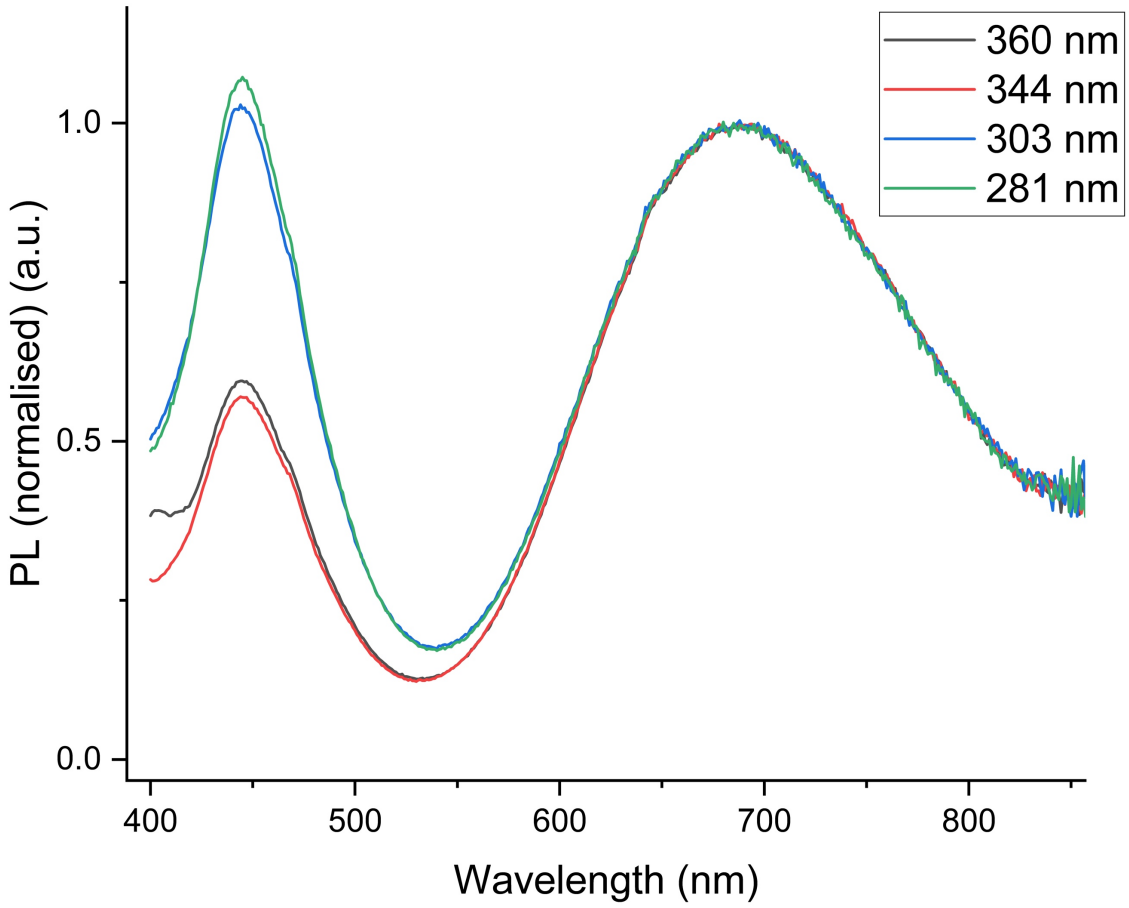
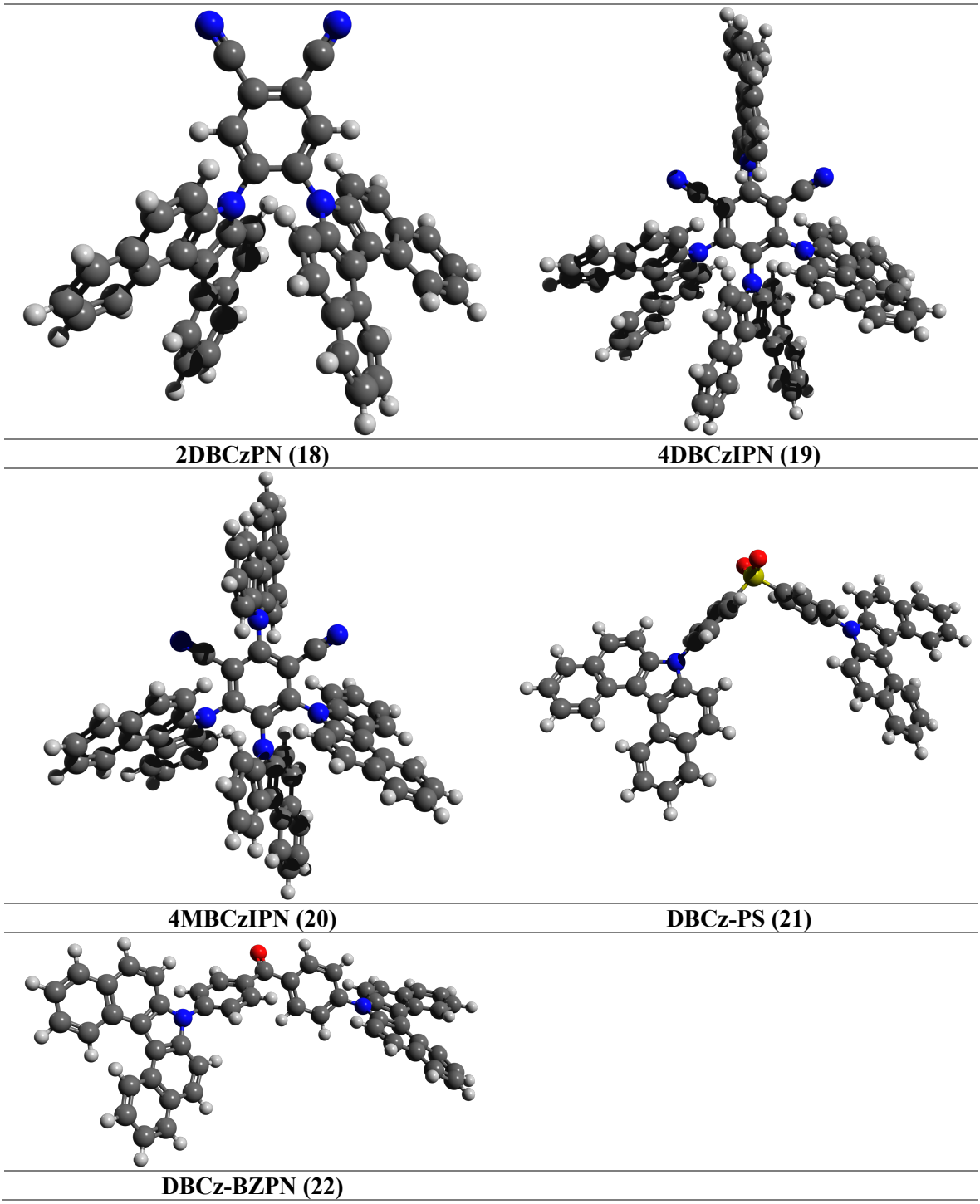


Figure 7-28 PL spectra of 4DBCzIPN (19) when excited at each of its UV-vis absorption peaks respective wavelengths in diethyl ether.

In the monobenzocarbazole derivative, 4MBCzIPN (**20**), no such blue-shifted emission component is present in any solvent, further supporting its origin in a localised excited state upon the dibenzocarbazole donor unit.

7.3.11 Computational chemistry

Structures of the four compounds in this study were optimised *via* DFT-B3LYP 6-31+G (d) in the gas phase and the results displayed below. As with the calculations in the previous structures, all optimised geometries produced real (non-negative) frequences and can be considered potential energy surface minima. Excited state energy calculations were performed to explore the S_1 and T_1 states *via* TD-DFT at PBE0 6-31+G (d).



2DBCzPN (18) | **4DBCzIPN (19)**

4MBCzIPN (20) | **DBCz-PS (21)**

DBCz-BZPN (22)

Figure 7-29 DFT optimised structures of compounds 18 to 22.

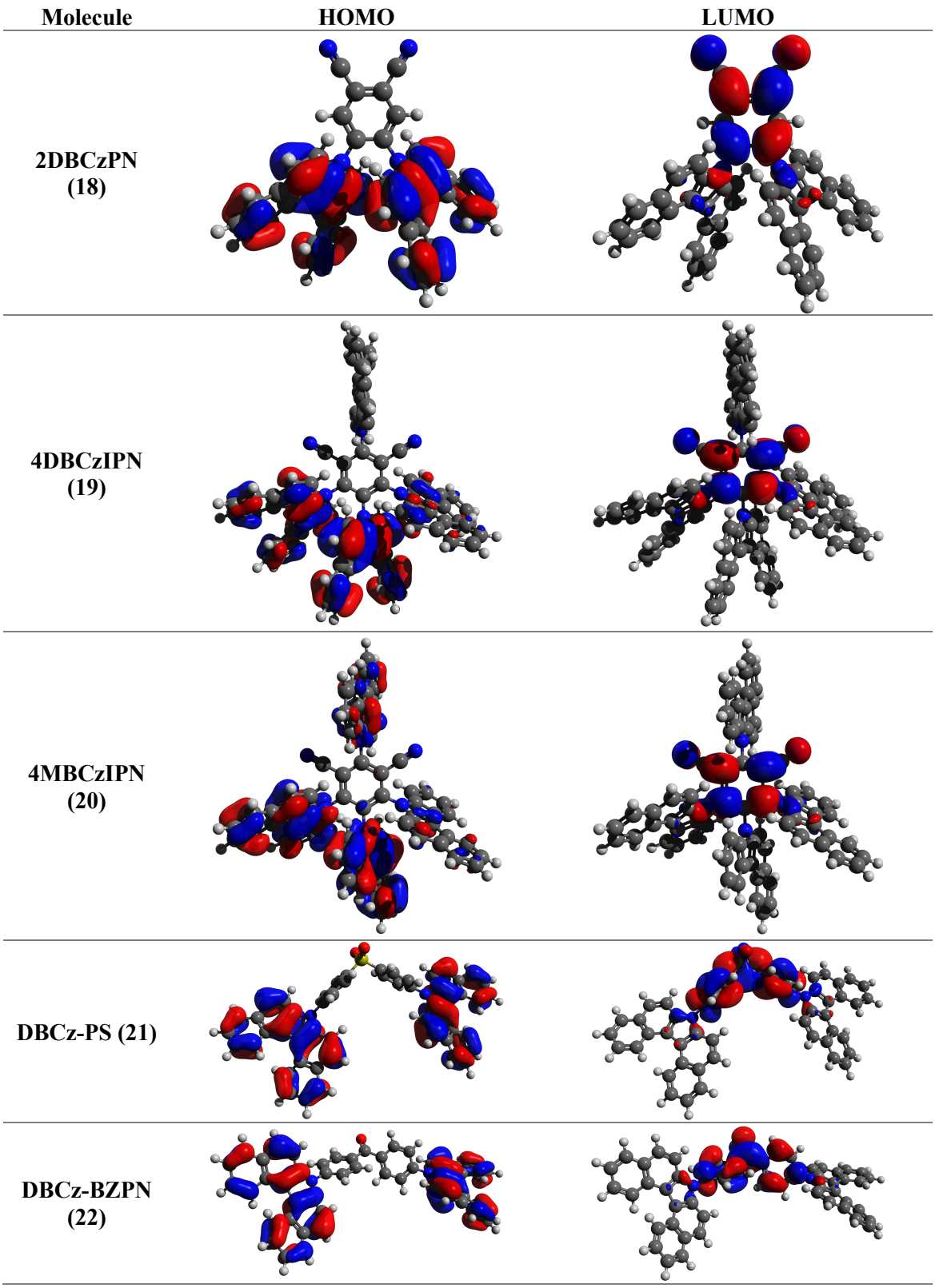


Figure 7-30 DFT optimised structures of compounds 18 to 22 and the structures of their respective HOMOs and LUMOs.

Based upon the results of TD-DFT calculations (PBE0 6-31+G (d)), the HOMO is delocalised over the two dibenzocarbazole moieties in compound **18** and on the lower three in compounds **19** and **20**. The LUMO is localised upon the central dicyanobenzene acceptor moiety, which suggests that the first singlet state (S_1) is of charge-transfer character.

Table 7-14 Key bond distances from DFT calculations for the three dicyano-benzene compounds.

	Bond distances (Å)							
Molecule	**C-N 1**	**C-N 2**	**C-N 3**	**C-N 4**	**C-C≡N 1**	**C-C≡N 2**	**C≡N 1**	**C≡N 2**
2DBCzPN (18)	1.41	1.411	-	-	1.43	1.43	1.16	1.16
4DBCzIPN (19)	1.41	1.41	1.41	1.41	1.43	1.43	1.16	1.16
4MBCzIPN (20)	1.41	1.41	1.41	1.41	1.43	1.43	1.16	1.16

Table 7-15 Key bond angles from DFT calculations for the three dicyano-benzene compounds.

	Dihedral angles (°)				Donor distortion angles (°)			
Molecule	**C-N 1**	**C-N 2**	**C-N 3**	**C-N 4**	**1**	**2**	**3**	**4**
2DBCzPN (18)	54	60	-	-	26	26	-	-
4DBCzIPN (19)	63	66	83	64	25	28	26	26
4MBCzIPN (20)	64	66	73	64	3.2	2.2	1.4	2.2

As can be seen in Table 7-14, the bond lengths remain largely unchanged regardless of what acceptor or donor moiety is used. From Table 7-15, it can be seen that in compound **18**, the dihedral angle between donors and acceptor is quite large (54° - 60°) and comparable to that of carbazole in 4CzIPN as reported by Uoyama *et al*.[33] and this is reflected in its calculated ΔE_{ST} of 0.25 eV. Compound **19** exceeds the dihedral angles of both compound **18** and its progenitor 4CzIPN, being between 63° and 83°. This helps to give rise to the even narrower calculated ΔE_{ST} of 0.10 eV. Further investigation using Peach *et al*.'s[369] orbital overlap methodology, reveals the presence of multiple CT triplet and singlet states in compound **19**.

For the monobenzocarbazole derivative, 4MBCzIPN (**20**), the dihedrals remain mostly similar to compound **19**, though the largest is 73° instead of 83° in the lower most congested central donor, a result of decreased steric hindrance losing one benzene ring per donor. All other C-N bonds (both D-A and the cyano groups) remain identical in all three compounds.

The quasi-helical nature of the dibenzocarbazole donors is revealed in their distortion angle (the dihedral from the outermost reaches of the benzo groups across the central C-C bond in the 5-membered heteroaromatic ring. In the two dibenzocarbazole compounds, this distortion ranges from 25° up to 28°. Switching to the monobenzocarbazole donor completely removes this helical character, with deviation from true planarity only being between 1.4° and 3.2°.

The HOMO in compound **19** is larger than compound **20**, owing to the larger surface area of the donor. As such, the overall percentage overlap between HOMO and LUMO in compound **19** would be less (which can be seen from the DFT calculations). Comparing the molar absorption coefficients of the two molecules in section 7.3.8) it can be seen at indeed the molecule with the largest mixing, compound **20** possesses the smallest coefficient of the two (1.85×10^4 $cm^{-1}M^{-1}$ as opposed to 9.34×10^4 $cm^{-1}M^{-1}$).

Table 7-16 Key bond distances from DFT structural calculations for the diphenyl sulfone and benzophenone compounds.

	Bond distances (Å)			
Molecule	**C-N 1**	**C-N 2**	**C - S 1 / C - C 1**	**C - S 1 / C - C 1**
2DBCz-PS (21)	1.418	1.418	1.802	1.802
2DBCz-BZPN (22)	1.42	1.42	1.5	1.5

Table 7-17 Key angular properties from DFT structural calculations for the diphenyl sulfone and benzophenone compounds.

	Dihedral angles (°)			Donor distortion angles (°)		Acceptor distortion angles (°)
Molecule	**C-N 1**	**C-N 2**	**Internal acceptor**	**Internal buckling 1**	**Internal buckling 2**	**C – S – C / C – CO – C**
2DBCz-PS (21)	59	59	91.4	27.0	27.0	105.0
2DBCz-BZPN (22)	57	57	31.2 / 51	26.2	26.2	120.5

DBCz-PS (**21**) demonstrates excellent HOMO-LUMO separation. As before, the HOMO is entirely localised upon the dibenzocarbazole donors with no seepage into the acceptor moiety. The LUMO resides upon the diphenyl sulfone acceptor, bleeding only by a tiny degree into the central five membered ring of the donor. This may permit a slight degree of mixing to allow for a narrow ΔE_{ST}. From Table 7-16 and Table 7-17 it can be seen that the donor and acceptor are calculated to be at dihedrals of 59° along both D-A bonds, with the D-A N-C bond lengths being 1.42 Å each.

The optimised structure for DBCz-BZPN (**22**) once again shows excellent confinement of the HOMO to the donor moiety, but the smallest degree of HOMO-LUMO mixing of all of the molecules studied. This may result in increased charge-transfer character, since the LUMO only spreads onto the nitrogen of the donor moieties. Interestingly, dihedrals of 57° are observed between the donors and acceptor – only slightly less than compound **21**, despite the greater degree of freedom the phenyl rings on the acceptor possess due to the lack of

additional bond connecting them. As Table 7-16 shows, the lack of connection between the benzophenone rings results in a 52° face-to-face dihedral between them (31° through the sulfur), with a 121° separation across the C-(CO)-C connection, which is much wider than the 105° C-S-C central angle in compound **21**. The C-N bond lengths are both 1.42 Å in compound **22**, exhibiting identical lengths to compound **21**.

On the matter of HOMO – LUMO separation, the molar absorption coefficients for compounds **21** and **22** would appear to support them being very similar in terms of their separation, being only 0.85×10^4 $cm^{-1}M^{-1}$ different.

Table 7-18 Excited state properties as calculated *via* TD-DFT PBE0.

Molecule	S_1 (eV)	S_1 (nm)	T_1 (eV)	T_1 (nm)	ΔE_{ST} (eV)
2DBCzPN (18)	2.40	565	2.16	575	0.24
4DBCzIPN (19)	2.16	575	2.06	603	0.10
4MBCzIPN (20)	2.44	507	2.33	532	0.11
2DBCz-PS (21)	3.19	389	3.16	392	0.02
2DBCz-BZPN (22)	2.80	442	2.82	439	-0.02

Table 7-19 HOMO and LUMO energies and HOMO-LUMO band-gap as calculated *via* TD-DFT PBE0.

Molecule	HOMO (eV)	LUMO (eV)	Eg (eV)
2DBCzPN (18)	-5.89	-2.87	3.02
4DBCzIPN (19)	-5.76	-2.95	2.81
4MBCzIPN (20)	-5.97	-2.84	3.13
2DBCz-PS (21)	-5.73	-2.41	3.32
2DBCz-BZPN (22)	-5.72	-2.42	3.30

Table 7-18 and Table 7-19 summarise the excited state energies and HOMO and LUMO energies respectively for the compounds in this chapter. The calculated HOMO-LUMO energy gaps follow the same trends as was observed with the cyclic voltammetry experiments.

As with DBCz-DMB (**3**) in Chapter 4, the HOMO in all five molecules in this chapter are significantly localised upon the donor moieties, with no trace of it shown over the acceptor. This is at odds with previous studies of carbazole based analogues (shown in Figure 7-31)

where the donors' HOMOs spread quite considerably into the acceptor moiety region in these types of molecules [33,338,356].

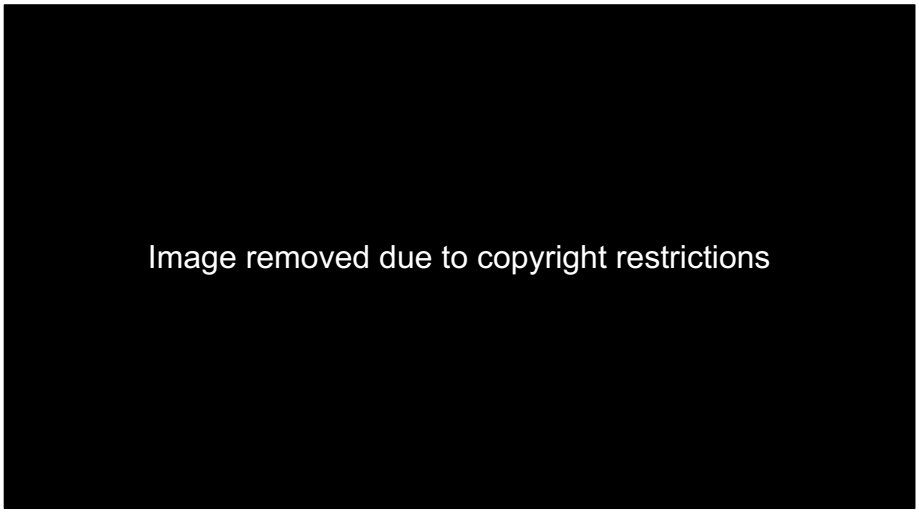


Figure 7-31 HOMOs and LUMOs from DFT calculations. Images taken from the original papers: 2CzPN from Wong *et al.*[338] , 4CzIPN from Uoyama *et al.*[33] and 4CzIPN-Me, 4CzIPN-*t*Bu and 4CzIPN-Ph from Ishimatsu *et al.*[356]

However, a recently studied dithienopyrrole derivative of 4CzIPN (4DTPIPN, shown in Figure 7-32), by Cardeynaels *et al*.[360] illustrates a similar phenomenon in their DFT calculations. In their work, they hypothesise that the greater HOMO localisation will give rise to enhanced CT character and narrower ΔE_{ST}. As we also observe better HOMO confinement to our dibenzocarbazole donors, the substantial solvatochromism and enhanced CT character can be ascribed to this electronic feature.

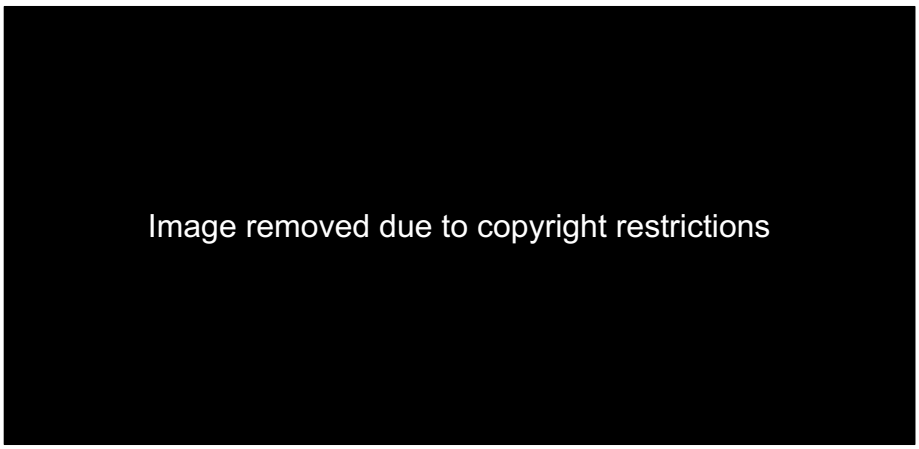


Figure 7-32 Cardeynaels *et al.*'s[360] DFT comparison of 4CzIPN's and 4DTPIPN's HOMOs and LUMOs. Not the enhanced confinement of the HOMO to the donors in 4DTPIPN.

CT and LE States

Exploring the degree of orbital overlap in compounds **18** to **22**, compound **19** appears to possess numerous triplet CT states, as well as a locally excited triplet state with energy of 2.19 eV. If true, then the energy gap between it and the first CT triplet state would be 0.13 eV, and with the first singlet CT state, 0.04 eV, potentially facilitating highly efficient rISC. Calculations reveal no triplet CT states for compound **18**, but four CT singlet states. This would explain its significant solvatochromism, but reduced lifetimes compared to 4DBCzIPN (although the accuracy of these calculations may not be overly reliable).

The monobenzocarbazole derivative, compound **20** shows a nearly locally excited triplet state which is close to CT in character at 2.06 eV, and a CT singlet state at 2.44 eV. While its ΔE_{ST} is slightly larger than compound **19** (by 0.01 eV), a ^{3}LE state at 2.35 eV could act as an intermediate state should the 2.06 eV triplet be truly CT in nature.

For compound **21**, a ^{3}CT state at 3.16 eV is observed, along with a ^{3}LE state at 3.09 eV, and a ^{1}CT state at 3.19 eV, resulting in a very narrow ΔE_{ST} of 0.02 eV. The strong solvatochromism supports the presence of CT states, but the lack of prolonged lifetimes for the emissions throws shade on the accuracy of the ΔE_{ST} energy gap value. Further work exploring the low temperature photoluminescence is required to determine whether rISC is truly occurring to this degree.

Compound **22** is also calculated to have a very narrow ΔE_{ST}, though surprisingly a negative value of -0.02 eV owing to a higher energy ^{3}CT triplet state at 2.82 eV and singlet state ^{1}CT of 2.80 eV. The nearby locally excited triplet state (^{3}LE) at 2.80 eV as well (if true) would act as a very effective intermediate state to facilitate rISC. The presence of the ^{1}CT states is supported with the incredibly strong solvatochromism of compound **22** observed experimentally. The significantly well separated HOMO and LUMO seen in the calculations could also explain why the LE emission observed in this compound is so strong in more polar solvents – with such solvents stabilising the structural conformation further separating the HOMO and LUMO.

7.3.12 Crystal structures

Crystals were grown by chloroform : methanol vapour diffusion and the single crystal XRD measurements were performed by Dr Laura McCormick at the University of Southampton.

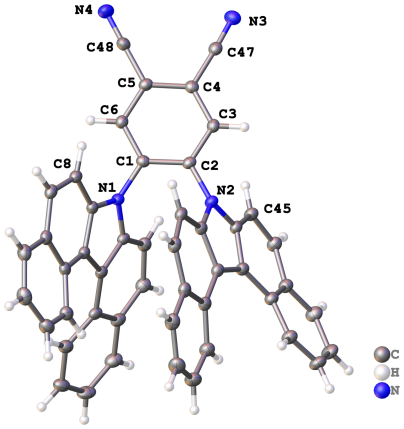
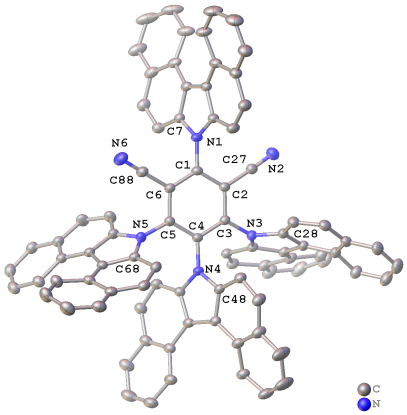
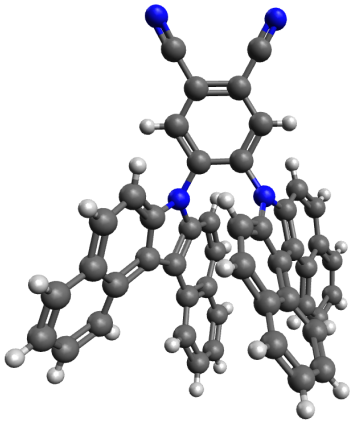
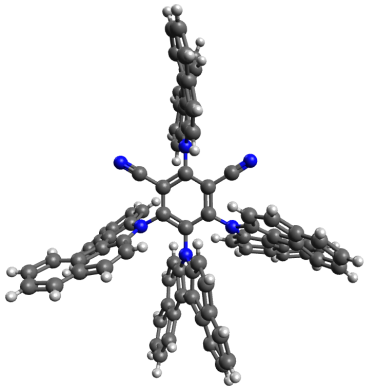
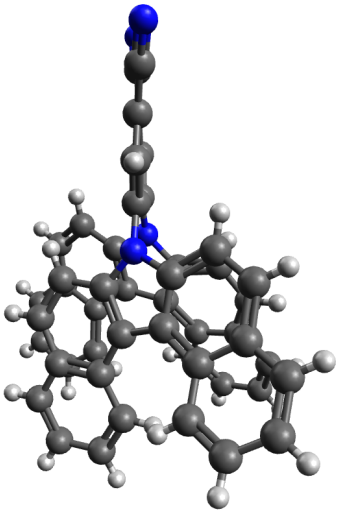
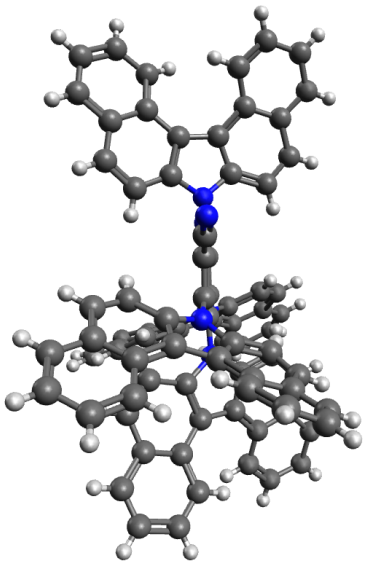
	2DBCzPN (18) (red square plates)	4DBCzIPN (19)
Ortep		
Front View		
Side View		

Figure 7-33 Single crystal XRD structures of 2DBCzPN (18) and 4DBCzIPN (19).

Unfortunately, the yellow needles polymorph crystals grown of compound **18** in dichloromethane were unsuitable for XRD analysis. Attempts to grow crystals of compound **20** yielded red crystals that were also unfortunately of too poor quality of XRD analysis as well.

Table 7-20 Summary of single crystal XRD bond distances.

	Bond distances (Å)							
Molecule	**C-N 1**	**C-N 2**	**C-N 3**	**C-N 4**	**C-C≡N 1**	**C-C≡N 2**	**C≡N 1**	**C≡N 2**
2DBCzPN (18) (red square plates)	1.41	1.41	-	-	1.44	1.44	1.15	1.15
4DBCzIPN (19)	1.41	1.41	1.41	1.41	1.44	1.44	1.15	1.14

Table 7-21 Summary of single crystal XRD angular measurements.

	Dihedral angles (°)				Donor distortion angles (°)			
Molecule	**C-N 1**	**C-N 2**	**C-N 3**	**C-N 4**	**1**	**2**	**3**	**4**
2DBCzPN (18) (red square plates)	67	52	-	-	27	30	-	-
4DBCzIPN (19)	64	58	66	59	35	33	28	30

From the single crystal XRD data (Table 7-20 and Table 7-21), there are no changes to the length of donor acceptor C-N bonds when the acceptor is switched from the ortho-substituted cyano groups to the meta-substituted analogue. Alongside this change, increased numbers of dibenzocarbazole groups bonded to the acceptor core makes no impact upon the C-N bond lengths (remaining at 1.41 Å for all D-A bonds), despite the increased crowding caused by greater numbers of bulky donor moieties. On average, increased numbers of donor groups also yields little change to the D-A dihedral angles – ranging from 52° to 67° in compound **18** and 58° to 66° in compound **19**. However, in the more congested molecule, the quasi-helical kink in the dibenzocarbazole moiety does increase – up to 35° in compound **19** up from a maximum of 30° in compound **18**. This flexibility may prove to be useful for maintaining high dihedral angles in this type of compound as a means of compensating for distortions caused by molecular packing. However, it may also act to counteract attempts to increase the dihedral. The single crystal XRD data from Wang *et al.*[370] reveals that 4CzIPN (*i.e.* the derivative of 4DBCzIPN (**19**) with standard carbazole donors), possesses C-N bond lengths of 1.40 Å - 1.41 Å, with a slight shortening observed at the link between the acceptor and donor situated directly between the two cyano groups. Wang's data also shows D-A dihedral angles ranging between 57° and 62°, suggesting that dibenzocarbazole is marginally better at sustaining high donor-acceptor dihedrals.

Interestingly, the bond distances are in very good agreement with those of the DFT calculations in section 7.3.12, with the C-N bond lengths being identical, and the C-C bond lengths in the cyano groups being 0.01 Å shorter in the calculations and the C≡N triple bond length being 0.01 – 0.02 Å longer. The dihedrals differ by 2° and 7° in the case of compound **18** and are almost identical for compound **19**, with the top donor moiety being calculated to be at a much larger dihedral angle than the value found experimentally. The calculations actually underestimate the quasi-helical bending across the dibenzocarbazole donor by an average of 5.2°. As such, despite not having crystal structures of compound **20** at the time of writing, we can with some confidence say that the structural features will resemble that which was calculated to a good degree of accuracy.

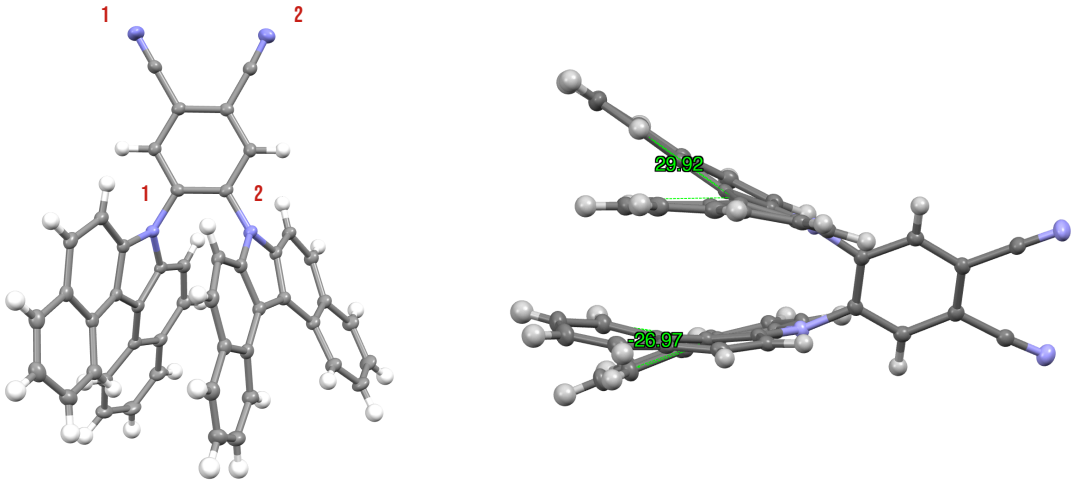


Figure 7-34 Molecular structure of compound 18 from single crystal XRD illustrating the quasi-helical nature of the donor moieties and their 'flapping' angles.

Figure 7-34 and Figure 7-35 for compounds **18** and **19** more clearly illustrate the deviation from planarity that the donor moieties demonstrate.

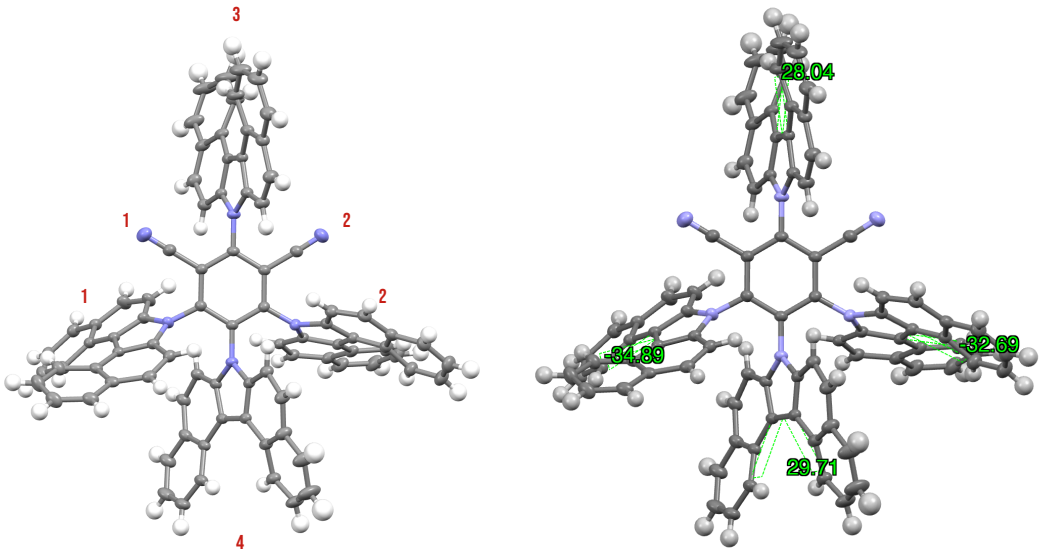


Figure 7-35 Molecular structure of compound 19 from single crystal XRD illustrating the quasi-helical nature of the donor moieties and their 'flapping' angles.

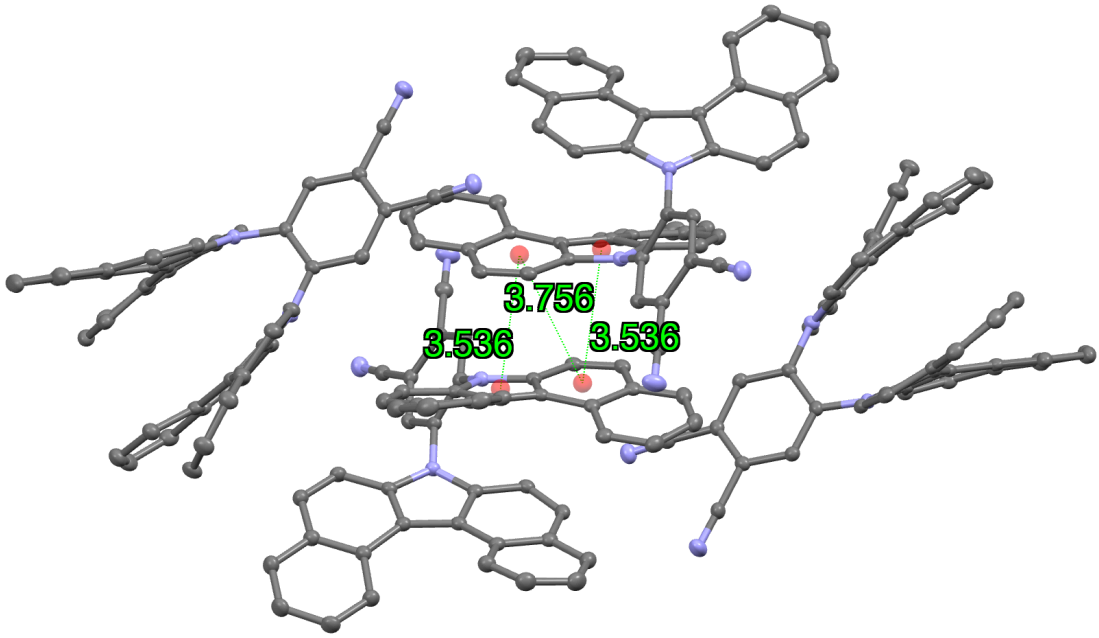


Figure 7-36 Crystal packing structure of compound 18 (red square plates) visualising π-π close contacts.

In compound **18**, the centroidal intermolecular π-π close contacts are between 3.54 Å and 3.76 Å are observed between the dibenzocarbazole moieties and those in their neighbouring molecules. This is within the range for non-covalent interactions between the molecules (see Figure 7-36). However, measuring the distances on an atom-by-atom basis (see Figure 7-37) this comes to as little as 3.28 Å, being sufficiently below the sum of the neighbouring carbon atoms' van der Waals radii, demonstrating the very close proximity to the dibenzocarbazole donors on neighbouring molecules.

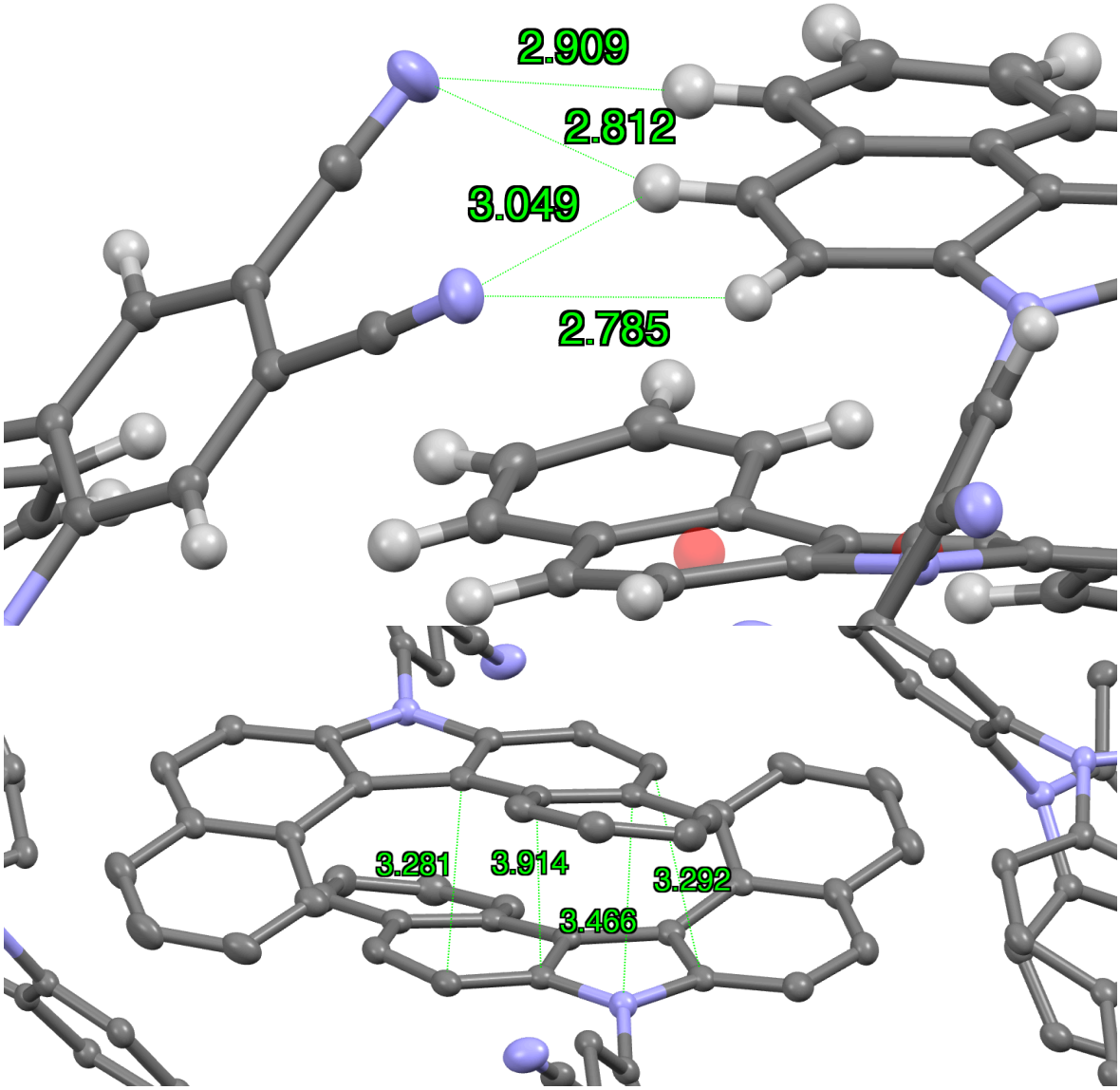


Figure 7-37 Close up of the atom-by-atom packing distances for compound 18.

In addition to this, there is potential for C≡N···H hydrogen bonding (2.79 Å), along with weak n-π interactions (C···N; 3.47 Å).

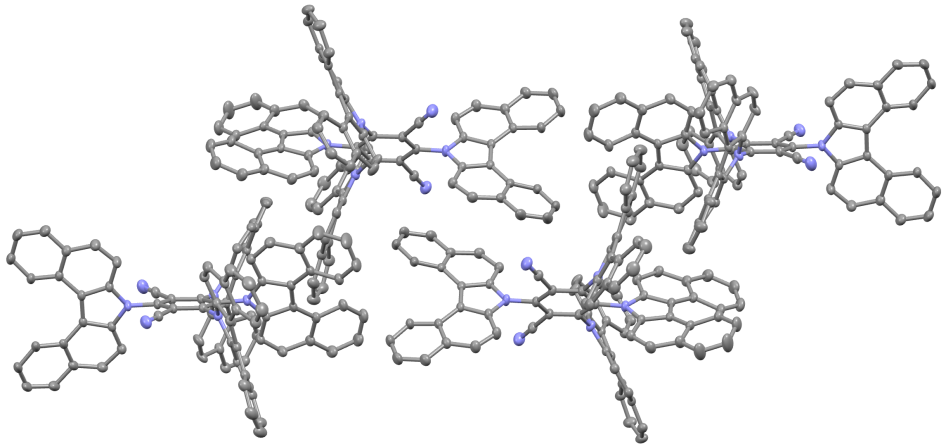


Figure 7-38 Crystal packing structure of compound 19. Hydrogen atoms omitted for clarity.

Unlike compound **18**, compound **19** molecules align such that neighbouring dibenzocarbazole groups are oriented to interlock at 87.6° to one another (see Figure 7-38 and Figure 7-39).

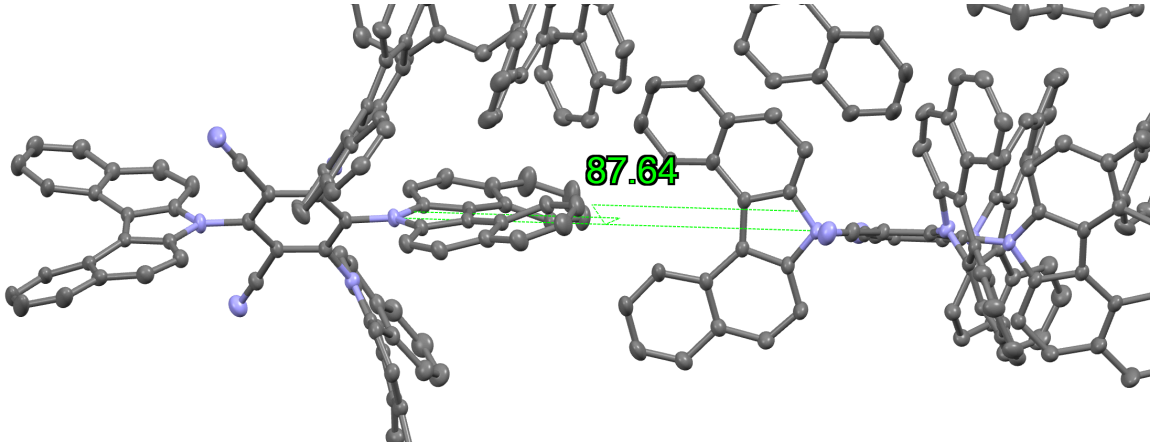


Figure 7-39 Near interlocking of two dibenzocarbazole groups on neighbouring molecules of compound 19.

Interestingly, this behaviour is completely absent in Wang *et al.*'s[370] XRD data for 4CzIPN, suggesting that the bulky quasi-helical donor moieties allow for much more complicated packing arrangements.

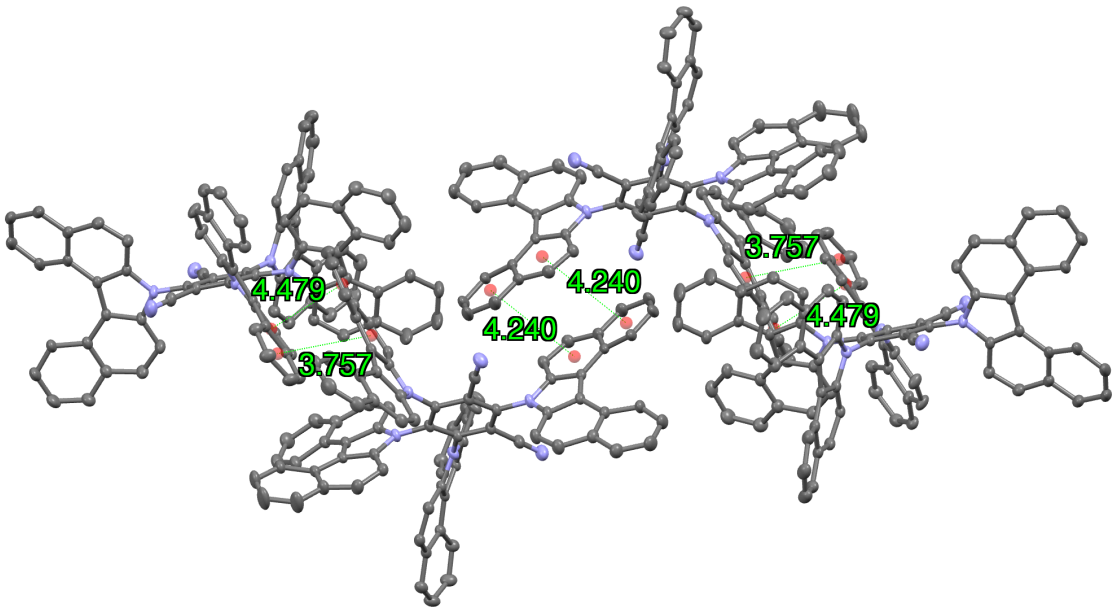


Figure 7-40 Crystal packing structure of compound 19 visualising π-π close contacts.

In compound **19**, the intermolecular centroidal π-π close contacts are between 3.76 Å and 4.48 Å, between the dibenzocarbazole moieties and those in their neighbouring molecules. This is too far to result in non-covalent aromatic interactions between the molecules.

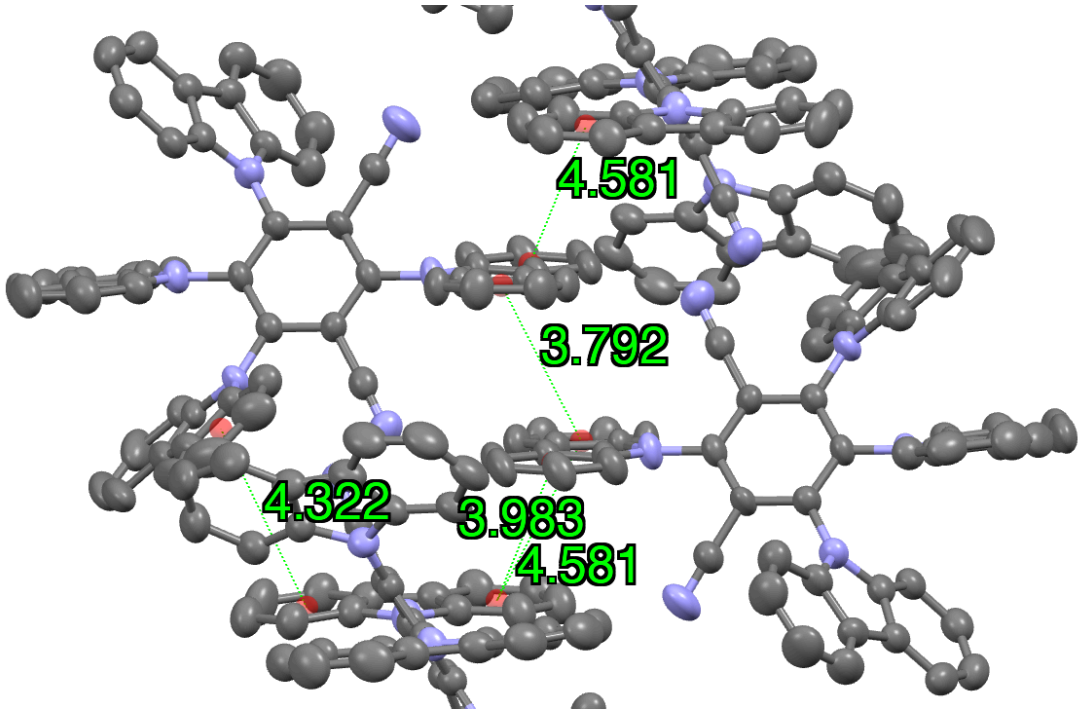


Figure 7-41 Visualisation of the centroidal close packing in 4CzIPN from the Wang *et al.*[370] XRD data in the CCD database.

For comparison, Wang's[370] data reveals the centroidal π-π close contacts are between 3.79 Å and 4.32 Å – the closest being further apart than in compound **19**, so the difference between the two molecules is negligible.

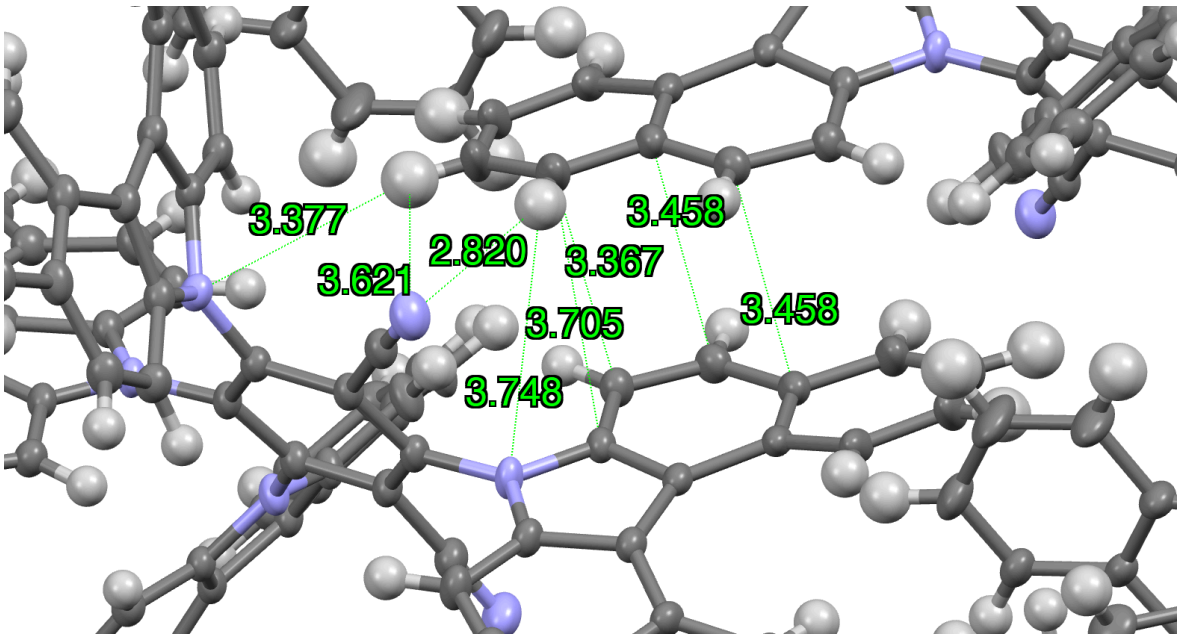


Figure 7-42 Atom-by-atom interatomic distances relative to the hydrogen atoms in compound 19.

Looking closer however (see Figure 7-42), the intersection of the quasi-helical donors permits the compound **19** molecules to be in close proximity to one another, and possess weak n-H interactions (C≡N···H, 2.82 Å), weak hydrogen bonds and n-π interactions (N: ···H / N: ···H; 3.75 Å/4.11 Å) and weak or partial π -π interactions (C···C; 3.37 Å, 3.46 Å).

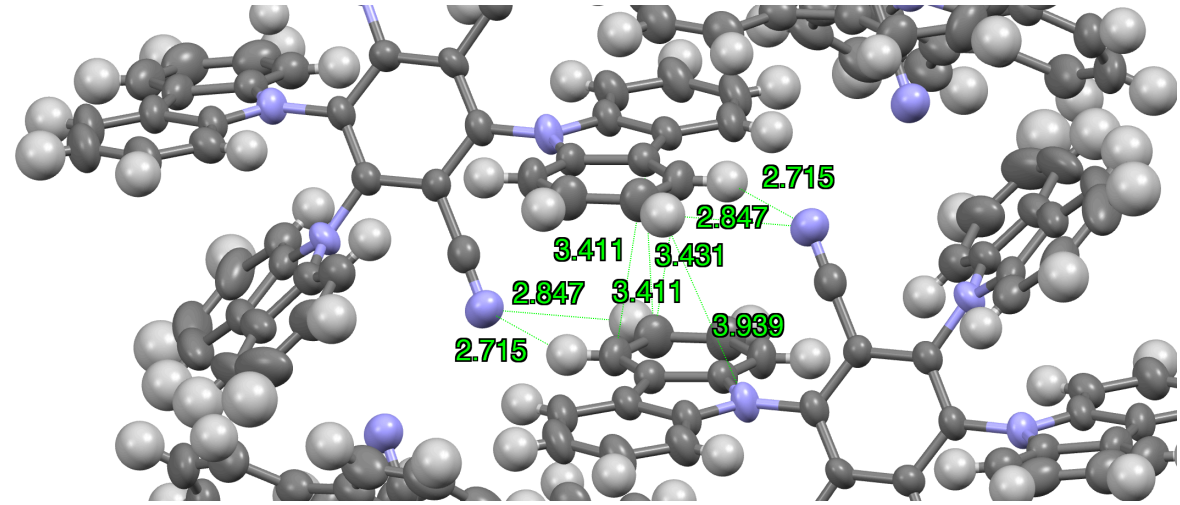


Figure 7-43 Closest points of contact between two neighbouring molecules of 4CzIPN from Wang *et al.*'s[370] paper.

The closest points of parallel carbazole donor moieties in 4CzIPN possess weak n-H interactions (C≡N···H, 2.72 Å), weak hydrogen bonds and n-π interactions (N: ···H 3.94 Å) and weak or partial π -π interactions (C···C; 3.43 Å).

From this, partial intermolecular π-π close contacts between the benzene rings of the carbazole moieties on neighbouring 2DBCzPN (**18**) and 4DBCzIPN (**19**) molecules are demonstrated[367].

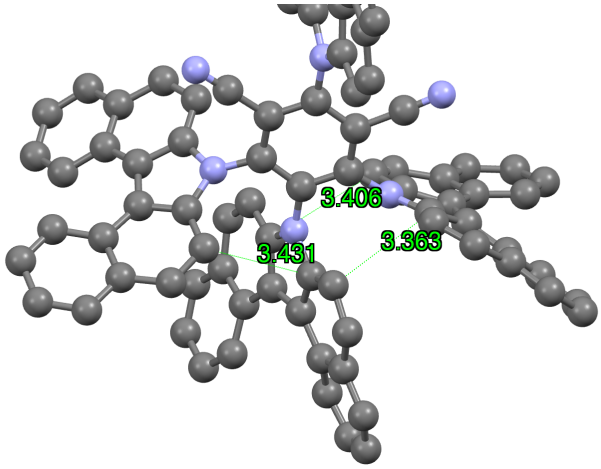


Figure 7-44 Intramolecular distances in compound 19.

Interestingly, as Figure 7-44 illustrates, the lower three neighbouring dibenzocarbazole moieties in compound **19** are in a congested environment such that their closest points are 3.36 Å - just below the sum of the van der Waals radius of two overlapping carbon atoms (3.40 Å). Since this is not a ring facial alignment, this suggest the potential for π-π intramolecular interactions between the donor moieties is weak, however interaction is most likely of a steric nature, thereby giving rise to locking the high dihedral angle between the donors and the acceptor.

7.3.13 Aggregation-induced emission of 2DBCzPN (18)

Samples were prepared of 2DBCzPN (**18**) in THF with increasing concentration of water (0 – 90% vol.). All spectrometer settings were left identical between each sample. The results are shown in Figure 7-45.

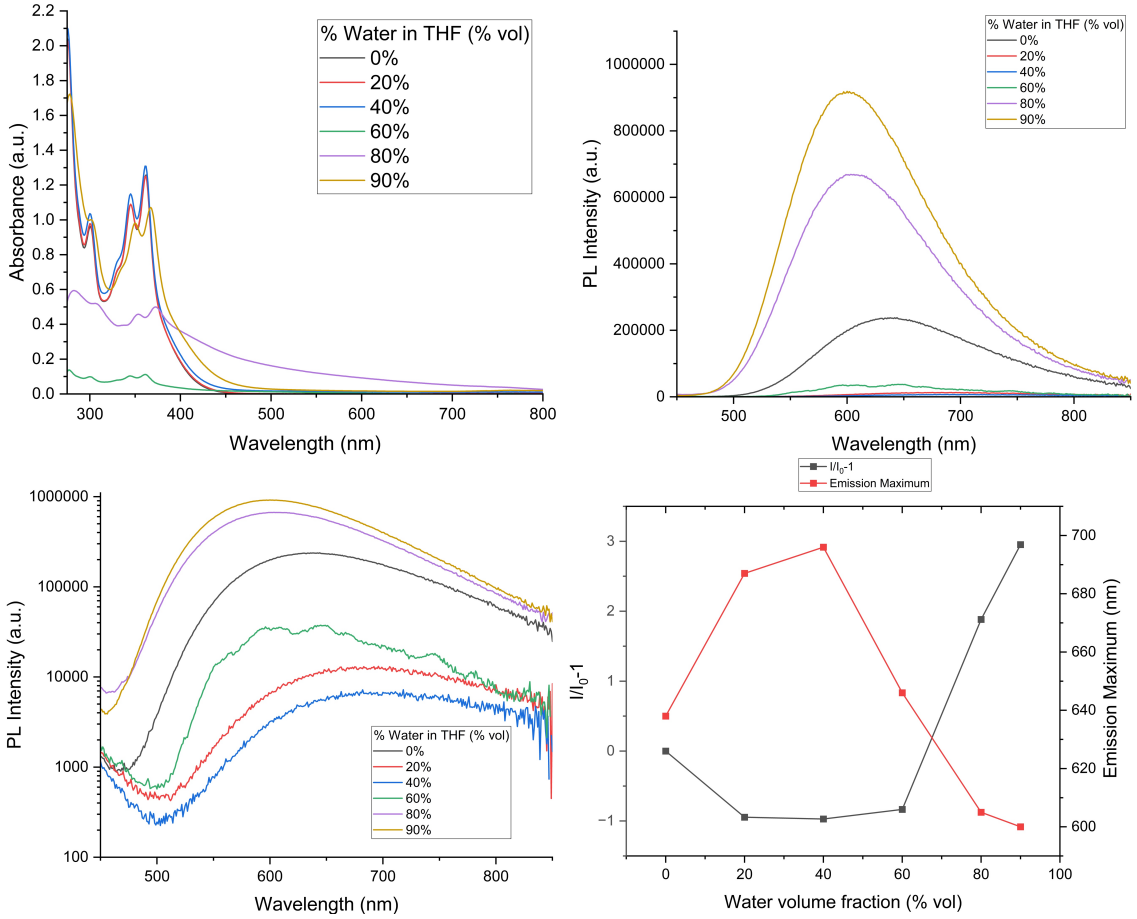


Figure 7-45 UV-vis absorption (top left) and PL spectra (top right) of compound 18 in varying concentrations of THF : water. The bottom left plot shows the PL on a log scale for clarity.

Emission increases dramatically at 90% vol suggesting effective aggregation effects on the emission. The emission is quite dull at 0% water content (100% THF) and is accompanied with an emission wavelength of 638 nm. Emission intensity initially decreases further from 0% to 40% vol., along with a red-shifted emission of 58 nm to 696 nm, presumably due to quenching from interactions with the water molecules. However, it increases from 60% vol, reaching peak intensity at 90% water content with a blue shift in emission wavelength from 40% to 90% of 96 nm, reaching 600 nm. This increase in intensity is likely due to aggregation induced emission cancelling out the negative impact of the water as the molecules of compound **18** are packed closer and closer together at 60% vol and beyond.

There is a curious dip in the absorption spectra at 60%, which coincides with the observation of particulates forming at that concentration – disappearing again at 80% (with a corresponding increase in absorption). This is likely a result of scattering due to nanoparticle formation[371].

7.3.14 Aggregation-induced emission of 4DBCzIPN (19) and 4MBCzIPN (20)

The two 4CzIPN derivatives, 4DBCzIPN (**19**) and 4MBCzIPN (**20**), were observed to posess rather dull photoluminescence under UV in solution, but much brighter in the solid or crystalline form (albeit quite close to their physical colour). To investigate the potential for aggregation-induced emissions (AIE), solutions of tetrahydrofuran : deionised water were prepared at different % vol of water concentrations. The concentration of the emitters was held the same in each sample (~1 × 10^{-4} M). Examples of the emissions from the solutions used are shown in Figure 7-46 and the UV-vis absorption and photoluminescence spectra are shown in Figure 7-67.



Figure 7-46 Samples of 10^{-4} M compound 19 (left) and compound 20 (right) in varying spiked mixtures of THF : deionised water ranging from 0% vol water on the left to 95% on the right.

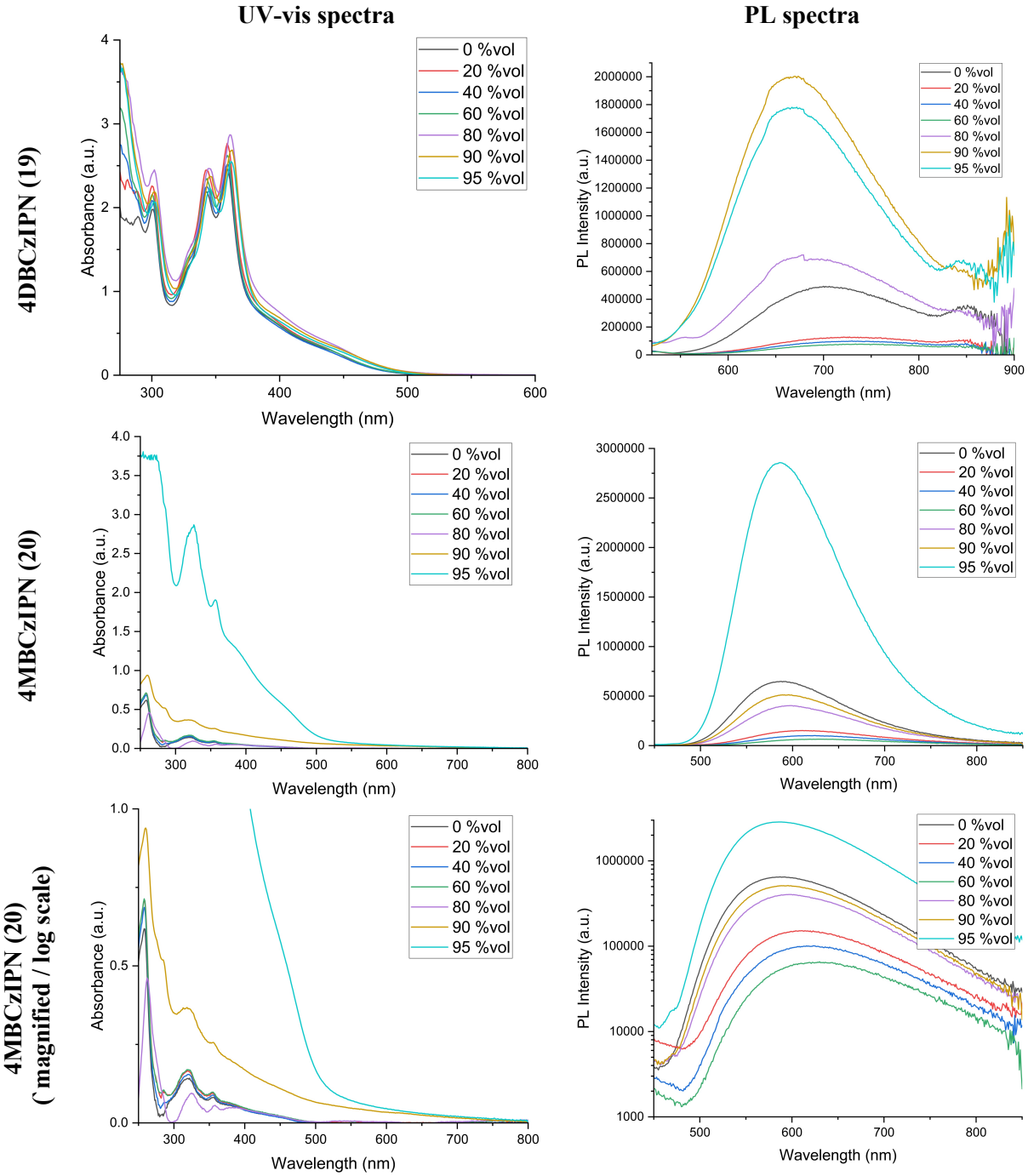


Figure 7-47 UV-vis absorption (left) and PL (right) spectra for compound 19 (top) and compound 20 (bottom two rows) in tetrahydrofuran spiked with different volumes of deionised water.

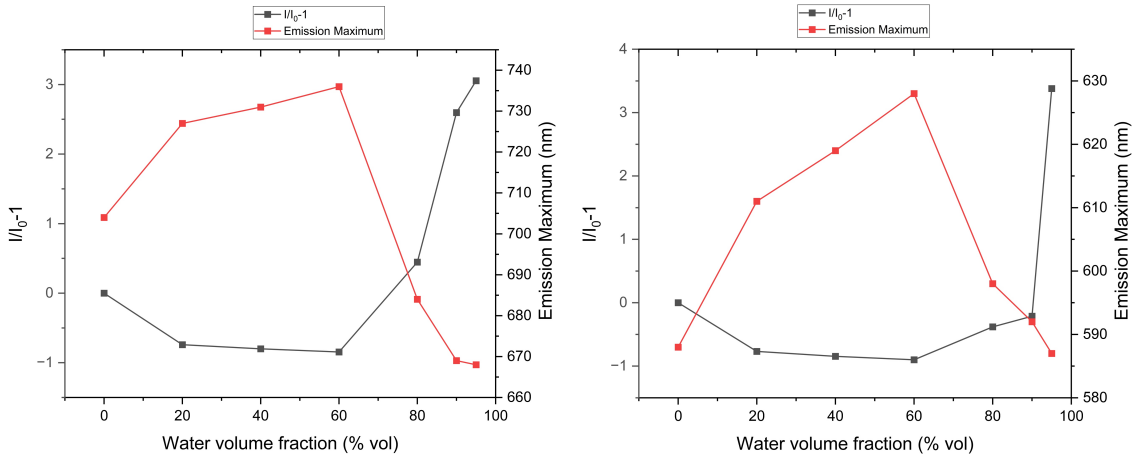


Figure 7-48 Change in emission intensity and emission wavelength shift with water volume fraction f_W for compound 19 (left) and compound 20 (right).

The AIE properties of compounds **19** and **20** were explored in tetrahydrofuran solutions, and the influence of water volume fraction on emission intensity shown in Figure 7-48. The PL intensity was low in pure THF for both compounds, decreasing further at low water spiking concentrations of $f_W \leq 60\%$ vol. Beyond this concentration the PL intensity increases dramatically for compound **19** until 95% vol, whereas for compound **20** the increase is gradual between 60 – 90% vol, before increasing dramatically at 95% vol. This emission enhancement reveals the AIE characteristics of the two compounds. For both compounds there is a red shift in emissions going from 0% vol to 60% vol. For compound **19** the red shift is 32 nm (shifting from 704 nm to 736 nm), followed by a blue shift at higher water concentrations to 668 nm (a shift of 68 nm). For compound **20**, the red shift is 40 nm at lower concentrations (going from 544 nm to 628 nm). This is followed by a blue shift of 41 nm to 587 nm by 95% vol. The bathochromic shifts are to be expected as, going from 0 to 60% vol, the solvent polarity is increasing (since water is more polar than THF). The hypsochromic shift beyond 60% vol is ascribed to AIE and formation of aggregates of the emitter material[372].

In both cases, the PL wavelength in the $f_W = 95\%$ vol samples is much closer to the thin film emission wavelengths of these compounds, indicating that during aggregation, crystalline or amorphous particles of compounds **19** and **20** are forming.

In the absorption spectra for compound **19**, the main absorption peak remains at 359 nm as the water fraction increases from 0% vol to 60% vol, however beyond this concentration it gradually increases by 4 nm to 363 nm. This suggests the potential formation of J-aggregates of this compound[373]. For compound **20**, the main absorption peak does not change in wavelength regardless of the water fraction concentration, however as more water is added,

the UV-vis absorption spectra become broader and more indistinct, indicating amorphous aggregation. The onset of AIE for compound **19** occurs at a lower water fraction concentration than compound **20** owing to its bulkier, quasi-helical donor moieties.

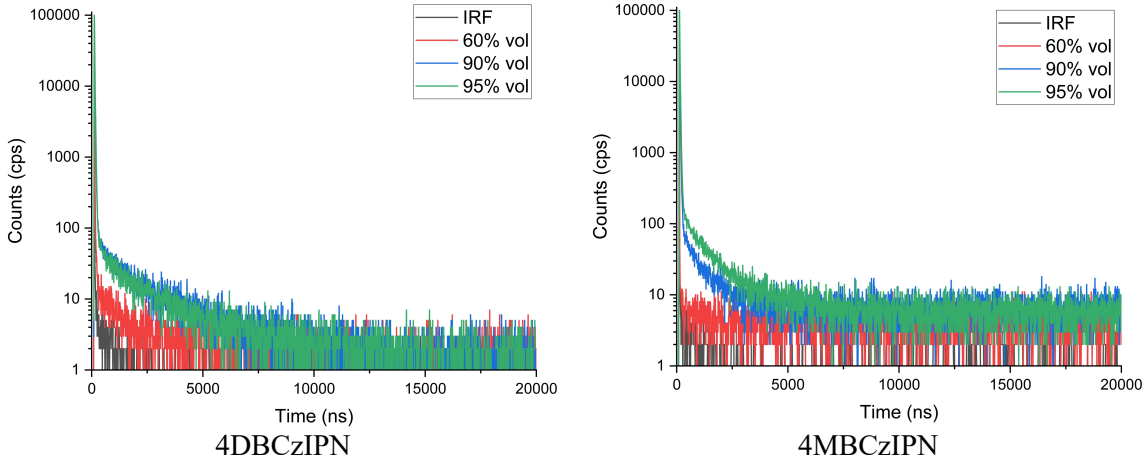


Figure 7-49 TCSPC plots for compound 19 (left) and compound 20 (right) of degassed solutions of THF : water looking at the transition concentrations 60%, 90% and 95% vol.

TCSPC measurements were performed under argon for the 60% vol, 90% vol and 95% vol samples to observe how the nature of the emission lifetimes changes as the aggregation effects increase. The TCSPC plots are shown in Figure 7-49 and the fittings are summarised in Table 7-22.

Table 7-22 Summary of the prompt and delayed component of the TCSPC measurements for compounds 19 and 20 at varying water concentrations in THF.

	4DBCzIPN (19)		4MBCzIPN (20)	
f_W (% vol)	τ_p (ns)	τ_d (ns)	τ_p (ns)	τ_d (ns)
60	8.81	776.6	8.79	119.4
90	19.4	1776.7	16.8	460.7
95	20.1	1846.2	19.1	741.9

In compound **19**, the TCSPC decays are all tri-exponential, with emission at $f_W = 60\%$ having a prompt component of 8.81 ns and a delayed component of 776.6 ns. This increases significantly at higher water fractions, reaching a prompt lifetime of 20.1 ns and delayed lifetime of 1.8 µs at $f_W = 95\%$. For compound **20**, the emission at $f_W = 60\%$ is bi-exponential, with a prompt component of 8.79 ns and a delayed component of 119.4 ns. As f_W increases, this becomes tri-exponential, yielding a prompt lifetime of 19.1 ns and delayed lifetime of 741.9 ns at $f_W = 95\%$. The increase in delayed component upon the formation of aggregates demonstrates that the aggregates possess TADF character.

7.4 Thermochromism

During melting point analysis, 2DBCzPN (**18**) was noticed to possess significant thermochromism from yellow to orange-red.

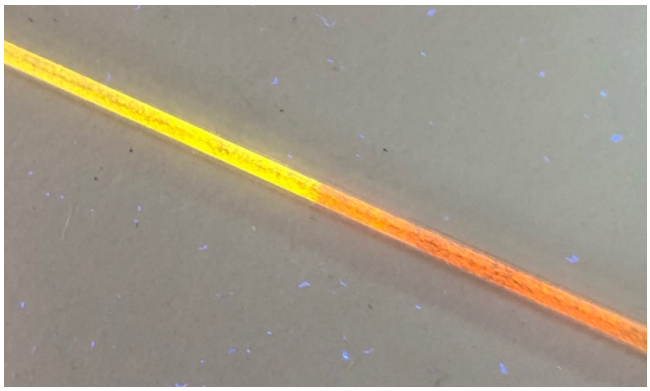


Figure 7-50 2DBCzPN (18) in a capillary tube after heating. The yellow fluorescence comes from the un-heated material (which was sticking out of the melting point apparatus) and the orange being the heated polymorph. Image was taken whilst the capillary tube was exposed to 365 nm UV light.

Considering the potential flexibility in the structure of 2DBCzPN (**18**), and potential for interactions between molecules in the solid state given the extended aromatic carbazole systems, thermochromic and mechanochromic behaviour was investigated.

Two quartz substrates were prepared with a 5 mg/mL solution of compound **18** drop-cast from dichloromethane.

The first substrate was measured as-is, whilst the second was annealed with a heat gun (T >300°C) for 2 minutes. The material was observed to turn orange, both physically and from its fluorescence spectrum under UV. UV-vis absorption, PL, TCSPC and PLQY measurements were performed on both substrates, then the annealed substrate was treated with dichloromethane fumes for 4 days (supported on a phial inside a jar partly filled with dichloromethane). Photophysical measurements were then repeated on the substrate after 4 days and are shown in Figure 7-51 and summarised in Table 7-23.

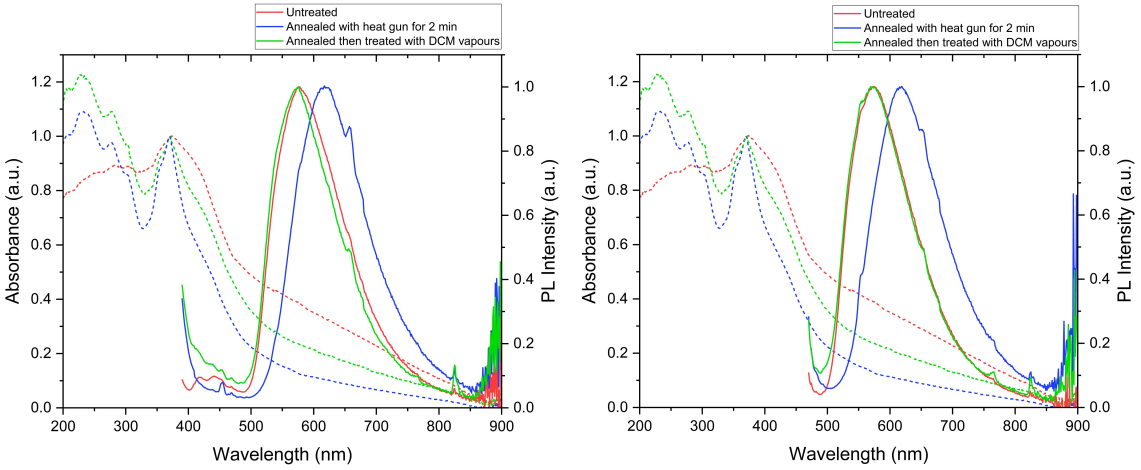


Figure 7-51 UV-vis absorbance and PL spectra of thermochromic samples of compound 18 drop-cast onto quartz substrates. Excited at 370 nm (left), excited at 450 nm CT peak (right).

Table 7-23 Photophysical data from thermochromic studies of drop-cast thin films of compound 18.

Sample type	λ_{abs} (nm)	λ_{PL} (nm)*	FWHM (nm)*	PLQY (%) (air)	τ_p (ns)	τ_d (ns)
Untreated	371	576 / 574	134 / 126	5.0	18.1	35.5
Annealed with heat gun for 2 minutes	371	620, 657 / 627, 651	135 / 134	5.8	14.4	34.6
Annealed then treated with CH_2Cl_2 vapours for 4 days	371	576 / 573	126 / 127	0.9	12.9	29.5

**360 nm excitation / 450 nm excitation*

The lack of a significant change in PLQY after heating suggests good stability of the material when undergoing thermochromic change. However, the decrease observed after treatment with dichloromethane is likely due to damage to the film over time with handling.

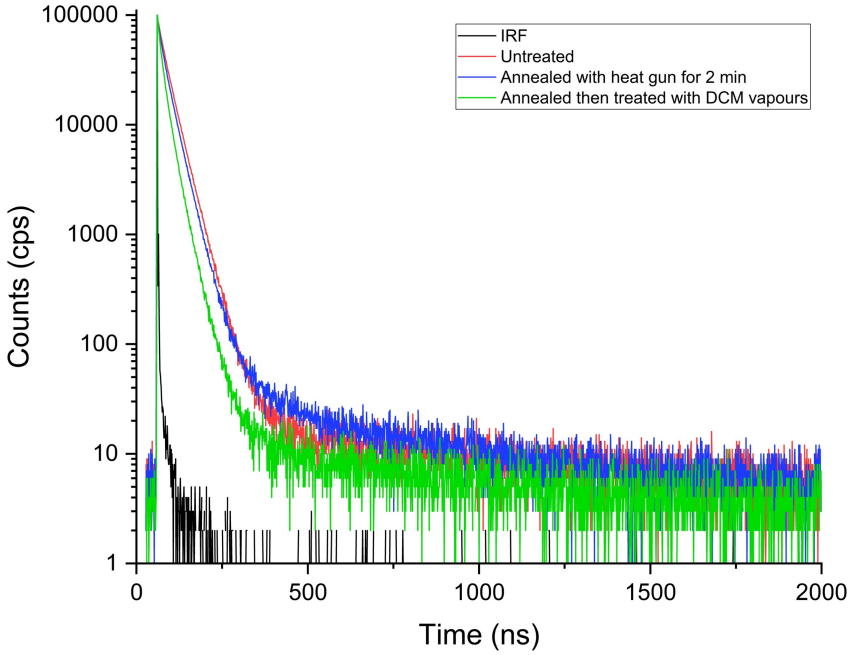


Figure 7-52 TCSPC plot of the three thermochromic samples of compound 18 excited with a 450 nm laser.

When treated with the heat gun, the lifetime of emissions from compound **18** changes very little, with τ_p decreasing by just 3.7 ns and τ_d decreasing by 0.9 ns (the TCSPC plot is shown in Figure 7-52). After treatment with dichloromethane fumes, a 1.5 ns decrease in τ_p is observed, along with a further 5.1 ns drop in τ_d. Since the changes are very small, it is more likely that they are also a result of degradation of the neat thin films through handling and chemical exposure.

Owing to the drop-casting method, there was some scattering noticed in the UV-vis absorption spectrum, but overall, there was no difference in the λ_{max} of 371 nm in each case. In the non-annealed sample, the fluorescence peak was 576 nm, with a FWHM of 134 nm. After annealing, the emission wavelength red shifts by 44 nm to 620 nm with the FWHM widening to 135 nm. After treatment with dichloromethane vapours, the emission peak shifts back to 574 nm, and the FWHM also returns to 126 nm, demonstrating excellent reversibility of the thermochromism in compound **18**.

To further investigate the temperature dependence of the emissions in the solid state, a small sample was placed in an aluminium pan on top of a hot plate. Directly above this was clamped a fibre optic spectrometer cable (Ocean Optics USB2000+ Miniature Fibre Optic Spectrometer) and a 365 nm UV torch was clamped into place and directed to illuminate the sample. The setup was shielded with a cardboard box covered in a black-out sheet. An initial measurement was performed at room temperature (25°C) yielding bright yellow

emissions. The hot plate was turned on, and the sample heated at several different temperatures for 5 minutes each to observe the thermochromic shift in emissions.

A dark measurement was performed with an empty pan, then measurements were performed at several temperatures (with the temperature maintained throughout the measurement). This allowed us to return to lower temperatures to see if the emission shifting was thermally reversible. Whilst this was found not to be the case, both compounds **18** and **19** exhibited fully reversible thermochromism when dissolved in dichloromethane after previously undergoing thermal annealing.

2DBCzPN (18)

Compound **18** showed the most noticeable thermochromism (to the human eye). The PL spectra are shown in Figure 7-53 and summarised in Table 7-24.

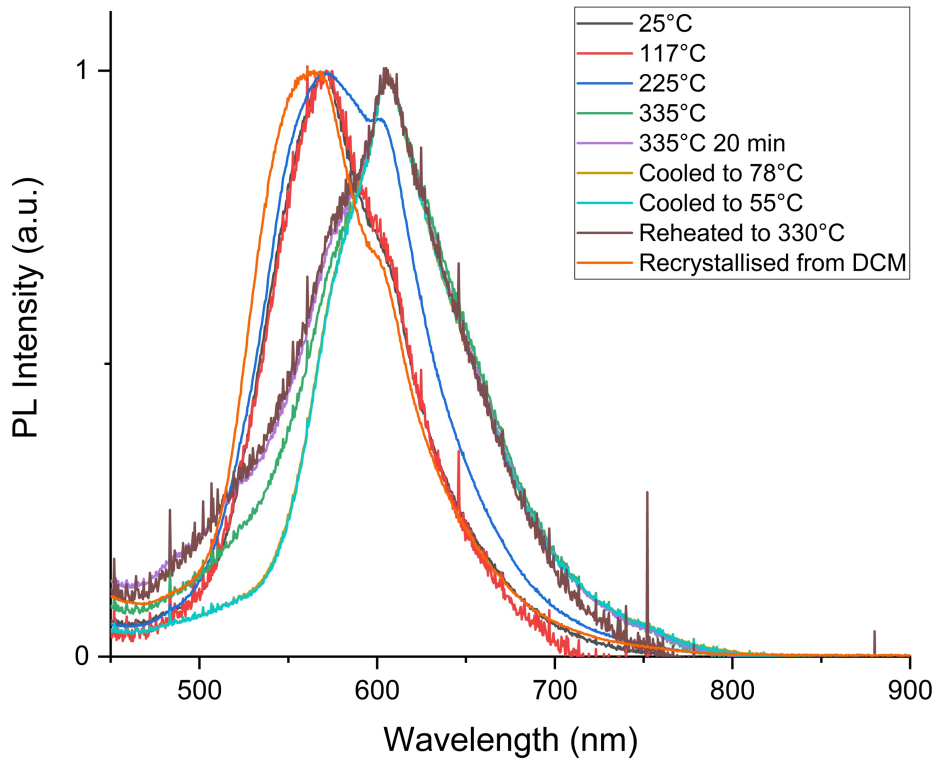


Figure 7-53 Fibre optic spectrometer measurements of compound 18 as a powder excited in an aluminium pan recorded at different thermal conditions. Excited with a 365 nm UV torch.

Table 7-24 Summary of the photophysical properties of the 2DBCzPN thermochromic measurments of compound 18 powder excited in an aluminium pan.

Sample treatment	λ_{PL} (nm)	FWHM
Untreated 25°C	571, 600 (sh)	66
Annealed to 117°C	571, 604 (sh)	84
Annealed to 225°C	571, 602	101
Annealed to 335°C 5 min	605, 582 (sh)	96
Annealed to 335°C 25 min	605, 578 (sh)	100
Cooled to 78°C	605, 585 (sh)	87
Cooled to 55°C	605, 580 (sh)	85
Reheated to 330°C	605, 577 (sh)	101
Recrystallised from CH_2Cl_2	563, 600 (sh)	90

At 25°C, there is a major emission peak at 571 nm, with a shoulder at 600 nm, with FWHM of 66 nm. Upon progressive heating, the major peak decreases in intensity, whilst the shoulder increases to become a second peak at 225°C and resolves into a new major peak at 605 nm by 335°C, with the original 571 nm peak becoming a shoulder, with the overall FWHM becoming 96 – 100 nm by this point. The FWHM is increasing as the emission spectra are seemingly the result of two emission peaks, with the 571 nm peak not decreasing to the same level that the 605 nm peak was at to begin with, giving the illusion of increasing spectral width. Exposing to dichloromethane fumes had no effect over 4 days (probably due to the powdered form), however dissolving and recrystallising from dichloromethane resets the emission spectrum back to its original yellow (563 nm), with the 600 nm shoulder diminished.

4DBCzIPN (19)

The blue-shifting thermochromism of compound **19** is shown below in Figure 7-54 and is summarised in Table 7-25.

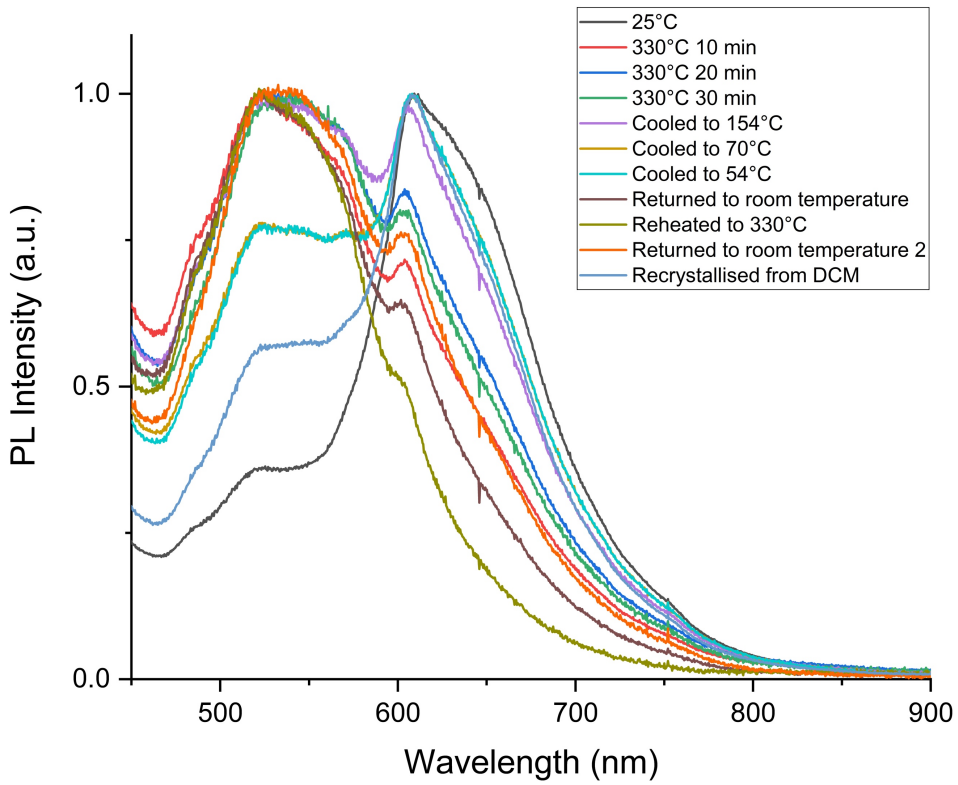


Figure 7-54 Fibre optic spectrometer measurements of compound 19 as a powder excited in an aluminium pan recorded at different thermal conditions. Excited with a 365 nm UV torch.

Table 7-25 Summary of the photophysical properties of the thermochromic measurements of compound 19 as a powder excited in an aluminium pan.

Sample treatment	λ_{PL} (nm)	FWHM
Untreated 25°C	608, 522 (sh), 644 (sh)	107
Annealed to 330°C for 10 min	520, 604	180
Annealed to 330°C for 20 min	523, 550 (sh), 604	196
Annealed to 330°C for 30 min	525, 540, 604	183
Cooled to 154°C	605, 523, 547 (sh), 567 (sh)	214
Cooled to 70°C	607, 570, 522	196
Cooled to 54°C	608, 569, 524	194
Returned to room temperature 20°C	523, 547 (sh), 601	155
Reheated to 330°C	523, 546 (sh), 600 (sh)	137
Returned to room temperature 20°C 2	603, 528, 542	162
Recrystallised from CH_2Cl_2	608, 648 (sh), 523	163

Neat films of compound **19** yielded PLQYs of 4.9% and 9.5% before and after being heated respectively, suggesting that the annealed polymorph is a more favourable conformation for emissions.

Neat films of compound **19** were prepared from 5% w.t. in dichloromethane and the resulting TCSPC plots shown in Figure 7-55 and the fittings summarised in Table 7-26.

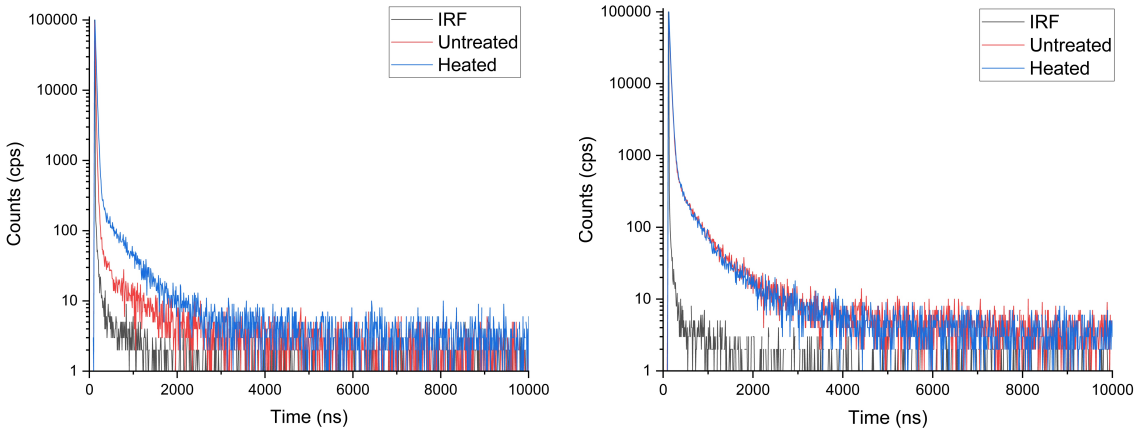


Figure 7-55 TCSPC plot of compound 19 prepared *via* drop-casting from dichloromethane on quartz substrates (left) and from toluene (right), with a 40 µs pulse 20 µs measurement. Response recorded prior to and after heating.

Upon heating (with a hot plate at 300°C for 2 hours, then heating with a heat gun a 450°C for 1 minute), the prompt component of the lifetime of the emissions increases by a factor of ~4 from 5.29 ns up to 20.3 ns. A dramatic increase is noticed for the delayed component, increasing by a factor of ~ 4.66 from 57.1 ns to 265.9 ns when heated.

Table 7-26 Summary of the lifetime fittings for the thin film of compound 19 from DCM and toluene, pre and post heating.

	Sample	τ_p (ns)	τ_d (ns)
From CH_2Cl_2	Untreated	5.29	57.1
	Post heating	20.3	265.9
From toluene	Untreated	29.6	512.7
	Post heating	30.3	467.6

When samples were prepared from toluene, both the prompt and delayed lifetimes increase substantially compared to the dichloromethane counterparts but do not change much upon heating. This suggested that the aggregation in the different polarity solvents had an effect on the arrangement of the molecules in the solid state, and that this orientation must result in similar environments (with the heating perhaps been insufficient to afford a complete transition to that produced by the action of toluene alone). Note that the lifetimes of the

toluene samples differ from those obtained in section 7.3.4. This is likely due to differences in the quality of the film morphology (experiments for both these sections were performed on different days with freshly prepared thin films). The films in section 7.3.4 were prepared from slightly more concentrated solutions (10% w.t.), whereas those in this section were 5% w.t. The difference in concentration was selected purely to obtain better quality films, but the overall difference between the dichloromethane and toluene films remained valid.

In an effort to gain a deeper understanding of the thermochromism in compounds **18** and **19**, thin films were prepared with each molecule doped at 5% w.t. in Zeonex. Thermochromic effects are often the result of changing the interactions between molecules such as overcoming π-π interactions. Held in a host matrix, the fluorescent molecules are held further apart, beyond the operational region of π-π interactions, therefore if such interactions are the reason for thermochromism, there should be a striking reduction in the thermochromic shift in emissions.

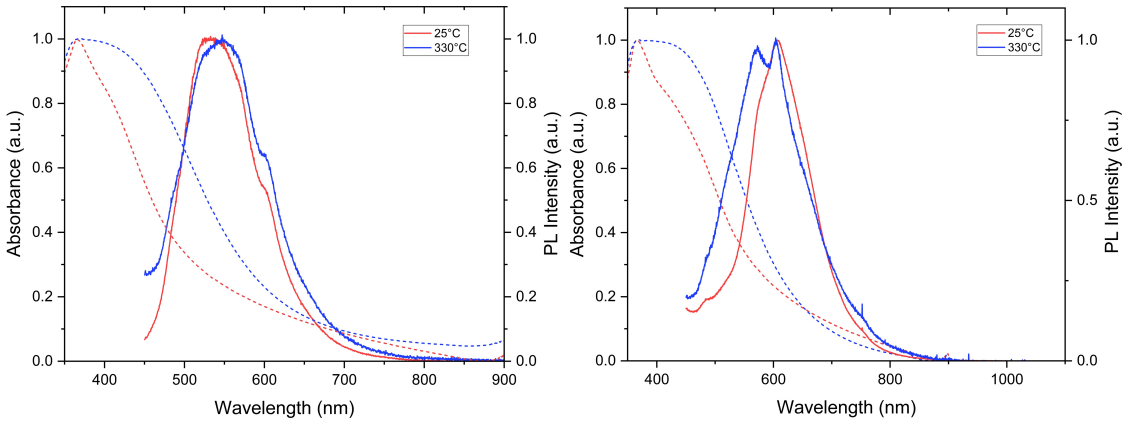


Figure 7-56 UV-vis absorption and PL Zeonex drop-cast thin films of compound 18 (left) and compound 19 (right). PL obtained *via* a fibre optic spectrometer with a 365 nm UV torch as the excitation source.

As can be seen from Figure 7-56, in both cases, the difference in emission profile before and after heating is negligible compared to the neat films (the slight differences can be ascribed to the slight melting or degradation to the Zeonex matrix at higher temperatures – evidenced by the broadening of the Zeonex absorption spectra).

Following the interesting thermochromic properties of compounds **18** and **19** being observed, it was decided that two further dibenzocarbazole based, multi-donor compounds would be synthesised. During the melting point analysis of DBCz-PS (**21**) and DBCz-BZPN (**22**), thermochromism was also noticed in the capillary tubes (with 3 or 4 components seen for compound **21** in Figure 7-57).

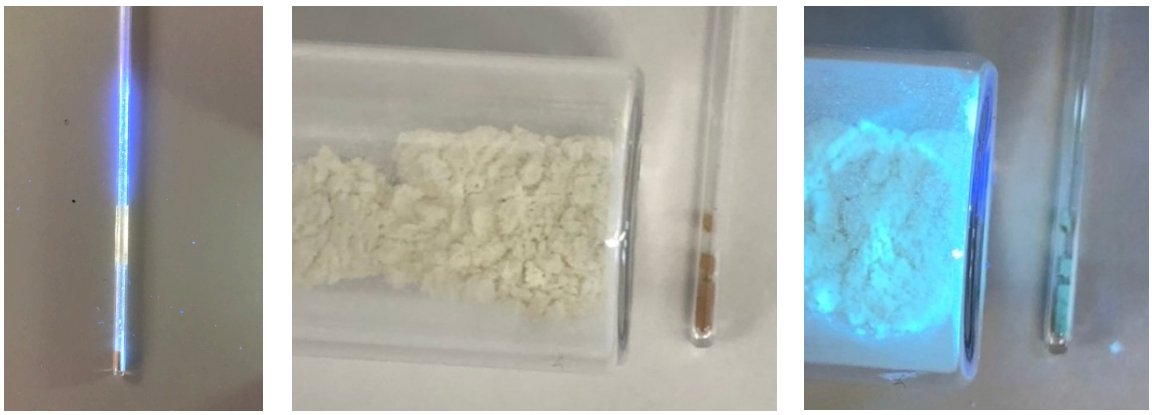


Figure 7-57 Left : compound 21 under UV after heating to 360°C in melting point apparatus. Note three different fluorescence colours. Middle compound 22 unheated (left) and heated (in capillary), note darkening of the material; Right compound 22 under UV, blue fluorescence turns green after heating to 360°C.

DBCz-PS (21)

For the data in Figure 7-58, compound **21** was heated in an aluminium pan and the PL spectra recorded at different temperatures, and the results are summarised in Table 7-27.

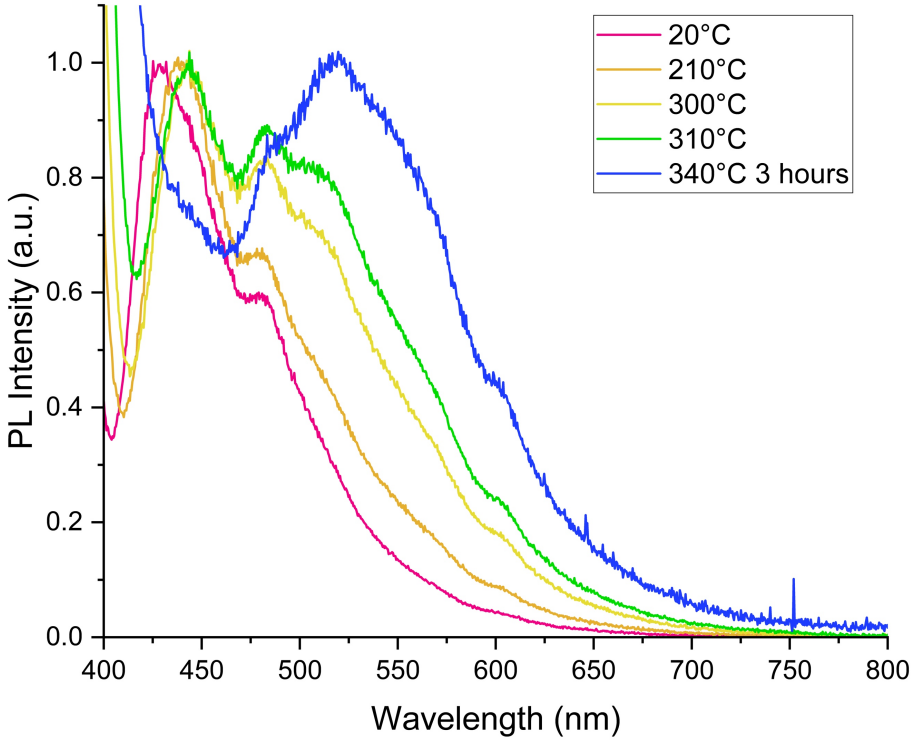


Figure 7-58 Fibre optic spectrometer measurements of compound 21 powder excited in an aluminium pan recorded at different temperatures. Excited with a 365 nm UV torch.

A clear additional peak is observed at 516 nm upon heating at the expense of the original 429 nm peak, suggesting structural changes in the bulk material. The broadening of the peak also suggests the new emission structure is of greater CT character.

Table 7-27 Summary of thermochromism spectra for compound 21 heated in an aluminium DSC pan.

Sample treatment	λ_{PL} (nm)	FWHM
20°C	429, 479sh	80
210°C	439, 479sh, 604	87
300°C	443, 482, 506sh, 600sh	122
310°C	443, 482, 506sh, 600sh	153
340°C	516, 489sh, 555sh, 600sh	~180*

*Estimating based on previous temperatures owing to scattering of the excitation peak hiding the onset.

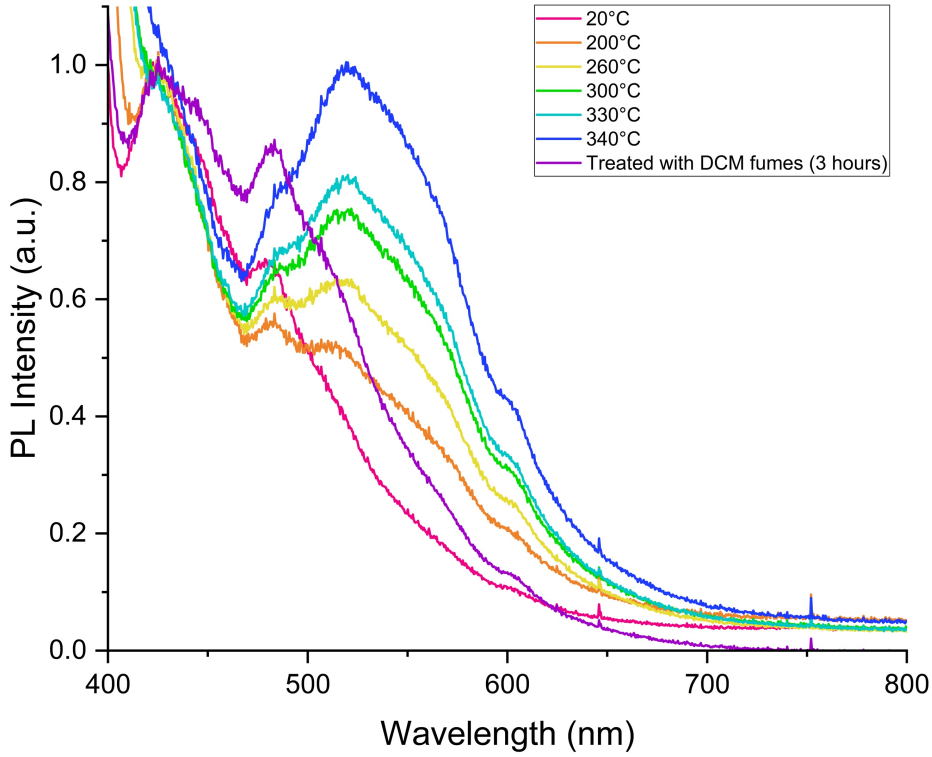


Figure 7-59 Fibre optic spectrometer measurements of compound 21 neat thin films on quartz substrates at different thermal conditions. Excited with a 365 nm UV torch.

Reducing the homogeneity of a bulk powder to a neat thin film shows that this transition is also occurring when compound **21** is in a much more homogeneous environment (see Figure 7-59 and Table 7-28 for a summary.

Table 7-28 Summary of thermochromism spectra for compound 21 thin films on quartz substrates.

Sample treatment	λ_{PL} (nm)
20°C	425, 480
200°C	426, 480, 512sh, 600sh
260°C	423, 485sh, 518, 553sh, 600sh
300°C	518, 485sh, 560sh, 600sh
330°C	518, 485sh, 560sh, 600sh
340°C	518, 485sh, 560sh, 600sh
Treated with DCM Vapours for 3 hours	425, 480, 600sh

*Not possible to measure FWHM due to overlap with excitation scattering.

The PLQY prior to heating was measured as 15% (in argon), however after heating it drops to 3.1%. Either heating results in significant degradation of compound **21** or this represents a new polymorph with much poorer emissive properties.

DBCz-BZPN (22)

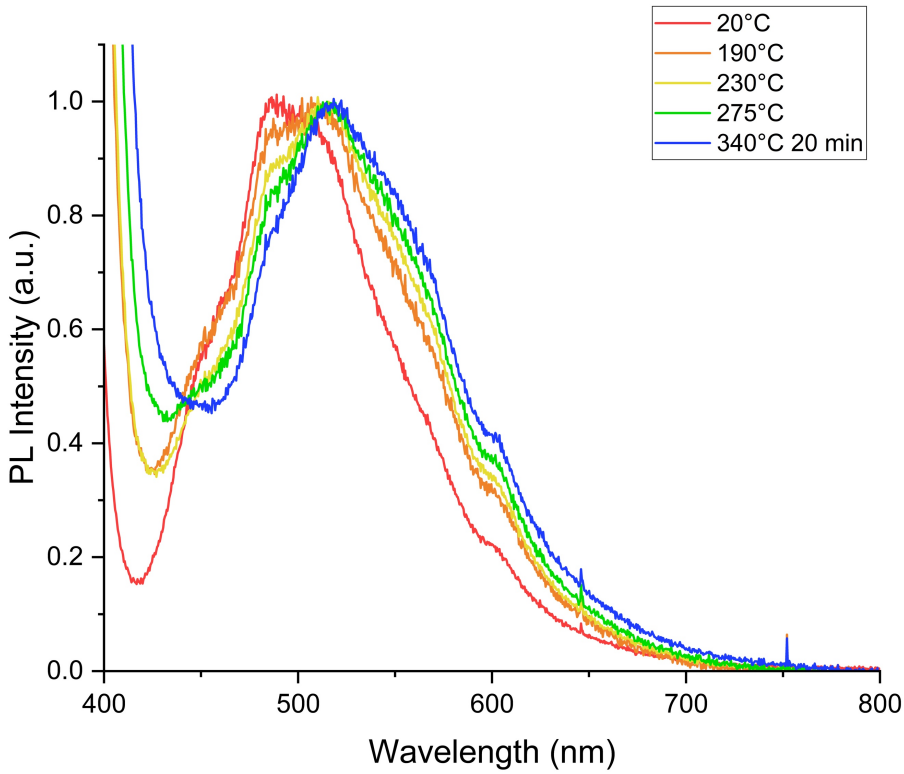


Figure 7-60 Fibre optic spectrometer measurements of compound 22 as a powder excited in an aluminium pan recorded at different thermal conditions. Excited with a 365 nm UV torch.

Swapping the diphenyl sulfone acceptor of compound **21** for a benzophenone acceptor in compound **22** produces much less noticeable thermochromism in the powdered form, as can be seen in Figure 7-60 and Table 7-29.

Table 7-29 Summary of thermochromism spectra for compound 22 heated in an aluminium DSC pan.

Sample treatment	λ_{PL} (nm)	FWHM
20°C	488, 456sh, 510sh, 597sh	112
190°C	508, 488sh, 455sh, 550sh, 598sh	133
230°C	514, 489sh, 456sh, 550sh, 598sh	129
275°C	516, 490sh, 546sh, 598sh	130
340°C	519, 490sh, 550sh, 599sh	122

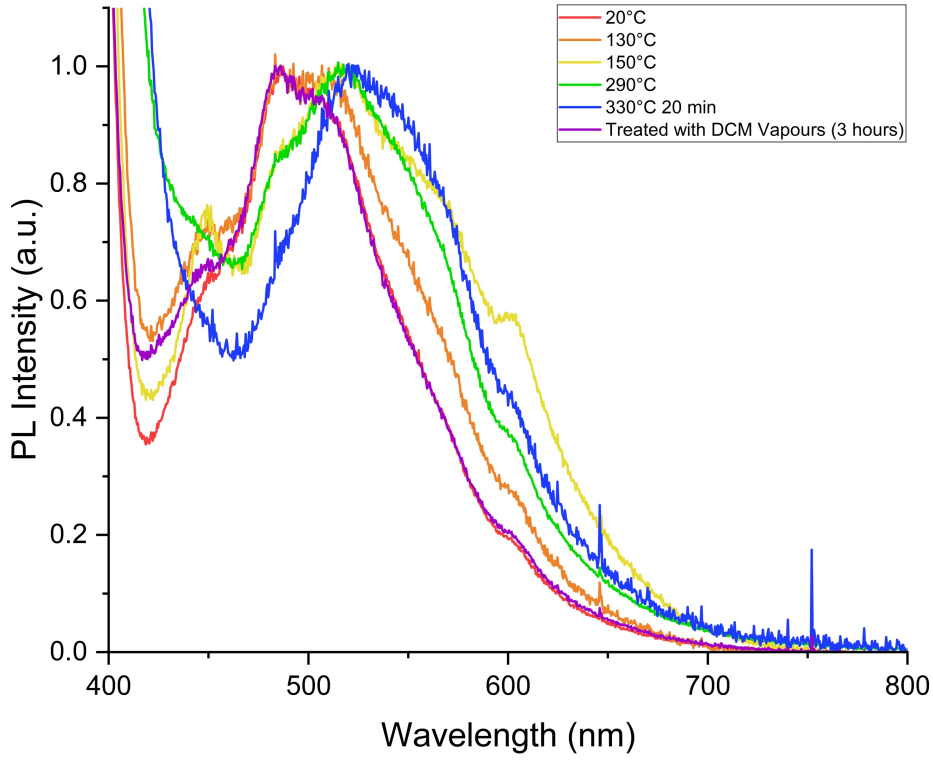


Figure 7-61 Fibre optic spectrometer measurements of compound 22 neat thin films on quartz substrates at different thermal conditions. Excited with a 365 nm UV torch.

However, when swapping to neat films of compound **22** in Figure 7-61, the thermochromism is much more pronounced. This is likely due to better morphology and contact with the heat source permitting the full thermochromic transition to occur. Table 7-30 summarises the main emission properties.

Table 7-30 Summary of thermochromism spectra for compound 22 thin films on quartz substrates.

Sample treatment	λ_{PL} (nm)	FWHM
20°C	487, 453sh, 510sh, 597sh	119
130°C	487, 510, 455sh, 597sh	156
150°C	515, 448, 448sh, 560sh, 600sh	178
290°C	516, 448sh, 560sh, 600sh	~130*
330°C	521, 486sh, 560sh, 600sh	127
Treated with DCM vapours	485, 450sh, 505sh, 550sh, 600sh	137

*Estimating based on previous temperatures owing to scattering of the excitation peak hiding the onset.

PLQY prior to heating for compound **22** is 5.5% and after heating decreases to 2.4%. Both compounds **21** and **22** exhibit a drop in PLQY along with red-shifted and broadened emissions upon heating.

To investigate whether steric effects from the quasi-helical bulk of the 7H-dibenzo[c,g]carbazole donors are to blame for the thermochromism, a less sterically hindered mono-benzo carbazole derivative of 4DBCzIPN (**19**) was synthesised and its thermochromic properties are herein reported.

As before, 4MBCzIPN (**20**) was first heated in an aluminium DSC pan under exposure to a 365 nm UV torch and its photoluminescence measured with a fibre optic spectrometer at varying temperatures (see Figure 7-62).

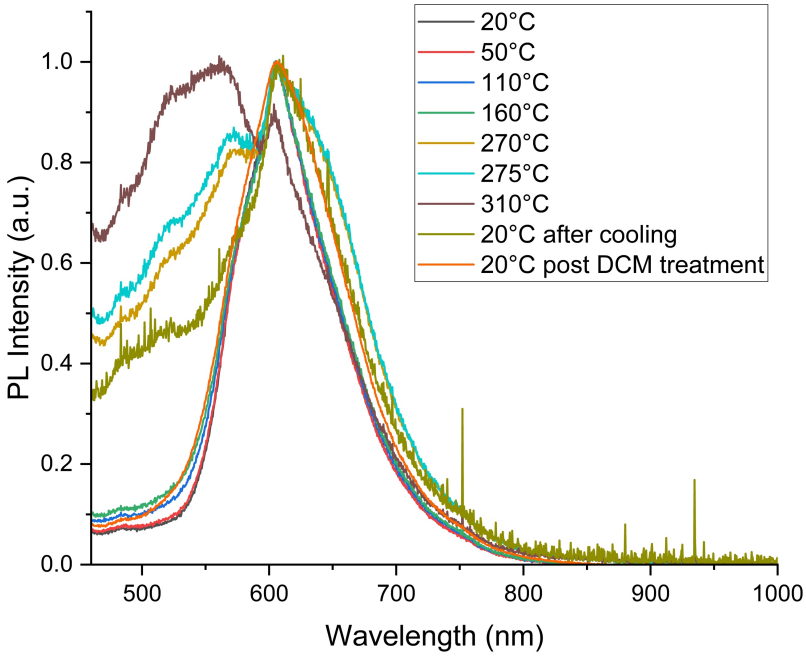


Figure 7-62 Fibre optic spectrometer measurements of compound 20 as a powder excited in an aluminium pan recorded at different thermal conditions. Excited with a 365 nm UV torch.

A major emission peak is present through all temperatures at 606 nm, however as the temperature increases, a shoulder emission appears at ~570 nm by 270°C, becoming the dominant emission at 562 nm by 310°C, with a shoulder at 522 nm. At this temperature, the material appeared glass-like and slightly molten – which is at odds with the melting point observed in DSC. Upon cooling back to room temperature, the blue-shifted emission diminishes, with the dominant emissions occurring at 606 nm once more, with a minor but broad shoulder at 522 nm. After recrystallising the contents of the pan from dichloromethane, the emissions returned to a single peak at 606 nm, demonstrating fully reversible thermochromism in compound **20**, albeit with a slightly wider FWHM. See Table 7-31 for a more detailed summary.

Table 7-31 Summary of thermochromism spectra for compound 20 heated in an aluminium DSC pan.

Sample treatment	λ_{PL} (nm)	FWHM
20°C	606	89
50°C	606	89
110°C	606	92
160°C	606	95
270°C	606, 571, 522(sh)	185
275°C	606, 571, 522(sh), 483(sh)	204
310°C	606, 571, 522(sh), 483(sh)	212
Cooled to 20°C	606, 568(sh), 522(sh), 491(sh)	123
Recrystallised from DCM	606	104

Thin films of neat compound **20** were prepared from toluene solution *via* drop-casting onto a quartz substrate and PL spectra obtained at varying temperature, along with PLQY measurements and TCSPC pre- and post-heating (see Figure 7-63 and Table 7-32).

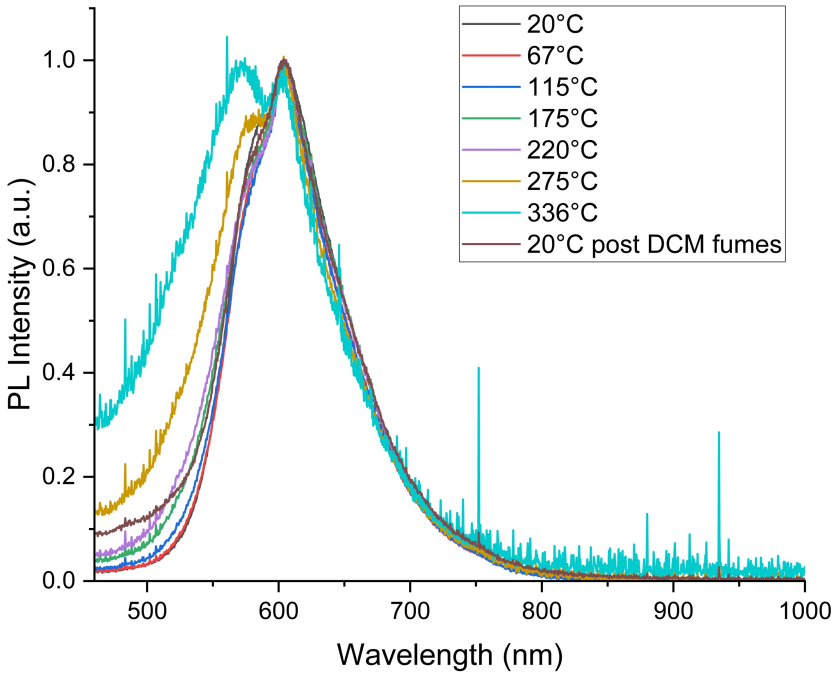


Figure 7-63 Fibre optic spectrometer measurements of compound 20 neat thin films on quartz substrates at different thermal conditions. Excited with a 365 nm UV torch.

Table 7-32 Summary of thermochromism spectra for thin films of compound 20 on a quartz substrate.

Sample treatment	λ_{PL} (nm)	FWHM
20°C	604, 583(sh)	95
67°C	604, 583(sh)	90
115°C	604, 583(sh)	90
175°C	604, 583(sh)	99
220°C	604, 583(sh)	100
275°C	604, 580(sh)	106
336°C	604, 580	141
20°C post DCM fumes	604, 583(sh)	97

For compound **20**, the PLQY prior to heating was 10.7% and decreased after heating to 6.0%.

Additionally, TCSPC measurements under argon were performed on a thin film of compound **20** pre- and post-heating.

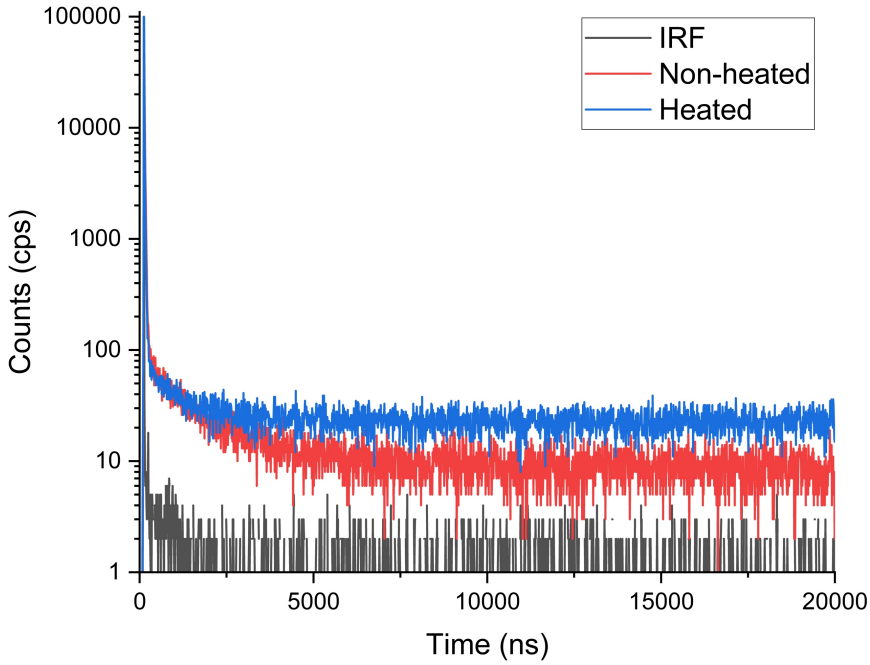


Figure 7-64 TCSPC measurement for compound 20 before and after heating a thin film on a quartz substrate.

After heating, the prompt lifetime of emissions seems to increase slightly, although there is a minor decrease in the delayed component (see Figure 7-64 and Table 7-33).

Table 7-33 Summary of the TCSPC measurement for compound 20 before and after heating a thin film on a quartz substrate.

	Sample	τ_p (ns)	τ_d (ns)
4MBCzIPN	Untreated	17.4	1373.7
	Post heating	23.2	1171.0

In order to address the influence of the polarity of the solvent used to prepare the thin films, samples of 4DBCzIPN (**19**) and 4MBCzIPN (**20**) were prepared via drop-casting from dichloromethane and toluene solvents.

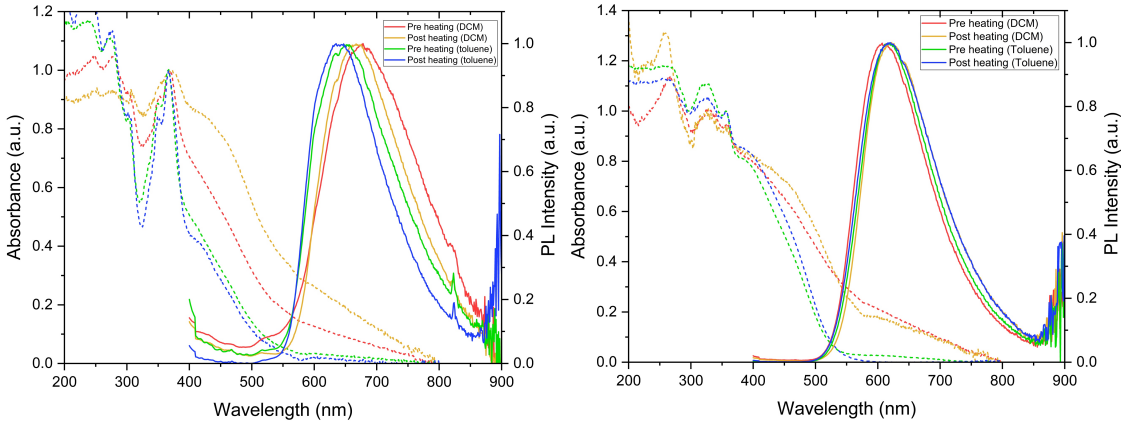


Figure 7-65 Comparison of the UV-vis absorption and PL spectra of thin films of compounds 19 (left) and 20 (right) when prepared from either dichloromethane or toluene prior to and after heating.

Thermochromism is clear regardless of solvent used to prepare the films (as illustrated in Figure 7-65), though how big a transition is largely dictated by the environment the molecules find themselves in upon solvent evaporation. Heating under the conditions used appears insufficient for complete conversion of the dichloromethane starting aggregation into one identical to that of toluene, once again suggesting that interactions between the solvent and the emitter are the primary control of orientation in the dried solid state. Interestingly, the UV-vis absorption spectra for the dichloromethane prepared sample post heating broadens significantly. This may be due to increased disorder caused by molecular reorientation yielding increased scatting effects.

With the same experiments performed with compound **20**, the differences in emissions are much less noticeable. This is likely due to reduced impact of solvent polarity on the crystallisation process of compound **20** compared to compound **19**. The impact of solvatochromism from residual solvent can be largely ruled out in both cases, as the same conditions were used for both molecules, yet here the shifting is much less, especially so since the sample prepared from the more polar dichloromethane is blue-shifted compared to toluene (ever so slightly). Once again, after heating the dichloromethane sample, the shoulder of the UV-vis absorption spectra broadens, suggesting increased scattering due to disorder.

The thermochromic potential of each compound can be described in the order of increasing sensitivity: DBCz-BZPN (**22**) < 2DBCzPN (**18**) < 4MBCzIPN (**20**) < DBCz-PS (**21**) < 4DBCzIPN (**19**), where the 4CzIPN based compounds **19** and **20** exhibited negative thermochromism. This is summarised in Table 7-34.

Table 7-34 Shift in wavelength caused by heating each of the molecules studied.

Compound	Thermochromic shift in powder (nm)
2DBCzPN (18)	31
4DBCzIPN (19)	-85
4MBCzIPN (20)	-35
DBCz-PS (21)	87
DBCz-BZPN (22)	28

7.4.1 Powder X-ray diffraction measurements

All dibenzocarbazole based materials were subject to variable temperature X-ray powder diffraction to observe the changes in structure as the thermochromism progressed. Before and after the thermochromic transition in both cases, the XRD diffraction patterns are sharp and clear, suggesting well defined changes to the crystal morphology, and lack of amorphous structural disorder[282]. The monobenzocarbaozle derivative, 4MBCzIPN (**20**) was omitted owing to time constraints.

The two compounds, 2DBCzPN (**18**) and 4DBCzIPN's (**19**) powder XRD plots are shown in Figure 7-66 and Figure 7-67.

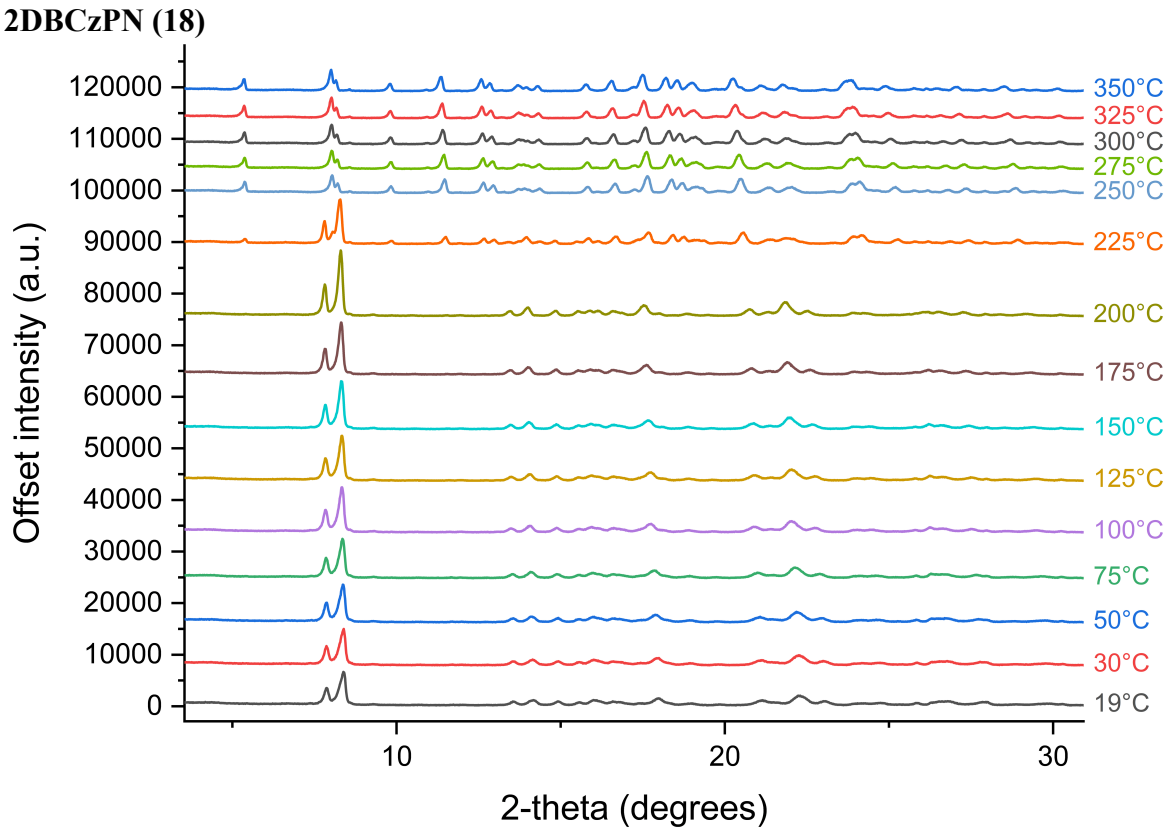


Figure 7-66 Variable temperature powder XRD plots for compound 18 ranging from 19°C to 350°C.

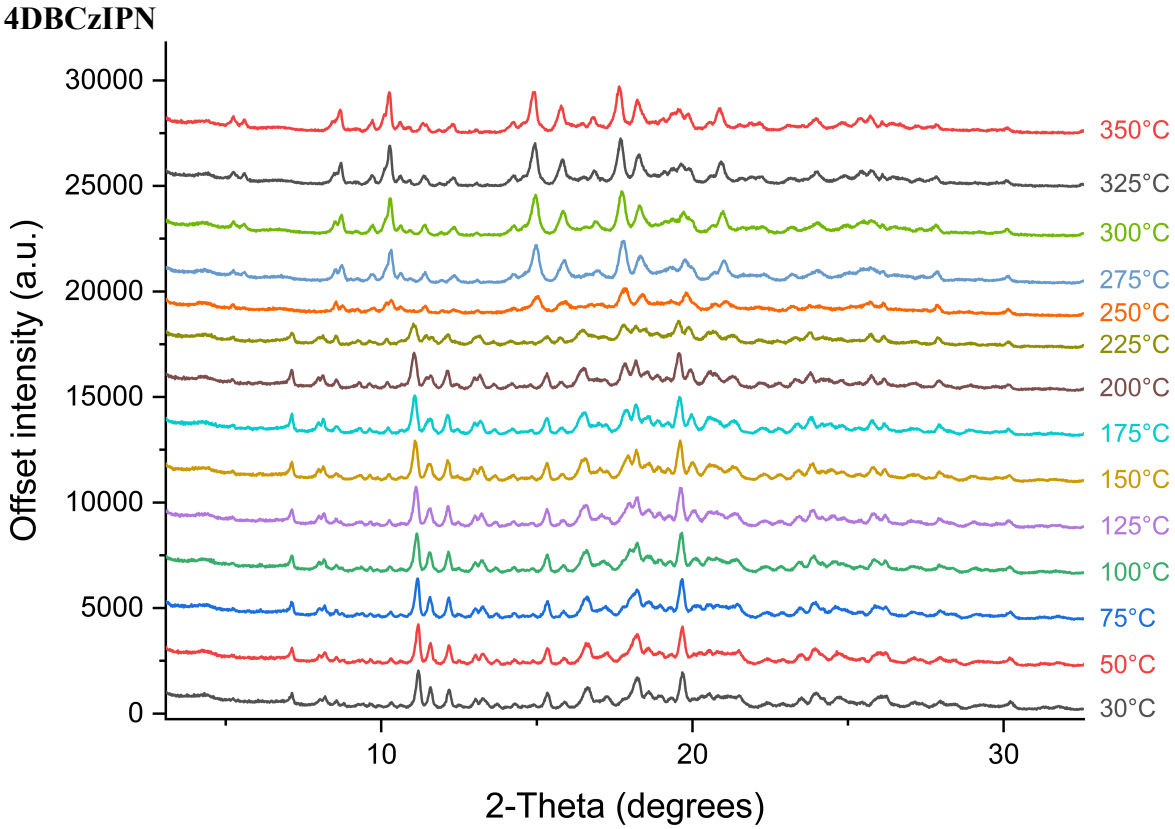


Figure 7-67 Variable temperature powder XRD plots for compound 19 ranging from 30°C to 350°C.

For compound **18**, a transition in crystal structure occurs between 225°C and 250°C, whereas compound **19** exhibits a crystal structure transition between 250°C and 275°C. This is in keeping with the observed transition in the DSC plots in which compound **18** possesses a transition at 240-250°C and compound **19** at 270°C.

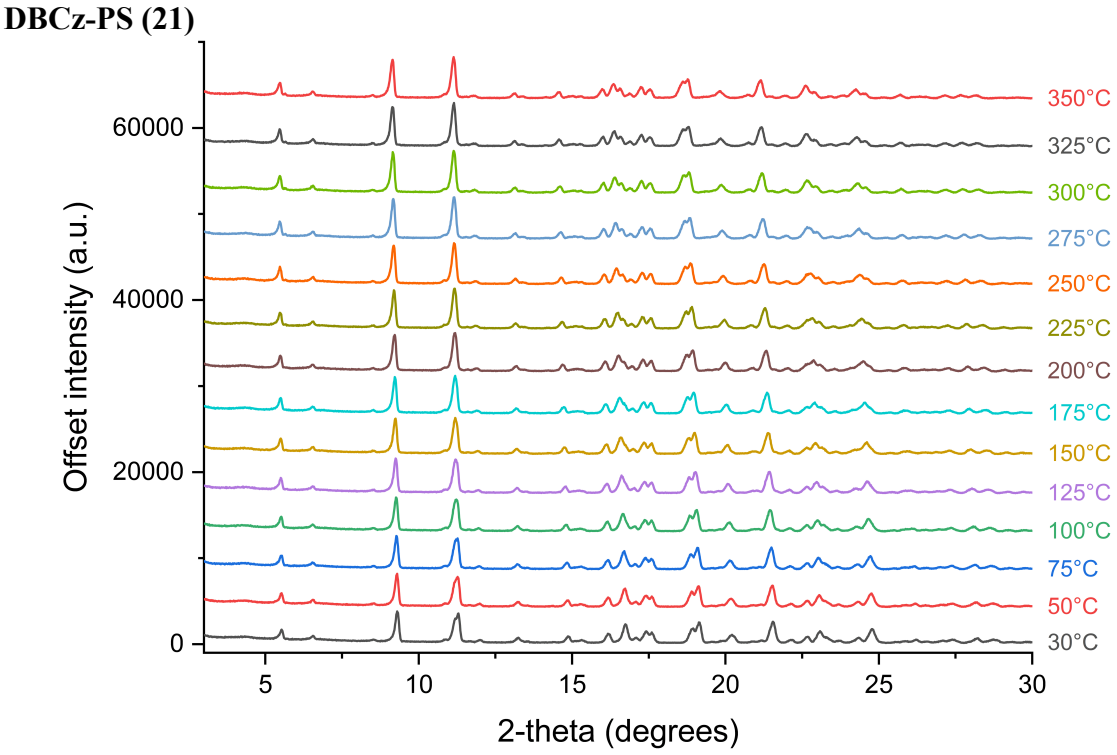


Figure 7-68 Variable temperature powder XRD plots for compound 21 ranging from 30°C to 350°C. The transition in this molecule is much more subtle.

Upon initial inspection, there appears to be little change in the apparent crystal structure for compound **21** (see Figure 7-68). However, closer inspection of the 15 – 30 2θ° region reveals a gradual change to the structures (see Figure 7-69 and Figure 7-70).

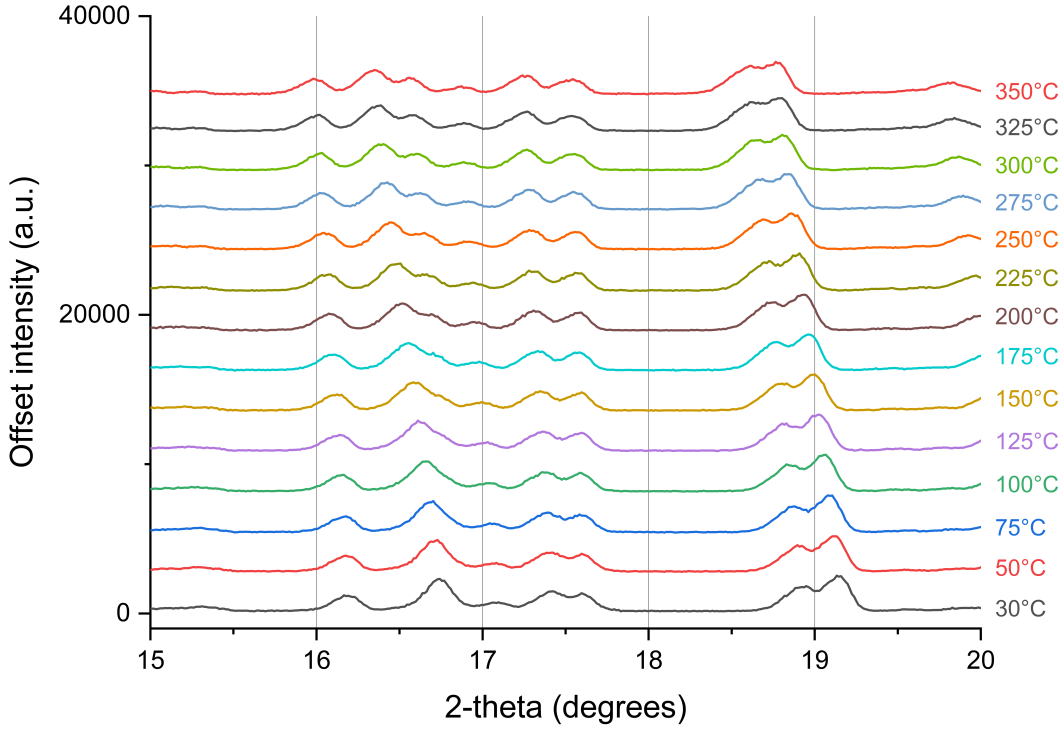


Figure 7-69 A close up view (15° – 20° 2*θ*) of variable temperature powder XRD plots for compound 21.

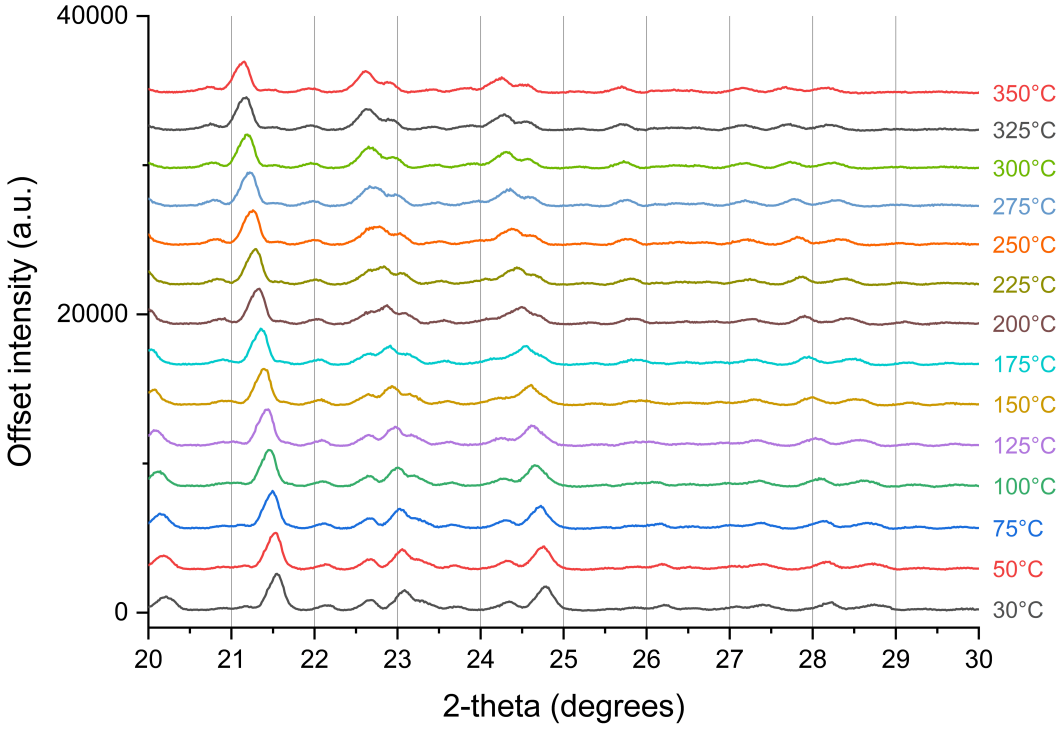


Figure 7-70 A close up view (20° – 30° 2*θ*) of variable temperature powder XRD plots for compound 21.

The transition appears complete by ~275°C, which is supported by the 270-273°C transition observed in the DSC plot for compound **21**. This is clearer still when focussing between the 30°C and 350°C patterns (see Figure 7-71).

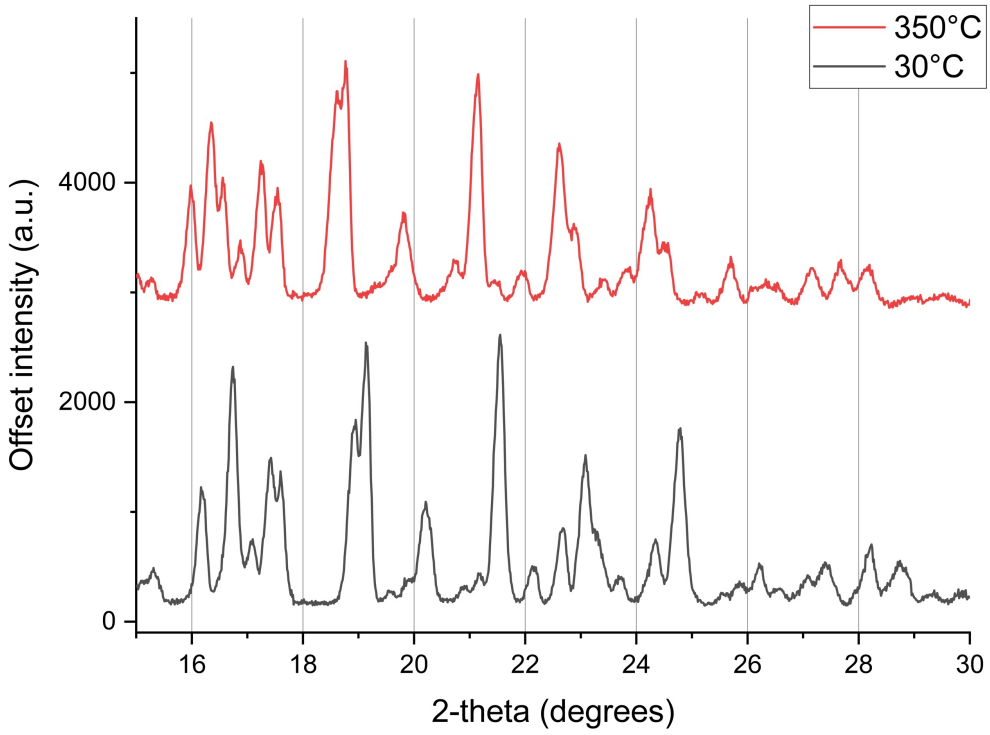


Figure 7-71 Comparing 30°C and 350°C powder XRD plots for compound 21 (from 15° – 30° 2*θ*).

Unlike the examples for compounds **18** and **19**, it seems that the transition to the thermochromic polymorph is gradual and proceeds even at lower temperatures.

To confirm that the transition is physical and not chemical, ^{1}H NMR spectroscopy was performed on pure DBCz-PS (**21**) and the same sample after heating (having exhibited thermochromism in its emissions when excited by UV), and is shown in Figure 7-72.

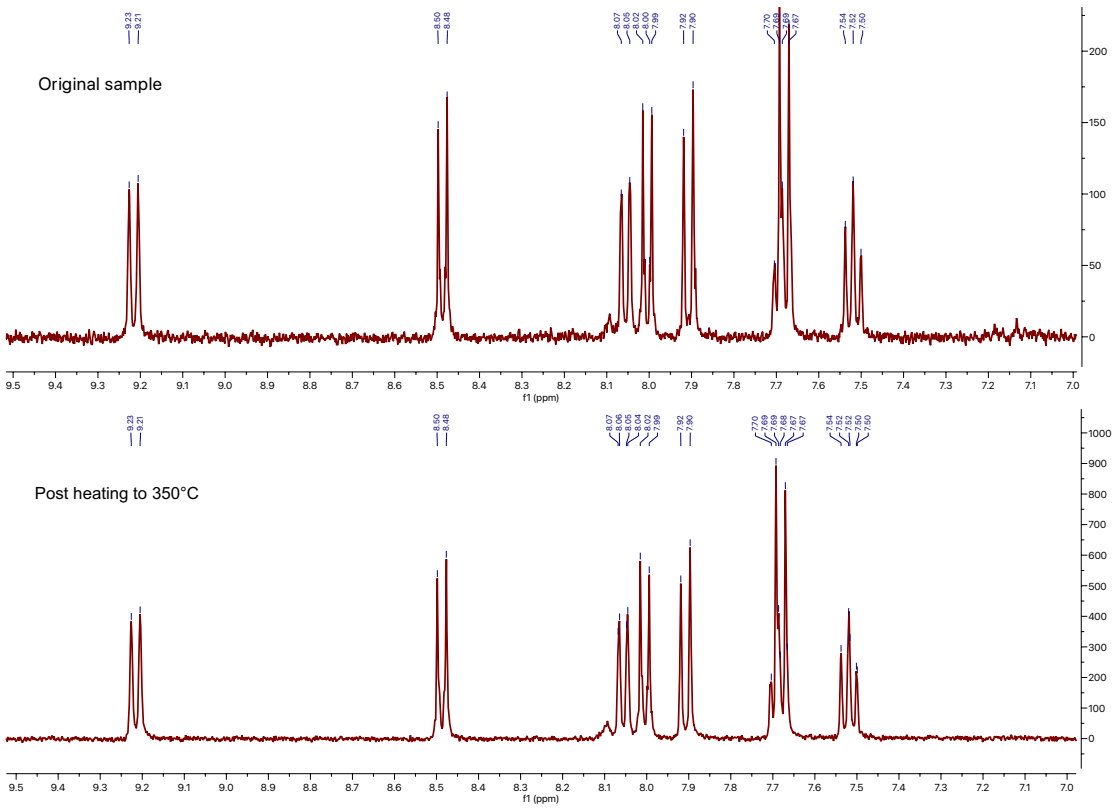


Figure 7-72 ^{1}H NMR spectra of the compound 21 sample prior and after heating to 350°C. Note the absence of any notable change.

Since there is no change in the proton NMR, we can safely say that no chemical change is occurring, and that the structural deviation resulting in thermochromic shifting in emissions is genuine.

DBCz-BZPN (22)

As with compound **21**, the thermochromic transition for compound **22** is difficult to see at first glance (see Figure 7-73).

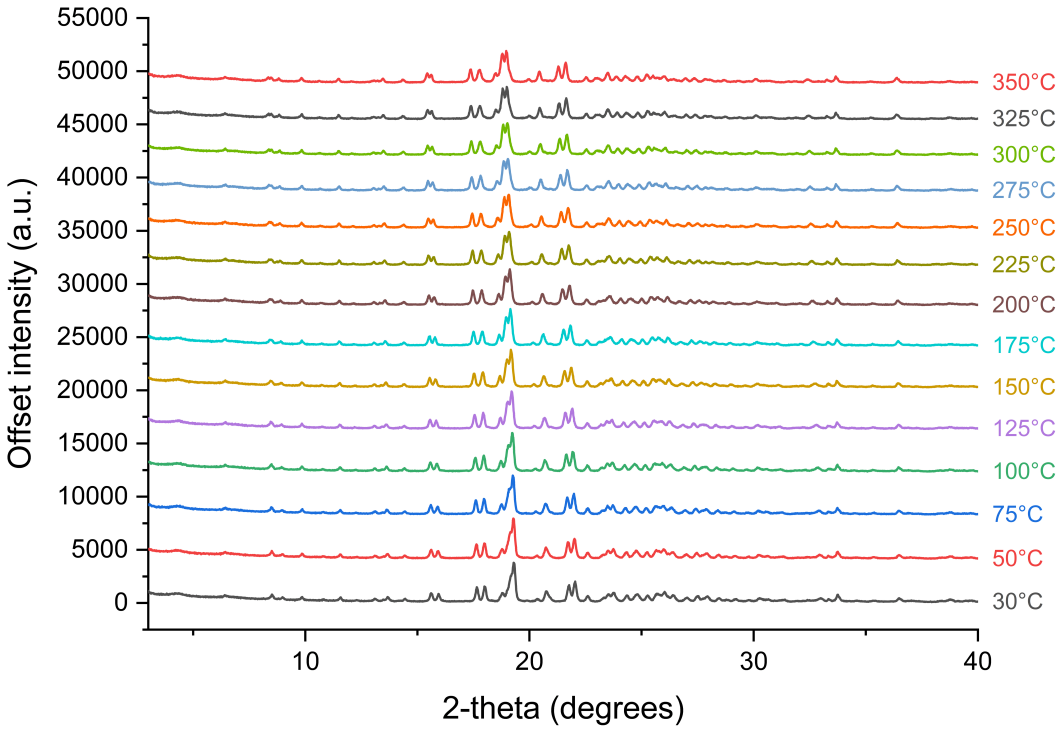


Figure 7-73 Variable temperature powder XRD plots for compound 22 ranging from 30°C to 350°C. As with compound 21, the thermochromic transition in this molecule is much more subtle.

Closer inspection of the 15 – 30 2θ° regions reveals it to be a gradual process as well (see Figure 7-74 and Figure 7-75).

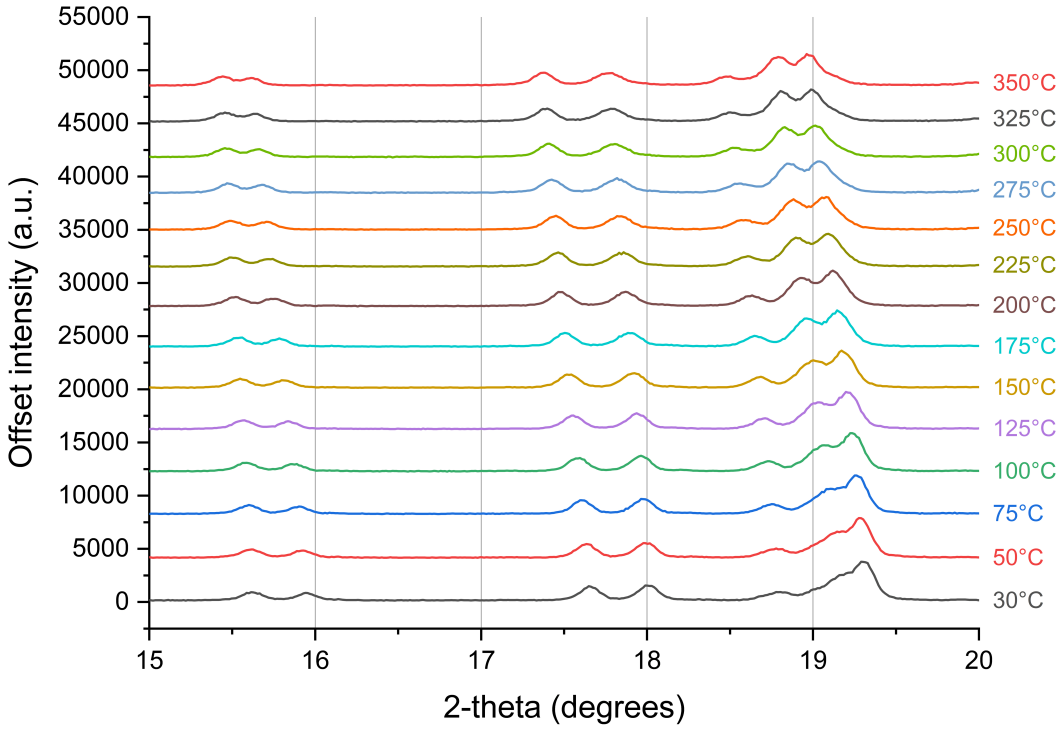


Figure 7-74 A close up view (15° – 20° 2*θ*) of the variable temperature powder XRD plots for compound 22, providing a better view of the thermochromic transition.

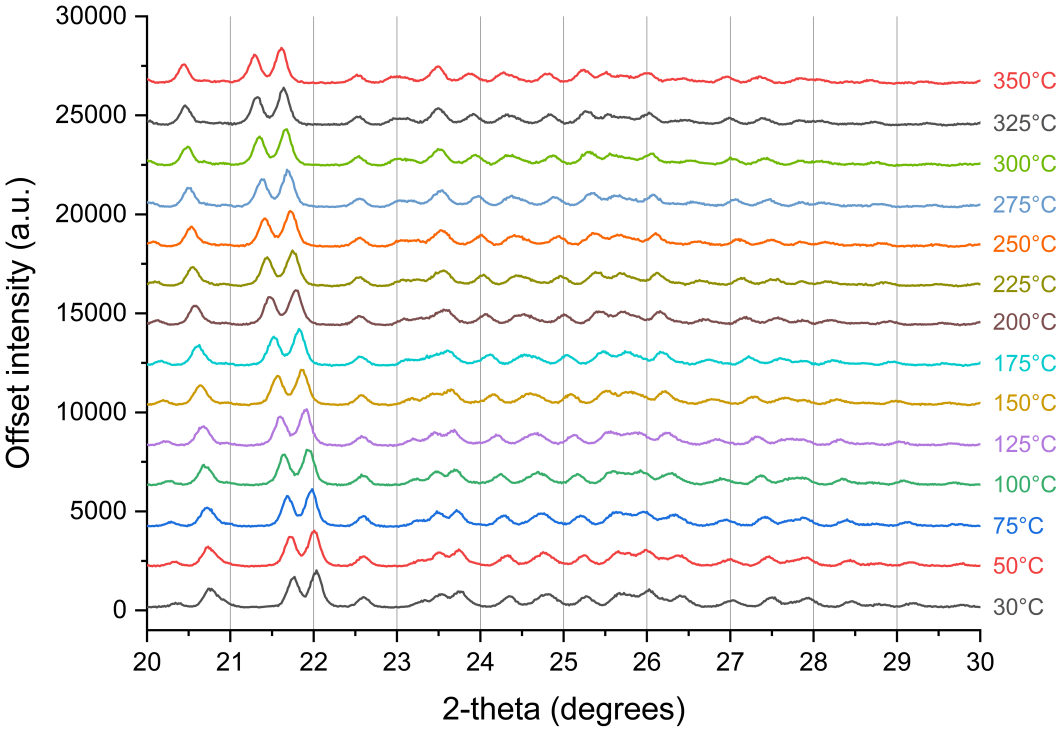


Figure 7-75 A second close up view (20° – 30° 2*θ*) of the variable temperature powder XRD plots for compound 22, providing a better view of the thermochromic transition.

The thermochromic transition is complete by 225 - 250°C, which is congruent with the observed transition peak in the DCS plot prior to the loss of thermal memory.

The complete transition can again be more clearly observed by comparing the 30°C and 350°C measurements (see Figure 7-76 and Figure 7-77).

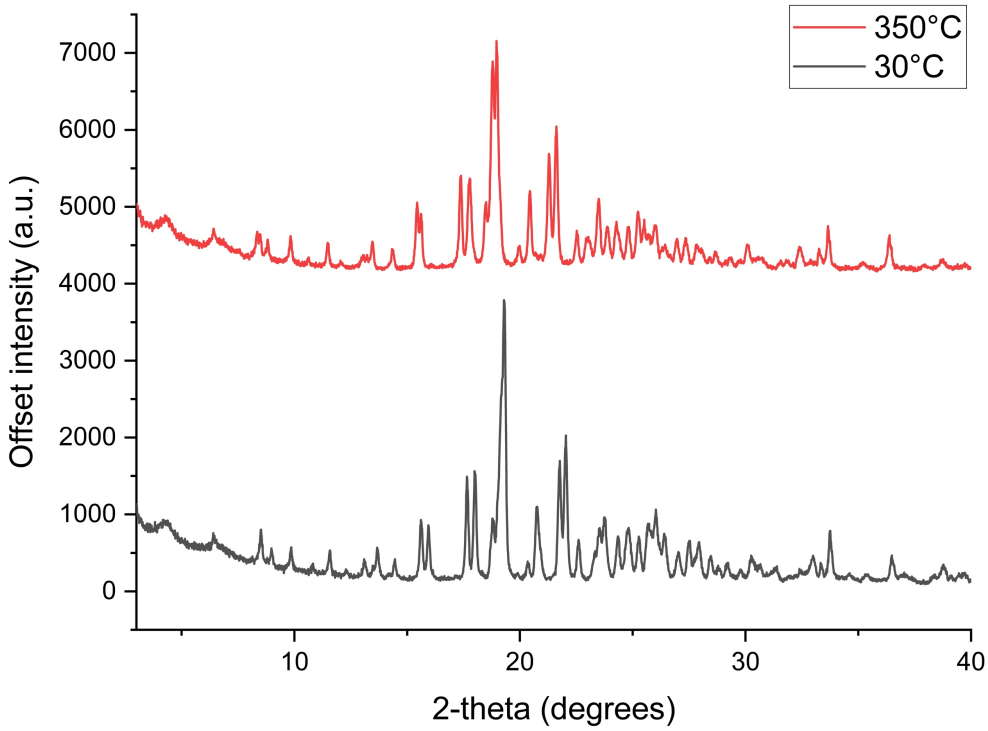


Figure 7-76 Comparing 30°C and 350°C powder XRD plots for compound 22.

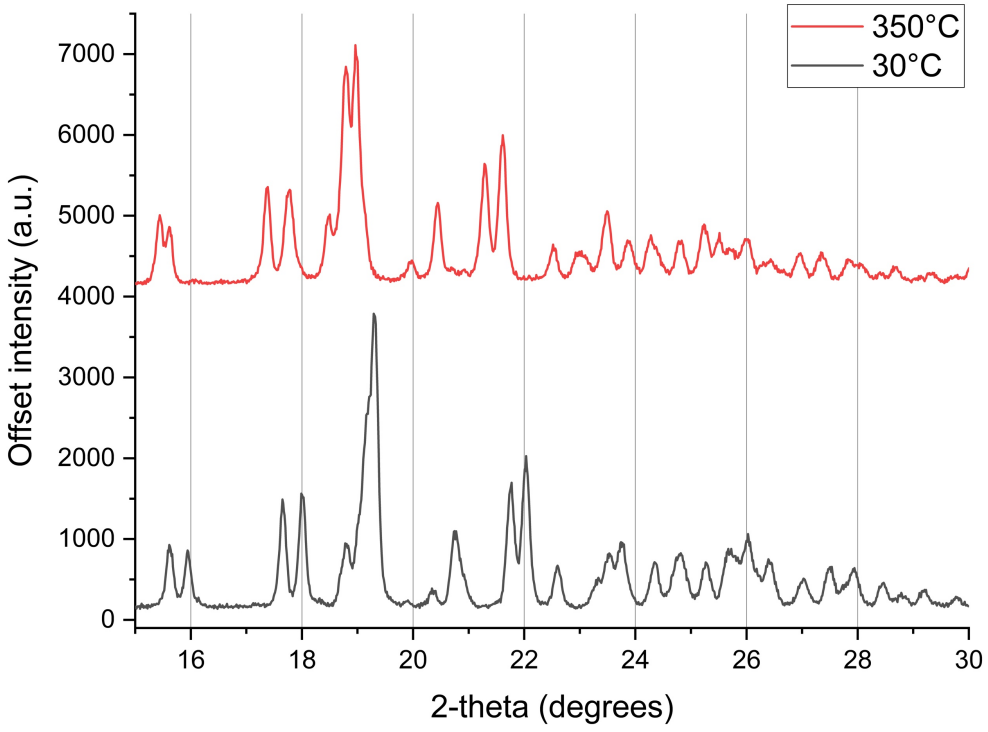


Figure 7-77 Comparing 30°C and 350°C powder XRD plots for compound 22 (close up 15° – 30° 2*θ*).

Once again, the ^{1}H NMR spectra in Figure 7-78 confirm that the thermochromism is not degradation of the compound since no changes are observed.

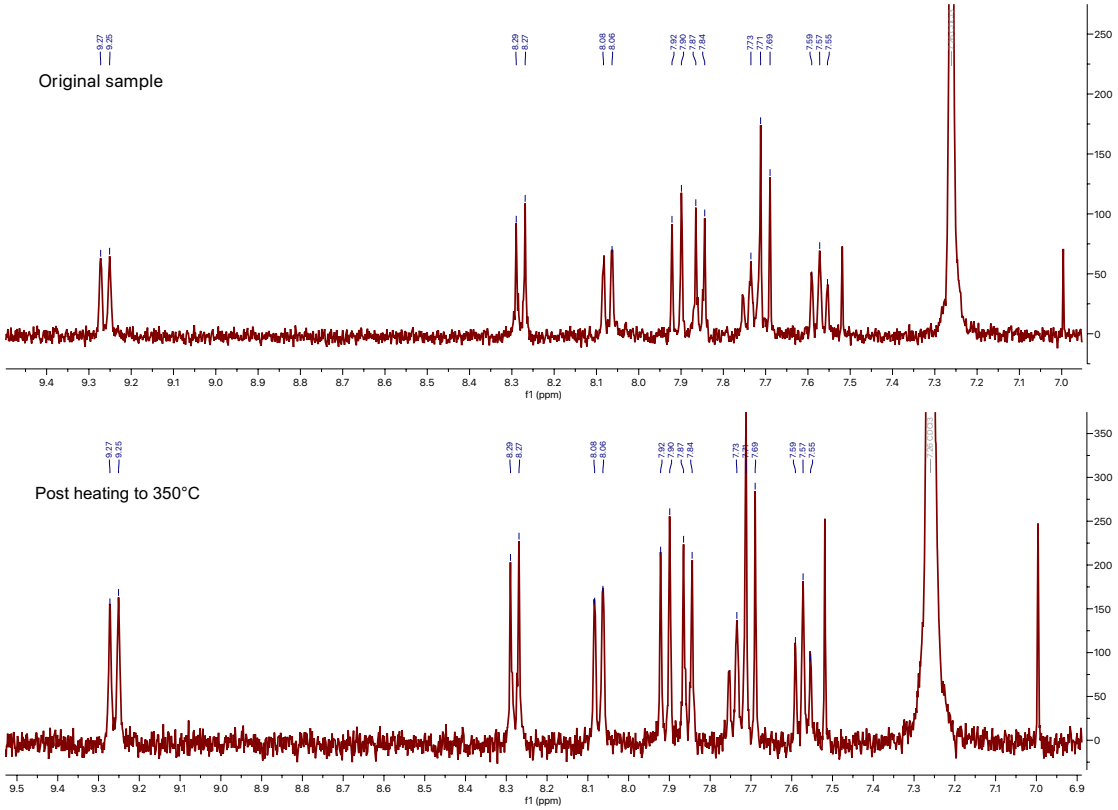


Figure 7-78 ^{1}H NMR spectra of the compound 22 sample prior and after heating to 350°C. Note the absence of any notable change.

7.5 Comparison to single crystal XRD

Single crystal XRD was performed by Dr Laura McCormick at the University of Southampton. Unfortunately, at the time of writing, only 2DBCzPN (**18**) (orange plates) and 4DBCzIPN (**19**) produced good enough quality crystals for analysis. Both were prepared *via* vapour diffusion from chloroform : methanol.

2DBCzPN (18)

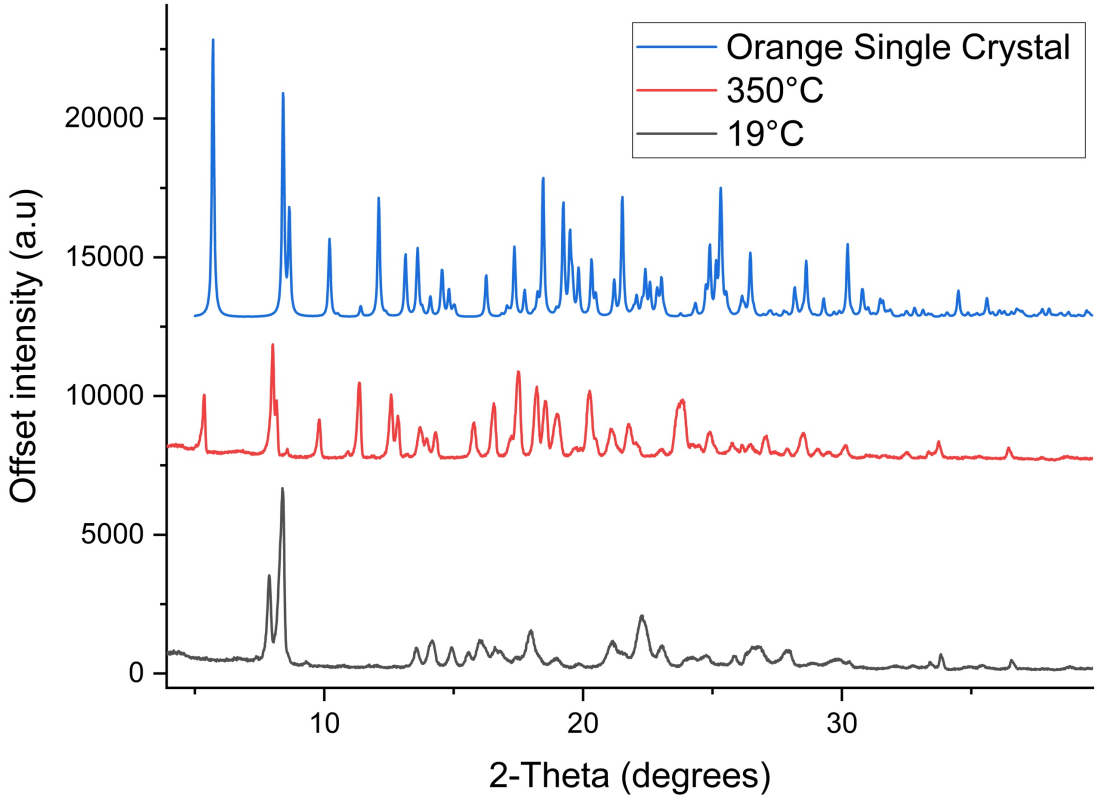


Figure 7-79 Comparison of single crystal XRD plot to powder XRD at room temperature and 350°C compound 18.

From Figure 7-79, it can be seen that the high temperature polymorph of compound **18** exhibits a powder XRD plot with very similar diffractogram to that of the single crystals obtained from chloroform : methanol vapour diffusion. This implies that the crystal structure adopted by compound **18** for the orange high temperature polymorph is indeed similar to the orange crystals produced in this manner, or is in the process of transitioning to that structure[374].

4DBCzIPN (19)

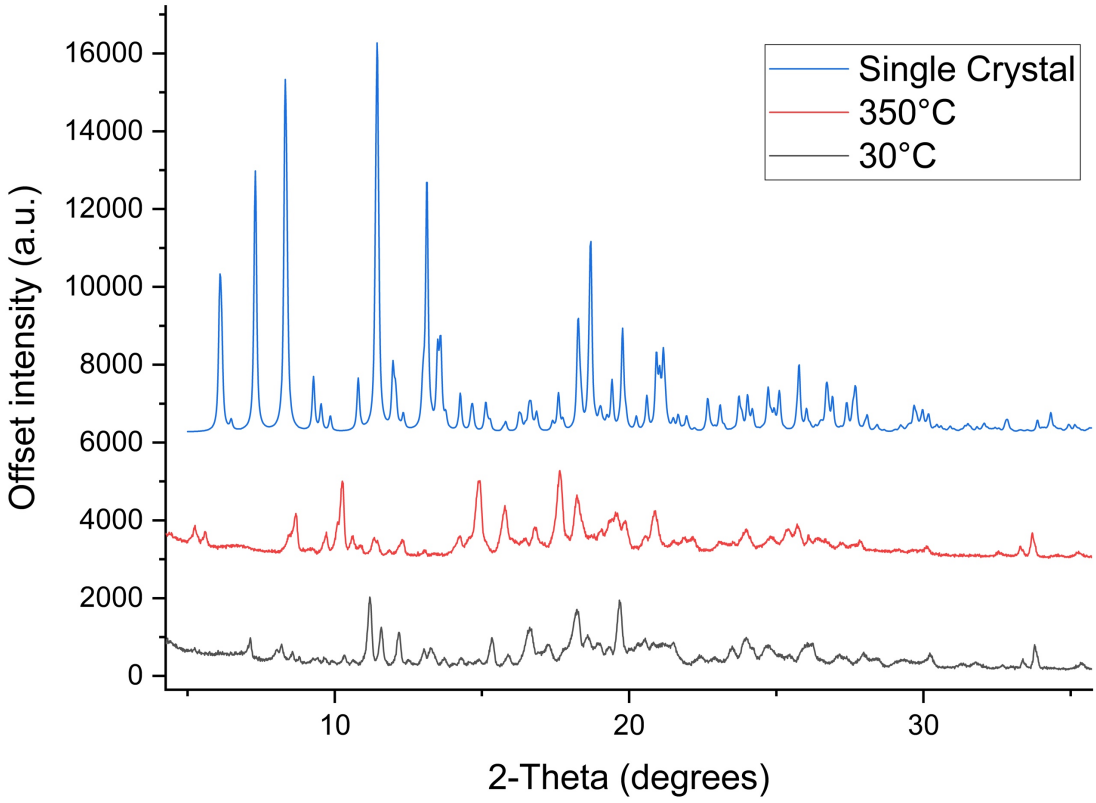


Figure 7-80 Comparison of single crystal XRD plot to powder XRD at room temperature and 350°C compound 19.

Unlike compound **18**, Figure 7-80 shows that compound **19** exhibits a completely different structure in the chloroform : methanol single crystal to that adopted by the high temperature polymorph. This suggests additional polymorphs available to this compound to adopt.

7.6 Mechanochromism

It was noticed upon growing single crystals of compound **18** for XRD analysis, that the square plate-like crystals formed from vapour diffusion (chloroform : methanol) were orange, differing substantially from the yellow powder of compound **18** used to grow them (see Figure 7-81 and Figure 7-82).



Figure 7-81 Solid powdered form of 2DBCzPN (18) under room light (left) and UV (right).

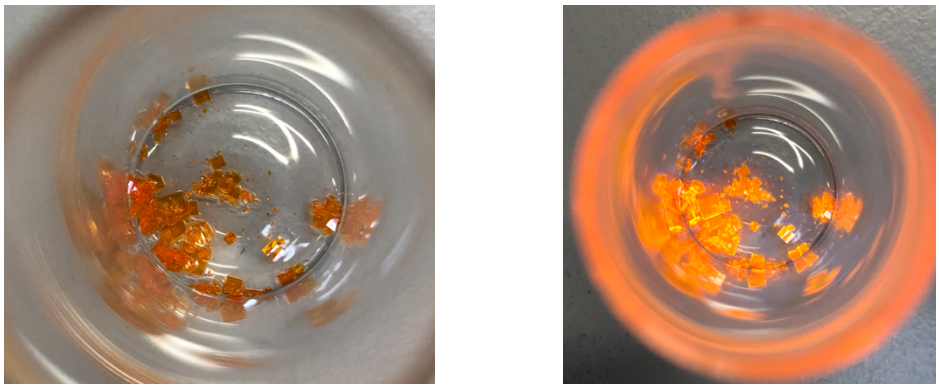


Figure 7-82 Orange crystalline sample of 2DBCzPN (18) under room light (left) and UV (right). The crystals were grown from vapour diffusion of chloroform : methanol.

Their luminescence under UV was also different – shifting from yellow to orange (λ_{max} = 604 nm, shoulder = 582 nm).

A small sample of compound **18** was dissolved in DCM and the solution heated at 50°C until the solvent evaporated to yield yellow needle-like crystals (see Figure 7-83).

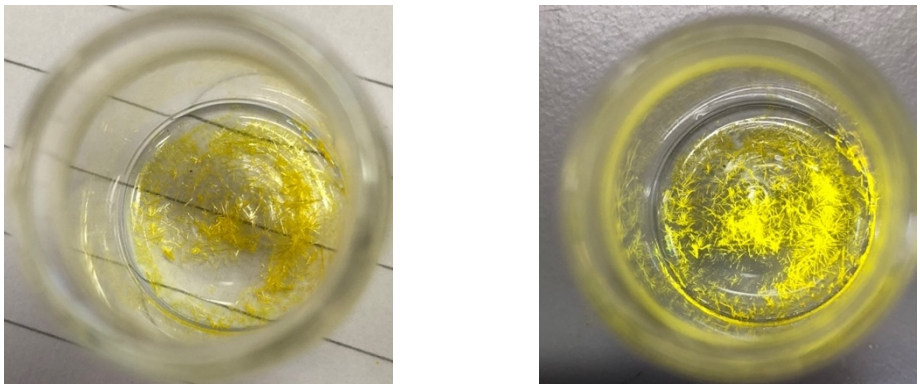


Figure 7-83 Yellow crystalline sample of 2DBCzPN (18) under room light (left) and UV (right). The crystals were grown from dichloromethane evaporated at 50°C.

These crystals fluoresced yellow under UV (λ_{max} = 564 nm, shoulder = 596 nm). A comparison of the PL spectra of the two crystalline polymorphs of compound **18** are shown in Figure 7-84.

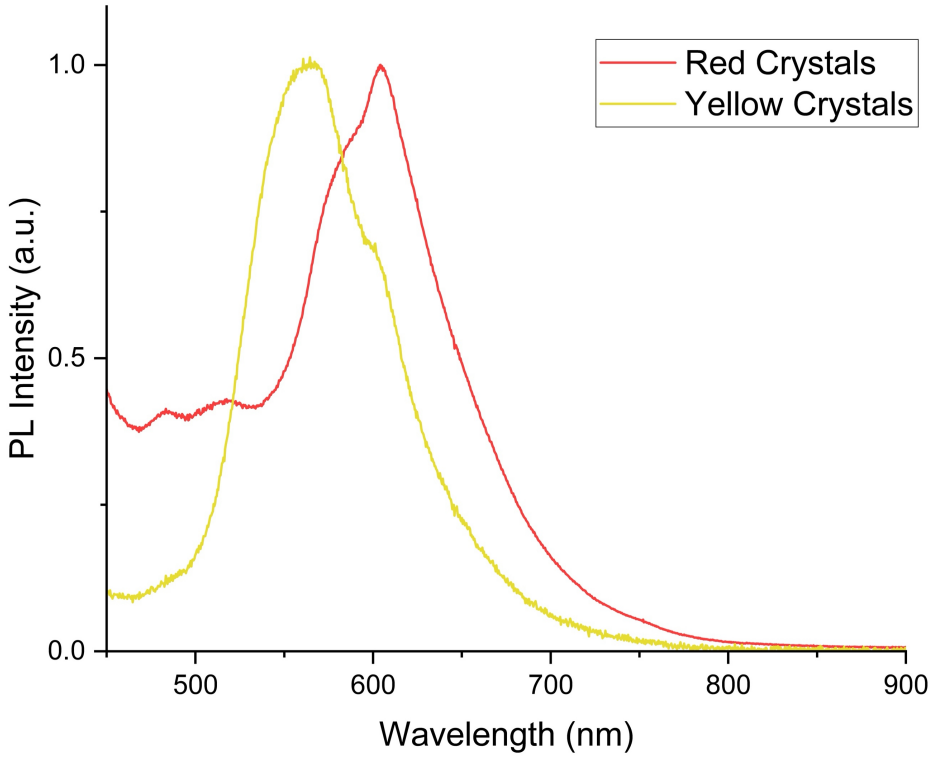


Figure 7-84 Fibre optic spectrometer PL spectra of crystals of compound 18. Yellow needle like crystals have blue-shifted emissions, whereas the red square-plate-like crystals have red-shifted emission.

The difference in structure and properties of the crystals suggests significant polymorphism in compound **18** which could potentially be the reason for the previously described thermochromism as well. Additionally, it was thought that if structural changes can be achieved *via* solvent effects, mechanical methods may also result in structural changes.

A small quantity of compound **18** was ground up with a pestle and mortar, yielding a yellow-orange solid with slight orange blemishes shown below in Figure 7-83.

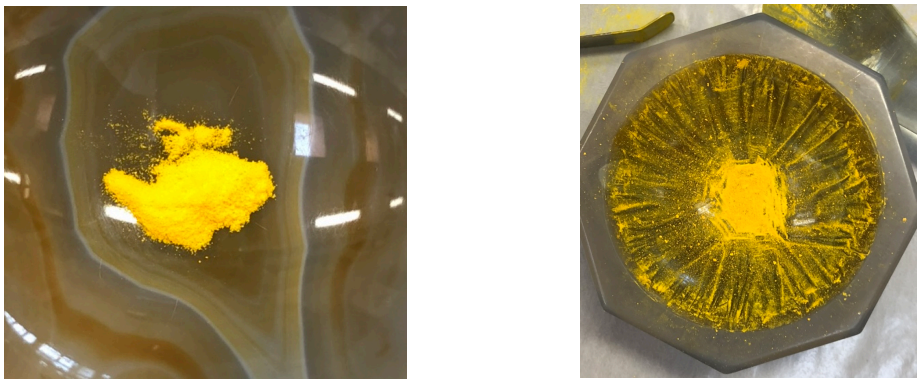


Figure 7-85 Compound 18 pre- and post-grinding under room lighting.

However, upon exposure to UV the solid emitted with an orange light after grinding, and this is shown below in Figure 7-86.

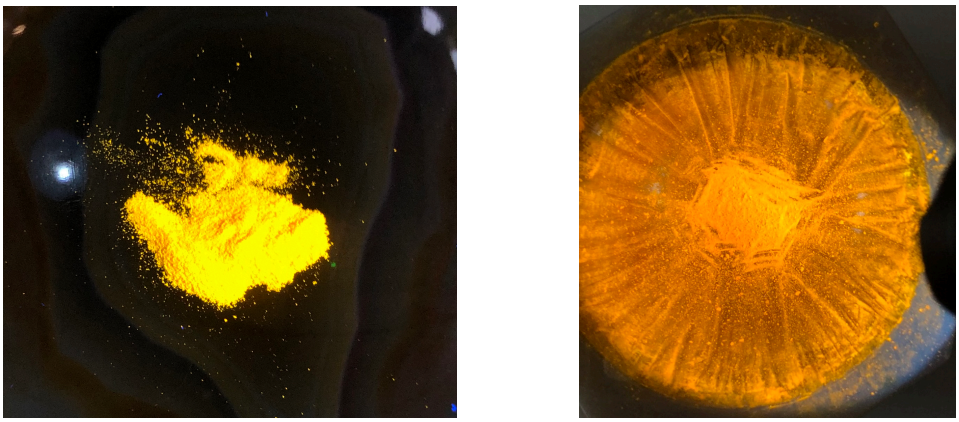


Figure 7-86 Compound 18 pre and post grinding under UV.

To further assess these changes, a chamber was constructed to shield a fibre optic spectrometer head from external light sources (cardboard box covered in a black-out shroud), with a 365 nm UV lamp clamped in place, in order to provide and excitation source.

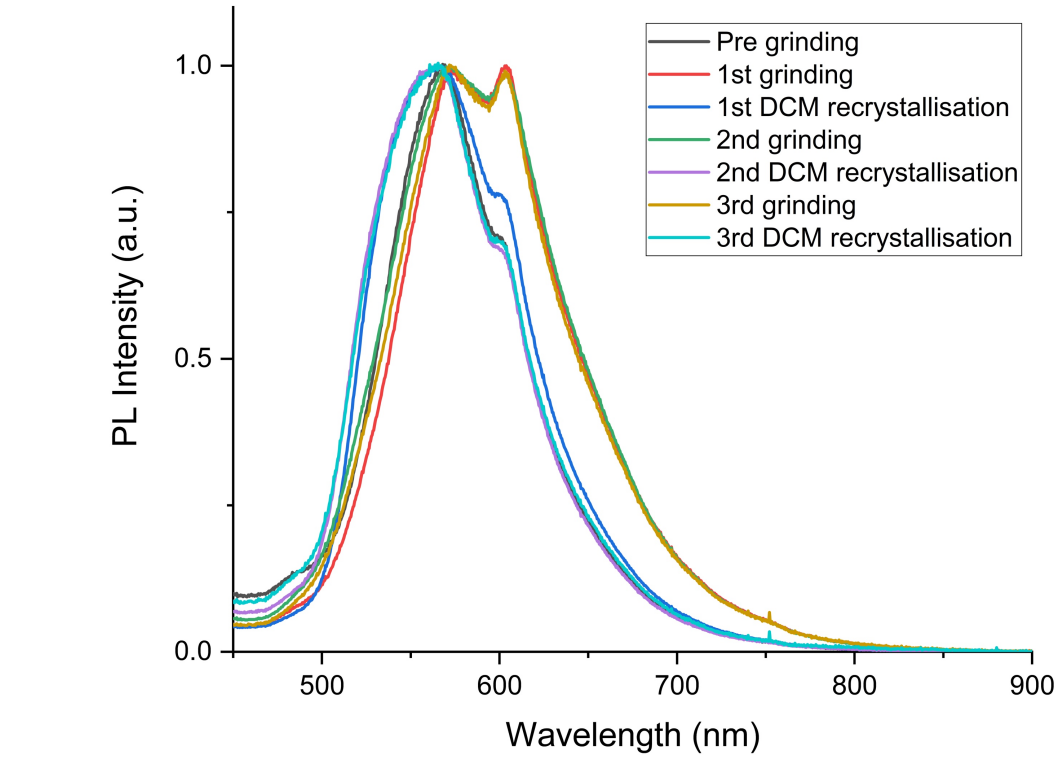
General mechanochromism procedure

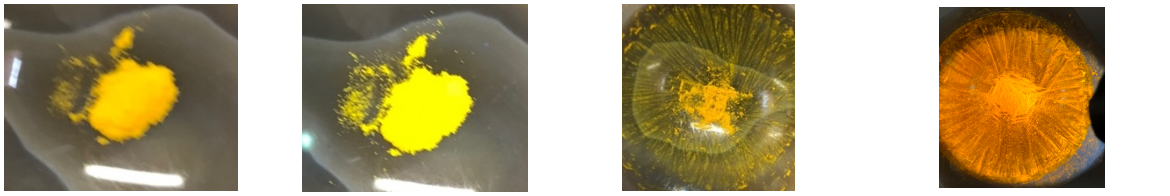
A mortar was placed in the chamber and a dark blank measurement take. Following this, a sample of compound **18** or **19**, was placed into the mortar and the UV lamp positioned to illuminate it, and a measurement was taken. Following this, the sample was ground up using the pestle, and a second measurement taken. The solid was then dissolved in dichloromethane and allowed to crystallise as the dichloromethane evaporated in order to

reset the mechanochromism, and a third measurement taken. This process was repeated three times for each sample.

2DBCzPN (18)

Compound **18** transitions from a bright yellow powder with bright yellow luminescence under UV, to an orange powder with bright orange luminescence upon grinding with a pestle and mortar (see Figure 7-87).





2DBCzPN | 2DBCzPN (UV) | 2DBCzPN post grinding | 2DBCzPN post grinding (UV)

Figure 7-87 Compound 18 mechanochromism PL spectra from fibre optic spectrometer, excited with 365 nm UV torch.

The PL shifts from yellow to orange luminescence upon grinding, with a subtle widening of the FWHM (see Table 7-35 for more detail). This is largely manifested as a main yellow peak with a redder shoulder morphing into two dual emissions peaks in the red and yellow upon grinding.

Table 7-35 Summary of the PL of compound 18 undergoing mechanochromism.

Sample treatment	λ_{PL} (nm)	FWHM
Pre-grinding	568, 600 (sh)	86
1st grinding	572, 603	108
1st CH_2Cl_2 recrystallisation	566, 600 (sh)	101
2nd grinding	571, 603	119
2nd CH_2Cl_2 recrystallisation	563, 600 (sh)	98
3rd grinding	573, 602	111
3rd CH_2Cl_2 recrystallisation	564, 599 (sh)	99

A ^{1}H-NMR was performed for the untreated sample and after grinding and the comparison shown in Figure 7-88.

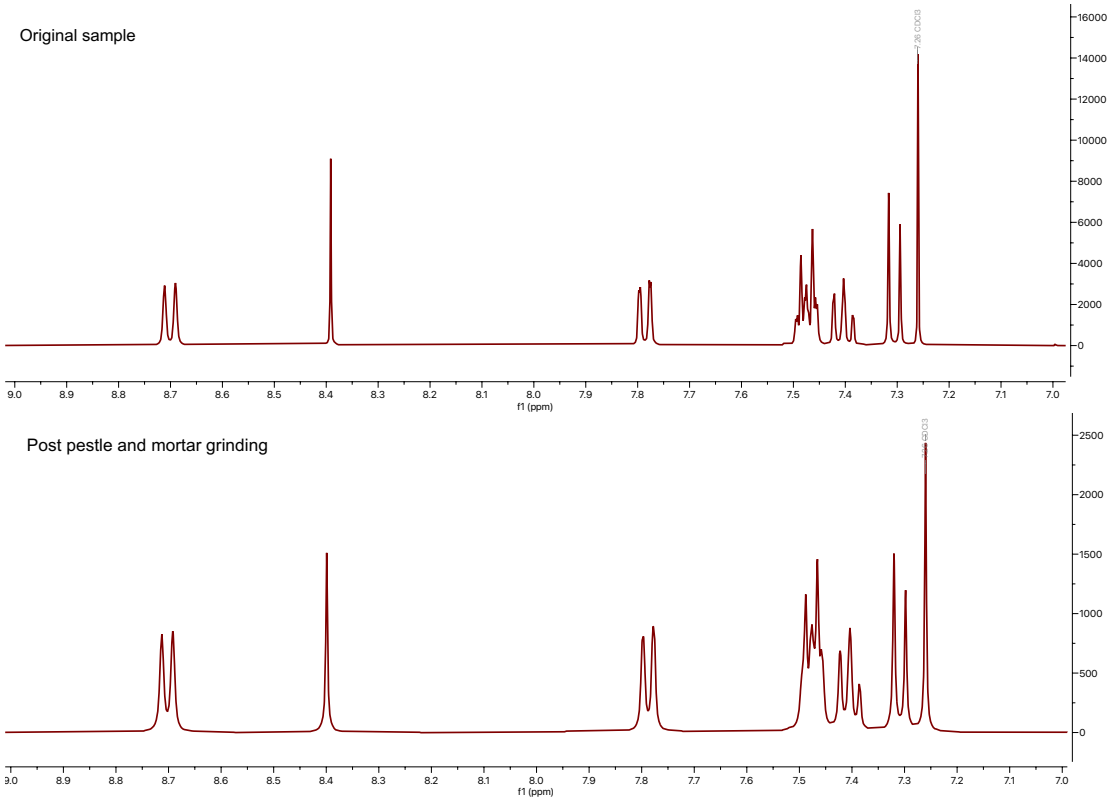


Figure 7-88 ^{1}H NMR spectra of compound 18 before and after grinding with a pestle and mortar. The material with red-shifted emissions is clearly the same compound, supporting the mechanochromic behaviour rather a change in the molecular structure.

Despite the change in physical appearance (yellow to orange-red) and change in emission (yellow to orange-red), there was no difference in the chemical structure of the molecule, concluding that no chemical change has occurred and that the mechanochromism must originate in changes to the crystal structure.

The post-grinding sample was also subject to DSC analysis and the results shown in Figure 7-89.

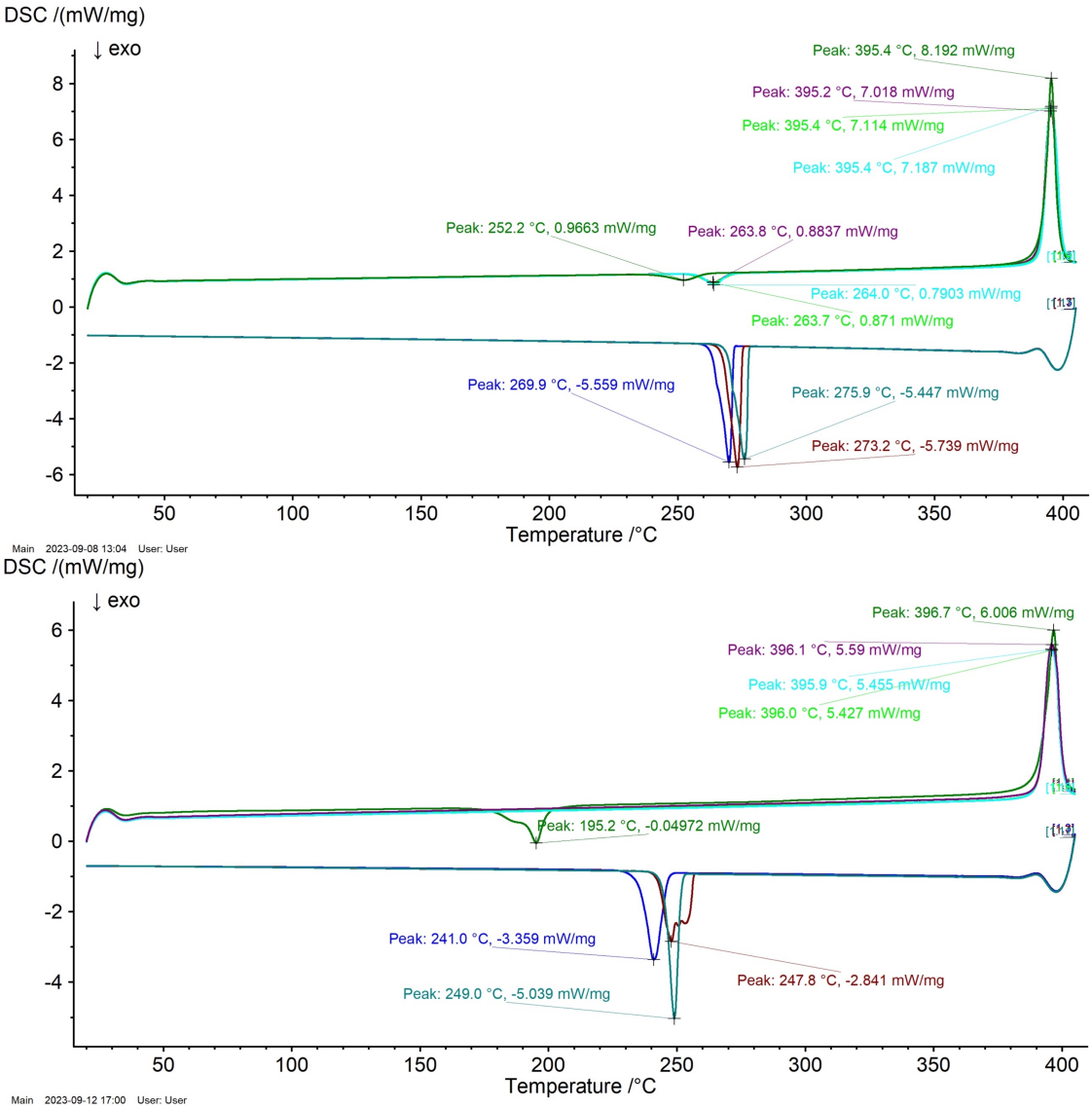
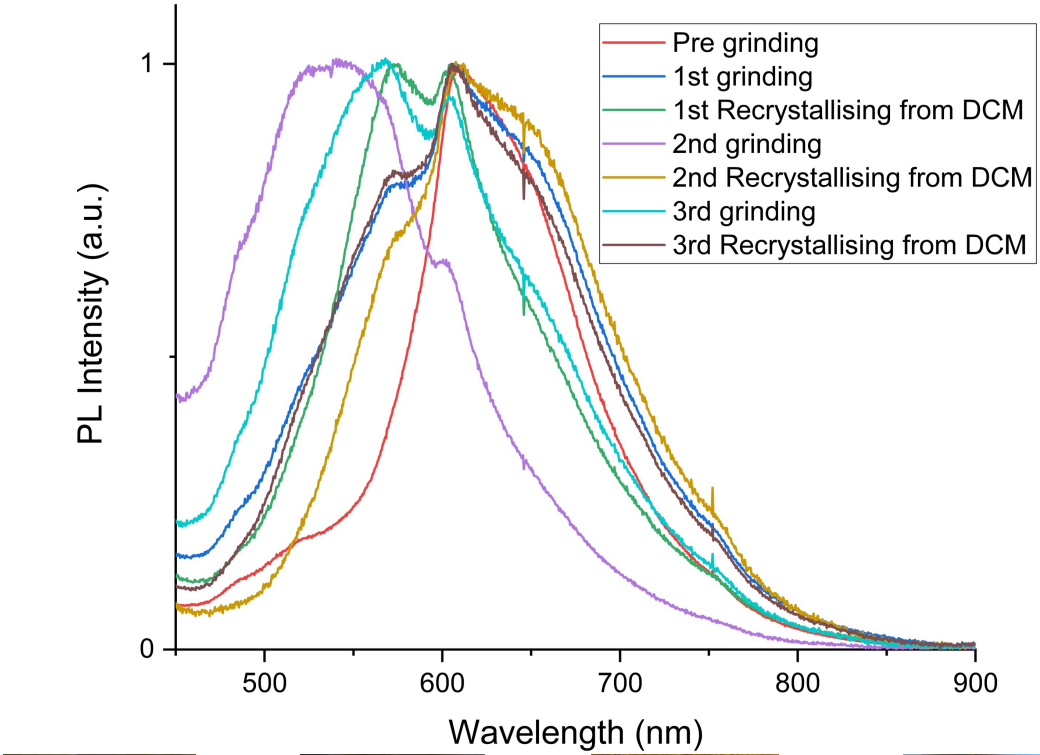


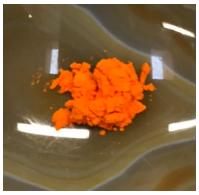
Figure 7-89 DSC plots of compound 18 untreated (top) and post grinding (bottom). *Dark green = First heating; blue = first cooling; purple = second heating; black = second cooling; light green = third heating; teal = third cooling; cyan = fourth heating.*

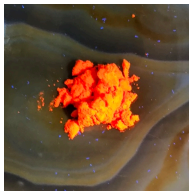
Upon removal of thermal history, the melting point of both ground and non-ground compound **18** remains identical, however the crystallisation temperature decreases by 30°C after grinding. This is likely due to the orange polymorph adopted by the ground material being closer in structure to a different thermochromic polymorph than the original yellow powder.

4DBCzIPN (19)

The same procedure as that for compound **18** was used for the mechanochromism study of compound **19** and the resulting PL spectra are shown in Figure 7-90 and summarised in Table 7-36.




4DBCzIPN


4DBCzIPN (UV)


4DBCzIPN post grinding


4DBCzIPN post grinding (UV)

Figure 7-90 Compound 19 mechanochromism PL spectra from fibreoptic spectrometer, excited with a 365 nm UV torch.

As with compound **18**, the mechanochromism manifests as a transition between a redder peak with bluer shoulder, with the shorter wavelength shoulder becoming the main peak upon grinding at the expense of the previous major peak, which in turn becomes a shoulder itself.

Table 7-36 Summary of the PL of compound 19 undergoing mechanochromism.

Sample treatment	λ_{PL} (nm)	FWHM
Pre-grinding	610, 646 (sh), 530 (sh)	101
1st grinding	572, 607, 645 (sh)	167
1st CH_2Cl_2 recrystallisation	603, 572, 645 (sh)	132
2nd grinding	543, 601 (sh)	146
2nd CH_2Cl_2 recrystallisation	609, 644 (sh), 575 (sh)	151
3rd grinding	604, 567, 647 (sh)	170
3rd CH_2Cl_2 recrystallisation	606, 573, 646 (sh)	161

Before and after grinding, compound **19** was dissolved in deuterated chloroform and the ^1H NMR compared, which can be seen in Figure 7-91.

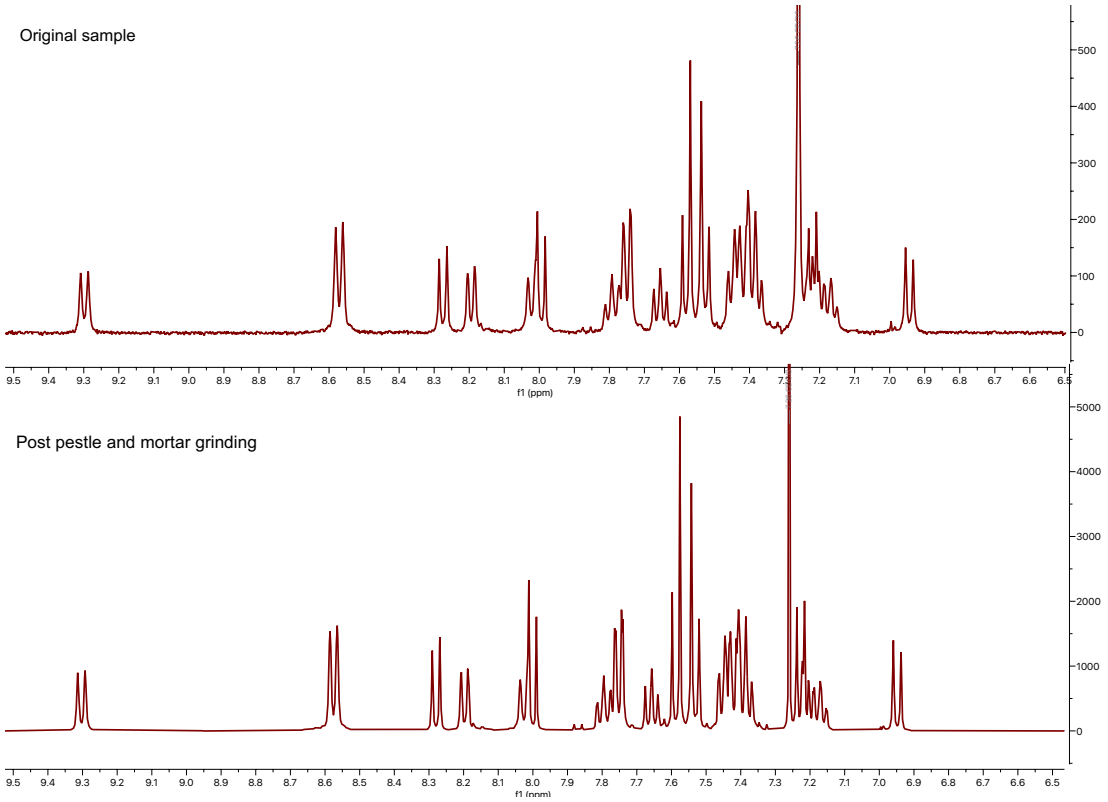


Figure 7-91 ^1H NMR spectra of compound 19 before and after grinding with a pestle and mortar. The material with red-shifted emissions is clearly the same compound, supporting the mechanochromic behaviour rather a change in the molecular structure.

Once again, after grinding there is no change in the identity of the molecule in the sample.

The post-grinding sample was also subject to DSC analysis, which is shown in Figure 7-92. The almost identical plots from each sample strongly supports the case for there being no chemical change post-grinding.

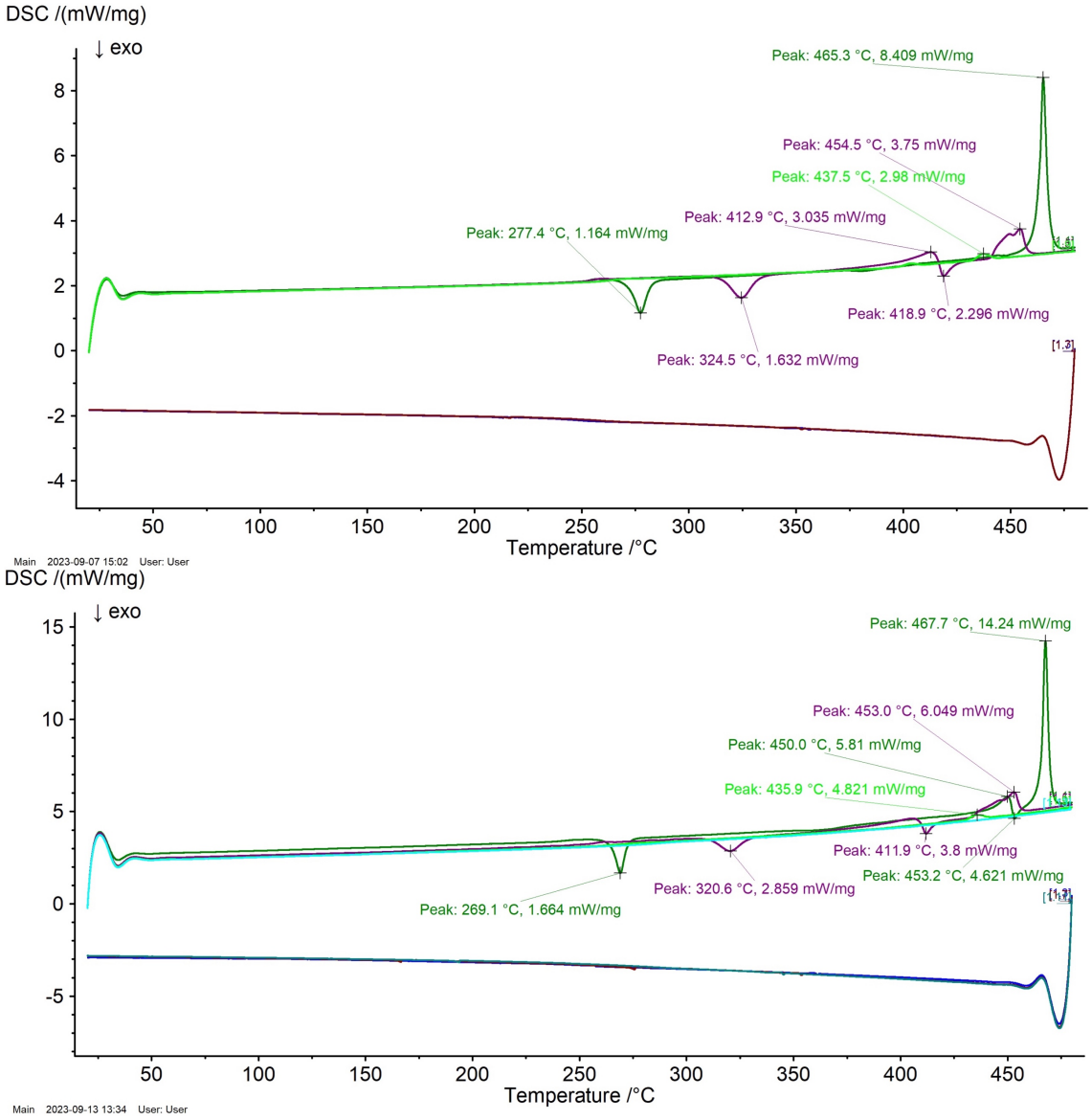


Figure 7-92 DSC plots of compound 19 untreated (top) and post grinding (bottom). Dark green = First heating; blue = first cooling; purple = second heating; black = second cooling; light green = third heating; teal = third cooling; cyan = fourth heating.

DBCz-PS (21)

A sample of compound **21** was also subjected to grinding and PL analysis. Figure 7-93 and Table 7-37 show that as with the previous compounds, mechanochromism in compound **21** is also characterised by a shoulder becoming a main emission peak at the expense of the intensity of the original pre-grinded emission peak.

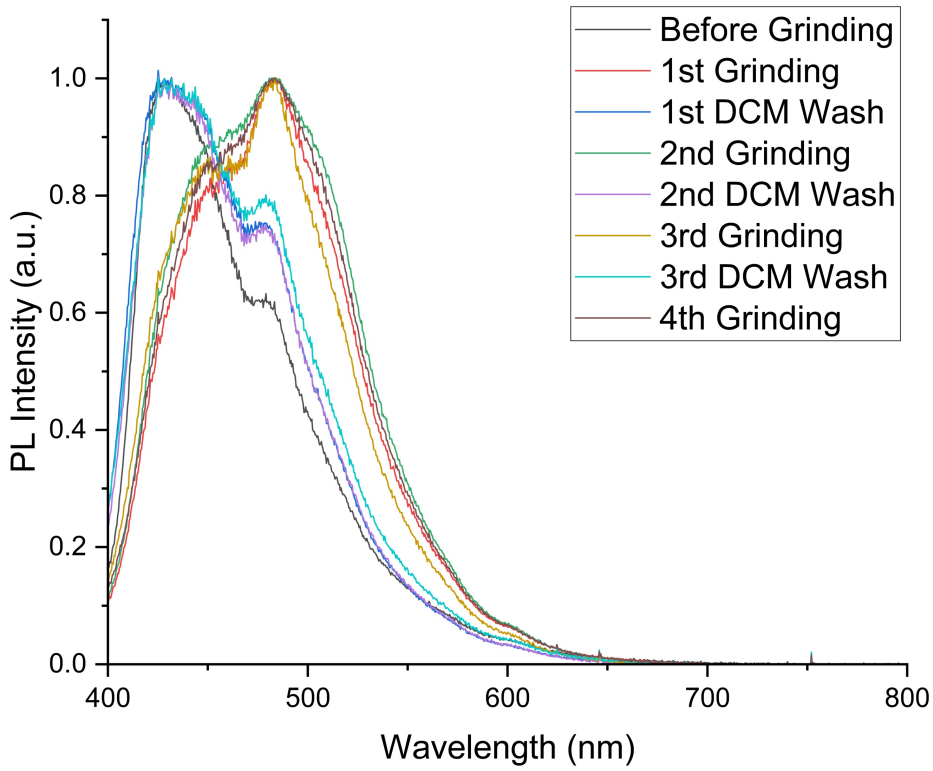


Figure 7-93 Fibre optic spectrometer PL spectra of powder of compound 21. Note the increase in intensity of the shoulder.

The mechanochromic shifting is summarised in Table 7-37.

Table 7-37 Summary of PL properties of mechanochromism in compound 21.

Sample treatment	λ_{PL} (nm)	FWHM (nm)
Before grinding	428, 477(sh)	81
1st grinding	483, 454(sh)	104
1st CH_2Cl_2 wash	428n 478(sh)	93
2nd grinding	483, 452(sh)	110
2nd CH_2Cl_2 wash	428, 478(sh)	91
3rd grinding	481, 450(sh)	105
3rd CH_2Cl_2 wash	428, 480(sh)	97
4th grinding	482, 450(sh)	108

Compound **21** exhibits distinct and fully reversible mechanochromism. The PL spectra reveal a transition between a dominant emission at 428 nm and a separate emission at 478 nm. A shoulder is present in both materials, with the ~450 nm shoulder in the grinded material possibly present and giving rise to a contribution to the broad main peak in the samples prior to grinding. This suggests multiple polymorphs – which supports the original multi-coloured emission from the melting point sample.

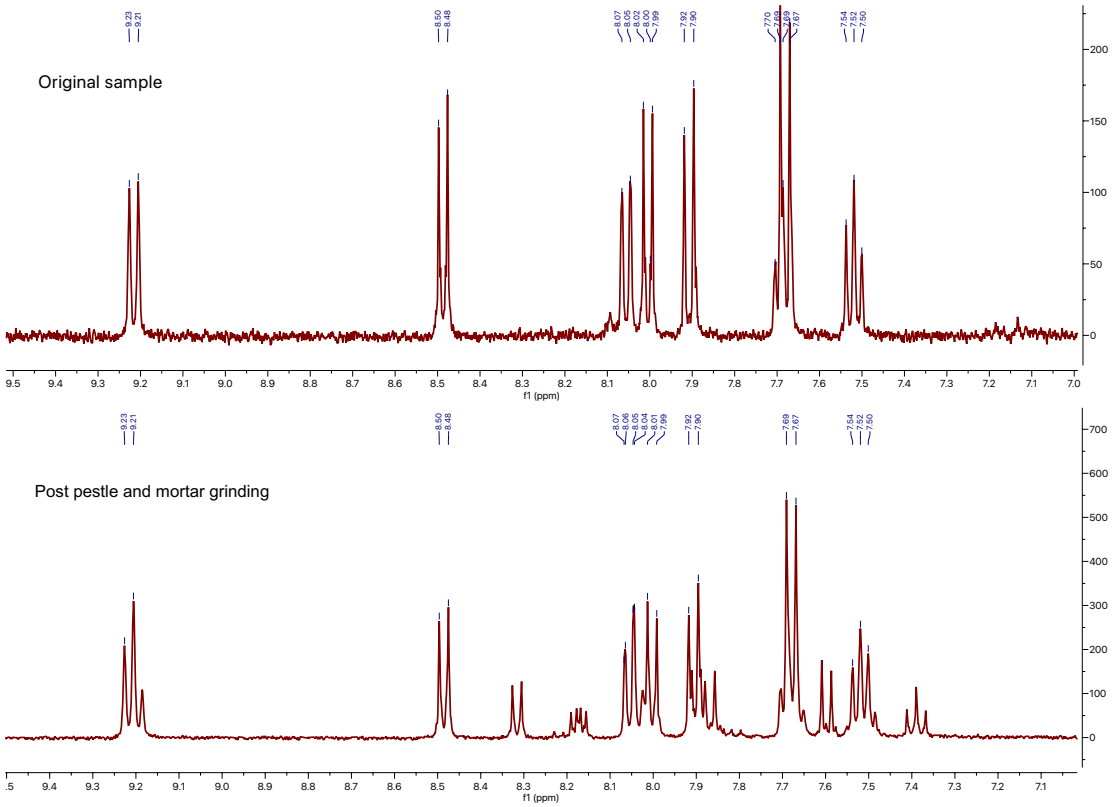


Figure 7-94 ^{1}H NMR spectra of compound 21 before and after grinding with a pestle and mortar. The material with red-shifted emissions is clearly the same compound, supporting the mechanochromic behaviour rather a change in the molecular structure. Interestingly, there does appear to be a slight degradation to the material.

From Figure 7-94, the ^{1}H NMR shows that the changes are not due to chemical breakdown, as the material is mostly the same after repeated grinding (the fact that it is fully reversible when recrystallised from DCM supports this). However, it must be noted that there is an additional doublet, quartet, singlet, triplet and pair of singlets at 8.32 ppm, 8.17 ppm, 7.86 ppm. 7.60 ppm, 7.58 ppm and 7.39 ppm respectively, which are likely from a small degree of decomposition. However, since they are absent in the thermochromic experiment's NMR, their presence is likely coincidental, unless mechanical stresses on the solid material imparts a greater C-N cleaving force than thermal action.

DBCz-BZPN (22)

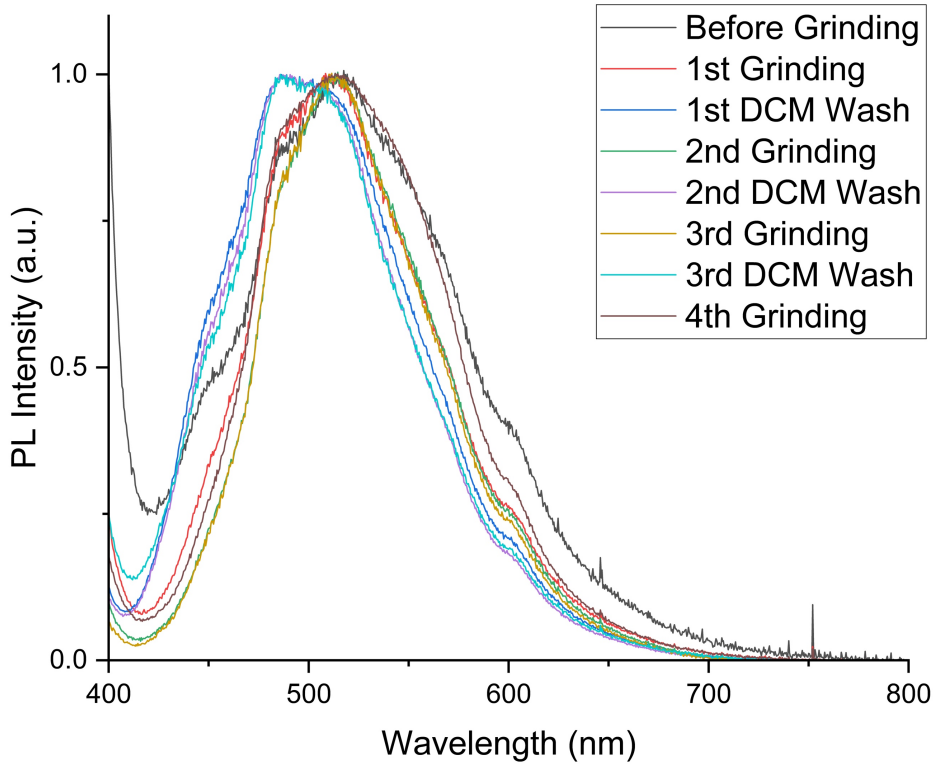


Figure 7-95 Fibre optic spectrometer PL spectra of powder of compounds 22.

Figure 7-95 shows that, as with its thermochromism, compound **22** demonstrates the least mechanochromic character of the four molecules. Grinding results in red-shifting of emissions, with what appears to be a decrease in the intensity of a ~487 nm emission, being replaced by a polymorph with emissions at ~512 nm. Interestingly, the first grinding had little effect on emissions, and washing in dichloromethane was required to instigate change to the PL spectra. This suggests that the polymorph obtained from the synthesis is the same as that which is obtained by grinding – material treated with dichloromethane being an alternative polymorph. The mechanochromic PL properties of compound **22** are summarised in Table 7-38.

Table 7-38 Summary of PL properties of mechanochromism in compound 22.

Sample treatment	λ_{PL} (nm)	FWHM (nm)
Before grinding	516, 487(sh), 597(sh)	127
1st grinding	512, 597(sh)	105
1st CH_2Cl_2 wash	486, 450(sh), 596(sh)	118
2nd grinding	514, 599(sh)	98
2nd CH_2Cl_2 wash	487, 451(sh), 597(sh)	112
3rd grinding	513, 598(sh)	96
3rd CH_2Cl_2 wash	487, 450(sh), 598(sh)	110
4th grinding	515, 597(sh)	111

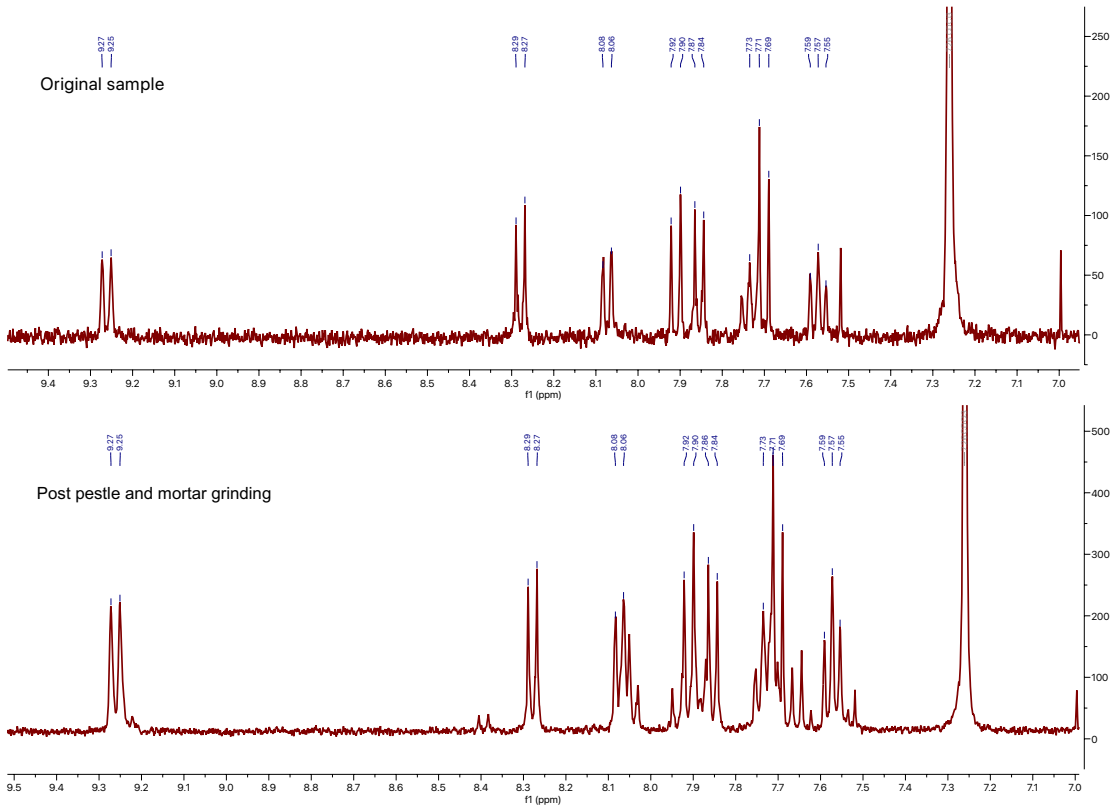
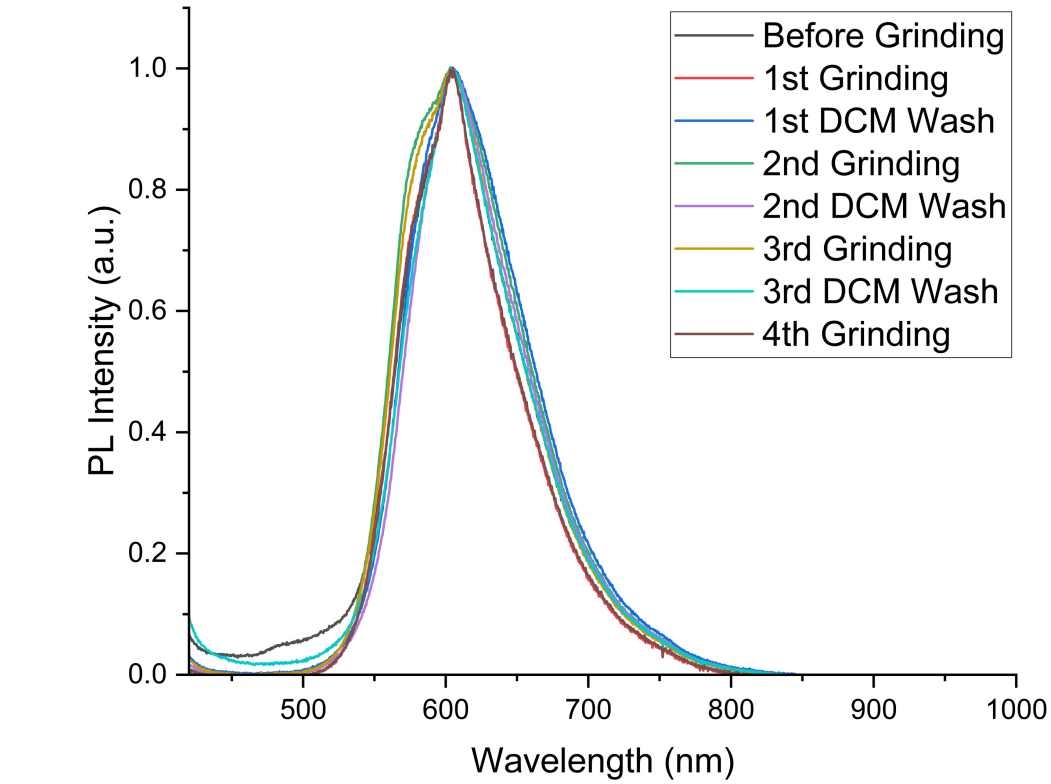
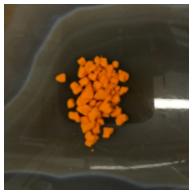


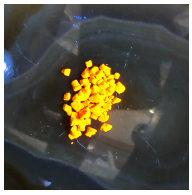
Figure 7-96 ^{1}H NMR spectra of compound 22 before and after grinding with a pestle and mortar. The material with red-shifted emissions is clearly the same compound, supporting the mechanochromic behaviour rather a change in the molecular structure. Interestingly, there appears to be only minimal degradation compared with compound 21.

After repeated grinding, the material is demonstrated to be chemically identical *via* ^{1}H NMR (see Figure 7-96). A small number of additional peaks in the NMR spectrum suggest minor degradation (doublets at 8.4 ppm, singlet at 8.04 ppm, singlet at 7.95 ppm, and three singlets at 7.62 – 7.68 ppm. This suggests that the C-N bond in compound **21** and compound **22** is slightly less stable than in compounds **18** and **19**.

As with the compound **19**, to investigate whether the quasi-helical dibenzo carbazole is the reason for mechanochromism, the monobenzocarbaozle derivative, compound **20** was synthesised and its mechanochromic properties explored (see Figure 7-97 for the mechanochromic PL spectra and Table 7-39 for a summary).




4MBCzIPN


4MBCzIPN (UV)


4MBCzIPN post grinding


4MBCzIPN post grinding (UV)

Figure 7-97 Compound 20 mechanochromism PL spectra from fibreoptic spectrometer, excited with 365 nm UV torch. The yellow tint of the pre-ground UV exposed sample is a misleading auto colour balance correction from the camera, in reality it is orange.

Table 7-39 Summary of the PL of compound 20 undergoing mechanochromism.

Sample treatment	λ_{PL} (nm)	FWHM
Pre-grinding	605	92
1st grinding	605	84
1st CH_2Cl_2 recrystallisation	605	97
2nd grinding	605, 589(sh)	101
2nd CH_2Cl_2 recrystallisation	605	88
3rd grinding	605, 589(sh)	96
3rd CH_2Cl_2 recrystallisation	605	89
4th Grinding	605	87

Unlike the dibenzocarbazole derivative, compound **20** shows only slight changes to its photoluminescence upon grinding. When recrystallised form dichloromethane, it forms a red crystalline solid, with dimmer emission than when ground. A slight shoulder in the emission spectrum can be observed at 589 nm upon grinding. This isn't present in the first

and fourth grindings, so it is possible that its more an artefact of increased surface area when particles of the material are scattering more light to the detector.

Removing the second benzene ring in the donor appears to be preventing the stark mechanochromism observed in compound **19**. This could be due to reduced steric bulk of the donors, changing the strength of any intermolecular forces between the molecules. It may therefore require a much greater grinding force to effect mechanochromic change to compound **20**. Indeed, it shows thermochromism at a similarly high temperature to that of compound **19**, but the DSC plots reveal that the thermally mediated transition in compound **20** is endothermic rather than the exothermic peak shown in compound **19**. This suggests the transition is different in nature between the two molecules. Further analysis *via* single crystal and powder XRD is required to explore this further.

For confirmation that no chemical degradation occurs upon grinding, ^{1}H NMR spectroscopy was performed on compound **20** before and after grinding.

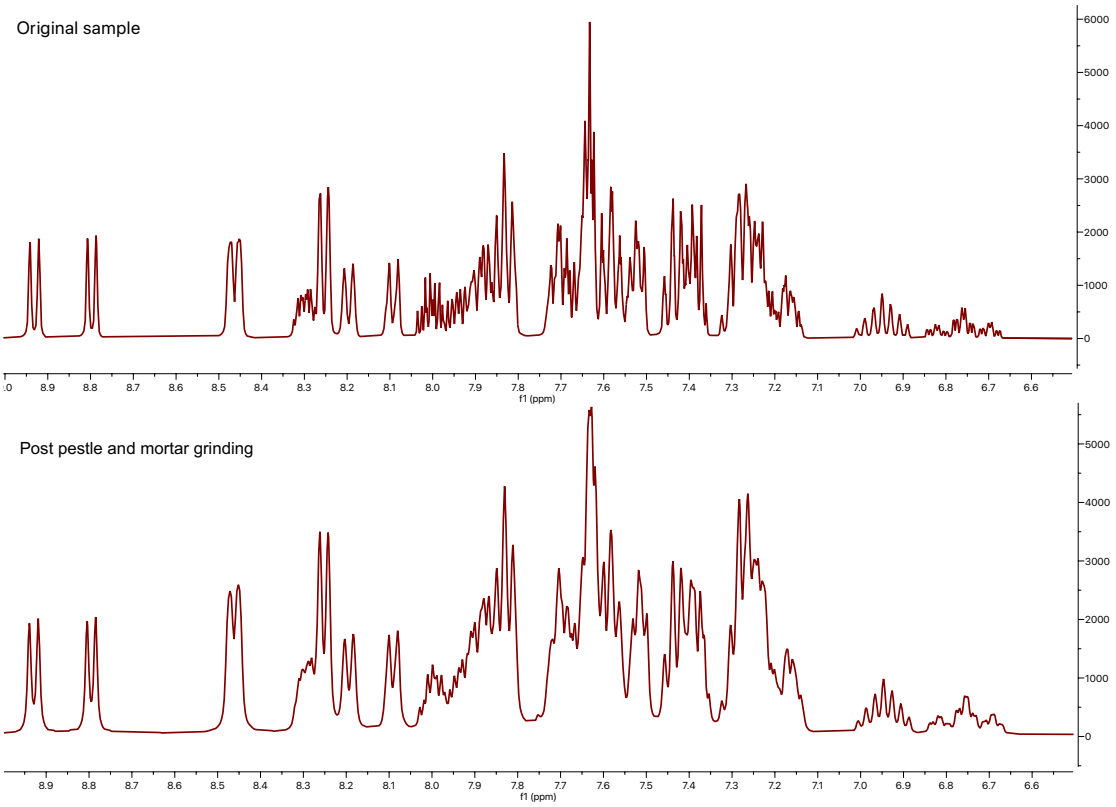


Figure 7-98 ^{1}H NMR spectra of compound 20 before and after grinding with a pestle and mortar. No chemical degradation is observed.

As can be seen in Figure 7-98, there is no chemical degradation to compound **20** upon grinding with a pestle and mortar. The differences in resolution are an artefact of the different concentrations of the NMR samples prepared.

7.6.1 Comparison of XRD data

Samples of both 2DBCzPN (**18**) and 4DBCzIPN (**19**) were ground up with a pestle and mortar and powder XRD analysis performed and compared to the previous powder XRD and single crystal XRD data.

2DBCzPN (18)

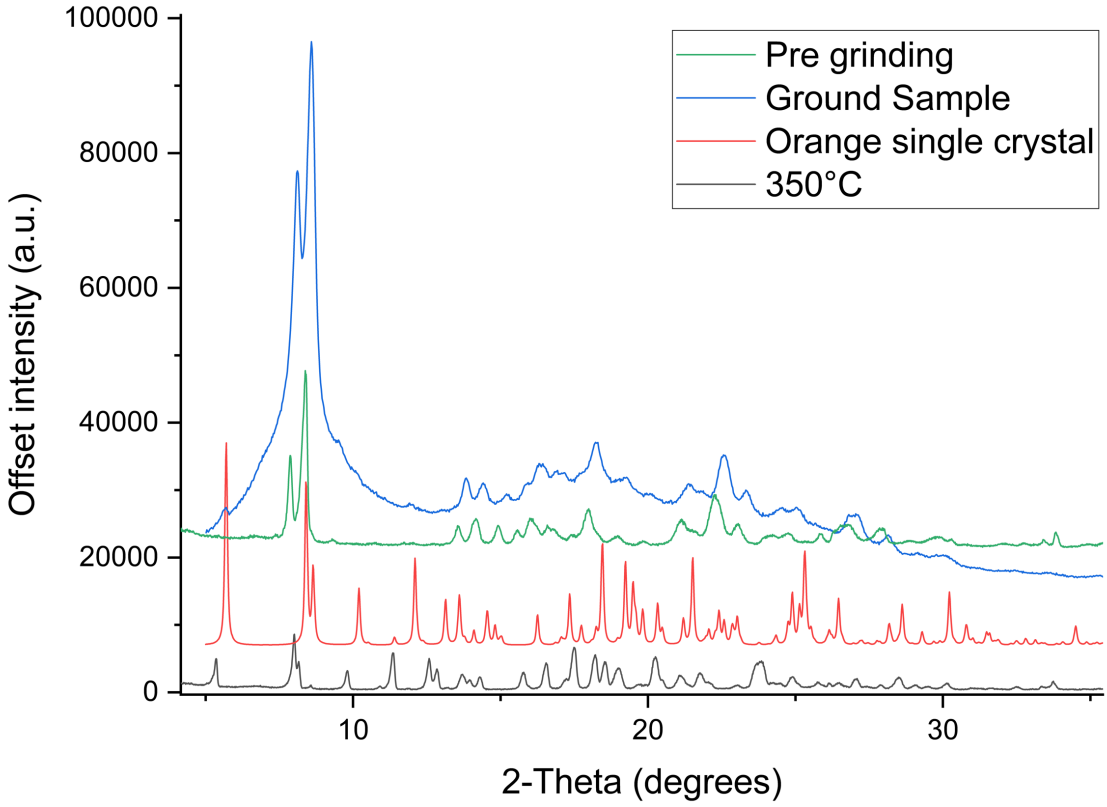


Figure 7-99 Combined powder XRD plots for compound 18 polymorphs comparing grinding, single crystal and heating.

In compound **18**, there appears to be at least 3 different polymorphs (see Figure 7-99). Closer inspection of the ground sample reveals there to be a mixture of crystal structures – most likely being the original, pre-ground structure along with the same structure as the orange single crystals (albeit in a lower quantity). The mixture may be a result of imperfect grinding when preparing the sample as the fluorescence under UV seemed to be not quite as orange as the heated sample appeared, and continued grinding resulted in significant sticking of the

material to the pestle and mortar, making extracting the sample for analysis difficult. Indeed, if disorder in the molecular packing is widespread, the diffraction pattern can have diminished clarity owing to more amorphous structures in the ground form[375,376]. The reduced quantity and potentially only partially ground sample would suggest that further grinding would possibly yield more complete conversion of the polymorph. The heated sample is similar, although slightly different from the orange single crystals.

4DBCzIPN (19)

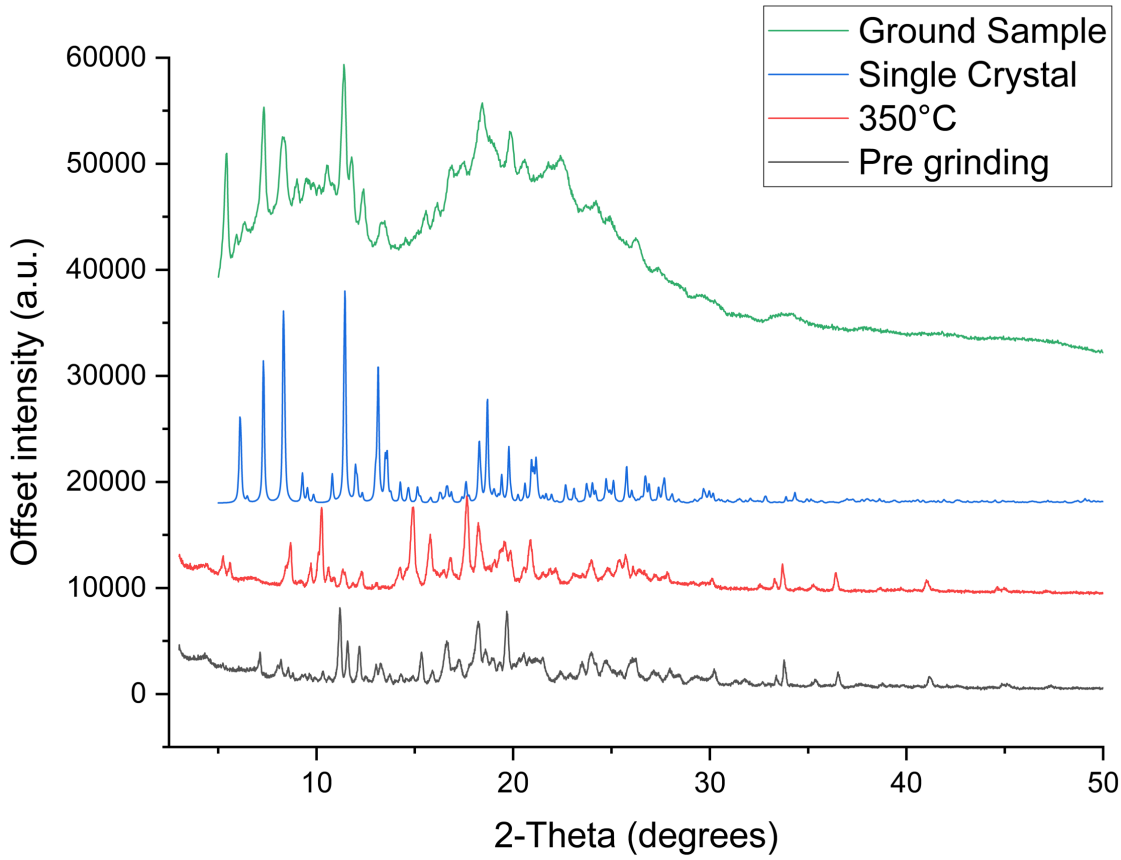


Figure 7-100 Combined powder XRD plots for compound 19 polymorphs comparing grinding, single crystal and heating.

The XRD data for compound **19** (see Figure 7-100) reveals the presence of at least three different polymorphs. The ground-up sample reveals the distinct peaks of the single crystal XRD sample, suggesting that in a perfectly ground sample, this is the structure that it adopts. Before grinding, the structure is different, lacking the three prominent peaks of the ground and single crystal sample, however it differs significantly compared to the sample which was heated to 350°C.

Unfortunately, owing to poorer yields, not enough material of compounds **21** and **22** was available to perform powder XRD measurements to explore the polymorphs involved in their mechanochromism. However, it is likely that different polymorphs exist since the thermochromism results also revealed polymorphism with similar changes to the photoluminescence spectra.

Gridneva *et al*.[341] also observed two different crystal structures for their dibenzocarbazole molecules (structures c) and d) in Figure 7-101), both exhibiting drastically different photoluminescent properties – one isomer emitting at 598 nm, and the other at 745 nm.

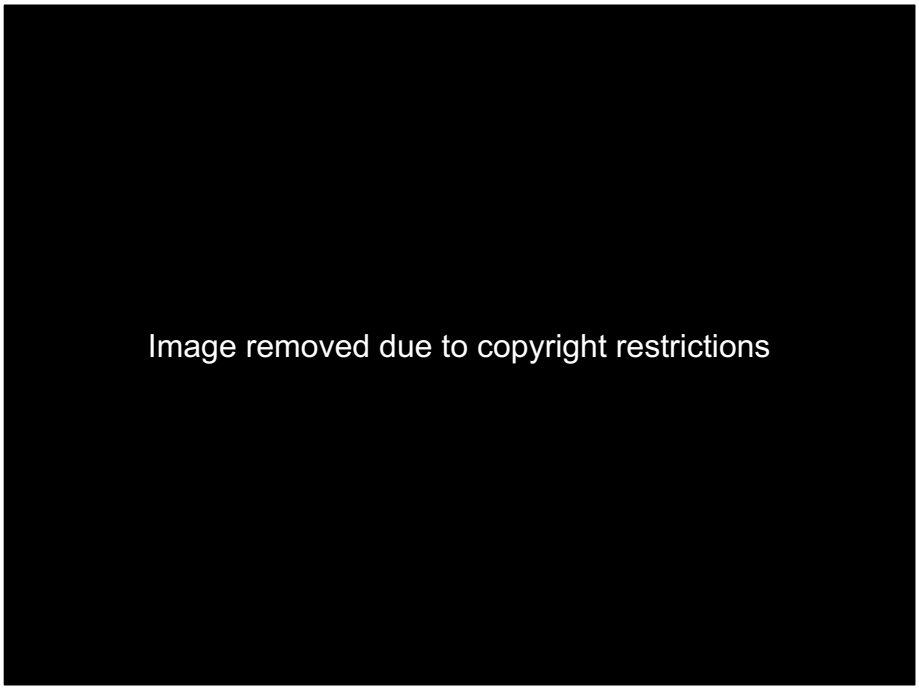


Figure 7-101 Ortep structures of the compounds studied in Gridneva el al.'s[341] work, taken from their paper.

Whilst these different structures were in fact driven by tridentate and tetradentate ligand bonding in each case, another work by Liang *et al*.[377] (also using dibenzocarbazole), observed effective co-facial π-π stacking between dibenzocarbazole donors. Since we observe suggestion of such interactions in section 7.3.12, our thermo- and mechanochromic properties are most likely a result of changes to such interactions, as is evidenced by the above powder diffraction spectra.

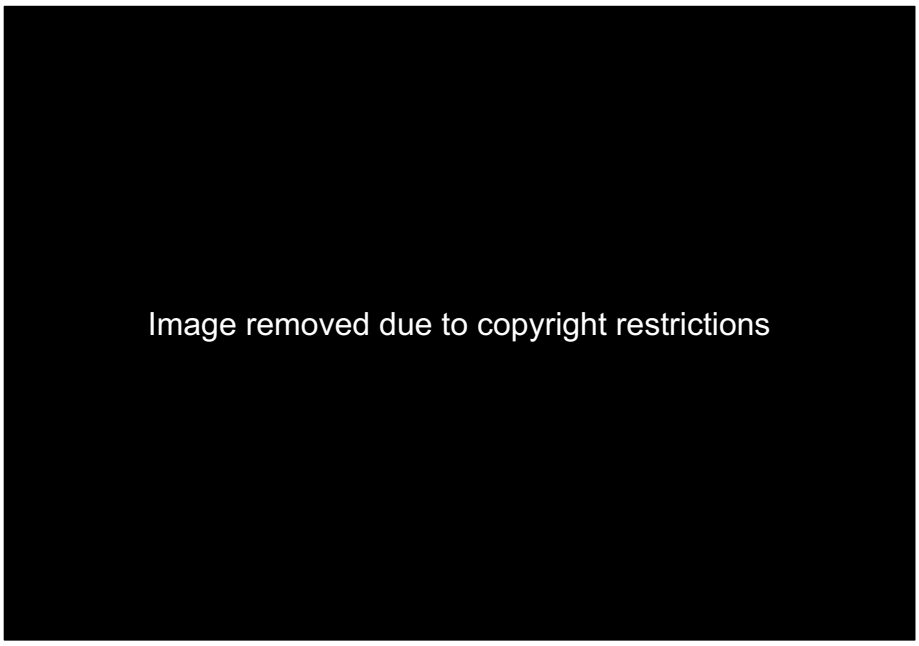


Figure 7-102 Ortep XRD structures of the compounds from Liang *et al*.s[377] work demonstrating the co-facial π-π stacking between dibenzocarbazole moieties. Image taken from their paper.

7.7 Variable temperature NMR

In order to investigate the presence of conformers, both compounds were dissolved in deuterated dimethyl sulfoxide and ^{1}H NMR performed at various temperatures. The resulting spectra are shown in Figure 7-103 and Figure 7-104.

2DBCzPN (18)

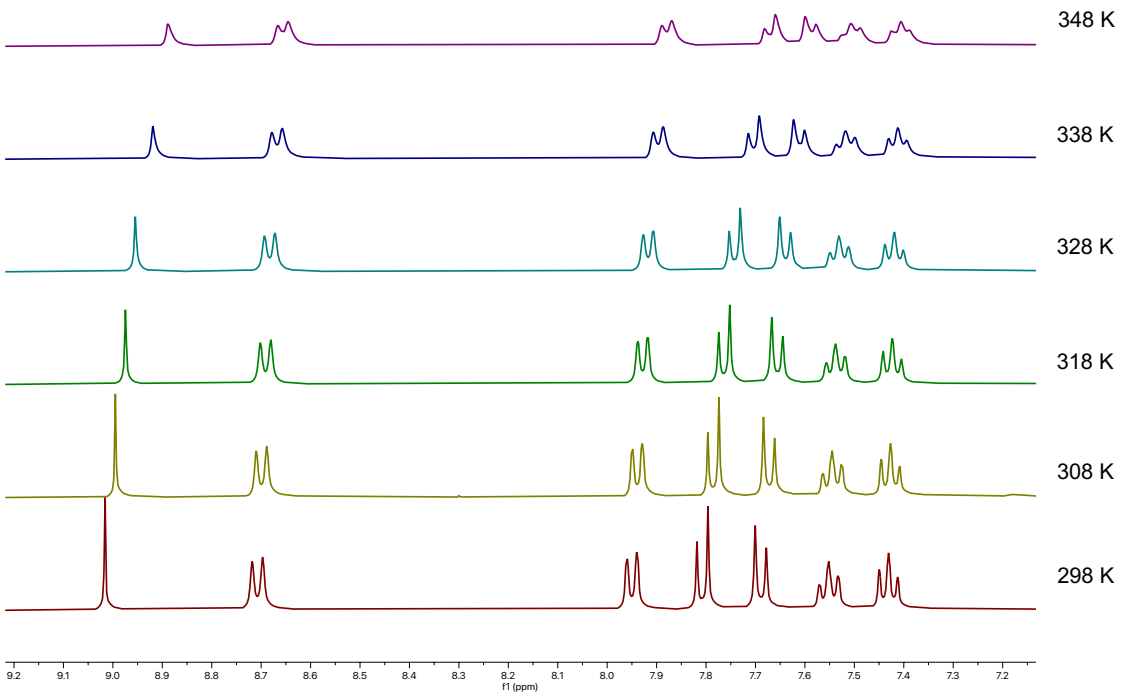


Figure 7-103 Variable temperature ^{1}H NMR spectra of compound 18 highlighting the aromatic region.

4DBCzIPN (19)

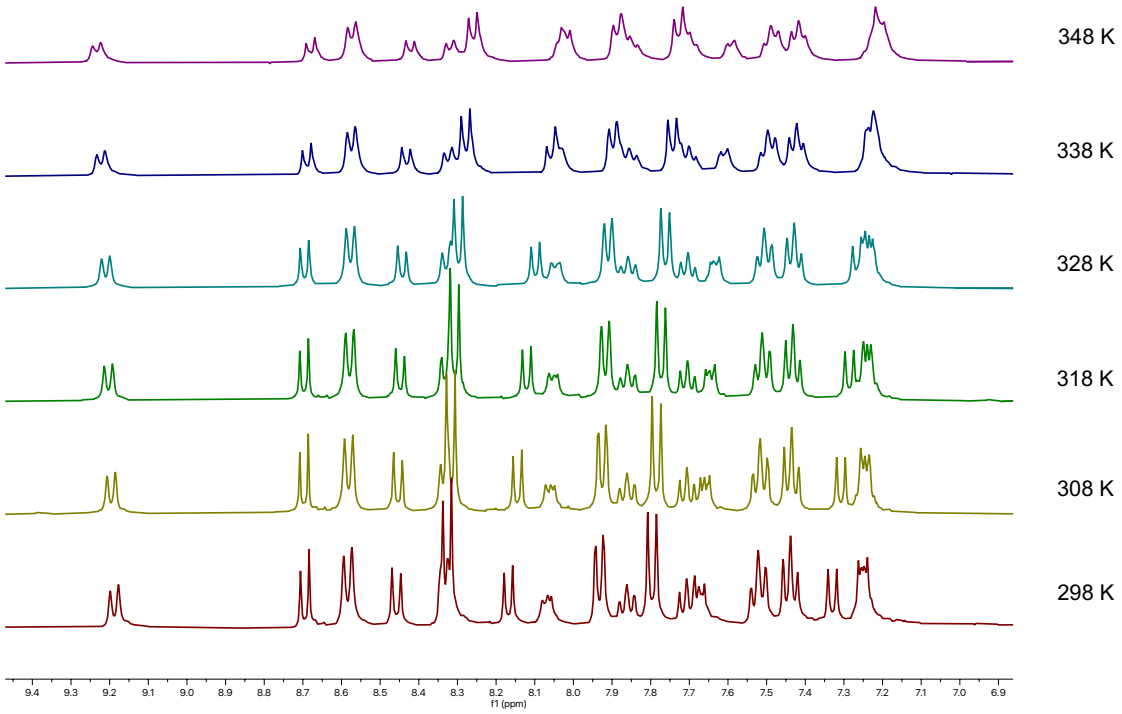


Figure 7-104 Variable temperature ^{1}H NMR spectra of compound 19 highlighting the aromatic region.

In both cases, peaks in the aromatic region broaden at higher temperatures. This suggests increased vibrational motion in these compounds caused by conformational changes due to the flexible quasi-helix in the donor moieties. The more prominent merger of peaks at high temperature for compound **19** suggests the presence of conformers in the more congested environment[367] (with the buckling of the dibenzocarbazole moieties being capable of misaligning with their neighbours).

7.8 Comparison to literature compounds

7.8.1 On thermal properties

Comparing the thermal properties of the compounds in this study to analogous reported literature compounds reveals some interesting trends.

Table 7-40 Comparison of the thermal properties of the compounds form this chapter with similar derivatives from the literature.

		Melting point (°C)	5% mass loss (°C)
2CzPN Derivatives	2CzPN	351.7[378]	322[379]
	2tBu-CzPN	340.2[378]	333[379]
	2Ph-CzPN	312[379]	447[379]
	2DBCzPN (**18**)*	395.4	466.1
4CzIPN Derivatives	4CzIPN	381[380]	403[351]
	4MBCzIPN (**20**)*	456	530.3
	4DBCzIPN (**19**)*	465.3	544.1
	4DTPIPN	-	414[360]
CzPS Derivatives	Cz-PS	-	311[336]
	MBCz-PS	-	502[381]
	DBCz-PS (**21**)*	386.9	495.3
Cz-BZPN Derivatives	Cz-BZPN	246[382]	382[382]
	MBCz-BZPN	-	453[381]
	DBCz-BZPN (**22**)*	407.5	531.3

* Refers to the compounds synthesised in this chapter; Cz-BZPN, MBCzPS and MBCz-BZPN are labelled O2C, BBCS and BBCC in the literature respectively, but were renamed here for ease of comparison (*i.e.* for *carbazole*, *monobenzocarbazole* and *dibenzocarbazole*).

From Table 7-40, it is clear that increasing conjugation of the carbazole-like donors, in almost all cases, leads to a dramatic increase in thermal stability. The only outlier is going from Cz-BZPN, to MBCz-BZPN and DBCz-BZPN (**22**), where the difference between mono- and dibenzocarbazole appears to suggest DBCz-BZPN (**22**) is less stable than MBCz-BZPN. However, it is more likely that this is an artefact of instrumental error since they are so close in value, and that in reality there will be little to no difference between the two molecules' thermal stability. Interestingly, adding two phenyl groups to the 3 and 6 positions on the carbazoles in 2Ph-CzPN – going from 2CzPN – we observe a 125°C increase in 5% mass loss temperature. However, when the additional phenyl rings are bonded with no means of rotation as part of a dibenzocarbazole donor in compound **18**, this increases by a further 19.1°C, showing that these benzene rings being fused to the carbazole rather than connected by a C-C bond makes for even more stable molecules.

A single extra benzene ring fused to the donor in compound **20** results in a massive increase in thermal stability compared to 4CzIPN, increasing the 5% mass loss temperature by 127°C, increasing further by 13.8°C for dibenzocarbazole in compound **19**. Whilst the gains in stability do not increase by as much with increasing numbers of fused aromatic rings, the enhanced thermal stability compared to the progenitor molecules in the literature is striking, especially since in 4CzIPN derivatives, significant steric congestion would suggest a potential for a weakening of the D – A bonds. Interestingly, in replacing two carbon atoms in each donor with slightly bulkier sulfur heteroatoms, causing slight structural contortions, Cardeynaels *et al.*[360] demonstrated a more modest 11°C increase in thermal stability. Compared to the rest of the survey in Table 7-40, this suggests that the enhancement in stability is more to do with steric effects rather than changes to the electronic properties of the donor moieties in these types of molecules.

The literature seems to be less forthcoming on reporting melting points for these compounds. However, from the values obtained, it can be seen in Table 7-40 that the melting points increase substantially upon increased conjugation of the donor. Interestingly, going from 2CzPN to its diphenyl derivative, 2Ph-CzPN, the melting point drops by ~40°C[378, 379]. On the other hand, using dibenzocarbazole as the donor, it increases by ~44°C. This suggests increased intermolecular interactions between the molecules when a dibenzocarbazole moiety is used, requiring increased thermal energy to overcome the weak forces holding the molecules close together. The face-to-face / edge-to-face contacts shown in the XRD data in section 7.3.12 supports this. This contrasts with the phenyl rings which presumably, possessing as they do, extra degrees of rotational freedom, makes for poorer alignment for face-to-face π-π interactions that would bring added stability to the dibenzocarbazole derivatives.

7.8.2 On photophysical and electrochemical properties

2DBCzPN (18) – 2CzPN

According to Wong *et al*.[338], in toluene, 2CzPN fluoresces at 485 nm, with a FWHM of 85 nm and 28.1% PLQY. The HOMO was measured as -5.88 eV and the LUMO -2.97 with an E_g of 2.91 eV. The dibenzocarbazole derivative, 2DBCzPN (**18**), on the other hand, fluoresces with a much redder 590 nm and broader 137 nm FWHM. The increased FWHM suggests increased CT character. The dibenzocarbazole also leads to a shallower HOMO at -5.64 eV and deeper LUMO at -3.15 eV, resulting in a 0.42 eV narrower HOMO-LUMO gap of 2.49 eV, suggesting better HOMO conjugation than standard carbazole donors.

4DBCzIPN (19) – 4CzIPN

The work of Uoyama *et al*.[33] reports 4CzIPN to have a PL of 507 nm and PLQY of 93.8% in toluene. Our compound, 4DBCzIPN (**19**), significantly red-shifts the emission to 678 nm – a bathochromic shift of 171 nm accompanied by a wide FWHM of 178 nm. Being a deep-red emitter, it is fairly unsurprising that compound **19** possesses a drop in its degassed PLQY to just 4.37% since, by their very nature, red emitters necessitate a lower lying triplet manifold, and therefore opens up more readily accessible lossy non-radiative decay pathways. Such non-radiative decays could conceivably occur *via* a flapping motion arising from the non-planar dibenzocarbazole moieties. The HOMO and LUMO values of 4CzIPN, as listed by Nakaotani *et al*.[383], are -5.8 eV and -3.4 eV respectively, giving an E_g of 2.4 eV. Swapping all four carbazole donors for 7H-dibenzo[c,g]carbazole results in a shallower HOMO at -5.55 eV and almost identical LUMO at -3.39 eV. The HOMO-LUMO energy gap is much narrower by swapping to the more conjugated dibenzocarbazole at 2.16 eV, a drop of 0.24 eV, supporting the idea that the HOMO is better conjugated[384] despite the kink to the donor revealed in the single crystal XRD.

In terms of thermochromism, Etherington *et al*.'s[351] 2019 study of 4CzIPN investigated annealing samples of 4CzIPN and their photophysical properties. Inspecting their prompt emission (in their supporting information, through pixel-by-pixel measurements in order to approximate), they show a ~26 nm blue-shift in emissions, compared to our observations with compound **19** of an up to 85 nm blue-shift. As such, it is clear that the larger dibenzocarbazole donor moieties lead to enhanced thermochromism in TADF compounds.

4MBCzIPN (20) – 4CzIPN

Like compound **19**, the monobenzocarbazole derivative, 4MBCzIPN (**20**), manifests a blue shift in its emissions, this time by a more modest 54 nm, albeit still larger than Etherington *et al*.'s[351] observations for 4CzIPN. The FWHM of the emission profile is much less for compound **20**, widening to only 117 nm, 61 nm narrower than its dibenzocarbazole counterpart, suggesting a slightly weaker CT state. Its PLQY on the other hand, jumps significantly to 54.8% owing to the significantly more rigid donor moieties reducing non-radiative decay pathways (with no flapping motion possible). The HOMO at -5.91 eV lies 0.11 eV deeper than 4CzIPN's[383] and the LUMO is only ever so slightly shallower at -3.39 eV (by only 0.01 eV). This differs from compound **19**, the HOMO of which was shallower – suggesting that increased HOMO conjugation in these compounds compared to 4CzIPN narrows the HOMO-LUMO energy gap[384]. It also suggests that the increased conjugation deepens the HOMO, but the quasi-helical nature of compound **19** acts counter to this to shallow it. However, we can rule out the kink in the dibenzocarbazole donor interrupting HOMO conjugation since, as stated before, the HOMO-LUMO gap for compound **19** is narrowing; the electrochemical energy gap between the HOMO and the LUMO in compound **20** is 2.52 eV, being 0.36 eV wider than compound **19**, and 0.12 eV wider even than 4CzIPN.

DBCz-PS (21) – Cz-PS

The compounds Cz-PS (bis(4-(3,6-di-tert-butylcarbazole)phenyl)sulfone (which is confusingly also known as DTC-DPS[358] and pDTCz-DPS[357] in the literature), is reported to emit at 404 nm with a degassed PLQY of 69% in toluene[359] along with a HOMO and LUMO of -5.81 eV and -2.52 eV respectively[359], giving an E_g of 3.29 eV. Replacing the two tert-butyl carbazole donors with 7H-dibenzo[c,g]carbazole raises the HOMO slightly to -5.77 eV and substantially deepens the LUMO to -3.46 eV. The resultant energy gap of 2.31 eV is much narrower than Cz-PS by 0.98 eV, also suggesting that the extension of the donor moiety is enhancing HOMO conjugation. In addition, the PL red-shifted by 38 nm to 442 nm, albeit with a much lower PLQY of 23.3% compared to Cz-PS.

Wu *et al*.[381] examine the monobenzocarbazole derivative of DBCz-PS (**21**), however they neglect to perform CV analysis, nor do they present a value for the optical HOMO-LUMO energy gap. The supplementary information does show the UV-vis absorption spectrum for this compound, however. Through pixel-by-pixel measurements, it is possible to extract a

value for the onset wavelength of the absorption of 381.6 nm, giving an optical HOMO-LUMO gap of 3.25 eV for a pure sample of their compound in an epoxy polymer host. Whilst an unconventional means of arriving at this property, it compares to our observed optical HOMO-LUMO gap (albeit in toluene) of 3.27 eV. Closer inspection of our pure-film sample's UV-vis absorption spectra reveals an optical HOMO-LUMO gap of 3.05 eV – slightly narrower, suggesting slightly better HOMO conjugation on the donor as was found above with compound **19**.

DBCz-BZPN (22) - Cz2BP

Lee *et al*.[334] characterised Cz2BP (effectively Cz-BZPN in our nomenclature), a carbazole derivative of our DBCz-BZPN (**22**), observing luminescence at 438 nm with a PLQY of 21% in degassed toluene. The HOMO and LUMO were measured to be -5.74 eV and -2.64 eV respectively, with a HOMO-LUMO gap of 3.1 eV. Compound **22** has redder emissions at 491 nm, with a significantly lower PLQY of 3.48%, a loss of efficiency which can be attributed to the flapping motion of the dibenzocarbazoles. The HOMO becomes shallower at -5.65 eV (which shows that 7H-dibenzo[c,g]carbazole is a stronger donor than 9H-carbazole) and the LUMO is much deeper at -3.54 eV. The electrochemical E_g narrows by 0.99 eV to 2.11 eV by swapping to dibenzocarbazole, again suggesting enhanced conjugation.

Wu *et al*.'s[381] paper examining the monobenzocarbazole derivative of DBCz-PS (**21**) and DBCz-BZPN (**22**) in an epoxy polymer host reveals an onset of 480 nm, equating to an optical HOMO-LUMO gap of ~2.58 eV for compound **22**, which sits between the carbazole and dibenzocarbazole derivatives values, as would be expected since conjugation length follows the order carbazole < monobenzocarbazole < dibenzocarbazole. It should be stressed here however, that Wu *et al*.'s[381] value comes from an optical HOMO-LUMO gap, so may not be comparable to our electrochemical HOMO-LUMO gap (and the value obtained for the Wu *et al*.[381] optical gap was acquired by pixel-by-pixel analysis, so may have a slightly larger degree of error).

Unfortunately, without cyclic voltammetry data from Wu *et al*.'s[381] work, or single crystal XRD from our own, this will have to remain supposition for the time being.

Two physical phenomena unite all compounds in this study: that they demonstrate both red-shifted emissions compared to their literature projenitors, and that they possess reduced PLQYs. The energy gap law[385,386] states that the greater the energy gap between two states (such as S_0 and T_1), the less likely the excited state is to decay non-radiatively[34]. This has implications for deep red and infrared emitting compounds since they will need a significantly low energy S_1 and T_1 state which would be close enough to the ground state that both radiative and non-radiative decay pathways would be competing with one another much more intensely. This means that the PLQYs of such compounds are much more likely to be low than those which emit with more blue-shifted wavelengths. When these molecules possess increased degrees of motion in the excited state[387] (such as dibenzocarbazole's flapping motion), this acts as a compounding factor, further lowing the emission efficiency.

As such, we can ascribe the poorer emissions and increased red-shifting observed to increased non-radiative decay pathways from the excited states of compounds **18** to **22**, brought about by a more flexible and non-planar donor moiety.

7.9 Conclusions

We demonstrate that 7H-dibenzo[c,g]carbazole, whilst understudied, can present a suitable donor moiety for TADF molecules (such as compound **19**). The flexibility of the quasi-helical aromatic system leads to redder emissions than other, more planar, comparable carbazole based systems. Of significant note is the fully reversible thermochromic and mechanochromic properties associated with 7H-dibenzo[c,g]carbazole-based molecules. From our results and the literature, the strength of the thermochromic blue-shifting observed in the 4CzIPN derivatives follows the order 4DBCzIPN (**19**) > 4MBCzIPN (**20**) > 4CzIPN, we can confidently establish that the size of the donor moieties strongly influence interactions between the molecules in the solid state giving rise to increased thermochromic action.

This presents interesting potential for these compounds to be used for encryption, anti-counterfeiting, data storage purposes, and sensors for thermal changes. Interestingly, both heating and grinding compound **19** resulted in a blue-shifting of emissions, compared to the red-shifting observed in the other compounds. This is likely due to different interactions between neighbouring molecules compared to this compound.

The larger HOMO spread across the donor moiety of 7H-dibenzo[c,g]carbazole compared to carbazole has yielded significant reductions in the E_g for each compound studied, relative to that of well-studied and previously reported carbazole-based analogues. When changing the conjugation length of the donors, the E_g values were demonstrated to follow the order carbazole > monobenzocarbazole > dibenzocarbazole regardless of acceptor moiety used, showing that the size of conjugation of the HOMO directly impacts the energy gap between HOMO and LUMO.

The 7H-dibenzo[c,g]carbazole donor also presents interesting aggregation effects, giving more intense luminescence in the solid state, with examination of the single-crystal X-ray diffraction data suggesting that in the crystalline form, the molecules of these compounds are just close enough to permit non-covalent interactions between them in some cases.

Further research exploiting the advantages of extended donor conjugation (namely, narrower HOMO-LUMO gap) by means of bridging the quasi-helical donor moieties should be investigated. This would undoubtedly result in higher PLQYs with the same deep red

emissions, due to the removal of lossy flapping motions in the donors. Furthermore, continuing with quasi-helical structures, by extending further may lead to interesting developments in thermo- and mechanochromic small molecules. Engineering of the HOMO-LUMO gap *via* substituent groups or even modified π-bridges attached to dibenzocarbazole donors as a means of decreasing the donor strength, may also result in thermo- and mechanochromism in the blue and green regions.

Chapter 8 Conclusions and future work

The main focus of this thesis has been the synthesis and photophysical characterisation of novel boron and carbazole-based TADF molecules for use as emitter molecules for OLEDs. An initial exploration of varying the conjugation of carbazole-like donor moieties in small dimesityl boron-based emitters was performed. This was followed by exploration of π-bridge modification to achieve non-covalent interactions with the empty p-orbital of boron to enhance dihedral separation of the HOMO and LUMO whilst maintaining charge transfer. Further exploration of a promising quasi-helical donor yielded a diverse family of emitters with intriguing thermochromic and mechanochromic properties.

In Chapter 4, four novel D-A-type molecules were synthesised and studied. The degree of conjugation in the structure of their donor moieties was varied, yielding room temperature phosphorescence and weak TADF in two. The dibenzocarbazole-based compound (DBCz-DMB (**3**), the most conjugated of the four) with its RTP served as the basis for further study in Chapter 7. Comparison to these molecules was achieved with the accompanying work of Dr Joseph Cameron, whereby methoxy groups were added to the carbazole moieties to yield TADF. Chemical and thermal stability of three of these compounds were revealed to be significantly poor, suggesting the B-N bond is particularly weak. XRD studies suggest that steric congestion around the boron atom helps to protect it from attack (as is well-demonstrated by IMSB-DMB (**1**), which informed the design of further molecules in chapter 5. Interesting aggregation induced emissions were observed for the iminostilbene-based compound, despite its poor emissions in solution.

In Chapter 5, the benefits of using the methoxy groups in Dr Joseph Cameron's molecules from Chapter 4 was further explored by attaching them to π-bridges in order to orientate them more favourably towards interacting with the empty p-orbital of a boron atom in the acceptor moiety. Whilst TADF was found to be absent in these compounds, significant blue-shifting and narrowing of the FWHM was observed. Further modification by Dr Andrea Pinto, produced phenoxy derivatives. These showed much more complicated photophysics, involving fluorescence, room temperature phosphorescence and TADF, all in the same molecule. Interestingly, the single crystal XRD data reveals co-facial orientations between the phenoxy rings on the π-bridge and the mesityl rings on the acceptor moiety, strongly suggesting this contorted structural feature between donor and acceptor leads to the observed properties.

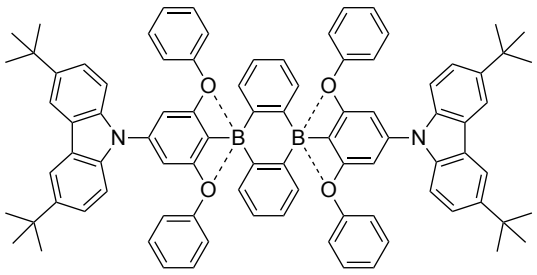
Chapter 6 culminates in two significant developments. Firstly, the synthesis of a novel TADF molecule with record-breaking long lifetimes for its structural type, striking solvatochromism and dual LE and CT emissions, suggesting that non-covalent interactions from the methoxy groups result in dihedral orientations, causing significant decoupling of the HOMO and LUMO in non-polar media. The interaction remains flexible enough that CT emissions dominate in polar media, being the sole emission type in DPEPO thin films. Secondly, a novel and much more efficient synthesis process for the increasingly attractive acceptor moiety, 9,10-dibromo-9,10-diboraanthracene (DBDBA), was developed. This utilises an alternative and cheaper precursor material than in previous reported works, which also happens to be readily commercially available, saving significant time and effort in the acceptor's preparation. This will open the door to more studies of this type of TADF emitter and allow for a much faster pace of research into its gallimaufry of potential derivatives, further developing our understanding of its complex photophysics.

Chapter 7 returns to the dibenzocarbazole donor which was established as a novel candidate for delayed emission in Chapter 4. The impressive confinement of its HOMO across the donor's surface with no spreading into the acceptor moiety (as demonstrated by DFT calculations) when compared to standard carbazole donors in previously reported compounds such as 4CzIPN, raises the intriguing possibility of its enhanced charge transfer character, despite its quasi-helical nature. A large family of novel emissive compounds, some of which possess TADF character, was produced. All of them displayed pronounced thermochromism and mechanochromism, which was extensively studied.

The main limitation of the compounds in Chapters 4 and 6 are their inherent lack of chemical stability. Extensive studies of the chemical stability were performed for all compounds in Chapters 4 – 6, producing three key discoveries. Firstly, the B-N bond is very weak (revealed by low decomposition temperatures for such compounds, if we assume this is where the molecule breaks first). Second, the B-N bond is highly susceptible to chemical attack *via* hydrolysis upon exposure to water (as illustrated by the cyclic voltammetry studies and water spiking experiments). This second point can be rectified by introducing steric hinderance to block attack at the boron's empty p-orbital, as is evidenced by the congestion of IMSB-DMB and the lack of such hydrolysis in Dr Joseph Cameron's compounds which incorporated methoxy and methyl groups on the donors, orientated such as to provide steric protection. Thirdly, introduction of π-bridges with methyl or methoxy substituents significantly protects boron from chemical attack. However, this is not universally true, as

in Chapter 6, tBu-MeOCzDBA is highly susceptible to hydrolysis. However, the highly planar nature of the DBA acceptor core may well be resulting in a slightly more exposed boron atom. Sadly, without adequate crystals of tBu-MeOCzDBA to illuminate its conformation and bond lengths, the true cause of its degradation shall have to remain a mystery for the time being.

The more complicated photophysics of the two compounds with phenoxy groups, namely, tBu-MPhOP-Cz-DMB (**14**) and tBu-DPhOP-Cz-DMB (**15**), warrants further study and OLEDs are currently being fabricated. Further exploration of phenoxy groups on π-bridges would also be interesting – pairing such donors with other aromatic rich acceptors such that more complete π-π interactions between donor and acceptor aromatic rings can be achieved. This may result in enhanced charge transfer, as well as stabilising the dihedral between donor and acceptor. One such avenue of research could be to produce a phenoxy analogue of the methoxy-based tBu-MeOCzDBA, replacing the anticipated methoxy oxygen – boron interactions with aromatic π-π interactions between the phenoxy rings of the donors and the DBA acceptor core (see Figure 8-1).



tBu-DPhOP-CzDBA

Figure 8-1 Proposed structure of a compound more likely to exhibit enhanced chemical stability as well as non-covalent interactions, tBu-DPhOP-CzDBA.

Overall, this body of work illustrates successful synthesis of novel boron and carbazole-based materials for luminescent applications, as well as exploration of their photophysical characteristics. Varying of structural features results in dramatic differences in emissive properties and chemical stabilities. Taking these into consideration, it is possible to design more effective materials, possessing high rISC rates for OLED applications.

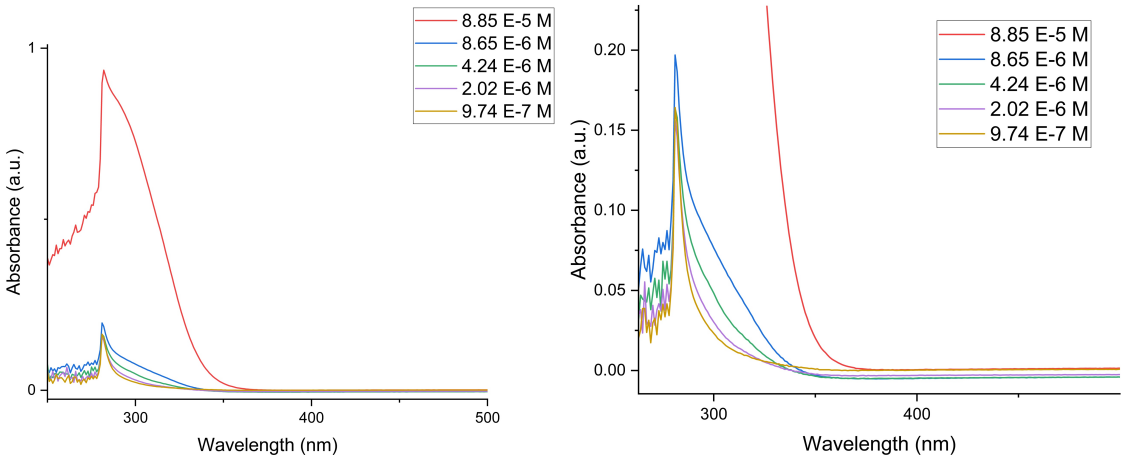
Chapter 9 Appendices

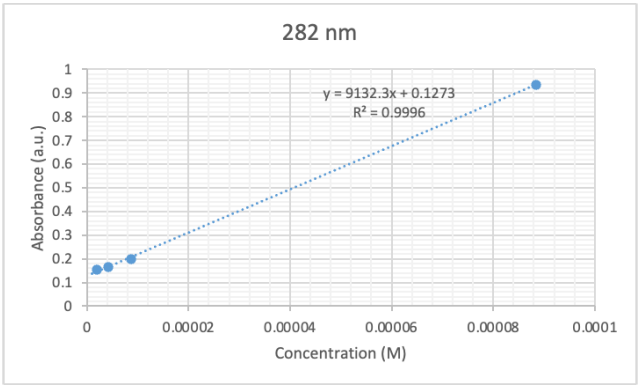
Appendix 1 – Molar absorption coefficients

Herein are the UV-vis absorption plots measured at various concentrations in dry toluene for each target compound in this thesis. Produced from the absorbance (a.u.) of key peaks and concentrations are the molar absorption plots, the gradient of which gives the value of ε for that particular absorption wavelength.

9.1 Chapter 4

9.1.1 IMDB (1)

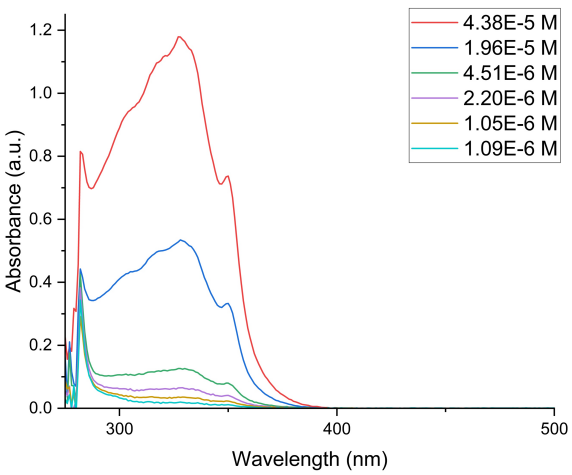


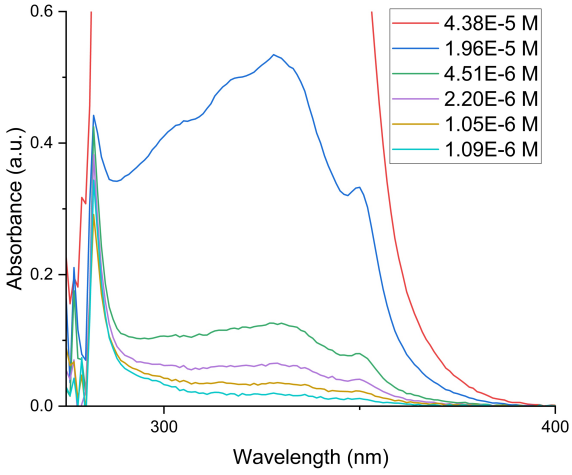


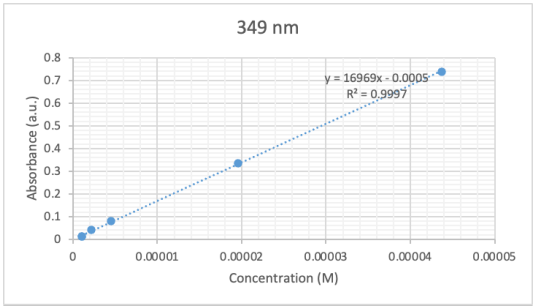
282 nm
$\varepsilon = 9.1323 \times 10^3\ cm^{-1}\ M^{-1}$

Figure 9-1 UV-vis absorption plots and absorption coefficient plots for IMSB-DMB (1) measured in toluene solution.

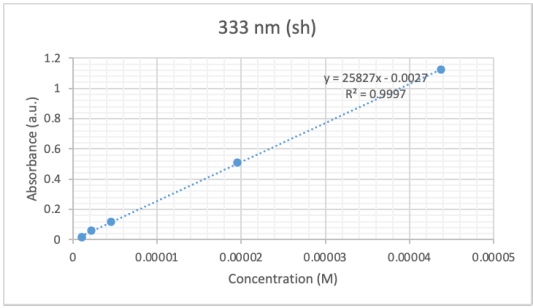
9.1.2 MBCz-DMB (2)



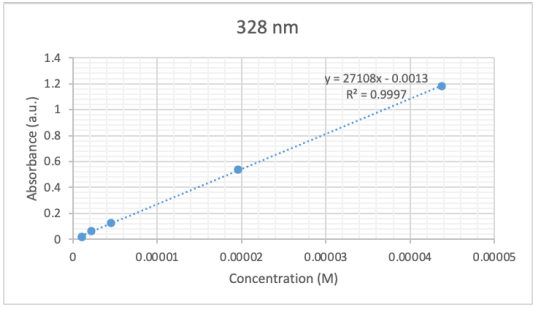




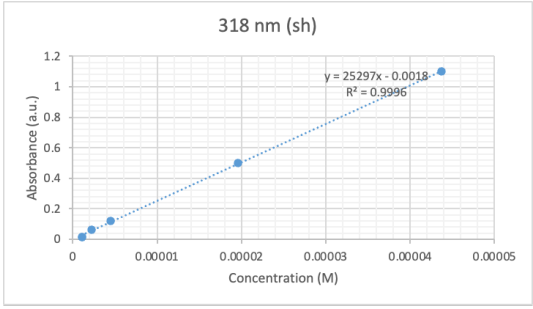
349 nm
$\varepsilon = 1.6969 \times 10^4\ cm^{-1}\ M^{-1}$



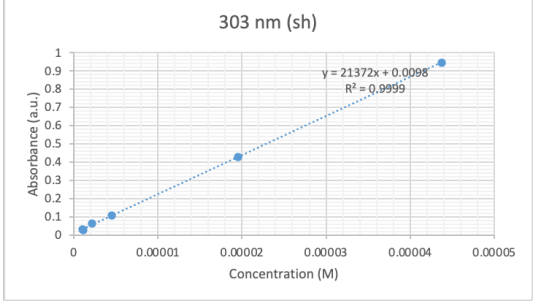
333 nm shoulder
$\varepsilon = 2.5827 \times 10^4\ cm^{-1}\ M^{-1}$



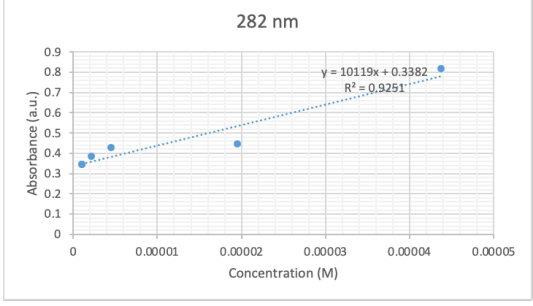
328 nm
$\varepsilon = 2.7108 \times 10^4\ cm^{-1}\ M^{-1}$



318 nm shoulder
$\varepsilon = 2.5297 \times 10^4\ cm^{-1}\ M^{-1}$



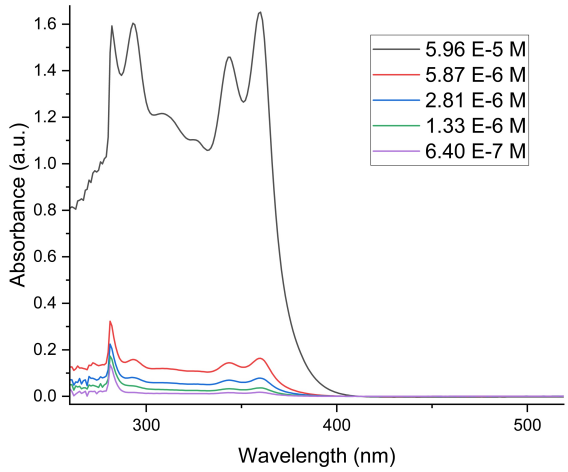
303 nm shoulder
$\varepsilon = 2.1372 \times 10^4\ cm^{-1}\ M^{-1}$

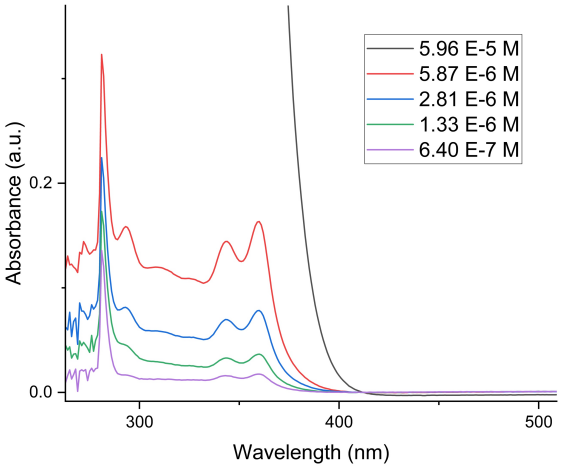


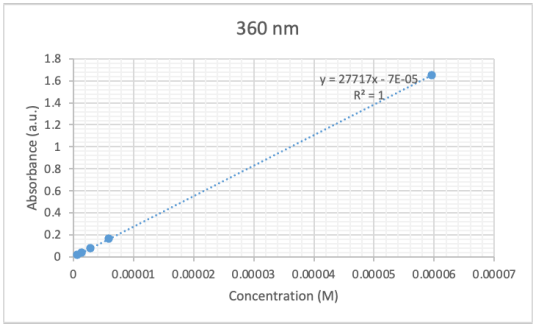
282 nm
$\varepsilon = 1.0119 \times 10^4\ cm^{-1}\ M^{-1}$

Figure 9-2 UV-vis absorption plots and absorption coefficient plots for MBCz-DMB (2) measured in toluene solution.

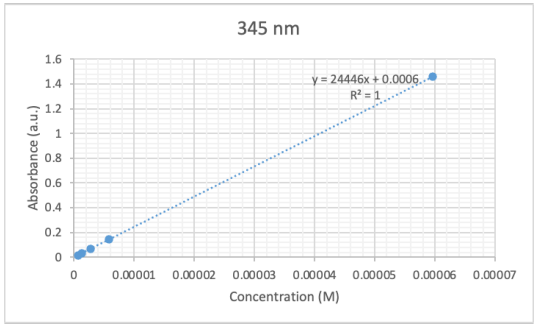
9.1.3 DBCz-DMB (3)



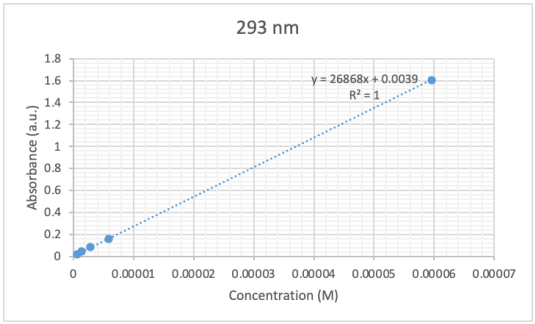




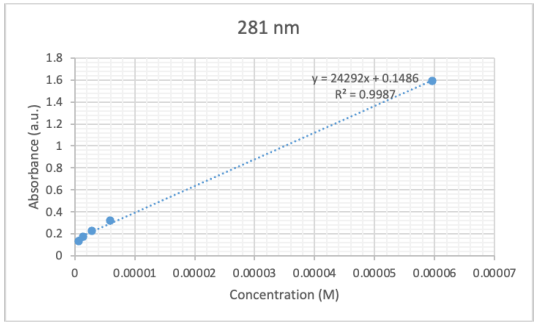
360 nm
$\varepsilon = 2.7717 \times 10^4\ cm^{-1}\ M^{-1}$



345 nm
$\varepsilon = 2.4446 \times 10^4\ cm^{-1}\ M^{-1}$



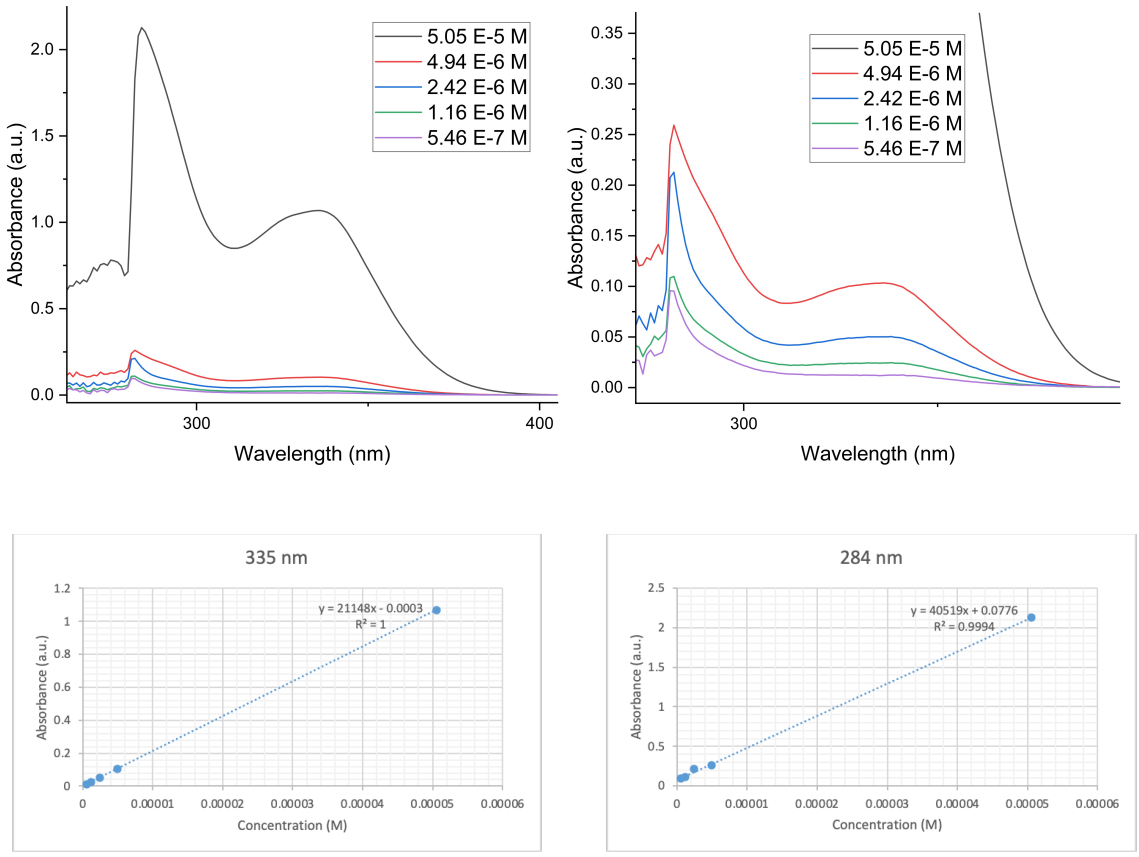
293 nm
$\varepsilon = 2.6868 \times 10^4\ cm^{-1}\ M^{-1}$



281 nm
$\varepsilon = 2.4392 \times 10^4\ cm^{-1}\ M^{-1}$

Figure 9-3 UV-vis absorption plots and absorption coefficient plots for DBCz-DMB (3) measured in toluene solution.

9.1.4 DPhCz-DMB (4)



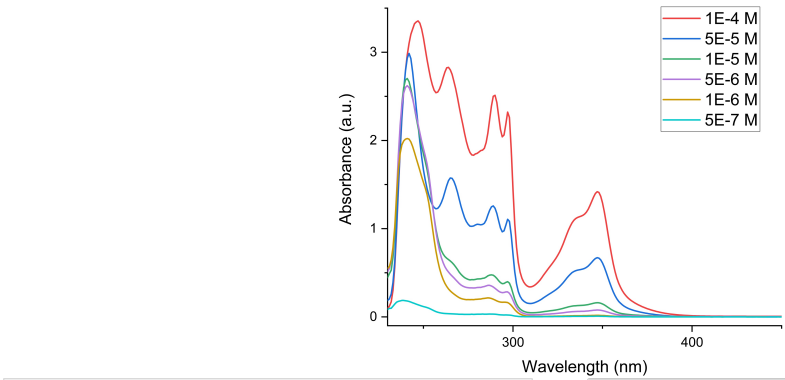
335 nm
$\varepsilon = 2.1148 \times 10^4\ cm^{-1}\ M^{-1}$

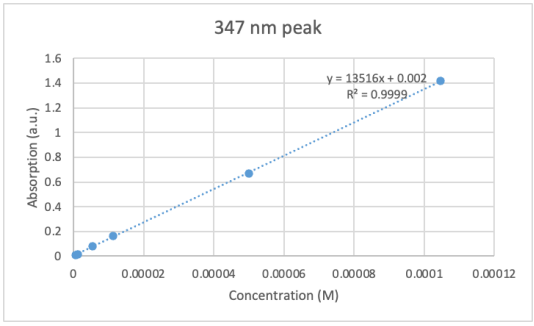
284 nm
$\varepsilon = 4.0519 \times 10^4\ cm^{-1}\ M^{-1}$

Figure 9-4 UV-vis absorption plots and absorption coefficient plots for DPhCz-DMB (4) measured in toluene solution.

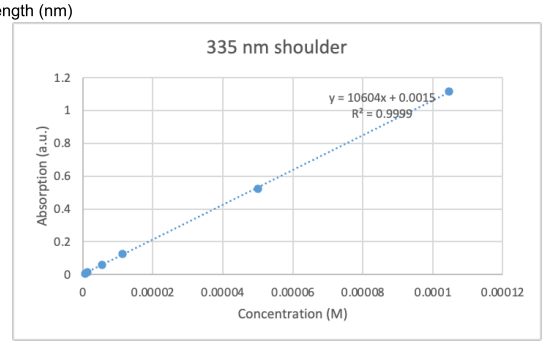
9.2 Chapter 5

9.2.1 tBu-DMP-Cz-OBA (10)

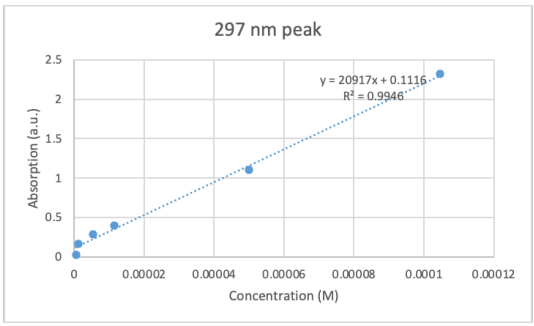




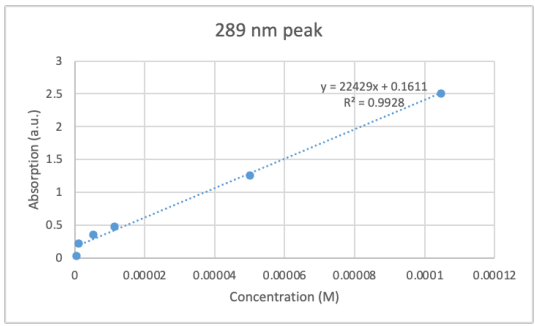
347 nm
$\varepsilon = 1.3516 \times 10^4\ cm^{-1}\ M^{-1}$



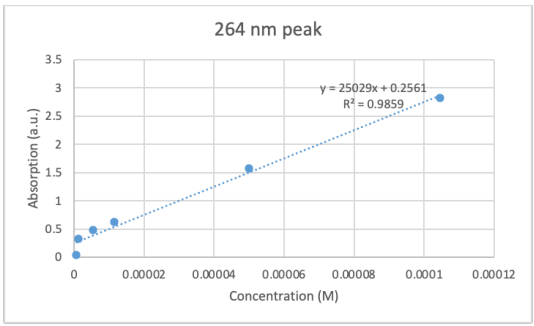
335 nm
$\varepsilon = 1.0604 \times 10^4\ cm^{-1}\ M^{-1}$



297 nm
$\varepsilon = 2.0917 \times 10^4\ cm^{-1}\ M^{-1}$



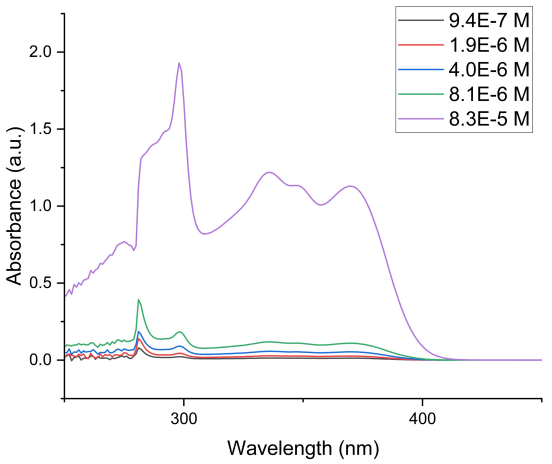
289 nm
$\varepsilon = 2.2429 \times 10^4\ cm^{-1}\ M^{-1}$

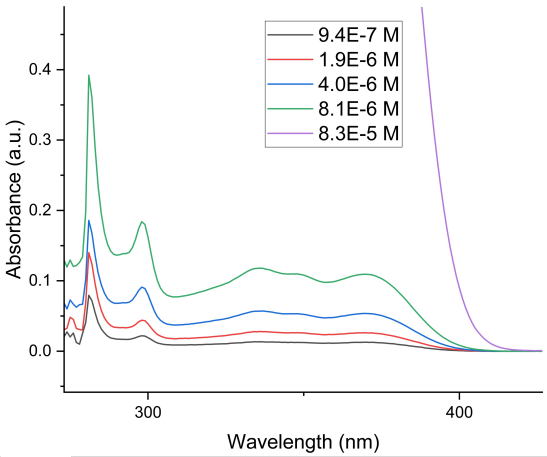


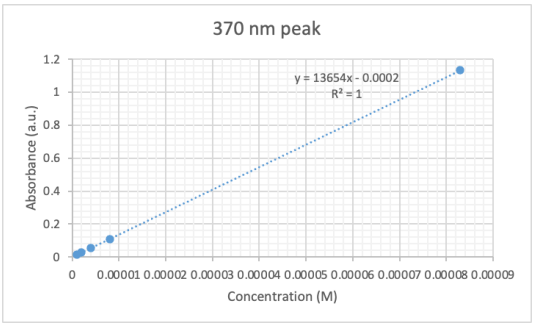
264 nm
$\varepsilon = 2.5029 \times 10^4\ cm^{-1}\ M^{-1}$

Figure 9-5 UV-vis absorption spectra and absorption coefficient plots for tBu-DMP-Cz-OBA (10) measured at various concentrations in toluene solution.

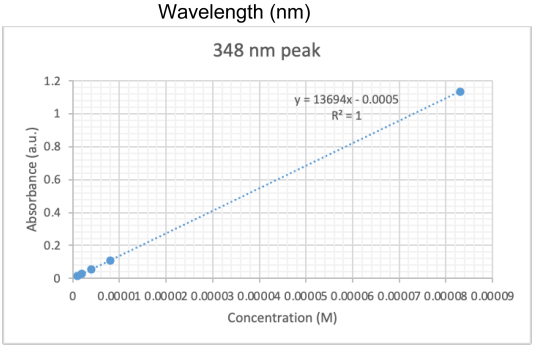
9.2.2 tBu-DMP-Cz-DMB (12)



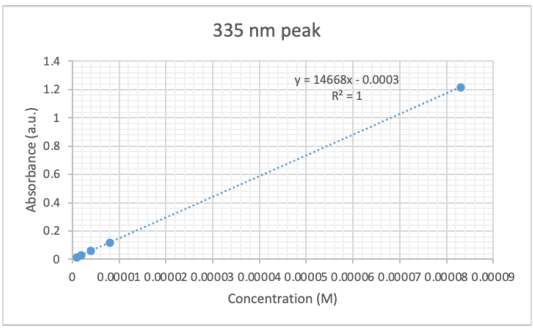




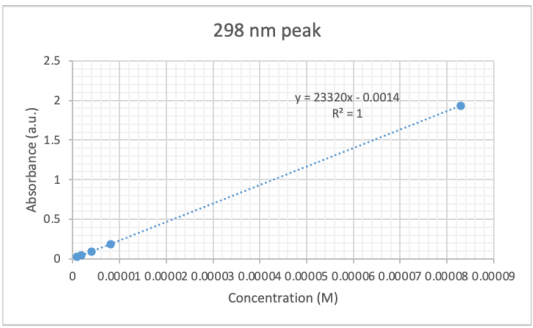
370 nm
$\varepsilon = 1.3654 \times 10^4\ cm^{-1}\ M^{-1}$



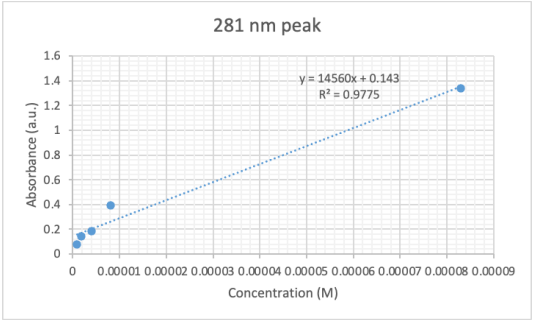
348 nm
$\varepsilon = 1.3694 \times 10^4\ cm^{-1}\ M^{-1}$



335 nm
$\varepsilon = 1.4668 \times 10^4\ cm^{-1}\ M^{-1}$



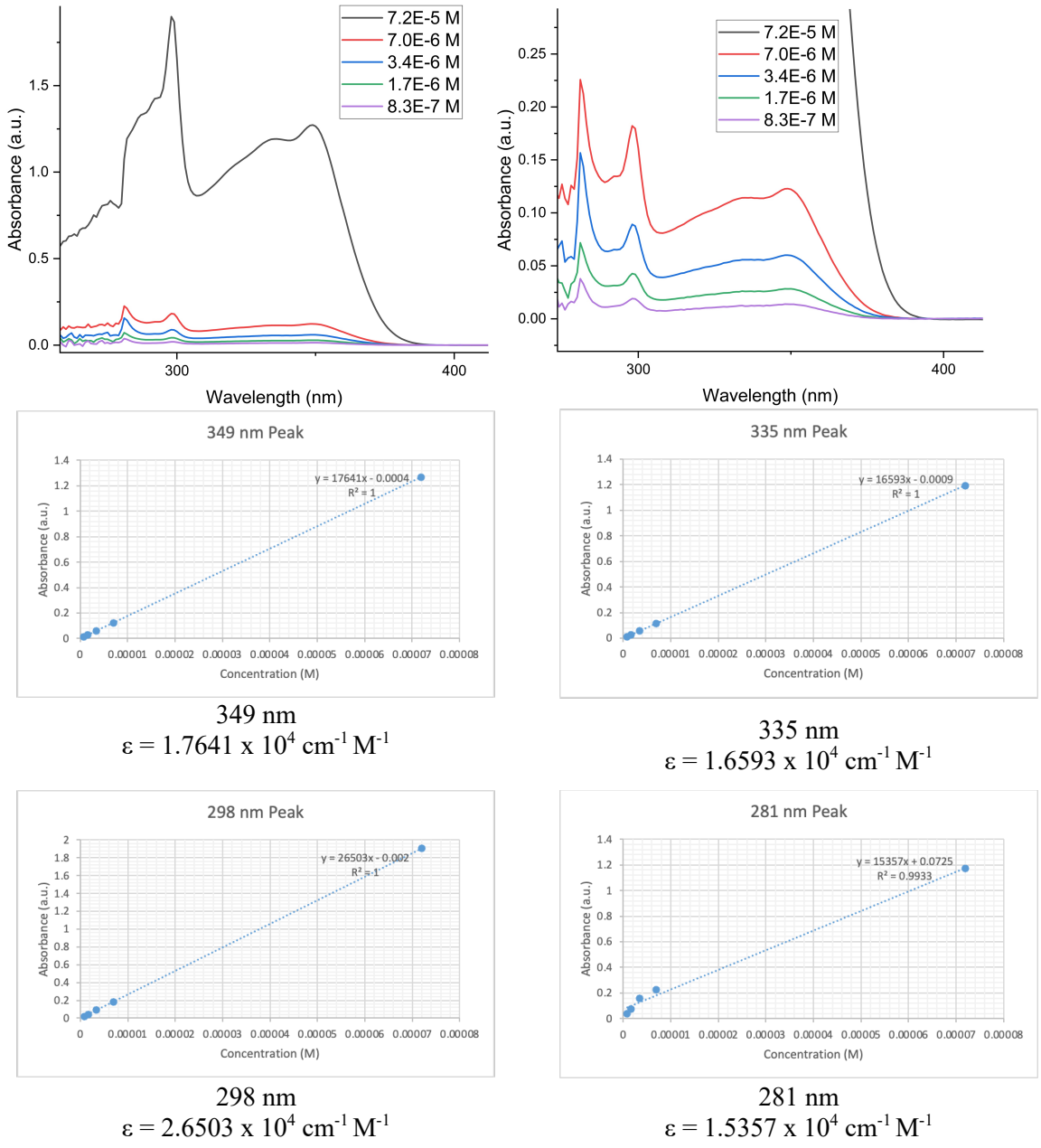
298 nm
$\varepsilon = 2.3320 \times 10^4\ cm^{-1}\ M^{-1}$



281 nm
$\varepsilon = 1.4560 \times 10^4\ cm^{-1}\ M^{-1}$

Figure 9-6 UV-vis absorption spectra and absorption coefficient plots for tBu-DMP-Cz-DMB (12) measured at various concentrations in toluene solution.

9.2.3 tBu-DMeOP-Cz-DMB (13)



349 nm
$\varepsilon = 1.7641 \times 10^4\ cm^{-1}\ M^{-1}$

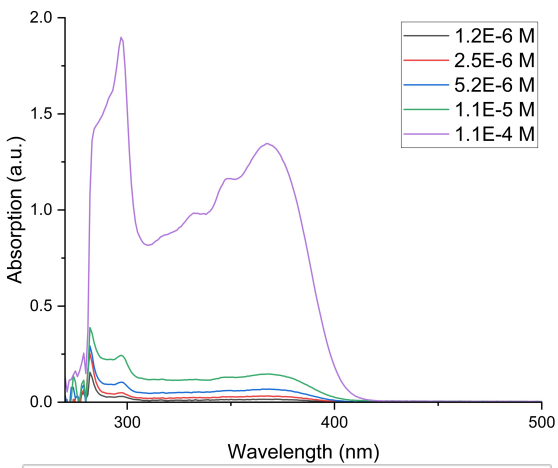
335 nm
$\varepsilon = 1.6593 \times 10^4\ cm^{-1}\ M^{-1}$

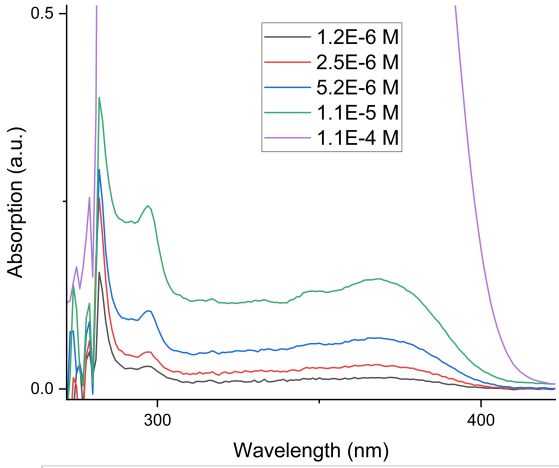
298 nm
$\varepsilon = 2.6503 \times 10^4\ cm^{-1}\ M^{-1}$

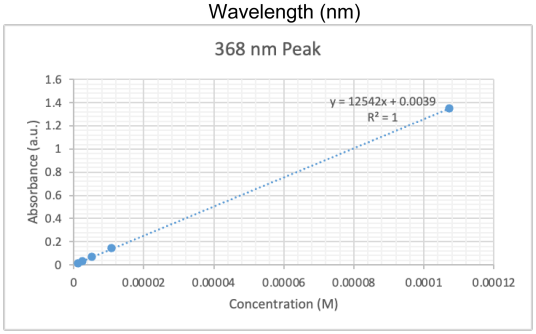
281 nm
$\varepsilon = 1.5357 \times 10^4\ cm^{-1}\ M^{-1}$

Figure 9-7 UV-vis absorption spectra and absorption coefficient plots for tBu-DMeOP-Cz-DMB (13) measured at various concentrations in toluene solution.

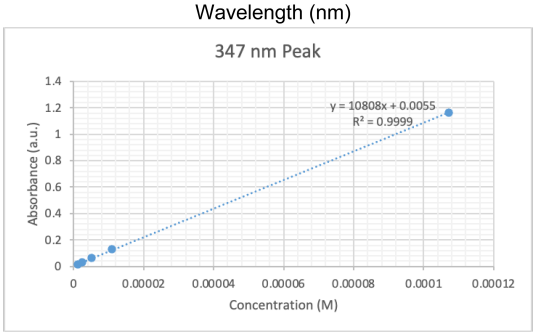
9.2.4 tBu-MPhOP-Cz-DMB (14)



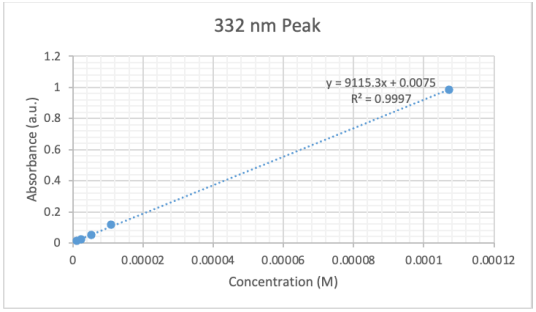




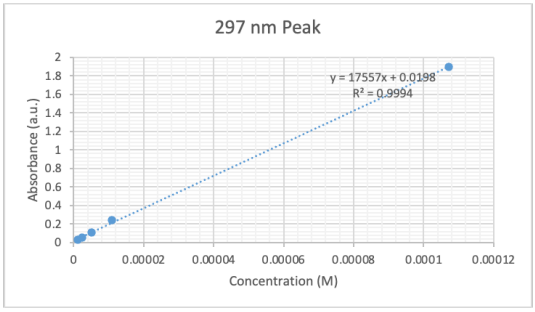
368 nm
$\varepsilon = 1.2542 \times 10^4\ cm^{-1}\ M^{-1}$



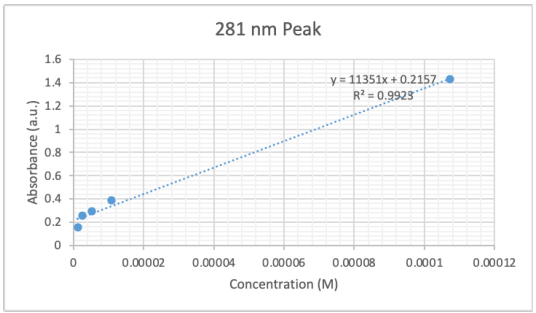
347 nm
$\varepsilon = 1.0808 \times 10^4\ cm^{-1}\ M^{-1}$



332 nm
$\varepsilon = 9.115 \times 10^3\ cm^{-1}\ M^{-1}$



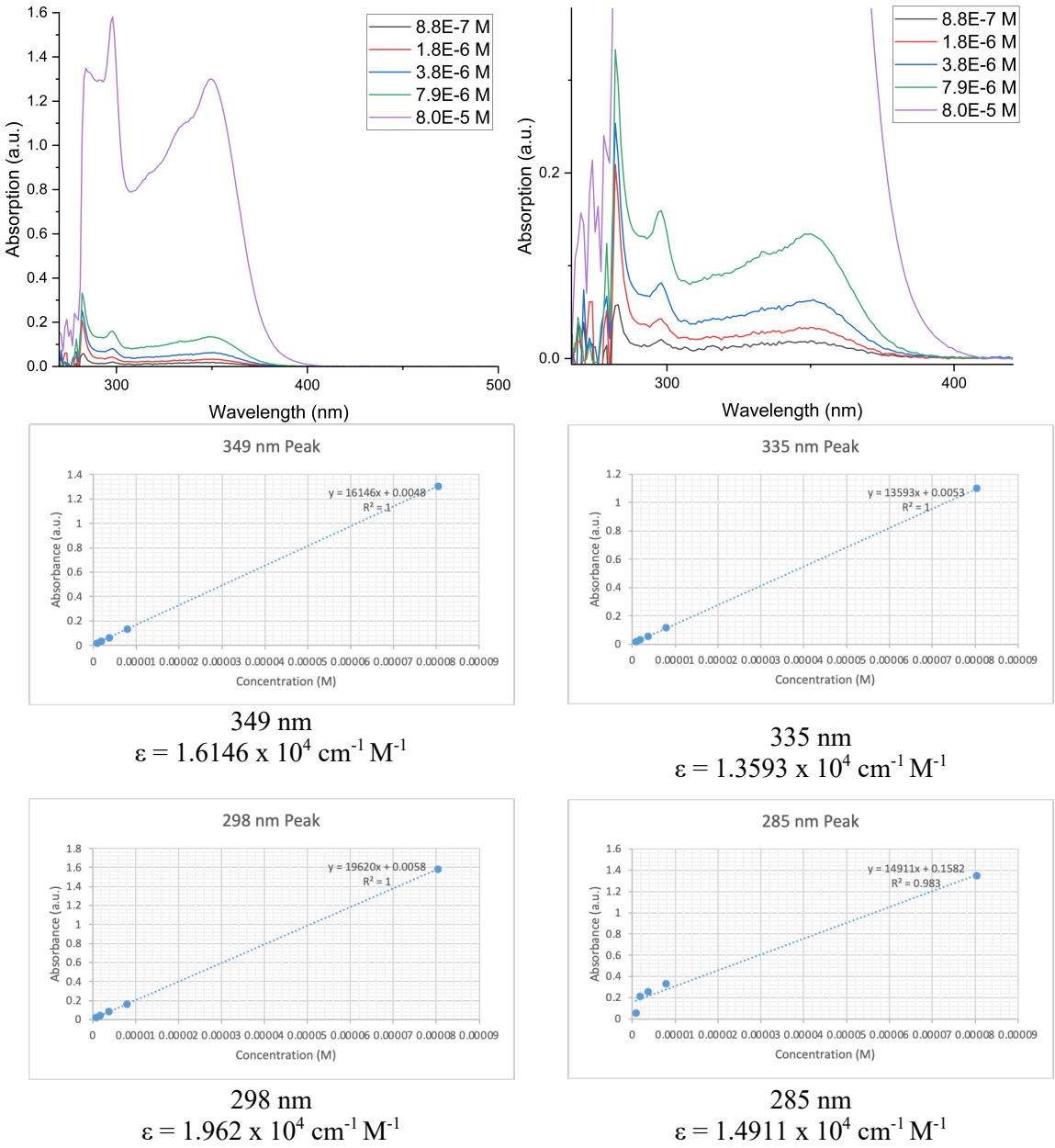
297 nm
$\varepsilon = 1.7557 \times 10^4\ cm^{-1}\ M^{-1}$



281 nm
$\varepsilon = 1.1351 \times 10^4\ cm^{-1}\ M^{-1}$

Figure 9-8 UV-vis absorption spectra and absorption coefficient plots for tBu-MPhOP-Cz-DMB (14) measured at various concentrations in toluene solution.

9.2.5 tBu-DPhOP-Cz-DMB (15)



349 nm
$\varepsilon = 1.6146 \times 10^4\ cm^{-1}\ M^{-1}$

335 nm
$\varepsilon = 1.3593 \times 10^4\ cm^{-1}\ M^{-1}$

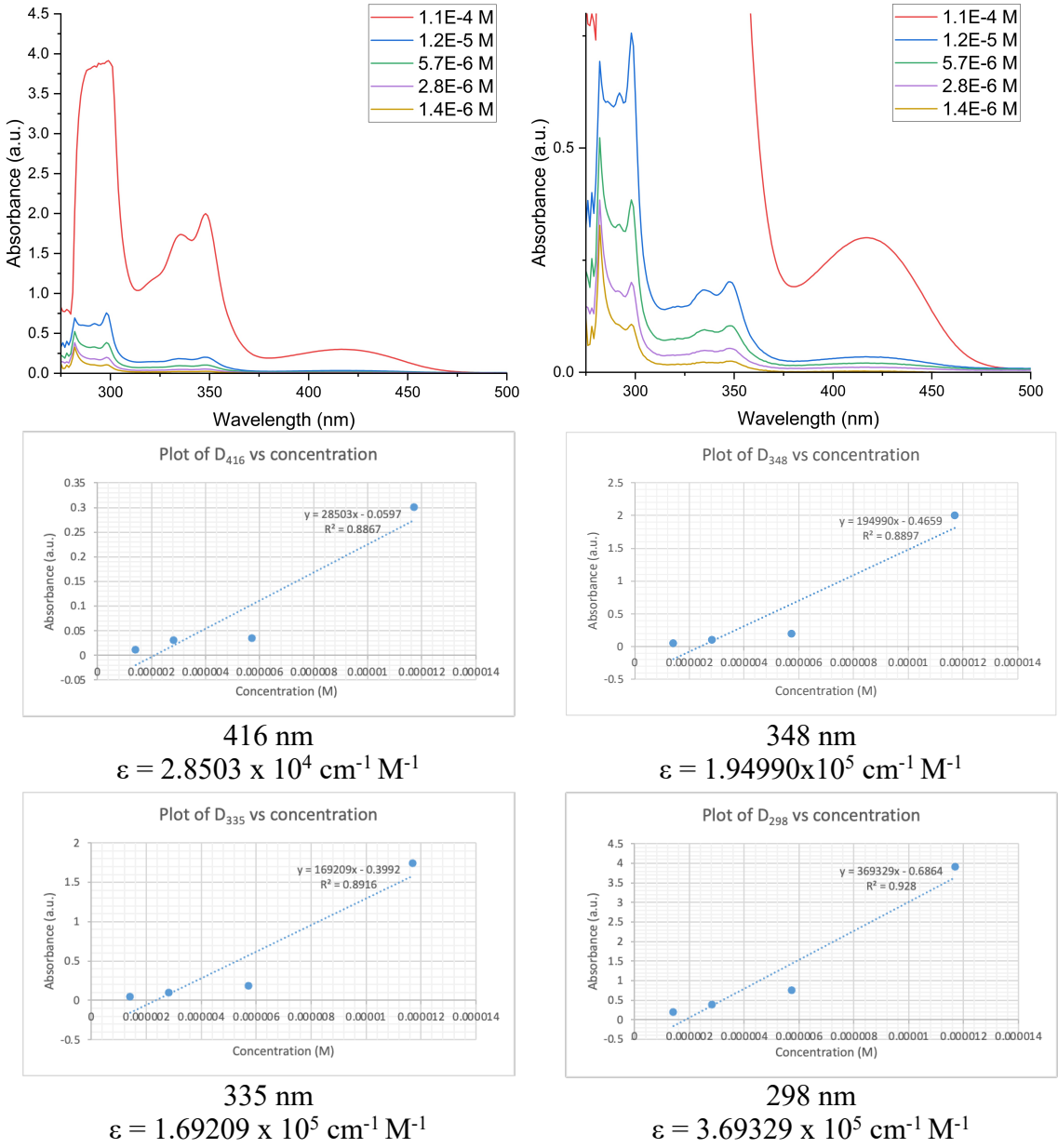
298 nm
$\varepsilon = 1.962 \times 10^4\ cm^{-1}\ M^{-1}$

285 nm
$\varepsilon = 1.4911 \times 10^4\ cm^{-1}\ M^{-1}$

Figure 9-9 UV-vis absorption spectra and absorption coefficient plots for tBu-DPhOP-Cz-DMB (15) measured at various concentrations in toluene solution.

9.3 Chapter 6

9.3.1 tBu-MeOCzDBA (17)



416 nm
$\varepsilon = 2.8503 \times 10^4\ cm^{-1}\ M^{-1}$

348 nm
$\varepsilon = 1.94990 \times 10^5\ cm^{-1}\ M^{-1}$

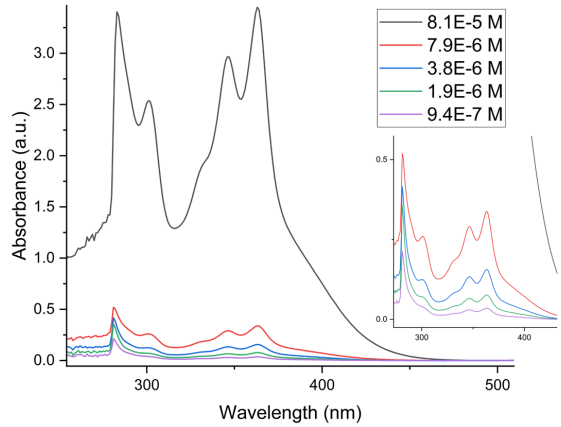
335 nm
$\varepsilon = 1.69209 \times 10^5\ cm^{-1}\ M^{-1}$

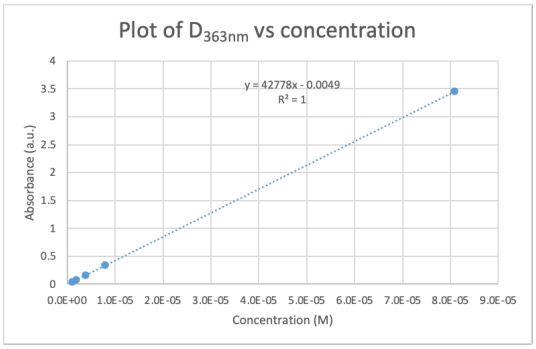
298 nm
$\varepsilon = 3.69329 \times 10^5\ cm^{-1}\ M^{-1}$

Figure 9-10 UV-vis absorption spectra of tBu-MeOCzDBA measured at different concentrations in toluene for molar absorption coefficient calculations. The top plot on the right is the same as the top plot on the left but magnified on the y-axis. Plots of the absorbance of each peak against the respective concentration of the tBu-MeOCzDBA samples are also shown producing the molar absorption coefficient (ε) as the gradient.

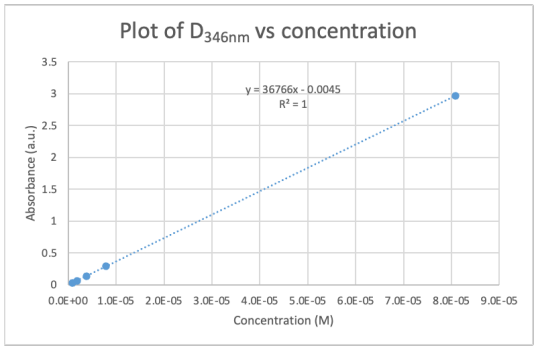
9.4 Chapter 7

9.4.1 2DBCzPN (18)

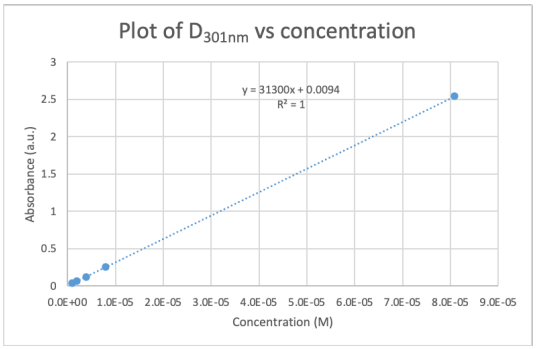




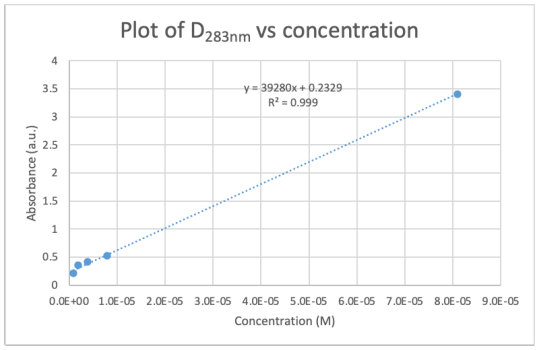
363 nm
$\varepsilon = 4.28 \times 10^4\ cm^{-1}\ M^{-1}$



346 nm
$\varepsilon = 3.68 \times 10^4\ cm^{-1}\ M^{-1}$



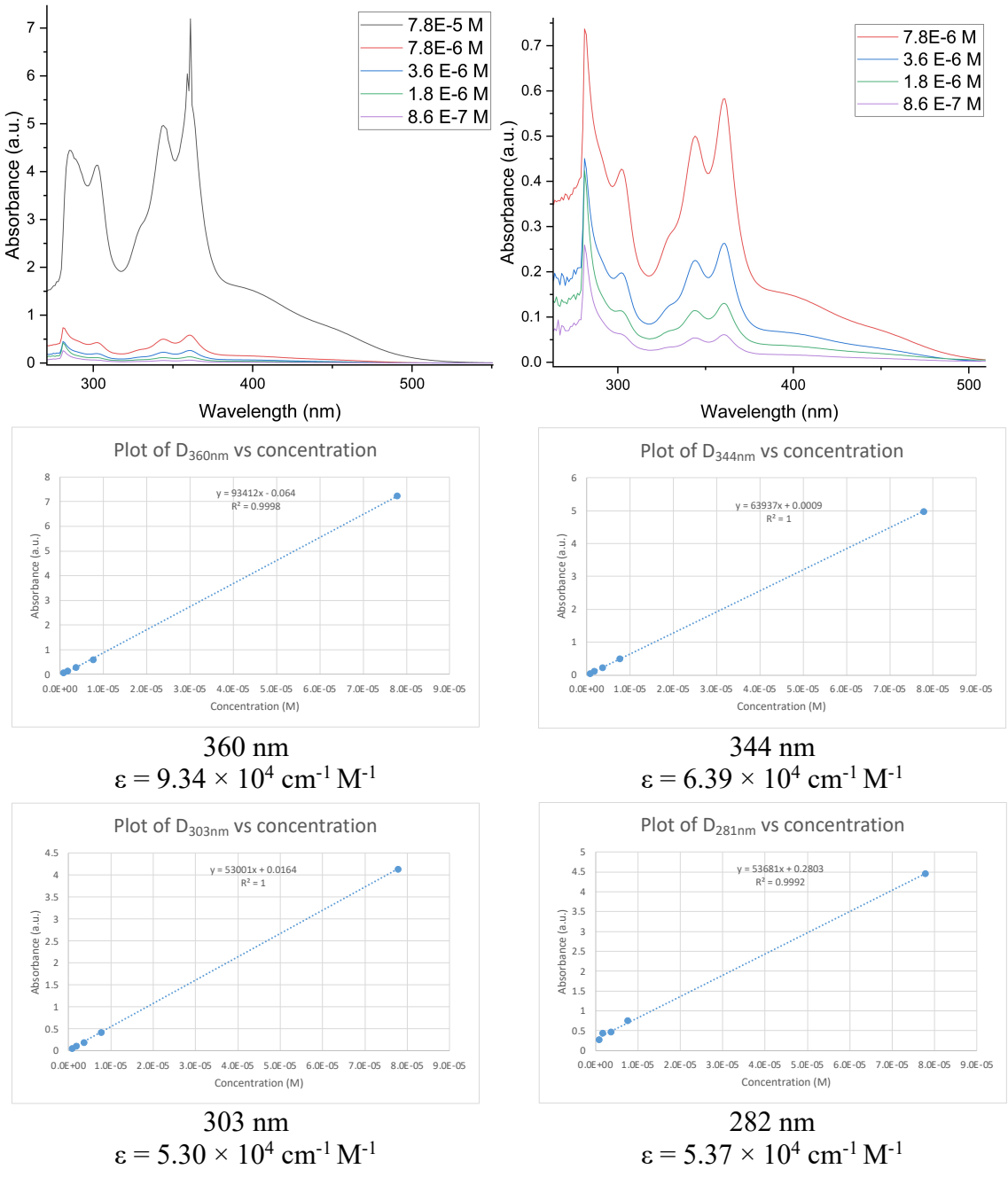
301 nm
$\varepsilon = 3.13 \times 10^4\ cm^{-1}\ M^{-1}$



283 nm
$\varepsilon = 3.93 \times 10^4\ cm^{-1}\ M^{-1}$

Figure 9-11 (Top) UV-vis absorption spectra of compound 18 measured at different concentrations in toluene for molar absorption coefficient calculations (the inset is magnified on the y-axis). (Bottom) Plots of the absorbance of each peak against the respective concentration of the compound 18 samples producing the molar absorption coefficient (ε) as the gradient.

9.4.2 4DBCzIPN (19)



360 nm
$\varepsilon = 9.34 \times 10^4\ cm^{-1}\ M^{-1}$

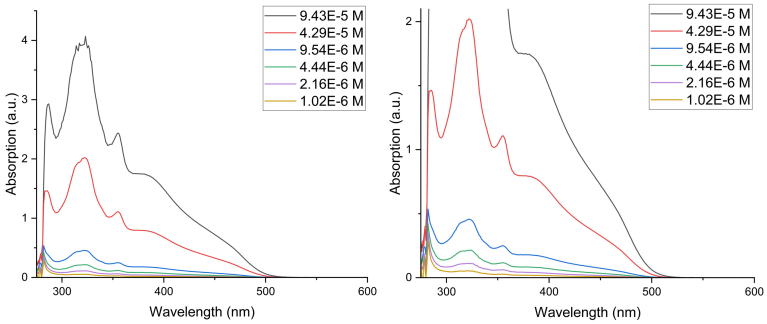
344 nm
$\varepsilon = 6.39 \times 10^4\ cm^{-1}\ M^{-1}$

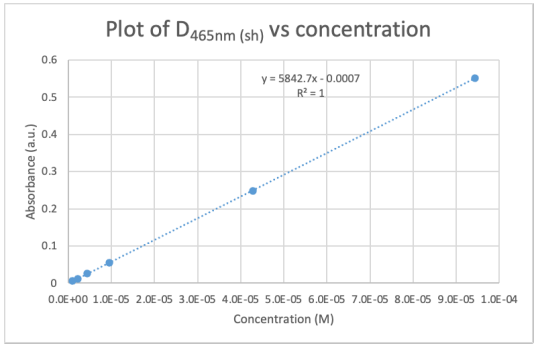
303 nm
$\varepsilon = 5.30 \times 10^4\ cm^{-1}\ M^{-1}$

282 nm
$\varepsilon = 5.37 \times 10^4\ cm^{-1}\ M^{-1}$

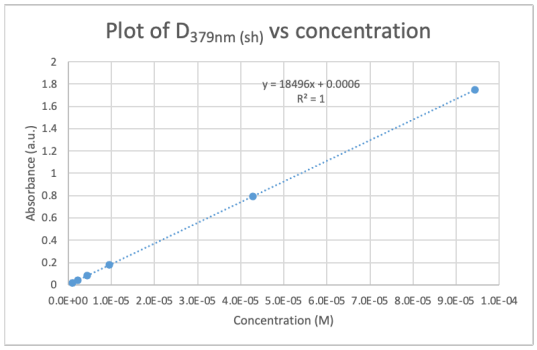
Figure 9-12 UV-vis absorption spectra of compound 19 measured at different concentrations in toluene for molar absorption coefficient calculations. The plot on the top right is the same as the top left, but magnified on the y-axis. Also shown are plots of the absorbance of each peak against the respective concentration of the compound 19 samples producing the molar absorption coefficient (ε) as the gradient.

9.4.3 4MBCzIPN (20)

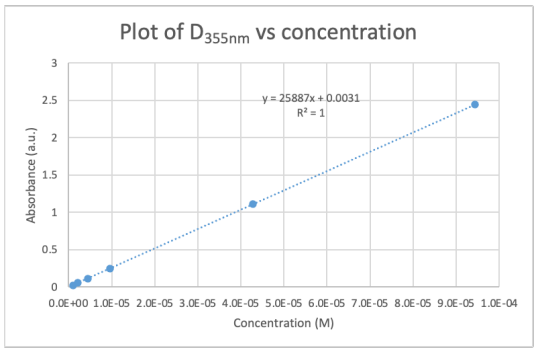




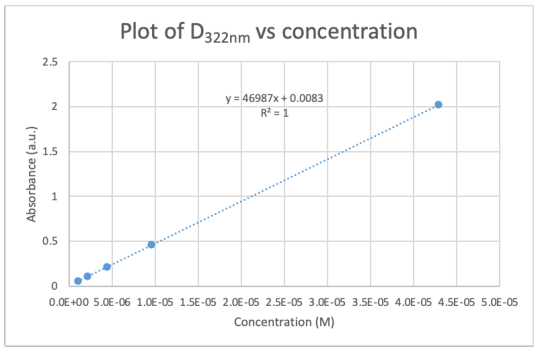
465 nm (sh)
$\varepsilon = 5.84 \times 10^3\ cm^{-1}\ M^{-1}$



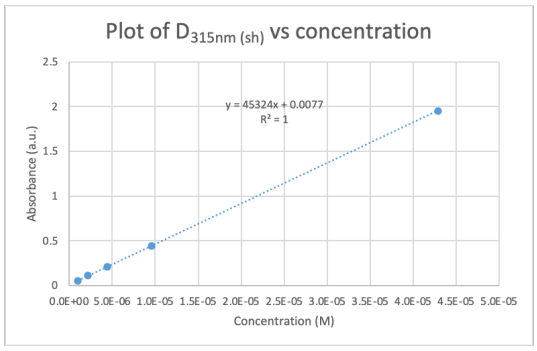
379 nm (sh)
$\varepsilon = 1.85 \times 10^4\ cm^{-1}\ M^{-1}$



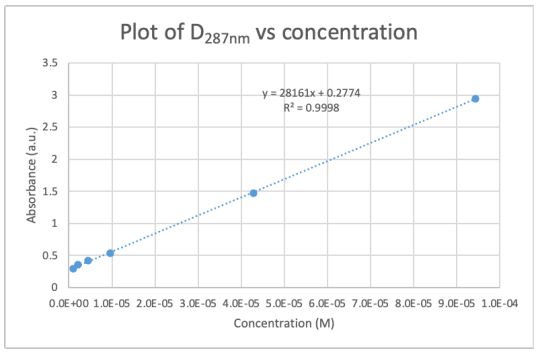
335 nm
$\varepsilon = 2.59 \times 10^4\ cm^{-1}\ M^{-1}$



322 nm
$\varepsilon = 4.70 \times 10^4\ cm^{-1}\ M^{-1}$



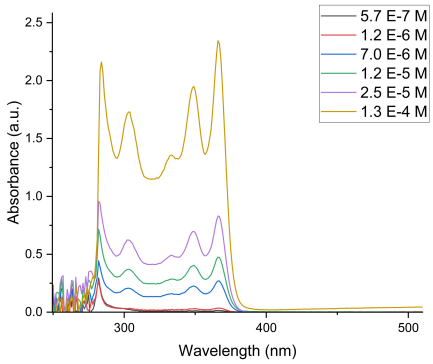
315 nm (sh)
$\varepsilon = 4.53 \times 10^4\ cm^{-1}\ M^{-1}$

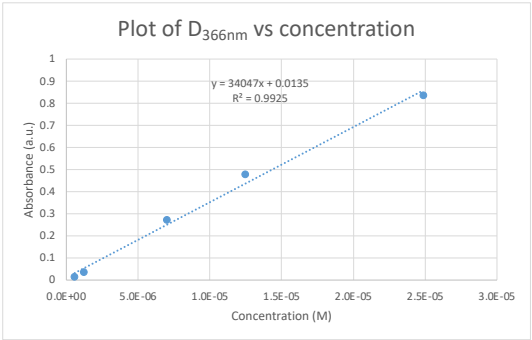


287 nm
$\varepsilon = 2.82 \times 10^4\ cm^{-1}\ M^{-1}$

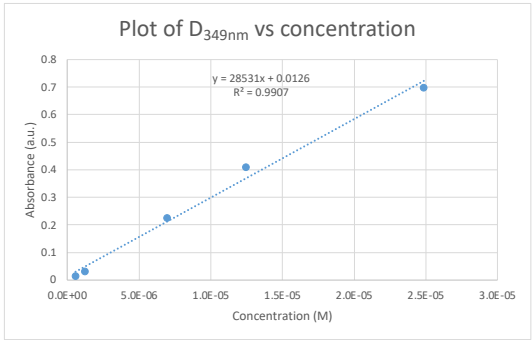
Figure 9-13 UV-vis absorption spectra of compound 20 measured at different concentrations in toluene for molar absorption coefficient calculations. (Top Right) shows the spectra magnified on the y-axis to show the concentrations used for the calculation. Under these spectra are shown plots of the absorbance of each peak against the respective concentration of the compound 20 samples producing the molar absorption coefficient (ε) as the gradient.

9.4.4 DBCz-PS (21)

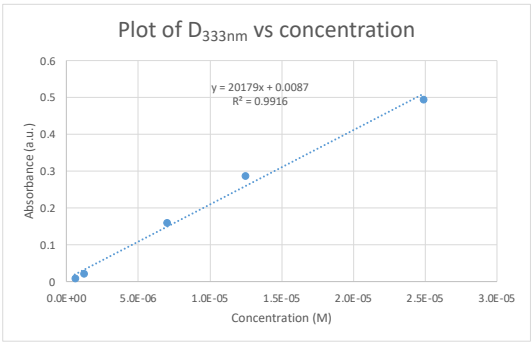




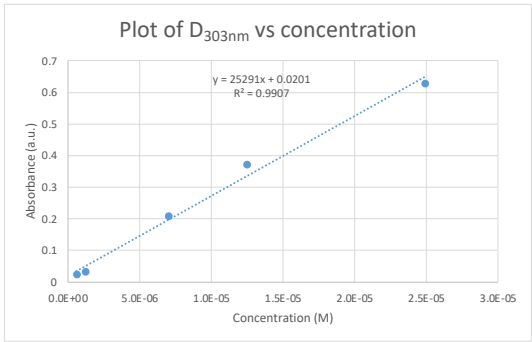
366 nm
$\varepsilon = 3.40 \times 10^4\ cm^{-1}\ M^{-1}$



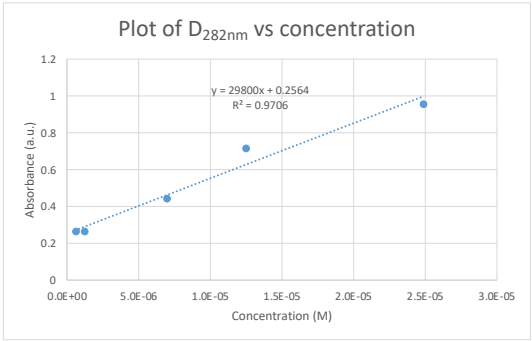
349 nm
$\varepsilon = 2.85 \times 10^4\ cm^{-1}\ M^{-1}$



333 nm
$\varepsilon = 2.02 \times 10^4\ cm^{-1}\ M^{-1}$



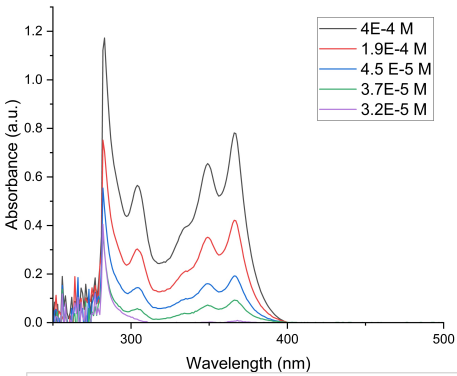
303 nm
$\varepsilon = 2.53 \times 10^4\ cm^{-1}\ M^{-1}$

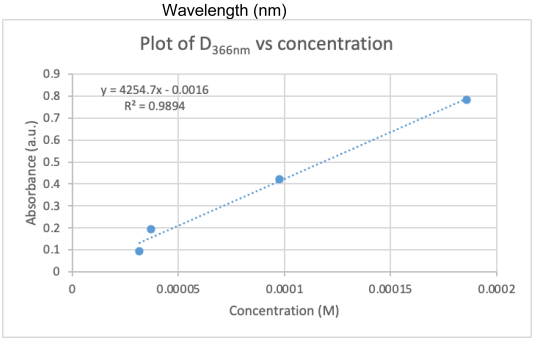


282 nm
$\varepsilon = 2.98 \times 10^4\ cm^{-1}\ M^{-1}$

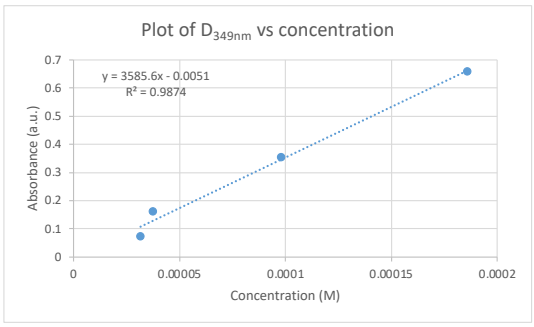
Figure 9-14 (Top) UV-vis absorption spectra of compound 21 measured at different concentrations in toluene for molar absorption coefficient calculations. Following this are plots of the absorbance of each peak against the respective concentration of the compound 21 samples producing the molar absorption coefficient (ε) as the gradient.

9.4.5 DBCz-BZPN (22)

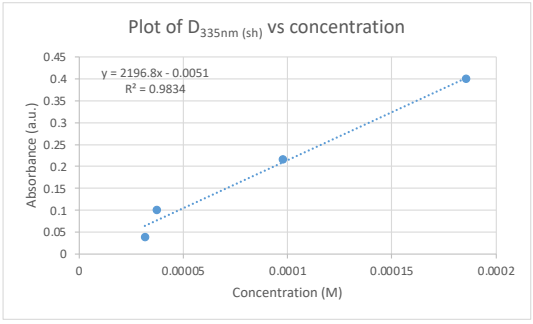




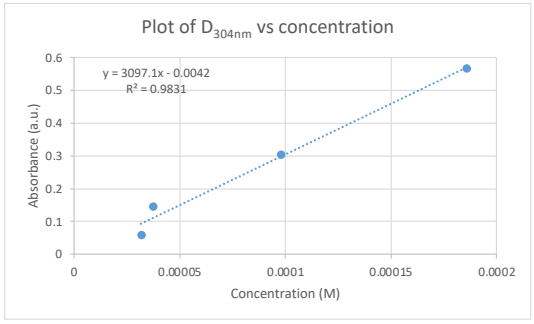
366 nm
$\varepsilon = 4.25 \times 10^3\ cm^{-1}\ M^{-1}$



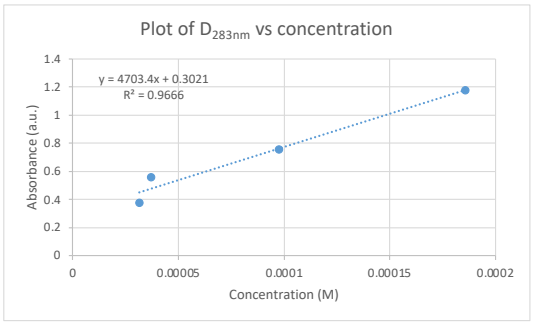
349 nm
$\varepsilon = 3.59 \times 10^3\ cm^{-1}\ M^{-1}$



335 nm (shoulder)
$\varepsilon = 2.20 \times 10^3\ cm^{-1}\ M^{-1}$



304 nm
$\varepsilon = 3.10 \times 10^3\ cm^{-1}\ M^{-1}$



283 nm
$\varepsilon = 4.70 \times 10^3\ cm^{-1}\ M^{-1}$

Figure 9-15 (Top) UV-vis absorption spectra of compound 22 measured at different concentrations in toluene for molar absorption coefficient calculations. Following this are plots of the absorbance of each peak against the respective concentration of the compound 22 samples producing the molar absorption coefficient (ε) as the gradient.

Appendix 2 – Experimental Procedures

9.5 General experimental details

For all reactions, to ensure anhydrous conditions, all glassware was dried in an oven at 120°C (typically overnight). Inert atmosphere was achieved via argon – vacuum purging cycles via a Schlenk line setup. Reagents were purchased commercially from Sigma Aldrich, Fluorochem, TCI, BLD Pharma and Alfa Aesar, without any additional purification. Dry solvents were obtained from the department's SPS system. Thin layer chromatography (TLC) was performed using Sigma Aldrich/Merck Silica Gel 60 F_{254} aluminium sheet TLC plates. For purification, column chromatography was performed using Sigma Aldrich/Merck Silica Gel high-purity grade, pore size 60Å, 230-400 mesh particle size 40-63 μm particle size. Melting points were measured using a Stuart Scientific SMP1 Melting Point apparatus (unless otherwise stated) and are uncorrected.

9.6 Analytical Characterisation

^{1}H and ^{13}C NMR was performed using a Bruker AVIII HD 400MHz or Bruker AVIII 400MHz spectrometer and chemical shifts are reported in ppm and *J* values in Hz. Mass spectrometry was performed on an Agilent 6546 Q-TOF-MS High Resolution Accurate Mass Spectrometer. Elemental micro analysis was performed with an Exeter CE-440 Elemental Analyser.

9.7 Thermal analysis

Thermogravimetric analysis (TGA) was performed on a NETZSCH TG 209 F3 - Tarsus thermogravimeter with a continuous nitrogen flow of 20 mL/min. A temperature increase rate of 20 K / min was used for all samples to a maximum temperature typically of 550°C - 650°C. Differential scanning calorimetry (DSC) was performed on a NETZSCH DSC 214 – Polyma differential. A heat-cool-reheat procedure was used for at least 3 heating cycles

at a rate of 20 K / min, typically ranging from 20°C or 25°C to a sufficiently high temperature for each compound in question such that thermal properties are observed, but sufficiently below the 5% mass loss temperature obtained via TGA to avoid irreversible degradation in each run.

9.8 Electrochemical characterisation

Cyclic voltammetry was employed to determine the oxidation and reduction potentials of all target compounds in order to characterise the HOMO and LUMO energies. A CH Instruments 660E electrochemical workstation was used, with a scan rate of 0.1 V s^{-1} using iR compensation. A glassy carbon working electrode, silver wire reference electrode and platinum wire working electrode were used to make up the electrochemical cell. 0.1 M solutions of tetrabutylammonium hexafluorophosphate was used as the electrolyte in anhydrous solvent. All values were corrected with respect to the redox potential of ferrocene. HOMO and LUMO energies were calculated by subtracting the oxidation and reduction potentials, respectively, from the HOMO of ferrocene (-4.8 eV).

9.9 X-ray crystallography

Single crystal X-ray diffractometry was performed by Dr Laura J. McCormick of the EPSRC National Crystallography Service at the University of Southampton's Department of Chemistry. Measurements were performed according to the following report:

"[a crystal was] *mounted on a Rigaku 007HF equipped with Arc)Sec VHF Varimax confocal mirrors and a UG2 goniometer and HyPix-Arc 100 detector. The crystal was kept at a steady T = 99.99(10) K during data collection. The structure was solved with the ShelXT 2018/2 (Sheldrick, 2018) structure solution program using the using dual methods solution method and by using Olex2 1.3 (Dolomanov et al., 2009) as the graphical interface. The model was refined with version 2018/3 of ShelXL 2018/3 (Sheldrick, 2015) using full matrix least squares minimisation on* $\boldsymbol{F^2}$ *minimisation*."

The structures rendered in this thesis were produced using the CCDC's crystal structure visualization, exploration and analysis software, Mercury.

Powder diffraction XRD was performed by Dr Claire Wilson at the University of Glasgow Department of Chemistry. An Anton-Paar XRK900 variable temperature platform was used to control the temperature for thermochromic materials on a Malvern Panalytical Empyrean multi-purpose platform powder diffractometer.

9.10 Molecular structures

All chemical structures shown in this thesis (other than those reproduced from the literature) were prepared on ChemDraw 20.1.

9.11 Computational Calculations

All structures were initially drawn in Avogadro software, version 1.2.0[388], initially optimised using a UFF or MMF94 force field to generate a starting geometry as a .mol file for computational calculations. GaussView 5 was used to set up input files for running in Gaussian09, or later, Gaussian16. Structures shown in this thesis were rendered in Avogadro software, version 1.2.0[388] using POV-Ray 3.7.0[389]. Owing to their size, the output files have been omitted from this thesis but are available upon request.

9.12 Photophysical properties

UV-vis absorption spectra were measured using a Shimadzu 2600 spectrophotometer and normalised to λ_{max} (except for the molar absorption coefficient measurements). Photoluminescence spectroscopy, time correlated single photon counting (TCSPC) spectroscopy and photoluminescence quantum yield (PLQY) were recorded using an Edinburgh Instruments FS5 spectrofluorometer. For solution and solid state photoluminescence and TCSPC measurements, a SC-05 cassette was employed, with a picosecond pulsed diode laser (365 nm, 375 nm or 450 nm) for the lifetime measurements. Instrument response factor (IRF) for the TCSPC measurements was obtained from a suspension of Ludox HS-40 40% water colloidal silica suspension for solution measurements and from scattering from a glass substrate for solid state measurements.

PLQY measurements were performed with a SC-30 integrating sphere. This was connected to an argon line and purged for 2 minutes before each inert atmosphere measurement. Solution PLQY measurements were degassed by bubbling argon through the solvent for 20 minutes and were of a concentration yielding 0.1 a.u. in the UV-vis absorption spectrum so as to prevent self-absorption.

The mechanochromism and thermochromism data was obtained using an Ocean Optics USB 2000 spectrometer clamped above either a substrate or aluminium TSC pan on top of a hot plate (for the thermochromism measurements), or dark marble pestle (for the mechanochromism measurements). A second clamp held in place a 365 nm UV torch to act as an excitation source. The setup was protected from ambient light by means of a large cardboard box covered in a blackout sheet.

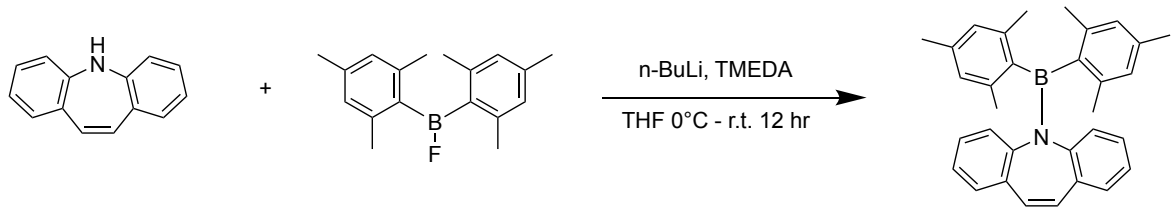
The time dependent measurements at Durham University by exciting with Nd:YAG laser (EKSPLA) at 355 nm and nitrogen laser at 337 nm. Measurements were obtained with a spectrograph and gated iCCD camera (Stanford Computer Optics).

9.13 Synthesis Procedures

9.13.1 Chapter 4

IMSB-DMB (**1**), MBCz-DMB (**2**), DBCz-DMB (**3**), DPhCz-DMB (**4**) were synthesised by myself and compounds Cz-$BMes_2$ (**5**), tBu_2CzOMe-$BMes_2$ (**6**), tBu_2CzOMe_2-$BMes_2$ (**7**), tBu_2-CzBMes_2 (**8**) and Me_4-Cz-$BMes_2$ (**9**) were synthesised by Dr Joseph Cameron from the University of Glasgow.

9.13.1.1 IMSB-DMB (1)



4.1 4.2 IMSB-DMB (**1**)

Under inert atmosphere, 1.01 g (5.23 mmol) of 9H-iminostilbene (**4.1**) was dissolved in 60 mL of dry tetrahydrofuran and 0.04 mL (0.27 mmol) of *N*,*N*,*N*′,*N*′-tetramethylethane-1,2-diamine was added dropwise with stirring. The reaction mixture was cooled to 0°C and 2.3 mL n-butyllithium (2.42 M, 5.57 mmol) added dropwise with stirring. The initially orange solution immediately turned a deep black/purple colour. Stirring was continued for 15 minutes at 0°C before the reaction mixture was allowed to return to room temperature to be stirred for 2 hours.

In a separate flask, a 13 mL solution of 1.41 g (5.26 mmol) dimesitylboron fluoride (**4.2**) was prepared. This was then added to the previous flask at 0°C dropwise with stirring. After 10 minutes at this temperature, the reaction mixture was permitted to return to room temperature and was stirred overnight at room temperature.

100 mL of saturated ammonium chloride solution was added to the reaction mixture, along with 100 mL of diethyl ether. The organic layer was separated and washed with a further 100 mL of ammonium chloride and 100 mL of deionised water. The aqueous layers were combined and washed with diethyl ether (3 × 100 mL). The organic extracts were combined

and washed with a 100 mL portion of brine, dried over magnesium sulfate and filtered. Volatiles were removed under reduced pressure and the resulting brown-orange solid was filtered *via* a silica plug on a fritted funnel using toluene as the eluent (TLC shows the product spot eluting with the toluene solvent front).

The product material was then recrystallised three times from hot dichloromethane/ethanol and the pale olive-green crystals were washed with methanol chilled to -78°C.

Yield : 1.61 g ; 70%; **Melting Point :** 191.1°C (DSC)

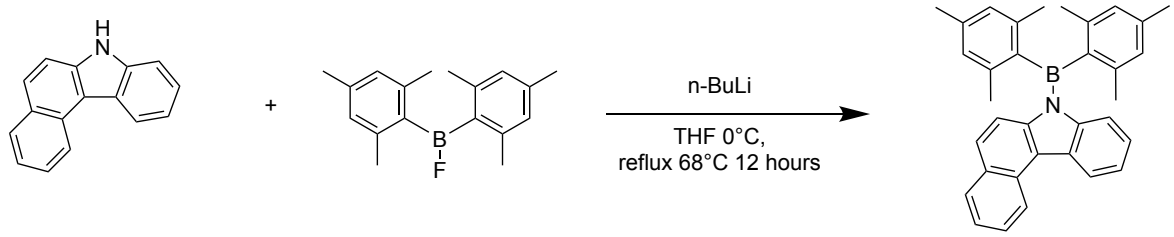
^{1}H NMR : δ_H (400 MHz, $CDCl_3$) 7.31 (dd, J = 7.8, 1.4, 2H), 7.17 (dd, J = 7.4, 1.9, 2H), 7.13 – 7.01 (m, 4H), 6.96 (s, 2H), 6.67 (s, 2H), 6.46 (s, 2H), 2.69 (s, 6H), 2.11 (s, 12H).

13C NMR : δ_C (101 MHz, $CDCl_3$) 145.5, 140.2, 136.3, 133.6, 131.5, 128.6, 128.5, 128.1, 128.0, 127.3, 125.8, 27.3, 24.7, 20.9.

MS m/z (ESI$^+$) : Calculated for molecular formula: 441.2628, found 464.2524 $[M+Na]^+$

Elemental Analysis: Calculated for molecular formula: C, 87.07; H, 7.31; N, 3.17; Found : C, 86.92; H, 7.36; N, 3.16;

9.13.1.2 MBCz-DMB (2)



4.3 4.2 MBCz-DMB (**2**)

Under inert atmosphere, 0.79 g (3.64 mmol) of 7H-Benzo[c]carbazole (**4.3**) was dissolved in 40 mL of dry tetrahydrofuran. The solution mixture was cooled to 0°C and 1.75 mL n-butyllithium (2.4 M, 4.2 mmol) added dropwise with stirring. The initially colourless solution gradually turned a peach-orange hue. Stirring was continued for 15 minutes at 0°C before the reaction mixture was allowed to return to room temperature to be stirred for 3.5 hours.

In a separate flask, a 10 mL solution of 1.41 g (5.26 mmol) dimesitylboron fluoride (**4.2**) in dry tetrahydrofuran was prepared. This was then added to the previous flask at 0°C dropwise with stirring. After 10 minutes at this temperature, the reaction mixture was permitted to return to room temperature and was stirred for 15 minutes before being refluxed at 68°C overnight.

The product solution was filtered through celite with tetrahydrofuran and the volatiles removed under reduced pressure. The peach crystalline solid yielded was recrystallised two times from hot dichloromethane : hexane to yield the product as a white solid.

Yield : 397 mg, 23.4%; **Melting Point :** 221.8°C (DSC)

^{1}H NMR : δ_H (400 MHz, $CDCl_3$) 8.85 (d, J = 8.4, 1H), 8.56 (d, J = 8.0, 1H), 7.91 (d, J = 8.1, 1H), 7.70 (t, J = 7.7, 1H), 7.59 – 7.46 (m, 2H), 7.45 – 7.34 (m, 1H), 7.23 (d, J = 9.1, 1H), 7.14 (s, 2H), 6.84 (s, 4H), 2.35 (s, 6H), 2.02 (s, 12H).

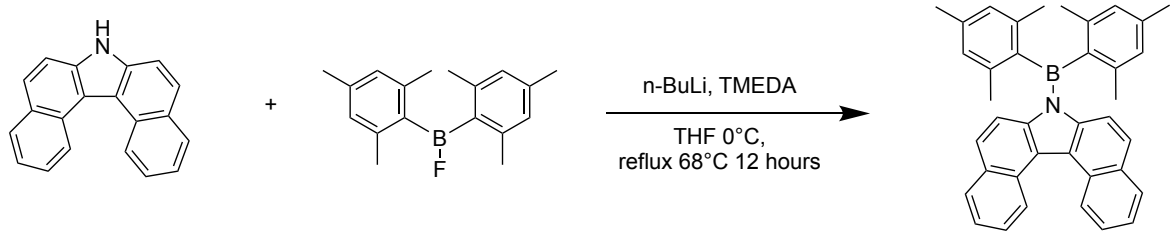
13C NMR : δ_C (101 MHz, $CDCl_3$) 142.9, 141.5, 141.4, 141.3, 139.7, 139.6, 130.8, 129.3, 129.1, 129.0, 129.0, 128.9, 127.3, 126.9, 125.1, 124.2, 123.8, 123.1, 121.8, 121.2, 115.9, 115.6, 22.2, 22.1, 21.5.

Slight splitting of a conjoined peak at 22.2 - 22.1 and the presence of 6 carbons associated with the dimesityl rings suggests a deviancy of symmetry induced by mono-benzocarbazole compared to the other donors in this series being symmetrical.

MS m/z (ESI$^+$) : Calculated for molecular formula: 465.2628, found 466.2700 $[M+H]^+$

Elemental Analysis: Calculated for molecular formula: C, 87.74; H, 6.93; N, 3.01; Found : C, 86.11; H, 6.82; N, 2.89;

9.13.1.3 DBCz-DMB (3)



4.4 4.2 DBCz-DMB (**3**)

Under inert atmosphere, 1.01 g (3.79 mmol) of 7H-dibenzo[c,g]carbazole (**4.4**) was dissolved in 40 mL of dry tetrahydrofuran and 0.03 mL (0.20 mmol) of *N*,*N*,*N*′,*N*′-Tetramethylethane-1,2-diamine was added dropwise with stirring. The reaction mixture was cooled to 0°C and 1.75 mL n-butyllithium (2.42 M, 4.24 mmol) added dropwise with stirring. The initially colourless solution gradually turned a yellow-orange hue. Stirring was continued for 15 minutes at 0°C before the reaction mixture was allowed to return to room temperature to be stirred for 4 hours.

In a separate flask, a 10 mL solution of 1.51 g (5.63 mmol) dimesitylboron fluoride (**4.2**) in dry tetrahydrofuran was prepared. This was then added to the previous flask at 0°C dropwise with stirring. After 10 minutes at this temperature, the reaction mixture was permitted to return to room temperature and was stirred for 15 minutes before being refluxed at 68°C overnight.

In the initial attempt, aqueous workup resulted in the decomposition of the bright green fluorescent product to the starting material, so a non-aqueous workup was used for subsequent attempts.

The product solution was filtered through celite with toluene, and all volatiles were removed under reduced pressure to yield an orange translucent paste with green-blue fluorescence.

The product was crudely purified through a silica gel column using toluene as the eluent. The product was the first fraction to elute. Final purification was achieved by recrystallisation from hot CH_2Cl_2 : hexane. The off-white crystals were washed with chilled hexane (<-50°C) to yield the product material.

Yield : 1.04 g, 53%; **Melting Point :** 176 - 178°C (conventional melting point kit)

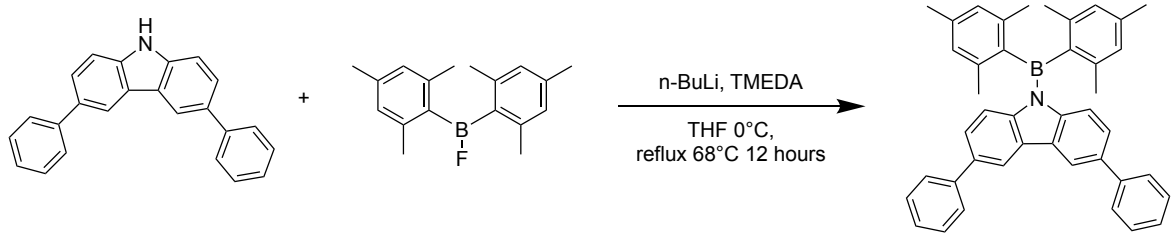
^{1}H NMR : δ_{H} (400 MHz, $CDCl_3$) 9.09 (d, *J* = 8.5, 2H), 7.94 (d, *J* = 7.3, 2H), 7.69 – 7.46 (m, 6H), 7.31 (d, *J* = 9.0, 2H), 6.85 (s, 4H), 2.36 (s, 6H), 2.00 (s, 12H).

^{13}C NMR : δ_{C} (101 MHz, $CDCl_3$) 141.5, 141.0, 140.0, 138.9, 131.2, 129.1, 128.8, 128.5, 126.8, 126.2, 125.1, 124.3, 123.1, 115.5, 22.2, 21.5.

MS m/z (ESI^{+}) : Calculated for molecular formula: 515.2784, found : 515.2785 $[M]^{+}$

Elemental Analysis: Calculated for molecular formula: C, 88.54; H, 6.65; N, 2.72; Found : C, 88.69; H, 6.62; N, 2.63;

9.13.1.4 DPhCz-DMB (4)



4.5 4.2 DPhCz-DMB (4)

Under inert atmosphere, 1.01 g (3.16 mmol) of 9H-3,6-diphenyl-9H-carbazole (**4.5**) was dissolved in 40 mL of dry tetrahydrofuran and 0.03 mL (0.20 mmol) of *N*,*N*,*N*′,*N*′-Tetramethylethane-1,2-diamine was added dropwise with stirring. The reaction mixture was cooled to 0°C and 1.50 mL n-butyllithium (2.42 M, 3.63 mmol) added dropwise with stirring. Stirring was continued for 15 minutes at 0°C before the reaction mixture was allowed to return to room temperature to be stirred for 4 hours.

In a separate flask, a 10 mL solution of 0.94 g (3.51 mmol) dimesitylboron fluoride (**4.2**) was prepared. This was then added to the previous flask at 0°C dropwise with stirring. After 10 minutes at this temperature, the reaction mixture was permitted to return to room temperature and was stirred for 15 minutes before being refluxed at 68°C overnight.

The product was noticed to decompose in water, so a non-aqueous workup was adopted. A short silica gel column was used to purify the compound using toluene as the eluent, with the product eluting with the solvent line. Further purification was achieved by recrystalising from hot CH_2Cl_2 : ethanol to yield a white crystalline solid.

Yield : 490 mg ; 27%; **Melting Point :** 251.1°C (DSC)

^{1}H NMR : δ_H (400 MHz, $CDCl_3$) 8.24 (d, *J* = 2.0, 2H), 7.68 (m, 4H), 7.45 (td, *J* = 8.3, 7.0, 4H), 7.39 – 7.30 (m, 4H), 6.98 (d, *J* = 0.6, 2H), 6.86 (s, 4H), 2.35 (s, 6H), 2.08 (s, 12H).

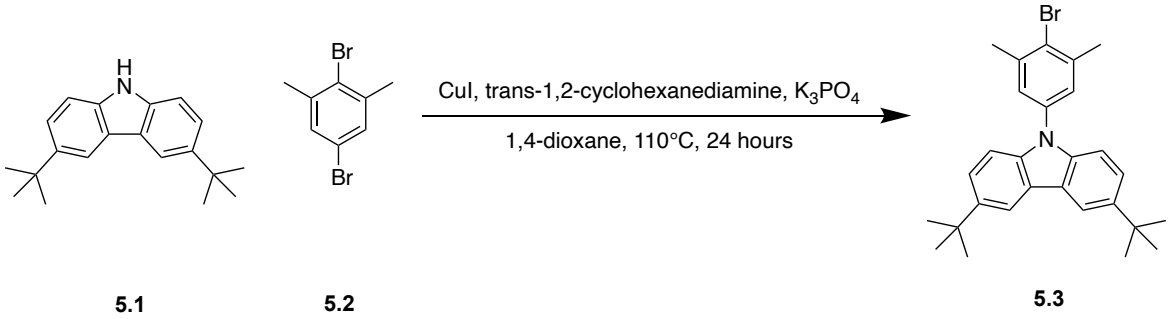
^{13}C NMR : δ_C (101 MHz, $CDCl_3$) 143.4, 141.5, 141.3, 139.5, 136.1, 129.0, 128.9, 127.3, 127.0, 126.0, 118.0, 115.9, 22.2, 21.5.

MS m/z (ESI$^+$) : Calculated for molecular formula: 567.3097, found : 567.3108 $[M]^+$

Elemental Analysis: Calculated for molecular formula: C, 88.88; H, 6.75; N, 2.47; Found : C, 88.61; H, 6.76; N, 2.17;

9.13.2 Chapter 5

9.13.2.1 9-(4-Bromo-3,5-dimethylphenyl)-9H-3,6-di-tert-butylcarbazole (5.3)



5.1 **5.2** **5.3**

The dimethyl donor moiety was synthesised from 8.29 g (29.7 mmol) of 3,6-di-tert-butylcarbazole (**5.1**), 0.40 mL (3.33 mmol) of trans-1,2-cyclohexanediamine, 8.74 g (33.1 mmol) of 2,5-dibromo-m-xylene (**5.2**), along with 22.21 g (105 mmol) of potassium phosphate and 0.33 g (1.73 mmol) of copper iodide were suspended in 50 mL of 1,4-dioxane under an argon atmosphere with stirring at 110°C for a period of 24 hours under reflux.

After the reaction had completed, the mixture was suspended in 200 mL dichloromethane, washed with 4 portions of deionised water (200 mL total). The aqueous phase was washed twice with 100 mL of dichloromethane, then all organic phases were combined and dried with $MgSO_4$. Volatiles were removed under reduced pressure and the solid dissolved in hot ethanol. Upon cooling, the solid precursor material was removed by filtration and the solvent removed from the filtrate to yield a pale orange solid.

Further purification was achieved by recrystallising from hot hexane : dichloromethane.

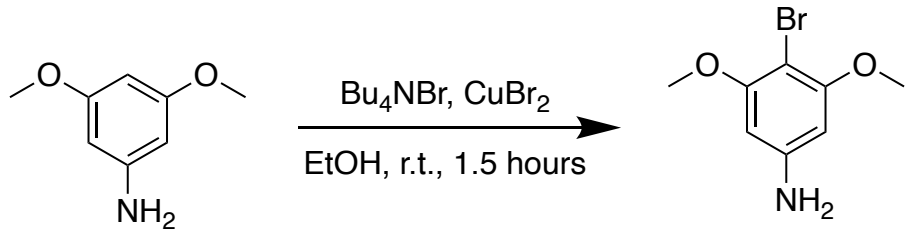
Yield : 5.43 g ; 40% ; **m.p. :** 189-190°C (conventional melting point kit)

^{1}H NMR (400MHz, $CDCl_3$) : 8.13 (d, J = 1.4, 2H), 7.46 (dd, J = 8.7, 2.0, 2H), 7.32 (d, J = 8.6, 2H), 7.27 (s, 2H), 2.51 (s, 6H), 1.46 (s, 18H).

^{13}C NMR δ_C (101 MHz, $CDCl_3$) 143.1, 140.1, 139.3, 136.8, 126.4, 125.7, 123.8, 123.5, 116.4, 109.3, 34.9, 32.2, 24.2.

MS m/z (ESI$^+$) : Calculated for molecular formula: 461.1718, found : 462.1787 $[M+H]^+$

9.13.2.2 4-Bromo-3,5-dimethoxyaniline (5.5)



5.4 **5.5**

The precursor for the methoxy donor moiety was synthesised from 1.93 g (12.63 mmol) of 3,5-dimethoxyaniline (**5.4**), 4.04 g (12.53 mmol) of tetrabutylammonium bromide which were placed into a 250 mL two necked round-bottom flask. The system was purged with argon and 50 mL of ethanol was added. The reaction mixture was stirred at room temperature (20°C) for 2 minutes, yielding an orange solution, then 4.27 g (18.28 mmol) $CuBr_2$ was added. After 20 minutes a precipitate was noticeable. The now black solution was stirred for 1.5 hours until the reaction was complete (determined by TLC).

The volatiles were removed under reduced pressure to yield a dark lilac solid. To this, 32 mL (35% w/v) of ammonium hydroxide was slowly added with stirring, followed by 32 mL of deionised water. The resultant brilliant blue solution was stirred for 30 minutes.

200 mL of dichloromethane was added in four portions and the organic phases extracted and combined, washed with brine, then dried with magnesium sulfate, filtered and the volatiles removed under reduced pressure and a dark brown/orange oil was obtained.

The oil was purified via silica gel column chromatography using diethyl ether : petroleum ether in a 5:1 ratio yielding **5.5**.

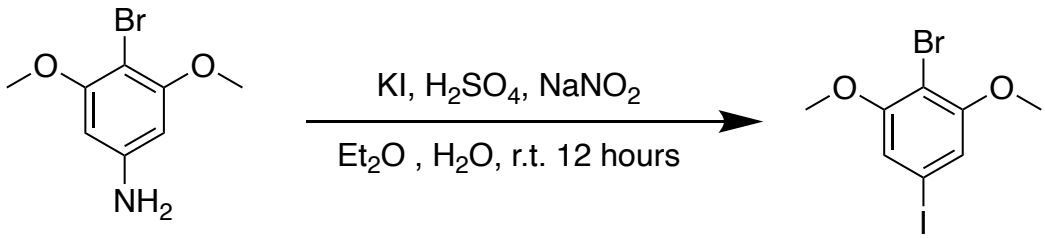
Yield : 1.16 g, 40%; **m.p.** 95.6°C (Stuart Automatic Melting Point SMP50)

^{1}H NMR (400MHz, $CDCl_3$) : 5.95 (s, 2H), 3.83 (s, 6H).

^{13}C NMR δ_C (101 MHz, $CDCl_3$) 157.7, 147.3, 92.6, 89.4, 56.4.

MS m/z (ESI$^+$) : Calculated for molecular formula: 230.9895, found : 253.9789 $[M+Na]^+$

9.13.2.3 2-Bromo-5-iodo-1,3-dimethoxybenzene (5.6)



5.5 **5.6**

The second step in the synthesis of the methoxy donor moiety was synthesised from 1.54 g (6.62 mmol) of 4-bromo-3,5-dimethoxyaniline (**5.5**) suspended in 60 mL (6 M) of H_2SO_4 with stirring, and cooled to -10℃ with ice and salt. 0.98 g (14.2 mmol) of sodium nitrite ($NaNO_2$) was dissolved in 6 mL of deionised water, and 2.21 g (13.3 mmol) of potassium iodide was dissolved in a separate 6 mL portion of deionised water. The sodium nitrite solution was added dropwise at -10℃ with stirring over the course of 5 minutes.

The potassium iodide solution was added dropwise with stirring at -10℃, and the resulting cloudy yellow solution stirred at this temperature for 15 minutes. The solution was allowed to slowly warm to 0℃ and stirring continued for 3 hours. After this time, it was noted that the solution had become caramel / orange in colour. The mixture was stirred overnight at room temperature, then neutralised with sodium carbonate solution.

The product solution was extracted with 200 mL diethyl ether, washed with 200 mL of deionised water, then quenched with two 100 mL portions of 1M sodium sulfite (Na_2SO_3) and two 100 mL portions of 2.5 M sodium hydroxide, followed by a final 100 mL portion of deionised water. The organic phase was dried with magnesium sulfate and filtered. The volatiles were removed under reduced pressure and the residue purified by silica gel column chromatography with a petroleum ether : ethyl acetate 1 : 1 mix as the eluent to yield **5.6**.

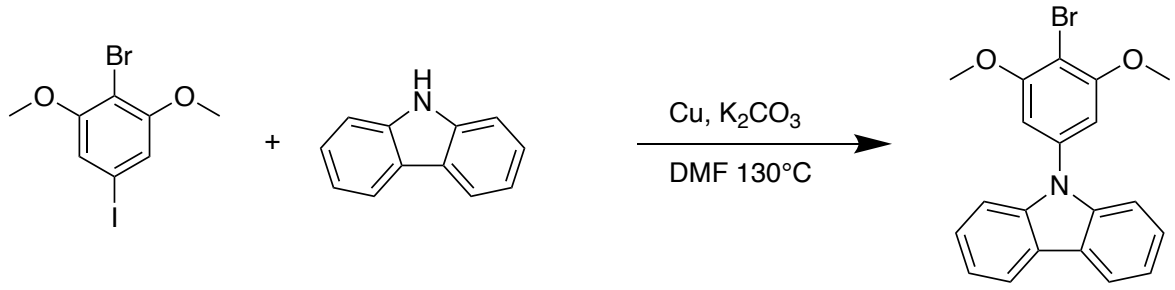
Yield : 1.18 g 51.9%; **m.p.** 84.8°C (Stuart Automatic Melting Point SMP50)

^{1}H NMR δ_H (400 MHz, $CDCl_3$) 6.87 (s, 2H), 3.88 (s, 6H).

^{13}C NMR δ_C (101 MHz, $CDCl_3$) 157.6, 114.5, 101.5, 92.2, 56.9.

MS m/z (ESI$^+$) : Calculated for molecular formula: 341.8752, found : 342.8835 $[M+H]^+$

9.13.2.4 9-(4-Bromo-3,5-dimethoxyphenyl)-9H-carbazole (5.8)



5.6 **5.7** **5.8**

Under inert atmosphere, 0.98 g (2.87 mmol) of 2-bromo-5-iodo-1,3-dimethoxybenzene (**5.6**), 0.52 g (3.13 mmol) 9H-carbazole (**5.7**), 0.56 g (8.88 mmol) copper powder and 1.22 g (8.81 mmol) potassium carbonate were suspended in 16 mL of N,N-dimethylformamide. After purging with argon, the mixture was refluxed at 130°C with stirring for 24 hours.

Upon cooling to room temperature, the resultant solution was filtered through celite, then washed with dichloromethane (100 mL), and deionised water. The organic layer was separated, and the aqueous washed thrice with 50 mL of dichloromethane. The combined organic layers were dried with magnesium sulfate, filtered and the volatiles removed under reduced pressure. The resultant brown sticky oil was purified via column chromatography (10 : 1 hexane : ethyl acetate, with the first eluent being the product) to yield a pale peach solid.

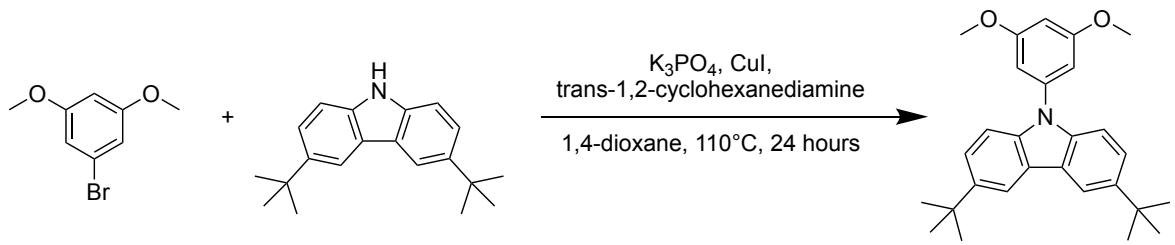
Yield : 534 mg 48.7%; **m.p.** 122-124°C (conventional melting point kit)

^{1}H NMR : δ_H (400 MHz, $CDCl_3$) 8.16 (d, J = 7.7, 2H), 7.47 – 7.41 (m, 4H), 7.35 – 7.27 (m, 2H), 6.79 (s, 2H), 3.92 (s, 6H)

^{13}C NMR : ^{13}C NMR (101 MHz, $CDCl_3$) δ 158.1, 140.8, 138.2, 126.3, 123.6, 120.6, 120.3, 109.9, 104.8, 104.0, 56.9

MS m/z (ESI$^+$) : Calculated for molecular formula: 381.0364; found : 382.0436 $[M+H]^+$

9.13.2.5 9-(1,3-Dimethoxyphenyl)-9H-3,6-di-tert-butyl-carbazole (5.10)



5.9 **5.1** **5.10**

Under inert atmosphere, 1.76 g (8.11 mmol) of 1,3-dimethoxy-5-bromobenzene (**5.9**), 3.05 g (10.92 mmol) of 9H-3,6-di-tert-butyl-carbzole (**5.10**), 5.20 g (24.50 mmol) of potassium phosphate, 78.4 mg (0.41 mmol) of copper iodide and 95 mg (0.162 mL, 0.83 mmol) of trans-1,2-cyclohexanediamine, were suspended in absolute 55 mL 1,4-dioxane and stirred under reflux at 110°C for 24 hours.

The solvent was removed under vacuum and the crude product was suspended in diethyl ether and washed with deionised water (3 portions of 20 mL). The aqueous layers were further extracted with diethyl ether (3 portions of 20 mL). The organic layers were combined and washed once with brine (30 mL), dried over magnesium sulfate, and the solvent removed under reduced pressure. The product was further purified via silica gel column chromatography. (hexane : dichloromethane 10 : 1).

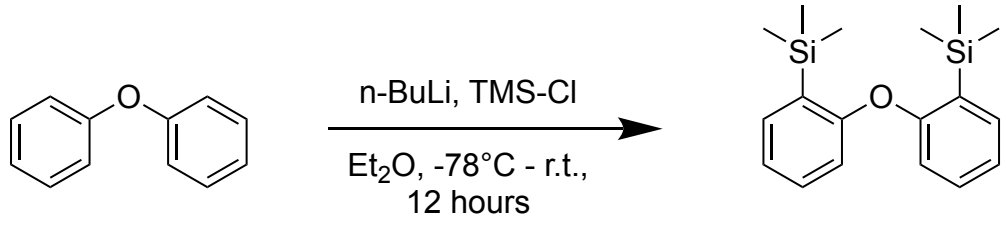
Yield : 1.21 g, 36%; **m.p.** 130-131°C (conventional melting point kit)

^{1}H NMR : δ_H (400 MHz, $CDCl_3$) 8.14 (d, J = 1.2, 2H), 7.51 – 7.39 (m, 4H), 6.73 (d, J = 2.3, 2H), 6.54 (t, J = 2.3, 1H), 3.84 (s, 6H), 1.47 (s, 18H).

^{13}C NMR : δ_C (101 MHz, $CDCl_3$) 161.7, 143.0, 140.0, 139.2, 123.7, 123.5, 116.3, 109.6, 105.0, 99.6, 55.7, 34.9, 32.2.

MS m/z (ESI$^+$) : Calculated for molecular formula: 415.2511, found : 416.2595 $[M+H]^+$

9.13.2.6 Bis-(2-trimethylsilylphenyl)ether (5.12)



5.11 **5.12**

Under inert atmosphere, 10.1 g (59.3 mmol) of diphenylether (**5.11**) was dissolved in dry dichloromethane under an argon atmosphere and to this 34 mL (151 mmol) of TMEDA was added. The solution was cooled to -78°C and 61 mL of n-BuLi (148 mmol, 2.43 M) was added dropwise with stirring. The solution was stirred at this temperature for 10 minutes, then allowed to return to room temperature over approximately 1 hour and stirred overnight.

The lithiated solution was cooled to -78° again and 19 mL (150 mmol) of trimethylsilyl chloride was added dropwise with stirring. The solution was stirred for 10 minutes at this temperature, and then allowed to return to room temperature whilst stirring for one hour, yielding a white precipitate suspended in a yellow solution. 166 mL of 1 M HCl was slowly added to the reaction mixture in order to perform hydrolysis, after which the precipitate dissolved.

The organic and aqueous layers were separated, and the aqueous layer was extracted twice with diethyl ether. The organic layers were combined, dried over magnesium sulfate, filtered and the volatiles removed under reduced pressure. A yellow oil of **5.12** was obtained and dried under high vacuum (10^{-2} mbar) overnight to remove residual solvent. The product had a slightly higher mass than expected owing to a small quantity of starting material remaining present. The crude product was used in the next step without any further purification.

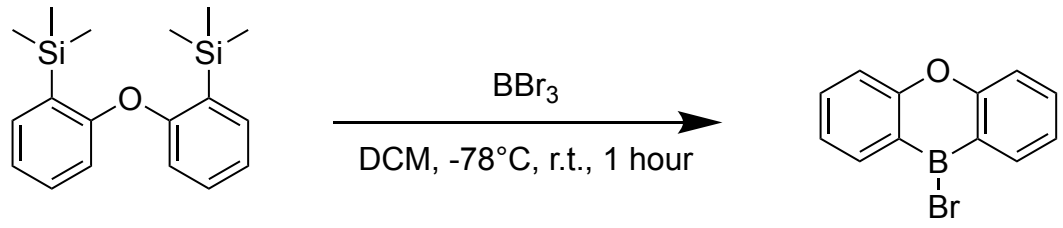
Yield : 22.23 g ; actual percentage yield uncertain as crude product was used as-is.

^{1}H NMR : δ_H (400 MHz, $CDCl_3$) 7.49 (dd, *J* = 7.3, 1.8, 2H), 7.31 – 7.22 (m, 2H), 7.08 (td, *J* = 7.3, 1.0, 2H), 6.64 (dd, *J* = 8.2, 1.0, 2H), 0.32 (s, 18H).

^{13}C NMR : Carbon-13 NMR not attempted owing to crude nature of the product material.

MS and **elemental analysis** not attempted owing to crude material and previously reported.

9.13.2.7 10-bromo-10H-dibenzo[b,e][1,4]oxaborinine (5.13)



5.12 **5.13**

Under inert atmosphere, 5.04 g (16.04 mmol) of bis-(2-trimethylsilylphenyl)ether (**5.12**) was dissolved in 40 mL of dry dichloromethane under argon atmosphere in a flask connected to a filter stick. In a separate flask, a solution of 4.6 mL (12.14 g, 48.5 mmol) of boron tribromide in 10 mL dry dichloromethane was prepared. The first solution was cooled to -78°C, and the boron tribromide solution added dropwise with stirring. After addition of the boron tribromide solution, the reaction mixture was stirred at this temperature for 10 minutes.

The reaction mixture was allowed to return to room temperature and was stirred for one hour. The volatiles were removed by vacuum, and the beige solid remaining was washed with 20 mL of cold dry diethyl ether. The resulting white suspension in yellow solution was filtered, leaving a white solid of **5.13**. This solid was washed a further two times with 10 mL portions of cold dry diethyl ether and dried overnight under vacuum.

The product is extremely oxygen and moisture sensitive, so it was used without any further purification in the next step. ^{13}C NMR and MS data were not obtained owing to the air and moisture sensitivity of the compound.

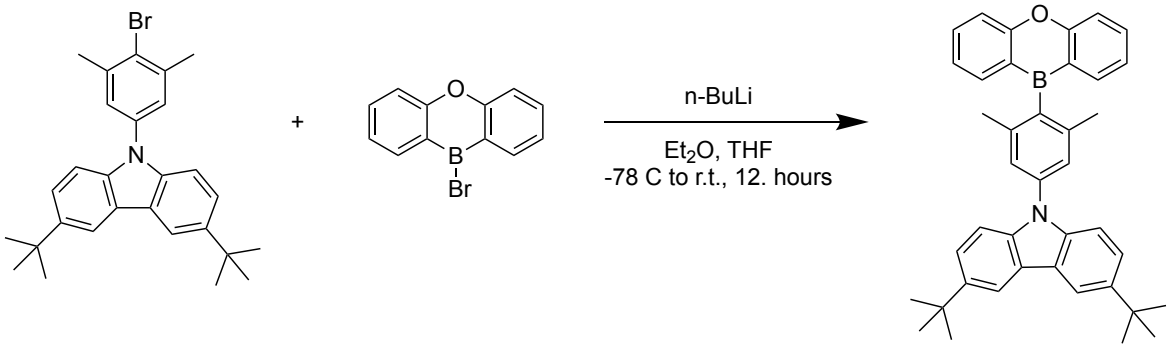
Yield : 2.18 g, 53%

^{1}H NMR : δ_H (400 MHz, $CDCl_3$) 7.96 (2 H, dd, *J* 7.5, 1.7), 7.66 (2 H, ddd, *J* 8.7, 7.1, 1.8), 7.48 – 7.41 (2 H, m), 7.32 – 7.26 (2 H, m)

MS and **Elemental analysis** not obtained due to significant air and moisture sensitivity of the product material.

9.13.2.8 tBu-DMP-Cz-OBA (10)

10-[(3,5-Dimethylphenyl)-3,6-di-tert-butyl-9H-carbazole]-9-oxa-10-boraanthracene



5.3 **5.13** **10**

Under inert atmosphere, 1.026 g (2.22 mmol) of (9-(4-bromo-3,5-dimethylphenyl)-3,6-di-tert-butyl-9H-carbazole) (**5.3**) was dissolved in 60 mL dry diethyl ether. 563 mg (2.17 mmol) of 10-bromo-10H-dibenzo[b,e][1,4]oxaborinine (**5.13**) was dissolved in 50 mL of dry THF. The solution of (**5.3**) was cooled to -78°C and 1.4 mL (3.5 mmol, 2.5 M in hexane) was added dropwise with stirring. The lithiation solution was stirred for 10 minutes, then allowed to warm to 0°C over a period of 30 minutes. The solution was cooled to -78°C again and the solution of (**5.13**) added dropwise with stirring. The solution was stirred for a further 15 minutes at -78°C, then was allowed to return to room temperature and stirred for 3 days.

The volatiles were removed under reduced pressure and the residue washed with saturated ammonium chloride solution and dichloromethane, separated and 3 portions of 50 mL dichloromethane used to wash the aqueous phases. The organic solutions were combined and dried with magnesium sulfate, filtered, and the solvent removed under reduced pressure. The crude product was purified via column chromatograph with silica gel, and using 10 : 1 hexane : toluene as the eluent.

A white crystalline solid was obtained with a deep blue fluorescence in the solid-state.

Yield : 239 mg, 20%; **m.p.** 260.0°C (DSC)

^{1}H NMR : δ_H (400 MHz, $CDCl_3$) 8.17 (d, J = 1.0, 2H), 7.85 (dd, J = 7.5, 1.8, 2H), 7.81 (ddd, J = 8.7, 7.0, 1.8, 2H), 7.67 (d, J = 8.6, 2H), 7.57 – 7.48 (m, 4H), 7.37 – 7.31 (m, 2H), 7.30 (s, 2H), 2.10 (s, 6H), 1.49 (s, 18H).

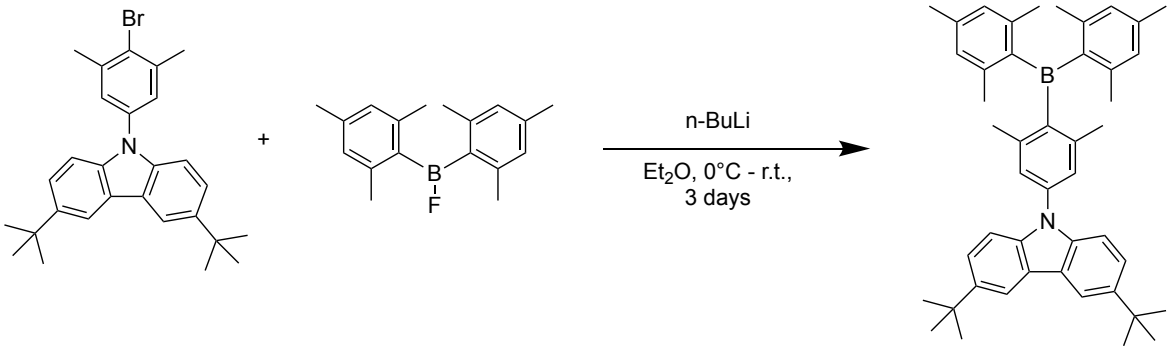
^{13}C NMR : δ_C (101 MHz, $CDCl_3$) 159.7, 142.7, 140.6, 139.6, 137.7, 136.4, 135.1, 124.9, 124.3, 123.6, 123.4, 122.9, 118.0, 116.3, 109.7, 77.4, 34.9, 32.2, 23.2.

MS m/z (ESI$^+$) : Calculated for molecular formula: 561.3203, Found : 562.3297 $[M+H]^+$

Elemental Analysis: Calculated for molecular formula: C, 85.55; H, 7.18; N, 2.49; Found : C, 83.68, H, 7.06, N, 2.32;

9.13.2.9 tBu-DMP-Cz-DMB (12)

9-(3,5-Dimethyphenyl)-3,6-di-tert-butyl-9H-carbazole dimesityl boron



5.3 **4.2** **12**

Under inert atmosphere, 1 g (2.23 mmol) of (9-(4-bromo-3,5-dimethylphenyl)-3,6-di-tert-butyl-9H-carbazole) (**5.3**) was dissolved in 50 mL dry diethyl ether. The solution was cooled to 0°C and 0.91 mL (2.5M, 2.2 mmol) of n-BuLi was added dropwise with stirring. The reaction mixture was stirred for 1 hour. A solution of 0.6148 g (2.29 mmol) of dimesitylboron fluoride (**4.2**) was prepared in 6 mL dry diethyl ether. This was then added dropwise to the solution of (**5.3**) and stirred for 1 hour at room temperature, then refluxed overnight.

The reaction mixture was quenched by addition of a small portion of water (5 mL) then was decanted into 100 mL of deionised water. The product material was extracted with 100 mL diethyl ether, which was then washed with 2 × 100 mL portions of deionised water. The organic phase was dried over magnesium sulfate and the volatiles were removed under reduced pressure. The crude product was purified via silica gel column chromatography using 10 : 1 hexane : toluene as the eluent, yielding **12** as a white solid.

Yield : 432 mg, 31%; **m.p.** 340.4°C (DSC)

^{1}H NMR : δ_H (400 MHz, $CDCl_3$) 8.16 – 8.12 (m, 2H), 7.51 – 7.39 (m, 4H), 7.13 (s, 2H), 6.80 (d, J = 10.4, 4H), 2.31 (s, 6H), 2.10 (s, 12H), 2.05 (s, 6H), 1.47 (s, 18H).

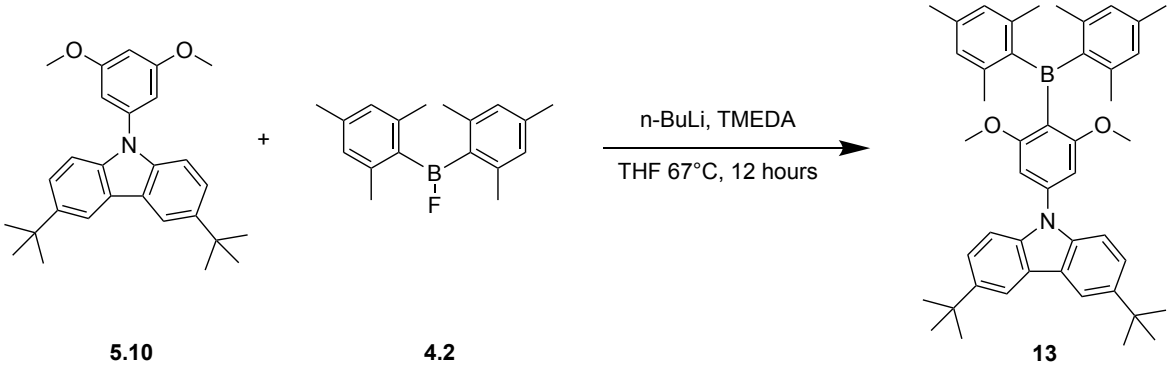
^{13}C NMR : δ_C (101 MHz, $CDCl_3$) 142.8, 142.4, 140.9, 140.7, 139.7, 139.2, 138.8, 128.9, 128.9, 125.4, 123.6, 123.5, 116.3, 109.7, 34.9, 32.2, 23.1, 23.1, 23.0, 21.4.

MS m/z (ESI$^+$) : Calculated for molecular formula: 631.4349; found : 632.4421 $[M+H]^+$

Elemental Analysis: Calculated for molecular formula: C, 87.46,; H, 8.62; N, 2.22 ; Found : C, 89.08,; H, 8.78; N, 2.13;

9.13.2.10 tBu-DMeOP-Cz-DMB (13)

9-(3,5-Dimethoxyphenyl)-3,6-di-tert-butyl-9H-carbazole dimesityl boron



5.10 **4.2** **13**

Under inert atmosphere, 1.21 g (2.91 mmol) of **5.10** was dissolved in 30 mL dry THF. To this a catalytic quantity (0.012 mL) of TMEDA was added. The solution was cooled to 0°C and 1.28 mL (2.27 M, 2.91 mmol) of n-BuLi was added dropwise with stirring. The reaction mixture was stirred for 4 hours.

A solution of 0.79 g (2.95 mmol) of dimesitylboron fluoride (**4.2**) was prepared in 7 mL dry THF. This was then added dropwise to the solution of **5.10** and stirred for 1 hour at room temperature, then refluxed overnight.

The reaction mixture was poured into a saturated solution of ammonium chloride (80 mL), washed with diethyl ether (100 mL) and separated. The aqueous phase was washed with 3 50 mL portions of diethyl ether. The combined organic solutions were washed with 1 x 100 mL portion of brine, dried over magnesium sulfate, filtered and the volatiles removed under reduced pressure. The crude solid was further purified by silica gel column chromatography using 2 : 1 petroleum ether : dichloromethane as the eluent to yield a white solid. Further purification by recrystallisation from hot ethanol / dichloromethane yielded white crystals of the product material **13**.

Yield : 157 mg, 8.2%; **m.p.** 274.7°C (DSC)

^{1}H NMR : δ_H (400 MHz, $CDCl_3$) 8.15 (d, J = 1.9, 2H), 7.53 – 7.40 (m, 4H), 6.77 (s, 4H), 6.68 (s, 2H), 3.52 (s, 6H), 2.29 (s, 6H), 2.16 (s, 12H), 1.48 (s, 18H).

^{13}C NMR : δ_C (101 MHz, $CDCl_3$) 162.2, 143.6, 143.0, 141.1, 140.2, 139.2, 138.3, 128.1, 123.8, 123.5, 116.4, 109.6, 103.4, 56.3, 34.9, 32.2, 22.4, 21.4.

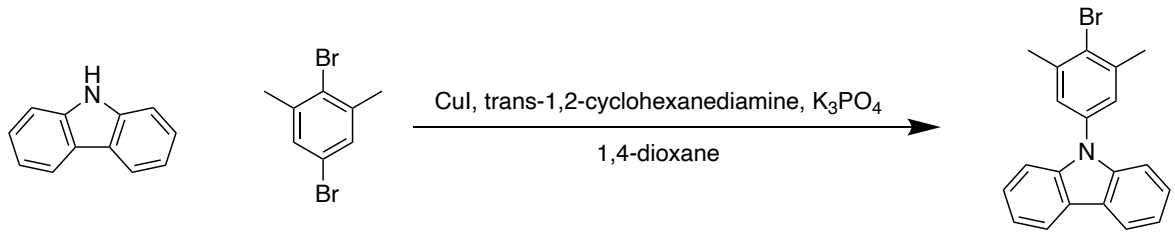
MS m/z (ESI$^+$) : Calculated for molecular formula: 663.4248 ; found : 664.4342 $[M+H]^+$

Elemental Analysis: Calculated for molecular formula: C, 83.24; H, 8.20; N, 2.11 ; Found : C, 83.39; H, 8.15; N, 1.85;

9.13.3 Chapter 6

The synthesis of the methoxy donor moiety in this chapter was performed by repeating the procedure outlined in chapter 5.

9.13.3.1 9-(4-Bromo-3,5-dimethylphenyl)-9H-carbazole (6.5)



5.7 **5.2** **6.5**

Under inert atmosphere, 8.28 g (50 mmol) of 9H-carbazole (**5.7**), 0.40 mL (3.33 mmol) of trans-1,2-cyclohexanediamine, 8.75 g (33 mmol) of 2,5-dibromo-m-xylene (**5.2**), along with 22.11 g (104 mmol) of potassium phosphate and 0.32 g (1.68 mmol) of copper iodide were suspended in 35 mL of 1,4-dioxane under an argon atmosphere with stirring at 110°C for a period of 24 hours in a 100 mL round-bottom flask.

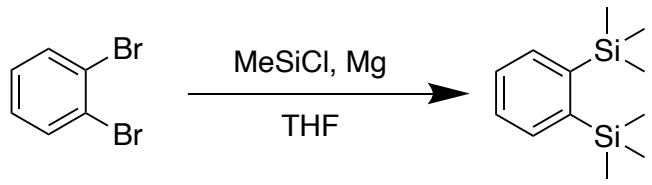
The reaction mixture was suspended in dichloromethane (200 mL), then washed with 4 × 100 mL portions of deionised water). The organic phase was extracted, and the aqueous phase washed twice with 100 mL of dichloromethane, then all organic phases were combined and dried with $MgSO_4$. The volatiles were removed under low pressure and the crude product purified via silica gel column chromatography using dichloromethane : petroleum ether in a 1:10 ratio. A pale pink crystalline solid was obtained.

Yield : 2.95 g, 25%; **m.p.** 121.1°C (Stuart Automatic Melting Point SMP50)

^{1}H NMR : δ_H (400 MHz, $CDCl_3$) 8.14 (d, J = 7.6, 2H), 7.44 – 7.36 (m, 4H), 7.32 – 7.26 (m, 4H), 2.52 (s, 6H).

^{13}C NMR : $\boldsymbol{\delta}_C$ (101 MHz, $CDCl_3$) 141.0, 140.3, 136.3, 126.8, 126.3, 126.1, 123.5, 120.5, 120.1, 109.9, 24.2.

9.13.3.2 1,2-Bis(trimethylsilyl)benzene (6.2)



6.1 **6.2**

Prior to synthesis, 1,2-dibromobenzene (**6.1**) was distilled under argon. The orange solution from the supplier condensed as a colourless liquid. The magnesium turnings were heated under vacuum to dry over the course of two hours and left under vacuum overnight.

31.84 g (2.07 mol) of dry magnesium turnings were suspended in 200 mL of dry tetrahydrofuran in a dry flask under inert atmosphere. To this, 170 mL (1.34 mol) of chlorotrimethyl silane was added with stirring, followed by slow addition of 10 mL (82.9 mmol) 1,2-dibromobenzene. The reaction mixture was cooled with a water bath (occasional addition of ice necessary as the reaction is exothermic). After around 10 minutes of stirring, a solution of 3 mL (44.9 mmol) 1,2-dibromoethane in 20 mL tetrahydrofuran was added dropwise over a period of 30 minutes.

The reaction mixture was allowed to stir overnight (20 hours in total) and then 120 mL of hexane (previously cooled in an ice bath) was added to the reaction mixture. The resulting solution was slowly poured onto ice with stirring. When effervescence had ceased, the excess magnesium was filtered off and the aqueous layer separated, washed three times with 100 mL portions of hexane, and all organic layers combined. The organic layers were then washed with three portions of 100 mL deionised water. The organic layers were then dried with magnesium sulphate, filtered, and the now very pale-yellow liquid concentrated under reduced pressure.

The resulting pale orange-yellow oil was purified via column chromatography, using a hexane as the eluent. The product was obtained from the first eluted fraction. Upon removal of the solvent, a colourless oil was obtained.

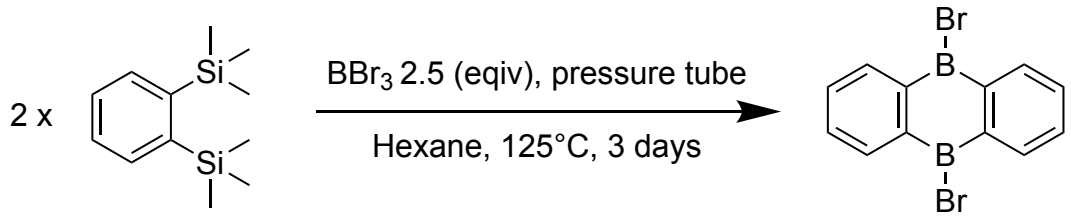
Yield : 5.06 g (22.7 mmol), 27%

^{1}H NMR : δ_H (400 MHz, $CDCl_3$) 7.67 (dd, J = 5.6, 3.4, 2H), 7.33 (dd, 2H), 0.37 (s, 18H).

^{13}C NMR : δ_C (101 MHz, $CDCl_3$) 146.2, 135.3, 127.9, 2.1

9.13.3.3 Dibromodiboraanthracene (DBDBA – 6.4)

9.13.3.3.1 From 1,2-bis(trimethylsilyl)benzene – hexane solvent



6.2 **DBDBA 6.4**

A 60 mL pressure tube was purged and 2.5 mL (10.1 mmol) of 1,2-bis(trimethylsilyl)benzene (**6.2**) was added, along with 15 mL of dry hexane and the reaction vessel purged with argon. The solution was stirred and 2.5 mL (25.9 mmol) of borontribromide was added dropwise. The reaction vessel was purged again to remove any HBr that formed in the process.

The reaction mixture (pale orange) was stirred at room temperature for 5 minutes, then the temperature was raised to 125°C and stirred for 3 days.

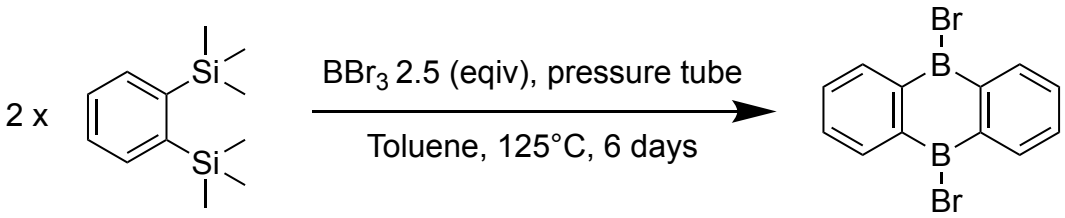
Upon completion the reaction mixture (now dark brown) was cooled to room temperature over the course of two hours, during which time, white crystals precipitated. The product mixture was then chilled with stirring to -77°C to crash out any further crystals, the solution filtered via cannula to yield a pale yellow-white solid. The solid was washed three times with anhydrous hexane and filtered in-situ via cannula.

The filtrate was collected and evaporated to dryness where a beige solid was obtained. This was further washed with 300 mL of anhydrous hexane in 50 mL portions and pale beige solid was obtained.

Owing to the need to prevent exposure to air and moisture to maximise the yield for the next step, no NMR or MS was attempted.

Yield : 0.69 g, 10% – unknown purity

9.13.3.3.2 From 1,2-bis(trimethylsilyl)benzene – toluene solvent



6.2 **DBDBA 6.4**

A 60 mL pressure tube was purged and 2.5 mL (10.1 mmol) of 1,2-bis(trimethylsilyl)benzene (**6.2**) was added, along with 15 mL of dry toluene and the reaction vessel purged with argon. The solution was stirred and 2.5 mL (25.9 mmol) of borontribromide was added dropwise. The reaction vessel was purged again to remove any HBr that formed in the process.

The reaction mixture (pale orange) was stirred at room temperature for 5 minutes, then the temperature was raised to 80°C for a period of 20 minutes, then stirred at 125°C for 6 days.

Upon completion the reaction mixture (now dark brown) was cooled to room temperature over the course of two hours, during which time, white crystals precipitated. The product mixture was then chilled with stirring to -77°C to crash out any further crystals, the solution filtered via cannula to yield a pale yellow-white solid. The solid was washed three times with anhydrous hexane and filtered in-situ via cannula.

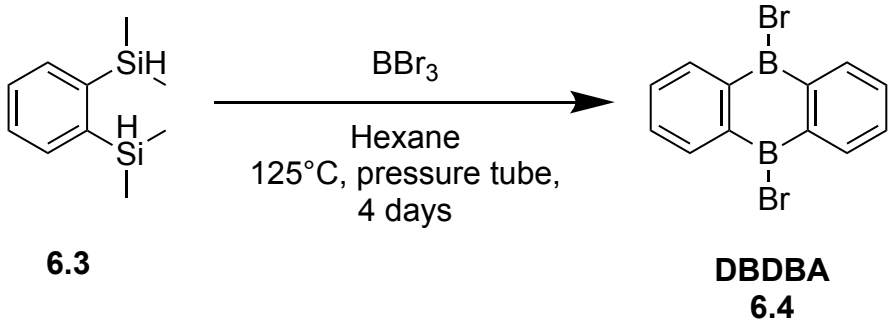
The filtrate was collected and evaporated to dryness where a blue/green/grey solid was obtained. This was further washed with 300 mL of anhydrous hexane in 50 mL portions and a white/grey solid was obtained.

Both solids were confirmed to be the DBDBA product via ^{1}H NMR. The product proved too unstable under atmospheric conditions to obtain ^{13}C NMR spectra or mass spectrometry data.

Yield : 426 mg, 25%

^{1}H NMR : δ_H (400 MHz, C_6D_6) 7.69 (dd, J = 5.4, 3.2, 4H), 7.28 (dd, J = 5.5, 3.2, 4H).

9.13.3.3.3 From 1,2-bis(dimethylsilyl)benzene – hexane solvent



6.3 **DBDBA 6.4**

In a pressure tube, 2.19 mL (1.07 g, 5.50 mmol) of 1,2-bis(dimethylsilyl)benzene (**6.3**) was dried under vacuum for 1 hour. 15 mL of dry hexane was purged with argon for 1 hour, then added to the pressure tube under argon. 2.5 mL of boron tribromide (6.6 g, 5.28 mmol) was added dropwise with stirring (a white precipitate was observed). Stirring was continued with 20 quick purges via a Schlenk, then the pressure tube was sealed and heated to 125°C and stirred for 4 days.

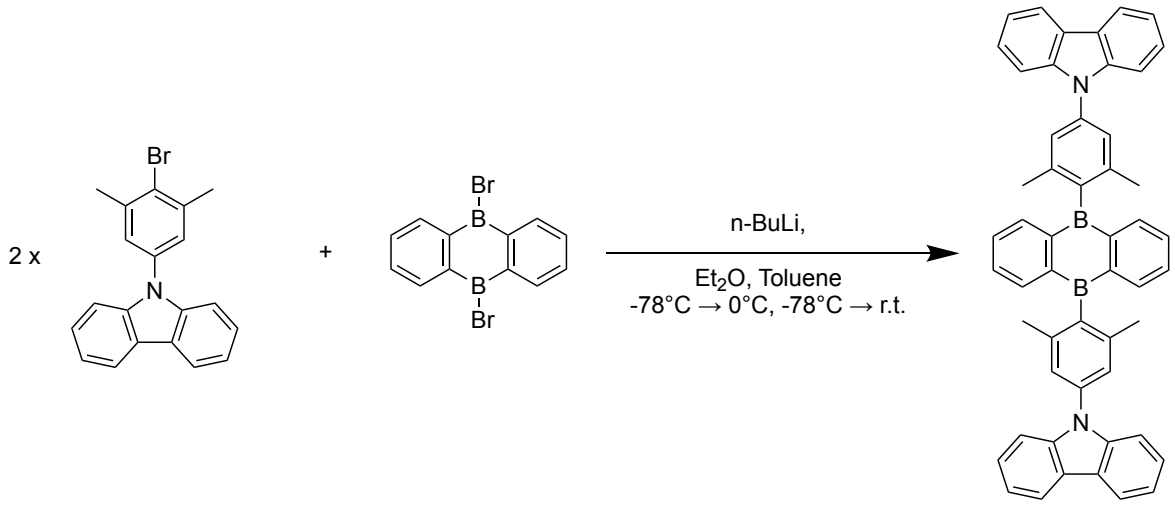
The pressure tube was allowed to return to room temperature, then was cooled to -78°C for 30 minutes to permit precipitation of additional product. The solvent and excess reagent was filtered off via cannula filtration and the solid washed with three 10 mL portions of dry hexane.

The beige-white solid was dried under high-vacuum for 3 hours and then used as-is for the next step in the synthesis of tBuMeOCzDBA.

Yield : 1.58 g, 90% (residual solvent present)

^{1}H NMR : δ_H (400 MHz, Tol) 7.61 (dd, J = 5.5, 3.2, 4H), 7.26 (dd, J = 5.4, 3.2, 4H)

9.13.3.4 CzDBA (16)



6.5 **DBDBA 6.4** **CzDBA 16**

Under inert atmosphere, 572 mg (1.63 mmol) of 9-(4-bromo-3,5-dimethylphenyl)-9H-carbazole, (**6.5**) was dissolved in 40 mL of dry diethyl ether. 268 mg (0.80 mmol) of 9,10-dibromo-9,10-diboraanthracene (**6.4**) was dissolved in 30 mL of dry toluene. The solution of **6.5** was cooled to -78°C and 1 mL (2.5 M, 2.5 mmol) of n-BuLi was added dropwise with stirring. The solution was stirred at -78°C for a further 10 minutes, then permitted to warm to 0°C over the course of half an hour. The solution was cooled again to -78°C, whereupon the solution of **6.4** was added dropwise, whilst maintaining -78°C throughout. After stirring for 15 minutes, the reaction mixture was allowed to return to room temperature and continued to be stirred for 15 hours.

The volatiles were removed under reduced pressure, and saturated ammonium chloride and dichloromethane added to the residue. The organic layer was separated, and the aqueous phase washed three times with 30 mL portions of dichloromethane. The organics were combined and dried over anhydrous magnesium sulfate, filtered and the solvent removed under reduced pressure.

The yellow/brown solid produced was further purified via a short silica gel column chromatography with 40% dichloromethane in hexane as the mobile phase.

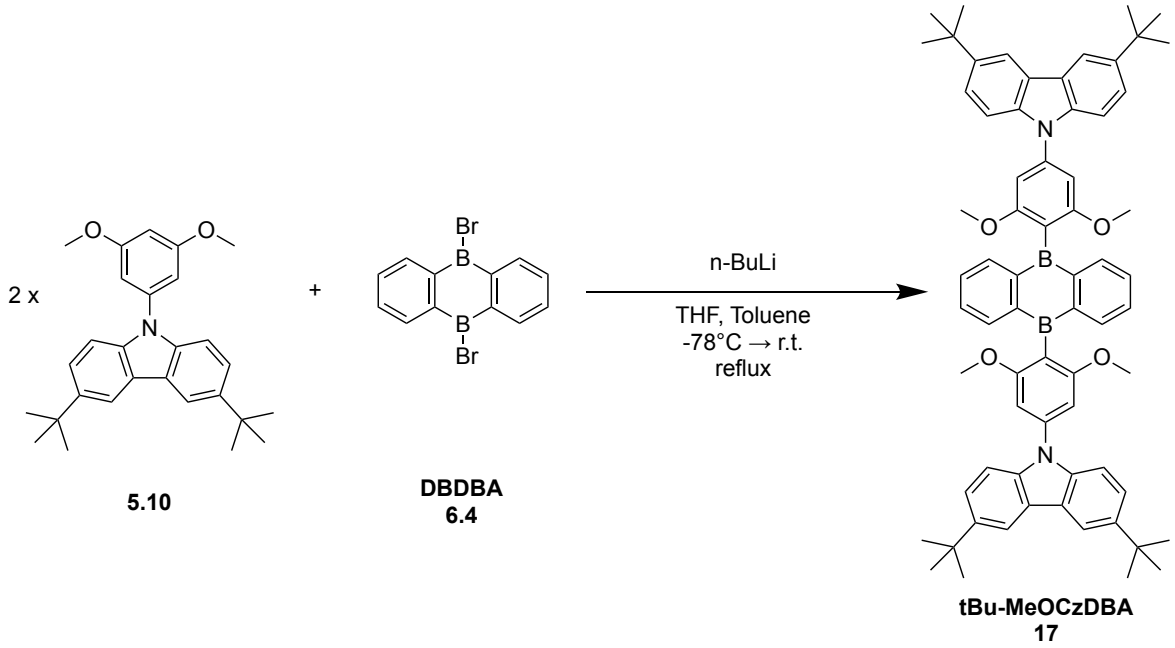
Yield : 113 mg, 20%; **m.p.** Not found

^{1}H NMR δ_H (400 MHz, $CDCl_3$) 8.19 (dd, *J* = 7.7, 1.0, 4H), 7.79 (dd, *J* = 5.3, 3.3, 4H), 7.66 – 7.59 (m, 8H), 7.49 (ddd, *J* = 8.3, 7.0, 1.2, 4H), 7.36 – 7.30 (m, 8H), 2.24 (s, 12H).

^{13}C NMR : Owing to the low yield and degradation of the product in the NMR tube, photophysics was prioritised over ^{13}C NMR. Identity of material was confirmed via ^{1}H NMR and MS as the compound is reported in the literature[238].

MS m/z (ESI$^+$) : Calculated : 714.3378; Found : 715.3454 $[M+H]^+$

9.13.3.5 tBu-MeOCzDBA (17)



Under inert atmosphere, 3.01 g (7.41 mmol, 2.06 eq) of (**5.10**) was dissolved in 60 mL of dry THF. 1.20 g (3.60 mmol) of 9,10-dibromo-9,10-diboraanthracene (**6.4**) was suspended in 20 mL of dry toluene. The solution of **5.10** was cooled to -78°C and 4.45 mL (2.5 M, 11.13 mmol, 1.50 eq) of n-BuLi was added dropwise with stirring. The solution was stirred at -78°C for a further 10 minutes, then permitted to warm to room temperature and stirred for 3 hours, becoming pale red in colour with weak blue fluorescence, then cooled again to -78°C. The suspension of **6.4** was added dropwise, whilst maintaining -78°C throughout. An additional 10 mL of dry toluene was added to the pressure tube to further extract the remains of **6.4**, followed by 2 × 10 mL portions of dry THF. Upon addition, the suspension was fully dissolved. After stirring for 10 minutes, the now orange-brown solution was allowed to return to room temperature and refluxed at 70°C for 48 hours.

The reaction was quenched via filtering through celite using THF as the eluent. Volatiles were removed under reduced pressure to yield a sticky yellow solid with bright blue-green fluorescence. The crude product was purified via a short silica gel chromatography column (300 g silica) so as to minimise the time the compound was spent on silica. 20% EtOAc in hexane was used as the eluent, to remove excess of **5.10** and the product eluted as a wide yellow band with bright green fluorescence.

The collected product was further purified by precipitation from hot dichloromethane : hexane as a bright green-yellow powder with brilliant blue-green fluorescence.

Yield : 46 mg, 1.3%; **m.p.** Not found

^{1}H NMR : δ_H (400 MHz, $CDCl_3$) 8.19 (d, *J* = 1.9, 4H), 7.83 (dd, *J* = 5.4, 3.3, 4H), 7.62 (d, *J* = 8.6, 4H), 7.60 – 7.53 (m, 8H), 6.89 (s, 4H), 3.67 (s, 12H), 1.51 (s, 36H).

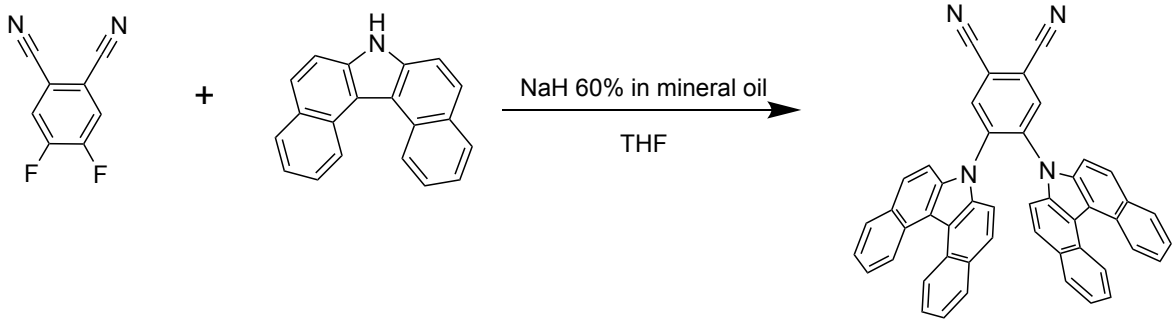
^{13}C NMR : δ_C (101 MHz, $CDCl_3$) 161.7, 143.0, 140.0, 139.2, 131.5, 131.4, 129.2, 123.7, 123.5, 116.3, 109.6, 105.0, 99.6, 55.7, 34.9, 32.2

MS m/z (ESI$^+$) : Calculated : 1002.5678; Found : 1002.5717 $[M]^+$

Elemental Analysis: Calculated : C, 81.43; H, 7.24; N. 2.79 ; Found : C, 81.68; H, 7.27; N. 2.86;

9.13.4 Chapter 7

9.13.4.1 2DBCzPN (18)



7.1 **4.4** **2DBCzPN**

To a round-bottom flask, 0.52 g of sodium hydride (60%) in mineral oil (giving 0.34 g, 13 mmol NaH) was added and washed with anhydrous hexane (3 × 20 mL), then dried under vacuum for 1.5 hours. 50 mL of dry tetrahydrofuran was added and the NaH suspended. 3.43 g (12.8 mmol) of 7H-dibenzo[c,g]carbazole (**4.4**) was added portion-wise and effervescence was noticed. The solution was stirred for 30 minutes at room temperature, then 1.24 g (7.56 mmol) of 4,5-difluorophthalonitrile (**7.1**) was added portion-wise. An additional 20 mL hexane was added to aid solvation.

The reaction mixture was stirred at room temperature for 24 hours. Quenching was performed by addition of deionised water (50 mL) and evolution of gas was noticed. 50 mL of methanol was also added to quench.

Extraction was performed with dichloromethane (100 mL) and the organic phase was washed with 3 × 100 mL portions of deionised water and 1 × 100 mL portion of brine. The organic phases were combined, dried over magnesium sulfate, filtered and the volatiles removed under reduced pressure.

The crude product was dissolved in boiling dichloromethane and methanol slowly added and an orange powder precipitated out. The product was filtered on a frit and the precipitation repeated to yield a bright yellow powder.

Yield : 1.53 g, 36%; **m.p.** 395.4°C (DSC)

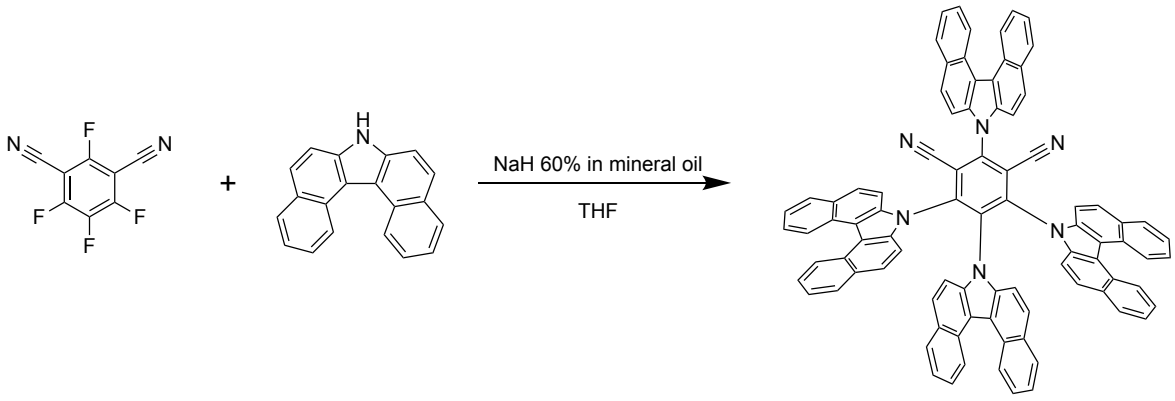
^{1}H NMR : δ_H (400 MHz, $CDCl_3$) 8.70 (d, *J* = 8.4 Hz, 4H), 8.39 (s, 2H), 7.79 (dd, *J* = 8.1 Hz, 4H), 7.55 – 7.44 (m, 8H), 7.40 (t, *J* = 7.0 Hz, 4H), 7.32 (s, 2H), 7.29 (s, 2H).

^{13}C NMR : δ_C (101 MHz, $CDCl_3$) 139.3, 136.7, 135.9, 130.6, 129.0, 128.5, 127.4, 125.8, 125.3, 124.2, 119.5, 116.1, 114.4, 110.0.

MS m/z (ESI$^+$) : Calculated for molecular formula: 658.2157, Found : 659.2221 $[M+H]^+$

Elemental Analysis: Calculated : C, 87.52; H, 3.98; N, 8.51; Found : C, 87.93; H, 3.96; N, 8.37;

9.13.4.2 4DBCzIPN (19)



7.2 4.4 4DBCzIPN

Using a similar approach as 2DBCzPN (**18**), 0.56 g of sodium hydride (60%) in mineral oil (giving 0.34 g, 14.2 mmol NaH) was added to a round-bottom flask, purged and washed with anhydrous hexane (3 × 20 mL), then dried under vacuum for 1.5 hours. 35 mL of dry tetrahydrofuran was added and the NaH suspended. 2.98 g (11.1 mmol) of 7H-dibenzo[c,g]carbazole (**4.4**) was added portion-wise and effervescence was noticed. The solution was stirred for 30 minutes at room temperature, then 0.45 g (2.25 mmol) of 2,4,5,6-tetrafluoroisophthalonitrile (**7.2**) was added portion-wise.

The reaction mixture was stirred at room temperature for 24 hours. Quenching was performed *via* addition of deionised water (50 mL) and evolution of gas was noticed. 50 mL of methanol was also added to quench.

Extraction was performed with dichloromethane (100 mL) and the organic phase was washed with 3 × 100 mL portions of deionised water and 1 × 100 mL portion of brine. The organic phases were combined, dried over magnesium sulfate, filtered and the volatiles removed under reduced pressure.

The crude product was dissolved in boiling dichloromethane and methanol slowly added and an orange powder precipitated out. The product was filtered on a frit and the precipitation repeated to yield a brilliant orange powder.

Yield : 2.00 g ; 75%; **m.p.** 465.3°C (DSC)

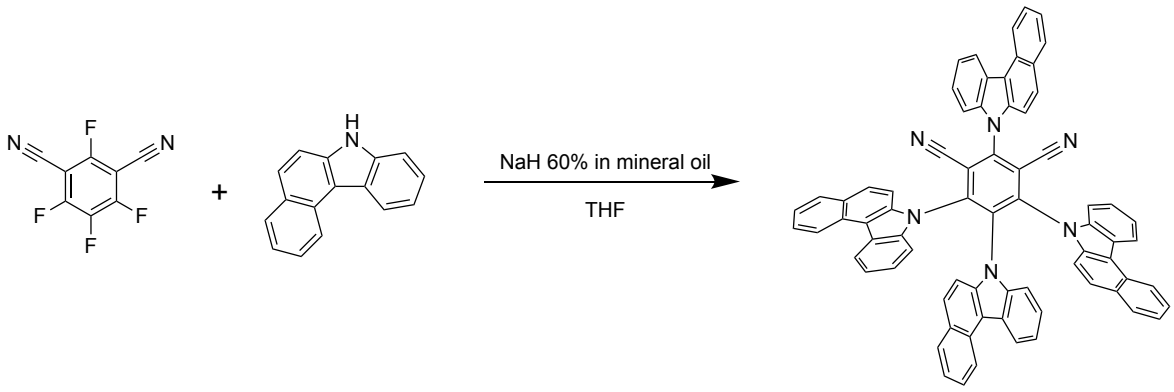
1H NMR : δ H (400 MHz, CDCl3) 9.30 (d, *J* = 8.5 Hz, 2H), 8.58 (d, *J* = 8.2 Hz, 4H), 8.28 (d, *J* = 8.8 Hz, 2H), 8.20 (d, *J* = 7.5 Hz, 2H), 8.01 (t, *J* = 9.3 Hz, 4H), 7.84 – 7.71 (m, 6H), 7.70 – 7.62 (m, 2H), 7.61 – 7.51 (m, 8H), 7.49 – 7.34 (m, 10H), 7.25 – 7.13 (m, 6H), 6.95 (d, *J* = 8.8 Hz, 2H).

^{13}C NMR : δ $_{C}$ (101 MHz, $CDCl_3$) 145.6, 137.4, 136.0, 135.1, 131.3, 130.8, 130.2, 129.6, 129.4, 129.2, 129.0, 128.7, 128.5, 128.5, 128.4, 127.9, 127.2, 126.5, 126.0, 125.8, 125.8, 125.5, 125.3, 125.0, 124.8, 124.3, 123.8, 120.5, 120.2, 119.5, 118.6, 111.3, 110.6, 110.5, 110.2.

MS m/z (ESI$^+$) : Calculated for molecular formula: 1188.3940, Found : 1189.4010 $[M+H]^+$

Elemental Analysis: Calculated : C, 88.87; H, 4.07; N, 7.07; Found : C, 88.30; H, 4.02; N, 6.81;

9.13.4.3 4MBCzIPN (20)



7.2 4.3 4MBCzIPN

As with 4DBCzIPN (**19**), 0.58 g of sodium hydride (60%) in mineral oil (giving 0.35 g, 14.1 mmol NaH) was washed three times with 10 mL portions of anhydrous hexane and dried under vacuum for 1 hour. The solid residue was suspended in 35 mL of dry tetrahydrofuran. To this, 2.42 g (11.1 mmol) of 7H-benzo[c]carbazole (**4.3**) was added portion wise and the resultant cloudy yellow solution quickly purged with argon and stirred at room temperature for 1 hour, by which time the solution resembled a deep orange. 0.45 g (2.25 mmol) of 2,4,5,6-tetrafluoroisophthalonitrile (**7.2**) was added portion wise with stirring, yielding a yellow-orange solution. The reaction mixture was then quickly purged with argon and stirred for 48 hours at room temperature.

50 mL of methanol and 50 mL of deionised water was added to quench the reaction and separation was performed with three 100 mL portions of dichloromethane and deionised water and brine. The organic phases were combined, dried over magnesium sulfate and filtered. The volatiles were removed under reduced pressure.

Purification was performed via silica gel chromatography using a 1 : 4 mix of ethyl acetate : petroleum ether as the eluent, increasing to 1 : 1 upon elution of the unreacted donor material. A crimson crystalline solid was obtained.

Initial ^{1}H NMR showed a pure compound with ethyl acetate still present after two days drying under high vacuum. This suggests coordination to the solvent in the crystalline form.

Further precipitation from hot dichloromethane : hexane and filtering was attempted to isolate the product without trapped solvent.

Yield : 991 mg ; 45%; **m.p.** 456.0°C (DSC)

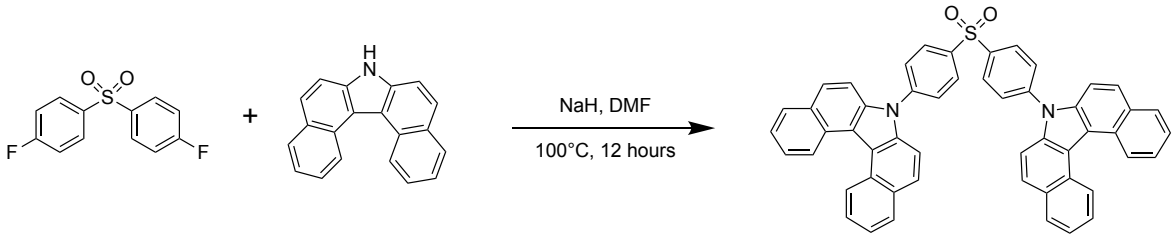
^{1}H NMR : δ_H (400 MHz, CD_2Cl_2) 8.93 (d, *J* = 8.4 Hz, 1H), 8.80 (d, *J* = 8.0 Hz, 1H), 8.46 (d, *J* = 8.7 Hz, 2H), 8.34 – 8.27 (m, 1H), 8.25 (d, *J* = 7.6 Hz, 2H), 8.20 (d, *J* = 8.3 Hz, 1H), 8.09 (d, *J* = 8.3 Hz, 1H), 8.05 – 7.86 (m, 4H), 7.83 (t, *J* = 7.2 Hz, 3H), 7.75 – 7.68 (m, 2H), 7.63 (t, *J* = 4.2 Hz, 4H), 7.58 (td, 3H), 7.55 – 7.49 (m, 2H), 7.47 – 7.35 (m, 4H), 7.34 – 7.13 (m, 7H), 6.93 (hept, 1H), 6.75 (ttd, 1H).

^{13}C NMR : δ_C (101 MHz, CD_2Cl_2) 145.9, 145.2, 139.7, 138.2, 138.1, 138.1, 137.2, 136.7, 136.6, 135.7, 130.9, 130.5, 130.1, 123.0, 129.9, 129.5, 129.5, 129.3, 129.2, 129.0, 128.3, 127.9, 127.8, 127.2, 126.8, 126.3, 125.9, 125.4, 125.1, 125.1, 125.0, 124.9, 124.6, 124.1, 124.1, 123.7, 123.7, 123.6, 123.5, 123.3, 123.0, 122.8, 122.2, 122.1, 118.3, 117.9, 117.3, 111.9, 111.2, 110.8, 110.7, 110.5, 110.4.

MS m/z (ESI$^+$) : Calculated for molecular formula: 988.3314; found : 1006.3672 $[M+NH_4]^+$

Elemental Analysis: Calculated : C, 87.43; H, 4.08; N, 8.50; Found : C, 87.05; H, 3.95; N, 8.43;

9.13.4.4 DBCz-PS (21)



7.3 **4.4** **DBCz-PS**

To a round-bottom flask, 0.42 g of sodium hydride (60% in mineral oil, 0.25 g, 10.5 mmol) was added, along with 1.49 g (5.57 mmol) of 7H-dibenzo[c,g]carbazole (**4.4**). The flask was cooled by means of an ice bath and 30 mL dry *N*,*N*,-dimethylformamide slowly added to form a suspension. The suspension was stirred at room temperature for 30 minutes, after which time it had formed a solution with bright blue fluorescence.

A solution of 0.62 g (2.44 mmol) bis-(p-fluorophenyl)-sulfone (**7.3**) in 15 mL dimethylformamide was prepared and added dropwise to the metalated solution of **4.4**. Stirring under reflux at 100°C was performed for 24 hours.

By the next day, the solution had formed a yellow suspension. The suspension was poured into 250 mL ice water, whereupon a white precipitate formed. The water was filtered off and the solid dried under vacuum.

Further purification was performed by suspending in hot ethanol and filtering, followed by washing with ethanol at room temperature to yield a white solid with bright blue fluorescence.

The material was found to be only sparingly soluble in most solvents, the most effective being tetrahydrofuran.

Yield : 1.03 g, 56%; **m.p.** 386.9°C (DSC)

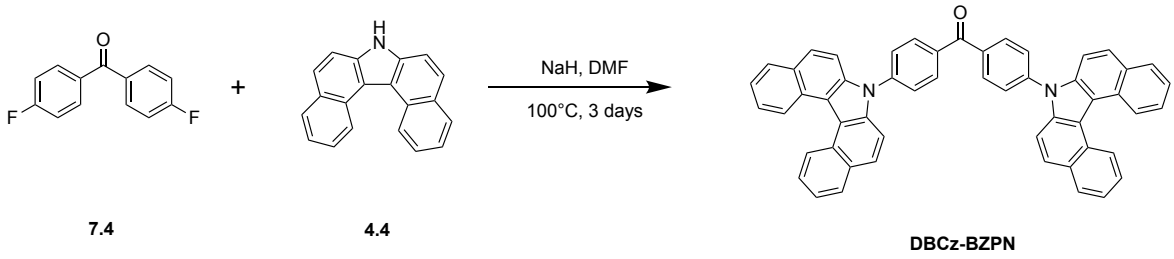
^{1}H NMR : δ_H (400 MHz, THF) 9.22 (d, J = 8.5 Hz, 4H), 8.49 (d, J = 8.5 Hz, 4H), 8.06 (d, J = 8.0 Hz, 4H), 8.00 (d, J = 8.5 Hz, 4H), 7.91 (d, J = 8.9 Hz, 4H), 7.69 (dd, J = 8.2, 5.6 Hz, 8H), 7.52 (t, J = 7.4 Hz, 4H).

^{13}C NMR : Too insoluble to prepare a concentration high enough without particulates

MS m/z (ESI$^+$) : Calculated for molecular formula: 748.2184; found : 749.2221 $[M+H]^+$

Elemental Analysis: Calculated : C, 83.40; H, 4.31; N, 3.74; Found : C, 83.56; H, 4.27; N, 3.78;

9.13.4.5 DBCz-BZPN (22)



7.4 4.4 DBCz-BZPN

Placed in a round-bottom flask were 1.48 g (5.54 mmol) of 7H-dibenzo[c,g]carbazole (**4.4**) and 0.26 g (10.8 mmol) sodium hydride (60% in mineral oil – 0.44 g total) and the flask connected to a condenser and purged with argon. 30 mL of dry *N*,*N*,-dimethylformamide was added with stirring at 0°C. Stirring was continued at room temperature for 1 hour, yielding a cloudy yellow suspension with bright blue fluorescence. To this 0.54 g (2.47 mmol) of 4,4'-difluorobenzophenone (**7.4**) was added portion wise, and the flask purged once more.

Stirring was maintained for a further 1 hour, then the reaction mixture was refluxed for 3 days at 100°C.

After 3 days a bright yellow precipitate had formed. The solution was decanted into ice water, filtered and recrystalised from hot ethanol : dichloromethane.

Yield : 131.4 mg 7.5%; **m.p.** 407.5°C (DSC)

^{1}H NMR : δ_H (400 MHz, $CDCl_3$) 9.26 (d, *J* = 8.5 Hz, 4H), 8.28 (d, *J* = 8.4 Hz, 4H), 8.07 (d, *J* = 8.1 Hz, 4H), 7.91 (d, *J* = 8.9 Hz, 4H), 7.85 (d, *J* = 8.4 Hz, 4H), 7.71 (t, *J* = 9.1 Hz, 8H), 7.57 (t, *J* = 7.4 Hz, 4H).

^{13}C NMR : To insoluble to prepare sample concentrated enough for ^{13}C NMR

MS m/z (ESI$^+$) : Calculated for molecular formula: 712.2515; found : 713.2595 $[M+H]^+$

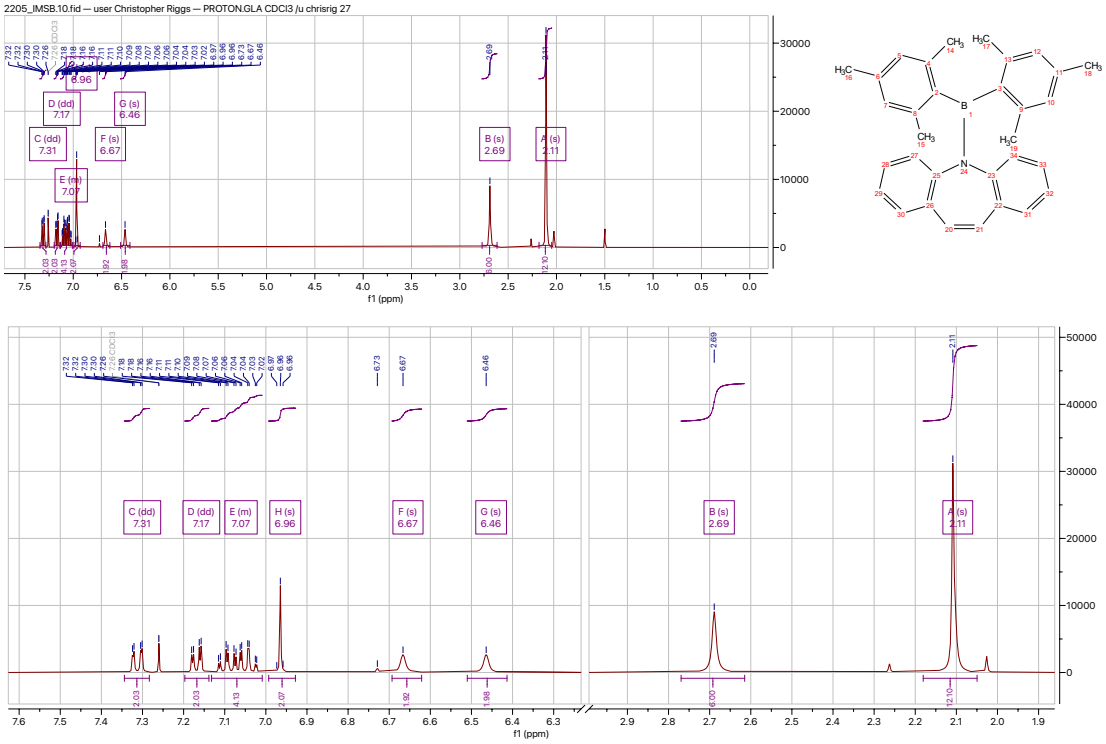
Elemental Analysis: Calculated : C, 89.30; H, 4.52; N, 3.93; Found : C, 88.20; H, 4.50; N, 3.92;

Appendix 3 NMR and mass spectrometry

9.14 Chapter 4

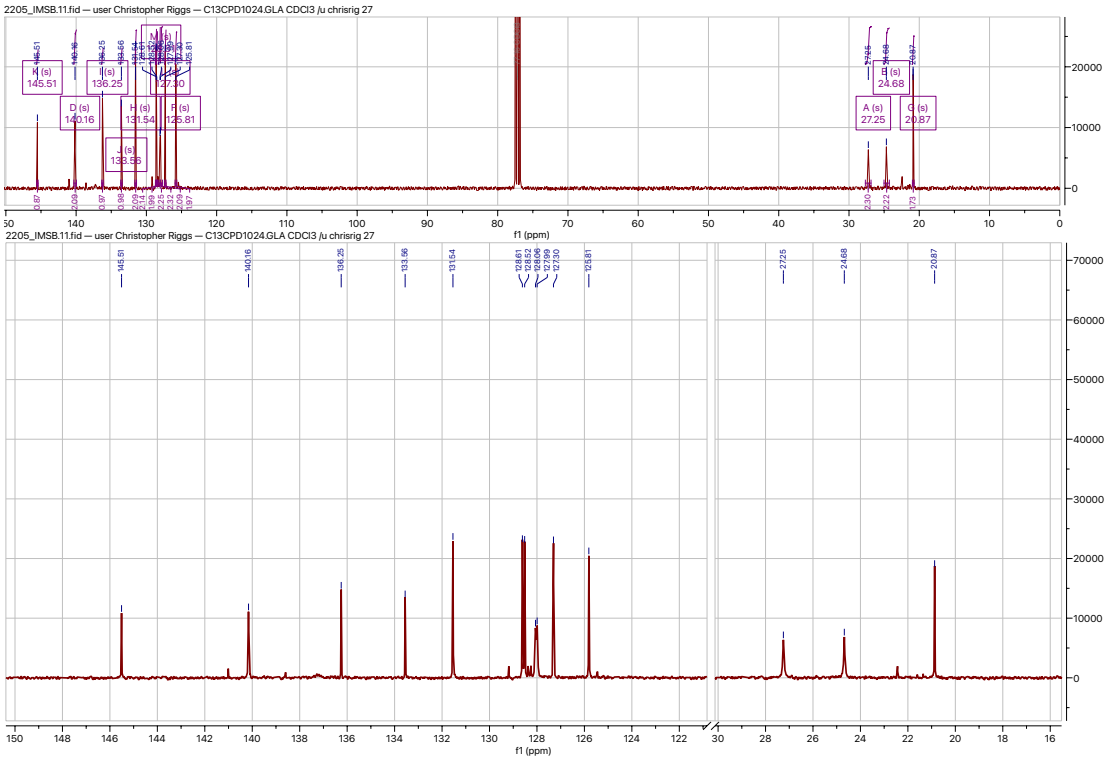
9.14.1 IMSB-DMB (1)

^{1}H NMR



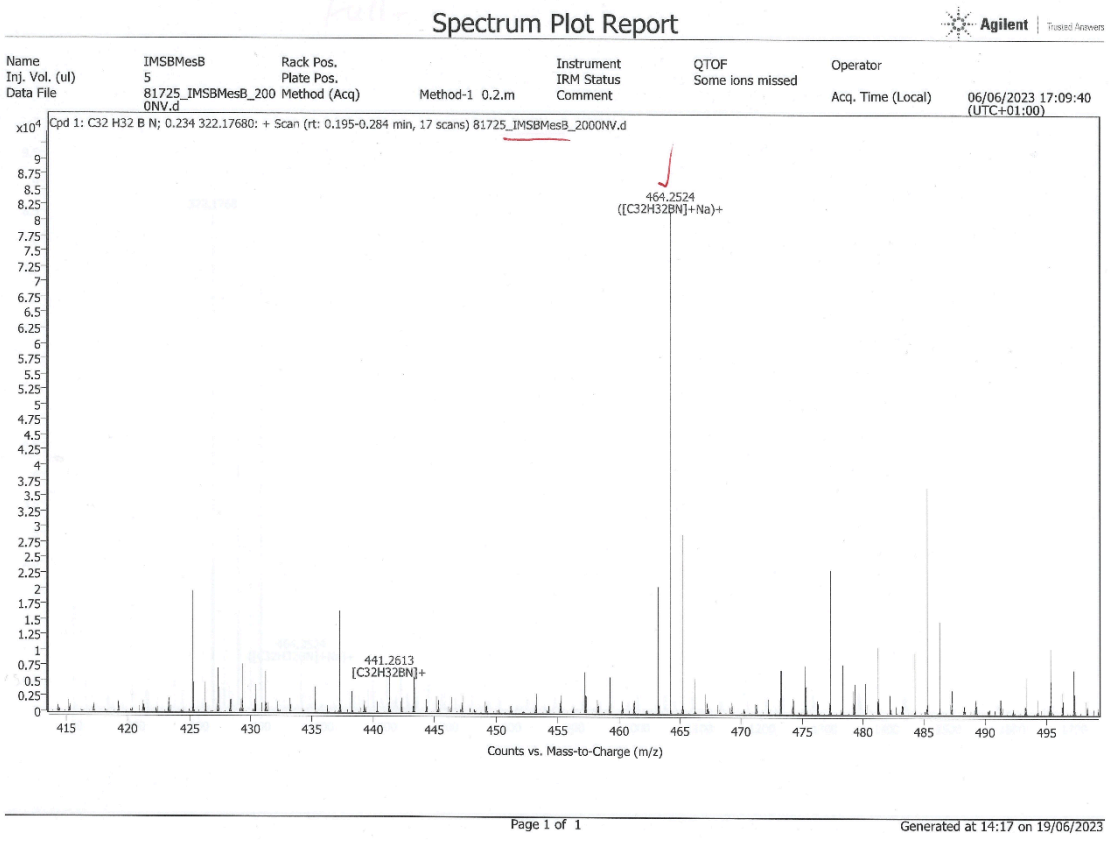
δ_H (400 MHz, $CDCl_3$) 7.31 (2 H, dd, *J* 7.8, 1.4), 7.17 (2 H, dd, *J* 7.4, 1.9), 7.13 – 7.01 (4 H, m), 6.96 (2 H, s), 6.67 (2 H, s), 6.46 (2 H, s), 2.69 (6 H, s), 2.11 (12 H, s).

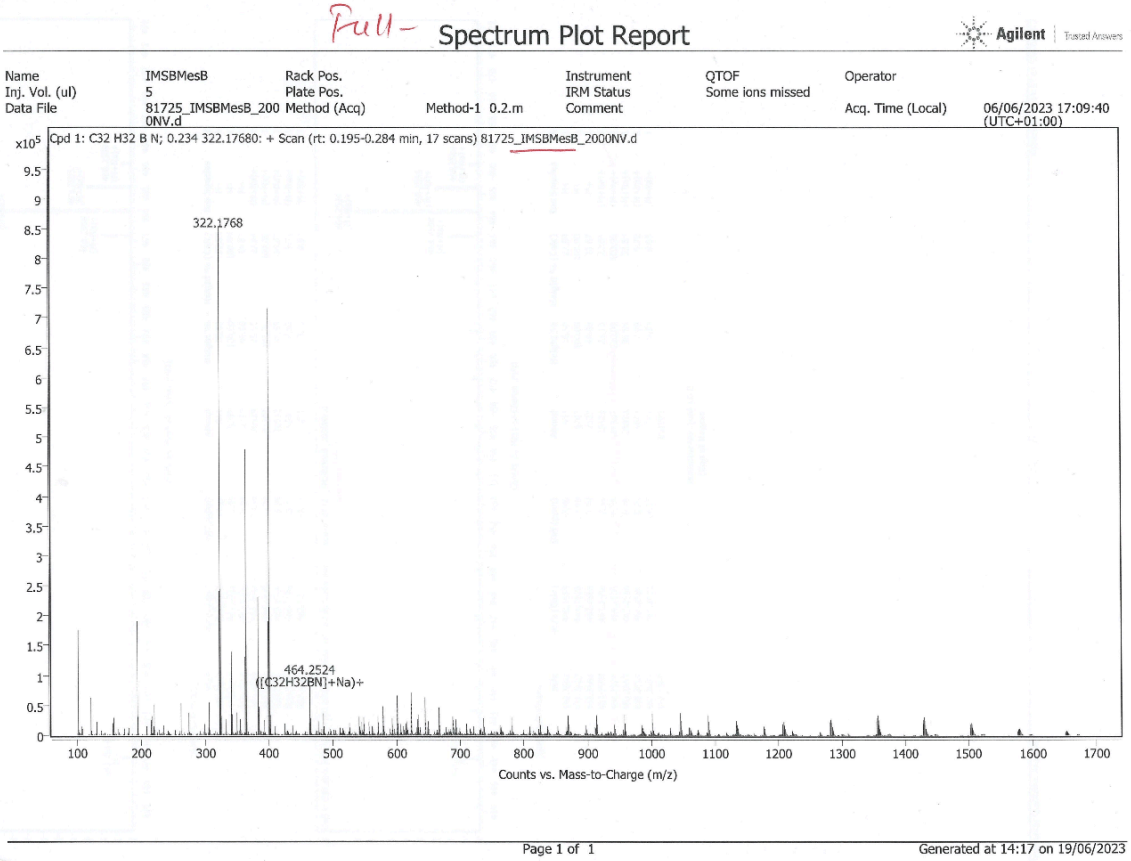
^{13}C NMR



δ_C (101 MHz, $CDCl_3$) 145.51, 140.16, 136.25, 133.56, 131.54, 128.61, 128.52, 128.06, 127.99, 127.30, 125.81, 27.25, 24.68, 20.87.

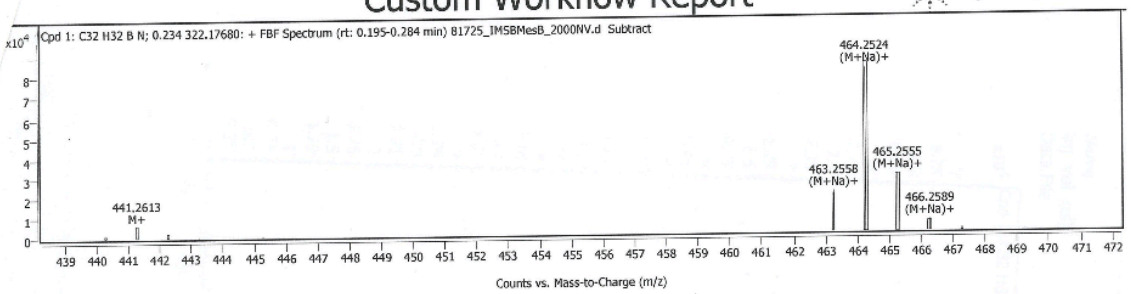
MS


Spectrum Plot Report
Agilent
Name IMSBMesB
Inj. Vol. (ul) 5
Data File 81725_IMSBMesB_2000NV.d
Rack Pos.
Plate Pos.
Method (Acq) Method-1 0.2.m
Instrument QTOF
IRM Status Some ions missed
Comment
Operator
Acq. Time (Local) 06/06/2023 17:09:40 (UTC+01:00)
Cpd 1: C32 H32 B N; 0.234 322.17680: + Scan (rt: 0.195-0.284 min, 17 scans) 81725_IMSBMesB_2000NV.d
x10^4
464.2524
([C32H32BN]+Na)+
441.2613
[C32H32BN]+
Counts vs. Mass-to-Charge (m/z)
Page 1 of 1
Generated at 14:17 on 19/06/2023


Full-
Spectrum Plot Report
Agilent
Name IMSBMesB
Inj. Vol. (ul) 5
Data File 81725_IMSBMesB_2000NV.d
Rack Pos.
Plate Pos.
Method (Acq) Method-1 0.2.m
Instrument QTOF
IRM Status Some ions missed
Comment
Operator
Acq. Time (Local) 06/06/2023 17:09:40 (UTC+01:00)
Cpd 1: C32 H32 B N; 0.234 322.17680: + Scan (rt: 0.195-0.284 min, 17 scans) 81725_IMSBMesB_2000NV.d
x10^5
322.1768
464.2524
([C32H32BN]+Na)+
Counts vs. Mass-to-Charge (m/z)
Page 1 of 1
Generated at 14:17 on 19/06/2023

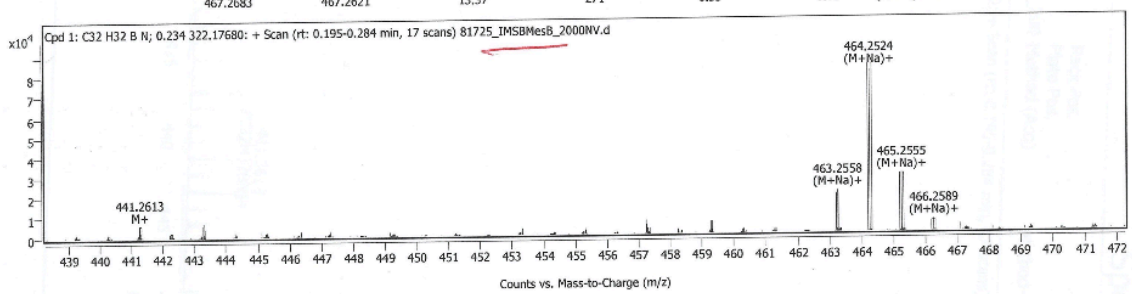
Custom Workflow Report

Agilent | Trusted Answers



Spectrum Peaks

m/z	m/z (Calc)	Diff (ppm)	Abund	Height %	Height % (Calc)	Ion Species	Z
440.2642	440.2659	-3.86	941	16.50	22.84	M+	1
441.2613	441.2628	-3.48	5703	100.00	100.00	M+	1
442.2663	442.2658	0.94	2327	40.80	33.87	M+	1
463.2558	463.2556	0.31	20429	25.10	22.84	(M+Na)+	1
464.2524	464.2526	-0.28	81387	100.00	100.00	(M+Na)+	1
465.2555	465.2556	-0.16	28933	35.55	33.87	(M+Na)+	1
466.2589	466.2588	0.25	5697	7.00	5.72	(M+Na)+	1
467.2683	467.2621	13.37	271	0.33	0.63	(M+Na)+	1



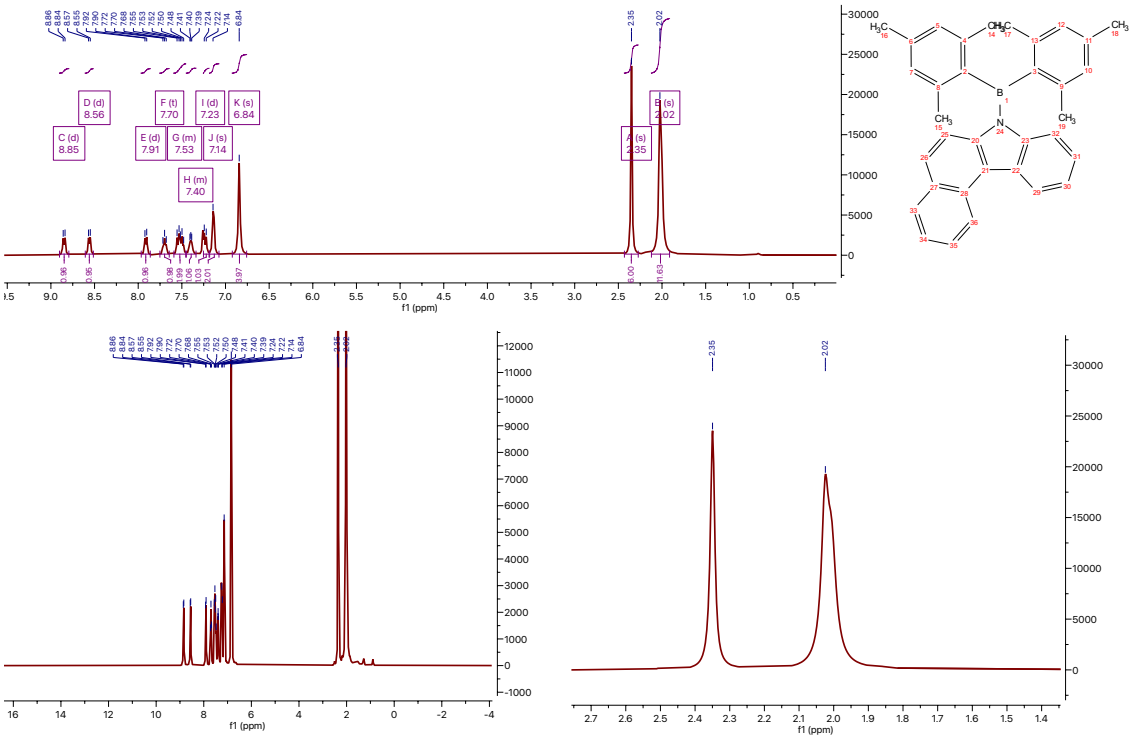
Spectrum Peaks

m/z	m/z (Calc)	Diff (ppm)	Abund	Height %	Height % (Calc)	Ion Species	Z
440.2642	440.2659	-3.86	941	16.50	22.84	M+	1
441.2613	441.2628	-3.48	5703	100.00	100.00	M+	1
442.2663	442.2658	0.94	2327	40.80	33.87	M+	1
463.2558	463.2556	0.31	20429	25.10	22.84	(M+Na)+	1
464.2524	464.2526	-0.28	81387	100.00	100.00	(M+Na)+	1
465.2555	465.2556	-0.16	28933	35.55	33.87	(M+Na)+	1
466.2589	466.2588	0.25	5697	7.00	5.72	(M+Na)+	1
467.2683	467.2621	13.37	271	0.33	0.63	(M+Na)+	1
322.1768			851909				

MassHunter Qual 10.0
(End of Report)

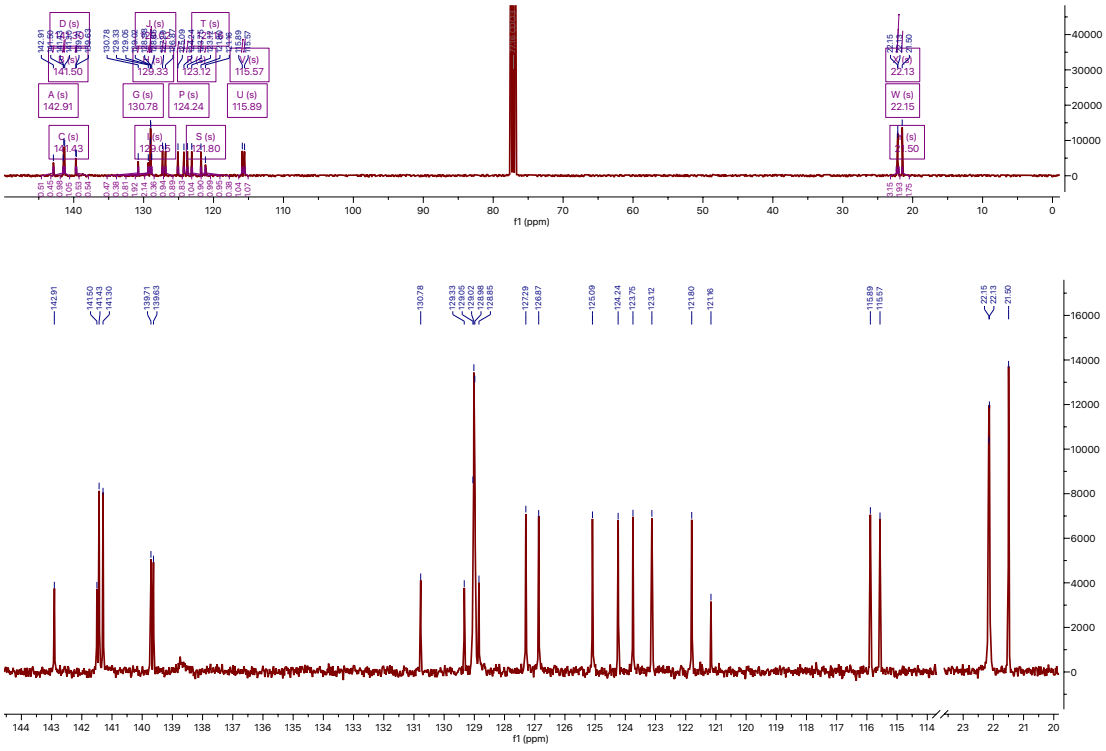
9.14.2 MBCz-DMB (2)

^{1}H NMR



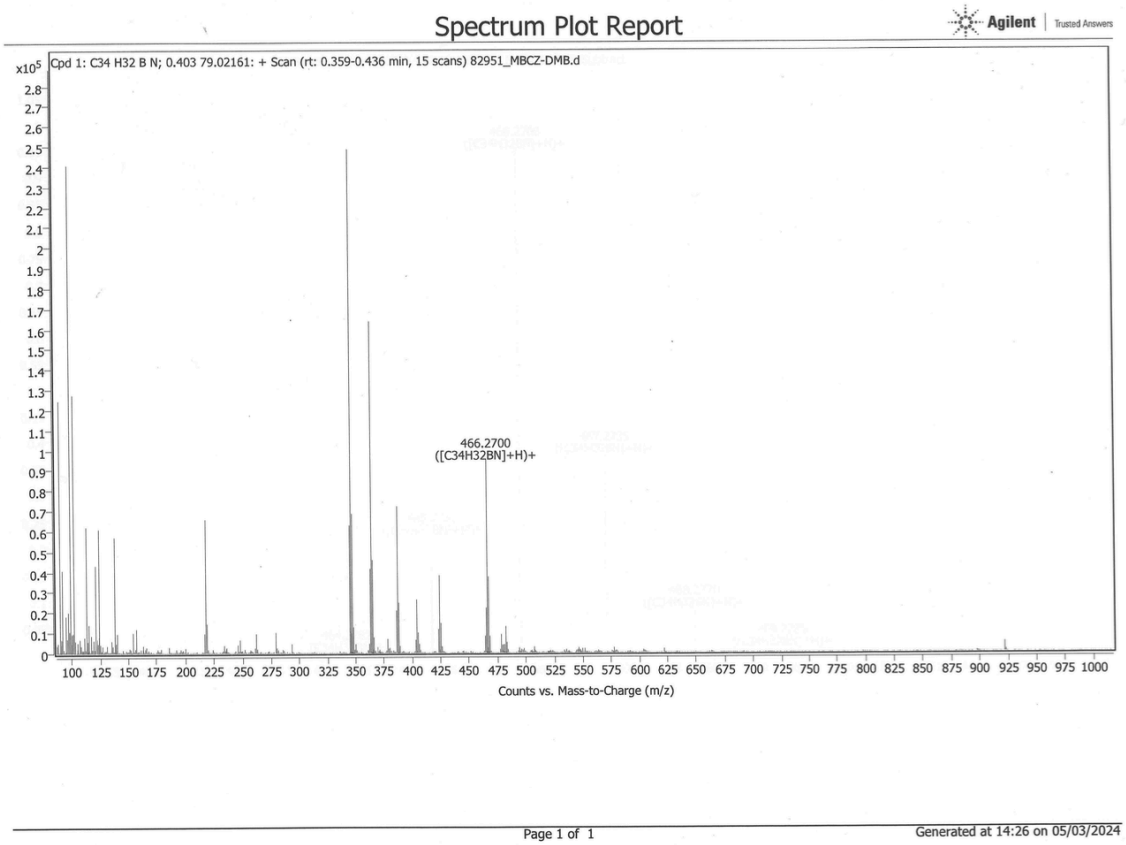
δ_H (400 MHz, $CDCl_3$) 8.85 (1 H, d, *J* 8.4), 8.56 (1 H, d, *J* 8.0), 7.91 (1 H, d, *J* 8.1), 7.70 (1 H, t, *J* 7.7), 7.59 – 7.46 (2 H, m), 7.45 – 7.34 (1 H, m), 7.23 (1 H, d, *J* 9.1), 7.14 (2 H, s), 6.84 (4 H, s), 2.35 (6 H, s), 2.02 (12 H, s).

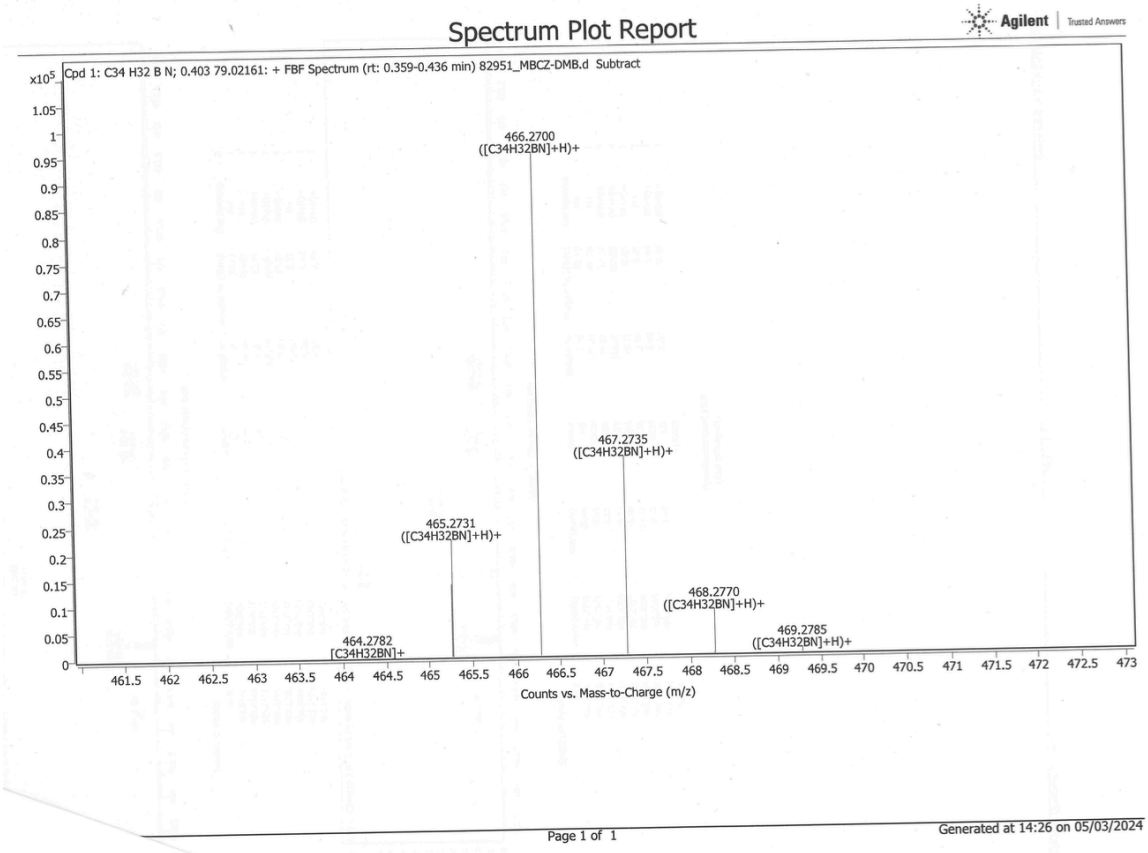
^{13}C NMR



δ_C (101 MHz, $CDCl_3$) 142.91, 141.50, 141.43, 141.30, 139.71, 139.63, 130.78, 129.33, 129.05, 129.02, 128.98, 128.85, 127.29, 126.87, 125.09, 124.24, 123.75, 123.12, 121.80, 121.16, 115.89, 115.57, 22.15, 22.13, 21.50.

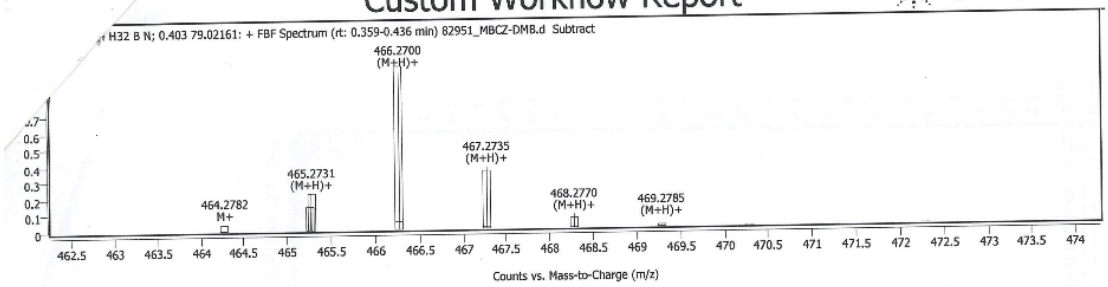
MS


Spectrum Plot Report
Agilent | Trusted Answers
Cpd 1: C34 H32 B N; 0.403 79.02161: + Scan (rt: 0.359-0.436 min, 15 scans) 82951_MBCZ-DMB.d
x10^5
466.2700
([C34H32BN]+H)+
Counts vs. Mass-to-Charge (m/z)
Page 1 of 1
Generated at 14:26 on 05/03/2024


Spectrum Plot Report
Agilent | Trusted Answers
Cpd 1: C34 H32 B N; 0.403 79.02161: + FBF Spectrum (rt: 0.359-0.436 min) 82951_MBCZ-DMB.d Subtract
x10^5
466.2700
([C34H32BN]+H)+
467.2735
([C34H32BN]+H)+
465.2731
([C34H32BN]+H)+
468.2770
([C34H32BN]+H)+
469.2785
([C34H32BN]+H)+
464.2782
[C34H32BN]+
Counts vs. Mass-to-Charge (m/z)
Page 1 of 1
Generated at 14:26 on 05/03/2024

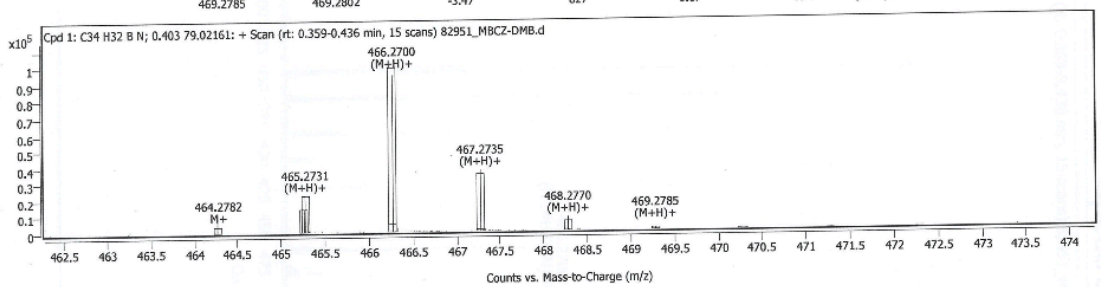
Custom Workflow Report

Agilent | Trusted Answers



Spectrum Peaks

m/z	m/z (Calc)	Diff (ppm)	Abund	Height %	Height % (Calc)	Ion Species	z
464.2782	464.2659	26.48	145	1.06	22.73	M+	1
465.2628	465.2628	-0.03	13630	100.00	100.00	M+	1
465.2731	465.2737	-1.32	22020	23.17	22.73	(M+H)+	1
466.2700	466.2706	-1.41	95029	100.00	100.00	(M+H)+	1
467.2735	467.2737	-0.30	37392	39.35	35.87	(M+H)+	1
468.2654	468.2723	-14.72	135	0.99	0.75	M+	1
468.2770	468.2769	0.23	8250	8.68	6.44	(M+H)+	1
469.2785	469.2802	-3.47	827	0.87	0.75	(M+H)+	1



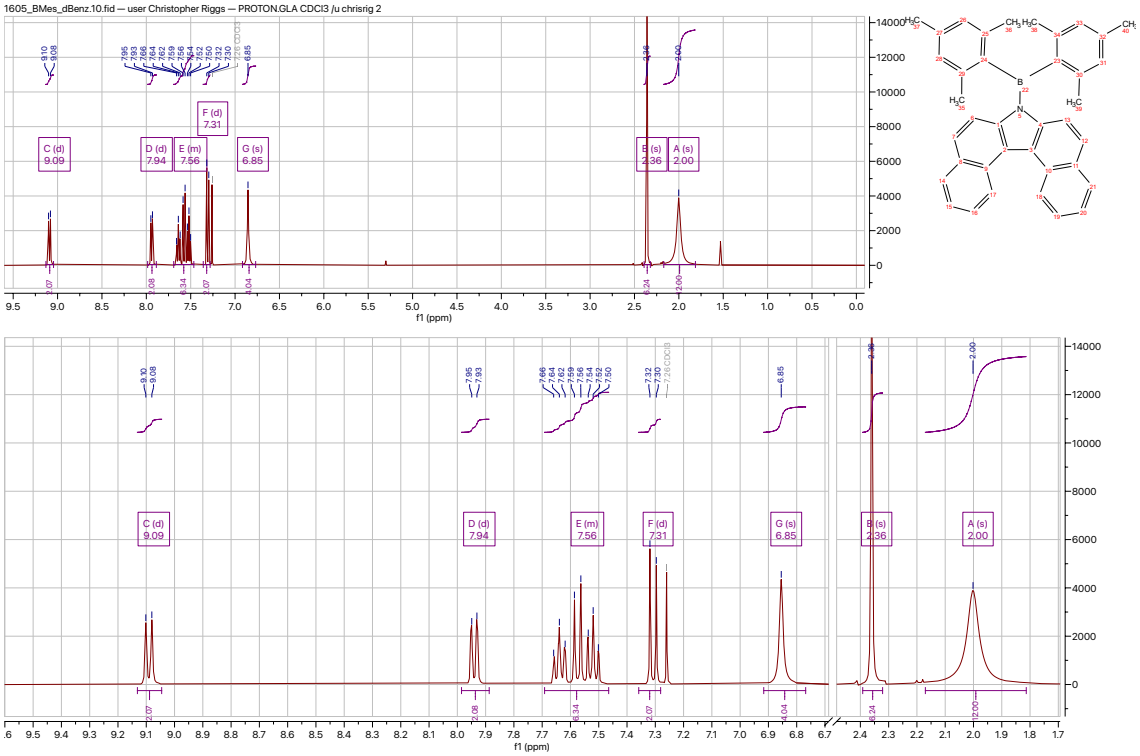
Spectrum Peaks

m/z	m/z (Calc)	Diff (ppm)	Abund	Height %	Height % (Calc)	Ion Species	z
464.2782	464.2659	26.48	145	1.06	22.73	M+	1
465.2628	465.2628	-0.03	13630	100.00	100.00	M+	1
465.2731	465.2737	-1.32	22020	23.17	22.73	(M+H)+	1
466.2700	466.2706	-1.41	95029	100.00	100.00	(M+H)+	1
467.2735	467.2737	-0.30	37392	39.35	35.87	(M+H)+	1
468.2654	468.2723	-14.72	135	0.99	0.75	M+	1
468.2770	468.2769	0.23	8250	8.68	6.44	(M+H)+	1
469.2785	469.2802	-3.47	827	0.87	0.75	(M+H)+	1
79.0216			5170325				

MassHunter Qual 10.0
(End of Report)

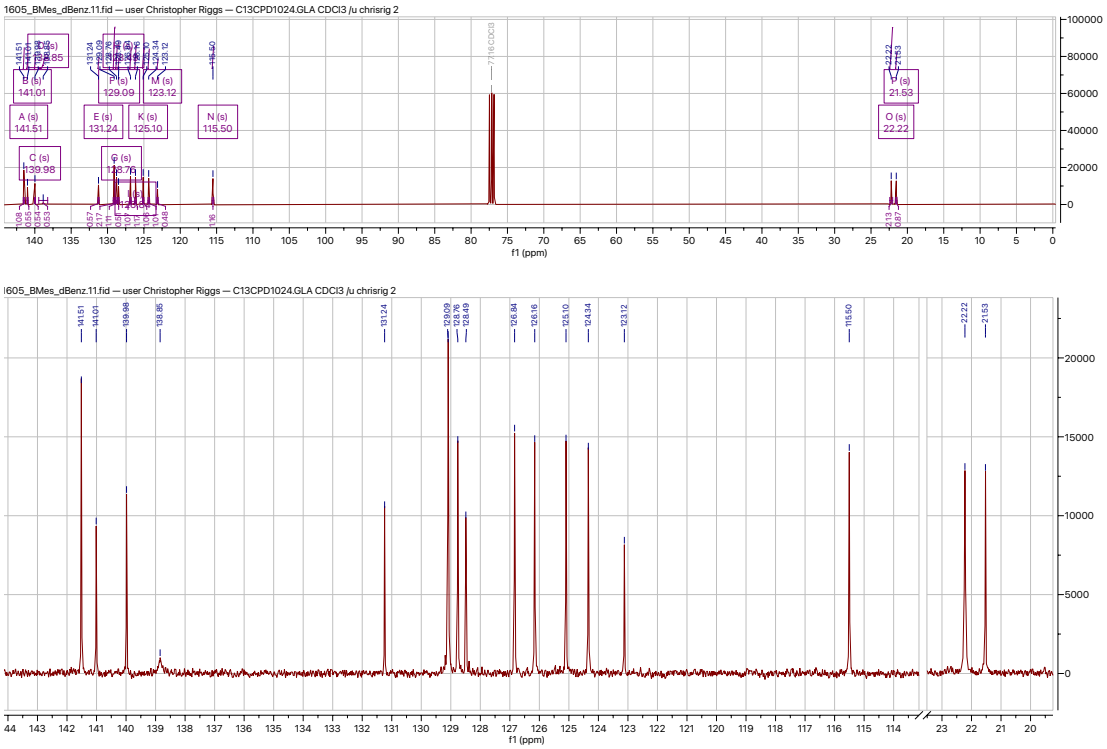
9.14.3 DBCz-DMB (3)

^{1}H NMR



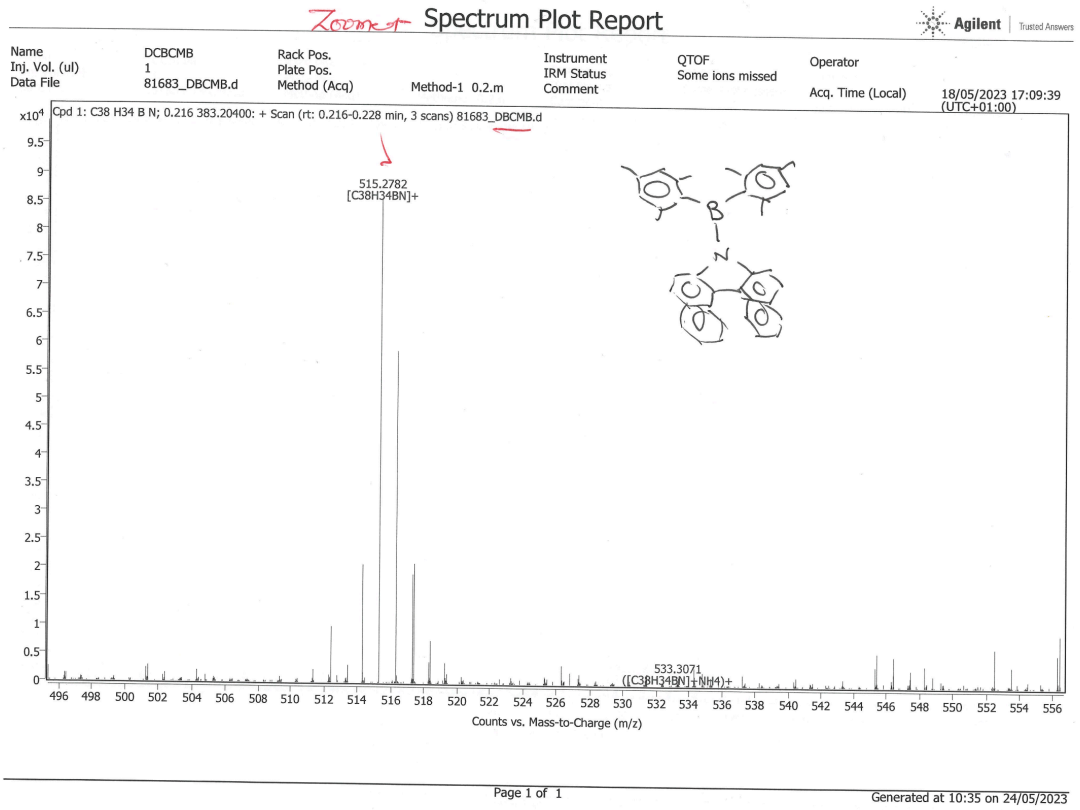
δ_{H} (400 MHz, $CDCl_3$) 9.09 (2 H, d, *J* 8.5), 7.94 (2 H, d, *J* 7.3), 7.69 – 7.46 (6 H, m), 7.31 (2 H, d, *J* 9.0), 6.85 (4 H, s), 2.36 (6 H, s), 2.00 (12 H, s).

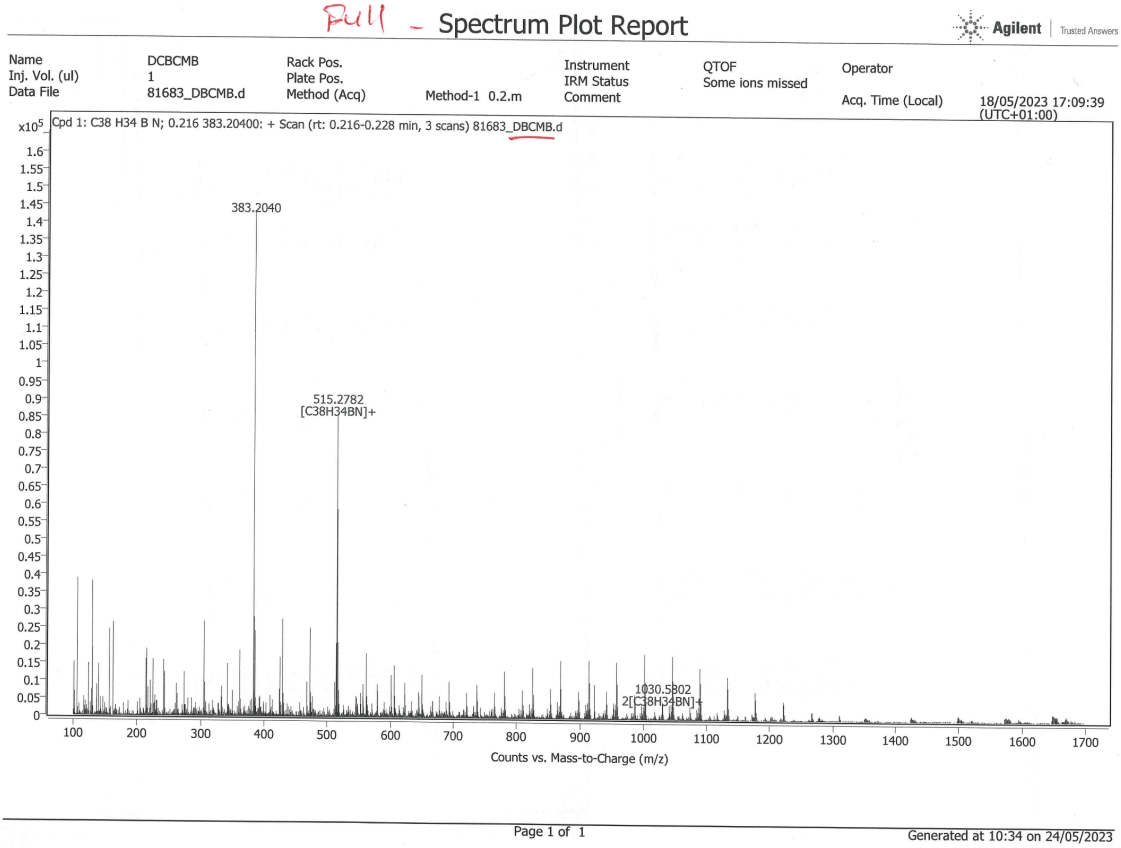
^{13}C NMR



δ_C (101 MHz, $CDCl_3$) 141.51, 141.01, 139.98, 138.85, 131.24, 129.09, 128.76, 128.49, 126.84, 126.16, 125.10, 124.34, 123.12, 115.50, 22.22, 21.53.

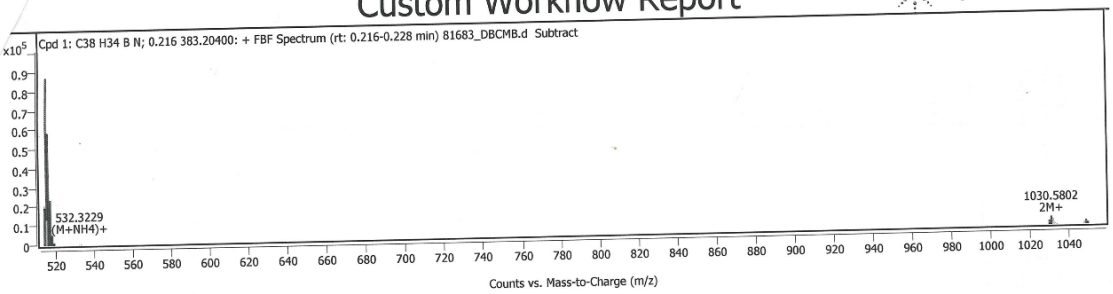
MS


Zoom in
Spectrum Plot Report
Agilent
Trusted Answers
Name DCBCMB
Inj. Vol. (ul) 1
Data File 81683_DBCMB.d
Rack Pos.
Plate Pos.
Method (Acq) Method-1 0.2.m
Instrument
IRM Status
Comment
QTOF
Some ions missed
Operator
Acq. Time (Local) 18/05/2023 17:09:39 (UTC+01:00)
Cpd 1: C38 H34 B N; 0.216 383.20400: + Scan (rt: 0.216-0.228 min, 3 scans) 81683_DBCMB.d
515.2782
[C38H34BN]+
533.3071
([C38H34BN]+NH4)+
Counts vs. Mass-to-Charge (m/z)
Page 1 of 1
Generated at 10:35 on 24/05/2023


Full
Spectrum Plot Report
Agilent
Trusted Answers
Name DCBCMB
Inj. Vol. (ul) 1
Data File 81683_DBCMB.d
Rack Pos.
Plate Pos.
Method (Acq) Method-1 0.2.m
Instrument
IRM Status
Comment
QTOF
Some ions missed
Operator
Acq. Time (Local) 18/05/2023 17:09:39 (UTC+01:00)
Cpd 1: C38 H34 B N; 0.216 383.20400: + Scan (rt: 0.216-0.228 min, 3 scans) 81683_DBCMB.d
383.2040
515.2782
[C38H34BN]+
1030.5802
2[C38H34BN]+
Counts vs. Mass-to-Charge (m/z)
Page 1 of 1
Generated at 10:34 on 24/05/2023

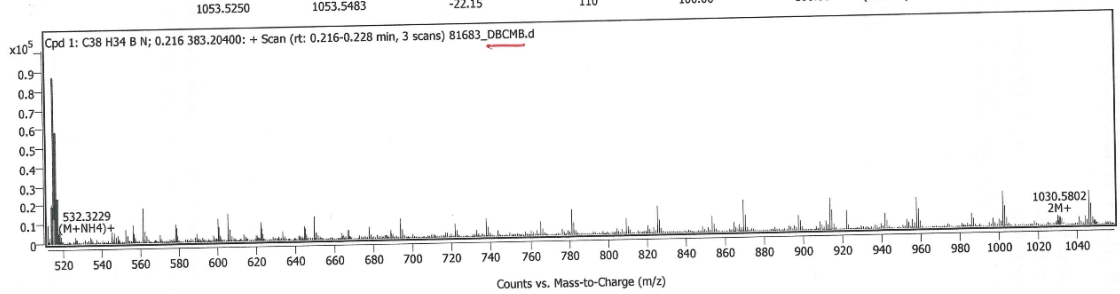
Custom Workflow Report

Agilent | Trusted Answers



Spectrum Peaks

m/z	m/z (Calc)	Diff (ppm)	Abund	Height %	Height % (Calc)	Ion Species	z
514.2813	514.2815	-0.48	20791	24.35	22.50	M+	1
515.2782	515.2785	-0.57	85401	100.00	100.00	M+	1
516.2838	516.2864	-4.90	58730	100.00	100.00	(M+H)+	1
517.2876	517.2894	-3.35	19120	32.55	39.85	(M+H)+	1
518.2915	518.2926	-2.17	3741	6.37	7.99	(M+H)+	1
519.2961	519.2959	0.48	997	1.70	1.05	(M+H)+	1
532.3229	532.3159	13.16	133	35.54	22.48	(M+NH4)+	1
533.3071	533.3129	-10.97	375	100.00	100.00	(M+NH4)+	1
534.3233	534.3159	13.84	110	29.20	40.21	(M+NH4)+	1
1029.5498	1029.5606	-10.51	309	7.50	38.17	2M+	1
1030.5802	1030.5585	21.05	4118	100.00	100.00	2M+	1
1031.5885	1031.5664	21.49	493	100.00	100.00	(2M+H)+	1
1032.5703	1032.5687	1.57	261	52.87	70.61	(2M+H)+	1
1033.5840	1033.5717	11.96	142	28.86	27.41	(2M+H)+	1
1048.5950	1048.5929	2.04	1553	100.00	100.00	(2M+NH4)+	1
1049.5968	1049.5952	1.50	552	35.52	70.91	(2M+NH4)+	1
1053.5250	1053.5483	-22.15	110	100.00	100.00	(2M+Na)+	1



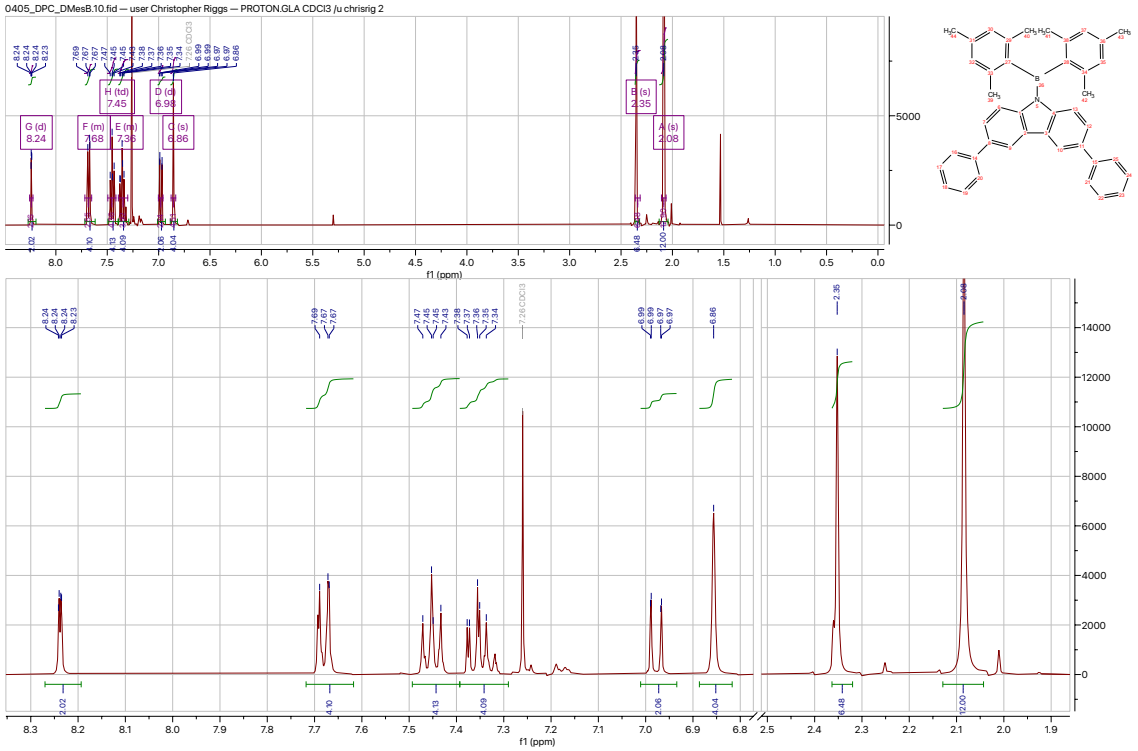
Spectrum Peaks

m/z	m/z (Calc)	Diff (ppm)	Abund	Height %	Height % (Calc)	Ion Species	z
514.2813	514.2815	-0.48	20791	24.35	22.50	M+	1
515.2782	515.2785	-0.57	85401	100.00	100.00	M+	1
516.2838	516.2864	-4.90	58730	100.00	100.00	(M+H)+	1
517.2876	517.2894	-3.35	19120	32.55	39.85	(M+H)+	1
518.2915	518.2926	-2.17	3741	6.37	7.99	(M+H)+	1
519.2961	519.2959	0.48	997	1.70	1.05	(M+H)+	1
532.3229	532.3159	13.16	133	35.54	22.48	(M+NH4)+	1
533.3071	533.3129	-10.97	375	100.00	100.00	(M+NH4)+	1
534.3233	534.3159	13.84	110	29.20	40.21	(M+NH4)+	1
1029.5498	1029.5606	-10.51	309	7.50	38.17	2M+	1
1030.5802	1030.5585	21.05	4118	100.00	100.00	2M+	1
1031.5885	1031.5664	21.49	493	100.00	100.00	(2M+H)+	1
1032.5703	1032.5687	1.57	261	52.87	70.61	(2M+H)+	1
1033.5840	1033.5717	11.96	142	28.86	27.41	(2M+H)+	1
1048.5950	1048.5929	2.04	1553	100.00	100.00	(2M+NH4)+	1
1049.5968	1049.5952	1.50	552	35.52	70.91	(2M+NH4)+	1
1053.5250	1053.5483	-22.15	110	100.00	100.00	(2M+Na)+	1
383.2040			142961				

MassHunter Qual 10.0
(End of Report)

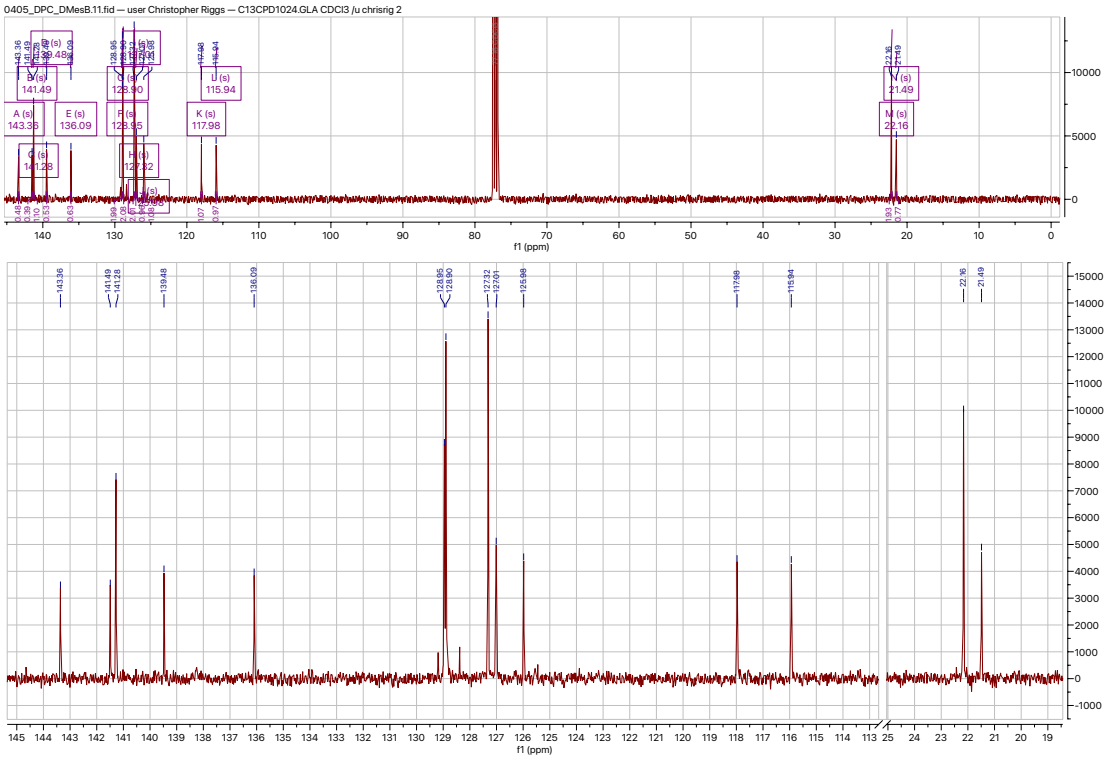
9.14.4 DPhCz-DMB (4)

^{1}H NMR



δ_H (400 MHz, $CDCl_3$) 8.24 (2 H, d, *J* 2.0), 7.72 – 7.65 (4 H, m), 7.45 (4 H, td, *J* 8.3, 7.0), 7.39 – 7.30 (4 H, m), 6.98 (2 H, d, *J* 0.6), 6.86 (4 H, s), 2.35 (6 H, s), 2.08 (12 H, s).

^{13}C NMR



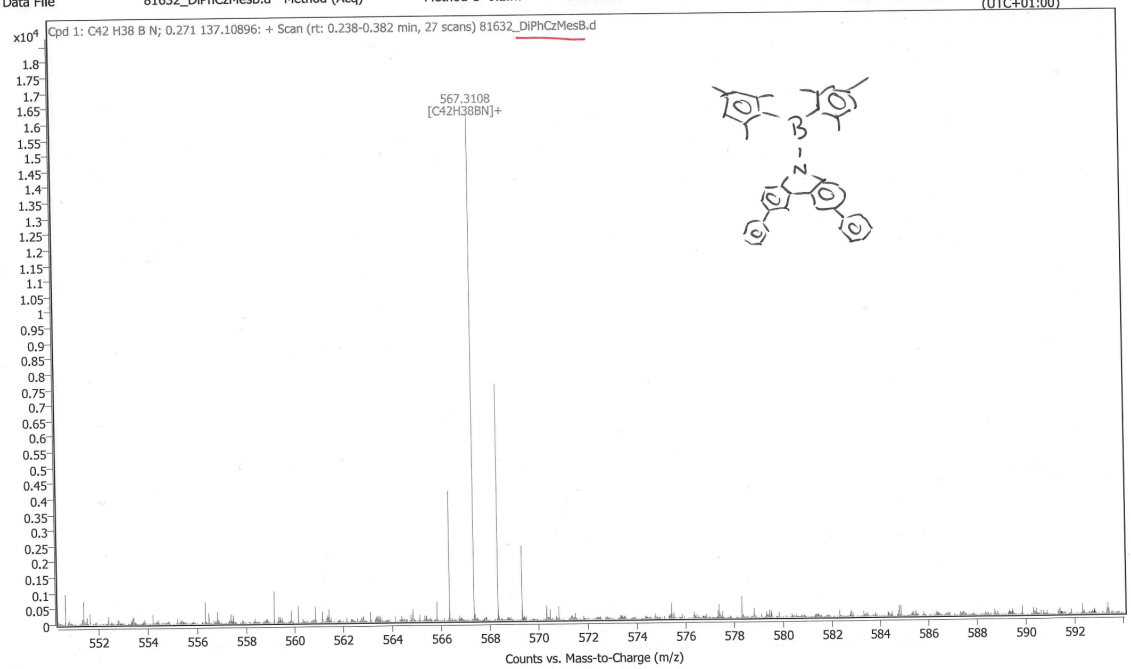
δ_C (101 MHz, $CDCl_3$) 143.36, 141.49, 141.28, 139.48, 136.09, 128.95, 128.90, 127.32, 127.01, 125.98, 117.98, 115.94, 22.16, 21.49.

MS

Zoomed - Spectrum Plot Report

Agilent | Trusted Answers

Name	DiPhCzMesB	Rack Pos.		Instrument	QTOF	Operator	
Inj. Vol. (ul)	1	Plate Pos.		IRM Status	Success		
Data File	81632_DiPhCzMesB.d	Method (Acq)	Method-1 0.2.m	Comment		Acq. Time (Local)	11/05/2023 14:55:14 (UTC+01:00)

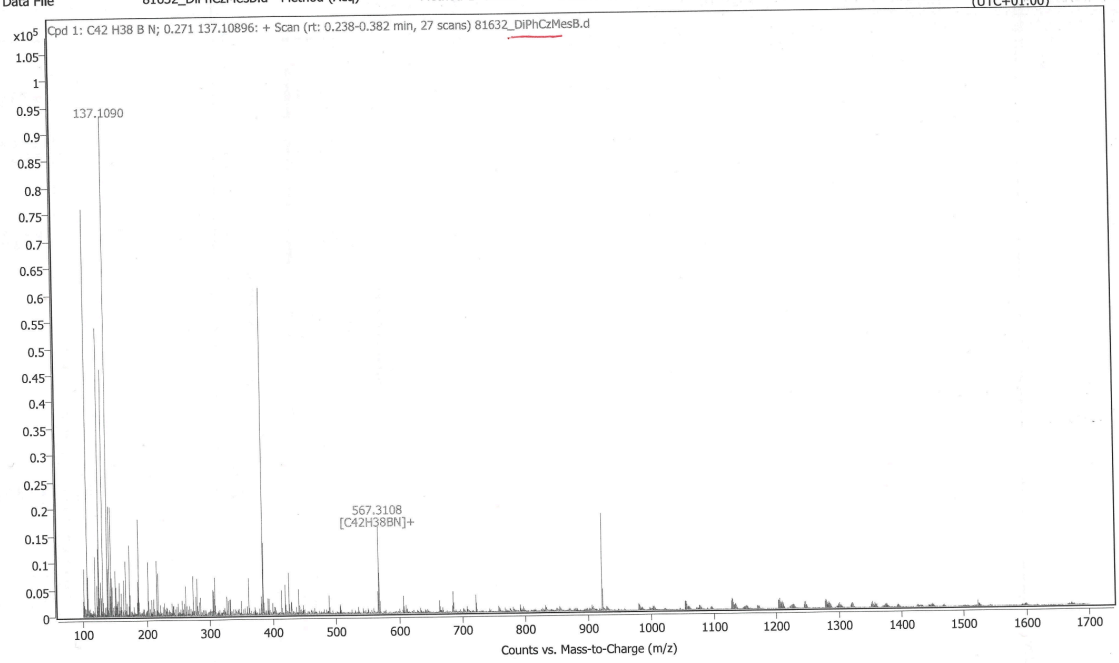


Generated at 16:21 on 11/05/2023

Full - Spectrum Plot Report

Agilent | Trusted Answers

Name	DiPhCzMesB	Rack Pos.		Instrument	QTOF	Operator	
Inj. Vol. (ul)	1	Plate Pos.		IRM Status	Success		
Data File	81632_DiPhCzMesB.d	Method (Acq)	Method-1 0.2.m	Comment		Acq. Time (Local)	11/05/2023 14:55:14 (UTC+01:00)



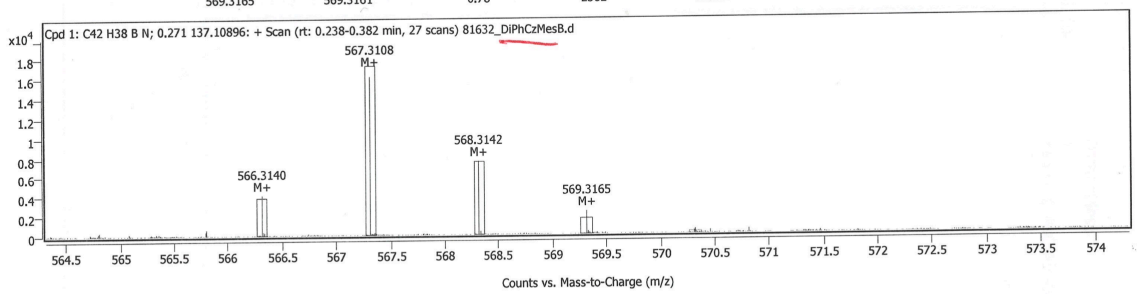
Generated at 16:20 on 11/05/2023

Custom Workflow Report

Agilent | Trusted Answers

Spectrum Peaks

m/z	m/z (Calc)	Diff (ppm)	Abund	Height %	Height % (Calc)	Ion Species	z
566.3140	566.3128	2.10	4135	25.56	22.28	M+	1
567.3108	567.3099	1.54	16176	100.00	100.00	M+	1
568.3142	568.3129	2.26	7555	46.70	43.79	M+	1
569.3165	569.3161	0.78	2362	14.60	9.71	M+	1



Spectrum Peaks

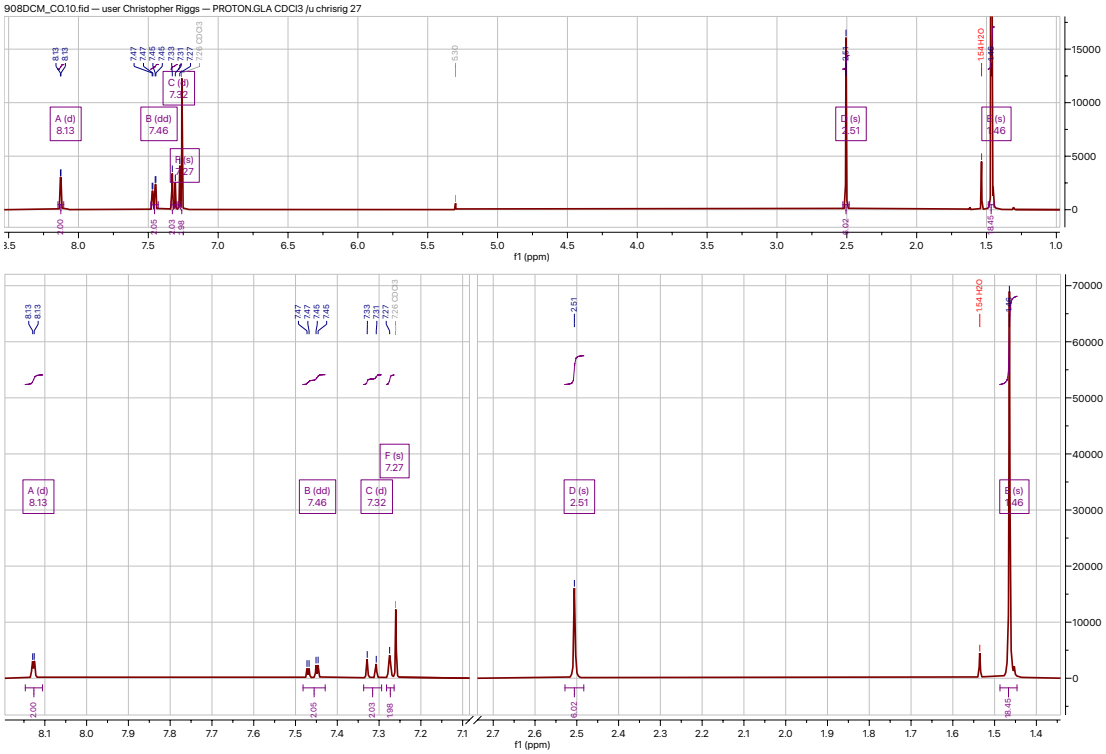
m/z	m/z (Calc)	Diff (ppm)	Abund	Height %	Height % (Calc)	Ion Species	z
566.3140	566.3128	2.10	4135	25.56	22.28	M+	1
567.3108	567.3099	1.54	16176	100.00	100.00	M+	1
568.3142	568.3129	2.26	7555	46.70	43.79	M+	1
569.3165	569.3161	0.78	2362	14.60	9.71	M+	1
137.1090			93215				

MassHunter Qual 10.0
(End of Report)

9.15 Chapter 5

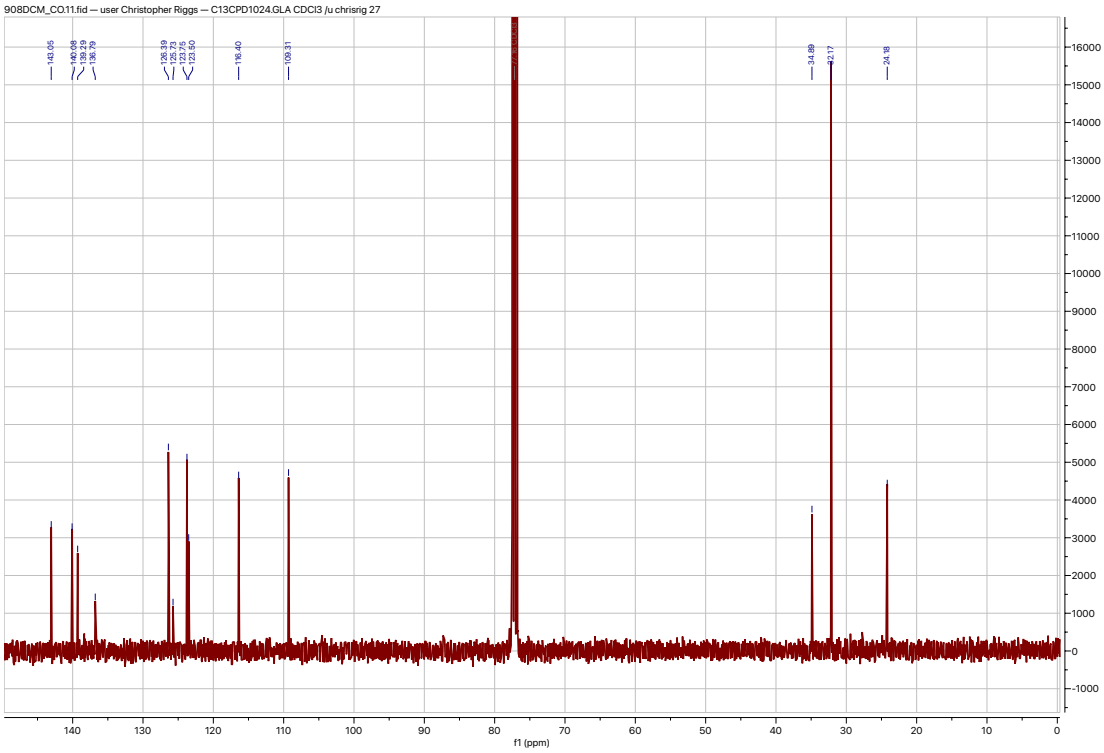
9.15.1 9-(4-bromo-3,5-dimethylphenyl)-9H-3,6-di-tert-butylcarbazole (5.3)

^{1}H NMR



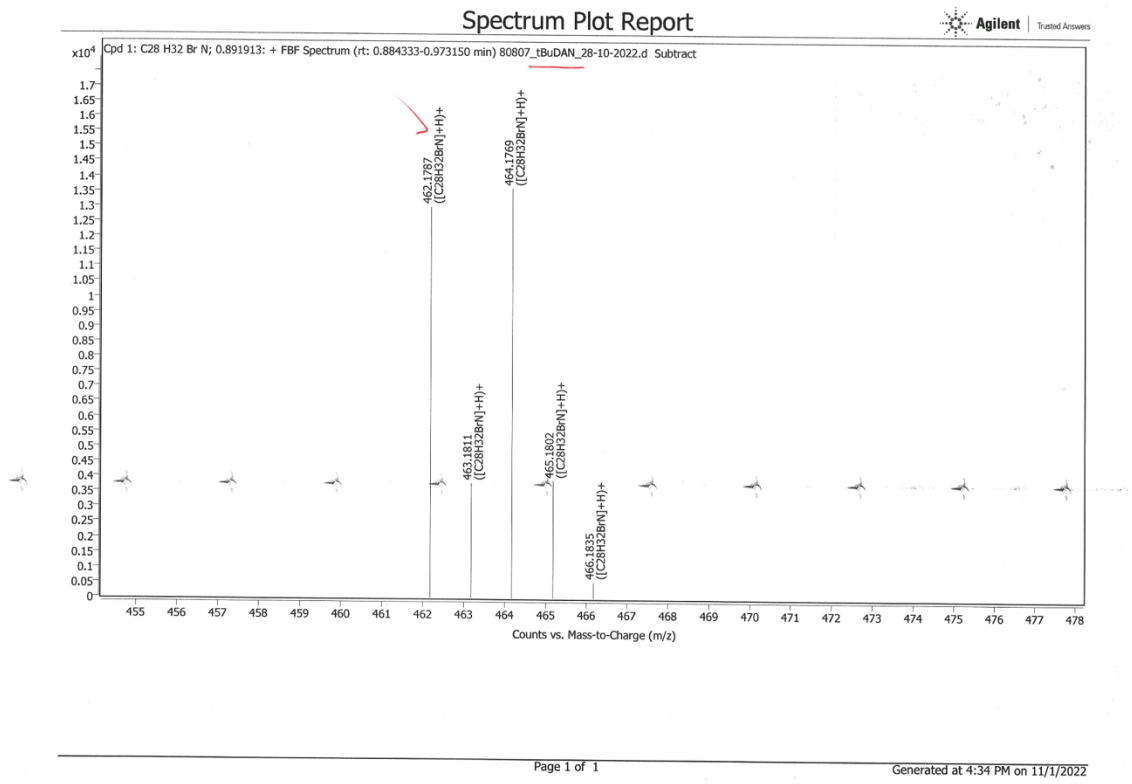
δ_H (400 MHz, $CDCl_3$) 8.13 (2 H, d, *J* 1.4), 7.46 (2 H, dd, *J* 8.7, 2.0), 7.32 (2 H, d, *J* 8.6), 7.27 (2 H, s), 2.51 (6 H, s), 1.46 (18 H, s).

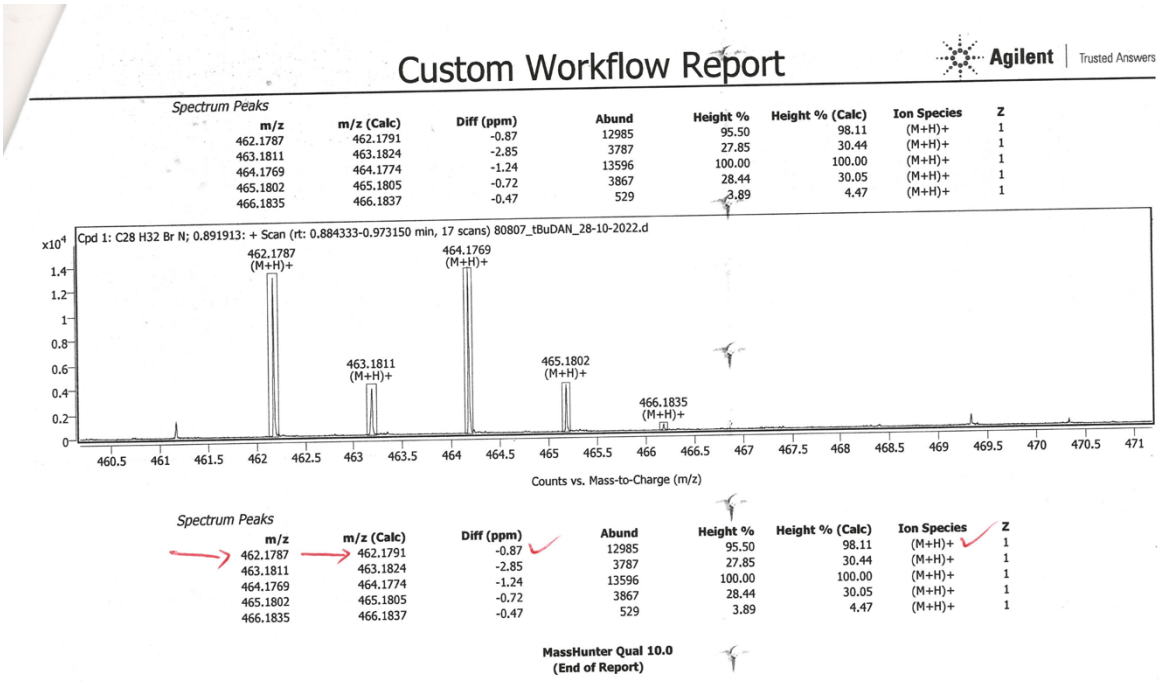
^{13}C NMR



δ_C (101 MHz, $CDCl_3$) 143.05, 140.08, 139.29, 136.79, 126.39, 125.73, 123.75, 123.50, 116.40, 109.31, 34.89, 32.17, 24.18.

MS

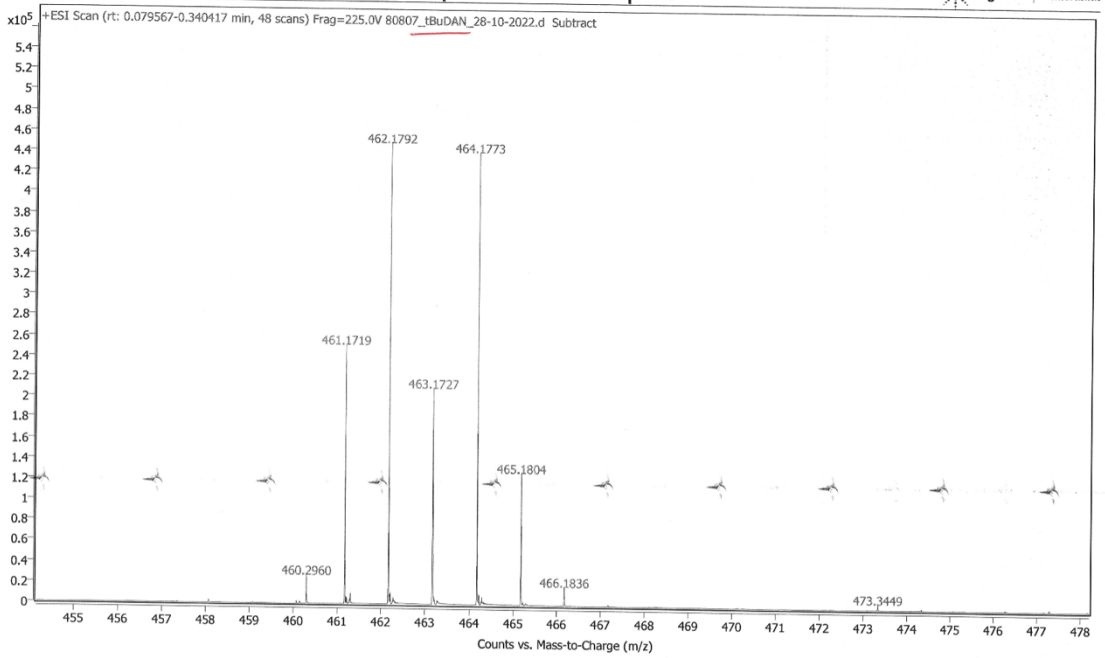

Spectrum Plot Report
Agilent | Trusted Answers
Cpd 1: C28 H32 Br N; 0.891913: + FBF Spectrum (rt: 0.884333-0.973150 min) 80807_tBuDAN_28-10-2022.d Subtract
462.1787 ((C28H32BrN)+H)+
464.1769 ((C28H32BrN)+H)+
463.1811 ((C28H32BrN)+H)+
465.1802 ((C28H32BrN)+H)+
466.1835 ((C28H32BrN)+H)+
Counts vs. Mass-to-Charge (m/z)
Page 1 of 1
Generated at 4:34 PM on 11/1/2022


Custom Workflow Report
Agilent | Trusted Answers
Spectrum Peaks
m/z | m/z (Calc) | Diff (ppm) | Abund | Height % | Height % (Calc) | Ion Species | z
462.1787 | 462.1791 | -0.87 | 12985 | 95.50 | 98.11 | (M+H)+ | 1
463.1811 | 463.1824 | -2.85 | 3787 | 27.85 | 30.44 | (M+H)+ | 1
464.1769 | 464.1774 | -1.24 | 13596 | 100.00 | 100.00 | (M+H)+ | 1
465.1802 | 465.1805 | -0.72 | 3867 | 28.44 | 30.05 | (M+H)+ | 1
466.1835 | 466.1837 | -0.47 | 529 | 3.89 | 4.47 | (M+H)+ | 1
Cpd 1: C28 H32 Br N; 0.891913: + Scan (rt: 0.884333-0.973150 min, 17 scans) 80807_tBuDAN_28-10-2022.d
462.1787 (M+H)+
464.1769 (M+H)+
463.1811 (M+H)+
465.1802 (M+H)+
466.1835 (M+H)+
Counts vs. Mass-to-Charge (m/z)
Spectrum Peaks
m/z | m/z (Calc) | Diff (ppm) | Abund | Height % | Height % (Calc) | Ion Species | z
462.1787 | 462.1791 | -0.87 | 12985 | 95.50 | 98.11 | (M+H)+ | 1
463.1811 | 463.1824 | -2.85 | 3787 | 27.85 | 30.44 | (M+H)+ | 1
464.1769 | 464.1774 | -1.24 | 13596 | 100.00 | 100.00 | (M+H)+ | 1
465.1802 | 465.1805 | -0.72 | 3867 | 28.44 | 30.05 | (M+H)+ | 1
466.1835 | 466.1837 | -0.47 | 529 | 3.89 | 4.47 | (M+H)+ | 1
MassHunter Qual 10.0
(End of Report)

Zoomed

Spectrum Plot Report

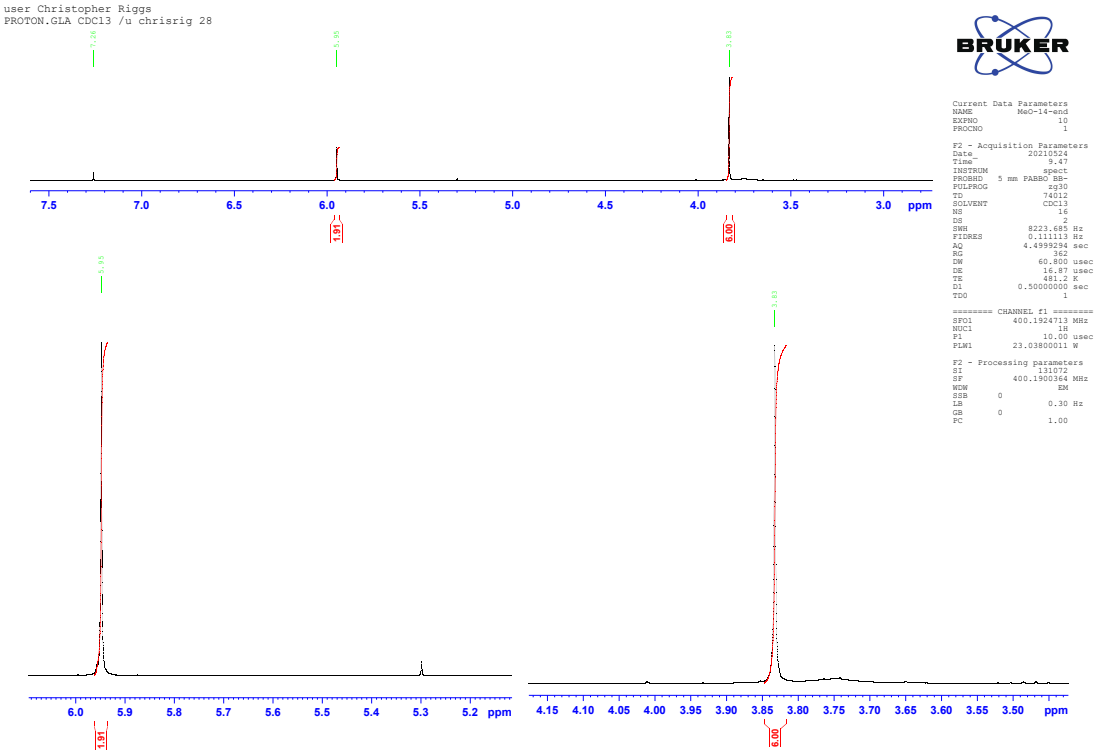
Agilent | Trusted Answers



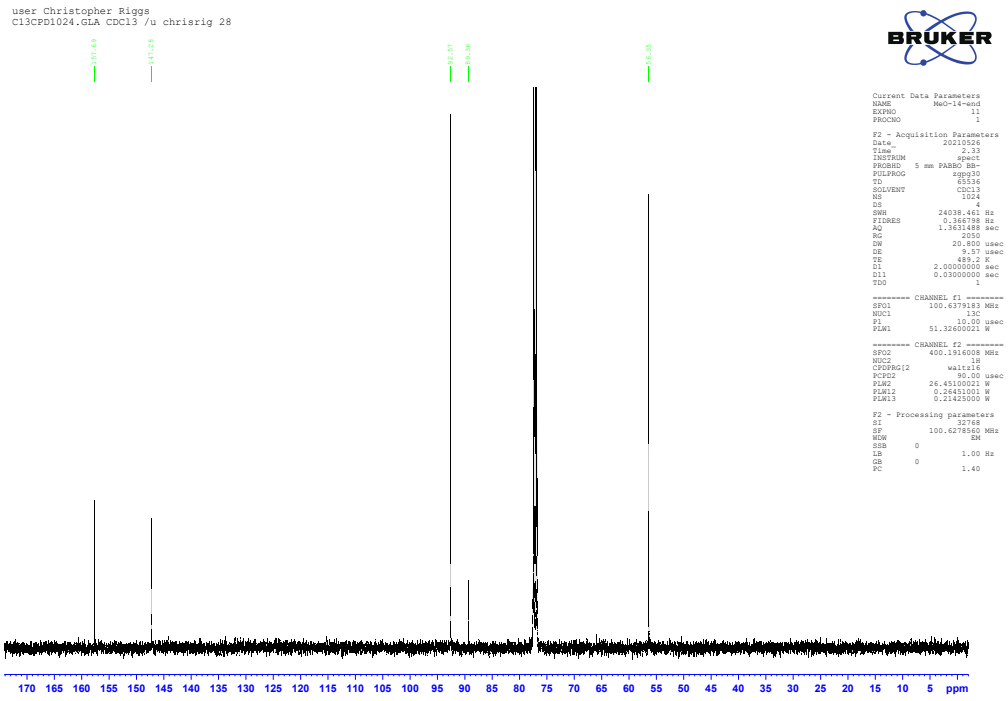
Generated at 4:35 PM on 11/1/2022

9.15.2 4-bromo-3,5-dimethoxyaniline (5.5)

^{1}H NMR



^{13}C NMR


user Christopher Riggs
C13CPD1024.GLA CDC13 /u chrisrig 28
157.69
147.28
82.57
79.36
56.35
BRUKER
Current Data Parameters
NAME MeO-14-end
EXPNO 11
PROCNO 1
F2 - Acquisition Parameters
Date 20210526
Time 2.33
INSTRUM spect
PROBHD 5 mm PABBO BB-
PULPROG zgpg30
TD 65536
SOLVENT CDCl3
NS 1024
DS 4
SWH 24038.461 Hz
FIDRES 0.366798 Hz
AQ 1.3631488 sec
RG 2050
DW 20.800 usec
DE 9.57 usec
TE 489.2 K
D1 2.00000000 sec
D11 0.03000000 sec
TD0 1
======== CHANNEL f1 ========
SFO1 100.6379183 MHz
NUC1 13C
P1 10.00 usec
PLW1 51.32600021 W
======== CHANNEL f2 ========
SFO2 400.1916008 MHz
NUC2 1H
CPDPRG[2 waltz16
PCPD2 90.00 usec
PLW2 26.45100021 W
PLW12 0.26451001 W
PLW13 0.21425000 W
F2 - Processing parameters
SI 32768
SF 100.6278560 MHz
WDW EM
SSB 0
LB 1.00 Hz
GB 0
PC 1.40
170 165 160 155 150 145 140 135 130 125 120 115 110 105 100 95 90 85 80 75 70 65 60 55 50 45 40 35 30 25 20 15 10 5 ppm

MS

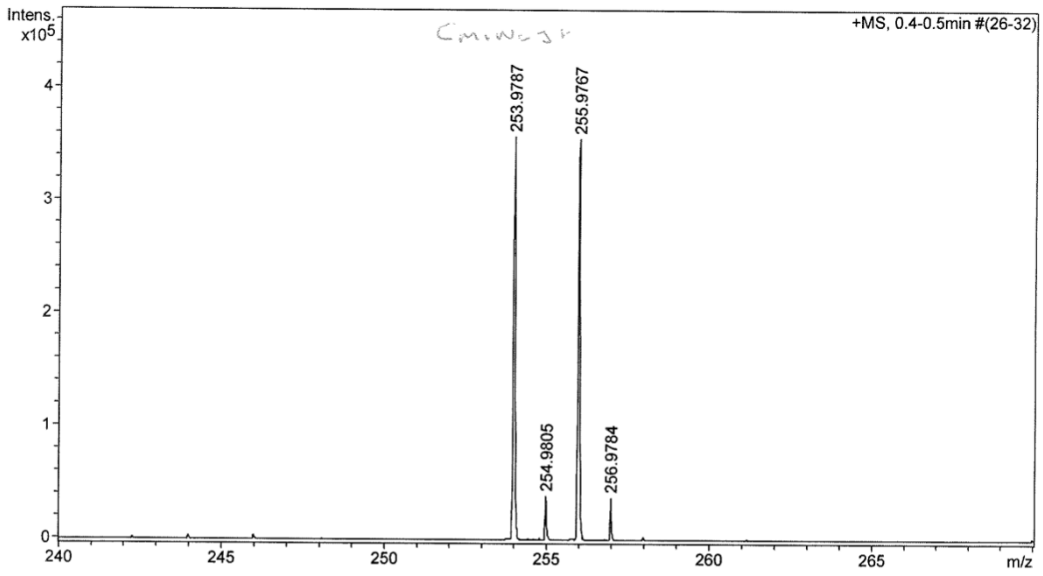
Mass Spectrum SmartFormula Report

Analysis Info

Analysis Name	D:\Data\Mass Spectrometry Service\77990-000003.d	Acquisition Date	7/5/2021 8:29:12 AM
Method	SM MS 50 to 600.m	Operator	user
Sample Name	Riggs-no name	Instrument / Ser#	micrOTOF-Q 74
Comment			

Acquisition Parameter

Source Type	ESI	Ion Polarity	Positive
Scan Begin	50 m/z		
Scan End	600 m/z		



Formula	z	m/z	Meas. m/z	err [ppm]	err [mDa]
	1+		253.9787		
C 8 H 10 N Na O 2 ^79Br		253.9787		-0.1	-0.0

FUTURE SAMPLES MUST HAVE A SAMPLE NAME + ARE SUPPLIED IN SCREW TOP VIALS

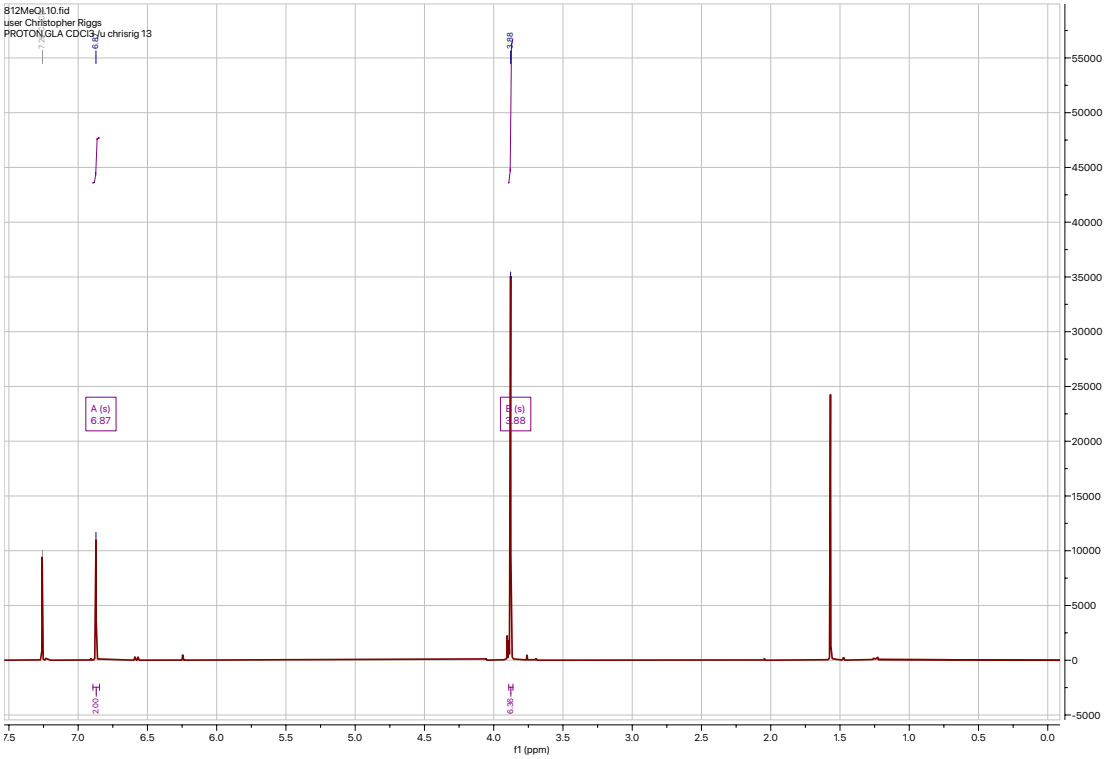
THANKS

Bruker Compass DataAnalysis 4.0 printed: 7/5/2021 8:34:27 AM Page 1 of 1

Accurate Mass

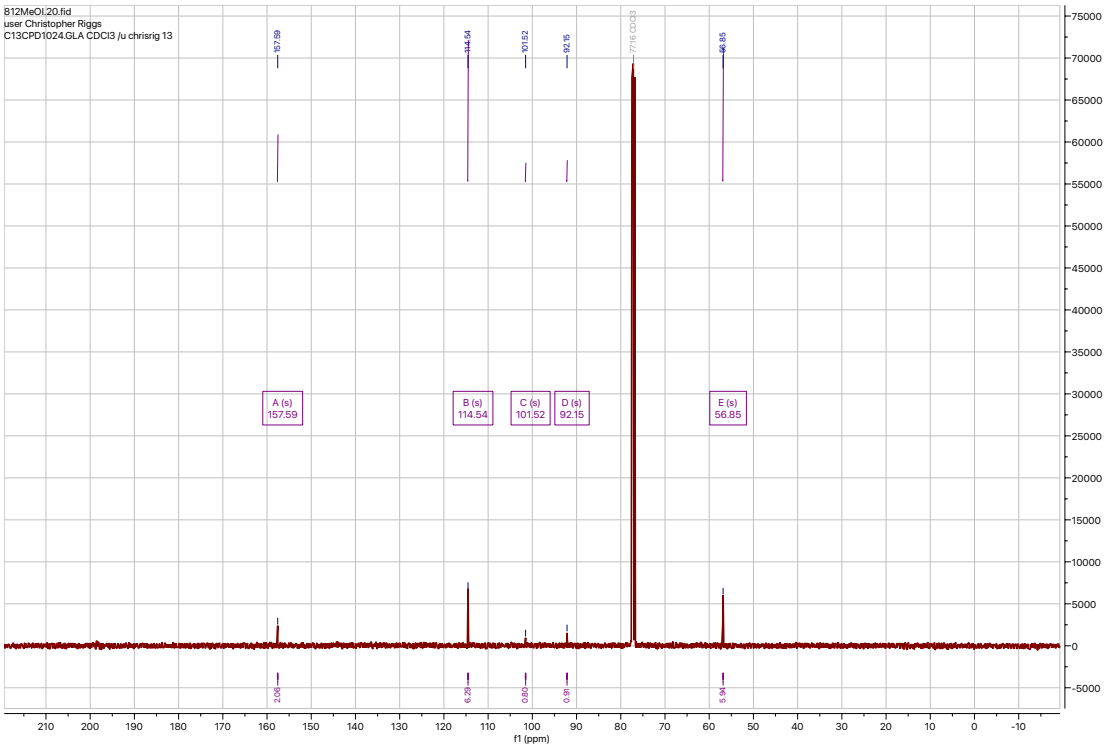
9.15.3 2-bromo-5-iodo-1,3-dimethoxybenzene (5.6)

^{1}H NMR



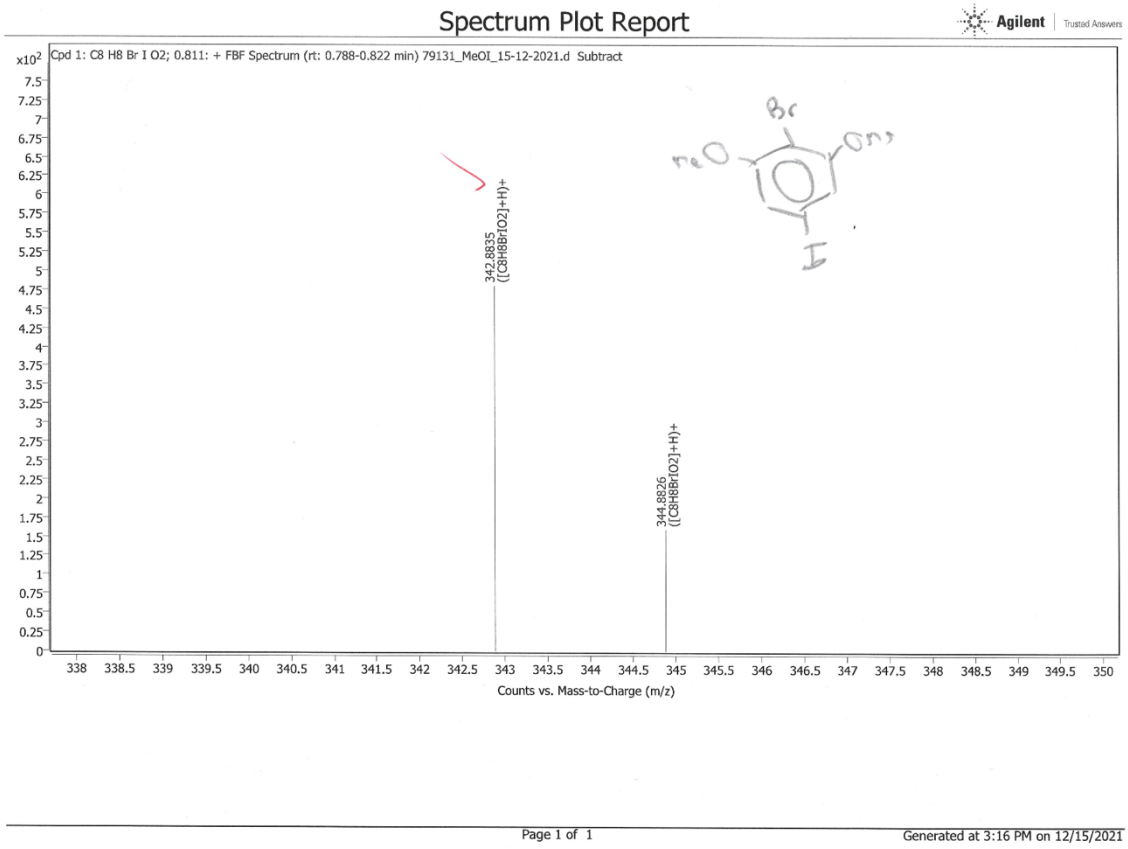
δ_H (400 MHz, $CDCl_3$) 6.87 (2 H, s), 3.88 (6 H, s).

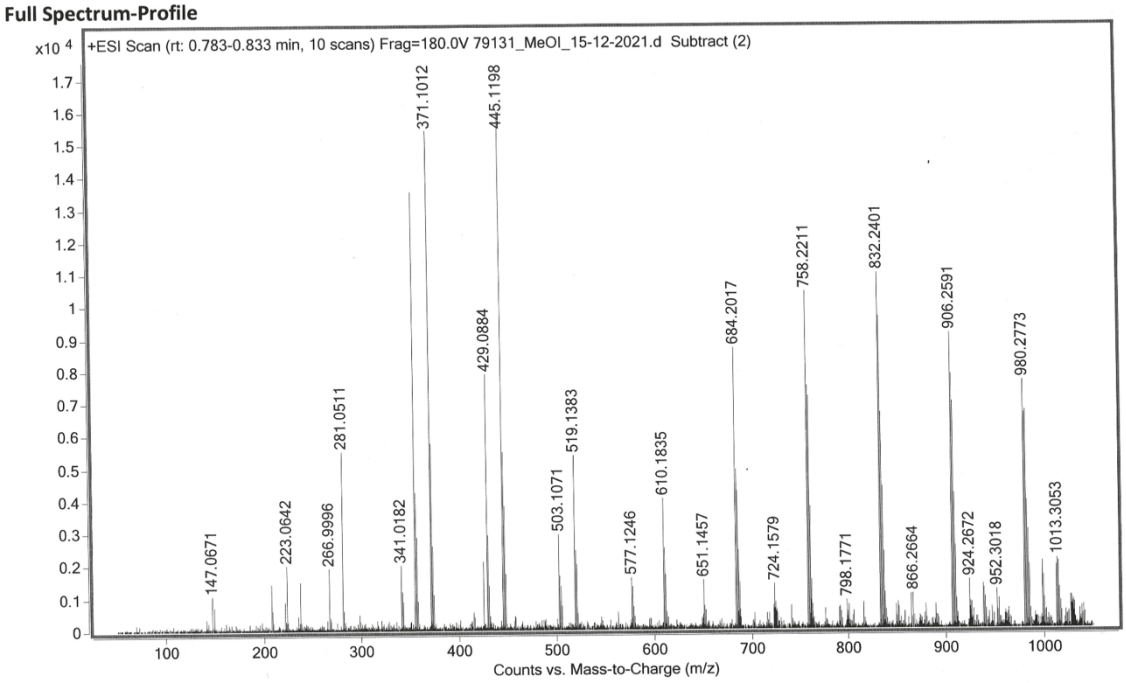
^{13}C NMR



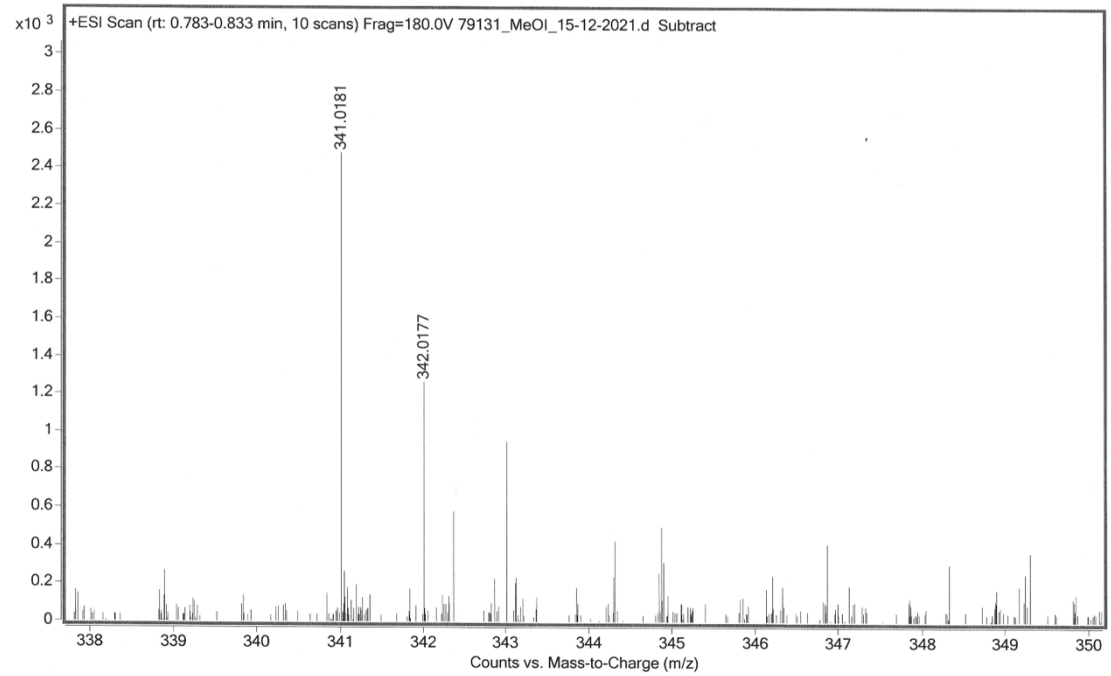
δ_C (101 MHz, $CDCl_3$) 157.59, 114.54, 101.52, 92.15, 56.85.

MS


Spectrum Plot Report
Agilent
Trusted Answers
Cpd 1: C8 H8 Br I O2; 0.811: + FBF Spectrum (rt: 0.788-0.822 min) 79131_MeOI_15-12-2021.d Subtract
x10²
342.8835
([C8H8BrIO2]+H)+
344.8826
([C8H8BrIO2]+H)+
Counts vs. Mass-to-Charge (m/z)
Page 1 of 1
Generated at 3:16 PM on 12/15/2021


Full Spectrum-Profile
+ESI Scan (rt: 0.783-0.833 min, 10 scans) Frag=180.0V 79131_MeOI_15-12-2021.d Subtract (2)
x10 4
147.0671
223.0642
266.9996
281.0511
341.0182
371.1012
429.0884
445.1198
503.1071
519.1383
577.1246
610.1835
651.1457
684.2017
724.1579
758.2211
798.1771
832.2401
866.2664
906.2591
924.2672
952.3018
980.2773
1013.3053
Counts vs. Mass-to-Charge (m/z)

Zoomed IN Spectra

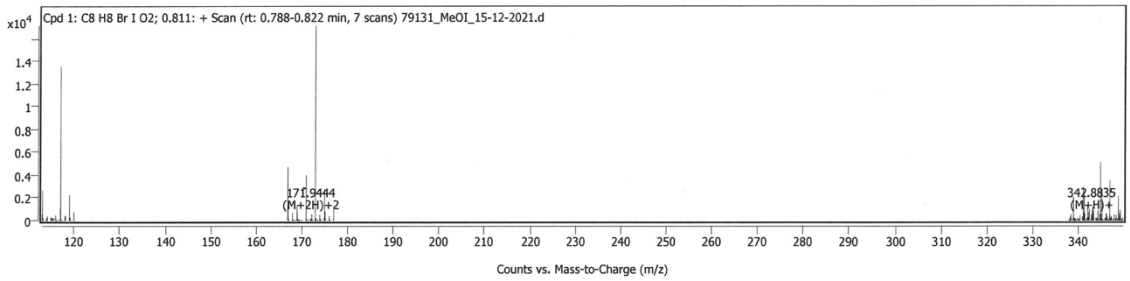


Custom Workflow Report

Agilent | Trusted Answers

Spectrum Peaks

m/z	m/z (Calc)	Diff (ppm)	Abund	Height %	Height % (Calc)	Ion Species	Z
114.9642	114.9657	-12.98	117	100.00	100.00	(M+3H)+3	3
171.9444	171.9449	-3.04	55	100.00	100.00	(M+2H)+2	2
342.8835	342.8825	2.94	480	100.00	100.00	(M+H)+	1
344.8826	344.8805	6.02	159	33.10	98.03	(M+H)+	1



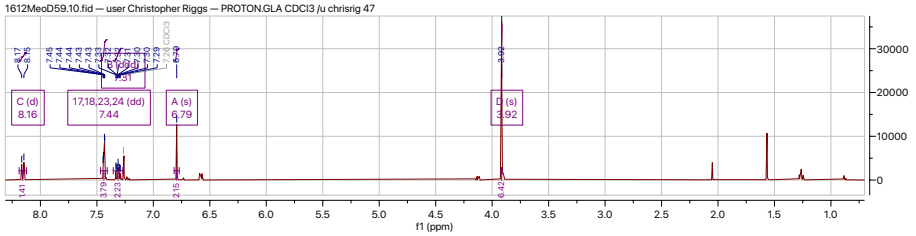
Spectrum Peaks

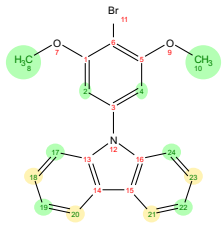
m/z	m/z (Calc)	Diff (ppm)	Abund	Height %	Height % (Calc)	Ion Species	Z
114.9642	114.9657	-12.98	117	100.00	100.00	(M+3H)+3	3
171.9444	171.9449	-3.04	55	100.00	100.00	(M+2H)+2	2
342.8835	342.8825	2.94	480	100.00	100.00	(M+H)+	1
344.8826	344.8805	6.02	159	33.10	98.03	(M+H)+	1

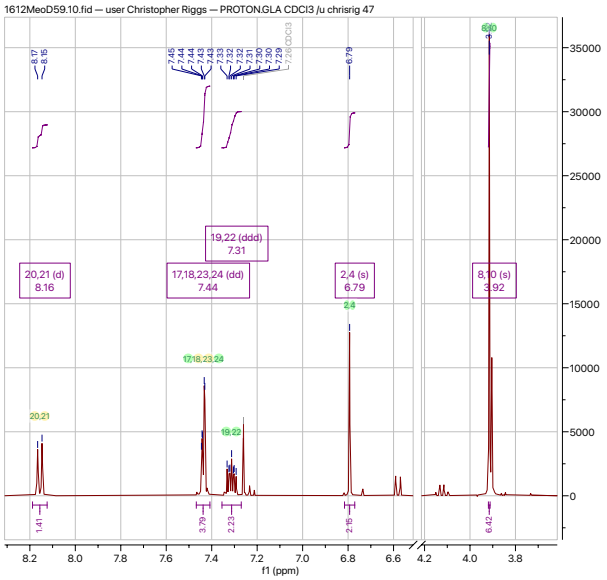
MassHunter Qual 10.0
(End of Report)

9.15.4 9-(4-bromo-3,5-dimethoxyphenyl)-9H-carbazole (5.8)

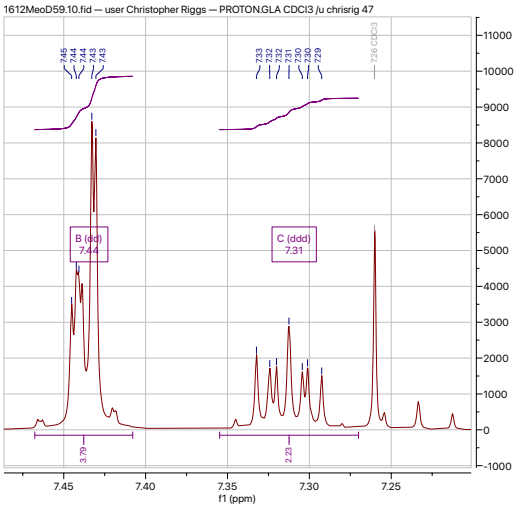
^{1}H NMR



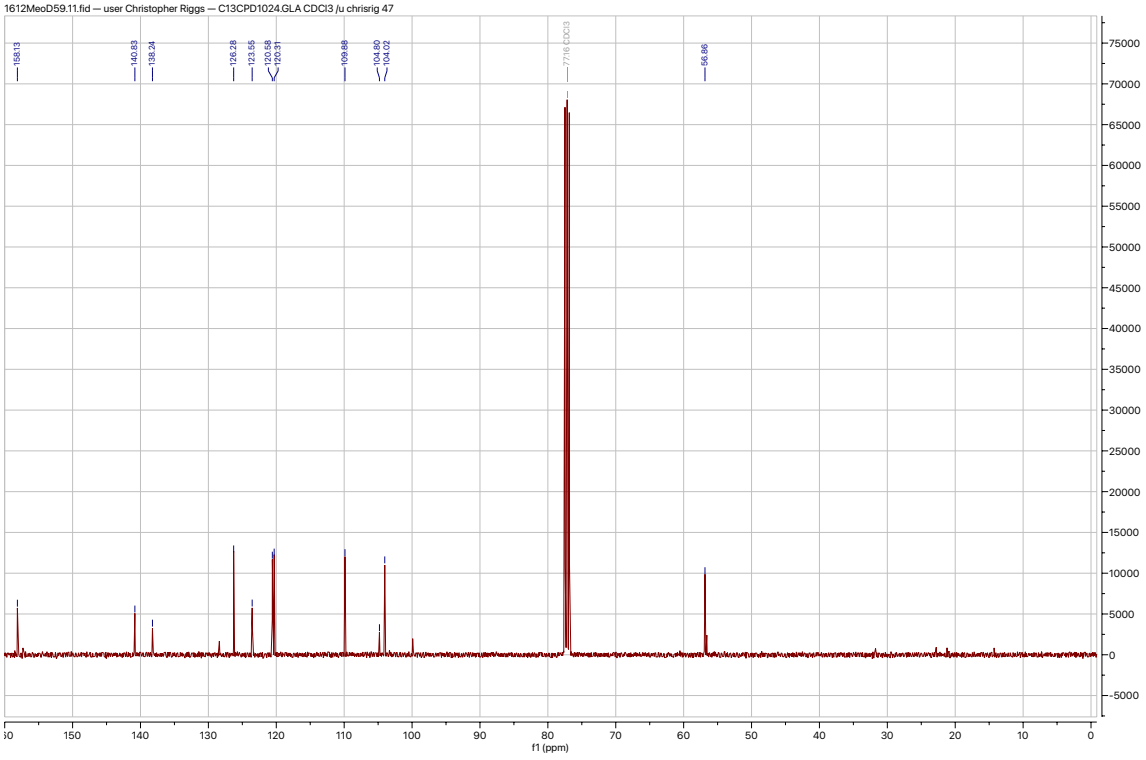




δ_H (400 MHz, $CDCl_3$) 8.16 (2 H, d, *J* 7.7), 7.47 – 7.41 (4 H, m), 7.35 – 7.27 (2 H, m), 6.79 (2 H, s), 3.92 (6 H, s).

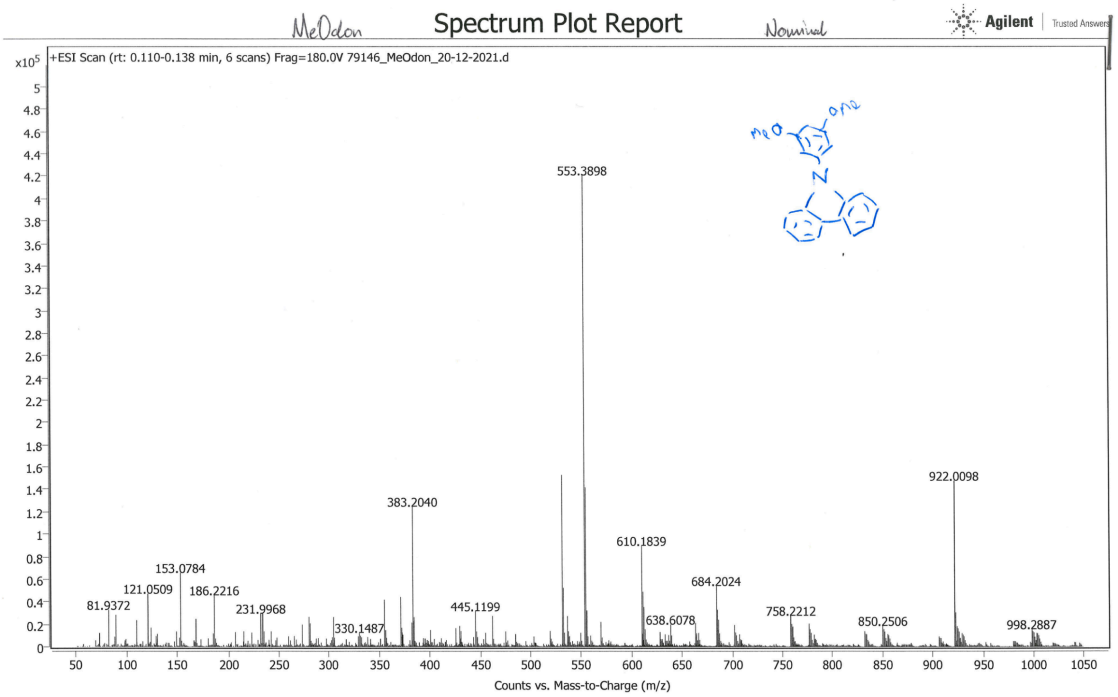


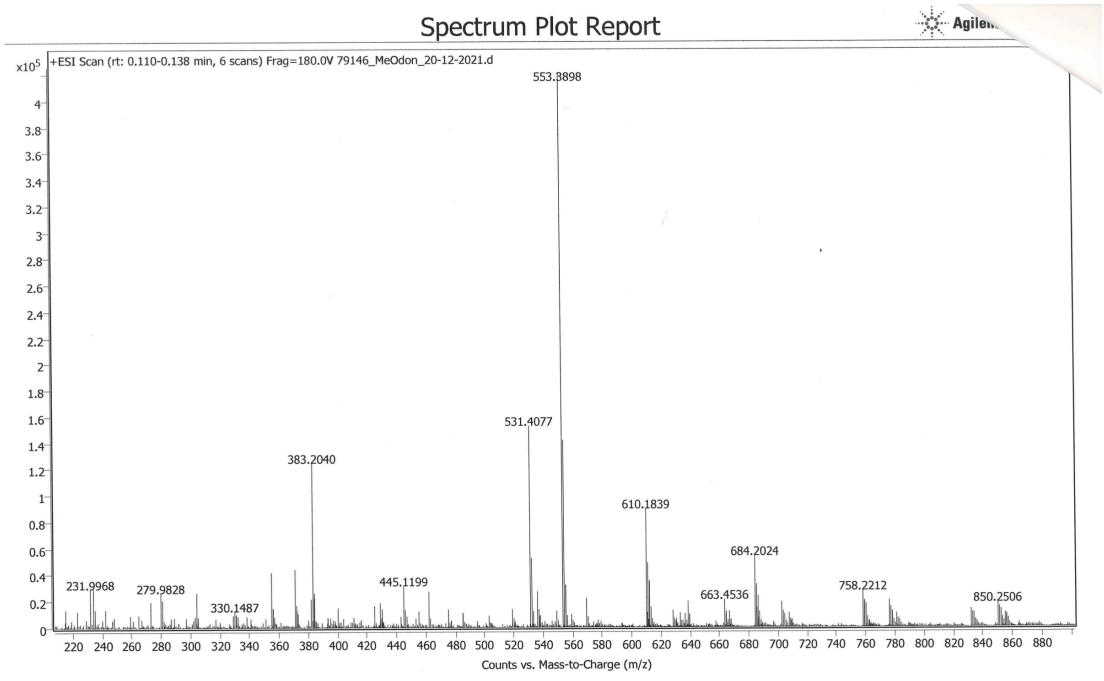
^{13}C NMR



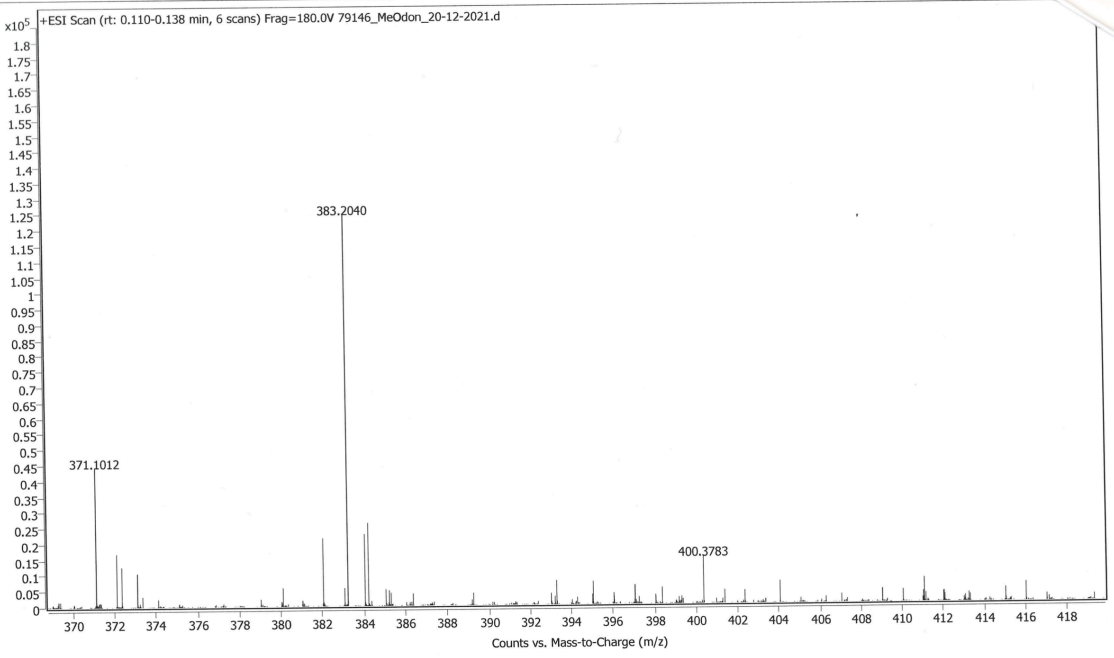
^{13}C NMR (101 MHz, $CDCl_3$) δ 158.13, 140.83, 138.24, 126.28, 123.55, 120.58, 120.31, 109.88, 104.80, 104.02, 56.86.

MS


MeOdon
Spectrum Plot Report
Nominal
Agilent
Trusted Answers
x10^5
+ESI Scan (rt: 0.110-0.138 min, 6 scans) Frag=180.0V 79146_MeOdon_20-12-2021.d
553.3898
922.0098
383.2040
610.1839
153.0784
684.2024
121.0509
186.2216
81.9372
231.9968
445.1199
758.2212
638.6078
850.2506
330.1487
998.2887
Counts vs. Mass-to-Charge (m/z)
Page 1 of 1
Generated at 1:02 PM on 12/20/2021


Spectrum Plot Report
Agilent
x10^5
+ESI Scan (rt: 0.110-0.138 min, 6 scans) Frag=180.0V 79146_MeOdon_20-12-2021.d
553.3898
531.4077
383.2040
610.1839
684.2024
231.9968
279.9828
445.1199
663.4536
758.2212
850.2506
330.1487
Counts vs. Mass-to-Charge (m/z)
Page 1 of 1
Generated at 1:02 PM on 12/20/2021

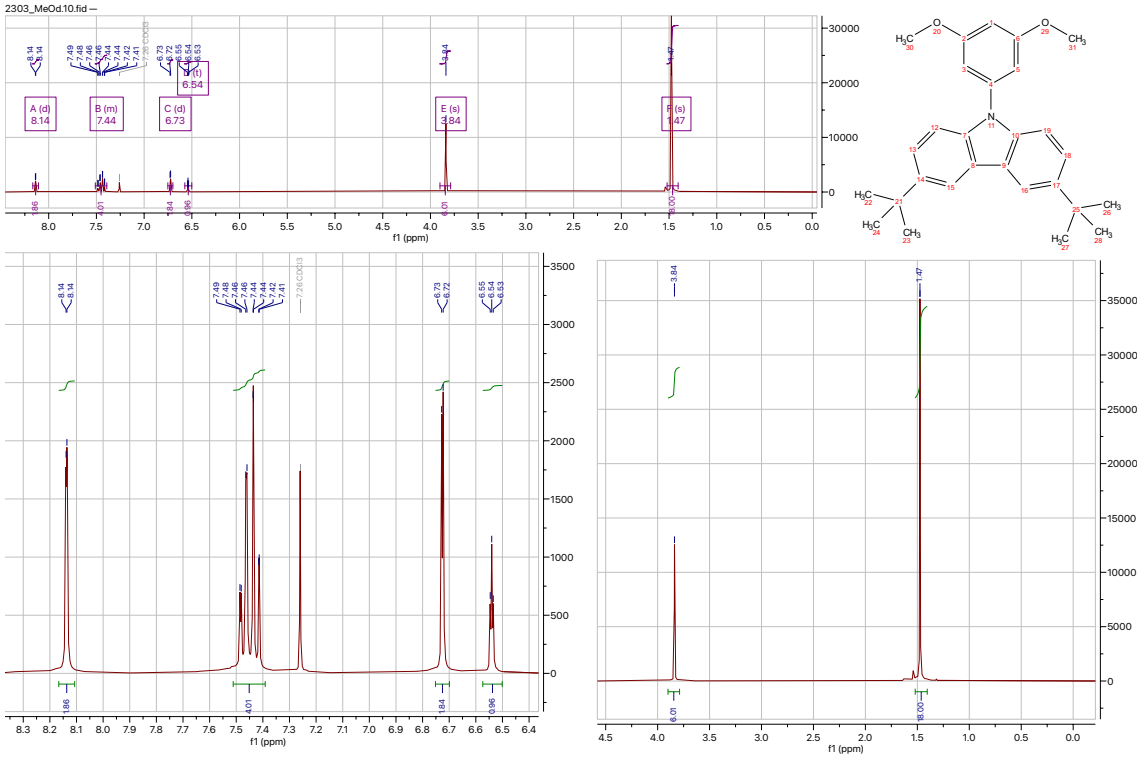
Spectrum Plot Report



Generated at 1:03 PM on 12/20/2021

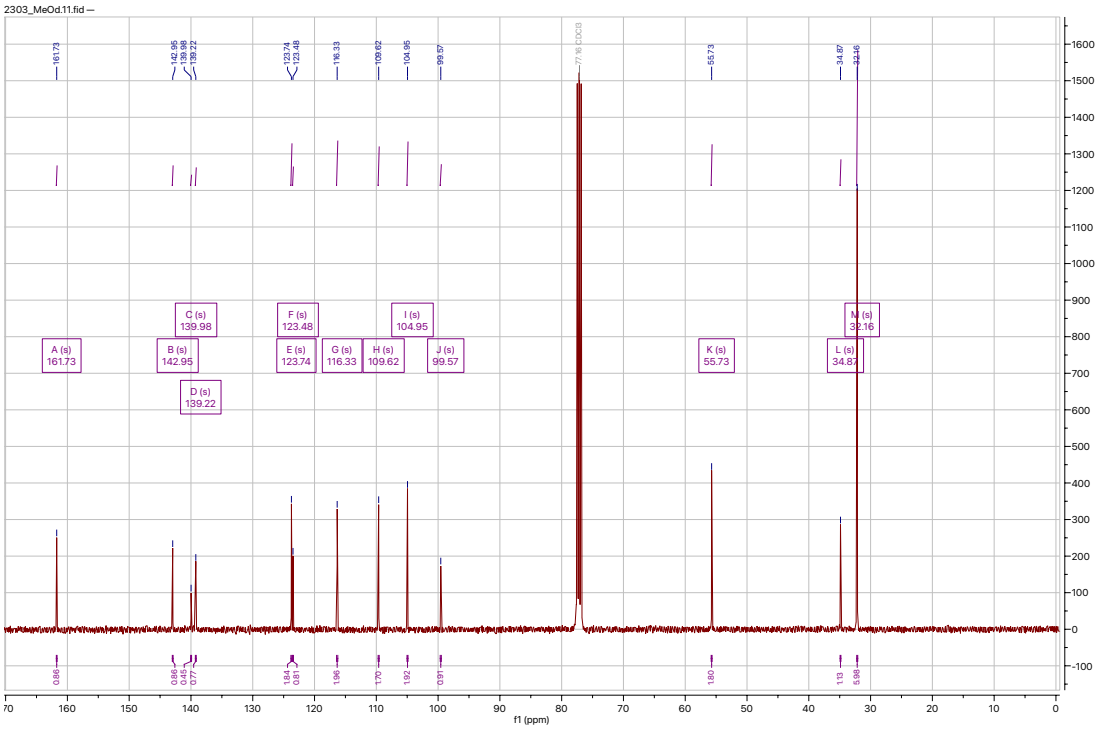
9.15.5 9-(1,3-dimethoxyphenyl)-9H-3,6-di-tert-butyl-carbazole (5.10)

^{1}H NMR



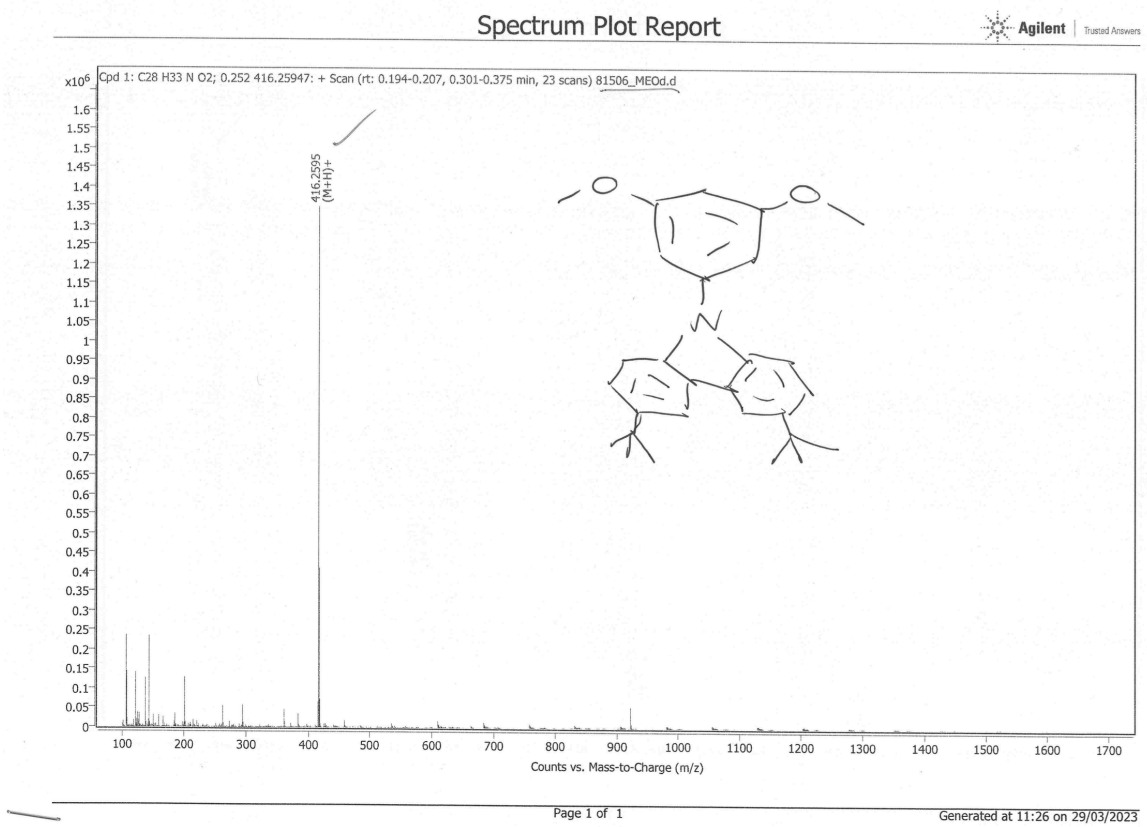
δ_H (400 MHz, $CDCl_3$) 8.14 (2 H, d, *J* 1.2), 7.51 – 7.39 (4 H, m), 6.73 (2 H, d, *J* 2.3), 6.54 (1 H, t, *J* 2.3), 3.84 (6 H, s), 1.47 (18 H, s).

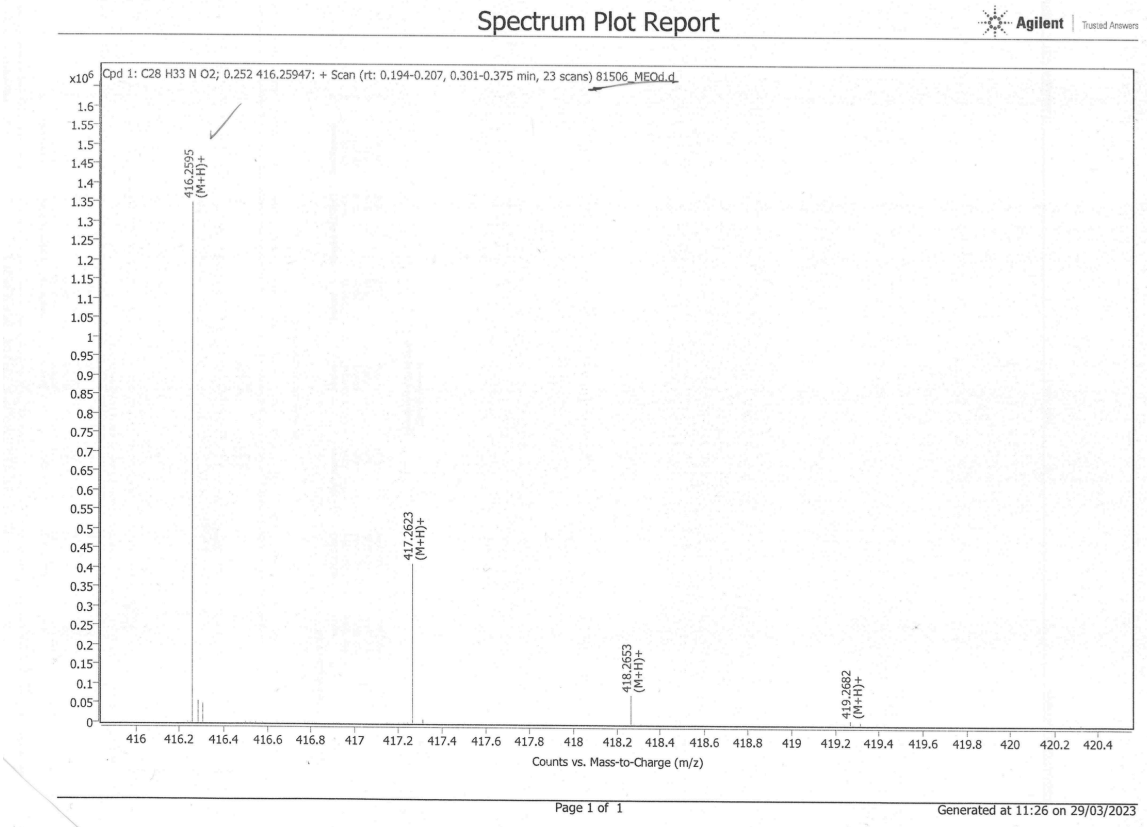
^{13}C NMR



δ_C (101 MHz, $CDCl_3$) 161.73, 142.95, 139.98, 139.22, 123.74, 123.48, 116.33, 109.62, 104.95, 99.57, 55.73, 34.87, 32.16.

MS


Spectrum Plot Report
Agilent | Trusted Answers
Cpd 1: C28 H33 N O2; 0.252 416.25947: + Scan (rt: 0.194-0.207, 0.301-0.375 min, 23 scans) 81506_MEOd.d
x10^6
416.2595 (M+H)+
Counts vs. Mass-to-Charge (m/z)
Page 1 of 1
Generated at 11:26 on 29/03/2023


Spectrum Plot Report
Agilent | Trusted Answers
Cpd 1: C28 H33 N O2; 0.252 416.25947: + Scan (rt: 0.194-0.207, 0.301-0.375 min, 23 scans) 81506_MEOd.d
x10^6
416.2595 (M+H)+
417.2623 (M+H)+
418.2653 (M+H)+
419.2682 (M+H)+
Counts vs. Mass-to-Charge (m/z)
Page 1 of 1
Generated at 11:26 on 29/03/2023

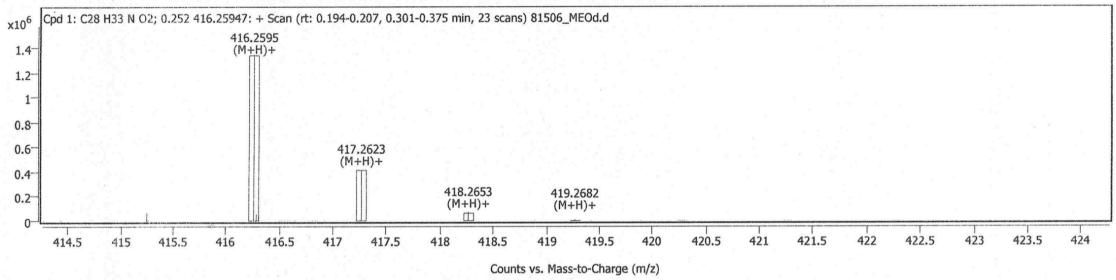
tel:419.2682

Custom Workflow Report

Agilent | Trusted Answers

Spectrum Peaks

m/z	m/z (Calc)	Diff (ppm)	Abund	Height %	Height % (Calc)	Ion Species	z
416.2595	416.2584	2.56	1348916	100.00	100.00	(M+H)+	1
417.2623	417.2617	1.44	411379	30.50	31.12	(M+H)+	1
418.2653	418.2649	1.01	73962	5.48	5.09	(M+H)+	1
419.2682	419.2678	0.99	9728	0.72	0.58	(M+H)+	1



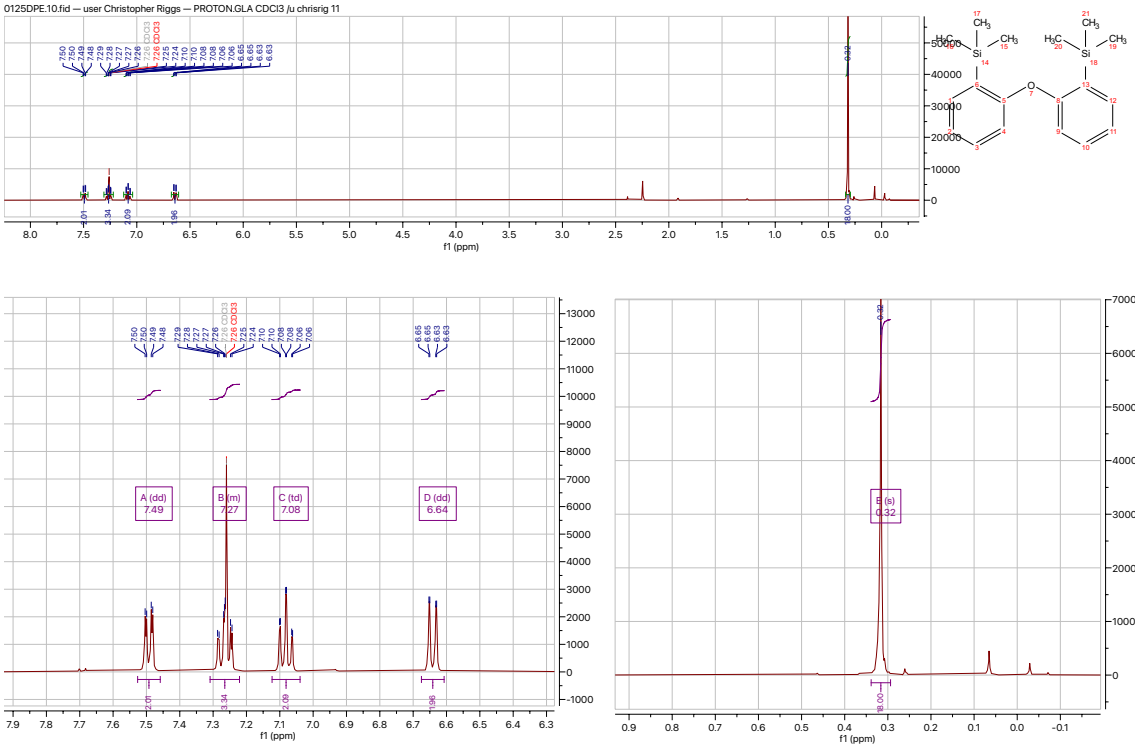
Spectrum Peaks

m/z	m/z (Calc)	Diff (ppm)	Abund	Height %	Height % (Calc)	Ion Species	z
416.2595	416.2584	2.56	1348916	100.00	100.00	(M+H)+	1
417.2623	417.2617	1.44	411379	30.50	31.12	(M+H)+	1
418.2653	418.2649	1.01	73962	5.48	5.09	(M+H)+	1
419.2682	419.2678	0.99	9728	0.72	0.58	(M+H)+	1

MassHunter Qual 10.0
(End of Report)

9.15.6 Bis-(2-trimethylsilylphenyl)ether (5.12)

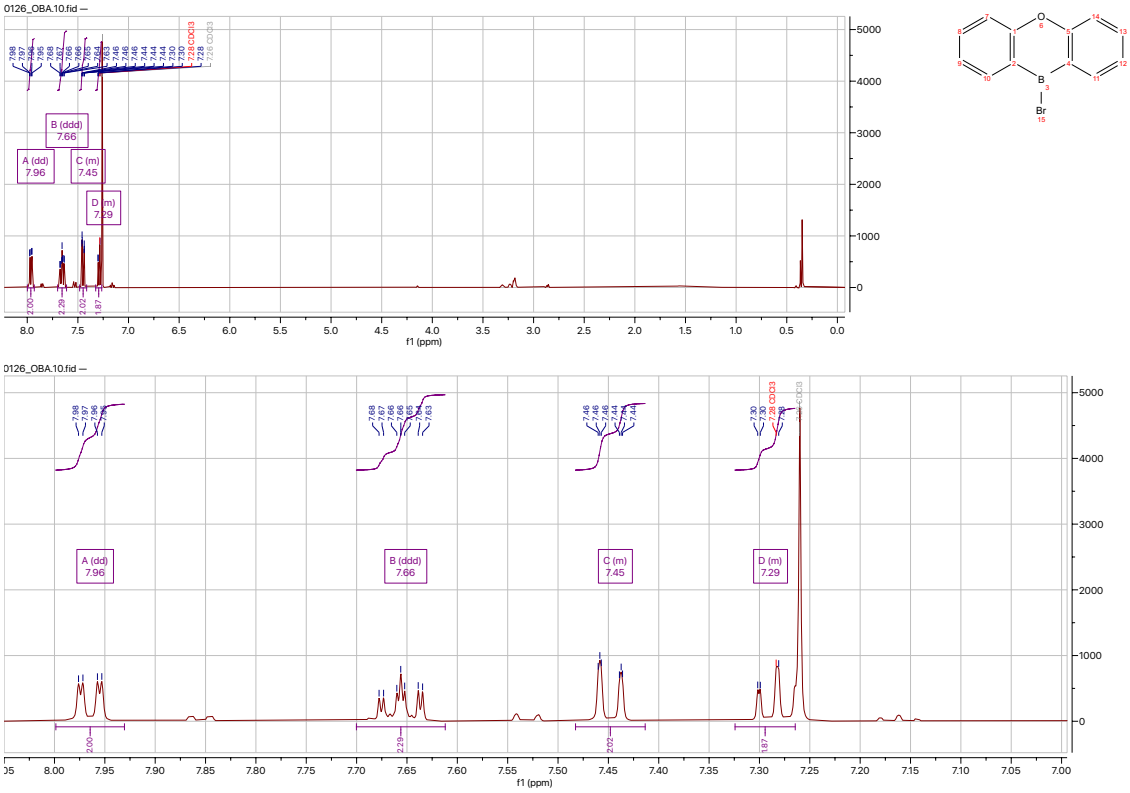
^{1}H NMR



δ_H (400 MHz, $CDCl_3$) 7.49 (2 H, dd, *J* 7.3, 1.8), 7.31 – 7.22 (2 H, m), 7.08 (2 H, td, *J* 7.3, 1.0), 6.64 (2 H, dd, *J* 8.2, 1.0), 0.32 (18 H, s).

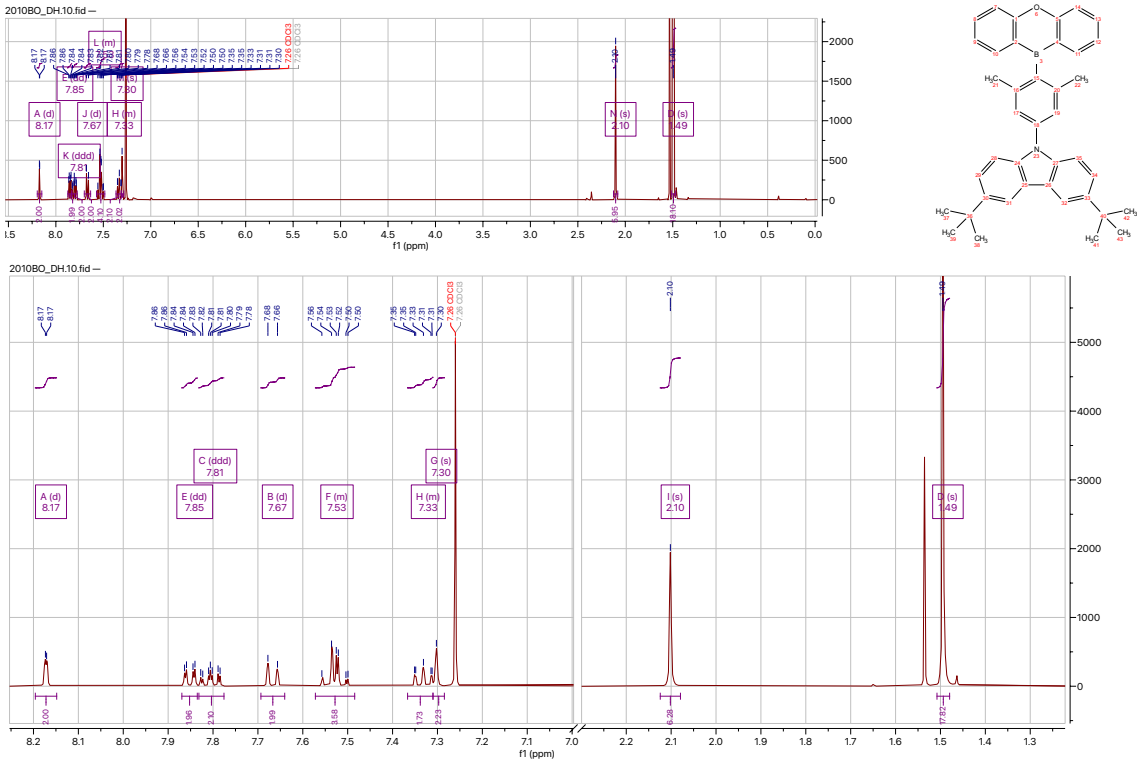
9.15.7 10-bromo-10H-dibenzo[b,e][1,4]oxaborinine (5.13)

^{1}H NMR



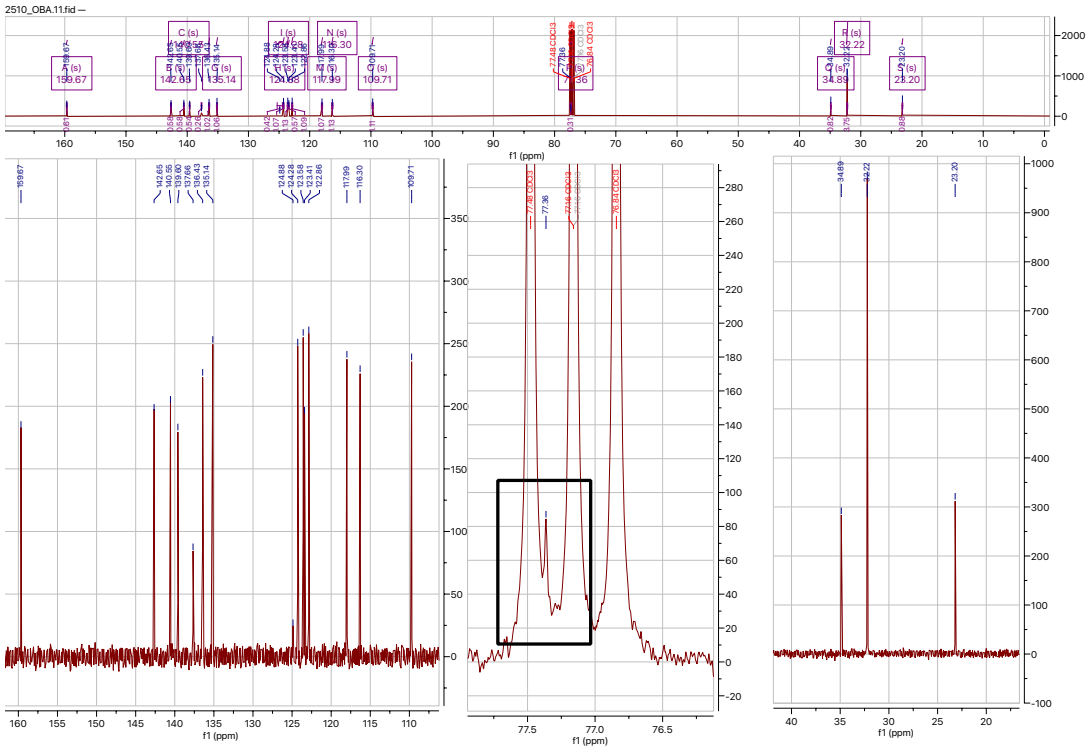
9.15.8 tBu-DMP-Cz-OBA (10)

^{1}H NMR



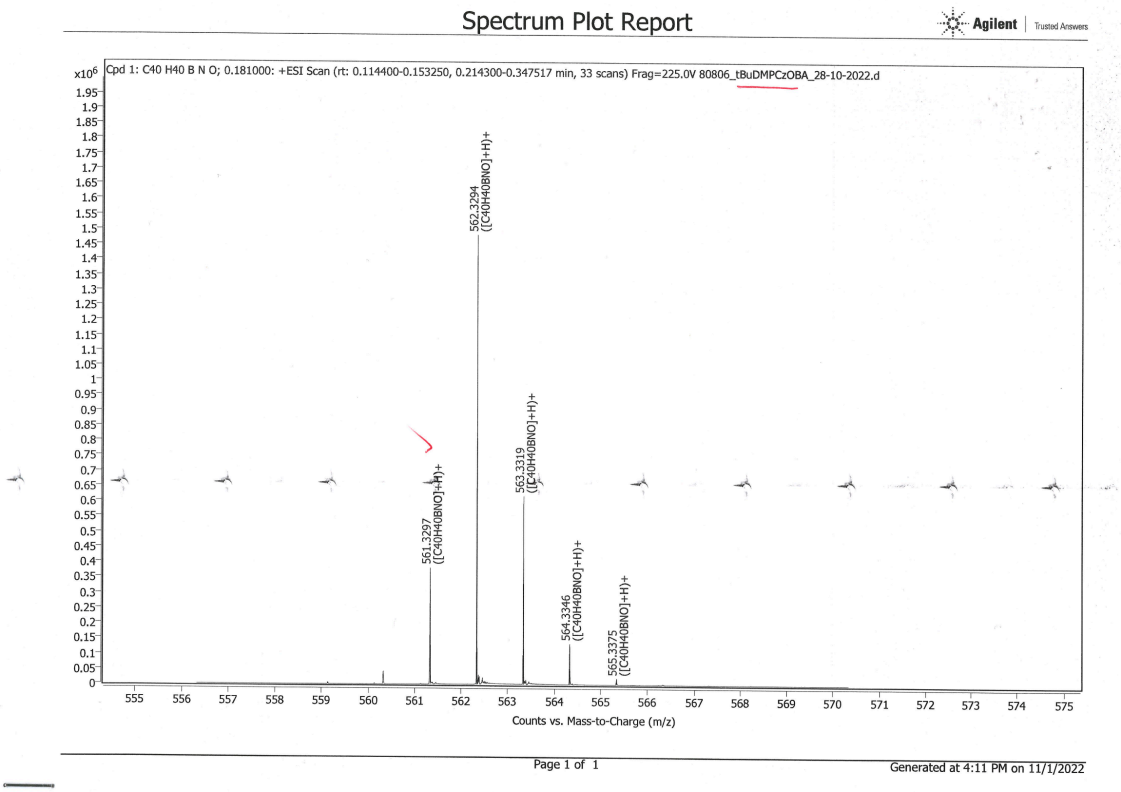
^{1}H (400 MHz, $CDCl_3$) 8.17 (2 H, d, *J* 1.0), 7.85 (2 H, dd, *J* 7.5, 1.8), 7.81 (2 H, ddd, *J* 8.7, 7.0, 1.8), 7.67 (2 H, d, *J* 8.6), 7.57 – 7.48 (4 H, m), 7.37 – 7.31 (2 H, m), 7.30 (2 H, s), 2.10 (6 H, s), 1.49 (18 H, s).

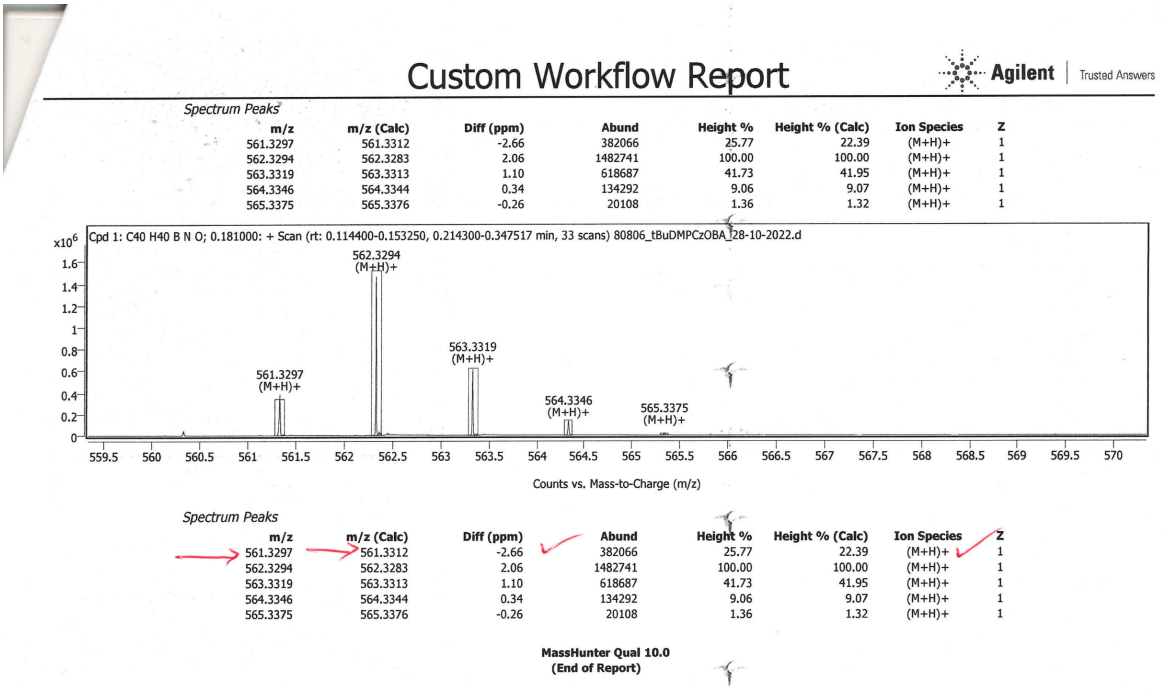
^{13}C NMR



δ_C (101 MHz, $CDCl_3$) 159.67, 142.65, 140.55, 139.60, 137.66, 136.43, 135.14, 124.88, 124.28, 123.58, 123.41, 122.86, 117.99, 116.30, 109.71, 77.36, 34.89, 32.22, 23.20.

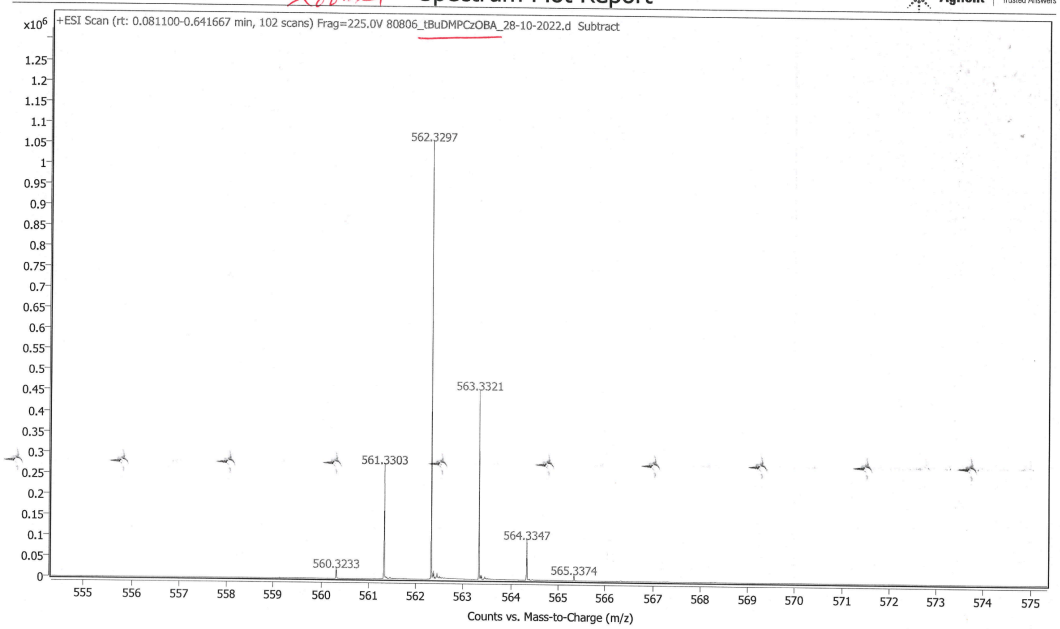
MS


Spectrum Plot Report
Agilent | Trusted Answers
Cpd 1: C40 H40 B N O; 0.181000: +ESI Scan (rt: 0.114400-0.153250, 0.214300-0.347517 min, 33 scans) Frag=225.0V 80806_tBuDMPCzOBA_28-10-2022.d
x10^6
562.3294 ([C40H40BNO]+H)+
563.3319 ([C40H40BNO]+H)+
561.3297 ([C40H40BNO]+H)+
564.3346 ([C40H40BNO]+H)+
565.3375 ([C40H40BNO]+H)+
Counts vs. Mass-to-Charge (m/z)
Page 1 of 1
Generated at 4:11 PM on 11/1/2022


Custom Workflow Report
Agilent | Trusted Answers
Spectrum Peaks
m/z | m/z (Calc) | Diff (ppm) | Abund | Height % | Height % (Calc) | Ion Species | Z
561.3297 | 561.3312 | -2.66 | 382066 | 25.77 | 22.39 | (M+H)+ | 1
562.3294 | 562.3283 | 2.06 | 1482741 | 100.00 | 100.00 | (M+H)+ | 1
563.3319 | 563.3313 | 1.10 | 618687 | 41.73 | 41.95 | (M+H)+ | 1
564.3346 | 564.3344 | 0.34 | 134292 | 9.06 | 9.07 | (M+H)+ | 1
565.3375 | 565.3376 | -0.26 | 20108 | 1.36 | 1.32 | (M+H)+ | 1
Cpd 1: C40 H40 B N O; 0.181000: + Scan (rt: 0.114400-0.153250, 0.214300-0.347517 min, 33 scans) 80806_tBuDMPCzOBA_28-10-2022.d
x10^6
562.3294 (M+H)+
563.3319 (M+H)+
561.3297 (M+H)+
564.3346 (M+H)+
565.3375 (M+H)+
Counts vs. Mass-to-Charge (m/z)
Spectrum Peaks
m/z | m/z (Calc) | Diff (ppm) | Abund | Height % | Height % (Calc) | Ion Species | Z
561.3297 | 561.3312 | -2.66 | 382066 | 25.77 | 22.39 | (M+H)+ | 1
562.3294 | 562.3283 | 2.06 | 1482741 | 100.00 | 100.00 | (M+H)+ | 1
563.3319 | 563.3313 | 1.10 | 618687 | 41.73 | 41.95 | (M+H)+ | 1
564.3346 | 564.3344 | 0.34 | 134292 | 9.06 | 9.07 | (M+H)+ | 1
565.3375 | 565.3376 | -0.26 | 20108 | 1.36 | 1.32 | (M+H)+ | 1
MassHunter Qual 10.0
(End of Report)

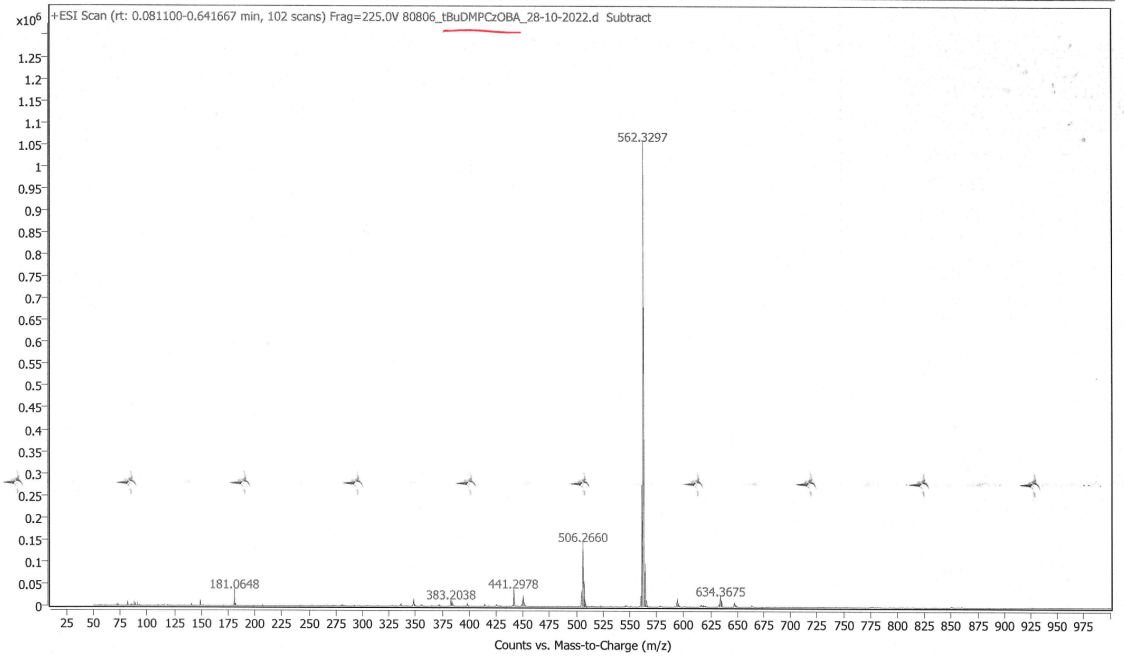
Zoomed – Spectrum Plot Report

Agilent | Trusted Answers



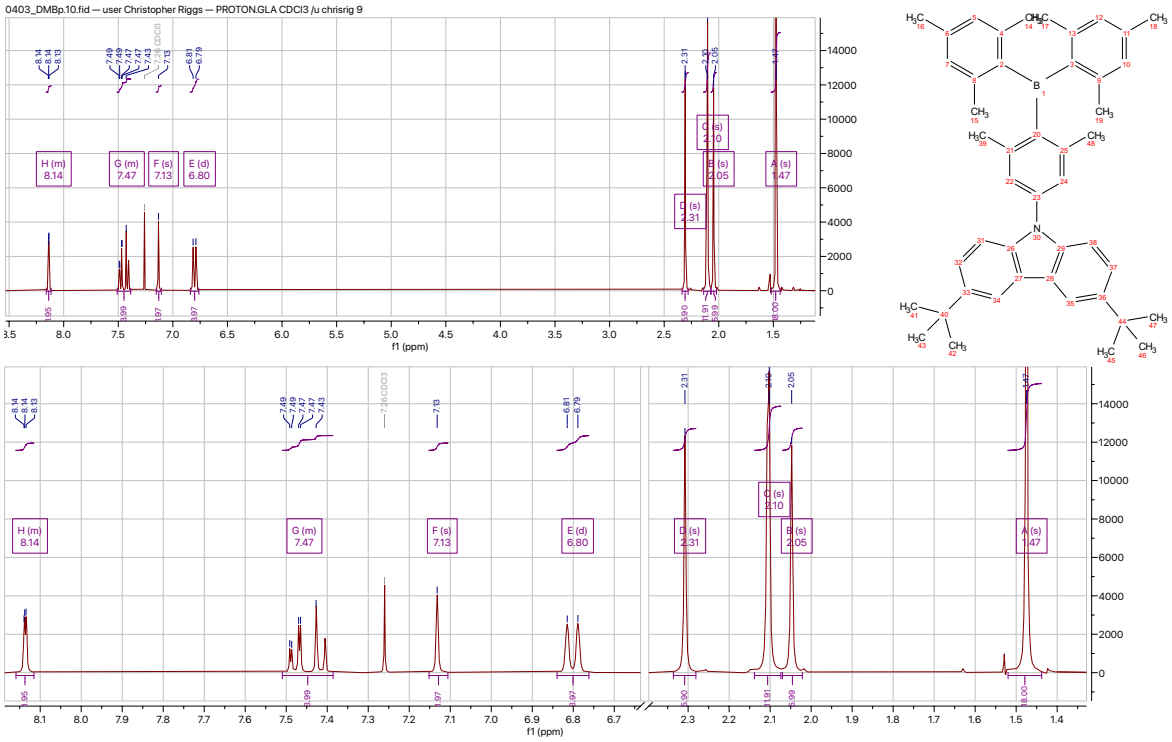
Full – Spectrum Plot Report

Agilent | Trusted Answers



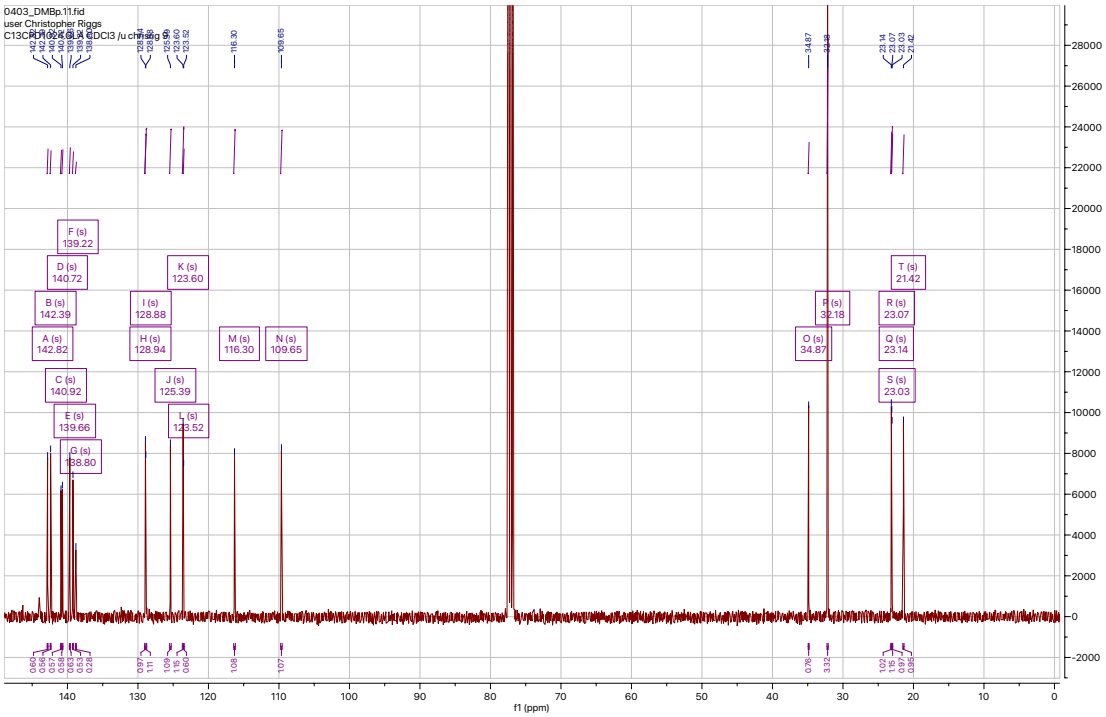
9.15.9 tBu-DMP-Cz-DMB (12)

^{1}H NMR



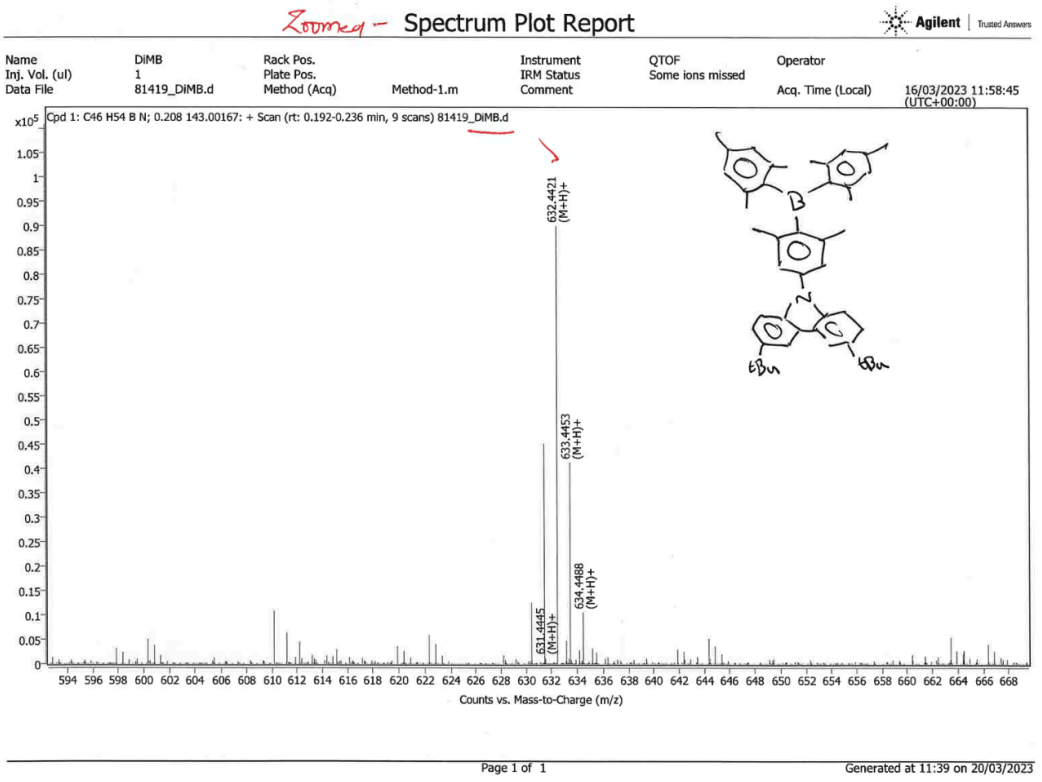
δ_H (400 MHz, $CDCl_3$) 8.16 – 8.12 (2 H, m), 7.51 – 7.39 (4 H, m), 7.13 (2 H, s), 6.80 (4 H, d, *J* 10.4), 2.31 (6 H, s), 2.10 (12 H, s), 2.05 (6 H, s), 1.47 (18 H, s).

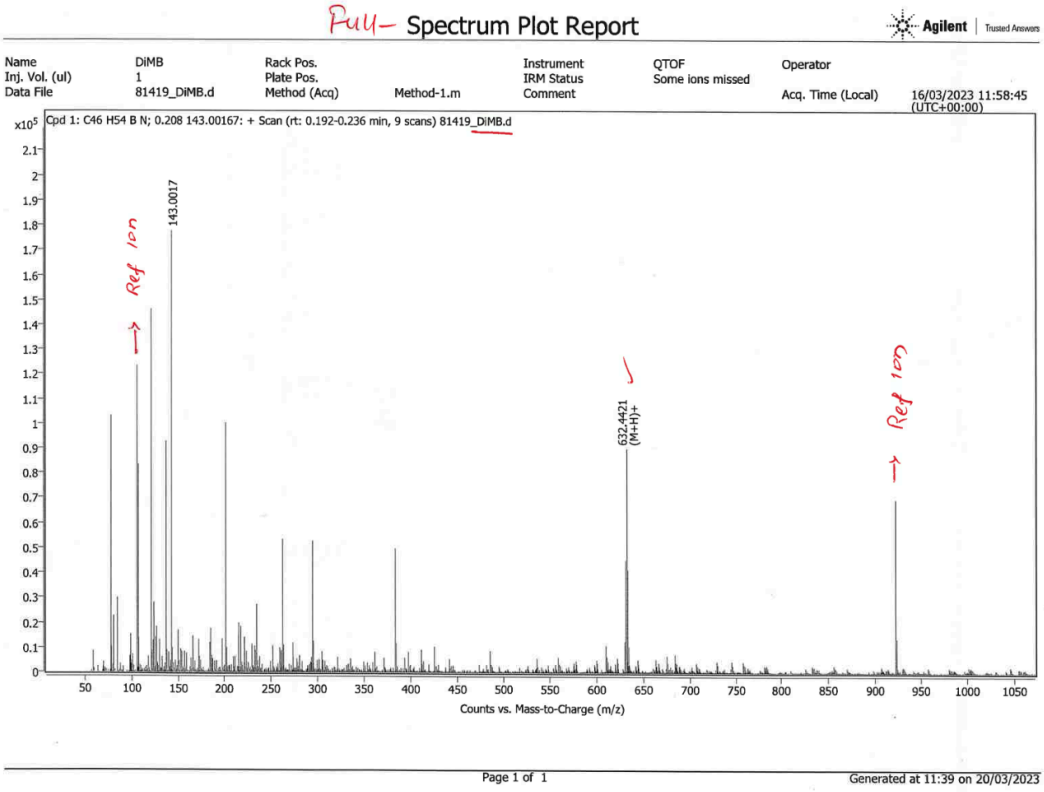
^{13}C NMR



δ_C (101 MHz, $CDCl_3$) 142.82, 142.39, 140.92, 140.72, 139.66, 139.22, 138.80, 128.94, 128.88, 125.39, 123.60, 123.52, 116.30, 109.65, 34.87, 32.18, 23.14, 23.07, 23.03, 21.42.

MS


Zoomed – Spectrum Plot Report
Agilent | Trusted Answers
Name DiMB
Inj. Vol. (ul) 1
Data File 81419_DiMB.d
Rack Pos.
Plate Pos.
Method (Acq) Method-1.m
Instrument
IRM Status
Comment
QTOF
Some ions missed
Operator
Acq. Time (Local) 16/03/2023 11:58:45 (UTC+00:00)
Cpd 1: C46 H54 B N; 0.208 143.00167: + Scan (rt: 0.192-0.236 min, 9 scans) 81419_DiMB.d
x10^5
632.4421 (M+H)+
633.4453 (M+H)+
634.4488 (M+H)+
631.4445 (M+H)+
Counts vs. Mass-to-Charge (m/z)
Page 1 of 1
Generated at 11:39 on 20/03/2023

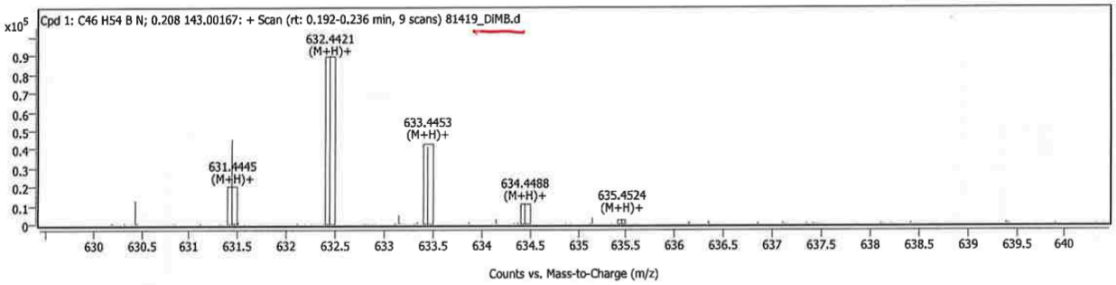

Full – Spectrum Plot Report
Agilent | Trusted Answers
Name DiMB
Inj. Vol. (ul) 1
Data File 81419_DiMB.d
Rack Pos.
Plate Pos.
Method (Acq) Method-1.m
Instrument
IRM Status
Comment
QTOF
Some ions missed
Operator
Acq. Time (Local) 16/03/2023 11:58:45 (UTC+00:00)
Cpd 1: C46 H54 B N; 0.208 143.00167: + Scan (rt: 0.192-0.236 min, 9 scans) 81419_DiMB.d
x10^5
143.0017
Ref ion
632.4421 (M+H)+
Ref ion
Counts vs. Mass-to-Charge (m/z)
Page 1 of 1
Generated at 11:39 on 20/03/2023

Custom Workflow Report

Agilent | Trusted Answers

Spectrum Peaks

m/z	m/z (Calc)	Diff (ppm)	Abund	Height %	Height % (Calc)	Ion Species	z
631.4445	631.4458	-2.05	1303	1.45	22.06	(M+H)+	1
632.4421	632.4430	-1.39	89990	100.00	100.00	(M+H)+	1
633.4453	633.4460	-1.01	41247	45.84	47.85	(M+H)+	1
634.4488	634.4492	-0.51	10534	11.71	11.65	(M+H)+	1
635.4524	635.4524	-0.02	2342	2.60	1.87	(M+H)+	1



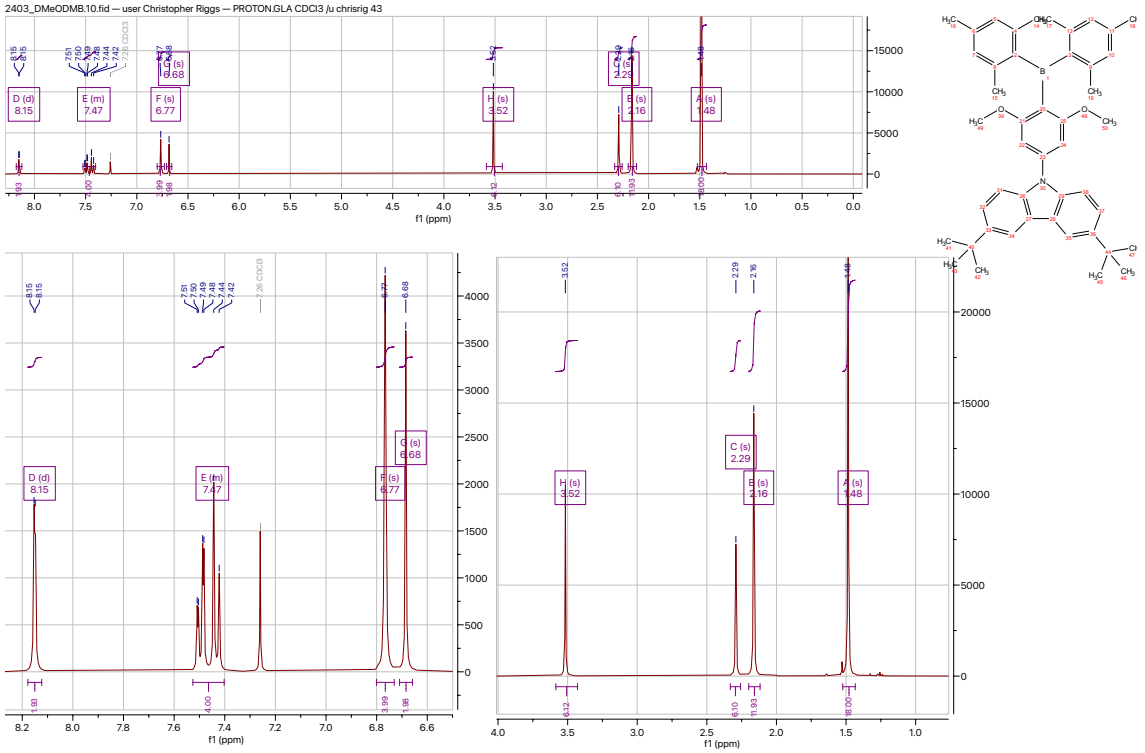
Spectrum Peaks

m/z	m/z (Calc)	Diff (ppm)	Abund	Height %	Height % (Calc)	Ion Species	z
631.4445	631.4458	-2.05	1303	1.45	22.06	(M+H)+	1
632.4421	632.4430	-1.39	89990	100.00	100.00	(M+H)+	1
633.4453	633.4460	-1.01	41247	45.84	47.85	(M+H)+	1
634.4488	634.4492	-0.51	10534	11.71	11.65	(M+H)+	1
635.4524	635.4524	-0.02	2342	2.60	1.87	(M+H)+	1
143.0017			177765				

MassHunter Qual 10.0
(End of Report)

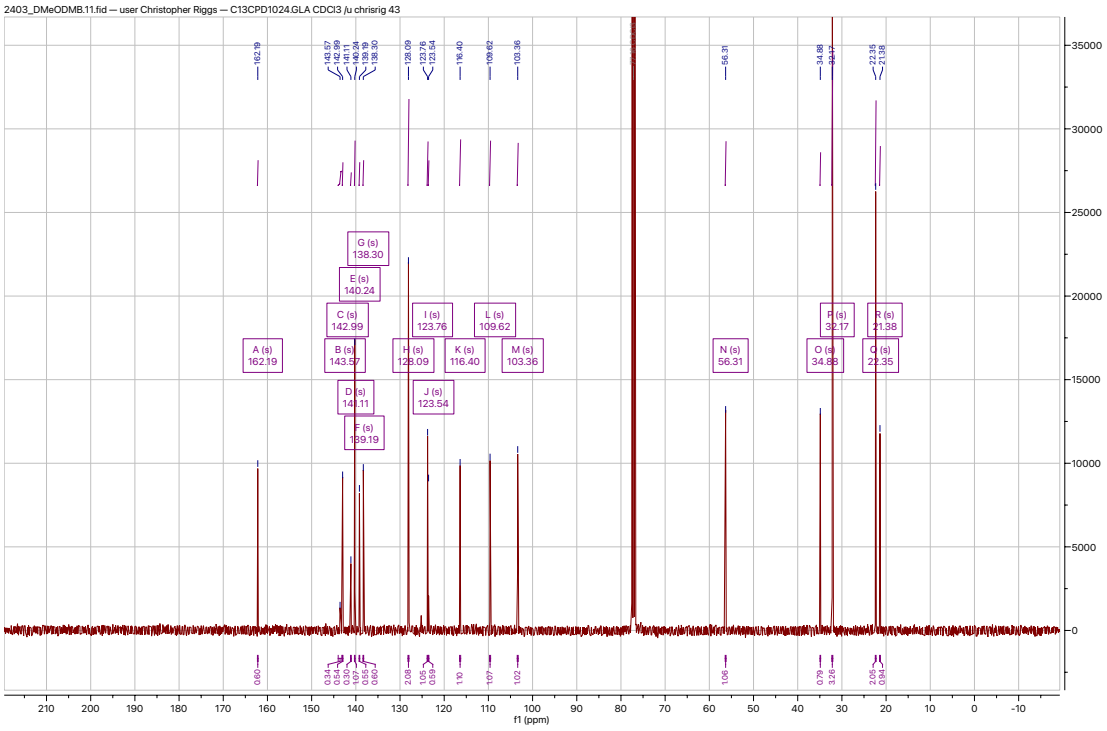
9.15.10 tBu-DMeOP-Cz-DMB (13)

^{1}H NMR



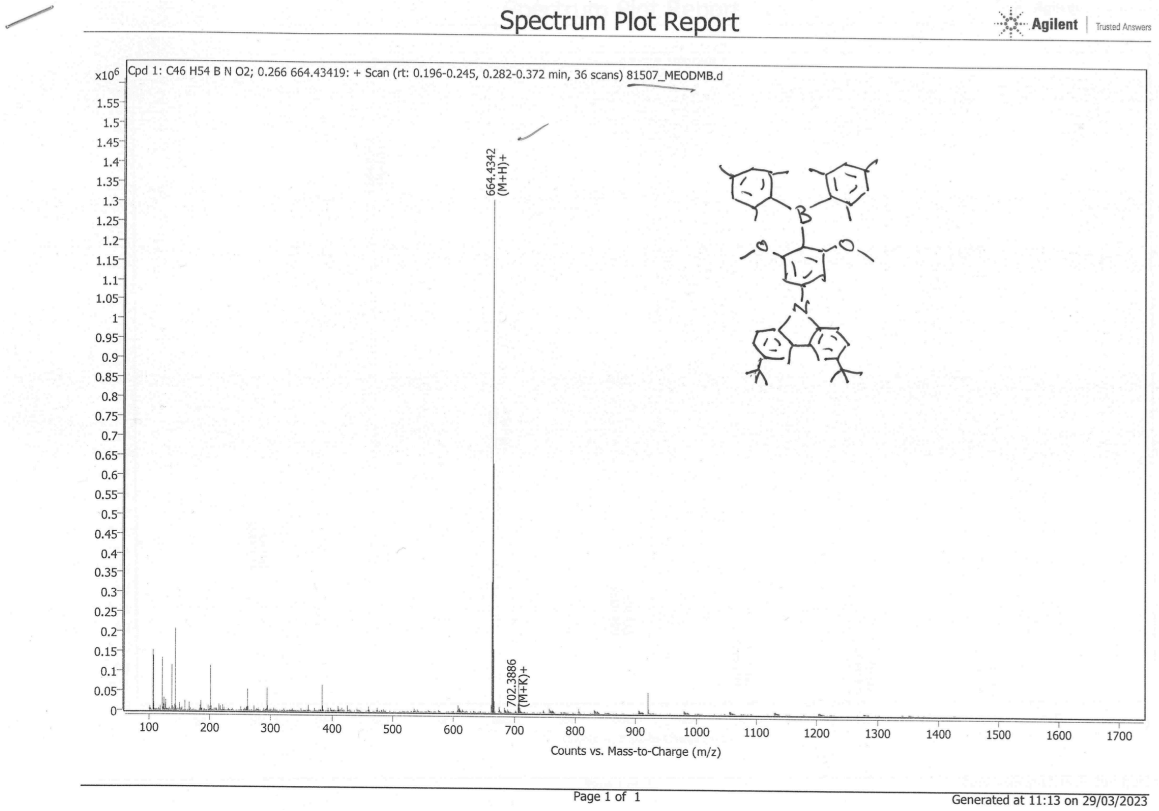
δ_H (400 MHz, $CDCl_3$) 8.15 (2 H, d, *J* 1.9), 7.53 – 7.40 (4 H, m), 6.77 (4 H, s), 6.68 (2 H, s), 3.52 (6 H, s), 2.29 (6 H, s), 2.16 (12 H, s), 1.48 (18 H, s).

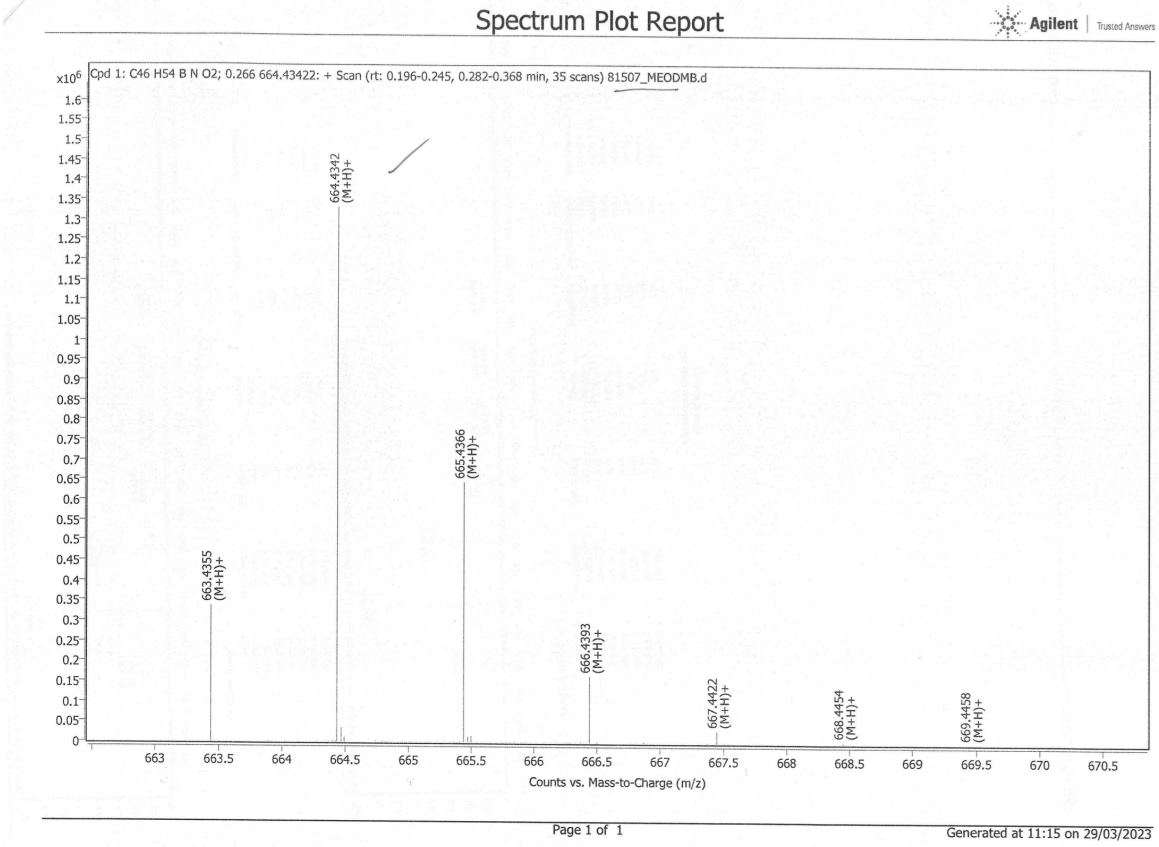
^{13}C NMR



δ_C (101 MHz, $CDCl_3$) 162.19, 143.57, 142.99, 141.11, 140.24, 139.19, 138.30, 128.09, 123.76, 123.54, 116.40, 109.62, 103.36, 56.31, 34.88, 32.17, 22.35, 21.38.

MS

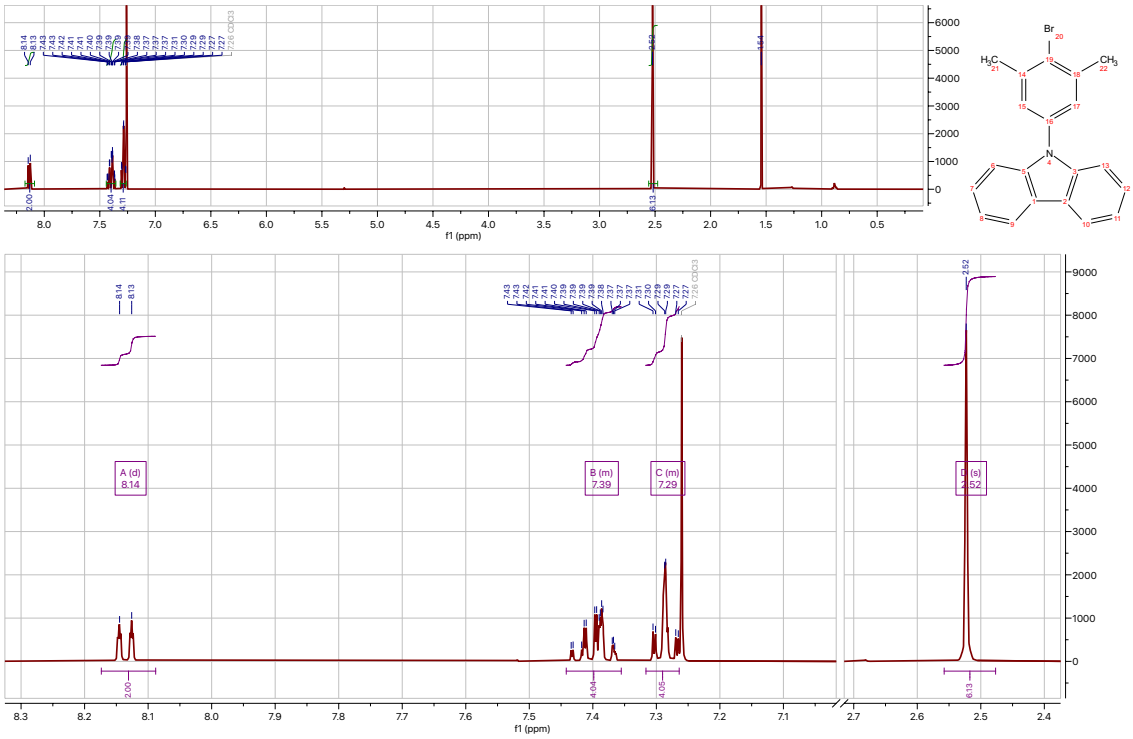

Spectrum Plot Report
Agilent Trusted Answers
Cpd 1: C46 H54 B N O2; 0.266 664.43419: + Scan (rt: 0.196-0.245, 0.282-0.372 min, 36 scans) 81507_MEODMB.d
x10^6
664.4342 (M+H)+
702.3886 (M+K)+
Counts vs. Mass-to-Charge (m/z)
Page 1 of 1
Generated at 11:13 on 29/03/2023


Spectrum Plot Report
Agilent Trusted Answers
Cpd 1: C46 H54 B N O2; 0.266 664.43422: + Scan (rt: 0.196-0.245, 0.282-0.368 min, 35 scans) 81507_MEODMB.d
x10^6
663.4355 (M+H)+
664.4342 (M+H)+
665.4366 (M+H)+
666.4393 (M+H)+
667.4422 (M+H)+
668.4454 (M+H)+
669.4458 (M+H)+
Counts vs. Mass-to-Charge (m/z)
Page 1 of 1
Generated at 11:15 on 29/03/2023

9.16 Chapter 6

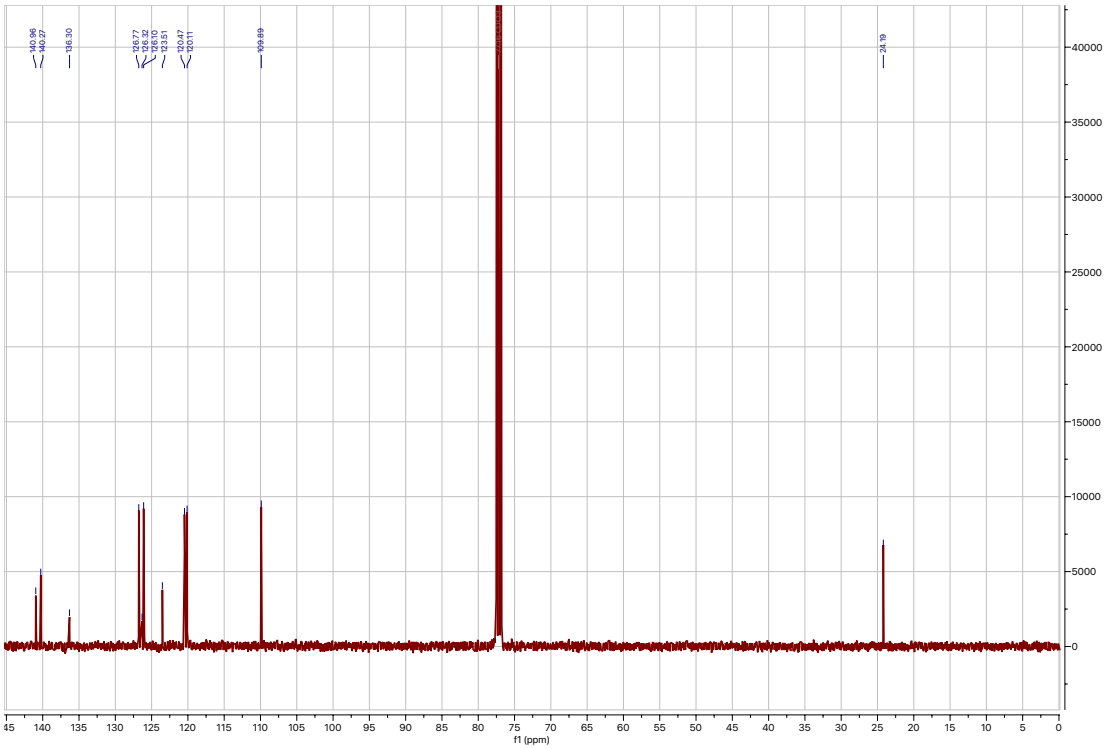
9.16.1 9-(4-bromo-3,5-dimethylphenyl)-9H-carbazole (6.5)

^{1}H NMR



δ_H (400 MHz, $CDCl_3$) 8.14 (2 H, d, *J* 7.6), 7.44 – 7.36 (4 H, m), 7.32 – 7.26 (4 H, m), 2.52 (6 H, s).

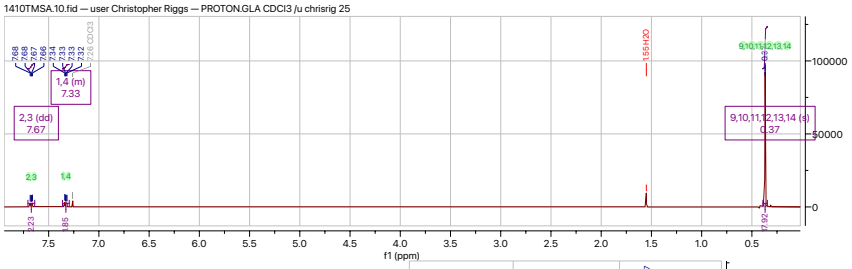
^{13}C NMR

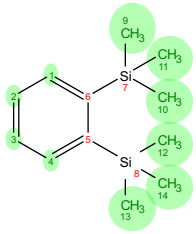


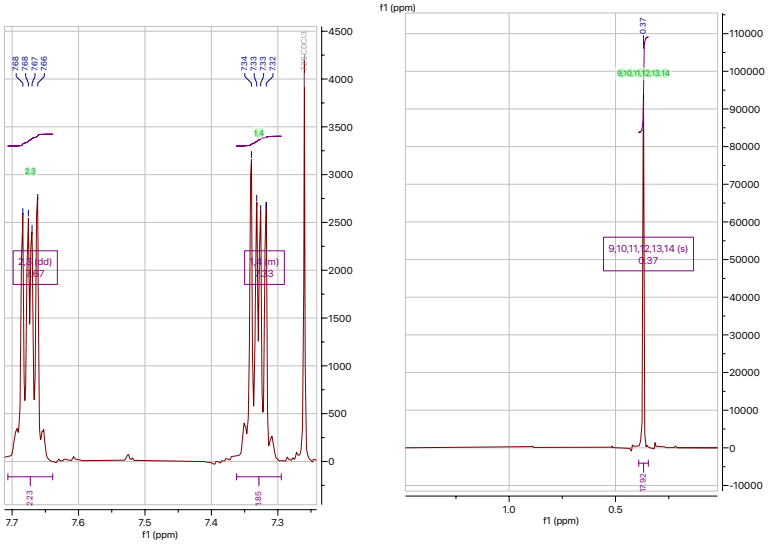
δ_C (101 MHz, $CDCl_3$) 140.96, 140.27, 136.30, 126.77, 126.32, 126.10, 123.51, 120.47, 120.11, 109.89, 24.19.

9.16.2 1,2-bis(trimethylsilyl)benzene (6.2)

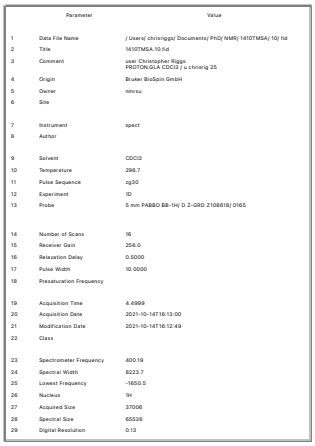
^{13}C NMR



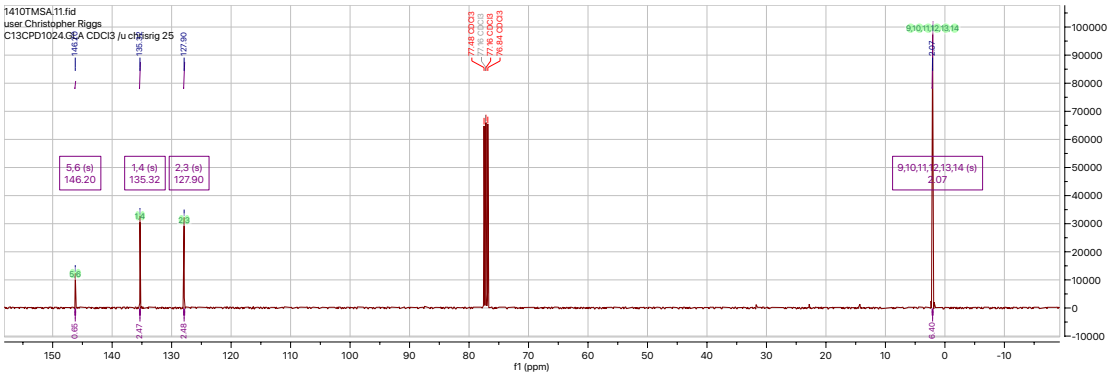


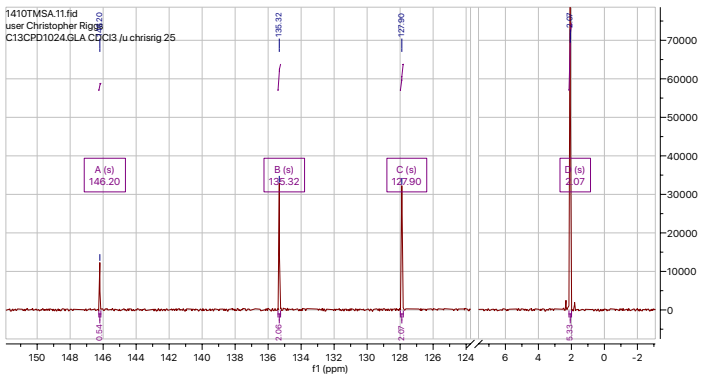


δ_H (400 MHz, $CDCl_3$) 7.67 (2 H, dd, *J* 5.6, 3.4), 7.33 (2 H, dd), 0.37 (18 H, s).

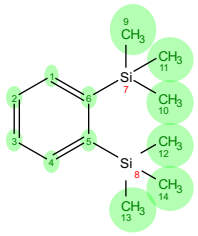


^{13}C NMR





δ_C (101 MHz, $CDCl_3$) 146.20, 135.32, 127.90, 2.07.

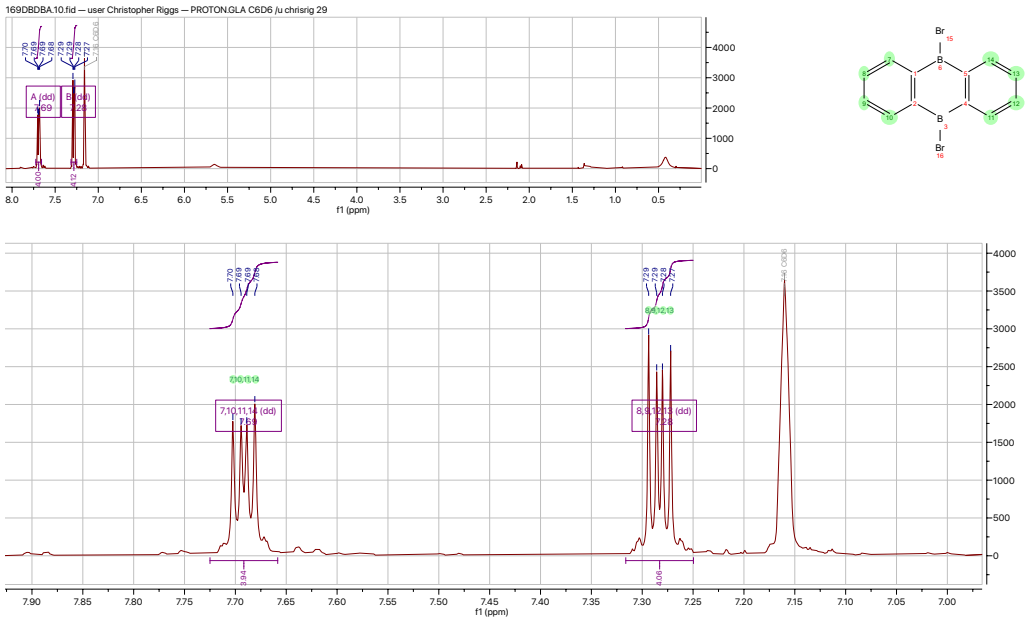


9.16.3 Dibromodiboraanthracene (DBDBA – 6.4)

9.16.3.1 From 1,2-bis(trimethylsilyl)benzene – toluene solvent

^{1}H NMR

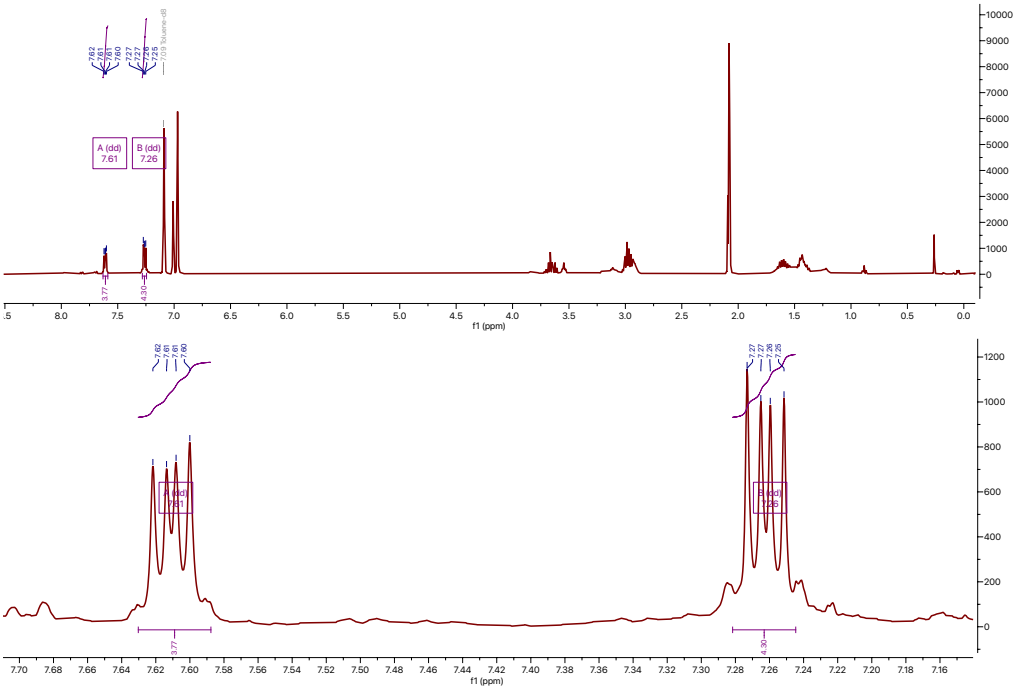
Crystal precipitate



δ_H (400 MHz, C_6D_6) 7.69 (4 H, dd, *J* 5.4, 3.2), 7.28 (4 H, dd, *J* 5.5, 3.2).

9.16.3.2 From 1,2-bis(dimethylsilyl)benzene – hexane solvent

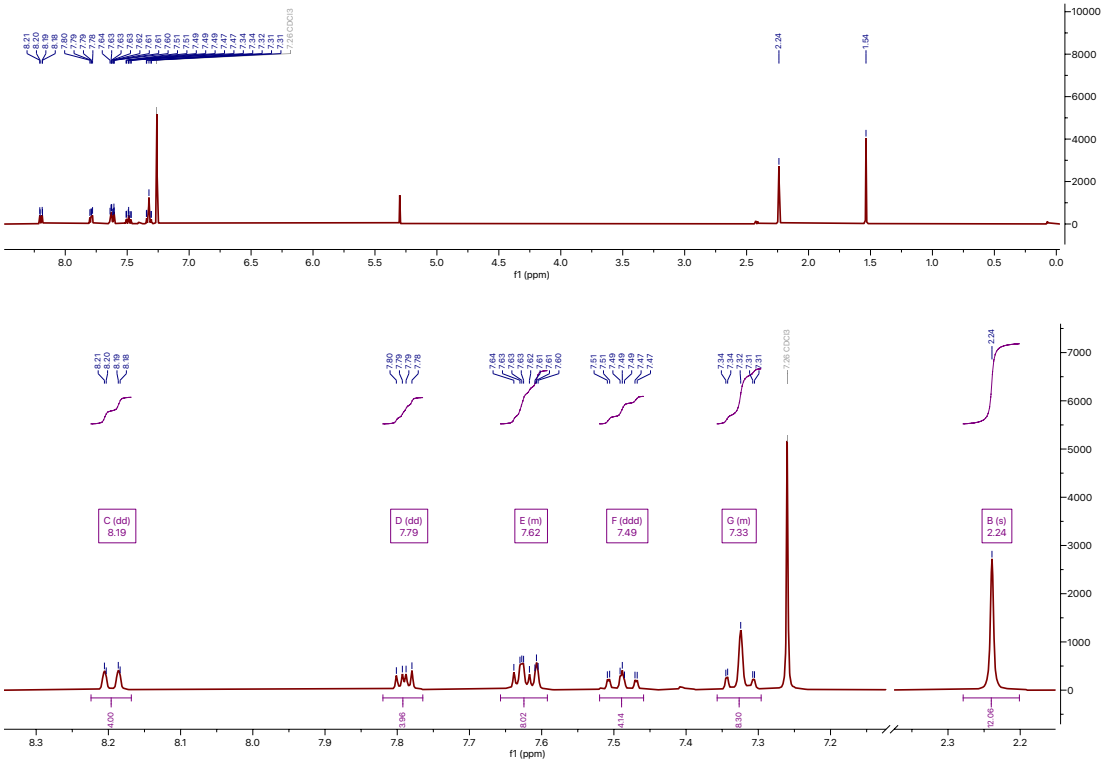
^{1}H NMR



δ_H (400 MHz, Tol) 7.61 (4 H, dd, *J* 5.5, 3.2), 7.26 (4 H, dd, *J* 5.4, 3.2).

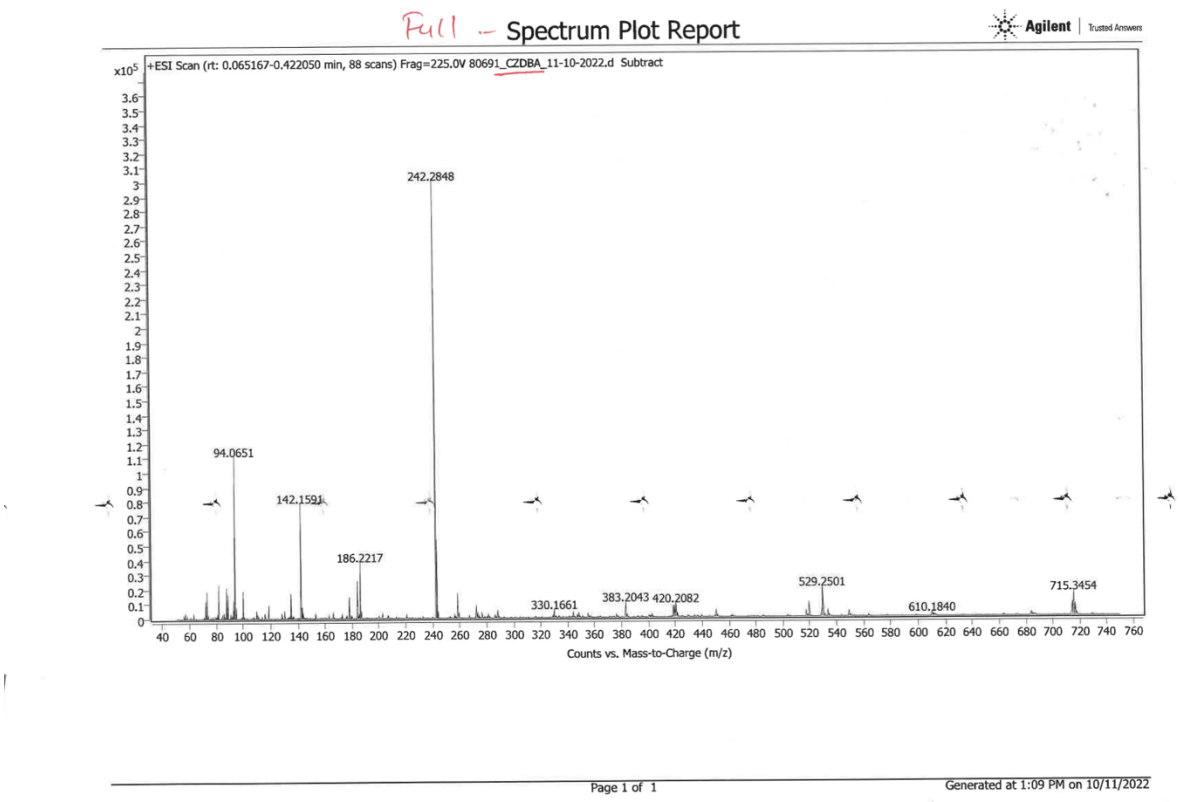
9.16.4 CzDBA (16)

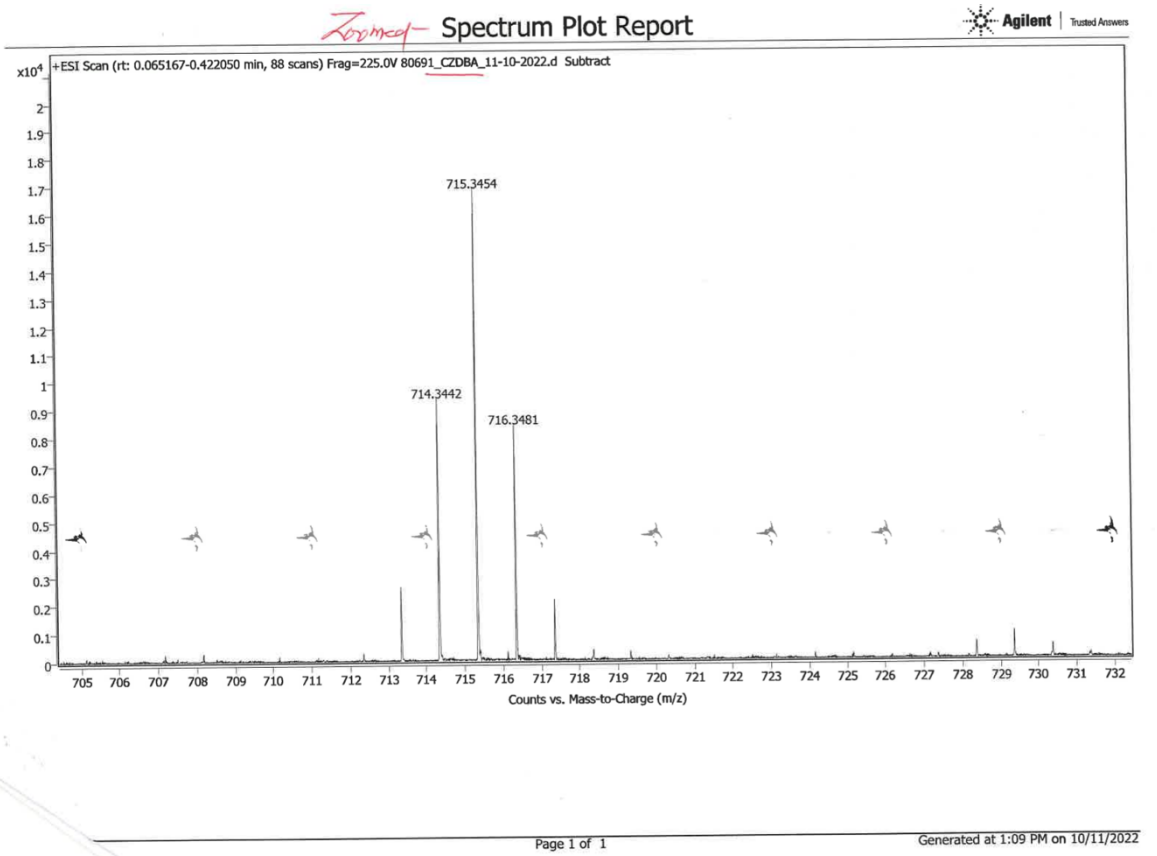
^{1}H NMR



δ_H (400 MHz, $CDCl_3$) 8.19 (4 H, dd, *J* 7.7, 1.0), 7.79 (4 H, dd, *J* 5.3, 3.3), 7.66 – 7.59 (8 H, m), 7.49 (4 H, ddd, *J* 8.3, 7.0, 1.2), 7.36 – 7.30 (8 H, m), 2.24 (12 H, s).

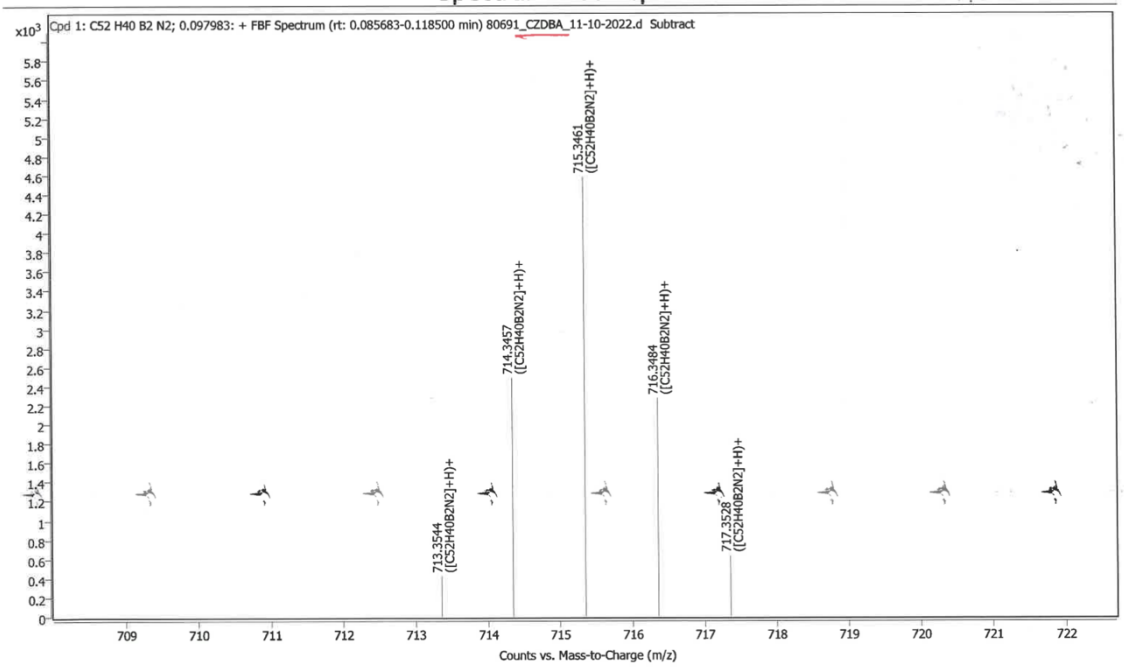
MS


Full – Spectrum Plot Report
Agilent | Trusted Answers
x10^5
+ESI Scan (rt: 0.065167-0.422050 min, 88 scans) Frag=225.0V 80691_CZDBA_11-10-2022.d Subtract
242.2848
94.0651
142.1591
186.2217
330.1661
383.2043
420.2082
529.2501
610.1840
715.3454
Counts vs. Mass-to-Charge (m/z)
Page 1 of 1
Generated at 1:09 PM on 10/11/2022


Zoomed – Spectrum Plot Report
Agilent | Trusted Answers
x10^4
+ESI Scan (rt: 0.065167-0.422050 min, 88 scans) Frag=225.0V 80691_CZDBA_11-10-2022.d Subtract
715.3454
714.3442
716.3481
Counts vs. Mass-to-Charge (m/z)
Page 1 of 1
Generated at 1:09 PM on 10/11/2022

Spectrum Plot Report

Agilent | Trusted Answers



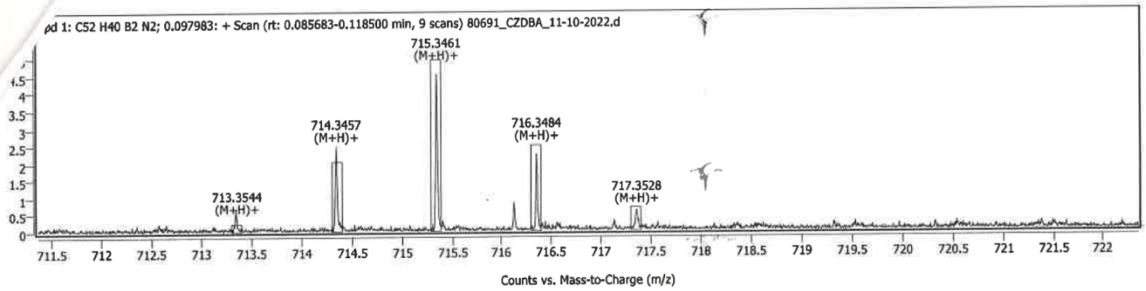
Generated at 1:06 PM on 10/11/2022

Custom Workflow Report

Agilent | Trusted Answers

Spectrum Peaks

m/z	m/z (Calc)	Diff (ppm)	Abund	Height %	Height % (Calc)	Ion Species	z
713.3544	713.3523	3.00	419	9.16	4.76	(M+H)+	1
714.3457	714.3491	-4.77	2485	54.31	41.09	(M+H)+	1
715.3461	715.3467	-0.81	4576	100.00	100.00	(M+H)+	1
716.3484	716.3492	-1.15	2270	49.62	50.70	(M+H)+	1
717.3528	717.3522	0.82	628	13.72	13.67	(M+H)+	1



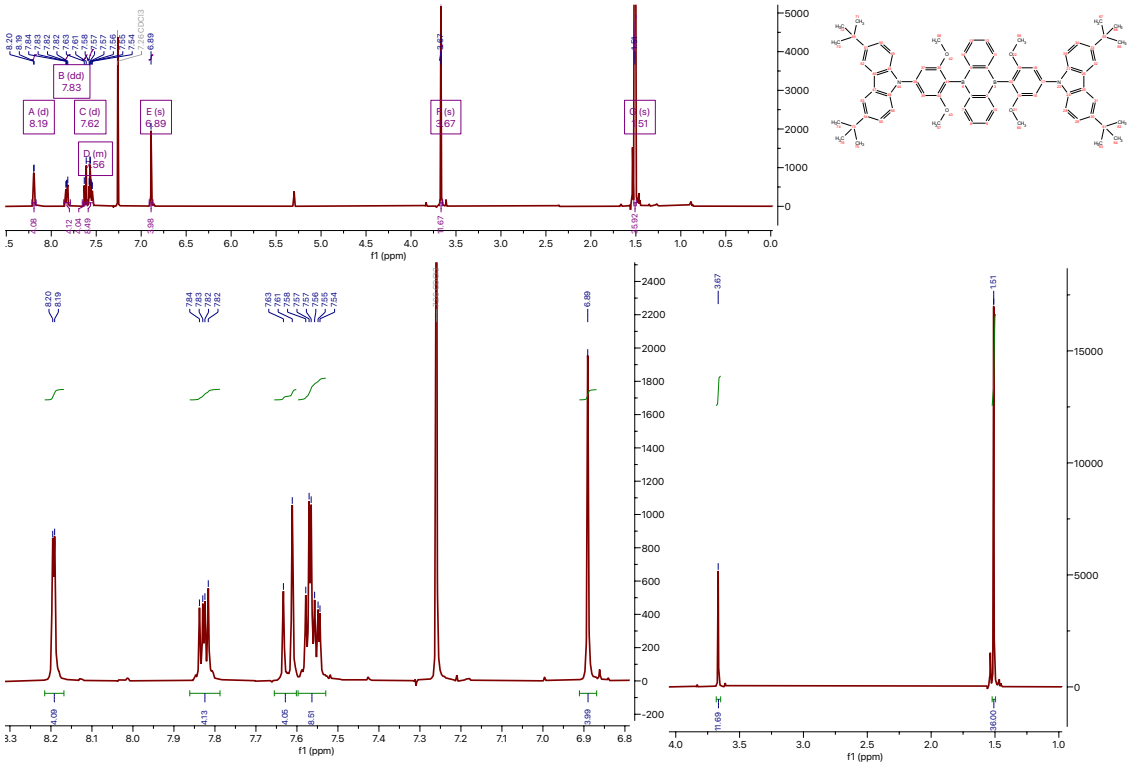
Spectrum Peaks

m/z	m/z (Calc)	Diff (ppm)	Abund	Height %	Height % (Calc)	Ion Species	z
713.3544	713.3523	3.00	419	9.16	4.76	(M+H)+	1
714.3457	714.3491	-4.77	2485	54.31	41.09	(M+H)+	1
715.3461	715.3467	-0.81	4576	100.00	100.00	(M+H)+	1
716.3484	716.3492	-1.15	2270	49.62	50.70	(M+H)+	1
717.3528	717.3522	0.82	628	13.72	13.67	(M+H)+	1

MassHunter Qual 10.0
(End of Report)

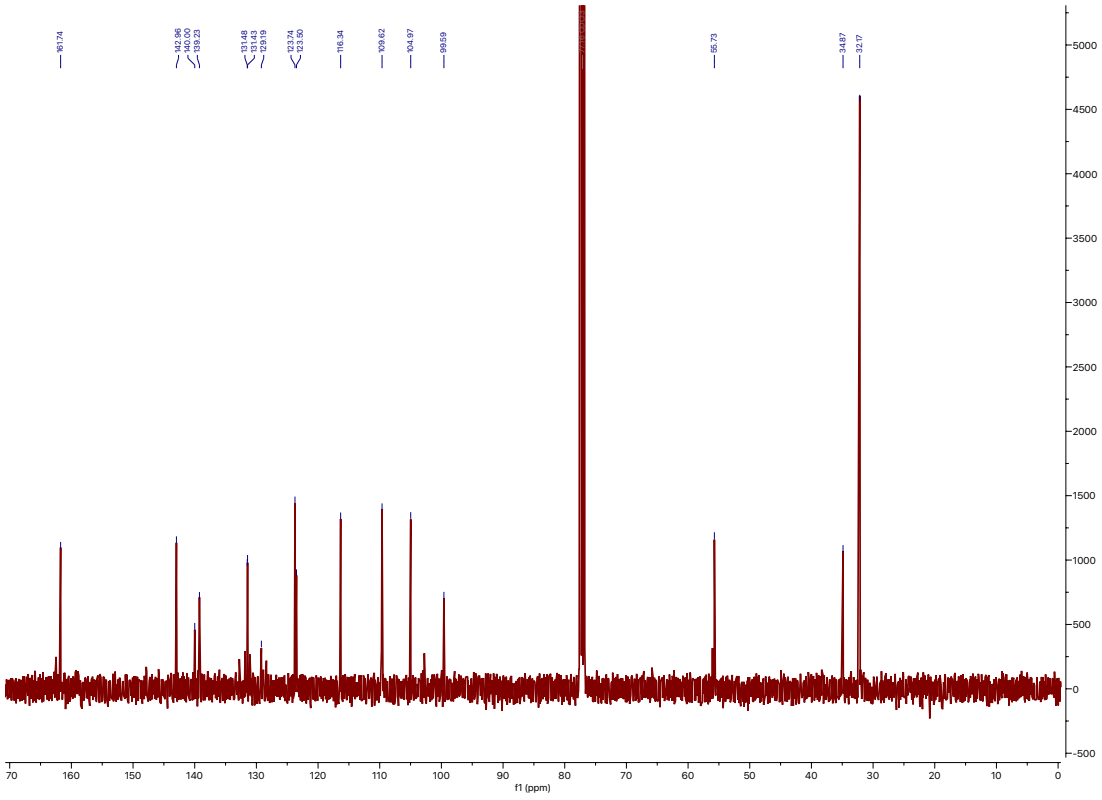
9.16.5 tBu-MeOCzDBA (17)

^{1}H NMR

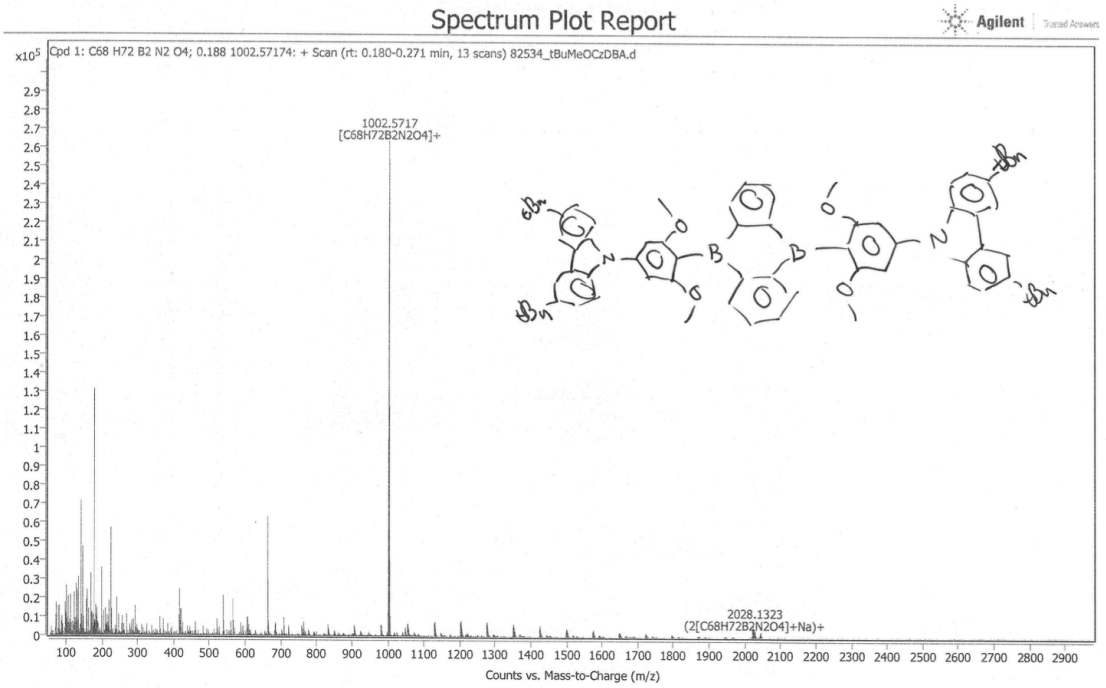


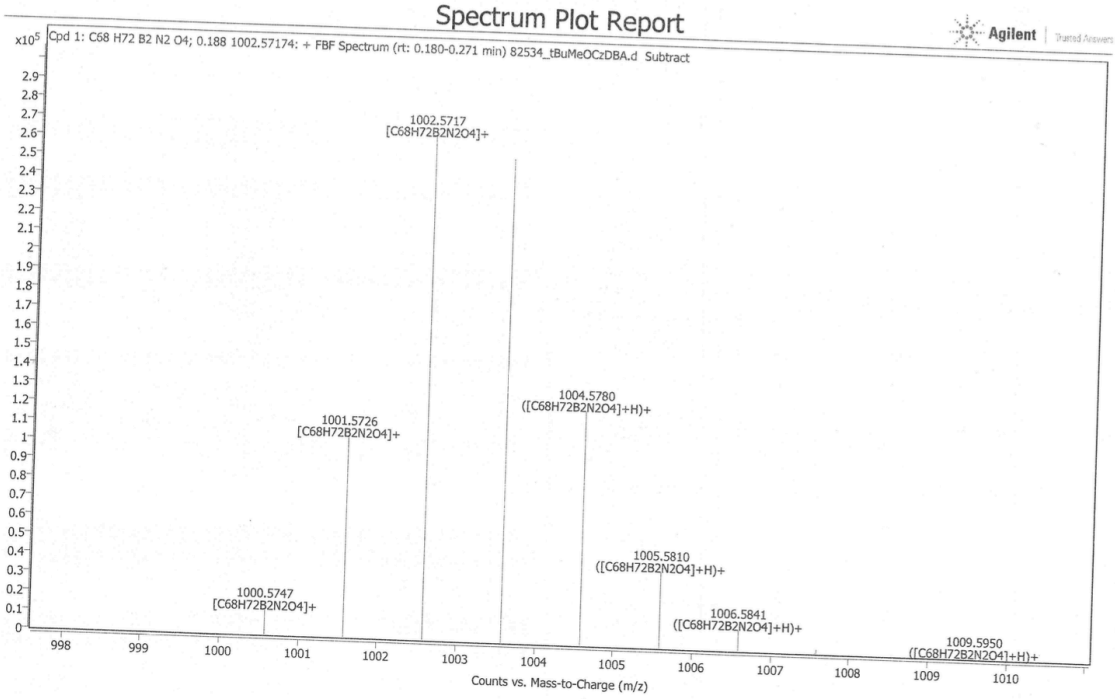
δ_H (400 MHz, $CDCl_3$) 8.19 (4 H, d, *J* 1.9), 7.83 (4 H, dd, *J* 5.4, 3.3), 7.62 (4 H, d, *J* 8.6), 7.60 – 7.53 (8 H, m), 6.89 (4 H, s), 3.67 (12 H, s), 1.51 (36 H, s).

^{13}C NMR


161.74
142.96
140.09
139.23
131.48
131.43
129.19
123.74
123.50
116.34
109.62
104.97
99.59
77.16
55.73
34.87
32.17
5000
4500
4000
3500
3000
2500
2000
1500
1000
500
0
-500
70
160
150
140
130
120
110
100
90
80
70
60
50
40
30
20
10
0
f1 (ppm)

MS


Spectrum Plot Report
Agilent
Cpd 1: C68 H72 B2 N2 O4; 0.188 1002.57174: + Scan (rt: 0.180-0.271 min, 13 scans) 82534_tBuMeOCzDBA.d
x10^5
1002.5717
[C68H72B2N2O4]+
2028.1323
(2[C68H72B2N2O4]+Na)+
Counts vs. Mass-to-Charge (m/z)

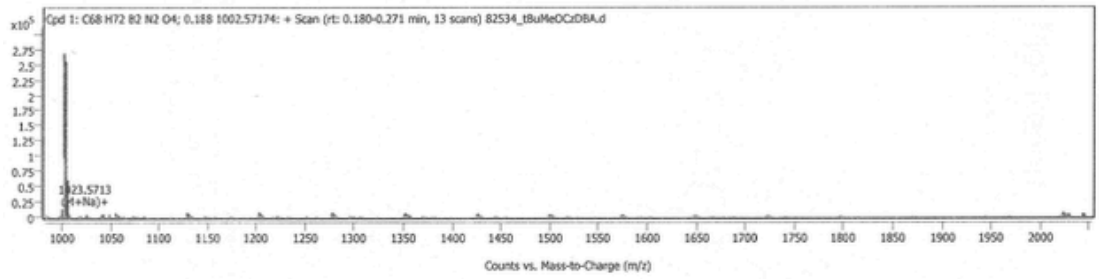

Spectrum Plot Report
Agilent
Cpd 1: C68 H72 B2 N2 O4; 0.188 1002.57174: + FBF Spectrum (rt: 0.180-0.271 min) 82534_tBuMeOCzDBA.d Subtract
x10^5
1002.5717
[C68H72B2N2O4]+
1001.5726
[C68H72B2N2O4]+
1004.5780
([C68H72B2N2O4]+H)+
1000.5747
[C68H72B2N2O4]+
1005.5810
([C68H72B2N2O4]+H)+
1006.5841
([C68H72B2N2O4]+H)+
1009.5950
([C68H72B2N2O4]+H)+
Counts vs. Mass-to-Charge (m/z)

Custom Workflow Report

Agilent | Trusted Answers

Spectrum Peaks

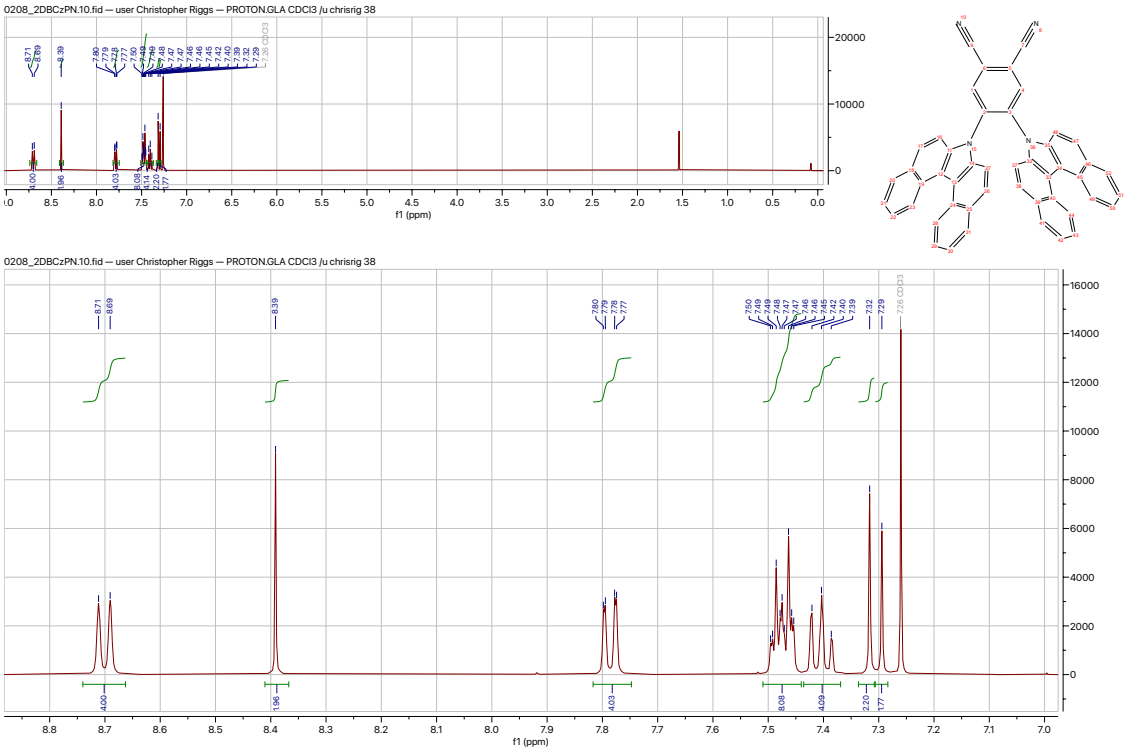
m/z	m/z (Calc)	Diff (ppm)	Abund	Height %	Height % (Calc)	Ion Species	Z
984.5484	984.5688	-20.66	132	51.75	39.05	(M+H)+[-H2O]	1
985.5431	985.5666	-23.80	255	100.00	100.00	(M+H)+[-H2O]	1
986.5641	986.5690	-5.03	66	25.83	64.56	(M+H)+[-H2O]	1
987.5683	987.5719	-3.66	75	29.38	23.14	(M+H)+[-H2O]	1
1000.5747	1000.5745	0.12	12817	4.85	4.44	M+	1
1001.5726	1001.5715	1.12	104906	39.69	39.04	M+	1
1002.5717	1002.5693	2.41	264329	100.00	100.00	M+	1
1003.5749	1003.5771	-2.23	253832	100.00	100.00	(M+H)+	1
1004.5780	1004.5796	-1.59	122589	48.30	64.68	(M+H)+	1
1005.5810	1005.5825	-1.46	39423	15.53	23.37	(M+H)+	1
1006.5841	1006.5855	-1.41	10656	4.20	5.87	(M+H)+	1
1007.5510	1007.5485	2.50	126	100.00	100.00	(M+Na)+[-H2O]	1
1007.5723	1007.5837	-11.35	316	0.12	0.18	M+	1
1007.5875	1007.5885	-1.00	2144	0.84	1.13	(M+H)+	1
1008.5402	1008.5510	-10.70	77	61.28	64.55	(M+Na)+[-H2O]	1
1009.5950	1009.5945	0.45	65	0.03	0.02	(M+H)+	1
1023.5713	1023.5643	6.88	110	5.16	4.44	(M+Na)+	1
1024.5596	1024.5613	-1.63	1019	47.67	39.04	(M+Na)+	1
1025.5589	1025.5591	-0.19	2139	100.00	100.00	(M+Na)+	1
1026.5614	1026.5615	-0.16	1184	55.37	64.67	(M+Na)+	1
1027.5829	1027.5644	18.01	458	21.40	23.37	(M+Na)+	1
1028.5484	1028.5674	-18.56	57	2.66	5.87	(M+Na)+	1
1039.5390	1039.5382	0.72	142	5.98	4.42	(M+K)+	1
1040.5351	1040.5352	-0.10	1204	50.74	38.92	(M+K)+	1
1041.5338	1041.5330	0.76	2372	100.00	100.00	(M+K)+	1
1042.5353	1042.5354	-0.04	1890	79.66	67.28	(M+K)+	1
1043.5372	1043.5367	0.54	880	37.08	30.49	(M+K)+	1
1044.5416	1044.5379	3.49	258	10.89	10.50	(M+K)+	1
1045.5288	1045.5397	-10.42	108	4.55	2.81	(M+K)+	1
2024.1282	2024.0970	15.41	115	26.09	15.64	(2M+K)+[-H2O]	1
2025.1132	2025.0949	9.07	185	41.91	54.50	(2M+K)+[-H2O]	1
2026.1270	2026.0940	16.30	441	100.00	100.00	(2M+K)+[-H2O]	1
2028.0699	2028.0971	-13.41	173	39.25	67.34	(2M+K)+[-H2O]	1
2028.1323	2028.1306	0.84	4112	100.00	100.00	(2M+Na)+	1
2029.1101	2029.0990	5.43	63	14.24	34.48	(2M+K)+[-H2O]	1
2029.1319	2029.1321	-0.07	3606	87.70	97.07	(2M+Na)+	1
2030.1338	2030.1344	-0.26	2169	52.75	61.11	(2M+Na)+	1
2031.1328	2031.1370	-2.07	1172	28.50	28.09	(2M+Na)+	1
2032.1375	2032.1399	-1.15	504	12.27	10.13	(2M+Na)+	1
2033.1468	2033.1428	1.99	105	2.55	3.00	(2M+Na)+	1
2043.1077	2043.1055	1.08	1192	40.88	54.48	(2M+K)+	1
2044.1057	2044.1046	0.55	2337	80.19	100.00	(2M+K)+	1
2045.1082	2045.1059	1.11	2915	100.00	99.90	(2M+K)+	1
2046.1083	2046.1077	0.31	1784	61.22	67.57	(2M+K)+	1
2047.1048	2047.1096	-2.32	922	31.64	34.70	(2M+K)+	1
2048.1100	2048.1116	-0.77	354	12.15	14.38	(2M+K)+	1



9.17 Chapter 7

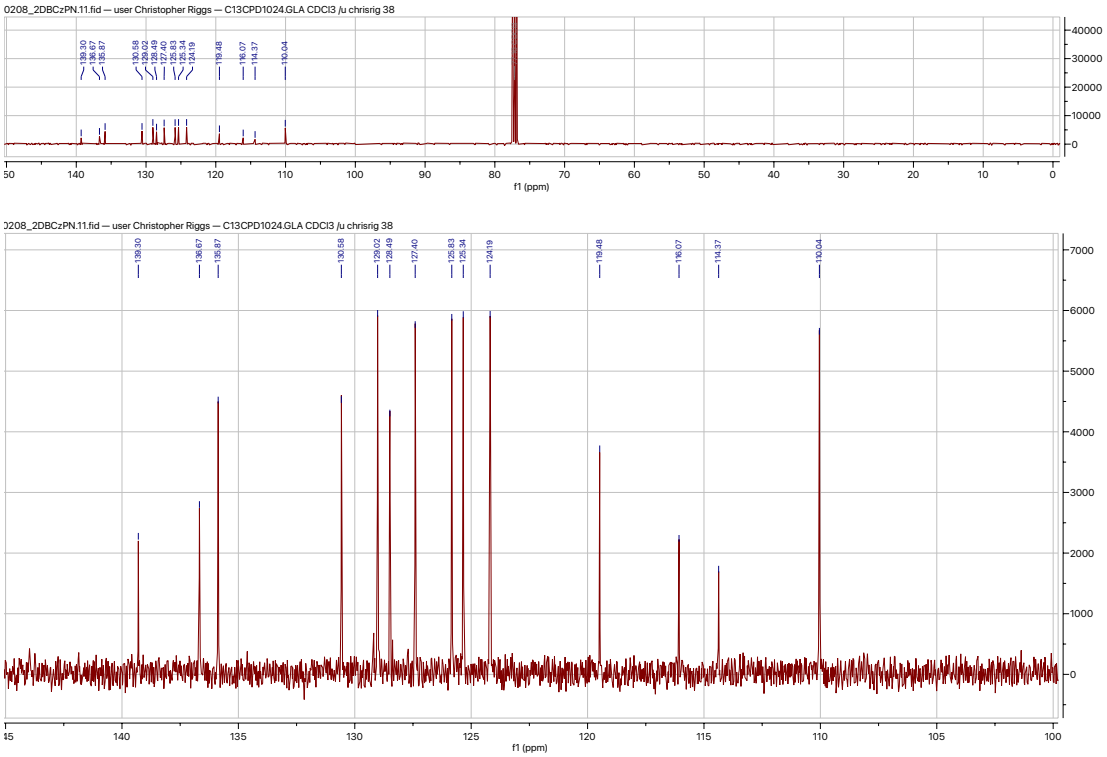
9.17.1 2DBCzPN (18)

^{1}H NMR



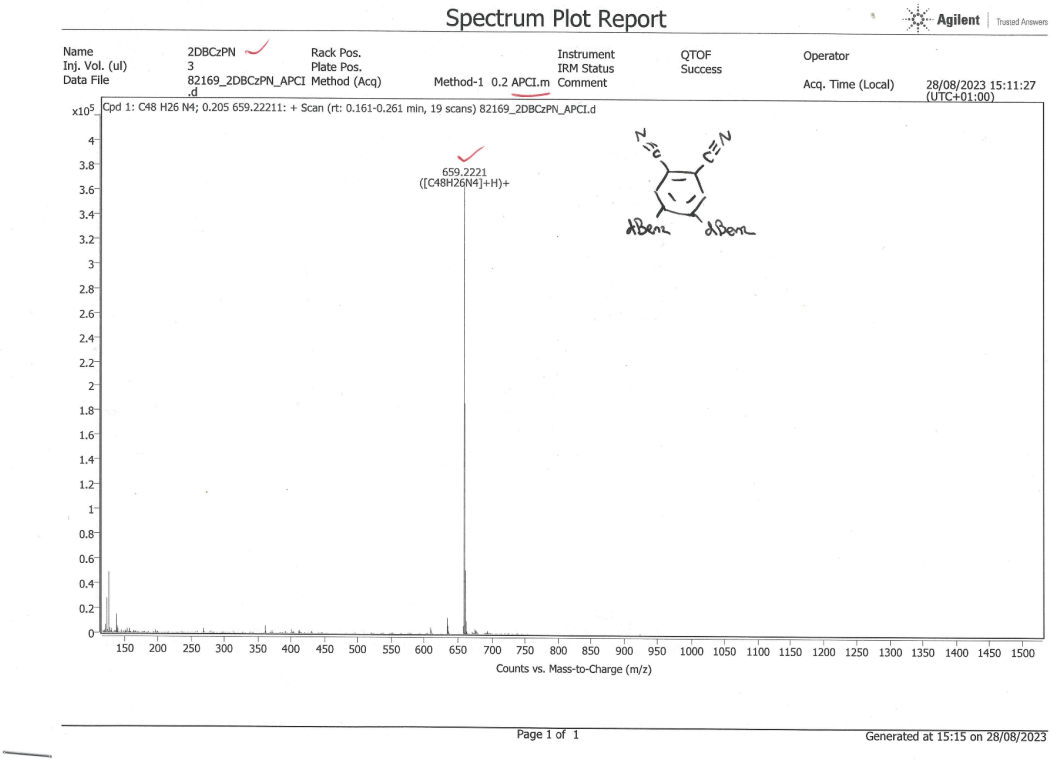
δ_H (400 MHz, $CDCl_3$) 8.70 (4 H, d, *J* 8.4), 8.39 (2 H, s), 7.79 (4 H, dd, *J* 8.1, 1.5), 7.55 – 7.44 (8 H, m), 7.40 (4 H, t, *J* 7.0), 7.32 (2 H, s), 7.29 (2 H, s).

^{13}C NMR



δ_C (101 MHz, $CDCl_3$) 139.30, 136.67, 135.87, 130.58, 129.02, 128.49, 127.40, 125.83, 125.34, 124.19, 119.48, 116.07, 114.37, 110.04.

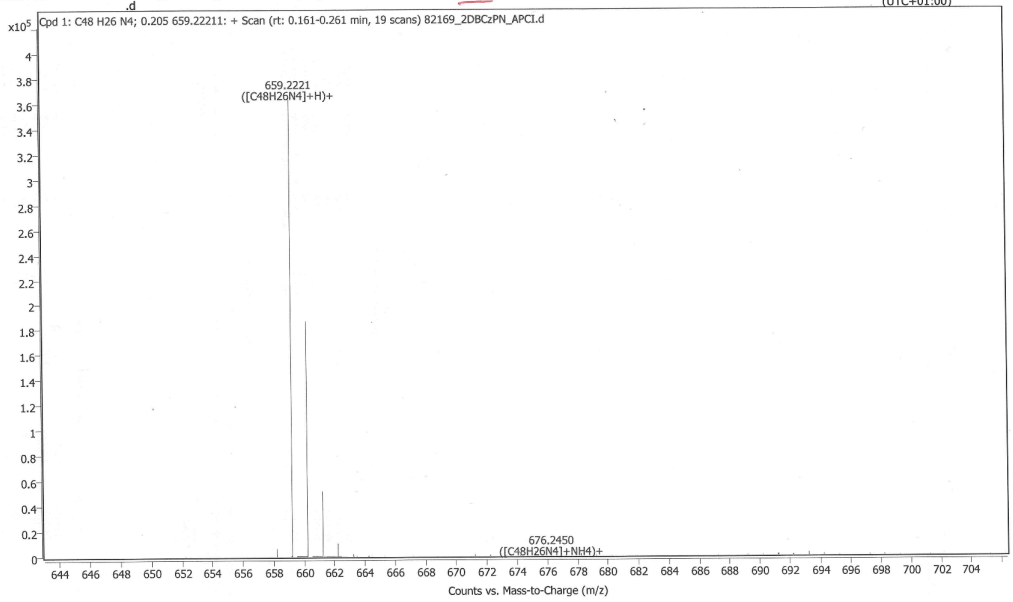
MS



Spectrum Plot Report

Agilent | Trusted Answers

Name	2DBCzPN	Rack Pos.		Instrument	QTOF	Operator	
Inj. Vol. (ul)	3	Plate Pos.		IRM Status	Success		
Data File	82169_2DBCzPN_APCI .d	Method (Acq)	Method-1 0.2 APCI.m	Comment		Acq. Time (Local)	28/08/2023 15:11:27 (UTC+01:00)



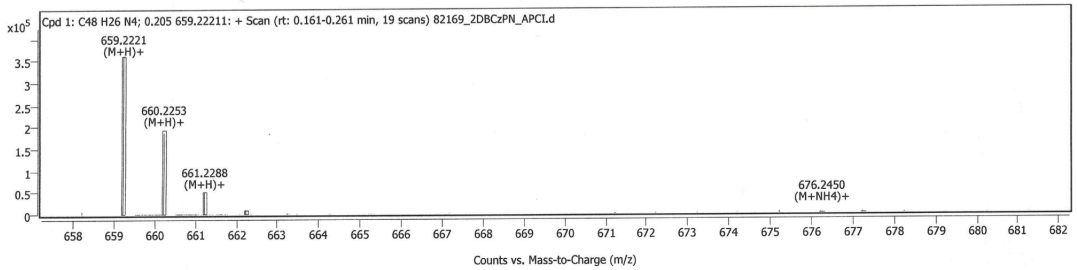
Generated at 15:17 on 28/08/2023

Custom Workflow Report

Agilent | Trusted Answers

Spectrum Peaks

m/z	m/z (Calc)	Diff (ppm)	Abund	Height %	Height % (Calc)	Ion Species	Z
659.2221	659.2230	-1.39	362786	100.00	100.00	(M+H)+	1
660.2253	660.2262	-1.45	186656	51.45	53.69	(M+H)+	1
661.2288	661.2294	-0.97	51432	14.18	14.13	(M+H)+	1
662.2328	662.2326	0.25	10265	2.83	2.43	(M+H)+	1
676.2450	676.2496	-6.76	147	100.00	100.00	(M+NH4)+	1
677.2582	677.2527	8.13	60	40.93	54.09	(M+NH4)+	1



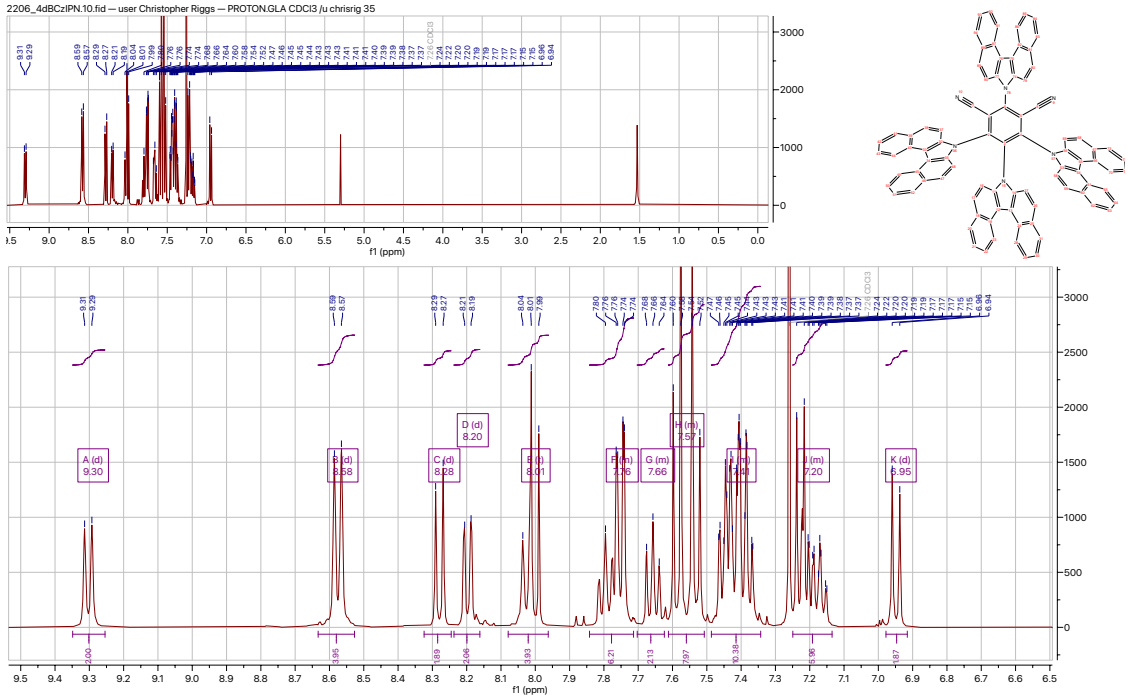
Spectrum Peaks

m/z	m/z (Calc)	Diff (ppm)	Abund	Height %	Height % (Calc)	Ion Species	Z
659.2221	659.2230	-1.39	362786	100.00	100.00	(M+H)+	1
660.2253	660.2262	-1.45	186656	51.45	53.69	(M+H)+	1
661.2288	661.2294	-0.97	51432	14.18	14.13	(M+H)+	1
662.2328	662.2326	0.25	10265	2.83	2.43	(M+H)+	1
676.2450	676.2496	-6.76	147	100.00	100.00	(M+NH4)+	1
677.2582	677.2527	8.13	60	40.93	54.09	(M+NH4)+	1

MassHunter Qual 10.0
(End of Report)

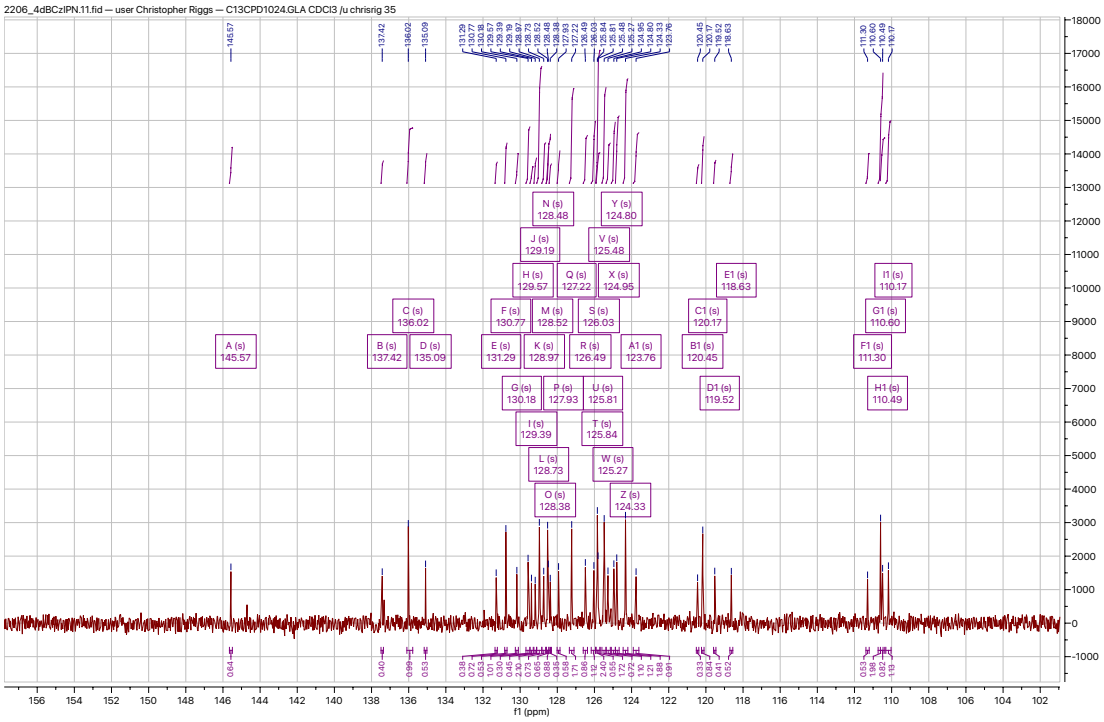
9.17.2 4DBCzIPN (19)

^{1}H NMR



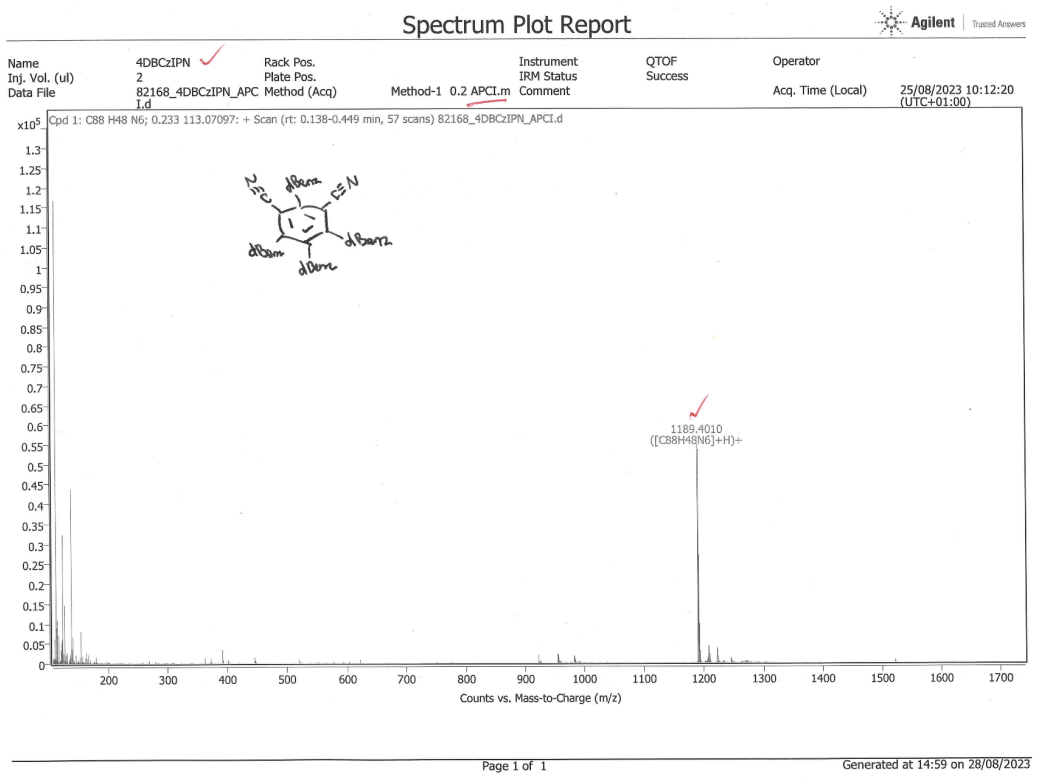
δ_H (400 MHz, $CDCl_3$) 9.30 (2 H, d, *J* 8.5), 8.58 (4 H, d, *J* 8.2), 8.28 (2 H, d, *J* 8.8), 8.20 (2 H, d, *J* 7.5), 8.01 (4 H, t, *J* 9.3), 7.84 – 7.71 (6 H, m), 7.70 – 7.62 (2 H, m), 7.61 – 7.51 (8 H, m), 7.49 – 7.34 (10 H, m), 7.25 – 7.13 (6 H, m), 6.95 (2 H, d, *J* 8.8).

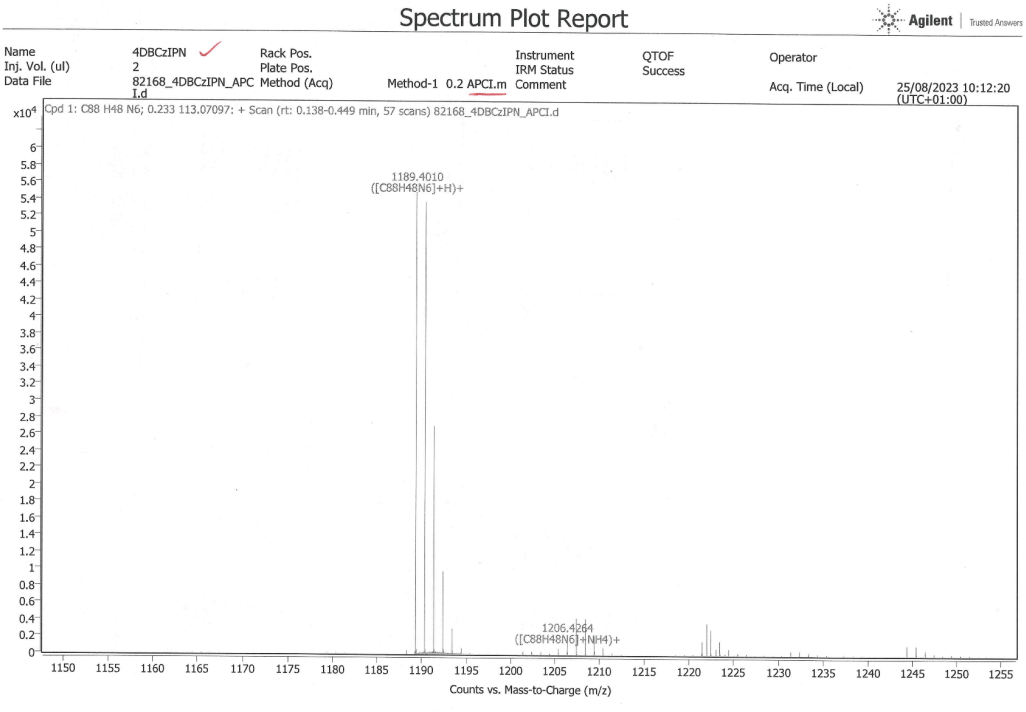
^{13}C NMR



δ_C (101 MHz, $CDCl_3$) 145.57, 137.42, 136.02, 135.09, 131.29, 130.77, 130.18, 129.57, 129.39, 129.19, 128.97, 128.73, 128.52, 128.48, 128.38, 127.93, 127.22, 126.49, 126.03, 125.84, 125.81, 125.48, 125.27, 124.95, 124.80, 124.33, 123.76, 120.45, 120.17, 119.52, 118.63, 111.30, 110.60, 110.49, 110.17.

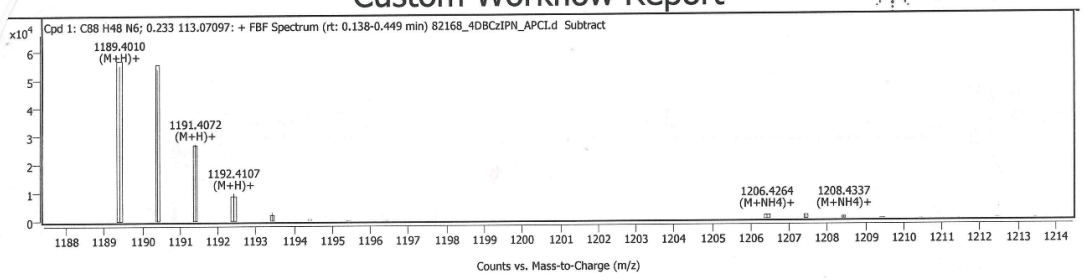
MS


Spectrum Plot Report
Agilent Trusted Answers
Name 4DBCzIPN
Inj. Vol. (ul) 2
Data File 82168_4DBCzIPN_APC I.d
Rack Pos.
Plate Pos.
Method (Acq) Method-1 0.2 APCI.m
Instrument IRM Status Comment
QTOF Success
Operator
Acq. Time (Local) 25/08/2023 10:12:20 (UTC+01:00)
Cpd 1: C88 H48 N6; 0.233 113.07097: + Scan (rt: 0.138-0.449 min, 57 scans) 82168_4DBCzIPN_APCI.d
x10^5
1189.4010
([C88H48N6]+H)+
Counts vs. Mass-to-Charge (m/z)
Page 1 of 1
Generated at 14:59 on 28/08/2023


Spectrum Plot Report
Agilent Trusted Answers
Name 4DBCzIPN
Inj. Vol. (ul) 2
Data File 82168_4DBCzIPN_APC I.d
Rack Pos.
Plate Pos.
Method (Acq) Method-1 0.2 APCI.m
Instrument IRM Status Comment
QTOF Success
Operator
Acq. Time (Local) 25/08/2023 10:12:20 (UTC+01:00)
Cpd 1: C88 H48 N6; 0.233 113.07097: + Scan (rt: 0.138-0.449 min, 57 scans) 82168_4DBCzIPN_APCI.d
x10^4
1189.4010
([C88H48N6]+H)+
1206.4264
([C88H48N6]+NH4)+
Counts vs. Mass-to-Charge (m/z)
Page 1 of 1
Generated at 15:00 on 28/08/2023

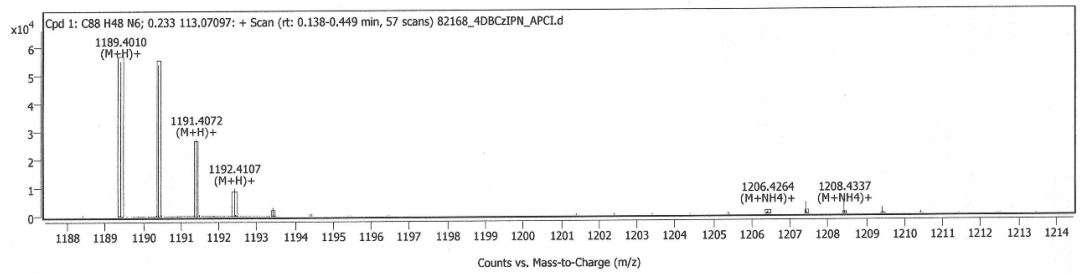
Custom Workflow Report

Agilent | Trusted Answers



Spectrum Peaks

m/z	m/z (Calc)	Diff (ppm)	Abund	Height %	Height % (Calc)	Ion Species	Z
1189.4010	1189.4013	-0.26	54864	100.00	100.00	(M+H)+	1
1190.4042	1190.4046	-0.30	53647	97.78	97.93	(M+H)+	1
1191.4072	1191.4078	-0.46	27005	49.22	47.44	(M+H)+	1
1192.4107	1192.4110	-0.29	9761	17.79	15.15	(M+H)+	1
1193.4141	1193.4142	-0.13	2990	5.45	3.59	(M+H)+	1
1206.4264	1206.4279	-1.21	1372	100.00	100.00	(M+NH4)+	1
1207.4276	1207.4311	-2.87	930	67.79	98.33	(M+NH4)+	1
1208.4337	1208.4343	-0.46	852	62.15	47.83	(M+NH4)+	1
1209.4504	1209.4375	10.64	139	10.11	15.34	(M+NH4)+	1



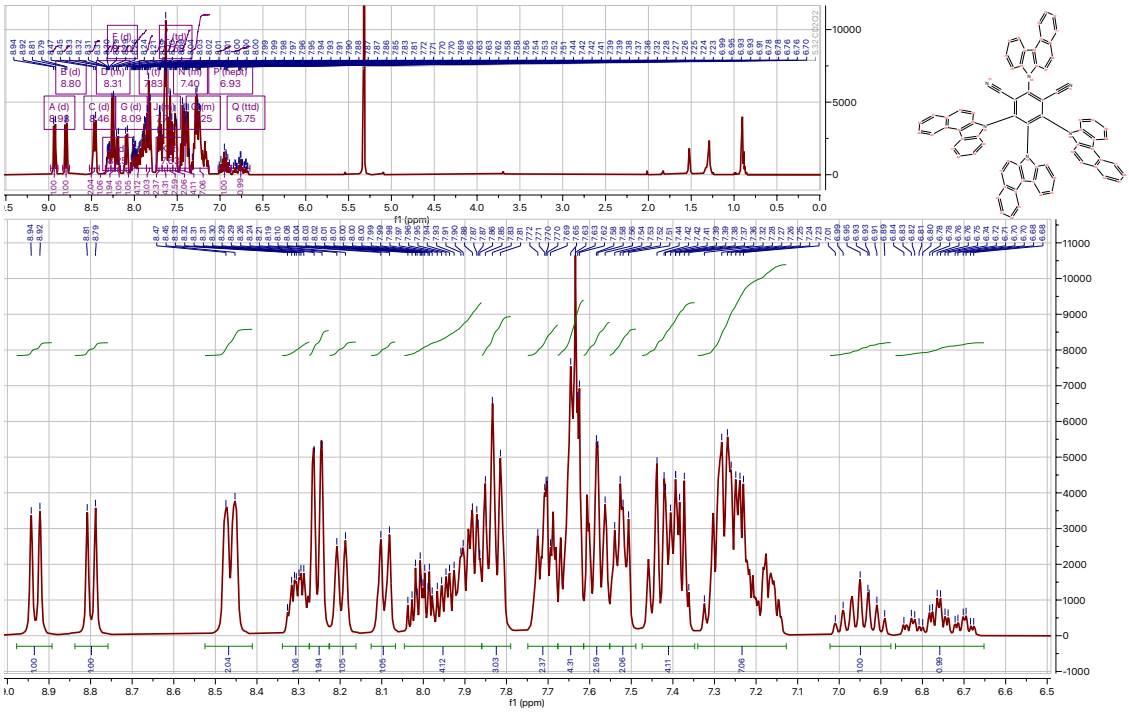
Spectrum Peaks

m/z	m/z (Calc)	Diff (ppm)	Abund	Height %	Height % (Calc)	Ion Species	Z
1189.4010	1189.4013	-0.26	54864	100.00	100.00	(M+H)+	1
1190.4042	1190.4046	-0.30	53647	97.78	97.93	(M+H)+	1
1191.4072	1191.4078	-0.46	27005	49.22	47.44	(M+H)+	1
1192.4107	1192.4110	-0.29	9761	17.79	15.15	(M+H)+	1
1193.4141	1193.4142	-0.13	2990	5.45	3.59	(M+H)+	1
1206.4264	1206.4279	-1.21	1372	100.00	100.00	(M+NH4)+	1
1207.4276	1207.4311	-2.87	930	67.79	98.33	(M+NH4)+	1
1208.4337	1208.4343	-0.46	852	62.15	47.83	(M+NH4)+	1
1209.4504	1209.4375	10.64	139	10.11	15.34	(M+NH4)+	1
113.0710			116761				

MassHunter Qual 10.0
(End of Report)

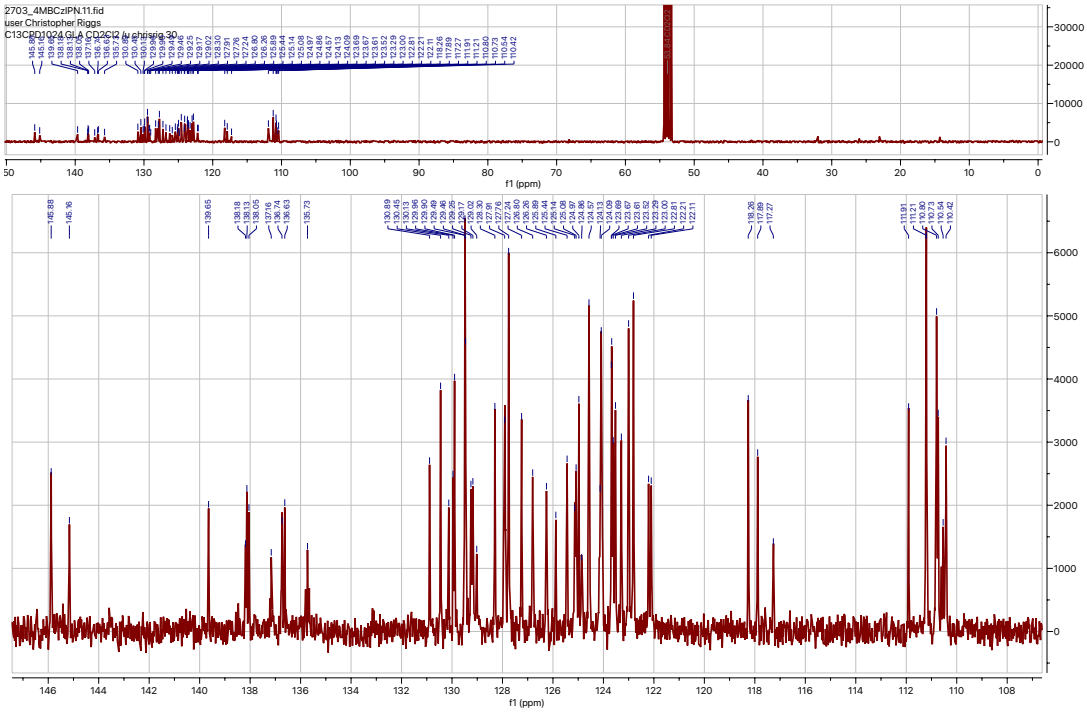
9.17.3 4MBCzIPN (20)

^{1}H NMR



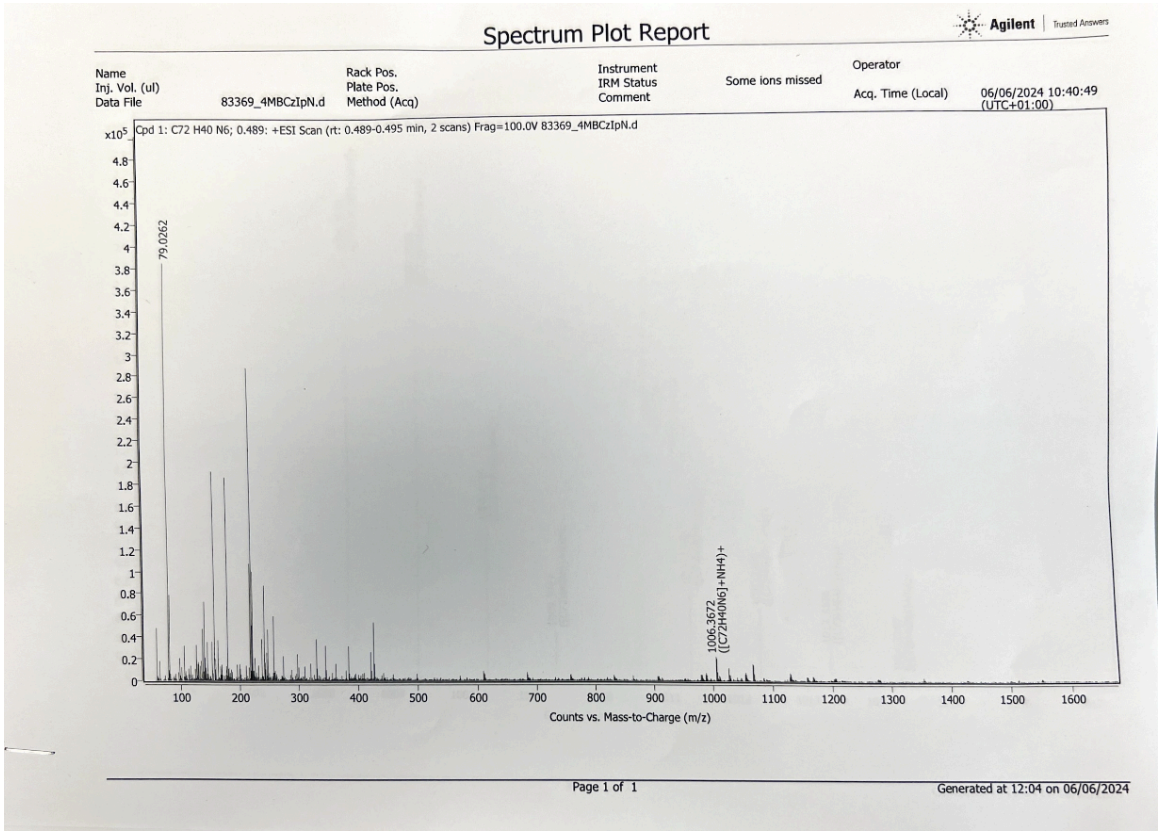
δ_H (400 MHz, CD_2Cl_2) 8.93 (1 H, d, *J* 8.4), 8.80 (1 H, d, *J* 8.0), 8.46 (2 H, d, *J* 8.7), 8.34 – 8.27 (1 H, m), 8.25 (2 H, d, *J* 7.6), 8.20 (1 H, d, *J* 8.3), 8.09 (1 H, d, *J* 8.3), 8.05 – 7.86 (4 H, m), 7.83 (3 H, t, *J* 7.2), 7.75 – 7.68 (2 H, m), 7.63 (4 H, t, *J* 4.2), 7.58 (3 H, td), 7.55 – 7.49 (2 H, m), 7.47 – 7.35 (4 H, m), 7.34 – 7.13 (7 H, m), 6.93 (1 H, hept), 6.75 (1 H, ttd).

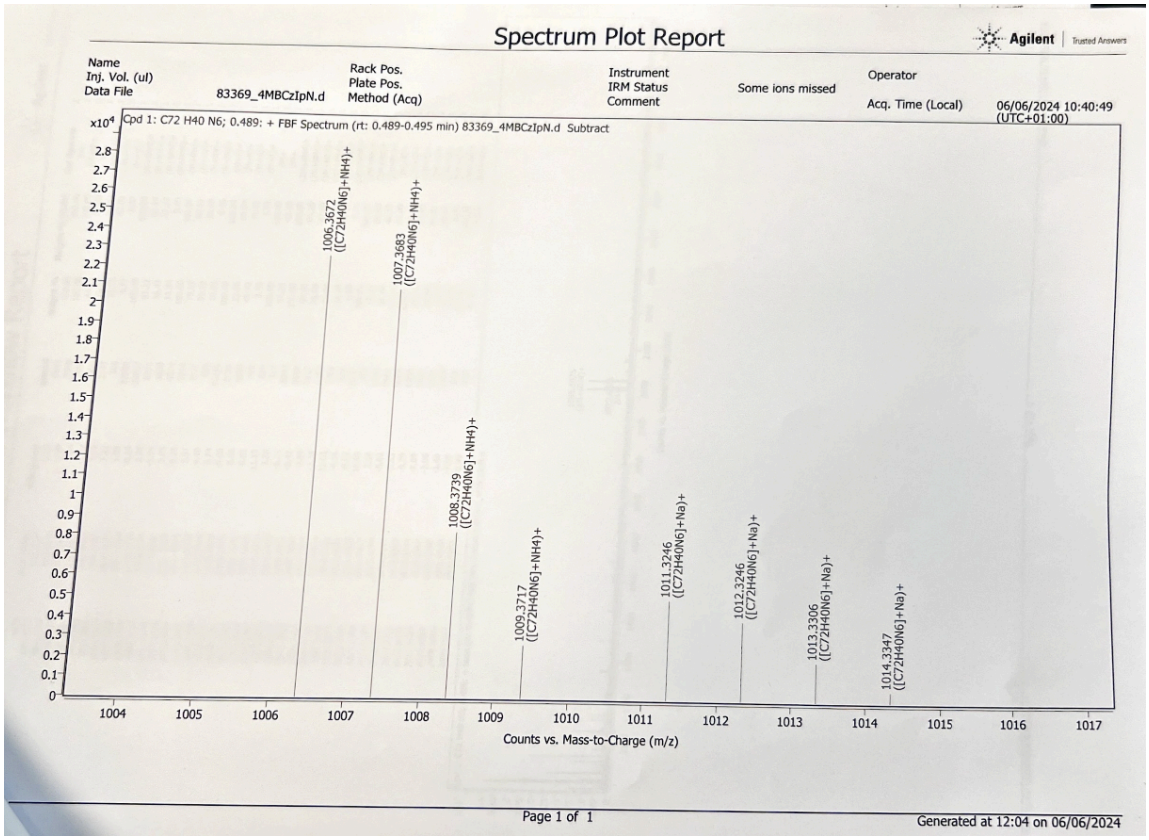
^{13}C NMR

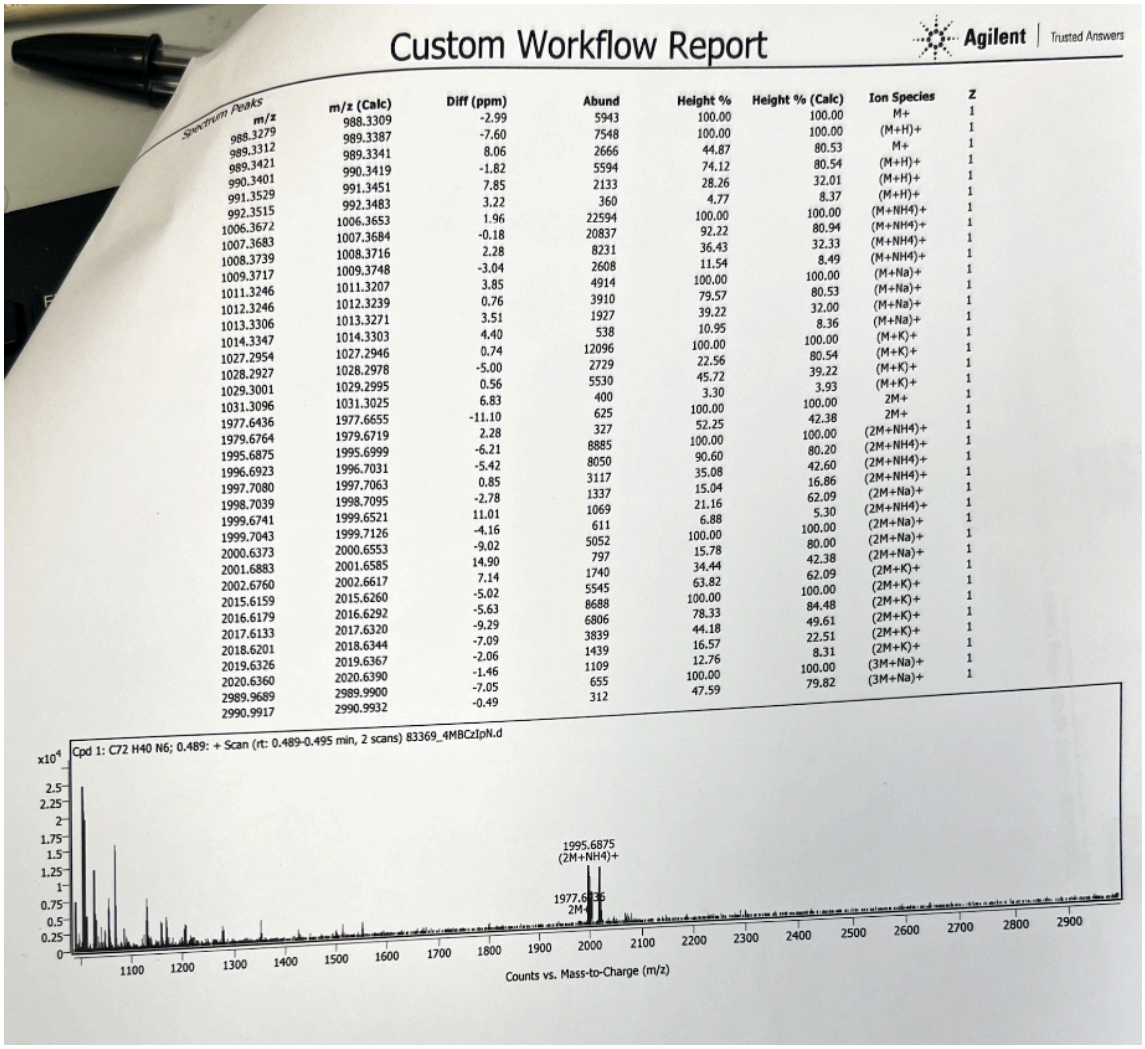


δ_C (101 MHz, CD_2Cl_2) 145.88, 145.16, 139.65, 138.18, 138.13, 138.05, 137.16, 136.74, 136.63, 135.73, 130.89, 130.45, 130.13, 129.96, 129.90, 129.49, 129.46, 129.25, 129.17, 129.02, 128.30, 127.91, 127.76, 127.24, 126.80, 126.26, 125.89, 125.44, 125.14, 125.08, 124.97, 124.86, 124.57, 124.13, 124.09, 123.69, 123.67, 123.61, 123.52, 123.29, 123.00, 122.81, 122.21, 122.11, 118.26, 117.89, 117.27, 111.91, 111.21, 110.80, 110.73, 110.54, 110.42.

MS


Spectrum Plot Report
Agilent | Trusted Answers
Name
Inj. Vol. (ul)
Data File 83369_4MBCzIpN.d
Rack Pos.
Plate Pos.
Method (Acq)
Instrument
IRM Status
Comment
Some ions missed
Operator
Acq. Time (Local) 06/06/2024 10:40:49 (UTC+01:00)
Cpd 1: C72 H40 N6; 0.489: +ESI Scan (rt: 0.489-0.495 min, 2 scans) Frag=100.0V 83369_4MBCzIpN.d
x10^5
79.0262
1006.3672 ((C72H40N6)+NH4)+
Counts vs. Mass-to-Charge (m/z)
Page 1 of 1
Generated at 12:04 on 06/06/2024


Spectrum Plot Report
Agilent | Trusted Answers
Name
Inj. Vol. (ul)
Data File 83369_4MBCzIpN.d
Rack Pos.
Plate Pos.
Method (Acq)
Instrument
IRM Status
Comment
Some ions missed
Operator
Acq. Time (Local) 06/06/2024 10:40:49 (UTC+01:00)
Cpd 1: C72 H40 N6; 0.489: + FBF Spectrum (rt: 0.489-0.495 min) 83369_4MBCzIpN.d Subtract
x10^4
1006.3672 ((C72H40N6)+NH4)+
1007.3683 ((C72H40N6)+NH4)+
1008.3739 ((C72H40N6)+NH4)+
1009.3717 ((C72H40N6)+NH4)+
1011.3246 ((C72H40N6)+Na)+
1012.3246 ((C72H40N6)+Na)+
1013.3306 ((C72H40N6)+Na)+
1014.3347 ((C72H40N6)+Na)+
Counts vs. Mass-to-Charge (m/z)
Page 1 of 1
Generated at 12:04 on 06/06/2024



Custom Workflow Report

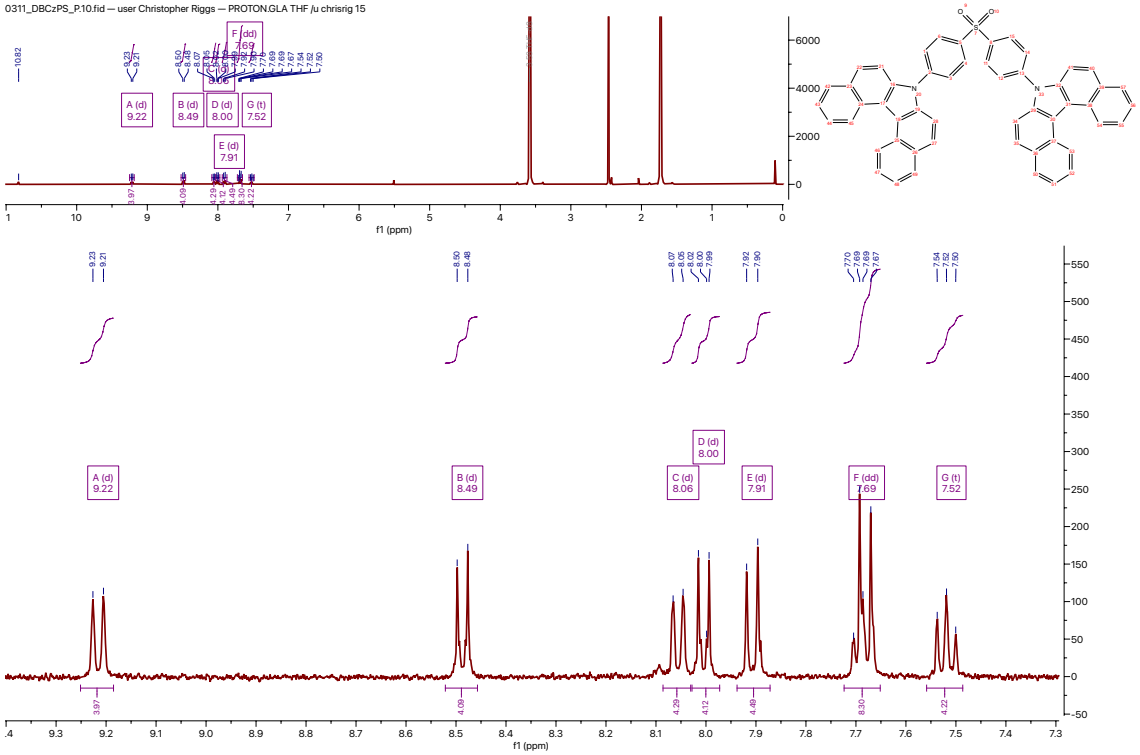
Agilent | Trusted Answers

Spectrum Peaks

m/z	m/z (Calc)	Diff (ppm)	Abund	Height %	Height % (Calc)	Ion Species	z
988.3279	988.3309	-2.99	5943	100.00	100.00	M+	1
989.3312	989.3387	-7.60	7548	100.00	100.00	(M+H)+	1
989.3421	989.3341	8.06	2666	44.87	80.53	M+	1
990.3401	990.3419	-1.82	5594	74.12	80.54	(M+H)+	1
991.3529	991.3451	7.85	2133	28.26	32.01	(M+H)+	1
992.3515	992.3483	3.22	360	4.77	8.37	(M+H)+	1
1006.3672	1006.3653	1.96	22594	100.00	100.00	(M+NH4)+	1
1007.3683	1007.3684	-0.18	20837	92.22	80.94	(M+NH4)+	1
1008.3739	1008.3716	2.28	8231	36.43	32.33	(M+NH4)+	1
1009.3717	1009.3748	-3.04	2608	11.54	8.49	(M+NH4)+	1
1011.3246	1011.3207	3.85	4914	100.00	100.00	(M+Na)+	1
1012.3246	1012.3239	0.76	3910	79.57	80.53	(M+Na)+	1
1013.3306	1013.3271	3.51	1927	39.22	32.00	(M+Na)+	1
1014.3347	1014.3303	4.40	538	10.95	8.36	(M+Na)+	1
1027.2954	1027.2946	0.74	12096	100.00	100.00	(M+K)+	1
1028.2927	1028.2978	-5.00	2729	22.56	80.54	(M+K)+	1
1029.3001	1029.2995	0.56	5530	45.72	39.22	(M+K)+	1
1031.3096	1031.3025	6.83	400	3.30	3.93	(M+K)+	1
1977.6436	1977.6655	-11.10	625	100.00	100.00	2M+	1
1979.6764	1979.6719	2.28	327	52.25	42.38	2M+	1
1995.6875	1995.6999	-6.21	8885	100.00	100.00	(2M+NH4)+	1
1996.6923	1996.7031	-5.42	8050	90.60	80.20	(2M+NH4)+	1
1997.7080	1997.7063	0.85	3117	35.08	42.60	(2M+NH4)+	1
1998.7039	1998.7095	-2.78	1337	15.04	16.86	(2M+NH4)+	1
1999.6741	1999.6521	11.01	1069	21.16	62.09	(2M+Na)+	1
1999.7043	1999.7126	-4.16	611	6.88	5.30	(2M+NH4)+	1
2000.6373	2000.6553	-9.02	5052	100.00	100.00	(2M+Na)+	1
2001.6883	2001.6585	14.90	797	15.78	80.00	(2M+Na)+	1
2002.6760	2002.6617	7.14	1740	34.44	42.38	(2M+Na)+	1
2015.6159	2015.6260	-5.02	5545	63.82	62.09	(2M+K)+	1
2016.6179	2016.6292	-5.63	8688	100.00	100.00	(2M+K)+	1
2017.6133	2017.6320	-9.29	6806	78.33	84.48	(2M+K)+	1
2018.6201	2018.6344	-7.09	3839	44.18	49.61	(2M+K)+	1
2019.6326	2019.6367	-2.06	1439	16.57	22.51	(2M+K)+	1
2020.6360	2020.6390	-1.46	1109	12.76	8.31	(2M+K)+	1
2989.9689	2989.9900	-7.05	655	100.00	100.00	(3M+Na)+	1
2990.9917	2990.9932	-0.49	312	47.59	79.82	(3M+Na)+	1

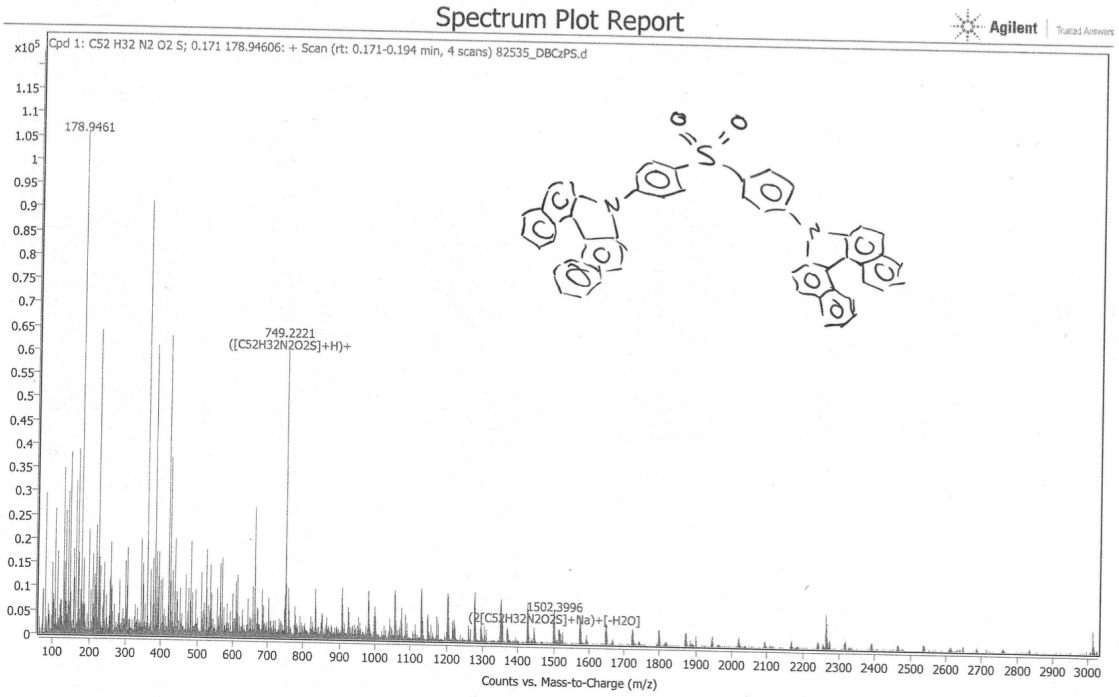
9.17.4 DBCz-PS (21)

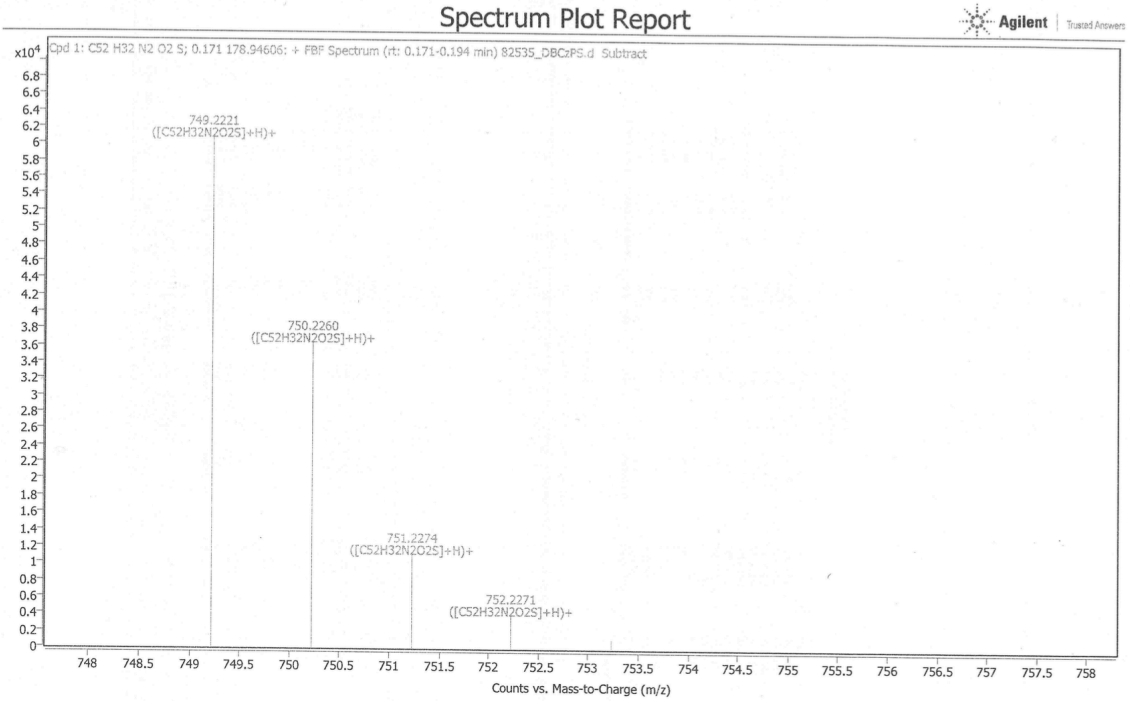
^{1}H NMR



δ_{H} (400 MHz, THF) 9.22 (4 H, d, *J* 8.5), 8.49 (4 H, d, *J* 8.5), 8.06 (4 H, d, *J* 8.0), 8.00 (4 H, d, *J* 8.5), 7.91 (4 H, d, *J* 8.9), 7.69 (8 H, dd, *J* 8.2, 5.6), 7.52 (4 H, t, *J* 7.4).

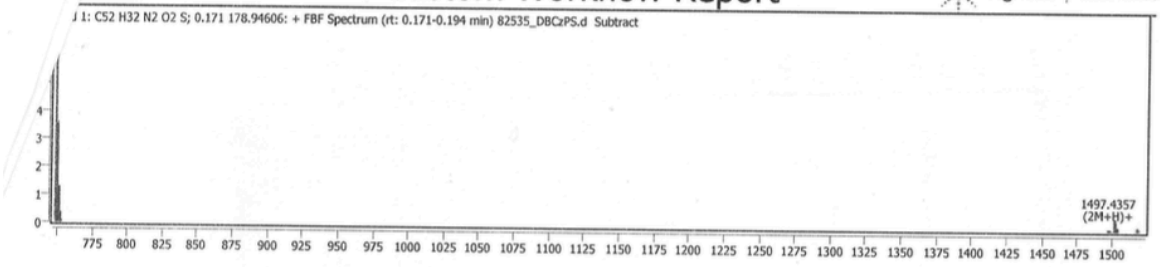
MS


Spectrum Plot Report
Agilent
Cpd 1: C52 H32 N2 O2 S; 0.171 178.94606: + Scan (rt: 0.171-0.194 min, 4 scans) 82535_DBCzPS.d
x10^5
178.9461
749.2221
([C52H32N2O2S]+H)+
1502.3996
(2[C52H32N2O2S]+Na)+[-H2O]
Counts vs. Mass-to-Charge (m/z)


Spectrum Plot Report
Agilent
Cpd 1: C52 H32 N2 O2 S; 0.171 178.94606: + FBF Spectrum (rt: 0.171-0.194 min) 82535_DBCzPS.d Subtract
x10^4
749.2221
([C52H32N2O2S]+H)+
750.2260
([C52H32N2O2S]+H)+
751.2274
([C52H32N2O2S]+H)+
752.2271
([C52H32N2O2S]+H)+
Counts vs. Mass-to-Charge (m/z)

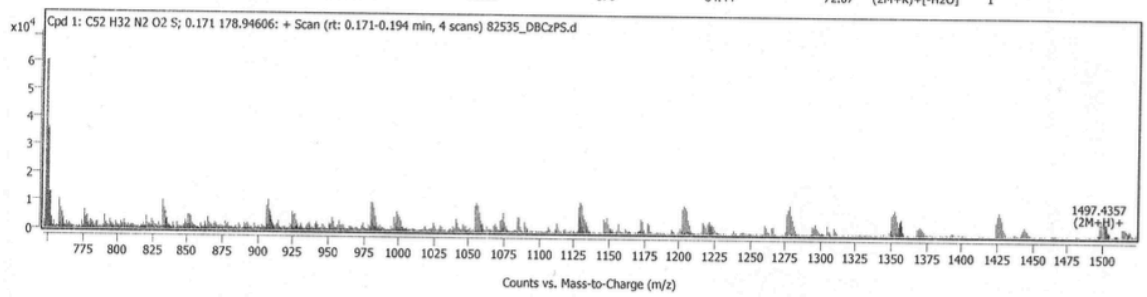
Custom Workflow Report

Agilent | Trusted Answers



Spectrum Peaks

m/z	m/z (Calc)	Diff (ppm)	Abund	Height %	Height % (Calc)	Ion Species	z
749.2221	749.2257	-4.80	60692	100.00	100.00	(M+H)+	1
750.2260	750.2290	-3.95	36327	59.85	58.22	(M+H)+	1
751.2274	751.2299	-3.41	11047	18.20	21.52	(M+H)+	1
752.2271	752.2307	-4.82	3849	6.34	5.92	(M+H)+	1
753.2313	753.2321	-1.08	1014	1.67	1.25	(M+H)+	1
1497.4357	1497.4442	-5.64	367	47.25	85.89	(2M+H)+	1
1498.4420	1498.4474	-3.63	777	100.00	100.00	(2M+H)+	1
1499.4540	1499.4494	3.09	491	63.17	66.07	(2M+H)+	1
1500.4589	1500.4508	5.39	274	35.32	31.69	(2M+H)+	1
1502.3996	1502.4188	-12.80	4135	100.00	100.00	(2M+Na)+[-H2O]	1
1503.3993	1503.4208	-14.29	3514	84.99	65.87	(2M+Na)+[-H2O]	1
1504.4094	1504.4222	-8.52	684	16.55	31.45	(2M+Na)+[-H2O]	1
1518.4101	1518.3927	11.41	1351	100.00	100.00	(2M+K)+[-H2O]	1
1519.4247	1519.3941	20.11	870	64.44	72.07	(2M+K)+[-H2O]	1



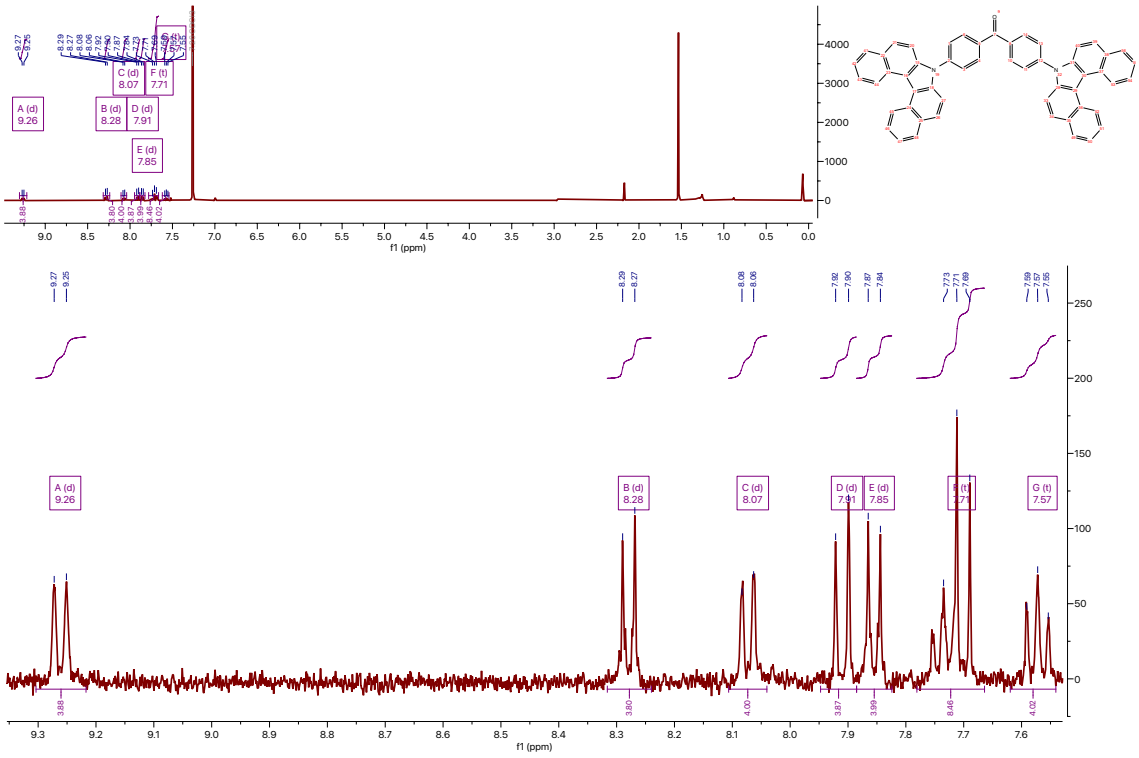
Spectrum Peaks

m/z	m/z (Calc)	Diff (ppm)	Abund	Height %	Height % (Calc)	Ion Species	z
749.2221	749.2257	-4.80	60692	100.00	100.00	(M+H)+	1
750.2260	750.2290	-3.95	36327	59.85	58.22	(M+H)+	1
751.2274	751.2299	-3.41	11047	18.20	21.52	(M+H)+	1
752.2271	752.2307	-4.82	3849	6.34	5.92	(M+H)+	1
753.2313	753.2321	-1.08	1014	1.67	1.25	(M+H)+	1
1497.4357	1497.4442	-5.64	367	47.25	85.89	(2M+H)+	1
1498.4420	1498.4474	-3.63	777	100.00	100.00	(2M+H)+	1
1499.4540	1499.4494	3.09	491	63.17	66.07	(2M+H)+	1
1500.4589	1500.4508	5.39	274	35.32	31.69	(2M+H)+	1
1502.3996	1502.4188	-12.80	4135	100.00	100.00	(2M+Na)+[-H2O]	1
1503.3993	1503.4208	-14.29	3514	84.99	65.87	(2M+Na)+[-H2O]	1
1504.4094	1504.4222	-8.52	684	16.55	31.45	(2M+Na)+[-H2O]	1
1518.4101	1518.3927	11.41	1351	100.00	100.00	(2M+K)+[-H2O]	1
1519.4247	1519.3941	20.11	870	64.44	72.07	(2M+K)+[-H2O]	1
178.9461			105737				

MassHunter Qual 10.0
(End of Report)

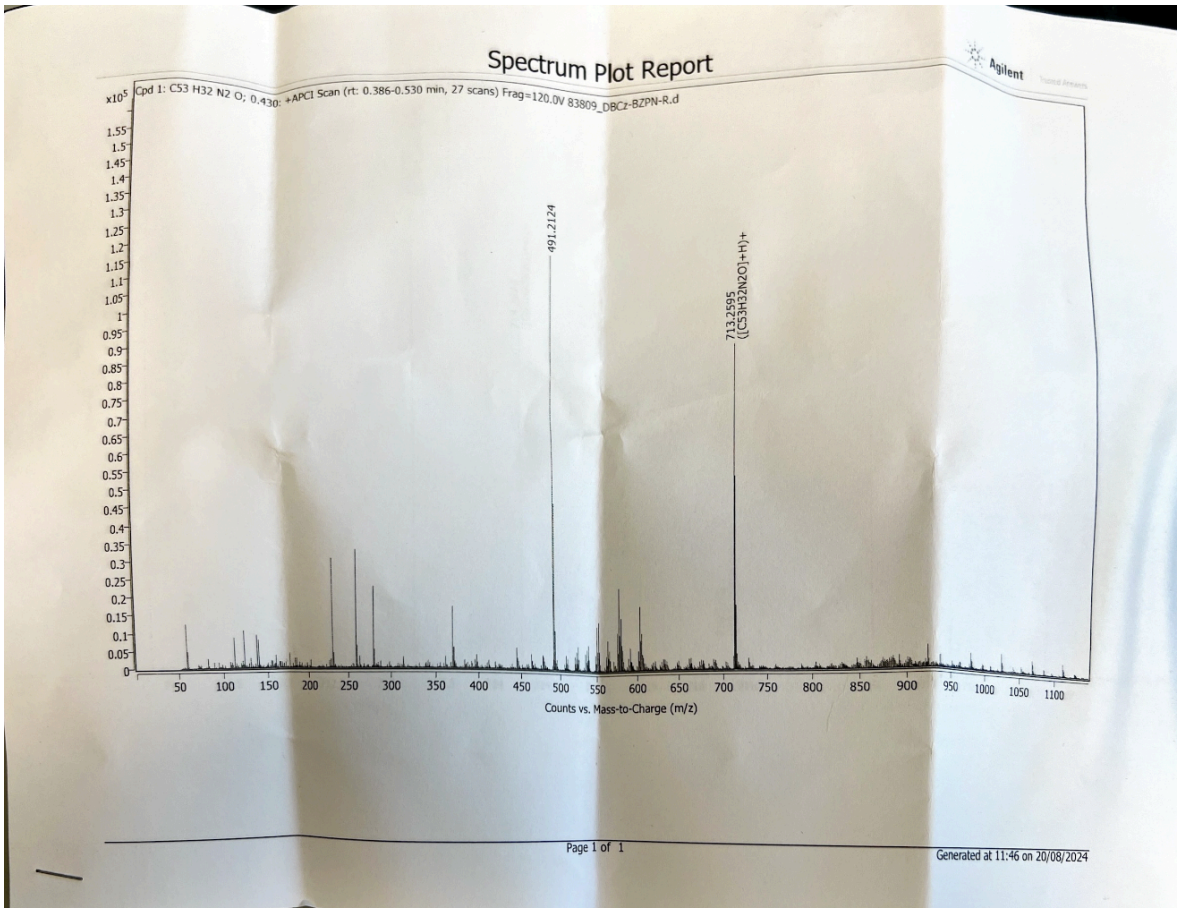
9.17.5 DBCz-BZPN (22)

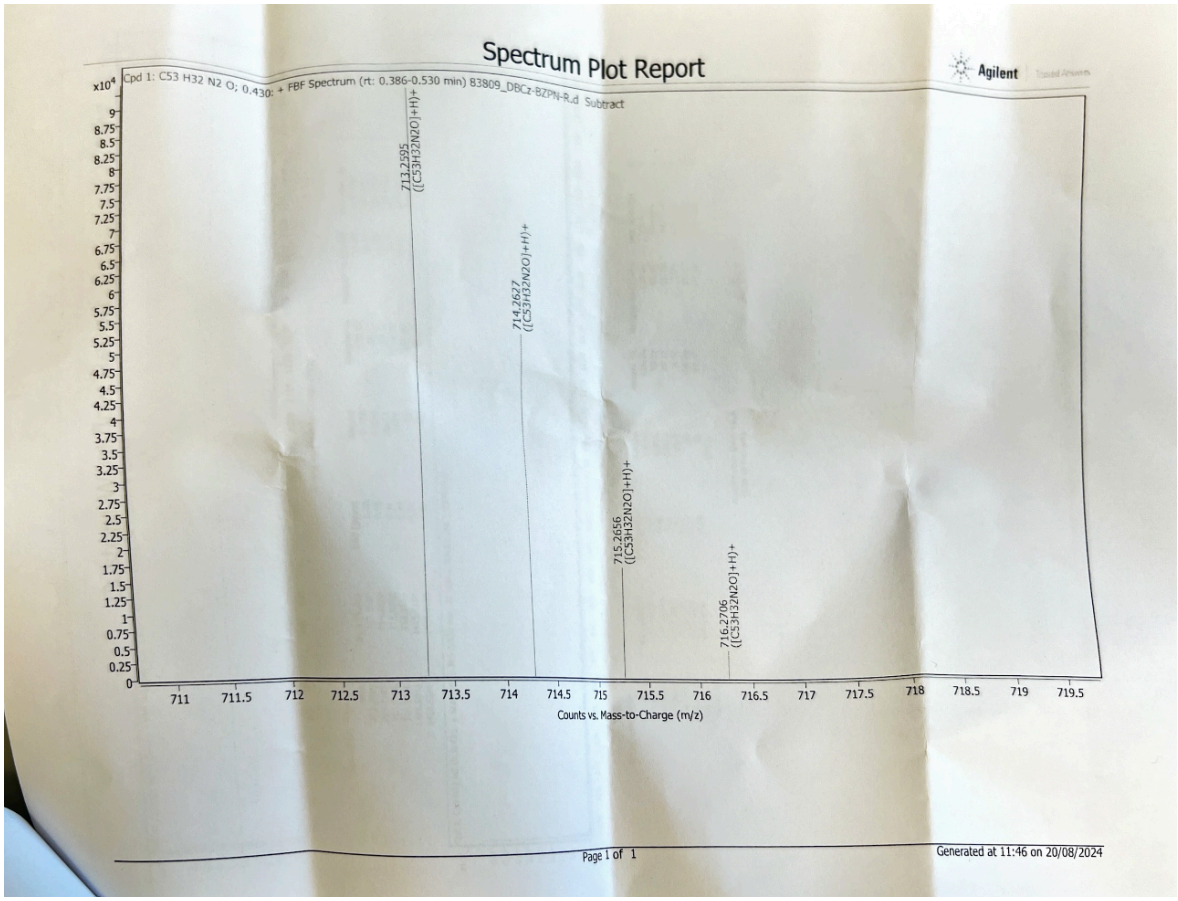
^{1}H NMR



δ_H (400 MHz, $CDCl_3$) 9.26 (4 H, d, *J* 8.5), 8.28 (4 H, d, *J* 8.4), 8.07 (4 H, d, *J* 8.1), 7.91 (4 H, d, *J* 8.9), 7.85 (4 H, d, *J* 8.4), 7.71 (8 H, t, *J* 9.1), 7.57 (4 H, t, *J* 7.4).

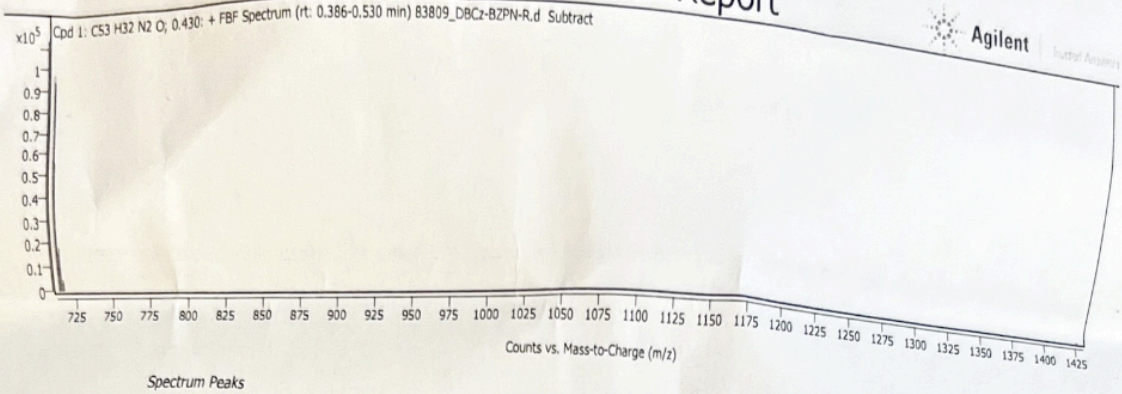
MS


Spectrum Plot Report
Agilent
Cpd 1: C53 H32 N2 O; 0.430: +APCI Scan (rt: 0.386-0.530 min, 27 scans) Frag=120.0V 83809_DBCz-BZPN-R.d
x10^5
491.2124
713.2595
((C53H32N2O)+H)+
Counts vs. Mass-to-Charge (m/z)
Page 1 of 1
Generated at 11:46 on 20/08/2024


Spectrum Plot Report
Agilent
Cpd 1: C53 H32 N2 O; 0.430: + FBF Spectrum (rt: 0.386-0.530 min) B3809_DBCz-BZPN-R.d Subtract
x10^4
713.2593
([C53H32N2O]+H)+
714.2627
([C53H32N2O]+H)+
715.2656
([C53H32N2O]+H)+
716.2706
([C53H32N2O]+H)+
Counts vs. Mass-to-Charge (m/z)
Page 1 of 1
Generated at 11:46 on 20/08/2024

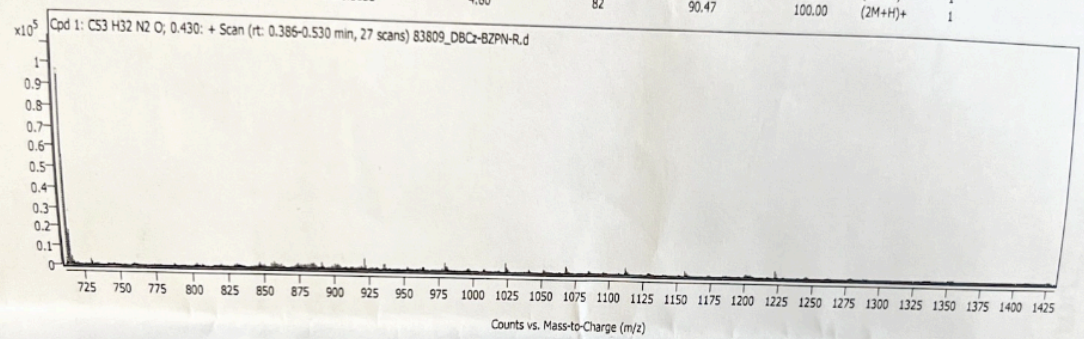
Custom Workflow Report

Agilent



Spectrum Peaks

m/z	m/z (Calc)	Diff (ppm)	Abund	Height %	Height % (Calc)	Ion Species	z
713.2595	713.2587	1.10	94268	100.00	100.00	(M+H)+	1
714.2627	714.2620	0.88	55636	59.02	58.47	(M+H)+	1
715.2656	715.2653	0.41	18212	19.32	16.99	(M+H)+	1
716.2706	716.2685	2.90	4473	4.75	3.27	(M+H)+	1
1425.5043	1425.5102	-4.14	90	100.00	85.52	(2M+H)+	1
1426.5201	1426.5135	4.60	82	90.47	100.00	(2M+H)+	1



Spectrum Peaks

m/z	m/z (Calc)	Diff (ppm)	Abund	Height %	Height % (Calc)	Ion Species	z
713.2595	713.2587	1.10	94268	100.00	100.00	(M+H)+	1
714.2627	714.2620	0.88	55636	59.02	58.47	(M+H)+	1
715.2656	715.2653	0.41	18212	19.32	16.99	(M+H)+	1
716.2706	716.2685	2.90	4473	4.75	3.27	(M+H)+	1
1425.5043	1425.5102	-4.14	90	100.00	85.52	(2M+H)+	1
1426.5201	1426.5135	4.60	82	90.47	100.00	(2M+H)+	1
491.2124			120530				

MassHunter Qual 10.0
(End of Report)

Appendix 4 – Crystallography data

All structures herein solved by Dr Laura J. McCormick McPherson of the University of Southampton.

9.18 Chapter 4

9.18.1 IMDB (1)

Table 9-1Crystal data and structural refinement details of IMSB-DMB (1)

Compound	**2023NCS0403_1a**
Formula	$C_{32}H_{32}BN$
$D_{calc.}$/ g cm^{-3}	1.188
μ/mm^{-1}	0.067
Formula Weight	441.39
Colour	colourless
Shape	prism-shaped
Size/mm^3	0.33◊0.21◊0.12
T/K	100(2)
Crystal System	monoclinic
Space Group	$P2_1/n$
a/≈	8.17240(10)
b/≈	14.6608(2)
c/≈	20.6431(3)
α/°	90
β/°	93.4960(10)
γ/°	90
V/≈^{3}	2468.73(6)
Z	4
Z'	1
Wavelength/≈	0.71073
Radiation type	Mo K_α
Θ_{min}/°	1.705
Θ_{max}/°	33.271
Measured Refl's.	65954
Indep't Refl's	8812
Refl's I≥2 σ(I)	7597
R_{int}	0.0271
Parameters	313
Restraints	0
Largest Peak	0.452
Deepest Hole	-0.283
GooF	1.046
wR_2 (all data)	0.1243
wR_2	0.1202
R_1 (all data)	0.0496
R_1	0.0428

Table 9-2 Fractional Atomic Coordinates (×10^4) and Equivalent Isotropic Displacement Parameters (Å2×10^3) for IMSB-DMB (1). U_{eq} is defined as 1/3 of the trace of the orthogonalised U_{ij}.

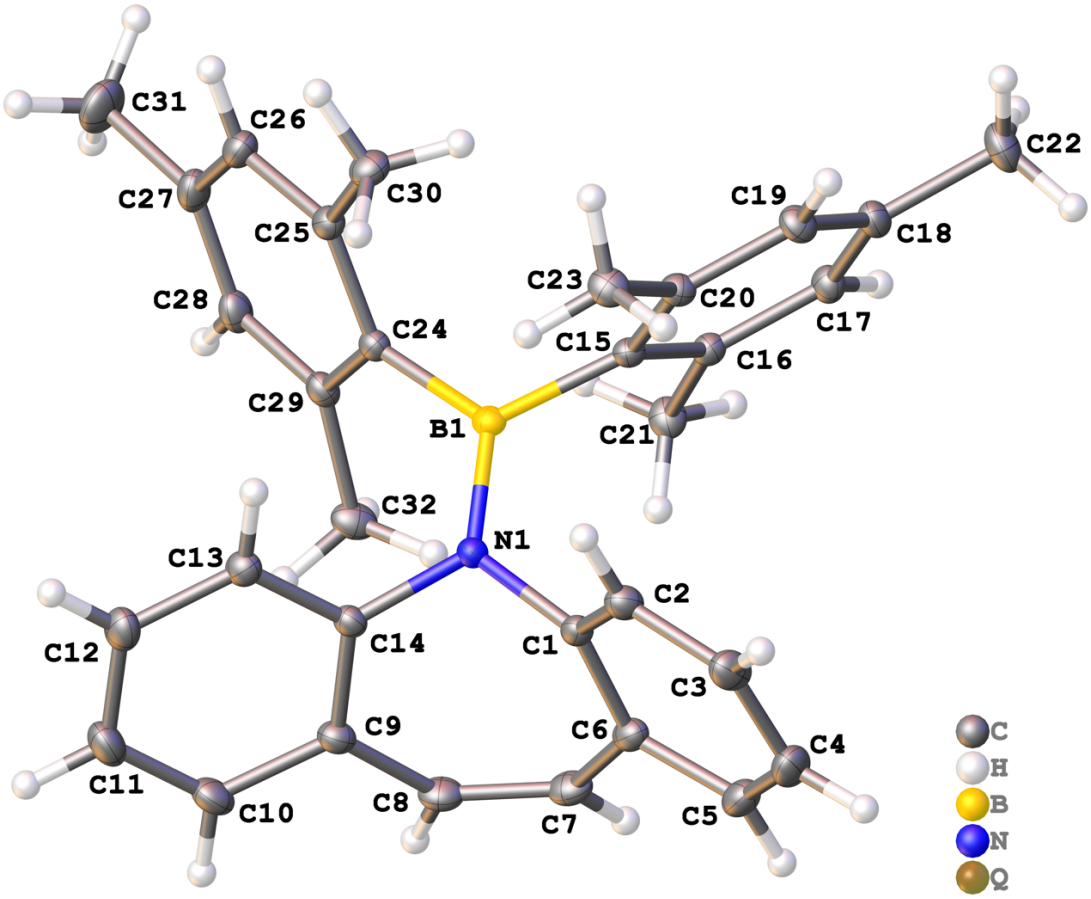
Atom	x	y	z	U_{eq}
N1	5479.1(8)	4240.6(4)	2262.5(3)	12.19(12)
C1	5775.3(9)	4960.0(5)	2736.7(4)	13.39(13)
C2	6790.2(10)	4798.8(6)	3289.5(4)	16.71(15)
C3	6999.9(12)	5457.9(6)	3771.9(4)	21.63(17)
C4	6176.1(12)	6284.0(6)	3703.7(4)	23.92(18)
C5	5215.8(11)	6461.6(6)	3143.3(4)	20.90(16)
C6	5046.8(10)	5819.9(5)	2639.0(4)	15.96(14)
C7	4256.0(10)	6109.2(5)	2018.9(4)	18.76(15)
C8	4721.8(11)	5851.0(6)	1433.9(4)	19.11(15)
C9	5960.7(10)	5169.6(5)	1291.9(4)	15.98(14)
C10	6765.2(11)	5257.1(6)	712.6(4)	21.17(16)
C11	7873.5(12)	4610.9(7)	523.1(4)	23.66(17)
C12	8203.2(11)	3848.5(6)	912.4(4)	20.85(16)
C13	7426.3(10)	3744.2(5)	1488.4(4)	15.73(14)
C14	6307.4(9)	4393.9(5)	1678.0(4)	13.24(13)
C15	3722.1(9)	3336.5(5)	3062.1(3)	12.12(13)
C16	2051.5(9)	3593.4(5)	3086.7(4)	13.19(13)
C17	1213.3(10)	3458.5(5)	3646.0(4)	15.58(14)
C18	1959.2(10)	3065.5(6)	4202.3(4)	16.38(14)
C19	3598.9(10)	2829.4(6)	4186.2(4)	16.74(15)
C20	4491.7(9)	2963.2(5)	3634.1(4)	14.03(13)
C21	1143.3(10)	4029.6(6)	2510.1(4)	17.03(15)
C22	1001.4(12)	2913.6(7)	4794.6(4)	23.80(18)
C23	6277.6(10)	2681.6(6)	3706.6(4)	17.55(15)
C24	4049.4(9)	2742.5(5)	1803.4(4)	12.86(13)
C25	4404.2(9)	1799.3(5)	1886.5(4)	14.71(14)
C26	3846.2(10)	1160.3(6)	1425.1(4)	18.36(15)
C27	2905.6(11)	1407.4(6)	868.0(4)	19.75(16)
C28	2588.1(10)	2328.0(6)	775.2(4)	18.15(15)
C29	3150.0(9)	2994.0(5)	1221.2(4)	14.69(14)
C30	5432.8(10)	1448.8(6)	2463.4(4)	18.27(15)
C31	2277.6(14)	693.6(7)	391.1(5)	30.2(2)
C32	2763.3(10)	3968.3(6)	1033.3(4)	18.99(15)
B1	4514.4(10)	3456.4(6)	2375.6(4)	12.03(14)

Table 9-3 Anisotropic Displacement Parameters (×10^4) for IMSB-DMB (1) The anisotropic displacement factor exponent takes the form: $-2\pi^2[h^2a^{*2} \times U_{11} + \ldots + 2hka^* \times b^* \times U_{12}]$

Atom	U_{11}	U_{22}	U_{33}	U_{23}	U_{13}	U_{12}
N^1	13.5(3)	11.3(3)	12.0(3)	0.2(2)	2.3(2)	-0.4(2)
C^1	14.0(3)	11.8(3)	14.8(3)	-0.8(2)	3.5(2)	-1.8(2)
C^2	18.4(3)	15.4(3)	16.4(3)	0.6(3)	1.1(3)	-2.6(3)
C^3	27.4(4)	21.3(4)	16.1(3)	-1.6(3)	0.7(3)	-6.8(3)
C^4	31.4(5)	19.6(4)	21.3(4)	-6.9(3)	6.1(3)	-6.0(3)
C^5	23.2(4)	14.7(3)	25.5(4)	-4.1(3)	7.0(3)	-1.0(3)
C^6	15.3(3)	12.8(3)	20.2(3)	-0.7(3)	4.7(3)	-0.3(3)
C^7	17.7(3)	13.1(3)	25.4(4)	2.0(3)	1.1(3)	2.1(3)
C^8	21.2(4)	14.5(3)	21.5(4)	4.9(3)	-0.3(3)	1.2(3)
C^9	17.9(3)	14.5(3)	15.6(3)	2.1(3)	1.3(3)	-1.6(3)
C^{10}	26.1(4)	20.8(4)	17.0(3)	4.6(3)	3.9(3)	-4.2(3)
C^{11}	26.0(4)	27.4(4)	18.5(4)	0.4(3)	8.5(3)	-4.9(3)
C^{12}	18.8(4)	22.7(4)	21.9(4)	-3.1(3)	7.4(3)	-1.7(3)
C^{13}	14.6(3)	15.3(3)	17.6(3)	-0.3(3)	2.7(3)	-0.4(3)
C^{14}	13.2(3)	13.4(3)	13.3(3)	0.8(2)	2.1(2)	-1.6(2)
C^{15}	13.2(3)	10.5(3)	12.7(3)	0.2(2)	1.1(2)	-0.7(2)
C^{16}	13.8(3)	12.1(3)	13.6(3)	-0.6(2)	0.6(2)	0.0(2)
C^{17}	14.0(3)	16.7(3)	16.2(3)	-1.1(3)	3.1(3)	0.3(3)
C^{18}	18.8(3)	17.2(3)	13.4(3)	-0.5(3)	4.0(3)	-1.9(3)
C^{19}	18.7(3)	18.3(3)	13.2(3)	2.4(3)	0.8(3)	-0.6(3)
C^{20}	14.7(3)	13.4(3)	14.0(3)	1.2(2)	0.4(2)	-0.5(2)
C^{21}	15.2(3)	19.8(4)	15.9(3)	1.3(3)	-0.2(3)	3.5(3)
C^{22}	24.2(4)	32.0(5)	15.9(3)	1.6(3)	7.1(3)	-1.1(3)
C^{23}	15.4(3)	19.1(4)	17.9(3)	2.8(3)	-0.9(3)	1.6(3)
C^{24}	12.9(3)	12.7(3)	13.2(3)	0.1(2)	3.0(2)	-1.0(2)
C^{25}	14.8(3)	13.5(3)	16.2(3)	-0.7(2)	4.1(2)	0.0(2)
C^{26}	20.7(4)	14.9(3)	19.9(3)	-3.7(3)	5.2(3)	-0.9(3)
C^{27}	21.6(4)	21.2(4)	16.9(3)	-6.2(3)	4.8(3)	-3.4(3)
C^{28}	19.0(3)	23.0(4)	12.6(3)	-2.5(3)	2.4(3)	-3.1(3)
C^{29}	14.4(3)	16.7(3)	13.2(3)	0.8(2)	2.8(2)	-1.8(3)
C^{30}	20.3(4)	13.8(3)	20.6(3)	-0.1(3)	0.8(3)	2.4(3)
C^{31}	36.9(5)	28.0(5)	25.5(4)	-13.1(4)	-0.3(4)	-4.1(4)
C^{32}	19.8(4)	19.0(4)	17.6(3)	4.6(3)	-2.9(3)	-2.0(3)
B^1	11.7(3)	10.8(3)	13.6(3)	1.5(3)	0.7(3)	0.8(3)

Table 9-4 Bond Angles in Å for IMDB-DMB (1).

Atom	Atom	Length/≈
N^{1}	C^{1}	1.4493(10)
N^{1}	C^{14}	1.4367(9)
N^{1}	B^{1}	1.4214(10)
C^{1}	C^{2}	1.3894(11)
C^{1}	C^{6}	1.4035(11)
C^{2}	C^{3}	1.3907(11)
C^{3}	C^{4}	1.3886(14)
C^{4}	C^{5}	1.3826(13)
C^{5}	C^{6}	1.4036(11)
C^{6}	C^{7}	1.4613(12)
C^{7}	C^{8}	1.3427(12)
C^{8}	C^{9}	1.4647(12)
C^{9}	C^{10}	1.4053(11)
C^{9}	C^{14}	1.4076(10)
C^{10}	C^{11}	1.3836(13)
C^{11}	C^{12}	1.3933(13)
C^{12}	C^{13}	1.3902(11)
C^{13}	C^{14}	1.3929(11)
C^{15}	C^{16}	1.4202(10)
C^{15}	C^{20}	1.4136(10)
C^{15}	B^{1}	1.6033(11)
C^{16}	C^{17}	1.3919(10)
C^{16}	C^{21}	1.5064(11)
C^{17}	C^{18}	1.3918(11)
C^{18}	C^{19}	1.3864(11)
C^{18}	C^{22}	1.5080(11)
C^{19}	C^{20}	1.4040(11)
C^{20}	C^{23}	1.5154(11)
C^{24}	C^{25}	1.4211(11)
C^{24}	C^{29}	1.4188(10)
C^{24}	B^{1}	1.6062(11)
C^{25}	C^{26}	1.3927(11)
C^{25}	C^{30}	1.5055(11)
C^{26}	C^{27}	1.3917(12)
C^{27}	C^{28}	1.3855(12)
C^{27}	C^{31}	1.5054(12)
C^{28}	C^{29}	1.4002(11)
C^{29}	C^{32}	1.5084(11)


C31
C26
C27
C30
C25
C28
C24
C29
B1
C32
N1
C13
C14
C12
C1
C2
C3
C9
C6
C4
C11
C10
C8
C7
C5
C22
C19
C18
C23
C20
C17
C15
C16
C21
C
H
B
N
Q

9.18.2 DBCz-DMB (3)

Table 9-5 Crystal data and structural refinement details of DBCz-DMB (3)

Compound	**2023NCS0405_1a_tw in1_hklf4**
Formula	$C_{38}H_{34}BN$
$D_{calc.}$/ g cm^{-3}	1.210
μ/mm^{-1}	0.516
Formula Weight	515.47
Colour	colourless
Shape	rod-shaped
Size/mm^3	0.43×0.06×0.04
T/K	100(2)
Crystal System	monoclinic
Space Group	$P2_1/n$
a/Å	9.62010(10)
b/Å	13.94030(10)
c/Å	21.2227(2)
α/°	90
β/°	96.0430(10)
γ/°	90
V/Å^3	2830.30(4)
Z	4
Z'	1
Wavelength/Å	1.54184
Radiation type	Cu K$_\alpha$
Θ_{min}/°	3.800
Θ_{max}/°	77.001
Measured Refl's.	12564
Indep't Refl's	12564
Refl's I≥2 σ(I)	11535
R_{int}	.
Parameters	368
Restraints	0
Largest Peak	0.202
Deepest Hole	-0.315
GooF	1.067
wR_2 (all data)	0.1562
wR_2	0.1525
R_1 (all data)	0.0545
R_1	0.0515

Table 9-6 Fractional Atomic Coordinates (×10^4) and Equivalent Isotropic Displacement Parameters (Å2×10^3) for DBCz-DMB (3). U_{eq} is defined as 1/3 of the trace of the orthogonalised U_{ij}.

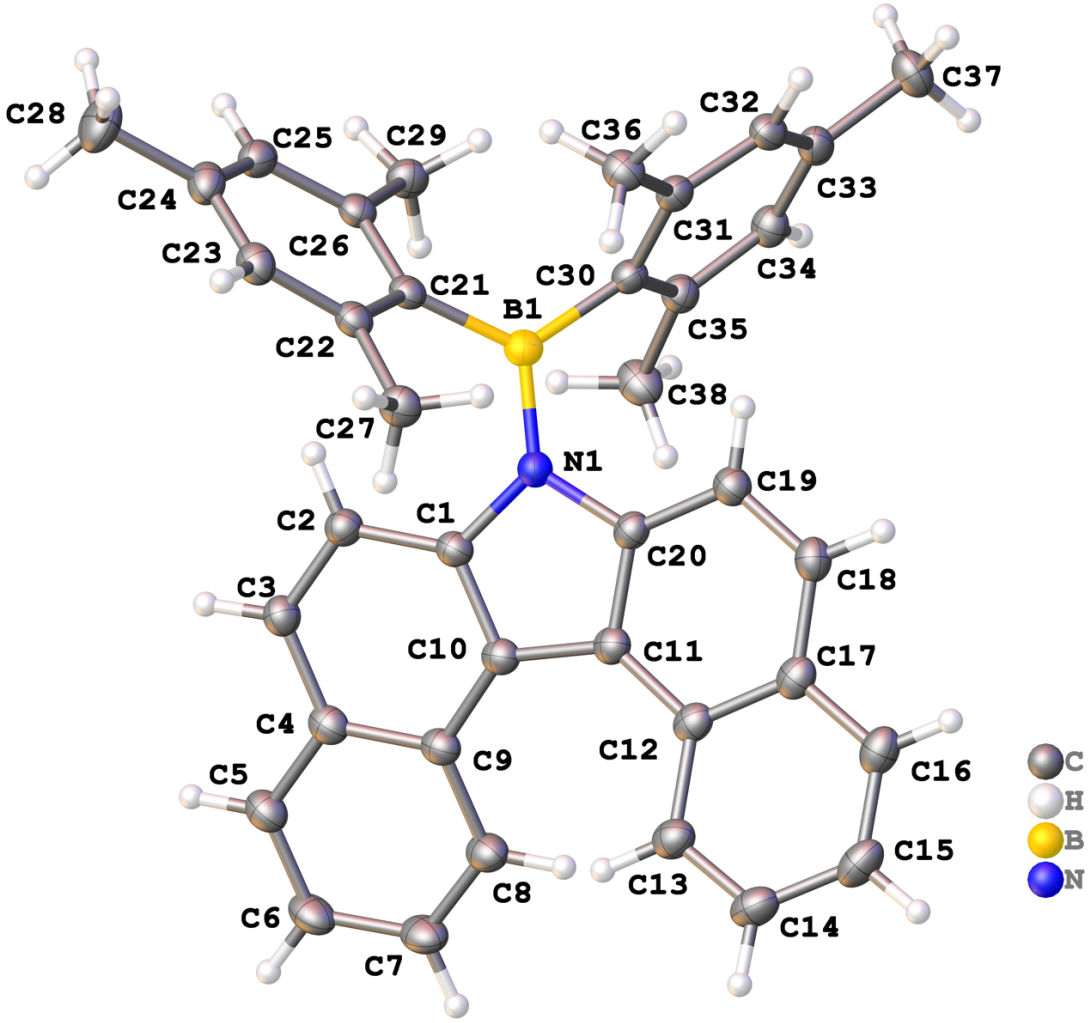
Atom	x	y	z	U_{eq}
N1	6931.1(12)	3343.6(9)	4213.5(6)	20.5(3)
C1	8184.1(15)	3317.5(11)	3924.9(7)	20.6(3)
C2	9499.0(15)	2978.5(11)	4198.3(7)	22.6(3)
C3	10563.3(15)	2928.6(11)	3820.7(7)	23.3(3)
C4	10346.6(15)	3131.5(11)	3161.2(7)	23.6(3)
C5	11426.0(16)	2953.9(12)	2769.9(8)	27.7(3)
C6	11213.6(17)	3078.4(13)	2129.3(8)	31.8(4)
C7	9888.7(18)	3358.0(14)	1848.5(8)	32.5(4)
C8	8813.5(17)	3525.7(12)	2211.8(8)	27.6(3)
C9	9017.9(15)	3459.4(11)	2881.1(7)	23.0(3)
C10	7950.9(15)	3622.5(11)	3296.5(7)	21.6(3)
C11	6514.2(14)	3970.1(11)	3205.6(7)	21.7(3)
C12	5710.1(15)	4542.4(11)	2732.1(7)	23.4(3)
C13	6270.7(17)	5020.8(12)	2222.4(8)	27.4(3)
C14	5439.7(18)	5556.3(13)	1790.1(8)	31.6(4)
C15	3999.0(18)	5646.9(12)	1839.9(8)	32.3(4)
C16	3439.8(17)	5245.9(12)	2345.2(8)	29.1(4)
C17	4281.5(16)	4713.7(11)	2810.4(8)	24.8(3)
C18	3716.4(15)	4404.7(11)	3369.7(8)	25.1(3)
C19	4513.2(15)	3947.5(11)	3846.1(7)	23.4(3)
C20	5915.5(15)	3731.3(11)	3757.6(7)	21.1(3)
C21	7891.1(14)	3099.7(11)	5405.2(7)	20.4(3)
C22	8478.8(14)	4015.9(11)	5551.7(7)	22.1(3)
C23	9448.6(15)	4129.6(12)	6083.6(8)	25.4(3)
C24	9892.0(15)	3359.7(13)	6471.6(8)	27.6(3)
C25	9339.9(15)	2458.3(12)	6318.2(8)	25.3(3)
C26	8340.7(14)	2320.8(11)	5799.1(7)	21.7(3)
C27	8077.7(16)	4894.2(11)	5156.5(8)	26.2(3)
C28	10945.2(19)	3506.1(16)	7041.8(9)	40.3(4)
C29	7794.2(16)	1316.6(12)	5668.5(8)	25.7(3)
C30	5260.4(14)	2490.3(11)	4918.6(7)	20.7(3)
C31	4373.5(14)	2823.2(11)	5359.6(7)	21.5(3)
C32	3106.7(15)	2359.1(11)	5417.9(7)	23.1(3)
C33	2721.6(15)	1535.5(11)	5074.3(8)	24.0(3)
C34	3611.7(15)	1198.5(11)	4648.0(7)	24.0(3)
C35	4848.0(15)	1672.7(11)	4551.2(7)	23.3(3)
C36	4765.2(16)	3685.6(12)	5770.2(8)	25.9(3)
C37	1389.9(16)	1008.9(13)	5171.9(9)	30.8(4)
C38	5713.4(17)	1273.2(13)	4054.2(8)	31.0(4)
B1	6707.6(16)	2986.8(12)	4836.8(8)	20.5(3)

Table 9-7 Anisotropic Displacement Parameters (×10^4) for DBCz-DMB (3) The anisotropic displacement factor exponent takes the form: $-2\pi^2[h^2a^{*2} \times U_{11} + \ldots + 2hka^* \times b^* \times U_{12}]$

Atom	U_{11}	U_{22}	U_{33}	U_{23}	U_{13}	U_{12}
N1	19.0(6)	22.5(6)	19.9(6)	-0.2(5)	1.8(4)	-0.1(4)
C1	21.6(7)	20.4(7)	20.1(7)	-1.8(6)	3.6(5)	-2.2(5)
C2	23.2(7)	23.1(7)	21.3(7)	-0.5(6)	1.9(5)	-0.3(5)
C3	21.8(7)	23.0(7)	25.1(8)	-2.4(6)	2.2(5)	-0.3(5)
C4	24.9(7)	22.3(7)	24.1(8)	-4.4(6)	4.6(6)	-4.1(5)
C5	25.8(7)	29.5(8)	28.6(8)	-5.5(6)	7.1(6)	-4.1(6)
C6	31.0(8)	38.7(10)	27.4(8)	-8.4(7)	12.0(6)	-6.8(7)
C7	35.6(8)	40.8(10)	21.8(8)	-5.4(7)	7.4(6)	-7.2(7)
C8	28.9(8)	32.3(8)	21.7(8)	-3.6(6)	3.1(6)	-5.6(6)
C9	24.9(7)	22.9(7)	21.5(8)	-2.9(6)	4.3(6)	-4.9(5)
C10	23.6(7)	21.1(7)	20.1(7)	-2.0(6)	2.3(5)	-3.9(5)
C11	23.0(7)	21.6(7)	20.2(7)	-2.0(6)	0.6(5)	-3.4(5)
C12	27.4(7)	20.8(7)	21.0(7)	-1.9(6)	-1.6(5)	-3.5(5)
C13	31.4(8)	27.0(8)	23.2(8)	-0.1(6)	-0.2(6)	-4.5(6)
C14	41.6(9)	28.3(9)	23.9(8)	3.0(7)	-1.4(6)	-5.4(7)
C15	40.6(9)	25.9(8)	27.6(8)	1.5(7)	-8.7(7)	1.1(6)
C16	29.7(8)	25.1(8)	30.6(9)	-1.9(6)	-5.3(6)	0.4(6)
C17	27.7(7)	20.9(7)	24.7(8)	-2.9(6)	-2.8(6)	-1.8(5)
C18	21.6(7)	24.6(8)	28.5(8)	-3.7(6)	0.0(6)	0.0(5)
C19	23.0(7)	24.2(7)	23.2(7)	-1.9(6)	2.6(5)	-1.4(5)
C20	22.1(7)	20.4(7)	20.1(7)	-1.3(6)	-0.7(5)	-1.4(5)
C21	20.0(6)	22.7(7)	19.2(7)	-1.6(6)	5.7(5)	-1.3(5)
C22	20.7(7)	24.3(8)	22.1(7)	-2.1(6)	5.9(5)	-1.5(5)
C23	23.2(7)	26.7(8)	26.7(8)	-6.0(6)	3.9(6)	-3.0(5)
C24	23.1(7)	35.7(9)	23.8(8)	-5.4(6)	1.1(6)	0.4(6)
C25	24.0(7)	29.6(8)	22.3(8)	1.4(6)	3.0(6)	2.8(5)
C26	20.4(6)	25.1(8)	20.5(7)	-0.5(6)	6.3(5)	0.2(5)
C27	28.5(7)	21.9(8)	28.4(8)	-1.3(6)	3.7(6)	-3.0(5)
C28	37.0(9)	46.8(11)	34.3(10)	-6.7(8)	-10.1(7)	0.2(8)
C29	27.9(7)	23.1(8)	26.2(8)	2.3(6)	3.4(6)	0.5(6)
C30	21.7(7)	22.0(7)	18.3(7)	1.3(5)	1.0(5)	-0.4(5)
C31	22.6(7)	21.4(7)	20.2(7)	1.5(6)	0.8(5)	1.0(5)
C32	21.7(7)	25.6(8)	22.5(7)	1.3(6)	4.3(5)	1.7(5)
C33	20.7(7)	24.9(8)	25.9(8)	3.6(6)	0.8(5)	-0.5(5)
C34	23.7(7)	21.7(7)	25.9(8)	-1.6(6)	-0.8(6)	-2.0(5)
C35	22.5(7)	24.4(8)	22.7(7)	-0.7(6)	1.8(5)	-0.3(5)
C36	27.5(7)	24.4(8)	26.5(8)	-4.2(6)	5.5(6)	-0.9(6)
C37	24.1(7)	29.7(9)	39.3(9)	-1.4(7)	6.5(6)	-4.3(6)
C38	31.0(8)	31.5(9)	31.4(9)	-10.3(7)	7.6(6)	-5.0(6)
B1	23.2(7)	18.1(8)	20.4(8)	-2.2(6)	3.7(6)	0.9(6)

Table 9-8 Bond Angles in Å for DBCz-DMB (3).

Atom	Atom	Length/Å
N^1	C^1	1.4089(18)
N^1	C^{20}	1.4085(19)
N^1	B^1	1.450(2)
C^1	C^2	1.416(2)
C^1	C^{10}	1.395(2)
C^2	C^3	1.367(2)
C^3	C^4	1.422(2)
C^4	C^5	1.418(2)
C^4	C^9	1.427(2)
C^5	C^6	1.364(2)
C^6	C^7	1.404(3)
C^7	C^8	1.374(2)
C^8	C^9	1.416(2)
C^9	C^{10}	1.440(2)
C^{10}	C^{11}	1.458(2)
C^{11}	C^{12}	1.442(2)
C^{11}	C^{20}	1.399(2)
C^{12}	C^{13}	1.424(2)
C^{12}	C^{17}	1.422(2)
C^{13}	C^{14}	1.373(2)
C^{14}	C^{15}	1.407(3)
C^{15}	C^{16}	1.369(3)
C^{16}	C^{17}	1.419(2)
C^{17}	C^{18}	1.423(2)
C^{18}	C^{19}	1.361(2)
C^{19}	C^{20}	1.414(2)
C^{21}	C^{22}	1.418(2)
C^{21}	C^{26}	1.410(2)
C^{21}	B^1	1.577(2)
C^{22}	C^{23}	1.396(2)
C^{22}	C^{27}	1.511(2)
C^{23}	C^{24}	1.392(2)
C^{24}	C^{25}	1.389(2)
C^{24}	C^{28}	1.508(2)
C^{25}	C^{26}	1.397(2)
C^{26}	C^{29}	1.511(2)
C^{30}	C^{31}	1.410(2)
C^{30}	C^{35}	1.414(2)
C^{30}	B^1	1.581(2)
C^{31}	C^{32}	1.397(2)
C^{31}	C^{36}	1.509(2)
C^{32}	C^{33}	1.389(2)
C^{33}	C^{34}	1.391(2)
C^{33}	C^{37}	1.510(2)
C^{34}	C^{35}	1.395(2)
C^{35}	C^{38}	1.517(2)


C28
C25
C29
C24
C23
C26
C21
B1
C22
C27
N1
C2
C1
C3
C10
C11
C4
C9
C5
C8
C6
C7
C36
C32
C37
C33
C31
C34
C30
C35
C38
C19
C20
C18
C17
C12
C16
C15
C13
C14
C
H
B
N

9.18.3 DPhCz-DMB (4)

Table 9-9 Crystal data and structural refinement details of DPhCz-DMB (4)

Compound	**2023CS0404_1a**
Formula	$C_{42}H_{38}BN$
$D_{calc.}$/ g cm^{-3}	1.201
μ/mm^{-1}	0.512
Formula Weight	567.54
Colour	colourless
Shape	prism-shaped
Size/mm^3	0.49×0.21×0.13
T/K	100(2)
Crystal System	triclinic
Space Group	P-1
a/Å	12.17890(10)
b/Å	16.08210(10)
c/Å	17.73730(10)
α/°	75.3820(10)
β/°	70.7970(10)
γ/°	77.3520(10)
V/Å^3	3139.24(4)
Z	4
Z'	2
Wavelength/Å	1.54184
Radiation type	Cu K$_\alpha$
Θ_{min}/°	2.690
Θ_{max}/°	76.790
Measured Refl's.	183362
Indep't Refl's	12594
Refl's I≥2 σ(I)	12068
R_{int}	0.0450
Parameters	805
Restraints	0
Largest Peak	0.247
Deepest Hole	-0.268
GooF	1.026
wR_2 (all data)	0.0938
wR_2	0.0929
R_1 (all data)	0.0398
R_1	0.0386

Table 9-10 Fractional Atomic Coordinates (×10^4) and Equivalent Isotropic Displacement Parameters (Å2×10^3) for DPhCz-DMB (4). U_{eq} is defined as 1/3 of the trace of the orthogonalised U_{ij}.

Atom	x	y	z	U_{eq}
N1	4998.6(8)	5746.4(6)	6604.3(5)	17.15(18)
C1	3974.6(9)	6196.2(7)	6379.4(6)	16.8(2)
C2	3861.1(9)	6635.8(7)	5616.9(6)	18.4(2)
C3	2747.4(9)	7003.6(7)	5553.9(6)	18.3(2)
C4	1732.0(9)	6944.5(7)	6226.5(6)	17.8(2)
C5	1855.1(9)	6478.8(7)	6978.4(6)	18.0(2)
C6	2972.7(9)	6106.2(7)	7054.5(6)	17.1(2)
C7	3372.6(9)	5587.5(7)	7736.4(6)	17.2(2)
C8	2776.0(9)	5315.4(7)	8555.3(6)	18.0(2)
C9	3399.7(9)	4812.7(7)	9085.9(6)	18.2(2)
C10	4628.7(9)	4598.4(7)	8781.4(6)	20.1(2)
C11	5239.3(9)	4876.0(7)	7973.1(6)	19.7(2)
C12	4598.1(9)	5368.2(7)	7446.1(6)	17.1(2)
C13	575.6(9)	7416.0(7)	6133.2(6)	18.7(2)
C14	298.4(10)	7551.3(7)	5402.0(7)	21.9(2)
C15	-741.0(10)	8067.1(8)	5303.7(7)	25.7(2)
C16	-1530.4(10)	8446.1(7)	5934.8(8)	25.8(2)
C17	-1281.4(10)	8296.7(7)	6671.2(7)	24.9(2)
C18	-238.2(9)	7790.6(7)	6767.2(7)	21.2(2)
C19	2784.6(9)	4491.9(7)	9955.7(6)	19.0(2)
C20	3304.5(10)	4418.8(8)	10567.7(7)	23.9(2)
C21	2732.3(10)	4109.7(8)	11379.2(7)	26.9(2)
C22	1630.0(10)	3865.9(7)	11593.7(7)	25.5(2)
C23	1102.7(10)	3938.1(7)	10990.1(7)	24.0(2)
C24	1669.2(10)	4248.0(7)	10179.6(7)	20.8(2)
C25	6546.4(9)	6427.6(7)	5309.9(6)	17.1(2)
C26	6352.0(9)	7304.4(7)	5397.4(6)	18.6(2)
C27	6679.6(9)	7957.2(7)	4719.5(7)	19.5(2)
C28	7196.9(9)	7775.1(7)	3941.1(7)	19.1(2)
C29	7405.9(9)	6911.3(7)	3859.7(6)	19.1(2)
C30	7100.8(9)	6238.3(7)	4526.1(6)	17.9(2)
C31	5795.4(10)	7554.3(7)	6220.6(7)	23.9(2)
C32	7546.8(10)	8490.0(7)	3212.4(7)	24.3(2)
C33	7371.0(11)	5318.7(7)	4377.4(7)	24.7(2)
C34	7113.2(9)	4874.9(7)	6284.1(6)	17.3(2)
C35	8225.0(9)	4964.1(7)	6323.0(6)	19.9(2)
C36	9021.7(10)	4228.5(7)	6484.2(7)	22.9(2)
C37	8777.6(9)	3394.7(7)	6585.7(7)	22.1(2)
C38	7700.6(9)	3308.9(7)	6522.5(6)	20.3(2)
C39	6864.9(9)	4027.7(7)	6383.7(6)	17.9(2)
C40	8581.5(10)	5844.5(8)	6193.3(8)	27.4(2)
C41	9666.6(10)	2613.6(8)	6752.5(8)	29.8(3)
C42	5709.4(9)	3864.0(7)	6342.6(7)	20.6(2)
B1	6195.3(10)	5685.9(8)	6081.3(7)	17.3(2)
N2	6675.0(7)	1178.7(6)	8383.9(5)	17.31(18)
C004	6996.4(9)	1049.4(7)	7569.9(6)	16.9(2)
C43	5508.0(9)	1644.4(7)	8535.9(6)	16.9(2)
C44	4742.8(9)	1884.6(7)	9255.7(6)	19.0(2)
C45	3626.9(9)	2311.8(7)	9248.6(6)	18.8(2)
C46	3247.3(9)	2515.9(7)	8547.6(6)	18.0(2)
C47	4009.2(9)	2260.3(7)	7838.2(6)	17.7(2)
C48	5125.8(9)	1808.2(6)	7840.2(6)	16.8(2)
C49	6067.6(9)	1410.3(6)	7228.8(6)	16.9(2)
C50	6162.0(9)	1340.4(7)	6439.2(6)	17.4(2)
C51	7198.0(9)	910.3(7)	5981.0(6)	17.8(2)
C52	8138.6(9)	601.9(7)	6321.1(6)	18.9(2)

Atom	x	y	z	U_{eq}
C^{53}	8063.0(9)	667.8(7)	7101.3(6)	18.8(2)
C^{54}	2043.9(9)	2991.6(7)	8582.1(6)	18.3(2)
C^{55}	1873.6(9)	3766.6(7)	8035.0(7)	20.1(2)
C^{56}	751.0(10)	4222.4(7)	8078.7(7)	23.2(2)
C^{57}	-220.3(10)	3905.3(8)	8671.2(8)	26.6(2)
C^{58}	-60.6(10)	3132.9(8)	9214.8(8)	26.8(2)
C^{59}	1063.3(10)	2679.6(7)	9174.5(7)	22.4(2)
C^{60}	7302.8(9)	779.1(6)	5157.0(6)	18.6(2)
C^{61}	6307.1(10)	717.9(7)	4956.5(7)	22.8(2)
C^{62}	6389.4(11)	622.1(8)	4184.0(7)	27.0(2)
C^{63}	7470.7(11)	581.9(7)	3591.0(7)	26.9(2)
C^{64}	8470.3(11)	621.0(7)	3783.1(7)	25.4(2)
C^{65}	8390.6(10)	715.2(7)	4558.6(7)	21.4(2)
C^{66}	7032.0(9)	1362.3(7)	9687.0(6)	17.9(2)
C^{67}	6988.2(9)	2275.5(7)	9542.3(7)	19.3(2)
C^{68}	6571.2(9)	2707.4(7)	10194.7(7)	22.0(2)
C^{69}	6159.9(10)	2270.5(8)	10991.6(7)	23.6(2)
C^{70}	6235.6(10)	1370.4(8)	11132.6(7)	23.6(2)
C^{71}	6681.6(9)	910.5(7)	10500.0(7)	20.2(2)
C^{72}	7341.2(10)	2812.5(7)	8693.3(7)	23.8(2)
C^{73}	5650.3(12)	2753.4(9)	11685.2(8)	32.8(3)
C^{74}	6720.4(11)	-65.1(8)	10709.5(7)	27.9(2)
C^{75}	8371.8(9)	77.6(7)	8834.5(6)	17.7(2)
C^{76}	8123.9(9)	-719.1(7)	8770.1(6)	18.5(2)
C^{77}	9015.2(10)	-1431.1(7)	8687.7(6)	20.5(2)
C^{78}	10162.8(10)	-1381.8(7)	8648.2(7)	21.8(2)
C^{79}	10397.0(9)	-602.9(7)	8720.1(7)	21.5(2)
C^{80}	9523.3(9)	118.6(7)	8824.7(6)	19.0(2)
C^{81}	6914.6(9)	-837.2(7)	8787.8(7)	21.3(2)
C^{82}	11126.2(11)	-2146.3(8)	8524.7(8)	29.9(3)
C^{83}	9855.0(10)	931.9(7)	8917.6(7)	23.8(2)
B^{2}	7365.3(10)	880.5(8)	8951.7(7)	17.5(2)

Table 9-11 Anisotropic Displacement Parameters (×10^4) for DPhCz-DMB (4) The anisotropic displacement factor exponent takes the form: $-2\pi^2[h^2a^{*2} \times U_{11} + \ldots + 2hka^* \times b^* \times U_{12}]$

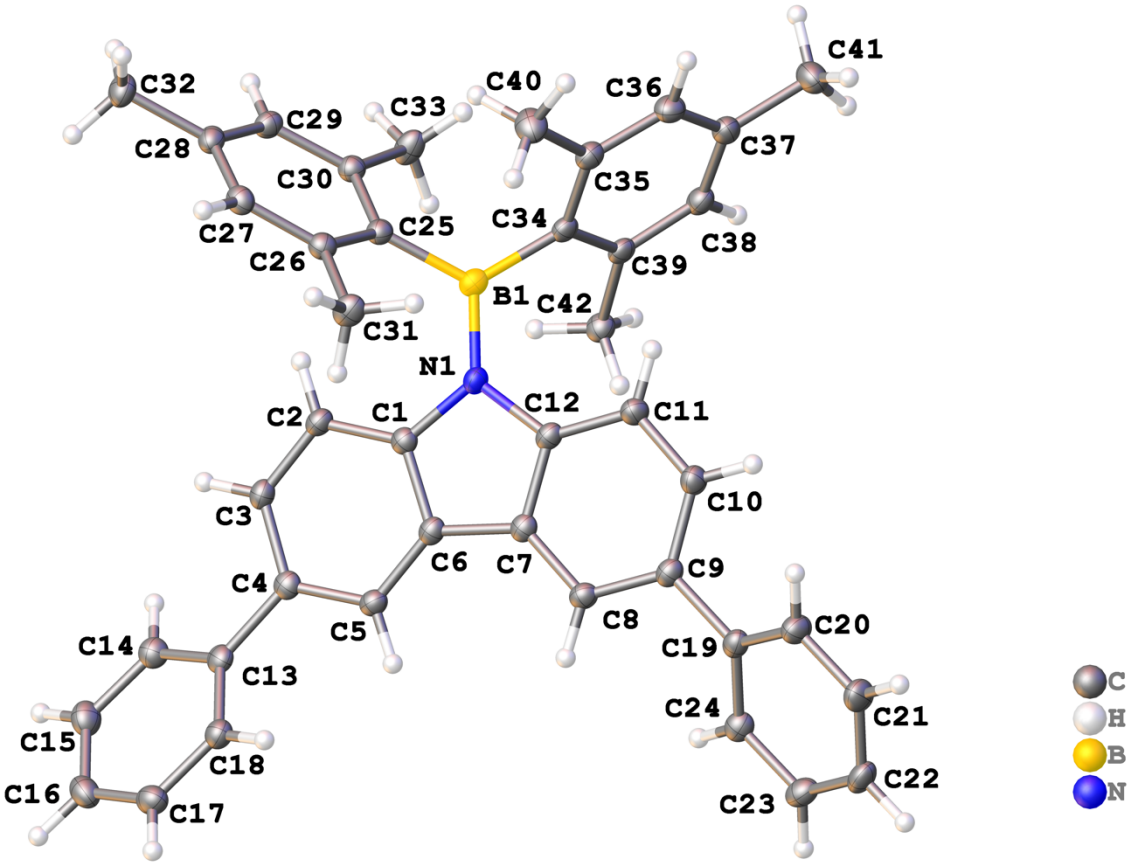
Atom	U_{11}	U_{22}	U_{33}	U_{23}	U_{13}	U_{12}
N1	19.0(4)	17.3(4)	13.8(4)	-1.2(3)	-4.4(3)	-2.7(3)
C1	18.3(5)	14.8(5)	17.4(5)	-3.7(4)	-4.6(4)	-2.6(4)
C2	20.5(5)	17.7(5)	15.3(5)	-2.2(4)	-2.7(4)	-4.7(4)
C3	22.8(5)	16.2(5)	15.8(5)	-1.2(4)	-6.1(4)	-3.9(4)
C4	20.5(5)	14.5(5)	19.0(5)	-3.8(4)	-5.4(4)	-3.6(4)
C5	18.5(5)	16.9(5)	17.1(5)	-3.6(4)	-2.5(4)	-3.4(4)
C6	20.9(5)	15.0(5)	15.3(5)	-3.1(4)	-4.1(4)	-3.7(4)
C7	20.2(5)	14.8(5)	16.7(5)	-3.7(4)	-4.5(4)	-3.5(4)
C8	18.2(5)	18.1(5)	16.8(5)	-4.5(4)	-2.7(4)	-3.3(4)
C9	21.5(5)	17.2(5)	15.4(5)	-3.2(4)	-3.9(4)	-4.3(4)
C10	21.7(5)	21.1(5)	16.6(5)	-2.0(4)	-6.3(4)	-1.9(4)
C11	18.7(5)	21.6(5)	17.0(5)	-3.9(4)	-3.8(4)	-1.8(4)
C12	20.2(5)	16.0(5)	14.3(5)	-3.1(4)	-2.8(4)	-4.3(4)
C13	20.2(5)	14.7(5)	20.2(5)	-0.6(4)	-5.0(4)	-5.1(4)
C14	23.3(5)	21.1(5)	22.0(5)	-4.0(4)	-7.0(4)	-4.4(4)
C15	27.5(6)	24.9(6)	27.3(6)	-1.5(5)	-13.4(5)	-5.0(5)
C16	21.6(5)	21.3(5)	34.4(6)	-2.1(5)	-11.1(5)	-1.7(4)
C17	22.0(5)	21.5(5)	27.1(6)	-4.2(5)	-3.2(4)	-1.7(4)
C18	22.4(5)	19.5(5)	19.7(5)	-1.0(4)	-5.1(4)	-4.0(4)
C19	21.8(5)	16.0(5)	16.3(5)	-2.4(4)	-3.2(4)	-1.3(4)
C20	22.0(5)	29.3(6)	18.4(5)	-1.5(5)	-4.9(4)	-4.7(4)
C21	27.9(6)	32.0(6)	17.4(5)	-1.0(5)	-6.7(4)	-2.2(5)
C22	30.0(6)	23.4(6)	16.2(5)	0.5(4)	-0.7(4)	-4.3(5)
C23	24.3(5)	21.5(5)	22.8(6)	-3.6(4)	-0.5(4)	-6.9(4)
C24	23.5(5)	19.2(5)	19.1(5)	-4.7(4)	-4.6(4)	-3.5(4)
C25	15.8(5)	18.1(5)	17.3(5)	-2.7(4)	-4.6(4)	-3.3(4)
C26	17.5(5)	19.5(5)	19.2(5)	-4.4(4)	-5.5(4)	-2.5(4)
C27	19.5(5)	15.9(5)	24.1(5)	-4.5(4)	-7.4(4)	-2.4(4)
C28	17.8(5)	19.3(5)	19.9(5)	-0.1(4)	-6.6(4)	-4.9(4)
C29	19.2(5)	21.6(5)	15.8(5)	-3.3(4)	-3.8(4)	-4.2(4)
C30	17.2(5)	18.0(5)	18.3(5)	-3.6(4)	-4.7(4)	-3.1(4)
C31	28.9(6)	20.2(5)	21.8(5)	-7.5(4)	-3.7(4)	-3.6(4)
C32	28.1(6)	20.3(5)	23.1(6)	1.6(4)	-7.9(5)	-6.8(4)
C33	35.0(6)	19.2(5)	17.8(5)	-5.0(4)	-2.9(4)	-5.6(4)
C34	18.5(5)	18.9(5)	12.3(5)	-1.9(4)	-1.6(4)	-4.2(4)
C35	20.8(5)	21.2(5)	16.6(5)	-2.3(4)	-3.8(4)	-5.3(4)
C36	18.5(5)	26.8(6)	22.8(5)	-2.4(5)	-5.5(4)	-5.5(4)
C37	20.3(5)	22.3(5)	19.1(5)	-1.2(4)	-2.9(4)	-1.5(4)
C38	22.0(5)	17.7(5)	18.0(5)	-1.5(4)	-2.3(4)	-4.5(4)
C39	18.9(5)	20.2(5)	12.1(5)	-1.8(4)	-1.2(4)	-4.4(4)
C40	26.5(6)	23.7(6)	35.3(7)	-2.4(5)	-12.9(5)	-7.9(5)
C41	23.0(6)	25.4(6)	36.3(7)	-0.9(5)	-8.3(5)	-0.5(5)
C42	21.8(5)	18.2(5)	21.5(5)	-3.1(4)	-5.2(4)	-5.1(4)
B1	20.1(6)	18.1(5)	15.2(5)	-5.1(4)	-4.3(4)	-5.4(4)
N2	17.7(4)	17.9(4)	15.2(4)	-4.5(3)	-3.3(3)	-1.1(3)
C004	20.0(5)	15.2(5)	15.2(5)	-2.3(4)	-4.4(4)	-3.9(4)
C43	16.8(5)	15.1(5)	18.0(5)	-2.3(4)	-4.7(4)	-2.5(4)
C44	20.4(5)	20.8(5)	16.2(5)	-4.4(4)	-4.9(4)	-3.6(4)
C45	19.3(5)	19.4(5)	16.9(5)	-5.7(4)	-2.5(4)	-3.0(4)
C46	18.7(5)	15.7(5)	19.3(5)	-3.1(4)	-4.5(4)	-4.1(4)
C47	19.8(5)	16.5(5)	17.0(5)	-2.1(4)	-6.1(4)	-3.6(4)
C48	19.2(5)	15.1(5)	15.5(5)	-2.3(4)	-3.7(4)	-4.5(4)
C49	18.6(5)	14.0(5)	16.8(5)	-2.0(4)	-3.6(4)	-3.7(4)
C50	20.2(5)	15.4(5)	16.4(5)	-1.6(4)	-5.6(4)	-3.4(4)
C51	21.9(5)	14.0(5)	15.8(5)	-1.3(4)	-3.4(4)	-4.3(4)
C52	19.4(5)	17.1(5)	17.2(5)	-3.3(4)	-1.8(4)	-2.2(4)
C53	19.0(5)	17.6(5)	18.1(5)	-2.4(4)	-5.0(4)	-1.2(4)
C54	19.5(5)	19.7(5)	18.2(5)	-8.8(4)	-5.4(4)	-2.1(4)

Atom	U_{11}	U_{22}	U_{33}	U_{23}	U_{13}	U_{12}
C^{55}	21.8(5)	20.8(5)	18.7(5)	-6.9(4)	-4.8(4)	-3.1(4)
C^{56}	26.2(6)	19.3(5)	25.7(6)	-6.5(4)	-10.9(5)	0.9(4)
C^{57}	19.0(5)	25.7(6)	37.3(7)	-12.2(5)	-10.2(5)	1.9(4)
C^{58}	18.6(5)	28.9(6)	32.2(6)	-8.7(5)	-3.1(5)	-5.8(4)
C^{59}	22.3(5)	21.1(5)	23.7(5)	-3.9(4)	-6.2(4)	-4.2(4)
C^{60}	25.4(5)	12.5(5)	16.6(5)	-2.0(4)	-5.4(4)	-2.1(4)
C^{61}	24.1(5)	21.4(5)	21.8(5)	-5.2(4)	-5.3(4)	-2.1(4)
C^{62}	33.3(6)	24.6(6)	27.5(6)	-7.5(5)	-13.7(5)	-3.1(5)
C^{63}	42.6(7)	21.4(6)	18.2(5)	-5.5(4)	-9.2(5)	-5.2(5)
C^{64}	33.2(6)	21.7(5)	18.5(5)	-5.7(4)	-0.8(5)	-6.9(5)
C^{65}	25.8(5)	18.4(5)	19.1(5)	-3.8(4)	-4.2(4)	-4.7(4)
C^{66}	15.6(5)	20.3(5)	18.6(5)	-4.8(4)	-6.4(4)	-0.8(4)
C^{67}	16.3(5)	21.1(5)	21.6(5)	-5.1(4)	-6.8(4)	-1.9(4)
C^{68}	20.8(5)	20.9(5)	26.5(6)	-8.1(4)	-8.1(4)	-1.9(4)
C^{69}	20.5(5)	29.9(6)	23.5(6)	-12.3(5)	-6.6(4)	-1.7(4)
C^{70}	23.9(5)	31.0(6)	16.0(5)	-4.1(5)	-4.9(4)	-5.8(4)
C^{71}	19.6(5)	23.2(5)	19.1(5)	-4.0(4)	-7.2(4)	-3.1(4)
C^{72}	26.3(6)	19.7(5)	24.3(6)	-3.3(4)	-6.7(4)	-3.2(4)
C^{73}	34.2(7)	39.2(7)	27.4(6)	-18.1(6)	-5.6(5)	-2.1(5)
C^{74}	38.3(7)	23.3(6)	19.9(5)	-0.9(5)	-6.2(5)	-7.4(5)
C^{75}	20.0(5)	19.6(5)	13.2(5)	-3.1(4)	-4.9(4)	-2.2(4)
C^{76}	20.8(5)	20.4(5)	13.6(5)	-2.7(4)	-4.8(4)	-2.7(4)
C^{77}	25.0(5)	18.3(5)	18.4(5)	-4.3(4)	-6.9(4)	-2.3(4)
C^{78}	23.9(5)	21.9(5)	18.7(5)	-5.0(4)	-7.4(4)	1.4(4)
C^{79}	19.6(5)	25.5(6)	20.3(5)	-5.4(4)	-7.5(4)	-1.4(4)
C^{80}	21.4(5)	20.6(5)	15.3(5)	-3.5(4)	-6.5(4)	-2.2(4)
C^{81}	21.6(5)	20.4(5)	21.9(5)	-4.1(4)	-5.6(4)	-4.2(4)
C^{82}	26.3(6)	26.2(6)	39.6(7)	-12.4(5)	-13.7(5)	4.4(5)
C^{83}	22.0(5)	23.6(6)	28.3(6)	-7.2(5)	-9.2(4)	-3.2(4)
B^{2}	17.9(5)	17.8(5)	16.3(5)	-1.4(4)	-3.8(4)	-5.4(4)

Table 9-12 Bond Angles in Å for DPhCz-DMB (4).

Atom	Atom	Length/Å
N^{1}	C^{1}	1.4228(13)
N^{1}	C^{12}	1.4247(13)
N^{1}	B^{1}	1.4451(14)
C^{1}	C^{2}	1.3947(15)
C^{1}	C^{6}	1.4045(14)
C^{2}	C^{3}	1.3847(15)
C^{3}	C^{4}	1.4090(14)
C^{4}	C^{5}	1.3928(15)
C^{4}	C^{13}	1.4860(15)
C^{5}	C^{6}	1.3974(15)
C^{6}	C^{7}	1.4477(15)
C^{7}	C^{8}	1.3977(14)
C^{7}	C^{12}	1.4046(14)
C^{8}	C^{9}	1.3906(15)
C^{9}	C^{10}	1.4097(15)
C^{9}	C^{19}	1.4881(14)
C^{10}	C^{11}	1.3888(15)
C^{11}	C^{12}	1.3951(15)
C^{13}	C^{14}	1.3988(15)
C^{13}	C^{18}	1.3990(15)
C^{14}	C^{15}	1.3904(16)
C^{15}	C^{16}	1.3887(17)
C^{16}	C^{17}	1.3878(17)
C^{17}	C^{18}	1.3875(16)
C^{19}	C^{20}	1.3959(16)
C^{19}	C^{24}	1.3988(15)
C^{20}	C^{21}	1.3911(16)
C^{21}	C^{22}	1.3857(17)
C^{22}	C^{23}	1.3888(17)
C^{23}	C^{24}	1.3884(15)
C^{25}	C^{26}	1.4172(14)
C^{25}	C^{30}	1.4098(14)
C^{25}	B^{1}	1.5787(15)
C^{26}	C^{27}	1.3920(15)
C^{26}	C^{31}	1.5097(14)
C^{27}	C^{28}	1.3928(15)
C^{28}	C^{29}	1.3920(15)
C^{28}	C^{32}	1.5086(15)
C^{29}	C^{30}	1.3959(15)
C^{30}	C^{33}	1.5138(14)
C^{34}	C^{35}	1.4179(15)
C^{34}	C^{39}	1.4152(14)
C^{34}	B^{1}	1.5715(16)
C^{35}	C^{36}	1.3899(16)
C^{35}	C^{40}	1.5117(15)
C^{36}	C^{37}	1.3915(16)
C^{37}	C^{38}	1.3914(16)
C^{37}	C^{41}	1.5051(16)
C^{38}	C^{39}	1.3924(15)
C^{39}	C^{42}	1.5146(14)
N^{2}	C^{004}	1.4231(13)
N^{2}	C^{43}	1.4273(13)
N^{2}	B^{2}	1.4450(15)
C^{004}	C^{49}	1.4028(15)
C^{004}	C^{53}	1.3975(14)
C^{43}	C^{44}	1.3987(14)
C^{43}	C^{48}	1.4031(14)
C^{44}	C^{45}	1.3846(15)
C^{45}	C^{46}	1.4048(15)

Atom	Atom	Length/Å
C^{46}	C^{47}	1.3925(14)
C^{46}	C^{54}	1.4869(14)
C^{47}	C^{48}	1.3953(14)
C^{48}	C^{49}	1.4532(14)
C^{49}	C^{50}	1.3983(14)
C^{50}	C^{51}	1.3993(14)
C^{51}	C^{52}	1.4061(15)
C^{51}	C^{60}	1.4893(14)
C^{52}	C^{53}	1.3858(15)
C^{54}	C^{55}	1.3953(16)
C^{54}	C^{59}	1.3975(15)
C^{55}	C^{56}	1.3901(15)
C^{56}	C^{57}	1.3928(17)
C^{57}	C^{58}	1.3869(18)
C^{58}	C^{59}	1.3911(16)
C^{60}	C^{61}	1.4001(16)
C^{60}	C^{65}	1.4009(15)
C^{61}	C^{62}	1.3859(16)
C^{62}	C^{63}	1.3895(17)
C^{63}	C^{64}	1.3854(18)
C^{64}	C^{65}	1.3913(15)
C^{66}	C^{67}	1.4177(15)
C^{66}	C^{71}	1.4113(15)
C^{66}	B^{2}	1.5780(15)
C^{67}	C^{68}	1.3944(15)
C^{67}	C^{72}	1.5094(15)
C^{68}	C^{69}	1.3890(17)
C^{69}	C^{70}	1.3931(17)
C^{69}	C^{73}	1.5069(15)
C^{70}	C^{71}	1.3938(15)
C^{71}	C^{74}	1.5123(16)
C^{75}	C^{76}	1.4185(15)
C^{75}	C^{80}	1.4125(15)
C^{75}	B^{2}	1.5772(15)
C^{76}	C^{77}	1.3952(15)
C^{76}	C^{81}	1.5150(15)
C^{77}	C^{78}	1.3950(15)
C^{78}	C^{79}	1.3884(16)
C^{78}	C^{82}	1.5072(15)
C^{79}	C^{80}	1.3969(15)
C^{80}	C^{83}	1.5116(15)


C41
C32
C40
C36
C33
C29
C28
C37
C30
C35
C27
C25
C34
C38
C26
C39
B1
C42
C31
N1
C2
C1
C12
C11
C3
C10
C6
C7
C4
C9
C5
C8
C14
C20
C19
C13
C24
C21
C15
C18
C22
C16
C17
C23
C
H
B
N

9.19 Chapter 5

9.19.1 tBu-DMP-Cz-OBA (10)

Table 9-13 Crystal data and structural refinement details of tBu-DMP-Cz-OBA (10)

Compound	**2023NCS0434_1b**
Formula	$C_{40}H_{40}BNO$
$D_{calc.}$/ g cm^{-3}	1.175
μ/mm^{-1}	0.522
Formula Weight	561.54
Colour	colourless
Shape	plate-shaped
Size/mm^3	0.33×0.10×0.06
T/K	100(2)
Crystal System	monoclinic
Space Group	$P2_1/c$
a/Å	26.8254(6)
b/Å	10.3230(3)
c/Å	11.5717(2)
α/°	90
β/°	97.755(2)
γ/°	90
V/Å^3	3175.11(13)
Z	4
Z'	1
Wavelength/Å	1.54184
Radiation type	Cu K$_\alpha$
Θ_{min}/°	1.662
Θ_{max}/°	72.116
Measured Refl's.	32366
Indep't Refl's	6267
Refl's I≥2 σ(I)	5591
R_{int}	0.0428
Parameters	516
Restraints	402
Largest Peak	0.404
Deepest Hole	-0.262
GooF	1.038
wR_2 (all data)	0.1217
wR_2	0.1186
R_1 (all data)	0.0527
R_1	0.0476

Table 9-14 Fractional Atomic Coordinates (×10^4) and Equivalent Isotropic Displacement Parameters (Å2×10^3) for tBu-DMP-Cz-OBA (10). U_{eq} is defined as 1/3 of the trace of the orthogonalised U_{ij}.

Atom	x	y	z	U_{eq}
O1	374.7(4)	3185.4(11)	-780.3(9)	22.9(2)
N1	2883.3(7)	7667.2(14)	2606.5(14)	17.4(3)
C1	2938.8(5)	8909.7(14)	2174.6(12)	16.1(3)
C2	2638.0(5)	9568.2(15)	1292.5(12)	18.7(3)
C3	2780.1(5)	10811.3(15)	1027.6(12)	18.8(3)
C4	3210.2(6)	11424.2(15)	1613.0(13)	17.2(3)
C5	3495.0(6)	10759.6(16)	2527.5(13)	16.9(3)
C6	3360.3(5)	9510.3(14)	2815.5(12)	15.4(3)
C7	3570.8(5)	8580.6(14)	3687.2(12)	15.6(3)
C8	3991.0(5)	8591.0(14)	4544.0(13)	17.7(3)
C9	4110.8(7)	7501.6(18)	5240.8(15)	18.5(3)
C10	3800.6(6)	6408.5(15)	5059.8(13)	18.8(3)
C11	3379.4(6)	6366.5(15)	4214.8(12)	17.9(3)
C12	3267.1(6)	7459.7(17)	3530.1(14)	15.8(3)
C13	3377.3(6)	12774.4(16)	1272.0(13)	20.3(3)
C14	3028.3(6)	13339.8(16)	242.1(14)	26.3(3)
C15	3907.8(8)	12684.6(17)	918(2)	26.6(4)
C16	3378.2(8)	13707.2(18)	2305.7(16)	29.7(4)
C17	4574.6(6)	7515(2)	6184.7(17)	22.2(4)
C18	5036.1(7)	7912(2)	5615.0(17)	40.8(5)
C19	4491.9(7)	8530.9(19)	7118.6(15)	34.3(4)
C20	4675.2(7)	6218.6(18)	6778.8(17)	33.6(4)
C21	2511.4(5)	6767.9(14)	2127.9(12)	16.5(3)
C22	2183.0(5)	6219.4(15)	2816.2(12)	18.4(3)
C23	1796.1(5)	5404.3(15)	2322.6(13)	18.7(3)
C24	1733.8(5)	5152.0(14)	1114.4(12)	17.8(3)
C25	2082.5(5)	5683.0(14)	437.1(12)	17.6(3)
C26	2469.6(5)	6477.7(14)	947.6(12)	17.5(3)
C27	1437.3(6)	4862.0(18)	3098.8(14)	26.8(4)
C28	2044.7(6)	5397.4(16)	-852.6(13)	21.3(3)
C29	1150.5(5)	2962.5(15)	573.9(12)	19.0(3)
C30	1458.1(6)	2064.8(17)	1272.2(13)	23.2(3)
C31	1324.9(6)	792.9(17)	1366.7(15)	26.2(3)
C32	871.6(6)	339.8(16)	752.7(14)	25.8(3)
C33	564.7(6)	1159.4(16)	36.2(13)	22.5(3)
C34	707.2(7)	2456.9(18)	-48.8(14)	19.7(3)
C35	851.0(6)	5165.7(16)	-313.4(13)	20.6(3)
C36	855.4(6)	6519.7(16)	-495.7(14)	25.8(3)
C37	481.1(7)	7139.8(18)	-1220.9(15)	30.0(4)
C38	81.4(6)	6421.6(18)	-1803.2(14)	28.6(4)
C39	58.9(6)	5104.9(17)	-1647.7(14)	25.6(3)
C40	440.5(6)	4493.8(15)	-901.5(13)	20.7(3)
B1	1258.6(6)	4412.7(18)	478.4(14)	19.5(3)
O1B	366(7)	11775(18)	-780(20)	70(3)
N1B	2939(10)	7380(20)	2730(20)	43.0(18)
C1B	2985(8)	6126(19)	2280(20)	43.0(18)
C2B	2651(8)	5440(20)	1340(20)	43.0(18)
C3B	2791(8)	4200(20)	1050(20)	43.0(18)
C4B	3220(8)	3540(20)	1650(20)	43.0(18)
C5B	3507(10)	4190(30)	2520(30)	43.0(18)
C6B	3387(8)	5460(20)	2850(20)	43.0(18)
C12B	3329(6)	7485(17)	3622(17)	43.0(18)
C11B	3455(6)	8561(13)	4324(18)	43.0(18)
C10B	3871(6)	8521(14)	5179(16)	43.0(18)
C9B	4163(6)	7405(17)	5331(17)	43.0(18)
C8B	4038(6)	6330(13)	4629(17)	43.0(18)

Atom	x	y	z	U_{eq}
C7B	3621(6)	6370(13)	3774(15)	43.0(18)
C13B	3358(7)	2184(18)	1289(17)	43.0(18)
C14B	2998(7)	1720(20)	216(18)	43.0(18)
C15B	3355(9)	1200(20)	2270(20)	43.0(18)
C16B	3889(10)	2320(30)	900(30)	43.0(18)
C17B	4692(14)	7510(40)	6000(40)	43.0(18)
C18B	4962(8)	8750(20)	6080(20)	43.0(18)
C19B	4522(8)	7180(20)	7260(20)	43.0(18)
C20B	5017(8)	6420(20)	5690(20)	43.0(18)
C21B	2546(8)	8250(20)	2220(30)	56(3)
C22B	2482(9)	8470(20)	1010(30)	56(3)
C23B	2112(9)	9300(20)	520(30)	56(3)
C24B	1747(9)	9830(20)	1140(30)	56(3)
C25B	1829(9)	9620(20)	2360(30)	56(3)
C26B	2214(9)	8820(20)	2830(30)	56(3)
C27B	2045(9)	9590(20)	-830(30)	56(3)
C28B	1469(9)	10130(20)	3110(30)	56(3)
C29B	1174(8)	12077(14)	630(20)	70(3)
C30B	1485(6)	12938(17)	1310(20)	70(3)
C31B	1343(6)	14228(16)	1380(20)	70(3)
C32B	892(6)	14657(13)	780(20)	70(3)
C33B	581(6)	13796(19)	90(20)	70(3)
C34B	722(7)	12506(19)	20(20)	70(3)
C35B	839(6)	9816(16)	-310(18)	70(3)
C40B	439(6)	10511(12)	-900(20)	70(3)
C39B	62(6)	9870(16)	-1623(19)	70(3)
C38B	86(6)	8534(16)	-1757(18)	70(3)
C37B	485(7)	7840(12)	-1170(20)	70(3)
C36B	862(6)	8481(16)	-445(19)	70(3)
B1B	1255(13)	10530(30)	570(50)	70(3)

Table 9-15 Anisotropic Displacement Parameters (×10^4) for tBu-DMP-Cz-OBA (10) The anisotropic displacement factor exponent takes the form: $-2\pi^2[h^2a^{*2} \times U_{11} + ... + 2hka^* \times b^* \times U_{12}]$

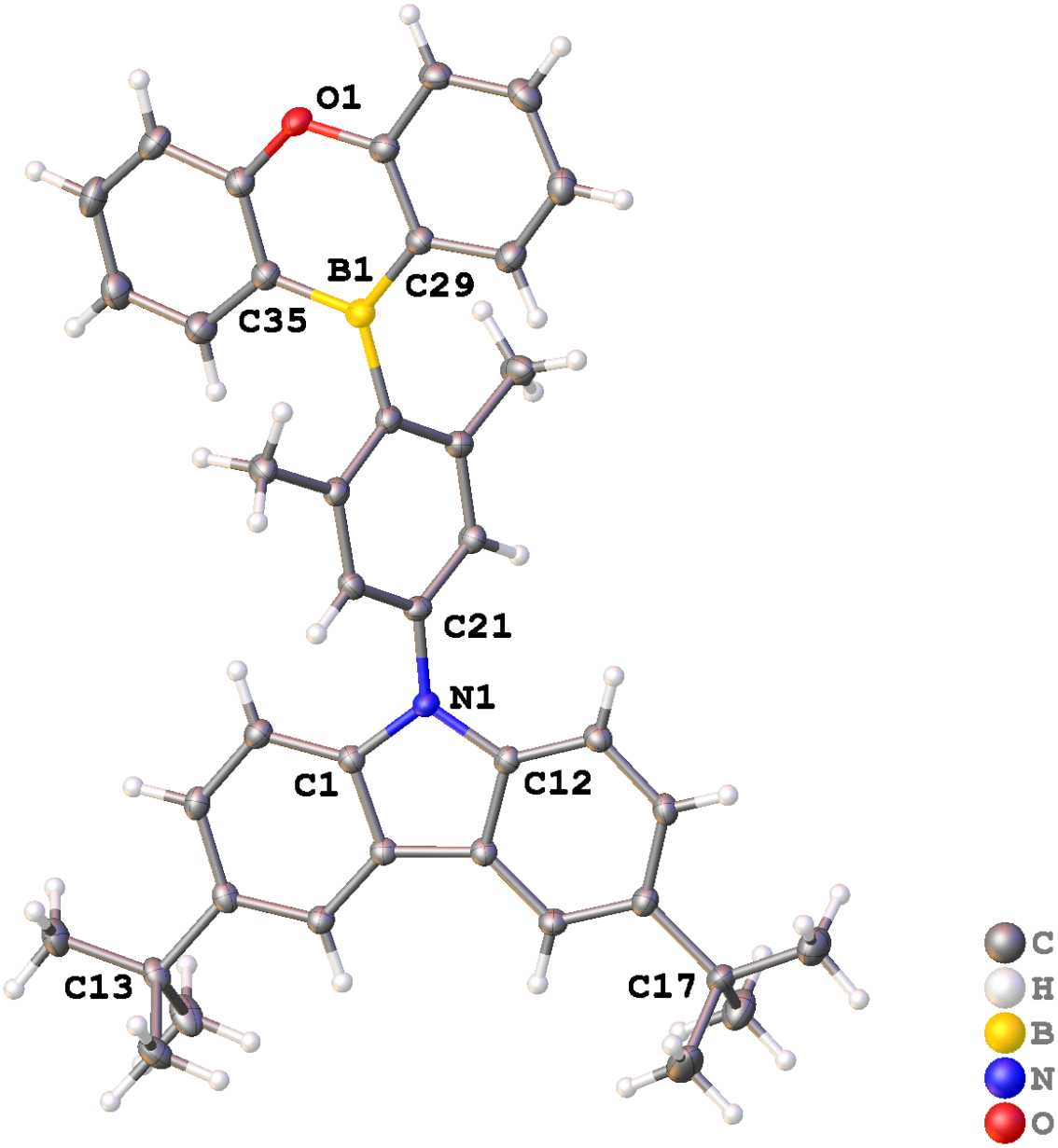
Atom	U_{11}	U_{22}	U_{33}	U_{23}	U_{13}	U_{12}
O1	22.2(5)	21.1(6)	23.3(5)	-0.4(4)	-4.8(4)	-3.4(4)
N1	17.5(7)	16.8(8)	16.7(6)	0.2(6)	-1.2(5)	-2.6(6)
C1	18.2(7)	15.1(7)	15.1(6)	-1.3(5)	2.9(5)	-0.1(5)
C2	18.8(7)	19.5(8)	17.2(7)	-1.5(6)	0.3(5)	0.7(6)
C3	22.2(7)	18.0(8)	16.0(7)	0.3(6)	1.3(5)	5.0(6)
C4	22.7(7)	13.3(7)	16.4(7)	-0.3(6)	4.8(6)	2.5(6)
C5	19.0(7)	14.6(8)	16.6(7)	-1.7(6)	1.3(5)	0.2(6)
C6	17.8(6)	13.6(7)	14.8(6)	-2.9(5)	2.5(5)	0.4(5)
C7	19.4(7)	12.9(7)	14.5(6)	-1.8(5)	2.2(5)	0.2(5)
C8	19.8(7)	14.9(7)	18.0(7)	-2.0(6)	1.1(6)	-1.9(5)
C9	19.8(7)	19.2(8)	15.8(7)	-0.4(6)	0.1(6)	1.3(6)
C10	24.0(7)	15.7(7)	16.4(7)	2.0(6)	2.0(6)	1.4(6)
C11	21.7(7)	14.8(7)	17.2(7)	-1.3(5)	2.8(6)	-2.3(6)
C12	17.0(7)	17.0(7)	13.4(7)	-1.4(6)	2.4(5)	0.5(6)
C13	29.2(8)	12.6(7)	19.6(7)	0.6(6)	5.3(6)	0.7(6)
C14	33.9(8)	19.4(8)	25.9(8)	6.7(6)	4.5(7)	3.3(7)
C15	28.5(8)	19.1(11)	33.6(9)	4.2(8)	8.7(7)	-2.8(8)
C16	50.4(12)	14.2(9)	25.1(9)	-1.9(7)	7.7(8)	-0.9(8)
C17	18.7(10)	25.0(9)	21.6(9)	2.7(7)	-2.0(7)	-2.9(8)
C18	21.9(8)	61.0(14)	37.8(10)	14.9(10)	-2.2(7)	-3.1(9)
C19	42.6(10)	30.7(10)	26.0(8)	-1.3(7)	-8.9(7)	0.2(8)
C20	32.6(9)	29.1(10)	35.7(9)	5.2(8)	-7.8(7)	1.8(7)
C21	16.1(6)	13.4(7)	19.1(7)	-1.7(5)	-0.6(5)	-1.1(5)
C22	20.2(7)	20.2(8)	14.5(6)	-1.4(6)	1.8(5)	-1.1(6)
C23	17.8(7)	19.3(8)	18.6(7)	0.7(6)	1.4(5)	-2.1(6)
C24	20.0(7)	15.3(7)	17.3(7)	0.7(6)	-0.5(5)	-0.3(6)
C25	20.2(7)	15.4(7)	16.6(7)	0.2(6)	0.3(5)	0.4(6)
C26	19.3(7)	15.7(7)	17.7(7)	1.3(6)	3.4(5)	-1.1(5)
C27	25.8(8)	34.8(10)	19.9(7)	-1.1(7)	3.8(6)	-9.6(7)
C28	26.3(7)	20.9(8)	16.3(7)	-0.7(6)	1.0(6)	-3.4(6)
C29	20.3(7)	19.7(8)	16.5(7)	-0.6(6)	0.6(5)	-2.5(6)
C30	23.4(7)	25.0(9)	20.1(7)	-0.8(6)	-1.6(6)	-1.3(6)
C31	31.9(8)	23.8(9)	22.0(8)	2.4(7)	0.5(6)	2.0(7)
C32	33.0(9)	18.8(8)	26.5(8)	0.3(6)	7.5(6)	-4.5(7)
C33	22.8(7)	22.1(8)	22.2(7)	-2.5(6)	1.8(6)	-5.6(6)
C34	19.8(7)	22.1(8)	17.3(7)	-1.3(6)	2.4(6)	-1.9(6)
C35	21.0(7)	21.1(8)	19.0(7)	0.6(6)	0.5(6)	-1.9(6)
C36	26.7(8)	21.5(8)	28.1(8)	1.8(7)	-1.1(6)	-1.9(6)
C37	34.3(9)	23.5(9)	31.5(9)	6.0(7)	1.3(7)	2.3(7)
C38	29.0(8)	33.1(10)	21.8(8)	4.0(7)	-3.2(6)	7.5(7)
C39	23.6(7)	30.3(9)	20.9(7)	-1.6(7)	-3.9(6)	1.1(6)
C40	23.5(7)	19.4(8)	18.6(7)	-0.6(6)	0.7(6)	-1.6(6)
B1	20.3(8)	22.5(9)	15.7(7)	-1.1(7)	2.0(6)	-2.9(7)
O1B	51(4)	40(4)	125(8)	2(4)	36(4)	5(3)
N1B	40(3)	32(3)	61(4)	-2(2)	19(3)	0(2)
C1B	40(3)	32(3)	61(4)	-2(2)	19(3)	0(2)
C2B	40(3)	32(3)	61(4)	-2(2)	19(3)	0(2)
C3B	40(3)	32(3)	61(4)	-2(2)	19(3)	0(2)
C4B	40(3)	32(3)	61(4)	-2(2)	19(3)	0(2)
C5B	40(3)	32(3)	61(4)	-2(2)	19(3)	0(2)
C6B	40(3)	32(3)	61(4)	-2(2)	19(3)	0(2)
C12B	40(3)	32(3)	61(4)	-2(2)	19(3)	0(2)
C11B	40(3)	32(3)	61(4)	-2(2)	19(3)	0(2)
C10B	40(3)	32(3)	61(4)	-2(2)	19(3)	0(2)
C9B	40(3)	32(3)	61(4)	-2(2)	19(3)	0(2)
C8B	40(3)	32(3)	61(4)	-2(2)	19(3)	0(2)

Atom	U_{11}	U_{22}	U_{33}	U_{23}	U_{13}	U_{12}
C7B	40(3)	32(3)	61(4)	-2(2)	19(3)	0(2)
C13B	40(3)	32(3)	61(4)	-2(2)	19(3)	0(2)
C14B	40(3)	32(3)	61(4)	-2(2)	19(3)	0(2)
C15B	40(3)	32(3)	61(4)	-2(2)	19(3)	0(2)
C16B	40(3)	32(3)	61(4)	-2(2)	19(3)	0(2)
C17B	40(3)	32(3)	61(4)	-2(2)	19(3)	0(2)
C18B	40(3)	32(3)	61(4)	-2(2)	19(3)	0(2)
C19B	40(3)	32(3)	61(4)	-2(2)	19(3)	0(2)
C20B	40(3)	32(3)	61(4)	-2(2)	19(3)	0(2)
C21B	44(4)	33(4)	98(7)	4(4)	36(4)	5(3)
C22B	44(4)	33(4)	98(7)	4(4)	36(4)	5(3)
C23B	44(4)	33(4)	98(7)	4(4)	36(4)	5(3)
C24B	44(4)	33(4)	98(7)	4(4)	36(4)	5(3)
C25B	44(4)	33(4)	98(7)	4(4)	36(4)	5(3)
C26B	44(4)	33(4)	98(7)	4(4)	36(4)	5(3)
C27B	44(4)	33(4)	98(7)	4(4)	36(4)	5(3)
C28B	44(4)	33(4)	98(7)	4(4)	36(4)	5(3)
C29B	51(4)	40(4)	125(8)	2(4)	36(4)	5(3)
C30B	51(4)	40(4)	125(8)	2(4)	36(4)	5(3)
C31B	51(4)	40(4)	125(8)	2(4)	36(4)	5(3)
C32B	51(4)	40(4)	125(8)	2(4)	36(4)	5(3)
C33B	51(4)	40(4)	125(8)	2(4)	36(4)	5(3)
C34B	51(4)	40(4)	125(8)	2(4)	36(4)	5(3)
C35B	51(4)	40(4)	125(8)	2(4)	36(4)	5(3)
C40B	51(4)	40(4)	125(8)	2(4)	36(4)	5(3)
C39B	51(4)	40(4)	125(8)	2(4)	36(4)	5(3)
C38B	51(4)	40(4)	125(8)	2(4)	36(4)	5(3)
C37B	51(4)	40(4)	125(8)	2(4)	36(4)	5(3)
C36B	51(4)	40(4)	125(8)	2(4)	36(4)	5(3)
B1B	51(4)	40(4)	125(8)	2(4)	36(4)	5(3)

Table 9-16 Bond Angles in Å for tBu-DMP-Cz-OBA (10).

Atom	Atom	Length/Å
O1	C34	1.369(2)
O1	C40	1.372(2)
N1	C1	1.392(2)
N1	C12	1.3968(19)
N1	C21	1.419(2)
C1	C2	1.390(2)
C1	C6	1.4093(19)
C2	C3	1.385(2)
C3	C4	1.407(2)
C4	C5	1.399(2)
C4	C13	1.532(2)
C5	C6	1.392(2)
C6	C7	1.450(2)
C7	C8	1.397(2)
C7	C12	1.413(2)
C8	C9	1.396(2)
C9	C10	1.401(2)
C9	C17	1.541(2)
C10	C11	1.392(2)
C11	C12	1.388(2)
C13	C14	1.528(2)
C13	C15	1.536(2)
C13	C16	1.535(2)
C17	C18	1.535(2)
C17	C19	1.543(3)
C17	C20	1.512(3)
C21	C22	1.386(2)
C21	C26	1.388(2)
C22	C23	1.397(2)
C23	C24	1.410(2)
C23	C27	1.510(2)
C24	C25	1.410(2)
C24	B1	1.580(2)
C25	C26	1.391(2)
C25	C28	1.511(2)
C29	C30	1.419(2)
C29	C34	1.405(2)
C29	B1	1.532(2)
C30	C31	1.369(2)
C31	C32	1.403(2)
C32	C33	1.377(2)
C33	C34	1.400(2)
C35	C36	1.414(2)
C35	C40	1.398(2)
C35	B1	1.539(2)
C36	C37	1.376(2)
C37	C38	1.399(3)
C38	C39	1.373(3)
C39	C40	1.398(2)
O1B	C34B	1.45(3)
O1B	C40B	1.33(2)
N1B	C1B	1.407(18)
N1B	C12B	1.372(18)
N1B	C21B	1.448(18)
C1B	C2B	1.49(3)
C1B	C6B	1.37(3)
C2B	C3B	1.39(3)
C3B	C4B	1.43(3)
C4B	C5B	1.36(4)

Atom	Atom	Length/Å
C4B	C13B	1.525(18)
C5B	C6B	1.42(3)
C6B	C7B	1.49(3)
C12B	C11B	1.3900
C12B	C7B	1.3900
C11B	C10B	1.3900
C10B	C9B	1.3900
C9B	C8B	1.3900
C9B	C17B	1.53(4)
C8B	C7B	1.3900
C13B	C14B	1.542(18)
C13B	C15B	1.520(19)
C13B	C16B	1.56(2)
C17B	C18B	1.47(5)
C17B	C19B	1.62(4)
C17B	C20B	1.50(4)
C21B	C22B	1.41(4)
C21B	C26B	1.35(3)
C22B	C23B	1.38(4)
C23B	C24B	1.40(3)
C23B	C27B	1.58(4)
C24B	C25B	1.42(4)
C24B	B1B	1.57(4)
C25B	C26B	1.38(4)
C25B	C28B	1.49(3)
C29B	C30B	1.3900
C29B	C34B	1.3900
C29B	B1B	1.61(4)
C30B	C31B	1.3900
C31B	C32B	1.3900
C32B	C33B	1.3900
C33B	C34B	1.3900
C35B	C40B	1.3900
C35B	C36B	1.3900
C35B	B1B	1.59(5)
C40B	C39B	1.3900
C39B	C38B	1.3900
C38B	C37B	1.3900
C37B	C36B	1.3900


O1
B1
C29
C35
C21
N1
C1
C12
C13
C17
C
H
B
N
O

9.19.2 tBu-DMP-Cz-DMB (12)

Table 9-17 Crystal data and structural refinement details of tBu-DMP-Cz-DMB (12)

Compound	**2023NCS0558_1b**
Formula	$C_{46}H_{54}BN$
$D_{calc.}$/ g cm^{-3}	1.094
μ/mm^{-1}	0.458
Formula Weight	631.71
Colour	colourless
Shape	block-shaped
Size/mm^3	0.24×0.15×0.13
T/K	100.00(10)
Crystal System	triclinic
Space Group	P-1
a/Å	10.87800(10)
b/Å	11.73450(10)
c/Å	16.2252(2)
α/°	105.9850(10)
β/°	98.4150(10)
γ/°	100.2640(10)
V/Å^3	1916.91(4)
Z	2
Z'	1
Wavelength/Å	1.54184
Radiation type	Cu K$_\alpha$
Θ_{min}/°	2.895
Θ_{max}/°	68.249
Measured Refl's.	57842
Indep't Refl's	7012
Refl's I≥2 σ(I)	6745
R_{int}	0.0235
Parameters	471
Restraints	0
Largest Peak	0.246
Deepest Hole	-0.228
GooF	1.046
wR_2 (all data)	0.0931
wR_2	0.0924
R_1 (all data)	0.0387
R_1	0.0377

Table 9-18 Fractional Atomic Coordinates (×10^4) and Equivalent Isotropic Displacement Parameters (Å2×10^3) for tBu-DMP-Cz-DMB (12). U_{eq} is defined as 1/3 of the trace of the orthogonalised U_{ij}.

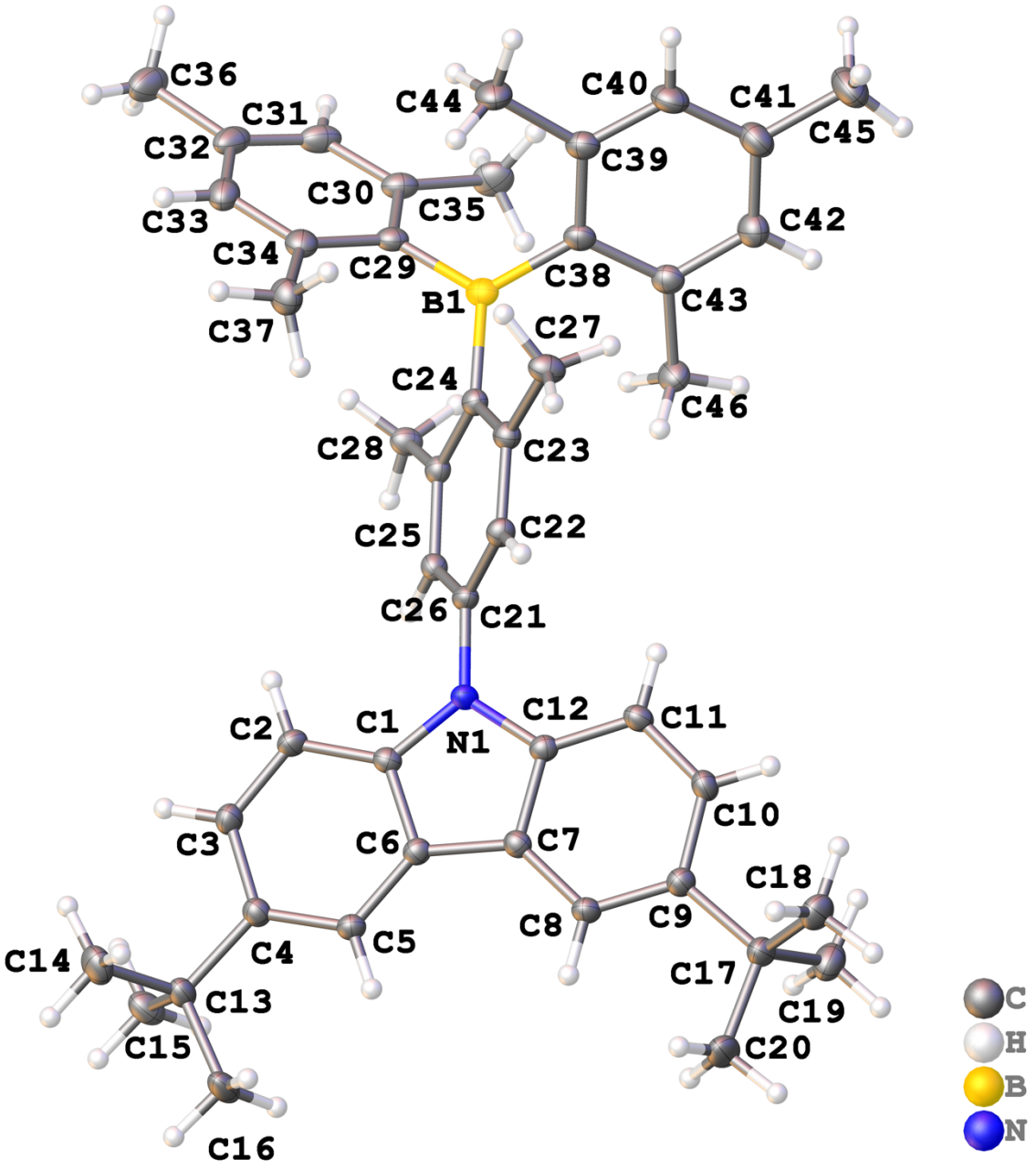
Atom	x	y	z	U_{eq}
N1	7952.7(8)	6395.4(8)	6036.8(6)	16.65(18)
C1	8273.6(9)	6400.8(9)	6901.7(7)	16.2(2)
C2	8276.3(10)	5430.1(9)	7240.2(7)	19.1(2)
C3	8600.0(10)	5700.3(10)	8139.7(7)	19.9(2)
C4	8922.3(10)	6902.1(10)	8720.8(7)	18.3(2)
C5	8888.9(10)	7850.3(9)	8368.6(7)	17.6(2)
C6	8562.8(9)	7608.0(9)	7460.7(7)	16.3(2)
C7	8429.3(10)	8375.9(9)	6907.8(7)	16.8(2)
C8	8643.6(10)	9637.7(9)	7075.9(7)	18.9(2)
C9	8506.7(10)	10120.0(10)	6385.9(7)	19.8(2)
C10	8146.5(10)	9307.8(10)	5521.9(7)	20.3(2)
C11	7913.2(10)	8060.1(10)	5336.2(7)	18.7(2)
C12	8053.0(10)	7598.2(9)	6040.7(7)	16.5(2)
C13	9306.3(11)	7110.9(10)	9707.5(7)	21.2(2)
C14	8224.5(13)	6410.2(12)	10014.0(8)	30.8(3)
C15	10524.6(12)	6656.1(11)	9892.6(8)	28.8(3)
C16	9572.3(14)	8459.1(11)	10234.4(7)	31.6(3)
C17	8789.0(12)	11492.7(10)	6516.5(7)	24.1(2)
C18	7644.2(12)	11811.9(10)	6027.4(8)	27.7(3)
C19	9975.4(12)	11825.4(11)	6143.3(9)	31.1(3)
C20	9070.0(15)	12248.8(11)	7483.8(8)	36.0(3)
C21	7591.9(10)	5365.6(9)	5268.2(7)	16.5(2)
C22	6478.2(10)	5212.3(9)	4668.0(7)	17.6(2)
C23	6132.1(10)	4248.4(9)	3889.9(7)	17.5(2)
C24	6897.5(10)	3388.2(9)	3708.9(7)	16.7(2)
C25	8019.0(10)	3549.2(9)	4334.2(7)	16.6(2)
C26	8360.2(10)	4537.1(9)	5100.7(7)	16.8(2)
C27	4909.9(10)	4151.5(10)	3268.6(7)	22.6(2)
C28	8927.5(11)	2712.4(10)	4176.9(7)	20.0(2)
C29	6499.7(10)	957.3(10)	2849.7(7)	19.4(2)
C30	7162.6(11)	220.9(10)	2318.5(7)	22.9(2)
C31	7141.3(11)	-959.1(11)	2343.4(8)	27.7(3)
C32	6458.9(12)	-1464.9(10)	2866.8(8)	28.6(3)
C33	5824.3(11)	-734.3(11)	3398.4(8)	27.3(3)
C34	5835.3(10)	457.2(10)	3403.5(7)	22.3(2)
C35	7927.8(12)	683.8(11)	1722.7(8)	29.5(3)
C36	6377.7(15)	-2773.5(11)	2840.8(9)	39.4(3)
C37	5077.6(12)	1159.9(12)	3982.1(8)	27.0(3)
C38	6176.9(10)	2554.5(9)	1925.8(7)	18.9(2)
C39	5098.6(11)	1824.3(10)	1270.1(7)	22.3(2)
C40	4820.2(11)	2079.0(11)	484.3(8)	27.2(3)
C41	5572.9(12)	3036.1(12)	307.4(8)	28.3(3)
C42	6624.1(11)	3753.4(11)	951.4(8)	25.2(2)
C43	6937.4(10)	3535.2(10)	1746.2(7)	20.7(2)
C44	4191.6(11)	777.2(11)	1398.2(8)	29.0(3)
C45	5270.0(14)	3281.8(14)	-555.2(9)	40.9(3)
C46	8134.9(11)	4355.5(11)	2380.1(8)	25.8(3)
B1	6517.6(11)	2294.1(11)	2823.6(8)	18.0(2)

Table 9-19 Anisotropic Displacement Parameters (×10^4) for tBu-DMP-Cz-DMB (12) The anisotropic displacement factor exponent takes the form: $-2\pi^2[h^2a^{*2} \times U_{11} + ... + 2hka^* \times b^* \times U_{12}]$

Atom	U_{11}	U_{22}	U_{33}	U_{23}	U_{13}	U_{12}
N^1	20.7(4)	14.2(4)	13.8(4)	2.7(3)	2.3(3)	4.3(3)
C^1	16.3(5)	16.7(5)	14.5(5)	3.4(4)	2.5(4)	3.9(4)
C^2	22.9(5)	13.8(5)	19.0(5)	3.0(4)	3.3(4)	4.2(4)
C^3	25.1(5)	16.5(5)	20.0(5)	7.5(4)	5.0(4)	6.2(4)
C^4	21.1(5)	18.3(5)	16.2(5)	5.4(4)	4.5(4)	5.6(4)
C^5	20.5(5)	14.8(5)	15.7(5)	2.7(4)	3.4(4)	3.5(4)
C^6	16.8(5)	14.9(5)	16.9(5)	4.2(4)	3.9(4)	3.9(4)
C^7	17.6(5)	17.4(5)	15.3(5)	4.6(4)	3.9(4)	4.5(4)
C^8	23.6(5)	15.9(5)	15.2(5)	2.6(4)	2.7(4)	3.9(4)
C^9	24.2(5)	16.6(5)	18.4(5)	5.2(4)	3.8(4)	5.0(4)
C^{10}	25.6(6)	20.7(5)	16.3(5)	7.9(4)	4.0(4)	6.3(4)
C^{11}	22.0(5)	18.9(5)	14.1(5)	3.3(4)	2.9(4)	5.1(4)
C^{12}	16.8(5)	15.3(5)	16.8(5)	3.8(4)	3.3(4)	4.1(4)
C^{13}	31.1(6)	18.2(5)	15.5(5)	5.7(4)	5.0(4)	7.8(4)
C^{14}	40.2(7)	33.9(7)	22.4(6)	12.5(5)	11.3(5)	8.7(5)
C^{15}	36.0(7)	30.4(6)	19.3(6)	6.5(5)	0.7(5)	12.1(5)
C^{16}	57.3(8)	22.6(6)	14.3(5)	4.6(5)	3.3(5)	12.4(6)
C^{17}	34.9(6)	16.6(5)	19.2(5)	6.1(4)	1.7(5)	4.0(5)
C^{18}	35.3(7)	18.5(5)	30.6(6)	8.5(5)	6.1(5)	8.8(5)
C^{19}	31.8(6)	25.8(6)	35.0(7)	14.7(5)	1.4(5)	1.2(5)
C^{20}	63.2(9)	16.6(6)	24.3(6)	5.0(5)	3.0(6)	6.5(6)
C^{21}	20.2(5)	14.0(5)	13.8(5)	2.9(4)	4.4(4)	1.9(4)
C^{22}	18.8(5)	16.5(5)	18.4(5)	5.0(4)	5.6(4)	5.7(4)
C^{23}	17.3(5)	18.2(5)	16.6(5)	5.4(4)	3.7(4)	2.7(4)
C^{24}	18.4(5)	16.1(5)	15.4(5)	5.0(4)	4.4(4)	2.4(4)
C^{25}	18.4(5)	15.7(5)	16.4(5)	5.8(4)	5.1(4)	3.0(4)
C^{26}	17.3(5)	17.3(5)	15.5(5)	5.9(4)	2.2(4)	2.8(4)
C^{27}	20.6(5)	24.1(6)	20.2(5)	2.3(4)	1.0(4)	7.4(4)
C^{28}	21.2(5)	19.0(5)	18.3(5)	3.4(4)	2.3(4)	6.6(4)
C^{29}	19.1(5)	17.7(5)	16.3(5)	1.1(4)	-0.7(4)	1.4(4)
C^{30}	22.4(5)	20.0(5)	20.3(5)	-0.1(4)	0.1(4)	3.4(4)
C^{31}	28.3(6)	20.8(6)	26.5(6)	-1.6(5)	-2.4(5)	7.7(5)
C^{32}	30.7(6)	18.7(6)	28.4(6)	4.5(5)	-9.1(5)	1.9(5)
C^{33}	27.0(6)	25.1(6)	25.9(6)	10.4(5)	-2.6(5)	-1.3(5)
C^{34}	20.8(5)	22.5(6)	19.5(5)	5.1(4)	-1.1(4)	0.9(4)
C^{35}	32.3(6)	25.8(6)	29.0(6)	1.2(5)	12.8(5)	9.5(5)
C^{36}	49.2(8)	21.7(6)	39.3(8)	8.8(6)	-10.2(6)	4.6(6)
C^{37}	27.1(6)	30.3(6)	25.4(6)	11.2(5)	8.7(5)	4.3(5)
C^{38}	20.4(5)	17.9(5)	16.1(5)	1.2(4)	4.1(4)	4.7(4)
C^{39}	22.7(5)	21.4(5)	19.2(5)	2.3(4)	3.1(4)	3.3(4)
C^{40}	26.0(6)	29.8(6)	18.9(6)	2.9(5)	-1.7(4)	1.5(5)
C^{41}	30.6(6)	34.1(7)	19.5(6)	8.8(5)	3.4(5)	6.1(5)
C^{42}	26.3(6)	26.4(6)	23.2(6)	9.2(5)	6.8(5)	3.4(5)
C^{43}	21.2(5)	20.7(5)	18.6(5)	3.2(4)	4.9(4)	4.7(4)
C^{44}	26.2(6)	27.4(6)	25.1(6)	5.6(5)	-3.0(5)	-3.8(5)
C^{45}	42.8(8)	50.9(9)	25.0(7)	17.2(6)	-1.4(6)	-1.0(6)
C^{46}	24.7(6)	25.9(6)	23.2(6)	8.3(5)	2.5(5)	-2.4(5)
B^1	12.7(5)	20.3(6)	19.2(6)	3.4(5)	4.5(4)	2.5(4)

Table 9-20 Bond Angles in Å for tBu-DMP-Cz-DMB (12).

Atom	Atom	Length/Å
N^{1}	C^{1}	1.3935(13)
N^{1}	C^{12}	1.3943(13)
N^{1}	C^{21}	1.4239(13)
C^{1}	C^{2}	1.3945(15)
C^{1}	C^{6}	1.4066(14)
C^{2}	C^{3}	1.3818(15)
C^{3}	C^{4}	1.4126(15)
C^{4}	C^{5}	1.3873(15)
C^{4}	C^{13}	1.5328(14)
C^{5}	C^{6}	1.3989(14)
C^{6}	C^{7}	1.4462(14)
C^{7}	C^{8}	1.3989(15)
C^{7}	C^{12}	1.4038(14)
C^{8}	C^{9}	1.3878(15)
C^{9}	C^{10}	1.4134(15)
C^{9}	C^{17}	1.5331(15)
C^{10}	C^{11}	1.3789(15)
C^{11}	C^{12}	1.3940(15)
C^{13}	C^{14}	1.5361(16)
C^{13}	C^{15}	1.5347(16)
C^{13}	C^{16}	1.5288(15)
C^{17}	C^{18}	1.5368(16)
C^{17}	C^{19}	1.5375(17)
C^{17}	C^{20}	1.5296(16)
C^{21}	C^{22}	1.3888(15)
C^{21}	C^{26}	1.3885(15)
C^{22}	C^{23}	1.3920(15)
C^{23}	C^{24}	1.4164(15)
C^{23}	C^{27}	1.5124(14)
C^{24}	C^{25}	1.4155(15)
C^{24}	B^{1}	1.5823(15)
C^{25}	C^{26}	1.3950(14)
C^{25}	C^{28}	1.5124(14)
C^{29}	C^{30}	1.4153(15)
C^{29}	C^{34}	1.4154(16)
C^{29}	B^{1}	1.5776(16)
C^{30}	C^{31}	1.3925(16)
C^{30}	C^{35}	1.5121(17)
C^{31}	C^{32}	1.3892(18)
C^{32}	C^{33}	1.3905(18)
C^{32}	C^{36}	1.5108(16)
C^{33}	C^{34}	1.3937(16)
C^{34}	C^{37}	1.5110(16)
C^{38}	C^{39}	1.4200(15)
C^{38}	C^{43}	1.4176(15)
C^{38}	B^{1}	1.5749(16)
C^{39}	C^{40}	1.3912(16)
C^{39}	C^{44}	1.5150(16)
C^{40}	C^{41}	1.3903(17)
C^{41}	C^{42}	1.3895(17)
C^{41}	C^{45}	1.5072(17)
C^{42}	C^{43}	1.3889(16)
C^{43}	C^{46}	1.5156(15)


C36
C31
C32
C33
C34
C37
C30
C35
C29
B1
C38
C44
C40
C41
C45
C39
C42
C43
C46
C27
C24
C28
C23
C25
C22
C26
C21
C2
C1
N1
C12
C11
C10
C3
C6
C7
C18
C14
C4
C5
C8
C9
C17
C13
C19
C15
C20
C16
C
H
B
N

9.19.3 tBu-DMeOP-Cz-DMB (13)

Table 9-21 Crystal data and structural refinement details of tBu-DMeOP-Cz-DMB (13)

Compound	**2023NCS0435_1b**
Formula	$C_{46}H_{54}BNO_2$
$D_{calc.}$/ g cm^{-3}	1.142
μ/mm^{-1}	0.517
Formula Weight	663.71
Colour	colourless
Shape	needle-shaped
Size/mm^3	0.75×0.02×0.02
T/K	100(2)
Crystal System	monoclinic
Space Group	$P2_1/c$
a/Å	16.0621(2)
b/Å	21.4856(3)
c/Å	11.65270(10)
α/°	90
β/°	106.3020(10)
γ/°	90
V/Å^3	3859.71(8)
Z	4
Z'	1
Wavelength/Å	1.54184
Radiation type	Cu K$_\alpha$
Θ_{min}/°	2.866
Θ_{max}/°	70.075
Measured Refl's.	37577
Indep't Refl's	7306
Refl's I≥2 σ(I)	5925
R_{int}	0.0604
Parameters	465
Restraints	0
Largest Peak	0.275
Deepest Hole	-0.222
GooF	1.038
wR_2 (all data)	0.1084
wR_2	0.1017
R_1 (all data)	0.0537
R_1	0.0409

Table 9-22 Fractional Atomic Coordinates (×10^4) and Equivalent Isotropic Displacement Parameters (Å2×10^3) for tBu-DMeOP-Cz-DMB (13). U_{eq} is defined as 1/3 of the trace of the orthogonalised U_{ij}.

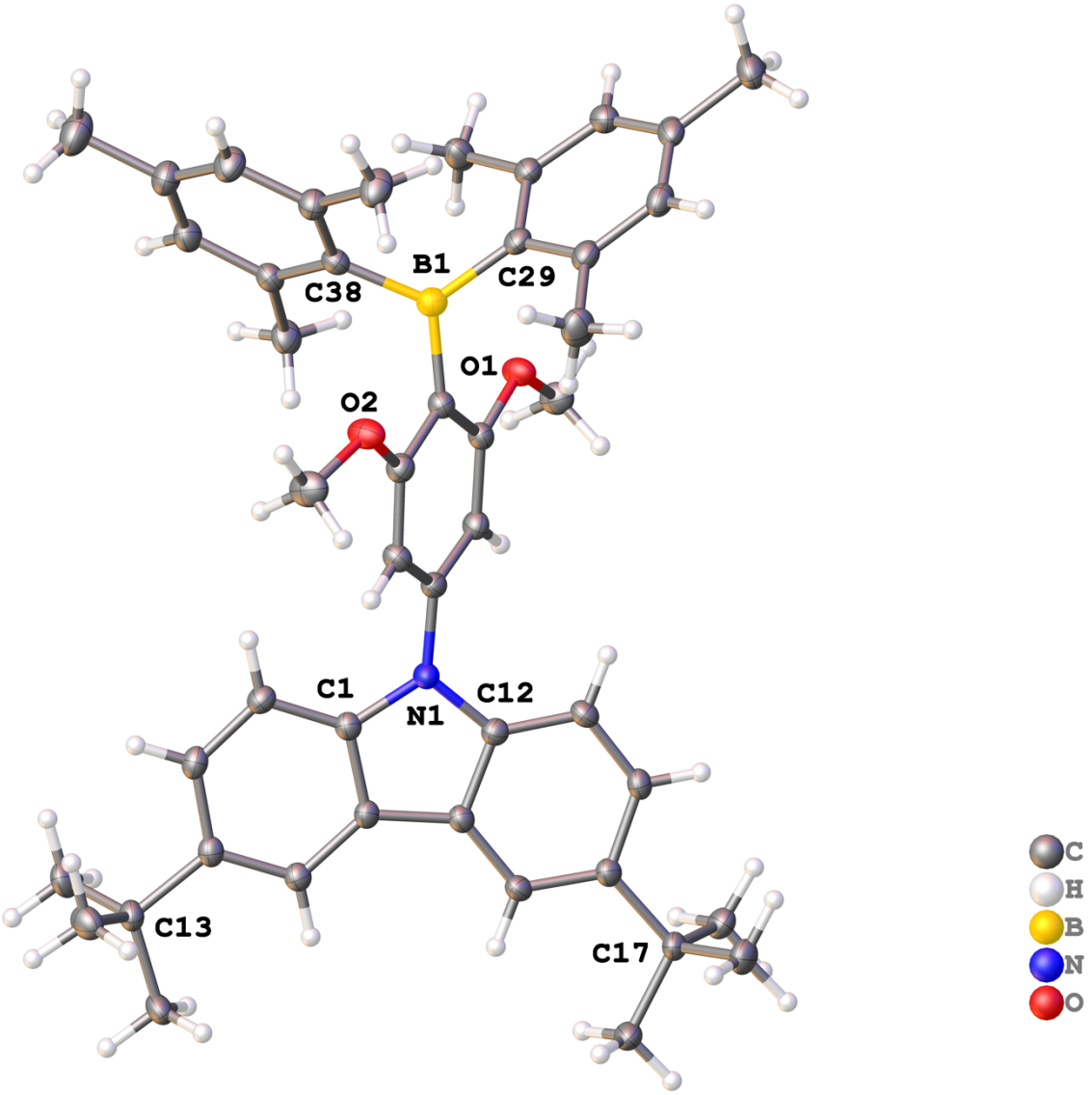
Atom	x	y	z	U_{eq}
O1	6963.9(6)	3005.8(5)	7576.4(8)	25.3(2)
O2	7128.1(7)	4971.9(5)	5979.5(8)	28.0(2)
N1	4882.8(7)	3556.8(5)	3813.8(9)	20.9(2)
C1	4856.8(9)	3671.3(6)	2621.7(11)	19.8(3)
C2	5510.4(9)	3881.1(6)	2140.1(12)	21.6(3)
C3	5324.2(9)	3910.5(6)	909.9(12)	22.2(3)
C4	4512.0(9)	3744.4(6)	134.0(11)	20.0(3)
C5	3867.3(9)	3543.5(6)	632.2(11)	20.0(3)
C6	4038.1(9)	3504.7(6)	1878.7(11)	19.0(3)
C7	3528.1(9)	3294.9(6)	2653.0(11)	19.5(3)
C8	2669.3(9)	3104.6(6)	2443.2(11)	20.4(3)
C9	2349.2(9)	2927.2(6)	3384.0(11)	20.7(3)
C10	2924.4(9)	2942.3(6)	4551.4(11)	21.8(3)
C11	3778.8(9)	3133.2(6)	4790.4(11)	21.9(3)
C12	4077.2(9)	3318.0(6)	3833.2(11)	20.2(3)
C13	4383.4(9)	3788.7(7)	-1220.3(12)	23.1(3)
C14	4517.5(11)	4466.4(7)	-1554.0(13)	31.1(3)
C15	5047.0(11)	3365.3(8)	-1556.5(13)	32.6(3)
C16	3474.6(10)	3587.6(8)	-1940.5(12)	27.7(3)
C17	1410.9(9)	2713.4(7)	3203.2(11)	23.3(3)
C18	901.5(9)	2688.6(8)	1878.5(12)	29.3(3)
C19	945.1(10)	3174.0(8)	3827.4(13)	30.8(3)
C20	1395.2(9)	2056.4(7)	3720.3(13)	27.8(3)
C21	5591.6(9)	3703.9(6)	4819.8(11)	20.4(3)
C22	5897.8(9)	3259.1(6)	5706.3(11)	20.8(3)
C23	6603.7(9)	3415.7(6)	6675.3(11)	20.5(3)
C24	7038.7(9)	3985.2(6)	6748.7(11)	21.0(3)
C25	6699.3(9)	4415.1(6)	5832.6(12)	21.8(3)
C26	5973.5(9)	4289.2(7)	4881.4(11)	22.3(3)
C27	6581.7(10)	2404.8(7)	7529.6(13)	27.1(3)
C28	6941.6(11)	5387.3(7)	4991.6(14)	33.1(3)
C29	8005.1(8)	4045.0(6)	9086.6(11)	21.1(3)
C30	7518.6(9)	4427.2(7)	9646.2(12)	24.0(3)
C31	7602.6(9)	4353.9(7)	10864.2(13)	26.4(3)
C32	8137.5(9)	3902.6(7)	11549.7(12)	25.8(3)
C33	8603.6(9)	3522.5(7)	10987.9(12)	25.5(3)
C34	8554.0(9)	3590.7(7)	9782.3(12)	22.7(3)
C35	6934.7(11)	4930.0(8)	8961.9(14)	34.4(4)
C36	8236.6(11)	3827.3(8)	12869.3(13)	33.8(4)
C37	9069.0(10)	3152.9(8)	9230.8(13)	29.7(3)
C38	8754.1(9)	4258.5(7)	7267.2(11)	21.8(3)
C39	9318.9(9)	4759.6(7)	7736.5(12)	25.5(3)
C40	10074.0(10)	4846.4(7)	7392.8(13)	30.3(3)
C41	10303.1(10)	4448.0(8)	6589.7(13)	30.0(3)
C42	9742.2(10)	3962.5(7)	6113.3(12)	26.4(3)
C43	8976.0(9)	3863.7(7)	6423.7(11)	23.2(3)
C44	9109.0(11)	5231.8(8)	8578.4(14)	33.3(3)
C45	11129.9(12)	4541.1(9)	6234.9(17)	41.5(4)
C46	8425.1(10)	3311.5(7)	5861.7(13)	27.9(3)
B1	7932.5(10)	4113.0(7)	7711.1(13)	21.1(3)

Table 9-23 Anisotropic Displacement Parameters (×10^4) for tBu-DMeOP-Cz-DMB (13) The anisotropic displacement factor exponent takes the form: $-2\pi^2[h^2a^{*2} \times U_{11} + ... + 2hka^* \times b^* \times U_{12}]$

Atom	U_{11}	U_{22}	U_{33}	U_{23}	U_{13}	U_{12}
O1	24.3(5)	25.5(5)	22.9(5)	5.9(4)	1.6(4)	-3.9(4)
O2	28.8(5)	23.8(5)	27.0(5)	3.2(4)	0.9(4)	-6.5(4)
N1	17.7(6)	28.2(6)	16.6(5)	-0.1(4)	4.6(4)	-3.4(5)
C1	19.7(7)	21.9(6)	18.3(6)	-0.2(5)	6.4(5)	0.4(5)
C2	17.8(6)	24.2(7)	22.8(6)	-0.6(5)	5.7(5)	-2.0(5)
C3	22.2(7)	22.4(7)	25.0(7)	0.1(5)	11.5(5)	-1.2(5)
C4	21.9(7)	20.1(6)	19.9(6)	0.2(5)	8.9(5)	0.8(5)
C5	20.2(7)	22.1(6)	18.4(6)	-0.9(5)	6.4(5)	-0.2(5)
C6	18.6(6)	21.5(6)	18.3(6)	-0.5(5)	7.4(5)	0.9(5)
C7	19.9(7)	22.7(6)	16.4(6)	-0.6(5)	6.1(5)	1.1(5)
C8	18.8(7)	26.9(7)	15.1(6)	-0.8(5)	3.9(5)	1.2(5)
C9	19.8(7)	25.7(7)	17.6(6)	-0.9(5)	6.8(5)	1.2(5)
C10	23.0(7)	27.0(7)	17.6(6)	-0.7(5)	9.3(5)	-0.6(6)
C11	22.5(7)	27.2(7)	15.0(6)	-0.5(5)	3.8(5)	-0.6(5)
C12	18.4(7)	23.4(6)	18.9(6)	-1.2(5)	5.3(5)	0.1(5)
C13	23.5(7)	29.2(7)	19.0(6)	0.5(5)	9.5(5)	-3.1(6)
C14	33.7(8)	34.9(8)	24.2(7)	5.6(6)	7.4(6)	-6.1(7)
C15	33.3(8)	45.5(9)	22.5(7)	-4.2(6)	13.5(6)	3.5(7)
C16	28.7(8)	39.4(8)	15.6(6)	-0.2(6)	7.0(5)	-6.5(6)
C17	18.9(7)	35.0(8)	17.8(6)	-0.2(5)	7.9(5)	-0.4(6)
C18	19.7(7)	47.3(9)	20.8(7)	-0.1(6)	5.7(5)	-5.1(6)
C19	25.2(8)	42.3(9)	28.6(7)	-2.4(6)	13.8(6)	1.7(7)
C20	20.0(7)	37.2(8)	27.1(7)	2.4(6)	8.3(6)	-3.5(6)
C21	16.9(6)	27.8(7)	16.4(6)	-1.1(5)	4.6(5)	-0.5(5)
C22	19.9(7)	23.5(7)	19.6(6)	-0.1(5)	6.7(5)	-3.4(5)
C23	19.4(7)	25.3(7)	17.1(6)	2.4(5)	5.7(5)	0.3(5)
C24	20.1(7)	25.3(7)	17.9(6)	0.9(5)	5.6(5)	-1.2(5)
C25	21.1(7)	23.0(7)	21.6(6)	-0.8(5)	6.7(5)	-2.0(5)
C26	23.1(7)	25.2(7)	18.1(6)	1.9(5)	4.7(5)	0.7(6)
C27	27.3(8)	24.1(7)	28.6(7)	5.3(6)	6.0(6)	-1.2(6)
C28	33.8(9)	27.1(7)	36.2(8)	9.0(6)	6.1(7)	-4.8(6)
C29	15.4(6)	26.1(7)	21.8(6)	-1.5(5)	5.3(5)	-4.3(5)
C30	18.5(7)	29.6(7)	25.2(7)	-2.6(6)	8.1(5)	-3.9(6)
C31	22.2(7)	33.2(8)	26.8(7)	-7.1(6)	11.8(6)	-4.5(6)
C32	21.6(7)	36.0(8)	20.7(6)	-3.7(6)	7.4(5)	-10.3(6)
C33	20.9(7)	33.7(8)	21.3(6)	2.6(6)	5.0(5)	-2.0(6)
C34	17.5(7)	30.5(7)	20.1(6)	0.2(5)	4.9(5)	-2.8(6)
C35	32.5(8)	37.9(9)	36.3(8)	3.7(7)	15.5(7)	10.1(7)
C36	33.5(9)	47.8(10)	22.6(7)	-2.4(6)	12.0(6)	-7.3(7)
C37	28.5(8)	38.5(8)	22.8(7)	4.9(6)	8.6(6)	9.6(6)
C38	21.4(7)	27.0(7)	15.9(6)	1.5(5)	3.4(5)	-0.7(6)
C39	23.8(7)	30.2(7)	23.3(7)	-1.6(6)	7.8(5)	-3.1(6)
C40	27.0(8)	33.4(8)	32.3(7)	-4.4(6)	11.3(6)	-8.5(6)
C41	25.7(8)	38.0(8)	29.3(7)	0.5(6)	12.3(6)	-1.8(6)
C42	26.6(7)	32.1(7)	22.2(6)	-0.9(6)	10.0(6)	1.6(6)
C43	23.7(7)	28.6(7)	17.4(6)	1.6(5)	5.9(5)	0.0(6)
C44	31.4(8)	35.3(8)	36.8(8)	-11.1(7)	15.2(7)	-11.0(7)
C45	34.0(9)	48.5(10)	49.2(10)	-8.7(8)	23.4(8)	-7.5(8)
C46	31.0(8)	31.2(8)	23.9(7)	-5.9(6)	11.4(6)	-3.2(6)
B1	21.4(8)	18.9(7)	22.4(7)	-0.7(6)	5.0(6)	0.2(6)

Table 9-24 Bond Angles in Å for tBu-DMeOP-Cz-DMB (13).

Atom	Atom	Length/Å
O1	C23	1.3682(16)
O1	C27	1.4243(17)
O2	C25	1.3671(17)
O2	C28	1.4205(18)
N1	C1	1.3998(16)
N1	C12	1.3981(17)
N1	C21	1.4216(17)
C1	C2	1.3968(19)
C1	C6	1.4028(19)
C2	C3	1.3812(19)
C3	C4	1.409(2)
C4	C5	1.3903(18)
C4	C13	1.5360(17)
C5	C6	1.4030(18)
C6	C7	1.4502(18)
C7	C8	1.3931(19)
C7	C12	1.4109(18)
C8	C9	1.3885(18)
C9	C10	1.4141(19)
C9	C17	1.5325(19)
C10	C11	1.384(2)
C11	C12	1.3897(18)
C13	C14	1.538(2)
C13	C15	1.533(2)
C13	C16	1.528(2)
C17	C18	1.5317(19)
C17	C19	1.541(2)
C17	C20	1.538(2)
C21	C22	1.3919(19)
C21	C26	1.392(2)
C22	C23	1.3981(19)
C23	C24	1.400(2)
C24	C25	1.4012(19)
C24	B1	1.578(2)
C25	C26	1.3911(19)
C29	C30	1.4129(19)
C29	C34	1.409(2)
C29	B1	1.5809(19)
C30	C31	1.396(2)
C30	C35	1.504(2)
C31	C32	1.390(2)
C32	C33	1.390(2)
C32	C36	1.5095(19)
C33	C34	1.3923(19)
C34	C37	1.510(2)
C38	C39	1.415(2)
C38	C43	1.4175(19)
C38	B1	1.578(2)
C39	C40	1.392(2)
C39	C44	1.514(2)
C40	C41	1.392(2)
C41	C42	1.388(2)
C41	C45	1.511(2)
C42	C43	1.393(2)
C43	C46	1.515(2)


B1
C38
C29
O1
O2
C1
N1
C12
C13
C17
C
H
B
N
O

9.19.4 tBu-MPhOP-Cz-DMB (14)

Table 9-25 Crystal data and structural refinement details of tBu-MPhOP-Cz-DMB (14)

Compound	**2024NCS0366_2a_twin1_hklf4**
Formula	$C_{50}H_{54}BNO$
$D_{calc.}$/ g cm^{-3}	1.166
μ/mm^{-1}	0.509
Formula Weight	695.75
Colour	colourless
Shape	needle-shaped
Size/mm^3	0.188×0.031×0.027
T/K	100(2)
Crystal System	orthorhombic
Flack Parameter	0.5(3)
Hooft Parameter	0.24(17)
Space Group	$P2_12_12_1$
a/Å	10.3173(4)
b/Å	12.1133(4)
c/Å	31.7172(8)
α/°	90
β/°	90
γ/°	90
V/Å^3	3963.9(2)
Z	4
Z'	1
Wavelength/Å	1.54184
Radiation type	Cu K$_\alpha$
Θ_{min}/°	3.906
Θ_{max}/°	73.941
Measured Refl's.	16924
Indep't Refl's	16924
Refl's I≥2 σ(I)	12931
R_{int}	.
Parameters	516
Restraints	3
Largest Peak	0.448
Deepest Hole	-0.251
GooF	1.025
wR_2 (all data)	0.2256
wR_2	0.2098
R_1 (all data)	0.1013
R_1	0.0810

Table 9-26 Fractional Atomic Coordinates (×10^4) and Equivalent Isotropic Displacement Parameters (Å2×10^3) for tBu-MPhOP-Cz-DMB (14). U_{eq} is defined as 1/3 of the trace of the orthogonalised U_{ij}.

Atom	x	y	z	U_{eq}
O1	3834(3)	2566(3)	6361.3(11)	38.0(8)
N1	1756(4)	2027(3)	7704.5(12)	33.5(9)
C1	1781(5)	2397(4)	8125.3(15)	34.2(10)
C2	1836(6)	3463(4)	8290.0(16)	40.2(12)
C3	1932(6)	3580(4)	8719.1(16)	41.1(12)
C4	1972(5)	2687(4)	9001.1(16)	37.7(11)
C5	1885(5)	1636(4)	8828.4(15)	33.6(10)
C6	1806(5)	1483(4)	8398.3(16)	34.4(10)
C7	1799(5)	511(4)	8133.1(15)	33.6(10)
C8	1870(5)	-622(4)	8226.6(16)	34.8(10)
C9	1908(5)	-1391(4)	7899.9(15)	33.7(10)
C10	1842(5)	-1009(4)	7486.3(16)	35.6(11)
C11	1750(5)	106(4)	7382.4(16)	36.5(11)
C12	1778(5)	861(4)	7713.8(15)	33.3(10)
C13	2132(6)	2898(5)	9474.5(17)	44.8(13)
C14	3484(8)	3387(9)	9551(2)	78(2)
C15	1118(8)	3705(6)	9632.5(19)	58.8(17)
C16	1984(10)	1840(5)	9730.1(18)	68(2)
C17	2059(5)	-2626(4)	8003.8(17)	39.1(12)
C18	3431(7)	-2809(6)	8169(3)	51(2)
C18A	3370(30)	-2980(30)	7821(18)	68(14)
C19A	1061(7)	-2965(5)	8335(2)	41.0(18)
C19B	2240(40)	-2870(30)	8488(10)	65(12)
C20A	1828(8)	-3349(5)	7615(2)	42.8(18)
C20B	1010(40)	-3360(30)	7875(13)	72(14)
C21	2529(5)	4044(4)	6638.9(15)	36.1(11)
C22	3019(5)	2973(4)	6673.4(15)	34.5(10)
C23	2814(5)	2325(4)	7024.9(16)	36.6(11)
C24	1984(5)	2694(4)	7344.6(15)	34.7(11)
C25	1402(5)	3724(4)	7305.2(16)	35.2(11)
C26	1714(5)	4399(4)	6967.4(15)	33.9(10)
C27	3317(6)	1803(4)	6083.1(15)	36.7(11)
C28	4157(6)	1354(5)	5794.3(19)	48.4(14)
C29	3710(7)	597(5)	5496.0(19)	52.7(15)
C30	2406(8)	315(5)	5493(2)	54.5(16)
C31	1579(7)	747(5)	5793.2(19)	51.4(15)
C32	2012(6)	1483(5)	6089.8(17)	43.8(12)
C33	3375(5)	6068(4)	6416.8(16)	37.5(11)
C34	2911(6)	7026(5)	6214.7(17)	41.2(12)
C35	3347(6)	8069(5)	6334.9(18)	44.8(13)
C36	4273(6)	8198(5)	6647(2)	46.4(13)
C37	4736(6)	7253(5)	6848.3(18)	44.6(13)
C38	4289(5)	6201(5)	6746.7(17)	38.2(12)
C39	1881(7)	6969(5)	5880.4(19)	50.5(14)
C40	4762(7)	9335(5)	6766(2)	57.4(16)
C41	4847(6)	5257(5)	6997(2)	46.3(14)
C42	2964(5)	4440(4)	5810.5(15)	34.2(11)
C43	4153(5)	4293(4)	5593.7(16)	38.0(12)
C44	4154(6)	3817(5)	5195.4(17)	41.1(12)
C45	3022(6)	3482(5)	4998.7(16)	43.8(13)
C46	1839(6)	3652(5)	5209.6(16)	42.3(12)
C47	1808(5)	4116(4)	5610.3(15)	36.9(11)
C48	5423(6)	4623(5)	5798.5(19)	46.4(14)
C49	3044(7)	2978(6)	4565.8(18)	57.2(16)
C50	501(5)	4244(5)	5825.7(19)	47.2(14)
B1	2957(6)	4857(5)	6281.4(19)	38.4(13)

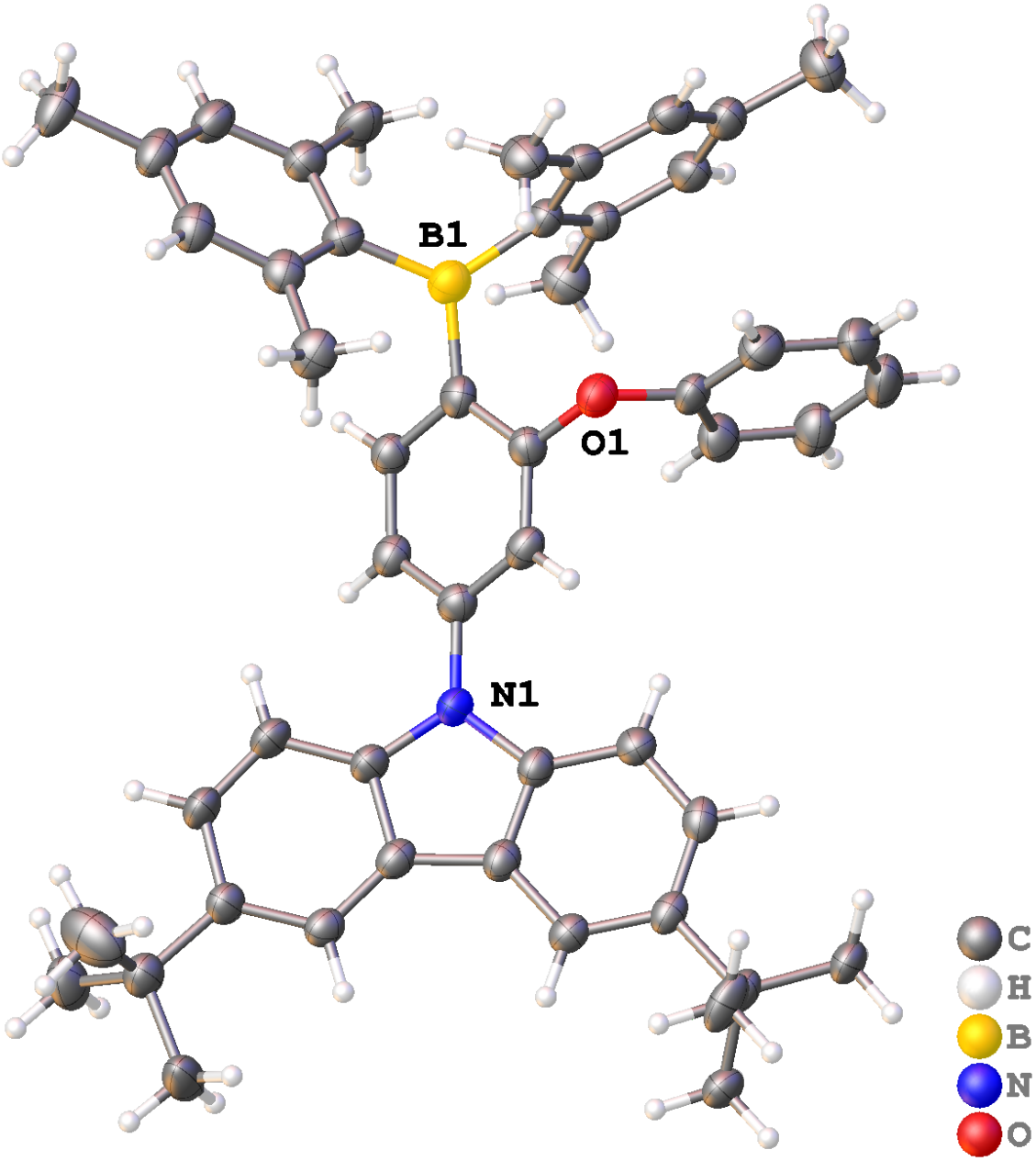
Table 9-27 Anisotropic Displacement Parameters (×10^4) for tBu-MPhOP-Cz-DMB (14) The anisotropic displacement factor exponent takes the form: $-2\pi^2[h^2a^{*2} \times U_{11} + ... + 2hka^* \times b^* \times U_{12}]$

Atom	U_{11}	U_{22}	U_{33}	U_{23}	U_{13}	U_{12}
O1	39.3(19)	32.3(19)	42.2(19)	-1.3(15)	2.5(15)	0.8(15)
N1	43(2)	24(2)	34(2)	-0.1(16)	3.4(17)	1.6(18)
C1	44(3)	25(2)	34(2)	2.3(19)	1(2)	3(2)
C2	55(3)	23(2)	42(3)	3(2)	2(2)	1(2)
C3	60(3)	22(2)	41(3)	0(2)	0(2)	1(3)
C4	48(3)	27(3)	37(3)	0(2)	2(2)	4(2)
C5	36(3)	27(2)	38(2)	2.2(19)	4(2)	3(2)
C6	37(3)	26(2)	41(3)	2(2)	2(2)	0(2)
C7	35(3)	26(2)	40(2)	-3(2)	3(2)	2(2)
C8	39(3)	27(2)	38(2)	2(2)	0(2)	-1(2)
C9	33(3)	23(2)	44(3)	-3(2)	2(2)	-1(2)
C10	35(3)	31(3)	42(3)	-9(2)	2(2)	-2(2)
C11	44(3)	31(3)	34(2)	0.5(19)	4(2)	-4(2)
C12	37(3)	25(2)	38(2)	-2.3(19)	4(2)	0(2)
C13	62(4)	31(3)	41(3)	-1(2)	2(2)	4(3)
C14	71(5)	112(7)	52(4)	-3(4)	-6(3)	-14(5)
C15	87(5)	44(4)	46(3)	-9(3)	2(3)	18(3)
C16	134(7)	34(3)	36(3)	0(2)	4(4)	11(4)
C17	47(3)	23(2)	47(3)	-1(2)	-1(2)	-2(2)
C18	50(4)	22(3)	82(6)	-3(3)	-12(4)	7(3)
C18A	40(20)	40(20)	120(40)	30(20)	10(20)	23(17)
C19A	55(4)	25(3)	43(4)	4(3)	3(3)	0(3)
C19B	80(30)	26(18)	90(30)	-2(18)	20(20)	-10(17)
C20A	60(4)	23(3)	45(4)	-4(3)	5(3)	-3(3)
C20B	130(40)	23(17)	70(30)	-10(16)	20(30)	-20(20)
C21	42(3)	30(3)	36(3)	-5(2)	-2(2)	-4(2)
C22	41(3)	31(3)	31(2)	-2(2)	-2(2)	3(2)
C23	42(3)	26(3)	42(3)	1(2)	-6(2)	-1(2)
C24	40(3)	31(3)	33(2)	1.4(19)	-3(2)	0(2)
C25	38(3)	28(3)	40(3)	-2(2)	1(2)	-1(2)
C26	38(3)	29(2)	34(2)	-1(2)	-2.4(19)	3(2)
C27	50(3)	23(2)	37(2)	-0.7(19)	-2(2)	1(2)
C28	55(3)	38(3)	51(3)	0(3)	9(3)	-2(3)
C29	74(4)	39(3)	45(3)	-6(3)	13(3)	4(3)
C30	81(5)	33(3)	50(3)	-9(3)	-8(3)	4(3)
C31	63(4)	41(3)	51(3)	-6(3)	-12(3)	-1(3)
C32	50(3)	37(3)	44(3)	-5(2)	2(2)	7(3)
C33	45(3)	33(3)	35(2)	2(2)	4(2)	-3(2)
C34	50(3)	33(3)	41(3)	2(2)	3(2)	1(2)
C35	54(3)	29(3)	52(3)	3(2)	7(3)	-1(2)
C36	48(3)	32(3)	60(3)	-5(3)	9(3)	-4(2)
C37	43(3)	40(3)	51(3)	-7(2)	1(2)	-2(2)
C38	35(3)	38(3)	42(3)	-3(2)	3(2)	-1(2)
C39	66(4)	33(3)	52(3)	10(2)	-11(3)	0(3)
C40	52(4)	31(3)	89(5)	-12(3)	6(3)	-6(3)
C41	43(3)	43(3)	53(3)	1(3)	-10(2)	1(2)
C42	44(3)	26(2)	32(2)	-0.5(19)	-2(2)	-3(2)
C43	47(3)	30(3)	36(3)	7(2)	1(2)	0(2)
C44	49(3)	32(3)	43(3)	7(2)	5(2)	3(2)
C45	62(4)	32(3)	38(3)	0(2)	-3(2)	-1(3)
C46	54(3)	38(3)	35(3)	2(2)	-4(2)	-6(3)
C47	47(3)	31(3)	33(2)	2.3(19)	-3(2)	-1(2)
C48	45(3)	49(4)	46(3)	0(3)	2(2)	-9(3)
C49	69(4)	59(4)	44(3)	-11(3)	3(3)	-5(3)
C50	42(3)	50(4)	50(3)	0(3)	-3(2)	-1(3)
B1	41(3)	33(3)	41(3)	1(2)	-3(2)	2(3)

Table 9-28 Bond Angles in Å for tBu-MPhOP-Cz-DMB (14).

Atom	Atom	Atom	Angle/°
C27	O1	C22	117.3(4)
C1	N1	C12	107.3(4)
C1	N1	C24	125.4(4)
C12	N1	C24	125.7(4)
C2	C1	N1	130.6(4)
C2	C1	C6	119.8(4)
C6	C1	N1	109.5(4)
C3	C2	C1	118.1(5)
C2	C3	C4	123.6(5)
C3	C4	C13	119.9(5)
C5	C4	C3	116.9(4)
C5	C4	C13	123.1(4)
C6	C5	C4	121.1(4)
C1	C6	C7	106.4(4)
C5	C6	C1	120.3(5)
C5	C6	C7	133.2(5)
C8	C7	C6	132.2(5)
C12	C7	C6	107.9(4)
C12	C7	C8	119.9(4)
C9	C8	C7	119.8(5)
C8	C9	C17	119.6(4)
C10	C9	C8	118.5(5)
C10	C9	C17	122.0(4)
C9	C10	C11	123.2(5)
C10	C11	C12	117.2(4)
C7	C12	N1	108.9(4)
C11	C12	N1	129.8(5)
C11	C12	C7	121.3(5)
C4	C13	C14	108.5(5)
C15	C13	C4	110.9(5)
C15	C13	C14	109.0(6)
C15	C13	C16	107.3(5)
C16	C13	C4	111.7(5)
C16	C13	C14	109.3(6)
C9	C17	C19B	113.8(14)
C18	C17	C9	108.0(5)
C18	C17	C19A	110.5(6)
C18	C17	C20A	109.7(6)
C18A	C17	C9	106.4(15)
C18A	C17	C19B	102(3)
C19A	C17	C9	109.9(5)
C19A	C17	C20A	107.2(5)
C20A	C17	C9	111.6(4)
C20B	C17	C9	117.2(18)
C20B	C17	C18A	112(3)
C20B	C17	C19B	104(2)
C22	C21	C26	116.2(5)
C22	C21	B1	122.6(5)
C26	C21	B1	120.9(5)
O1	C22	C21	119.5(4)
C23	C22	O1	117.8(4)
C23	C22	C21	122.5(5)
C22	C23	C24	119.8(5)
C23	C24	N1	120.1(5)
C25	C24	N1	120.8(5)
C25	C24	C23	119.0(5)
C26	C25	C24	119.9(5)
C25	C26	C21	122.1(5)
O1	C27	C32	123.0(5)

Atom	Atom	Atom	Angle/°
C28	C27	O1	116.5(5)
C28	C27	C32	120.5(5)
C27	C28	C29	120.2(6)
C30	C29	C28	119.1(6)
C31	C30	C29	120.0(6)
C32	C31	C30	121.2(6)
C31	C32	C27	118.9(5)
C34	C33	C38	117.9(5)
C34	C33	B1	123.0(5)
C38	C33	B1	119.0(5)
C33	C34	C39	121.6(5)
C35	C34	C33	120.8(5)
C35	C34	C39	117.5(5)
C36	C35	C34	121.4(5)
C35	C36	C37	118.1(5)
C35	C36	C40	120.7(6)
C37	C36	C40	121.2(6)
C38	C37	C36	122.1(5)
C33	C38	C41	123.8(5)
C37	C38	C33	119.7(5)
C37	C38	C41	116.5(5)
C43	C42	B1	120.3(5)
C47	C42	C43	118.6(4)
C47	C42	B1	120.9(5)
C42	C43	C48	120.5(5)
C44	C43	C42	119.6(5)
C44	C43	C48	119.9(5)
C45	C44	C43	122.1(5)
C44	C45	C46	118.3(5)
C44	C45	C49	121.2(6)
C46	C45	C49	120.5(5)
C47	C46	C45	121.0(5)
C42	C47	C50	121.4(4)
C46	C47	C42	120.4(5)
C46	C47	C50	118.2(5)
C21	B1	C33	117.5(4)
C21	B1	C42	119.1(5)
C42	B1	C33	123.4(5)


B1
O1
N1
C
H
B
N
O

9.19.5 tBu-DPhOP-Cz-DMB (15)

Table 9-29 Crystal data and structural refinement details of tBu-DPhOP-Cz-DMB (15)

Compound	**2024NCS0367r2_1 a**
Formula	$C_{56}H_{58}BNO_2$
$D_{calc.}$/ g cm^{-3}	1.139
μ/mm^{-1}	0.067
Formula Weight	787.914
Colour	colourless
Shape	block-shaped
Size/mm^3	0.170×0.150×0.120
T/K	100(2)
Crystal System	monoclinic
Space Group	$P2_1/n$
a/Å	12.8463(1)
b/Å	27.3003(2)
c/Å	13.1851(1)
α/°	90
β/°	96.580(1)
γ/°	90
V/Å^3	4593.66(6)
Z	4
Z'	1
Wavelength/Å	0.71073
Radiation type	Mo K$_\alpha$
Θ_{min}/°	1.72
Θ_{max}/°	36.32
Measured Refl's.	853583
Indep't Refl's	22272
Refl's I≥2 σ(I)	20680
R_{int}	0.0378
Parameters	1063
Restraints	0
Largest Peak	0.2706
Deepest Hole	-0.2078
GooF	1.1053
wR_2 (all data)	0.0444
wR_2	0.0434
R_1 (all data)	0.0255
R_1	0.0222

Table 9-30 Fractional Atomic Coordinates (×10^4) and Equivalent Isotropic Displacement Parameters (Å2×10^3) for tBu-DPhOP-Cz-DMB (15). U_{eq} is defined as 1/3 of the trace of the orthogonalised U_{ij}.

Atom	x	y	z	U_{eq}
O1	2850.49(16)	6643.93(7)	3972.88(17)	16.98(4)
O2	5169.71(15)	5515.06(7)	5834.74(15)	14.46(3)
N1	1627.77(17)	5027.37(8)	4677.62(17)	13.59(4)
C1	1018.14(19)	4906.07(9)	3763.12(19)	12.78(4)
C2	966.8(2)	5121.97(10)	2799.3(2)	15.47(4)
C3	285.4(2)	4918.49(10)	2019.6(2)	15.82(4)
C4	-354.3(2)	4509.63(9)	2163.84(19)	13.40(4)
C5	-258.5(2)	4288.28(9)	3121.84(19)	13.01(4)
C6	432.53(19)	4482.03(9)	3917.36(19)	12.02(4)
C7	715.89(19)	4331.31(9)	4962.00(18)	11.95(4)
C8	445.5(2)	3924.26(9)	5520.31(19)	13.13(4)
C9	866.0(2)	3869.12(10)	6534.45(19)	14.19(4)
C10	1531.1(2)	4242.27(10)	6979.7(2)	16.07(4)
C11	1828.2(2)	4644.13(10)	6437.2(2)	14.98(4)
C12	1438.24(19)	4677.15(9)	5407.88(19)	12.51(4)
C13	-1107.8(2)	4321.61(10)	1267.2(2)	15.32(4)
C14	-1784.6(3)	4744.82(12)	785.5(3)	23.17(6)
C15	-1851.6(2)	3930.21(12)	1601.8(2)	20.52(5)
C16	-474.5(3)	4100.85(14)	460.1(3)	24.20(6)
C17	621.9(2)	3428.54(10)	7182.9(2)	16.85(4)
C18	-5.8(3)	3603.06(12)	8040.7(2)	22.20(5)
C19	1647.8(3)	3192.06(14)	7658.4(3)	27.14(6)
C20	-17.6(3)	3036.73(11)	6556.1(3)	22.81(6)
C21	2417.7(2)	5386.87(9)	4790.0(2)	13.27(4)
C22	2235.0(2)	5849.05(9)	4350.8(2)	15.12(4)
C23	3051.5(2)	6185.17(9)	4404.0(2)	14.44(4)
C24	4038.9(2)	6098.57(9)	4940.5(2)	13.75(4)
C25	4173.33(19)	5633.35(9)	5388.3(2)	12.98(4)
C26	3402.6(2)	5274.91(9)	5302.0(2)	13.63(4)
C27	2823.5(2)	6682.94(10)	2926.3(2)	17.40(5)
C28	2581.6(3)	7145.46(11)	2520.9(3)	23.70(6)
C29	2554.3(3)	7219.48(13)	1476.6(3)	31.93(8)
C30	2771.0(4)	6836.51(15)	835.4(3)	34.01(8)
C31	3011.9(3)	6376.61(13)	1251.4(3)	27.60(6)
C32	3036.4(2)	6294.99(11)	2296.9(2)	20.43(5)
C33	5328.2(2)	5411.28(10)	6862.2(2)	14.98(4)
C34	6340.1(2)	5266.37(13)	7230.1(2)	23.24(6)
C35	6589.4(3)	5177.58(17)	8266.4(3)	31.48(8)
C36	5836.4(3)	5233.89(16)	8939.5(3)	31.69(8)
C37	4828.0(3)	5377.49(15)	8560.3(3)	27.29(6)
C38	4565.8(2)	5465.40(12)	7521.2(2)	19.93(5)
C39	5190.6(2)	6797.31(10)	4118.6(2)	15.24(4)
C40	5095.1(2)	7313.14(10)	4093.9(2)	19.19(5)
C41	5230.7(3)	7571.08(13)	3206.2(3)	26.00(6)
C42	5474.3(3)	7335.58(15)	2326.5(3)	28.35(7)
C43	5586.9(3)	6828.47(14)	2357.9(2)	25.15(6)
C44	5446.3(2)	6557.53(11)	3229.6(2)	18.66(5)
C45	4772.9(4)	7598.13(12)	4984.2(3)	28.72(7)
C46	5598.2(6)	7621.4(2)	1374.6(4)	48.17(12)
C47	5620.1(3)	6011.44(13)	3196.6(3)	25.05(6)
C48	5461.5(2)	6584.54(10)	6202.8(2)	16.27(4)
C49	4863.7(3)	6676.62(11)	7017.7(2)	22.06(5)
C50	5352.9(4)	6699.89(13)	8018.5(3)	32.02(8)
C51	6423.9(4)	6622.04(14)	8251.3(3)	36.28(9)
C52	7011.1(3)	6534.54(14)	7448.1(3)	31.63(8)
C53	6552.7(2)	6520.51(11)	6435.0(2)	21.70(5)

Atom	x	y	z	U_{eq}
C54	3695.0(3)	6756.61(14)	6842.7(3)	29.50(7)
C55	6934.0(8)	6631.2(3)	9337.2(4)	62.05(19)
C56	7245.9(3)	6405.08(17)	5623.3(3)	31.96(8)
B1	4923.7(2)	6503.12(10)	5080.0(2)	13.74(4)

Table 9-31 Anisotropic Displacement Parameters (×10^4) for tBu-DPhOP-Cz-DMB (15) The anisotropic displacement factor exponent takes the form: $-2\pi^2[h^2a^{*2} \times U_{11} + ... + 2hka^* \times b^* \times U_{12}]$

Atom	U_{11}	U_{22}	U_{33}	U_{23}	U_{13}	U_{12}
O1	16.54(8)	10.75(7)	23.19(9)	0.66(6)	0.37(7)	3.52(6)
O2	11.41(7)	15.74(8)	15.93(8)	1.24(6)	0.30(6)	0.99(6)
N1	13.25(9)	12.04(8)	15.00(9)	-2.27(7)	-0.49(7)	2.39(7)
C1	12.36(9)	11.88(9)	13.80(9)	-1.17(7)	0.23(7)	2.70(7)
C2	15.12(10)	15.11(10)	15.71(10)	-2.97(8)	-0.21(8)	5.05(8)
C3	16.33(10)	16.82(10)	13.92(10)	-2.34(8)	0.05(8)	4.63(8)
C4	13.86(9)	14.27(10)	11.89(9)	-0.61(8)	0.69(7)	1.74(7)
C5	14.23(9)	12.67(9)	11.92(9)	-1.68(7)	0.64(7)	1.29(7)
C6	12.71(9)	11.35(9)	11.86(9)	-1.10(7)	0.84(7)	1.50(7)
C7	13.17(9)	11.26(9)	11.38(9)	-1.17(7)	1.29(7)	1.01(7)
C8	15.54(10)	12.05(9)	11.85(9)	-1.98(7)	1.77(7)	1.22(7)
C9	16.58(10)	14.08(10)	12.02(9)	-1.27(8)	2.03(8)	1.95(7)
C10	18.80(11)	17.48(11)	11.66(9)	-3.05(8)	0.59(8)	1.24(8)
C11	16.83(10)	15.23(10)	12.57(9)	-2.95(8)	0.26(8)	-0.10(8)
C12	13.19(9)	11.70(9)	12.48(9)	-1.24(7)	0.81(7)	0.62(7)
C13	16.58(10)	17.18(10)	11.92(9)	-1.17(8)	0.47(8)	0.57(8)
C14	23.61(13)	22.90(13)	20.80(13)	0.61(11)	-6.9(1)	3.44(10)
C15	20.28(12)	24.03(13)	16.59(11)	-6.9(1)	-0.71(9)	1.32(10)
C16	26.62(14)	28.66(15)	18.31(12)	-2.98(12)	6.81(11)	-5.80(11)
C17	19.30(11)	16.09(10)	15.22(10)	-0.25(9)	2.19(8)	4.67(8)
C18	26.84(14)	23.67(13)	17.27(12)	-0.92(11)	7.59(10)	4.62(10)
C19	23.55(14)	25.20(15)	31.92(16)	4.46(11)	-0.08(12)	10.70(13)
C20	30.04(15)	16.32(11)	22.03(13)	-4.76(10)	2.79(11)	3.88(10)
C21	11.74(9)	10.66(9)	16.97(10)	-0.68(7)	-0.27(7)	1.95(7)
C22	11.78(9)	11.35(9)	21.54(11)	-0.23(7)	-1.03(8)	3.25(8)
C23	12.28(9)	10.38(9)	20.17(11)	-0.08(7)	-0.34(8)	2.70(8)
C24	11.97(9)	10.78(9)	18.11(10)	-0.57(7)	0.08(8)	1.60(8)
C25	11.23(9)	11.07(9)	16.26(10)	0.18(7)	-0.06(7)	1.35(7)
C26	12.40(9)	10.58(9)	17.41(10)	-0.09(7)	-0.40(8)	2.01(8)
C27	15.82(10)	12.42(10)	22.78(12)	-1.33(8)	-2.82(9)	4.41(9)
C28	27.65(14)	14.22(11)	27.57(14)	-0.55(10)	-3.96(11)	7.0(1)
C29	44.4(2)	20.86(14)	27.75(16)	-3.01(13)	-7.95(14)	10.17(12)
C30	49.5(2)	27.79(16)	22.04(15)	-7.06(15)	-7.69(14)	6.45(12)
C31	36.09(17)	23.74(14)	21.22(13)	-5.02(12)	-4.32(12)	0.87(11)
C32	22.12(12)	16.19(11)	21.78(12)	-1.48(9)	-2.67(10)	2.11(9)
C33	12.8(1)	15.32(10)	16.57(10)	1.59(8)	0.62(8)	2.73(8)
C34	15.25(11)	34.82(16)	19.25(12)	7.21(11)	0.21(9)	6.07(11)
C35	21.54(14)	50.8(2)	21.23(14)	10.42(14)	-1.14(11)	11.90(14)
C36	27.49(16)	47.9(2)	19.39(14)	6.46(15)	1.47(11)	13.05(14)
C37	24.00(14)	39.44(18)	19.14(13)	4.37(13)	5.52(11)	9.02(12)
C38	16.07(11)	25.58(13)	18.45(11)	3.05(9)	3.29(9)	4.75(10)
C39	15.2(1)	15.03(10)	15.53(10)	-3.26(8)	1.96(8)	-0.15(8)
C40	24.76(12)	14.57(11)	17.86(11)	-6.08(9)	0.84(9)	1.36(9)
C41	34.04(16)	21.63(13)	21.89(13)	-8.84(12)	1.27(11)	6.28(11)
C42	31.53(16)	33.92(17)	19.92(13)	-7.76(13)	4.38(11)	7.98(12)
C43	23.67(13)	35.16(17)	17.43(12)	-2.42(12)	5.81(10)	1.56(11)
C44	16.40(11)	23.06(12)	16.92(11)	-0.79(9)	3.63(8)	-1.30(9)
C45	50.2(2)	13.34(12)	22.25(14)	-0.55(13)	2.71(14)	-1.43(10)

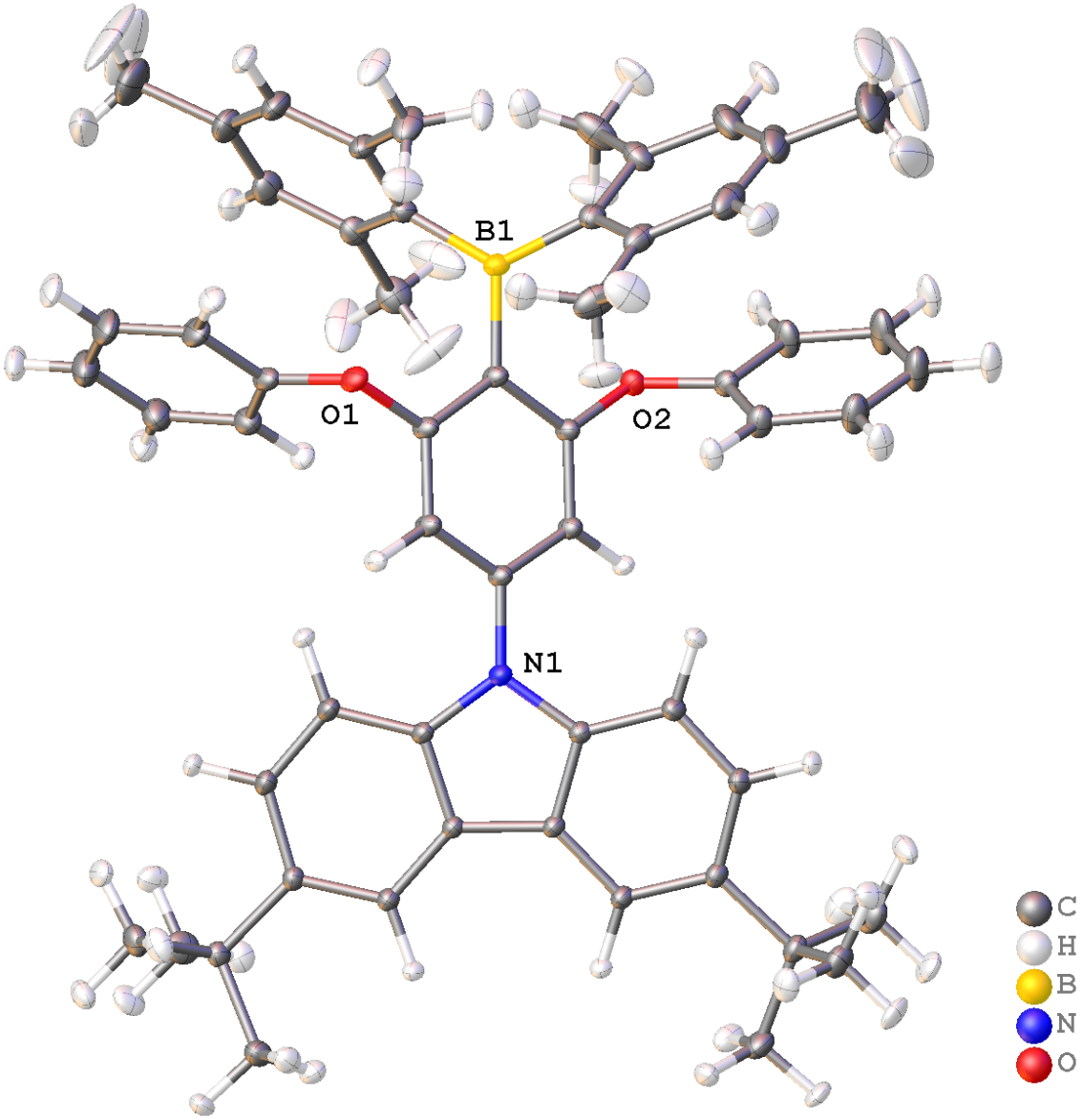
Atom	U_{11}	U_{22}	U_{33}	U_{23}	U_{13}	U_{12}
C46	64.8(3)	54.2(3)	26.82(19)	-11.2(3)	11.0(2)	16.77(19)
C47	24.42(14)	26.11(14)	25.18(14)	6.34(11)	5.32(11)	-5.61(11)
C48	19.42(11)	13.67(10)	15.7(1)	-1.94(8)	1.84(8)	-1.33(8)
C49	32.85(15)	16.31(11)	18.45(12)	-4.06(10)	9.09(11)	-1.31(9)
C50	56.3(2)	23.90(14)	16.74(13)	-9.05(15)	8.01(14)	-2.33(11)
C51	58.9(3)	28.60(16)	18.41(14)	-8.88(16)	-8.34(15)	-1.00(12)
C52	37.13(19)	27.11(15)	26.73(16)	-1.89(13)	-13.28(14)	-3.19(12)
C53	21.46(13)	19.82(12)	22.16(13)	-0.06(10)	-4.67(10)	-4.52(10)
C54	33.14(17)	23.49(14)	35.69(18)	-1.71(13)	20.41(15)	-2.34(13)
C55	96.6(5)	60.5(4)	23.1(2)	-18.4(4)	-18.8(3)	-0.3(2)
C56	17.53(13)	40.4(2)	36.65(19)	4.56(13)	-2.36(12)	-15.23(16)
B1	13.21(11)	11.96(10)	16.11(11)	-1.45(8)	2.02(9)	-0.36(9)
H26	27(3)	20(2)	35(3)	-2(2)	-1(2)	5(2)
H22	22(3)	24(3)	42(3)	1(2)	-6(2)	8(2)
H32	46(3)	26(3)	37(3)	5(3)	0(3)	1(2)
H31	68(4)	42(4)	37(3)	1(3)	3(3)	-3(3)
H30	94(5)	52(4)	26(3)	-6(4)	-7(3)	7(3)
H29	85(5)	34(3)	45(4)	3(3)	-10(3)	18(3)
H28	53(4)	25(3)	47(4)	1(3)	0(3)	4(3)
H52	45(4)	64(5)	56(4)	5(3)	-29(3)	-9(3)
H50	87(5)	52(4)	35(3)	-11(4)	24(3)	-5(3)
H43	53(4)	57(4)	29(3)	1(3)	14(3)	2(3)
H41	69(4)	32(3)	41(4)	-7(3)	4(3)	12(3)
H5	33(3)	26(3)	25(3)	-8(2)	0(2)	0(2)
H3	37(3)	36(3)	25(3)	-9(2)	-1(2)	11(2)
H2	37(3)	29(3)	31(3)	-11(2)	-1(2)	8(2)
H11	34(3)	35(3)	24(3)	-11(2)	-3(2)	0(2)
H10	40(3)	36(3)	21(3)	-7(2)	-1(2)	5(2)
H8	33(3)	22(3)	27(3)	-5(2)	1(2)	1(2)
H38	25(3)	58(4)	31(3)	12(3)	4(2)	5(3)
H37	40(3)	83(5)	34(3)	12(3)	15(3)	10(3)
H36	50(4)	96(6)	28(3)	13(4)	8(3)	21(3)
H35	38(4)	106(6)	41(4)	23(4)	-5(3)	18(4)
H34	26(3)	77(5)	31(3)	13(3)	7(2)	10(3)
H14a	45(4)	50(4)	43(4)	18(3)	-3(3)	-6(3)
H14b	43(4)	38(3)	50(4)	-2(3)	-11(3)	17(3)
H14c	47(4)	41(3)	41(3)	2(3)	-14(3)	1(3)
H15a	41(3)	33(3)	46(4)	-7(3)	0(3)	8(3)
H15b	37(3)	49(4)	34(3)	-6(3)	8(3)	-1(3)
H15c	40(3)	52(4)	34(3)	-20(3)	-8(3)	3(3)
H16a	46(4)	53(4)	40(3)	-12(3)	15(3)	-6(3)
H16b	43(4)	50(4)	47(4)	10(3)	10(3)	-5(3)
H16c	55(4)	64(4)	29(3)	-9(3)	7(3)	-22(3)
H18a	68(4)	42(3)	38(3)	-3(3)	24(3)	16(3)
H18b	53(4)	55(4)	31(3)	-13(3)	9(3)	-10(3)
H18c	33(3)	55(4)	46(4)	16(3)	6(3)	10(3)
H19a	52(4)	39(3)	48(4)	2(3)	-20(3)	3(3)
H19b	51(4)	40(4)	59(4)	5(3)	0(3)	28(3)
H19c	48(4)	47(4)	73(5)	24(3)	24(3)	16(3)
H20a	60(4)	29(3)	44(3)	-12(3)	6(3)	15(3)
H20b	30(3)	39(3)	44(3)	-6(3)	-8(3)	7(3)
H20c	65(4)	32(3)	36(3)	-6(3)	18(3)	-8(3)
H45a	134(7)	24(3)	49(4)	-3(4)	19(4)	-3(3)
H45b	65(5)	61(5)	69(5)	2(4)	22(4)	-22(4)
H45c	95(5)	47(4)	27(3)	18(4)	-4(3)	0(3)
H46a	450(20)	32(5)	95(8)	-11(9)	117(12)	21(5)
H46b	167(12)	241(17)	134(10)	85(11)	117(10)	114(11)
H46c	165(11)	241(16)	91(7)	-127(11)	-67(8)	96(9)
H47a	221(11)	48(5)	53(5)	23(6)	4(6)	-20(4)
H47b	59(5)	61(5)	212(11)	24(4)	-41(6)	-24(6)

Atom	U_{11}	U_{22}	U_{33}	U_{23}	U_{13}	U_{12}
H47c	167(9)	36(4)	162(9)	22(5)	135(8)	23(5)
H54a	37(4)	79(5)	61(4)	13(3)	12(3)	13(4)
H54b	44(4)	48(4)	101(6)	-9(3)	25(4)	-5(4)
H54c	65(5)	104(6)	72(5)	9(4)	30(4)	-41(5)
H55a	270(17)	115(9)	73(7)	-35(11)	-67(8)	-30(7)
H55b	200(15)	264(17)	66(7)	-142(14)	-12(8)	22(9)
H55c	193(15)	370(20)	81(9)	176(17)	-66(10)	-48(12)
H56a	62(5)	66(5)	93(6)	-8(4)	25(4)	-48(4)
H56b	43(4)	89(6)	44(4)	15(4)	16(3)	-3(4)
H56c	23(3)	112(6)	70(5)	11(4)	-6(3)	-23(4)

Table 9-32 Bond Angles in Å for tBu-DPhOP-Cz-DMB (15).

Atom	Atom	Length/Å
O1	C23	1.3873(3)
O1	C27	1.3805(4)
O2	C25	1.3844(3)
O2	C33	1.3761(3)
N1	C1	1.4002(3)
N1	C12	1.3979(3)
N1	C21	1.4073(3)
C1	C2	1.3956(4)
C1	C6	1.4080(3)
C2	C3	1.3875(4)
C3	C4	1.4118(4)
C4	C5	1.3929(4)
C4	C13	1.5283(4)
C5	C6	1.3981(4)
C6	C7	1.4436(3)
C7	C8	1.3986(3)
C7	C12	1.4047(3)
C8	C9	1.3917(4)
C9	C10	1.4133(4)
C9	C17	1.5288(4)
C10	C11	1.3869(4)
C11	C12	1.3947(4)
C13	C14	1.5388(4)
C13	C15	1.5316(4)
C13	C16	1.5350(4)
C17	C18	1.5380(4)
C17	C19	1.5353(4)
C17	C20	1.5318(4)
C21	C22	1.3969(4)
C21	C26	1.3979(4)
C22	C23	1.3893(4)
C23	C24	1.3999(4)
C24	C25	1.4029(4)
C24	B1	1.5804(4)
C25	C26	1.3874(4)
C27	C28	1.3923(4)
C27	C32	1.3918(4)
C28	C29	1.3881(5)
C29	C30	1.3926(6)
C30	C31	1.3907(5)
C31	C32	1.3932(5)
C33	C34	1.3917(4)
C33	C38	1.3897(4)
C34	C35	1.3885(5)
C35	C36	1.3941(5)
C36	C37	1.3903(5)
C37	C38	1.3938(4)
C39	C40	1.4136(4)
C39	C44	1.4137(4)
C39	B1	1.5713(4)
C40	C41	1.3939(4)
C40	C45	1.5054(5)
C41	C42	1.3927(5)
C42	C43	1.3921(5)
C42	C46	1.5017(5)
C43	C44	1.3959(4)
C44	C47	1.5089(5)
C48	C49	1.4130(4)
C48	C53	1.4110(4)

Atom	Atom	Length/Å
C48	B1	1.5760(4)
C49	C50	1.3965(5)
C49	C54	1.5086(5)
C50	C51	1.3913(7)
C51	C52	1.3894(6)
C51	C55	1.5049(6)
C52	C53	1.3973(5)
C53	C56	1.5020(5)



9.20 Chapter 6

9.20.1 tBu-MeOCzDBA (17)

Still awaiting XRD data.

9.21 Chapter 7

9.21.1 2DBCzPN (18)

Table 9-33 Crystal data and structural refinement details of 2DBCzPN (18)

Compound	**2023NCS0559_1b**
Formula	$C_{48}H_{26}N_4$
$D_{calc.}$/ g cm^{-3}	1.350
μ/mm^{-1}	0.620
Formula Weight	658.73
Colour	orange
Shape	plate-shaped
Size/mm^3	0.68×0.32×0.05
T/K	99.99(10)
Crystal System	monoclinic
Space Group	$P2_1/c$
a/Å	15.52100(10)
b/Å	14.29070(10)
c/Å	14.63110(10)
α/°	90
β/°	92.7440(10)
γ/°	90
V/Å^3	3241.54(4)
Z	4
Z'	1
Wavelength/Å	1.54184
Radiation type	Cu K$_\alpha$
Θ_{min}/°	2.850
Θ_{max}/°	70.073
Measured Refl's.	50168
Indep't Refl's	6148
Refl's I≥2 σ(I)	5658
R_{int}	0.0436
Parameters	469
Restraints	0
Largest Peak	0.164
Deepest Hole	-0.237
GooF	1.048
wR_2 (all data)	0.0895
wR_2	0.0876
R_1 (all data)	0.0368
R_1	0.0341

Table 9-34 Fractional Atomic Coordinates (×10^4) and Equivalent Isotropic Displacement Parameters (Å2×10^3) for 2DBCzPN (18). U_{eq} is defined as 1/3 of the trace of the orthogonalised U_{ij}.

Atom	x	y	z	U_{eq}
N1	5928.0(6)	6470.1(6)	5284.9(6)	16.73(19)
N2	7147.5(6)	7741.4(6)	6125.7(6)	17.20(19)
N3	4609.5(6)	10852.8(7)	6302.5(7)	25.0(2)
N4	2922.7(6)	8941.8(8)	5577.2(8)	30.8(2)
C1	5666.2(7)	7358.4(7)	5591.2(7)	16.7(2)
C2	6273.8(7)	7999.7(7)	5974.2(7)	16.7(2)
C3	6012.7(7)	8904.2(8)	6180.9(7)	17.7(2)
C4	5149.5(7)	9162.0(7)	6048.3(7)	17.4(2)
C5	4537.0(7)	8495.2(8)	5736.2(7)	17.7(2)
C6	4800.7(7)	7603.7(8)	5499.9(7)	17.6(2)
C7	5746.7(7)	5619.0(7)	5698.9(7)	16.5(2)
C8	5082.8(7)	5432.3(8)	6296.1(7)	18.3(2)
C9	5014.5(7)	4541.5(8)	6616.6(7)	19.6(2)
C10	5647.3(7)	3849.1(8)	6447.0(7)	18.8(2)
C11	5619.4(8)	2957.6(8)	6868.6(8)	23.3(2)
C12	6280.2(8)	2331.6(8)	6798.9(8)	25.8(3)
C13	7006.3(8)	2577.4(8)	6314.4(8)	24.3(2)
C14	7038.9(7)	3418.1(8)	5861.1(7)	20.4(2)
C15	6343.5(7)	4060.8(7)	5874.4(7)	17.8(2)
C16	6324.9(7)	4943.0(7)	5409.5(7)	16.7(2)
C17	6820.6(6)	5376.9(8)	4708.4(7)	16.6(2)
C18	7356.6(7)	5036.3(8)	4005.1(7)	18.3(2)
C19	7487.7(7)	4079.2(8)	3806.8(8)	21.4(2)
C20	8004.7(7)	3807.0(9)	3115.3(8)	25.4(3)
C21	8411.2(8)	4474.5(9)	2583.1(8)	28.2(3)
C22	8261.6(7)	5406.9(9)	2721.7(8)	25.7(3)
C23	7721.8(7)	5712.5(8)	3416.8(7)	20.6(2)
C24	7504.9(7)	6678.1(8)	3486.8(7)	21.5(2)
C25	6914.0(7)	6983.6(8)	4079.4(7)	19.7(2)
C26	6583.9(6)	6321.2(8)	4682.6(7)	16.8(2)
C27	7431.2(7)	6906.0(8)	6537.8(7)	17.4(2)
C28	6983.5(7)	6369.6(8)	7172.0(7)	18.6(2)
C29	7378.0(7)	5583.2(8)	7514.4(7)	20.4(2)
C30	8182.0(7)	5272.1(8)	7192.4(7)	20.5(2)
C31	8523.0(8)	4390.2(8)	7473.1(8)	24.6(2)
C32	9237.8(8)	4027.3(9)	7089.7(9)	28.7(3)
C33	9632.7(8)	4524.0(9)	6395.5(9)	27.3(3)
C34	9341.4(7)	5399.1(8)	6135.6(8)	23.1(2)
C35	8629.4(7)	5816.7(8)	6548.4(7)	19.0(2)
C36	8272.2(7)	6717.3(8)	6294.9(7)	17.9(2)
C37	8545.1(7)	7516.2(8)	5764.9(7)	17.7(2)
C38	9346.7(7)	7827.6(8)	5410.3(7)	19.1(2)
C39	10166.5(7)	7442.2(8)	5651.6(8)	22.5(2)
C40	10902.2(7)	7794.7(9)	5297.9(8)	25.8(3)
C41	10864.0(7)	8546.9(9)	4680.9(8)	26.2(3)
C42	10086.9(7)	8955.4(9)	4451.6(8)	24.6(3)
C43	9318.7(7)	8628.9(8)	4824.5(7)	20.7(2)
C44	8536.5(7)	9139.5(8)	4663.7(8)	21.1(2)
C45	7804.4(7)	8907.1(8)	5087.0(8)	20.0(2)
C46	7828.8(7)	8103.3(8)	5643.6(7)	17.7(2)
C47	4865.8(7)	10104.7(8)	6211.0(7)	19.0(2)
C48	3638.3(7)	8743.8(8)	5640.3(8)	21.1(2)

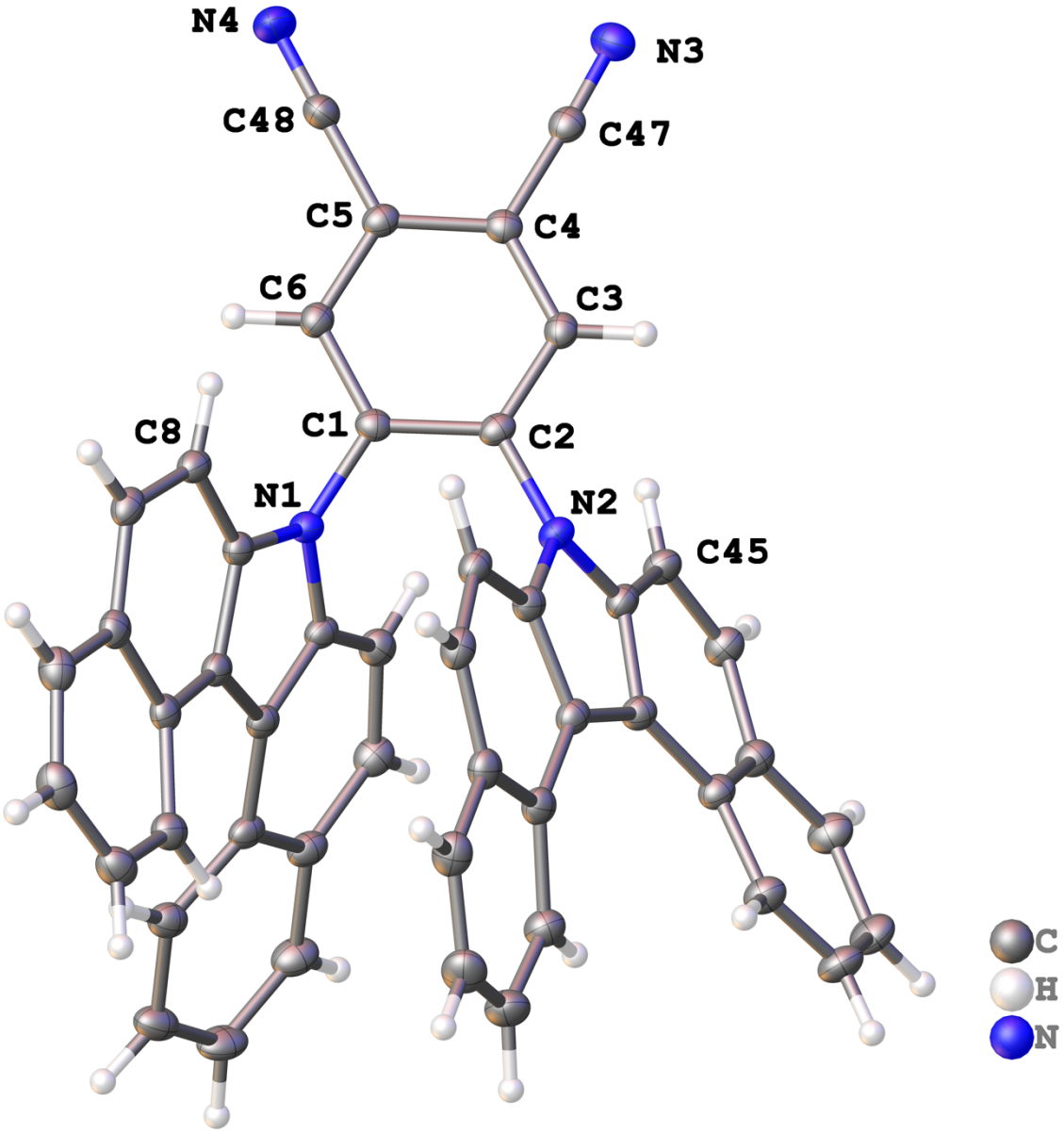
Table 9-35 Anisotropic Displacement Parameters (×10^4) for 2DBCzPN (18) The anisotropic displacement factor exponent takes the form: $-2\pi^2[h^2a^{*2} \times U_{11} + \ldots + 2hka^* \times b^* \times U_{12}]$

Atom	U_{11}	U_{22}	U_{33}	U_{23}	U_{13}	U_{12}
N^1	14.9(4)	17.9(4)	17.4(4)	-1.5(3)	2.0(3)	0.9(3)
N^2	13.9(4)	19.5(5)	18.3(4)	1.1(4)	1.3(3)	0.3(3)
N^3	26.6(5)	21.9(5)	27.1(5)	-0.5(4)	6.1(4)	1.7(4)
N^4	20.0(5)	31.0(6)	41.0(6)	-9.1(5)	-2.5(4)	5.1(4)
C^1	17.7(5)	18.3(5)	14.3(5)	-0.3(4)	2.3(4)	1.5(4)
C^2	14.3(5)	21.4(5)	14.5(5)	1.4(4)	2.1(4)	0.8(4)
C^3	17.1(5)	20.1(5)	15.9(5)	-0.8(4)	2.2(4)	-2.5(4)
C^4	18.7(5)	19.1(5)	14.5(5)	0.2(4)	2.9(4)	0.9(4)
C^5	15.9(5)	21.5(5)	15.8(5)	0.6(4)	1.9(4)	1.3(4)
C^6	16.4(5)	20.3(5)	16.1(5)	-1.2(4)	1.0(4)	-1.0(4)
C^7	15.1(5)	18.8(5)	15.5(5)	-2.1(4)	-1.6(4)	-0.6(4)
C^8	15.2(5)	22.9(5)	16.6(5)	-3.9(4)	0.5(4)	0.1(4)
C^9	17.1(5)	26.5(6)	15.1(5)	-1.9(4)	0.8(4)	-3.9(4)
C^{10}	19.2(5)	21.9(6)	15.0(5)	-2.7(4)	-2.1(4)	-2.9(4)
C^{11}	26.6(6)	24.7(6)	18.4(5)	0.1(4)	1.0(4)	-5.6(5)
C^{12}	33.2(6)	20.5(6)	23.3(6)	3.0(5)	-2.2(5)	-2.3(5)
C^{13}	26.9(6)	21.9(6)	23.8(6)	-1.2(4)	-3.3(5)	3.9(5)
C^{14}	20.6(5)	22.5(6)	17.8(5)	-2.8(4)	-1.1(4)	0.6(4)
C^{15}	18.6(5)	19.5(5)	15.0(5)	-3.1(4)	-2.3(4)	-1.7(4)
C^{16}	14.1(5)	19.8(5)	15.9(5)	-3.1(4)	-1.4(4)	-1.0(4)
C^{17}	13.4(5)	20.5(5)	15.8(5)	-1.2(4)	-1.9(4)	0.5(4)
C^{18}	13.5(5)	25.8(6)	15.3(5)	-1.6(4)	-1.7(4)	1.8(4)
C^{19}	19.3(5)	25.6(6)	19.2(5)	-2.6(4)	-1.0(4)	3.6(4)
C^{20}	24.5(6)	30.0(6)	21.5(6)	-6.6(5)	-0.7(5)	8.0(5)
C^{21}	23.5(6)	41.9(7)	19.7(6)	-5.1(5)	5.2(5)	7.9(5)
C^{22}	21.4(6)	36.3(7)	19.8(6)	1.4(5)	4.4(4)	2.3(5)
C^{23}	16.0(5)	28.9(6)	16.9(5)	0.0(4)	0.3(4)	1.9(4)
C^{24}	20.7(5)	26.3(6)	17.4(5)	3.4(4)	1.4(4)	-1.0(4)
C^{25}	19.2(5)	20.8(6)	18.9(5)	0.4(4)	-1.2(4)	0.8(4)
C^{26}	12.9(5)	22.0(5)	15.3(5)	-1.9(4)	-0.4(4)	0.6(4)
C^{27}	16.8(5)	19.6(5)	15.5(5)	-1.3(4)	-1.8(4)	-0.2(4)
C^{28}	15.0(5)	23.9(6)	16.9(5)	-2.0(4)	0.1(4)	-2.2(4)
C^{29}	20.3(5)	23.9(6)	16.8(5)	1.7(4)	-0.1(4)	-4.5(4)
C^{30}	20.2(5)	22.5(6)	18.3(5)	-0.8(4)	-3.4(4)	-1.9(4)
C^{31}	25.5(6)	23.8(6)	24.3(6)	3.8(5)	-2.2(5)	-1.4(5)
C^{32}	28.5(6)	22.5(6)	34.5(7)	3.1(5)	-4.2(5)	4.7(5)
C^{33}	22.6(6)	27.4(6)	32.0(6)	-1.7(5)	0.9(5)	5.3(5)
C^{34}	20.0(5)	24.8(6)	24.4(6)	0.3(5)	1.2(4)	1.5(4)
C^{35}	17.6(5)	21.4(5)	17.7(5)	-0.7(4)	-2.7(4)	-0.2(4)
C^{36}	15.9(5)	22.0(5)	15.6(5)	-1.0(4)	-0.6(4)	-0.8(4)
C^{37}	16.2(5)	20.8(5)	16.1(5)	-0.3(4)	0.0(4)	0.8(4)
C^{38}	16.6(5)	22.9(5)	17.9(5)	-0.6(4)	2.0(4)	-0.3(4)
C^{39}	18.6(5)	25.3(6)	23.6(6)	3.1(4)	1.6(4)	1.9(4)
C^{40}	15.5(5)	32.3(6)	29.8(6)	2.0(5)	2.3(4)	3.0(5)
C^{41}	18.0(6)	32.7(6)	28.2(6)	3.6(5)	6.2(5)	-1.8(5)
C^{42}	22.0(6)	27.8(6)	24.3(6)	5.4(5)	5.0(5)	-0.3(5)
C^{43}	18.3(5)	24.2(6)	19.6(5)	0.7(4)	1.7(4)	-0.1(4)
C^{44}	19.7(5)	22.7(6)	20.8(5)	3.4(4)	0.5(4)	-0.2(4)
C^{45}	16.0(5)	21.8(6)	22.2(5)	1.3(4)	-0.2(4)	1.6(4)
C^{46}	14.2(5)	21.5(5)	17.3(5)	-1.6(4)	0.4(4)	-1.6(4)
C^{47}	17.5(5)	22.7(6)	17.0(5)	-0.2(4)	2.5(4)	-0.9(4)
C^{48}	20.7(6)	19.3(5)	23.3(6)	-4.5(4)	0.5(4)	1.6(4)

Table 9-36 Bond Angles in Å for 2DBCzPN (18).

Atom	Atom	Length/Å
N^{1}	C^{1}	1.4124(14)
N^{1}	C^{7}	1.3936(14)
N^{1}	C^{26}	1.3942(13)
N^{2}	C^{2}	1.4127(13)
N^{2}	C^{27}	1.3989(14)
N^{2}	C^{46}	1.3979(13)
N^{3}	C^{47}	1.1508(15)
N^{4}	C^{48}	1.1456(15)
C^{1}	C^{2}	1.4116(15)
C^{1}	C^{6}	1.3886(15)
C^{2}	C^{3}	1.3923(15)
C^{3}	C^{4}	1.3941(15)
C^{4}	C^{5}	1.4067(15)
C^{4}	C^{47}	1.4406(15)
C^{5}	C^{6}	1.3869(15)
C^{5}	C^{48}	1.4396(15)
C^{7}	C^{8}	1.4081(15)
C^{7}	C^{16}	1.3979(15)
C^{8}	C^{9}	1.3625(16)
C^{9}	C^{10}	1.4243(16)
C^{10}	C^{11}	1.4170(16)
C^{10}	C^{15}	1.4311(15)
C^{11}	C^{12}	1.3684(17)
C^{12}	C^{13}	1.4044(17)
C^{13}	C^{14}	1.3744(16)
C^{14}	C^{15}	1.4181(15)
C^{15}	C^{16}	1.4322(15)
C^{16}	C^{17}	1.4505(15)
C^{17}	C^{18}	1.4389(14)
C^{17}	C^{26}	1.3985(15)
C^{18}	C^{19}	1.4149(16)
C^{18}	C^{23}	1.4292(16)
C^{19}	C^{20}	1.3772(16)
C^{20}	C^{21}	1.4005(18)
C^{21}	C^{22}	1.3693(18)
C^{22}	C^{23}	1.4173(16)
C^{23}	C^{24}	1.4252(16)
C^{24}	C^{25}	1.3636(16)
C^{25}	C^{26}	1.4075(15)
C^{27}	C^{28}	1.4118(15)
C^{27}	C^{36}	1.3955(15)
C^{28}	C^{29}	1.3637(16)
C^{29}	C^{30}	1.4259(16)
C^{30}	C^{31}	1.4200(16)
C^{30}	C^{35}	1.4276(16)
C^{31}	C^{32}	1.3689(17)
C^{32}	C^{33}	1.4039(18)
C^{33}	C^{34}	1.3772(17)
C^{34}	C^{35}	1.4164(15)
C^{35}	C^{36}	1.4428(15)
C^{36}	C^{37}	1.4546(15)
C^{37}	C^{38}	1.4410(15)
C^{37}	C^{46}	1.3974(15)
C^{38}	C^{39}	1.4156(15)
C^{38}	C^{43}	1.4299(15)
C^{39}	C^{40}	1.3719(16)
C^{40}	C^{41}	1.4030(17)
C^{41}	C^{42}	1.3672(17)
C^{42}	C^{43}	1.4140(15)

Atom	Atom	Length/Å
C^{43}	C^{44}	1.4263(15)
C^{44}	C^{45}	1.3611(15)
C^{45}	C^{46}	1.4075(15)



9.21.2 4DBCzIPN (19)

Table 9-37 Crystal data and structural refinement details of 4DBCzIPN (19)

Compound	**2023NCS0569_1a**
Formula	$C_{93.25}H_{58.5}N_6O_{1.75}$
$D_{calc.}$/ g cm^{-3}	1.279
μ/mm^{-1}	0.077
Formula Weight	1290.96
Colour	orange
Shape	plate-shaped
Size/mm^3	0.140×0.090×0.050
T/K	100(2)
Crystal System	monoclinic
Space Group	$P2_1/n$
a/Å	14.9898(2)
b/Å	15.4406(2)
c/Å	29.6184(4)
α/°	90
β/°	102.0890(10)
γ/°	90
V/Å^3	6703.20(16)
Z	4
Z'	1
Wavelength/Å	0.71073
Radiation type	Mo K_α
Θ_{min}/°	1.916
Θ_{max}/°	30.508
Measured Refl's.	142744
Indep't Refl's	20459
Refl's I≥2 σ(I)	16312
R_{int}	0.0281
Parameters	847
Restraints	0
Largest Peak	0.571
Deepest Hole	-0.437
GooF	1.022
wR_2 (all data)	0.1509
wR_2	0.1427
R_1 (all data)	0.0684
R_1	0.0553

Table 9-38 Fractional Atomic Coordinates (×10^4) and Equivalent Isotropic Displacement Parameters (Å2×10^3) for 4DBCzIPN (19). U_{eq} is defined as 1/3 of the trace of the orthogonalised U_{ij}.

Atom	x	y	z	U_{eq}
N1	5177.2(7)	7417.5(7)	5581.9(3)	24.8(2)
N2	6866.9(8)	6600.4(9)	6471.4(4)	36.0(3)
N3	5302.3(7)	6900.2(7)	7212.4(3)	22.96(19)
N4	3520.4(7)	7592.1(7)	7125.2(3)	23.2(2)
N5	2502.3(7)	7984.3(7)	6211.6(4)	24.5(2)
N6	3013.6(10)	8320.0(10)	5121.9(4)	41.3(3)
C1	4764.6(8)	7467.2(8)	5966.6(4)	22.7(2)
C2	5246.3(8)	7225.2(8)	6405.0(4)	22.2(2)
C3	4830.1(8)	7243.9(8)	6788.4(4)	21.6(2)
C4	3919.9(8)	7523.3(8)	6736.1(4)	21.9(2)
C5	3426.9(8)	7742.7(8)	6292.3(4)	23.1(2)
C6	3857.0(8)	7730.5(8)	5913.6(4)	23.5(2)
C7	4929.0(8)	6836.3(8)	5216.1(4)	22.6(2)
C8	4207.6(9)	6236.8(9)	5151.0(4)	27.5(2)
C9	4081.4(10)	5728.1(9)	4766.5(5)	31.0(3)
C10	4703.5(10)	5748.1(8)	4464.7(4)	30.3(3)
C11	4589.2(14)	5167.2(10)	4087.2(5)	42.3(4)
C12	5232.6(16)	5104.5(10)	3822.3(6)	52.2(5)
C13	6034.5(15)	5590.7(10)	3936.1(6)	48.6(5)
C14	6159.2(12)	6185.8(9)	4292.2(5)	35.5(3)
C15	5469.4(10)	6315.0(8)	4548.6(4)	26.4(2)
C16	5523.0(8)	6942.6(8)	4912.6(4)	22.3(2)
C17	6094.7(8)	7683.3(8)	5075.8(4)	22.9(2)
C18	6682.9(9)	8242.3(8)	4880.6(4)	25.7(2)
C19	6779.6(11)	8203.9(9)	4415.4(5)	33.2(3)
C20	7333.6(13)	8774.1(10)	4248.0(6)	42.9(4)
C21	7822.3(12)	9413.7(10)	4532.5(6)	42.0(4)
C22	7714.5(10)	9492.5(10)	4979.1(5)	35.0(3)
C23	7133.9(9)	8926.8(9)	5161.0(5)	28.5(3)
C24	6965.7(10)	9073.4(10)	5610.9(5)	32.5(3)
C25	6332.8(10)	8604.7(9)	5777.7(4)	30.6(3)
C26	5894.1(8)	7928.2(8)	5499.3(4)	24.2(2)
C27	6151.9(9)	6876.8(8)	6450.0(4)	25.7(2)
C28	6156.8(8)	7155.7(8)	7466.6(4)	24.1(2)
C29	6632.8(9)	7920.9(9)	7414.6(4)	27.3(2)
C30	7420.8(9)	8081.6(9)	7732.5(5)	29.0(3)
C31	7715.6(9)	7526.8(9)	8119.8(4)	28.4(3)
C32	8460.6(10)	7765.7(10)	8477.3(5)	34.8(3)
C33	8703.4(11)	7281.7(12)	8870.6(5)	41.5(3)
C34	8197.7(11)	6538.9(12)	8930.0(5)	41.0(3)
C35	7479.1(10)	6280.5(10)	8587.5(5)	33.7(3)
C36	7233.7(9)	6749.8(9)	8167.4(4)	26.8(2)
C37	6472.1(8)	6531.3(8)	7803.1(4)	24.2(2)
C38	5837.9(8)	5809.6(8)	7718.5(4)	24.2(2)
C39	5851.3(9)	4924.5(9)	7867.9(4)	27.8(2)
C40	6638.0(11)	4486.5(10)	8113.1(5)	34.5(3)
C41	6604.4(12)	3626.9(10)	8226.3(5)	40.5(3)
C42	5792.1(13)	3157.1(10)	8108.7(5)	41.8(4)
C43	5023.8(12)	3551.0(9)	7863.3(5)	36.8(3)
C44	5042.4(10)	4427.0(9)	7723.3(4)	28.7(3)
C45	4274.1(9)	4785.6(9)	7412.7(4)	27.4(2)
C46	4313.3(8)	5586.3(8)	7222.2(4)	24.2(2)
C47	5105.3(8)	6081.2(8)	7373.9(4)	22.7(2)
C48	3874.4(8)	8102.8(8)	7511.0(4)	22.7(2)
C49	4608.1(9)	8685.2(8)	7559.3(4)	26.6(2)
C50	4843.9(10)	9118.7(10)	7968.4(5)	33.4(3)

Atom	x	y	z	U_{eq}
C51	4411.5(11)	8946.0(10)	8345.8(5)	33.9(3)
C52	4737.3(14)	9332.6(13)	8782.8(6)	53.5(5)
C53	4413.6(15)	9073.0(15)	9161.5(6)	58.2(5)
C54	3765.6(12)	8419.3(12)	9124.0(5)	42.3(4)
C55	3392.6(10)	8073.8(9)	8699.8(4)	29.7(3)
C56	3678.4(9)	8347.5(8)	8294.9(4)	26.0(2)
C57	3347.2(8)	7987.5(8)	7844.4(4)	22.7(2)
C58	2586.3(8)	7439.8(8)	7636.3(4)	23.0(2)
C59	1749.4(9)	7187.0(8)	7761.2(4)	26.0(2)
C60	1404.3(9)	7572.1(9)	8123.7(5)	30.4(3)
C61	577.9(10)	7328.8(11)	8214.2(5)	37.9(3)
C62	54.4(11)	6683.2(11)	7950.4(6)	41.9(4)
C63	353.2(10)	6316.4(10)	7587.1(6)	37.8(3)
C64	1187.8(9)	6572.4(9)	7474.5(5)	29.2(3)
C65	1441.1(9)	6258.7(9)	7064.9(5)	29.8(3)
C66	2188.5(9)	6571.5(9)	6921.5(4)	26.9(2)
C67	2737.9(8)	7182.2(8)	7204.5(4)	23.2(2)
C68	2141.3(8)	8735.1(8)	6362.9(4)	22.3(2)
C69	2618.0(9)	9372.0(8)	6658.6(4)	25.2(2)
C70	2133.0(9)	10076.9(8)	6748.0(4)	26.2(2)
C71	1213.3(9)	10209.4(8)	6515.1(4)	25.0(2)
C72	777.7(10)	11007.0(8)	6564.6(5)	30.5(3)
C73	-53.6(10)	11205.6(9)	6295.5(6)	35.9(3)
C74	-481.7(10)	10616.5(9)	5959.4(6)	36.0(3)
C75	-99.6(9)	9813.7(9)	5916.8(5)	29.4(3)
C76	742.8(8)	9574.9(8)	6202.3(4)	23.7(2)
C77	1207.2(8)	8772.5(8)	6165.0(4)	22.0(2)
C78	971.3(8)	7958.5(8)	5920.0(4)	22.9(2)
C79	138.3(8)	7498.5(8)	5745.9(4)	23.9(2)
C80	-732.7(9)	7769.8(9)	5802.7(5)	28.2(2)
C81	-1494.0(9)	7267.5(9)	5661.4(5)	31.2(3)
C82	-1435.2(9)	6466.9(9)	5445.2(5)	30.8(3)
C83	-604.9(9)	6177.1(9)	5388.9(4)	29.5(3)
C84	200.1(9)	6666.0(9)	5543.9(4)	27.0(2)
C85	1068.8(9)	6308.9(10)	5525.3(5)	33.2(3)
C86	1860.1(9)	6708.0(10)	5727.7(5)	32.1(3)
C87	1793.2(8)	7521.0(9)	5934.1(4)	25.1(2)
C88	3378.5(9)	8049.9(9)	5471.9(4)	28.9(3)

Table 9-39 Anisotropic Displacement Parameters (×10^4) for 4DBCzIPN (19) The anisotropic displacement factor exponent takes the form: $-2\pi^2[h^2a^{*2} \times U_{11} + \ldots + 2hka^* \times b^* \times U_{12}]$

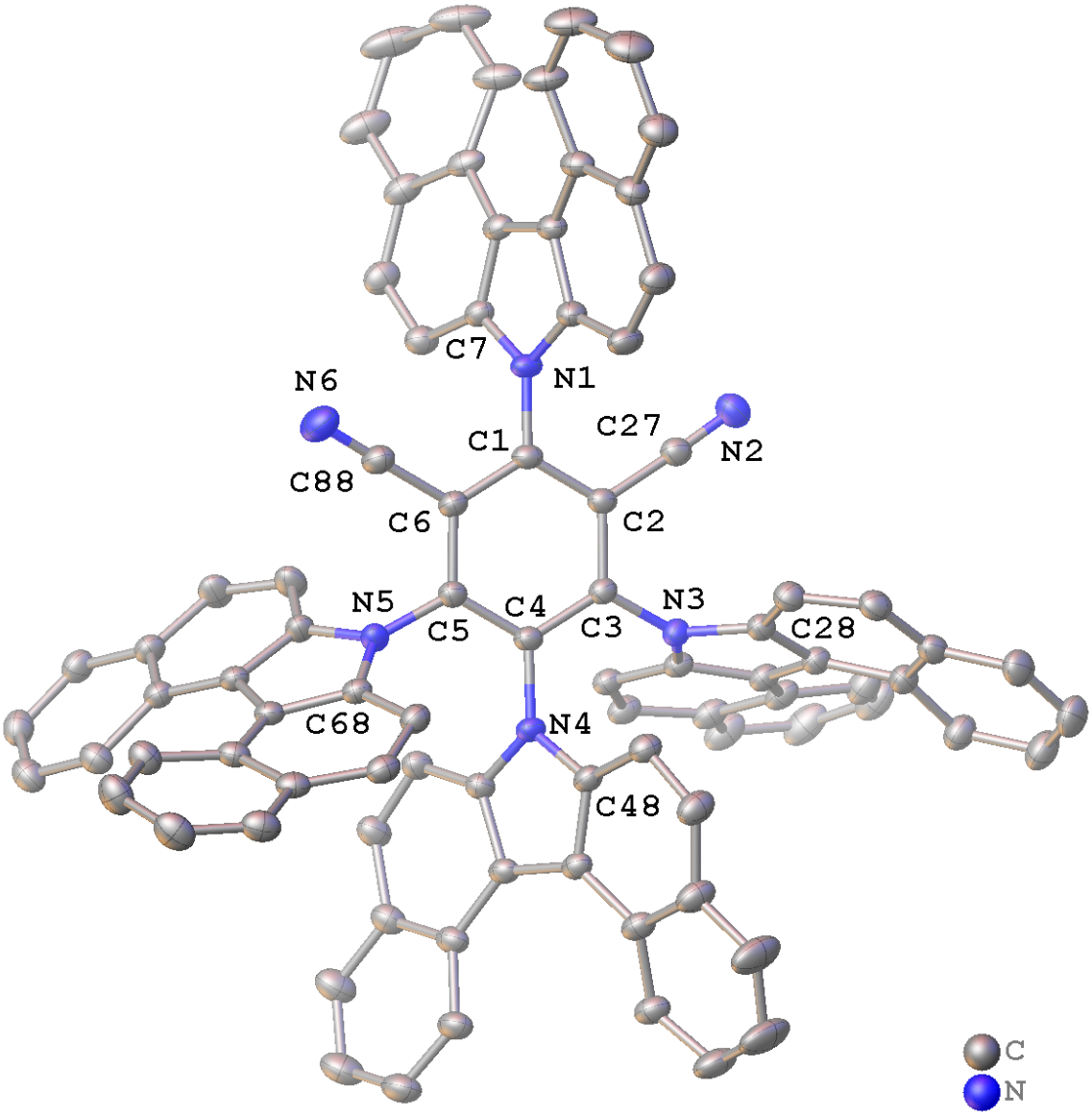
Atom	U_{11}	U_{22}	U_{33}	U_{23}	U_{13}	U_{12}
N1	24.9(5)	32.5(5)	19.0(4)	-5.3(4)	9.3(4)	-4.4(4)
N2	28.1(6)	43.8(7)	37.1(6)	-6.4(5)	8.9(5)	1.8(5)
N3	20.8(5)	28.3(5)	19.4(4)	-0.5(4)	3.2(4)	-2.1(4)
N4	23.2(5)	29.8(5)	17.7(4)	-4.5(4)	6.8(4)	-1.5(4)
N5	21.1(5)	30.4(5)	21.8(5)	-6.9(4)	4.0(4)	1.9(4)
N6	47.7(8)	47.9(7)	27.5(6)	1.1(5)	6.4(5)	9.8(6)
C1	23.7(5)	26.4(5)	19.8(5)	-2.7(4)	8.9(4)	-2.1(4)
C2	21.6(5)	25.7(5)	20.3(5)	-3.5(4)	6.9(4)	-2.0(4)
C3	22.1(5)	24.4(5)	18.6(5)	-1.8(4)	4.8(4)	-1.5(4)
C4	22.0(5)	26.2(5)	18.6(5)	-3.7(4)	6.9(4)	-1.4(4)
C5	22.2(5)	26.9(6)	20.7(5)	-3.7(4)	5.8(4)	0.3(4)
C6	24.2(5)	28.3(6)	18.4(5)	-2.1(4)	5.5(4)	0.6(4)
C7	25.0(5)	24.8(5)	18.2(5)	-1.7(4)	5.4(4)	2.2(4)
C8	29.7(6)	28.9(6)	25.6(6)	-2.9(5)	9.3(5)	-1.9(5)
C9	37.8(7)	27.5(6)	27.4(6)	-3.6(5)	6.3(5)	-4.0(5)
C10	47.0(8)	23.1(6)	21.4(5)	-1.1(4)	8.2(5)	0.7(5)
C11	75.0(11)	27.0(6)	28.3(7)	-5.6(5)	18.1(7)	-8.6(7)
C12	104.3(15)	27.1(7)	34.6(8)	-8.9(6)	36.4(9)	-9.2(8)
C13	91.0(14)	26.7(7)	41.4(8)	-2.5(6)	44.1(9)	1.4(8)
C14	57.8(9)	24.6(6)	31.4(7)	2.6(5)	26.0(6)	5.4(6)
C15	40.2(7)	21.3(5)	19.8(5)	2.3(4)	10.9(5)	5.4(5)
C16	26.3(5)	23.4(5)	17.8(5)	1.7(4)	6.0(4)	4.4(4)
C17	24.3(5)	26.4(5)	19.4(5)	0.7(4)	7.5(4)	2.6(4)
C18	29.5(6)	26.6(6)	23.6(5)	2.7(4)	11.5(5)	2.5(5)
C19	49.9(8)	28.2(6)	27.1(6)	0.8(5)	20.9(6)	-0.8(6)
C20	66.8(11)	34.5(7)	36.5(8)	1.6(6)	31.8(8)	-4.5(7)
C21	52.5(9)	35.7(7)	45.5(8)	5.0(6)	28.3(7)	-6.2(7)
C22	37.1(7)	33.5(7)	37.3(7)	1.8(6)	14.4(6)	-5.7(6)
C23	28.3(6)	31.1(6)	27.8(6)	1.7(5)	9.8(5)	-1.6(5)
C24	34.3(7)	36.4(7)	27.6(6)	-4.6(5)	8.3(5)	-8.8(6)
C25	33.6(7)	37.5(7)	22.4(6)	-5.9(5)	9.7(5)	-7.3(5)
C26	23.5(5)	30.9(6)	19.5(5)	-0.4(4)	7.3(4)	-0.8(5)
C27	24.9(6)	29.2(6)	23.7(5)	-4.4(4)	6.9(4)	-2.0(5)
C28	21.5(5)	30.3(6)	20.7(5)	-3.9(4)	4.9(4)	-1.3(4)
C29	26.2(6)	30.5(6)	25.9(6)	-1.2(5)	6.9(5)	-3.4(5)
C30	25.1(6)	33.3(6)	30.1(6)	-4.4(5)	9.1(5)	-5.6(5)
C31	22.7(6)	36.8(7)	26.2(6)	-8.0(5)	6.5(5)	-2.0(5)
C32	27.2(6)	41.5(8)	34.1(7)	-9.1(6)	2.9(5)	-7.3(6)
C33	34.8(7)	52.5(9)	32.2(7)	-8.8(6)	-4.9(6)	-6.0(7)
C34	41.7(8)	51.1(9)	26.0(7)	-2.0(6)	-2.6(6)	-2.9(7)
C35	33.9(7)	40.2(7)	24.7(6)	-1.8(5)	1.0(5)	-3.6(6)
C36	23.4(6)	34.6(6)	21.8(5)	-5.1(5)	3.7(4)	-0.5(5)
C37	23.1(5)	29.6(6)	19.8(5)	-3.4(4)	4.4(4)	-0.9(4)
C38	26.0(6)	28.8(6)	17.6(5)	-3.3(4)	4.0(4)	-1.0(5)
C39	35.5(7)	28.9(6)	18.4(5)	-2.4(4)	4.5(5)	1.9(5)
C40	39.4(7)	36.2(7)	25.4(6)	-1.9(5)	0.8(5)	4.2(6)
C41	54.5(9)	35.8(7)	27.5(7)	0.6(6)	0.5(6)	11.6(7)
C42	66.4(11)	28.2(7)	27.2(7)	1.0(5)	2.1(7)	3.8(7)
C43	54.1(9)	28.9(6)	25.7(6)	-1.5(5)	4.5(6)	-5.1(6)
C44	38.6(7)	27.9(6)	19.4(5)	-3.1(4)	6.0(5)	-0.8(5)
C45	31.7(6)	29.9(6)	21.1(5)	-3.3(4)	6.5(5)	-5.4(5)
C46	25.0(6)	29.6(6)	18.4(5)	-2.5(4)	5.8(4)	-1.2(5)
C47	24.6(5)	26.4(5)	17.8(5)	-2.1(4)	6.0(4)	-0.6(4)
C48	25.6(5)	25.6(5)	17.0(5)	-1.9(4)	4.1(4)	2.0(4)
C49	29.9(6)	28.7(6)	21.9(5)	-0.4(4)	6.9(5)	-1.9(5)
C50	40.8(7)	33.5(7)	25.2(6)	-2.7(5)	5.7(5)	-10.6(6)
C51	45.5(8)	33.8(7)	22.8(6)	-5.5(5)	7.6(5)	-8.0(6)
C52	70.7(12)	61.7(11)	28.8(7)	-15.6(7)	12.4(8)	-31.5(10)

Atom	U_{11}	U_{22}	U_{33}	U_{23}	U_{13}	U_{12}
C53	76.3(13)	75.0(13)	25.4(7)	-18.0(8)	15.0(8)	-29.3(11)
C54	54.8(9)	53.1(9)	21.1(6)	-6.3(6)	12.6(6)	-8.5(8)
C55	36.3(7)	32.3(6)	21.7(5)	-2.2(5)	9.3(5)	2.2(5)
C56	34.0(6)	25.0(5)	19.9(5)	-2.6(4)	7.4(5)	2.5(5)
C57	26.5(6)	23.5(5)	18.8(5)	-0.9(4)	5.9(4)	3.8(4)
C58	25.0(5)	25.5(5)	19.9(5)	-0.3(4)	8.0(4)	4.5(4)
C59	26.0(6)	29.0(6)	25.1(6)	1.1(5)	10.2(5)	5.1(5)
C60	30.2(6)	36.5(7)	27.0(6)	-0.6(5)	11.8(5)	6.6(5)
C61	35.6(7)	48.2(8)	34.4(7)	-0.5(6)	17.7(6)	6.3(6)
C62	37.0(8)	46.4(9)	48.9(9)	0.5(7)	24.1(7)	-0.2(7)
C63	33.1(7)	38.0(7)	46.6(8)	-4.2(6)	18.3(6)	-3.3(6)
C64	26.8(6)	30.6(6)	32.8(6)	-1.2(5)	11.7(5)	2.2(5)
C65	26.4(6)	32.0(6)	32.5(6)	-6.3(5)	9.7(5)	-1.6(5)
C66	25.0(6)	32.2(6)	24.3(6)	-6.2(5)	7.4(5)	-1.1(5)
C67	21.9(5)	26.8(6)	22.1(5)	-2.4(4)	7.3(4)	1.2(4)
C68	25.5(5)	24.2(5)	18.1(5)	-1.5(4)	6.8(4)	0.5(4)
C69	26.5(6)	27.6(6)	21.1(5)	-1.2(4)	4.1(4)	-2.7(5)
C70	32.8(6)	24.9(6)	21.6(5)	-1.7(4)	7.8(5)	-4.9(5)
C71	30.2(6)	23.7(5)	23.9(5)	-0.3(4)	12.4(5)	-2.3(5)
C72	36.2(7)	23.5(6)	35.1(7)	-3.9(5)	15.0(5)	-3.1(5)
C73	36.1(7)	24.0(6)	50.5(8)	-3.6(6)	15.4(6)	2.5(5)
C74	29.0(7)	29.6(7)	48.9(8)	-1.1(6)	7.3(6)	4.4(5)
C75	26.1(6)	27.2(6)	35.6(7)	-2.3(5)	7.9(5)	0.6(5)
C76	25.5(6)	23.6(5)	24.6(5)	-0.6(4)	11.1(4)	-0.2(4)
C77	23.5(5)	25.8(5)	18.3(5)	-1.2(4)	7.9(4)	0.1(4)
C78	23.7(5)	28.0(6)	17.9(5)	-2.5(4)	6.3(4)	1.2(4)
C79	24.2(5)	28.5(6)	19.1(5)	-1.6(4)	4.9(4)	0.7(4)
C80	26.5(6)	28.1(6)	31.1(6)	-0.1(5)	8.8(5)	1.5(5)
C81	25.0(6)	32.9(7)	36.9(7)	2.7(5)	8.8(5)	1.0(5)
C82	26.9(6)	33.3(7)	30.1(6)	2.1(5)	1.3(5)	-3.8(5)
C83	31.2(6)	31.9(6)	23.9(6)	-4.7(5)	2.4(5)	-2.6(5)
C84	26.6(6)	32.5(6)	21.6(5)	-6.5(5)	4.5(4)	-0.3(5)
C85	30.2(6)	36.6(7)	33.0(7)	-17.4(6)	6.9(5)	-0.1(5)
C86	25.1(6)	37.6(7)	34.1(7)	-14.0(6)	7.0(5)	3.5(5)
C87	23.2(5)	31.1(6)	20.9(5)	-6.7(4)	4.4(4)	0.4(5)
C88	30.7(6)	34.1(6)	22.7(6)	-1.5(5)	7.4(5)	3.5(5)

Table 9-40 Bond Angles in Å for 4DBCzIPN (19).

Atom	Atom	Length/Å
N1	C1	1.4077(14)
N1	C7	1.3960(15)
N1	C26	1.3951(16)
N2	C27	1.1429(17)
N3	C3	1.4098(15)
N3	C28	1.3998(15)
N3	C47	1.4050(16)
N4	C4	1.4097(14)
N4	C48	1.3982(15)
N4	C67	1.3954(16)
N5	C5	1.4066(15)
N5	C68	1.3926(15)
N5	C87	1.3968(16)
N6	C88	1.1446(18)
C1	C2	1.3979(17)
C1	C6	1.3969(17)
C2	C3	1.4059(16)
C2	C27	1.4402(17)
C3	C4	1.4083(16)
C4	C5	1.4077(17)
C5	C6	1.4061(16)
C6	C88	1.4410(17)
C7	C8	1.4058(18)
C7	C16	1.4010(16)
C8	C9	1.3637(18)
C9	C10	1.421(2)
C10	C11	1.4153(18)
C10	C15	1.424(2)
C11	C12	1.368(2)
C12	C13	1.397(3)
C13	C14	1.381(2)
C14	C15	1.4194(18)
C15	C16	1.4393(16)
C16	C17	1.4500(17)
C17	C18	1.4387(17)
C17	C26	1.4019(16)
C18	C19	1.4169(17)
C18	C23	1.4242(19)
C19	C20	1.372(2)
C20	C21	1.401(2)
C21	C22	1.371(2)
C22	C23	1.4167(19)
C23	C24	1.4252(18)
C24	C25	1.3654(19)
C25	C26	1.4059(18)
C28	C29	1.4052(18)
C28	C37	1.3961(18)
C29	C30	1.3702(18)
C30	C31	1.426(2)
C31	C32	1.4175(18)
C31	C36	1.4226(19)
C32	C33	1.368(2)
C33	C34	1.406(2)
C34	C35	1.375(2)
C35	C36	1.4201(19)
C36	C37	1.4371(17)
C37	C38	1.4520(17)
C38	C39	1.4354(18)
C38	C47	1.3979(17)

Atom	Atom	Length/Å
C39	C40	1.4201(19)
C39	C44	1.4236(19)
C40	C41	1.372(2)
C41	C42	1.397(3)
C42	C43	1.369(2)
C43	C44	1.4167(19)
C44	C45	1.4267(19)
C45	C46	1.3653(18)
C46	C47	1.4042(17)
C48	C49	1.4045(18)
C48	C57	1.3993(16)
C49	C50	1.3643(18)
C50	C51	1.4298(19)
C51	C52	1.416(2)
C51	C56	1.419(2)
C52	C53	1.372(2)
C53	C54	1.389(3)
C54	C55	1.3716(19)
C55	C56	1.4198(18)
C56	C57	1.4347(16)
C57	C58	1.4496(18)
C58	C59	1.4344(17)
C58	C67	1.4025(16)
C59	C60	1.4165(17)
C59	C64	1.4250(19)
C60	C61	1.374(2)
C61	C62	1.401(2)
C62	C63	1.372(2)
C63	C64	1.4169(19)
C64	C65	1.4297(18)
C65	C66	1.3668(18)
C66	C67	1.4075(17)
C68	C69	1.4081(17)
C68	C77	1.4013(17)
C69	C70	1.3652(18)
C70	C71	1.4213(18)
C71	C72	1.4159(18)
C71	C76	1.4289(17)
C72	C73	1.366(2)
C73	C74	1.401(2)
C74	C75	1.3824(19)
C75	C76	1.4136(18)
C76	C77	1.4366(17)
C77	C78	1.4572(17)
C78	C79	1.4353(17)
C78	C87	1.3981(17)
C79	C80	1.4143(17)
C79	C84	1.4290(17)
C80	C81	1.3707(19)
C81	C82	1.403(2)
C82	C83	1.3652(19)
C83	C84	1.4159(18)
C84	C85	1.4257(18)
C85	C86	1.3595(19)
C86	C87	1.4089(18)


C7
N1
N6
C1
C27
N2
C88
C6
C2
N5
C4
N3
C5
C3
C28
C68
N4
C48
C
N

Appendix 5 List of conferences

1. RSC Materials Chemistry MC15 2021 (Online) – attended.

2. ICSM 2022 (Glasgow) – absent due to coronavirus, but *Poster 1* was submitted and displayed.

3. Molecular Photophysics Conference III 2022 (Newcastle) – attended and presented *Poster 1*.

4. RSC Materials Chemistry MC16 2023 (Dublin) – attended and presented a talk on our paper: *A Study on Varying the Number of Fluorene Units in 2, 1, 3-Benzothiadiazole-Containing Oligomers and the Effect on OLED Performance and Stability, ChemPhotoChem, 2022, e202200256*. This also included a discussion of the follow up work I investigated on hyperfluorescence with these molecules in collaboration with Sebastian Reineke's group at TU Dresden as part of MEGA H2020, as well as additional work completed upon my return to Glasgow.

   For this I was awarded an RSC Researcher Development and Travel Grant to fund the travel and accommodation costs.

5. RSC Photophysics and Photochemistry conference 2024 (Sheffield) – attended and presented *Poster 2*.

6. International Conference on Electronic Luminescence ICEL 2024 (Kyoto, Japan) – attended and presented *Poster 3*.

9.22 Poster 1

University of Glasgow

rISC - The Game of Strategic Molecular Design for High Efficiency OLEDs

Christopher J. Riggs, {xxxxx@student.gla.ac.uk} Skabara Group, University of Glasgow

Professor Pete Skabara[1], Dr Joseph Cameron[1] , Dr Oleksandr Kanibolotsky[1], Dr Lyuda Kanibolotsky [1], Professor Sebastian Reineke[2], Dr Sebastian Schellhammer[2], Dr Paulius Imbrasas[2] and Dr Heidi Thomas[2]

[1]Skabara Group, University of Glasgow; [2]LEXOS group, TU Dresden / Creaphys

REFERENCES

[1] Etherington et al. Nature Communications. (2016). 1-7. 7

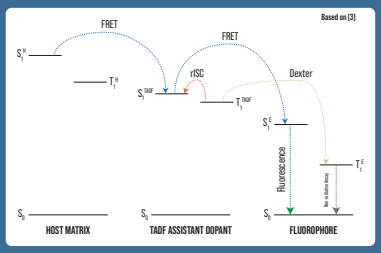
[2] Nakanotani et al. Nature Communications. (2014). 1-7. 5(May)

[3] Wallwork et al. Journal of Materials Chemistry C. (2022). 4767-4774. 10(12)

[4] Adachi et al. Proceedings of the International Display Workshops. (2021). 399-401. 27

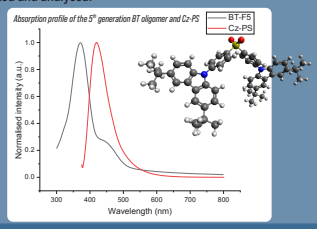
WHAT ARE OLEDS?

- Light emitting diodes with a purely organic material as the emissive layer.
- Can be formed on flexible substrates, allowing for a diverse array of form factors and flexible displays.
- Made from recyclable, biodegradeable and sustainable materials.
- Allow for displays with deep blacks; but high brightness lead to shorter lifetimes.



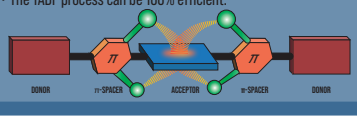
SAMPLE PREPARATION

- Thin films were prepared of all the BT oligomers and potential TADF assistant dopants via spin coating (Cz-PS and 5tCzCF$_3$Ph).
- Pairings with appropriate HOMO-LUMO encompassment, S_1 energies, and emission and absorption profile overlap were selected and binary (1% w.t.) and tertiary blends (30% w.t. TADF, 0.5% w.t. and 1% w.t. fluorophore concentrations) were spin coated and analysed.



rISC AND TADF

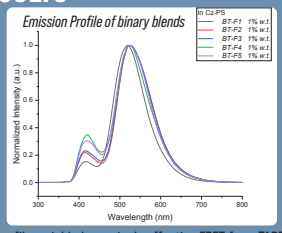
- rISC is the process of harvesting non-emissive excited triplet states and converting them into emissive singlet states.
- Thermally activated delayed fluorescence (TADF) achieves this by applying thermal energy (from room temperature) to convert triplets to singlets.
- TADF can be achieved with purely organic materials (no metals or toxic materials) by exploiting charge transfer (CT) states and donor-acceptor - donor structrual motifs incorporating locally excited (LE) states[1].
- Susceptable to roll-off effects and has broad emission profiles.
- The TADF process can be 100% efficient.



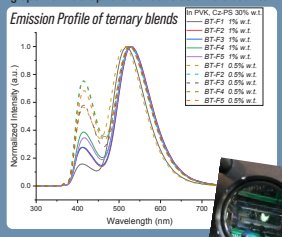
SELECTING FLUOROPHORES

- When designing a hyperfluorescent devices, two processes must be considered: Förster resonance energy transfer and Dexter energy transfer.
- Dexter energy transfer is driven by molecular collisions, and results in energy transfer from the TADF molecule's triplet state to the fluorescent molecule's dark triplet state - which is non-emissive. As such, the fluorophore must be diluted within the emitter layer (typically ~0.5 - 1% w.t.)[3].
- There are two types of hyperfluorescent devices - binary (where the host is a TADF molecule), and ternary (where a host matrix holds both a TADF molecule (~15 - 50% w.t.) and the fluorophore).
- To maximise Förster resonance energy transfer, the S_1 energy of the TADF molecule must exceed that of the fluorophore's, and its emission spectra must overlap with the fluorophore's absorption profile.

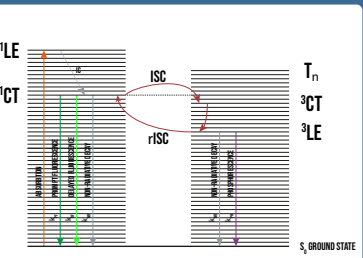
RESULTS

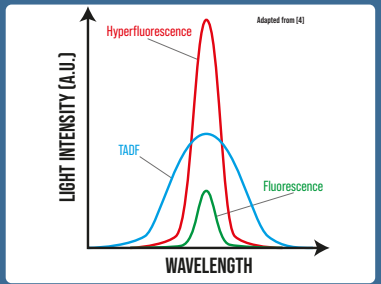


- Binary films yielded seemingly effective FRET from TADF to BT oligomer, with more pronounced results in the smaller molecules.
- PLQYs from 75-85% for the Cz-PS s binary film samples suggest good energy transfer.
- Almost 100% PLQY from 1% w.t. ternary films suggest lower concentrations are further enhancing FRET, and that Dexter interactions are more prominant in binary films.
- 0.5% w.t. flims have intermediate PLQYs from 77% - 82%, suggesting optimal fluorophore concentration is closer to 1% w.t.







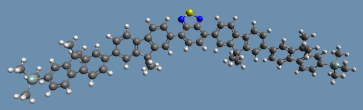


HYPERFLUORESCENCE

- Hyperfluorescence allows for purer colour emissions and significantly higher luminance than TADF and standard fluorescence[2].
- Involves a TADF molecule as a host generating singlet states that exploits Förster resonance energy transfer to drive singlets from the TADF molecule to the fluorophore which then emit as fluorescence with 100% efficiency.
- No triplet states formed in the fluorophore, and no CT states used in emission, so if TADF is 100% efficient, narrower FWHM and brighter emissions.

THE PROJECT

- A family of benzothiadiazole and fluorene based fluorescent emitters are investigated as potential hyperfluorescent fluorophores, owing to their absorptive fluorene arms.
- Paired with a selection of TADF emitters (host and assistant dopant) with matching HOMOs, LUMOS, and excited states, as well as overlapping emission and absorption spectra.



ONGOING RESEARCH

- OLEDs are being fabricated based on the most promising blends.
- Synthesis of a novel TADF molecule more suited to the properties of the BT oligomers.
- Synthesis of a novel family of fluoroene based oligomers with a different acceptor core to further enhance the Förster resonance energy transfer.

ACKNOWLEDGEMENTS

Thanks to the coauthors for their help and support with this project, as well as the MEGA H2020 scheme for sponsoring my secondment to TU Dresden.

MEGA TECHNISCHE UNIVERSITÄT DRESDEN @F2Chemistry

9.23 Poster 2

University of Glasgow

Durham University

A quasi-helical, flappable donor

Dibenzocarbazole - from thermochromism, to TADF and polymorphism

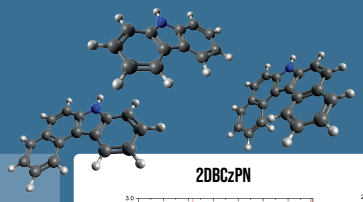
Christopher J. Riggs[1,2], (christopher.j.riggs@durham.ac.uk)

Dr Joseph Cameron[1], Dr Andrea Pinto[1], Dr Suman Kulia[2], Dr Andrew Danos[2], Kamile Bareikaite[2], Professor Andrew Monkman[2], Professor Pete Skabara[1]

[1]Skabara Group, University of Glasgow; [2]OEM Group, Durham University

REFERENCES

[1] Wong et al., ACS Applied Materials and Interfaces, (2018), 33360-33372, 10(39)
[2] Uoyama et al., Nature, (2012), 234-238, 492(7428)
[3] Ishimatsu et al., Chemistry - A European Journal, (2016), 4889-4898, 22(14)
[4] Cardeynaels et al., J. Mater. Chem. C, 2022, 10, 5840-5848
[5] Shu et al., Dyes and Pigments 195 (2021) 109708



DIBENZOCARBAZOLE

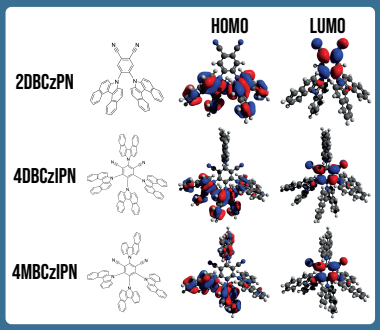
Carbazole has been well established as a suitable donor moiety for TADF molecules. *7H-Dibenzo[c,g]carbazole* presents a slightly stronger donor with increased conjugation. Our previous studies indicate significant HOMO confinement and excellent HOMO-LUMO separation, regardless of acceptor used with this donor - rivalling that observed with 2CzPN[1] and 4CzIPN[2,3], potentially giving rising to enhanced rISC.

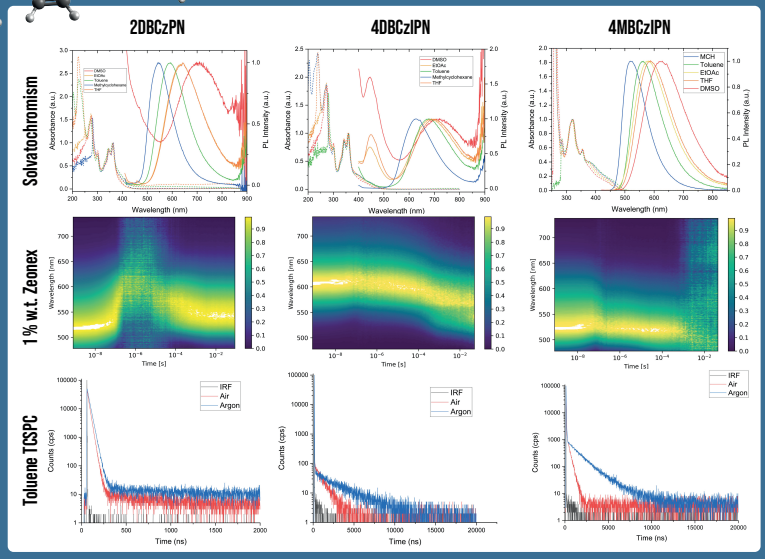
Two acceptor moieties were paired with dibenzocarbazole, and a monobenzocarbazole molecule was prepared for comparison.

PHOTOPHYSICS AND DFT

All three compounds demonstrate substantial solvatochromism and delayed emissions. Whilst 2DBCzPN and 4DBCzIPN have low PLQYs in degassed toluene (4% and 10% respectively), 4MBCzIPN has a PLQY of 55%. This increases in the solid-state, with 4MBCzIPN reaching 90% in mCP. The oxygen sensitivity of the emissions strongly suggests the action of rISC, with the 4CzIPN derivatives having substantially longer emission lifetimes when degassed.

As with out other work, the DFT calculations (*PBE0 6-31+G (d)*) reveal complete confinement of the HOMO to the donor moiety with significantly less mixing with the LUMO observed than is reported in the literature for 4CzIPN. Interestingly, the dibenzocarbazole moieties are revealed to be quasi-helical. This better confinement is likely to lead to increased CT character[4].





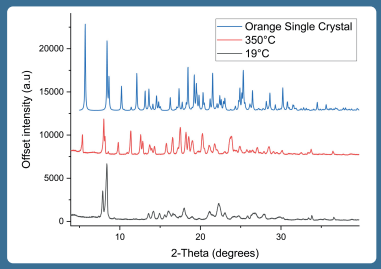
THERMOCHROMISM, MECHANOCHROMISM AND POLYMORPHISM

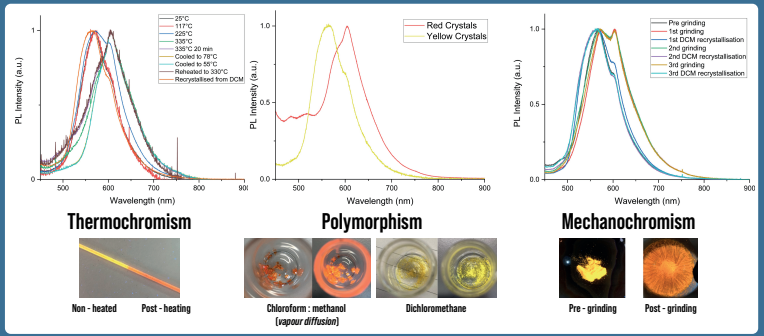
All three compounds exhibit significant thermo- and mechanochromism, with 2DBCzPN red-shifting up to 75 nm when heated, 31 nm when ground up and a 40 nm difference observed between two different crystalline polymorphs.

4DBCzIPN and 4MBCzIPN both exhibit blue-shifted thermochromic and mechanochromic emissions.

Powder diffraction XRD reveals the existence of different polymorphic forms for each compound.

From single crystal XRD studies, close contacts of as little as 3.28 Å along with face-to-face contacts, suggest changes to the crystal structure are facilitating the changes to the photophysical properties of these compounds.[5]





CONCLUSIONS

UV-vis absorption spectroscopy and cyclic voltammetry reveal a narrowing of the HOMO-LUMO energy gaps upon increased conjugation of the donor moieties. The HOMO confinement observed in our DFT calculations is supported by the significant charge transfer character of the emissive properties.

Furthermore, thermochromic blue-shifting follows the order of 4DBCzIPN > 4MBCzIPN > 4CzIPN at 171 nm, 85 nm and 26 nm respectively, demonstrating enhanced thermochromic character as conjugation of the donor moiety is increased owing to increased intermolecular interactions.

Additional novel dibenzocarbazole based compounds under study suggest thermo- and mechanochromism is common to all dibenzocarbazole based emitters.

ONGOING RESEARCH

- Further investigation of the changing photophysics at different temperatures.
- Potential applications into devices or cryptographic applications.
- Further photophysics on an extended family of dibenzocarbazole derivatives showing similar properties with significantly increased PLQYs.

ACKNOWLEDGEMENTS

Thanks to the coauthors for their help and support with this project. In addition, thanks to Dr Laura McCormick from the University of Southampton for performing single crystal XRD for us and to Dr Claire Wilson for assisting with variable temperature powder XRD studies. Thanks also to Dr Suman Kulia[2] for performing the initial CCD measurements for this project.

@F2Chemistry

9.24 Poster 3

University of Glasgow

Durham University

A Game of rISC

Engineering non-covalent interactions to drive TADF in boron-based compounds

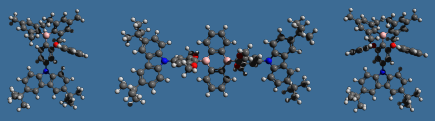
Christopher J. Riggs[1,2], (christopher.j.riggs@durham.ac.uk)

Kamile Bareikaite[2], Dr Joseph Cameron[1], Dr Andrea Pinto[1], Dr Suman Kulia[2,3], Professor Andrew Monkman[2], Professor Thomas Penfold[4], Professor Pete Skabara[1]

[1] Skabara Group, University of Glasgow; [2] OEM Group, Durham University; [3] University of Colorado, Boulder, [4] Newcastle University

REFERENCES

[1] Lee et al., Adv Opt Mater, 2018, 6, 1800385-1800407
[2] Kitamoto et al., J Mater Chem C Mater, 2015, 3, 9122-9130
[3] Kitamoto et al., Org Electron, 2016, 34, 208-217.
[4] Wu et al., Nat Photonics, 2018, 12, 235-240



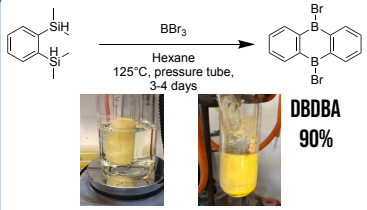
INTRODUCTION

Boron has been reported as a suitable component of electron-accepting moieties owing to its electron deficient empty p-orbital. Lee et al.[1] demonstrated that combining carbazole-based donors with dimesityl boron, separated by means of an ortho-substituted π-bridge, can yield blue emitters with high PLQYs and attractively high EQEs. Kitamoto et al.[2,3] showed that when paired with phenoxazine or dimethyl acridine donors, 10H-phenoxaborin and dimesityl boron acceptors can yield TADF. Whilst they found two factors resulted in no TADF with carbazole based donors – namely it being too weakly electron donating, and the π-bridge not being sterically hindered enough to yield adequate HOMO-LUMO separation via a high dihedral. We sought to improve upon this in two ways – increased steric hinderance between donor π-bridge and acceptor, as well as introducing non-covalent interactions to sustain a large dihedral twist, whilst also facilitating increased charge transfer.

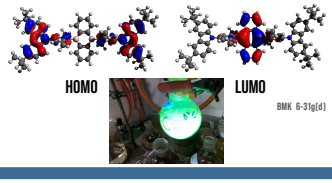
RESULTS

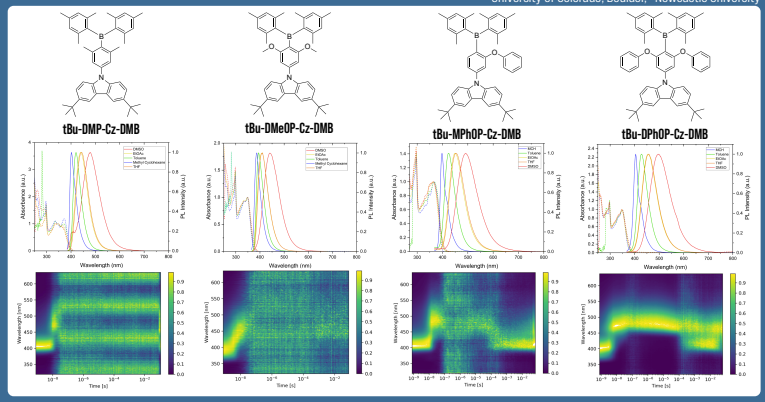
All the compounds studied produced significant solvatochromism, indicative of CT character, as well as relatively high PLQYs (70 - 80%). Their lifetimes demonstrate that no delayed component is present in the methyl and methoxy derivatives, likely due to enhanced flexibility of the acceptor moiety despite steric interactions, although they have excellent FWHM of 29 and 28 nm, respectively. In the phenoxy compounds, solvatochromism is enhanced further and very long delayed lifetimes are observed (20 ms and 12 ms for **mono-** and **diphenoxy** compounds, respectively), with the **diphenoxy** compound demonstrating fluorescence, RTP and TADF.

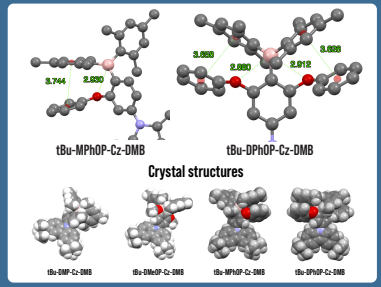
Crystal structures of the compounds indicate proximity for non-covalent interactions between the **methoxy** and **phenoxy** oxygens, and boron. However, in the two **phenoxy** compounds, the aromatic rings of the **phenoxy** groups orient such that they exhibit face-to-face contacts with the two mesityl rings, allowing for π- π interactions, and permitting charge transfer and further stabilising the structures and reducing non-radiative decay.

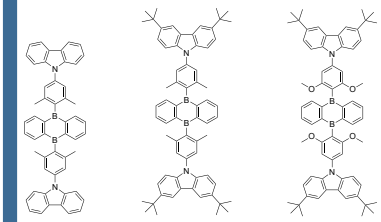


DBDBA
90%









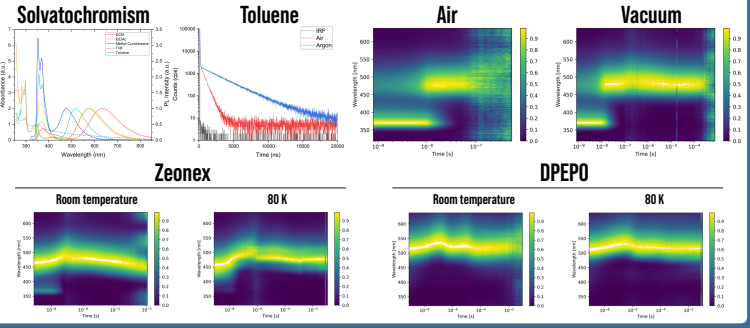
CZDBA

In 2018, Wu et al.[4] demonstrated a highly efficient green emitter, **CzDBA**. The planar DBA acceptor moiety and methyl substituted π-bridge results in well-separated HOMO and LUMO leading to an exceedingly high rISC rate. In solution, PLQYs are very low, owing to multiple decay pathways and molecule flexibility. We sought to improve upon this design, replacing the methyl groups with methoxy groups to induce non-covalent interactions, resulting in a rigid structure with enough flexibility to permit SOC.

The DBA acceptor core is based on **DBDBA**, a notoriously air sensitive material with a long synthesis procedure with mediocre to low yields. We have substantially improved upon this with a new synthetic method which halves the synthesis time with cheap, commercially available starting material in a single step, with a staggeringly high yield of 90%.

Impressive solvatochromism was observed in our target compound, **tBu-MeOCzDBA**, with exceedingly long decay lifetimes (up to 30 s in neat films). Interestingly, in non-polar solvents, dual emission is observed – a green CT emission and blue LE emission. Switching to polar media and the LE peak is suppressed (completely switched off in DPEPO) and CT emission dominates. This suggests that in non-polar media, the rigidity of the molecule is such that the HOMO and LUMO are almost completely decoupled, yielding emission from both the CT state and the individual donor moieties.

In a compelling twist, in solution, we observed PLQYs of 91%, a significant increase from the 14% observed by Wu et al.[4] for their analogues. This also reaches 100% in Zeonex and mCP hosts. This suggests that in **tBu-MeOCzDBA**, the methoxy – boron non-covalent interaction is highly effective at suppressing any non-radiative decay pathways that are present in the progenitor molecules.



CONCLUSIONS

Five novel boron-based emitters have been developed. **Methoxy** groups have yielded very narrow FWHMs and deep-blue fluorescent emissions. Switching to **phenoxy** groups activates an RTP and TADF pathway thanks to stronger non-covalent interactions preventing losses from the rotation of mesityl rings in the acceptor moieties. With a planar and rigid acceptor, our methoxy modification to **CzDBA** has resulted in a significant increase in PLQYs in solution and the solid state thanks to a substantial reduction in non-radiative decay pathways. We have established the methoxy – boron non-covalent interaction as a viable means of aiding high dihedral angles with enough flexibility to facilitate effective SOC resulting in rISC and hence TADF.

ONGOING RESEARCH

- Further alternative modifications to further stablise the target molecules, protecting them from degradation and fabrication of OLED devices.
- Investigation into the application of phenoxy groups into moleucles with planar acceptors

ACKNOWLEDGEMENTS

Thanks to the coauthors for their help and support with this project. In addition, thanks to Dr Laura McCormick from the University of Southampton for performing single crystal XRD for us. Thanks also to Dr Suman Kulia[2,3] for performing the initial CCD measurements for this project.

@F2Chemistry

Appendix 6 List of collaborative visits

7. MEGA H2020 secondment to Sebastian Reineke's Lexos group at the Integrated Centre for Applied Physics and Photonic Materials at Technische Universität Dresden (2.5 months). This project involved exploring the photophysics of BT-Fx_2 oligomers prepared in the Skabara group by Dr Joseph Cameron and Dr Luis-Abraham Lozano-Hernández and pairing them with appropriate TADF molecules to achieve hyperfluorescence through FRET. The blends were incorporated into OLEDs which I fabricated myself. Work here contributed to our paper: *A Study on Varying the Number of Fluorene Units in 2, 1, 3-Benzothiadiazole-Containing Oligomers and the Effect on OLED Performance and Stability, ChemPhotoChem, 2022, e202200256.* The project continued upon my return to Glasgow with some success with device work and photophysics and was featured in my talk in Dublin at MC16 in 2023. Work for this project is ongoing during my post doc position at Durham University.

8. rISC project collaborator's meeting in Newcastle (February 2023). Current results at the time were presented (for the first molecule of Chapter 5, tBu-DMP-Cz-OBA) and next steps discussed.

9. rISC project collaborator's meeting at Ross-Priory (December 2023). The combined work of Chapters 4, 5, 6 and 7 was presented and discussed, with particular focus on the non-covalent interactions of tBu-MeOCzDBA in Chapter 6.

10. Photophysics for tBu-MeOCzDBA. In November 2023 and January 2024, I visited the OEM group of Professor Andy Monkman at Durham University where I worked with Kamile Bareikaite to perform solution and solid state CCD lifetime studies of the compound.

Bibliography

1 M. S. Shur and A. Žukauskas, Solid-state lighting: Toward superior illumination, *Proceedings of the IEEE*, 2005, **93**, 1691–1703.
2 A. Volta, II. Of the method of rendering very sensible the weakest natural or artificial electricity, *Philos Trans R Soc Lond*, 1782, **72**, 4653.
3 M. Faraday, Experimental Researches in Electricity — Fourth Series, *Philos Trans R Soc Lond*, 1833, **123**, 507–522.
4 J. W. Orton, in *The Story of Semiconductors*, Oxford University Press, 2008.
5 A. H. Wilson, The theory of electronic semi-conductors, *Proceedings of the Royal Society of London. Series A, Containing Papers of a Mathematical and Physical Character*, 1931, **133**, 458–491.
6 A. Bernanose, Electroluminescence of organic compounds, *British Journal of Applied Physics*, 1955, **6**, 54.
7 Sony α7 III, https://www.sony.co.uk/electronics/interchangeable-lens-cameras/ilce-7m3-body-kit#product_details_default, (accessed 26 May 2020).
8 LG OLED TVs, https://www.lg.com/uk/oled-tvs, (accessed 26 May 2020).
9 Apple iPhone 11, https://www.apple.com/uk/iphone-11-pro/, (accessed 26 May 2020).
10 D. Dilaura, 22 | OPN September 2008 www.osa-opn.org, 2008, 22–28.
11 M. Guarnieri, An Historical Survey on Light Technologies, *IEEE Access*, 2018, **6**, 25881–25897.
12 L. Figuier, Fig. 10 -- verre du bec d'Argand, http://hdl.loc.gov/loc.pnp/cph.3c10395, (accessed 6 June 2024).
13 D. E. Nye, *American Illuminations*, The MIT Press, 2018.
14 W. T. Sedgewick and F. J. Schnider, The relation of illuminating gas to public health, *Journal of the American Public Health Association*, 1911, **1**, 385–390.
15 L. Worsley, A quick history of domestic lighting, https://www.lucyworsley.com/a-quick-history-of-domestic-lighting/, (accessed 25 March 2020).
16 K. Wallis-Smith, Gas Lighting in Victorian times, http://www.countrylife.co.uk/property/guides-advice/gas-lighting-in-victorian-times-16562.
17 H. Davy, I. On the fire-damp of coal mines, and on methods of lighting the mines so as to prevent its explosion, *Philos Trans R Soc Lond*, 1816, **106**, 1–22.
18 Kobo and Wikipedia, Image of Humphry Davy lamp, https://en.wikipedia.org/wiki/Davy_lamp#/media/File:Davy_lamp.png, (accessed 6 June 2024).
19 V. B. Lewes, Gas mantle, incandescent, and its uses, *Journal of the Society of Arts; London*, 1899, **48**, 853–860.
20 D. Voss, L. Poffenberger and Alaina. G. Levine, *APS News*, 2018, 27, 3.
21 A. Bateson, The chemistry of 'being in the limelight'., https://www.ool.co.uk/blog/the-chemistry-of-being-in-the-limelight/, (accessed 25 March 2020).
22 C. M. Carver, *A History of English in its Own Words*, Harper Collins, 1991.
23 D. MacIsaac, G. Kanner and G. Anderson, Basic physics of the incandescent lamp (lightbulb), *Phys Teach*, 1999, **37**, 520–525.
24 T. A. Edison, *Patent: Electric lamp, US Patent Number US223898*, United States Patent Office, United States, 1880.
25 M. Schiler, *Simplified Design of Building Lighting*, Wiley, 1997.
26 H. J. Round, A note on carborundum, *Electrical World*, 1907, **49**, 309.

27 N. Holonyak and S. F. Bevacqua, Coherent (visible) light emission from Ga(As1-xPx) Junctions, *Semiconductor Devices: Pioneering Papers*, 1991, **82**, 898–899.

28 R. N. Hall, G. E. Fenner, J. D. Kingsley, T. J. Soltys and R. O. Carlson, Coherent Light Emission From GaAs Junctions, *Phys Rev Lett*, 1962, **9**, 366–368.

29 S. Nakamura, T. Mukai and M. Senoh, Candela-class high-brightness InGaN/AlGaN double-heterostructure blue-light-emitting diodes, *Appl Phys Lett*, 1994, **64**, 1687–1689.

30 The Nobel Prize in Physics 2014, https://www.nobelprize.org/prizes/physics/2014/press-release/, (accessed 26 March 2020).

31 M. Pope, H. P. Kallmann and P. Magnante, Electroluminescence in organic crystals [16], *J Chem Phys*, 1963, **38**, 2042–2043.

32 G. Hong, X. Gan, C. Leonhardt, Z. Zhang, J. Seibert, J. M. Busch and S. Bräse, A Brief History of OLEDs—Emitter Development and Industry Milestones, *Advanced Materials*, 2021, **33**, 5630–5654.

33 H. Uoyama, K. Goushi, K. Shizu, H. Nomura and C. Adachi, Highly efficient organic light-emitting diodes from delayed fluorescence, *Nature*, 2012, **492**, 234–238.

34 S. R. Forrest, *Organic Electronics: Foundations to Applications*, Oxford University Press, Oxford, 2020.

35 M. P. Bracciale, *Sustainable Strategies in Organic Electronics*, Elsevier, 2022.

36 L. Kelion and J. Whitwell, Galaxy Fold: The internet reacts to Samsung's flexible phone, https://www.bbc.co.uk/news/technology-47313049, (accessed 5 February 2021).

37 V. Savov, Flexible Phone Screens That Roll and Fold Are Liberating Boring Design, https://www.bloomberg.com/news/articles/2021-01-28/flexible-mobile-phone-screens-that-fold-are-liberating-boring-design, (accessed 5 February 2021).

38 S. J. Benight, C. Wang, J. B. H. Tok and Z. Bao, Stretchable and self-healing polymers and devices for electronic skin, *Prog Polym Sci*, 2013, **38**, 1961–1977.

39 M. Irimia-Vladu, P. A. Troshin, M. Reisinger, L. Shmygleva, Y. Kanbur, G. Schwabegger, M. Bodea, R. Schwödiauer, A. Mumyatov, J. W. Fergus, V. F. Razumov, H. Sitter, N. S. Sariciftci and S. Bauer, Biocompatible and biodegradable materials for organic field-effect transistors, *Adv Funct Mater*, 2010, **20**, 4069–4076.

40 Y. Zhou, T. M. Khan, J. C. Liu, C. Fuentes-Hernandez, J. W. Shim, E. Najafabadi, J. P. Youngblood, R. J. Moon and B. Kippelen, Efficient recyclable organic solar cells on cellulose nanocrystal substrates with a conducting polymer top electrode deposited by film-transfer lamination, *Org Electron*, 2014, **15**, 661–666.

41 Y. Xie, F. Guan, Z. Li, Y. Meng, J. Cheng, L. Li and Q. Pei, A Phase-Changing Polymer Film for Broadband Smart Window Applications, *Macromol Rapid Commun*, 2020, **41**, 290–297.

42 NOWOFOL, What is ETFE?, https://www.nowofol.com/en/etfe-architecture/etfe-membrane/#:~:text=ETFE%20film%20is%20highly%20flame,a%20wide%20range%20of%20applications., (accessed 20 May 2024).

43 Y. Li, X. Huang, K. Ding, H. K. M. Sheriff, L. Ye, H. Liu, C.-Z. Li, H. Ade and S. R. Forrest, Non-fullerene acceptor organic photovoltaics with intrinsic operational lifetimes over 30 years, *Nat Commun*, 2021, **12**, 5419–5428.

44 Hayley Hanway, Organic photovoltaics offer realistic pathway to power-generating windows, https://ece.engin.umich.edu/stories/organic-photovoltaics-offer-realistic-pathway-to-power-generating-windows#:~:text=Organic%20solar%20cells%20can%20absorb,creating%20a%20stained%2Dglass%20appearance., (accessed 20 May 2024).

45 LG, LG Signature Rollable OLED, https://www.lg.com/global/lg-signature/rollable-oled-tv-r, (accessed 20 May 2024).
46 Google, Pixel Fold, https://store.google.com/gb/product/pixel_fold?hl=en-GB, (accessed 20 May 2024).
47 OnePlus, OnePlus Open, https://www.oneplus.com/uk/oneplus-open, (accessed 20 May 2024).
48 Honor, Honor Magic V2, https://www.honor.com/uk/phones/honor-magic-v2/, (accessed 20 May 2024).
49 Samsung, Samsung Galaxy Flip/Fold, https://www.samsung.com/uk/smartphones/galaxy-z/, (accessed 20 May 2024).
50 Oppo, Oppo X 2021, https://www.oppo.com/en/smartphones/oppo-x-2021/, (accessed 22 September 2024).
51 David Lumb, I Felt the Motorola Rizr's Rollable Screen Move Under My Hand, https://www.cnet.com/tech/mobile/i-felt-the-motorola-rizrs-rollable-screen-move-under-my-hand/, (accessed 20 May 2024).
52 Panasonic, Panasonic VITRINE, https://panasonic.net/design/works/milan2019/, (accessed 5 February 2021).
53 H. Akamatu and H. Inokuchi, On the Electrical Conductivity of Violanthrone, Iso-Violanthrone, and Pyranthrone, *J Chem Phys*, 1950, **18**, 810–811.
54 H. Inokuchi, The discovery of organic semiconductors. Its light and shadow, *Org Electron*, 2006, **7**, 62–76.
55 H. Inokuchi, Photoconductivity of the Condensed Polynuclear Aromatic Compounds, *Bull Chem Soc Jpn*, 1954, **27**, 22–27.
56 Y. Liu, X. Wu, Z. Xiao, J. Gao, J. Zhang, H. Rui, X. Lin, N. Zhang, Y. Hua and S. Yin, Highly efficient tandem OLED based on C 60 /rubrene: MoO 3 as charge generation layer and LiF/Al as electron injection layer, *Appl Surf Sci*, 2017, **413**, 302–307.
57 H. Spanggaard and F. C. Krebs, A brief history of the development of organic and polymeric photovoltaics, *Solar Energy Materials and Solar Cells*, 2004, **83**, 125–146.
58 R. C. Nelson, Organic photoconductors. I. The kinetics of photoconductivity in rhodamine B, *J Chem Phys*, 1954, **22**, 885–889.
59 A. K. Ghosh, D. L. Morel, T. Feng, R. F. Shaw, C. A. Rowe, A. Schottky-barrier and C. A. R. Jr, Photovoltaic and rectification properties of Al/Mg phthalocyanine/Ag Schottkybarrier cells Photovoltaic and rectification properties of All Mg, *J. Appl. Phys.*, 1974, **45**, 230–236.
60 D. L. Morel, A. K. Ghosh, T. Feng, E. L. Stogryn, P. E. Purwin, R. F. Shaw and C. Fishman, High-efficiency organic solar cells, *Appl Phys Lett*, 1978, **32**, 495–497.
61 G. A. Chamberlain and P. J. Cooney, Photoelectric properties of aluminium/copper phthalocyanine/gold photovoltaic cells, *Chem Phys Lett*, 1979, **66**, 88–94.
62 C. W. Tang, Two-layer organic photovoltaic cell, *Appl Phys Lett*, 1986, **48**, 183–185.
63 C. Wang, H. Dong, W. Hu, Y. Liu and D. Zhu, Semiconducting π-conjugated systems in field-effect transistors: A material odyssey of organic electronics, *Chem Rev*, 2012, **112**, 2208–2267.
64 S. Park, M. Takakuwa, K. Fukuda, S. Lee, T. Yokota and T. Someya, Toward ultraflexible organic electronic devices, *MRS Bull*, 2023, **48**, 999–1012.
65 K. Liu, B. Ouyang, X. Guo, Y. Guo and Y. Liu, Advances in flexible organic field-effect transistors and their applications for flexible electronics, *npj Flexible Electronics*, 2022, **6**, 1.
66 M. Pope, H. P. Kallmann and P. Magnante, Electroluminescence in Organic Crystals, *J Chem Phys*, 1963, **38**, 2042–2043.

67 S. A. Vanslyke, C. W. Tang and R. C. Luther, *Patent: Electroluminescent Device with Organic Luminescent Medium, Patent Number US4720432A*, United States, 1988.

68 T. H. Han, W. Song and T. W. Lee, Elucidating the crucial role of hole injection layer in degradation of organic light-emitting diodes, *ACS Appl Mater Interfaces*, 2015, **7**, 3117–3125.

69 TCTA - Ossila, https://www.ossila.com/products/tcta, (accessed 23 February 2022).

70 H. Shi, L. Deng, S. Chen, Y. Xu, H. Zhou, F. Cheng, X. Li, L. Wang and W. Huang, Flexible top-emitting warm-white organic light-emitting diodes with highly luminous performances and extremely stable chromaticity, *Org Electron*, 2014, **15**, 1465–1475.

71 C.-S. Ho, W.-C. Hsu, Y.-N. Lai, C.-S. Lee, W.-M. Chen, E.-L. Huang, E.-P. Yao and C.-W. Wang, Performance Improvement in Poly(3-hexylthiophene):[6,6]-Phenyl C $_{61}$ Butyric Acid Methyl Ester Polymer Solar Cell by Doping Wide-Gap Material Tris(phenylpyrazole)iridium, *Applied Physics Express*, 2013, **6**, 423011–423014.

72 M. Kumar and L. Pereira, Mixed-Host Systems with a Simple Device Structure for Efficient Solution-Processed Organic Light-Emitting Diodes of a Red-Orange TADF Emitter, *ACS Omega*, 2020, **5**, 2196–2204.

73 T. Chatterjee and K. T. Wong, Perspective on Host Materials for Thermally Activated Delayed Fluorescence Organic Light Emitting Diodes, *Adv Opt Mater*, 2019, **7**, 1800565.

74 G. W. Kim, Y. H. Son, H. I. Yang, J. H. Park, I. J. Ko, R. Lampande, J. Sakong, M. J. Maeng, J. A. Hong, J. Y. Lee, Y. Park and J. H. Kwon, Diphenanthroline electron transport materials for the efficient charge generation unit in tandem organic light-emitting diodes, *Chemistry of Materials*, 2017, **29**, 8299–8312.

75 T. Furukawa, H. Nakanotani, M. Inoue and C. Adachi, Dual enhancement of electroluminescence efficiency and operational stability by rapid upconversion of triplet excitons in OLEDs, *Sci Rep*, 2015, **5**, 8429–8437.

76 C.-C. Chang, M.-T. Hsieh, J.-F. Chen, S.-W. Hwang and C. H. Chen, Highly power efficient organic light-emitting diodes with a p-doping layer, *Appl Phys Lett*, 2006, **89**, 253504.

77 H. Ahn, H. Lee, J. Yang and C. Lee, in *Digest of Technical Papers - SID International Symposium*, Blackwell Publishing Ltd, 2012, vol. 43, pp. 1481–1483.

78 Precedence Research, OLED Market (By Technology: Active-matrix OLED (AMOLED), Passive-matrix OLED (PAMOLED), Foldable OLED, White OLED, Transparent OLED, Others; By Product Type: Display, Lighting; By Display Panel Type: Rigid, Flexible, Others; By Application: Smartphone & Tablet, Smartwatches & Wearables, Television, Digital Signage Systems, PC Monitors, Laptop, Others) - Global Industry Analysis, Size, Share, Growth, Trends, Regional Outlook, and Forecast 2023-2032, https://www.precedenceresearch.com/oled-market, (accessed 21 May 2024).

79 Motorola, Motorola Razr, https://www.motorola.co.uk/smartphones-motorola-razr-40/p?skuId=701, (accessed 21 May 2024).

80 Fitbit, Fitbit Luxe, https://www.fitbit.com/global/us/products/trackers/luxe?sku=422GLWT, (accessed 28 February 2022).

81 Apple, Apple Watch Series 7, https://www.apple.com/uk/apple-watch-series-7/, (accessed 28 February 2022).

82 Samsung, Samsung Galaxy Watch 4, https://www.samsung.com/uk/watches/galaxy-watch/galaxy-watch4-pink-gold-lte-sm-r865fzdaeua/, (accessed 28 February 2022).

83 LG, Transparent OLED Automatic Door, https://www.lg-informationdisplay.com/product/oled-signage/transparent-oled-automatic-door, (accessed 22 May 2024).

84 LG, LG Objet Collection – Posé 42 inch TV 2022, https://www.lg.com/uk/tvs-soundbars/oled-evo/42lx1q6la/, (accessed 22 May 2024).

85 lights.co.uk, OMLED One d2, https://www.lights.co.uk/p/omled-one-d2-desk-lamp-with-oleds-white-3063009.html, (accessed 22 May 2024).

86 lights.co.uk, Trae Jade OLED desk lamp, https://www.lights.co.uk/p/trae-jade-oled-desk-lamp-qi-white-9048001.html?lw_om_view=recotop&utm_source=google&utm_medium=cpc&utm_campaign=PMAX_Villains&utm_content=&utm_term=&gad_source=1&gclid=EAIaIQobChMIyaKoyfqghgMVqJJQBh18YgymEAQYAyABEgIz2vD_BwE&et_uk=6b336a43d295485791125174e5050074&et_gk=Y2Y3NmU0NmE2NmY3NGM5ODgyZWZjM2RkZDI2MzFjNWMlN0MyMS4wNy4yMDI0KzA5JTNBMzYlM0EwNg, (accessed 22 May 2024).

87 Audi, Lighting technology pioneer Audi fields next-generation OLED technology, https://press.audi.co.uk/en-gb/releases/74, (accessed 12 October 2024).

88 Architonic, LivingShapes interactive wall, https://www.architonic.com/en/product/philips-lumiblade-oled-livingshapes-interactive-wall/1201916, (accessed 22 May 2024).

89 Corning, Corning - Emerging Innovations, https://www.corning.com/emea/en/innovation/corning-emerging-innovations/oled-lighting-corning-emerging-innovations.html, (accessed 22 May 2024).

90 LG, LG Chem Develops World's First High-Efficacy OLED Light Panels, https://www.lgcorp.com/media/release/3695, (accessed 22 May 2024).

91 C. M. Lochner, Y. Khan, A. Pierre and A. C. Arias, All-organic optoelectronic sensor for pulse oximetry, *Nat Commun*, 2014, **5**, 5745–5752.

92 I. D. W. Samuel, C. Lian, M. Piksa, K. Matczyszyn, K. Yoshida, S. Persheyev, K. Pawlik, F. Cabral, M. Ribeiro and J. Lindoso, in *Organic and Hybrid Sensors and Bioelectronics XIII, 114750C*, eds. R. Shinar, I. Kymissis and E. J. List-Kratochvil, Proc. SPIE 11475, 2020, p. 10.

93 E. Tankelevičiūtė, I. D. W. Samuel and E. Zysman-Colman, The Blue Problem: OLED Stability and Degradation Mechanisms, *American Chemical Society*, 2024, preprint, DOI: 10.1021/acs.jpclett.3c03317.

94 Ossila, How Long Do OLEDs Last?, https://www.ossila.com/pages/oled-lifetime, (accessed 22 May 2024).

95 E. F. Schubert, *Light-Emitting Diodes*, Cambridge University Press, 2006.

96 Y. Ohno, in *Fourth International Conference on Solid State Lighting*, Proc. SPIE 5530, 2004, vol. 5530, p. 88.

97 Lesker, Lesker Super-SPECTROS 200 product page, https://www.lesker.com/process-equipment-division/thin-film-systems/super-spectros-200-deposition-platform.cfm, (accessed 6 June 2024).

98 D. Deganello, in *Organic Light-Emitting Diodes (OLEDs): Materials, Devices and Applications*, Elsevier Ltd., 2013.

99 T. Gao, H. Wang, Z. Chen, Z. Wang, M. Zhou, B. Zhao, F. Chen and Q. Zou, Performance improved white full-organic light emitting diodes (WOLED) based on tricolor dual-layer of hyperfluorescence (HF), *Org Electron*, 2023, **120**, 106845.

100 M. Cocchi, M. Bertoldo, M. Seri, P. Maccagnani, C. Summonte, S. Buoso, G. Belletti, F. Dinelli and R. Capelli, Fully Recyclable OLEDs Built on a Flexible Biopolymer Substrate, *ACS Sustain Chem Eng*, 2021, **9**, 12733–12737.

101 Kenneth R. Spring, Thomas J. Fellers and Michael W. Davidson, Human Vision and Color Perception, https://www.olympus-lifescience.com/en/microscope-

resource/primer/lightandcolor/humanvisionintro/#:~:text=When%20fully%20light%2Dadapted%2C%20the,of%20the%20visible%20light%20spectrum), (accessed 25 May 2024).
102 H. Young and R. Freedman, *University Physics with Modern Physics 14th Edition*, Pearson, 2016.
103 C. Housecroft and E. Constable, *Chemistry*, Pearson Education, 3rd edn., 2006.
104 J. W. Orton, *The Story of Semiconductors*, Oxford University Press, 2008.
105 J. J. Quinn and K.-S. Yi, *Solid State Physics: Principles and modern applications*, Springer, 2009.
106 H. Shirakawa, E. J. Louis, A. G. MacDiarmid, C. K. Chiang and A. J. Heeger, Synthesis of electrically conducting organic polymers: Halogen derivatives of polyacetylene, (CH)x, *J Chem Soc Chem Commun*, 1977, 578–580.
107 H. Inokuchi, G. Saito, P. Wu, K. Seki, T. B. Tang, T. Mori, K. Imaeda, T. Enoki, Y. Higuchi, K. Inaka and N. Yasuoka, A Novel Type of Organic Semiconductors. Molecular Fastener, *Chem Lett*, 1986, **15**, 1263–1266.
108 D. Bloor, Totally organic transistors, *Nature*, 1991, **349**, 738–740.
109 N. A. Ran, J. A. Love, C. J. Takacs, A. Sadhanala, J. K. Beavers, S. D. Collins, Y. Huang, M. Wang, R. H. Friend, G. C. Bazan and T. Q. Nguyen, Harvesting the Full Potential of Photons with Organic Solar Cells, *Advanced Materials*, 2016, **28**, 1482–1488.
110 M. Y. Wong and E. Zysman-Colman, Purely Organic Thermally Activated Delayed Fluorescence Materials for Organic Light-Emitting Diodes, *Advanced Materials*, 2017, **29**, 1605444.
111 D. T. Chase, A. G. Fix, S. J. Kang, B. D. Rose, C. D. Weber, Y. Zhong, L. N. Zakharov, M. C. Lonergan, C. Nuckolls and M. M. Haley, 6,12-Diarylindeno[1,2- b]fluorenes: Syntheses, photophysics, and ambipolar OFETs, *J Am Chem Soc*, 2012, **134**, 10349–10352.
112 V. Coropceanu, J. Cornil, D. A. da Silva Filho, Y. Olivier, R. Silbey and J. L. Brédas, Charge transport in organic semiconductors, *Chem Rev*, 2007, **107**, 926–952.
113 N. T. Kalyani, H. Swart and S. J. Dhoble, in *Principles and Applications of Organic Light Emitting Diodes (OLEDs)*, Elsevier, 2017.
114 M. Irimia-Vladu, E. D. Głowacki, G. Voss, S. Bauer and N. S. Sariciftci, Green and biodegradable electronics, *Materials Today*, 2012, **15**, 340–346.
115 M. Irimia-Vladu, 'Green' electronics: Biodegradable and biocompatible materials and devices for sustainable future, *Chem Soc Rev*, 2014, **43**, 588–610.
116 M. Godumala, S. Choi, M. J. Cho and D. H. Choi, Recent breakthroughs in thermally activated delayed fluorescence organic light emitting diodes containing non-doped emitting layers, *J Mater Chem C Mater*, 2019, **7**, 2172–2198.
117 K. L. Kohlstedt, N. E. Jackson, B. A. Savoie and M. A. Ratner, Introduction to Organic Semiconductors Using Accessible Undergraduate Chemistry Concepts, *J Chem Educ*, 2018, **95**, 1500–1511.
118 U. Salzner, J. B. Lagowski, P. G. Pickup and R. A. Poirier, Comparison of geometries and electronic structures of polyacetylene, polyborole, polycyclopentadiene, polypyrrole, polyfuran, polysilole, polyphosphole, polythiophene, polyselenophene and polytellurophene, *Synth Met*, 1998, **96**, 177–189.
119 K. W. Böer and U. W. Pohl, *Semiconductor Physics*, Springer International Publishing, 2018.
120 K. Hannewald, V. M. Stojanović, J. M. T. Schellekens, P. A. Bobbert, G. Kresse and J. Hafner, Theory of polaron bandwidth narrowing in organic molecular crystals, *Phys Rev B*, 2004, **69**, 075211.

121 B. Valeur and M. N. Berberan-Santos, *Molecular Fluorescence*, Wiley, 2012.
122 A. Köhler and H. Bässler, Triplet states in organic semiconductors, *Materials Science and Engineering R: Reports*, 2009, **66**, 71–109.
123 T. Ogiwara, Y. Wakikawa and T. Ikoma, Mechanism of intersystem crossing of thermally activated delayed fluorescence molecules, *Journal of Physical Chemistry A*, 2015, **119**, 3415–3418.
124 A. Jablonski, Efficiency of Anti-Stokes Fluorescence in Dyes, *Nature*, 1933, **131**, 839–840.
125 M. Hutchings and P. Bamfield, *Chromic Phenomena*, Royal Society of Chemistry, Cambridge, 2018.
126 J. L. Bredas, Mind the gap!, *Mater Horiz*, 2014, **1**, 17–19.
127 J. C. Koziar and D. O. Cowan, Photochemical Heavy-Atom Effects, *Acc Chem Res*, 1978, **11**, 334–341.
128 P. Atkins and J. de Paula, *Elements of Physical Chemistry 5th Edition*, Oxford University Press, 5th edn., 2009.
129 J. Chen, Y. Wu, X. Wang, Z. Yu, H. Tian, J. Yao and H. Fu, A soluble cryogenic thermometer with high sensitivity based on excited-state configuration transformations, *Physical Chemistry Chemical Physics*, 2015, **17**, 27658–27664.
130 J. B. Birks and L. G. Christophorou, Excimer fluorescence spectra of pyrene derivatives, *Spectrochimica Acta*, 1963, **19**, 401–410.
131 P. Atkins and J. De Paula, *Physical Chemistry 9th Edition*, Oxford University Press, 9th edn., 2010.
132 M. Tonet, Fluorescence Quenching & the Stern-Volmer Plot, https://www.edinst.com/wp-content/uploads/2024/05/Spectral_School_Quenching_Stern_Volmer-1.pdf, (accessed 22 September 2024).
133 Th. Főrster, 10th Spiers Memorial Lecture. Transfer mechanisms of electronic excitation, *Discuss. Faraday Soc.*, 1959, **27**, 7–17.
134 D. Ma, Z. Xu, B. Z. Tang and Y. Wang, Recent advances in high performance blue organic light-emitting diodes based on fluorescence emitters, *J Mater Chem C Mater*, 2020, 2614–2642.
135 B. Valeur and M. N. Berberan-Santos, A brief history of fluorescence and phosphorescence before the emergence of quantum theory, *J Chem Educ*, 2011, **88**, 731–738.
136 Y. Pan, W. Li, S. Zhang, L. Yao, C. Gu, H. Xu, B. Yang and Y. Ma, High Yields of Singlet Excitons in Organic Electroluminescence through Two Paths of Cold and Hot Excitons, *Adv Opt Mater*, 2014, **2**, 510–515.
137 C. A. Parker and C. G. Hatchard, Triplet-singlet emission in fluid solutions. Phosphorescence of eosin, *Transactions of the Faraday Society*, 1961, **57**, 1894–1904.
138 M. A. Baldo, D. F. O'Brien, Y. You, A. Shoustikov, S. Sibley, M. E. Thompson and S. R. Forrest, Highly efficient phosphorescent emission from organic electroluminescent devices, *Nature*, 1998, **395**, 151–154.
139 R. Czerwieniec and H. Yersin, Diversity of copper(I) complexes showing thermally activated delayed fluorescence: Basic photophysical analysis, *Inorg Chem*, 2015, **54**, 4322–4327.
140 A. Monkman, in *Highly Efficient OLEDs*, Wiley, 2018, vol. 5, pp. 425–463.
141 F. B. Dias, J. Santos, D. R. Graves, P. Data, R. S. Nobuyasu, M. A. Fox, A. S. Batsanov, T. Palmeira, M. N. Berberan-Santos, M. R. Bryce and A. P. Monkman, The Role of Local Triplet Excited States and D-A Relative Orientation in Thermally Activated Delayed Fluorescence: Photophysics and Devices, *Advanced Science*, 2016, **3**, 1600080.

142 C. Baleizão and M. N. Berberan-Santos, *Thermally Activated Delayed Fluorescence in Fullerenes*, *Ann N Y Acad Sci*, 2008, **1130**, 224–234.
143 C. A. Parker and C. G. Hatchard, Delayed fluorescence of pyrene in ethanol, *Transactions of the Faraday Society*, 1963, **59**, 284–295.
144 C. J. Chiang, A. Kimyonok, M. K. Etherington, G. C. Griffiths, V. Jankus, F. Turksoy and A. P. Monkman, Ultrahigh efficiency fluorescent single and bi-layer organic light emitting diodes: The key role of triplet fusion, *Adv Funct Mater*, 2013, **23**, 739–746.
145 C. Ringemann, A. Schönle, A. Giske, C. Von Middendorff, S. W. Hell and C. Eggeling, Enhancing fluorescence brightness: Effect of reverse intersystem crossing studied by fluorescence fluctuation spectroscopy, *ChemPhysChem*, 2008, **9**, 612–624.
146 A. Endo, M. Ogasawara, A. Takahashi, D. Yokoyama, Y. Kato and C. Adachi, Thermally activated delayed fluorescence from Sn4+-porphyrin complexes and their application to organic light-emitting diodes -A novel mechanism for electroluminescence, *Advanced Materials*, 2009, **21**, 4802–4806.
147 K. Goushi, K. Yoshida, K. Sato and C. Adachi, Organic light-emitting diodes employing efficient reverse intersystem crossing for triplet-to-singlet state conversion, *Nat Photonics*, 2012, **6**, 253–258.
148 I. A. Wright, A. Danos, S. Montanaro, A. S. Batsanov, A. P. Monkman and M. R. Bryce, Conformational Dependence of Triplet Energies in Rotationally Hindered N- and S-Heterocyclic Dimers: New Design and Measurement Rules for High Triplet Energy OLED Host Materials, *Chemistry - A European Journal*, 2021, **27**, 6545–6556.
149 R. Scholz, P. Kleine, R. Lygaitis, L. Popp, S. Lenk, M. K. Etherington, A. P. Monkman and S. Reineke, Investigation of Thermally Activated Delayed Fluorescence from a Donor-Acceptor Compound with Time-Resolved Fluorescence and Density Functional Theory Applying an Optimally Tuned Range-Separated Hybrid Functional, *Journal of Physical Chemistry A*, 2020, **124**, 1535–1553.
150 Y. Long, M. Mamada, C. Li, P. L. Dos Santos, M. Colella, A. Danos, C. Adachi and A. Monkman, Excited State Dynamics of Thermally Activated Delayed Fluorescence from an Excited State Intramolecular Proton Transfer System, *J Phys Chem Lett*, 2020, **11**, 3305–3312.
151 L. G. Franca, A. Danos and A. Monkman, Donor, Acceptor, and Molecular Charge Transfer Emission All in One Molecule, *Journal of Physical Chemistry Letters*, 2023, **14**, 2764–2771.
152 L. G. Franca, A. Danos, R. Saxena, S. Kuila, K. Stavrou, C. Li, S. Wedler, A. Köhler and A. P. Monkman, Exploring the Early Time Behavior of the Excited States of an Archetype Thermally Activated Delayed Fluorescence Molecule, *Journal of Physical Chemistry Letters*, 2024, **15**, 1734–1740.
153 M. K. Etherington, J. Gibson, H. F. Higginbotham, T. J. Penfold and A. P. Monkman, Revealing the spin–vibronic coupling mechanism of thermally activated delayed fluorescence, *Nat Commun*, 2016, **7**, 13680.
154 L. S. Cui, A. J. Gillett, S. F. Zhang, H. Ye, Y. Liu, X. K. Chen, Z. Sen Lin, E. W. Evans, W. K. Myers, T. K. Ronson, H. Nakanotani, S. Reineke, J. L. Bredas, C. Adachi and R. H. Friend, Fast spin-flip enables efficient and stable organic electroluminescence from charge-transfer states, *Nat Photonics*, 2020, **14**, 636–642.
155 D. Sasikumar, A. T. John, J. Sunny and M. Hariharan, Access to the triplet excited states of organic chromophores, *Chem Soc Rev*, 2020, **49**, 6122–6140.
156 A. Mohan, E. Sebastian, M. Gudem and M. Hariharan, Near-Quantitative Triplet State Population via Ultrafast Intersystem Crossing in Perbromoperylenediimide, *Journal of Physical Chemistry B*, 2020, **124**, 6867–6874.

157 D. S. Mcclure, Triplet-singlet transitions in organic molecules. Lifetime measurements of the triplet state, *J Chem Phys*, 1949, **17**, 905–913.
158 M. Kasha, Collisional perturbation of spin-orbital coupling and the mechanism of fluorescence quenching. a visual demonstration of the perturbation, *J Chem Phys*, 1952, **20**, 71–74.
159 F. B. Dias, J. Santos, D. R. Graves, P. Data, R. S. Nobuyasu, M. A. Fox, A. S. Batsanov, T. Palmeira, M. N. Berberan-Santos, M. R. Bryce and A. P. Monkman, The Role of Local Triplet Excited States and D-A Relative Orientation in Thermally Activated Delayed Fluorescence: Photophysics and Devices, *Advanced Science*, 2016, **3**, 1600080.
160 J. Gibson, A. P. Monkman and T. J. Penfold, The Importance of Vibronic Coupling for Efficient Reverse Intersystem Crossing in Thermally Activated Delayed Fluorescence Molecules, *ChemPhysChem*, 2016, 2956–2961.
161 P. Data, P. Pander, M. Okazaki, Y. Takeda, S. Minakata and A. P. Monkman, Dibenzo[a,j]phenazine-Cored Donor-Acceptor-Donor Compounds as Green-to-Red/NIR Thermally Activated Delayed Fluorescence Organic Light Emitters, *Angewandte Chemie - International Edition*, 2016, **55**, 5739–5744.
162 F. B. Dias, K. N. Bourdakos, V. Jankus, K. C. Moss, K. T. Kamtekar, V. Bhalla, J. Santos, M. R. Bryce and A. P. Monkman, Triplet harvesting with 100% efficiency by way of thermally activated delayed fluorescence in charge transfer OLED emitters, *Advanced Materials*, 2013, **25**, 3707–3714.
163 P. L. Santos, J. S. Ward, P. Data, A. S. Batsanov, M. R. Bryce, F. B. Dias and A. P. Monkman, Engineering the singlet-triplet energy splitting in a TADF molecule, *J Mater Chem C Mater*, 2016, **4**, 3815–3824.
164 P. L. Dos Santos, J. S. Ward, M. R. Bryce and A. P. Monkman, Using Guest-Host Interactions to Optimize the Efficiency of TADF OLEDs, *Journal of Physical Chemistry Letters*, 2016, **7**, 3341–3346.
165 M. K. Etherington, F. Franchello, J. Gibson, T. Northey, J. Santos, J. S. Ward, H. F. Higginbotham, P. Data, A. Kurowska, P. L. Dos Santos, D. R. Graves, A. S. Batsanov, F. B. Dias, M. R. Bryce, T. J. Penfold and A. P. Monkman, Regio- and conformational isomerization critical to design of efficient thermally-activated delayed fluorescence emitters, *Nat Commun*, 2017, **8**, 14987.
166 P. L. dos Santos, J. S. Ward, A. S. Batsanov, M. R. Bryce and A. P. Monkman, Optical and Polarity Control of Donor–Acceptor Conformation and Their Charge-Transfer States in Thermally Activated Delayed-Fluorescence Molecules, *The Journal of Physical Chemistry C*, 2017, **121**, 16462–16469.
167 T. J. Penfold, E. Gindensperger, C. Daniel and C. M. Marian, Spin-Vibronic Mechanism for Intersystem Crossing, *Chem Rev*, 2018, **118**, 6975–7025.
168 P. L. Dos Santos, M. K. Etherington and A. P. Monkman, Chemical and conformational control of the energy gaps involved in the thermally activated delayed fluorescence mechanism, *J Mater Chem C Mater*, 2018, **6**, 4842–4853.
169 K. Shizu, H. Tanaka, M. Uejima, T. Sato, K. Tanaka, H. Kaji and C. Adachi, Strategy for designing electron donors for thermally activated delayed fluorescence emitters, *Journal of Physical Chemistry C*, 2015, **119**, 1291–1297.
170 R. S. Nobuyasu, Z. Ren, G. C. Griffiths, A. S. Batsanov, P. Data, S. Yan, A. P. Monkman, M. R. Bryce and F. B. Dias, Rational Design of TADF Polymers Using a Donor-Acceptor Monomer with Enhanced TADF Efficiency Induced by the Energy Alignment of Charge Transfer and Local Triplet Excited States, *Adv Opt Mater*, 2016, **4**, 597–607.
171 W. Li, D. Liu, F. Shen, D. Ma, Z. Wang, T. Feng, Y. Xu, B. Yang and Y. Ma, A twisting donor-acceptor molecule with an intercrossed excited state for highly efficient, deep-blue electroluminescence, *Adv Funct Mater*, 2012, **22**, 2797–2803.

172 X. Zhang, W. Shen, D. Zhang, Y. Zheng, R. He and M. Li, Theoretical investigation of dihydroacridine and diphenylsulphone derivatives as thermally activated delayed fluorescence emitters for organic light-emitting diodes, *RSC Adv*, 2015, **5**, 51586–51591.

173 F. B. Dias, T. J. Penfold and A. P. Monkman, Photophysics of thermally activated delayed fluorescence molecules, *Methods Appl Fluoresc*, 2017, **5**, 012001.

174 B. T. Lim, S. Okajima, A. K. Chandra and E. C. Lim, Radiationless transitions in electron donor-acceptor complexes: selection rules for S1 → T intersystem crossing and efficiency of S1 → S0 internal conversion, *Chem Phys Lett*, 1981, **79**, 22–27.

175 M. Wang, T. Chatterjee, C. J. Foster, T. Wu, C. L. Yi, H. Yu, K. T. Wong and B. Hu, Exploring mechanisms for generating spin-orbital coupling through donor-acceptor design to realize spin flipping in thermally activated delayed fluorescence, *J Mater Chem C Mater*, 2020, **8**, 3395–3401.

176 C. Reichardt and T. Welton, *Solvents and Solvent Effects in Organic Chemistry*, Wiley, 4th edn., 2010.

177 A. V. Kulinich, E. K. Mikitenko and A. A. Ishchenko, Scope of negative solvatochromism and solvatofluorochromism of merocyanines, *Physical Chemistry Chemical Physics*, 2016, **18**, 3444–3453.

178 Michael Evans, Georgia Tech Lecture Series: Molecular Photochemistry (CHEM 4801): 4.4 Förster Resonance Energy Transfer, https://www.youtube.com/watch?v=UBvnNhwtQH8, (accessed 8 June 2024).

179 Michael Evans, Georgia Tech Lecture Series: Molecular Photochemistry (CHEM 4801): 4.3 Dexter (Exchange) Energy Transfer and Trivial Energy Transfer, https://www.youtube.com/watch?v=Jqv1lYCGsgk, (accessed 8 June 2024).

180 M. C. Gather, A. Köhnen and K. Meerholz, White organic light-emitting diodes, *Advanced Materials*, 2011, **23**, 233–248.

181 C. Gartner, C. Karnutsch and U. Lemmer, in *2007 European Conference on Lasers and Electro-Optics and the International Quantum Electronics Conference*, IEEE, 2007, vol. 101, p. 1.

182 M. Koschorreck, R. Gehlhaar, V. G. Lyssenko, M. Swoboda, M. Hoffmann and K. Leo, Dynamics of a high-Q vertical-cavity organic laser, *Appl Phys Lett*, 2005, **87**, 181108.

183 C. Murawski, K. Leo and M. C. Gather, Efficiency roll-off in organic light-emitting diodes, *Advanced Materials*, 2013, **25**, 6801–6827.

184 K. Masui, H. Nakanotani and C. Adachi, Analysis of exciton annihilation in high-efficiency sky-blue organic light-emitting diodes with thermally activated delayed fluorescence, *Org Electron*, 2013, **14**, 2721–2726.

185 D. Kasemann, R. Brückner, H. Fröb and K. Leo, Organic light-emitting diodes under high currents explored by transient electroluminescence on the nanosecond scale, *Phys Rev B*, 2011, **84**, 115208.

186 S. D. Babenko, V. A. Benderskii, V. I. Gol'danskii, A. G. Lavrushko and V. P. Tychinskii, Annihilation of singlet excited states in anthracene solutions, *Chem Phys Lett*, 1971, **8**, 598–600.

187 J. Eng, J. Hagon and T. J. Penfold, D–A $_3$ TADF emitters: the role of the density of states for achieving faster triplet harvesting rates, *J Mater Chem C Mater*, 2019, **7**, 12942–12952.

188 C. S. Oh, D. de S. Pereira, S. H. Han, H.-J. Park, H. F. Higginbotham, A. P. Monkman and J. Y. Lee, Dihedral Angle Control of Blue Thermally Activated Delayed Fluorescent Emitters through Donor Substitution Position for Efficient Reverse Intersystem Crossing, *ACS Appl Mater Interfaces*, 2018, **10**, 35420–35429.

189 Y. Kawamura, J. Brooks, J. J. Brown, H. Sasabe and C. Adachi, Intermolecular interaction and a concentration-Quenching mechanism of phosphorescent Ir(III) complexes in a solid film, *Phys Rev Lett*, 2006, **96**, 11–14.
190 E. B. Namdas, A. Ruseckas, I. D. W. Samuel, S. C. Lo and P. L. Burn, Photophysics of fac-tris(2-phenylpyridine) iridium(III) cored electroluminescent dendrimers in solution and films, *Journal of Physical Chemistry B*, 2004, **108**, 1570–1577.
191 E. B. Namdas, A. Ruseckas, I. D. W. Samuel, S.-C. Lo and P. L. Burn, Triplet exciton diffusion in *fac* -tris(2-phenylpyridine) iridium(III)-cored electroluminescent dendrimers, *Appl Phys Lett*, 2005, **86**, 091104.
192 L. Han, D. Yang, W. Li, B. Chu, Y. Chen, Z. Su, D. Zhang, F. Yan, Z. Hu and Z. Zhang, The reduced triplet-triplet annihilation of electrophosphorescent device doped by an iridium complex with active hydrogen, *Appl Phys Lett*, 2008, **93**, 153303.
193 M. A. Baldo, C. Adachi and S. R. Forrest, Transient analysis of organic electrophosphorescence. II. Transient analysis of triplet-triplet annihilation, *Phys Rev B*, 2000, **62**, 10967–10977.
194 W. Ji, L. Zhang and W. Xie, Improving efficiency roll-off in phosphorescent OLEDs by modifying the exciton lifetime, *Opt Lett*, 2012, **37**, 2019–2021.
195 S. H. Kim, J. Jang, K. S. Yook and J. Y. Lee, Stable efficiency roll-off in phosphorescent organic light-emitting diodes, *Appl Phys Lett*, 2008, **92**, 023513.
196 B. D. Chin, Enhancement of efficiency and stability of phosphorescent OLEDs based on heterostructured light-emitting layers, *J Phys D Appl Phys*, 2011, **44**, 115103.
197 N. C. Erickson and R. J. Holmes, Relating charge transport and performance in single-layer graded-composition organic light-emitting devices, *J Appl Phys*, 2011, **110**, 084515.
198 X.-K. Liu, C.-J. Zheng, J. Xiao, J. Ye, C.-L. Liu, S.-D. Wang, W.-M. Zhao and X.-H. Zhang, Novel bipolar host materials based on 1,3,5-triazine derivatives for highly efficient phosphorescent OLEDs with extremely low efficiency roll-off, *Physical Chemistry Chemical Physics*, 2012, **14**, 14255–14261.
199 Y. Zhang, M. Whited, M. E. Thompson and S. R. Forrest, Singlet-triplet quenching in high intensity fluorescent organic light emitting diodes, *Chem Phys Lett*, 2010, **495**, 161–165.
200 Y. Zhang, M. Slootsky and S. R. Forrest, Enhanced efficiency in high-brightness fluorescent organic light emitting diodes through triplet management, *Appl Phys Lett*, 2011, **99**, 4–7.
201 N. B. Kotadiya, P. W. M. Blom and G. J. A. H. Wetzelaer, Efficient and stable single-layer organic light-emitting diodes based on thermally activated delayed fluorescence, *Nat Photonics*, 2019, **13**, 765–769.
202 X. Tang, R. Pan, H. Zhu, X. Zhao, L. Tu and Z. Xiong, The origin of interlayer-induced significant enhancement of EQE in CzDBA-based OLEDs studied by magneto-electroluminescence, *Appl Phys Lett*, 2021, **118**, 013503.
203 R. S. Nobuyasu, J. S. Ward, J. Gibson, B. A. Laidlaw, Z. Ren, P. Data, A. S. Batsanov, T. J. Penfold, M. R. Bryce and F. B. Dias, The influence of molecular geometry on the efficiency of thermally activated delayed fluorescence, *J Mater Chem C Mater*, 2019, **7**, 6672–6684.
204 H. Li, J. Li, D. Liu, T. Huang and D. Li, Effects of Electron Affinity and Steric Hindrance of the Trifluoromethyl Group on the π-Bridge in Designing Blue Thermally Activated Delayed Fluorescence Emitters, *Chemistry – A European Journal*, 2020, **26**, 6899–6909.

205 T. Nakagawa, S. Y. Ku, K. T. Wong and C. Adachi, Electroluminescence based on thermally activated delayed fluorescence generated by a spirobifluorene donor–acceptor structure, *Chemical Communications*, 2012, **48**, 9580–9582.
206 T. T. Bui, F. Goubard, M. Ibrahim-Ouali, D. Gigmes and F. Dumur, Recent advances on organic blue thermally activated delayed fluorescence (TADF) emitters for organic light-emitting diodes (OLEDs), *Beilstein Journal of Organic Chemistry*, 2018, **14**, 282–308.
207 Y. Xiang, Z. L. Zhu, D. Xie, S. Gong, K. Wu, G. Xie, C. S. Lee and C. Yang, Revealing the new potential of an indandione unit for constructing efficient yellow thermally activated delayed fluorescence emitters with short emissive lifetimes, *J Mater Chem C Mater*, 2018, **6**, 7111–7118.
208 W. Wei, Z. Yang, X. Chen, T. Liu, Z. Mao, J. Zhao and Z. Chi, Modulation of π-linkers in asymmetric thermally activated delayed fluorescence molecules enabling high performance OLEDs, *J Mater Chem C Mater*, 2020, **8**, 3663–3668.
209 H. Li, J. Li, D. Liu, T. Huang and D. Li, Effects of Electron Affinity and Steric Hindrance of the Trifluoromethyl Group on the π-Bridge in Designing Blue Thermally Activated Delayed Fluorescence Emitters, *Chemistry - A European Journal*, 2020, **26**, 6899–6909.
210 J. Clayden, N. Greeves and S. Warren, *Organic Chemistry*, Oxford University Press, Oxford, 2nd edn., 2012.
211 F. A. Carey and R. J. Sundberg, *Advanced Organic Chemistry Part A: Structure and Mechanisms*, Springer, 5th edn., 2007.
212 L. S. Cui, Y. M. Xie, Y. K. Wang, C. Zhong, Y. L. Deng, X. Y. Liu, Z. Q. Jiang and L. S. Liao, Pure Hydrocarbon Hosts for ≈100% Exciton Harvesting in Both Phosphorescent and Fluorescent Light-Emitting Devices, *Advanced Materials*, 2015, **27**, 4213–4217.
213 M. Stanoppi and A. Lorbach, Boron-based donor-spiro-acceptor compounds exhibiting thermally activated delayed fluorescence (TADF), *Dalton Transactions*, 2018, **47**, 10394–10398.
214 Y. J. Shiu, Y. C. Cheng, W. L. Tsai, C. C. Wu, C. T. Chao, C. W. Lu, Y. Chi, Y. T. Chen, S. H. Liu and P. T. Chou, Pyridyl Pyrrolide Boron Complexes: The Facile Generation of Thermally Activated Delayed Fluorescence and Preparation of Organic Light-Emitting Diodes, *Angewandte Chemie - International Edition*, 2016, **55**, 3017–3021.
215 Y. J. Shiu, Y. T. Chen, W. K. Lee, C. C. Wu, T. C. Lin, S. H. Liu, P. T. Chou, C. W. Lu, I. C. Cheng, Y. J. Lien and Y. Chi, Efficient thermally activated delayed fluorescence of functional phenylpyridinato boron complexes and high performance organic light-emitting diodes, *J Mater Chem C Mater*, 2017, **5**, 1452–1462.
216 P. Ganesan, D.-G. Chen, J.-L. Liao, W.-C. Li, Y.-N. Lai, D. Luo, C.-H. Chang, C.-L. Ko, W.-Y. Hung, S.-W. Liu, G.-H. Lee, P.-T. Chou and Y. Chi, Isomeric spiro-[acridine-9,9′-fluorene]-2,6-dipyridylpyrimidine based TADF emitters: insights into photophysical behaviors and OLED performances, *J Mater Chem C Mater*, 2018, **6**, 10088–10100.
217 W.-C. Chen, C.-S. Lee and Q.-X. Tong, Blue-emitting organic electrofluorescence materials: progress and prospective, *J Mater Chem C Mater*, 2015, **3**, 10957–10963.
218 Z. He, W. Zhao, J. W. Y. Lam, Q. Peng, H. Ma, G. Liang, Z. Shuai and B. Z. Tang, White light emission from a single organic molecule with dual phosphorescence at room temperature, *Nat Commun*, 2017, **8**, 416.
219 T. Miwa, S. Kubo, K. Shizu, T. Komino, C. Adachi and H. Kaji, Blue organic light-emitting diodes realizing external quantum efficiency over 25% using thermally activated delayed fluorescence emitters, *Sci Rep*, 2017, **7**, 284.

220 P. Ganesan, D. G. Chen, W. C. Chen, P. Gnanasekaran, J. A. Lin, C. Y. Huang, M. C. Chen, C. S. Lee, P. T. Chou and Y. Chi, Methoxy substituents activated carbazole-based boron dimesityl TADF emitters, *J Mater Chem C*, 2020, **8**, 4780–4788.

221 Y. Im, M. Kim, Y. J. Cho, J. A. Seo, K. S. Yook and J. Y. Lee, Molecular Design Strategy of Organic Thermally Activated Delayed Fluorescence Emitters, *Chemistry of Materials*, 2017, **29**, 1946–1963.

222 K. Suzuki, S. Kubo, K. Shizu, T. Fukushima, A. Wakamiya, Y. Murata, C. Adachi and H. Kaji, Triarylboron-Based Fluorescent Organic Light-Emitting Diodes with External Quantum Efficiencies Exceeding 20 %, *Angewandte Chemie - International Edition*, 2015, **54**, 15231–15235.

223 R. S. of Chemistry, Royal Society of Chemistry Periodic Table Website, https://www.rsc.org/periodic-table/element/5/boron, (accessed 25 June 2021).

224 M. Yamashita, Y. Yamamoto, K. Y. Akiba, D. Hashizume, F. Iwasaki, N. Takagi and S. Nagase, Syntheses and structures of hypervalent pentacoordinate carbon and boron compounds bearing an anthracene skeleton - Elucidation of hypervalent interaction based on X-ray analysis and DFT calculation, *J Am Chem Soc*, 2005, **127**, 4354–4371.

225 S. S. Kothavale and J. Y. Lee, Three- and Four-Coordinate, Boron-Based, Thermally Activated Delayed Fluorescent Emitters, *Adv Opt Mater*, 2020, **8**, 2000922.

226 A. Kumar, W. Lee, T. Lee, J. Jung, S. Yoo and M. H. Lee, Triarylboron-based TADF emitters with perfluoro substituents: High-efficiency OLEDs with a power efficiency over 100 lm W-1, *J Mater Chem C Mater*, 2020, **8**, 4253–4263.

227 A. Kumar, H. Y. Shin, T. Lee, J. Jung, B. J. Jung and M. H. Lee, Doubly Boron-Doped TADF Emitters Decorated with ortho-Donor Groups for Highly Efficient Green to Red OLEDs, *Chemistry - A European Journal*, 2020, **26**, 16793–16801.

228 H. Lee, D. Karthik, R. Lampande, J. H. Ryu and J. H. Kwon, Recent Advancement in Boron-Based Efficient and Pure Blue Thermally Activated Delayed Fluorescence Materials for Organic Light-Emitting Diodes, *Front Chem*, 2020, **8**, 373.

229 X. Liang, Z. L. Tu and Y. X. Zheng, Thermally Activated Delayed Fluorescence Materials: Towards Realization of High Efficiency through Strategic Small Molecular Design, *Chemistry - A European Journal*, 2019, **25**, 5623–5642.

230 Y. Kondo, K. Yoshiura, S. Kitera, H. Nishi, S. Oda, H. Gotoh, Y. Sasada, M. Yanai and T. Hatakeyama, Narrowband deep-blue organic light-emitting diode featuring an organoboron-based emitter, *Nat Photonics*, 2019, **13**, 678–682.

231 A. Escande and M. J. Ingleson, Fused polycyclic aromatics incorporating boron in the core: Fundamentals and applications, *Chemical Communications*, 2015, **51**, 6257–6274.

232 C. Dou, S. Saito and S. Yamaguchi, A pentacoordinate boron-containing π-electron system with Cl-B-Cl three-center four-electron bonds, *J Am Chem Soc*, 2013, **135**, 9346–9349.

233 C. Dou, S. Saito, K. Matsuo, I. Hisaki and S. Yamaguchi, A Boron-Containing PAH as a Substructure of Boron-Doped Graphene, *Angewandte Chemie International Edition*, 2012, **51**, 12206–12210.

234 Z. Zhou, A. Wakamiya, T. Kushida and S. Yamaguchi, Planarized triarylboranes: Stabilization by structural constraint and their plane-to-bowl conversion, *J Am Chem Soc*, 2012, **134**, 4529–4532.

235 D. H. Ahn, S. W. Kim, H. Lee, I. J. Ko, D. Karthik, J. Y. Lee and J. H. Kwon, Highly efficient blue thermally activated delayed fluorescence emitters based on symmetrical and rigid oxygen-bridged boron acceptors, *Nat Photonics*, 2019, **13**, 540–546.

236 B. Wex and B. R. Kaafarani, Perspective on carbazole-based organic compounds as emitters and hosts in TADF applications, *J Mater Chem C Mater*, 2017, **5**, 8622–8653.

237 H. Liu, J. Li, G. Li, B. Zhang, Q. Zhan, Z. Liu, C. Zhou, K. Li, Z. Wang and C. Yang, A simple strategy to achieve efficient thermally activated delayed fluorescent emitters via enhancing electron donating ability of donors, *Dyes and Pigments*, 2020, **180**, 108521–108527.

238 T. L. Wu, M. J. Huang, C. C. Lin, P. Y. Huang, T. Y. Chou, R. W. Chen-Cheng, H. W. Lin, R. S. Liu and C. H. Cheng, Diboron compound-based organic light-emitting diodes with high efficiency and reduced efficiency roll-off, *Nat Photonics*, 2018, **12**, 235–240.

239 M. H. Tsai, H. W. Lin, H. C. Su, T. H. Ke, C. C. Wu, F. C. Fang, Y. L. Liao, K. T. Wong and C. I. Wu, Highly efficient organic blue electrophosphorescent devices based on 3,6-Bis(triphenylsilyl)carbazole as the host material, *Advanced Materials*, 2006, **18**, 1216–1220.

240 X. Sallenave, A. Bucinskas, S. Salman, D. Volyniuk, O. Bezvikonnyi, V. Mimaite, J. V. Grazulevicius and G. Sini, Sensitivity of Redox and Optical Properties of Electroactive Carbazole Derivatives to the Molecular Architecture and Methoxy Substitutions, *The Journal of Physical Chemistry C*, 2018, **122**, 10138–10152.

241 M. Okazaki, Y. Takeda, P. Data, P. Pander, H. Higginbotham, A. P. Monkman and S. Minakata, Thermally activated delayed fluorescent phenothiazine-dibenzo[a,j]phenazine-phenothiazine triads exhibiting tricolor-changing mechanochromic luminescence, *Chem Sci*, 2017, **8**, 2677–2686.

242 P. Data, M. Okazaki, S. Minakata and Y. Takeda, Thermally activated delayed fluorescence: Vs. room temperature phosphorescence by conformation control of organic single molecules, *J Mater Chem C Mater*, 2019, **7**, 6616–6621.

243 G. Conboy, H. J. Spencer, E. Angioni, A. L. Kanibolotsky, N. J. Findlay, S. J. Coles, C. Wilson, M. B. Pitak, C. Risko, V. Coropceanu, J. L. Brédas and P. J. Skabara, To bend or not to bend-are heteroatom interactions within conjugated molecules effective in dictating conformation and planarity?, *Mater Horiz*, 2016, **3**, 333–339.

244 T. Kharandiuk, E. J. Hussien, J. Cameron, R. Petrina, N. J. Findlay, R. Naumov, W. T. Klooster, S. J. Coles, Q. Ai, S. Goodlett, C. Risko and P. J. Skabara, Noncovalent Close Contacts in Fluorinated Thiophene-Phenylene-Thiophene Conjugated Units: Understanding the Nature and Dominance of O···H versus S···F and O···F Interactions with Respect to the Control of Polymer Conformation, *Chemistry of Materials*, 2019, **31**, 7070–7079.

245 X. K. Chen, B. W. Bakr, M. Auffray, Y. Tsuchiya, C. D. Sherrill, C. Adachi and J. L. Bredas, Intramolecular Noncovalent Interactions Facilitate Thermally Activated Delayed Fluorescence (TADF), *Journal of Physical Chemistry Letters*, 2019, **10**, 3260–3268.

246 J. R. Cha, C. W. Lee, J. Y. Lee and M. S. Gong, Design of ortho-linkage carbazole-triazine structure for high-efficiency blue thermally activated delayed fluorescent emitters, *Dyes and Pigments*, 2016, **134**, 562–568.

247 C. Peng, S. Yang, H. Li, G. Xie, L. Cui, S. Zou, C. Poriel, Z. Jiang and L. Liao, Highly Efficient Thermally Activated Delayed Fluorescence via an Unconjugated Donor–Acceptor System Realizing EQE of Over 30%, *Advanced Materials*, 2020, **32**, 2003885.

248 Z. Yang, Z. Mao, C. Xu, X. Chen, J. Zhao, Z. Yang, Y. Zhang, W. Wu, S. Jiao, Y. Liu, M. P. Aldred and Z. Chi, A sterically hindered asymmetric D-A-D′ thermally activated delayed fluorescence emitter for highly efficient non-doped organic light-emitting diodes, *Chem Sci*, 2019, **10**, 8129–8134.

249 C. S. Oh, S. H. Han and J. Y. Lee, Molecular design of thermally activated delayed fluorescent emitters for blue-shifted emission by methoxy substitution, *J Mater Chem C Mater*, 2017, **5**, 9106–9114.

250 R. Ansari, W. Shao, S.-J. Yoon, J. Kim and J. Kieffer, Charge Transfer as the Key Parameter Affecting the Color Purity of Thermally Activated Delayed Fluorescence Emitters, *ACS Appl Mater Interfaces*, 2021, **13**, 28529–28537.

251 D.-Y. Chen, W. Liu, C.-J. Zheng, K. Wang, F. Li, S. Tao, X.-M. Ou and X.-H. Zhang, Isomeric Thermally Activated Delayed Fluorescence Emitters for Color Purity-Improved Emission in Organic Light-Emitting Devices, *ACS Appl Mater Interfaces*, 2016, **8**, 16791–16798.

252 P. Rajamalli, N. Senthilkumar, P.-Y. Huang, C.-C. Ren-Wu, H.-W. Lin and C.-H. Cheng, New Molecular Design Concurrently Providing Superior Pure Blue, Thermally Activated Delayed Fluorescence and Optical Out-Coupling Efficiencies, *J Am Chem Soc*, 2017, **139**, 10948–10951.

253 J. Luo, Z. Xie, Z. Xie, J. W. Y. Lam, L. Cheng, H. Chen, C. Qiu, H. S. Kwok, X. Zhan, Y. Liu, D. Zhu and B. Z. Tang, Aggregation-induced emission of 1-methyl-1,2,3,4,5-pentaphenylsilole, *Chemical Communications*, 2001, **18**, 1740–1741.

254 S. W. Thomas, G. D. Joly and T. M. Swager, Chemical Sensors Based on Amplifying Fluorescent Conjugated Polymers, *Chem Rev*, 2007, **107**, 1339–1386.

255 Z. Wang, Z. Wang, P. Lu and Y. Wang, Preparation and Photoluminescent Properties of Three 5-Amino Benzothiadiazoles (5-amBTDs), *Chem Asian J*, 2020, **15**, 3519–3526.

256 Y. Ren, J. W. Y. Lam, Y. Dong, B. Z. Tang and K. S. Wong, Enhanced emission efficiency and excited state lifetime due to restricted intramolecular motion in silole aggregates, *Journal of Physical Chemistry B*, 2005, **109**, 1135–1140.

257 Y. F. Shen, M. Li, W. L. Zhao, Y. F. Wang, H. Y. Lu and C. F. Chen, Quinoline-based TADF emitters exhibiting aggregation-induced emission for efficient non-doped organic light-emitting diodes, *Mater Chem Front*, 2021, **5**, 834–842.

258 Q. Wei, J. Zhang and Z. Ge, *Handbook of Aggregation-Induced Emission*, Wiley, 2022, vol. 3.

259 P. Ganesan, D.-G. Chen, W.-C. Chen, P. Gnanasekaran, J.-A. Lin, C.-Y. Huang, M.-C. Chen, C.-S. Lee, P.-T. Chou and Y. Chi, Methoxy substituents activated carbazole-based boron dimesityl TADF emitters, *J Mater Chem C*, 2020, **8**, 4780–4788.

260 Y. H. Lee, S. Park, J. Oh, S. Woo, A. Kumar, J. Kim, J. Jung, S. Yoo and M. H. Lee, High-Efficiency Sky Blue to Ultradeep Blue Thermally Activated Delayed Fluorescent Diodes Based on *Ortho* -Carbazole-Appended Triarylboron Emitters: Above 32% External Quantum Efficiency in Blue Devices, *Adv Opt Mater*, 2018, **6**, 1800385.

261 Q. Wei, P. Imbrasas, E. Caldera-Cruz, L. Cao, N. Fei, H. Thomas, R. Scholz, S. Lenk, B. Voit, S. Reineke and Z. Ge, Conjugation-induced thermally activated delayed fluorescence: Photophysics of a carbazole-benzophenone monomer-to-tetramer molecular series, *Journal of Physical Chemistry A*, 2021, **125**, 1345–1354.

262 T. Taniguchi, J. Wang, S. Irle and S. Yamaguchi, TICT fluorescence of N-borylated 2,5-diarylpyrroles: A gear like dual motion in the excited state, *Dalton Transactions*, 2013, **42**, 620–624.

263 P. Zimmermann Crocomo, T. Kaihara, S. Kawaguchi., P. Stachelek, S. Minakata, P. de Silva, P. Data and Y. Takeda, The Impact of C $_2$ Insertion into a Carbazole Donor on the Physicochemical Properties of Dibenzo[*a,j*]phenazine-Cored Donor–Acceptor–Donor Triads, *Chemistry – A European Journal*, 2021, **27**, 13390–13398.

264 D. Hamdane, C. Bou-Nader, D. Cornu, G. Hui-Bon-Hoa and M. Fontecave, Flavin-Protein Complexes: Aromatic Stacking Assisted by a Hydrogen Bond, *Biochemistry*, 2015, **54**, 4354–4364.

265 E. R. Johnson, S. Keinan, P. Mori-Sánchez, J. Contreras-García, A. J. Cohen and W. Yang, Revealing noncovalent interactions, *J Am Chem Soc*, 2010, **132**, 6498–6506.

266 T. Chen, M. Li and J. Liu, π-π Stacking Interaction: A Nondestructive and Facile Means in Material Engineering for Bioapplications, *Cryst Growth Des*, 2018, **18**, 2765–2783.

267 X. Zhang, G. P. Lu, Z. B. Xu and C. Cai, Facile Synthesis of Indolizines via 1,3-Dipolar Cycloadditions in [Omim]Br: The Promotion of the Reaction through Noncovalent Interactions, *ACS Sustain Chem Eng*, 2017, **5**, 9279–9285.

268 A. Zheng, J. Wang, N. Xu, R. Zhu, Y. Yuan, J. Zhang, J. Zhang, Z. Li and P. Wang, Control of π-π Stacking of Dithienopyrrole-Based, Hole-Transporting Materials via Lateral Substituents for High-Efficiency Perovskite Solar Cells, *ACS Photonics*, 2018, **5**, 4694–4701.

269 D. Tu, J. Li, F. Sun, H. Yan, J. Poater and M. Solà, Cage-···Cage-Interaction: Boron Cluster-Based Noncovalent Bond and Its Applications in Solid-State Materials, *JACS Au*, 2021, **1**, 2047–2057.

270 D. Tu, H. Yan, J. Poater and M. Solà, The nido-Cage···π Bond: A Non-covalent Interaction between Boron Clusters and Aromatic Rings and Its Applications, *Angewandte Chemie - International Edition*, 2020, **59**, 9018–9025.

271 R. Báez-Grez and R. Pino-Rios, On the Importance of Noncovalent Interactions in the Stabilization of Nonconventional Compounds Using Bulky Groups, *ACS Omega*, 2023, **8**, 23168–23173.

272 H. Huang, L. Yang, A. Facchetti and T. J. Marks, Organic and Polymeric Semiconductors Enhanced by Noncovalent Conformational Locks, *Chem Rev*, 2017, **117**, 10291–10318.

273 Yale Chemistry, Yale University Department of Chemistry Organic Chemistry Study Aids, https://ursula.chem.yale.edu/~chem220/chem220js/STUDYAIDS/vanderwaalsradius.html, (accessed 20 July 2024).

274 G. Mierzwa, A. J. Gordon and S. Berski, The nature of multiple boron-nitrogen bonds studied using electron localization function (ELF), electron density (AIM), and natural bond orbital (NBO) methods, *J Mol Model*, 2020, **26**, 136–159.

275 S. Berski, Z. Latajka and A. J. Gordon, On the multiple B-N bonding in boron compounds using the topological analysis of electron localization function (ELF), *New Journal of Chemistry*, 2011, **35**, 89–96.

276 C. Arivazhagan, A. Maity, K. Bakthavachalam, A. Jana, S. K. Panigrahi, E. Suresh, A. Das and S. Ghosh, Phenothiazinyl Boranes: A New Class of AIE Luminogens with Mega Stokes Shift, Mechanochromism, and Mechanoluminescence, *Chemistry - A European Journal*, 2017, **23**, 7046–7051.

277 H. Yersin, *Highly Efficient OLEDs*, Wiley, Weinheim, Germany, 2018.

278 J. Sworakowski, How accurate are energies of HOMO and LUMO levels in small-molecule organic semiconductors determined from cyclic voltammetry or optical spectrosco, *Synth Met*, 2018, **235**, 125–130.

279 R. Stenutz, Stetnutz Chemistry Tables, http://www.stenutz.eu/chem/solv23.php, (accessed 18 July 2024).

280 F. Würthner, Aggregation-Induced Emission (AIE): A Historical Perspective, *Wiley-VCH Verlag*, 2020, preprint, DOI: 10.1002/anie.202007525.

281 E. E. Jelley, Spectral Absorption and Fluorescence of Dyes in the Molecular State, *Nature*, 1936, **138**, 1009–1010.

282 J. Shu, T. Ni, X. Liu, B. Xu, L. Liu, W. Chu, K. Zhang and W. Jiang, Mechanochromism, thermochromism, protonation effect and discrimination of CHCl3 from organic solvents in a Et2N-substituted Salicylaldehyde Schiff base, *Dyes and Pigments*, 2021, **195**, 109708.
283 J. Mei, Y. Hong, J. W. Y. Lam, A. Qin, Y. Tang and B. Z. Tang, Aggregation-Induced Emission: The Whole Is More Brilliant than the Parts, *Advanced Materials*, 2014, **26**, 5429–5479.
284 J. Mei, N. L. C. Leung, R. T. K. Kwok, J. W. Y. Lam and B. Z. Tang, Aggregation-Induced Emission: Together We Shine, United We Soar!, *Chem Rev*, 2015, **115**, 11718–11940.
285 K. K. Neena, P. Sudhakar, K. Dipak and P. Thilagar, Diarylboryl-phenothiazine based multifunctional molecular siblings, *Chemical Communications*, 2017, **53**, 3641–3644.
286 Y.-J. Lien, T.-C. Lin, C.-C. Yang, Y.-C. Chiang, C.-H. Chang, S.-H. Liu, Y.-T. Chen, G.-H. Lee, P.-T. Chou, C.-W. Lu and Y. Chi, First N-Borylated Emitters Displaying Highly Efficient Thermally Activated Delayed Fluorescence and High-Performance OLEDs, *ACS Appl Mater Interfaces*, 2017, **9**, 27090–27101.
287 C. C. Tsai, W. C. Huang, H. Y. Chih, Y. C. Hsh, C. W. Liao, C. H. Lin, Y. X. Kang, C. H. Chang, Y. J. Chang and C. W. Lu, Efficient donor-acceptor-donor borylated compounds with extremely small ΔEST for thermally activated delayed fluorescence OLEDs, *Org Electron*, 2018, **63**, 166–174.
288 Y. Kitamoto, T. Namikawa, D. Ikemizu, Y. Miyata, T. Suzuki, H. Kita, T. Sato and S. Oi, Light blue and green thermally activated delayed fluorescence from 10H-phenoxaborin-derivatives and their application to organic light-emitting diodes, *J Mater Chem C Mater*, 2015, **3**, 9122–9130.
289 Y. Kitamoto, T. Namikawa, T. Suzuki, Y. Miyata, H. Kita, T. Sato and S. Oi, Dimesitylarylborane-based luminescent emitters exhibiting highly-efficient thermally activated delayed fluorescence for organic light-emitting diodes, *Org Electron*, 2016, **34**, 208–217.
290 R. Stahl, C. Lambert, C. Kaiser, R. Wortmann and R. Jakober, Electrochemistry and photophysics of donor-substituted triarylboranes: Symmetry breaking in ground and excited state, *Chemistry - A European Journal*, 2006, **12**, 2358–2370.
291 H. Y. Zhao, X. Y. Yang, H. Lei, M. Xin and S. Q. Zhang, Cu-mediated selective bromination of aniline derivatives and preliminary mechanism study, *Synth Commun*, 2019, **49**, 1406–1415.
292 T. Fujihara, Y. Tomike, T. Ohtake, J. Terao and Y. Tsuji, Ruthenium-catalyzed ring-closing metathesis accelerated by long-range steric effect, *Chemical Communications*, 2011, **47**, 9699–9701.
293 Doug Discovery, Fluorochem - 1-bromo-3,5-dimethoxybenzene, https://dougdiscovery.com/p/F092710, (accessed 30 August 2024).
294 S. Solé and F. P. Gabbaï, A bidentate borane as colorimetric fluoride ion sensor, *Chemical Communications*, 2004, **4**, 1284–1285.
295 M. K. Etherington, Thermally Activated Delayed Fluorescence: Beyond the Single Molecule, *Front Chem*, 2020, **8**, 716.
296 S. Madayanad Suresh, L. Zhang, D. Hall, C. Si, G. Ricci, T. Matulaitis, A. M. Z. Slawin, S. Warriner, Y. Olivier, I. D. W. Samuel and E. Zysman-Colman, A Deep-Blue-Emitting Heteroatom-Doped MR-TADF Nonacene for High-Performance Organic Light-Emitting Diodes**, *Angewandte Chemie International Edition*, 2023, **62**, e202215522.
297 B. Chen, C. Liao, D. Li, H. Liu and S. Wang, Ultra-deep-blue thermally actrivated delayed fluorescence emitters constructed by carbazole derivatives enable efficient

solution-processed OLED with a CIEy of < 0.05, *J Mater Chem C Mater*, 2023, **11**, 8767–8775.

298 D. K. A. Phan Huu, S. Saseendran, R. Dhali, L. G. Franca, K. Stavrou, A. Monkman and A. Painelli, Thermally Activated Delayed Fluorescence: Polarity, Rigidity, and Disorder in Condensed Phases, *J Am Chem Soc*, 2022, **144**, 15211–15222.

299 V. M. Divac, D. Šakić, T. Weitner and M. Gabričević, Solvent effects on the absorption and fluorescence spectra of Zaleplon: Determination of ground and excited state dipole moments, *Spectrochim Acta A Mol Biomol Spectrosc*, 2019, **212**, 356–362.

300 K. Stavrou, L. G. Franca and A. P. Monkman, Photophysics of TADF Guest-Host Systems: Introducing the Idea of Hosting Potential, *ACS Appl Electron Mater*, 2020, **2**, 2868–2881.

301 Y. Takeda, T. Kaihara, M. Okazaki, H. Higginbotham, P. Data, N. Tohnai and S. Minakata, Conformationally-flexible and moderately electron-donating units-installed D-A-D triad enabling multicolor-changing mechanochromic luminescence, TADF and room-temperature phosphorescence, *Chemical Communications*, 2018, **54**, 6847–6850.

302 I. Bhattacharjee, N. Acharya, H. Bhatia and D. Ray, Dual Emission through Thermally Activated Delayed Fluorescence and Room-Temperature Phosphorescence, and Their Thermal Enhancement via Solid-State Structural Change in a Carbazole-Quinoline Conjugate, *Journal of Physical Chemistry Letters*, 2018, **9**, 2733–2738.

303 M. S. Kwon, D. Lee, S. Seo, J. Jung and J. Kim, Tailoring Intermolecular Interactions for Efficient Room-Temperature Phosphorescence from Purely Organic Materials in Amorphous Polymer Matrices, *Angewandte Chemie International Edition*, 2014, **53**, 11177–11181.

304 H. Bhatia and D. Ray, Asymmetric-donor (D2D2′)-acceptor (A) conjugates for simultaneously accessing intrinsic blue-RTP and blue-TADF, *Mater Adv*, 2020, **1**, 1858–1865.

305 C. Avila-Montiel, A. R. Tapia-Benavides, E. Islas-Trejo, A. Ariza, H. Tlahuext and M. Tlahuextl, Non-covalent interactions in organic-inorganic hybrid compounds derived from amino amides, *J Mol Struct*, 2020, **1202**, 127258.

306 C. Janiak, A critical account on n-n stacking in metal complexes with aromatic nitrogen-containing ligands, *Journal of the Chemical Society, Dalton Transactions*, 2000, 3885–3896.

307 Z. Yang, Z. Mao, C. Xu, X. Chen, J. Zhao, Z. Yang, Y. Zhang, W. Wu, S. Jiao, Y. Liu, M. P. Aldred and Z. Chi, A sterically hindered asymmetric D–A–D′ thermally activated delayed fluorescence emitter for highly efficient non-doped organic light-emitting diodes, *Chem Sci*, 2019, **10**, 8129–8134.

308 H. Narita, H. Min, N. Kubo, I. Hattori, T. Yasuda and S. Yamaguchi, Bis- *Ortho* -Donor-Modification of Boracyclic π-Electron Systems beyond Steric Protection to Produce Thermally Activated Delayed Fluorescence Materials, *Angewandte Chemie International Edition*, 2024, **63**, e202405412.

309 T. Nishiuchi, K. Kisaka and T. Kubo, Synthesis of Anthracene-Based Cyclic π-Clusters and Elucidation of their Properties Originating from Congested Aromatic Planes, *Angewandte Chemie - International Edition*, 2021, **60**, 5400–5406.

310 T. Nishiuchi, S. Y. Uno, Y. Hirao and T. Kubo, Intramolecular Interaction, Photoisomerization, and Mechanical C-C Bond Dissociation of 1,2-Di(9-anthryl)benzene and Its Photoisomer: A Fundamental Moiety of Anthracene-Based π-Cluster Molecules, *Journal of Organic Chemistry*, 2016, **81**, 2106–2112.

311 T. Nishiuchi, H. Sotome, K. Shimizu, H. Miyasaka and T. Kubo, 1,2,3-Tri(9-anthryl)benzene: Photophysical Properties and Solid-State Intermolecular

Interactions of Radially Arranged, Congested Aromatic π-Planes**, *Chemistry – A European Journal*, 2022, **28**, e202104245.
312 H. Tsujimoto, D. G. Ha, G. Markopoulos, H. S. Chae, M. A. Baldo and T. M. Swager, Thermally Activated Delayed Fluorescence and Aggregation Induced Emission with Through-Space Charge Transfer, *J Am Chem Soc*, 2017, **139**, 4894–4900.
313 G. B. McGaughey, M. Gagné and A. K. Rappé, π-Stacking Interactions: Alive and Well in Proteins, *Journal of Biological Chemistry*, 1998, **273**, 15458–15463.
314 C. M. Hsieh, T. L. Wu, J. Jayakumar, Y. C. Wang, C. L. Ko, W. Y. Hung, T. C. Lin, H. H. Wu, K. H. Lin, C. H. Lin, S. Hsieh and C. H. Cheng, Diboron-Based Delayed Fluorescent Emitters with Orange-to-Red Emission and Superior Organic Light-Emitting Diode Efficiency, *ACS Appl Mater Interfaces*, 2020, **12**, 23199–23206.
315 Y. Tao, C. Yang and J. Qin, Organic host materials for phosphorescent organic light-emitting diodes, *Chem Soc Rev*, 2011, **40**, 2943–2970.
316 C. Reus, S. Weidlich, M. Bolte, H. W. Lerner and M. Wagner, C-functionalized, air- and water-stable 9,10-dihydro-9,10- diboraanthracenes: Efficient blue to red emitting luminophores, *J Am Chem Soc*, 2013, **135**, 12892–12907.
317 T. Matsumoto, H. Takamine, K. Tanaka and Y. Chujo, Design of bond-cleavage-induced intramolecular charge transfer emission with dibenzoboroles and their application to ratiometric sensors for discriminating chain lengths of alkanes, *Mater Chem Front*, 2017, **1**, 2368–2375.
318 Y. G. Shi, J. W. Wang, H. Li, G. F. Hu, X. Li, S. K. Mellerup, N. Wang, T. Peng and S. Wang, A simple multi-responsive system based on aldehyde functionalized amino-boranes, *Chem Sci*, 2018, **9**, 1902–1911.
319 Q. Hou, L. Liu, S. K. Mellerup, N. Wang, T. Peng, P. Chen and S. Wang, Stimuli-Responsive B/N Lewis Pairs Based on the Modulation of B-N Bond Strength, *Org Lett*, 2018, **20**, 6467–6470.
320 S. K. Mellerup and S. Wang, Boron-based stimuli responsive materials, *Chem Soc Rev*, 2019, **48**, 3537–3549.
321 Y. Wang, K. Liu, P. Chen, X. Yin, T. Peng, J. Iqbal and N. Wang, A multi-responsive system based on intramolecular B ← O=P Lewis acid–base pairs, *J Mater Chem C Mater*, 2022, **10**, 10981–10987.
322 J. Wang, N. Wang, G. Wu, S. Wang and X. Li, Multicolor Emission from Non-conjugated Polymers Based on a Single Switchable Boron Chromophore, *Angewandte Chemie*, 2019, **131**, 3114–3118.
323 S. J. Cassidy, I. Brettell-Adams, L. E. McNamara, M. F. Smith, M. Bautista, H. Cao, M. Vasiliu, D. L. Gerlach, F. Qu, N. I. Hammer, D. A. Dixon and P. A. Rupar, Boranes with Ultra-High Stokes Shift Fluorescence, *Organometallics*, 2018, **37**, 3732–3741.
324 E. Januszewski, A. Lorbach, R. Grewal, M. Bolte, J. W. Bats, H. Lerner and M. Wagner, Unsymmetrically Substituted 9,10-Dihydro-9,10-diboraanthracenes as Versatile Building Blocks for Boron-Doped π-Conjugated Systems, *Chemistry – A European Journal*, 2011, **17**, 12696–12705.
325 S. Bieller, F. Zhang, M. Bolte, J. W. Bats, H. W. Lerner and M. Wagner, Bitopic bis- and tris(1-pyrazolyl)borate ligands: Syntheses and structural characterization, *Organometallics*, 2004, **23**, 2107–2113.
326 S. Kirschner, J. M. Mewes, M. Bolte, H. W. Lerner, A. Dreuw and M. Wagner, How Boron Doping Shapes the Optoelectronic Properties of Canonical and Phenylene-Containing Oligoacenes: A Combined Experimental and Theoretical Investigation, *Chemistry - A European Journal*, 2017, **23**, 5104–5116.
327 Fluorochem, Dougdiscovery page for 1,2-Bis(trimethylsilyl)benzene, https://dougdiscovery.com/p/F733402, (accessed 16 January 2024).

328 Fluorochem, Dougdiscovery page for 1,2-Bis(dimethylsilyl)benzene, https://dougdiscovery.com/p/S01774, (accessed 16 January 2024).
329 G. Méhes, K. Goushi, W. J. Potscavage and C. Adachi, Influence of host matrix on thermally-activated delayed fluorescence: Effects on emission lifetime, photoluminescence quantum yield, and device performance, *Org Electron*, 2014, **15**, 2027–2037.
330 M. Kawashiro, T. Mori, M. Ito, N. Ando and S. Yamaguchi, Photodissociative Modules that Control Dual-Emission Properties in Donor–π–Acceptor Organoborane Fluorophores, *Angewandte Chemie International Edition*, 2023, **62**, e202303725.
331 C. J. Berger, G. He, C. Merten, R. McDonald, M. J. Ferguson and E. Rivard, Synthesis and luminescent properties of lewis base-appended borafluorenes, *Inorg Chem*, 2014, **53**, 1475–1486.
332 A. Wakamiya, K. Mishima, K. Ekawa and S. Yamaguchi, Kinetically stabilized dibenzoborole as an electron-accepting building unit, *Chemical Communications*, 2002, **8**, 579–581.
333 E. Von Grotthuss, S. E. Prey, M. Bolte, H. W. Lerner and M. Wagner, Dual Role of Doubly Reduced Arylboranes as Dihydrogen- and Hydride-Transfer Catalysts, *J Am Chem Soc*, 2019, **141**, 6082–6091.
334 S. Y. Lee, T. Yasuda, Y. S. Yang, Q. Zhang and C. Adachi, Luminous butterflies: Efficient exciton harvesting by benzophenone derivatives for full-color delayed fluorescence OLEDs, *Angewandte Chemie - International Edition*, 2014, **53**, 6402–6406.
335 E. E. Bas, P. Ulukan, A. Monari, V. Aviyente and S. Catak, Photophysical Properties of Benzophenone-Based TADF Emitters in Relation to Their Molecular Structure, *Journal of Physical Chemistry A*, 2022, **126**, 473–484.
336 J. Li, X. Liao, H. Xu, L. Li, J. Zhang, H. Wang and B. Xu, Deep-blue thermally activated delayed fluorescence dendrimers with reduced singlet-triplet energy gap for low roll-off non-doped solution-processed organic light-emitting diodes, *Dyes and Pigments*, 2017, **140**, 79–86.
337 Y. Luo, S. Li, Y. Zhao, C. Li, Z. Pang, Y. Huang, M. Yang, L. Zhou, X. Zheng, X. Pu and Z. Lu, An Ultraviolet Thermally Activated Delayed Fluorescence OLED with Total External Quantum Efficiency over 9%, *Advanced Materials*, 2020, **32**, 2001248.
338 M. Y. Wong, S. Krotkus, G. Copley, W. Li, C. Murawski, D. Hall, G. J. Hedley, M. Jaricot, D. B. Cordes, A. M. Z. Slawin, Y. Olivier, D. Beljonne, L. Muccioli, M. Moral, J.-C. Sancho-Garcia, M. C. Gather, I. D. W. Samuel and E. Zysman-Colman, Deep-Blue Oxadiazole-Containing Thermally Activated Delayed Fluorescence Emitters for Organic Light-Emitting Diodes, *ACS Appl Mater Interfaces*, 2018, **10**, 33360–33372.
339 F. Hundemer, L. Graf von Reventlow, C. Leonhardt, M. Polamo, M. Nieger, S. M. Seifermann, A. Colsmann and S. Bräse, Acceptor Derivatization of the 4CzIPN TADF System: Color Tuning and Introduction of Functional Groups, *ChemistryOpen*, 2019, **8**, 1413–1420.
340 K. Chen, Y. Zhang, Y. Lei, W. Dai, M. Liu, Z. Cai, H. Wu, X. Huang and X. Ma, Twofold rigidity activates ultralong organic high-temperature phosphorescence, *Nat Commun*, 2024, **15**, 1269–1280.
341 T. Gridneva, A. Karimata, R. Bansal, R. R. Fayzullin, S. Vasylevskyi, A. Bruhacs and J. R. Khusnutdinova, Deep-red photoluminescent mechanoresponsive polymers with dynamic CuI-arylamide mechanophores, *Chemical Communications*, 2023, **60**, 212–215.

342 K. Albrecht, K. Matsuoka, D. Yokoyama, Y. Sakai, A. Nakayama, K. Fujita and K. Yamamoto, Thermally activated delayed fluorescence OLEDs with fully solution processed organic layers exhibiting nearly 10% external quantum efficiency, *Chemical Communications*, 2017, **53**, 2439–2442.
343 V. V. Patil, K. H. Lee and J. Y. Lee, Dibenzo[*c* , *g*]indolo[3,2,1- *jk*]carbazole as a new chromophore for blue organic light-emitting diodes, *J Mater Chem C Mater*, 2019, **7**, 14301–14305.
344 K. Matsuda, R. Xiaotian, K. Nakamura, M. Furukori, T. Hosokai, K. Anraku, K. Nakao and K. Albrecht, Photostability of luminescent tris(2,4,6-trichlorophenyl)methyl radical enhanced by terminal modification of carbazole donor, *Chemical Communications*, 2022, **58**, 13443–13446.
345 J. H. Day, Thermochromism., *Chem Rev*, 1963, **63**, 65–80.
346 A. A. Dar and A. A. Ganie, Irreversible Thermochromism in Organic Salts of Sulfonated Anils, *Cryst Growth Des*, 2020, **20**, 3888–3897.
347 M. Wan, H. R. Chen, Y. N. Wang, K. Shi, J. Y. Liu, Z. M. Li, S. Y. Ye, J. Y. Li and L. Z. Chen, Reversible thermochromism to tune the bandgap of organic-inorganic hybrid materials, *Mater Chem Front*, 2022, **6**, 3094–3101.
348 B. Xu, Z. Song, M. Zhang, Q. Zhang, L. Jiang, C. Xu, L. Zhong, C. Su, Q. Ban, C. Liu, F. Sun, Y. Zhang, Z. Chi, Z. Zhao and G. Shi, Controlling the thermally activated delayed fluorescence of axially chiral organic emitters and their racemate for information encryption, *Chem Sci*, 2021, **12**, 15556–15562.
349 B. Yu, D. Liu, Y. Wang, T. Zhang, Y. M. Zhang, M. Li and S. X. A. Zhang, A solid-state emissive and solvatofluorochromic fluorophore and its application in high-contrast, fast, and repeatable thermochromic blends, *Dyes and Pigments*, 2019, **163**, 412–419.
350 A. Alconchel, O. Crespo, P. García-Orduña and M. C. Gimeno, *Closo* - or *Nido* - Carborane Diphosphane as Responsible for Strong Thermochromism or Time Activated Delayed Fluorescence (TADF) in [Cu(N^N)(P^P)] $^{0/+}$, *Inorg Chem*, 2021, **60**, 18521–18528.
351 M. K. Etherington, N. A. Kukhta, H. F. Higginbotham, A. Danos, A. N. Bismillah, D. R. Graves, P. R. McGonigal, N. Haase, A. Morherr, A. S. Batsanov, C. Pflumm, V. Bhalla, M. R. Bryce and A. P. Monkman, Persistent Dimer Emission in Thermally Activated Delayed Fluorescence Materials, *The Journal of Physical Chemistry C*, 2019, **123**, 11109–11117.
352 N. Willis-Fox, E. Watchorn-Rokutan, E. Rognin and R. Daly, Technology pull: scale-up of polymeric mechanochemical force sensors, *Trends Chem*, 2023, **5**, 415–431.
353 F. Khan, A. Ekbote and R. Misra, Reversible mechanochromism and aggregation induced enhanced emission in phenothiazine substituted tetraphenylethylene, *New Journal of Chemistry*, 2019, **43**, 16156–16163.
354 V. Thanikachalam, U. Karunakaran, J. Jayabharathi and S. Thilagavathy, Multifunctional pyrenoimidazole substituted tetraphenylethylene derivatives: Mechanochromism and aggregation-induced emission, *J Photochem Photobiol A Chem*, 2021, **420**, 113489.
355 M. Sarma and K. T. Wong, Exciplex: An Intermolecular Charge-Transfer Approach for TADF, *ACS Appl Mater Interfaces*, 2018, **10**, 19279–19304.
356 R. Ishimatsu, T. Edura, C. Adachi, K. Nakano and T. Imato, Photophysical Properties and Efficient, Stable, Electrogenerated Chemiluminescence of Donor-Acceptor Molecules Exhibiting Thermal Spin Upconversion, *Chemistry - A European Journal*, 2016, **22**, 4889–4898.
357 P. Rajamalli, D. Chen, W. Li, I. D. W. Samuel, D. B. Cordes, A. M. Z. Slawin and E. Zysman-Colman, Enhanced thermally activated delayed fluorescence through

bridge modification in sulfone-based emitters employed in deep blue organic light-emitting diodes, *J Mater Chem C Mater*, 2019, **7**, 6664–6671.

358 S. Wu, M. Aonuma, Q. Zhang, S. Huang, T. Nakagawa, K. Kuwabara and C. Adachi, High-efficiency deep-blue organic light-emitting diodes based on a thermally activated delayed fluorescence emitter, *J Mater Chem C Mater*, 2014, **2**, 421–424.

359 Q. Zhang, J. Li, K. Shizu, S. Huang, S. Hirata, H. Miyazaki and C. Adachi, Design of efficient thermally activated delayed fluorescence materials for pure blue organic light emitting diodes, *J Am Chem Soc*, 2012, **134**, 14706–14709.

360 T. Cardeynaels, M. K. Etherington, S. Paredis, A. S. Batsanov, J. Deckers, K. Stavrou, D. Vanderzande, A. P. Monkman, B. Champagne and W. Maes, Dominant dimer emission provides colour stability for red thermally activated delayed fluorescence emitter, *J Mater Chem C Mater*, 2022, **10**, 5840–5848.

361 X. Yang, F.-I. Wu, H. Haverinen, J. Li, C.-H. Cheng and G. E. Jabbour, Efficient organic light-emitting devices with platinum-complex emissive layer, *Appl Phys Lett*, 2011, **98**, 033302.

362 Y. Kawamura, K. Goushi, J. Brooks, J. J. Brown, H. Sasabe and C. Adachi, 100% phosphorescence quantum efficiency of Ir(III) complexes in organic semiconductor films, *Appl Phys Lett*, 2005, **86**, 071104.

363 C. W. Lee and J. Y. Lee, Above 30% external quantum efficiency in blue phosphorescent organic light-emitting diodes using pyrido[2,3-b]indole derivatives as host materials, *Advanced Materials*, 2013, **25**, 5450–5454.

364 D. Zhang, M. Cai, Y. Zhang, D. Zhang and L. Duan, Highly Efficient Simplified Single-Emitting-Layer Hybrid WOLEDs with Low Roll-off and Good Color Stability through Enhanced Förster Energy Transfer, *ACS Appl Mater Interfaces*, 2015, **7**, 28693–28700.

365 Q. Zhang, T. Komino, S. Huang, S. Matsunami, K. Goushi and C. Adachi, Triplet exciton confinement in green organic light-emitting diodes containing luminescent charge-transfer Cu(I) complexes, *Adv Funct Mater*, 2012, **22**, 2327–2336.

366 S. Paredis, T. Cardeynaels, J. Deckers, A. Danos, D. Vanderzande, A. P. Monkman, B. Champagne and W. Maes, Bridge control of photophysical properties in benzothiazole-phenoxazine emitters - from thermally activated delayed fluorescence to room temperature phosphorescence, *J Mater Chem C Mater*, 2022, **10**, 4775–4784.

367 A. Klimash, P. Pander, W. T. Klooster, S. J. Coles, P. Data, F. B. Dias and P. J. Skabara, Intermolecular interactions in molecular crystals and their effect on thermally activated delayed fluorescence of helicene-based emitters, *J Mater Chem C Mater*, 2018, **6**, 10557–10568.

368 J. S. Ward, R. S. Nobuyasu, A. S. Batsanov, P. Data, A. P. Monkman, F. B. Dias and M. R. Bryce, The interplay of thermally activated delayed fluorescence (TADF) and room temperature organic phosphorescence in sterically-constrained donor-acceptor charge-transfer molecules, *Chemical Communications*, 2016, **52**, 2612–2615.

369 M. J. G. Peach, P. Benfield, T. Helgaker and D. J. Tozer, Excitation energies in density functional theory: An evaluation and a diagnostic test, *J Chem Phys*, 2008, **128**, 044118.

370 S. Wang, Y. Zhang, W. Chen, J. Wei, Y. Liu and Y. Wang, Achieving high power efficiency and low roll-off OLEDs based on energy transfer from thermally activated delayed excitons to fluorescent dopants, *Chemical Communications*, 2015, **51**, 11972–11975.

371 A. Qin, L. Tang, J. W. Y. Lam, C. K. W. Jim, Y. Yu, H. Zhao, J. Z. Sun and B. Z. Tang, Metal-free click polymerization: Synthesis and photonic properties of poly(aroyltriazole)s, *Adv Funct Mater*, 2009, **19**, 1891–1900.

372 M. A. Potopnyk, J. Mech-Piskorz, G. Angulo, M. Ceborska, R. Luboradzki, E. Andresen, A. Gajek, A. Wisniewska and U. Resch-Genger, Aggregation/Crystallization-Induced Emission in Naphthyridine-Based Carbazolyl-Modified Donor-Acceptor Boron Dyes Tunable by Fluorine Atoms, *Chemistry – A European Journal*, 2024, **30**, e202400004.

373 G. A. Zalmi, D. N. Nadimetla, P. Kotharkar, A. L. Puyad, M. Kowshik and S. V. Bhosale, Aggregation-Induced Emission-Based Material for Selective and Sensitive Recognition of Cyanide Anions in Solution and Biological Assays, *ACS Omega*, 2021, **6**, 16704–16713.

374 F. Sánchez-Férez, X. Solans-Monfort, T. Calvet, M. Font-Bardia and J. Pons, Controlling the Formation of Two Concomitant Polymorphs in Hg(II) Coordination Polymers, *Inorg Chem*, 2022, **61**, 4965–4979.

375 P. Xue, Z. Yang and P. Chen, Hiding and revealing information using the mechanochromic system of a 2,5-dicarbazole-substituted terephthalate derivative, *J Mater Chem C Mater*, 2018, **6**, 4994–5000.

376 T. Zhang, Y. Han, K. Wang, M. Liang, W. Bian, Y. Zhang, X. Li, C. Zhang and P. Xue, Alkyl chain-dependent ESIPT luminescent switches of phenothazine derivatives in response to force, *Dyes and Pigments*, 2020, **172**, 107835.

377 Z. Liang, M. Wei, S. Zhang, W. Huang, N. Shi, A. Lv, H. Ma and Z. He, Activating Molecular Room-Temperature Phosphorescence by Manipulating Excited-State Energy Levels in Poly(vinyl alcohol) Matrix, *ACS Appl Mater Interfaces*, 2023, **15**, 35534–35542.

378 S. A. Majeed, B. Ghazal, D. E. Nevonen, P. C. Goff, D. A. Blank, V. N. Nemykin and S. Makhseed, Evaluation of the Intramolecular Charge-Transfer Properties in Solvatochromic and Electrochromic Zinc Octa(carbazolyl)phthalocyanines, *Inorg Chem*, 2017, **56**, 11640–11653.

379 Y. Zhang, D. Zhang, T. Tsuboi, Y. Qiu and L. Duan, Simultaneous enhancement of efficiency and stability of OLEDs with thermally activated delayed fluorescence materials by modifying carbazoles with peripheral groups, *Sci China Chem*, 2019, **62**, 393–402.

380 Y. Tsuchiya, N. Nakamura, S. Kakumachi, K. Kusuhara, C.-Y. Chan and C. Adachi, A convenient method to estimate the glass transition temperature of small organic semiconductor materials, *Chemical Communications*, 2022, **58**, 11292–11295.

381 S. Wu, H. Zhang, Z. Mao, Y. Liang, J.-A. Li, P. Hu, Q. Zhang, C. Liu, S. Luo, Y. Wang, G. Shi and B. Xu, Achieving Stable and Switchable Ultralong Room-Temperature Phosphorescence from Polymer-Based Luminescent Materials with Three-Dimensional Covalent Networks for Light-Manipulated Anticounterfeiting, *ACS Appl Mater Interfaces*, 2023, **15**, 39896–39904.

382 Z. Xie, C. Chen, S. Xu, J. Li, Y. Zhang, S. Liu, J. Xu and Z. Chi, White-Light Emission Strategy of a Single Organic Compound with Aggregation-Induced Emission and Delayed Fluorescence Properties, *Angewandte Chemie*, 2015, **127**, 7287–7290.

383 H. Nakanotani, K. Masui, J. Nishide, T. Shibata and C. Adachi, Promising operational stability of high-efficiency organic light-emitting diodes based on thermally activated delayed fluorescence, *Sci Rep*, 2013, **3**, 2127–2132.

384 A. Shimizu, Y. Ishizaki, S. Horiuchi, T. Hirose, K. Matsuda, H. Sato and J. I. Yoshida, HOMO-LUMO Energy-Gap Tuning of π-Conjugated Zwitterions Composed of Electron-Donating Anion and Electron-Accepting Cation, *Journal of Organic Chemistry*, 2021, **86**, 770–781.

385 R. Englman and J. Jortner, The energy gap law for non-radiative decay in large molecules, *J Lumin*, 1970, **1–2**, 134–142.
386 J. Jortner, Radiationless transitions, *Pure and Applied Chemistry*, 1971, **27**, 389–420.
387 W. Siebrand, Radiationless transitions in polyatomic molecules. II. Triplet-ground-state transitions in aromatic hydrocarbons, *J Chem Phys*, 1967, **47**, 2411–2422.
388 M. D. Hanwell, D. E. Curtis, D. C. Lonie, T. Vandermeersch, E. Zurek and G. R. Hutchison, *SOFTWARE Open Access Avogadro: an advanced semantic chemical editor, visualization, and analysis platform*, 2012, vol. 4.
389 Persistence of Vision Pty. Ltd. (2004), Persistence of Vision Raytracer (Version 3.6), http://www.povray.org/download/, (accessed 21 September 2024).

1 M. S. Shur and A. Žukauskas, Solid-state lighting: Toward superior illumination, *Proceedings of the IEEE*, 2005, **93**, 1691–1703.
2 A. Volta, II. Of the method of rendering very sensible the weakest natural or artificial electricity, *Philos Trans R Soc Lond*, 1782, **72**, 4653.
3 M. Faraday, Experimental Researches in Electricity — Fourth Series, *Philos Trans R Soc Lond*, 1833, **123**, 507–522.
4 J. W. Orton, in *The Story of Semiconductors*, Oxford University Press, 2008.
5 A. H. Wilson, The theory of electronic semi-conductors, *Proceedings of the Royal Society of London. Series A, Containing Papers of a Mathematical and Physical Character*, 1931, **133**, 458–491.
6 A. Bernanose, Electroluminescence of organic compounds, *British Journal of Applied Physics*, 1955, **6**, 54.
7 Sony α7 III, https://www.sony.co.uk/electronics/interchangeable-lens-cameras/ilce-7m3-body-kit#product_details_default, (accessed 26 May 2020).
8 LG OLED TVs, https://www.lg.com/uk/oled-tvs, (accessed 26 May 2020).
9 Apple iPhone 11, https://www.apple.com/uk/iphone-11-pro/, (accessed 26 May 2020).
10 D. Dilaura, 22 | OPN September 2008 www.osa-opn.org, 2008, 22–28.
11 M. Guarnieri, An Historical Survey on Light Technologies, *IEEE Access*, 2018, **6**, 25881–25897.
12 L. Figuier, Fig. 10 -- verre du bec d'Argand, http://hdl.loc.gov/loc.pnp/cph.3c10395, (accessed 6 June 2024).
13 D. E. Nye, *American Illuminations*, The MIT Press, 2018.
14 W. T. Sedgewick and F. J. Schnider, The relation of illuminating gas to public health, *Journal of the American Public Health Association*, 1911, **1**, 385–390.
15 L. Worsley, A quick history of domestic lighting, https://www.lucyworsley.com/a-quick-history-of-domestic-lighting/, (accessed 25 March 2020).
16 K. Wallis-Smith, Gas Lighting in Victorian times, http://www.countrylife.co.uk/property/guides-advice/gas-lighting-in-victorian-times-16562.
17 H. Davy, I. On the fire-damp of coal mines, and on methods of lighting the mines so as to prevent its explosion, *Philos Trans R Soc Lond*, 1816, **106**, 1–22.
18 Kobo and Wikipedia, Image of Humphry Davy lamp, https://en.wikipedia.org/wiki/Davy_lamp#/media/File:Davy_lamp.png, (accessed 6 June 2024).
19 V. B. Lewes, Gas mantle, incandescent, and its uses, *Journal of the Society of Arts; London*, 1899, **48**, 853–860.
20 D. Voss, L. Poffenberger and Alaina. G. Levine, *APS News*, 2018, 27, 3.

21 A. Bateson, The chemistry of 'being in the limelight'., https://www.ool.co.uk/blog/the-chemistry-of-being-in-the-limelight/, (accessed 25 March 2020).
22 C. M. Carver, *A History of English in its Own Words*, Harper Collins, 1991.
23 D. MacIsaac, G. Kanner and G. Anderson, Basic physics of the incandescent lamp (lightbulb), *Phys Teach*, 1999, **37**, 520–525.
24 T. A. Edison, *Patent: Electric lamp, US Patent Number US223898*, United States Patent Office, United States, 1880.
25 M. Schiler, *Simplified Design of Building Lighting*, Wiley, 1997.
26 H. J. Round, A note on carborundum, *Electrical World*, 1907, **49**, 309.
27 N. Holonyak and S. F. Bevacqua, Coherent (visible) light emission from Ga(As1-xPx) Junctions, *Semiconductor Devices: Pioneering Papers*, 1991, **82**, 898–899.
28 R. N. Hall, G. E. Fenner, J. D. Kingsley, T. J. Soltys and R. O. Carlson, Coherent Light Emission From GaAs Junctions, *Phys Rev Lett*, 1962, **9**, 366–368.
29 S. Nakamura, T. Mukai and M. Senoh, Candela-class high-brightness InGaN/AlGaN double-heterostructure blue-light-emitting diodes, *Appl Phys Lett*, 1994, **64**, 1687–1689.
30 The Nobel Prize in Physics 2014, https://www.nobelprize.org/prizes/physics/2014/press-release/, (accessed 26 March 2020).
31 M. Pope, H. P. Kallmann and P. Magnante, Electroluminescence in organic crystals [16], *J Chem Phys*, 1963, **38**, 2042–2043.
32 G. Hong, X. Gan, C. Leonhardt, Z. Zhang, J. Seibert, J. M. Busch and S. Bräse, A Brief History of OLEDs—Emitter Development and Industry Milestones, *Advanced Materials*, 2021, **33**, 5630–5654.
33 H. Uoyama, K. Goushi, K. Shizu, H. Nomura and C. Adachi, Highly efficient organic light-emitting diodes from delayed fluorescence, *Nature*, 2012, **492**, 234–238.
34 S. R. Forrest, *Organic Electronics: Foundations to Applications*, Oxford University Press, Oxford, 2020.
35 M. P. Bracciale, *Sustainable Strategies in Organic Electronics*, Elsevier, 2022.
36 L. Kelion and J. Whitwell, Galaxy Fold: The internet reacts to Samsung's flexible phone, https://www.bbc.co.uk/news/technology-47313049, (accessed 5 February 2021).
37 V. Savov, Flexible Phone Screens That Roll and Fold Are Liberating Boring Design, https://www.bloomberg.com/news/articles/2021-01-28/flexible-mobile-phone-screens-that-fold-are-liberating-boring-design, (accessed 5 February 2021).
38 S. J. Benight, C. Wang, J. B. H. Tok and Z. Bao, Stretchable and self-healing polymers and devices for electronic skin, *Prog Polym Sci*, 2013, **38**, 1961–1977.
39 M. Irimia-Vladu, P. A. Troshin, M. Reisinger, L. Shmygleva, Y. Kanbur, G. Schwabegger, M. Bodea, R. Schwödiauer, A. Mumyatov, J. W. Fergus, V. F. Razumov, H. Sitter, N. S. Sariciftci and S. Bauer, Biocompatible and biodegradable materials for organic field-effect transistors, *Adv Funct Mater*, 2010, **20**, 4069–4076.
40 Y. Zhou, T. M. Khan, J. C. Liu, C. Fuentes-Hernandez, J. W. Shim, E. Najafabadi, J. P. Youngblood, R. J. Moon and B. Kippelen, Efficient recyclable organic solar cells on cellulose nanocrystal substrates with a conducting polymer top electrode deposited by film-transfer lamination, *Org Electron*, 2014, **15**, 661–666.
41 Y. Xie, F. Guan, Z. Li, Y. Meng, J. Cheng, L. Li and Q. Pei, A Phase-Changing Polymer Film for Broadband Smart Window Applications, *Macromol Rapid Commun*, 2020, **41**, 290–297.

42 NOWOFOL, What is ETFE?, https://www.nowofol.com/en/etfe-architecture/etfe-membrane/#:~:text=ETFE%20film%20is%20highly%20flame,a%20wide%20range%20of%20applications., (accessed 20 May 2024).

43 Y. Li, X. Huang, K. Ding, H. K. M. Sheriff, L. Ye, H. Liu, C.-Z. Li, H. Ade and S. R. Forrest, Non-fullerene acceptor organic photovoltaics with intrinsic operational lifetimes over 30 years, *Nat Commun*, 2021, **12**, 5419–5428.

44 Hayley Hanway, Organic photovoltaics offer realistic pathway to power-generating windows, https://ece.engin.umich.edu/stories/organic-photovoltaics-offer-realistic-pathway-to-power-generating-windows#:~:text=Organic%20solar%20cells%20can%20absorb,creating%20a%20stained%2Dglass%20appearance., (accessed 20 May 2024).

45 LG, LG Signature Rollable OLED, https://www.lg.com/global/lg-signature/rollable-oled-tv-r, (accessed 20 May 2024).

46 Google, Pixel Fold, https://store.google.com/gb/product/pixel_fold?hl=en-GB, (accessed 20 May 2024).

47 OnePlus, OnePlus Open, https://www.oneplus.com/uk/oneplus-open, (accessed 20 May 2024).

48 Honor, Honor Magic V2, https://www.honor.com/uk/phones/honor-magic-v2/, (accessed 20 May 2024).

49 Samsung, Samsung Galaxy Flip/Fold, https://www.samsung.com/uk/smartphones/galaxy-z/, (accessed 20 May 2024).

50 Oppo, Oppo X 2021, https://www.oppo.com/en/smartphones/oppo-x-2021/, (accessed 22 September 2024).

51 David Lumb, I Felt the Motorola Rizr's Rollable Screen Move Under My Hand, https://www.cnet.com/tech/mobile/i-felt-the-motorola-rizrs-rollable-screen-move-under-my-hand/, (accessed 20 May 2024).

52 Panasonic, Panasonic VITRINE, https://panasonic.net/design/works/milan2019/, (accessed 5 February 2021).

53 H. Akamatu and H. Inokuchi, On the Electrical Conductivity of Violanthrone, Iso-Violanthrone, and Pyranthrone, *J Chem Phys*, 1950, **18**, 810–811.

54 H. Inokuchi, The discovery of organic semiconductors. Its light and shadow, *Org Electron*, 2006, **7**, 62–76.

55 H. Inokuchi, Photoconductivity of the Condensed Polynuclear Aromatic Compounds, *Bull Chem Soc Jpn*, 1954, **27**, 22–27.

56 Y. Liu, X. Wu, Z. Xiao, J. Gao, J. Zhang, H. Rui, X. Lin, N. Zhang, Y. Hua and S. Yin, Highly efficient tandem OLED based on C 60 /rubrene: MoO 3 as charge generation layer and LiF/Al as electron injection layer, *Appl Surf Sci*, 2017, **413**, 302–307.

57 H. Spanggaard and F. C. Krebs, A brief history of the development of organic and polymeric photovoltaics, *Solar Energy Materials and Solar Cells*, 2004, **83**, 125–146.

58 R. C. Nelson, Organic photoconductors. I. The kinetics of photoconductivity in rhodamine B, *J Chem Phys*, 1954, **22**, 885–889.

59 A. K. Ghosh, D. L. Morel, T. Feng, R. F. Shaw, C. A. Rowe, A. Schottky-barrier and C. A. R. Jr, Photovoltaic and rectification properties of Al/Mg phthalocyanine/Ag Schottkybarrier cells Photovoltaic and rectification properties of All Mg, *J. Appl. Phys.*, 1974, **45**, 230–236.

60 D. L. Morel, A. K. Ghosh, T. Feng, E. L. Stogryn, P. E. Purwin, R. F. Shaw and C. Fishman, High-efficiency organic solar cells, *Appl Phys Lett*, 1978, **32**, 495–497.

61 G. A. Chamberlain and P. J. Cooney, Photoelectric properties of aluminium/copper phthalocyanine/gold photovoltaic cells, *Chem Phys Lett*, 1979, **66**, 88–94.

62 C. W. Tang, Two-layer organic photovoltaic cell, *Appl Phys Lett*, 1986, **48**, 183–185.

63 C. Wang, H. Dong, W. Hu, Y. Liu and D. Zhu, Semiconducting π-conjugated systems in field-effect transistors: A material odyssey of organic electronics, *Chem Rev*, 2012, **112**, 2208–2267.

64 S. Park, M. Takakuwa, K. Fukuda, S. Lee, T. Yokota and T. Someya, Toward ultraflexible organic electronic devices, *MRS Bull*, 2023, **48**, 999–1012.

65 K. Liu, B. Ouyang, X. Guo, Y. Guo and Y. Liu, Advances in flexible organic field-effect transistors and their applications for flexible electronics, *npj Flexible Electronics*, 2022, **6**, 1.

66 M. Pope, H. P. Kallmann and P. Magnante, Electroluminescence in Organic Crystals, *J Chem Phys*, 1963, **38**, 2042–2043.

67 S. A. Vanslyke, C. W. Tang and R. C. Luther, *Patent: Electroluminescent Device with Organic Luminescent Medium, Patent Number US4720432A*, United States, 1988.

68 T. H. Han, W. Song and T. W. Lee, Elucidating the crucial role of hole injection layer in degradation of organic light-emitting diodes, *ACS Appl Mater Interfaces*, 2015, **7**, 3117–3125.

69 TCTA - Ossila, https://www.ossila.com/products/tcta, (accessed 23 February 2022).

70 H. Shi, L. Deng, S. Chen, Y. Xu, H. Zhou, F. Cheng, X. Li, L. Wang and W. Huang, Flexible top-emitting warm-white organic light-emitting diodes with highly luminous performances and extremely stable chromaticity, *Org Electron*, 2014, **15**, 1465–1475.

71 C.-S. Ho, W.-C. Hsu, Y.-N. Lai, C.-S. Lee, W.-M. Chen, E.-L. Huang, E.-P. Yao and C.-W. Wang, Performance Improvement in Poly(3-hexylthiophene):[6,6]-Phenyl C $_{61}$ Butyric Acid Methyl Ester Polymer Solar Cell by Doping Wide-Gap Material Tris(phenylpyrazole)iridium, *Applied Physics Express*, 2013, **6**, 423011–423014.

72 M. Kumar and L. Pereira, Mixed-Host Systems with a Simple Device Structure for Efficient Solution-Processed Organic Light-Emitting Diodes of a Red-Orange TADF Emitter, *ACS Omega*, 2020, **5**, 2196–2204.

73 T. Chatterjee and K. T. Wong, Perspective on Host Materials for Thermally Activated Delayed Fluorescence Organic Light Emitting Diodes, *Adv Opt Mater*, 2019, **7**, 1800565.

74 G. W. Kim, Y. H. Son, H. I. Yang, J. H. Park, I. J. Ko, R. Lampande, J. Sakong, M. J. Maeng, J. A. Hong, J. Y. Lee, Y. Park and J. H. Kwon, Diphenanthroline electron transport materials for the efficient charge generation unit in tandem organic light-emitting diodes, *Chemistry of Materials*, 2017, **29**, 8299–8312.

75 T. Furukawa, H. Nakanotani, M. Inoue and C. Adachi, Dual enhancement of electroluminescence efficiency and operational stability by rapid upconversion of triplet excitons in OLEDs, *Sci Rep*, 2015, **5**, 8429–8437.

76 C.-C. Chang, M.-T. Hsieh, J.-F. Chen, S.-W. Hwang and C. H. Chen, Highly power efficient organic light-emitting diodes with a p-doping layer, *Appl Phys Lett*, 2006, **89**, 253504.

77 H. Ahn, H. Lee, J. Yang and C. Lee, in *Digest of Technical Papers - SID International Symposium*, Blackwell Publishing Ltd, 2012, vol. 43, pp. 1481–1483.

78 Precedence Research, OLED Market (By Technology: Active-matrix OLED (AMOLED), Passive-matrix OLED (PAMOLED), Foldable OLED, White OLED, Transparent OLED, Others; By Product Type: Display, Lighting; By Display Panel Type: Rigid, Flexible, Others; By Application: Smartphone & Tablet, Smartwatches & Wearables, Television, Digital Signage Systems, PC Monitors, Laptop, Others) - Global Industry Analysis, Size, Share, Growth, Trends, Regional Outlook, and

Forecast 2023-2032, https://www.precedenceresearch.com/oled-market, (accessed 21 May 2024).
79 Motorola, Motorola Razr, https://www.motorola.co.uk/smartphones-motorola-razr-40/p?skuId=701, (accessed 21 May 2024).
80 Fitbit, Fitbit Luxe, https://www.fitbit.com/global/us/products/trackers/luxe?sku=422GLWT, (accessed 28 February 2022).
81 Apple, Apple Watch Series 7, https://www.apple.com/uk/apple-watch-series-7/, (accessed 28 February 2022).
82 Samsung, Samsung Galaxy Watch 4, https://www.samsung.com/uk/watches/galaxy-watch/galaxy-watch4-pink-gold-lte-sm-r865fzdaeua/, (accessed 28 February 2022).
83 LG, Transparent OLED Automatic Door, https://www.lg-informationdisplay.com/product/oled-signage/transparent-oled-automatic-door, (accessed 22 May 2024).
84 LG, LG Objet Collection – Posé 42 inch TV 2022, https://www.lg.com/uk/tvs-soundbars/oled-evo/42lx1q6la/, (accessed 22 May 2024).
85 lights.co.uk, OMLED One d2, https://www.lights.co.uk/p/omled-one-d2-desk-lamp-with-oleds-white-3063009.html, (accessed 22 May 2024).
86 lights.co.uk, Trae Jade OLED desk lamp, https://www.lights.co.uk/p/trae-jade-oled-desk-lamp-qi-white-9048001.html?lw_om_view=recotop&utm_source=google&utm_medium=cpc&utm_campaign=PMAX_Villains&utm_content=&utm_term=&gad_source=1&gclid=EAIaIQobChMIyaKoyfqghgMVqJJQBh18YgymEAQYAyABEgIz2vD_BwE&et_uk=6b336a43d295485791125174e5050074&et_gk=Y2Y3NmU0NmE2NmY3NGM5ODgyZWZjM2RkZDI2MzFjNWMlN0MyMS4wNy4yMDI0KzA5JTNBMzYlM0EwNg, (accessed 22 May 2024).
87 Audi, Lighting technology pioneer Audi fields next-generation OLED technology, https://press.audi.co.uk/en-gb/releases/74, (accessed 12 October 2024).
88 Architonic, LivingShapes interactive wall, https://www.architonic.com/en/product/philips-lumiblade-oled-livingshapes-interactive-wall/1201916, (accessed 22 May 2024).
89 Corning, Corning - Emerging Innovations, https://www.corning.com/emea/en/innovation/corning-emerging-innovations/oled-lighting-corning-emerging-innovations.html, (accessed 22 May 2024).
90 LG, LG Chem Develops World's First High-Efficacy OLED Light Panels, https://www.lgcorp.com/media/release/3695, (accessed 22 May 2024).
91 C. M. Lochner, Y. Khan, A. Pierre and A. C. Arias, All-organic optoelectronic sensor for pulse oximetry, *Nat Commun*, 2014, **5**, 5745–5752.
92 I. D. W. Samuel, C. Lian, M. Piksa, K. Matczyszyn, K. Yoshida, S. Persheyev, K. Pawlik, F. Cabral, M. Ribeiro and J. Lindoso, in *Organic and Hybrid Sensors and Bioelectronics XIII, 114750C*, eds. R. Shinar, I. Kymissis and E. J. List-Kratochvil, Proc. SPIE 11475, 2020, p. 10.
93 E. Tankelevičiūtė, I. D. W. Samuel and E. Zysman-Colman, The Blue Problem: OLED Stability and Degradation Mechanisms, *American Chemical Society*, 2024, preprint, DOI: 10.1021/acs.jpclett.3c03317.
94 Ossila, How Long Do OLEDs Last?, https://www.ossila.com/pages/oled-lifetime, (accessed 22 May 2024).
95 E. F. Schubert, *Light-Emitting Diodes*, Cambridge University Press, 2006.
96 Y. Ohno, in *Fourth International Conference on Solid State Lighting*, Proc. SPIE 5530, 2004, vol. 5530, p. 88.

97 Lesker, Lesker Super-SPECTROS 200 product page, https://www.lesker.com/process-equipment-division/thin-film-systems/super-spectros-200-deposition-platform.cfm, (accessed 6 June 2024).

98 D. Deganello, in *Organic Light-Emitting Diodes (OLEDs): Materials, Devices and Applications*, Elsevier Ltd., 2013.

99 T. Gao, H. Wang, Z. Chen, Z. Wang, M. Zhou, B. Zhao, F. Chen and Q. Zou, Performance improved white full-organic light emitting diodes (WOLED) based on tricolor dual-layer of hyperfluorescence (HF), *Org Electron*, 2023, **120**, 106845.

100 M. Cocchi, M. Bertoldo, M. Seri, P. Maccagnani, C. Summonte, S. Buoso, G. Belletti, F. Dinelli and R. Capelli, Fully Recyclable OLEDs Built on a Flexible Biopolymer Substrate, *ACS Sustain Chem Eng*, 2021, **9**, 12733–12737.

101 Kenneth R. Spring, Thomas J. Fellers and Michael W. Davidson, Human Vision and Color Perception, https://www.olympus-lifescience.com/en/microscope-resource/primer/lightandcolor/humanvisionintro/#:~:text=When%20fully%20light%2Dadapted%2C%20the,of%20the%20visible%20light%20spectrum), (accessed 25 May 2024).

102 H. Young and R. Freedman, *University Physics with Modern Physics 14th Edition*, Pearson, 2016.

103 C. Housecroft and E. Constable, *Chemistry*, Pearson Education, 3rd edn., 2006.

104 J. W. Orton, *The Story of Semiconductors*, Oxford University Press, 2008.

105 J. J. Quinn and K.-S. Yi, *Solid State Physics: Principles and modern applications*, Springer, 2009.

106 H. Shirakawa, E. J. Louis, A. G. MacDiarmid, C. K. Chiang and A. J. Heeger, Synthesis of electrically conducting organic polymers: Halogen derivatives of polyacetylene, (CH)x, *J Chem Soc Chem Commun*, 1977, 578–580.

107 H. Inokuchi, G. Saito, P. Wu, K. Seki, T. B. Tang, T. Mori, K. Imaeda, T. Enoki, Y. Higuchi, K. Inaka and N. Yasuoka, A Novel Type of Organic Semiconductors. Molecular Fastener, *Chem Lett*, 1986, **15**, 1263–1266.

108 D. Bloor, Totally organic transistors, *Nature*, 1991, **349**, 738–740.

109 N. A. Ran, J. A. Love, C. J. Takacs, A. Sadhanala, J. K. Beavers, S. D. Collins, Y. Huang, M. Wang, R. H. Friend, G. C. Bazan and T. Q. Nguyen, Harvesting the Full Potential of Photons with Organic Solar Cells, *Advanced Materials*, 2016, **28**, 1482–1488.

110 M. Y. Wong and E. Zysman-Colman, Purely Organic Thermally Activated Delayed Fluorescence Materials for Organic Light-Emitting Diodes, *Advanced Materials*, 2017, **29**, 1605444.

111 D. T. Chase, A. G. Fix, S. J. Kang, B. D. Rose, C. D. Weber, Y. Zhong, L. N. Zakharov, M. C. Lonergan, C. Nuckolls and M. M. Haley, 6,12-Diarylindeno[1,2- b]fluorenes: Syntheses, photophysics, and ambipolar OFETs, *J Am Chem Soc*, 2012, **134**, 10349–10352.

112 V. Coropceanu, J. Cornil, D. A. da Silva Filho, Y. Olivier, R. Silbey and J. L. Brédas, Charge transport in organic semiconductors, *Chem Rev*, 2007, **107**, 926–952.

113 N. T. Kalyani, H. Swart and S. J. Dhoble, in *Principles and Applications of Organic Light Emitting Diodes (OLEDs)*, Elsevier, 2017.

114 M. Irimia-Vladu, E. D. Głowacki, G. Voss, S. Bauer and N. S. Sariciftci, Green and biodegradable electronics, *Materials Today*, 2012, **15**, 340–346.

115 M. Irimia-Vladu, 'Green' electronics: Biodegradable and biocompatible materials and devices for sustainable future, *Chem Soc Rev*, 2014, **43**, 588–610.

116 M. Godumala, S. Choi, M. J. Cho and D. H. Choi, Recent breakthroughs in thermally activated delayed fluorescence organic light emitting diodes containing non-doped emitting layers, *J Mater Chem C Mater*, 2019, **7**, 2172–2198.

117 K. L. Kohlstedt, N. E. Jackson, B. A. Savoie and M. A. Ratner, Introduction to Organic Semiconductors Using Accessible Undergraduate Chemistry Concepts, *J Chem Educ*, 2018, **95**, 1500–1511.

118 U. Salzner, J. B. Lagowski, P. G. Pickup and R. A. Poirier, Comparison of geometries and electronic structures of polyacetylene, polyborole, polycyclopentadiene, polypyrrole, polyfuran, polysilole, polyphosphole, polythiophene, polyselenophene and polytellurophene, *Synth Met*, 1998, **96**, 177–189.

119 K. W. Böer and U. W. Pohl, *Semiconductor Physics*, Springer International Publishing, 2018.

120 K. Hannewald, V. M. Stojanović, J. M. T. Schellekens, P. A. Bobbert, G. Kresse and J. Hafner, Theory of polaron bandwidth narrowing in organic molecular crystals, *Phys Rev B*, 2004, **69**, 075211.

121 B. Valeur and M. N. Berberan-Santos, *Molecular Fluorescence*, Wiley, 2012.

122 A. Köhler and H. Bässler, Triplet states in organic semiconductors, *Materials Science and Engineering R: Reports*, 2009, **66**, 71–109.

123 T. Ogiwara, Y. Wakikawa and T. Ikoma, Mechanism of intersystem crossing of thermally activated delayed fluorescence molecules, *Journal of Physical Chemistry A*, 2015, **119**, 3415–3418.

124 A. Jablonski, Efficiency of Anti-Stokes Fluorescence in Dyes, *Nature*, 1933, **131**, 839–840.

125 M. Hutchings and P. Bamfield, *Chromic Phenomena*, Royal Society of Chemistry, Cambridge, 2018.

126 J. L. Bredas, Mind the gap!, *Mater Horiz*, 2014, **1**, 17–19.

127 J. C. Koziar and D. O. Cowan, Photochemical Heavy-Atom Effects, *Acc Chem Res*, 1978, **11**, 334–341.

128 P. Atkins and J. de Paula, *Elements of Physical Chemistry 5th Edition*, Oxford University Press, 5th edn., 2009.

129 J. Chen, Y. Wu, X. Wang, Z. Yu, H. Tian, J. Yao and H. Fu, A soluble cryogenic thermometer with high sensitivity based on excited-state configuration transformations, *Physical Chemistry Chemical Physics*, 2015, **17**, 27658–27664.

130 J. B. Birks and L. G. Christophorou, Excimer fluorescence spectra of pyrene derivatives, *Spectrochimica Acta*, 1963, **19**, 401–410.

131 P. Atkins and J. De Paula, *Physical Chemistry 9th Edition*, Oxford University Press, 9th edn., 2010.

132 M. Tonet, Fluorescence Quenching & the Stern-Volmer Plot, https://www.edinst.com/wp-content/uploads/2024/05/Spectral_School_Quenching_Stern_Volmer-1.pdf, (accessed 22 September 2024).

133 Th. Főrster, 10th Spiers Memorial Lecture. Transfer mechanisms of electronic excitation, *Discuss. Faraday Soc.*, 1959, **27**, 7–17.

134 D. Ma, Z. Xu, B. Z. Tang and Y. Wang, Recent advances in high performance blue organic light-emitting diodes based on fluorescence emitters, *J Mater Chem C Mater*, 2020, 2614–2642.

135 B. Valeur and M. N. Berberan-Santos, A brief history of fluorescence and phosphorescence before the emergence of quantum theory, *J Chem Educ*, 2011, **88**, 731–738.

136 Y. Pan, W. Li, S. Zhang, L. Yao, C. Gu, H. Xu, B. Yang and Y. Ma, High Yields of Singlet Excitons in Organic Electroluminescence through Two Paths of Cold and Hot Excitons, *Adv Opt Mater*, 2014, **2**, 510–515.

137 C. A. Parker and C. G. Hatchard, Triplet-singlet emission in fluid solutions. Phosphorescence of eosin, *Transactions of the Faraday Society*, 1961, **57**, 1894–1904.
138 M. A. Baldo, D. F. O'Brien, Y. You, A. Shoustikov, S. Sibley, M. E. Thompson and S. R. Forrest, Highly efficient phosphorescent emission from organic electroluminescent devices, *Nature*, 1998, **395**, 151–154.
139 R. Czerwieniec and H. Yersin, Diversity of copper(I) complexes showing thermally activated delayed fluorescence: Basic photophysical analysis, *Inorg Chem*, 2015, **54**, 4322–4327.
140 A. Monkman, in *Highly Efficient OLEDs*, Wiley, 2018, vol. 5, pp. 425–463.
141 F. B. Dias, J. Santos, D. R. Graves, P. Data, R. S. Nobuyasu, M. A. Fox, A. S. Batsanov, T. Palmeira, M. N. Berberan-Santos, M. R. Bryce and A. P. Monkman, The Role of Local Triplet Excited States and D-A Relative Orientation in Thermally Activated Delayed Fluorescence: Photophysics and Devices, *Advanced Science*, 2016, **3**, 1600080.
142 C. Baleizão and M. N. Berberan-Santos, *Thermally Activated Delayed Fluorescence in Fullerenes*, *Ann N Y Acad Sci*, 2008, **1130**, 224–234.
143 C. A. Parker and C. G. Hatchard, Delayed fluorescence of pyrene in ethanol, *Transactions of the Faraday Society*, 1963, **59**, 284–295.
144 C. J. Chiang, A. Kimyonok, M. K. Etherington, G. C. Griffiths, V. Jankus, F. Turksoy and A. P. Monkman, Ultrahigh efficiency fluorescent single and bi-layer organic light emitting diodes: The key role of triplet fusion, *Adv Funct Mater*, 2013, **23**, 739–746.
145 C. Ringemann, A. Schönle, A. Giske, C. Von Middendorff, S. W. Hell and C. Eggeling, Enhancing fluorescence brightness: Effect of reverse intersystem crossing studied by fluorescence fluctuation spectroscopy, *ChemPhysChem*, 2008, **9**, 612–624.
146 A. Endo, M. Ogasawara, A. Takahashi, D. Yokoyama, Y. Kato and C. Adachi, Thermally activated delayed fluorescence from Sn4+-porphyrin complexes and their application to organic light-emitting diodes -A novel mechanism for electroluminescence, *Advanced Materials*, 2009, **21**, 4802–4806.
147 K. Goushi, K. Yoshida, K. Sato and C. Adachi, Organic light-emitting diodes employing efficient reverse intersystem crossing for triplet-to-singlet state conversion, *Nat Photonics*, 2012, **6**, 253–258.
148 I. A. Wright, A. Danos, S. Montanaro, A. S. Batsanov, A. P. Monkman and M. R. Bryce, Conformational Dependence of Triplet Energies in Rotationally Hindered N- and S-Heterocyclic Dimers: New Design and Measurement Rules for High Triplet Energy OLED Host Materials, *Chemistry - A European Journal*, 2021, **27**, 6545–6556.
149 R. Scholz, P. Kleine, R. Lygaitis, L. Popp, S. Lenk, M. K. Etherington, A. P. Monkman and S. Reineke, Investigation of Thermally Activated Delayed Fluorescence from a Donor-Acceptor Compound with Time-Resolved Fluorescence and Density Functional Theory Applying an Optimally Tuned Range-Separated Hybrid Functional, *Journal of Physical Chemistry A*, 2020, **124**, 1535–1553.
150 Y. Long, M. Mamada, C. Li, P. L. Dos Santos, M. Colella, A. Danos, C. Adachi and A. Monkman, Excited State Dynamics of Thermally Activated Delayed Fluorescence from an Excited State Intramolecular Proton Transfer System, *J Phys Chem Lett*, 2020, **11**, 3305–3312.
151 L. G. Franca, A. Danos and A. Monkman, Donor, Acceptor, and Molecular Charge Transfer Emission All in One Molecule, *Journal of Physical Chemistry Letters*, 2023, **14**, 2764–2771.

152 L. G. Franca, A. Danos, R. Saxena, S. Kuila, K. Stavrou, C. Li, S. Wedler, A. Köhler and A. P. Monkman, Exploring the Early Time Behavior of the Excited States of an Archetype Thermally Activated Delayed Fluorescence Molecule, *Journal of Physical Chemistry Letters*, 2024, **15**, 1734–1740.

153 M. K. Etherington, J. Gibson, H. F. Higginbotham, T. J. Penfold and A. P. Monkman, Revealing the spin–vibronic coupling mechanism of thermally activated delayed fluorescence, *Nat Commun*, 2016, **7**, 13680.

154 L. S. Cui, A. J. Gillett, S. F. Zhang, H. Ye, Y. Liu, X. K. Chen, Z. Sen Lin, E. W. Evans, W. K. Myers, T. K. Ronson, H. Nakanotani, S. Reineke, J. L. Bredas, C. Adachi and R. H. Friend, Fast spin-flip enables efficient and stable organic electroluminescence from charge-transfer states, *Nat Photonics*, 2020, **14**, 636–642.

155 D. Sasikumar, A. T. John, J. Sunny and M. Hariharan, Access to the triplet excited states of organic chromophores, *Chem Soc Rev*, 2020, **49**, 6122–6140.

156 A. Mohan, E. Sebastian, M. Gudem and M. Hariharan, Near-Quantitative Triplet State Population via Ultrafast Intersystem Crossing in Perbromoperylenediimide, *Journal of Physical Chemistry B*, 2020, **124**, 6867–6874.

157 D. S. Mcclure, Triplet-singlet transitions in organic molecules. Lifetime measurements of the triplet state, *J Chem Phys*, 1949, **17**, 905–913.

158 M. Kasha, Collisional perturbation of spin-orbital coupling and the mechanism of fluorescence quenching. a visual demonstration of the perturbation, *J Chem Phys*, 1952, **20**, 71–74.

159 F. B. Dias, J. Santos, D. R. Graves, P. Data, R. S. Nobuyasu, M. A. Fox, A. S. Batsanov, T. Palmeira, M. N. Berberan-Santos, M. R. Bryce and A. P. Monkman, The Role of Local Triplet Excited States and D-A Relative Orientation in Thermally Activated Delayed Fluorescence: Photophysics and Devices, *Advanced Science*, 2016, **3**, 1–10.

160 J. Gibson, A. P. Monkman and T. J. Penfold, The Importance of Vibronic Coupling for Efficient Reverse Intersystem Crossing in Thermally Activated Delayed Fluorescence Molecules, *ChemPhysChem*, 2016, 2956–2961.

161 P. Data, P. Pander, M. Okazaki, Y. Takeda, S. Minakata and A. P. Monkman, Dibenzo[a,j]phenazine-Cored Donor-Acceptor-Donor Compounds as Green-to-Red/NIR Thermally Activated Delayed Fluorescence Organic Light Emitters, *Angewandte Chemie - International Edition*, 2016, **55**, 5739–5744.

162 F. B. Dias, K. N. Bourdakos, V. Jankus, K. C. Moss, K. T. Kamtekar, V. Bhalla, J. Santos, M. R. Bryce and A. P. Monkman, Triplet harvesting with 100% efficiency by way of thermally activated delayed fluorescence in charge transfer OLED emitters, *Advanced Materials*, 2013, **25**, 3707–3714.

163 P. L. Santos, J. S. Ward, P. Data, A. S. Batsanov, M. R. Bryce, F. B. Dias and A. P. Monkman, Engineering the singlet-triplet energy splitting in a TADF molecule, *J Mater Chem C Mater*, 2016, **4**, 3815–3824.

164 P. L. Dos Santos, J. S. Ward, M. R. Bryce and A. P. Monkman, Using Guest-Host Interactions to Optimize the Efficiency of TADF OLEDs, *Journal of Physical Chemistry Letters*, 2016, **7**, 3341–3346.

165 M. K. Etherington, F. Franchello, J. Gibson, T. Northey, J. Santos, J. S. Ward, H. F. Higginbotham, P. Data, A. Kurowska, P. L. Dos Santos, D. R. Graves, A. S. Batsanov, F. B. Dias, M. R. Bryce, T. J. Penfold and A. P. Monkman, Regio- and conformational isomerization critical to design of efficient thermally-activated delayed fluorescence emitters, *Nat Commun*, 2017, **8**, 14987.

166 P. L. dos Santos, J. S. Ward, A. S. Batsanov, M. R. Bryce and A. P. Monkman, Optical and Polarity Control of Donor–Acceptor Conformation and Their Charge-Transfer States in Thermally Activated Delayed-Fluorescence Molecules, *The Journal of Physical Chemistry C*, 2017, **121**, 16462–16469.

167 T. J. Penfold, E. Gindensperger, C. Daniel and C. M. Marian, Spin-Vibronic Mechanism for Intersystem Crossing, *Chem Rev*, 2018, **118**, 6975–7025.

168 P. L. Dos Santos, M. K. Etherington and A. P. Monkman, Chemical and conformational control of the energy gaps involved in the thermally activated delayed fluorescence mechanism, *J Mater Chem C Mater*, 2018, **6**, 4842–4853.

169 K. Shizu, H. Tanaka, M. Uejima, T. Sato, K. Tanaka, H. Kaji and C. Adachi, Strategy for designing electron donors for thermally activated delayed fluorescence emitters, *Journal of Physical Chemistry C*, 2015, **119**, 1291–1297.

170 R. S. Nobuyasu, Z. Ren, G. C. Griffiths, A. S. Batsanov, P. Data, S. Yan, A. P. Monkman, M. R. Bryce and F. B. Dias, Rational Design of TADF Polymers Using a Donor-Acceptor Monomer with Enhanced TADF Efficiency Induced by the Energy Alignment of Charge Transfer and Local Triplet Excited States, *Adv Opt Mater*, 2016, **4**, 597–607.

171 W. Li, D. Liu, F. Shen, D. Ma, Z. Wang, T. Feng, Y. Xu, B. Yang and Y. Ma, A twisting donor-acceptor molecule with an intercrossed excited state for highly efficient, deep-blue electroluminescence, *Adv Funct Mater*, 2012, **22**, 2797–2803.

172 X. Zhang, W. Shen, D. Zhang, Y. Zheng, R. He and M. Li, Theoretical investigation of dihydroacridine and diphenylsulphone derivatives as thermally activated delayed fluorescence emitters for organic light-emitting diodes, *RSC Adv*, 2015, **5**, 51586–51591.

173 F. B. Dias, T. J. Penfold and A. P. Monkman, Photophysics of thermally activated delayed fluorescence molecules, *Methods Appl Fluoresc*, 2017, **5**, 012001.

174 B. T. Lim, S. Okajima, A. K. Chandra and E. C. Lim, Radiationless transitions in electron donor-acceptor complexes: selection rules for S1 → T intersystem crossing and efficiency of S1 → S0 internal conversion, *Chem Phys Lett*, 1981, **79**, 22–27.

175 M. Wang, T. Chatterjee, C. J. Foster, T. Wu, C. L. Yi, H. Yu, K. T. Wong and B. Hu, Exploring mechanisms for generating spin-orbital coupling through donor-acceptor design to realize spin flipping in thermally activated delayed fluorescence, *J Mater Chem C Mater*, 2020, **8**, 3395–3401.

176 C. Reichardt and T. Welton, *Solvents and Solvent Effects in Organic Chemistry*, Wiley, 4th edn., 2010.

177 A. V. Kulinich, E. K. Mikitenko and A. A. Ishchenko, Scope of negative solvatochromism and solvatofluorochromism of merocyanines, *Physical Chemistry Chemical Physics*, 2016, **18**, 3444–3453.

178 Michael Evans, Georgia Tech Lecture Series: Molecular Photochemistry (CHEM 4801): 4.4 Förster Resonance Energy Transfer, https://www.youtube.com/watch?v=UBvnNhwtQH8, (accessed 8 June 2024).

179 Michael Evans, Georgia Tech Lecture Series: Molecular Photochemistry (CHEM 4801): 4.3 Dexter (Exchange) Energy Transfer and Trivial Energy Transfer, https://www.youtube.com/watch?v=Jqv1lYCGsgk, (accessed 8 June 2024).

180 M. C. Gather, A. Köhnen and K. Meerholz, White organic light-emitting diodes, *Advanced Materials*, 2011, **23**, 233–248.

181 C. Gartner, C. Karnutsch and U. Lemmer, in *2007 European Conference on Lasers and Electro-Optics and the International Quantum Electronics Conference*, IEEE, 2007, vol. 101, p. 1.

182 M. Koschorreck, R. Gehlhaar, V. G. Lyssenko, M. Swoboda, M. Hoffmann and K. Leo, Dynamics of a high-Q vertical-cavity organic laser, *Appl Phys Lett*, 2005, **87**, 181108.

183 C. Murawski, K. Leo and M. C. Gather, Efficiency roll-off in organic light-emitting diodes, *Advanced Materials*, 2013, **25**, 6801–6827.

184 K. Masui, H. Nakanotani and C. Adachi, Analysis of exciton annihilation in high-efficiency sky-blue organic light-emitting diodes with thermally activated delayed fluorescence, *Org Electron*, 2013, **14**, 2721–2726.
185 D. Kasemann, R. Brückner, H. Fröb and K. Leo, Organic light-emitting diodes under high currents explored by transient electroluminescence on the nanosecond scale, *Phys Rev B*, 2011, **84**, 115208.
186 S. D. Babenko, V. A. Benderskii, V. I. Gol'danskii, A. G. Lavrushko and V. P. Tychinskii, Annihilation of singlet excited states in anthracene solutions, *Chem Phys Lett*, 1971, **8**, 598–600.
187 J. Eng, J. Hagon and T. J. Penfold, D–A $_3$ TADF emitters: the role of the density of states for achieving faster triplet harvesting rates, *J Mater Chem C Mater*, 2019, **7**, 12942–12952.
188 C. S. Oh, D. de S. Pereira, S. H. Han, H.-J. Park, H. F. Higginbotham, A. P. Monkman and J. Y. Lee, Dihedral Angle Control of Blue Thermally Activated Delayed Fluorescent Emitters through Donor Substitution Position for Efficient Reverse Intersystem Crossing, *ACS Appl Mater Interfaces*, 2018, **10**, 35420–35429.
189 Y. Kawamura, J. Brooks, J. J. Brown, H. Sasabe and C. Adachi, Intermolecular interaction and a concentration-Quenching mechanism of phosphorescent Ir(III) complexes in a solid film, *Phys Rev Lett*, 2006, **96**, 11–14.
190 E. B. Namdas, A. Ruseckas, I. D. W. Samuel, S. C. Lo and P. L. Burn, Photophysics of fac-tris(2-phenylpyridine) iridium(III) cored electroluminescent dendrimers in solution and films, *Journal of Physical Chemistry B*, 2004, **108**, 1570–1577.
191 E. B. Namdas, A. Ruseckas, I. D. W. Samuel, S.-C. Lo and P. L. Burn, Triplet exciton diffusion in *fac* -tris(2-phenylpyridine) iridium(III)-cored electroluminescent dendrimers, *Appl Phys Lett*, 2005, **86**, 091104.
192 L. Han, D. Yang, W. Li, B. Chu, Y. Chen, Z. Su, D. Zhang, F. Yan, Z. Hu and Z. Zhang, The reduced triplet-triplet annihilation of electrophosphorescent device doped by an iridium complex with active hydrogen, *Appl Phys Lett*, 2008, **93**, 153303.
193 M. A. Baldo, C. Adachi and S. R. Forrest, Transient analysis of organic electrophosphorescence. II. Transient analysis of triplet-triplet annihilation, *Phys Rev B*, 2000, **62**, 10967–10977.
194 W. Ji, L. Zhang and W. Xie, Improving efficiency roll-off in phosphorescent OLEDs by modifying the exciton lifetime, *Opt Lett*, 2012, **37**, 2019–2021.
195 S. H. Kim, J. Jang, K. S. Yook and J. Y. Lee, Stable efficiency roll-off in phosphorescent organic light-emitting diodes, *Appl Phys Lett*, 2008, **92**, 023513.
196 B. D. Chin, Enhancement of efficiency and stability of phosphorescent OLEDs based on heterostructured light-emitting layers, *J Phys D Appl Phys*, 2011, **44**, 115103.
197 N. C. Erickson and R. J. Holmes, Relating charge transport and performance in single-layer graded-composition organic light-emitting devices, *J Appl Phys*, 2011, **110**, 084515.
198 X.-K. Liu, C.-J. Zheng, J. Xiao, J. Ye, C.-L. Liu, S.-D. Wang, W.-M. Zhao and X.-H. Zhang, Novel bipolar host materials based on 1,3,5-triazine derivatives for highly efficient phosphorescent OLEDs with extremely low efficiency roll-off, *Physical Chemistry Chemical Physics*, 2012, **14**, 14255–14261.
199 Y. Zhang, M. Whited, M. E. Thompson and S. R. Forrest, Singlet-triplet quenching in high intensity fluorescent organic light emitting diodes, *Chem Phys Lett*, 2010, **495**, 161–165.
200 Y. Zhang, M. Slootsky and S. R. Forrest, Enhanced efficiency in high-brightness fluorescent organic light emitting diodes through triplet management, *Appl Phys Lett*, 2011, **99**, 4–7.

201 N. B. Kotadiya, P. W. M. Blom and G. J. A. H. Wetzelaer, Efficient and stable single-layer organic light-emitting diodes based on thermally activated delayed fluorescence, *Nat Photonics*, 2019, **13**, 765–769.

202 X. Tang, R. Pan, H. Zhu, X. Zhao, L. Tu and Z. Xiong, The origin of interlayer-induced significant enhancement of EQE in CzDBA-based OLEDs studied by magneto-electroluminescence, *Appl Phys Lett*, 2021, **118**, 013503.

203 R. S. Nobuyasu, J. S. Ward, J. Gibson, B. A. Laidlaw, Z. Ren, P. Data, A. S. Batsanov, T. J. Penfold, M. R. Bryce and F. B. Dias, The influence of molecular geometry on the efficiency of thermally activated delayed fluorescence, *J Mater Chem C Mater*, 2019, **7**, 6672–6684.

204 H. Li, J. Li, D. Liu, T. Huang and D. Li, Effects of Electron Affinity and Steric Hindrance of the Trifluoromethyl Group on the π-Bridge in Designing Blue Thermally Activated Delayed Fluorescence Emitters, *Chemistry – A European Journal*, 2020, **26**, 6899–6909.

205 T. Nakagawa, S. Y. Ku, K. T. Wong and C. Adachi, Electroluminescence based on thermally activated delayed fluorescence generated by a spirobifluorene donor–acceptor structure, *Chemical Communications*, 2012, **48**, 9580–9582.

206 T. T. Bui, F. Goubard, M. Ibrahim-Ouali, D. Gigmes and F. Dumur, Recent advances on organic blue thermally activated delayed fluorescence (TADF) emitters for organic light-emitting diodes (OLEDs), *Beilstein Journal of Organic Chemistry*, 2018, **14**, 282–308.

207 Y. Xiang, Z. L. Zhu, D. Xie, S. Gong, K. Wu, G. Xie, C. S. Lee and C. Yang, Revealing the new potential of an indandione unit for constructing efficient yellow thermally activated delayed fluorescence emitters with short emissive lifetimes, *J Mater Chem C Mater*, 2018, **6**, 7111–7118.

208 W. Wei, Z. Yang, X. Chen, T. Liu, Z. Mao, J. Zhao and Z. Chi, Modulation of π-linkers in asymmetric thermally activated delayed fluorescence molecules enabling high performance OLEDs, *J Mater Chem C Mater*, 2020, **8**, 3663–3668.

209 H. Li, J. Li, D. Liu, T. Huang and D. Li, Effects of Electron Affinity and Steric Hindrance of the Trifluoromethyl Group on the π-Bridge in Designing Blue Thermally Activated Delayed Fluorescence Emitters, *Chemistry - A European Journal*, 2020, **26**, 6899–6909.

210 J. Clayden, N. Greeves and S. Warren, *Organic Chemistry*, Oxford University Press, Oxford, 2nd edn., 2012.

211 F. A. Carey and R. J. Sundberg, *Advanced Organic Chemistry Part A: Structure and Mechanisms*, Springer, 5th edn., 2007.

212 L. S. Cui, Y. M. Xie, Y. K. Wang, C. Zhong, Y. L. Deng, X. Y. Liu, Z. Q. Jiang and L. S. Liao, Pure Hydrocarbon Hosts for ≈100% Exciton Harvesting in Both Phosphorescent and Fluorescent Light-Emitting Devices, *Advanced Materials*, 2015, **27**, 4213–4217.

213 M. Stanoppi and A. Lorbach, Boron-based donor-spiro-acceptor compounds exhibiting thermally activated delayed fluorescence (TADF), *Dalton Transactions*, 2018, **47**, 10394–10398.

214 Y. J. Shiu, Y. C. Cheng, W. L. Tsai, C. C. Wu, C. T. Chao, C. W. Lu, Y. Chi, Y. T. Chen, S. H. Liu and P. T. Chou, Pyridyl Pyrrolide Boron Complexes: The Facile Generation of Thermally Activated Delayed Fluorescence and Preparation of Organic Light-Emitting Diodes, *Angewandte Chemie - International Edition*, 2016, **55**, 3017–3021.

215 Y. J. Shiu, Y. T. Chen, W. K. Lee, C. C. Wu, T. C. Lin, S. H. Liu, P. T. Chou, C. W. Lu, I. C. Cheng, Y. J. Lien and Y. Chi, Efficient thermally activated delayed fluorescence of functional phenylpyridinato boron complexes and high performance organic light-emitting diodes, *J Mater Chem C Mater*, 2017, **5**, 1452–1462.

216 P. Ganesan, D.-G. Chen, J.-L. Liao, W.-C. Li, Y.-N. Lai, D. Luo, C.-H. Chang, C.-L. Ko, W.-Y. Hung, S.-W. Liu, G.-H. Lee, P.-T. Chou and Y. Chi, Isomeric spiro-[acridine-9,9′-fluorene]-2,6-dipyridylpyrimidine based TADF emitters: insights into photophysical behaviors and OLED performances, *J Mater Chem C Mater*, 2018, **6**, 10088–10100.

217 W.-C. Chen, C.-S. Lee and Q.-X. Tong, Blue-emitting organic electrofluorescence materials: progress and prospective, *J Mater Chem C Mater*, 2015, **3**, 10957–10963.

218 Z. He, W. Zhao, J. W. Y. Lam, Q. Peng, H. Ma, G. Liang, Z. Shuai and B. Z. Tang, White light emission from a single organic molecule with dual phosphorescence at room temperature, *Nat Commun*, 2017, **8**, 416.

219 T. Miwa, S. Kubo, K. Shizu, T. Komino, C. Adachi and H. Kaji, Blue organic light-emitting diodes realizing external quantum efficiency over 25% using thermally activated delayed fluorescence emitters, *Sci Rep*, 2017, **7**, 284.

220 P. Ganesan, D. G. Chen, W. C. Chen, P. Gnanasekaran, J. A. Lin, C. Y. Huang, M. C. Chen, C. S. Lee, P. T. Chou and Y. Chi, Methoxy substituents activated carbazole-based boron dimesityl TADF emitters, *J Mater Chem C*, 2020, **8**, 4780–4788.

221 Y. Im, M. Kim, Y. J. Cho, J. A. Seo, K. S. Yook and J. Y. Lee, Molecular Design Strategy of Organic Thermally Activated Delayed Fluorescence Emitters, *Chemistry of Materials*, 2017, **29**, 1946–1963.

222 K. Suzuki, S. Kubo, K. Shizu, T. Fukushima, A. Wakamiya, Y. Murata, C. Adachi and H. Kaji, Triarylboron-Based Fluorescent Organic Light-Emitting Diodes with External Quantum Efficiencies Exceeding 20 %, *Angewandte Chemie - International Edition*, 2015, **54**, 15231–15235.

223 R. S. of Chemistry, Royal Society of Chemistry Periodic Table Website, https://www.rsc.org/periodic-table/element/5/boron, (accessed 25 June 2021).

224 M. Yamashita, Y. Yamamoto, K. Y. Akiba, D. Hashizume, F. Iwasaki, N. Takagi and S. Nagase, Syntheses and structures of hypervalent pentacoordinate carbon and boron compounds bearing an anthracene skeleton - Elucidation of hypervalent interaction based on X-ray analysis and DFT calculation, *J Am Chem Soc*, 2005, **127**, 4354–4371.

225 S. S. Kothavale and J. Y. Lee, Three- and Four-Coordinate, Boron-Based, Thermally Activated Delayed Fluorescent Emitters, *Adv Opt Mater*, 2020, **8**, 2000922.

226 A. Kumar, W. Lee, T. Lee, J. Jung, S. Yoo and M. H. Lee, Triarylboron-based TADF emitters with perfluoro substituents: High-efficiency OLEDs with a power efficiency over 100 lm W-1, *J Mater Chem C Mater*, 2020, **8**, 4253–4263.

227 A. Kumar, H. Y. Shin, T. Lee, J. Jung, B. J. Jung and M. H. Lee, Doubly Boron-Doped TADF Emitters Decorated with ortho-Donor Groups for Highly Efficient Green to Red OLEDs, *Chemistry - A European Journal*, 2020, **26**, 16793–16801.

228 H. Lee, D. Karthik, R. Lampande, J. H. Ryu and J. H. Kwon, Recent Advancement in Boron-Based Efficient and Pure Blue Thermally Activated Delayed Fluorescence Materials for Organic Light-Emitting Diodes, *Front Chem*, 2020, **8**, 373.

229 X. Liang, Z. L. Tu and Y. X. Zheng, Thermally Activated Delayed Fluorescence Materials: Towards Realization of High Efficiency through Strategic Small Molecular Design, *Chemistry - A European Journal*, 2019, **25**, 5623–5642.

230 Y. Kondo, K. Yoshiura, S. Kitera, H. Nishi, S. Oda, H. Gotoh, Y. Sasada, M. Yanai and T. Hatakeyama, Narrowband deep-blue organic light-emitting diode featuring an organoboron-based emitter, *Nat Photonics*, 2019, **13**, 678–682.

231 A. Escande and M. J. Ingleson, Fused polycyclic aromatics incorporating boron in the core: Fundamentals and applications, *Chemical Communications*, 2015, **51**, 6257–6274.

232 C. Dou, S. Saito and S. Yamaguchi, A pentacoordinate boron-containing π-electron system with Cl-B-Cl three-center four-electron bonds, *J Am Chem Soc*, 2013, **135**, 9346–9349.
233 C. Dou, S. Saito, K. Matsuo, I. Hisaki and S. Yamaguchi, A Boron-Containing PAH as a Substructure of Boron-Doped Graphene, *Angewandte Chemie International Edition*, 2012, **51**, 12206–12210.
234 Z. Zhou, A. Wakamiya, T. Kushida and S. Yamaguchi, Planarized triarylboranes: Stabilization by structural constraint and their plane-to-bowl conversion, *J Am Chem Soc*, 2012, **134**, 4529–4532.
235 D. H. Ahn, S. W. Kim, H. Lee, I. J. Ko, D. Karthik, J. Y. Lee and J. H. Kwon, Highly efficient blue thermally activated delayed fluorescence emitters based on symmetrical and rigid oxygen-bridged boron acceptors, *Nat Photonics*, 2019, **13**, 540–546.
236 B. Wex and B. R. Kaafarani, Perspective on carbazole-based organic compounds as emitters and hosts in TADF applications, *J Mater Chem C Mater*, 2017, **5**, 8622–8653.
237 H. Liu, J. Li, G. Li, B. Zhang, Q. Zhan, Z. Liu, C. Zhou, K. Li, Z. Wang and C. Yang, A simple strategy to achieve efficient thermally activated delayed fluorescent emitters via enhancing electron donating ability of donors, *Dyes and Pigments*, 2020, **180**, 108521–108527.
238 T. L. Wu, M. J. Huang, C. C. Lin, P. Y. Huang, T. Y. Chou, R. W. Chen-Cheng, H. W. Lin, R. S. Liu and C. H. Cheng, Diboron compound-based organic light-emitting diodes with high efficiency and reduced efficiency roll-off, *Nat Photonics*, 2018, **12**, 235–240.
239 M. H. Tsai, H. W. Lin, H. C. Su, T. H. Ke, C. C. Wu, F. C. Fang, Y. L. Liao, K. T. Wong and C. I. Wu, Highly efficient organic blue electrophosphorescent devices based on 3,6-Bis(triphenylsilyl)carbazole as the host material, *Advanced Materials*, 2006, **18**, 1216–1220.
240 X. Sallenave, A. Bucinskas, S. Salman, D. Volyniuk, O. Bezvikonnyi, V. Mimaite, J. V. Grazulevicius and G. Sini, Sensitivity of Redox and Optical Properties of Electroactive Carbazole Derivatives to the Molecular Architecture and Methoxy Substitutions, *The Journal of Physical Chemistry C*, 2018, **122**, 10138–10152.
241 M. Okazaki, Y. Takeda, P. Data, P. Pander, H. Higginbotham, A. P. Monkman and S. Minakata, Thermally activated delayed fluorescent phenothiazine-dibenzo[a,j]phenazine-phenothiazine triads exhibiting tricolor-changing mechanochromic luminescence, *Chem Sci*, 2017, **8**, 2677–2686.
242 P. Data, M. Okazaki, S. Minakata and Y. Takeda, Thermally activated delayed fluorescence: Vs. room temperature phosphorescence by conformation control of organic single molecules, *J Mater Chem C Mater*, 2019, **7**, 6616–6621.
243 G. Conboy, H. J. Spencer, E. Angioni, A. L. Kanibolotsky, N. J. Findlay, S. J. Coles, C. Wilson, M. B. Pitak, C. Risko, V. Coropceanu, J. L. Brédas and P. J. Skabara, To bend or not to bend-are heteroatom interactions within conjugated molecules effective in dictating conformation and planarity?, *Mater Horiz*, 2016, **3**, 333–339.
244 T. Kharandiuk, E. J. Hussien, J. Cameron, R. Petrina, N. J. Findlay, R. Naumov, W. T. Klooster, S. J. Coles, Q. Ai, S. Goodlett, C. Risko and P. J. Skabara, Noncovalent Close Contacts in Fluorinated Thiophene-Phenylene-Thiophene Conjugated Units: Understanding the Nature and Dominance of O···H versus S···F and O···F Interactions with Respect to the Control of Polymer Conformation, *Chemistry of Materials*, 2019, **31**, 7070–7079.
245 X. K. Chen, B. W. Bakr, M. Auffray, Y. Tsuchiya, C. D. Sherrill, C. Adachi and J. L. Bredas, Intramolecular Noncovalent Interactions Facilitate Thermally Activated

Delayed Fluorescence (TADF), *Journal of Physical Chemistry Letters*, 2019, **10**, 3260–3268.

246 J. R. Cha, C. W. Lee, J. Y. Lee and M. S. Gong, Design of ortho-linkage carbazole-triazine structure for high-efficiency blue thermally activated delayed fluorescent emitters, *Dyes and Pigments*, 2016, **134**, 562–568.

247 C. Peng, S. Yang, H. Li, G. Xie, L. Cui, S. Zou, C. Poriel, Z. Jiang and L. Liao, Highly Efficient Thermally Activated Delayed Fluorescence via an Unconjugated Donor–Acceptor System Realizing EQE of Over 30%, *Advanced Materials*, 2020, **32**, 2003885.

248 Z. Yang, Z. Mao, C. Xu, X. Chen, J. Zhao, Z. Yang, Y. Zhang, W. Wu, S. Jiao, Y. Liu, M. P. Aldred and Z. Chi, A sterically hindered asymmetric D-A-D′ thermally activated delayed fluorescence emitter for highly efficient non-doped organic light-emitting diodes, *Chem Sci*, 2019, **10**, 8129–8134.

249 C. S. Oh, S. H. Han and J. Y. Lee, Molecular design of thermally activated delayed fluorescent emitters for blue-shifted emission by methoxy substitution, *J Mater Chem C Mater*, 2017, **5**, 9106–9114.

250 R. Ansari, W. Shao, S.-J. Yoon, J. Kim and J. Kieffer, Charge Transfer as the Key Parameter Affecting the Color Purity of Thermally Activated Delayed Fluorescence Emitters, *ACS Appl Mater Interfaces*, 2021, **13**, 28529–28537.

251 D.-Y. Chen, W. Liu, C.-J. Zheng, K. Wang, F. Li, S. Tao, X.-M. Ou and X.-H. Zhang, Isomeric Thermally Activated Delayed Fluorescence Emitters for Color Purity-Improved Emission in Organic Light-Emitting Devices, *ACS Appl Mater Interfaces*, 2016, **8**, 16791–16798.

252 P. Rajamalli, N. Senthilkumar, P.-Y. Huang, C.-C. Ren-Wu, H.-W. Lin and C.-H. Cheng, New Molecular Design Concurrently Providing Superior Pure Blue, Thermally Activated Delayed Fluorescence and Optical Out-Coupling Efficiencies, *J Am Chem Soc*, 2017, **139**, 10948–10951.

253 J. Luo, Z. Xie, Z. Xie, J. W. Y. Lam, L. Cheng, H. Chen, C. Qiu, H. S. Kwok, X. Zhan, Y. Liu, D. Zhu and B. Z. Tang, Aggregation-induced emission of 1-methyl-1,2,3,4,5-pentaphenylsilole, *Chemical Communications*, 2001, **18**, 1740–1741.

254 S. W. Thomas, G. D. Joly and T. M. Swager, Chemical Sensors Based on Amplifying Fluorescent Conjugated Polymers, *Chem Rev*, 2007, **107**, 1339–1386.

255 Z. Wang, Z. Wang, P. Lu and Y. Wang, Preparation and Photoluminescent Properties of Three 5-Amino Benzothiadiazoles (5-amBTDs), *Chem Asian J*, 2020, **15**, 3519–3526.

256 Y. Ren, J. W. Y. Lam, Y. Dong, B. Z. Tang and K. S. Wong, Enhanced emission efficiency and excited state lifetime due to restricted intramolecular motion in silole aggregates, *Journal of Physical Chemistry B*, 2005, **109**, 1135–1140.

257 Y. F. Shen, M. Li, W. L. Zhao, Y. F. Wang, H. Y. Lu and C. F. Chen, Quinoline-based TADF emitters exhibiting aggregation-induced emission for efficient non-doped organic light-emitting diodes, *Mater Chem Front*, 2021, **5**, 834–842.

258 Q. Wei, J. Zhang and Z. Ge, *Handbook of Aggregation-Induced Emission*, Wiley, 2022, vol. 3.

259 P. Ganesan, D.-G. Chen, W.-C. Chen, P. Gnanasekaran, J.-A. Lin, C.-Y. Huang, M.-C. Chen, C.-S. Lee, P.-T. Chou and Y. Chi, Methoxy substituents activated carbazole-based boron dimesityl TADF emitters, *J Mater Chem C*, 2020, **8**, 4780–4788.

260 Y. H. Lee, S. Park, J. Oh, S. Woo, A. Kumar, J. Kim, J. Jung, S. Yoo and M. H. Lee, High-Efficiency Sky Blue to Ultradeep Blue Thermally Activated Delayed Fluorescent Diodes Based on *Ortho* -Carbazole-Appended Triarylboron Emitters: Above 32% External Quantum Efficiency in Blue Devices, *Adv Opt Mater*, 2018, **6**, 1800385.

261 Q. Wei, P. Imbrasas, E. Caldera-Cruz, L. Cao, N. Fei, H. Thomas, R. Scholz, S. Lenk, B. Voit, S. Reineke and Z. Ge, Conjugation-induced thermally activated delayed fluorescence: Photophysics of a carbazole-benzophenone monomer-to-tetramer molecular series, *Journal of Physical Chemistry A*, 2021, **125**, 1345–1354.

262 T. Taniguchi, J. Wang, S. Irle and S. Yamaguchi, TICT fluorescence of N-borylated 2,5-diarylpyrroles: A gear like dual motion in the excited state, *Dalton Transactions*, 2013, **42**, 620–624.

263 P. Zimmermann Crocomo, T. Kaihara, S. Kawaguchi., P. Stachelek, S. Minakata, P. de Silva, P. Data and Y. Takeda, The Impact of C $_2$ Insertion into a Carbazole Donor on the Physicochemical Properties of Dibenzo[*a,j*]phenazine-Cored Donor–Acceptor–Donor Triads, *Chemistry – A European Journal*, 2021, **27**, 13390–13398.

264 D. Hamdane, C. Bou-Nader, D. Cornu, G. Hui-Bon-Hoa and M. Fontecave, Flavin-Protein Complexes: Aromatic Stacking Assisted by a Hydrogen Bond, *Biochemistry*, 2015, **54**, 4354–4364.

265 E. R. Johnson, S. Keinan, P. Mori-Sánchez, J. Contreras-García, A. J. Cohen and W. Yang, Revealing noncovalent interactions, *J Am Chem Soc*, 2010, **132**, 6498–6506.

266 T. Chen, M. Li and J. Liu, π-π Stacking Interaction: A Nondestructive and Facile Means in Material Engineering for Bioapplications, *Cryst Growth Des*, 2018, **18**, 2765–2783.

267 X. Zhang, G. P. Lu, Z. B. Xu and C. Cai, Facile Synthesis of Indolizines via 1,3-Dipolar Cycloadditions in [Omim]Br: The Promotion of the Reaction through Noncovalent Interactions, *ACS Sustain Chem Eng*, 2017, **5**, 9279–9285.

268 A. Zheng, J. Wang, N. Xu, R. Zhu, Y. Yuan, J. Zhang, J. Zhang, Z. Li and P. Wang, Control of π-π Stacking of Dithienopyrrole-Based, Hole-Transporting Materials via Lateral Substituents for High-Efficiency Perovskite Solar Cells, *ACS Photonics*, 2018, **5**, 4694–4701.

269 D. Tu, J. Li, F. Sun, H. Yan, J. Poater and M. Solà, Cage-···Cage-Interaction: Boron Cluster-Based Noncovalent Bond and Its Applications in Solid-State Materials, *JACS Au*, 2021, **1**, 2047–2057.

270 D. Tu, H. Yan, J. Poater and M. Solà, The nido-Cage···π Bond: A Non-covalent Interaction between Boron Clusters and Aromatic Rings and Its Applications, *Angewandte Chemie - International Edition*, 2020, **59**, 9018–9025.

271 R. Báez-Grez and R. Pino-Rios, On the Importance of Noncovalent Interactions in the Stabilization of Nonconventional Compounds Using Bulky Groups, *ACS Omega*, 2023, **8**, 23168–23173.

272 H. Huang, L. Yang, A. Facchetti and T. J. Marks, Organic and Polymeric Semiconductors Enhanced by Noncovalent Conformational Locks, *Chem Rev*, 2017, **117**, 10291–10318.

273 Yale Chemistry, Yale University Department of Chemistry Organic Chemistry Study Aids, https://ursula.chem.yale.edu/~chem220/chem220js/STUDYAIDS/vanderwaalsradius.html, (accessed 20 July 2024).

274 G. Mierzwa, A. J. Gordon and S. Berski, The nature of multiple boron-nitrogen bonds studied using electron localization function (ELF), electron density (AIM), and natural bond orbital (NBO) methods, *J Mol Model*, 2020, **26**, 136–159.

275 S. Berski, Z. Latajka and A. J. Gordon, On the multiple B-N bonding in boron compounds using the topological analysis of electron localization function (ELF), *New Journal of Chemistry*, 2011, **35**, 89–96.

276 C. Arivazhagan, A. Maity, K. Bakthavachalam, A. Jana, S. K. Panigrahi, E. Suresh, A. Das and S. Ghosh, Phenothiazinyl Boranes: A New Class of AIE Luminogens with Mega Stokes Shift, Mechanochromism, and Mechanoluminescence, *Chemistry - A European Journal*, 2017, **23**, 7046–7051.

277 H. Yersin, *Highly Efficient OLEDs*, Wiley, Weinheim, Germany, 2018.
278 J. Sworakowski, How accurate are energies of HOMO and LUMO levels in small-molecule organic semiconductors determined from cyclic voltammetry or optical spectrosco, *Synth Met*, 2018, **235**, 125–130.
279 R. Stenutz, Stetnutz Chemistry Tables, http://www.stenutz.eu/chem/solv23.php, (accessed 18 July 2024).
280 F. Würthner, Aggregation-Induced Emission (AIE): A Historical Perspective, *Wiley-VCH Verlag*, 2020, preprint, DOI: 10.1002/anie.202007525.
281 E. E. Jelley, Spectral Absorption and Fluorescence of Dyes in the Molecular State, *Nature*, 1936, **138**, 1009–1010.
282 J. Shu, T. Ni, X. Liu, B. Xu, L. Liu, W. Chu, K. Zhang and W. Jiang, Mechanochromism, thermochromism, protonation effect and discrimination of CHCl3 from organic solvents in a Et2N-substituted Salicylaldehyde Schiff base, *Dyes and Pigments*, 2021, **195**, 109708.
283 J. Mei, Y. Hong, J. W. Y. Lam, A. Qin, Y. Tang and B. Z. Tang, Aggregation-Induced Emission: The Whole Is More Brilliant than the Parts, *Advanced Materials*, 2014, **26**, 5429–5479.
284 J. Mei, N. L. C. Leung, R. T. K. Kwok, J. W. Y. Lam and B. Z. Tang, Aggregation-Induced Emission: Together We Shine, United We Soar!, *Chem Rev*, 2015, **115**, 11718–11940.
285 K. K. Neena, P. Sudhakar, K. Dipak and P. Thilagar, Diarylboryl-phenothiazine based multifunctional molecular siblings, *Chemical Communications*, 2017, **53**, 3641–3644.
286 Y.-J. Lien, T.-C. Lin, C.-C. Yang, Y.-C. Chiang, C.-H. Chang, S.-H. Liu, Y.-T. Chen, G.-H. Lee, P.-T. Chou, C.-W. Lu and Y. Chi, First N-Borylated Emitters Displaying Highly Efficient Thermally Activated Delayed Fluorescence and High-Performance OLEDs, *ACS Appl Mater Interfaces*, 2017, **9**, 27090–27101.
287 C. C. Tsai, W. C. Huang, H. Y. Chih, Y. C. Hsh, C. W. Liao, C. H. Lin, Y. X. Kang, C. H. Chang, Y. J. Chang and C. W. Lu, Efficient donor-acceptor-donor borylated compounds with extremely small ΔEST for thermally activated delayed fluorescence OLEDs, *Org Electron*, 2018, **63**, 166–174.
288 Y. Kitamoto, T. Namikawa, D. Ikemizu, Y. Miyata, T. Suzuki, H. Kita, T. Sato and S. Oi, Light blue and green thermally activated delayed fluorescence from 10H-phenoxaborin-derivatives and their application to organic light-emitting diodes, *J Mater Chem C Mater*, 2015, **3**, 9122–9130.
289 Y. Kitamoto, T. Namikawa, T. Suzuki, Y. Miyata, H. Kita, T. Sato and S. Oi, Dimesitylarylborane-based luminescent emitters exhibiting highly-efficient thermally activated delayed fluorescence for organic light-emitting diodes, *Org Electron*, 2016, **34**, 208–217.
290 R. Stahl, C. Lambert, C. Kaiser, R. Wortmann and R. Jakober, Electrochemistry and photophysics of donor-substituted triarylboranes: Symmetry breaking in ground and excited state, *Chemistry - A European Journal*, 2006, **12**, 2358–2370.
291 H. Y. Zhao, X. Y. Yang, H. Lei, M. Xin and S. Q. Zhang, Cu-mediated selective bromination of aniline derivatives and preliminary mechanism study, *Synth Commun*, 2019, **49**, 1406–1415.
292 T. Fujihara, Y. Tomike, T. Ohtake, J. Terao and Y. Tsuji, Ruthenium-catalyzed ring-closing metathesis accelerated by long-range steric effect, *Chemical Communications*, 2011, **47**, 9699–9701.
293 Doug Discovery, Fluorochem - 1-bromo-3,5-dimethoxybenzene, https://dougdiscovery.com/p/F092710, (accessed 30 August 2024).
294 S. Solé and F. P. Gabbaï, A bidentate borane as colorimetric fluoride ion sensor, *Chemical Communications*, 2004, **4**, 1284–1285.

295 M. K. Etherington, Thermally Activated Delayed Fluorescence: Beyond the Single Molecule, *Front Chem*, 2020, **8**, 716.

296 S. Madayanad Suresh, L. Zhang, D. Hall, C. Si, G. Ricci, T. Matulaitis, A. M. Z. Slawin, S. Warriner, Y. Olivier, I. D. W. Samuel and E. Zysman-Colman, A Deep-Blue-Emitting Heteroatom-Doped MR-TADF Nonacene for High-Performance Organic Light-Emitting Diodes**, *Angewandte Chemie International Edition*, 2023, **62**, e202215522.

297 B. Chen, C. Liao, D. Li, H. Liu and S. Wang, Ultra-deep-blue thermally actrivated delayed fluorescence emitters constructed by carbazole derivatives enable efficient solution-processed OLED with a CIEy of < 0.05, *J Mater Chem C Mater*, 2023, **11**, 8767–8775.

298 D. K. A. Phan Huu, S. Saseendran, R. Dhali, L. G. Franca, K. Stavrou, A. Monkman and A. Painelli, Thermally Activated Delayed Fluorescence: Polarity, Rigidity, and Disorder in Condensed Phases, *J Am Chem Soc*, 2022, **144**, 15211–15222.

299 V. M. Divac, D. Šakić, T. Weitner and M. Gabričević, Solvent effects on the absorption and fluorescence spectra of Zaleplon: Determination of ground and excited state dipole moments, *Spectrochim Acta A Mol Biomol Spectrosc*, 2019, **212**, 356–362.

300 K. Stavrou, L. G. Franca and A. P. Monkman, Photophysics of TADF Guest-Host Systems: Introducing the Idea of Hosting Potential, *ACS Appl Electron Mater*, 2020, **2**, 2868–2881.

301 Y. Takeda, T. Kaihara, M. Okazaki, H. Higginbotham, P. Data, N. Tohnai and S. Minakata, Conformationally-flexible and moderately electron-donating units-installed D-A-D triad enabling multicolor-changing mechanochromic luminescence, TADF and room-temperature phosphorescence, *Chemical Communications*, 2018, **54**, 6847–6850.

302 I. Bhattacharjee, N. Acharya, H. Bhatia and D. Ray, Dual Emission through Thermally Activated Delayed Fluorescence and Room-Temperature Phosphorescence, and Their Thermal Enhancement via Solid-State Structural Change in a Carbazole-Quinoline Conjugate, *Journal of Physical Chemistry Letters*, 2018, **9**, 2733–2738.

303 M. S. Kwon, D. Lee, S. Seo, J. Jung and J. Kim, Tailoring Intermolecular Interactions for Efficient Room-Temperature Phosphorescence from Purely Organic Materials in Amorphous Polymer Matrices, *Angewandte Chemie International Edition*, 2014, **53**, 11177–11181.

304 H. Bhatia and D. Ray, Asymmetric-donor (D2D2′)-acceptor (A) conjugates for simultaneously accessing intrinsic blue-RTP and blue-TADF, *Mater Adv*, 2020, **1**, 1858–1865.

305 C. Avila-Montiel, A. R. Tapia-Benavides, E. Islas-Trejo, A. Ariza, H. Tlahuext and M. Tlahuextl, Non-covalent interactions in organic-inorganic hybrid compounds derived from amino amides, *J Mol Struct*, 2020, **1202**, 127258.

306 C. Janiak, A critical account on n-n stacking in metal complexes with aromatic nitrogen-containing ligands, *Journal of the Chemical Society, Dalton Transactions*, 2000, 3885–3896.

307 Z. Yang, Z. Mao, C. Xu, X. Chen, J. Zhao, Z. Yang, Y. Zhang, W. Wu, S. Jiao, Y. Liu, M. P. Aldred and Z. Chi, A sterically hindered asymmetric D–A–D′ thermally activated delayed fluorescence emitter for highly efficient non-doped organic light-emitting diodes, *Chem Sci*, 2019, **10**, 8129–8134.

308 H. Narita, H. Min, N. Kubo, I. Hattori, T. Yasuda and S. Yamaguchi, Bis- *Ortho* -Donor-Modification of Boracyclic π-Electron Systems beyond Steric Protection to Produce Thermally Activated Delayed Fluorescence Materials, *Angewandte Chemie International Edition*, 2024, **63**, e202405412.

309 T. Nishiuchi, K. Kisaka and T. Kubo, Synthesis of Anthracene-Based Cyclic π-Clusters and Elucidation of their Properties Originating from Congested Aromatic Planes, *Angewandte Chemie - International Edition*, 2021, **60**, 5400–5406.
310 T. Nishiuchi, S. Y. Uno, Y. Hirao and T. Kubo, Intramolecular Interaction, Photoisomerization, and Mechanical C-C Bond Dissociation of 1,2-Di(9-anthryl)benzene and Its Photoisomer: A Fundamental Moiety of Anthracene-Based π-Cluster Molecules, *Journal of Organic Chemistry*, 2016, **81**, 2106–2112.
311 T. Nishiuchi, H. Sotome, K. Shimizu, H. Miyasaka and T. Kubo, 1,2,3-Tri(9-anthryl)benzene: Photophysical Properties and Solid-State Intermolecular Interactions of Radially Arranged, Congested Aromatic π-Planes**, *Chemistry – A European Journal*, 2022, **28**, e202104245.
312 H. Tsujimoto, D. G. Ha, G. Markopoulos, H. S. Chae, M. A. Baldo and T. M. Swager, Thermally Activated Delayed Fluorescence and Aggregation Induced Emission with Through-Space Charge Transfer, *J Am Chem Soc*, 2017, **139**, 4894–4900.
313 G. B. McGaughey, M. Gagné and A. K. Rappé, π-Stacking Interactions: Alive and Well in Proteins, *Journal of Biological Chemistry*, 1998, **273**, 15458–15463.
314 C. M. Hsieh, T. L. Wu, J. Jayakumar, Y. C. Wang, C. L. Ko, W. Y. Hung, T. C. Lin, H. H. Wu, K. H. Lin, C. H. Lin, S. Hsieh and C. H. Cheng, Diboron-Based Delayed Fluorescent Emitters with Orange-to-Red Emission and Superior Organic Light-Emitting Diode Efficiency, *ACS Appl Mater Interfaces*, 2020, **12**, 23199–23206.
315 Y. Tao, C. Yang and J. Qin, Organic host materials for phosphorescent organic light-emitting diodes, *Chem Soc Rev*, 2011, **40**, 2943–2970.
316 C. Reus, S. Weidlich, M. Bolte, H. W. Lerner and M. Wagner, C-functionalized, air- and water-stable 9,10-dihydro-9,10- diboraanthracenes: Efficient blue to red emitting luminophores, *J Am Chem Soc*, 2013, **135**, 12892–12907.
317 T. Matsumoto, H. Takamine, K. Tanaka and Y. Chujo, Design of bond-cleavage-induced intramolecular charge transfer emission with dibenzoboroles and their application to ratiometric sensors for discriminating chain lengths of alkanes, *Mater Chem Front*, 2017, **1**, 2368–2375.
318 Y. G. Shi, J. W. Wang, H. Li, G. F. Hu, X. Li, S. K. Mellerup, N. Wang, T. Peng and S. Wang, A simple multi-responsive system based on aldehyde functionalized amino-boranes, *Chem Sci*, 2018, **9**, 1902–1911.
319 Q. Hou, L. Liu, S. K. Mellerup, N. Wang, T. Peng, P. Chen and S. Wang, Stimuli-Responsive B/N Lewis Pairs Based on the Modulation of B-N Bond Strength, *Org Lett*, 2018, **20**, 6467–6470.
320 S. K. Mellerup and S. Wang, Boron-based stimuli responsive materials, *Chem Soc Rev*, 2019, **48**, 3537–3549.
321 Y. Wang, K. Liu, P. Chen, X. Yin, T. Peng, J. Iqbal and N. Wang, A multi-responsive system based on intramolecular B ← O=P Lewis acid–base pairs, *J Mater Chem C Mater*, 2022, **10**, 10981–10987.
322 J. Wang, N. Wang, G. Wu, S. Wang and X. Li, Multicolor Emission from Non-conjugated Polymers Based on a Single Switchable Boron Chromophore, *Angewandte Chemie*, 2019, **131**, 3114–3118.
323 S. J. Cassidy, I. Brettell-Adams, L. E. McNamara, M. F. Smith, M. Bautista, H. Cao, M. Vasiliu, D. L. Gerlach, F. Qu, N. I. Hammer, D. A. Dixon and P. A. Rupar, Boranes with Ultra-High Stokes Shift Fluorescence, *Organometallics*, 2018, **37**, 3732–3741.
324 E. Januszewski, A. Lorbach, R. Grewal, M. Bolte, J. W. Bats, H. Lerner and M. Wagner, Unsymmetrically Substituted 9,10-Dihydro-9,10-diboraanthracenes as Versatile Building Blocks for Boron-Doped π-Conjugated Systems, *Chemistry – A European Journal*, 2011, **17**, 12696–12705.

325 S. Bieller, F. Zhang, M. Bolte, J. W. Bats, H. W. Lerner and M. Wagner, Bitopic bis- and tris(1-pyrazolyl)borate ligands: Syntheses and structural characterization, *Organometallics*, 2004, **23**, 2107–2113.
326 S. Kirschner, J. M. Mewes, M. Bolte, H. W. Lerner, A. Dreuw and M. Wagner, How Boron Doping Shapes the Optoelectronic Properties of Canonical and Phenylene-Containing Oligoacenes: A Combined Experimental and Theoretical Investigation, *Chemistry - A European Journal*, 2017, **23**, 5104–5116.
327 Fluorochem, Dougdiscovery page for 1,2-Bis(trimethylsilyl)benzene, https://dougdiscovery.com/p/F733402, (accessed 16 January 2024).
328 Fluorochem, Dougdiscovery page for 1,2-Bis(dimethylsilyl)benzene, https://dougdiscovery.com/p/S01774, (accessed 16 January 2024).
329 G. Méhes, K. Goushi, W. J. Potscavage and C. Adachi, Influence of host matrix on thermally-activated delayed fluorescence: Effects on emission lifetime, photoluminescence quantum yield, and device performance, *Org Electron*, 2014, **15**, 2027–2037.
330 M. Kawashiro, T. Mori, M. Ito, N. Ando and S. Yamaguchi, Photodissociative Modules that Control Dual-Emission Properties in Donor–π–Acceptor Organoborane Fluorophores, *Angewandte Chemie International Edition*, 2023, **62**, e202303725.
331 C. J. Berger, G. He, C. Merten, R. McDonald, M. J. Ferguson and E. Rivard, Synthesis and luminescent properties of lewis base-appended borafluorenes, *Inorg Chem*, 2014, **53**, 1475–1486.
332 A. Wakamiya, K. Mishima, K. Ekawa and S. Yamaguchi, Kinetically stabilized dibenzoborole as an electron-accepting building unit, *Chemical Communications*, 2002, **8**, 579–581.
333 E. Von Grotthuss, S. E. Prey, M. Bolte, H. W. Lerner and M. Wagner, Dual Role of Doubly Reduced Arylboranes as Dihydrogen- and Hydride-Transfer Catalysts, *J Am Chem Soc*, 2019, **141**, 6082–6091.
334 S. Y. Lee, T. Yasuda, Y. S. Yang, Q. Zhang and C. Adachi, Luminous butterflies: Efficient exciton harvesting by benzophenone derivatives for full-color delayed fluorescence OLEDs, *Angewandte Chemie - International Edition*, 2014, **53**, 6402–6406.
335 E. E. Bas, P. Ulukan, A. Monari, V. Aviyente and S. Catak, Photophysical Properties of Benzophenone-Based TADF Emitters in Relation to Their Molecular Structure, *Journal of Physical Chemistry A*, 2022, **126**, 473–484.
336 J. Li, X. Liao, H. Xu, L. Li, J. Zhang, H. Wang and B. Xu, Deep-blue thermally activated delayed fluorescence dendrimers with reduced singlet-triplet energy gap for low roll-off non-doped solution-processed organic light-emitting diodes, *Dyes and Pigments*, 2017, **140**, 79–86.
337 Y. Luo, S. Li, Y. Zhao, C. Li, Z. Pang, Y. Huang, M. Yang, L. Zhou, X. Zheng, X. Pu and Z. Lu, An Ultraviolet Thermally Activated Delayed Fluorescence OLED with Total External Quantum Efficiency over 9%, *Advanced Materials*, 2020, **32**, 2001248.
338 M. Y. Wong, S. Krotkus, G. Copley, W. Li, C. Murawski, D. Hall, G. J. Hedley, M. Jaricot, D. B. Cordes, A. M. Z. Slawin, Y. Olivier, D. Beljonne, L. Muccioli, M. Moral, J.-C. Sancho-Garcia, M. C. Gather, I. D. W. Samuel and E. Zysman-Colman, Deep-Blue Oxadiazole-Containing Thermally Activated Delayed Fluorescence Emitters for Organic Light-Emitting Diodes, *ACS Appl Mater Interfaces*, 2018, **10**, 33360–33372.
339 F. Hundemer, L. Graf von Reventlow, C. Leonhardt, M. Polamo, M. Nieger, S. M. Seifermann, A. Colsmann and S. Bräse, Acceptor Derivatization of the 4CzIPN

TADF System: Color Tuning and Introduction of Functional Groups, *ChemistryOpen*, 2019, **8**, 1413–1420.

340 K. Chen, Y. Zhang, Y. Lei, W. Dai, M. Liu, Z. Cai, H. Wu, X. Huang and X. Ma, Twofold rigidity activates ultralong organic high-temperature phosphorescence, *Nat Commun*, 2024, **15**, 1269–1280.

341 T. Gridneva, A. Karimata, R. Bansal, R. R. Fayzullin, S. Vasylevskyi, A. Bruhacs and J. R. Khusnutdinova, Deep-red photoluminescent mechanoresponsive polymers with dynamic CuI-arylamide mechanophores, *Chemical Communications*, 2023, **60**, 212–215.

342 K. Albrecht, K. Matsuoka, D. Yokoyama, Y. Sakai, A. Nakayama, K. Fujita and K. Yamamoto, Thermally activated delayed fluorescence OLEDs with fully solution processed organic layers exhibiting nearly 10% external quantum efficiency, *Chemical Communications*, 2017, **53**, 2439–2442.

343 V. V. Patil, K. H. Lee and J. Y. Lee, Dibenzo[*c* , *g*]indolo[3,2,1- *jk*]carbazole as a new chromophore for blue organic light-emitting diodes, *J Mater Chem C Mater*, 2019, **7**, 14301–14305.

344 K. Matsuda, R. Xiaotian, K. Nakamura, M. Furukori, T. Hosokai, K. Anraku, K. Nakao and K. Albrecht, Photostability of luminescent tris(2,4,6-trichlorophenyl)methyl radical enhanced by terminal modification of carbazole donor, *Chemical Communications*, 2022, **58**, 13443–13446.

345 J. H. Day, Thermochromism., *Chem Rev*, 1963, **63**, 65–80.

346 A. A. Dar and A. A. Ganie, Irreversible Thermochromism in Organic Salts of Sulfonated Anils, *Cryst Growth Des*, 2020, **20**, 3888–3897.

347 M. Wan, H. R. Chen, Y. N. Wang, K. Shi, J. Y. Liu, Z. M. Li, S. Y. Ye, J. Y. Li and L. Z. Chen, Reversible thermochromism to tune the bandgap of organic-inorganic hybrid materials, *Mater Chem Front*, 2022, **6**, 3094–3101.

348 B. Xu, Z. Song, M. Zhang, Q. Zhang, L. Jiang, C. Xu, L. Zhong, C. Su, Q. Ban, C. Liu, F. Sun, Y. Zhang, Z. Chi, Z. Zhao and G. Shi, Controlling the thermally activated delayed fluorescence of axially chiral organic emitters and their racemate for information encryption, *Chem Sci*, 2021, **12**, 15556–15562.

349 B. Yu, D. Liu, Y. Wang, T. Zhang, Y. M. Zhang, M. Li and S. X. A. Zhang, A solid-state emissive and solvatofluorochromic fluorophore and its application in high-contrast, fast, and repeatable thermochromic blends, *Dyes and Pigments*, 2019, **163**, 412–419.

350 A. Alconchel, O. Crespo, P. García-Orduña and M. C. Gimeno, *Closo* - or *Nido* - Carborane Diphosphane as Responsible for Strong Thermochromism or Time Activated Delayed Fluorescence (TADF) in [Cu(N^N)(P^P)] $^{0/+}$, *Inorg Chem*, 2021, **60**, 18521–18528.

351 M. K. Etherington, N. A. Kukhta, H. F. Higginbotham, A. Danos, A. N. Bismillah, D. R. Graves, P. R. McGonigal, N. Haase, A. Morherr, A. S. Batsanov, C. Pflumm, V. Bhalla, M. R. Bryce and A. P. Monkman, Persistent Dimer Emission in Thermally Activated Delayed Fluorescence Materials, *The Journal of Physical Chemistry C*, 2019, **123**, 11109–11117.

352 N. Willis-Fox, E. Watchorn-Rokutan, E. Rognin and R. Daly, Technology pull: scale-up of polymeric mechanochemical force sensors, *Trends Chem*, 2023, **5**, 415–431.

353 F. Khan, A. Ekbote and R. Misra, Reversible mechanochromism and aggregation induced enhanced emission in phenothiazine substituted tetraphenylethylene, *New Journal of Chemistry*, 2019, **43**, 16156–16163.

354 V. Thanikachalam, U. Karunakaran, J. Jayabharathi and S. Thilagavathy, Multifunctional pyrenoimidazole substituted tetraphenylethylene derivatives:

Mechanochromism and aggregation-induced emission, *J Photochem Photobiol A Chem*, 2021, **420**, 113489.
355 M. Sarma and K. T. Wong, Exciplex: An Intermolecular Charge-Transfer Approach for TADF, *ACS Appl Mater Interfaces*, 2018, **10**, 19279–19304.
356 R. Ishimatsu, T. Edura, C. Adachi, K. Nakano and T. Imato, Photophysical Properties and Efficient, Stable, Electrogenerated Chemiluminescence of Donor-Acceptor Molecules Exhibiting Thermal Spin Upconversion, *Chemistry - A European Journal*, 2016, **22**, 4889–4898.
357 P. Rajamalli, D. Chen, W. Li, I. D. W. Samuel, D. B. Cordes, A. M. Z. Slawin and E. Zysman-Colman, Enhanced thermally activated delayed fluorescence through bridge modification in sulfone-based emitters employed in deep blue organic light-emitting diodes, *J Mater Chem C Mater*, 2019, **7**, 6664–6671.
358 S. Wu, M. Aonuma, Q. Zhang, S. Huang, T. Nakagawa, K. Kuwabara and C. Adachi, High-efficiency deep-blue organic light-emitting diodes based on a thermally activated delayed fluorescence emitter, *J Mater Chem C Mater*, 2014, **2**, 421–424.
359 Q. Zhang, J. Li, K. Shizu, S. Huang, S. Hirata, H. Miyazaki and C. Adachi, Design of efficient thermally activated delayed fluorescence materials for pure blue organic light emitting diodes, *J Am Chem Soc*, 2012, **134**, 14706–14709.
360 T. Cardeynaels, M. K. Etherington, S. Paredis, A. S. Batsanov, J. Deckers, K. Stavrou, D. Vanderzande, A. P. Monkman, B. Champagne and W. Maes, Dominant dimer emission provides colour stability for red thermally activated delayed fluorescence emitter, *J Mater Chem C Mater*, 2022, **10**, 5840–5848.
361 X. Yang, F.-I. Wu, H. Haverinen, J. Li, C.-H. Cheng and G. E. Jabbour, Efficient organic light-emitting devices with platinum-complex emissive layer, *Appl Phys Lett*, 2011, **98**, 033302.
362 Y. Kawamura, K. Goushi, J. Brooks, J. J. Brown, H. Sasabe and C. Adachi, 100% phosphorescence quantum efficiency of Ir(III) complexes in organic semiconductor films, *Appl Phys Lett*, 2005, **86**, 071104.
363 C. W. Lee and J. Y. Lee, Above 30% external quantum efficiency in blue phosphorescent organic light-emitting diodes using pyrido[2,3-b]indole derivatives as host materials, *Advanced Materials*, 2013, **25**, 5450–5454.
364 D. Zhang, M. Cai, Y. Zhang, D. Zhang and L. Duan, Highly Efficient Simplified Single-Emitting-Layer Hybrid WOLEDs with Low Roll-off and Good Color Stability through Enhanced Förster Energy Transfer, *ACS Appl Mater Interfaces*, 2015, **7**, 28693–28700.
365 Q. Zhang, T. Komino, S. Huang, S. Matsunami, K. Goushi and C. Adachi, Triplet exciton confinement in green organic light-emitting diodes containing luminescent charge-transfer Cu(I) complexes, *Adv Funct Mater*, 2012, **22**, 2327–2336.
366 S. Paredis, T. Cardeynaels, J. Deckers, A. Danos, D. Vanderzande, A. P. Monkman, B. Champagne and W. Maes, Bridge control of photophysical properties in benzothiazole-phenoxazine emitters - from thermally activated delayed fluorescence to room temperature phosphorescence, *J Mater Chem C Mater*, 2022, **10**, 4775–4784.
367 A. Klimash, P. Pander, W. T. Klooster, S. J. Coles, P. Data, F. B. Dias and P. J. Skabara, Intermolecular interactions in molecular crystals and their effect on thermally activated delayed fluorescence of helicene-based emitters, *J Mater Chem C Mater*, 2018, **6**, 10557–10568.
368 J. S. Ward, R. S. Nobuyasu, A. S. Batsanov, P. Data, A. P. Monkman, F. B. Dias and M. R. Bryce, The interplay of thermally activated delayed fluorescence (TADF) and room temperature organic phosphorescence in sterically-constrained donor-

acceptor charge-transfer molecules, *Chemical Communications*, 2016, **52**, 2612–2615.

369 M. J. G. Peach, P. Benfield, T. Helgaker and D. J. Tozer, Excitation energies in density functional theory: An evaluation and a diagnostic test, *J Chem Phys*, 2008, **128**, 044118.

370 S. Wang, Y. Zhang, W. Chen, J. Wei, Y. Liu and Y. Wang, Achieving high power efficiency and low roll-off OLEDs based on energy transfer from thermally activated delayed excitons to fluorescent dopants, *Chemical Communications*, 2015, **51**, 11972–11975.

371 A. Qin, L. Tang, J. W. Y. Lam, C. K. W. Jim, Y. Yu, H. Zhao, J. Z. Sun and B. Z. Tang, Metal-free click polymerization: Synthesis and photonic properties of poly(aroyltriazole)s, *Adv Funct Mater*, 2009, **19**, 1891–1900.

372 M. A. Potopnyk, J. Mech-Piskorz, G. Angulo, M. Ceborska, R. Luboradzki, E. Andresen, A. Gajek, A. Wisniewska and U. Resch-Genger, Aggregation/Crystallization-Induced Emission in Naphthyridine-Based Carbazolyl-Modified Donor-Acceptor Boron Dyes Tunable by Fluorine Atoms, *Chemistry – A European Journal*, 2024, **30**, e202400004.

373 G. A. Zalmi, D. N. Nadimetla, P. Kotharkar, A. L. Puyad, M. Kowshik and S. V. Bhosale, Aggregation-Induced Emission-Based Material for Selective and Sensitive Recognition of Cyanide Anions in Solution and Biological Assays, *ACS Omega*, 2021, **6**, 16704–16713.

374 F. Sánchez-Férez, X. Solans-Monfort, T. Calvet, M. Font-Bardia and J. Pons, Controlling the Formation of Two Concomitant Polymorphs in Hg(II) Coordination Polymers, *Inorg Chem*, 2022, **61**, 4965–4979.

375 P. Xue, Z. Yang and P. Chen, Hiding and revealing information using the mechanochromic system of a 2,5-dicarbazole-substituted terephthalate derivative, *J Mater Chem C Mater*, 2018, **6**, 4994–5000.

376 T. Zhang, Y. Han, K. Wang, M. Liang, W. Bian, Y. Zhang, X. Li, C. Zhang and P. Xue, Alkyl chain-dependent ESIPT luminescent switches of phenothazine derivatives in response to force, *Dyes and Pigments*, 2020, **172**, 107835.

377 Z. Liang, M. Wei, S. Zhang, W. Huang, N. Shi, A. Lv, H. Ma and Z. He, Activating Molecular Room-Temperature Phosphorescence by Manipulating Excited-State Energy Levels in Poly(vinyl alcohol) Matrix, *ACS Appl Mater Interfaces*, 2023, **15**, 35534–35542.

378 S. A. Majeed, B. Ghazal, D. E. Nevonen, P. C. Goff, D. A. Blank, V. N. Nemykin and S. Makhseed, Evaluation of the Intramolecular Charge-Transfer Properties in Solvatochromic and Electrochromic Zinc Octa(carbazolyl)phthalocyanines, *Inorg Chem*, 2017, **56**, 11640–11653.

379 Y. Zhang, D. Zhang, T. Tsuboi, Y. Qiu and L. Duan, Simultaneous enhancement of efficiency and stability of OLEDs with thermally activated delayed fluorescence materials by modifying carbazoles with peripheral groups, *Sci China Chem*, 2019, **62**, 393–402.

380 Y. Tsuchiya, N. Nakamura, S. Kakumachi, K. Kusuhara, C.-Y. Chan and C. Adachi, A convenient method to estimate the glass transition temperature of small organic semiconductor materials, *Chemical Communications*, 2022, **58**, 11292–11295.

381 S. Wu, H. Zhang, Z. Mao, Y. Liang, J.-A. Li, P. Hu, Q. Zhang, C. Liu, S. Luo, Y. Wang, G. Shi and B. Xu, Achieving Stable and Switchable Ultralong Room-Temperature Phosphorescence from Polymer-Based Luminescent Materials with Three-Dimensional Covalent Networks for Light-Manipulated Anticounterfeiting, *ACS Appl Mater Interfaces*, 2023, **15**, 39896–39904.

382 Z. Xie, C. Chen, S. Xu, J. Li, Y. Zhang, S. Liu, J. Xu and Z. Chi, White-Light Emission Strategy of a Single Organic Compound with Aggregation-Induced

Emission and Delayed Fluorescence Properties, *Angewandte Chemie*, 2015, **127**, 7287–7290.

383 H. Nakanotani, K. Masui, J. Nishide, T. Shibata and C. Adachi, Promising operational stability of high-efficiency organic light-emitting diodes based on thermally activated delayed fluorescence, *Sci Rep*, 2013, **3**, 2127–2132.

384 A. Shimizu, Y. Ishizaki, S. Horiuchi, T. Hirose, K. Matsuda, H. Sato and J. I. Yoshida, HOMO-LUMO Energy-Gap Tuning of π-Conjugated Zwitterions Composed of Electron-Donating Anion and Electron-Accepting Cation, *Journal of Organic Chemistry*, 2021, **86**, 770–781.

385 R. Englman and J. Jortner, The energy gap law for non-radiative decay in large molecules, *J Lumin*, 1970, **1–2**, 134–142.

386 J. Jortner, Radiationless transitions, *Pure and Applied Chemistry*, 1971, **27**, 389–420.

387 W. Siebrand, Radiationless transitions in polyatomic molecules. II. Triplet-ground-state transitions in aromatic hydrocarbons, *J Chem Phys*, 1967, **47**, 2411–2422.

388 M. D. Hanwell, D. E. Curtis, D. C. Lonie, T. Vandermeersch, E. Zurek and G. R. Hutchison, *SOFTWARE Open Access Avogadro: an advanced semantic chemical editor, visualization, and analysis platform*, 2012, vol. 4.

389 Persistence of Vision Pty. Ltd. (2004), Persistence of Vision Raytracer (Version 3.6), http://www.povray.org/download/, (accessed 21 September 2024).